Publication Year	2015
Acceptance in OA	2020-04-15T16:04:46Z
Title	Advancing Astrophysics with the Square Kilometre Array (AASKA14)
Authors	Bourke, Tyler. L., Braun, Robert, Fender, Rob, GOVONI, FEDERICA, Green, Jimi, Hoare, Melvin, Jarvis, Matt, Johnston-Hollitt, Melanie, Keane, Evan, Koopmans, Leon, Kramer, Michael, Maartens, Roy, Macquart, Jean-Pierre, Mellema, Garrelt, Oosterloo, Tom, PRANDONI, ISABELLA, Pritchard, Jonathan, Santos, Mario, Seymour, Nick, Stappers, Ben, Staveley-Smith, Lister, Wu Tian, Wen, UMANA, Grazia Maria Gloria, Wagg, Jeff
Handle	http://hdl.handle.net/20.500.12386/24059
Journal	POS PROCEEDINGS OF SCIENCE
Volume	215

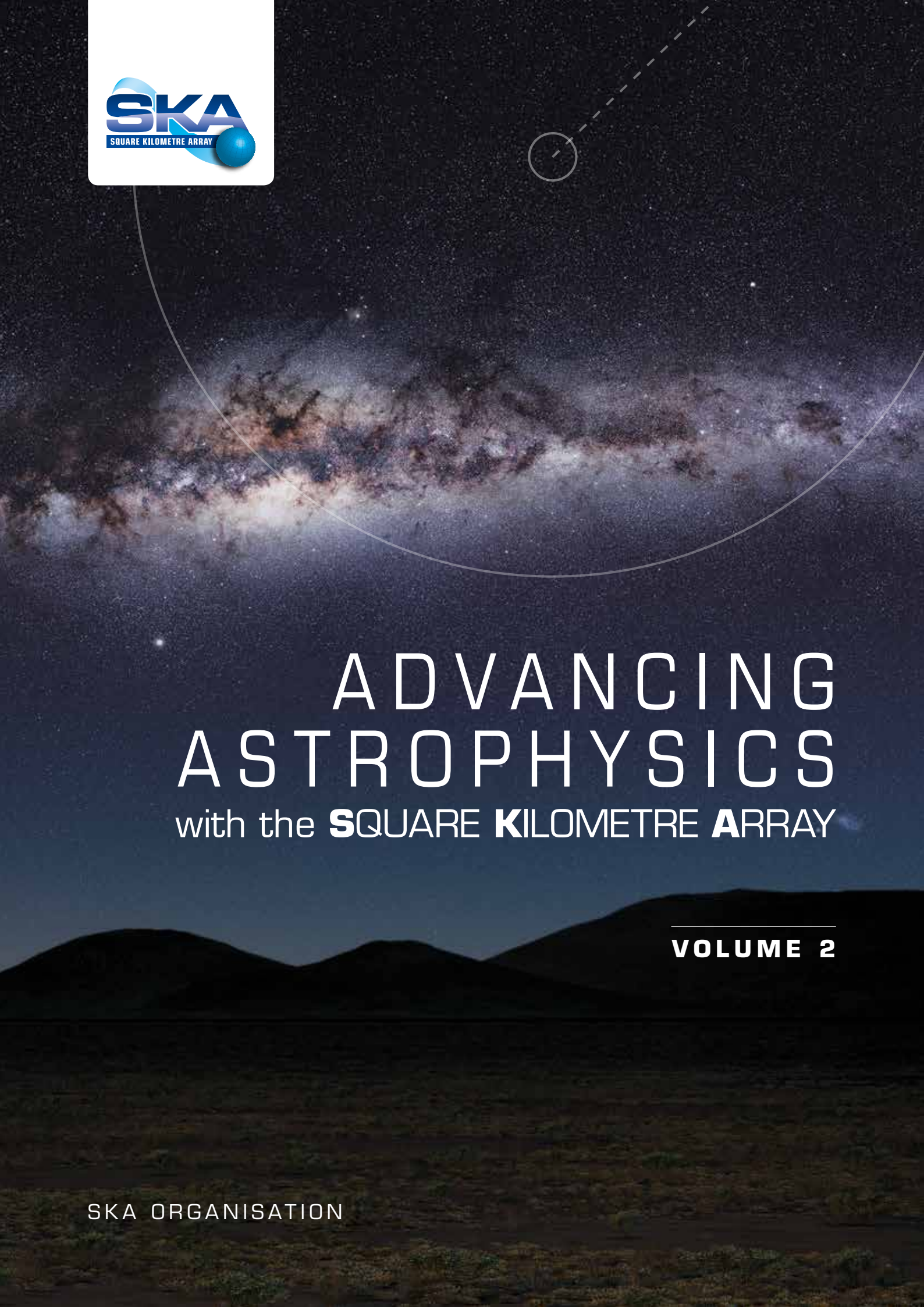

ADVANCING ASTROPHYSICS

with the SQUARE KILOMETRE ARRAY

VOLUME 2

SKA ORGANISATION

Advancing Astrophysics with the Square Kilometre Array

Volume 2

ISBN: 978-1-909204-71-3

Cover design: Carbon Creative | www.carboncreative.net
Cover: Artist impression of the SKA sites at night, Credit: SKA Organisation; The Milky Way panorama, Credit: ESO/S. Brunier

Design, layout and production by Bookcreateservice Ltd
for the SKA Organisation Communications, Outreach and Education Office.

First published in 2015 by Dolman Scott Ltd for SKA Organisation.

©Copyright of the papers owned by the author(s) under the terms of the Creative Commons Attribution-Non Commercial-Share Alike Licence.

Advancing Astrophysics with the Square Kilometre Array © 2015 by SKA Organisation.

All rights reserved. No part of this publication may be copied, stored in a retrieval system, or transmitted in any form, or by any means electronic, mechanical, optical, or otherwise except with written permission of the publisher. Except for review purposes only.

About the SKA

The Square Kilometre Array (SKA) project is an international collaboration to build the world's largest radio telescope. The SKA aims to conduct transformational science that will improve our understanding of the Universe and the laws of fundamental physics. It will monitor the sky in unprecedented detail and map it hundreds of times faster than any current facility.

The SKA is not a single telescope but a collection of telescopes called an array, working together over long distances – tens to hundreds of kilometres and eventually thousands of kilometres. The SKA's construction is divided into two phases: Phase 1 in Australia for SKA1-LOW and South Africa for SKA1-MID; and Phase 2 for SKA2 expanding further in Australia and South Africa as well as into other African countries. Scientific operations are scheduled to begin in the early 2020s.

Supported by 20 countries around the world, the SKA is being designed by more than 500 of the world's finest scientists and engineers drawn from more than 100 companies and research institutions.

Panorama of the Karoo near the SKA site in South Africa. Credit: Rob Millenaar (ASTRON)

Panorama of the Murchison from the SKA site in Australia. Credit: CSIRO

Preface

In 2014 it was 10 years since the publication of the comprehensive *Science with the Square Kilometre Array* book and 15 years since the first such volume appeared in 1999. In that time numerous and unexpected advances have been made in the fields of astronomy and physics relevant to the capabilities of the Square Kilometre Array (SKA). The SKA itself progressed from an idea to a developing reality with a Phase 1 design (SKA1) now well-advanced and scientific operations scheduled to begin in the early 2020s.

To facilitate the publication of a new, updated science book relevant to the current astrophysical context, the meeting *Advancing Astrophysics with the Square Kilometre Array* was held from 9 - 13 June, 2014, in Giardini Naxos, Sicily.

Articles were solicited from the scientific community for that meeting to document the scientific advances enabled by the first phase of the SKA and those pertaining to future SKA deployments. The chapters reproduced in these volumes are the direct result of that meeting.

The papers are published online in the Proceedings of Science (PoS) at:

http://pos.sissa.it/

This book is available in electronic format on the SKA website at

www.skatelescope.org/books/

The conference was considered by all participants to have been a major success and the organisers would like to thank the following event sponsors for their generous support of the event:

The research leading to these results has received funding from the European Commission Seventh Framework Programme (FP/2007-2013) under grant agreement No 283393 (RadioNet3).

The editorial board

Tyler L. Bourke, Robert Braun, Rob Fender, Federica Govoni, Jimi Green, Melvin Hoare, Matt Jarvis, Melanie Johnston-Hollitt, Evan Keane, Leon Koopmans, Michael Kramer, Roy Maartens, Jean-Pierre Macquart, Garrelt Mellema, Tom Oosterloo, Isabella Prandoni, Jonathan Pritchard, Mario Santos, Nick Seymour, Ben Stappers, Lister Staveley-Smith, Wen Wu Tian, Grazia Umana, Jeff Wagg.

27 July 2015

Contents
Volume 1

Introduction

Advancing Astrophysics with the Square Kilometre Array
R. Braun , T.L Bourke, J.A Green, E. Keane and J. Wagg 3

The Cradle of Life

SKA and the Cradle of Life
M. Hoare, L Perez, T.L Bourke, L Testi, I Jimenez-Serra, P Zarka, A.P.V. Siemion, H.J. van-Langevelde, L Loinard, G Anglada, A Belloche, P Bergman, R. Booth, P Caselli, C.J Chandler, C Codella, G Hallinan, J Lazio, I.S Morrison, L Podio, A Remijan and J Tarter 15

Searching for Extraterrestrial Intelligence with the Square Kilometre Array
A. Siemion, J. Benford, J. Cheng-Jin, J. Chennamangalam, J.M. Cordes, H.D.E. Falcke, S.T. Garrington, M.A. Garrett, L. Gurvits, M. Hoare, E. Korpela, J. Lazio, D. Messerschmitt, I. Morrison, T. O'Brien, Z. Paragi, A. Penny, L. Spitler, J. Tarter and D. Werthimer 27

Protoplanetary disks and the dawn of planets with SKA
L. Testi, L Perez, I Jimenez-Serra, M.G Hoare, A Boley, T.L Bourke, J.R Brucato, P Caselli, C.J Chandler, A Isella, J Lazio, M.E Palumbo, L Podio, A Remijan, J Tarter and D.J Wilner 43

The impact of SKA on Galactic Radioastronomy: continuum observations
G. Umana, C. Trigilio, L. Cerrigone, R. Cesaroni, A.A Zijlstra, M. Hoare, K. Weis, A. Beasley, D. Bomans, G. Hallinan, S. Molinari, R. Taylor, L. Testi and M. Thompson 55

Maser Astrometry with VLBI and the SKA
J. Green, H.J. Van Langevelde, A. Brunthaler, S. Ellingsen, H. Imai, W.H.T. Vlemmings, M.J. Reid and A.M.S. Richards 73

Magnetospheric Radio Emissions from Exoplanets with the SKA
P. Zarka, J. Lazio and G. Hallinan 83

Radio Jets in Young Stellar Objects with the SKA
G. Anglada, L.F. Rodríguez and C. Carrasco-Gonzalez 101

Complex organic molecules in protostellar environments in the SKA era
C. Codella, L Podio, F Fontani, I Jimenez-Serra, P Caselli, M.E Palumbo, A Lopez-Sepulcre, M.T Beltran, B Lefloch, J.R Brucato, S Viti and L Testi 109

Studies of Anomalous Microwave Emission (AME) with the SKA
C. Dickinson, Y. Ali-Hamoud, R.J. Beswick, S. Casassus, K. Cleary, B. Draine, R. Genova-Santos, K. Grainge, T.C Hoang, A. Lazarian, E. Murphy, R. Paladini, M.W Peel, Y. Perrott, J.A. Rubino-Martin, A. Scaife, C. Tibbs, L. Verstraete, M. Vidal, R.A. Watson and N. Ysard 127

OH masers in the Milky Way and Local Group galaxies in the SKA era
S. Etoka, D. Engels, H. Imai, J. Dawson, S. Ellingsen, L. Sjouwerman and H. van Langevelde 139

The ionised,radical and molecular Milky Way: spectroscopic surveys with the SKA
M. Thompson, H. Beuther, C. Dickinson, J. Mottram, P. Klaassen, A. Ginsburg,S. Longmore, A. Remijan and K.M. Menten 153

SKA tomography of Galactic star-forming regions and spiral arms
L. Loinard, M. Thompson, M. Hoare, H.J. van Langevelde, S. Ellingsen, A. Brunthaler, J. Forbrich, K. Rygl, L.F Rodriguez, A.J Mioduszewski, R.M Torres-Lopez, S.A Dzib, G.N Ortiz-Leon, T.L Bourke and J.A Green 163

Fundamental Physics with Pulsars

Pulsar Science with the SKA
M. Kramer and B. Stappers 173

Gravitational Wave Astronomy with the SKA
G. Janssen, G. Hobbs, M. McLaughlin, C. Bassa, A. Deller, M. Kramer, K. Lee, C. Mingarelli, P. Rosado, S. Sanidas, A. Sesana, L. Shao, I. Stairs, B. Stappers and J. Verbiest 185

Understanding pulsar magnetospheres with the SKA
A. Karastergiou, S. Johnston, A Karastergiou, S Johnston, N Andersson, R Breton, P Brook, C Gwinn, N Lewandowska, E Keane, M Kramer, J.P Macquart, M Serylak, R Shannon, B Stappers, J van Leeuwen, J Verbiest, P Weltevrede and G Wright 205

Understanding the Neutron Star Population with the SKA
T.M Tauris, V.M Kaspi, R.P Breton, A.T Deller, E.F Keane, M Kramer, D.R Lorimer, M.A McLaughlin, A Possenti, P.S Ray, B.W Stappers and P Weltevrede 225

A Cosmic Census of Radio Pulsars with the SKA
E.F Keane, B Bhattacharyya, M Kramer, B.W Stappers, S.D Bates, M Burgay, S Chatterjee, D.J Champion, R.P Eatough, J.W.T Hessels, G Janssen, K.J Lee, J van Leeuwen, J. Margueron, M Oertel, A Possenti, S Ransom, G. Theureau and P Torne 251

Three-dimensional Tomography of the Galactic and Extragalactic Magnetoionic Medium with the SKA
J. Han, W. van Straten, J. Lazio, A. Deller, C. Sobey, J. Xu, D. Schnitzeler, H. Imai, S. Chatterjee, J.P. Macquart, M. Kramer and J.M. Cordes 273

Testing Gravity with Pulsars in the SKA Era
L. Shao, I. Stairs, J. Antoniadis, A. Deller, P. Freire, J. Hessels, G. Janssen, M. Kramer, J. Kunz, C. Laemmerzahl, V. Perlick, A. Possenti, S. Ransom, B. Stappers and W. van Straten 289

Probing the neutron star interior and the Equation of State of cold dense matter with the SKA
A. Watts, C.M. Espinoza, R. Xu, N. Andersson, J. Antoniadis, D. Antonopoulou, S. Buchner, S. Datta, P. Demorest, P. Freire, J. Hessels, J. Margueron, M. Oertel, A. Patruno, A. Possenti, S. Ransom, I. Stairs and B. Stappers 309

Observing Radio Pulsars in the Galactic Centre with the Square Kilometre Array
R. Eatough, T.J.W Lazio, J Casanellas, S Chatterjee, J.M Cordes, P.B Demorest, M Kramer, K.J Lee, K Liu, S.M Ransom and N Wex 331

Pulsar Wind Nebulae in the SKA era
J. Gelfand, R. Breton, C.U. Ng, J. Hessels, B. Stappers, M. Roberts and A. Possenti 345

Pulsars in Globular Clusters with the SKA
J. Hessels, A Possenti, M Bailes, C. Bassa, P.C.C Freire, D.R Lorimer, R Lynch, S.M Ransom and I.H Stairs 355

Magnetism

Using SKA Rotation Measures to Reveal the Mysteries of the Magnetised Universe
M. Johnston-Hollitt, F. Govoni, R. Beck, S. Dehghan, L. Pratley, T. Akahori, G. Heald, I. Agudo, A. Bonafede, E. Carretti, T. Clarke, S. Colafrancesco, T.A. Ensslin, L. Feretti, B. Gaensler, M. Haverkorn, S.A. Mao, N. Oppermann, L. Rudnick, A. Scaife, D. Schnitzeler, J. Stil, A.R. Taylor and V. Vacca 371

Studies of Relativistic Jets in Active Galactic Nuclei with SKA
I. Agudo, M. Boettcher, H.D.E. Falcke, M. Georganopoulos, G. Ghisellini, G. Giovannini, M. Giroletti, L. Gurvits, J.L. Gómez, R. Laing, M. Lister, J.M. Martí, E. Meyer, Y. Mizuno, S. O'Sullivan, P. Padovani, Z. Paragi, M. Perucho, D. Schleicher, L. Stawarz, N. Vlahakis and J. Wardle 389

Structure, dynamical impact and origin of magnetic fields in nearby galaxies in the SKA era
R. Beck, D. Bomans, S. Colafrancesco, R.J. Dettmar, K. Ferrière, A. Fletcher, G. Heald, V. Heesen, C. Horellou, M. Krause, Y.Q. Lou, S.A. Mao, R. Paladino, E. Schinnerer, D. Sokoloff, J. Stil and F. Tabatabaei 407

Unravelling the origin of large-scale magnetic fields in galaxy clusters and beyond through Faraday Rotation Measures with the SKA
A. Bonafede, F. Vazza, M. Brüggen, T. Akahori, E. Carretti, S. Colafrancesco, L. Feretti, C. Ferrari, G. Giovannini, F. Govoni, M. Johnston-Hollitt, M. Murgia, A. Scaife, V. Vacca, F. Govoni, L. Rudnick and A. Scaife 425

Measuring magnetism in the Milky Way with the Square Kilometre Array
M. Haverkorn, T. Akahori, E. Carretti, K. Ferrière, P. Frick, B. Gaensler, G. Heald, M. Johnston-Hollitt, D. Jones, T. Landecker, S.A. Mao, A. Noutsos, N. Oppermann, W. Reich, T. Robishaw, A. Scaife, D. Schnitzeler, R. Stepanov, X. Sun and R. Taylor 435

Filaments of the radio cosmic web: opportunities and challenges for SKA
F. Vazza, C. Ferrari, A. Bonafede, M. Brüggen, C. Gheller, R. Braun and S. Brown 453

Probing the nature of Dark Matter with the SKA
S. Colafrancesco, M. Regis, P. Marchegiani, G. Beck, R. Beck, H. Zechlin, A. Lobanov and D. Horns 463

Using Tailed Radio Galaxies to Probe the Environment and Magnetic Field of Galaxy Clusters in the SKA Era
M. Johnston-Hollitt, S. Dehghan and L. Pratley 473

SKA studies of in situ synchrotron radiation from molecular clouds
C. Dickinson, R. Beck, R. Crocker, R.M Crutcher, R.D. Davies, K. Ferrière, G. Fuller, T.R. Jaffe, D. Jones, P. Leahy, E. Murphy, M.W Peel, E. Orlando, T. Porter, R.J Protheroe, A. Strong, T. Robishaw, R.A. Watson and F. Yusef-Zadeh 483

Broadband Polarimetry with the Square Kilometre Array: A Unique Astrophysical Probe
B. Gaensler, I. Agudo, T. Akahori, J. Banfield, R. Beck, E. Carretti, J. Farnes, M. Haverkorn, G. Heald, D. Jones, T. Landecker, S.A. Mao, R. Norris, S. O'Sullivan, L. Rudnick, D. Schnitzeler, N. Seymour and X. Sun 493

Mega-parsec scale magnetic fields in low density regions in the SKA era: filaments connecting galaxy clusters and groups
G. Giovannini, A. Bonafede, S. Brown, L. Feretti, C. Ferrari, M. Gitti, F. Govoni, M. Murgia and V. Vacca 505

Cluster magnetic fields through the study of polarized radio halos in the SKA era
F. Govoni, M. Murgia, H. Xu, H. Li, M. Norman, L. Feretti, G. Giovannini, V. Vacca, G. Bernardi, A. Bonafede, G. Brunetti, E. Carretti, S. Colafrancesco, J. Donnert, C. Ferrari, M. Gitti, L. Iapichino, M. Johnston-Hollitt, R. Pizzo and L. Rudnick 515

Magnetic Field Tomography in Nearby Galaxies with the Square Kilometre Array
G. Heald, R. Beck, W.J.G. de Blok, R.J. Dettmar, A. Fletcher, B. Gaensler, M. Haverkorn, V. Heesen, C. Horellou, M. Krause, S.A. Mao, N. Oppermann, A. Scaife, D. Sokoloff, J. Stil, F. Tabatabaei, K. Takahashi, A.R. Taylor and A. Williams 525

Kinematics and Dynamics of kiloparsec-scale Jets in Radio Galaxies with SKA
R. Laing 537

Giant radio galaxies as probes of the ambient WHIM in the era of the SKA
B. Peng, R.R. Chen and R. Strom 547

Measuring Magnetic Fields Near and Far with the SKA via the Zeeman Effect
T. Robishaw, J. Green, G. Surcis, W.H.T. Vlemmings, A.M.S. Richards, S. Etoka, T.L Bourke, V. Fish, M.D Gray, H. Imai, B. Kramer, J. McBride, E. Momjian, A.P. Sarma and A.A Zijlstra 557

Stacking for Cosmic Magnetism with SKA Surveys
J. Stil and B. Keller 569

SKA Deep Polarization and Cosmic Magnetism
R. Taylor, I. Agudo, T. Akahori, R. Beck, B. Gaensler, G. Heald, M. Johnston-Hollitt, M. Langer, L. Rudnick, A. Scaife, D. Schleicher, J. Stil and D. Ryu 579

Statistical methods for the analysis of rotation measure grids in large scale structures in the SKA era
V. Vacca, N. Oppermann, T.A. Ensslin, M. Selig, H. Junklewitz, M. Greiner, J. Jasche, C.A Hales, M. Reneicke, E. Carretti, L. Feretti, C. Ferrari, G. Giovannini, F. Govoni, C. Horellou, S. Ideguchi, M. Johnston-Hollitt, M. Murgia, R. Paladino, R. Pizzo and A. Scaife 589

The Hydrogen Universe

HI Science with the Square Kilometre Array
L. Staveley-Smith and T. Oosterloo 601

Exploring Neutral Hydrogen and Galaxy Evolution with the SKA
S. Blyth, T.M. van der Hulst, M.A.W. Verheijen, B. Catinella, F. Fraternali, M.P. Haynes, K.M. Hess, B. Koribalski, C. Lagos, M. Meyer, D. Obreschkow, A. Popping, C. Power, L.L. Verdes-Montenegro and M. Zwaan 611

The SKA view of the Neutral Interstellar Medium in Galaxies
E. de Blok, F. Fraternali, G. Heald, B. Adams, A. Bosma and B. Koribalski 633

Galactic and Magellanic Evolution with the SKA
N.M. McClure-Griffiths, S. Stanimirovic, C. Murray, D. Li, J.M Dickey, E. Vazquez-Semadeni, J.E.G. Peek, M. Putman, S.E. Clark, M.A. Miville-Deschenes, J. Bland-Hawthorn and L. Staveley-Smith 655

Connecting the Baryons: Multiwavelength Data for SKA HI Surveys
M. Meyer, A. Robotham, D. Obreschkow, S. Driver, L. Staveley-Smith and M. Zwaan 679

Observations of the Intergalactic Medium and the Cosmic Web in the SKA era
A. Popping, M. Meyer, L. Staveley-Smith, D. Obreschkow, G. Jozsa and D.J. Pisano 695

Galaxy Formation & Dark Matter Modelling in the Era of the Square Kilometre Array
C. Power, C. Lagos, B. Qin, C. Baugh, D. Cunnama, J. Fu, H. Kim, C. Lacey, L. Li, D. Obreschkow, J. Wang, Y. Wang and M. Zhu 715

Cool Outflows and HI absorbers with SKA
R. Morganti, E.M. Sadler and S. Curran 733

The SKA as a Doorway to Angular Momentum
D. Obreschkow, M. Meyer, A. Popping, C. Power, P. Quinn and L. Staveley-Smith 751

The Physics of the Cold Neutral Medium: Low-frequency Radio Recombination Lines with the Square Kilometre Array
R. Oonk, L. Morabito, F. Salgado, M.C. Toribio, R.J. van Weeren, A.G.G.M. Tielens and H.J.A. Rottgering 765

The Transient Universe

The Transient Universe with the Square Kilometre Array
R. Fender, A. Stewart, J.P. Macquart, I. Donnarumma, T. Murphy, A. Deller, Z. Paragi and S. Chatterjee 781

The SKA View of Gamma-Ray Bursts
D. Burlon, G. Ghirlanda, A. van der Horst, T. Murphy, R.A.M.J. Wijers, B. Gaensler, G. Ghisellini and I. Prandoni 803

Incoherent transient radio emission from stellar-mass compact objects in the SKA era
S. Corbel, J.C.A. Miller-Jones, R. Fender, E. Gallo, T. Maccarone, T. O'Brien, Z. Paragi, M. Rupen, A. Rushton, S. Sabatini, G. Sivakoff, J. Strader and P.A. Woudt 821

SKA as a powerful hunter of jetted Tidal Disruption Events
I. Donnarumma, E.M Rossi, R Fender, S Komossa, Z Paragi, S Van Velzen and I Prandoni 841

Fast Transients at Cosmological Distances with the SKA
J.P. Macquart, E. Keane, K. Grainge, M. McQuinn, R. Fender, J. Hessels, A. Deller, R. Bhat, R. Breton, S. Chatterjee, C. Law, D. Lorimer, E.O. Ofek, M. Pietka, L. Spitler, B. Stappers and C.Trott 857

The SKA contribution to GRB cosmology
L. Amati, S. Capozziello, A.C. Ruggeri, M. De Laurentis, M. Della Valle, O. Luongo and G. Stratta 873

Time domain studies of Active Galactic Nuclei with the Square Kilometre Array
H.E. Bignall, S.D. Croft, T. Hovatta, J.Y. Koay, J. Lazio, J.P. Macquart and C. Reynolds 885

Core-collapse and Type Ia supernovae with the SKA
M. Perez Torres, A Alberdi, R.J. Beswick, P Lundqvist, R Herrero-Illana, C Romero-Canizales, S Ryder, M della Valle, J Conway, J.M. Marcaide, S Mattila, T Murphy and E. Ros 905

Thermal radio emission from novae & symbiotics with the Square Kilometre Array
T. O'Brien, M. Rupen, L. Chomiuk, V. Ribeiro, M. Bode, J. Sokoloski and P.A. Woudt 921

Investigations of supernovae and supernova remnants in the era of SKA
L. Wang, X. Cui, H. Zhu and W. Tian 933

The SKA and the Unknown Unknowns
P. Wilkinson 943

Early Phase Detection and Coverage of Extragalactic and Galactic Black Hole X-ray Transients with SKA
W. Yu, H. Zhang, Z. Yan and W. Zhang 951

Lunar detection of ultra-high-energy cosmic rays and neutrinos with the Square Kilometre Array
J. Bray, J. Alvarez-Muniz, S. Buitink, R. Dagkesamanskii, R.D Ekers, H.D.E. Falcke, K. Gayley, T. Huege, C. James, M. Mevius, R. Mutel, R.J Protheroe, O. Scholten, F. Schroeder, R.E. Spencer and S. ter Veen 961

Precision measurements of cosmic ray air showers with the SKA
T. Huege, J. Bray, S. Buitink, R. Dallier, R.D Ekers, H.D.E. Falcke, C. James, L. Martin, B. Revenu, O. Scholten and F. Schroeder 979

Contents
Volume 2

The Continuum Universe

Revealing the Physics and Evolution of Galaxies and Galaxy Clusters with SKA Continuum Surveys
I. Prandoni and N. Seymour 991

The star-formation history of the Universe with the SKA
M. Jarvis, N. Seymour, J. Afonso, P. Best, R. Beswick, M. Huynh, E. Murphy, I. Prandoni, E. Schinnerer, C. Simpson, M. Vaccari, S. White and I. Heywood 1009

Exploring AGN Activity over Cosmic Time with the SKA
V. Smolcic, P. Padovani, J. Delhaize, I. Prandoni, N. Seymour, M. Jarvis, J. Afonso, M. Magliocchetti, M. Huynh, M. Vaccari and A. Karim 1027

SKA studies of nearby galaxies: star-formation, accretion processes and molecular gas across all environments
R. Beswick, E. Brinks, M. Perez Torres, A.M.S. Richards, S. Aalto, A. Alberdi, M.K. Argo, I. van Bemmel, J.E. Conway, C. Dickinson, D. Fenech, M.D Gray, H.R. Kloeckner, E. Murphy, T.W.B. Muxlow, M.W Peel, A. Rushton and E. Schinnerer 1041

Identifying the first generation of radio powerful AGN in the Universe with the SKA
J. Afonso, J. Casanellas, I. Prandoni, M. Jarvis, S. Lorenzoni, M. Magliocchetti and N. Seymour 1063

Cluster Radio Halos at the crossroads between astrophysics and cosmology in the SKA era
R. Cassano, G. Bernardi, G. Brunetti, M. Brüggen, T. Clarke, D. Dallacasa, K. Dolag, S. Ettori, S. Giacintucci, C. Giocoli, M. Gitti, M. Johnston-Hollitt, R. Kale, M. Markevich, R. Norris, M.P. Pommier, G. Pratt, H.J.A. Rottgering and T. Venturi 1073

Non-thermal emission from galaxy clusters: feasibility study with SKA
C. Ferrari, A. Dabbech, O. Smirnov, S. Makhathini, J.S. Kenyon, M. Murgia, F. Govoni, D. Mary, E. Slezak, F. Vazza, A. Bonafede, M. Brugger, M. Johnston-Hollitt, S. Dehghan, L. Feretti, G. Giovannini, V. Vacca, M.W. Wise, M. Gitti, M. Arnaud, G. Pratt, K. Zarb Adami and S. Colafrancesco 1087

The SKA view of cool-core clusters: evolution of radio mini-halos and AGN feedback
M. Gitti, P. Tozzi, G. Brunetti, R. Cassano, D. Dallacasa, A. Edge, S. Ettori, L. Feretti, C. Ferrari, S. Giacintucci, G. Giovannini, M. Hogan and T. Venturi 1097

Morphological classification of radio sources for galaxy evolution and cosmology with the SKA
S. Makhathini, M. Jarvis, O. Smirnov and I. Heywood 1115

Radio Observations of Star Forming Galaxies in the SKA era
C. Mancuso, A. Lapi, Z.Y. Cai, M. Negrello, G. De Zotti, F. Perrotta and L. Danese 1127

The SKA view of the Interplay between SF and AGN Activity and its role in Galaxy Evolution
K. McAlpine, I. Prandoni, M. Jarvis, N. Seymour, P. Padovani, P. Best, C. Simpson, D. Guidetti, E. Murphy, M. Huynh, M. Vaccari, S. White, R. Beswick, J. Afonso, M. Magliocchetti and M. Bondi 1137

Strong Gravitational Lensing with the SKA
J. McKean, N. Jackson, S Vegetti, M Rybak, S Serjeant, L.V.E. Koopmans, R.B Metcalf, C. Fassnacht, P.J Marshall and M Pandey-Pommier 1151

The Astrophysics of Star Formation Across Cosmic Time at >10 GHz with the Square Kilometre Array
E. Murphy, M. Sargent, R. Beswick, C. Dickinson, L. Hunt, M. Huynh, M. Jarvis, A. Karim, M. Krause, I. Prandoni, N. Seymour, E. Schinnerer, F. Tabatabaei, J. Wagg and I. Heywood 1169

The SKA Mid-frequency All-sky Continuum Survey: Discovering the unexpected and transforming radio-astronomy
R. Norris, K. Basu, M. Brown, E. Carretti, A.D Kapinska, I. Prandoni, L. Rudnick and N. Seymour 1183

The physics of the radio emission in the quiet side of the AGN population with the SKA
M. Orienti, F. D'Ammando, M. Giroletti, G. Giovannini and F. Panessa 1201

Radio investigation of Ultra-Luminous X-ray (ULX) Sources in the SKA Era
A. Wolter, A. Rushton, M. Mezcua, D. Cseh, F. Pintore, I. Prandoni, Z. Paragi and L. Zampieri 1209

The SKA and Galaxy Cluster Science with the Sunyaev-Zel'dovich Effect
K. Grainge, S. Borgani, S. Colafrancesco, C. Ferrari, A. Scaife, P. Marchegiani, S. Emritte and J. Weller 1221

Astronomy Below the Survey Threshold in the SKA Era
J. Zwart, J. Wall, A. Karim, C. Jackson, R. Norris, J. Condon, J. Afonso, M. Jarvis, F. Navarrete, I. Prandoni, E. Rigby, H.J.A. Rottgering, M. Santos, M. Sargent, N. Seymour, R. Taylor, T. Vernstrom and I. Heywood 1233

Unravelling lifecycles and physics of radio-loud AGN in the SKA Era
A.D Kapinska, M. Hardcastle, C. Jackson, T. An, W. Baan and M. Jarvis 1247

Cosmology

Overview of Cosmology with the SKA
R. Maartens, F.B. Abdalla, M. Jarvis and M.G Santos 1271

Cosmology from HI galaxy surveys with the SKA
F.B. Abdalla, P. Bull, S. Camera, A. Benoit Levy, B. Joachimi, D. Kirk, H.R. Kloeckner, R. Maartens, A. Raccanelli, M.G Santos and G.B. Zhao 1283

Cosmology with SKA Radio Continuum Surveys
M. Jarvis, D. Bacon, C. Blake, M. Brown, S. Lindsay, A. Raccanelli, M. Santos and D.J. Schwarz 1299

Cosmology from a SKA HI intensity mapping survey
M. Santos, P. Bull, D. Alonso, S. Camera, P. Ferreira, G. Bernardi, R. Maartens, M. Viel, F. Villaescusa-Navarro, F.B. Abdalla, M. Jarvis, R.B. Metcalf, A. Pourtsidou and L. Wolz 1315

Cross correlation surveys with the Square Kilometre Array
D. Kirk, F.B. Abdalla, A. Benoit Levy, P. Bull and B. Joachimi 1341

HI galaxy simulations for the SKA: number counts and bias
M. Santos, D. Alonso, P. Bull, M.B. Silva and S. Yahya 1353

Weak gravitational lensing with the Square Kilometre Array
M. Brown, D. Bacon, S. Camera, I. Harrison, B. Joachimi, R.B. Metcalf, A. Pourtsidou, K. Takahashi, J. Zuntz, F.B. Abdalla, S. Bridle, M. Jarvis, T. Kitching, L. Miller and P. Patel 1365

Measuring baryon acoustic oscillations with future SKA surveys
P. Bull, S. Camera, A. Raccanelli, C. Blake, P. Ferreira, M. Santos and D.J. Schwarz 1383

Cosmology on the Largest Scales with the SKA
S. Camera, A. Raccanelli, P. Bull, D. Bertacca, X. Chen, P. Ferreira, M. Kunz, R. Maartens, Y. Mao, M. Santos, P.R. Shapiro, M. Viel and Y. Xu 1399

Real time cosmology - A direct measure of the expansion rate of the Universe with the SKA
H.R. Kloeckner, D. Obreschkow, C. Martins, A. Raccanelli, D. Champion, A.L. Roy, A. Lobanov, J. Wagner and R. Keller 1417

Weak Lensing Simulations for the SKA
P. Patel, I. Harrison, S. Makhathini, F.B. Abdalla, D. Bacon, M. Brown, M. Jarvis, O. Smirnov and I. Heywood 1427

Measuring redshift-space distortion with future SKA surveys
A. Raccanelli, P. Bull, S. Camera, C. Blake, P. Ferreira, R. Maartens, M. Santos, P. Bull, D. Bacon, O. Dore, P. Ferreira, M.G Santos, M. Viel and G.B. Zhao 1445

Testing foundations of modern cosmology with SKA all-sky surveys
D.J. Schwarz, D. Bacon, S. Chen, C. Clarkson, D. Huterer, M. Kunz, R. Maartens, A. Raccanelli, M. Rubart and J.L. Starck 1461

Topology of neutral hydrogen distribution with the Square Kilometre Array
Y. Wang, Y. Xu, F. Wu, X. Chen, X. Wang, J. Kim, C. Park, K.G. Lee and R. Cen 1473

Cosmology with galaxy clusters: studying the Dark Ages and the Epoch of Reionization in the SKA era
S. Colafrancesco, P. Marchegiani and M.S. Emritte 1483

Foreground Subtraction in Intensity Mapping with the SKA
L. Wolz, F.B. Abdalla, D. Alonso, C. Blake, P. Bull, T.C. Chang, P. Ferreira, C.Y. Kuo, M. Santos and J.R. Shaw 1493

Model-independent constraints on dark energy and modified gravity with the SKA
G. Zhao, D. Bacon, R. Maartens, M. Santos and A. Raccanelli 1507

Stacking of SKA data: comparing uv-plane and and image-plane stacking .
K.K. Knudsen, L. Lindroos, W.H.T. Vlemmings, J.E. Conway and I. Marti-Vidal 1519

Epoch of Reionisation

The Cosmic Dawn and Epoch of Reionisation with SKA
L. Koopmans, J Pritchard, G Mellema, J Aguirre, K Ahn, R Barkana, I van Bemmel, G Bernardi, A Bonaldi, F Briggs, A.G. de Bruyn, T.C. Chang, E Chapman, X Chen, B Ciardi, P. Dayal, A. Ferrara, A. Fialkov, F Fiore, K. Ichiki, I.T. Illiev, S Inoue, V Jelic, M Jones, J Lazio, U Maio, S Majumdar, K.J. Mack, A. Mesinger, M.F. Morales, A. Parsons, U.L. Pen, M Santos, R Schneider, B Semelin, R.S de Souza, R Subrahmanyan, T Takeuchi, H Vedantham, J Wagg, R Webster, S Wyithe, K.K. Datta and C. Trott 1529

Probing the First Galaxies and Their Impact on the Intergalactic Medium through 21-cm Observations of the Cosmic Dawn with the SKA
K. Ahn, A. Mesinger, M.A Alvarez and X. Chen 1557

Synergy of CO/[CII]/Lya Line Intensity Mapping with the SKA
T.C. Chang, Y. Gong, M. Santos, M.B. Silva, J. Aguirre, O. Dore and J. Pritchard 1567

Cosmic Dawn and Epoch of Reionization Foreground Removal with the SKA
E. Chapman, A. Bonaldi, G. Harker, V. Jelic, F.B. Abdalla, G. Bernardi, J. Bobin, F. Dulwich, B. Mort, M. Santos and J.L. Starck 1577

21-cm forest with the SKA
B. Ciardi, S. Inoue, K. Mack, Y. Xu and G. Bernardi 1595

Epoch of Reionization modelling and simulations for SKA
I. Iliev, M. Santos, A. Mesinger, S. Majumdar and G. Mellema 1605

SKA - EoR correlations and cross-correlations: kSZ, radio galaxies, and NIR background
V. Jelic, B. Ciardi, E. Fernandez, H. Tashiro and D. Vrbanec 1617

Bulk Flows and End of the Dark Ages with the SKA
U. Maio, B. Ciardi and L. Koopmans 1627

HI tomographic imaging of the Cosmic Dawn and Epoch of Reionization with SKA
G. Mellema, L. Koopmans, H. Shukla, K.K. Datta, A. Mesinger and S. Majumdar 1637

Constraining the Astrophysics of the Cosmic Dawn and the Epoch of Reionization with the SKA .
A. Mesinger, A. Ferrara, B. Greig, I. Iliev, G. Mellema, J. Pritchard and M. Santos 1651

Cosmology from EoR/Cosmic Dawn with the SKA
J. Pritchard, K. Ichiki, A. Mesinger, R.B. Metcalf, A. Pourtsidou, M. Santos, F.B. Abdalla, T.C. Chang, X. Chen, J. Weller and S. Zaroubi 1665

The physics of Reionization: processes relevant for SKA observations
B. Semelin and I. Iliev 1683

All-sky signals from recombination to reionization with the SKA
R. Subrahmanyan, U.N Shankar, J. Pritchard and H.K Vedantham 1693

Imaging HII Regions from Galaxies and Quasars During Reionisation with SKA
S. Wyithe, P. Geil and H. Kim 1705

Synergies and Other Science

Very Long Baseline Interferometry with the SKA
Z. Paragi, L. Godfrey, C. Reynolds, M.J. Rioja, A. Deller, B. Zhang, L. Gurvits, et al. 1719

Synergy between the Large Synoptic Survey Telescope and the Square Kilometre Array
D. Bacon, S. Bridle, F.B. Abdalla, M. Brown, P. Bull, S. Camera, R. Fender, K. Grainge, Z. Ivezic, M. Jarvis, N. Jackson, D. Kirk, B. Mann, J. McEwen, J. McKean, J.A. Newman, A. Raccanelli, M. Sahlen, M. Santos, T. Tyson and G. Zhao 1739

Euclid & SKA Synergies
T. Kitching, D. Bacon, M. Brown, P. Bull, J. McEwen, M. Oguri, R. Scaramella, K. Takahashi, K. Wu and D. Yamauchi 1761

SKA synergy with Microwave Background studies
C. Burigana, P. Alexander, C. Baccigalupi, D.S. Barbosa, A. Blanchard, A. De Rosa, G. De Zotti, F. Finelli, A. Gruppuso, M. Jones, S. Matarrese, A. Melchiorri, D. Molinari, M. Negrello, D. Paoletti, F. Perrotta, R. Scaramella and T. Trombetti 1777

Synergistic science with Euclid and SKA: the nature and history of Star Formation
P. Ciliegi and S. Bardelli 1793

Multiple supermassive black hole systems: SKA's future leading role
R. Deane, Z. Paragi, M. Jarvis, M. Coriat, G. Bernardi, S. Frey, H.R. Kloeckner and I. Heywood 1805

Star and Stellar Cluster Formation: ALMA-SKA Synergies
G. Fuller, J. Forbrich, J. Rathborne, S. Longmore and S. Molinari 1817

The connection between radio and high energy emission in black hole powered systems in the SKA era
M. Giroletti, M. Orienti, F. D'Ammando, F. Massaro, G. Tosti, R. LICO, G. Giovannini, I. Agudo, A. Alberdi, H.E. Bignall, M.P. Pommier and A. Wolter 1829

Synergies between SKA and ALMA: observations of Nearby Galaxies
R. Paladino, E.O. Orru, J. Brand, V. Casasola, E. Liuzzo, M. Massardi and A. Mignano 1841

Multi-wavelength, Multi-Messenger Pulsar Science in the SKA Era
J. Antoniadis, L. Guillemot, A. Possenti, S. Bogdanov, J. Gelfand, M. Kramer, R. Mignani, B. Stappers and P. Torne 1849

Overview of Complementarity and Synergy with Other Wavelengths in Cosmology in the SKA era
K. Takahashi, M. Brown, C. Burigana, C. Jackson, M. Jarvis, K.D Thomas D. Kitching, J.P. Jean-Paul Kneib, M. Masamune Oguri, S. Prunet, H. Shan, J.L. Starck and D. Yamauchi 1863

Solar and Heliospheric Physics with the Square Kilometre Array
V. Nakariakov, M.M Bisi, P.K Browning, D. Maia, E.P Kontar, D. Oberoi, P.T. Gallagher, I.H Cairns and H. Ratcliffe 1875

Extragalactic jets in the SKA era: solving the mystery of Ultra High Energy Cosmic Rays?
S. Turriziani 1889

Enabling the next generation of cm-wavelength studies of high-redshift molecular gas with the SKA
J. Wagg, E. da Cunha, C. Carilli, F. Walter, M. Aravena, J. Hodge, E. Murphy, D. Riechers, M. Sargent, R. Wang and I. Heywood 1901

Enhancing Science from Future Space Missions and Planetary Radar with the SKA
D. Jones and J. Lazio 1911

Delivering SKA Science
P. Quinn, T Axelrod, I Bird, R Dodson, A Szalay and A Wicenec 1921

Summary and Future Directions

Square Kilometre Array key science: a progressive retrospective
C. Carilli 1949

The Continuum Universe

PROCEEDINGS OF SCIENCE

Revealing the Physics and Evolution of Galaxies and Galaxy Clusters with SKA Continuum Surveys*

Isabella Prandoni[†1] **& Nicholas Seymour**[2]

[1] *INAF - IRA, Via P. Gobetti 101, 40129 Bologna (Italy)*

[2] *12Curtin Institute of Radio Astronomy, Curtin University, GPO Box U1987, Perth WA 6845, Australia*

E-mail: prandoni@ira.inaf.it , nick.seymour@curtin.edu.au

In this chapter we provide an overview of the science enabled by radio continuum surveys in the SKA era, focusing on galaxy/galaxy cluster physics and evolution studies, and other relevant continuum science in the > 2020 scientific framework. We outline a number of *reference* radio-continuum surveys for SKA1 that can address such topics, and comprehensively discuss the most critical science requirements that we have identified. We highlight what should be achieved by SKA1, to guarantee a major leap forwards with respect to the pre-SKA era, considering the science advances expected in the coming years with existing and upcoming telescopes (JVLA, LOFAR, eMERLIN, and the three SKA precursors: MWA, ASKAP and MeerKAT). In this exercise we take in due account also the other waveband facilities coming online at the same time (e.g. *Euclid*, LSST, etc.), which tackle overlapping scientific goals, but in a different manner. In this respect particular attention has been payed to ensure that the proposed *reference* surveys are able to exploit the existing synergies with such facilities, so as to generate strong involvement from all astronomical communities, and leave a lasting legacy value. It is clear that a certain degree of freedom is allowed to some of the observational parameters. We believe it is very important to best fine-tune such parameters taking into proper account existing commensalities with SKA1 surveys addressing other science areas (HI galaxy science, magnetism, cosmology).

Advancing Astrophysics with the Square Kilometre Array
June 8-13, 2014
Giardini Naxos, Italy

*This chapter is presented on behalf of the *SKA Continuum Science Working Group*, and builds upon work done in consultation with a wider expert community. A comprehensive discussion of the various science topics summarized here is presented in a number of dedicated chapters.

[†]Speaker.

PoS(AASKA14)067

1. Preamble

Radio continuum surveys are a common tool that can be exploited to address several scientific areas like galaxy evolution, magnetism, transients, cosmology etc. Here we present those science cases that are the focus of the *SKA Continuum Science Working Group (WG)*, primarily in the field of galaxy/galaxy clusters' physics and evolution.

The WG covers a wide range of science areas and represents a diverse cross-section of the astronomy community, demonstrating that a wide census of galactic and extra-galactic research areas can be addressed by the SKA, provided that key continuum science requirements are met. Such diversity is comprehensively illustrated in the collection of *Continuum Science* chapters presented in this Volume.

The top science priorities/drivers for continuum SKA1 surveys are based on the *Continuum Science* chapters, and have been identified from the WG after a long process that involved the wider community through a dedicated *Science Assessment Workshop* (Sept. 2013), the establishment of an *ad-hoc* SKA1-LOW *tiger team* (October-March 2014), and a breakout session on radio–continuum surveys at the AASKA14 Conference (June 2014).

The WG scientific discussion took into account (a) the expected scientific framework in years 2020-2025; (b) the fact that SKA1 should go a major step further with respect to its pathfinders (e.g. JVLA, LOFAR, eMERLIN, etc.) and precursors (Meerkat, MWA and ASKAP); (c) other facilities coming online at the same time (i.e. the planned facilities in the other wavebands, e.g. *Euclid*, LSST, etc.) which tackle overlapping scientific goals, but in a different manner.

With all this in mind, four *reference* radio–continuum surveys were defined, that are considered to have relevant scientific impact in the SKA1 era. Such surveys are designed and optimized so as to respond to specific major scientific drivers, in key research areas like galaxy evolution and cosmology, but will be able to address a much broader range of science cases. As with most modern radio continuum surveys, these are naturally of the form of a nested 'wedding cake' going from all-sky/wide to deep/ultra-deep fields. We note that the surveys presented here have been made compliant with the outcome of the SKA1 rebaselining process.

2. Top Priority Continuum Science Cases

In this section we briefly summarize the top priority science cases in the field of galaxy/galaxy cluster physics and evolution, that we use as the main drivers for our *reference* surveys. For a more comprehensive discussion of such science cases, we refer to the dedicated chapters in the present Volume, as detailed below. It s clear that radio–continuum surveys can serve other relevant research fields. Key science drivers for magnetism, transients, cosmology, etc. are summarized by the relevant overview chapters in this Volume.

◇ The Star Formation History of the Universe

Measuring the Star Formation History of the Universe (SFHU) is a key goal of modern astrophysics, as it allows us to determine the how, when and why of star formation across the whole of cosmic time. Radio continuum observations provide a unique way of measuring the star formation rate (SFR) in galaxies, as the synchrotron emission from relativistic supernova particles and free-free

PoS(AASKA14)067

emission from HII regions are unaffected by dust obscuration (unlike optical/UV) and directly scale to SFR. The SKA can potentially play a major role in assessing the SFHU since its phase 1, as the sensitivity and resolution of the SKA1 at Band 1 and/or 2 provide the means to reach much lower SFRs than confusion limited far-IR surveys.

Observations at $\nu \geq 10$ GHz (Band 5) will provide higher resolution imaging and probe higher rest-frame frequencies with increasing redshift, where free-free processes dominate. In doing so, Band 5 surveys can provide a more direct, dust-unbiased measurement of the massive star formation rate by being highly sensitive to the number of ionizing photons that are produced. Having observations at both Bands 1 (or 2) and 5 we can have insights on the ISM properties at high redshifts, and compare RC (Radio Continuum) - SFR relations independently obtained from thermal and non-thermal physical processes. In addition Band 5 will provide angular resolutions of the order of 0.05-0.1 arcsec, needed to map the distribution of active star formation within galaxies, and morphologically separate out AGN contributions to total energetics for unbiased measurements of star formation rates. This type of imaging is extremely complementary to ALMA imaging of CO for resolved studies of the Schmidt law at very early epochs.

Galaxy evolution is best addressed through a tiered survey strategy whereby enough volume is sampled at each cosmic epoch of interest in order to overcome sample variance and gain a representative view of the Universe, from voids to clusters.

For more details see Jarvis et al.; Murphy et al.; McAlpine et al.; Mancuso et al.; Ciliegi & Bardelli (2015, this Volume).

◇ **The Role of Black Holes in Galaxy Evolution**

Super Massive Black Hole (SMBH) accretion occurs in at least two different modes: (a) a radiatively efficient *fast* accretion mode, also known as *quasar mode*, typically associated with radio-quiet (RQ) active galactic nuclei (AGN), (b) a radiatively inefficient *slow* accretion mode, also known as *radio mode*, typically associated with radio-loud (RL) AGN. Each mode is associated with different "feedback" processes. AGN feedback processes have become a standard ingredient in semi-analytic models of galaxy evolution in order to reproduce observed galaxy properties, but a clear understanding of these complex processes and their true role in shaping galaxy evolution remains elusive: what is the relative importance of the two feedback modes as a function of galaxy mass and epoch? Which role is played by the environment? What drives these processes?
Large-areas are particularly important for AGN feedback studied as a sufficicient volume has to be probed to include the full range of galaxy environments, given the very important role that large-scale environment can play in triggering radio-mode feedback.

The discovery of an increasing fraction of RQ AGNs in the current deepest radio fields means that future sensitive radio surveys can in principle probe the entire AGN population, and not only the tiny (10%) RL AGN fraction. The advantage of radio over e.g. X-ray/optical studies is that radio emission is not affected by gas obscuration, so μJy and sub-μJy radio surveys are sensitive to all types of AGN, independently of obscuration and their orientation (i.e., Type 1s and Type 2s).

SKA1 will push evolutionary studies into the realm of the RQ AGN regime, at the same time being

PoS(AASKA14)067

sensitive to the onset and earliest evolution of the RL AGN phenomenon in the Universe. By achieving a much higher sensitivity over very large survey areas, SKA1 will be able to reach well into the epoch of formation of the earliest AGN ($z > 7$). Besides the immediate interest for galaxy evolution, the successful detection of a RL AGN at very high redshifts would allow for the direct study of neutral Hydrogen in the Epoch of Reionization, through observations of the HI 21 cm forest against such a background source.

For more details see Smolcic et al.; Afonso et al.; McAlpine et al.; Makhathini et al. (2015, this Volume).

◇ **Diffuse Non-Thermal Emission from Galaxy Clusters and Cosmic Filaments**

Radio Halos (RH) are known to be present in a high fraction of massive and merging clusters. The current prevalent view is that they trace turbulent regions, developed in merging clusters, where relativistic particles are trapped and accelerated. According to such a scenario the synchrotron spectra of RH become increasingly steep above a certain frequency, whose value is determined by the efficiency of turbulent-acceleration. Relaxed clusters are expected to host the so-called "off-state" RH, produced by secondary particles, that can be potentially used to detect galaxy clusters in blind radio surveys, providing a powerful cosmological tool, in synergy with upcoming X-ray and Sunyev-Zeldovitch (SZ) surveys (also possible with SKA1 at Band 5). Such off-state RH are predicted by modelling but not yet observed, due to lack of sensitivity.

The phenomenon of mini radio halos, on the other hand, seems to be closely related to AGN feedback in galaxy clusters. Mini-halos are detected around a number of radio-loud brightest cluster galaxies (BCG), on scales comparable to that of the cooling region. Mini-halos are not directly connected with radio bubbles, but the emission is on larger scales and is truly generated from the intra-cluster medium (ICM).

Predictions at low and mid frequencies show that the SKA1 will step into an unexplored territory allowing us to study the formation and evolution of radio halos in a totally new range of cluster masses, dynamical status and redshift. Ongoing simulations of SKA1 observations of galaxy cluster halos show promising results, in particular thanks to the development of deconvolution and source detection algorithms optimized for the analysis of extended and diffuse radio sources.

Even more excitingly the SKA1 may, for the first time, detect synchrotron emission produced by stationary accretion shocks in the warm-hot intergalactic medium associated with cosmic filaments. This is a very challenging task, but even a non-detection at SKA1 sensitivities will give an extremely important upper-limit on the magnetization of the Cosmic Web on its largest scales.

For more details see Cassano et al.; Ferrari et al.; Gitti et al.; Grainge et al.; Vazza et al. (2015, this Volume).

◇ **Detailed Astrophysics of Star Formation and Accretion Processes**

SKA1 continuum surveys covering a wide range of frequencies will provide μJy sensitivities with exquisite image fidelity over a wide range of spatial scales for all nearby galaxies. This will produce a complete census of star-formation and AGN activity as a function of galaxy mass, morphology

PoS(AASKA14)067

and spectral type, black-hole mass and luminosity. This, alongside UV/optical/IR surveys (see §6) will be the cornerstone of multi-wavelength studies of the Local Universe. By providing high resolution ($0.5''$ or better at ~ 1 GHz) the SKA will be able to decompose individual galaxies into their compact radio source populations (accretion dominated AGN, compact HII regions, superstar clusters, X-ray binaries, planetary nebulae, supernovae and their remnants).

The high resolution provided by the SKA1, even over wide areas, will mean that high-resolution, multi-frequency total intensity and polarization imaging of a large sample of RL AGN will become available. Our developing understanding of the dynamics and the spectral/polarization evolution of RL AGN means that it will be possible to make relatively accurate estimates of the kinetic luminosity function of the AGN and their environmental properties from radio observations alone. The ability to do this will be very important both for our understanding of the physics of the RL AGN population and for models of galaxy formation and evolution that rely on feedback processes from RL objects.

The main physical processes at work in RQ AGN, particularly the origin of the radio emission, are still under debate, mainly due to the weakness of these objects. So far high-resolution studies have been possible only for local RQ AGN where high brightness temperature radio cores have been detected. The main processes proposed to explain such emission are synchrotron radiation from mildly relativistic mini-jets, thermal cyclo-synchrotron emission by low-efficient accretion flow, or thermal free-free emission from the X-ray heated corona or wind. Multi-frequency, high-sensitivity polarimetric radio observations are, thus, crucial to constrain the nature of the power engine, and may help in distinguishing between the contribution from star formation and AGN activity.

For more details see Beswick et al.; Kapinska et al.; Orienti et al.; Wolter et al. (2015, this Volume).

◇ Strong Gravitational Lensing

Strong gravitational lenses (GL) provide an important tool to measure masses in the distant Universe, thus (a) testing models for galaxy formation and dark matter, (b) investigate structure at the Epoch of Reionization, and (c) measuring the Hubble constant, and possibly the w parameter (from the cosmology equation of state), as a function of redshift. The limiting factor in all of these studies is the currently small samples of known GL ($\sim 10^2$). SKA will transform our understanding of the Universe with gravitational lensing, as the number of radio-detected GL will increase to $\sim 10^5$. Depending on splitted image separation, relative brightness and total flux density, between 10^3 and 10^4 of such systems will be identified in an all-sky SKA1 mid-frequency survey. This requires a large area, sub-arcsecond angular resolution survey. SKA1 lensing simulations show that angular resolutions of $0.25 - 0.5$ arcsec are required for identifying most of the lens candidates for follow-up imaging. Resolution of $\leq 0.2''$ is required to follow-up these sources.

For more details see McKean et al. (2015, this Volume).

◇ Legacy Value/Serendipity/Rare

Experience shows that when telescopes enter unexplored areas of observational phase space, they make unexpected discoveries. Even more importantly, experience shows that the most significant

PoS (AASKA14) 067

discoveries with major telescopes are unexpected. For example, of the top ten discoveries with *HST*, only one was listed amongst the key goals used to justify *HST*. So while specific science goals are useful to focus the SKA design, they are unlikely to appear amongst its greatest scientific achievements. So in addition to achieving known science goals, the SKA must be designed to maximise its ability to discover the (potentially more important) unknown science goals. Moreover, the sensitivity of SKA1 means that all-sky surveys will result in a radio measurement of most galaxies detected in upcoming all-sky optical surveys. So SKA1 will transform radio-astronomy from a niche field focused on RL AGNs to a mainstream field producing data on most objects of interest by astronomers at other wavelengths.

One particular area where the legacy added-value of an all-sky survey is significant is Galactic science. The SKA1 unique spatial resolution, sensitivity and survey speed at 1-2 GHz, will provide us with a valuable and unprecedented wide-field atlas of the Galactic continuum emission. SKA1 will give the opportunity to create a sensitive catalog of discrete Galactic radio sources, most of them representing the interaction of stars at various stages of their evolution with the environment: complete census of all stage of HII regions evolution; complete census of late stages of stellar evolution such as PNe and SNRs; detection of stellar winds, thermal jets, Symbiotic systems, Chemically Peculiar and dMe stars, active binary systems in both flaring and quiescent states. Coherent emission events as Cyclotron Maser due to particle acceleration and interaction with exoplanets can be detected.

For more details see Norris et al.; Umana et al. (2015, this Volume).

3. Reference Surveys

We have identified four *reference* surveys for SKA1, that we consider best suited to address the aforementioned top priority science cases, as listed below:

- Three-tiered survey at Band 1 or 2
- Two-tiered survey at Band 5
- All-sky survey with SKA1-LOW
- All-sky survey at Band 2

Their observational parameters (observing frequency, 1σ rms sensitivity, surveyed sky area, angular resolution) are summarized in Table 1, as well as their main science drivers. Such surveys are defined so as to provide significant advances over pre-SKA surveys (as illustrated in the last column of Table 1). The *reference* surveys are compared to existing and planned surveys (with SKA pathfinders and precursors) in Figure 1: the three panels illustrate the increment over a pre-SKA scenario in terms of flux limit (top right), angular resolution (top left) and area covered (bottom). Our reference surveys were originally based on full sensitivity capabilities as advertised in Dewdney et al. (2013) and Braun (2014)[1], by assuming 30% fractional bandwidths (i.e. $BW = 0.3\nu$,

[1]Such sensitivity performance is summarized in the Appendix.

PoS(AASKA14)067

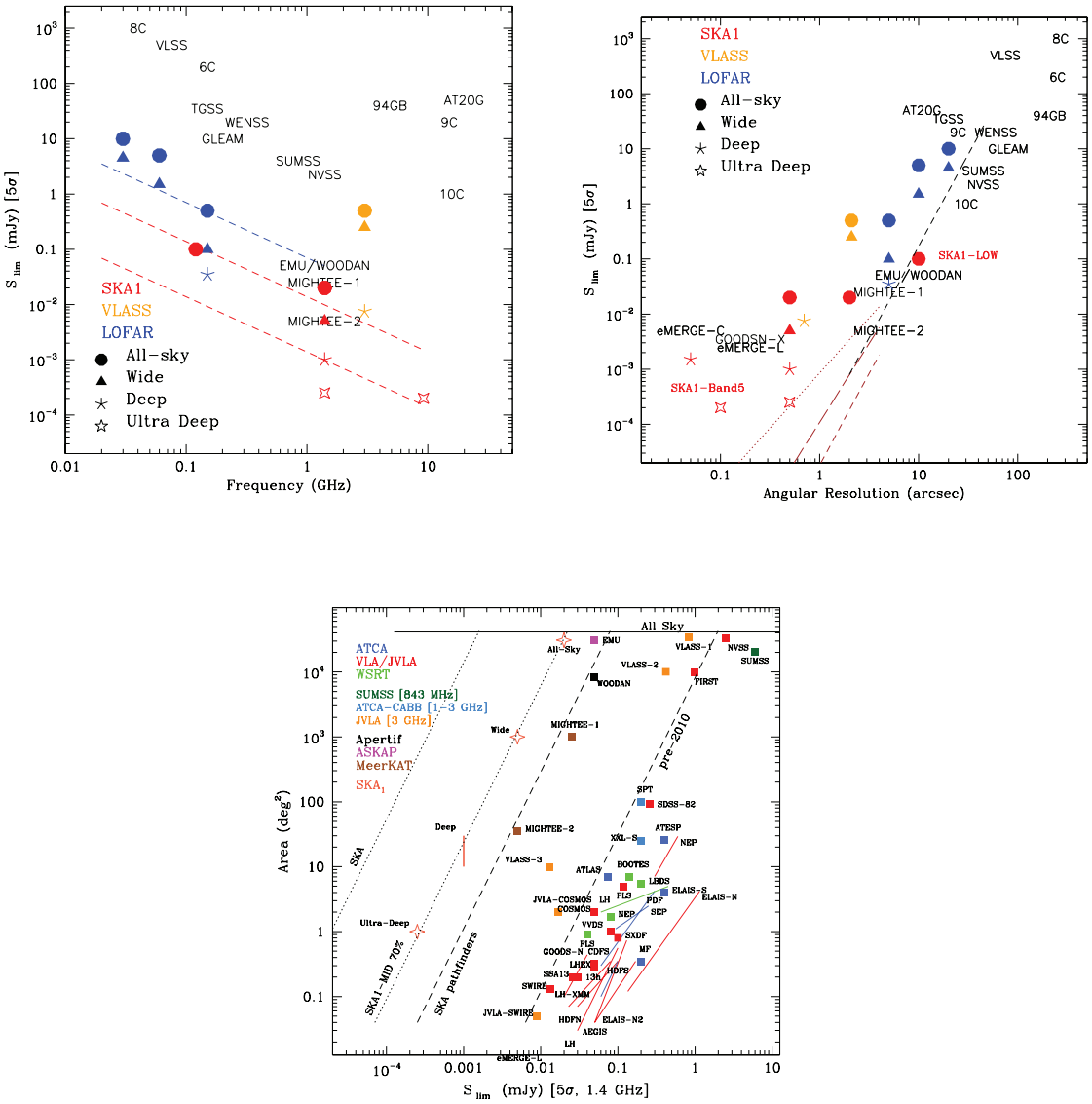

Figure 1: *Top Panels:* SKA1 *reference* surveys in comparison with existing $> 2\pi$ steradian surveys and/or surveys planned for the next future with SKA pathfinders and precursors. LOFAR, VLASS and SKA1 *reference* surveys are highlighted in blue, orange and red respectively. Different symbols refer to different a survey coverage: all-sky (filled circles); wide tiers (filled triangles); deep tiers (asterisks); ultra deep tiers (starred symbols). *Left:* Depth (5σ flux limit) vs. frequency. Band 1 and/or 2 SKA surveys are all shown at a reference frequency of 1.4 GHz. The red and blue dashed lines indicate a slope of $\sim \nu^{-1}$ for different 1.4 GHz flux normalizations. *Right:* Depth (5σ flux limit) vs. angular resolution. The black and brown lines represent approximate estimates of the confusion limit at 120 MHz and 1 GHz respectively (see Appendix for more details). *Bottom panel:* SKA1 *reference* surveys in comparison with existing or planned surveys. Only surveys with observing frequencies in the range 1-3 GHz are shown. Area coverage vs depth (5σ flux limit); for 3 GHz VLA surveys the flux limit has been rescaled to 1.4 GHz.

PoS(AASKA14)067

Table 1: Outline of *Reference* Surveys

#	Science Drivers	ν_{obs} (GHz)	Tier	rms (μJy/b)	Area (deg^2)	θ ($''$)	Increment over pre-SKA
1	SFHU SMBH/gal co-evolution	$\sim 1^a$	Ultra Deep	0.05	1	0.5^b	40× deeper than VLASS-3; 10× smaller area; similar resolution
			Deep	0.2	10-30	0.5	10× deeper than VLASS-3; same area; similar resolution
			Wide	1	1 10^3	0.5	Same sensitivity as MIGHTEE-2 survey; 30× larger area; 8× higher resolution
2	SFHU SMBH/gal co-evolution	~ 10	Ultra Deep	0.04	0.0081	0.1	20× deeper than JVLA 8 GHz GOODS-N field; similar area; 2× better resolution
			Deep	0.3	1	0.1	2× deeper than 5 GHz tier of eMERGE legacy survey; 20× larger area; similar resolution
3	Clusters and Filaments	0.12	All-sky	$\sim 20^c$	31 10^3	10	3× better surface brightness sensitivity than LOFAR all sky surveys, corresponding to the detection of 10× fainter radio halos/relics
4	Strong GL	1.4	All-sky	4	31 10^3	$\leq 0.5^d$	$2-3\times$ deeper sensitivity than ASKAP all sky survey (EMU); 20× better angular resolution; $\sim 1000\times$ more radio-loud strong GL than currently known
	Legacy/Rare Serendipity					$\sim 2^d$	$2-3\times$ deeper sensitivity than ASKAP all sky survey (EMU); 5× better angular resolution

[a] Reference value. The observing frequency can be fine-tuned within Band 1 and/or 2
[b] Reference value at 1 GHz. <1 arcsec required to avoid confusion (see text)
[c] may be confusion limited (see Appendix)
[d] Different angular resolution requirements reflect in distinct surveys, unless we can assume that the same survey can be processed at both the required resolutions

where ν is the observing frequency). Since SKA1-SUR has been deferred as a result of the re-baselining process, all Band 1/2 surveys now refer to SKA1-MID. In addition we now fully exploit the large bandwidths available on MID. This change allows us to fully compensate the factor ~ 2 longer integration times due to the 30% reduced collecting area if SKA1-MID introduced by the re-baselining, at least for the high resolution (sub-arcsec) surveys. The low resolution Band 2 all-sky survey, on the other hand, would be better done with SKA1-SUR (a factor ~ 4 faster at a few arcsec resolution). This means that the original case for a 2 μJy, 2 arcsec resolution survey with SKA1-SUR (extensively discussed in Norris et al. 2015), is not achievable, and a 4 μJy rms is now

PoS(AASKA14)067

Table 2: Tiered surveys at Band 1/2 and at Band 5

Survey	Science Requirements	Addressed Science
1 - UD	will detect $SFR > 10M_{\odot}/yr$ galaxies up to $z \sim 3-4$, and $SFR > 50M_{\odot}/yr$ galaxies up to $z \sim 6$ to probe the SFHU in the very early phases of galaxy evolution	W/D/UD: SFHU non-thermal W/D/UD: SMBH/gal co-evolution W: SF/AGN astro-physics and resolved SF in nearby Universe W/D: RL/RQ AGN dichotomy
1 - D	will detect $SFR > 10M_{\odot}/yr$ galaxies at $z \sim 1-2$, the epoch of maximum star formation activity, for detailed SFG studies as a function of stellar mass, environment and galaxy morphology	
1 - W	will probe the bulk of the SFG population (0.5 < SFR < 10 $M_{\odot}$/yr) over a wide range of environments, for detailed studies as a function of stellar mass, environment and galaxy morphology, in the redshift range where the evolution function presents a strong derivative ($0 < z < 1$)	
2 - UD	- will detect galaxies forming stars at a rate of $\sim 50M_{\odot}/yr$ out to $z \sim 6$ in their rest-frame 70 GHz emission; - will map the distribution of star formation on kpc ($\lesssim$ 0.2 arcsec) scales in galaxies forming stars at $\sim 100M_{\odot}/yr$ out to the peak of the cosmic star formation rate density ($z \lesssim 2$; rest-frame 30 GHz); - will resolve $SFR > 100M_{\odot}/yr$ galaxies on sub-kpc ($\sim$ 0.1 arcsec) scales up to $z \sim 1$ to map out the distribution of active star formation and morphologically separate out AGN contributions to total energetics for unbiased measurements of SFRs, and detailed studies of AGN-galaxy co-evolution/feedback	D/UD: SFHU thermal and resolved SF at medium/high-z D/UD: SF/AGN Interplay
2 - D	- will detect galaxies forming stars at a rate of $\sim 100M_{\odot}/yr$ out to $z \lesssim 3$ (rest-frame 40 GHz) - will resolve $SFR > 100M_{\odot}/yr$ galaxies on sub-kpc ($\lesssim$ 0.1 arcsec) scales out to $z \sim 0.5$ to map out the distribution of active star formation and morphologically separate out AGN contributions to total energetics for unbiased measurements of SFRs, and detailed studies of AGN-galaxy co-evolution/feedback	

quoted. We also note that the 50% reduced collecting area of SKA1-LOW implies a factor 4 longer timescale for the (confusion-limited) all-sky survey, bringing the original 6 months integration time to 2 years. Similar timescales are also needed for the Band 1 and/or 2 surveys, while the Band 5 survey could be in principle run in 6 months. It is worth noting, however, that the actual survey parameters can be fine-tuned to a certain degree to meet tighter time constraints and dependent on refined science goals. For example, the use of the wide bandwidth introduces non-uniform sensitivity as a function of frequency due to the varying primary beam. Note that the details of the rebaselined SKA (version 2) are described in Braun et al. (2015) and Cornwell et al. (2015).

3.1 Science Requirements and Critical Parameters

The observational parameters of our *reference* surveys have been chosen so as to respond to specific science requirements, as detailed In Tables 2, 3, 4, and as such they guarantee a significant impact in the research areas that we have identified as top-priority. It s clear however that a certain degree of freedom is allowed to some of them. We believe it is very important to best fine-tune the observational parameters of SKA1 surveys, to fully exploit existing commensalities and synergies

PoS(AASKA14)067

Table 3: All-sky survey with SKA1-LOW

Science Requirements	Addressed Science
- will detect ~ 2600 RHs up to $z \sim 0.6$, including ~ 1000 USSRH, a factor $\sim 7\times$ increase over LOFAR All Sky Surveys - will probe for the very first time the existence of hadronic 'off-state' radio halos, predicted for virialized clusters; - will be able to detect RHs in clusters up to $z \sim 1$ and with masses down to $M_{500} \sim 10^{14} M_{\odot}$, thus competing with *eROSITA* and SZ surveys in blind cluster searches; - will detect $> 1-10\%$ fraction of the diffuse non-thermal emission in massive $B \sim 0.1-0.3\ \mu$G cosmic filaments, or provide an upper limit in case of lower magnetic fields; - will find powerful RL AGN in the Epoch of Reionisation	RH and USSRH hadronic 'off-state' RH cosmic filaments RL AGN physics RL AGN in the EoR rare populations

Table 4: All-sky Survey at Band 2

Survey	Science Requirements	Addressed Science
4 μJy rms $< 0.5''$ res.	- will detect $\sim 10^4$ new strong lens systems ($\sim 0.25\,\mathrm{deg}^{-2}$) for VLBI follow-up; - will resolve 100 pc scales at distances of $D \sim 40$ Mpc, for detailed studies of ISM in nearby galaxies	Strong GL SF/AGN astrophysics in nearby galaxies rare populations
4 μJy rms $\sim 2''$ res.	- will provide a radio counterpart for most galaxies detected in upcoming all-sky optical surveys; **a resolution of ~ 2 arcsec is optimized for radio-optical identification experiments;** - will provide a complete and unprecedented census of Galaxy Plane radio sources (stellar winds, PN, HII, active binary systems, flare stars etc.), increasing the number of detections by a factor $100\times$; - will provide high-ν information for cluster non-thermal emission, by detecting ~ 500 new halos (in both merging and relaxed clusters) and ~ 300 new mini-halos (in cool core clusters) up to $z \sim 0.6$; - will provide $200\times$ more radio sources than currently known (from 2.5 million to 500 million), allowing to identify rare populations and probably discovering unknown classes of objects	Legacy Galaxy Plane Clusters/mini-halos Serendipity rare populations

among different science areas (HI galaxy science, magnetism, cosmology, transients, etc.). The most critical observational parameters for our science objectives are discussed below.

Observing Frequency: For most continuum science cases we are frequency agnostic as long as the requisite source density, galaxy star-formation rates, AGN radio powers are met. Therefore, our quoted sensitivities (see Table 1) should be scaled by the average spectral index of the dominant extragalactic source population at these flux densities, i.e. star-forming galaxies, which have a spectral index of $\nu^{-0.7}$. Hence, as long as the required resolution is retained, continuum surveys are generally better done at as low frequency as feasible, albeit before becoming dominated by the sky temperature. For the mid-frequency arrays however, this should not be an issue and observing down to a frequency of$\sim 600-700$ MHz could be advantageous. It is worth noting that for observations

PoS(AASKA14)067

with a lower central frequency field-of-view, and hence survey speed, increases. Observing at low frequency would also exploit commensality with cosmological HI surveys, and provide HI line information (HI masses/redshifts) for at least some classes of galaxies. Observations at higher frequency (e.g. ~ 1.4 GHz), on the other hands, would exploit commensality with polarization surveys (magnetism). As extensively discussed by Murphy et al. (2015, this Volume), we gain significantly by having Band 5 as second band, as this would provide complementary significantly higher resolution information ($0.05-0.1$ arcsec), very important for detailed astrophysical studies at high redshift and AGN identification (see below). In addition Band 5 allows us to probe a different emission process at high redshift (thermal vs non-thermal). Band 5 is also crucial for Galactic studies, not only because of the high resolution and the spectral index information it provides, but also because it allows to detect particular classes of sources, like Hypercompact HII regions or a quiescent Solar analogue at 10 pc (see Umana et al. 2015, this Volume).

Angular Resolution at Mid/High Frequency:

• *Galaxy Evolution:* Angular resolution is a critical parameter for galaxy evolution studies for several reasons. The most obvious one is confusion from background sources. Our *reference* Ultra Deep and Deep Band 1/2 tiers would be confusion-limited at $\sim 1-2$ arcsec resolution, assuming the latest 1.4 GHz source counts predictions (Condon et al. 2012; see Appendix for more details). Another critical aspect is the ability to identify and reliably classify different classes of sources at any redshift. This requires extensive, deep multi-wavelength information in the surveyed areas, as well as sub-arcsec resolution radio observations. Galaxy H_α disks are found to shrink to 0.7 arcsec sizes at redshifts $z \gtrsim 1$ (based on HST Grism imaging; e.g. Nelson et al. 2013), corresponding to $5-6$ kpc physical scales. So radio observations of similar or better resolution are needed to distinguish emission triggered by star formation from emission from $\gtrsim 10-30$ kpc radio jets possibly associated to RQ AGNs. Assuming a 0.5 arcsec resolution at 1 GHz (achievable with ≥ 120 km maximum baselines), we allow for resolution values from 0.4 (1.4 GHz) to 0.7 (700 MHz) arcsec, depending on the actual observing frequency. Such values provide a good match with the resolution of next generation optical/NIR surveys (0.2 arcsec *Euclid*; 0.7 arcsec LSST). A factor $10-100$ better resolution would be needed to resolve star formation from embedded AGN radio cores. Galaxy-AGN co-evolution studies will significantly benefit from the implementation of Band 5 in phase 1 (0.05-0.1 arcsec at 10 GHz), that would allow to pinpoint flat-spectrum radio core candidates (see McAlpine et al. 2015, this Volume). Crucial in this respect is the implementation of VLBI capabilities for SKA1.

• *Strong Lensing:* The main requirement for gravitational lens surveys is resolution. Retaining the post-rebaselining 150 km maximum baseline for SKA1-MID is therefore crucial. For maximum efficiency, resolutions of about 0.2 arcsec are required, as was used in the CLASS survey. However, surveys of 0.5 arcsec resolution are still useful, at the expense of completeness of samples (the smaller-separation lenses will be missed) and false positives (requiring more follow-up). Nevertheless, this problem has been investigated in the past and tricks are available to find lenses with the lower-resolution surveys. A particularly promising approach is to use two surveys - here, SKA1 together with *Euclid* - as this should allow much more efficient rejection of false positives. In principle, 1 in every $\sim 600-1000$ background sources is strongly lensed, the main dependency being on source redshift (approximately as $(1+z)^4$); the likely redshift distribution

PoS(AASKA14)067

of SKA objects suggests that this will be continued, although detailed simulations including the various source populations have yet to be done. A survey of a few $\times 10^8$ objects, e.g. all-sky with SKA1, should in theory yield a few hundred thousand lenses (McKean et al. 2015, this Volume). SKA1 VLBI capability is critical to follow up the most promising strong lens candidates.

Angular Resolution for SKA1-LOW: The lack of baselines longer than ~ 80 km for SKA1-LOW limits the overall sensitivity of the instrument which is confusion limited at ~ 20 μJy/b rms (at 120 MHz, 10 arcsec resolution). Nevertheless SKA1-LOW (even with its post-rebaselining 50% sensitivity performance) will provide a significant improvement in studies of cluster diffuse emission (Cassano et al. 2015, this Volume), at least up to $z \sim 0.5-1$ (at higher redshifts a 4-5 arcsec resolution become critical to reliably separating diffuse emission from contaminating point sources), and can potentially provide a first detection of the diffuse synchrotron emission in massive cosmic filaments (see simulations by Vazza et al. 2015, this Volume). For other key continuum science cases, better sensitivity and/or better resolution than currently designed, are necessary to make a significant step forwards with respect to SKA pathfinders (and in particular LOFAR, that already offers better spatial resolution). We therefore envisage the implementation of significanly longer baselines (ideally by a factor 4) for the full SKA.

Beam Shape: At μJy flux density levels the source counts are such that effective beam solid angle is extremely sensitive to extended (large Ω) low-level "pedestals" and other sidelobes of the dirty beam. The naturally weighted beam of SKA1-MID, in particular, has large pedestals produced by the 1 km core array optimized for pulsars and the 8 km halo array for HI observations. Consequently it is important that the (u,v) be weighted sufficiently to remove the pedestals from the compact cores of the SKA arrays. It is also important to investigate further the effect of sidelobes to confusion noise which cannot be curtailed by weighting.

Dynamic Range: The sensitivities possible over wide areas with SKA1 naturally raise the requirement of high dynamic range for even the smallest survey tier (this is closely related to the beam shape and sidelobes discussed above). While some effort can be made to avoid the brightest sources, that will not always be possible. The use of an accurate sky model can help mitigate this issue, but there will undoubtedly be regions of enhanced noise (above thermal) around bright source. For these to be minimized we require a dynamic range of ~ 60 dB for the survey scenarios outlined above, but ultimately ~ 70 dB will be required for the full SKA.

Short Baselines: The detection of diffuse non-thermal emission in cosmic filaments needs the availability of good UV coverage at the shortest baselines, ie those sensitive to diffuse emission on scales $\gg 1$ Mpc (corresponding to angular scales of degrees at redshift $z \sim 0.05-0.1$). This requirement is fulfilled for SKA1-LOW (and not for SKA1-MID or SUR), which therefore plays a unique role for this experiment. On the oher hand, current simulations show that better surface brightness sensitivity is needed to fully probe diffuse radio-continuum emission from the cosmic web (Vazza et al. 2015, this Volume). This will be achieved by the full SKA, with longer baselines.

Spectral Index Information: Several continuum science cases benefit from spectral index measurements. This is essential to identify classes of very steep spectrum sources (non thermal emis-

PoS(AASKA14)067

sion in galaxy clusters, very high redshift AGNs, etc.). The proposed *reference* surveys at different frequencies have matched sensitivity for ν^{-1} sources (see Figure 1, top right panel).

Strategy: Here we note a few points on general survey strategy. The use of nested "wedding-cake" surveys reduces the overall observing time by not requiring the duplication of observation over the same areas. Hence a natural strategy is to incrementally build up depth in all-sky surveys, but go deep first in the best understood areas where you plan to go deepest. Related to this approach is the fact that the deepest pointings will be constrained by both the location of the best ancillary data as well as bright, dynamic-range limiting sources. As confusion noise is the ultimate constraint on any survey we advocate that long baselines be kept (over sensitivity) and built early to maintain the SKA's position as a transformational observatory.

Data Archiving and Processing: The possibility to store visibilities and re-process the data at different resolutions/bandwidths etc. would have a huge commensality/synergy added-value for continuum surveys. At the very least, if visibilities are not retained, we must plan for multiple processing paths to produce images with different resolutions.

4. Synergies and Commensalities

For many, if not most, of the science goals listed in §2 multi-wavelength, ancillary data is key for a plethora of reasons, e.g. determining redshifts, measuring other properties. In Table 5 we list those facilities and surveys which will best complement the proposed survey tiers at the time the SKA1 surveys will be conducted. These include imaging and spectroscopic surveys from optical to far-IR wavelengths. Of note, but not included in Table 5, are ALMA and *JWST*, as detailed deep survey plans have not yet been defined for those facilities.

A full exploitation of the existing synergies between the SKA surveys and those at other wavelengths is key to maximise the science return from the continuum surveys and to generate a strong involvement in all astronomical communities. This requires more detailed examination of these other surveys and coordination with them over issues such as depth and areas covered, although observations at different wavelengths have different observational constraints. By ensuring careful coordination of the SKA tiers with all these surveys we can provide the richest possible legacy value for the community.

Potential commensalities exist between the survey tiers proposed here and those proposed by other WGs, namely Cosmology, HI, Magnetism and Transients. While it is beyond the scope of this document to examine this issue in detail we note that finding a common ground between these different surveys will greatly decrease the total demand on SKA1 time for large projects as well as providing valuable ancillary radio data products. For example, the same set of observations with the Australian SKA Pathfinder will provide different data products for the HI, continuum and polarisation legacy projects ensuring close collaboration of the different science teams. Hence, due to the huge benefit of commensality, we propose it be discussed in subsequent fora.

5. Conclusions

We have highlighted the major science areas in which continuum surveys with SKA1, and

PoS(AASKA14)067

Table 5: Table of key multi-wavelength surveys for SKA surveys in the 2020 era. All magnitudes are given in AB. The final column indicates the estimated release date of the data after survey completion.

SKA Tier	Observatory /Survey Name	Area (deg^2)	Wavelength Bands	Limiting Mag. or flux[a]	Data Release Date
All-sky	ALL*WISE*[a]	42,195	3.4, 4.6, 12, 22 μm	70 μJy	2013
All-sky	PanSTARRS[b]	31k	g, r, i, z, y	$r < 24.0$	2020[b]
All-sky	LSST[c]	20k	u, g, r, i, z, y	$r < 27.5$	2020
All-sky	VISTA-VHS[d]	20	Y, J, H, K	$K < 20.0$	2011+
All-sky	*eROSITA*[e]	$\sim$ 42k	$0.5 - 10$ keV	$\sim 10^{-14}$ ergcm^{-2}s^{-1}	2018
All-sky	*EUCLID*[f]	15k	$0.55 - 2.0\,\mu$m+spec.	$YJH < 24$	2020+
All-sky	TAIPAN[g]	20k	$0.37 - 0.87\,\mu$m spec.	$R < 17.5$	2015
All-sky	4MOST[h]	15-20k	$0.39 - 1.05\,\mu$m spec.	$r < 22$	2019+
All-sky	MOONS[i]	15k	$0.8 - 1.8\,\mu$m spec.	(TBD)	2019+
Wide	H-ATLAS[j]	570	$70 - 500\,\mu$m	$S_{250\mu m} > 44.5$ mJy	2015
Wide	DES[k]	5000	g, r, i, z, y	$r < 25$	2017
Wide	VISTA-Viking[d]	1500	Y, J, H, K_s	$K_s < 21.2$	2012
Wide	VST-ATLAS[d]	4500	u', g', r', i', z'	$r' < 22.2$	2016
Wide	VST-KIDS[d]	1500	u', g', r', i'	$r' < 24.2$	2016
Wide	PanSTARRS Deep[b]	1200	$0.5 - 0.8, g, r, i, z, y$	$g < 27.0$	2020
Deep	SCUBA2[l]	1/6	450/850 μm	$S_{850\mu m} > 3.5$ mJy	????
Deep	HerMES[m]	1...270	$70 - 500\,\mu$m	$S_{250\mu m} > 3.8...64$ mJy	2016
Deep	SERVS[n]	18	$3.4, 4.6\,\mu$m	$\sim 2\,\mu$Jy	2013
Deep	VISTA-VIDEO[d]	12	Z, J, H, K_s	$K_s < 23.5$	2016
Deep	LSST (deep drilling)[o]	38.4	(some of) u, g, r, i, z, y	$r < 30$	2020
Deep	UltraVISTA[d]	0.73	Y, J, H, K_s, NB	$K_s < 25.6$	2016
Deep	DES[k]				

[a]http://wise2.ipac.caltech.edu/docs/release/allwise/
[b]http://www.ps1sc.org
[c]http://www.lsst.org/files/docs/LSSToverview.pdf
[d]http://www.eso.org/sci/observing/PublicSurveys/sciencePublicSurveys.html
[e]http://www.mpe.mpg.de/erosita
[f]http://www.euclid-ec.org/
[g]http://www.taipan-survey.org/
[h]http://workshop.4most.eu/doc/4most_poster_121019s.pdf
[i]http://www.roe.ac.uk/ ciras/MOONS/VLT-MOONS.html
[j]http://www.h-atlas.org/
[k]http://www.darkenergysurvey.org/
[l]http://www.jach.hawaii.edu/JCMT/surveys/Cosmology.html
[m]http://hermes.sussex.ac.uk/
[n]http://www.cv.nrao.edu/ mlacy/servs.html
[o]http://www.lsst.org/News/enews/deep-drilling-201202.html

PoS(AASKA14)067

ultimately the full SKA, will have. We have come up with a list of *reference* surveys which are designed to examine how we can address a wide range of science goals. Such *reference* surveys are just the starting point for planning real surveys with SKA1 and considerable more conversation within the community is required. However, they bring into sharp focus the technical requirements and critical parameters which must be achievable, as well as the need to consult other WGs in designing surveys which address more than just continuum science and make the most efficient use the world's most powerful radio telescope.

We finish by noting that surveys, while driven by headline science goals, can address an extremely wide range of science, and hence, be of benefit to a wide section of the astronomical community. By presenting a transformational step in sensitivities and capabilities well designed surveys with SKA1 will provide huge science return for the widest possible number of astronomers.

Acknowledgments

NS is the recipient of an ARC Future Fellowship.

References

Afonso J., et al. 2015, "Identifying the first generation of radio powerful AGN in the Universe with the SKA", in proceedings of "Advancing Astrophysics with the Square Kilometre Array", PoS(AASKA14)071

Beswick R. J., et al. 2015, "SKA studies of nearby galaxies: star-formation, accretion processes and molecular gas across all environments" , in proceedings of "Advancing Astrophysics with the Square Kilometre Array", PoS(AASKA14)070

Braun R. 2014, "SKA1 Imaging Science Performance Document", SKA Document, Rev A Draft 5

Braun R. et al. 2015, "SKA1 Science (Level 0) Requirements", SKA-TEL-SKO-0000007 Rev 2

Cassano R., et al. 2015, "Cluster Radio Halos at the crossroads between astrophysics and cosmology in the SKA era", in proceedings of "Advancing Astrophysics with the Square Kilometre Array", PoS(AASKA14)073

Ciliegi P. & Bardelli S. 2015, "Synergistic science with Euclid and SKA: the nature and history of Star Formation", in proceedings of "Advancing Astrophysics with the Square Kilometre Array", PoS(AASKA14)150

Condon J. J. 1987, in Proceedings of the Arecibo UpgradingWorkshop, ed. J. H. Taylor & M. M. Davis (Arecibo:NAIC), 89

Condon J. J., Cotton W. D., Fomalont E. B., et al. 2012, ApJ, 758, 23

Cornwell T. et al. 2015 "SKA1 Baseline Design", SKA-TEL-SKO-0000002 Rev 2"

Dewdney P., Turner W., Millenaar R., McCool R., Lazio J., Cornwell T. 2013, "SKA1 System Baseline Design", Document number SKA-TEL-SKO-DD-001 Revision 1

Ferrari C., et al. 2015, "Non-thermal emission from galaxy clusters: feasibility study with SKA", in proceedings of "Advancing Astrophysics with the Square Kilometre Array", PoS(AASKA14)075

PoS(AASKA14)067

Gitti M., et al. 2015, "The SKA view of cool-core clusters: evolution of radio mini-halos and AGN feedback", in proceedings of "Advancing Astrophysics with the Square Kilometre Array", PoS(AASKA14)076

Grainge K., et al. 2015, "The SKA and Galaxy Cluster Science with the Sunyaev-Zel'dovich Effect", in proceedings of "Advancing Astrophysics with the Square Kilometre Array", PoS(AASKA14)170

Jarvis M. J., et al. 2015, "The star-formation history of the Universe with the SKA", in proceedings of "Advancing Astrophysics with the Square Kilometre Array", PoS(AASKA14)068

Kapinska A. D., et al. 2015, "Unravelling lifecycles & physics of radio-loud AGN in the SKA era", in proceedings of "Advancing Astrophysics with the Square Kilometre Array", PoS(AASKA14)173

Makhathini S., Smirnov O. M., Jarvis M. J. and Heywood I. 2015, "Morphological classification of radio sources for galaxy evolution and cosmology with the SKA", in proceedings of "Advancing Astrophysics with the Square Kilometre Array", PoS(AASKA14)81

Mancuso C., et al. 2015, "Radio Observations of Star Forming Galaxies in the SKA era", in proceedings of "Advancing Astrophysics with the Square Kilometre Array", PoS(AASKA14)82

McAlpine K., et al. 2015, "The SKA view of the Interplay between SF and AGN Activity, and its role in Galaxy Evolution", in proceedings of "Advancing Astrophysics with the Square Kilometre Array", PoS(AASKA14)83

McKean J. P., et al. 2015, "Strong gravitational lensing with the SKA", in proceedings of "Advancing Astrophysics with the Square Kilometre Array", PoS(AASKA14)84

Murphy E. J., et al. 2015, "The Astrophysics of Star Formation Across Cosmic Time at $\gtrsim$ 10 GHz with the Square Kilometer Array", in proceedings of "Advancing Astrophysics with the Square Kilometre Array", PoS(AASKA14)85

Nelson E. J., van Dokkum P. G., Momcheva I., et al. 2013, ApJ, 763, L16

Norris R. P., et al. 2015, "The SKA Mid-frequency All-sky Continuum Survey: Discovering the unexpected and transforming radio-astronomy", in proceedings of "Advancing Astrophysics with the Square Kilometre Array", PoS(AASKA14)86

Orienti M., D'Ammando F., Giroletti M., Giovannini G. and Panessa F. 2015, "The physics of the radio emission in the quiet side of the AGN population with the SKA", in proceedings of "Advancing Astrophysics with the Square Kilometre Array", PoS(AASKA14)87

Smolcic V., et al. 2015, "Exploring AGN Activity over Cosmic Time with the SKA", in proceedings of "Advancing Astrophysics with the Square Kilometre Array", PoS(AASKA14)69

Umana G., et al. 2015, "The impact of SKA on Galactic Radioastronomy: continuum observations", in proceedings of "Advancing Astrophysics with the Square Kilometre Array", PoS(AASKA14)118

Vazza F., et al. 2015, "Filaments of the radio cosmic web: opportunities and challenges for SKA", in proceedings of "Advancing Astrophysics with the Square Kilometre Array", PoS(AASKA14)97

Wolter A., et al. 2015, "Radio investigation of Ultra-Luminous X-ray Sources in the SKA Era", in proceedings of "Advancing Astrophysics with the Square Kilometre Array", PoS(AASKA14)91

Zwart J., et al. 2015, "Astronomy below the Survey Threshold in the SKA Era", in proceedings of

PoS(AASKA14)067

"Advancing Astrophysics with the Square Kilometre Array", PoS(AASKA14)172

Appendix: SKA1 Sensitivity Performance

As a common reference we summarize here the set of telescope parameters used to estimate the sensitivity of SKA1, as advertised in Dewdney et al. (2013) and/or Braun (2014) (see Table 6). Using the parameters in Table 6 one can compute the thermal RMS sensitivity (ΔS) of each array/band as follows:

$$\Delta S^{\rm Jy} = \frac{SEFD^{\rm Jy}}{\eta_S \sqrt{2\Delta\nu_{\rm Hz}\, t_{\rm s}}} = 1.31\times10^{-5}\frac{SEFD^{\rm Jy}}{\sqrt{\Delta\nu_{\rm MHz}\, t_{\rm h}}} \tag{5.1}$$

where $\Delta\nu$ is the assumed instantaneous bandwidth ($\leq \Delta\nu_{\rm max}$), t is the integration time in hours, and the system efficiency η_S is assumed equal to 0.9. It is important to note that the tabulated sensitivities are just reference values. Simulations (see e.g. Figure 2 of Braun 2014) show that the actual sensitivities measured in CLEANed images are typically a factor of 1.5-2 larger for a range of restoring beams around natural resolution, and degrade very rapidly at the highest and lowest resolutions. This has to be taken into account when estimating the actual expected sensitivities.

Please note that as a consequence of the re-baselining process SKA1-MID and SKA1-LOW have collecting areas reduced by a factor 30 and 50 per cent respectively (note that the details of the rebaselined SKA (version 2) are described in Braun et al. (2015) and Cornwell et al. (2015)). This means that the ΔS quoted for SKA1-MID and SKA1-LOW in Table 6 should be increased by the same factor. We also notice that SKA1-SUR has been deferred, and is not relevant anymore for the definition of our continuum surveys. Another important parameter to take into proper account when designing a deep continuum survey, and strictly related to spatial resolution is (*classical*) confusion noise, which limits the actual depth of a survey, due to the presence of unresolved background sources, below the detection limit. The confusion limit critically depends on the assumed sources counts (typically approximated by a power-law, $n(S) \sim kS^{-\gamma}$). We used the scaling relation presented in Condon et al. (2012, see their eq. 27) to estimate 120 MHz and 1 GHz confusion limits as a function of angular resolution (see black and brown short-dashed lines in Figure 1, top right panel). This scaling relation assumes $\gamma = 1.6$. For 1 GHz surveys we also show other two estimates: one (brown long-dashed line) obtained by converting to 1 GHz the $\gamma = 1.7$ power-law fit to the 3 GHz source counts recently derived for the JVLA SWIRE field (Condon et al. 2012); the other one obtained by using an older scaling relation presented in Condon (1987), where $\gamma = 2$ (brown dotted line). The latter estimate, which better match confusion limits for existing low frequency surveys (see Cassano et al. 2015, this Volume), is shown to illustrate a worst-case scenario. It is clear that SKA1-LOW surveys are likely to be confusion limited at the angular resolutions accessible with $\sim$ 90 km maximum baselines. At Band 1/2 confusion is less of a problem, and deep surveys at 1-2 arcsec resolution should be feasible, even though there is a clear intrinsic uncertainty in the extrapolation of the measured number counts to sub-μJy sensitivities. For a more comprehensive discussion of confusion we refer to Zwart et al. (2015, this Volume), where different estimates are presented (see their § 6).

PoS(AASKA14)067

Table 6: Telescope Performance assumed for SKA1 before rebaselining.

Telescope	Band	Freq. Range GHz	$\Delta\nu_{\rm max}{}^a$ MHz	ν_0 GHz	$\rm FoV^b_{eff}$ deg^2	SEFD‡ Jy		$\Delta S^{c\ddagger}$ μJy h$^{-1/2}$	
SKA1-MID	1a	0.35-1.05	700	0.7	1.4	3.5		4.6	
	1b	0.58-1.02	440	0.7	1.4	2.8^d		3.7	
	2	0.95-1.76	810	1.4	0.35	1.7^d		2.2	
	3	1.65-3.05	1400	2.35	0.124	2.1		2.8	
	4	2.8-5.18	2380	4.0	0.043	2.3		3.0	
	5	4.6-13.8	2×2500	9.2	0.0081	2.8		3.7	
SKA1-SUR	1	0.35-0.9	500	0.625	61	11.8^e	(16.3)	15.5	(21.4)
	2	0.65-1.67	500	1.4	18	7.1^e	(9.8)	9.3	(12.8)
	3	1.5-4.0	500	2.8	3.1	9.4^e	(13.0)	12.3	(17.0)
SKA1-LOW		0.05-.35	250	0.05	39	19		24.9^f	
				0.11	8	2.9		3.8^f	
				0.16	3.8	2.6		3.4^f	
				0.22	2.0	2.6		3.4^f	

‡ require an increase of 30% for MID and 50% for LOW post-rebaselining.

^{a} Maximum instantaneous bandwidth.

^{b} *Effective* FoV, i.e. the FoV you have to sum up to cover areas larger than the primary beam with uniform noise. For MID and LOW $\rm FOV_{eff} = 0.5\,\Theta_P$, where Θ_P is the Gaussian primary beam in square degrees ($\Theta_P = (\pi/4)(66\lambda_0/d_{\rm dish/station})^2$). For LOW we assume $d_{\rm station} = 45$ m. For SUR $\rm FOV_{eff} = FOV_{PAF} = 36\,\Theta_P$, where Θ is computed as above, assuming $\lambda_0 = \lambda_{\rm min}$, i.e. the minimum wavelength in the band.

^{c} RMS sensitivity reached in 1^h of integration assuming the tabulated SEFD and $\Delta\nu$ =100 MHz (see eq. 5.1).

^{d} Includes Meerkat dishes.

^{e} Includes ASKAP dishes. Note that ASKAP can be included in only one of the three available bands, at your choice. For the other bands you have to use SEFD values for SUR dishes only, (reported in parenthesis in the table).

^{f} Note that with the current Baseline Design (maximum baseline $\sim$ 90 km), SKA1-LOW is confusion limited and cannot reach the tabulated noise levels (see text for more details.

PoS(AASKA14)067

PROCEEDINGS OF SCIENCE

The star-formation history of the Universe with the SKA

Matt J. Jarvis[1,2], **Nick Seymour**[3*], **Jose Afonso**[4,5], **Philip Best**[6], **Rob Beswick**[7], **Ian Heywood**[8,9], **Minh Huynh**[10], **Eric Murphy**[11], **Isabella Prandoni**[12], **Eva Schinnerer**[13], **Chris Simpson**[14], **Mattia Vaccari**[2], **Sarah White**[1]

[1]*Astrophysics, University of Oxford, Keble Road, Oxford, OX1 3RH, UK;* [2]*Physics Department, University of the Western Cape, Bellville 7535, South Africa;* [3]*International Centre for Radio Astronomy Research, Curtin University, Perth, Australia;* [4] *Instituto de Astrofísica e Ciências do Espaço, Universidade de Lisboa, OAL, Tapada da Ajuda, PT1349-018 Lisboa, Portugal;* [5] *Departamento de Física, Faculdade de Ciências, Universidade de Lisboa, Edifício C8, Campo Grande, PT1749-016 Lisbon, Portugal;* [6] *Institute for Astronomy, University of Edinburgh, Royal Observatory, Blackford Hill, Edinburgh EH9 3HJ, UK;* [4] *Jodrell Bank Centre for Astrophysics, Alan Turing Building, University of Manchester, Oxford Road, Manchester, M13 9PL, UK;* [8]*CSIRO Astronomy & Space Science, P.O. Box 76, Epping, NSW 1710, Australia* [9]*RATT, Department of Physics and Electronics, Rhodes University, P.O. Box 94, Grahamstown, South Africa* [10]*International Centre for Radio Astronomy Research, University of Western Australia, Perth, Australia;* [11]*IPAC, Caltech, MC 220-6, Pasadena CA, 91125, USA;* [12]*INAF-IRA Bologna, Via Gobetti 101, I-40129 Bologna, Italy;* [13]*Max-Planck-Institut fuür Astronomie, Königstuhl 17, 69117 Heidelberg, Germany;* [14]*Astrophysics Research Institute, Liverpool John Moores University, ic2 Building, 146 Brownlow Hill, Liverpool L3 5RF*
E-mail: matt.jarvis@astro.ox.ac.uk

Radio wavelengths offer the unique possibility of tracing the total star-formation rate in galaxies, both obscured and unobscured. As such, they may provide the most robust measurement of the star-formation history of the Universe. In this chapter we highlight the constraints that the SKA can place on the evolution of the star-formation history of the Universe, the survey area required to overcome sample variance, the spatial resolution requirements, along with the multi-wavelength ancillary data that will play a major role in maximising the scientific promise of the SKA. The required combination of depth and resolution means that a survey to trace the star formation in the Universe should be carried out with a facility that has a resolution of at least ~ 0.5 arcsec, with high sensitivity at < 1 GHz. We also suggest a strategy that will enable new parameter space to be explored as the SKA expands over the coming decade.

Advancing Astrophysics with the Square Kilometre Array
June 8-13, 2014
Giardini Naxos, Italy

*Speaker

PoS(AASKA14)068

1. Introduction

Gaining a full understanding of the formation and evolution of galaxies relies on our ability to trace the build-up of stellar mass over the history of the Universe. Therefore we are required to obtain observations that allow us to measure both ongoing star-formation activity and the stellar populations that are already in place. The older stars, which contain the bulk of the stellar mass, emit the majority of their radiation towards the near-infrared part of the electromagnetic spectrum. Ongoing surveys with the Visible-Infrared Survey Telescope for Astronomy (VISTA), the *Spitzer Space Telescope* and the *Hubble Space Telescope* (HST) are adept at tracing such emission to very high redshifts. However, tracing the current star-formation activity in distant galaxies is a much more difficult problem. This is because the hot young stars are very blue and consequently are much more susceptible to obscuration by dust, making ultra-violet and optical surveys incomplete (for a review see Madau & Dickinson 2014). Indeed, from measurements of the integrated optical and infrared background radiation we know that around 50 per cent of the light from stellar processes is obscured by dust (e.g. Takeuchi et al. 2005; Dole et al. 2006).

This property has motivated a long line of telescopes with the aim of detecting the reprocessed dust emission from these young stars at far-infrared wavelengths. The most recent of these, the *Herschel Space Observatory*, has provided a wealth of new information on the total star-formation rate (SFR) density in the Universe and how this evolves (e.g. Vaccari et al. 2010; Dye et al. 2010; Lapi et al. 2011; Burgarella et al. 2013; Gruppioni et al. 2013; Magnelli et al. 2013). However, even *Herschel* does not have the ability to track the star formation in galaxies to faint levels at high redshift, and the differences in dust temperature may also lead to systematic biases (e.g. Smith et al. 2014). The relatively poor spatial resolution means that imaging surveys with *Herschel* are confusion-noise dominated, rather than instrumental or sky-background dominated. Other types of survey such as those targeting galaxies with emission-lines excited by the young stars have also been successful, but are generally limited to either expensive follow-up spectroscopy of known galaxies (e.g. Erb et al. 2003; Gilbank et al. 2010), or narrow-band imaging campaigns that are limited in the volume that they can survey, due to the width of the specific filter (e.g. Sobral et al. 2012; Drake et al. 2013). Both of these methods are also affected by dust obscuration, and multiple lines of the same atomic species are required to obtain an estimate of the dust extinction, and thus obtain an accurate star-formation rate (SFR). Therefore, we are currently unable to obtain a clear view of the total star formation occurring over cosmic time, what galaxies this occurs in and when, and also in what environments such activity is stimulated or truncated.

As we move towards the next generation of deep radio continuum surveys, the dominant radio source population will no longer be active galactic nuclei (AGN), but star-forming galaxies (e.g. Cram et al. 1998; Haarsma et al. 2000; Afonso et al. 2005; Seymour et al. 2008; Padovani et al. 2009; McAlpine et al. 2013), although radio-quiet AGN may still make a significant contribution (e.g. Jarvis & Rawlings 2004; Simpson et al. 2006; Smolčić et al. 2009b; Bonzini et al. 2013; White et al. 2014). The radio emission from these star-forming galaxies is predominantly in the form of synchrotron emission from relativistic electrons accelerated in supernova remnants, and free-free emission from HII regions (for a review see Condon 1992). Both of these emission processes are linked to stars of masses $M \gtrsim 8$ M$_\odot$ that end in core-collapse supernovae, and dominate the ionisation of HII regions. Thus, it is not surprising that radio continuum emission, where dust

PoS(AASKA14)068

obscuration is no longer an issue, has been used to infer the SFRs of galaxies. However, current observations at high redshift are limited to stacking experiments, where only average properties of galaxies selected at other wavelengths are determined (e.g. Karim et al. 2011; Zwart et al. 2014). This constraint will be overcome with the vast sensitivity of the SKA.

Therefore, as we move into the SKA era, using the radio continuum emission to trace the star-formation history of the Universe will potentially provide us with the first unbiased view of star formation using a single waveband. Such surveys will happen on the same time frame as other major imaging facilities and multi-object spectrographs on 8-m class telescopes (see Section 7). The combination of these major facilities will enable us to investigate galaxy evolution from the perspective of both massive statistical studies, coupled with detailed studies of well-selected samples, focusing on the role of redshift, galaxy mass, environment and feedback from both supernovae and active galactic nuclei. The SKA will contribute to all of these types of study. In this chapter we provide an overview of the statistical power of the SKA in determining the history of star formation in the Universe and how this may depend on galaxy mass and environment.

2. Assumptions

In what follows we will assume that we have both the ability to disentangle star-formation from AGN emission, and photometric redshifts with an uncertainty of $\Delta z/(1+z) \sim 0.05$ up to $z \sim 6$, based on current optical and near-infrared surveys (e.g. Jarvis et al. 2013). We note that such a precision for emission-line objects is difficult but feasible over the coming decade.

We also base our estimates of the star-formation history on the luminosity functions that underpin the semi-empirical extragalactic sky simulations of Wilman et al. (2008, 2010). These simulations continue to provide a very good description of the latest source counts from various deep field surveys with the JVLA (e.g. Condon et al. 2012; Vernstrom et al. 2014). Although modifications may be required to accurately reproduce the most recent results from e.g. *Herschel*, the general trends and evolution prescribed are relatively well-matched to our current understanding, and the extrapolations to flux-density levels yet to be reached in the radio band are constrained by observations at a range of other wavelengths. For full details see Wilman et al. (2010).

The receivers being considered for both SKA1-SUR and SKA1-MID means that any observations will cover a large bandwidth of around 1 GHz, however, for ease of comparison with previous work, we adopt a single frequency. However, see Section 8 for a discussion of the impact of this assumption.

SFRs derived from radio observations have predominantly been calibrated to the integrated far-infrared emission, which is one of the most accurate and unbiased tracers of star-formation in galaxies, due to the optically thin nature of the dust to far-infrared emission (de Jong et al. 1985; Appleton et al. 2004; Ivison et al. 2010; Jarvis et al. 2010; Bourne et al. 2011). In this chapter we use the relation between star-formation rate and radio luminosity as provided by Yun et al. (2001), although we note that similar results are obtained if we use the relation of Bell (2003), to investigate how the SKA can contribute to this field.

PoS(AASKA14)068

3. The evolution of radio luminosity function of star-forming galaxies

The most straightforward experiment to trace the star-formation history of the Universe is to measure the evolution of the radio luminosity function of star-forming galaxies (e.g. Hopkins 2004; Smolčić et al. 2009a). We can then use the relation between radio luminosity and star-formation rate derived by several authors (e.g. Condon 1992; Yun et al. 2001; Bell 2003) to estimate the total star-formation rate in the galaxy.

This requires several key measurements: 1) the radio flux density, 2) the redshift of the source, 3) the fraction of radio emission that is due to star formation, rather than from an AGN. The first of these is obviously measured directly from the radio continuum emission, however 2) and 3) are more problematic. We discuss 2) in Section 7 and defer details of 3) to separate chapters (see McAlpine et al. 2015; Makhatini et al. 2015). We note that the large bandwidth will also allow in-band spectral index measurements (see e.g. Rau et al. 2014), thus removing a source of uncertainty in measuring a monochromatic rest-frame luminosity.

To address the evolution of star-forming galaxies from radio surveys, one also needs a tiered survey strategy whereby enough volume is sampled at each cosmic epoch of interest in order to overcome sample variance and gain a representative view of the Universe, from the sparsest voids through to the densest clusters. We therefore consider three tiers that we believe to be representative of the survey strategy that could be conducted with the SKA in phase 1.

In the following sections and in Figures 1, 2 and 3, we show the predicted measured radio luminosity function of star-forming galaxies for three surveys. These are based on the simulations of Wilman et al. (2008, 2010), assuming a moderate decline in the star-formation rate density at $z > 2$. Together they cover enough cosmic volume from $z = 0 \rightarrow 6$ to minimise the Poisson uncertainty, and in the case of the wide and deep surveys, sample variance (see Section 4). We note that the uncertainties on the luminosity function as presented are entirely Poissonian and therefore depend on the volume surveyed, which is why the uncertainties in Figure 1 generally exceed those on the shallower tiers in Figures 2 and 3.

3.1 Ultra Deep

A single deep pointing with the SKA1-MID will be comparable in size to the deepest fields currently surveyed at other wavelengths, although the SKA1-MID deep field would be over a somewhat wider area (1-2 deg^2) than the bulk of the ancillary data, which will come from *HST*, *JWST* and ALMA, covering optical through to far-infrared wavelengths. This may also warrant a multi-frequency approach with SKA1-MID, where we sample from the synchrotron dominant regime at low frequencies through to the free-free emission that is detectable at higher frequencies, and where the limited primary beam is not a significant problem (e.g. Murphy et al. 2015).

The key science for this tier would be to probe the extremely faint star-forming populations to the highest redshifts (well into the Epoch of Reionisation). For example, to detect a galaxy with a SFR=20 $M_\odot$ yr^{-1}at $z \sim 7$ would require a 100 nJy detection threshold (or an rms of $\sim$ 20 nJy). Such a limit would also allow detection of the star-formation occurring in dwarf galaxies (M$< 10^8$ $M_\odot$) to cosmologically significant distances (e.g. $z \sim 0.3$ for a galaxy forming stars at 0.01 $M_\odot$ yr^{-1}).

Figure 1 shows the constraints that would be achieved for the radio luminosity function from such a survey for three survey areas. We note that the primary beam of SKA1-MID at 1000 MHz

PoS(AASKA14)068

and 700 MHz are around 0.4 deg^2 and 1.5 deg^2 respectively, but utilising the full bandwidth increases the effective sensitivity substantially, at the cost of a reduced field-of-view at the top end of the frequency band. Therefore, for the ultra-deep tier we only consider a very small "single-pointing" strategy, which means that the central, highest-sensitivity part of the primary beam can be considered separately to a strategy that utilises the full area of the primary beam, which naturally has a fall off in sensitivity aligned with the beam shape. In practice alternative strategies, which involve some level of mosaicking, should be considered to ensure a more uniform sensitivity across the preferred survey area.

Figure 1 shows that sample-variance limited constraints can be made on the evolution of the star-formation in galaxies with SFR$\sim$ 10 M$_\odot$ yr^{-1} out to $z \sim 4$, and that we can determine the evolution of galaxies with SFR$\sim$ 100 M$_\odot$ yr^{-1}to $z \sim 8$. Furthermore, such surveys are feasible over $\sim$ 1 deg^2, and as such provide an interesting complement to surveys that will be carried out with the *JWST*, which will have the sensitivity to detect similar galaxies at near-infrared wavelengths.

3.2 Deep

The role of the deep survey is to provide a census of the Universe since the epoch of reionisation ($z < 6$) through to $z \sim 1$. In order to probe all environments at these redshifts a survey area of 15-30 deg^2 is required, and there are trade-offs in depth versus area that can be made within this specification. However, given that the key multi-wavelength data will come from LSST (see e.g. Bacon et al. 2015) and complementary near-infrared surveys, then it would be sensible to survey the LSST deep drilling fields, four of which are likely to be the COSMOS/UltraVISTA, XMM-LSS, CDFS and ELAIS-S1 fields. LSST will provide around 35 deg^2 over these fields with contiguous coverage over 9 deg^2 patches of sky in each.

A detection threshold sensitive to $\sim 50-100$ M$_\odot$ yr^{-1}at $z \sim 6$, suggests a flux-density limit of 0.2μJy rms over this area. In Figure 2 it is clear that a 30 deg^2 survey to a 5σ flux-density limit 1μJy will provide sample-variance limited constraints on the evolution of Milky Way-type galaxies to $z \sim 2$, whilst providing sufficient area to detect the rarest and more luminous starbursts out to the epoch of reionisation. There is evidence for the most massive galaxies at high redshifts to be more dusty than their lower-mass counterparts (e.g. Willott et al. 2013). This may give the SKA a unique niche in the study of the high-redshift Universe, because although such dusty objects could be detected by far-infrared/submm observatories, the resolution of such facilities is generally prohibitive to identifying their optical/near-infrared counterparts. Indeed, radio observations have been used to associate such sources in the past (e.g. Ivison et al. 2007; Heywood et al. 2013). Furthermore, ALMA may be very efficient at studying such galaxies in detail once they are found, but the small field-of-view of ALMA essentially precludes it from discovering the rarest and most extreme galaxies in the early Universe.

3.3 Wide

We also need to relate the findings on the high-redshift Universe from the deep tier to the lower redshift Universe, therefore we also support a wider, shallower tier that will provide a census of the $z < 1$ Universe. To sample the full range of environments at $0.3 < z < 1$ requires a few thousand square degrees. We again use a 20 M$_\odot$ yr^{-1}galaxy at $z = 1$ to determine the depth required. This

PoS(AASKA14)068

dictates a depth of around 1μJy rms (see Fig. 3). Based on the existence of ancillary data over the KIDS/VIKING area (1500 deg^2) and the Dark Energy Survey (5000 deg^2) we suggest a combination of these will provide the necessary ancillary data for the science in this tier, at least until LSST and *Euclid* are well underway.

4. The star-formation main sequence and the build-up of galaxies

Up until now we have only considered how the evolution of star formation in the Universe evolves in a general sense, and have not considered how this may be linked to the evolutionary state of the galaxy, i.e. how much stellar mass is already in place, and also how star formation may be related to environmental effects.

The past decade has seen a marked increase in the study of the relation between the stellar mass and star-formation rate in galaxies, or when considered together, the specific star-formation rate (e.g. Erb et al. 2006; Daddi et al. 2007; Noeske et al. 2007).

The power of the *Herschel Space Observatory* has also opened up a new window on the star-formation history of the Universe, providing us with a census of obscured star formation from the low-redshift Universe through to $z > 2$. One of the key results to come out of these surveys is a reinforcement of the relation between star-formation and stellar mass, the so-called star-formation main sequence (e.g. Elbaz et al. 2011; Magnelli et al. 2014; Rodighiero et al. 2014). We can use this link to estimate how radio continuum surveys with the SKA will be able to provide an in-depth understanding of the link between the stellar mass build-up, and the current star formation rate. We assume that the measurement of the stellar mass in galaxies will come from a combination of optical (e.g. DES, KIDS, LSST) and near-infrared surveys (e.g. VIKING, VIDEO, UltraVISTA) and also *Euclid*) (e.g. Ciliegi & Bardelli 2015), i.e. the same data that are also used to determine the photometric redshifts.

In Figure 4 we show the predicted average radio flux-density that would be detected from galaxies of a given mass as a function of redshift, if they lie on the star-formation main sequence, based on the work of Whitaker et al. (2012) and Johnston et al. (in prep.). This assumes an intrinsic relationship between the stellar mass of a galaxy and its star-formation rate, which evolves strongly with redshift. However, we note that the constraints beyond $z \sim 2$ are very poor and thus the form of the curves at high redshift should be considered highly uncertain, and this is borne out by the divergence in the curves at $z > 2$ using the two different studies. We note that many of the most massive galaxies do not exhibit such levels of star formation. On the other hand there is also a significant fraction of starburst galaxies that have higher star-formation rates than those galaxies on the star-formation main sequence.

Therefore, up to the redshift where the current data are constrained ($z \sim 2$), a survey flux density threshold of $S_{1\mathrm{GHz}} > 1$ μJy is sufficient to determine the SFR of a 10^9 M$_\odot$ galaxy, if it lies on the star-formation main sequence. Given that such data is free from dust extinction (cf. ultraviolet/optical measurements) and does not suffer from confusion (cf. submm/far-infrared imaging), the SKA will provide the ideal way to push the study of the relation between stellar mass and star-formation to the highest redshifts.

However, when considering the relation between star-formation rate and stellar mass, one needs to consider whether the survey covers enough cosmic volume to not be severely limited by

PoS(AASKA14)068

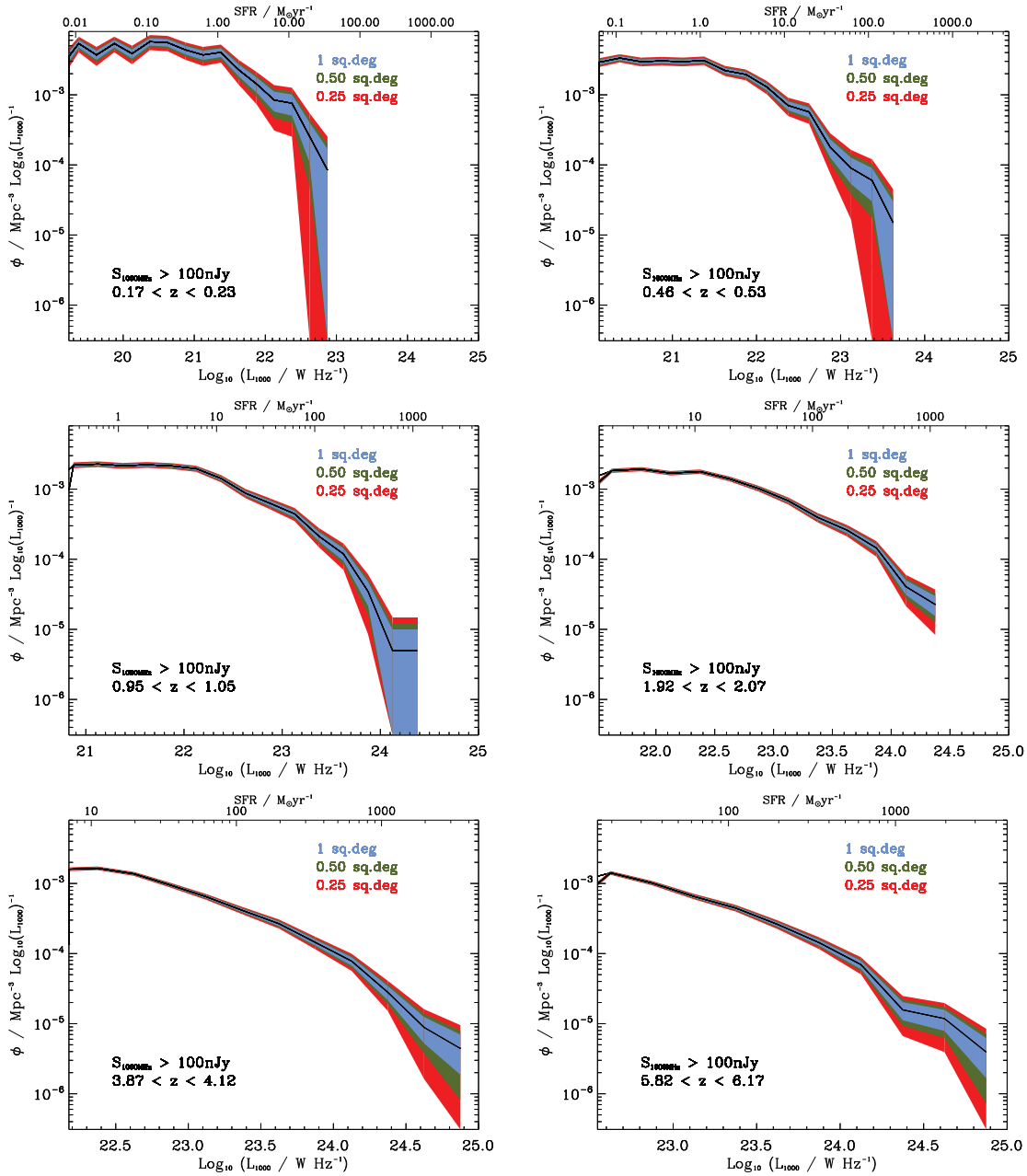

Figure 1: Radio luminosity functions (LFs) for star-forming galaxies with $\Delta(\log_{10} L_{1000}) = 0.25$, in six redshift bins of width typical of expected photometric redshift uncertainties, to a flux-density (5σ) limit of 100 nJy. The red region corresponds to the Poisson uncertainties for a 0.25 deg^2 survey, green is for 0.5 deg^2 and blue is for 1 deg^2. The upper axis shows the star-formation rate determined from the radio luminosity, extrapolated from 1.4 GHz using a spectral index of $\alpha = 0.7$. Note that the range on the abscissa-axis change from panel to panel to aid the reader in assessing the uncertainty boundaries.

PoS(AASKA14)068

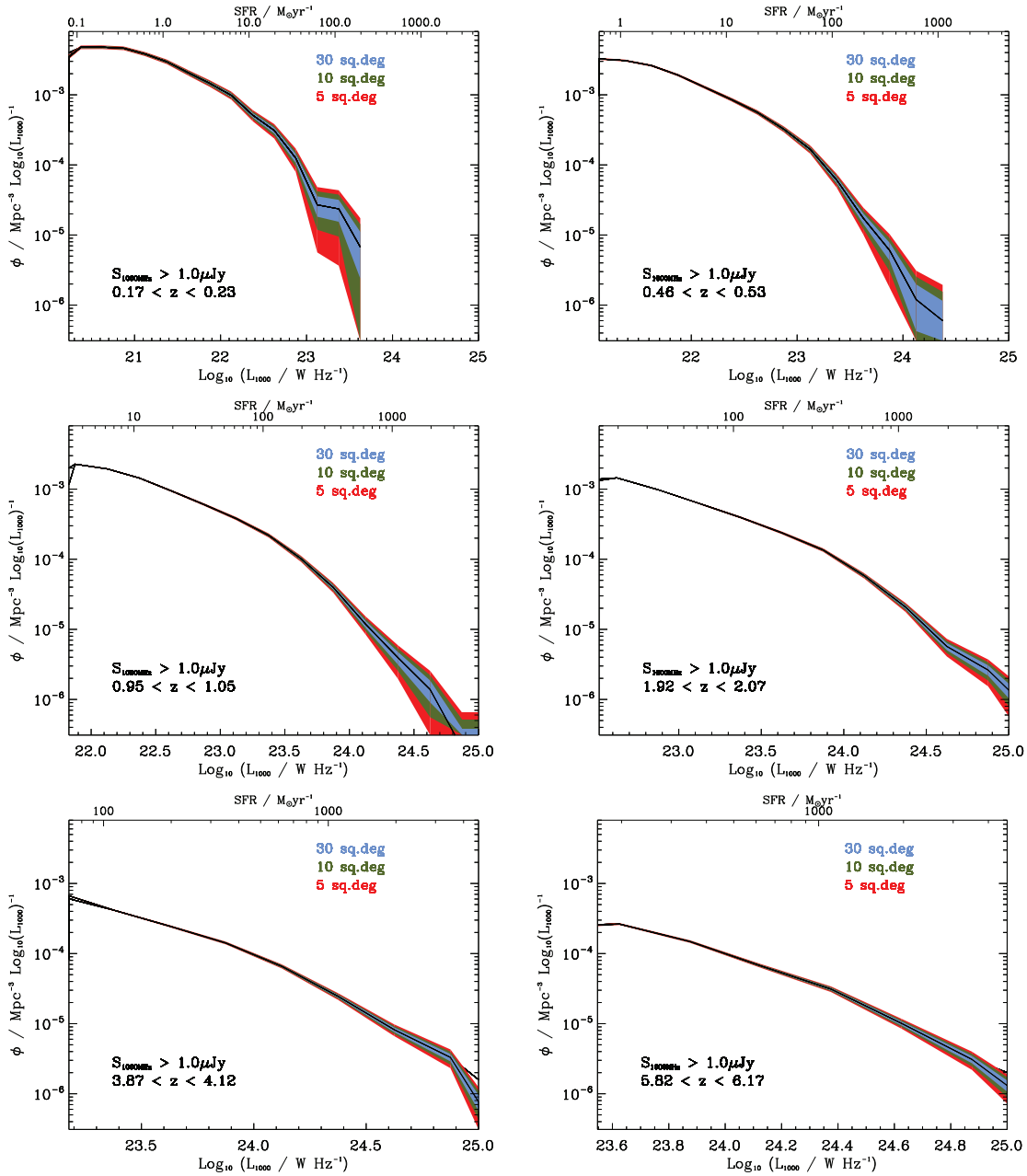

Figure 2: Radio luminosity functions (LFs) for star-forming galaxies with $\Delta(\log_{10} L_{1000}) = 0.25$, in six redshift bins of width typical of expected photometric redshift uncertainties, to a flux-density (5σ) limit of 1 μJy. The red region corresponds to the Poisson uncertainties for a 5 deg^2 survey, green is for 10 deg^2 and blue is for 30 deg^2. The upper axis shows the star-formation rate determined from the radio luminosity, extrapolated from 1.4 GHz using a spectral index of $\alpha = 0.7$. Note that the range on the abscissa-axis change from panel to panel to aid the reader in assessing the uncertainty boundaries.

PoS(AASKA14)068

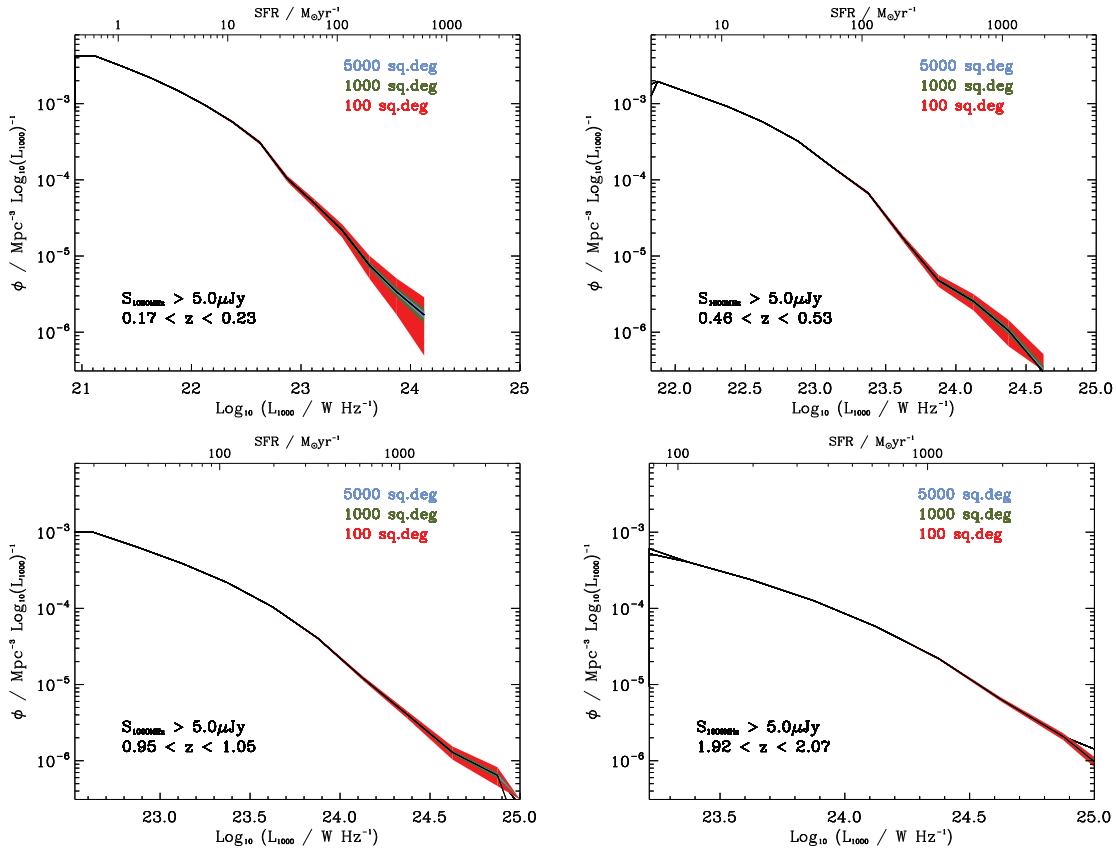

Figure 3: Radio luminosity functions (LFs) for star-forming galaxies with $\Delta(\log_{10} L_{1000}) = 0.25$, in four redshift bins of width typical of expected photometric redshift uncertainties, to a flux-density (5σ) limit of 5 μJy. The red region corresponds to the Poisson uncertainties for a 100 deg^2 survey, green is for 1000 deg^2 and blue is for 5000 deg^2. Note that the blue and green are invisible in some figures due to the Poisson uncertainties being so small. The upper axis shows the star-formation rate determined from the radio luminosity, extrapolated from 1.4 GHz using a spectral index of $\alpha = 0.7$. Note that the range on the abscissa-axis change from panel to panel to aid the reader in assessing the uncertainty boundaries.

sample variance, in particular for the most massive and highly-clustered galaxies. Therefore, in Figure 5 we show the expected level of sample variance for a given survey area as a function of redshift [of bin width $\Delta z = 0.05(1+z)$], for two values of stellar mass, using the prescription of Moster et al. (2011).

It is clear that in order to overcome significant sample variance for the most massive galaxies at $z > 1$ then a minimum of 10 deg^2 is needed. Such an area means that the sample variance is of the order of 10 per cent, but increases towards higher redshift. Thus, 30 deg^2 is a more appropriate survey area, and having this area comprised of sub-areas helps further in overcoming sample variance. Thus targeting 3-4 distinct areas that are part of the LSST deep drilling fields, covering a total area of around 30 deg^2, would provide the ideal balance between survey execution time and overcoming sample variance.

PoS(AASKA14)068

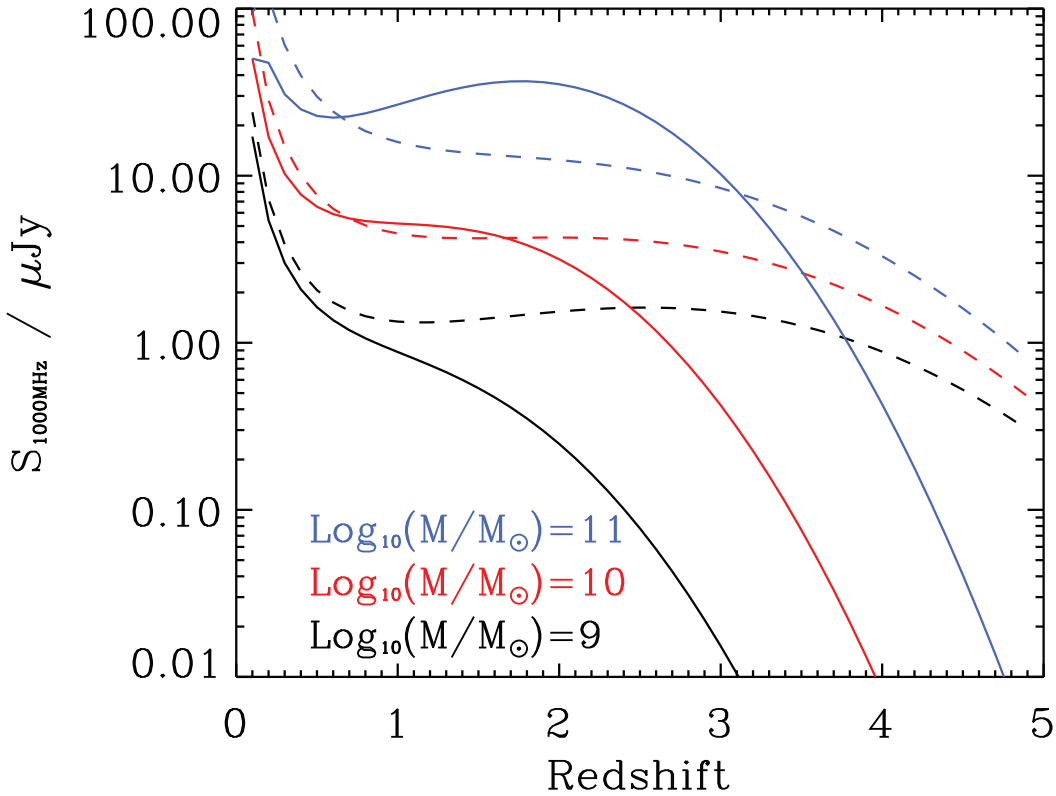

Figure 4: The radio flux-density for galaxies of 10^9, 10^{10} and 10^{11} $M_\odot$, that lie on the star-formation main sequence as modelled by Whitaker et al. (2012) (*dashed lines*) and Johnston et al. (in prep.) (*solid lines*). Note that the form of the relation at $z > 2$ is highly uncertain, which can explain the large dichotomy between the two prescriptions.

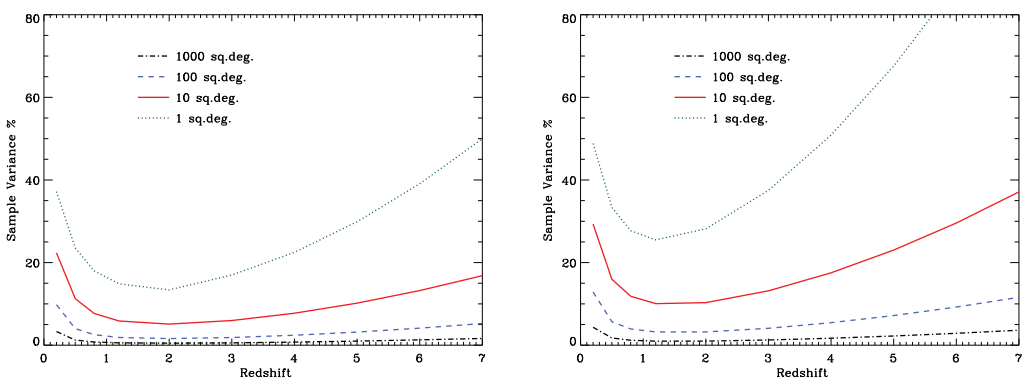

Figure 5: Percentage sample variance for massive galaxies; (*left*) 10^{10} $M_\odot$ and (*right*) 10^{11} $M_\odot$, for four surveys covering 1, 10, 100 and 1000 deg^2. Based on the prescription of Moster et al. (2011).

PoS(AASKA14)068

5. The role of environment

The specific star-formation rate has been shown to correlate with both mass and environment (e.g. Baldry et al. 2006; Scoville et al. 2013). This implies that an environmental mechanism is actively influencing galaxy evolution within the densest environments through the truncation of star formation. This raises an important consideration with respect to which correlations are actually dependent on environment and which reflect other correlations that are independent of environment. Recent studies investigating the relationship between mass and environment have concluded that the quenching effects of environment on the star-formation rate in galaxies are separable from the quenching processes traced by stellar mass. Peng et al. (2010) argue that the quenching of star formation in passive red galaxies is distinct from the general decline in the global specific star-formation rate of galaxies since $z \sim 2$. They showed that the specific SFRs of star-forming galaxies are, at most, a weak function of stellar mass and completely independent of environment. For passive galaxies however, they conclude that environment has little impact on the evolution of the most massive ($> 10^{10}$ $M_{\odot}$) galaxies, where stellar-mass related quenching dominates through feedback effects. However, for lower-mass passive galaxies ($< 10^{10}$ $M_{\odot}$), this quenching is the product of environmental interaction processes.

Therefore, surveys with the SKA, which are both sensitive enough to gain a full census of star formation in the high-redshift Universe, but also cover enough cosmic volume to sample the full range in environmental density, will provide the requisite data to significantly enhance our understanding of the evolution of galaxies. Therefore a tiered survey that samples enough cosmic volume at each epoch is required to address these issues.

6. Spatially resolving star-forming galaxies

Studies using MERLIN, Muxlow et al. (2005) have demonstrated that the typical size of high-redshift star-forming galaxies is around $0.5 - 1$ arcsec, similar to what is found at optical wavelengths. Adopting a spatial resolution at radio observations that is poorer than the complementary data at other wavelengths will weaken the impact of SKA radio continuum observations from a purely multi-wavelength perspective. However, there are extremely strong scientific reasons for requiring high resolution.

High resolution has been key for determining energetics through brightness temperature measurements of sources to distinguish between accretion and star formation (e.g. Condon et al. 1991), and to directly resolve the impact of jets on star formation in the host galaxy (e.g. McAlpine et al. 2015; Makhatini et al. 2015). To understand star formation we are required to account for the contribution from AGN, and we can only do this with a spatial resolution that allows us to resolve the global star formation activity in the host galaxy.

Furthermore, it is only by resolving such galaxies in the radio that we will be able to measure their disk-averaged star formation rates using a wavelength that is both not obscured by dust or can be confused with the underlying stellar population. When combined with observations of the molecular gas content of such systems (e.g., CO with ALMA), we are able to look for differences in gas depletion times for sources at high redshift, allowing us to investigate whether the modes of star formation in galaxy disks is actually different at high redshift relative to the local universe, for

PoS(AASKA14)068

statistically significant samples of sources. The SKA will make a huge impact in this area with the requisite long baselines.

Finally, high resolution is key to understanding star formation in the low-redshift Universe. Although not discussed in this chapter, only with < 0.5 arcsec angular resolution continuum imaging capability, the SKA will be able study the individual components of star-formation and accretion within local (< 100 Mpc) galaxies. Such a capability will allow the SKA to be transformational in this area, providing a complete census of star-formation and low to high luminosity accretion powered objects, thus allowing the study of physics of individual object and the characterisation of the role of these processes more widely within the context of galaxy evolution.

We also note that high spatial resolution is key for other extragalactic science, in galaxy evolution (e.g. Smolčić et al. 2015; McAlpine et al. 2015), strong lensing (McKean et al. 2015) and cosmology (Ferramacho et al. 2014; Brown et al. 2015; Jarvis et al. 2015).

7. The multi-wavelength requirements

The key quantity that is critical for understanding the star-formation history of the Universe derived from radio continuum observations is the redshift of the sources. Radio continuum observations generally provide no indication of the redshift, therefore we require ancillary data from a range of other wavelengths. This could be achieved with broad-band photometry and/or more precise spectroscopic redshifts from future large-format multi-object spectrographs, or indeed using the SKA itself for measuring the HI 21-cm line.

7.1 Spectroscopic redshifts

Even in 2020 it will not be possible to obtain spectroscopic redshifts for large areas of sky to the faint limits required to gain a census of star-forming galaxies. However, future spectrographs on 8-m class telescopes; e.g. Prime Focus Spectrograph (PFS) on Subaru (Takada et al. 2014), the Maunakea Spectroscopic Explorer[1] (MSE), and the Multi-Object Optical and Near-infrared Spectrograph (MOONS) on the VLT (Cirasuolo et al. 2012) may provide the survey power to gain a very good census of the radio sources in the deeper fields. In particular, at $z < 1.2$ and $z > 2.2$, PFS and MSE will have the spectral coverage at visible wavelengths to obtain emission-line redshifts based on the usual star-formation tracers, e.g. [OII], Hα etc. Both are situated in the northern hemisphere so will not be able to cover the whole of the SKA sky, however in terms of the deep fields suggested, only ELAIS-S1 at a declination of < -40 deg would be difficult to observe. Moreover, obscured systems that we detect at radio wavelengths but not at optical wavelengths will still be a problem. The proposed near-infrared multi-object spectrograph for the VLT (MOONS) could fill in some of this parameter space, with the redshift desert ($1.2 < z < 2.2$) difficult to access with optical spectrographs.

For wider and shallower surveys, the proposed 4MOST spectrograph, aiming to survey the entire southern sky in spectroscopy to $r < 22$ would provide a basis for obtaining redshifts for the brighter star-forming galaxies, predominantly in the low-redshift Universe. If 4MOST adopted a tiered survey (e.g. WAVES) whereby the integration time was well-matched to the survey strategy

[1] http://mse.cfht.hawaii.edu

PoS(AASKA14)068

for the SKA continuum survey, then it could fill the gap between the ultra-deep pointings one might expect to carry out with MOONS and PFS, and the wide-area tiers.

The additional benefit of spectroscopy over imaging is that the emission lines can be used to determine the level of AGN activity (e.g. Jackson & Rawlings 1997; Herbert et al. 2010) or star formation (e.g. Baldwin et al. 1981; Kewley et al. 2013) in the galaxy, complementing the radio data.

7.2 Photometric redshifts

The majority of the radio sources detected at these faint levels will be too faint at optical wavelengths to obtain spectroscopic redshifts. We are therefore reliant on photometric redshifts based on the deep imaging data that will be available on the same timescale as the SKA. In the early phases this will be from surveys that are currently underway, such as COSMOS/UltraVISTA (Scoville et al. 2007; McCracken et al. 2012), SXDF/UDS (Furusawa et al. 2008; Foucaud et al. 2007) and the VIDEO survey fields (Jarvis et al. 2013) for the deep surveys, and KIDS/VIKING (de Jong et al. 2013; Edge et al. 2013), DES/VHS (e.g. Banerji et al. 2014) and *WISE* (Wright et al. 2010) for the wider areas.

As we move to the full operation of SKA1 then we should also have LSST and *Euclid* imaging, which will provide very deep imaging from the g-band through to H-band across a large swathe of the southern sky. The expected photometric redshift accuracy from such surveys is $\Delta z \sim 0.05(1+z)$ and we have assumed this in our predictions for the luminosity function evolution based on the SKA continuum surveys. However, we note that it is impossible to quantify the accuracy of photometric redshifts of objects that are fainter than the limits possible with spectroscopy. Furthermore, emission-line galaxies are generally more difficult to estimate the photometric redshifts for, due to the uncertainty surrounding the strength of emission lines which pass through various filters.

In addition to the photometric redshifts, these surveys provide the necessary data from which to derive other properties of the galaxies, e.g. stellar mass, optical reddening and morphology.

8. The SKA

In this section we discuss the technical requirements of the science presented in this chapter.

The key argument revolves around the need to have high resolution, in order to avoid the confusion limit and allow the characterisation of the radio sources based on their morphology (Section 6), whilst also aiming to observe at relatively low frequency to maximise the observed flux density of the sources, due to the steep synchrotron-emission spectrum ($S_\nu \propto \nu^{0.7}$ for star-forming galaxies). This is particularly pertinent at high redshift, where the synchrotron spectrum may steepen towards high-frequency due to synchrotron losses off CMB photons (e.g. Murphy 2009). The adopted central frequency of 1000 MHz, used in this chapter corresponds to a resolution of ~ 0.4 arcsec for SKA1-MID, whereas SKA1-SUR would provide a resolution of ~ 1.5 arcsec, i.e. much larger than the typical angular extent of galaxies at $z > 0.5$.

Furthermore, given a typical spectral index of $\alpha = -0.7$[2], then sources that are detected at 20σ at 700 MHz will be detected at $\sim 12\sigma$ at 1.4 GHz in the same receiver band, with a resolution

[2] $S_\nu \propto \nu^\alpha$.

PoS(AASKA14)068

of ~ 0.3 arcsec with SKA1-MID (compared to 1 arcsec for SKA1-SUR). This will allow detailed morphologies to be measured for a large fraction of the sources using SKA1-MID, and certainly to a better accuracy than non-AO assisted ground-based optical imaging, although obviously the primary beam is smaller at 1.4 GHz compared to 700 MHz so a different survey strategy would be required to obtain uniform coverage at the higher frequency (we note that this would apply to SKA1-SUR as well if the PAF was optimised towards the lower frequency end of the band using the maximum number of beams). If SKA1-SUR was to be used then we would lose all of our ability to obtain morphological measurements of star-forming galaxies at high redshift, where the typical size is of order $0.5-1$ arcsec, and therefore much of the unique science that can be achieved with the SKA.

We also note that SKA1-MID is a faster survey instrument than SKA1-SUR at the required resolution (~ 0.5 arcsec) at all frequencies below 1.4 GHz. For a fixed resolution this advantage increases with decreasing frequency. As a resolution of 0.5 arcsec is essential for this science, then the number of sources is maximised by going to the lowest frequency.

Therefore, the combination of longer maximum baselines and higher instantaneous sensitivity makes SKA1-MID the preferred facility for this science case, as the higher surveys speeds at high frequencies for the PAF technology is negated for the majority of radio continuum science, due to ability to move to lower frequency with single-pixel feeds. For the shallower tier SKA1-SUR is more competitive, and the key limiting factor is the angular resolution.

8.1 Towards SKA1

Given that the SKA will be built up over the coming decade, in this section we highlight the preferred build-out strategy for the science case outlined above.

In order to make the most informative surveys as the SKA is expanded, then enhancing the ability to reach the full depth at the full resolution as quickly as possible will ensure that the new continuum surveys for studying the star-formation history of the Universe will surpass what is possible with the JVLA (e.g. Hales 2013; Brown et al. 2013; Jarvis et al. 2014). Initially this should be done at the expense of survey area. Given that the requisite multi-wavelength surveys will not exist to the required depth over the survey areas described in Section 3, then it makes perfect sense to start the surveys on smaller scales, but retaining the final depth. As such, for 50 per cent of SKA1-MID, surveying the 13.5 deg^2 covered by the combination of the VIDEO and UltraVISTA near-infrared surveys would provide the greatest leap in our understanding of the total star-formation rate in galaxies, over the epoch where the Universe was undergoing its most active phase at $1 < z < 4$. This would also enable the study of the environmental dependence of star formation over the vast majority of environments, and provide sufficient area in four independent fields to reduce the significant effects of sample variance.

Given that low-surface brightness sensitivity is not a key element for such surveys, then this means that in order to obtain the requisite resolution, the core of SKA1-MID could be delayed with respect to the long baselines, which are critical to retain the resolution for morphological studies and to avoid confusion at these very deep levels. This would require a similar time to complete as the full 30 deg^2 survey, as the poorer sensitivity is balanced by the reduced survey area.

PoS(AASKA14)068

8.2 SKA1

The three surveys in Section 3 could be carried out fully with SKA1-MID, providing a unique census of star formation from the local Universe through to the epoch of reionisation. The key elements of SKA1-MID are the high sensitivity, large bandwidth in Band 1 or 2, along with the high resolution at relatively low frequency, which are required to push to low star-formation rates at high redshift whilst retaining morphological information.

8.3 SKA2

SKA2, with a factor of 10 increase in sensitivity and resolution, will be unrivalled for studying the total star formation rate in galaxies. Although at this stage it would be possible to extend the deep field and ultra-deep fields described in Section 3 to much wider areas, there may be little gained if this was seen as the default approach. By the mid-2020s our understanding of the evolution of star formation will have changed significantly, and it is really the new parameter space that is most likely to add to our understanding. For example, obtaining *JWST*-like resolution over enough cosmic volume that all environments are probed, out to the highest redshifts, would be a significant advancement over the foreseeable surveys with SKA1-MID. Therefore, the highest priority in our opinion would be to; a) cover the 30 deg^2 where the best ancillary data lies, to the depth of the ultra-deep survey described above, but at a resolution of 30 milli-arcseconds. This would allow the study of star forming regions on the scale of 200 pc (i.e. the size of the Tarantula Nebula in the LMC) up to the highest redshifts, and, b) conduct ultra-deep surveys of dense regions to better understand the role of environment.

9. Conclusions

The SKA promises to be the premier facility for understanding the evolution of star formation in the Universe. Unlike optical and ultra-violet observations, the radio emission is not extinguished by dust, and thus provides a unique method to trace the total star-formation rate in galaxies. Furthermore, the resolution that is possible with the SKA surpasses what will be possible with the *JWST*, allowing morphologies and individual star-forming regions to be observed to the highest redshifts. Such observations, which will also cover enough area of sky to overcome sample variance, and allow star-formation to be studied as a function of galaxy environment, will provide the best method for understanding the build up of stellar mass in the Universe.

References

Afonso, J., Georgakakis, A., Almeida, C., Hopkins, A. M., Cram, L. E., Mobasher, B., & Sullivan, M. 2005, ApJ, 624, 135

Appleton, P. N. et al. 2004, ApJS, 154, 147

Bacon, D. et al. 2015, "Synergy between the Large Synoptic Survey Telescope and the Square Kilometre Array", in "Advancing Astrophysics with the SKA", PoS(AASKA14)145

Baldry, I. K., Balogh, M. L., Bower, R. G., Glazebrook, K., Nichol, R. C., Bamford, S. P., & Budavari, T. 2006, MNRAS, 373, 469

PoS(AASKA14)068

Baldwin, J. A., Phillips, M. M., & Terlevich, R. 1981, PASP, 93, 5
Banerji, M. et al. 2014, ArXiv.1407.3801
Bell, E. F. 2003, ApJ, 586, 794
Bonzini, M., Padovani, P., Mainieri, V., Kellermann, K. I., Miller, N., Rosati, P., Tozzi, P., & Vattakunnel, S. 2013, MNRAS, 436, 3759
Bourne, N., Dunne, L., Ivison, R. J., Maddox, S. J., Dickinson, M., & Frayer, D. T. 2011, MNRAS, 410, 1155
Brown, M. et al. 2015, "Weak gravitational lensing with the Square Kilometre Array", in "Advancing Astrophysics with the SKA", PoS(AASKA14)023
Brown, M. L. et al. 2013, ArXiv.1312.5618
Burgarella, D. et al. 2013, A&A, 554, A70
Ciliegi, P. & Bardelli, S. 2015, "Synergistic science with Euclid and SKA : the nature and history of Star Formation", in "Advancing Astrophysics with the SKA", PoS(AASKA14)150
Cirasuolo, M. et al. 2012, in Society of Photo-Optical Instrumentation Engineers (SPIE) Conference Series, Vol. 8446, Society of Photo-Optical Instrumentation Engineers (SPIE) Conference Series
Condon, J. J. 1992, ARA&A, 30, 575
Condon, J. J., Cotton, W. D., Fomalont, E. B., Kellermann, K. I., Miller, N., Perley, R. A., Scott, D., Vernstrom, T., & Wall, J. V. 2012, ApJ, 758, 23
Condon, J. J., Huang, Z.-P., Yin, Q. F., & Thuan, T. X. 1991, ApJ, 378, 65
Cram, L., Hopkins, A., Mobasher, B., & Rowan-Robinson, M. 1998, ApJ, 507, 155
Daddi, E. et al. 2007, ApJ, 670, 156
de Jong, J. T. A. et al. 2013, The Messenger, 154, 44
de Jong, T., Klein, U., Wielebinski, R., & Wunderlich, E. 1985, A&A, 147, L6
Dole, H. et al. 2006, A&A, 451, 417
Drake, A. B. et al. 2013, MNRAS, 433, 796
Dye, S. et al. 2010, A&A, 518, L10
Edge, A., Sutherland, W., Kuijken, K., Driver, S., McMahon, R., Eales, S., & Emerson, J. P. 2013, The Messenger, 154, 32
Elbaz, D. et al. 2011, A&A, 533, A119
Erb, D. K., Shapley, A. E., Steidel, C. C., Pettini, M., Adelberger, K. L., Hunt, M. P., Moorwood, A. F. M., & Cuby, J.-G. 2003, ApJ, 591, 101
Erb, D. K., Steidel, C. C., Shapley, A. E., Pettini, M., Reddy, N. A., & Adelberger, K. L. 2006, ApJ, 647, 128
Ferramacho, L. D., Santos, M. G., Jarvis, M. J., & Camera, S. 2014, MNRAS, 442, 2511
Foucaud, S. et al. 2007, MNRAS, 376, L20
Furusawa, H. et al. 2008, ApJS, 176, 1
Gilbank, D. G., Baldry, I. K., Balogh, M. L., Glazebrook, K., & Bower, R. G. 2010, MNRAS, 405, 2594
Gruppioni, C. et al. 2013, MNRAS, 432, 23
Haarsma, D. B., Partridge, R. B., Windhorst, R. A., & Richards, E. A. 2000, ApJ, 544, 641
Hales, C. A. 2013, ArXiv.1312.4602
Herbert, P. D., Jarvis, M. J., Willott, C. J., McLure, R. J., Mitchell, E., Rawlings, S., Hill, G. J., &

PoS(AASKA14)068

Dunlop, J. S. 2010, MNRAS, 406, 1841
Heywood, I., Bielby, R. M., Hill, M. D., Metcalfe, N., Rawlings, S., Shanks, T., & Smirnov, O. M. 2013, MNRAS, 428, 935
Hopkins, A. M. 2004, ApJ, 615, 209
Ivison, R. J. et al. 2007, MNRAS, 380, 199
—. 2010, A&A, 518, L31
Jackson, N. & Rawlings, S. 1997, MNRAS, 286, 241
Jarvis, M. J. et al. 2014, ArXiv.1401.4018
—. 2013, MNRAS, 428, 1281
Jarvis, M. J. & Rawlings, S. 2004, NewAR, 48, 1173
Jarvis, M. J. et al. 2015, "Cosmology with SKA Radio Continuum Surveys" in "Advancing Astrophysics with the SKA", PoS(AASKA14)018
Jarvis, M. J. et al. 2010, MNRAS, 409, 92
Karim, A. et al. 2011, ApJ, 730, 61
Kewley, L. J., Maier, C., Yabe, K., Ohta, K., Akiyama, M., Dopita, M. A., & Yuan, T. 2013, ApJL, 774, L10
Lapi, A. et al. 2011, ApJ, 742, 24
Madau, P. & Dickinson, M. 2014, ARA&A, 52, 415
Magnelli, B. et al. 2014, A&A, 561, A86
—. 2013, A&A, 553, A132
Makhatini, S., Smirnov, O., Jarvis, M., & Heywood, I. 2015, in PoS, Vol. 1, Advancing Astrophysics with the SKA
McAlpine, K., Jarvis, M. J., & Bonfield, D. G. 2013, MNRAS, 436, 1084
McAlpine, K. et al. 2015, "The SKA view of the interplay between SF and AGN Activity and its role in Galaxy Evolution", in "Advancing Astrophysics with the SKA", PoS(AASKA14)083
McCracken, H. J. et al. 2012, A&A, 544, A156
McKean, J. et al. 2015, in PoS, Vol. 1, "Advancing Astrophysics with the SKA", PoS(ASKAA14)084
Moster, B. P., Somerville, R. S., Newman, J. A., & Rix, H.-W. 2011, ApJ, 731, 113
Murphy, E. et al. 2015, "The Astrophysics of Star Formation Across Cosmic Time at >10 GHz with the Square Kilometre Array" in "Advancing Astrophysics with the SKA", PoS(AASKA14)085
Murphy, E. J. 2009, ApJ, 706, 482
Muxlow, T. W. B. et al. 2005, MNRAS, 358, 1159
Noeske, K. G. et al. 2007, ApJL, 660, L43
Padovani, P., Mainieri, V., Tozzi, P., Kellermann, K. I., Fomalont, E. B., Miller, N., Rosati, P., & Shaver, P. 2009, ApJ, 694, 235
Peng, Y.-j. et al. 2010, ApJ, 721, 193
Rau, U., Bhatnagar, S., & Owen, F. N. 2014, ArXiv.1403.5242
Rodighiero, G. et al. 2014, MNRAS, 443, 19
Scoville, N. et al. 2013, ApJS, 206, 3
—. 2007, ApJS, 172, 1
Seymour, N., Dwelly, T., Moss, D., McHardy, I., Zoghbi, A., Rieke, G., Page, M., Hopkins, A., & Loaring, N. 2008, MNRAS, 386, 1695

PoS(AASKA14)068

Simpson, C., Martínez-Sansigre, A., Rawlings, S., Ivison, R., Akiyama, M., Sekiguchi, K., Takata, T., Ueda, Y., & Watson, M. 2006, MNRAS, 372, 741
Smith, D. J. B. et al. 2014, MNRAS, 445, 2232
Smolčić, E. et al. 2015, "Exploring AGN Activity over Cosmic Time with the SKA" in "Advancing Astrophysics with the SKA", PoS(AASKA14)069
Smolčić, V. et al. 2009a, ApJ, 690, 610
—. 2009b, ApJ, 696, 24
Sobral, D., Best, P. N., Matsuda, Y., Smail, I., Geach, J. E., & Cirasuolo, M. 2012, MNRAS, 420, 1926
Takada, M. et al. 2014, PASJ, 66, 1
Takeuchi, T. T., Buat, V., & Burgarella, D. 2005, A&A, 440, L17
Vaccari, M. et al. 2010, A&A, 518, L20
Vernstrom, T., Scott, D., Wall, J. V., Condon, J. J., Cotton, W. D., Fomalont, E. B., Kellermann, K. I., Miller, N., & Perley, R. A. 2014, MNRAS, 440, 2791
Whitaker, K. E., van Dokkum, P. G., Brammer, G., & Franx, M. 2012, ApJL, 754, L29
White, S. V., Jarvis, M. J., Häußler, B., & Maddox, N. 2014, ArXiv.1410.3892
Willott, C. J. et al. 2013, AJ, 145, 4
Wilman, R. J., Jarvis, M. J., Mauch, T., Rawlings, S., & Hickey, S. 2010, MNRAS, 405, 447
Wilman, R. J. et al. 2008, MNRAS, 388, 1335
Wright, E. L. et al. 2010, AJ, 140, 1868
Yun, M. S., Reddy, N. A., & Condon, J. J. 2001, ApJ, 554, 803
Zwart, J. T. L., Jarvis, M. J., Deane, R. P., Bonfield, D. G., Knowles, K., Madhanpall, N., Rahmani, H., & Smith, D. J. B. 2014, MNRAS, 439, 1459

PoS(AASKA14)068

PROCEEDINGS OF SCIENCE

Exploring AGN Activity over Cosmic Time with the SKA

Vernesa Smolčić[*1], **Paolo Padovani**[2], **Jacinta Delhaize**[1], **Isabella Prandoni**[3], **Nicholas Seymour**[4], **Matt Jarvis**[5,6], **Jose Afonso**[7,8], **Manuela Magliocchetti**[9] **Minh Huynh**[10], **Mattia Vaccari**[6], **Alexander Karim**[11]

[1]*University of Zagreb, Physics Department, Bijenička cesta 32, 10002 Zagreb, Croatia;* [2]*European Southern Observatory, Karl-Schwarzschild-Strasse 2, 85748 Garching b. München, Germany;* [3]*INAF - Istituto di Radioastronomia, Bologna, Italy;* [4]*International Centre for Radio Astronomy Research, Curtin University, Perth, Australia;* [5] *Astrophysics, University of Oxford, Keble Road, Oxford, OX1 3RH, UK;* [6] *Physics Department, University of the Western Cape, Bellville 7535, South Africa;* [7]*Instituto de Astrofísica e Ciências do Espaço, Universidade de Lisboa, OAL, Tapada da Ajuda, PT1349-018 Lisboa, Portugal;* [8]*Departamento de Física, Faculdade de Ciências, Universidade de Lisboa, Edifício C8, Campo Grande, PT1749-016 Lisbon, Portugal;* [9]*INAF-IAPS, Via Fosso del Cavaliere 100, I-00133 Roma, Italy;* [10]*International Center for Radio Astronomy Research, M468, University of Western Australia, Crawley, WA 6009, Australia;* [11]*Argelander Institut for Astronomy, Auf dem Hügel 71, Bonn D-53121, Germany*

E-mail: vs@phy.hr

In this Chapter we present the motivation for undertaking both a wide and deep survey with the SKA in the context of studying AGN activity across cosmic time. With an rms down to 1 μJy/beam at 1 GHz over 1,000 – 5,000 deg^2 in 1 year (wide tier band 1/2) and an rms down to 200 nJy/beam over 10 – 30 deg^2 in 2000 hours (deep tier band 1/2), these surveys will directly detect faint radio-loud and radio-quiet AGN (down to a 1 GHz radio luminosity of about 2×10^{23} W/Hz at $z = 6$). For the first time, this will enable us to conduct detailed studies of the cosmic evolution of radio AGN activity to the cosmic dawn ($z \gtrsim 6$), covering all environmental densities.

Advancing Astrophysics with the Square Kilometre Array
June 8-13, 2014
Giardini Naxos, Italy

[*]Speaker.

PoS(AASKA14)069

1. Introduction

Galaxies are thought to evolve over time from an initial stage of blue star forming galaxies with spiral morphology towards quiescent red galaxies with spheroidal morphologies and the highest stellar masses (e.g., Faber et al. 2007). A galaxy evolves through interspersed episodes of intensive mass accretion onto the stellar body, as well as the central super-massive black hole (SMBH), creating a powerful active galactic nucleus (AGN; Sanders & Mirabel 1996). This is consistent with the ΛCDM paradigm, in which structure in the Universe grows hierarchically in such a way that small structures evolve into larger ones. In this context, faint ($L_{1.4GHz} < 10^{25}$ W/Hz) but still radio-loud AGN remain puzzling.[1] These faint radio loud AGN are found in red, quiescent galaxies that would not be identified as AGN at any other wavelength (e.g., Hickox et al. 2009) and they do not seem to fit into the Unified Model for AGN (e.g., Hardcastle et al. 2007). They often reside at the bottom of the galaxy cluster/group potential wells and their radio-bright outflows heat the intra-cluster/group gas and the hot gas halo of the host galaxy (e.g. Fabian 2012; Best et al. 2006). This heating, deemed crucial in cosmological models of galaxy formation, has been termed 'radio-mode' feedback (Granato et al. 2004; Croton et al. 2006; Bower et al. 2006). However, both on group/cluster and galaxy scales, feedback is still poorly understood.[2]

In the context of the most powerful AGN, Type 1 (broad line) AGN (quasars hereafter), are a population that experiences the most intense SMBH growth. Quasar winds associated with this intense SMBH growth are thought to quench their galactic star formation by expelling a fraction of the interstellar gas (so called 'quasar mode AGN feedback'; e.g. Hopkins et al. 2006). The existence of two, physically distinct, radio-loud (RL hereafter) and radio-quiet (RQ hereafter)[3] quasar populations is a long debated issue that has far-reaching implications for astrophysical models, including unified models for AGN and the evolution of star formation. Although the quasar radio-loudness distribution has been carefully studied in many different quasar samples over the past few decades (e.g. Strittmatter et al. 1980; Ivezić et al. 2002; White et al. 2000, 2007; Cirasuolo et al. 2003; Baloković et al. 2012), there is still no definite understanding or consensus. The bimodality could imply two physically distinct types of quasars (pointing to e.g. different SMBH accretion/spin mechanisms or physically different sources of synchrotron emission) or be due to differing geometries (e.g. Fanidakis et al. 2011). Furthermore, recent studies suggest that, in general, radio emission in radio-quiet AGN may arise from star formation related processes (e.g. Kimball et al. 2011; Padovani et al. 2011; Condon et al. 2012; Bonzini et al. submitted). However,

[1] For Type 1 AGN we here define radio loudness (R') following White et al. (2000) and Ivezić et al. (2002) as the logarithm of the ratio of radio-to-optical fluxes: $R' = \log \frac{F_{\rm radio}}{F_{\rm optical}} = 0.4(i-t)$ where i is the optical i-band AB magnitude and $t = -2.5 \log\left(\frac{F_{1.4GHz}}{3631\ Jy}\right)$ is the AB magnitude at 1.4 GHz. The adopted radio-loud vs. radio-quiet threshold is $R' = 1$. For Type 2 AGN we define radio-loud sources as those with $q = \log\left[(F_{\rm FIR}/3.75\times10^{12})/F_{1.4GHz}\right] < 1.7$, where $F_{\rm FIR}$ is the far-IR flux between 42.5 μm and 122.5 μm (e.g., Machalski & Condon 1999; Padovani et al. 2011) .

[2] We note that powerful ($L_{1.4GHz} > 10^{25}$ W/Hz), high-excitation AGN, that fit into the Unified model for AGN, also can exert feedback through their jets (e.g. Shabala et al. 2011; Zakamska & Greene 2014). However, cosmological models assume that 'radio-mode' feedback is cosmologically important through feedback exerted by galaxies that have reached their 'quiescent' phase of black-hole accretion (e.g. Croton et al. 2006). This 'quiescent' galaxy phase is directly linked to low-excitation radio AGN (Smolčić 2009) predominantly found at low radio luminosities (e.g. Kauffmann et al. 2008; Best & Heckman 2012).

[3] We here refer to radio luminous Type 1, broad line AGN as quasars.

PoS(AASKA14)069

this is contradicted by White et al. (2014), who find evidence for black-hole accretion still making a significant contribution to the total radio emission. We note that such studies are subject to biases in terms of the luminosity and redshift ranges studied. For example, the deep-field work of Bonzini et al. (submitted) is sensitive to fainter AGN which may be hosted in spiral galaxies which are likely to have ongoing star formation, whereas the wide-field work of Kimball et al. (2011) and Condon et al. (2012) detect the more luminous AGN, which are more likely to be hosted by massive ellipticals (e.g. Dunlop et al. 2003).

In extragalactic radio surveys, two dominant galaxy populations are observed. These are AGN and star forming galaxies. At the bright end ($\gtrsim$ 1 mJy), the GHz radio-bright sky consists mainly of "classical" radio AGN, i.e. radio quasars and radio galaxies. Their radio emission is generated from the gravitational energy associated with a SMBH and emitted through relativistic jets of particles as synchrotron radiation. Below 1 mJy there is an increasing contribution to the radio source population from massive star formation. In this case, synchrotron emission is produced via relativistic plasma ejected from supernovae. However, such star forming galaxies (SFGs) appear not to be the only component of the faint radio sky, at least down to $\sim$ 50 μJy at a few GHz (e.g., Gruppioni et al. 2003; Jarvis & Rawlings 2004; Simpson et al. 2006a; Smolčić et al. 2008; Mignano et al. 2008; Padovani et al. 2009). At the faint radio levels ($<$ 1 mJy) the source counts are still well populated by both RQ and RL AGN.

Sensitive radio continuum surveys, as will be provided with the SKA1 wide and deep tier band 1/2 surveys, are of extreme relevance for a variety of reasons: (1) Only deep radio observations trace AGN hosted by otherwise quiescent galaxies, thought to be the main drivers of the radio-mode feedback; (2) The least luminous RQ AGN reside typically in spiral galaxies, which are still forming stars, and therefore are likely to provide a vital contribution to our understanding of AGN – galaxy co-evolution; (3) Radio observations are unaffected by absorption and therefore sensitive to all types of AGN, independently of obscuration and their orientation (i.e., Type 1s and Type 2s); (4) Finally and most importantly, sensitive radio observations, that only the new-generation radio interferometers can provide, will start to detect the bulk ($\sim$ 90%) of the AGN population, currently missed by the majority of existing radio surveys (e.g. Ivezić et al. 2002; Baloković et al. 2012).

For the remainder of the Chapter we assume the following SKA1 deep and wide tier band 1/2 survey characteristics. For the wide survey we assume an rms of $\sim$ 1 μJy/beam over 1,000 – 5,000 deg^2 reached in 1 year of observations, and for the deep survey we assume an rms of 0.2 μJy/beam over 10 – 30 deg^2 for 2,000 hours of observations at an observing frequency of 1 GHz (see Prandoni & Seymour 2015, for more details on the surveys).

2. AGN activity in the faint radio sky

Radio source counts are the most straight-forward information drawn from a radio survey and are commonly used to predict source counts in future deeper surveys. They flatten below 1 mJy and are generally expected to decrease again at fainter fluxes (e.g. Hopkins et al. 2000; Wilman et al. 2008; Condon et al. 2012). In Fig. 1 we show a compilation of various survey results and the simulated results for presently unreached levels, separated for RL and RQ AGN. Various methods, all relying on multi-wavelength data, have been employed to separate the radio faint population into star forming and AGN galaxies (e.g. Smolčić et al. 2008; Seymour et al. 2008; Simpson et al.

PoS(AASKA14)069

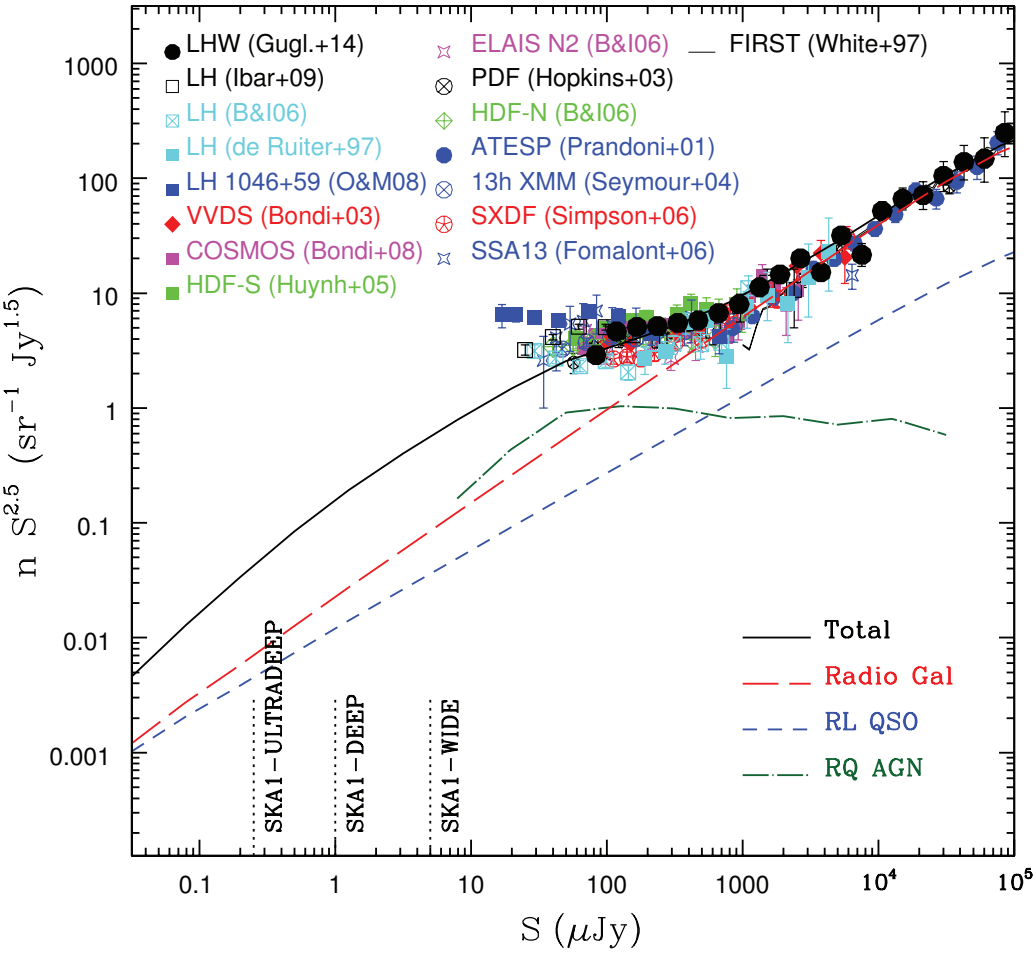

Figure 1: A compilation of observed radio source counts and simulated counts, divided into radio-loud quasars, radio-quiet AGN, and radio galaxies (as indicated in the legend, the data are taken from Guglielmino et al., in preparation; Ibar et al. 2009; Biggs & Ivison 2006; de Ruiter et al. 1997; Owen & Morrison 2008; Bondi et al. 2003, 2008; Huynh et al. 2005; Biggs & Ivison 2006; Hopkins et al. 2003; Prandoni et al. 2001; Seymour et al. 2004; Simpson et al. 2006b; Fomalont et al. 2006; White et al. 1997). The simulated counts are taken from the SKADS model (Wilman et al. 2008). Also indicated are the 5σ SKA1 wide, deep and Ultradeep limits.

2012; McAlpine et al. 2013; Bonzini et al. 2013). For example, using optical, IR, X-ray and radio data, Bonzini et al. (2013) disentangle the SFG, RQ, and RL AGN in the Extended *Chandra* deep Field South (ECDFS) survey ($\sim$ 6 μJy rms noise in a 2.8" x 1.6" beam over 0.3 deg^2 containing 900 radio sources; see also Miller et al. 2008, 2013; Bonzini et al. 2012; Padovani et al. 2011).

Fig. 2, adapted from Bonzini et al. (2013), shows the relative fractions of the various radio source classes as a function of radio flux density. As expected, AGN dominate at large flux densities ($\gtrsim$ 1 mJy). Above $\sim$ 0.1 mJy RL AGN are the predominant type of AGN, however their fractional contribution steeply decreases towards lower flux densities. On the other hand, below 0.1 mJy the radio sky is dominated by star-formation-related processes, rather than RL and/or RQ AGN. Thus, deep observations of large areas of the sky are needed to assemble statistically-sound samples of the faintest RQ and RL AGN and to study their physical properties and cosmic evolution. Such surveys will be provided by SKA1 and SKA2. At the above assumed depth and area of the wide (5000 deg^2,

PoS(AASKA14)069

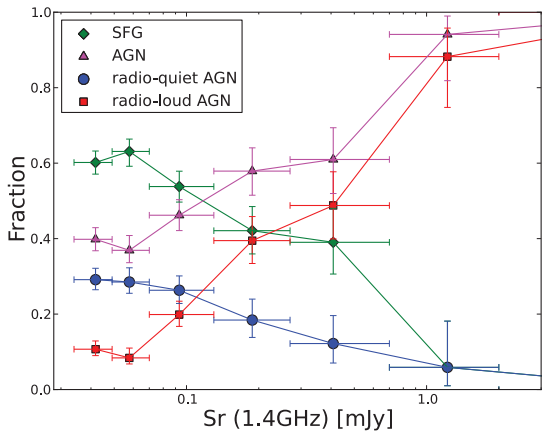

Figure 2: Relative fraction of the various classes of E-CDFS sources as a function of radio flux density: SFG (green diamonds), all AGN (magenta triangles), radio-quiet AGN (blue circles) and radio-loud AGN (red squares). Adapted from Bonzini et al. (2013).

rms ~ 1 μJy/beam) and deep (30 deg^2, rms ~ 0.2 μJy/beam) tier SKA1 surveys, about 3×10^7 and 4×10^5 AGN, respectively, are predicted using the SKADS (Wilman et al. 2008, 2010) simulations of the extragalactic radio sky based on models of the evolution of the radio luminosity function. This is orders of magnitude larger than the number of sources detected in the deepest radio surveys to-date, e.g. COSMOS (rms $\sim 10-15$ μJy/beam, 2 deg^2, $\sim 2,500$ sources, Schinnerer et al. 2007, 2010) and ECDFS (rms ~ 6 μJy/beam, 0.3 deg^2, ~ 900 sources, Miller et al. 2008, 2013). For comparison, MeerKAT-MIGHTEE (rms ~ 1 μJy/beam, 35 deg^2, 1.4 GHz) is expected to detect about 174,000 AGN, while ASKAP-EMU (rms ~ 10 μJy/beam, 30,000 deg^2, 1.4 GHz) will detect $\sim 2.8 \times 10^7$ AGN.

2.1 Radio emission in radio-quiet AGN

RQ AGN are characterized by relatively low radio-to-optical flux density ratios and radio powers and, until recently, have been found predominantly in optically selected samples. We note that the distinction between RQ and RL AGN is not simply a matter of semantics - the two classes represent intrinsically different objects. RL AGN emit most of their energy over the entire electromagnetic spectrum non-thermally and in association with powerful relativistic jets. The multi-wavelength emission of RQ AGN is dominated by thermal emission and is related to the accretion disk. The exact mechanism responsible for radio emission in RQ AGN has been a matter of debate for the past fifty years. Explanations have included, for example, a scaled down version of the RL AGN mechanism (e.g., Miller et al. 1993; Ulvestad et al. 2005), and star formation (Sopp & Alexander 1991).

There is still no clear consensus on the existence of a bimodality in the radio-loudness distribution of quasars. A bimodality would imply two physically distinct types of quasars in the Universe and would point to, for instance, different SMBH accretion/spin mechanisms, geometries or physical properties (e.g. Fanidakis et al. 2011; Kimball et al. 2011; Condon et al. 2013). This issue is still open mainly due to the overwhelmingly high fraction of RQ quasars that regularly go undetected

PoS(AASKA14)069

in radio surveys. As shown in Fig. 3 all current radio surveys (even the deepest ones) barely sample even the loudest end of the radio-quiet part of the distribution. Hence, as only $\sim 10\%$ of optically selected quasars are RL (e.g. Ivezić et al. 2002), this means that a major fraction of quasars still remains undetected and unexplored at radio wavelengths (see also Baloković et al. 2012). Only observations of large sky areas to the depths reachable with the SKA1 deep and wide surveys will directly reveal the radio properties of roughly 90% of optically detected quasars.

Recent studies of radio-quiet AGN suggest different radio emitting mechanisms in RL and RQ AGN (e.g. Kimball et al. 2011; Padovani et al. 2011; Condon et al. 2013; Bonzini et al. 2013). For example, investigating the cosmic evolution of RQ AGN and SFGs, the results presented in Padovani et al. (2011) suggest very close ties between star formation and radio emission in RQ AGN at $z \sim 1.5-2$. They find that the evolution of RQ AGN is similar to that of SFG (see also Smolčić et al. 2009b, and references therein) and that their luminosity function appears to be an extension of the SFG LF (see also Kimball et al. 2011; Condon et al. 2013). If RQ AGN were simply scaled-down versions of RL AGN, it could be expected that they share the evolutionary properties of the latter and their luminosity function should also be an extrapolation of the RL luminosity function at low powers, however this does not appear to be the case (e.g. Fernandes et al. 2011). This has prompted studies of the emission mechanism of synchrotron radiation from RQ AGN. For example, Kimball et al. (2011); Padovani et al. (2011); Condon et al. (2013); Bonzini et al. (2013) suggest that star formation in the host galaxy of RQ AGN may be the dominant contributor to the radio continuum emission, whereas White et al. (2014) compare the radio emission from a sample of faint radio-quiet quasars with the massive galaxy population, and suggest that the radio emission in optically-selected radio-quiet quasars is consistent with being due to the AGN. These studies envelope different luminosity (both optical and radio) and redshift ranges, and some of the differences may be attributable to to the diversity of the samples. Furthermore, a close link between star formation and radio emission in RQ AGN is further affirmed by the comparison of the star formation rates (SFRs) derived from the far-IR luminosities and the radio luminosities, assuming that all the radio emission is due to star formation (Bonzini et al. submitted). For RQ AGN and SFGs, the two SFR estimates are consistent. For RL AGN, the agreement is poor due to the large contribution of the relativistic jet to their radio luminosity (Morić et al. 2010; Bonzini et al. submitted). Another intriguing possibility is that both AGN and SF processes contribute to the total radio (and IR) emission, in some relative proportion (e.g. Morić et al. 2010). Seyfert 2 galaxies are a well-established example in the local Universe (e.g. Roy et al. 1998) and recent studies indicate that composite AGN/SF systems may constitute a significant fraction of the galaxy population at high redshifts (e.g. Daddi et al. 2007; Gruppioni et al. 2011; Del Moro et al. 2013).

The SKA1 wide and deep surveys, in conjunction with multi-wavelength data will provide the basis to resolve the long-standing quasar radio-loudness dichotomy, and the possible interplay between coexisting AGN and star formation phenomena. However, only once star-formation and AGN activity are reliably separated, and/or their fractional contribution to individual sources is determined, it is possible to derive unbiased radio luminosity functions and disentangle the contributions of each type of activity over cosmic time via direct radio detections and stacking in the radio map (e.g. Smolčić et al. 2008; Karim et al. 2011; Zwart et al. 2014).

PoS(AASKA14)069

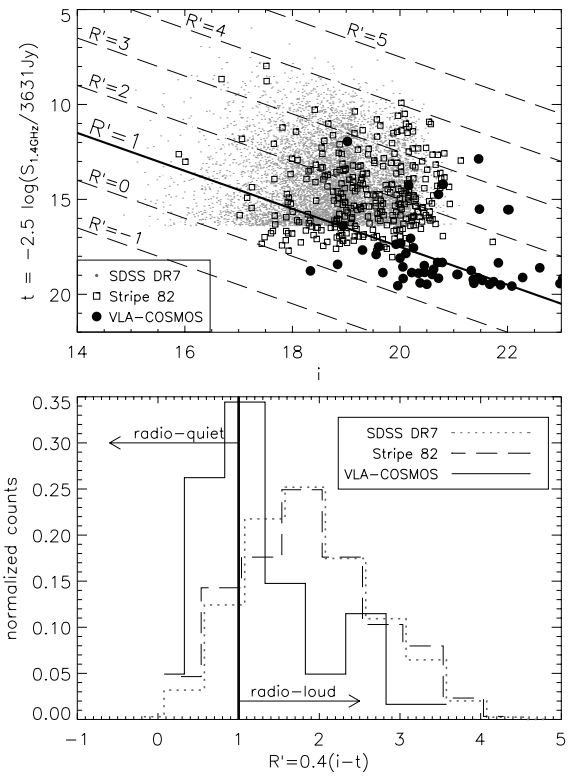

Figure 3: Top: *i*-band vs. 1.4 GHz radio magnitude (t) distribution for optically selected quasars (i.e. broad line AGN) drawn from current state-of-the-art surveys: SDSS DR7 - FIRST ($\sim 9,000$ deg^2, $S_{1.4\mathrm{GHz}} \gtrsim 1$ mJy; Schneider et al. 2010), Stripe 82 (92 deg^2, $S_{1.4\mathrm{GHz}} \gtrsim 260$ μJy; Hodge et al. 2011), and COSMOS (2 deg^2, $S_{1.4\mathrm{GHz}} \gtrsim 12$ μJy; Schinnerer et al. 2007, 2010; Lilly et al. 2007, 2009). The bottom panel shows the distribution of radio loudness, $R' = 0.4(i-t)$, for quasars in these three surveys.

3. Radio-loud AGN: Relevance for feedback in massive galaxy formation

By now, negative AGN feedback has become a standard ingredient in semi-analytic models and is required to reproduce the observed galaxy properties (e.g. Granato et al. 2004; Croton et al. 2006; Bower et al. 2006; Sijacki et al. 2007). In the models, this type of feedback, referred to as radio-mode feedback, is related to radio AGN outflows as the main source that heats the gas halo surrounding a massive galaxy. This heating thereby quenches the star formation and limits growth, thus avoiding the creation of overly high-mass galaxies. A detailed description of radio feedback is given in McAlpine et al. (2015).

The first observational support for AGN feedback was found using the combination of radio and X-ray data by McNamara et al. (2000), and Best et al. (2006) quantitatively showed that, in the local Universe, radio outflows may indeed balance the radiative cooling of the hot gas surrounding elliptical galaxies. Furthermore, it has been both theoretically postulated and observationally supported that this 'radio-mode' heating occurs during a quiescent phase of black-hole accretion

PoS(AASKA14)069

(presumably via advection dominated accretion flows) and manifests as low-power radio AGN activity ($L_{1.4GHz} < 10^{25}$ W/Hz; Evans et al. 2006; Hardcastle et al. 2006, 2007; Kauffmann et al. 2008; Smolčić et al. 2009a; Smolčić 2009; Smolčić & Riechers 2011). Such low-power radio AGN, and the evolution of their comoving volume density (i.e. their radio luminosity function) through cosmic times, can be studied in detail only via simultaneously deep and large radio surveys with supplementary panchromatic data (Sadler et al. 2007; Donoso et al. 2009; Smolčić et al. 2009b; Simpson et al. 2012; McAlpine et al. 2013).

To date, the 20 cm radio luminosity function for low radio power AGN ($L_{1.4GHz} \lesssim 10^{25}$ W/Hz) has been mostly derived out to $z = 1.3$ (Sadler et al. 2007; Donoso et al. 2009; Smolčić et al. 2009b; Simpson et al. 2012; McAlpine et al. 2013). This also provided the first direct, radio-based, (albeit uncertain) observational support for radio-mode AGN feedback beyond the local universe (Smolčić et al. 2009b). This is illustrated in Figures 4 and 5. In Fig. 4 we show the 1.4 GHz radio luminosity functions for red, quiescent galaxies drawn from the COSMOS two square degree survey (Scoville et al. 2007; Ilbert et al. 2010) out to $z = 3$ (Smolčić et al., in prep). The luminosity functions were derived from the VLA-COSMOS 1.4 GHz Large Project (Schinnerer et al. 2007) reaching an rms of 10(15) μJy/beam over an area of 1(2) deg^2. Stacking of the red, quiescent host galaxy population, selected following Ilbert et al. (2010), in the radio map constrained the luminosity function beyond $z = 1.3$. The monochromatic luminosity was then converted to a kinetic power via scaling relations drawn from Bîrzan et al. (2008) and O'Sullivan et al. (2011). Integrating over the kinetic power averaged over comoving volume then yielded the heating rate exerted by radio luminous AGN onto their surroundings as a function of cosmic time out to $z = 3$, as shown in Fig. 5 (see e.g. Smolčić et al. 2009b, for details). We stress that the result strongly depends on the i) knowledge of the low-luminosity end of the RL AGN luminosity function, and ii) conversion between monochromatic radio luminosity and kinetic power. As shown in the top panel of Fig. 5 when using the Bîrzan et al. scaling relation to convert between monochromatic radio luminosity and kinetic power the overall heating curve systematically rises depending on the low-luminosity boundary applied to the integral. This clearly illustrates the importance of both, i) constraining the conversion between monochromatic radio luminosity and kinetic power, and ii) constraining the luminosity functions of low-power radio AGN with high precision, especially at the low-luminosity end and out to the highest redshifts possible. The first is described in more detail in Kapińska et al. (2015), and the latter, a topic of this Chapter, will be possible to resolve with the SKA1 deep and wide continuum surveys, in conjunction with deep multi-wavelength data-sets. The assumed 5σ limits of the wide and deep SKA1 surveys correspond to a 1.4 GHz luminosity limit of 10^{23} W/Hz (wide) and 2×10^{22} W/Hz (deep) at $z = 2$, and 10^{24} W/Hz (wide) and 2×10^{23} W/Hz (deep) at $z = 6$. This will allow a direct examination of the faint end of the radio AGN luminosity function. Stacking in the radio maps will push this limit even further, while SKA2 will provide an order of magnitude push in sensitivity and determination of the faint end of the radio AGN luminosity function, as illustrated in Figs. 6 and 7.

4. Studying AGN activity over cosmic time with the SKA

SKA1 will provide a vital contribution to the science cases described above. Based on the SKADS (Wilman et al. 2008, 2010) simulation the SKA1 wide survey (assuming an rms of $\sim$

PoS(AASKA14)069

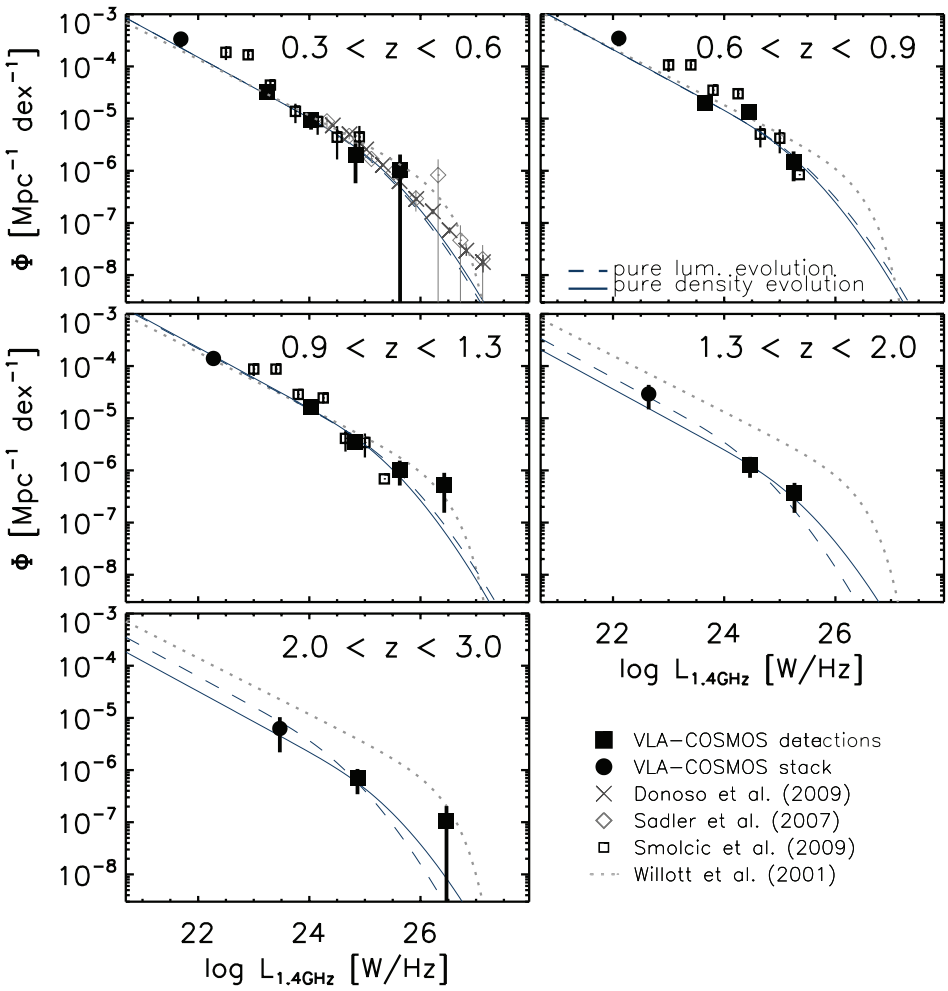

Figure 4: Radio luminosity functions (LFs) in five redshift bins out to $z = 3$ for quiescent galaxies in the COSMOS field with stellar masses $M_* \gtrsim 3 \times 10^{10}$ $M_\odot\,yr^{-1}$ (Ilbert et al. 2010, filled circles and squares). The volume densities derived based on a volume limited radio detected sample are shown by the filled black squares, while those based on stacked data are shown by the filled black circles. The (full and dashed) lines show the best fit evolution to the COSMOS data in a given redshift range (blue curves) using the Sadler et al. (2002) local LF (dashed line: pure luminosity evolution; full line: pure density evolution). Various results from the literature, indicated in the legend, are also shown.

1 μJy/beam over 5000 deg^2 achieved in 1 year of observations) is expected to detect about 3×10^7, while the SKA1 deep survey (assuming an rms of 0.2 μJy/beam over 30 deg^2 for 2000 hours of observations) is expected to detect 4×10^5 AGN at 1 GHz. SKA2 will provide 10$\times$ higher sensitivities at this frequency. The results discussed above can serve as a path-finder for SKA survey planning, outlined as follows:

- At flux densities $\lesssim 100$ μJy, most sources will be SFGs and most AGN will be of the radio-quiet type. Since the radio emission of these two classes may be powered by the same

PoS(AASKA14)069

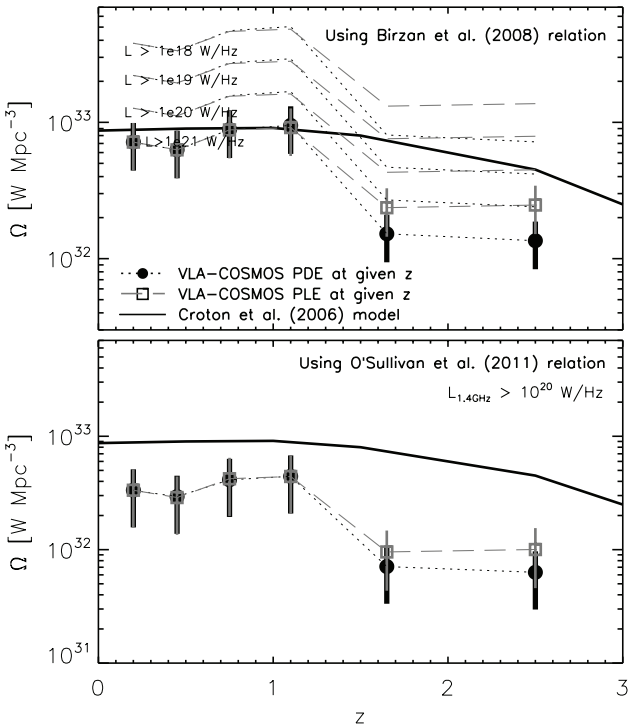

Figure 5: Comoving volume averaged heating rate (Ω) performed by quiescent massive galaxies in the COSMOS field as a function of redshift. Ω was derived by integrating the kinetic power per comoving volume over radio luminosity (see Smolčić et al. 2009b, for details). The COSMOS data points were derived by assuming pure density (filled circles), and pure luminosity (open squares) evolution best fit to the data in a given redshift bin. The upper and lower panels show Ω when using the relation between kinetic and 1.4 GHz radio luminosity from Bîrzan et al. (2008) and O'Sullivan et al. (2011), respectively. The (dotted and dashed) lines in the upper panel illustrate the discrepancy in Ω if various lower limit integral values are assumed (indicated in the panel). No such discrepancy is present when using the O'Sullivan et al. (2011) relation. The thick solid line in both panels shows the 'radio-mode feedback' heating rate drawn from the Croton et al. (2006) cosmological model, and required to reproduce observed galaxy properties.

mechanism pure continuum radio observations alone will not be able to distinguish between these populations;

- The classification of SKA radio sources will require ancilliary, multi-wavelength information. The location of the SKA surveys will therefore need to be planned carefully, in conjunction with existing and planned multi-wavelength surveys;
- The radio band, at sensitivities that will be provided by the SKA, carries the potential of becoming the optimal band to study the evolution of the most common types of AGN (the radio-quiet ones) given that radio emission is simultaneously insensitive to dust and provides high angular resolution, contrary to most other wavelength regimes;
- The SKA1 wide and deep surveys, in conjunction with multi-wavelength data will provide the basis to resolve the long-standing quasar radio-loudness dichotomy, unambiguously de-

PoS(AASKA14)069

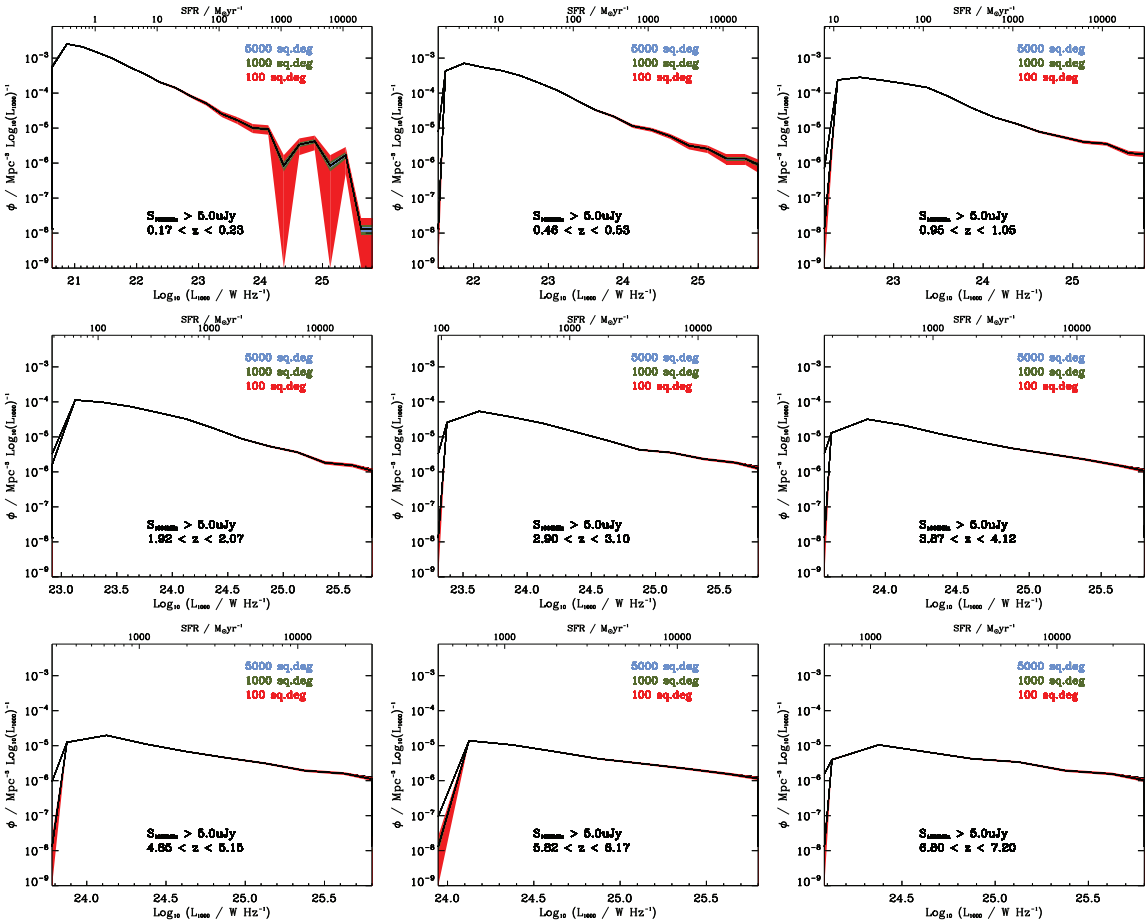

Figure 6: Radio AGN luminosity functions in various redshift bins (indicated in the panels) predicted for the wide SKA1 tier based on the SKADS simulations (Wilman et al. 2008, 2010).

termine the source of radio-emission in RQ AGN, and study the cosmic evolution of faint radio AGN out to the highest redshifts ($z \sim 6$);

- Radio surveys have reached such depths that they are now dominated by the same galaxies detected by IR, optical and X-ray surveys. As a result, the SKA radio surveys will be an increasingly important component of multi-wavelength studies of galaxy formation and evolution and will therefore be useful to a very broad community.

Acknowledgments

VS acknowledges support from the European Union's Seventh Frame-work program under grant agreements 337595 and 333654. MJJ and MV acknowledge support by the South African Square Kilometre Array Project, the South African National Research Foundation. J.A. gratefully acknowledges support from the Science and Technology Foundation (FCT, Portugal) through the research grant PTDC/FIS-AST/2194/2012 and PEst-OE/FIS/UI2751/2014.

PoS(AASKA14)069

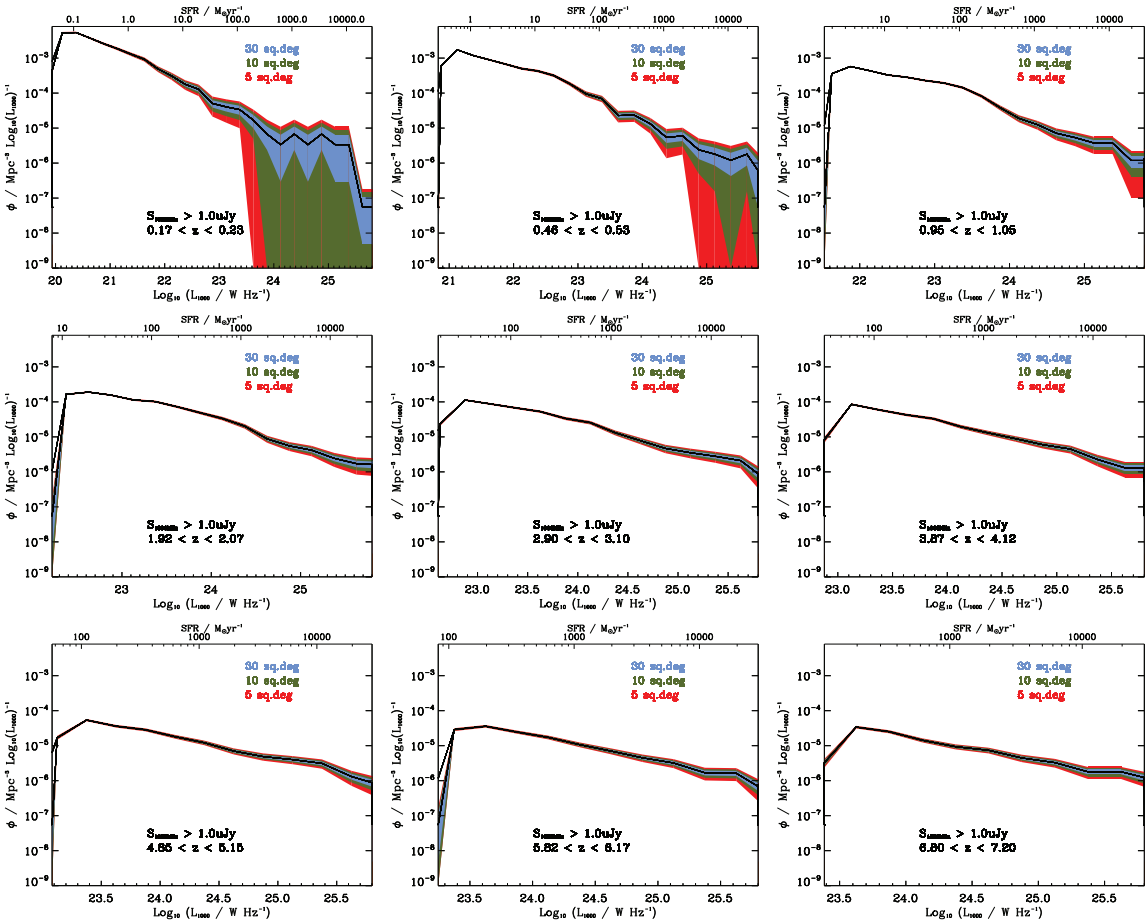

Figure 7: Radio AGN luminosity functions in various redshift bins (indicated in the panels) predicted for the deep SKA1 tier based on the SKADS simulations (Wilman et al. 2008, 2010).

References

Baloković, M., Smolčić, V., Ivezić, Ž., et al. 2012, ApJ, 759, 30
Best, P. N., & Heckman, T. M. 2012, MNRAS, 421, 1569
Best, P. N., Kaiser, C. R., Heckman, T. M., & Kauffmann, G. 2006, MNRAS, 368, L67
Biggs, A. D., & Ivison, R. J. 2006, MNRAS, 371, 963
Bîrzan, L., McNamara, B. R., Nulsen, P. E. J., Carilli, C. L., & Wise, M. W. 2008, ApJ, 686, 859
Bondi, M., Ciliegi, P., Schinnerer, E., et al. 2008, ApJ, 681, 1129
Bondi, M., Ciliegi, P., Zamorani, G., et al. 2003, A&A, 403, 857
Bonzini, M., Padovani, P., Mainieri, V., et al. 2013, MNRAS, 436, 3759
Bonzini, M., Mainieri, V., Padovani, P., et al. 2012, ApJSS, 203, 15
—. submitted, MNRAS
Bower, R. G., Benson, A. J., Malbon, R., et al. 2006, MNRAS, 370, 645
Cirasuolo, M., Magliocchetti, M., Celotti, A., & Danese, L. 2003, MNRAS, 341, 993
Condon, J. J., Kellermann, K. I., Kimball, A. E., Ivezić, Ž., & Perley, R. A. 2013, ApJ, 768, 37
Condon, J. J., Cotton, W. D., Fomalont, E. B., et al. 2012, ApJ, 758, 23

PoS(AASKA14)069

Croton, D. J., Springel, V., White, S. D. M., et al. 2006, MNRAS, 365, 11
Daddi, E., Alexander, D. M., Dickinson, M., et al. 2007, ApJ, 670, 173
de Ruiter, H. R., Zamorani, G., Parma, P., et al. 1997, A&A, 319, 7
Del Moro, A., Alexander, D. M., Mullaney, J. R., et al. 2013, A&A, 549, A59
Donoso, E., Best, P. N., & Kauffmann, G. 2009, MNRAS, 392, 617
Dunlop, J. S., McLure, R. J., Kukula, M. J., et al. 2003, MNRAS, 340, 1095
Evans, D. A., Worrall, D. M., Hardcastle, M. J., Kraft, R. P., & Birkinshaw, M. 2006, ApJ, 642, 96
Faber, S. M., Willmer, C. N. A., Wolf, C., et al. 2007, ApJ, 665, 265
Fabian, A. C. 2012, ARAA, 50, 455
Fanidakis, N., Baugh, C. M., Benson, A. J., et al. 2011, MNRAS, 410, 53
Fernandes, C. A. C., Jarvis, M. J., Rawlings, S., et al. 2011, MNRAS, 411, 1909
Fomalont, E. B., Kellermann, K. I., Cowie, L. L., et al. 2006, ApJSS, 167, 103
Granato, G. L., De Zotti, G., Silva, L., Bressan, A., & Danese, L. 2004, ApJ, 600, 580
Gruppioni, C., Pozzi, F., Zamorani, G., et al. 2003, MNRAS, 341, L1
Gruppioni, C., Pozzi, F., Zamorani, G., & Vignali, C. 2011, MNRAS, 416, 70
Hardcastle, M., Evans, D., & Croston, J. 2007, MNRAS, 376, 1849
Hardcastle, M. J., Evans, D. A., & Croston, J. H. 2006, MNRAS, 370, 1893
Hickox, R. C., Jones, C., Forman, W. R., et al. 2009, ApJ, 696, 891
Hodge, J. A., Becker, R. H., White, R. L., Richards, G. T., & Zeimann, G. R. 2011, AJ, 142, 3
Hopkins, A., Georgakakis, A., Cram, L., Afonso, J., & Mobasher, B. 2000, ApJSS, 128, 469
Hopkins, A. M., Afonso, J., Chan, B., et al. 2003, AJ, 125, 465
Hopkins, P. F., Somerville, R. S., Hernquist, L., et al. 2006, ApJ, 652, 864
Huynh, M. T., Jackson, C. A., Norris, R. P., & Prandoni, I. 2005, AJ, 130, 1373
Ibar, E., Ivison, R. J., Biggs, A. D., et al. 2009, MNRAS, 397, 281
Ilbert, O., Salvato, M., Le Floc'h, E., et al. 2010, ApJ, 709, 644
Ivezić, Ž., Menou, K., Knapp, G. R., et al. 2002, AJ, 124, 2364
Jarvis, M. J., & Rawlings, S. 2004, New Astronomy Reviews, 48, 1173
Kapińska, A. D., Hardcastle, M. J., Jackson, C. A., et al. 2015, "Unravelling lifecycles and physics of radio-loud AGN in the SKA Era", in "Advancing Astrophysics with the Square Kilometre Array", PoS(AASKA14)173
Karim, A., Schinnerer, E., Martínez-Sansigre, A., et al. 2011, ApJ, 730, 61
Kauffmann, G., Heckman, T. M., & Best, P. N. 2008, MNRAS, 384, 953
Kimball, A. E., Kellermann, K. I., Condon, J. J., Ivezić, Ž., & Perley, R. A. 2011, ApJL, 739, L29
Lilly, S. J., Le Fèvre, O., Renzini, A., et al. 2007, ApJSS, 172, 70
Lilly, S. J., Le Brun, V., Maier, C., et al. 2009, ApJSS, 184, 218
McAlpine, K., Jarvis, M. J., & Bonfield, D. G. 2013, MNRAS, 436, 1084
McAlpine, K., Prandoni, I., Jarvis, M., et al. 2015, "The SKA view of the Interplay between SF and AGN Activity and its role in Galaxy Evolution", in "Advancing Astrophysics with the Square Kilometre Array", PoS(AASKA14)083
McNamara, B. R., Wise, M., Nulsen, P. E. J., et al. 2000, ApJL, 534, L135
Mignano, A., Prandoni, I., Gregorini, L., et al. 2008, A&A, 477, 459
Miller, N. A., Fomalont, E. B., Kellermann, K. I., et al. 2008, ApJSS, 179, 114
Miller, N. A., Bonzini, M., Fomalont, E. B., et al. 2013, ApJSS, 205, 13

PoS(AASKA14)069

Miller, P., Rawlings, S., & Saunders, R. 1993, MNRAS, 263, 425
Morić, I., Smolčić, V., Kimball, A., et al. 2010, ApJ, 724, 779
O'Sullivan, E., Giacintucci, S., David, L. P., et al. 2011, ApJ, 735, 11
Owen, F. N., & Morrison, G. E. 2008, AJ, 136, 1889
Padovani, P., Mainieri, V., Tozzi, P., et al. 2009, ApJ, 694, 235
Padovani, P., Miller, N., Kellermann, K. I., et al. 2011, ApJ, 740, 20
Prandoni, I., Gregorini, L., Parma, P., et al. 2001, A&A, 365, 392
Prandoni, I., & Seymour, N. 2015, "Revealing the Physics and Evolution of Galaxies and Galaxy Clusters with SKA Continuum Surveys", in "Advancing Astrophysics with the Square Kilometre Array", PoS(AASKA14)067
Roy, A. L., Norris, R. P., Kesteven, M. J., Troup, E. R., & Reynolds, J. E. 1998, MNRAS, 301, 1019
Sadler, E. M., Jackson, C. A., Cannon, R. D., et al. 2002, MNRAS, 329, 227
Sadler, E. M., Cannon, R. D., Mauch, T., et al. 2007, MNRAS, 381, 211
Sanders, D. B., & Mirabel, I. F. 1996, ARAA, 34, 749
Schinnerer, E., Smolčić, V., Carilli, C. L., et al. 2007, ApJSS, 172, 46
Schinnerer, E., Sargent, M. T., Bondi, M., et al. 2010, ApJSS, 188, 384
Schneider, D. P., Richards, G. T., Hall, P. B., et al. 2010, AJ, 139, 2360
Scoville, N., Aussel, H., Brusa, M., et al. 2007, ApJSS, 172, 1
Seymour, N., McHardy, I. M., & Gunn, K. F. 2004, MNRAS, 352, 131
Seymour, N., Dwelly, T., Moss, D., et al. 2008, MNRAS, 386, 1695
Shabala, S. S., Kaviraj, S., & Silk, J. 2011, MNRAS, 413, 2815
Sijacki, D., Springel, V., Di Matteo, T., & Hernquist, L. 2007, MNRAS, 380, 877
Simpson, C., Martínez-Sansigre, A., Rawlings, S., et al. 2006a, MNRAS, 372, 741
—. 2006b, MNRAS, 372, 741
Simpson, C., Rawlings, S., Ivison, R., et al. 2012, MNRAS, 421, 3060
Smolčić, V. 2009, ApJL, 699, L43
Smolčić, V., & Riechers, D. A. 2011, ApJ, 730, 64
Smolčić, V., Schinnerer, E., Scodeggio, M., et al. 2008, ApJSS, 177, 14
Smolčić, V., Zamorani, G., Schinnerer, E., et al. 2009a, ApJ, 696, 24
Smolčić, V., Schinnerer, E., Zamorani, G., et al. 2009b, ApJ, 690, 610
Sopp, H. M., & Alexander, P. 1991, MNRAS, 251, 14P
Strittmatter, P. A., Hill, P., Pauliny-Toth, I. I. K., Steppe, H., & Witzel, A. 1980, A&A, 88, L12
Ulvestad, J. S., Antonucci, R. R. J., & Barvainis, R. 2005, ApJ, 621, 123
White, R. L., Becker, R. H., Helfand, D. J., & Gregg, M. D. 1997, ApJ, 475, 479
White, R. L., Helfand, D. J., Becker, R. H., Glikman, E., & de Vries, W. 2007, ApJ, 654, 99
White, R. L., Becker, R. H., Gregg, M. D., et al. 2000, ApJSS, 126, 133
White, S. V., Jarvis, M. J., Häußler, B., & Maddox, N. 2014, ArXiv e-prints, arXiv:1410.3892
Wilman, R. J., Jarvis, M. J., Mauch, T., Rawlings, S., & Hickey, S. 2010, MNRAS, 405, 447
Wilman, R. J., Miller, L., Jarvis, M. J., et al. 2008, MNRAS, 388, 1335
Zakamska, N. L., & Greene, J. E. 2014, MNRAS, 442, 784
Zwart, J. T. L., Jarvis, M. J., Deane, R. P., et al. 2014, MNRAS, 439, 1459

PoS(AASKA14)069

PROCEEDINGS OF SCIENCE

SKA studies of nearby galaxies: star-formation, accretion processes and molecular gas across all environments

R. J. Beswick[*1†], **E. Brinks**[2], **M. A. Pérez-Torres**[3], **A. M. S. Richards**[1], **S. Aalto**[4], **A. Alberdi**[2], **M. K. Argo**[1], **I. van Bemmel**[5], **J. E. Conway**[4], **C. Dickinson**[1] **D. M. Fenech**[6], **M. D. Gray**[1], **H-R Klöckner**[7], **E. J. Murphy**[8], **T. W. B. Muxlow**[1], **M. Peel**[1], **A. P. Rushton**[9,10], **E. Schinnerer**[11]

[1] *Jodrell Bank Centre for Astrophysics/e-MERLIN, The University of Manchester, M13 9PL, UK*
[2] *Centre for Astrophysics Research, University of Hertfordshire, AL10 9AB, UK*
[3] *Instituto de Astrofisica de Andalucia (IAA-CSIC), E-18008 Granada, Spain*
[4] *Department of Eath and Space Sciences, Chalmers University of Technology, Onsala Space Observatory, SE-439 92, Onsala, Sweden*
[5] *Netherlands Institute for Radio Astronomy (ASTRON), Postbus-2, NL-7990 AA Dwingeloo, The Netherlands*
[6] *Department of Physics and Astronomy, University College London, London, WC1E 6BT, UK*
[7] *Max-Planck-Institut für Radioasronomie, Auf dem Hügel 69, D-53121 Bonn, Germany*
[8] *IPAC, Caltech, MC 220-6, Pasadena CA, 91125, USA*
[9] *Department of Physics, Astrophysics, University of Oxford, Keble Road, Oxford, OX1 3RH, UK*
[10] *School of Astronomy and Physics, Univeristy of Southampton, highfield, Southampton, SO17 1BJ, UK*
[11] *Max-Planck-Institut für Astronomie, Königstuhl 17, D-69117, Heidelberg, Germany*

The SKA will be a transformational instrument in the study of our local Universe. In particular, by virtue of its high sensitivity (both to point sources and diffuse low surface brightness emission), angular resolution and the frequency ranges covered, the SKA will undertake a very wide range of astrophysical research in the field of nearby galaxies. By surveying vast numbers of nearby galaxies of all types with μJy sensitivity and sub-arcsecond angular resolutions at radio wavelengths, the SKA will provide the cornerstone of our understanding of star-formation and accretion activity in the local Universe. In this chapter we outline the key continuum and molecular line science areas where the SKA, both during phase-1 and when it becomes the full SKA, will have a significant scientific impact.

Advancing Astrophysics with the Square Kilometre Array
June 8-13, 2014
Giardini Naxos, Italy

*Speaker.
†Robert.Beswick@manchester.ac.uk

PoS(AASKA14)070

1. Introduction

The appearance of galaxies, and by this virtue, our Universe as a whole is dominated by two physical processes: star-formation and accretion. Star-formation (SF) is fundamental to the formation and evolution of galaxies, whilst accretion provides a major power source in the Universe, dominating the emission from distant quasars down to nearby X-ray binary systems. The feedback between these two processes is also crucial, e.g., in reconciling the observed galaxy luminosity function with predictions from the standard hierarchical clustering models. Radio observations provide by far the best single diagnostic of these two processes, allowing a direct view of SF even in dusty environments and the detection of AGN and measurement of their accretion rate at bolometric luminosities far below anything detectable at higher energies.

In this chapter we outline the scientific motivation for undertaking large surveys and deep observations of galaxies in the local Universe across all available frequency bands of SKA1 and look forward to the full SKA. The high sensitivity, resolution and imaging fidelity capabilities of SKA1, and the expected enhanced capabilities of the full SKA, will ensure that the SKA will become a dominant instrument for the detailed study of nearby galaxies over the coming decades.

Continuum surveys, undertaken during phase-1 covering the expected SKA dish (MID/SUR) frequency ranges of 0.35–3 GHz and higher (see also Murphy et al., 2015, in this proceedings), will provide μJy sensitivities with exquisite image fidelity over a wide range of spatial scales for all nearby galaxies. This will produce a complete census of SF and AGN activity as a function of galaxy mass, morphology and spectral type, black-hole mass and luminosity; alongside optical/IR/mm surveys and observations from ALMA, LSST, VISTA, *Spitzer*, *Herschel* and *WISE*, this will be the cornerstone of multi-wavelength studies of the local Universe.

By providing high angular resolution observations ($\sim$0.″5 or better) the SKA will be able to decompose individual galaxies into their compact radio source populations comprising accretion dominated AGN plus the tracers of the early stages of SF, such as compact HII regions, super star clusters (SSCs), as well as stellar end-points like X-ray binaries, planetary nebulae, supernovae (SNe) and their remnants (SNR). In nearby galaxies the SKA will image these sources at physically important size scales ($\sim$few to tens of parsecs) characterising individual sources and providing a detailed extinction-free census of the compact SF products across a wide range of galaxy types and the environment parameter space they inhabit. For example, at a sensitivity of a few μJy at $\sim$GHz frequencies, a census of this type will detect all of the long-lived radio SNR within several tens of Mpc, thus providing a measure of SF rates (SFRs) within local galaxies, independent of the IR-radio correlation and obscuration corrections. The mismatch between the measured Core Collapse SN (CCSNe) rates and the cosmic massive SFR (Mattila et al., 2012) should be corrected. Such a measure will preferentially trace high mass SF ($M>8M_{\odot}$), providing a direct tracer of the upper part of the galaxy Initial Mass Function (IMF). The SKA will detect all AGN activity in the local Universe. By resolving and measuring the AGN and SF contributions, local Universe studies of galaxies with the SKA will be vital in determining the contributions and interplay of these two key physical processes which are critical for our interpretation of the high redshift Universe. On larger scales the SKA will image the diffuse radio emission structure of nearby galaxies across a range of frequencies (few hundred MHz – several GHz, ideally up to at least 13GHz) thus allowing the separation of synchrotron and thermal radio emission. The component separation of the thermal

PoS(AASKA14)070

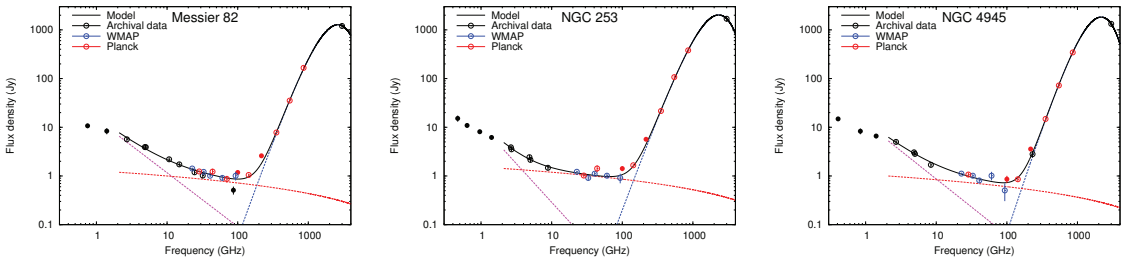

Figure 1: Spectral energy distribution of the nearby star-forming galaxies M82, NGC253 and NGC4945. Spectral fits to synchrotron (magenta), thermal (free-free - red) and thermal (dust - blue) are shown alongside the combination of these products as a solid line (Peel et al., 2011).

emission of galaxies provides another unobscured measure of the massive SF activity spanning a diverse range of galaxy types and environments, and providing a local Universe reference point.

Observations of this type will be undertaken both commensally with other wide-area or pointed observations (Prandoni & Seymour, 2015), along with specific targeted pointings focusing on this science theme. Complementing the continuum science for nearby galaxies, high sensitivity cold neutral, molecular and ionised ISM observations (the fuel for the SF and accretion processes traced via continuum observations, see section 4, also see de Blok et al. 2015; Paladino et al. 2015; Oonk et al. 2015 - this proceedings), and polarization observations of galaxies (Beck et al., 2015; Heald et al., 2015, also in these proceedings) will also be made by the SKA. This combined information will allow the SKA to fully characterise the ongoing physics and fueling of SF and accretion within the nearby galaxy population.

2. Radio continuum tracers of star-formation in the local Universe

The SF history, along with current levels of SF, within individual galaxies still remains a crucial physical parameter that observations are only now beginning to accurately characterise. Traditionally, observations of optical line, IR and the global synchrotron emission from galaxies have been used as proxies for SF. However, these tracers have some fundamental flaws. In many galaxies optical emission lines are heavily obscured towards their centres, this can require potentially large corrections, whilst IR emission, which essentially traces the light from young stars reprocessed by dust and re-radiated at longer wavelengths, relies upon empirical interpretation of physically complex processes in order for it to be related to SF. Global radio synchrotron emission provides an alternative, and extinction-free, indication of SF, however, the link between radio synchrotron emission and SF is also via complex physical mechanisms (see section 2.1.1) which are generally calibrated using the radio-to-IR correlation (Yun, Reddy & Condon, 2001; Bell, 2003; Beswick et al., 2008). The long-standing critical issue which remains is how to calibrate either global radio or IR emission as a measure of SF, and how this calibration varies as a function of galaxy properties (e.g. gas content, SFR, specific SFR, interaction/merger state) and their global environment (Kennicutt, 1998).

PoS(AASKA14)070

2.1 Thermal and non-thermal radio emission as star-formation tracers

2.1.1 Radio-Infrared correlation and star-formation

The physical underpinning of the radio–continuum (RC) — Far–Infrared (FIR) correlation is broadly understood to be the formation of massive stars, which can believably be associated with the dominant contributions to both the FIR and RC emission of galaxies. The IR contribution is due to the hot dust envelopes surrounding the massive stars, which are energised by the copious amounts of Lyman continuum radiation that those stars emit. The radio contribution includes two components (see Fig. 1). The first is the thermal continuum, free-free emission, which predominantly comes from HII regions, associated with massive ($M \geq 8\ M_{\odot}$) stars. The second is the non-thermal, synchrotron emission from relativistic electrons. These electrons are accelerated in the SNe shocks that occur when massive stars explode as CCSNe (type Ibc and type II SNe). When the supernova blast wave interacts with the outer material a shell is formed, and radio emission is generated initially due to the interaction with the circumstellar medium (CSM), fading away with time as the supernova continues to expand. Eventually, the supernova shock meets the uniform interstellar medium (ISM), at which time the SN suffers a re-brightening and continues emitting at radio wavelengths for thousands of years, now as a SNR, which is also a very efficient cosmic ray electron (CRe) accelerator. If all CRe lose their energy exclusively within the galaxy, it can be considered a calorimeter (Völk, 1989; Lisenfeld, Völk & Xu, 1996).

Both continuum thermal free-free radio emission and synchrotron radio emission can be considered as SF tracers. Thus if the presence of an AGN can be excluded (or its contribution neglected), one could then obtain independent estimates of the SF rate, and thus check the linearity of the RC(thermal)–FIR and RC(sync)–FIR correlations.

RC and FIR emission both depend on (recent) SF and will thus be correlated. Surprisingly, this RC–FIR relation of galaxies holds over 4 orders of magnitude in luminosity, irrespective of galaxy type (Helou et al., 1985; de Jong et al., 1985; Beswick et al., 2008); displays only a 0.26 dex scatter, and has been observed to hold out to a redshift of about 3 (Garrett, 2002; Appleton et al., 2004). Fig. 2 (left hand panel) taken from Kitchener et al. (2014), which is based on data from Yun, Reddy & Condon (2001), shows the RC–FIR relation based on the integrated emission from star forming (spiral) galaxies. The RC–FIR relation can be understood if not only the CRe lose all their energy within the galaxy but also the dust absorbs and transforms all the emission related to recent SF into FIR. More realistically, a galaxy is a leaky box, and models become far more involved (e.g., Bell, 2003; Beswick et al., 2008; Lacki, Thompson & Quataert, 2010). Despite the leaky nature of galaxies, the relative successes of theoretical models lend confidence that massive SF and RC emission are indeed closely tied together. A well calibrated RC–FIR relation offers a powerful method to probe the cosmic SFR out to intermediate redshifts, initially with SKA pathfinders and precursors, and eventually with the SKA (e.g., Murphy, 2009; Lacki, Thompson & Quataert, 2010; Murphy et al., 2012; Norris et al., 2013). This will be an essential prerequisite for deep extragalactic surveys with the SKA since measuring the cosmic SF history will be limited by our understanding of the radio continuum-to-SF relationship rather than the number count statistics which limit today's observations.

Rather than relying on the FIR, which at best provides modest angular resolution and relies on the availability of suitable satellites, one can use the RC to determine directly the current SFR

PoS(AASKA14)070

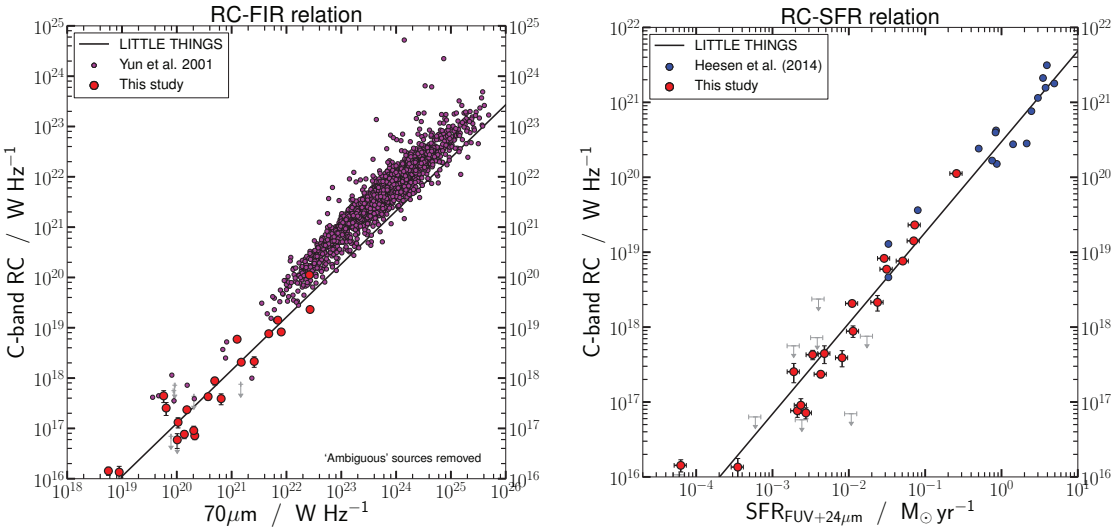

Figure 2: *left: RC–FIR relation* Filled purple symbols are integrated values for the galaxies taken from the sample collected by Yun, Reddy & Condon (2001). Their VLA 1.4 GHz data have been corrected to what would be expected at 6 GHz and their IRAS 60 μm data to the Spitzer 70 μm passband. The red circles and upper limits (downward arrows) come from the 6 cm VLA survey of 40 dwarf irregular galaxies by Kitchener et al. (2014) and are listed as "This study" in the legend. The line is a fit through the red circles and corresponds to a power law slope of 0.9 ± 0.1 and a dispersion of 0.3 dex. *right: RC–SFR relation* The blue circles are from Heesen et al. (2014) who mainly studied spiral galaxies observed with the WSRT at 22 cm from the SINGS survey. The WSRT 22 cm fluxes have been corrected to 6 GHz. The red circles and upper limits (downward arrows) are from Kitchener et al. (2014).

in galaxies (see Condon, 1992, for a review). The thermal and non–thermal emission are the result of fundamentally different processes, with different RC–SFR relations expected for each component. The thermal RC is expected to be directly proportional to the SFR, depending as it does on the ionised flux from massive stars. This makes it an ideal, virtually extinction–free proxy for SF (Murphy et al., 2011). The non–thermal RC depends on the magnetic field strength as well as the cosmic–ray energy density, unless one assumes an electron calorimeter which is unlikely, particularly for dwarf galaxies, or in general those galaxies with large–scale outflows. Usually one assumes energy equipartition between the CRe and the magnetic field, so that the RC–SFR relation is closely connected to a relation between the magnetic field and gas. Price & Duric (1992) separated the RC into its thermal and non–thermal components and found both to follow their own unique RC–FIR relation; the thermal relation being indistinguishable from a one–to–one relation (power law slope of 0.97 ± 0.02) whereas the non–thermal relation is steeper, at 1.33 ± 0.10. Although it is less obvious why the non–thermal RC would form a tight relation with SF, empirically it does and recent theoretical work suggests the non–thermal RC–SFR follows a super–linear (e.g., Niklas & Beck, 1997; Schleicher & Beck, 2013) relation with a slope of RC$\sim$SFR$^{1.3}$. Given that, at the lower frequencies, non–thermal emission related to SF can be 1–2 orders of magnitude brighter than the thermal counterpart, there is great potential in arriving at a well calibrated and understood RC-SFR relation. A recent compilation is shown in Fig. 2 (right hand panel) taken from Kitchener et al. (2014) which is based on data from Heesen et al. (2014). It shows the RC–SFR relation based on the integrated emission from star forming galaxies.

PoS(AASKA14)070

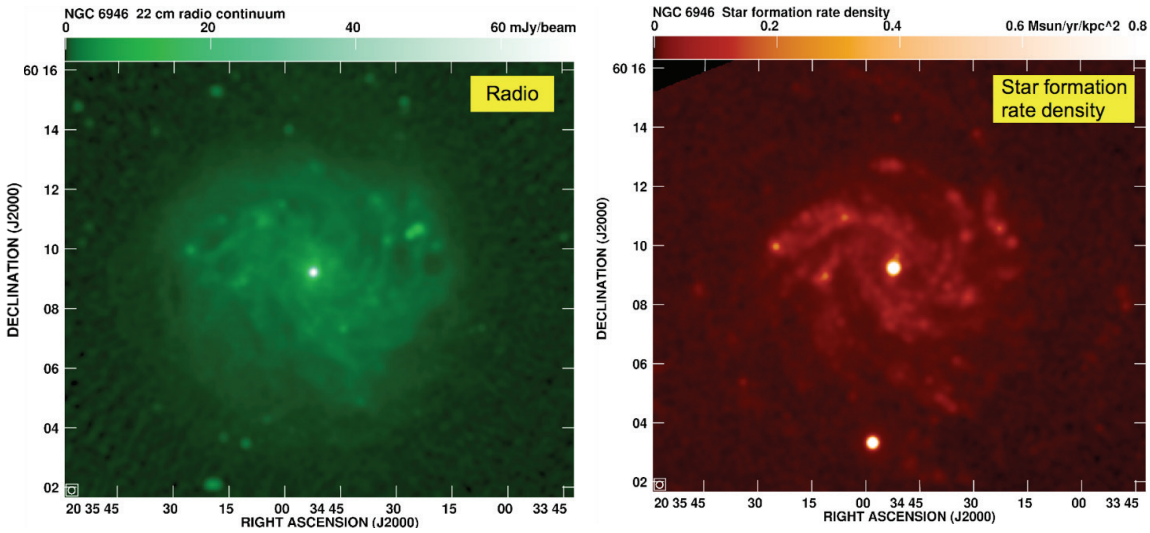

Figure 3: Images of the 22 cm radio continuum and derived star-formation rate density for the nearby face-on star-forming galaxy NGC 6946.

2.1.2 From existing capabilities to the SKA

Upgrades to existing instruments (in the form of wide–band end-to-end systems) have opened up a number of possibilities including i) spatially resolved imaging of dozens of spirals in the Local Universe down to μJy levels, ii) extending those studies to the low mass, low metallicity regime of dwarf irregular galaxies, and iii) mapping of nearby galaxies at parsec resolution which, via a headcount of individual SNRs, gives an independent handle on the SFR (Fenech et al., 2008, 2010). Murphy et al. (2006, 2008) provide spatially resolved information at ~ 1 kpc scale, using Westerbork Synthesis Radio Telescope (WSRT) 20 cm observations (Braun et al., 2007) combined with *Spitzer* 70 μm maps. They find that the RC emission mimics a smoothed version of the FIR map, a consequence of CR electrons diffusing over their $\sim 10^8$ yr lifetime across typically ~ 1 kpc. They also find that the slope of the RC–FIR relation, q_{70}, varies with radius and with surface brightness. Fig. 3 shows the stunning similarity between 22 cm radio continuum emission from Braun et al. (2007) and a map tracing the current SFR which is based on a linear combination of *GALEX* FUV and *Spitzer* 24 μm emission (based on Heesen et al., 2014). These authors, based on a sample of 18 nearby spirals, conclude that the RC–SFR relation as posited by Condon (1992) holds for their integrated luminosities. When averaging azimuthally, the ratio of 22 cm surface brightness to the SFR surface density is remarkably constant as well. Diffusion of CRe flattens the local (averaged over a 0.7 to 1.2 kpc diameter area) RC–SFR relation, and this is compatible with magnetic field amplification by a small–scale dynamo, powered by SF-driven turbulence.

Kitchener et al. (2014) push these results to the low-mass, low SFR regime of dwarf irregulars (the red symbols in Fig. 2). They find that dwarf galaxies follow the same RC–FIR slope as that defined by the larger spirals, but are systematically fainter by a factor of about two. Assuming equipartition, the strength of the B–field is 9 μG, which is of the same order as that in spirals. Resolved studies in nearby spiral galaxies such as M51 (Dumas et al., 2011) and NGC6946

PoS(AASKA14)070

(Tabatabaei et al., 2013) show deviations in the RC–IR slope as a function of environment (e.g. arm vs. inter-arm, SFR, gas density and radiation field). These studies find evidence of clear variations of the synchrotron emission with SFR thus providing further evidence for coupling of the gas density and magnetic field strength. At SFRs lower than 1 $M_\odot$ yr^{-1}, the RC deviates increasingly from the Condon relation, which is interpreted as being due to a deficiency of non–thermal emission as a result of CRe escape.

SKA1–MID will transform what can be achieved. Rather than monochromatic (or at best in–band spectral index) information, observations of about 1 hr per band will sample the entire radio continuum spectrum between 1.67 and 10 GHz (about 4 hr total per target), down to μJy sensitivity. This will allow the above mentioned relations to be put on a much more robust footing as we will be able to separate off the thermal contribution, leaving just the non–thermal fraction. In addition to extending the work quoted above by Murphy et al. (2011), Heesen et al. (2014) and Kitchener et al. (2014) to larger samples, the spatially resolved spectral index distribution will come within reach, which should provide a lever on the propagation and aging of CRe as they diffuse from their sites of origin.

2.2 Decomposition of local galaxies into their constituent parts

Sensitive and critically high angular resolution ($\leq 0\farcs5$) radio images of nearby galaxies such as will be provided by the SKA1-MID and by the complete SKA, provide one method by which observations can directly probe SF and SF processes in a way which is independent of complex physical emission mechanisms. Whereas lower resolution radio observations of normal and star-forming galaxies trace the diffuse radio emission (see Section 2.1.1), sub-arcsecond angular resolution observations are required to systematically characterise the populations of individual compact SF products on a galaxy by galaxy basis by resolving away the diffuse emission. This population census can hence be used to directly infer the levels of SF.

Observed with $<0\farcs5$ angular resolution, each individual galaxy can be considered as a laboratory containing a large sample of discrete radio sources, all at essentially the same distance, which can be studied in a systematic way. At μJy and sub-μJy sensitivities and between frequencies of 1 and 7 GHz this source population, with the exception of accretion dominated objects and in particular AGN (see Section 3), will consist exclusively of sources related to various key phases of the stellar evolutionary sequence. This population will be a mixture of sources from the early stages of SF, such as compact HII regions, through SSCs, and stellar end-points like X-ray binaries, planetary nebulae, SNe (see also Pérez-Torres et al., 2015, in this proceedings) and their SNR.

By first detecting and then identifying the physical nature of these objects using a combination of radio morphologies and spectral indices, alongside extensive multi-wavelength ancillary data, high angular resolution radio observations will provide the first detailed extinction-free census of SF products within nearby galaxies. The majority of core-collapse SNe evolve to form long-lived radio SNR (Weiler et al., 2002; Gendre et al., 2013), hence this statistically well-constrained census combined with information regarding the sizes and hence canonical ages of SNR (for the nearest galaxies observed with sub-arcsecond resolution available in higher bands with SKA1–MID), can be used to directly infer levels of SF in individual galaxies (e.g. Pedlar, 2001; Fenech et al., 2008, 2010). This will provide a further obscuration-independent SFR tracer and, because it detects massive stars which form CCSNe, will preferentially probe the top part of the IMF. When combined

PoS(AASKA14)070

with other SFR measures such as IR/UV or global RC free-free and synchrotron emission (e.g. Section 2.1.1) this will provide constraints on the universality of the IMF as a function of galaxy type, evolution and environment within the local volume.

Importantly, such a local galaxy radio survey will also identify populations of sources that trace earlier stages in stellar evolution, such as HII regions and SSCs, placing useful constraints on the levels of SF at various phases in the evolution of individual galaxies. When compared with other wavelength tracers, which probe different ranges of SF age and different spatial regions, these radio diagnostics will provide significant new insights.

Whilst this will be achievable on a galaxy-by-galaxy basis, the power and importance of an SKA survey of nearby galaxies arises from its large size and the available complementary multi-wavelength data-sets. By combining these direct radio tracers of SF products, with other multi-wavelength SF proxies (e.g. IR), significant constraints will be placed on their calibration and interpretation, with important implications across a wide range of observational astrophysics. Large-area SKA1 continuum surveys with both SKA-MID and SKA-SUR with sensitivities of $\sim 4\mu$Jy will be capable of detecting all local galaxies thus spanning a complete range of types and levels of both historical and ongoing SF, and allowing this census of SF products to be applied over the wide range of luminosity and environment parameter space inhabited by galaxies. Such a survey will provide the radio benchmark for studies of local galaxies with application to all observational astronomers.

2.3 Towards higher redshift

Intermediate redshift ($0.1<z<0.3$) and some local Luminous Infrared Galaxies (LIRGs) and Ultra-Luminous Infrared Galaxies (ULIRGs) are thought to be nearby versions of high-z star-forming galaxies (see also Mancuso et al., 2015, in this proceedings). Since a major science goal for the SKA and its pathfinders is the study of SF across cosmic time, it is crucial to i) have a detailed and accurate knowledge of local star-forming galaxies, and ii) test the radio-infrared (radio-IR) relation. Since radio emission is a dust-unbiased SF tracer, an accurate calibration of the radio-IR relation will be needed to determine the SFRs at high-z. Indeed, at $z \geq 1$, 1 arcsec corresponds to 8 kpc, so that disentangling AGN from star-forming activity is challenging, unless angular resolutions better than $\sim 0\farcs1$ are provided, so that one starts to separate a putative AGN from a compact starburst at essentially any redshift. This capability will be provided by the full SKA.

A large fraction of massive SF at both low- and high-z has taken place in (U)LIRGs. Their implied high SFRs are expected to result in CCSN rates a couple of orders of magnitude higher than in normal galaxies. Therefore, a powerful tracer for starburst activity in (U)LIRGs is the detection of CCSNe, since the SFR is directly related to the CCSN rate. However, most SNe occurring in ULIRGs are optically obscured by large amounts of dust in the nuclear starburst environment, and have therefore remained undiscovered by (optical) SN searches. Fortunately, it is possible to discover these CCSNe through high-resolution radio observations, as radio emission is free from extinction effects. Furthermore, CCSNe are expected (unlike thermonuclear SNe) to become strong radio emitters when the SN ejecta interact with the CSM that was ejected by the progenitor star before its explosion as a supernova. Therefore, if (U)LIRGs are starburst-dominated, bright radio SNe are expected to occur. Given their compactness and characteristic radio behavior of radio SNe they can be pinpointed with high-resolution, high-sensitivity radio observations (e.g., SN 2000ft in

PoS(AASKA14)070

NGC 7469 Colina et al. 2001; Alberdi et al. 2006; Pérez-Torres et al. 2009b; SN 2004ip in IRAS 18293-3413, Pérez-Torres et al. 2007; SN 2008cs in IRAS 17138-1017, Pérez-Torres et al. 2008; Kankare et al. 2008; supernovae in Arp 299 Neff, Ulvestad & Teng 2004, Arp 220 Smith et al. 1998; Lonsdale et al. 2006; Parra et al. 2007, Mrk 273 Bondi et al. 2005). However, since (U)LIRGs are likely to have an AGN contribution, high-sensitivity, high-resolution radio observations are required to disentangle the nuclear and stellar (mainly from young SNe) contributions to the radio emission, thus probing the mechanisms responsible for the heating of the dust in their (circum-)nuclear regions.

In view of the importance of (U)LIRGs in tracing the SF history across cosmic time, a targeted survey of local (U)LIRGs using SKA1–MID, up to a distance of 100 Mpc, will be essential. The sub-arcsecond angular resolution in band 2/3 will be well-matched to current (J)VLA-A images at higher frequencies, permitting the thermal and non-thermal contribution to be disentangled in the very centres of galaxies. Considering the continuum sensitivity provided by SKA1–MID, as little as 2 minutes per source would be sufficient to produce 1.7 GHz images of a similar depth to those currently provided by the JVLA at 8.4 GHz in 1 hour. A census of all local (U)LIRGs could be obtained in just a few hours with SKA1–MID. Even if the specifications deviate by as much as 30% in terms of sensitivity, this science will not be severely affected. However, baseline lengths of at least 200 km are required, to provide the necessary angular resolution. An SKA-MID survey providing an angular resolution of $0\farcs5$ corresponds to a physically interesting resolving linear scale of $\sim$250 pc at 100 Mpc.

Similarly, SKA1–MID will be a game–changer when it comes to providing a benchmark study for relating the CCSN rate to the SFR in both star-forming and normal spirals, and down to dwarf irregulars. With sensitivities of over an order of magnitude better than current instruments, and sub-arcsecond resolutions providing linear resolution scales of a few tens of pc within nearby galaxies, SKA1–MID will be well matched to spatially separate CCSNe from their surrounding diffuse emission, thus enabling a complete census.

With the 20 fold increase in angular resolution expected with the full SKA (resolution of about 10 mas at 1.67 GHz (see also Paragi et al., 2015), it will be possible to locate individual core-collapse supernovae (or supernova remnants) within the nuclear regions of all local starburst galaxies, similar to detailed studies in e.g., Arp 220 and Arp 299 (see Fig. 4, taken from Pérez-Torres et al. 2009a, 2010), but with the potential of unveiling the much more numerous, fainter radio supernovae and supernova remnants. In turn, this will allow us to test scenarios of SN/CSM-ISM interaction, including estimates of the energy budgets in particles and magnetic fields, and determine the SNR luminosity vs. size relation for essentially all local (U)LIRGs. In addition, we will be able to extend the study described above to essentially all redshifts, as the 10 mas beam at 1.67 GHz will yield spatial resolutions of 80 pc, or better, at all redshifts.

3. Accretion sources in the nearest galaxies

The sensitivity and frequency coverage of SKA1 will enable a complete census of accretion powered sources in the local Universe. Such sources encompass multiple orders of magnitude in mass and luminosity, from supermassive black-holes (SMBH) and low-luminosity AGN, through Sgr A$*$–like luminosities, to intermediate-mass black-holes and down to stellar mass black-hole

PoS(AASKA14)070

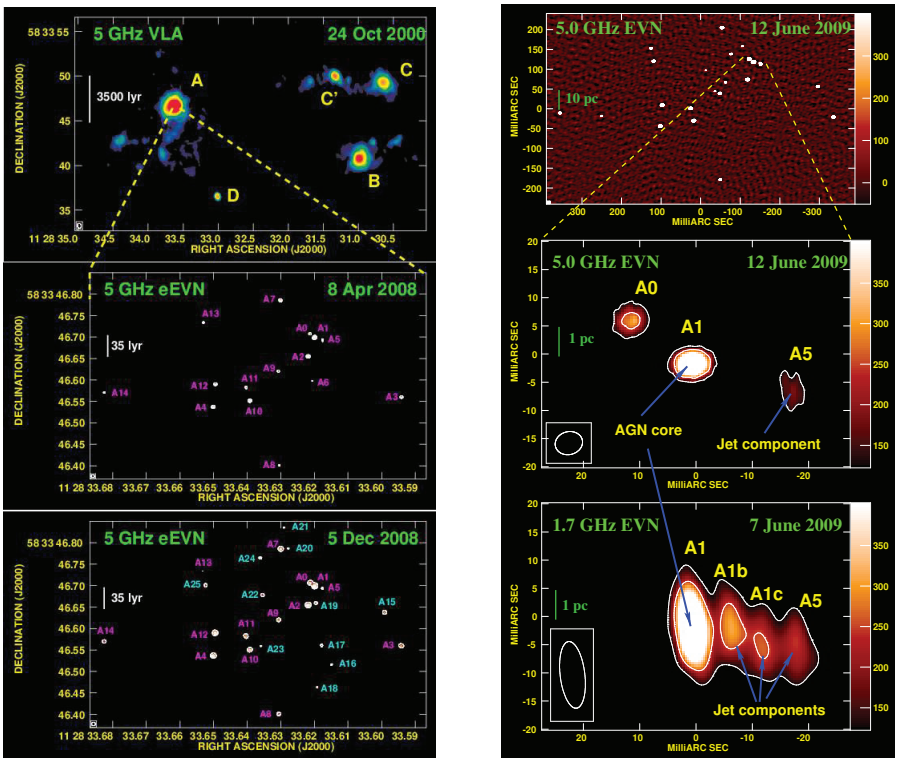

Figure 4: *Top left:* 5 GHz VLA archival observations of Arp 299 on 24 October 2000, displaying the five brightest knots of radio emission in this merging galaxy. *Middle and bottom left:* Contour maps drawn at five times the r.m.s. noise of our 5 GHz eEVN observations of the central 500 light years of the luminous infrared galaxy Arp 299-A on 8 April 2008 and 5 December 2008, revealing a large population of bright, compact, non-thermal emitting sources. To guide the reader's eye, we show in cyan the components detected only at the 5 December 2008 epoch. *Top right:* 5.0 GHz full EVN image of the central 150 parsec region of the luminous infrared galaxy Arp 299-A, displaying a large number of bright, compact, non-thermal emitting sources, mostly identified with young RSNe and SNRs. *Middle and bottom right:* Blow-ups of the inner 8 parsec of the nuclear region of Arp 299-A, as imaged with the full EVN at 1.7 and 5.0 GHz. The core-jet morphology, spectral index and luminosity of the A1–A5 region clearly revealed the location of the long-sought AGN in Arp 299A.

systems such as microquasars. The sensitivity of the SKA during a deep pointed survey will show accretion-dominated objects in a variety of environments within an individual galaxy, not constrained just to the nucleus.

3.1 Accretion onto supermassive Black-holes

Accretion onto SMBHs is one of the most significant energy sources in the universe, with the potential to clear star-forming gas from galactic bulges and even to regulate the growth of entire galaxies in galaxy clusters (e.g. di Matteo, Springel & Hernquist, 2005). The mechanism for this feedback is mechanical, through jets and outflows powered by accretion. However, despite the importance of SMBH activity in regulating galaxy formation, comparatively little is known about SMBH activity towards low radiative luminosities. This is a significant gap in our understanding

PoS(AASKA14)070

of feedback and the role of SMBHs in galaxy growth and evolution, since it is now known that mechanical jet power can be energetically more significant than supernova feedback, even at low AGN luminosities (Nagar, Falcke & Wilson, 2005; Körding, Jester, & Fender, 2008). The major difficulty in studying low luminosity AGN is precisely their low radiative output with respect to their surrounding host galaxy, especially since many LLAGN are embedded in nuclear SF regions (see Fig. 4; and work of Ho et al., 1997, and references therein). For these LLAGN, large amounts of mechanical energy are shed by massive stars into their surrounding medium which significantly increases its temperature. Thus those massive stars would hinder the accretion of material to the central black-hole, resulting in a less powerful AGN. The problem is compounded because at low-luminosities AGN become radiatively inefficient, and lose the strong optical and X-ray signatures commonly used to identify AGN activity. However, just because an AGN is radiatively inefficient does not make it mechanically inefficient, in fact at low luminosities the total power is almost certainly mechanically-dominated via the jet.

Radio imaging is also essential to unambiguously identify activity due to SMBH accretion. For example, even with more sensitive optical spectroscopy, it will be difficult to distinguish the weak optical emission from faint AGN against the contribution from nuclear SF. In contrast, a separation of AGN and SF components can be made with the moderate resolution ($\sim 0\farcs5$) obtained by SKA1–MID initially in the most local systems, coupled with the leverage of multiple frequency bands to distinguish flat-spectrum AGN cores. Finally, using radio data circumvents the problem of where to draw the dividing line between a galaxy being "active" or "normal". This is because one can not only estimate the jet power from core radio luminosities, but also measure the absolute mass accretion rate, which appears to be well-correlated with radio luminosity for the lowest luminosity objects, and where beaming effects do not play an important role, scaling as $L_R \propto M_\odot^{1.4}$ (Körding, Jester, & Fender, 2006). Thus we can classify all galaxies according to their SMBH accretion power, tying the lowest accretion "quiescent" SMBH to the LINERs and classical Seyferts.

3.2 Accretion from intermediate to stellar mass black-holes

Deep radio surveys of the local Universe with the SKA will prove critically important to our further understanding of high-energy accretion processes across a wide mass-function of compact objects. Bright off-nuclear X-ray point sources with luminosities in excess of 10^{39} erg s^{-1}, known as Ultra-Luminous X-ray sources (ULXs), are among the most energetic mass-accretion processes in the local Universe (Roberts, 2007). Due to their defining characteristics, ULXs could be explained by stellar-mass black-holes with global accretion rates at or in excess of their Eddington limit or represent a population of intermediate mass black-holes (IMBH) with masses between $10^{2-3} M_\odot$ (e.g., King, 2009). Some evidence for the latter has arisen through the discovery of radio emitting 'bubble nebulae', 100s of parsecs in diameter surrounding the X-ray sources (e.g., Pakull & Mirioni, 2002), and transient radio outbursts from a 'hyper-Luminous X-ray' source at a distance of $\sim$ 100 Mpc (Webb et al., 2012). These may be photo-ionised by the central X-ray source (Pakull & Mirioni, 2002; Kaaret, Ward & Zezas, 2004), shock-heated through the interaction of outflows with the ambient medium (Pakull & Mirioni, 2002, 2003) or both. As the bolometric radiative efficiency of these sources provides an unreliable measure of the black-hole mass, it is by studying these surrounding radio nebulae and jets that we could estimate the true kinetic power of these

PoS(AASKA14)070

compact objects and gain insight to their mass-function (see more extensive chapter on this area by Wolter et al., 2015).

IMBHs and stellar-mass black-hole systems (e.g. microquasars) also provide a hitherto sparsely investigated population of transient or variable faint compact radio sources in galaxies and are expected in larger numbers in high SFR systems than are found in our own Galaxy (see Fender et al., 2015; Corbel et al., 2015, for more information on radio transients and the SKA). To date few dedicated radio searches have been performed of nearby star-forming galaxies and only a handful of candidate sources have been detected serendipitously (e.g., potenial microquasars in M82, Arp220 and Arp299; Muxlow et al., 2010; Joseph et al., 2011; Batejat et al., 2012; Bondi et al., 2012, respectively). Whilst the current radio instruments, such as JVLA and e-MERLIN, are only just starting to explore the brightest and nearest of this population. Via large-area and pointed SKA survey observations with sub-arcsecond angular resolution the entire population of accreting objects in galaxies across all mass scales and environments will be charactised. Searches for radio emission from star clusters and dwarf satellite galaxies around local galaxies will provide constraints on what fraction of each class of object shows evidence for containing black-holes of $\sim$1/1000 of their total masses, in the same way that giant galaxies seem to do nearly universally. Several visits to the fields my be required to clarify the nature of the sources.

4. Tracing the fuel for, and influence of SF and accretion: Molecular Gas tracers of kinematics and properties

4.1 OH masers and Circumnuclear starbursts

Masers are the radio analogues of lasers, and occur when there is an excess of molecules in a higher energy state – a non-thermal or inverted population distribution. This gives a negative optical depth so that ambient or background radiation is amplified. Intrinsically compact both spatially and spectrally (extragalactic masers are detectable down to μas scales in $<$km s^{-1} channels), masers provide the best directly-mappable tracers of high-resolution kinematics. They demonstrate the presence of more compact molecular regions than any other cm-wave tracer and increasingly sophisticated models (e.g. Gray 2012) place tight limits on the density-temperature parameter space required to pump the maser inversion. The most intense Milky Way masers are associated with individual star forming regions, and similar phenomena have been detected from Local Group galaxies, (water, methanol and hydroxl; Brunthaler et al., 2006; Sjouwerman et al., 2010; Argo et al., 2013, respectively). So called Mega- or kilo-masers can be more than a thousand time brighter and hence can be detected from within more distant galaxies (see Tarchi, 2012, for a recent review). Some of the potential science applications of the SKA for investigating nearby and Galactic masers is covered by Etoka et al. (2015) and Robishaw et al. (2015) in this proceedings.

OH masers, rest frequencies 1.6-1.7 GHz, have been found in over 100 (U)LIRGs out to z=0.27 (Darling & Giovanelli, 2002; Willet, 2012). There is a strong relationship $L_{\rm OH} \propto (L_{\rm IR})^{\alpha}$, explained by the rôle of radiation from dust in the maser pumping (Lockett & Elizur, 2008). The corresponding OH IR lines at 35 and 53μm have recently been detected in both absorption (53μm) and emission by *Herschel* (González-Alfonso et al., 2014) providing important constraints on pumping schemes. Values of $0.5 < \alpha < 2$ have been reported, however these are sensitive to the angular resolution of the observations and the orientation of the emission region. Dust temperatures

PoS(AASKA14)070

$45 < T < 200$ K (optimally 80–140 K) and a number density $10^9 < n < 10^{12}$ m^{-3} (Darling 2007; Lockett & Elizur 2008) are also required.

Images of extra-galactic OH masers have only been published for around a dozen galaxies further away than the Magellanic Clouds, out to $z \sim 0.045$. In approximate order of increasing distance, these are: M82 (Argo et al., 2010, 2013), NGC 1068 (Gallimore et al., 1996), III Zw35 (Parra et al., 2005), Arp 220 (Rovilos et al., 2003), Arp 299 (Polatidis & Aalto, 2001), II Zw096 (Migenes et al., 2011), Mrk 273 (Yates et al., 2000), Mrk 213 (Richards et al., 2005), IRAS 17208-0014 (Momjian et al., 2006), IRAS 12032+1707, IRAS 1407+0525 (Pihlström et al., 2005) and IRAS 10173+0828 (Yu, 2005). All these galaxies show evidence for interactions or mergers and some masers are found at two or more sites hundreds of pc apart (e.g., in Arp220; Rovilos et al., 2003).

In most of the more distant objects, the brightest masers trace a rotating disc, typically a (few) hundred mas (a few hundred pc) in diameter, suggesting enclosed masses between $10^6 - 10^9$ M$_\odot$, possibly evidence for massive black-holes, but dense nuclear starburst regions, or both (Richards et al., 2005), cannot be ruled out without higher-resolution data (Klöckner, Baan & Garrett, 2003). These Mega-masers are generally inside the extent of discs traced by HI. VLBI observations, and modelling of lower resolution data, show that the OH masers mostly emanate from clouds within a factor of four of 1pc in diameter (Lonsdale et al., 2003; Richards et al., 2005). The discs may also be warped or interact with jets, requiring sensitive high-resolution imaging for good models (e.g., Klöckner, Baan & Garrett, 2003).

The OH ground state main lines, rest frequencies 1667.359 and 1665.402-MHz are brightest, with intensity ratio ≥ 1.8 (the value expected for unsaturated emission) and (in accordance with predictions), the highest brightness temperature masers have higher ratios (Lonsdale et al., 1998). The OH satellite lines at 1612- and 1720-MHz are fainter and masers have only been detected in 6 objects (McBride, Heiles & Elitzur, 2013). There are cases where 1720-MHz absorption accompanies 1612-MHz emission, requiring a different pumping mechanism even if mainline masers are also seen. A number of OH Mega-masers have line wings at up to 800 km s^{-1} from the systemic velocity (Baan, 1989), but neither these nor the satellite lines have ever been imaged.

4.2 Other cm-wave extragalactic masers

Bright 22-GHz extragalactic masers are best known thanks to their location in sub-pc tori around supermassive black-holes. Both Doppler and (with VLBI) proper motions were measured for NGC 4258 (Herrnstein et al., 1999; Green et al., 2015; Paragi et al., 2015). This gives the most precisely-known estimates of the enclosed black-hole mass and the distance, providing the disc kinematics are modelled accurately (Humphreys et al., 2013). The Hubble constant could thus be measured very accurately from a larger sample of such galaxies (e.g., the Mega-maser cosmology project Kuo et al., 2013). VLBI with the SKA will push this to far greater distances. A water maser at z=2.6 has already been detected at 6.1 GHz (Impellizzeri et al., 2008) in a lensed galaxy. H_2O masers are also found in interactions between jets and the ISM, (e.g. Kondratko, Greenhill & Moran, 2003). Such galaxies do not usually have high SFRs and only a few nearby merger systems, e.g. NGC 1068, also host OH masers.

Excited OH lines occur in the rest frequency range 4-6.7 GHz; extragalactic thermal emission is known (Impellizzeri et al., 2006), but as yet these lines have not been observed as masers.

PoS(AASKA14)070

Formaldehyde masers (rest frequency 4.8 GHz) are known from a handful of ULIRGs, all with OH Mega-masers (Araya et al., 2004). The inversion has the interesting property that maser amplification occurs at $n \geq 10^{11.6}\,\mathrm{m}^{-3}$ and the excitation temperature exceeds the CMB temperature; at lower densities supercooling and strong absorption occurs (Mangum et al., 2013). Molecules, such as OH and CH, with multiple masing transitions can be not only good thermometers, but also can be used as probes of any cosmological variation in fundamental constants.

4.3 SKA phase 1 and SKA observations of Mega-maser molecules

There are several complementary modes whereby SKA1–MID can locate and measure Mega-maser properties. Spectral surveys would be very valuable in finding Mega-masers associated with galaxies out to the peak of the merger rate around redshift 1–2, helping to provide an estimate of the galaxy merger rate (Aharonian et al., 2013), and in identifying candidates for imaging. Searches are optimised by providing at least 3 samples across the line peak, i.e. a few tens $\mathrm{km\,s^{-1}}$ channels, with angular resolution ≤ 1 arcsec, not greatly exceeding the size of the emission area. Nonetheless, piggyback observations at coarser resolution would be worthwhile. Selection criteria are described based on IR properties (Darling & Giovanelli, 2002) including deep silicate 9.8μm absorption (Willett et al., 2011). The 18 sources detected at $0.1 < z < 0.27$ have OH peaks of 1.8–40 mJy and line widths (FWHM) of 50–600 $\mathrm{km\,s^{-1}}$, with some of the most distant being among the brightest. This suggests that a few percent of similarly selected candidates would have a flux density $\sim$0.6 mJy at $z = 1$ and the brightest might reach $\sim$0.2 mJy at $z = 2$. Assuming that a sensitivity of 0.13 mJy can be reached in 20 $\mathrm{km\,s^{-1}}$ channels in ≤ 1 hr (depending on Dec.) at 1 arcsec resolution, this would give a 5σ detection for 0.6 mJy masers in 1-2 hr, at modest redshifts around 1.6 GHz. At 555 MHz, $z \sim 2$, the lower sensitivity requires ~ 24 hr to detect 0.2 mJy lines. McKean & Roy (2009) describe a strategy using APERTIF or ASKAP for a blind search which would detect ~ 1 mJy masers (5σ) at the highest accessible redshift of $z = 1.39$, but in several hours (per tuning) and 150 $\mathrm{km\,s^{-1}}$ resolution.

The known satellite lines are 1–10% of the main line peaks in Mega-maser galaxies, but are often brighter in Milky-Way-like star-forming regions. McBride, Heiles & Elitzur (2013) detected 5 out of 77 sources at $z < 0.05$, at a few mJy. The 1-hr sensitivity of SKA will go at least twice as deep. Detection of multiple maser lines places tighter constraints on the parameter space of temperature-density-velocity coherence. Such a survey may also produce a large enough sample of satellite maser lines to help identify the pumping mechanism responsible for conjugate behavior, especially for any bright enough to image.

The enclosed mass density derived from resolved maser PV diagrams can be compared with predictions from thermal tracers of high-density, warm gas, for example HCN, which has excitational properties correlated with OH Mega-masers (Darling, 2007; Kandalyan & Al-Zyout, 2010, and see Section 4.5) and with HC_3N (Lindberg et al., 2011). The position of maser components can be measured with a precision (for reasonable uv coverage) of 0.5$\times$(beamsize/signal-to-noise ratio), so, at 250 mas resolution, a signal-to-noise of 5 across a few hundred $\mathrm{km\,s^{-1}}$, sampled by 5 or more channels, would resolve a $\sim$ 150 pc radius edge-on disc at $z \sim 0.2$. The 2-hr sensitivity at this resolution in 30 $\mathrm{km\,s^{-1}}$ channels is $\sim$ 0.5 mJy, allowing emission above 2.5 mJy to be resolved sufficiently. This would typically correspond to a 10 mJy spectral peak.

PoS(AASKA14)070

Selected objects should be imaged for 12–24 hr, to allow higher sensitivity or higher resolution. This will allow detection of multiple components per channel from discs tilted enough to be spatially resolved, and define the angle of inclination. The 1665-MHz line is typically fainter and lacks the compact hot-spots seen in the 1667-MHz line; imaging this avoids blending ambiguities as well as providing material for maser modelling. Higher sensitivity will provide the first imaging of the satellite lines, providing tighter constrains on physical conditions. It will also reveal the origin of the high-velocity mainline emission, which could be fast-rotating regions in the inner disc, or material entrained by jets (Klöckner, Baan & Garrett, 2003), since at least some of the host galaxies contain weak AGN, although the fraction has been variously estimated at 45% (Baan et al., 1998) or 10–25% (Willett et al., 2011). Another possibility is a molecular outflow as suggested by the velocity dispersion within the III Zw35 disc (Parra et al., 2005) since the superwind from NGC 253 has recently been shown by ALMA to be laden with molecules as well as the better-known light, ionised component (Walter et al., 2013).

Searches and rapid imaging of extragalactic masers requires a channel width of a few tens of $\mathrm{km\,s^{-1}}$ at most, since maser lines tend to be narrow and diluted at too-coarse a resolution. Spectra can be decomposed into a mixture of broad features and few $\mathrm{km\,s^{-1}}$ details, and a resolution of $\sim 1\ \mathrm{km\,s^{-1}}$ is needed to measure Zeeman splitting (Robishaw et al., 2015), or even finer for the measurement of fundamental constants. Similarly, comparison of single dish, WSRT, MERLIN and EVN spectra (Klöckner, 2004) shows that the brightest peaks are often almost as bright at ~ 30 mas resolution as at a resolution of a few arcsec or more, but the weaker emission is partly or completely resolved out on scales of a few hundred mas or less. The SKA will provide the first opportunity to sample emission on MERLIN to WSRT scales simultaneously (and eventually on VLBI scales). Flexible data reduction is needed, with weighting-up of short baselines for maximum sensitivity at high spectral resolution, and channel averaging to allow high spatial resolution making full use of long baselines.

Finally, another motive for characterising OH masers is to avoid contamination of HI surveys; the maser lines can be distinguished at higher spectral resolution or by anomalous redshift and excess brightness with respect to other lines and continuum/optical properties (Haynes et al., 2011).

4.4 Summary of Mega-maser requirements

The basic requirement is the frequency range. Ground-state OH masers at $0 < z < 2$ need frequencies from about 1721 down to 530 MHz. Searches are optimized at a velocity resolution of ten or a few tens of $\mathrm{km\,s^{-1}}$. Follow-up of brighter objects at resolution down to $\leq 1\ \mathrm{km\,s^{-1}}$ in full polarization is desirable, with a coverage of a few thousand $\mathrm{km\,s^{-1}}$ and angular resolution as fine as possible (ideally 100 mas or less). However, it will not be possible to achieve many detections simultaneously at full spectral and spatial resolution. To achieve this the use of different weighting may be required to produce the highest spectral or spatial resolution images.

The (to date) rarer extragalactic masers such as CH, formaldehyde, methanol and excited OH require frequencies up to just above 6 GHz (potentially higher, since Galactic OH and methanol are known up to 13 GHz). In fact, any expansion of frequency range will allow detection of masers at some redshift, notably for the 22-GHz water masers. In the more advanced stages of the SKA, VLBI at up to 22 GHz is essential for the Megamaser Cosmology Project.

PoS(AASKA14)070

4.5 Molecular line and other tracers

There is now mounting evidence that cold, neutral/molecular outflows are extremely important carriers of momentum and mass within galaxies. We are beginning to see that the properties and mass balance atomic/molecular/ionised change along individual outflows as well as among outflows. In this area HI absorption studies are absolutely fundamental, however observations of OH maser emission in dense outflows in ULIRGs also have a critical role and radio recombination lines (RRLs) also potential can play an important part in nearby sources (see section 4 and Morganti et al., 2015; Oonk et al., 2015, for HI absorption and RRL opportunities with the SKA). Very recently it has also become clear that AGN driven outflows may also have extremely interesting molecular properties (linked to their evolution) that can be studied in exquisite detail with the SKA. The ISM properties of galaxies throughout the Universe can be investigated via HI and radio recombination studies which probe the atomic and ionized medium and are a key complement to the molecular cloud structure/mass/dynamics probed by mm-telescopes such as ALMA. This area is of fundamental importance to the understanding of cloud and SF processes in galaxies both near and far.

In this area the sensitivity and frequency coverage of the SKA, even in phase-1, provides a unique opportunity to study these processes via centimetric molecular lines that have hitherto been ill explored (preliminary JVLA and Arceibo studies have been made on selected sources e.g., Rickert, 2011; Salter et al., 2008). A number of molecular tracers, which include several prebiotic molecules, are available within the proposed SKA-1 bands (see Table 1) and will be observable as kinematic and ISM tracers within local galaxies.

For example the SKA's capabilities provide the possibility of studying the properties of the extreme nuclear regions of Compact Obscured Nuclei (CONs) - and dust obscured galaxies (DOGs). Here, activity may be buried behind $N_H > 1 \times 10^{25}\,cm^{-2}$ of gas which means that these Compton thick, high pressure regions are the realm of molecules (not even X-rays will penetrate to help fingerprint the activity). Molecular emission can probe behind the optically thick dust veil to reveal temperature gradients and field strengths at SKA spatial resolution. Thus these studies will trace the impact and structure of the deeply buried activity in a unique way. The properties of these galactic nuclei may only be accessible with molecules.

Why SKA and not ALMA? Many of these line species are accessible at mm and submm wavelengths (and studies are underway with ALMA). However, some of the heavier molecules have their primary transitions in the SKA bands, plus critically at submm wavelengths the line confusion and line blending is so severe that using these lines sometimes becomes extremely difficult. Pilot studies on nearby galaxies are underway on the JVLA at 6, 9 and 20 GHz, however these will remain sensitivity limited with current facilities. The sensitivity and frequency range covered by the SKA make this it an ideal instrument to open up this new field. Furthermore initial modelling work predicts that several of these molecules will have maser transitions at the very lowest frequencies (e.g. 0.3 GHz) rendering them as potentially extremely important probes of circumnuclear extreme regions around AGNs.

5. Conclusions

The major endeavor that is the SKA will create a general user facility which will produce

PoS(AASKA14)070

Table 1: Selection of molecular line tracers between 1-10 GHz and within the bands of SKA-1. Lines of the OH radical and various other species are also of key importance but for brevity not included below.

Line	Rest freq (MHz)	SKA-1 MID band	SKA-1-SUR band
HCN $v_2 = 1, \Delta J = 0, J = 2$	1346.765	2	2
HCN $v_2 = 1, \Delta J = 0, J = 4$	4488.4718	4	-
H_2CO	4829	4/5	-
N_2H+	5009.8278	4/5	-
H_2CNH $1_{10} - 1_{11}$,$\Delta F = 0, \pm 1$	5289.813	5	-
HCO+	6350.908	5	-
HNC	6484.497	5	-
CH_3OH $5_1 - 6_0 A^+$	6668.5192	5	-
HCN $v_2 = 1, \Delta J = 0, J = 5$	6731.9098	5	-
HCO+	8890.452	5	-
HCN $v_2 = 1, \Delta J = 0, J = 6$	9423.3338	5	-
HNC	9724.644	5	-

transformational science across a wide range of astrophysics for many decades to come. For studies of the galaxy population within the local Universe these broad, general user capabilities, will enable an extremely wide range of science covering many areas of astrophysics, and will form the bridge between the detailed studies of objects in our own Galaxy and the distant high-redshift Universe. Deep and moderate-resolution (few arcsec) continuum and spectral line surveys of large numbers of nearby galaxies will be provided by projected SKA1 "all-sky" surveys at frequencies of $\sim$1-2 GHz. Such large area surveys will essentially provide a full radio atlas of the local Universe and allow detailed studies of the non-thermal radio component of galaxies. However, multiple, pointed observations covering a wide range of frequency bands, in particular higher band SKA1–MID (band 5), will be required to characterise the non-thermal components of local galaxies. Even with modest capability reductions, SKA1 will make significant advances in this field. This will, for the first time, allow the determination of SF within galaxies covering the full range of type and environments which will be critical to our understanding of galaxy evolution and SF through cosmic time.

Via higher frequency bands in SKA1 and later baseline extensions during the full SKA high angular resolution ($> 0\farcs5$ to mas) continuum and spectral line (maser and absorption studies) of nearby galaxies will allow the physical composition of these galaxies to be decomposed. Even with the modest resolution of SKA1, this will result in the detection and study of many thousands of individual SF and accretion-related components such as SNe, SNR, HII and their like. Via such observations the SKA will not only be able to study the physics of SF and extreme physics in accretion dominated sources on an individual basis in nearby galaxies, but also allow statistical properties of these sources to be investigated, how they interact with the ISM and how they affect galaxy evolution.

PoS(AASKA14)070

References

Aharonian, F., Arshakian, T. G., Allen, B., et al. 2013, Pathway to the Square Kilometre Array - The German White Paper, Ed. Köckner et al.
Alberdi, A., Colina, L., Torrelles, J. M., et al. 2006, ApJ, 638, 938
Araya, E., Hofner, P., Kurtz, S., et al., 2004, ApJ, 154, 541
Argo, M. K., Pedlar, A., Beswick. R. J., et al, 2010, MNRAS, 402, 2703
Argo, M. K., Beswick, R. J., Muxlow, T. W. B., et al., 2013, POS(11th EVN Symposium)05
Appleton, P. N., Fadda, D. T., Marleau, F. R. et al. 2004, ApJS, 154, 147
Baan, W. A., 1989, ApJ, 346, 680
Baan, W. A. Salzer, J. J., LeWinter, R. D, 1998, ApJ, 509, 633
Batejat, F., Conway, J. E., Rushton, A., et al. 2012, A&A, 542, 24
Beck, R., & Krause, M. 2005, Astronomische Nachrichten, 326, 414
Beck, R. et al. "Structure, dynamical impact and origin of magnetic fields in nearby galaxies in the SKA era", in proceedings of "Advancing Astrophysics with the Square Kilometre Array", 2015, PoS(AASKA14)094
Beswick, R. J., Muxlow, T. W. B. Thrall, H., et al 2008, MNRAS, 385, 1143
Bell, E. F. 2003, ApJ, 586, 794
de Blok, E. et al. "The SKA view of the Neutral Interstellar Medium in Galaxies", in proceedings of "Advancing Astrophysics with the Square Kilometre Array", 2015, PoS(AASKA14)129
Bondi. M., Perez-Torres, M. P., Dallacasa, D., et al. 2005, MNRAS, 361, 748
Bondi, M., Perez-Torres, M. A., Herrero-Illana, R, et al. 2012, A&A, 539, 134
Braun, R., Oosterloo, T. A., Morganti, R., et al. 2007, A&A, 461, 455
Brunthaler, A., Henkel, C, de Blok et al., 2006, A&A, 457, 109
Colina, L., Alberdi, A., Torrelles, J. M., et al. 2001, ApJ, 553, L19
Condon, J. J. 1992, ARA&A, 30, 575
Condon, J. J., Cotton, W. D., & Broderick, J. J. 2002, AJ, 124, 675
Corbel, S. et al. "Incoherent transient radio emission from stellar-mass compact objects in the SKA era", in proceedings of "Advancing Astrophysics with the Square Kilometre Array", 2015, PoS(AASKA14)053
Darling, J. & Giovanelli, R., 2002, AJ, 124, 100
Darling, J., 2007, ApJ, 669, L9
Dumas, G., Schinnerer, E., Tabatabaei, F. S, et al, 2011, AJ, 141, 41
Etoka, S. et al. "OH masers in the Milky Way and Local group galaxies in the SKA era", in proceedings of "Advancing Astrophysics with the Square Kilometre Array", 2015, PoS(AASKA14)125
Fender, R. et al. "The Transient Universe with the Square Kilometre Array ", in proceedings of "Advancing Astrophysics with the Square Kilometre Array", 2015, PoS(AASKA14)051
Fenech, D. M., Muxlow, T. W. B., Beswick, R. J., et al. 2008, MNRAS, 391, 1384
Fenech, D. M., Beswick, R. J., Muxlow, T. W. B., et al. 2010, MNRAS, 408, 607
Gallimore, J. F., Baum, S. A., O'Dea C. P., et al., 1996, ApJ, 462, 740
Garrett, M. A. 2002, A&A, 384, 19
Gebhardt, K., Rich, R. M., & Ho, L. C. 2005, ApJ, 634, 1093

PoS(AASKA14)070

Gendre, M. A., Fenech, D. M., Beswick, R. J., et al. 2013, MNRAS, 431, 1107
González-Alfonso, E., Fischer, J., Garciá-Carpio J., et al., 2014, A&A, 561, A27
Gray, M., Maser Sources in Astrophysics, CUP 2012
Green, J., et al. "Maser Astrometry with VLBI and the SKA", in proceedings of "Advancing Astrophysics with the Square Kilometre Array", 2015, PoS(AASKA14)119
Haynes, M. P., Giovanelli, R., Martin, A. M., et al., 2011, AJ, 142, 170
Heald, G. et al. "Magnetic field tomography in nearby galaxies with the Square Kilometre Array", in proceedings of "Advancing Astrophysics with the Square Kilometre Array", 2015, PoS(AASKA14)106
Heesen, V., Rau, U., Rupen, M. P., et al. 2011, ApJ, 739, L23
Heesen, V., Brinks, E., Leroy, A. K. et al. 2014, AJ, 147, 103
Helou, G., Soifer, B. T. & Rowan-Robinson, M. 1985, ApJ, 298, L7
Herrnstein, J. R., Moran, J. M., Greenhill, L. J., et al., 1999, Nature., 400, 539
Ho, L. C., Filippenko, A. V., Sargent, W. L. W. 1997, ApJ, 487, 568
Humphreys, E. M. L., Reid, M. J., Moran, J. M., et al., 2013, ApJ, 755, 13
Impellizzeri, C. M. V., Roy, A. L. & Henkel, C. 2006, PoS(8th EVN Symposium)
Impellizzeri, C. M. V., McKean, J. P., Castangia, P., et al., 2008, Nature., 456, 927
de Jong, T., Klein, U., Wielebinski, R., & Wunderlich, E. 1985, A&A, 147, L6
Joseph, T. D., Maccarone, T. J., & Fender, R. P. 2011, MNRAS, 415, 59
Kaaret, P., Ward, M. J., & Zezas, A., 2004 MNRAS, 351, 83
Kandalyan, R. A. & Al-Zyout, M. M.,2010 Astrophysics, 53, 475
Kankare, E., Mattila, S., Ryder, S., et al., 2008, ApJ, 687, 97
Kennicutt, R. C., Jr. 1998, ApJ, 498, 541
King, A. R., 2009, MNRAS, 393, 41
Kitchener, B., Brinks, E., Heesen, V., et al. 2014, AJ, (submitted)
Klöckner, H.-R., Baan, W. A. & Garrett, M. A. 2003, Nature, 421, 821
Klöckner, H.-R., 2004, PhD Thesis, University of Groningen
Kondratko, P. T., Greenhil L. J. & Moran, J. M., 2003, ApJ, 618, 618
Körding, E. G., Colbert, E. & Falcke, H. 2005, A&A, 436, 427
Körding, E. G., Jester, S. & Fender, R. 2006, MNRAS, 372, 1366
Körding, E. G., Jester, S. & Fender, R. 2008, MNRAS, 383, 277
Kuo, C. Y., Braatz, J. A., Reid, M. J., et al., 2013, ApJ, 767, 155
Lacki, B. C., & Thompson, T. A. 2010, ApJ, 717, 196
Lacki, B. C., Thompson, T. A., & Quataert, E. 2010, ApJ, 717, 1
Li, Y., Calzetti, D., Kennicutt, R. C., et al. 2010, ApJ, 725, 677
Lindberg, J. E., Aalto, S., Costagliola, F., et al., 2011, A&A, 527, A150
Lisenfeld, U., Völk, H. J., & Xu, C. 1996, A&A, 314, 745
Lockett, P. & Elizur, M., 2008, ApJ, 677, 985
Lonsdale, C. J., Lonsdale, C. J., Smith, H. E., et al., 1998 ApJ, 493, L13
Lonsdale, C. J., Lonsdale, C. J., Smith, H. E., et al., 2003, ApJ, 592, 804
Lonsdale, C. J., Diamond, P. J., Thrall, H., et al. 2006, ApJ, 647, L185
Mancuso, C. et al. "Radio Observations of Star-forming Galaxies in the SKA era", in proceedings of "Advancing Astrophysics with the Square Kilometre Array", 2015, PoS(AASKA14)082

PoS(AASKA14)070

Mangum, J. G., Darling, J., Henkel, C. et al., 2013, AJ, 766, 108
di Matteo, T., Springel, V. & Herquits, L. 2005, Nature, 433, 605
Mattila, S., Dahlen, T., Efstathiou, A., et al., 2012, ApJ, 756, 111
McBride, J., Heiles, C., Elitzur, M. 2013, ApJ, 774, 35
McKean, J. &Roy, A. L., 2009, Panoramic Radio Astronomy, PoS, 89, 60
Migenes, V., Coziol, R., Cooprider, K., et al., 2011, MNRAS, 416, 12
Momjian, E., Romney, J. D., Carilli, C. L., et al., 2006, ApJ, 653, 1172
Morganti, R. et al. "Cool Outflows and HI absorbers with SKA", in proceedings of "Advancing Astrophysics with the Square Kilometre Array", 2015, PoS(AASKA14)134
Murphy, E. J., Braun, R., Helou, G., et al. 2006, ApJ, 638, 157
Murphy, E. J., Helou, G., Kenney, J. D. P., et al. 2008, ApJ, 678, 828
Murphy, E. J. 2009, ApJ, 706, 482
Murphy, E. J., Condon, J. J., Schinnerer, E. et al. 2011, ApJ, 737, 67
Murphy, E. J., Bremseth, J., Mason, B. S., et al. 2012, ApJ, 761, 97
Murphy, E. J., Sargent, M., T, Beswick, R. J., et al. "The Astrophysics of Star Formation Across Cosmic Time at >10GHz with the Square Kilometer Array", in proceedings of "Advancing Astrophysics with the Square Kilometre Array", 2015, PoS(AASKA14)085
Muxlow, T. W. B., Beswick, R. J., Garrington, S. T., et al. 2010, MNRAS, 404, 109
Nagar, N. M., Falcke, H. & Wilson, A. S. 2005, A&A, 435, 521
Neff, S. G., Ulvestad J. S., Teng, S. H. 2004, ApJ, 611, 186
Niklas, S., & Beck, R. 1997, A&A, 320, 54
Norris, R. P., Afonso, J., Bacon, R. D., et al 2013, PASA, 30, 20
Oonk, R., et al. "The Physics of the Cold neutral Medium: Low-frequency Radio recombination Lines with the SKA", in proceedings of "Advancing Astrophysics with the Square Kilometre Array", 2015, PoS(AASKA14)139
Pakull, M. W., & Mirioni, L., 2002, in proceedings of “New Visions of the X-ray Universe in the XMM-Newton and Chandra Era, astro-ph/0202488
Pakull, M. W., & Mirioni, L., 2003, Rev. Mexicana Astron. Astrofis.15, 197
Paladino, R. et al. "Synergies between SKA and ALMA: observations of Nearby Galaxies", in proceedings of "Advancing Astrophysics with the Square Kilometre Array", 2015, PoS(AASKA14)156
Paragi, Z., Godfrey, L., Reynolds, C., et al. "Very Long baseline Interferometry with the SKA", in proceedings of "Advancing Astrophysics with the Square Kilometre Array", 2015, PoS(AASKA14)143
Parra, R., Conway, J. E., Elitzur, M. et al., 2005, A&A, 443, 383
Parra, R., Conway, J. E., Diamond, P. J., et al. 2007, ApJ, 659, 314
Pedlar, A 2001, IAU Symp., 205, 366
Peel, M. W., Dickinson, C., Davies, R. D., et al. 2011, MNRAS, 416, 99
Pérez-Torres, M. A., Mattila, S., Alberdi, A., et al. 2007, ApJ, 671, L21
Pérez-Torres, M. A., Romero, C., Alberdi, A., et al. 2008, *C*BET, 1392, 2P
Pérez-Torres, M. A., Romero-Cañizales, C., Alberdi, A., et al 2009a, A&A, 507, L17
Pérez-Torres, M. A., Alberdi, A., Colina, L., et al 2009b MNRAS399, 1641
Pérez-Torres, M. A., Alberdi, A., Romero-Cañizales, C., et al 2010, A&A, 519, L5

PoS(AASKA14)070

Pérez-Torres, M. et al. "Radio emission from young CCSNe and Type Ia SNe with the SKA", in proceedings of "Advancing Astrophysics with the Square Kilometre Array", 2015, PoS(AASKA14)060
Pihlström Y. M., Baan, W. A., Darling, J., et al. 2005, ApJ, 618, 705
Planck Collaboration, 2013, 2013arXiv1303.5076P
Polatidis, A. G. & Aalto, S., 2001, IAU Symp. 205, 2011
Prandoni, I. & Seymour, N, "Revealing the Physics and Evolution of Galaxies and Galaxy Clusters with SKA Continuum Surveys", in proceedings of "Advancing Astrophysics with the Square Kilometre Array", 2015, PoS(AASKA14)067
Price, R., & Duric, N. 1992, ApJ, 401, 81
Richards, A. M. S., Knapen, J. H., Yates, J. A. et al., 2005, MNRAS, 364, 353
Rickert, M. 2011 MSc thesis, DePaul University, Chicago
Roberts, T. P., 2007, Ap&SS, 311, 203
Robishaw, T. et al. "Measuring Magnetic Fields Near and Far with the SKA via the Zeeman Effect", in proceedings of "Advancing Astrophysics with the Square Kilometre Array", 2015, PoS(AASKA14)110
Rovilos, E., Diamond, P. J., Lonsdale, C. J., et al., 2003, MNRAS, 342, 373
Rovilos, E., Diamond, P. J., Lonsdale, C. J., et al. 2005, MNRAS, 359, 827
Salter, C. J., Ghosh, T., Catinella, B. et al. 2008, AJ, 136, 389
Schleicher, D. R. G., & Beck, R. 2013, A&A, 556, A142
Sjouwerman, L. O., Murray, C. E., Pihlström, Y. M., et al. 2010 ApJ, 724, 158
Smith, H. E., Lonsdale, C. J., Lonsdale, C. J., et al. 1998,ApJ, 493, L17
Tabatabaei, F. S,. Schinnerer, E. Murphy, E. J., et al. 2013, A&A, 552, 19
Tarchi, A., 2012, IAU Symposium 287, CUP, 323
Trudolyubov & Priedhorsky 2004 ApJ, 616, 821
Ulvestad, Greene & Ho 2007, ApJ, 616, 151
Völk, H. J. 1989, A&A, 218, 67
Walter, F., Bolatto, A. D., Leroy, A. K., et al. 2013, AAS, 22122105
Wehner, E. H., & Harris, W. E. 2006, ApJ, 644, L17
Webb, N., Cseh, D., Lenc, E., et al. 2012, Science, 337, 554
Weiler, K. W., Panagia, N., Montes, M .J., et al. 2002, ARA&A, 40, 387
Willett, K. W., Darling, J., Spoon, H. W. W., et al., 2011, AJ, 730 56
Willett, K. W., 2012, IAU Symposium 287, CUP, 345
Wolter, A. et al "Radio investigations of Ultra-luminous X-ray (ULX) sources in the SKA Era", in proceedings of "Advancing Astrophysics with the Square Kilometre Array", 2015, PoS(AASKA14)091
Yates, J. A., Richards, A. M. S., Wright, M. M. et al., 2000, MNRAS, 317, 28
Yu, Z.-Y., 2005, Chin. JAA, 5, 2, 159
Yun, M. S., Reddy, N. A., & Condon, J. J. 2001, ApJ, 554, 803

PoS(AASKA14)070

PROCEEDINGS OF SCIENCE

Identifying the first generation of radio powerful AGN in the Universe with the SKA

Jose Afonso[*1,2], **Jordi Casanellas**[3], **Isabella Prandoni**[4], **Matt Jarvis**[5,6], **Silvio Lorenzoni**[1], **Manuela Magliocchetti**[7], **Nick Seymour**[8]

[1] *Instituto de Astrofísica e Ciências do Espaço, Universidade de Lisboa, OAL, Tapada da Ajuda, PT1349-018 Lisboa, Portugal;* [2] *Departamento de Física, Faculdade de Ciências, Universidade de Lisboa, Edifício C8, Campo Grande, PT1749-016 Lisbon, Portugal;* [3] *Max Planck Institut fur Gravitationsphysik (Albert-Einstein- Institut), D-14476 Potsdam, Germany;* [4]*INAF - Istituto di Radioastronomia, Bologna, Italy;* [5]*Astrophysics, University of Oxford, Keble Road, Oxford, OX1 3RH, UK;* [6]*Physics Department, University of the Western Cape, Bellville 7535, South Africa;* [7]*INAF-IAPS, Via Fosso del Cavaliere 100, I-00133 Roma, Italy;* [8]*International Centre for Radio Astronomy Research, Curtin University, Perth, Australia*

E-mail: jafonso at oal.ul.pt

One of the most challenging and exciting subjects in modern astrophysics is that of galaxy formation at the epoch of reionisation. The SKA, with its revolutionary capabilities in terms of frequency range, resolution and sensitivity, will allow to explore the first Gyr of structure formation in the Universe, in particular, with the detection and study of the earliest manifestations of the AGN phenomenon. The tens of QSOs that are currently known out to the highest redshifts ($z \sim 7$), many of them exhibiting powerful radio emission, imply that super-massive black holes can be grown on a very short timescale and support the existence of very high redshift ($z > 7$) radio loud sources - sources that have so far escaped detection. Not only would such detections be paramount to the understanding of the earliest stages of galaxy evolution, they are necessary for the direct study of neutral hydrogen in the Epoch of Reionisation, through observations of the HI 21cm forest against such background sources.

In order to understand how SKA and SKA1 observations can be optimised to reveal these earliest AGN, we have examined the effect of a hot CMB on the emission of powerful and young radio galaxies. By looking at the SKA1 capabilities, in particular in terms of wavelength coverage and resolution, we determine how the effects of "CMB-muting" of a radio loud source can be observationally minimised and how to identify the best highest-redshift radio candidates. Considering different predictions for the space density of radio loud AGN at such redshifts, we identify the survey characteristics necessary to optimize the detection and identification of the very first generation of radio loud AGN in the Universe.

Advancing Astrophysics with the Square Kilometre Array
June 8-13, 2014
Giardini Naxos, Sicily, Italy

[*]Speaker.

PoS(AASKA14)071

1. Introduction

The epoch of "the first light" in the Universe, or Epoch of Reionisation (EoR), is one of the most exciting frontiers in current astrophysical knowledge. When (and how) did the first galaxies form? When (and how) did their first stars and supermassive black holes start to shine and how did the first light they produced rapidly ionise the entire Universe? In the quest to understand the earliest phases of galaxy evolution, one requires even more powerful telescopes than available today, capable of reaching faint and rare sources and, even more importantly, to understand how to fine-tune observations for the identification of such "holy-grail" objects.

Over the last few years, observations have been focusing on two fundamental processes for early galaxy evolution: star-formation and AGN activity. If the radiation from the first stars is often assumed to be the major culprit for the Reionisation of the Universe, recent work (Giallongo et al. 2012; Fontanot et al. 2012; Robertson et al. 2013; Fontanot et al. 2014) has raised some doubts over the contribution of accretion to early supermassive black holes (SMBHs). This is particularly relevant to radio observations with the upcoming Square Kilometre Array (SKA), as radio emission from the earliest AGN should be well within its reach. The detection of such very high redshift radio galaxies would be even more exciting for SKA, as it would then be feasible to consider the direct study of neutral hydrogen and its evolution *in the Epoch of Reionisation itself*, through observations of the HI 21cm forest against such background sources (Carilli et al. 2004; Khatri & Wandelt 2010).

In this chapter we aim to explore how SKA, and in particular SKA phase 1, can be optimised to identify these earliest examples of AGN activity in the Universe. We focus on quantifying the "CMB-muting" of young radio sources - the inverse Compton scattering of synchrotron-emitting electrons off energetic CMB photons, an effect that can be substantial at very high redshifts, and on how SKA radio surveys can be fine-tuned to not only detect but identify the earliest bouts of powerful AGN activity.

2. The onset of very high redshift AGN activity

The first sources of light, responsible for the transition from a neutral Universe to a completely ionised one, must have appeared sometime between $z \sim 30$ and $z \sim 7$ (e.g., Barkana & Loeb 2001; Zaroubi 2013). However, the fundamental observation of sources in the EoR is still only barely manageable: distant powerful quasars, out to $z \sim 7$, showing increasingly strong signatures of neutral hydrogen (HI) absorption in their optical spectra (e.g., Fan et al. 2006; Mortlock et al. 2011); $z \sim 6-9$ star-forming galaxies selected from Lyman-break techniques (e.g., Bouwens et al. 2011; Ono et al. 2012; Finkelstein et al. 2013; Bowler et al. 2014); the occasional detection (and very limited study) of elusive gamma-ray burst hosts (Tanvir et al. 2009; Cucchiara et al. 2011). Confirmation and detailed investigation of such distant sources is often impossible with current instrumentation, which has prevented expanding our knowledge of the EoR. The very origin of the reionisation mechanism itself is still unclear. Different studies have pointed to star formation as the origin of the photons that ionise the neutral hydrogen - if enough (proto-)galaxies start forming stars, even if at relatively low levels, and if these stars are hot and energetic enough, a few hundred Myr will be enough to completely ionise the Universe (Robertson et al. 2013). On the

PoS(AASKA14)071

other hand, accretion to a SMBH, another process that can produce the necessary ionising radiation, was deemed unlikely, as the time needed to nurture and grow such a "beast" seemed prohibitive, and the apparent break in the luminosity function of powerful AGN at high redshifts made such a significant population of ionising sources unlikely.

However, there has been an increasing number of detections of high redshift luminous ($L > 10^{44}$ erg/s) quasars, out to the current record breaker ULASJ1120+0641, at $z = 7.1$ (Mortlock et al. 2011). By themselves, these observations show that 10^8-10^9 $M_\odot$ SMBHs already exist well within the first Gyr of the Universe, implying a very early formation and a surprisingly rapid growth. Since observations are obviously biased towards the most powerful objects, this raises the intriguing question about the ionising contribution of a possibly significant number of slightly less luminous AGN in the first Gyr (Giallongo et al. 2012).

Anchored by these observations, theory has advanced significantly over the last few years (e.g., Haiman et al. 2004; Di Matteo et al. 2008, 2012; see Volonteri 2010 for a review). The problem is now not if a SMBH can be grown quickly enough (observations show that they can), but how to produce a sufficiently massive (10^2 to 10^5 $M_\odot$) BH seed a few hundred Myr before. If such BH seeds exist, they can lead to suitable SMBHs at $z > 7$, even without a continuous, and difficult to envisage, accretion at the Eddington rate for the entire period of growth. The remnants of the first generation (Pop. III) stars now appear *not* to be the such seeds, as sufficiently high stellar masses are less common than previously though (Turk et al. 2009; Clark et al. 2011; Greif et al. 2011; Stacy et al. 2012). Suitable seeds are nevertheless possible via direct gas collapse, quasi-stars produced by very high gas infall rates, the collapse of star clusters or even primordial black holes, formed much before the epoch of galaxy formation (e.g., Carr 2003; Bromm & Loeb 2003; Mayer et al. 2010; Begelman 2010; Devecchi et al. 2010, 2012; Khlopov 2010).

Whatever the process, the end result - the existence of SMBHs well within the first Gyr of the Universe - now seems established, and their detection and study is fundamental to understand the earliest phases of galaxy formation. The SKA, with its revolutionary capabilities, will be fundamental to explore these elusive sources, revealing the first steps of the AGN phenomenon in the Universe and the role of SMBHs to the development of galaxies from the earliest times.

3. The space density of very high redshift radio powerful AGN

A crucial ingredient to understand the role of a revolutionary telescope such as SKA for the observation of the first powerful AGN, is an estimate of their expected *space density*. Several models, taking different approaches to early AGN evolution, are currently available to produce such estimates.

A simple physically motivated semianalytic model for the SMBH population out to very high redshifts is presented by Haiman et al. (2004). Constrained by the optical-IR and X-ray quasar luminosity functions (LFs) at lower redshifts ($z \sim 5$), the Luminosity Function and number counts of bright (~ 1 mJy) radio sources at high redshift and the counts at the $10\,\mu$Jy level in deep radio observations, this model predicts the detection of ~ 60 AGN per deg^2 for $z > 6$, ~ 20 for $z > 8$, and ~ 10 for $z > 10$, for a radio survey with a detection threshold of $10\,\mu$Jy. In this model, a discrepancy in the predicted source counts at $\sim 10\,\mu$Jy is solved by assuming that SMBHs with masses $M < 10^7$ $M_\odot$ are either rare or are inefficient at producing radio emission. If that is the case,

PoS(AASKA14)071

then the detection rate of very high redshift AGN does not change significantly even if reaching lower observed radio fluxes – essentially all radio emitting AGN, those with $M > 10^7\,\mathrm{M}_\odot$, are already detected at $10\,\mu$Jy in this model. Another point to notice is that a flat spectral index is assumed – if this is relaxed to $\alpha \sim 0.5$ ($F_\nu \propto \nu^{-\alpha}$) the counts are reduced by a factor of a few, at most, and only for the highest frequencies of ~ 10 GHz.

Another model appropriate to estimate the abundance of very high redshift AGN is the SKADS Simulated Skies (S3, Wilman et al. 2008, 2010). The model predicts the detection of ~ 160 AGN per deg^2 for $z > 6$, ~ 100 for $z > 8$, and ~ 70 for z>10, for a radio survey complete to $10\,\mu$Jy. The AGN type separation therein indicates that one third of the detected AGN in the model at $z > 6$ are young Gigahertz-Peaked Sources (GPS), while the other two thirds are essentially composed of FRI sources. The AGN mix changes at $z > 10$ to a 50/50 ratio between FRIs and GPS sources.

Although the difference between the Haiman et al. (2004) and S3 predictions is significant, both models suggest a very substantial presence of detectable AGN at the highest redshifts. However, in spite of the optimistic predictions, the unavoidable fact is that very high redshift radio AGN have not been easy to detect, even after years of dedicated efforts by several teams. The highest redshift purely radio selected AGN continues to be TN J0924-2201, at a redshift of $z = 5.2$ (van Breugel et al. 1999). More recently, selection based on a radio-to-near-infrared criterion led to the discovery of a $z = 4.9$ radio powerful source (Jarvis et al. 2009). The combination of optical quasar selection criteria with a radio detection has also resulted in the identification of a number of radio luminous AGN at high redshifts ($z \sim 6$, e.g. McGreer et al. 2006; Zeimann et al. 2011).

One of the major difficulties is certainly the *confirmation* of radio-selected very high redshift candidates, as this relies in lengthy optical/NIR spectroscopy observations with the largest telescopes available. However, given that we currently know a few tens of optical/NIR selected QSOs at $z \sim 6-7$ (e.g., Fan et al. 2006; Willott et al. 2007, 2009; Jiang et al. 2008; Mortlock et al. 2011; Venemans et al. 2013), even selection biases start having a rough time explaining the sparseness of very high redshift radio sources. This naturally leads to analysing more deeply the physics of radio emission within the first Gyr after the Big Bang: are there physical processes that will lead to a decreased radio emission that can explain the difficulty in finding the earliest examples of AGN activity? And, if so, can one tune a radio survey in the frequency vs. sensitivity parameter space in order to optimize the probability of finding such early sources?

4. The physics of continuum radio emission at very high redshift

The continuum radio emission from AGN is dominated by synchrotron emission produced by highly energetic charged particles powered by the collapse of matter to a SMBH. In the early Universe, this process will happen with two important differences with respect to what happens at more recent epochs: the environment will be denser and the interaction with the cosmic microwave background (CMB) will be more significant, given the higher energy density of its radiation field ($U_{CMB} \propto (1+z)^4$).

In a recent work, Ghisellini et al. (2014) have considered the interaction between the extended emission of a radio jet and the CMB, concluding that energy losses of emitting electrons by Inverse Compton (IC) to the hot CMB may overcome synchrotron losses for epochs earlier than by $z \sim 3-5$ (an effect we will call here CMB-muting, and which can easily reach factors of 10 at GHz

PoS(AASKA14)071

frequencies, depending on the strength of the magnetic field in the emitting region). This is more significant at higher radio frequencies, which suggests that finding powerful AGN at high redshift based on the identification of extended radio structures should be better performed at lower radio frequencies (e.g., observing in the $10-100$ MHz range instead of ~ 10 GHz).

Given that early galaxy formation happened in much denser environments, the expansion of radio emitting material must also have been more difficult. Hence, environment, age, and significant CMB-muting for very high redshifts, all combine to favour looking for compact radio sources in the highest redshift Universe. Even if the jets are able to expand and form extended lobes, which will likely be severely CMB-muted at the highest redshifts, their compact radio cores may still be detectable as compact radio sources.

We have recently started looking at the effects of CMB-muting in compact radio sources (Casanellas et al. 2015), namely Compact Steep Spectrum (CSS) sources or Gigahertz Peaked-Spectrum (GPS) sources (e.g., Falcke et al. 2004). These are radio AGN at their early evolutionary stages, with GPS sources being considered to evolve into CSS sources in a self-similar way at later stages, displaying increasing sizes (up to a few kpc) and radio spectra peaking at lower frequencies (to below ~ 500 MHz, see e.g., O'Dea 1998). GPS and CSS sources are thought to be the progenitors of larger classical radio galaxies (Carvalho 1985; Readhead et al. 1996), and GPS or CSS-like radio spectra are also found in the inner jets or radio cores of AGNs with extended lobes.

The main emission mechanism in these radio sources is the synchrotron radiation from the relativistic electrons in their jets, as in classical radio galaxies but with the hot spots located closer to the nucleus. The physical processes governing the energy balance of the electrons in these sources at high redshift are similar to those in the nearby Universe, with the difference that the denser radiation field of the CMB which may play a more important role.

By modelling the balance between synchrotron emission (including the effects of synchrotron self-absorption, important for sources in their early evolutionary stages, such as GPS and CSS) and CMB-muting in the core of radio-powerful AGN, we find that in contrast with extended sources, compact radio cores such as CSS and GPS sources do not generally suffer significant radiative losses due to inverse Compton with the CMB – even at the highest redshifts ($z \gtrsim 10$). Only for CSS sources with weaker magnetic fields ($\lesssim 200\,\mu$G) do we find significant CMB-muting, resulting in a reduction of the expected flux density at high frequencies ($\gtrsim 1$ GHz). In this case, the flux density is much less affected at lower frequencies and, with the decrease of the break frequency above which the CMB-muting is most obvious, the radio SED becomes steeper between MHz and GHz frequencies.

As an illustration of the potential effect of CMB-muting in compact radio sources with weaker magnetic fields, we show in Figure 1 how the observed radio SED of the CSS source 3C455 ($z = 0.543$) would change if it was placed at increasing redshifts. The substantial CMB-muting at high redshift steepens the spectrum of the source, strongly reducing the flux density at the higher frequencies. On the other hand, the impact is weaker at low frequencies, as the CMB-muting preferentially reduces the population of the more energetic electrons, the main contributors to the high frequency region of the spectra.

A significant reduction of the flux density at high frequencies would be observed for 3C455 at $z \gtrsim 5$ due to the energy losses by CMB-muting. For example, at $z = 8$ the flux density at ~ 1 GHz would decrease by a factor of 3 when CMB-muting is taken into account (see Figure 1). On the

PoS(AASKA14)071

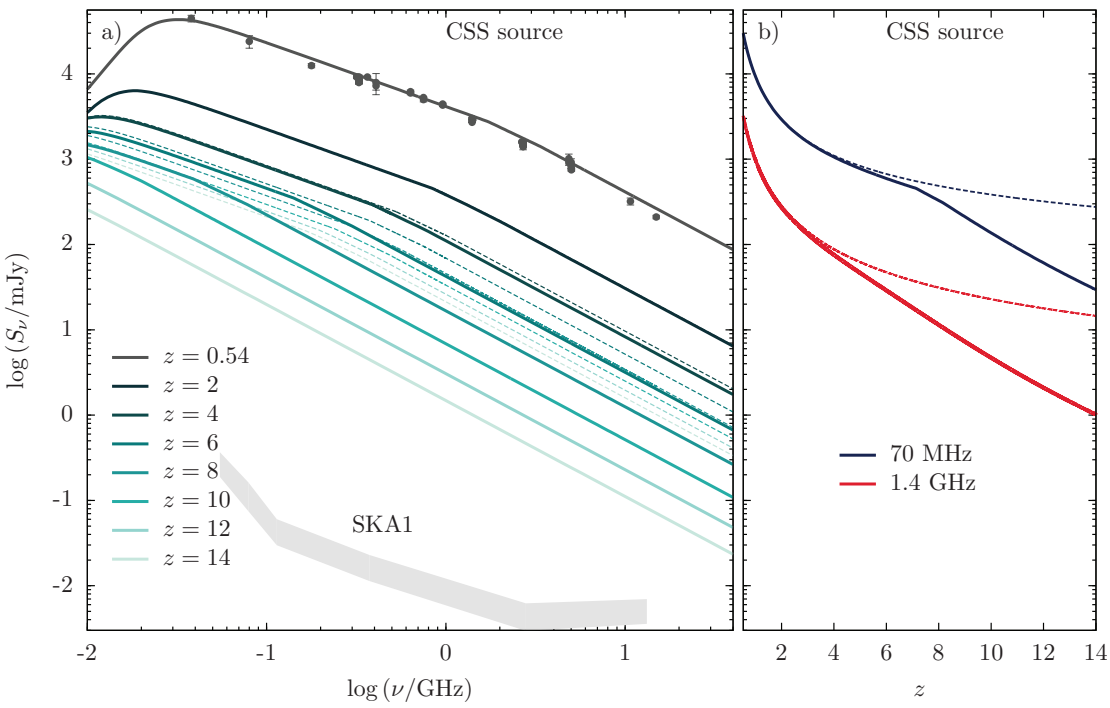

Figure 1: a) Observed radio SED of the CSS source, 3C455, if placed at different redshifts. The effect of redshift (dashed lines) and considering also CMB-muting (solid lines) is shown. A magnetic field of $B = 200\,\mu$G (Murgia et al. 1999) was assumed. The gray region marks the sensitivity limits (5 to 10 σ) of SKA1 for an integration time of 30 minutes; b) Flux densities at 70 MHz and 1.4 GHz from the same CSS source.

other hand, the reduction of the flux density at 70 MHz is more moderate at the same redshift.

We note that such low magnetic fields as those in 3C455 are observed in a very small percentage of the observed CSS population (Murgia et al. 1999). For the vast majority of known CSS and GPS sources, CMB-muting will not have an appreciable effect on their observed radio SEDs. An example is shown in Figure 2, for the GPS source GPS 2352+495 ($z = 0.237$). In contrast to the CSS source, the IC/CMB mechanism does not produce significant radiative losses due to the larger magnetic fields. One should note that the flux density at low frequencies does not decline with redshift as quickly as at high frequencies, pointing to the interest in considering the lower frequency regime ($\sim$ 100 MHz) when searching for the highest redshift sources.

Furthermore, it is also noteworthy that the detection of the turnover frequency, due to synchrotron self-absorption, for compact radio sources is particularly relevant for their potential identification from radio observations alone – fundamental at the highest redshifts. The coverage of the low frequency regime ($\nu \sim 10 - 500$ MHz) with a sensitive radio telescope would thus be of particular interest.

5. Identifying the highest redshift radio sources with SKA

In terms of continuum detection of the highest redshift radio powerful AGN, SKA1 should

PoS(AASKA14)071

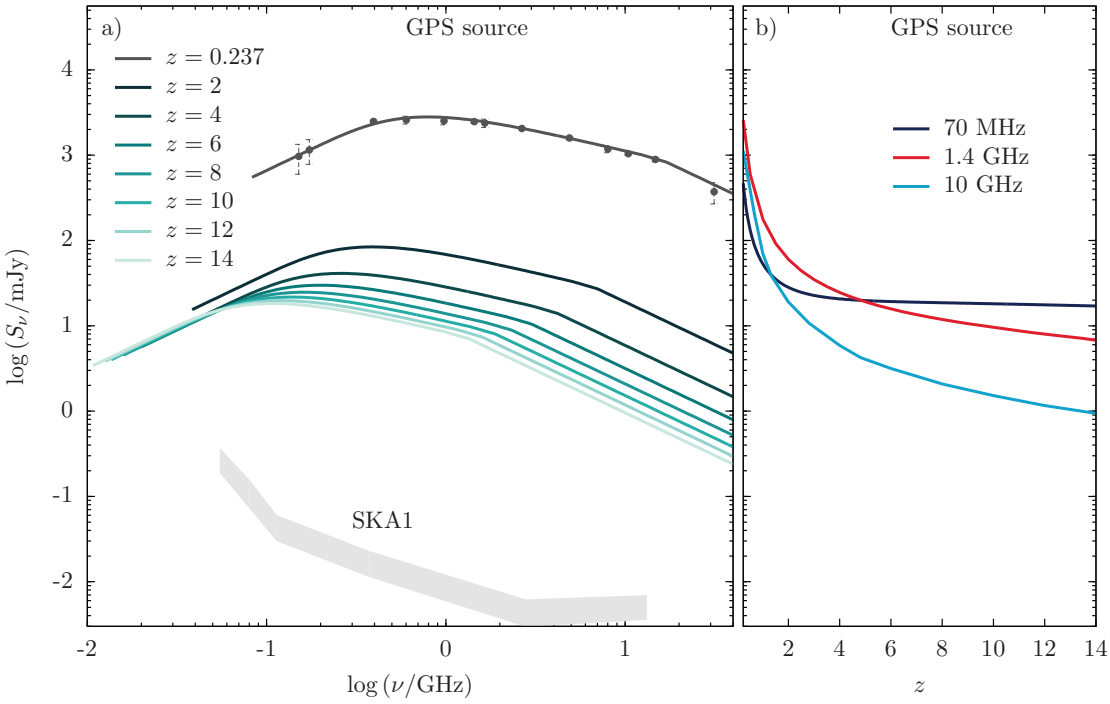

Figure 2: a) Observed radio SED of a representative GPS source, GPS 2352+495, at different redshifts, as in Figure 1. A magnetic field of $B = 5\,\mathrm{mG}$ was considered (O'Dea 1998). The gray region marks the sensitivity limits (5 to 10 σ) of SKA1 for an integration time of 30 minutes; b) Flux densities at 70 MHz, 1.4 GHz and 20 GHz from the same GPS source.

be able to detect thousands of such sources at redshifts $z \sim 6-10$. As seen above, both Haiman et al. (2004) and the S3 models predict that a wide (1000-5000 deg^2) survey at ~ 1 GHz reaching a detection level of $10\,\mu$Jy will reveal as many as $\sim 10^5$ powerful AGN at $z > 6$, several tens of thousands at $z > 8$ and even $\sim 10^4$ at $z > 10$. Even considering the indication of the S3 models that up to half of these sources (the extended FRIs in the sample) may be affected by considerable CMB-muting, that still leaves a few thousand AGN (the young and compact ones) detectable even at $z > 10$. Naturally, the huge uncertainties about a possible large decrease of the luminosity function of AGN at the highest redshifts (e.g., Rigby et al. 2011) advise some caution in using these numbers, but, as far as we can tell, even the shallower SKA1 surveys (see Prandoni & Seymour 2015, this volume) will reveal a large number of very high redshift powerful AGN.

As can be seen in Figure 1 and Figure 2, the exploration of radio observations can provide some indication about the redshift of the source, in particular when considering low-frequency radio observations – either from the SKA itself, or adding observations from observatories like LOFAR, at even lower frequencies ($\sim 10-100$ MHz). Nevertheless, the radio SED shape alone will likely not be sufficient to provide more than a way to help selecting potentially interesting sources for follow-up work. In order to confirm that radio sources are indeed at high-redshift (say, $z > 6$) multi-wavelength data will be crucial. Deep imaging above and below the Lyman-α line will be required, which consequently means a combination of optical and near-infrared observations as even at $z = 6$ Lyman-α is at ~ 8500Å, and as we push to much higher redshifts then the short wavelength band

PoS(AASKA14)071

is pushed well into the near-infrared window. Therefore the key surveys for this science case are LSST (see Bacon et al. 2015, this volume), to essentially rule out low-redshift interlopers from the high-redshift radio galaxy sample, and a combination of wide-area, deep near-infrared imaging from *Euclid* and deep field near-infrared imaging from either ground-based facilities such as VISTA now (see e.g. McCracken et al. 2012; Jarvis et al. 2013) but possibly crucially the *JWST* which will be able to detect these galaxies individually with relatively short exposures, thus confirming the likelihood of the source being within the epoch of reionisation. Nevertheless, one should not neglect the upcoming availability of powerful near-infrared spectrographs, like *MOONS* (Cirasuolo et al. 2012) at the VLT, which will be able to confirm a very high redshift nature for many of the brightest candidates.

6. Conclusions

The unparalleled capabilities of SKA, in terms of sensitivity but mostly in terms of survey speed and wide frequency coverage, will allow for the detection of young powerful radio galaxies at very high redshifts (even out to $z \gtrsim 8$). The first powerful radio sources, whenever they exist, will be amongst the sources revealed by the early SKA1 surveys, allowing for the study of the first bouts of AGN activity in the Universe. The biggest challenge will be to identify such sources amongst the millions that will be observed. The use of the wide frequency range of SKA, possibly together with other radio observations at lower frequencies, will allow for the identification of robust candidates for such high redshift sources. Still, the combination of SKA surveys with optical and NIR surveys will be necessary for the confirmation of sources well within the epoch of reionisation. Given the availability of such complementary data in the near future, the study of the very first generation of radio loud AGN in the Universe will be well within our reach.

Acknowledgments

JA and SL gratefully acknowledge support from the Science and Technology Foundation (FCT, Portugal) through the research grants PTDC/FIS-AST/2194/2012 and PEst-OE/FIS/UI2751/2014, and the fellowship (SL) SFRH/ BPD/89554/2012. JC acknowledges support from the Alexander von Humboldt Foundation. MJ acknowledges support by the South African Square Kilometre Array Project, the South African National Research Foundation.

References

Bacon, D., et al. 2015, “Synergy between the Large Synoptic Survey Telescope and the Square Kilometre Array”, in proceedings of "Advancing Astrophysics with the Square Kilometre Array", PoS(AASKA14)145.

Barkana, R., & Loeb, A., 2001, Physics Reports, 349, 125

Begelman, M. C. 2010, MNRAS, 402, 673

Bouwens, R. J., Illingworth, G. D., Labbe, I., et al. 2011, Nature, 469, 504

Bowler, R. A. A., Dunlop, J. S., McLure, R. J., et al. 2014, MNRAS, 440, 2810

Bromm, V., & Loeb, A. 2003, ApJ, 596, 34

PoS(AASKA14)071

Casanellas, J., Afonso, J., Brito, R., et al., in preparation
Carilli, C. L., Furlanetto, S., Briggs, F., et al. 2004, New Astron. Rev., 48, 1029
Carvalho, J. C. 1985, MNRAS, 215, 463
Carr, B. J. 2003, Quantum Gravity: From Theory to Experimental Search, 631, 301
Cirasuolo, M., Afonso, J., Bender, R., et al. 2012, SPIE Conf. Ser., 8446,
Clark, P. C., Glover, S. C. O., Klessen, R. S., & Bromm, V. 2011, ApJ, 727, 110
Cucchiara, A., Levan, A. J., Fox, D. B., et al. 2011, ApJ, 736, 7
Devecchi, B., Volonteri, M., Colpi, M., & Haardt, F. 2010, MNRAS, 409, 1057
Devecchi, B., Volonteri, M., Rossi, E. M., et al. 2012, MNRAS, 421, 1465
Di Matteo, T., Colberg, J., Springel, V., Hernquist, L., & Sijacki, D. 2008, ApJ, 676, 33
Di Matteo, T., Khandai, N., DeGraf, C., et al. 2012, ApJL, 745, L29
Falcke, H., Körding, E., & Nagar, N. M. 2004, New Astron. Rev., 48, 1157
Fan, X., Strauss, M. A., Richards, G. T., et al. 2006, AJ, 131, 1203
Finkelstein, S. L., Papovich, C., Dickinson, M., et al. 2013, Nature, 502, 524
Fontanot, F., Cristiani, S., & Vanzella, E. 2012, MNRAS, 425, 1413
Fontanot, F., Cristiani, S., Pfrommer, C., Cupani, G., & Vanzella, E. 2014, MNRAS, 438, 2097
Giallongo, E., Menci, N., Fiore, F., et al. 2012, ApJ, 755, 124
Ghisellini, G., Celotti, A., Tavecchio, F., Haardt, F., & Sbarrato, T. 2014, MNRAS, 438, 2694
Greif, T. H., Springel, V., White, S. D. M., et al. 2011, ApJ, 737, 75
Haiman, Z., Quataert, E., & Bower, G. C. 2004, ApJ, 612, 698
Jarvis, M. J., Teimourian, H., Simpson, C., et al. 2009, MNRAS, 398, L83
Jarvis, M. J., Bonfield, D. G., Bruce, V. A., et al. 2013, MNRAS, 428, 1281
Jiang, L., Fan, X., Annis, J., et al. 2008, AJ, 135, 1057
Khatri, R. & Wandelt, B. D. 2010, Highlights of Astronomy, 15, 312
Khlopov, M. Y. 2010, Research in Astronomy and Astrophysics, 10, 495
Mayer, L., Kazantzidis, S., Escala, A., & Callegari, S. 2010, Nature, 466, 1082
McCracken, H. J., Milvang-Jensen, B., Dunlop, J., et al. 2012, A&A, 544, A156
McGreer, I. D., Becker, R. H., Helfand, D. J., & White, R. L. 2006, ApJ, 652, 157
Mortlock, D. J., Warren, S. J., Venemans, B. P., et al. 2011, Nature, 474, 616
Murgia, M., Fanti, C., Fanti, R., et al. 1999, A&A, 345, 769
O'Dea, C. P. 1998, PASP, 110, 493
Ono, Y., Ouchi, M., Mobasher, B., et al. 2012, ApJ, 744, 83
Prandoni, I. & Seymour, N. 2015, "Revealing the Physics and Evolution of Galaxies and Galaxy Clusters with SKA Continuum Surveys", in proceedings of "Advancing Astrophysics with the Square Kilometre Array", PoS(AASKA14)067
Readhead, A. C. S., Taylor, G. B., Pearson, T. J., & Wilkinson, P. N. 1996, ApJ, 460, 634
Rigby, E. E., Best, P. N., Brookes, M. H., et al. 2011, MNRAS, 416, 1900
Robertson, B. E., Furlanetto, S. R., Schneider, E., et al. 2013, ApJ, 768, 71
Stacy, A., Greif, T. H., & Bromm, V. 2012, MNRAS, 422, 290
Tanvir, N. R., Fox, D. B., Levan, A. J., et al. 2009, Nature, 461, 1254
Turk, M. J., Abel, T., & O'Shea, B. 2009, Science, 325, 601
van Breugel, W., De Breuck, C., Stanford, S. A., et al. 1999, ApJ, 518, L61
Venemans, B. P., Findlay, J. R., Sutherland, W. J., et al. 2013, ApJ, 779, 24

PoS(AASKA14)071

Volonteri, M. 2010, Astronomy and Astrophysics Review, 18, 279
Willott, C. J., Delorme, P., Omont, A., et al. 2007, AJ, 134, 2435
Willott, C. J., Delorme, P., Reylé, C., et al. 2009, AJ, 137, 3541
Wilman, R. J., Miller, L., Jarvis, M. J., et al. 2008, MNRAS, 388, 1335
Wilman, R. J., Jarvis, M. J., Mauch, T., Rawlings, S., & Hickey, S. 2010, MNRAS, 405, 447
Zaroubi, S. 2013, Astrophysics and Space Science Library, 396, 45 (arXiv:1206.0267)
Zeimann, G. R., White, R. L., Becker, R. H., et al. 2011, ApJ, 736, 57

PoS(AASKA14)071

PROCEEDINGS OF SCIENCE

Cluster Radio Halos at the crossroads between astrophysics and cosmology in the SKA era

R. Cassano[*1], **G. Bernardi**[2], **G. Brunetti**[1], **M. Brüggen**[3], **T. Clarke**[4], **D. Dallacasa**[1,5], **K. Dolag**[6], **S. Ettori**[7], **S. Giacintucci**[8], **C. Giocoli**[5], **M. Gitti**[1,5], **M. Johnston-Hollitt**[9], **R. Kale**[1,10], **M. Markevitch**[11], **R. Norris**[12], **M. Pandey-Pommier**[13], **G.W. Pratt**[14], **H. Röttgering**[15], **T. Venturi**[1]

[1] *INAF-IRA, Bologna, IT;* [2] *SKA SA, Rhodes University, SA ;* [3] *Hamburg University, Germany;* [4] *NRL, US;* [5] *DIFA, University of Bologna, IT;* [6] *USM, DE;* [7] *INAF - OAB, IT;* [8] *University of Maryland, US;* [9] *University of Wellington, NZ;* [10] *NCRA, Pune, IN;* [11] *NASA/GSFC, US;* [12] *CSIRO, AU;* [13] *CRAL, Lyon, FR;* [14] *CEA Saclay - IRFU, Service d' Astrophysique, FR;* [15] *Leiden Observatory, NL*

E-mail: rcassano@ira.inaf.it

Giant Radio Halos (**RH**) are diffuse, Mpc-sized, synchrotron radio sources observed in a fraction of galaxy clusters. They probe the energy content and properties of relativistic particles and magnetic fields in galaxy clusters and their imprint on cluster formation and evolution. RHs are found in merging clusters, suggesting that they are generated as a result of the dissipation of gravitational energy during the hierarchical sequence of mergers that leads to the formation of clusters themselves. The current leading scenario for the origin of RHs assumes that turbulence generated during cluster mergers re-accelerates pre-existing fossil and/or secondary electrons in the intra-cluster-medium (ICM) to the energies necessary to produce the observed radio emission. Moreover, more relaxed clusters could host diffuse "off state" halos, fainter than classical RHs, produced by secondary electrons. In this Chapter we use Monte Carlo simulations, that combine turbulent-acceleration physics and the generation of secondaries in the ICM, to calculate the occurrence of RHs in the Universe, their spectral properties and connection with properties of the hosting clusters at different cosmic epochs. Predictions for SKA1 surveys are presented at low (100-300 MHz) and mid (1-2 GHz) frequencies assuming the expected sensitivities and spatial resolutions of SKA1. SKA1 will step into an unexplored territory allowing us to study the formation and evolution of RHs in a totally new range of cluster masses and redshift. Based on our study, SKA1 observations will allow firm tests of the current theoretical hypothesis. In particular we show that the combination of SKA1-LOW and SUR will allow the discovery of ~ 1000 ultra-steep-spectrum halos and to detect for the very first time "off state" RHs. We expect that at least ~ 2500 giant RHs will be discovered by SKA1-LOW surveys up to $z \sim 0.6$. Remarkably these surveys will be sensitive to RHs in a cluster mass range (down to $\sim 10^{14} M_{\odot}$) and redshifts (up to ~ 1) that are unexplored by current observations. SKA1 surveys will be highly competitive with present and future SZ-surveys in the detection of high-redshift massive objects.

Advancing Astrophysics with the Square Kilometre Array
June 8-13, 2014
Giardini Naxos, Italy

PoS(AASKA14)073

1. Introduction

Giant Radio Halos (RHs) are diffuse, Mpc-sized, synchrotron radio sources with steep radio spectra ($\alpha > 1$, with $f(\nu) \propto \nu^{-\alpha}$) that are observed in the central regions of a fraction of galaxy clusters (*e.g.,* Feretti et al. 2012, for a review of the observational properties). They probe the energy content and properties of relativistic particles and magnetic fields in galaxy clusters and their imprint on cluster formation and evolution. RHs are always found in merging clusters[1], suggesting that they are generated as a result of the dissipation of gravitational energy during the hierarchical sequence of mergers that leads to the formation of clusters themselves (*e.g.,* Brunetti & Jones 2014, for a recent review). A popular idea for the origin of RHs is based on the hypothesis that turbulence generated during cluster mergers re-accelerates pre-existing fossil and/or secondary electrons in the intra-cluster-medium (ICM) to the energies necessary to produce the observed radio emission (*e.g.,* Brunetti et al. 2001; Petrosian 2001). According to turbulence-acceleration models the formation history of RHs depends on the cluster merging rate throughout cosmic epochs and on the mass of the hosting clusters themselves, which ultimately sets the energy budget that is available for the acceleration of relativistic particles. A key expectation is that RHs should preferentially be found in massive objects undergoing energetic merging events, whereas they should be rarer in less massive merging-systems. The reason making RHs less common in smaller systems is that the acceleration mechanism in the case of less energetic mergers is expected to generate increasingly steep spectra which become under luminous at higher frequencies (*e.g.,* Cassano et al. 2006, 2010a). This theoretical conjecture is consistent with the observed radio bimodality in galaxy clusters and its connection to cluster dynamics (*e.g.,* Cassano et al. 2010b), it is also supported by the discovery of RHs with very-steep spectrum (*e.g.,* Brunetti et al. 2008; Dallacasa et al. 2009).

The generation of secondary particles due to inelastic collisions between relativistic protons and thermal protons in the ICM is another mechanism for the generation of cluster-scale diffuse emission (*e.g.,* Dennison 1980; Blasi & Colafrancesco 1999). Studies in the radio and gamma-rays suggest that the contribution to RHs due to this latter mechanism is sub-dominant (Ackermann et al. 2010; Brunetti et al. 2012), however in more relaxed clusters it is expected to produce diffuse radio sources, called "off state" halos, fainter than classical RHs (*e.g.,* Brunetti & Lazarian 2011; Brown et al. 2011; Donnert et al. 2013).

In this Chapter we will adopt the theoretical framework described above and use Monte Carlo simulations, that combine turbulent-acceleration physics and the generation of secondaries in the ICM, to calculate the occurrence of RHs in the Universe and their spectral properties. These simulations provide a physically motivated way to model the connection between RHs (and their characteristics) and the thermodynamical properties and mass of the hosting clusters at different cosmic epochs. Predictions for SKA1 surveys are presented at low (100-300 MHz) and mid (1-2 GHz) frequencies assuming the expected sensitivities and spatial resolutions of SKA1 (SKA1 Performance Memo by R. Braun).

A ΛCDM cosmology ($H_o = 70\,\mathrm{km\,s^{-1}\,Mpc^{-1}}$, $\Omega_m = 0.3$, $\Omega_\Lambda = 0.7$) is adopted.

*Speaker.

[1] An exception is the halo in the cool-core cluster CL1821+643 (Bonafede et al 2014). One hypothesis suggested by these authors is however that this cluster is undergoing a minor or off-axis merger.

PoS(AASKA14)073

2. Statistical modeling of diffuse radio emission in clusters: "turbulent" and "off-state" halos

A detailed description of the theoretical-statistical model that we will use in this Chapter can be found in Cassano & Brunetti (2005) and Cassano et al. (2006), while applications to RH predictions for future surveys (with LOFAR, Apertif on WSRT, and ASKAP) can be found in Cassano et al. (2010a, 2012). In this section we provide a summary of the theoretical framework and of the most important implications for RH statistical properties and connection with the host clusters. In this contribution we follow the formation and evolution of two populations of cluster RHs: *(i)* "turbulent" halos generated in merging clusters by turbulent re-acceleration of relativistic particles, and *(ii)* "off-state" halos generated by secondary electrons in more relaxed clusters. The maximum emitted frequency, ν_s,[2] in turbulent halos depends ultimately on the turbulent energy budget that is available in the hosting cluster. We follow a simplified approach based on two separate cluster radio-populations. Specifically, we assume that those clusters where turbulence is not sufficient to generate RHs emitting at the observing frequency, ν_o, host "off-state" halos. We assume that presently observed giant RHs, those following the RH power – cluster X-ray luminosity correlation (see Fig.1, left panel), are mainly driven by turbulent re-acceleration in merging clusters. Whereas the radio power of clusters hosting "off-state" halos is constrained by using limits derived for "radio quiet" galaxy clusters (see upper limits in Fig.1; Brunetti et al. 2007; Brown et al. 2011). Brown et al. (2011) claimed the detection of diffuse emission from "off-state" galaxy clusters by stacking SUMSS images of ~ 100 clusters at a luminosity-level slightly below that constrained by the upper-limits in Fig.1. Optimistically in our modelling we shall assume that this is the level of the hadronically-induced "off state" halos.

We model the properties of the "turbulent" and "off-state" halos and their cosmic evolution by means of a Monte Carlo approach, which is based on the semi-analytic model of Lacey & Cole (1993; *i.e.,* extended Press & Schechter 1974) to describe the hierarchical process of formation of galaxy cluster dark matter halos. The merger history of a synthetic population of galaxy clusters is followed back in time and the generation of the turbulence in the ICM is estimated for each merger identified in the *merger trees*. It is assumed that turbulence is generated in the volume swept by the subcluster infalling into the main cluster and that a fixed fraction ($\sim 0.1-0.3$) of the PdV work done by this subcluster goes into MHD turbulence, which in turn becomes available for particle acceleration on Mpc-scale. We do not follow directly the process of magnetic field growth and amplification in the ICM, but this is anchored to the evolution of the host cluster, assuming a scaling between the mean rms magnetic field $\langle B\rangle$ and the virial cluster mass, M_v, $\langle B\rangle \propto M_v^b$, with $b \gtrsim 0.5$ (*e.g.,* Dolag et al. 2002).

The most important expectation of turbulent re-acceleration scenarios is that the synchrotron spectrum of RHs (see Fig.1, right panel) should become gradually steeper above a frequency, ν_s, that is determined by the competition between acceleration and energy losses and which is connected to the energetics of the merger events that generate the halos (*e.g.,* Fujita et al. 2003; Cassano & Brunetti 2005). The frequency ν_s depends on the acceleration efficiency , χ, and on

[2] at larger frequencies the synchrotron spectrum of halos steepens. Following Cassano et al. (2010) we adopt the convention that RHs have spectral index $\alpha = 1.9$ between $\nu_s/2.5$ and ν_s.

PoS(AASKA14)073

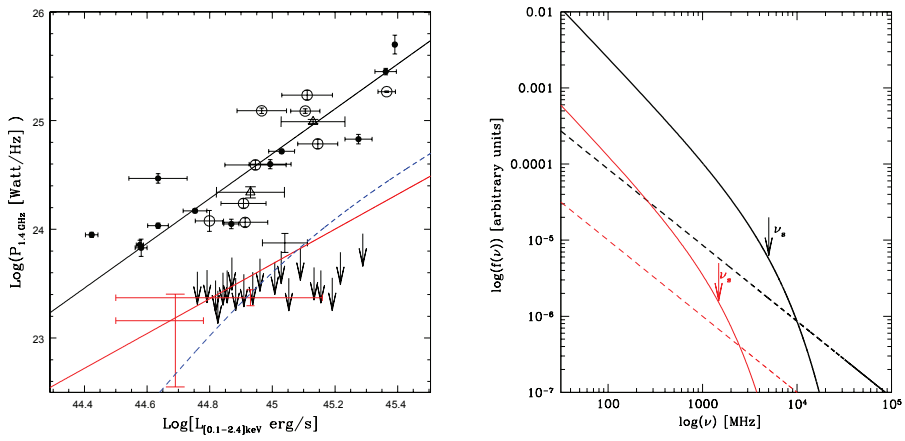

Figure 1: *Left Panel* Distribution of clusters in the $P_{1.4} - L_X$ plane (from Brunetti et al. 2009). Clusters from the literature (black filled circles) and clusters belonging to the "GMRT RH Survey" (open circles and arrows) are reported. The red crosses are obtained by staking the radio images of clusters from the SUMSS survey (Brown et al. 2011). On the same figure we also report the scalings adopted here for halos produced by secondary electrons (red solid line;see text for details). *Right Panel*: Reference spectra of "turbulent" RHs (solid lines) and "off-state" (hadronic) halos (dashed lines) in a massive (*i.e.,* $M_v \sim 2.5 \times 10^{15} M_\odot$; black thick lines) and less massive (*i.e.,* $M_v \sim 10^{15} M_\odot$; red thin lines) cluster. Arrows indicate the position of the steepening frequency, ν_s, in the two cases. The turbulent spectra are computed assuming in both cases a merger event with a sub-clump of mass $\Delta M = 5 \times 10^{14} M_\odot$ at $z = 0.023$.

$\langle B \rangle$, as $\nu_s \propto \langle B \rangle \chi^2 / (\langle B \rangle^2 + B_{cmb}^2)^2$ (*e.g.,* Cassano et al. 2006, 2010a)[3]. Monte Carlo simulations of cluster mergers that occur during the hierarchical process of cluster formation allow for evaluating χ from the estimated rate of turbulence-generation and the physical condition in the ICM, and consequently to explore the dependence of ν_s on cluster mass, redshift, and merger parameters in a statistical sample of synthetic clusters. Consequently, in the adopted scenario the population of RHs is expected to be made of a complex mixture of sources with different spectra, with massive (and hot) clusters that have a tendency to generate halos with spectra, measured between two frequencies, that are flatter than those in less massive systems (Fig.1, right panel).

Contrary to turbulent halos, "off-state" halos are expected with power-law spectra with fairly similar slopes (Fig.1, right panel), independently of the cluster mass. Consequently, surveying the sky at different radio frequencies and with appropriate sensitivities allows to disentangle these two populations.

In order to estimate the occurrence of RHs in surveys at different observing frequencies we assume that only those halos with $\nu_s \geq \nu_o$ can be observable, ν_o being the observing frequency. Energy arguments imply that giant RHs with $\nu_s \geq 1$ GHz are generated in connection with the most energetic merger-events in the Universe. Only these mergers can generate enough turbulence on Mpc scales and potentially produce the acceleration rate that is necessary to maintain the relativistic electrons emitting at these frequencies (Cassano & Brunetti 2005). In general, in this model the fraction of clusters with radio halos increases with the cluster mass, since more massive clusters

[3] $B_{cmb} = 3.2(1+z)^2 \mu$G is the equivalent magnetic field of the cosmic microwave background (CMB) radiation

PoS(AASKA14)073

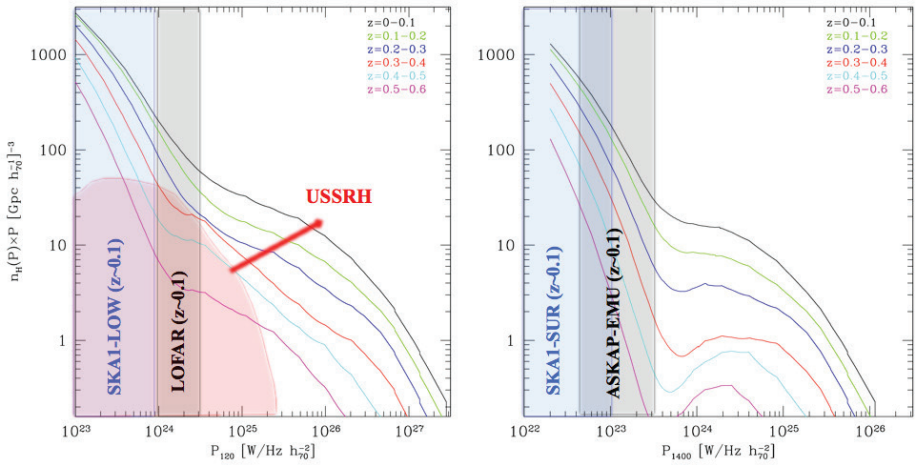

Figure 2: Total RHLFs obtained by combining the contributions from "turbulent" and from "off-state" (hadronic) halos at 120 MHz (left panel) and 1400 MHz (right panel) are reported at different redshifts (see figure panels). The local RHLF of USSRH is also highlighted (shaded red region). The expected sensitivities to RHs of SKA1-LOW and SUR, LOFAR and EMU are shown at $z \sim 0.1$ (shaded vertical regions).

are more turbulent (*e.g.,* Vazza et al. 2006; Hallman & Jeltema 2011), and thus are more likely to host a turbulent RH. Present surveys carried out at $\nu_o \sim 1$ GHz detect RHs only in the most massive and merging clusters (*e.g.,* Cassano et al. 2013).

For similar energy arguments RH with lower values of ν_s, or with ultra-steep radio spectra (USSRH[4]), must be more common, since they can be generated in connection with less energetic phenomena, *e.g.,* major mergers between less massive systems or minor mergers in massive systems, that are more common in the Universe.

3. The luminosity function of radio halos

The luminosity functions of turbulent RHs (RHLFs) with $\nu_s \geq \nu_0$ (*i.e.,* the expected number of halos per comoving volume and radio power "observable" at frequency ν_0) can be estimated by :

$$\frac{dN_H(z)}{dV\,dP(\nu_0)} = \frac{dN_H(z)}{dM\,dV} \Big/ \frac{dP(\nu_0)}{dM}\,, \tag{3.1}$$

where M is the virial cluster mass and $dN_H(z)/dM\,dV$ is the theoretical mass function of clusters hosting radio halos with $\nu_s \geq \nu_0$, that is obtained by combining Monte Carlo calculations of the fraction of clusters with RHs and the Press & Schechter (PS) mass function of clusters (*e.g.,* Cassano et al. 2006). Following Cassano et al. (2006) we estimate $dP(\nu_0)/dM$ from the correlation observed for giant RHs between the 1.4 GHz radio power, $P(1.4)$, and the mass of the parent clusters (*e.g.,* Govoni et al. 2001; Cassano et al. 2006, Fig.1, left panel).
The luminosity function of "off-state" halos is:

[4]Operatively, in this paper we define USSRH as those halos with $\alpha > 1.9$ between 250-600 MHz.

PoS (AASKA14) 073

$$\frac{dN_H^{sec}(z,\nu_o)}{dV\,dP} = \frac{dN_H^{sec}(z,\nu_o)}{dV\,dM} \times \frac{dM}{dP}\,, \tag{3.2}$$

where $dN_H(z)/dM\,dV$ is the massfunction of clusters hosting "off-state" halos, which is given by:

$$\frac{dN_H^{sec}(z,\nu_o)}{dV\,dM} = (1 - f_{RH}(M,\nu_o)) \times \frac{dN_M^{cl}}{dV\,dM} \tag{3.3}$$

where $f_{RH}(M,\nu_o)$ is the fraction of clusters of mass M with RHs due to turbulent re-acceleration (with $\nu_s \geq \nu_o$) and $dN_M^{cl}/dV\,dM$ is the cluster mass function. We derive dM/dP from the expected relation between the radio luminosity of "off-state" halos and the mass (or L_X) of the host clusters (*e.g.,* Kushnir et al. 2009) that is slightly flatter than that of giant RHs. In this Chapter, we adopt a simplified scaling in which we consider a constant magnetic field $\langle B \rangle = 3\mu$G and a normalization $P \approx 5 \times 10^{23}$ Watt/Hz for $L_X = 10^{45}$ erg/sec (red line in Fig.1, left panel, see also Sect.3 in Cassano et al. 2012, for details on the adopted values for the parameters).

In Fig. 2 we report the total RHLF, obtained by combining the contributions from "turbulent" RHs and from (purely hadronic) "off-state" halos and its redshift evolution (see figure panel). Under our assumptions, "off-state" halos dominate the RHLF at lower radio luminosities where the RHLF due to turbulent RHs flattens. The luminosity functions are derived for RHs with $\nu_s \geq 120$ MHz (left panel) and for halos with $\nu_s \geq 1000$ MHz (right panel). The contribution of USSRH to the local ($z \sim 0.05$) RHLF at 120 MHz is also highlighted (shaded red region) showing that these systems contribute substantially to the RHLF at low radio powers, $P_{120} \sim 3 - 30 \times 10^{23}$ W/Hz.

4. Detecting giant radio halos in clusters

To estimate the minimum flux of a RH (integrated over a scale of $\sim$ 1 Mpc) that can be detected in a survey we will consider two possible approaches: *(i)* a brightness-based criterion and *(ii)* a flux-based criterion[5].

The criterion based on a threshold in brightness guarantees that halos are detected in the images generated by the survey. We know that the typical brightness profiles of RH smoothly decrease with distance from the cluster center, so the outermost regions are very difficult to detect. Based on a sample of well-studied RHs, Brunetti et al. (2007) found that about half ($\sim 58\%$) of the total radio flux of a RH is contained in about half radius of the halo. What is important is thus the capability of the survey to detect at least the brightest central regions of the RH. The minimum flux, $f_{min}(z)$, of a 1 Mpc RH that can be detected in a survey can be obtained by requiring that the mean halo brightness within half halo radius is ξ_1 times ($\xi_1 \approx 2-3$) the noise level in the map:

$$f_{min}(z) \simeq 1.2 \times 10^{-4} \xi_1 \left(\frac{\mathrm{F_{rms}}}{10\mu\mathrm{Jy}}\right)\left(\frac{100\,\mathrm{arcsec}^2}{\theta_b^2}\right)\left(\frac{\theta_H^2(z)}{\mathrm{arcsec}^2}\right)\,[\mathrm{mJy}]\,, \tag{4.1}$$

where $\theta_H(z)$ is the apparent angular radius of the halo at a given redshift in arcseconds, θ_b is the beam angular size in arcseconds and F_{rms} is the rms noise per beam.

[5]Simulations of SKA1 observations of galaxy clusters are necessary to study the capability of the radio telescope to detect faint diffuse emission on different physical scales (see *e.g.,* Ferrari et al., this Volume).

PoS(AASKA14)073

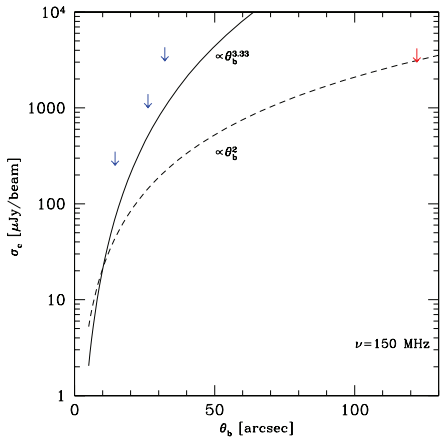

Figure 3: Confusion noise, σ_c, as a function of θ_b as provided by Eq. 4.3 (dashed line) and by Condon et al. (2012) using 3 GHz deep JVLA observations (solid line). The red arrow shows a measure of σ_c at 150 MHz with WSRT (Bernardi et al. 2009), the blue arrows are measures of the rms noise at 150 MHz on deep GMRT fields (from left to right: Ishwara-Chandra et al. 2010; Intema et al. 2011; George & Stevens 2008). Since these GMRT observations are not limited by confusion, the measured rms noise at different θ_b could be considered as upper limits on σ_c.

configurations	rms μJy/beam	θ_b arcesc
LOFAR (120 MHz)	400	25
SKA1-LOW (120 MHz)	20	10
EMU (1.4 GHz)	13	15
SKA1-SUR (1.4 GHz)	5	15

Table 1: Survey performance assumptions adopted in this Chapter.

A second possible approach to derive f_{min} is to assume that the halo is detectable when the integrated flux within $0.5\,\theta_H$ gives a signal to noise ratio ξ_2, *i.e.*, $f_{min}(<0.5\,\theta_H) \simeq 0.58 f_{min}(<\theta_H) \simeq \xi_2\sqrt{N_b}\times F_{rms}$, where N_b is the number of independent beam within $0.5\theta_H$, it follows:

$$f_{min}(z) \simeq 1.43\times 10^{-3}\,\xi_2\left(\frac{\mathrm{F_{rms}}}{10\mu\mathrm{Jy}}\right)\left(\frac{10\,\mathrm{arcsec}}{\theta_b}\right)\left(\frac{\theta_H(z)}{\mathrm{arcsec}}\right)\,[\mathrm{mJy}]\,, \tag{4.2}$$

Here we adopt $\xi_1 = 2$ and $\xi_2 = 7$ as reference values for calculations, these values are constrained through the detection of fake RHs in real *uv* radio data (NVSS, GMRT) and through the comparison between model expectations and observations (see Brunetti et al. 2007; Venturi et al. 2008; Cassano et al. 2012; for more details).

In this Chapter we consider the radio surveys reported in Tab.1: the *LOFAR Tier 1* survey and SKA1-LOW survey at 120 MHz, and the EMU (ASKAP) and SKA1-SUR at 1400 MHz.

It is important, especially for observations at low radio frequency, to evaluate the role of confusion. Indeed, as reported in Braun (2014), most of the SKA1-LOW continuum configurations

PoS(AASKA14)073

would be limited by the confusion noise. The classical confusion noise due to faint radio sources have been estimated at GHz frequencies (Condon 1987):

$$\left(\frac{\sigma_{\rm c}}{\rm mJy\,beam^{-1}}\right) \approx 0.2\left(\frac{\nu}{\rm GHz}\right)^{-0.7}\left(\frac{\theta_{\rm b}}{\rm arcmin}\right)^{2} \tag{4.3}$$

As illustrated in Fig.3, this is roughly consistent with recent results by Condon et al. (2012; obtained with the JVLA at 3 GHz and with 8 arcsec resolution, continuum line) for resolutions $\sim 5-15$ arcsec, while for larger beams Eq. 4.3 provides a more reliable estimate of σ_c in comparison with some observed values (arrows). For the *LOFAR Tier 1* survey (*e.g.,* Röttgering 2010) we will assume F_{rms}=0.4 mJy/beam and $\theta_b \sim 25$ arcsec [6]; according to Eq.4.3 this is still far from being confusion-limited. On the other hand, considering Eq.4.3 a SKA1-LOW continuum survey with $F_{rms} = 20\mu$Jy/beam, $\theta_b = 10$ arcesc is already confusion limited.

At higher frequency, corresponding to the SKA1-SUR band, ASKAP can perform cluster science improving the sensitivity and resolution with respect to current radio surveys at ~ 1 GHz (such as the NVSS). One important key project of ASKAP will be EMU, the "Evolutionary Map of the Universe" (Norris et al. 2011), an all-sky continuum survey with a sensitivity of 10 μJy/beam and an angular resolution of 10 arcsec. For the EMU survey we consider a configuration with $\theta_b = 15$ arcsec and $rms = 13\mu$Jy/beam. On the other hand SKA1-SUR could be able to perform all-sky surveys in 1-2 GHz band with $rms = 2\mu$Jy/beam and $\theta_b = 2$ arcsec. Such a survey would be far from confusion and can be used to make source-subtracted images, that can be tapered up to a resolution of 15 arcsec to increase the sensitivity to the extended emission. In this case we can consider a survey at 1.4 GHz with $rms = 5\mu$Jy/beam and $\theta_b = 15$ arcsec.[7] The equivalent of EMU in the northern sky will be the WODAN (Westerbork Observations of the Deep APERTIF Northern-Sky) survey (Röttgering et al. 2011); the expectations that we will derive in next Sections for EMU can be used also for WODAN.

Fig. 4 shows the resulting minimum power of RHs detectable in the considered surveys.

5. Number of Radio Halos in surveys with SKA1-LOW and SUR

The number of RHs with $flux \geq f_{min}(z)$ in the redshift interval, $\Delta z = z_2 - z_1$, can be obtained by combining the RHLF $(dN_H(z)/dP(\nu_o)dV)$ and $f_{min}(z)$:

$$N_H^{\Delta_z} = \int_{z=z_1}^{z=z_2} dz'(\frac{dV}{dz'})\int_{P_{min}(f^*_{min},z')} \frac{dN_H(P(\nu_o),z')}{dP(\nu_o)\,dV}\,dP(\nu_o) \tag{5.1}$$

In Fig.5 we show the all-sky number of RHs expected in the LOFAR (black) and SKA1-LOW (blue) surveys (left panels) and in the EMU (black) and SKA1-SUR (blue) surveys (right panel). We consider both giant RHs that originate from turbulent re-acceleration in merging clusters and "off-state" halos. We consider the flux limit derived according to Eq. 4.1 with $\xi_1 = 2$ (solid lines) and that obtained by Eq. 4.2 with $\xi_2 = 7$ (dashed lines).

[6] this is a conservative assumption, since pointed LOFAR observations obtained using configurations similar to the *Tier 1* survey reached rms values ~ 0.1 mJy/beam at ~ 5 arcsec resolution and $\sim 0.2-0.3$ mJy/beam at $\sim 20-30$ arcsec (van Weeren et al. in prep.)

[7] Our estimates of telescope sensitivities to diffuse emission are probably conservative, because it might be possible to mitigate confusion by subtracting compact sources (see *e.g.,* Vernstrom et al 2014).

PoS(AASKA14)073

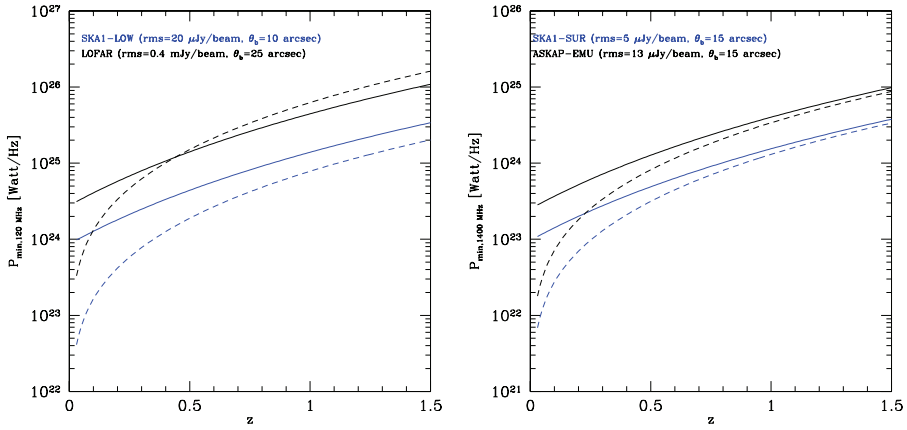

Figure 4: Minimum power of RHs detectable at 120 MHz (left panel) and at 1400 MHz (right panel) in different radio surveys (see figure panels) as a function of redshift. The minimum radio power has been computed according to Eqs.4.1 (dashed lines) and 4.2 (solid lines).

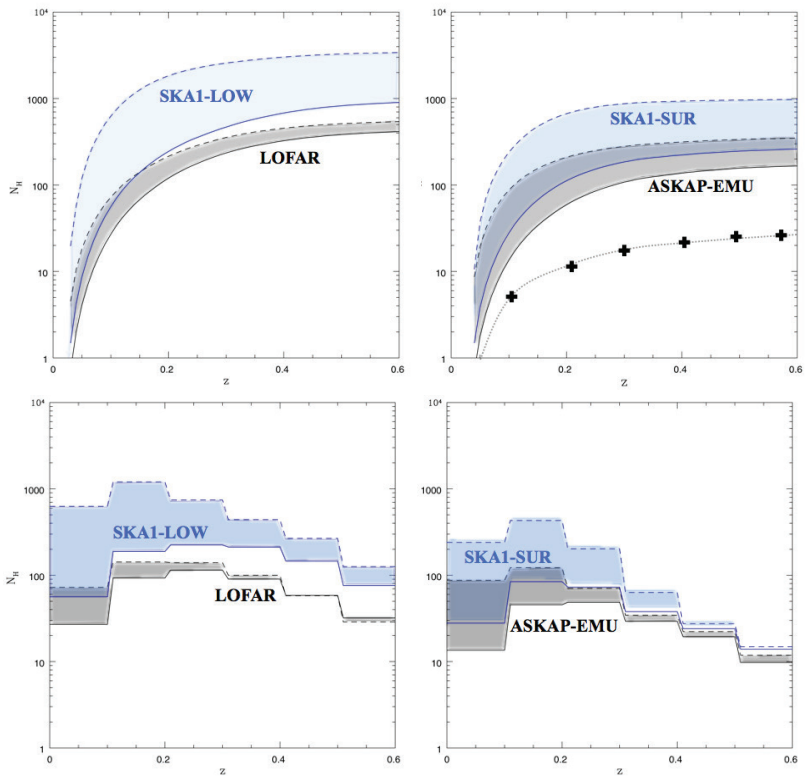

Figure 5: *Upper Panels*: expected integral number (all-sky) of RHs as a function of redshift at 120 MHz (left panel) and 1400 MHz (right panel). Black crosses show the integral number of RHs observed so far at ~ 1 GHz. *Lower Panels*: expected number of RH (all-sky) in redshift intervals at 120 MHz (left panel) and 1400 MHz (right panel). In all plots, the shaded regions show the ranges obtained considering the two methods (Eq.4.1 and Eq.4.2) to derive the RH detection limit in the considered survey (see figure panels).

PoS(AASKA14)073

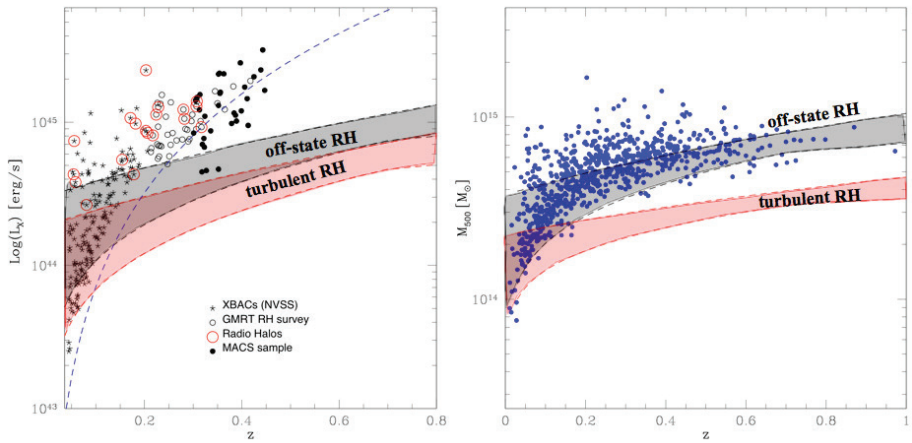

Figure 6: *Left Panel*: distribution of clusters in the $L_X - z$ plane (see legend in the figure panel). The sensitivity limit of the Reflex sample (blue dashed line) is reported. *Right Panel*: distribution of clusters detected by *Planck* in the $M_{500} - z$ plane. In both panels, the shaded regions show the minimum X-ray luminosity and mass of clusters with "turbulent" halos (red regions) and with "off-state" halos (black regions) detectable in the SKA1-LOW survey.

As a general consideration, we note that with the current design SKA1-LOW is much more efficient in the detection of RHs than SKA1-SUR. Given the typical RHLF (Fig.2) "off-state" halos are expected to contribute significantly to the total number of RHs in both low frequency and mid frequency surveys at lower redshift ($z < 0.3$). LOFAR would mainly detect RH generated in turbulent merging clusters, while SKA1-LOW and SKA1-SUR could start to test *for the very first time* the presence of hadronic halos in relaxed clusters. In both cases, LOFAR and SKA1-LOW would be able to detect USSRH, with the number of these sources being larger in SKA1-LOW surveys thanks to the better sensitivity. The detection of a number of these USSRH is a powerful test for models (Brunetti et al. 2008).

SKA1-LOW and SKA1-SUR could be able to detect up to ~ 2600 and ~ 750 halos, respectively, on 3π sr and out to $z \sim 0.6$. We note that this difference is due both to the better sensitivity of SKA1-LOW to the detection of diffuse steep-spectrum cluster scale emission and to the presence of USSRH, which would be detectable preferentially at lower radio frequency. For comparison, the maximum number of halos detectable by LOFAR and EMU would be ~ 400 and ~ 260, respectively. At both low and mid frequency SKA1 promises a tangible gain in the RH detection with respect to precursors and pathfinders. A major step can be already obtained with the early phase of SKA1-LOW (50% of SKA1-LOW sensitivity) that could be able to detect more than 1000 RH. The SKA2 at low frequency would be sensitive to RHs that are two times less powerful than those visible by SKA1-LOW, with the potential to increase by an order of magnitude the number of RH detected by SKA1, because the number counts of "off-state" halos are expected to be very steep.

6. Radio Halos to detect galaxy clusters in radio surveys

In this Section we compare the potential of the SKA1-LOW survey to discover galaxy clusters

PoS(AASKA14)073

using RHs with that of other surveys in the X-ray and SZ. By using Eq. 4.1 and Eq. 4.2 we derive the minimum power of giant RH detectable in the SKA1-LOW survey as a function of redshift. Then, using the scaling relations $P_{1.4} - L_X$ (*e.g.,* Cassano et al. 2006) and $P_{1.4} - M_{500}$ (*e.g.,* Basu 2012; Cassano et al. 2013) for "turbulent" RH and "off-state" halos separately, we derive the minimum X-ray luminosity and mass of clusters that can be detected in SKA1-LOW as a function of z. Fig.6, left panel shows that SKA1-LOW would be more powerful in the detection of galaxy clusters with respect to present X-ray surveys, especially at $z \geq 0.2$. In Fig.6, right panel, we show the distribution of *Planck* clusters in the $M_{500} - z$ plane. Because of the very steep relation between the RH power and the cluster mass ($P_{1.4} \propto M_{500}^{3.7}$, Cassano et al. 2013), the cluster selection function provided by SKA1-LOW in the $M_{500} - z$ plane is relatively flat, becoming competitive with the Planck SZ cluster survey in the detection of high-z clusters. A preliminary analysis suggest that SKA1-LOW offers the unique opportunity to detect high-z clusters through their diffuse radio emission in the form of both "turbulent" and "off-state" halos. Clearly at these redshifts the possibility to separate the truly diffuse emission from the contribution of discrete sources becomes challenging. Although simulations of SKA1 observations are needed (see Ferrari et al., this Volume), we note that the $10''$ resolution of SKA1-LOW correspond to a physical scale of ~ 80 kpc at $z \sim 1$, suggesting that a first order estimate of the contribution of the discrete sources will be possible.

7. Radio halos at high-z: caution

In the previous Section we showed that SKA1-LOW is potentially powerful in the detection of high-z clusters through the detection of their RH emission. On the other hand, only a few massive high-z ($z > 0.5 - 0.6$) clusters are know to host giant RH (*e.g.,* Bonafede et al. 2009, 2012; van Weeren et al. 2009, 2014; Lindner et al. 2014). This number starts to increase only recently thanks to the detection of high-z massive clusters via SZ-based cluster surveys (with SPT, Planck, etc.).

Theoretically, the generation of high-z RH is challenging due to the increase with z of the Inverse Compton losses of the radio emitting electrons ($dE/dt \propto (1+z)^4$). Present models, based on semi-analytical calculations of cluster formation and turbulence generation, are only able to make trustworthy expectations for moderate-z ($z < 0.5 - 0.6$) clusters. This is because the PS-based Monte Carlo method starts to underproduce the number and merging rate of high-z clusters. This means that in the adopted formalism the formation of massive clusters is delayed (massive clusters start to form at lower z) with respect to what is observed in cosmological simulations or predicted by more refined semi-analytic models (*e.g.,* Giocoli 2012, 2013). This implies that the expectations presented for RH at $z \sim 0.5 - 0.6$ (Fig.5) should be taken as lower limits. More refined semi-analytical models to describe the formation and evolution of galaxy clusters (*e.g.,* Giocoli 2012, 2013) combined with our formalism for non-thermal components will allow to obtain more reliable expectations at higher redshift (Cassano et al in prep).

References

Ackermann, M., Ajello, M., Allafort, A., et al. 2010, ApJ, 717, L71
Basu, K. 2012, MNRAS, 421, L112

PoS(AASKA14)073

Bernardi, G., de Bruyn, A. G., Brentjens, M. A., et al. 2009, A&A, 500, 965
Blasi, P., & Colafrancesco, S. 1999, Astroparticle Physics, 12, 169
Bonafede, A., Feretti, L., Giovannini, G., et al. 2009, A&A, 503, 707
Bonafede, A., Brüggen, M., van Weeren, R., et al. 2012, MNRAS, 426, 40
Bonafede, A., Intema, H. T., Brüggen, M., et al. 2014, MNRAS, 444, L44
Braun, R., "SKA1 Imaging Science Performance", Document number SKA-TEL-SKO-DD-XXX Revision A Draft 2
Brown, S., Emerick, A., Rudnick, L., & Brunetti, G. 2011, ApJ, 740, L28
Brunetti, G., & Jones, T. W. 2014, International Journal of Modern Physics D, 23, 30007
Brunetti G., Setti G., Feretti L., Giovannini G., 2001, MNRAS 320, 365
Brunetti, G.; Venturi, T.; Dallacasa, D., 2007, et al. ApJ, 670, L5
Brunetti G., Giacintucci S., Cassano R., et al., 2008, Nature 455, 944.
Brunetti, G., Cassano, R., Dolag, K., & Setti, G. 2009, A&A, 507, 661
Brunetti, G., & Lazarian, A. 2011, MNRAS, 410, 127
Brunetti, G., Blasi, P., Reimer, O., et al. 2012, MNRAS, 426, 956
Cassano R. & Brunetti G., 2005, MNRAS 357, 1313
Cassano R., Brunetti G., Setti G., 2006, MNRAS 369,1577
Cassano, R.; Brunetti, G.; Venturi, T., et al., 2008, A&A, 480, 687
Cassano, R., Brunetti, G., Röttgering, H. J. A., & Brüggen, M. 2010a, A&A, 509, A68
Cassano, R., Ettori, S., Giacintucci, S., et al. 2010b, ApJ, 721, L82
Cassano, R., Brunetti, G., Norris, R. P., et al. 2012, A&A, 548, A100
Cassano, R., Ettori, S., Brunetti, G., et al. 2013, ApJ, 777, 141
Condon, J. J. 1987, in Proceedings of the Arecibo Upgrading Workshop, ed. J. H. Taylor & M. M. Davis (Arecibo:NAIC), 89
Condon, J. J., Cotton, W. D., Fomalont, E. B., et al. 2012, ApJ, 758, 23
Dallacasa, D., Brunetti, G., Giacintucci, S., et al. 2009, ApJ, 699, 1288
Dennison B., 1980, ApJ 239
Dolag, K., Bartelmann, M., & Lesch, H. 2002, A&A, 387, 383
Donnert, J., Dolag, K., Brunetti, G., & Cassano, R. 2013, MNRAS, 429, 3564
Feretti, L., Giovannini, G., Govoni, F., & Murgia, M. 2012, A&A Rev.,, 20, 54
Ferrari et al. 2015, "Non-thermal emission from galaxy clusters: feasibility study with SKA", in "Advancing Astrophysics with the Square Kilometre Array", PoS(AASKA14)075
Fujita Y., Takizawa M., Sarazin C.L., 2003, ApJ 584, 190
George, S. J., & Stevens, I. R. 2008, MNRAS, 390, 741
Giocoli, C., Tormen, G., & Sheth, R. K. 2012, MNRAS, 422, 185
Giocoli, C., Marulli, F., Baldi, M., Moscardini, L., & Metcalf, R. B. 2013, MNRAS, 434, 2982
Govoni, F., Feretti, L., Giovannini, G., et al. 2001, A&A, 376, 803
Hallman, E. J., & Jeltema, T. E. 2011, MNRAS, 418, 2467
Intema, H. T., van Weeren, R. J., Röttgering, H. J. A., & Lal, D. V. 2011, A&A, 535, AA38
Ishwara-Chandra, C. H., Sirothia, S. K., Wadadekar, Y., Pal, S., & Windhorst, R. 2010, MNRAS, 405, 436
Kushnir, D., Katz, B., & Waxman, E. 2009, J. Cosmology Astropart. Phys., 9, 24
Lacey, C., & Cole, S. 1993, MNRAS, 262, 627

PoS(AASKA14)073

Lindner, R. R., Baker, A. J., Hughes, J. P., et al. 2014, ApJ, 786, 49
Norris, R. P., Hopkins, A. M., Afonso, J., et al. 2011, PASA, 28, 215
Petrosian V., 2001, ApJ 557, 560
Press W.H., Schechter P., 1974, ApJ 187, 425
Röttgering, H. J. A. 2010, ISKAF2010 Science Meeting
Röttgering, H., Afonso, J., Barthel, P., et al. 2011, Journal of Astrophysics and Astronomy, 32, 557
van Weeren, R. J., Röttgering, H. J. A., Brüggen, M., & Cohen, A. 2009, A&A, 505, 991
van Weeren, R. J., Intema, H. T., Lal, D. V., et al. 2014, ApJ, 781, L32
Vazza, F., Tormen, G., Cassano, R., Brunetti, G., & Dolag, K. 2006, MNRAS, 369, L14
Venturi T., Giacintucci S., Brunetti G., et al. 2007, A&A 463, 937
Venturi, T., Giacintucci, S., Dallacasa, et al. 2008, A&A, 484, 327
Vernstrom, T., Norris, R. P., Scott, D., & Wall, J. V. 2014, arXiv:1408.4160

PoS(AASKA14)073

PROCEEDINGS OF SCIENCE

Non-thermal emission from galaxy clusters: feasibility study with the SKA

Chiara Ferrari[*1], **Arwa Dabbech**[1], **Oleg Smirnov**[2,3], **Sphesihle Makhathini**[2], **Jonathan S. Kenyon**[2], **Matteo Murgia**[4], **Federica Govoni**[4], **David Mary**[1], **Eric Slezak**[1], **Franco Vazza**[5], **Annalisa Bonafede**[5], **Marcus Brüggen**[5], **Melanie Johnston-Hollitt**[6], **Siamak Dehghan**[6], **Luigina Feretti**[7], **Gabriele Giovannini**[7,8], **Valentina Vacca**[9], **Michael Wise**[10], **Myriam Gitti**[7,8], **Monique Arnaud**[11], **Gabriel W. Pratt**[11], **Kristian Zarb Adami**[12,13], **Sergio Colafrancesco**[14]

[1] *Laboratoire Lagrange, UMR 7293, UNS, CNRS, OCA, 06300 Nice (FR);* [2] *Department of Physics and Electronics, Rhodes University, PO Box 94, Grahamstown, 6140;* [3] *SKA South Africa, 3rd Floor, The Park, Park Road, Pinelands, 7405 (ZA);* [4] *INAF - Osservatorio Astronomico di Cagliari, Via della Scienza 5, 09047 Selargius (IT);* [5] *Universität Hamburg, Hamburger Sternwarte, Gojenbergsweg 112, D-21029, Hamburg (DE);* [6] *School of Chemical & Physical Sciences, Victoria University of Wellington, PO Box 600, Wellington, 6140 (NZ);* [7] *INAF – Istituto di Radioastronomia, Via Gobetti 101, I–40129 Bologna (IT);* [8] *Dipartimento di Fisica e Astronomia, Università di Bologna, Via Ranzani 1, I–40127 Bologna (IT);* [9] *Max Planck Institute for Astrophysics, Karl-Schwarzschild-Str. 1, 85748 Garching (DE);* [10] *Netherlands Institute for Radio Astronomy (ASTRON), Postbus 2, 7990 AA Dwingeloo (NL);* [11] *Laboratoire AIM, IRFU/Service d'Astrophysique – CEA F–91191 Gif-sur-Yvette Cedex (FR);* [12] *Physics Department, University of Malta, Msida, MSD 2080 (MT);* [13] *Physics Department, University of Oxford, Oxford, OX1 3RH (UK);* [14] *School of Physics, University of the Witwatersrand, Private Bag 3, 2050-Johannesburg (ZA)*

E-mail: chiara.ferrari at oca.eu

Galaxy clusters are known to host a variety of extended radio sources: tailed radio galaxies whose shape is modelled by the interaction with the intra-cluster medium (ICM); radio bubbles filling cavities in the ICM distribution and rising buoyantly through the thermal gas; diffuse giant radio sources ("halos" and "relics") revealing the presence of relativistic electrons and magnetic fields in the intra-cluster volume. It is currently the subject of an active debate how the non-thermal components that we observe at radio wavelengths affect the physical properties of the ICM and depend on the dynamical state of galaxy clusters.

In this work we start our SKA1 feasibility study of the "radio cluster zoo" through simulations of a typical radio-loud cluster, hosting several bright tailed radio galaxies and a diffuse radio halo. Realistic simulations of SKA1 observations are obtained through the `MeqTrees` software. A new deconvolution algorithm, based on sparse representations and optimised for the detection of faint diffuse astronomical sources, is tested and compared to the classical `CLEAN` method.

Advancing Astrophysics with the Square Kilometre Array
June 8-13, 2014
Giardini Naxos, Sicily, Italy

[*]Speaker.

PoS(AASKA14)075

1. Science case

The discovery of diffuse radio sources up to Mpc scales (called "halos", "mini-halos" or "relics", depending on their position in the cluster, size, morphology and polarization properties) in more than 70 galaxy clusters has pointed out the existence of a non-thermal (NT) component (relativistic electrons with Lorentz factor $>>1000$ and magnetic fields of the order of μG) in the intracluster volume (e.g. Ferrari et al. (2008); see also Chapters by Cassano et al.; Govoni et al.; Gitti et al., this Volume). Through NT studies of galaxy clusters we can estimate the cosmic-ray and magnetic field energy budget and pressure contribution to the intracluster medium (ICM), as well as get clues about energy redistribution during cluster mergers. NT analyses can elucidate non-equilibrium physical processes whose deep understanding is essential to do high-precision cosmology using galaxy clusters (Vazza et al. 2012a).

A detailed understanding of the origin of the intracluster NT component is still missing. A current status of this research area is summarised here and is presented in more detail in the Chapter by R. Cassano et al. While magnetic fields have been proven to be ubiquitous in the intracluster volume (Bonafede et al. 2011), it is still debated how the thermal electrons of the ICM can be accelerated to relativistic energies. Since the radiative lifetime of electrons is much shorter than their crossing time over Mpc scales, cosmic ray acceleration has to be related to "in situ" physical processes. Diffuse radio emission has generally been detected in massive merging clusters. The most widely accepted acceleration models are thus those that predict electron acceleration by shocks (in the case of relics) and turbulence (in the case of halos) that develop within the ICM during cluster interactions (e.g. Brunetti & Jones 2014). Note, however, that recently Bonafede et al. (2014b) have pointed out the existence of a giant radio halo in a cluster characterised by a cool-core, i.e. either a nearly relaxed or a minor merger system. Relativistic electrons are also expected to be produced in clusters as a secondary product of hadronic collisions between the ions of the ICM and relativistic protons, characterised by significantly longer lifetime compared to relativistic electrons (Enßlin et al. 2011, and refs. therein). Even if most evidence indicates that secondary electrons are not expected to give rise to diffuse radio emission at levels detectable by current instruments (but see Enßlin et al. 2011), they could provide the seeds for further re-acceleration by merger induced turbulence and shocks. There is therefore still the need to disentangle their possible contribution to the total cluster radio emission through the next generation of radio telescopes (Brunetti & Lazarian 2011). Theoretical models of electron acceleration need to be compared to statistical samples of clusters emitting at radio wavelengths, while only a few tens of radio relics and halos are known up to now and mostly at low/moderate redshift ($z \lesssim 0.4$, Feretti et al. 2012). Of great importance for characterising the origin of intracluster cosmic rays is the possibility to perform spectral analyses of diffuse radio sources (e.g. Orrú et al. 2007; Stroe et al. 2013). While currently deep pointed radio observations have allowed to detect radio emission from a few cases of high-z clusters ($z > 0.5$, see van Weeren et al. 2014, and references therein), it is crucial to perform radio studies of statistical cluster samples up to z$\sim$1 (to follow the assembly process from the epoch of massive cluster formation) and get detailed information about the mass and dynamical state of "radio loud" vs. "radio quiet" clusters (e.g. Govoni et al. 2004; Cassano et al. 2013).

Apart from radio halos and relics, galaxy clusters host a wider variety of extended radio sources, such as tailed radio galaxies whose shape is modelled by the interaction with the ICM

PoS(AASKA14)075

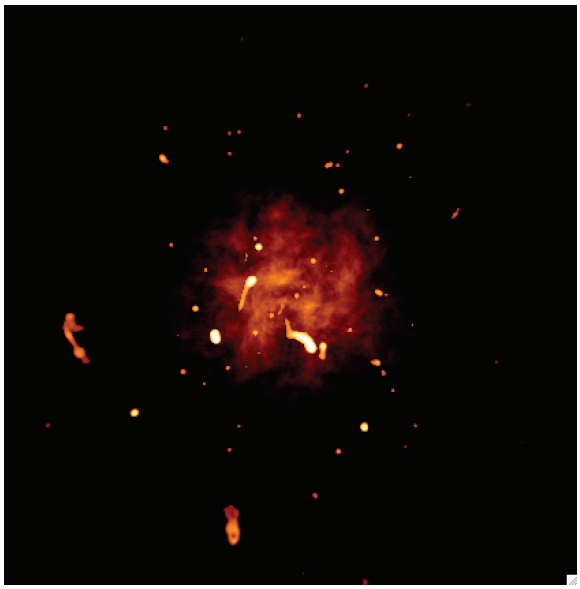

Figure 1: Simulated radio emission at 1.4 GHz from a galaxy cluster (FARADAY tool, Murgia et al. 2004) at z=0.5. The radio galaxy population is extracted from the cluster A 2255 (Govoni et al. 2006).

(e.g. Dehghan et al. 2011; Pfrommer & Jones 2011; Pratley et al. 2013) and radio bubbles filling holes in the ICM distribution and rising buoyantly through the thermal gas (e.g. de Gasperin et al. 2012; Gitti et al. 2012). Joint studies of all types of extended radio sources in clusters allow us to address the complex physical processes regulating the interaction between the different components of galaxy clusters (e.g. Bonafede et al. 2014a). For this, it is of course crucial to be able to identify separately the different kinds of radio sources in galaxy clusters (i.e. to discriminate between the radio emission related to active galaxies or to the NT ICM). In this paper we start our SKA1 feasibility study of the "radio cluster zoo" through a model radio-loud cluster presented in Sect. 2.1. Realistic simulations of SKA1 observations of this model cluster are described in Sect. 2.2. Sect. 3 focuses on the results of a new deconvolution algorithm (MORESANE, Dabbech et al. 2012, 2015) optimised for the detection of faint diffuse astronomical sources. We conclude with some remarks about the feasibility of cluster studies with SKA1 and with future plans in Sect. 4.

2. Simulations of a radio-loud galaxy cluster

2.1 The model cluster

While with current facilities radio halos have been mostly discovered in low-redshift clusters ($< z > \sim 0.2$, Feretti et al. 2012), with this study we aim at analysing up to which redshift we can detect diffuse cluster radio emission with SKA1. We are particularly interested to test if we can reach the epoch in which massive clusters that we observe today are forming, i.e. $z \approx 1$. By modelling both the gas and energy density distributions of the thermal and relativistic electron populations, and the characterisation of the magnetic field fluctuation and radial scaling similarly to Govoni et al. (2006), we perform simulations of a galaxy cluster at z=0.5 using the FARADAY tool (Murgia et al. 2004). The resulting model cluster hosts a diffuse radio halo, several tailed radio galaxies and point sources (see Fig. 1). The total power of the simulated radio halo is $P_{1.4\ \mathrm{GHz}} \sim 1.2 \times 10^{24}$ W/Hz, roughly corresponding to the luminosity limit of currently detected radio halos (left panel

PoS(AASKA14)075

of Fig. 1 in Cassano et al., this Volume). The overlaid radio galaxy population is extracted from the galaxy cluster A 2255 (Govoni et al. 2006). The simulated model cluster is then redshifted up to z=1.0 by taking into account the scaling of size, surface brightness and radio luminosity with redshift (e.g. Enßlin & Röttgering 2002).

2.2 Simulations of SKA1-MID and SKA1-SUR observations

In this work, we start from our model cluster described in Sect. 2.1 and we perform realistic simulations of SKA1-MID and SKA1-SUR observations using the `MeqTrees` software (Noordam & Smirnov 2010). We provide as input currently available antenna configurations and, similarly to the "SKA1 imaging science performance" document by R. Braun, a total observing time of 8h. Note that, based on the bigger field-of-view (FoV) of SKA-SUR with respect to SKA1-MID ($\sim$ 18 deg^2 *vs* 0.38 deg^2 at 1.4 GHz), the first instrument would approximately allow an all-sky survey within 2 years with the adopted observation time per field. Conversely, the higher sensitivity of SKA1-MID provides a significantly better detection of cluster radio emission, as discussed in the following. In order to limit the simulated data volume, a 60s integration time is assumed and no time averaging is applied. A 50 MHz bandwidth of a single channel and starting at 1415 MHz is considered. The simulated observations are treated as essentially monochromatic. No primary beam corrections are applied: the size of the input model map is selected to be 2048 $\times$ 2048 pixels^2, with the 512 $\times$ 512 pixels^2 sky image shown in Fig. 1 padded with zeros in its external regions. We use SEFDs[1] as set out in the baseline design (Dewdney et al. 2013) and rescale the noise to simulate the 8 hours of synthesis.

We have performed different imaging tests both for SKA1-SUR and SKA1-MID with w-projection correction included and no other wide-field effects simulated. In the following we will present results for: *Case A)* a uniform weighting scheme with 1 arcsec taper; *Case B)* a uniform weighting scheme with 5 arcsec taper; *Case C)* natural weighting. Examples of the resulting dirty maps for the cluster at z=0.5 are shown in Fig. 2. Despite the fact that nearly no convolution artefacts are present in the images, at the highest resolution (*Case A*) only the brightest radio sources are visible and the diffuse radio emission is completely below the noise. The diffuse emission of the radio halo is instead already distinguishable on the dirty map in *Case B*.

Note that our approach, based on simulated observations, differs from the feasibility study presented by Cassano et al., this Volume. In that case, similarly to Ferrari (2011), the authors use a criterion based on a threshold in surface brightness to estimate if a radio halo of a given luminosity can be detected by SKA. For this, they need to assume a certain, generalised surface brightness profile for radio halos (e.g. Cassano et al. (2015) assume that about half of the total halo flux is contained in about half halo radius, while Ferrari (2011) adopts a brightness profile as a function of radius derived from Govoni et al. (2001)).

3. New deconvolution and source detection method

We run both Högbom and Multi-Scale (`MS-CLEAN`)[2] algorithms (Högbom 1974; Cornwell 2008) on the dirty maps down to 2σ level. In both cases, we use the `lwimager` software imple-

[1] System Equivalent Flux Densities

[2] Eigth scales are used for `MS-CLEAN`: [0,2,4,8,16,32,64,128].

PoS(AASKA14)075

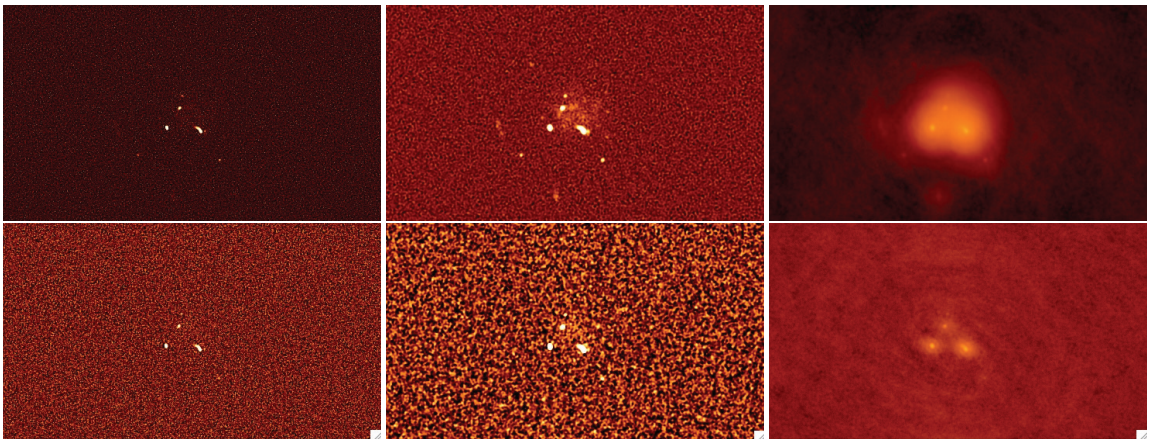

Figure 2: Dirty maps resulting from simulated observations of the model cluster at z=0.5 for *Cases A*, *B* and *C* (from *left* to *right*). *Top* panels show results for SKA1-MID, *bottom* panel for SKA1-SUR.

Cases	*A* at z=0.5	*B* at z=0.5	*C* at z=0.5	*A* at z=1.0	*B* at z=1.0	*C* at z=1.0
SKA1-MID						
Resolution [arcsec]	1.8	4.5	10.4	1.8	4.5	10.4
Sensitivity [μJy/beam]	2.4	1.7	0.8	2.5	1.9	1.2
SKA1-SUR						
Resolution [arcsec]	1.8	4.9	7.4	1.8	4.9	7.4
Sensitivity [μJy/beam]	6.9	7.0	5.6	6.5	7.0	6.0

Table 1: Final resolution and rms sensitivity of the restored maps obtained with a total observing time of 8 hours and using `MS-CLEAN` (see Sect. 2.2 for more details).

mented in `MeqTrees`, a stand-alone imager based on the `CASA` libraries and providing `CASA`-equivalent implementations of various `CLEAN` algorithms. No `CLEAN` boxes are used in our tests, since we aim at verifying results for a fully automatic data reduction (as required for SKA). The rms sensitivity and final resolution (determined by a combination of the adopted taper, weighting and uv-coverage) of the restored maps both for SKA1-SUR and SKA1-MID tests are given in Table 1. The `MS-CLEAN` components (convolved at the same resolution of simulated observations) and maps of residuals are shown in the fourth and fifth columns of Figs. 3 and 4.

We then run the deconvolution algorithm `MORESANE` (Dabbech et al. 2012, 2015) on dirty maps. `MORESANE`, whose results are shown in the second and third columns of Figs. 3 and 4, belongs to the family of new algorithms based on the theory of Compressed Sensing (see Sect. 4.4.2 in Norris et al. 2013). More specifically, `MORESANE` allies complementary types of sparse image models (Dabbech et al. 2015). The clear advantage is that its reconstructed image allows the detection of both extended and compact radio sources, reproducing in a accurate way their morphologies (see Fig. 3). Further tests indicate that flux measurements can be derived as a direct

PoS (AASKA14) 075

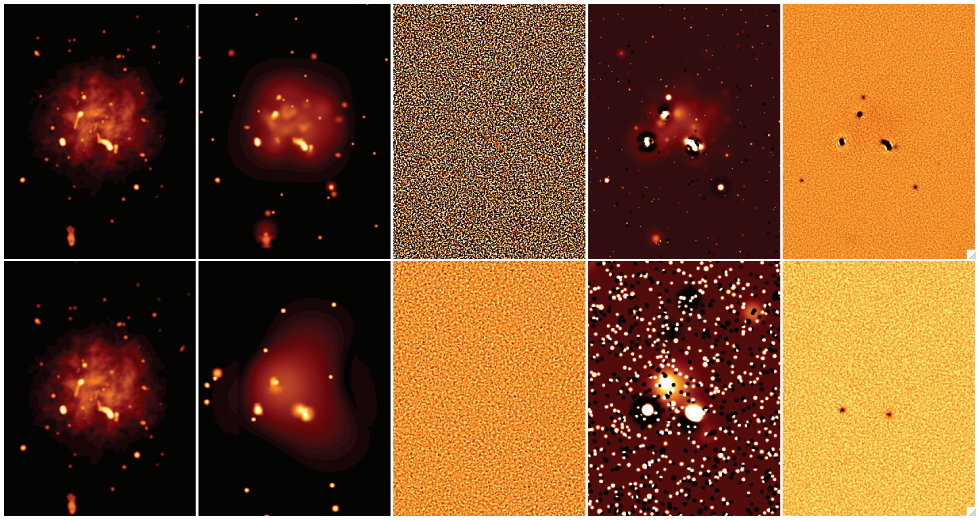

Figure 3: Results of deconvolution for the model cluster at z=0.5 (*top*) and z=1.0 (*bottom*) observed with SKA1-MID and adopting the imaging parameters of *Case A*. From *left* to *right*: model cluster map convolved at the same resolution of simulated observations; source model resulting from `MORESANE` deconvolution algorithm convolved at the same resolution of simulated observations; `MORESANE` maps of residuals; `MS-CLEAN` components convolved at the same resolution of simulated observations; `MS-CLEAN` maps of residuals. The model images are saturated at the same level.

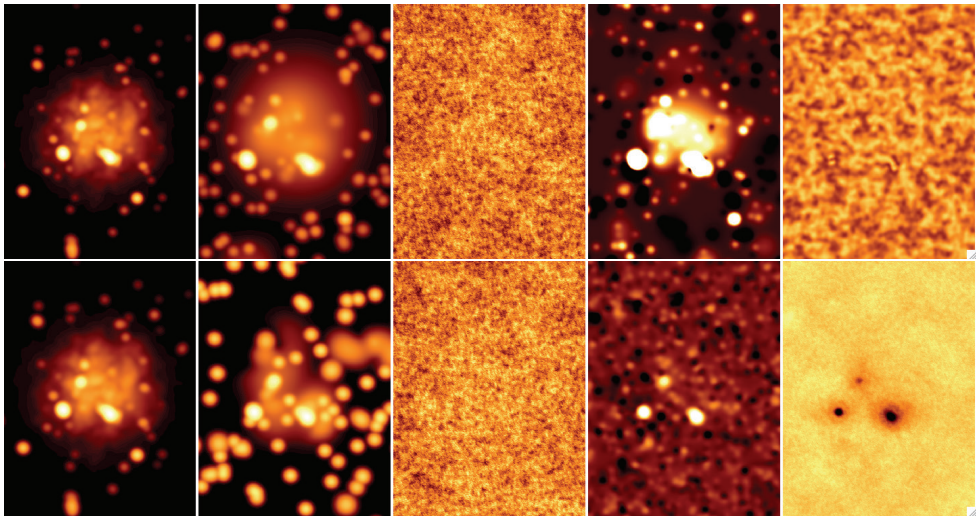

Figure 4: Results of deconvolution for the model cluster at z=0.5 (*top*) and z=0.7 (*bottom*) observed with SKA1-SUR and adopting the imaging parameters of *Case C*. Columns are the same as in Fig. 3.

PoS(AASKA14)075

output of MORESANE, since the photometry of the input model sky is conserved in the deconvolved image (Dabbech et al. 2015). The algorithm has been conceived and optimised for the detection and characterisation of very low-surface brightness and extended radio sources, resulting in the case presented here in the non-trivial detection of the very weak radio halo as well as in the good recovery of tailed radio galaxy morphologies. In addition, contrarily to CLEAN, the contamination by fake model components has been proven to be extremely weak, when not absolutely zero. Based on all these elements, the output of MORESANE can therefore be used for source catalog purposes (see Dabbech et al. 2015, for a detailed description of MORESANE and a quantitative comparison with other existing deconvolution methods).

Thanks to the image reconstructed by MORESANE, we can conclude that 8 hour observations with SKA1-MID will allow us to easily detect the different components of our model cluster (from tailed radio galaxies to the low surface brightness radio halo) up to z=1 and with an excellent resolution ($\sim$ 1 arcsec, *Case A*). Through 8 hours of observation with SKA1-SUR, we are instead able to get hints of the possible presence of a diffuse radio source up to z $\sim$ 0.7 only when adopting a higher sensitivity natural weighting scheme (*Case C*).

3.1 Notes on SKA1-LOW

Diffuse intracluster radio sources are generally characterised by steep synchrotron spectra. This, together with their low-surface brightness and the possible spectral steepening at high radio frequencies due to electron ageing, make them more easily detectable at long wavelengths. In addition, a unique prediction of turbulence acceleration models is the existence of ultra-steep radio halos, not associated to major cluster mergers, but to less energetic merging events (Cassano et al. 2013). Low-frequency observations are required to detect this kind of sources, as well as old population of electrons, for instance in dying or re-started radio galaxies at the center of galaxy clusters.

With a maximum baseline of 100 km, we can expect a maximum resolution of about 5 arcsec at 150 MHz and about 9 arcsec at 70 MHz, resulting in surface brightness confusion levels of the order of 140 and 245 nJy/arcsec^2 (see Fig. 4 in Ferrari et al. 2013, courtesy J. Condon)[3]. This imposes a much more severe limit in the sensitivity of SKA1-LOW to diffuse emission from clusters compared to, for instance, the lowest frequency part of SKA1-MID (see Fig. 6 in Ferrari et al. 2013). Higher resolution SKA1-LOW observations could not only allow us to achieve a higher sensitivity to diffuse radio emission by removing point sources and by re-imaging at lower resolution the subtracted data (see e.g. Vazza et al. 2015), but are also absolutely required to discriminate between the radio emission from active galaxies and from diffuse intra-cluster radio sources, particularly at high-redshift (z$\gtrsim$1). Current resolutions achieved by SKA1-LOW are therefore limiting low-frequency high/intermediate-z cluster science in Phase 1.

4. Conclusions and future plans

In this work, based on simulated SKA1 observations of galaxy clusters, we show that prospects are good for the study of non-thermal cluster physics, in particular thanks to new developments in

[3]Assuming a confusion noise that scales proportionally to $\nu^{-0.7}$, as a typical radio source.

PoS(AASKA14)075

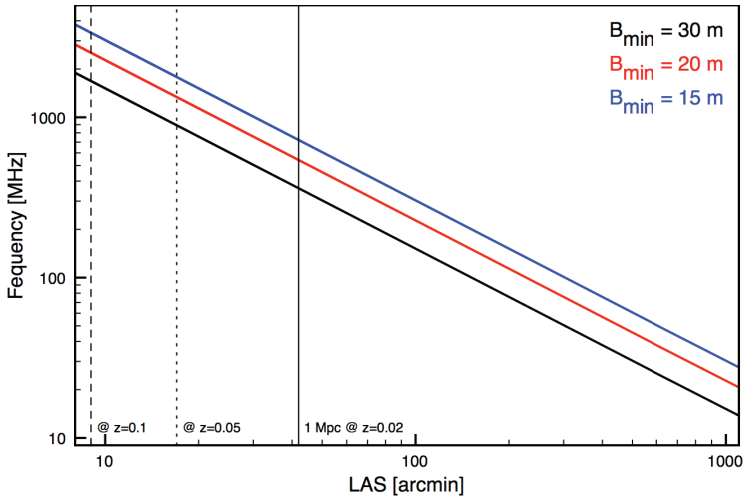

Figure 5: Frequency *vs.* largest angular scale (LAS) detectable as a function of three different array minimum baselines (B_{min}). The angular scale corresponding to a typical 1 Mpc intra-cluster radio source at different redshifts is also indicated (we assume a ΛCDM cosmology with $\Omega_\Lambda = 0.7$ and $\Omega_M = 0.3$).

the deconvolution and source detection steps that are here optimised for the analysis of extended and diffuse radio sources. Note that, in our simulations, we adopt a narrow band-width (50 MHz, Sect. 2.2). The quality of the results indicate that we will be able to get multi-frequency images of diffuse cluster radio sources within each of the large SKA1 bands, thus enabling detailed spectral index studies of galaxy clusters, an essential tool for our understanding of their NT physics (e.g. Orrú et al. 2007).

Based on the results highlighted in Sect. 2.2, we conclude that SKA1-MID is an extremely powerful instrument for radio analyses of galaxy clusters: relatively deep ($\lesssim$8 hours) follow-up observations of interesting targets from multi-wavelength (optical, X-ray, Sunyaev-Z'eldovich, ..., see the Chapter by Grainge et al., this Volume) cluster catalogs can allow detailed studies of both tailed radio galaxies and relatively low-luminosity ($P_{1.4\ \mathrm{GHz}} \approx 10^{24}$ W/Hz, see Sect. 2.1) diffuse radio halos up to at least z=1.0. A 2-years all-sky survey with SKA1-SUR can provide a completely independent interesting catalog of new candidates of diffuse cluster sources up to z$\sim$0.7, to be possibly followed up with SKA1-MID.

On a final cautionary note, Fig. 5 shows the largest angular scale (LAS, in arcmin) that can be detected as a function of the observed frequency and minimum array baseline. For reference, we show the angular scale corresponding to a typical 1 Mpc intra-cluster radio source at different redshifts. We can note, for instance, that, at 1.4 GHz, a minimum baseline of approximately 20-30 m does not allow to detect structures larger than $\sim$ 1 Mpc at z $<$ 0.05. In order to image giant radio sources down to very low–redshifts, we can either combine single-dish and interferometric data to completely fill in the gap down to 0m-spacing or perform coherent mosaicking observations by scanning the interferometer over the extended source with a regular (at least Nyquist–spaced) grid (see e.g. Holdaway 1999, and references therein).

The analysis developed in this paper will be extended in future works, in particular:

- the detectability with SKA1 of simulated radio relics and radio bubbles (e.g. Vazza et al. 2012b; Roediger et al. 2007) will be investigated and compared to similar feasibility studies for SKA precursors and pathfinders (JVLA, LOFAR, GMRT, MeerKAT, ASKAP, ...). Polarisation studies for targeted observations might also be included;

PoS(AASKA14)075

- due to the importance of low-frequency observations for cluster science, a more extended feasibility study will be taken into account for SKA1-LOW;
- on longer time-scale, we would like to develop similar observational simulations for the Phase 2 configuration of the SKA array. At present, we are limited by computer resources for performing this part of the work.

Acknowledgements
We thank the referees of this paper for their useful comments and the SKA office for the conference organisation. We acknowledge financial support by the "*Agence Nationale de la Recherche*" through grant ANR-09-JCJC-0001-01, the "*Programme National Cosmologie et Galaxies (2014)*", the *BQR* program of Lagrange Laboratory (2014), the "PHC PROTEA" programme (2013), the joint doctoral program "*région PACA-OCA*" (2011). S. Makhathini acknowledges financial support from the National Research Foundation of South Africa. O. Smirnov's research is supported by the South African Research Chairs Initiative of the Department of Science and Technology and National Research Foundation.

References

Bonafede, A., Govoni, F., Feretti, L., et al. 2011, A&A, 530, A24
Bonafede, A., Intema, H. T., Brüggen, M., et al. 2014a, ApJ, 785, 1
Bonafede, A., Intema, H. T., Brüggen, M., et al. 2014b, MNRAS, 444, 44
Brunetti, G. & Jones, T. W. 2014, International Journal of Modern Physics D, 23, 30007
Brunetti, G. & Lazarian, A. 2011, MNRAS, 410, 127
Cassano, R., Bernardi, G. G. B., Brüggen, M., et al., 2015, "Cluster Radio Halos at the crossroads between astrophysics and cosmology in the SKA era", in proceedings of *Advancing Astrophysics with the Square Kilometre Array* PoS(AASKA14)073
Cassano, R., Ettori, S., Brunetti, G., et al. 2013, ApJ, 777, 141
Cornwell, T. J. 2008, IEEE Journal of Selected Topics in Signal Processing, 2, 793
Dabbech, A., Ferrari, C., Mary, D., et al. 2015, A&A, 576, 7
Dabbech, A., Mary, D., & Ferrari, C. 2012, in Acoustics, Speech and Signal Processing (ICASSP), 2012 IEEE International Conference on, 3665–3668
de Gasperin, F., Orrú, E., Murgia, M., et al. 2012, A&A, 547, A56
Dehghan, S., Johnston-Hollitt, M., Mao, M., et al. 2011, Journal of Astrophysics and Astronomy, 32, 491
Dewdney, P., Turner, W., Millenaar, R., McCool, R., Lazio, J., Cornwell, T., 2013, "SKA1 System Baseline Design", Document number SKA-TEL-SKO-DD-001 Revision 1, SKA Organisation
Enßlin, T., Pfrommer, C., Miniati, F., et al. 2011, A&A, 527, A99
Enßlin, T. A. & Röttgering, H. 2002, A&A, 396, 83
Feretti, L., Giovannini, G., Govoni, F., et al. 2012, A&A Rev., 20, 54
Ferrari, C. 2011, Memorie della Societa Astronomica Italiana Supplementi, 17, 79
Ferrari, C., Condon, J., Govoni, F., et al. 2013, SKA1 baseline design – Diffuse radio sources in galaxy clusters: internal report after the Continuum W.G. meeting

PoS(AASKA14)075

Ferrari, C., Govoni, F., Schindler, S., et al. 2008, Space Sci. Rev., 134, 93

Gitti, M., Brighenti, F., McNamara, B. R. 2012, AdAst, 2012 6

Gitti, M., Tozzi, P., Brunetti, G., et al. 2015, "The SKA view of cool-core clusters: evolution of radio mini-halos and AGN feedback", in proceedings of *Advancing Astrophysics with the Square Kilometre Array* PoS(AASKA14)076

Govoni, F., Enßlin, T. A., Feretti, L., et al. 2001, A&A, 369, 441

Govoni, F., Markevitch, M., Vikhlinin, A., et al. 2004, ApJ, 605, 695

Govoni, F., Murgia, M., Feretti, L., et al. 2006, A&A, 460, 425

Govoni, F., Murgia, M., Xu, H., et al. 2015, "Cluster magnetic fields through the study of polarized radio halos in the SKA era", in proceedings of *Advancing Astrophysics with the Square Kilometre Array* PoS(AASKA14)105

Grainge, K., Borgani, S., Colafrancesco, S., et al. 2015, "Galaxy Cluster Science with the Sunyaev-Zeldovich Effect", in proceedings of *Advancing Astrophysics with the Square Kilometre Array* PoS(AASKA14)170

Högbom, J. A. 1974, A&AS, 15, 417

Holdaway, M. A. 1999, ASPC, 180, 401

Murgia, M., Govoni, F., Feretti, L., et al. 2004, A&A, 424, 429

Noordam, J. E. & Smirnov, O. M. 2010, A&A, 524, A61

Norris, R. P., Afonso, J., Bacon, D., et al. 2013, PASA, 30, 20

Orrú, E., Murgia, M., Feretti, L., Govoni, F., Brunetti, G., Giovannini, G., Girardi, M., & Setti, G. 2007, A&A, 467, 943

Pfrommer, C. & Jones, T. W. 2011, ApJ, 730, 22

Pratley, L., Johnston-Hollitt, M., Dehghan, S., et al. 2013, MNRAS, 432, 243

Roediger, E., Brüggen, M., Rebusco, P., et al. 2007, MNRAS, 375, 15

Stroe, A., van Weeren, R. J., Intema, H. T., Röttgering, H. J. A., Brüggen, M., & Hoeft, M. 2013, A&A, 555, A110

van Weeren, R. J., Intema, H. T., Lal, D. V., et al. 2014, ApJ, 781, 32

Vazza, F., Brüggen, M., Gheller, C., & Brunetti, G. 2012a, MNRAS, 421, 3375

Vazza, F., Brüggen, M., van Weeren, R., Bonafede, A., Dolag, K., & Brunetti, G. 2012b, MNRAS, 421, 1868

Vazza, F., Ferrari, C., Bonafede, A., et al. 2015, "Filaments of the radio cosmic web: opportunities and challenges for SKA", in proceedings of *Advancing Astrophysics with the Square Kilometre Array* PoS(AASKA14)097

PoS(AASKA14)075

PROCEEDINGS OF SCIENCE

The SKA view of cool-core clusters: evolution of radio mini-halos and AGN feedback

Myriam Gitti[*1,2], **Paolo Tozzi**[3], **Gianfranco Brunetti**[2], **Rossella Cassano**[2], **Daniele Dallacasa**[1,2], **Alastair Edge**[4], **Stefano Ettori**[5], **Luigina Feretti**[2], **Chiara Ferrari**[6], **Simona Giacintucci**[7,8], **Gabriele Giovannini**[1,2], **Michael Hogan**[4], **Tiziana Venturi**[2]

[1] *Dipartimento di Fisica e Astronomia - Università di Bologna, via Ranzani 1, I-40127 Bologna, Italy;* [2] *INAF - Istituto di Radioastronomia, via Gobetti 101, I-40129 Bologna, Italy;* [3] *INAF - Osservatorio Astrofisico di Arcetri, Largo E. Fermi 5, I-50125 Firenze, Italy;* [4] *Department of Physics, Durham University, Durham, DH1 3LE UK;* [5] *INAF - Osservatorio Astronomico di Bologna, via Ranzani 1, I-40127 Bologna, Italy;* [6] *Laboratoire Lagrange, UMR 7293, Université de Nice Sophia-Antipolis, CNRS, Observatoire de la Côte d'Azur, 06300 Nice (FR);*
[7] *Department of Astronomy, University of Maryland, College Park, MD 20742, USA;* [8] *Joint Space-Science Institute, University of Maryland, College Park, MD, 20742-2421, USA*
E-mail: myriam.gitti at unibo.it

In about 70% of the population of relaxed, cool-core galaxy clusters, the brightest cluster galaxy (BCG) is radio loud, showing non-thermal radio jets and lobes ejected by the central active galactic nucleus (AGN). In recent years such relativistic plasma has been unambiguously shown to interact with the surrounding thermal intra-cluster medium (ICM) thanks to spectacular images where the lobe radio emission is observed to fill the cavities in the X-ray-emitting gas. This *'radio feedback'* phenomenon is widespread and is critical to understand the physics of the inner regions of galaxy clusters and the properties of the central BCG. At the same time, mechanically-powerful AGN are likely to drive turbulence in the central ICM which may also play a role for the origin of non-thermal emission on cluster-scales. Diffuse non-thermal emission has been observed in a number of cool-core clusters in the form of a radio mini-halo surrounding the radio-loud BCG on scales comparable to that of the cooling region. Large mini-halo samples are necessary to establish their origin and connection with the cluster thermal properties and dynamics, especially in light of future X-ray characterization of the cluster cores as it is expected by Athena-XIFU. We show that All-Sky reference survey at Band 2 with SKA1 at confusion limit (rms $\sim$2 μJy per beam) has the potential to detect up to $\sim$ 620 mini-halos at redshift $z < 0.6$, whereas Deep Tier reference surveys at Band 1/2 with SKA1 at sub-arcsec resolution (rms $\sim 0.2\mu$Jy per beam) will allow a complete census of the radio-loud BCGs at any redshift down to a 1.4 GHz power of $10^{22}\,\mathrm{W\,Hz^{-1}}$. We further anticipate that SKA2 might detect up to $\sim$ 1900 new mini-halos at redshift $z < 0.6$ and characterize the radio-mode AGN feedback in every cluster and group up to redshift $z \sim 1.7$ (the highest-z where virialized clusters are currently detected) and even beyond, thus providing a complete picture of the feedback phenomenon in clusters and its role in shaping the large scale structure of the Universe.

Advancing Astrophysics with the Square Kilometre Array
June 8-13, 2014
Giardini Naxos, Sicily, Italy

PoS(AASKA14)076

1. Introduction

The majority of baryons in galaxy clusters are in the form of diffuse hot plasma, the intra-cluster medium (ICM), heated mostly by gravitational processes at temperatures in the range 1-10 keV (going from groups to massive clusters) and visible in the X-ray band thanks to its thermal Bremsstrahlung emission. However the catastrophic cooling of the gas expected at the center of relaxed systems under these conditions (Fabian 1994) is not observed (e.g., Peterson & Fabian 2006), suggesting that complex non-gravitational physical processes must be at work in the ICM to provide smoothly distributed heating on scales of about 100 kpc and then stop the cooling process. Understanding the interplay of gravitational and non-gravitational physics in the ICM and its interaction with the relativistic plasma ejected by the central active galactic nucleus (AGN) is key for understanding the growth and evolution of galaxies and their central black holes, the history of star formation and the assembly of large-scale structures. In particular, the feedback from the central black hole has turned out to be an essential ingredient that must be taken into account in any model of galaxy formation and evolution. The main evidence of the action of radio-mode AGN feedback is in these *'cool-core'* galaxy clusters, which hold a special place in the entire field of extragalactic astrophysics.

The central dominant (cD) galaxies of cool-core clusters (which are characterized by short cooling times, high gas densities and low temperatures in the central regions) have a high incidence of radio activity, showing the presence of central FR-I radiogalaxies (Fanaroff & Riley 1974) in 70% of the cases (Burns 1990; Dunn & Fabian 2006; Best et al. 2007; Mittal et al. 2009). In particular, high-resolution X-ray observations performed with Chandra and XMM-Newton showed that the central radio sources have a fundamental and persistent effect on the ICM – the central hot gas in many cool-core systems is not smoothly distributed, but shows instead "holes" coincident with lobes of extended radio emission. The most typical configuration is for jets from the central dominant elliptical of a cluster to extend outwards in a bipolar flow, inflating lobes of radio-emitting plasma (radio *'bubbles'*) which are spatially separated from the thermal ICM component. The interpretation is that these lobes push aside the X-ray-emitting gas of the cluster atmosphere, thus excavating *'cavities'* in the ICM which are detectable as deficits in the X-ray images. Thanks to spectacular images where the radio emission is observed to fill the cavities in the X-ray emitting ICM, the radio galaxies have thus been identified as a primary source of feedback to solve the so–called 'cooling flow problem' (for recent reviews see Gitti et al. 2012; McNamara & Nulsen 2012; Fabian 2012). In Figure 1 we show clear examples of radio lobes (black contours) filling the cavities in the ICM in a galaxy group (left panel) and in a massive cluster (right panel).

The detailed mechanism to transfer the mechanical energy of the radio jets into thermal energy of the ICM is still unclear. It has been proposed that mechanically-powerful AGN are responsible for driving turbulence in the central ICM, which must eventually dissipate into heat thus contributing to offsetting radiative cooling (e.g., Zhuravleva et al. 2014). On the other hand, such a turbulence may also contribute to re-accelerating a seed population of (sub-)relativistic particles naturally present in the ICM, and producing diffuse non-thermal emission. Obvious sources of the seed relativistic electrons are, for example, the buoyant radio bubbles that are inflated by the radio activity of the central AGN itself and disrupted by gas motions in the core.

*Speaker.

PoS(AASKA14)076

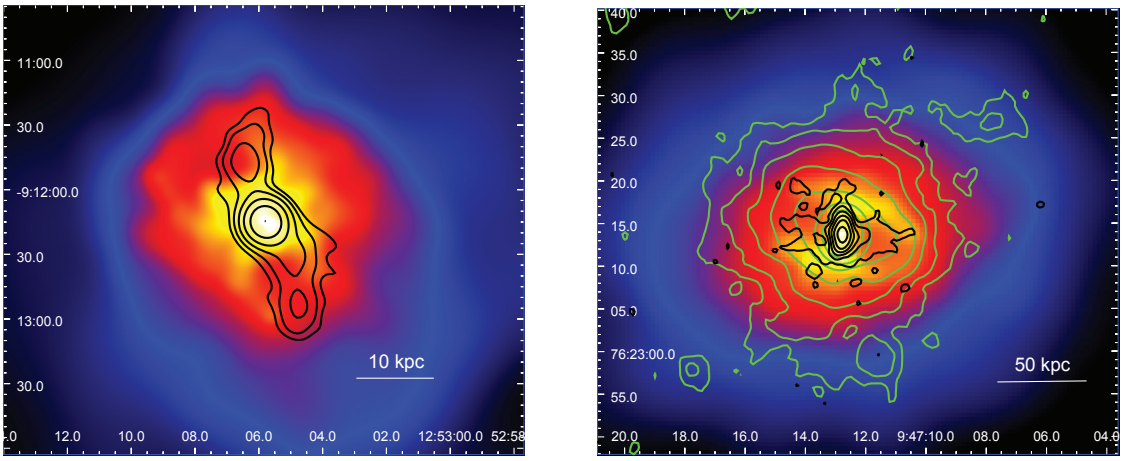

Figure 1: *Left panel:* X-ray image of the galaxy group HCG 62 at $z = 0.0137$ (Gitti et al. 2010) with superimposed GMRT radio contours at 610 MHz. *Right panel:* X-ray image of the galaxy cluster RBS 797 at $z = 0.35$ with superimposed VLA radio contours at 1.4 GHz (green contours, Gitti et al. 2012; Doria et al. 2012) and at 5 GHz (black contours, Gitti et al. 2013). In both cases X-ray cavities in the ICM are observed to be coincident with the BCG radio lobes (black contours), and in the case of RBS 797 a large-scale radio mini-halo is also detected (green contours).

Diffuse non-thermal emission has been observed in a number of cool-core clusters, where the radio-loud brightest cluster galaxy (BCG) is surrounded by a so-called *'radio mini-halo'*. Mini-halos are diffuse, faint radio sources observed at the cluster center on scales (total size) ~100-500 kpc comparable to that of the cooling region, with steep radio spectra and amorphous (roundish) shape. The typical mini-halo power at 1.4 GHz is of the order of $\sim 10^{23}$ - 10^{24} W Hz^{-1}. These radio sources are not directly connected with the radio bubbles, but the mini-halo emission is on larger scales and is truly generated from the ICM where the thermal plasma and the relativistic electron population are mixed (see in the right panel of Figure 1 the example of the cluster RBS 797 which hosts both a mini-halo, in green contours, and a cavity-bubble system, in black contours). Therefore, the synchrotron emission from radio mini-halos proves that ~GeV electrons are diffusing through $\sim \mu$G magnetic fields permeating the ICM, as in the case of giant radio halos and relics (see also Cassano et al. 2015; Ferrari et al. 2015; Govoni et al. 2015). Mini-halos are qualitatively similar to the most extreme case of giant radio halos and relics that however are typically found in disturbed/non cool-core clusters and are most likely powered by cluster mergers. In fact, radio mini-halos indicate that, in addition to mergers, diffuse non-thermal emission can be powered also by less extreme processes that dissipate energy associated to large-scale (tens-hundreds kpc) motions at micro-physical scales and are connected at some level with the mechanisms responsible for the heating of the cooling gas. Although mini-halos are not directly sustained by the central engine, it is nonetheless likely that the AGN plays a role for the origin of these sources. For example, it has been proposed that the relativistic electrons that generate mini-halos are released in the ICM by the central AGN and then can be transported and re-accelerated by turbulent motions in the cool cores (Gitti et al. 2002; Mazzotta & Giacintucci 2008; ZuHone et al. 2013).

Only about twenty mini-halos (or candidates) are known so far, all at redshift $z < 0.6$ (Giacin-

PoS(AASKA14)076

tucci et al. 2014b; van Weeren et al. 2014). Due to the limitations of current radio interferometers it is difficult to assess the occurrence of radio mini-halos in clusters. In particular, the mini-halo detection is complicated by the need of separating their diffuse, low surface brightness emission (at a level of few μJy arcsec^{-2} at 1.4 GHz) from the bright emission of the central radio BCG. This requires a very good sensitivity to diffuse emission, high dynamic range and good spatial resolution, which will be achievable with SKA only. A large mini-halo sample observed by SKA will allow us to reach a better understanding of this class of sources, in particular to establish their origin and connection with the cluster thermal properties and dynamics which will be characterized at unprecedented levels by the next-generation of X-ray instruments like XIFU, the X-ray Integral Field Unit covering the 0.2 to 10 keV energy range with unrivalled energy resolution, that will flight onboard of the ESA-L2 mission Athena[1] (expected launch in 2028). Furthermore, at present the study of the radio-mode feedback in clusters is limited to $z < 0.7$ with very few cases at high redshift (Hlavacek-Larrondo et al. 2012), while virialized clusters are currently detected up to redshifts of 1.6 or larger (at present the highest redshift, massive cluster whose virialization is confirmed by deep X-ray study is XDCP J0044.0−2033 at $z = 1.58$, Tozzi et al., submitted). Therefore, there is a wide redshift range where radio-mode feedback is still unexplored. In addition, recent studies show that cool cores are already present and well developed at least at $z \sim 1$, suggesting that cool-core formation takes place on a short time-scale after the formation of the cluster (Santos et al. 2010, 2012). Since the association of cool cores with radio mini-halos and radio AGN is ubiquitous (Feretti et al. 2012; Sun 2009), with SKA we expect to be able to trace the non-thermal emission and feedback activity in clusters, and therefore to study the interplay between thermal and non-thermal plasma in the central regions of galaxy clusters, up to the highest redshift where clusters are found.

The non-thermal activity and radio-mode feedback in clusters of galaxies is a scientific case key to the physics of the ICM and the evolution of the cosmic large scale structures. Radio astronomy in the SKA era can be the main scientific driver in these fields.

In the rest of this chapter we assume a ΛCDM cosmology with $H_0 = 70$ km s^{-1} Mpc^{-1} and $\Omega_M = 1 - \Omega_\Lambda = 0.3$.

2. Origin of radio mini-halos

At a first glance, radio mini-halos may resemble a small-scale version of giant radio halos, extending on scales of the order of few hundred kpc size rather than Mpc size. However, the two classes of radio sources show prominent differences. First of all, in clear contrast to giant radio halos[2], mini-halos are always found in dynamically relaxed systems suggesting that cluster mergers do not play a major role for their origin. Also the synchrotron volume emissivity of mini-halos is typically larger than that of giant halos (Cassano et al. 2008; Murgia et al. 2009). On the other hand, it is yet not well established whether the underlying physical mechanisms that accelerate the cosmic ray electrons (CRe) in mini-halos differ substantially from the analogous mechanisms in giant radio halos. Clusters hosting mini-halos always have a central radio-loud AGN, which often exhibits outflows in the form of radio lobes and bubbles injecting CRe into the central regions of

[1] http://www.the-athena-x-ray-observatory.eu/

[2] note that there are also two atypical cases of giant halos, that apparently are in clusters without strong merging activity (Farnsworth et al. 2013; Bonafede et al. 2014)

PoS(AASKA14)076

galaxy clusters. In principle these AGN could represent the primary source of the CRs in mini-halos, however they are not sufficient by themselves, at least without some dynamical contribution, to explain the diffuse radio emission. In particular, a slow diffusion problem exists for mini-halos (as for giant halos); that is, the energy loss time scale of the radio emitting CRe ($\approx 10^8$ yr) is much shorter than the time needed by these particles to diffuse efficiently across the emitting volume (e.g., Gitti et al. 2004). Similarly to giant halos, two physical mechanisms have been identified as possibly responsible for the radio emission in mini-halos: i) re-acceleration of CRe (*leptonic* models or re-acceleration models) where electrons are reaccelerated by micro-turbulence in the radio-emitting region, and ii) generation of secondary CRe (*hadronic* or secondary models) where the radio-emitting region is continuously supplied with secondary electrons generated by inelastic collisions between cosmic-ray protons (CRp) and thermal protons (see Brunetti & Jones 2014, for a review).

A key question in the re-acceleration models is the origin of the turbulence responsible for re-accelerating the electrons. Gitti et al. (2002) originally considered magnetohydrodynamic (MHD) turbulence amplified by compression in the cool cores, where the necessary energetics to power radio mini-halos is supplied by the cooling flow process itself. This model predicts a direct connection between the synchrotron emitted power in mini-halos and the energetics of (or energy available into) the cooling flow. Remarkably a trend between the radio power and the cooling flow power is observed in mini-halo clusters (Gitti et al. 2004, 2007, 2012), where the strongest radio mini–halos are associated with the most powerful cooling flows, thus hinting at a direct connection between the thermal properties of cooling flows and the non-thermal emission of radio mini-halos. Although these observations support a connection between synchrotron and (gas-)cooling power, the physical mechanisms responsible for the acceleration of the emitting electrons are still poorly constrained. In particular, in the re-acceleration model the origin of the turbulence necessary to trigger the electron re-acceleration is still debated. As already mentioned in the Introduction, one possibility is that the turbulence is powered by AGN activity. In this case the mechanisms responsible for particles re-acceleration in mini-halos and for the gas heating should be intimately connected. This scenario can be tested by investigating whether all mini-halo clusters show evidence of AGN feedback (see Sect. 4). On the other hand, the signatures of minor dynamical activity have recently been detected in some mini-halo clusters, thus suggesting that additional or alternative turbulent energy may be provided by minor mergers (Gitti et al. 2007; Cassano et al. 2008) and related gas sloshing mechanism in cool-core clusters (Mazzotta & Giacintucci 2008; Giacintucci et al. 2014a), which is also supported by recent simulations (ZuHone et al. 2013). The clearest observational signatures of these large-scale gas motions are spiral-shaped cold fronts seen in the majority of cool-core clusters (Markevitch & Vikhlinin 2007). These cold fronts are believed to be produced by the cold gas of the core sloshing in the clusters deep potential well, in response to crossing dark matter subhalo motions, for example. Those sloshing motions can advect ICM across the cluster core where turbulence can also be produced (Fujita et al. 2004; Ascasibar & Markevitch 2006; ZuHone et al. 2010).

Understanding the nature of mini-halos would provide invaluable information on the micro-physics of the ICM, including the process of amplification and dissipation of the magnetic field, and on the diffusion/transport of CRs in these environments. Both understanding the nature of turbulence in cool-core clusters and discriminating between a leptonic and hadronic origin of radio

PoS(AASKA14)076

mini-halos is however very challenging due to severe limitations of current observational constraints. A leap forward is expected from future spectral and polarimetric information in the radio band, that will become available with SKA, combined with constraints in other bands (e.g., hard X-rays and gamma-rays). For example, the combination of SKA1-LOW and SKA1-MID/SUR observations will allow us to establish whether the spectrum of mini-halos is curved or if it is a pure power-law. Compelling evidence for very steep spectra and/or for the existence of spectral breaks at high frequencies would favour a re-acceleration scenario rather than a hadronic origin of the mini halos (Brunetti & Jones 2014). At the same time, polarimetric information will allow us to probe the turbulent status of the magnetic field in the radio-emitting region, whereas the degree of circular polarization will allow us to poinpoint the CRe to CRp ratio, thus constraining the hadronic or re-acceleration origin of radio mini-halos.

In this chapter we focus on the crucial information that will be obtained by statistical studies with SKA. Although a correspondence between radio mini-halos and cool-core clusters is well established, current radio studies do not provide an exhaustive view of the occurrence of radio mini-halos in galaxy clusters more generally. For example, it is still not clear whether these radio sources are common or rare in cool cores. Statistical studies of large cluster samples are necessary to reach a better understanding of these sources, investigating in particular the following key points:

- Do all cool-core clusters host a radio mini-halo? How does the mini-halo/cool-core fraction evolve with redshift? How do the radio properties correlate with the X-ray properties?
  (radio power-limited sample with wider redshift distribution, synergy with eROSITA and Athena X-ray satellites)
- Does the central AGN play a significant role in powering radio mini-halos? What is the fraction of mini-halo clusters that show evidence of AGN feedback?
  (spectral studies, radio bubbles filling the X-ray cavities)
- Are mini-halos intrinsically different from giant halos, or do they represent a different evolutionary stage of the same non-thermal phenomenon? In particular, if non cool-core clusters evolve into cool-core clusters as believed, do giant radio halos evolve into mini-halos?
  (polarimetric studies, evolutive models and synergy with Athena X-ray satellite)

We will present evidence that surveys with SKA1 and eventually with SKA2 will have the capabilities to address the above questions.

3. Statistics of radio mini-halos

We start from the list of mini-halos reported in Giacintucci et al. (2014b) who recently selected a large sample of X-ray-luminous clusters with available high-quality radio data, and discovered four new mini-halos. By excluding the objects that they classify as "candidate" or "uncertain", and by including the new detection in the Phoenix cluster (van Weeren et al. 2014), the mini-halo sample used in this work comprises the following 16 objects (sorted by decreasing radio power at 1.4 GHz): RX J1347.5−1145 (z=0.451), Phoenix (z=0.596), RX J1720.1+2638 (z=0.159), A 2390 (z=0.23), RX J1532.9+3021 (z=0.362), RXC J1504.1−0248 (z=0.215), RBS 797 (z=0.35), Perseus (z=0.018), MS 1455.0+2232 (z=0.258), ZwCl 3146 (z=0.290), A 1835 (z=0.252), A 2204 (z=0.152), A 478 (z=0.088), A 2029 (z=0.077), Ophiuchus (z=0.028), 2A 0335+096 (z=0.035).

PoS(AASKA14)076

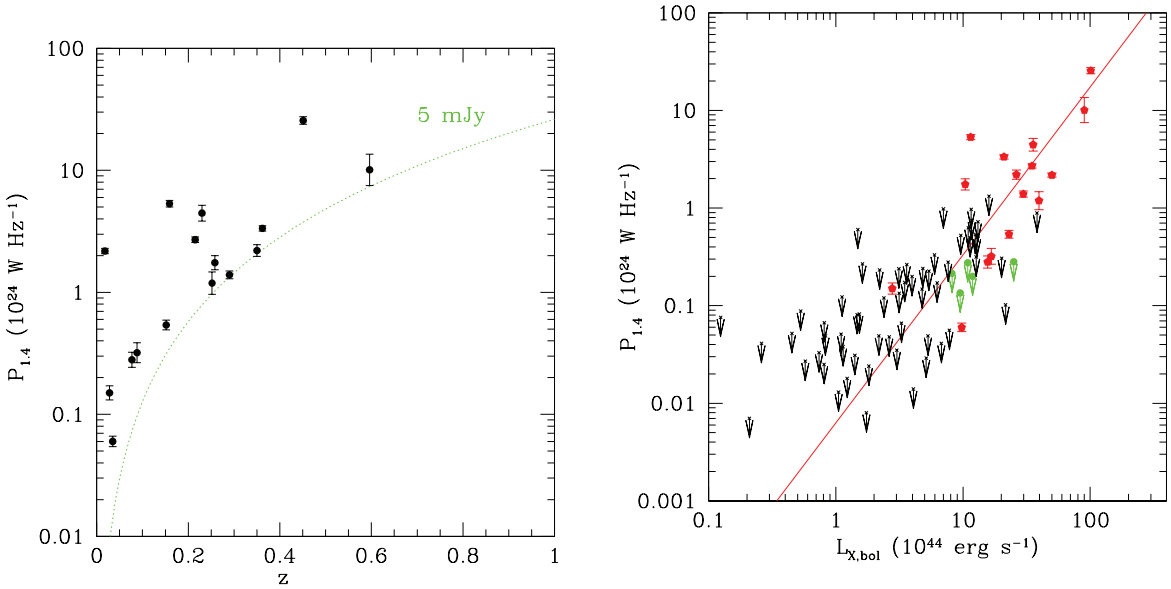

Figure 2: *Left panel:* Radio power at 1.4 GHz versus redshift for the mini-halo sample. The green dotted line represents the radio power corresponding to a flux density of 5 mJy. *Right panel:* Radio power at 1.4 GHz versus the cool-core-excised bolometric X-ray luminosity for the mini-halo sample (red filled circles). The red solid line is the best fit relation to the red points from bisector BCES regression to the parameters in log space (see Eq. 3.1). The green points are the observed upper limits from Kale et al. (2013), whereas the black crosses are the current upper limits estimated for the ACCEPT clusters which are candidates to host radio mini-halos.

We note that all these mini-halo clusters have a central entropy $K_0 = kT_0 n_0^{-2/3} \lesssim 25$ keV cm^2 (where $K0$ values are taken from the Chandra ACCEPT[3] sample of Cavagnolo et al. 2009), that according to the classification of Hudson et al. (2010) defines the population of strong cool cores (SCC). Recently, Panagoulia et al. (2014) take issues with the ACCEPT sample, arguing that the flattening of the entropy profile towards smaller radii, that is, the measured excess 'floor' K_0 of the core entropy above the best-fitting power-law profile for the entropy at larger radii, could be a resolution effect. Since the measured central entropy is correlated with the central bin size, this problem is enhanced for clusters with poor data quality, or poor spatial resolution, where the inner regions are under-sampled. However, we note that this effect is not an issue in this context, as it simply implies that the true central entropy value could be even lower, thus strengthening the SCC classification of our mini-halo sample (see also Giacintucci et al. in preparation for a more detailed investigation).

In Figure 2 (left panel) we plot the 1.4 GHz radio power of the mini-halos (taken from Giacintucci et al. 2014b; van Weeren et al. 2014) versus redshift. For comparison we overlay the

[3]Archive of Chandra Cluster Entropy Profile Tables

PoS(AASKA14)076

radio power corresponding to a flux of 5 mJy (green dotted line), which is roughly the lowest mini-halo flux detected up to now. It is evident that there is a strong observational bias that limits our present ability of detecting mini-halos; that is, we are currently missing many faint mini-halos simply because of the limited sensitivity of present radio telescopes. But how many mini-halos await discovery? The technical improvement reachable with SKA will be fundamental to answer to this question. To estimate the quantum leap produced by SKA in the ability of detecting radio mini-halos, we must link the non-thermal properties of these sources with the thermal properties of their host galaxy clusters. Being dominated by selection effects, the current radio information on mini-halos does not allow us to make predictions on future discoveries. By contrast, cluster statistics in terms of X-ray properties is already available from Chandra and XMM studies, and can be exploited to forecast future detections of radio mini-halos, provided an intrinsic relation between the thermal and non-thermal cluster properties exists.

To link the properties of the mini-halos with the global X-ray properties of the host clusters, in Figure 2 (right panel) we plot with red filled circles the mini-halo radio power at 1.4 GHz versus the cool-core-excised bolometric X-ray luminosity of the cluster, taken from the ACCEPT sample. We used the bivariate correlated error and intrinsic scatter (BCES) algorithm (Akritas & Bershady 1996) to perform regression fits to the data in log space, determining the best-fitting powerlaw relationship (bisector method) between the radio power, $P_{1.4}$, and the bolometric X-ray luminosity, $L_{\rm X,bol}$ (overlaid as a red solid line in Figure 2, right panel):

$$\log P_{1.4} = 1.72(\pm 0.28)\,\log L_{\rm X,bol} - 2.20(\pm 0.46) \tag{3.1}$$

where $P_{1.4}$ is in units of 10^{24} W Hz^{-1} and $L_{\rm X,bol}$ is in units of 10^{44} erg s^{-1}. We note that our analysis improve significantly the previous ones (e.g., Cassano et al. 2008; Kale et al. 2013) thanks to the better statistics, and that a similar scaling (with slope 1.76 ± 0.16) is obtained for giant radio halos (Brunetti et al. 2009). It is also entirely plausible that the flux density of mini-halos scales, perhaps even better, with other X-ray properties as well, such the cool-core strength[4]. However, we stress that for statistical studies of large cluster samples it is essential to link the non-thermal properties of the mini-halos to the thermal properties of the ICM which are easily observable with X-ray surveys, such as the X-ray luminosity.

Our starting point is the *optimistic* zero-th order assumption that every SCC cluster hosts a radio mini-halo, and that such a mini-halo follows the radio–X-ray power correlation. To check whether our hypothesis is consistent with the current independent constraints, in Figure 2 (right panel) we report in green the observed upper limits to the mini-halo emission in 5 SCC clusters from Kale et al. (2013). Although these limits appear systematically lower than the correlation, they are still consistent with the scatter of the observed trend. In Figure 2 (right panel) we also report the radio upper limit distribution of all SCC clusters in the ACCEPT sample which are candidate to host radio mini-halos; that is, according to our assumption, clusters having a central entropy $K0 \lesssim 25$ keV cm^2. Although most of these clusters have radio observations, there is no evidence for the presence of mini-halos in these clusters (see Giacintucci et al. 2014b). Thus a mandatory point is to check whether the absence of mini-halos in these SCC clusters is still consistent with

[4]a detailed investigation of this correlation, which requires accurate model fits to the X-ray spectra extracted inside the cooling region, is currently underway and will be presented in a forthcoming paper

PoS(AASKA14)076

our assumptions. We did that by estimating the radio upper limits in Figure 2 (right panel) based on the capabilities of current radio telescopes. In particular we adapted to mini-halos the criterion of Cassano et al. (2012) based on a threshold in flux for giant halos. From this threshold we derive the minimum flux of radio mini-halos that can be detected by assuming a spatial distribution of their brightness, and use this value to derive the upper limit to the luminosity of mini-halos in each SCC cluster. Murgia et al. (2009) modeled the radio brightness profile $I(r)$ of radio mini-halos with an exponential of the form $I(r) = I_0 \exp(-r/r_e)$, where r_e is the effective radius. This implies that the outermost, low brightness, regions of mini-halos are very difficult to detect. However, what is important is the capability to detect at least the brightest mini-halo regions. By considering the brightness profile of Murgia et al. (2009), we estimate that radio mini-halos emit about half of their total radio flux within their half radius $r_{50} \sim 1.68\, r_e$. Following Cassano et al. (2015) we can derive the minimum detectable flux, $f_{\rm min}(z)$, by assuming that the mini-halo is detected when the integrated flux within r_{50} gives a signal to noise ratio ξ_2. In particular, for each low-entropy cluster selected in the ACCEPT sample, we estimate $f_{\rm min}(z)$ from Eq. 4.2 of Cassano et al. (2015) by considering the angular size of the radio mini-halo in arcseconds, $\theta_{\rm MH}(z)$, which corresponds to $2\, r_{50}$ at the given cluster redshift. We adopt typical values of the current sample of observed mini-halos (e.g., Giacintucci et al. 2014b) of half radius $r_{50} \sim 100$ kpc, rms noise per beam $F_{\rm rms}$ = 25 μJy, $\xi_2 = 10$, beam angular size $\theta_b = 10$ arcsec. The observed (green points) and estimated (black crosses) upper limits in Figure 2 (right panel) do not violate the $P_{1.4}$-$L_{\rm X,bol}$ correlation, therefore we shall proceed with the assumption that all SCC clusters host a mini-halo that follows the radio–X-ray power correlation.

To derive a zeroth-order estimate of the detection limit reachable by SKA, in Figure 3 (left panel) we plot the clusters in the ACCEPT sample which are candidates to host radio mini-halos (i.e., having $K0 \lesssim 25$ keV cm^2) as a function of redshift. In red we highlight the objects that are known to possess a mini-halo, and in blue overlay the threshold in X-ray bolometric luminosity obtained by converting the upper limits on $P_{1.4}$ (black points in Figure 2, right panel) to upper limits on $L_{\rm X,bol}$ by means of Eq. 3.1. The blue line thus is representative of the current mini-halo detection limit on the population of SCC clusters. As clear, at present we are able to investigate only the "tip of the iceberg" of the population of SCC clusters. We then estimate the minimum flux as described above by assuming values in the reach of SKA1-SUR surveys at confusion limit (see Prandoni & Seymour 2015; Cassano et al. 2015, for more discussion on the role of confusion). In particular, the red solid line in Figure 3 (left panel) represents the minimum X-ray bolometric luminosity obtained (via the $P_{1.4}$-$L_{\rm X,bol}$ correlation given by Eq. 3.1) from the minimum 1.4 GHz radio power calculated for observations at 1.4 GHz with $F_{\rm rms}$ = 2 μJy, $\xi_2 = 10$, $\theta_b = 8$ arcsec. We also estimate that the scientific outcomes delivered in this field during early science operations of SKA1 (with performances at $\sim$50%) will be significant, allowing the radio follow-up to more than 70% of the ACCEPT sample (see red dotted line in Figure 3, left panel). Our anticipations for SKA2 are shown in Figure 3, left panel (red dashed line).

3.1 Number of radio mini-halos expected in surveys with SKA1-SUR

Given the large number of stations and the unprecedented *(u,v)* coverage of SKA, the detection will depend only on the mini-halo flux density. The number of mini-halos that can be detected from a radio survey with a given sensitivity up to a certain redshift z is computed by integrating the radio

PoS(AASKA14)076

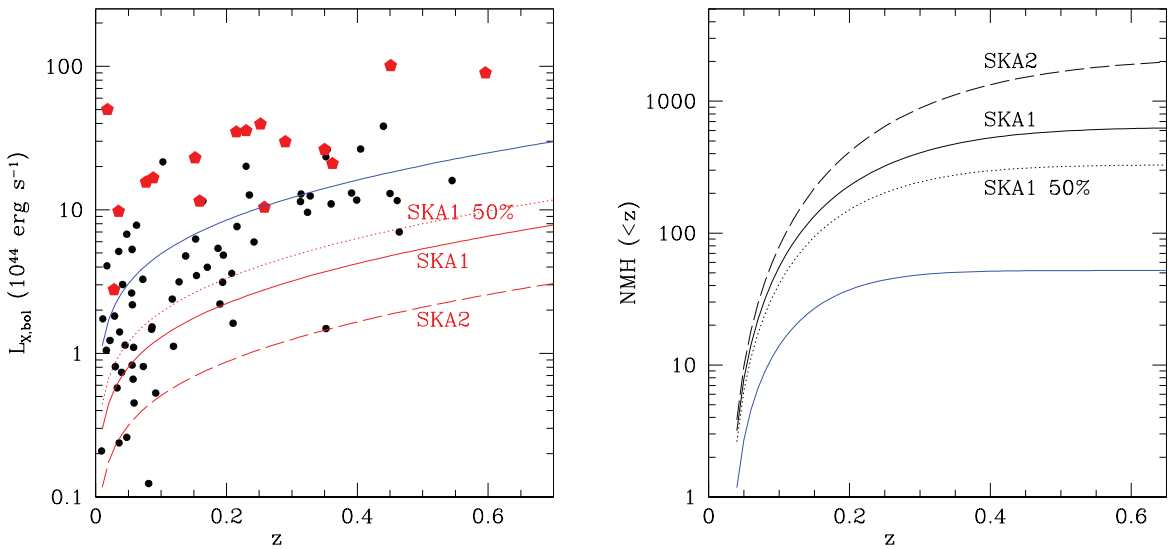

Figure 3: *Left panel:* Cool-core-excised bolometric X-ray luminosity, $L_{\rm X,bol}$, versus redshift for the ACCEPT clusters with central entropy $K0 \lesssim 25$ keV cm^2 (Cavagnolo et al. 2009). The clusters hosting a radio mini-halo are highlighted in red. The blue solid line is indicative of the current mini-halo detection limit on the population of SCC clusters ($F_{\rm rms}$ = 25 μJy, $\theta_b = 10$ arcsec), whereas the red solid line represents the detection limit reachable by SKA1-SUR surveys at confusion limit (obtained from the minimum radio power calculated for observations at 1.4 GHz with $F_{\rm rms}$ = 2 μJy, $\theta_b = 8$ arcsec). The red dotted lines and red dashed lines represent the detection limit reachable by early science operations of SKA1-SUR ($F_{\rm rms}$ = 4 μJy, $\theta_b = 8$ arcsec), and by SKA2 (rms = 0.2 μJy, $\theta_b = 4$ arcsec), respectively. *Right panel:* Integrated number of radio mini-halos detectable at 1.4 GHz out to z, NMH ($< z$), as a function of redshift. The predictions for All Sky surveys with SKA1, early SKA1 and SKA2 are shown with black solid lines, black dotted lines and black dashed lines, respectively. The prediction for a hypothetical survey conducted with current telescopes is also shown for comparison (blue solid line). The survey performances adopted to estimate the integrated number of mini-halos are the same as in left panel. The uncertainty envelopes driven by the $P_{1.4}$-$L_{\rm X}$ correlation alone are of the order of $\sim$30% at z=0.1, $\sim$40% at z=0.3 and $\sim$50% at z=0.6, but are not shown here to avoid confusion among different lines.

luminosity function (RLF) of mini-halos $\frac{dN_{\rm MH}}{dP_{1.4}dV}$ over radio luminosity and redshift (cf. Eq. 5.1 of Cassano et al. 2015), where the minimum radio luminosity detectable at a given redshift can be estimated from $f_{\rm min}(z)$ as described above (Eq. 4.2 of Cassano et al. 2015). Under our assumptions the RLF of mini-halos (per sky area surveyed in steradians) is

$$\frac{dN_{\rm MH}}{dPdV} = {\rm f_{SCC}} \frac{dN_{\rm cl}}{dL_{\rm X}dV} \frac{dL_{\rm X}}{dP_{1.4}} \tag{3.2}$$

where $\frac{dN_{\rm cl}}{dL_{\rm X}dV}$ is the X-ray luminosity function (XLF) of galaxy clusters (e.g., Mullis et al. 2004;

PoS (AASKA14) 076

Böhringer et al. 2014), f_{SCC} is the fraction of clusters with SCC (e.g., Hudson et al. 2010; Bharadwaj et al. 2014) and $\frac{dL_X}{dP_{1.4}}$ can be obtained from the observed radio–X-ray power correlation for mini-halos.

In particular, here we adopt the evolving XLF derived from the high-redshift, X-ray–selected 160 Square Degree *ROSAT* Cluster Survey (160SD) by Mullis et al. (2004) in a Λ-dominated universe, assuming the local XLF determined from the REFLEX survey (Böhringer et al. 2002). For consistency with the 160SD, where L_X is calculated in the 0.5-2.0 keV band, we derive the $P_{1.4}$-L_X correlation for mini-halos by estimating L_X in the same energy band. For each cluster in our mini-halo sample, we take the X-ray luminosity from the meta-catalogue of Piffaretti et al. (2011), which is given in the 0.1-2.4 keV energy band inside the radius R_{500}, and convert it to the 0.5-2.0 keV energy band assuming an Xspec `mekal` plasma model at the observed cluster temperature (taken from Cavagnolo et al. 2009), redshift, and assuming a metallicity of 0.3. We derive a correlation in the form $\log P_{1.4} = 2.03(\pm 0.20)\log L_X - 1.65(\pm 0.21)$, where $P_{1.4}$ is in units of 10^{24} W Hz^{-1} and L_X is in units of 10^{44} erg s^{-1}. Hence in Eq. 3.2 we can substitute

$$\frac{dL_X}{dP_{1.4}} = \frac{L_X}{P_{1.4}}\frac{d\log L_X}{d\log P_{1.4}} = \frac{1}{2.03}\frac{L_X}{P_{1.4}} \tag{3.3}$$

By further assuming $f_{SCC} \sim 0.40$ (Hudson et al. 2010), we estimate the number counts of radio mini-halos as a function of redshift from the All Sky surveys (3π) with SKA1, early SKA1 and SKA2 (see Fig. 3, right panel); we predict that they will be able to detect up to ~ 620, ~ 330 and ~ 1900 mini-halos, respectively, out to redshift $z \sim 0.6$. If the cluster XLF is taken as known, a measure of the error on such estimates can be obtained by considering the combined maximum variation of the $P_{1.4}$-L_X correlation parameters. This leads to uncertainties of the order of $\sim$30%, $\sim$40% and $\sim$50% at z=0.1, 0.3 and 0.6, respectively.

4. BCG radio properties and interaction with the ICM as a function of cosmic epoch

The radio-mode feedback is expected to be efficient in any cool core, in order to prevent complete cooling and provide a smooth temperature profile in the ICM as observed (McNamara et al. 2006; Rafferty et al. 2008). The presence of a radio galaxy in the BCG of a cluster is predicted to be generally associated to cavities in the ICM, as a result of the interaction between the population of relativistic electrons and the thermal electrons of the diffuse, X-ray emitting plasma. The study of cavities in the ICM inflated by relativistic electrons has been the subject of several studies aimed at understanding the energetics of the feedback processes, and the mechanism by which the mechanical energy is transferred to the ICM. The energetics can be estimated thanks to the enthalpy ($4PV$ for relativistic plasma) of the bubbles (Bîrzan et al. 2004; Bîrzan et al. 2008), while the heating mechanism is still strongly debated. This mechanism is important also because it is thought to be responsible for the heating of the gas at galactic scales, efficiently quenching the star formation processes and therefore setting the stellar mass scales and colors for massive galaxies (Croton et al. 2006). In addition, strong radio sources can be the beacon of massive protoclusters at redshift 2 and larger (see, e.g., Miley et al. 2006). Therefore, radio selection of clusters and protoclusters may be an efficient method to find the progenitor of massive clusters at $z > 2$, where the red sequence of the cluster galaxies may not be fully established, and the ICM is not shining in the X-ray band yet, indicating an incomplete virialization (Chiaberge et al. 2010).

PoS(AASKA14)076

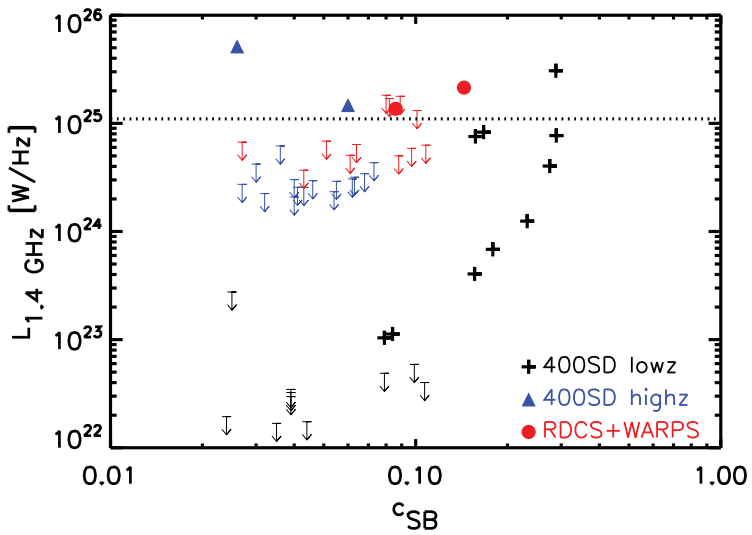

Figure 4: Relation between the radio luminosity of sources in close proximity to the cluster cores, $L_{1.4}$ GHz, and the surface brightness concentration, C_{SB}. Arrows refer to upper limits of non-detections. The dotted line at 1.1×10^{25} W Hz^{-1} marks the luminosity limit at $z = 1$ for NVSS sources, corresponding to the flux limit of 2.5 mJy (from Santos et al. 2010).

Tracing the feedback in galaxy clusters in the radio band consists of detecting the presence of radio AGN in the central galaxy, measuring its total power and resolving the radio emission in the radio lobes filling the cavities in the ICM. These studies have been very successful for local targets, where deep radio and X-ray data are both available, but they become increasingly difficult at higher redshifts. Recently, a few studies focused on high-redshift clusters and on the evolution of their properties with cosmic time. In particular, it has been realized that the evolution of the cool-core phenomenon is mirrored by the evolution of the feedback process itself. A simple correlation of the radio power and the cool-core strength (quantified through the concentration parameter C_{SB}) has been shown for low and medium redshift clusters (see Figure 4 right panel, Santos et al. 2010). It is observed that the luminosity of radio galaxies in the center of cool-core cluster have radio powers ranging from $\sim 10^{23}$ W Hz^{-1} to 10^{25} W Hz^{-1}. Ongoing JVLA programs (PI P. Tozzi) are being carried out to target the majority of the high redshift clusters with X-ray data known to date, to extend this relation up to $z \sim 1$, and to perform a systematic investigations of the radio-mode feedback in a representative sample of massive clusters in the CLASH sample (Postman et al. 2012). A comprehensive study of the radio properties of BCGs in X-ray selected galaxy clusters is in preparation (Hogan et al., submitted), in which multi-frequency radio observations allow one to investigate how the BCG properties vary with cluster environmental factors.

From a simple visual inspection of Figure 4, we conclude that we need to detect every radio galaxy at least down to 10^{23} W Hz^{-1} (at 1.4 GHz) in order to explore the same dynamical range

PoS(AASKA14)076

at high redshift. In the left panel of Figure 5 we show the radio power in unresolved sources corresponding to detection limits of 20, 10 and 1 μJy from top to bottom. Assuming that typically a detection requires a signal to noise ratio $S/N \sim 5$, these values correspond to 4 μJy, 2μJy and 0.2μJy per beam rms, which will be achieved by SKA1 (50% sensitivity), SKA1 All Sky and SKA1 Deep Tier, respectively. With early SKA1 (50% sensitivity) it will be possible to detect all the feedback process involving radio galaxies with power larger than 10^{23} W Hz^{-1} up to $z \leq 1$. We find that sources above 10^{23} W Hz^{-1} can be detected up to redshift $z \sim 1.7$ (the largest redshift where virialized galaxy clusters are currently found) and beyond with a sensitivity of 10 μJy per beam, which is easily achieved by SKA1-MID on the entire sky (3π) with a subarcsec resolution. At this sensitivity, confusion is avoided for a beam FWHM smaller than 4 arcsec (see Prandoni & Seymour 2015). A ten time lower detection threshold, corresponding to an rms of 0.2μJy per beam (blue line in Figure 5, left panel) is reached in the Deep Tier (2000 hrs) reference surveys (over about 10-30 deg^2) with SKA1-MID. This sensitivity is obtained at an angular resolution below 1 arcsec, thus easily allowing a complete census of the radio properties of the BCG at any redshift down to a total power of 10^{22} W Hz^{-1} at 1.4 GHz. In this case, even in the presence of a strong negative evolution with redshift, all the BCG in massive clusters with cool core and feedback activity will be detected and characterized. Considering that on the entire sky there are potentially 4×10^4 massive clusters at $z > 0.5$ which are within the reach of Athena or any X-ray survey mission with an average resolution of ≤ 10 arcsec (like the Wide Field X-ray Telescope[5]), the number of galaxies with radio activity in cool cores at $z > 0.5$ can be as high as $\sim 2 \times 10^4$, assuming little or no evolution in the population of cool core clusters, or few thousands assuming a strong evolution by a factor of 10. At present, there is large uncertainty on the evolution of cool cores (Santos et al. 2010; McDonald et al. 2013), and only a strong synergy of SKA1 with deep and wide X-ray data will answer to this question. Clearly SKA, when completed, will allow one to investigate the presence of radio galaxies also in groups at high redshift, a completely new window for which it is impossible to make predictions given the present knowledge of the feedback processes. SKA therefore offers a unique opportunity to constrain the duty cycle of radio galaxies in groups and cluster of galaxies across the cosmic epochs. Another relevant aspect to consider is that radio BCGs often show variabiliy and a high complexity in their radio spectra (Hogan et al., submitted), with $\sim$80% of them showing a flat-spectrum/self-absorbed core. These flatter/active components will often be distinguishable only at frequencies larger than 5 GHz, making it desirable to have coverage at these frequencies.

A further major breakthrough in the investigation of radio-mode AGN feedback at high redshift is the detection and characterization of the radio lobes produced by the relativistic electrons which are responsible for carving the cavities in the ICM clearly observed in X-ray local clusters. If we use as a reference the bubble size in the two objects shown in Figure 1, we can directly compute the typical angular size of the bubbles as a function of the redshift. For the group HCG 62 ($z = 0.0137$) the average size for a single bubble, assuming a spherical shape, is 5 kpc, while for the medium-mass cluster RBS 797 ($z = 0.35$) is 12 kpc. If we focus on targets at $z > 1$ the angular size turns out to be about 0.6 and 1.5 arcsec, respectively, with a weak dependence on the redshift. For these objects we measure a total radio power at 1.4 GHz of 2.0×10^{21} W Hz^{-1} and 10^{24} W Hz^{-1} for

[5] see www.wfxt.eu

PoS(AASKA14)076

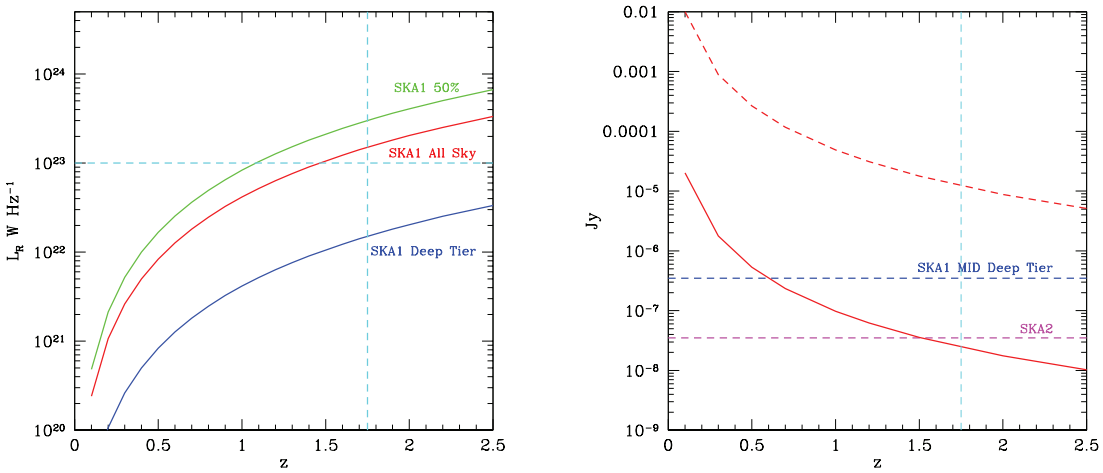

Figure 5: *Left panel:* Radio power at 1.4 GHz detectable with a sensitivity of 1-10-20 μJy (defined as 5× rms noise) are shown in blue, red, and green lines, respectively, as a function of redshift. Green corresponds to early SKA, red to SKA1 All Sky, and blue to SKA1 Deep Tier. The horizontal dashed line shows the minimum radio luminosity currently measured in a radio galaxy hosting a cool core in local clusters. *Right panel:* the dashed red line shows the flux density per beam with a resolution of 0.75 arcsec for a bubble with radio power of 10^{24} W Hz^{-1} as observed in the cluster RBS 797. The dashed horizontal blue line marks the sensitivity of Deep Tier (2000 hrs) reference surveys with SKA1-MID at the same angular resolution. The solid red line shows the flux density per beam with a resolution of 0.3 arcsec for a bubble with radio power of 2×10^{21} W Hz^{-1} as observed in the group HCG 62. The magenta dashed line shows the sensitivity reacheble with SKA2. In both panels the vertical dashed lines mark the highest redshift where virialized, X-ray emitting clusters are currently detected.

a single cavity in HCG 62 and RBS 797, respectively. We conservatively assume that a beam FWHM of half the size of the bubble is sufficient to resolve it. Therefore, we compute the radio flux density at 1.4 GHz from a single cavity as a function of redshift, assuming a spectral index $\alpha \sim 1$, and a beam FWHM of 0.3 arcsec and 0.75 arcsec for the reference cases of HCG 62 and RBS 797, respectively. We show in Figure 5 (right panel) that the signal from a single cavity in medium and large clusters is always well above the sensitivity of Deep Tier (2000 hrs) reference surveys with SKA1-MID, which is computed as 5×70 nJy per beam rms (see Prandoni & Seymour 2015). At this resolution, we are also well above the confusion level. Therefore the detection and characterization of typical cavities in medium or large mass cluster is within the reach of SKA1-MID surveys at any relevant redshift.

On the other hand, to detect a single cavity in a small group a beam FWHM of 0.3 arcsec is required, and given the much lower radio power of $\sim 2.0 \times 10^{21}$ W Hz^{-1}, the expected radio flux density in the beam rapidly falls below the sensitivity limit of SKA1-MID (see red lines in Figure 5, right panel). According to the current specifics, SKA1-MID allows detection and characterization of radio bubbles only up to $z \sim 0.5$. If a ~ 10 times better sensitivity can be reached with SKA2 at the resolution of 0.3 arcsec, the investigation of the radio-mode feedback becomes feasible also in groups up to $z \sim 1.3$. We also note that the fraction of BCGs that show clear radio lobes in local X-ray selected clusters is about 10% (Hogan et al., submitted). This leaves room for several

PoS(AASKA14)076

thousands of clusters in the entire sky potentially hosting bubbles and cavities, but it may also indicate that most of the activity we actually observe around radio galaxies is either the aftermath of lobe creation and dissipation, or, more likely, low power outbursts that are confined within a few hundreds pc of the core. In this case at high redshift the full resolution SKA images will likely appear unresolved or amorphous. Nevertheless, the subarcsec angular resolution provided by the long baselines are essential to investigate the feedback process in details in relatively low and medium redshift clusters.

To summarize, our preliminary feasibility study shows that the radio-mode feedback will be unveiled practically at any level in clusters up to $z \sim 1.7$, the maximum redshift where virialized clusters have been detected in the X-ray band so far. The same study will be possible also in high-redshift groups if SKA2 will improve the sensitivity by an order of magnitude at the same angular resolution. When SKA will be fully operational, the knowledge of distant galaxy clusters will be largely but unpredictably changed. A large number of optically and IR selected clusters will be available thanks to the forthcoming surveys of the Euclid[6] satellite and of the LSST project[7]. Thanks to the ICM X-ray characterization of the cluster cores achievable with the Athena mission, these can be directly combined with the radio data to search for cavities. However, an efficient synergy with SKA will depend on the on-axis angular resolution of the X-ray telescope, which should be of the order of 1 arcsec. In the field of high-z clusters, as in many others, the advent of SKA will provide access to incredibly deep and high quality data, which are hardly matched by any planned of foreseen facility in other wavebands.

References

Akritas, M. G. & Bershady, M. A. 1996, ApJ, 470, 706
Ascasibar, Y. & Markevitch, M. 2006, ApJ, 650, 102
Best, P. N. et al.. 2007, MNRAS, 379, 894
Bharadwaj, V. et al.. 2014, ArXiv e-prints
Bîrzan, L. et al.. 2008, ApJ, 686, 859
Bîrzan, L. et al.. 2004, ApJ, 607, 800
Böhringer, H. et al.. 2014, ArXiv e-prints
—. 2002, ApJ, 566, 93
Bonafede, A. et al.. 2014, MNRAS, 444, L44
Brunetti, G. et al.. 2009, A&A, 507, 661
Brunetti, G. & Jones, T. W. 2014, International Journal of Modern Physics D, 23, 30007
Burns, J. O. 1990, Astronomical Journal, 99, 14
Cassano, R. et al.. 2015, “Cluster Radio Halos at the crossroads between astrophysics and cosmology in the SKA era”, in proceedings of "Advancing Astrophysics with the Square Kilometre Array", PoS(AASKA14)073
—. 2012, A&A, 548, A100
—. 2008, A&A, 486, L31
Cavagnolo, K. W. et al.. 2009, ApJ Supplement Series, 182, 12

[6]http://sci.esa.int/euclid/
[7]http://www.lsst.org/lsst/

PoS(AASKA14)076

Chiaberge, M. et al.. 2010, ApJ, 710, L107
Croton, D. J. et al.. 2006, MNRAS, 365, 11
Doria, A. et al.. 2012, ApJ, 753, 47
Dunn, R. J. H. & Fabian, A. C. 2006, MNRAS, 373, 959
Fabian, A. C. 1994, Annual Rev. of Astronomy & Astrophysics, 32, 277
—. 2012, Annual Rev. of Astronomy & Astrophysics, 50, 455
Fanaroff, B. L. & Riley, J. M. 1974, MNRAS, 167, 31P
Farnsworth, D. et al.. 2013, ApJ, 779, 189
Feretti, L. et al.. 2012, Astronomy & Astrophysics Rev., 20, 54
Ferrari, C. et al.. 2015, "Non-thermal emission from galaxy clusters: feasibility study with SKA", in proceedings of "Advancing Astrophysics with the Square Kilometre Array", PoS(AASKA14)075
Fujita, Y. et al.. 2004, Journal of Korean Astronomical Society, 37, 571
Giacintucci, S. et al.. 2014a, ArXiv e-prints
—. 2014b, ApJ, 781, 9
Gitti, M. et al.. 2012, Advances in Astronomy, 2012
—. 2004, A&A, 417, 1
—. 2002, A&A, 386, 456
—. 2007, A&A, 470, L25
—. 2013, A&A, 557, L14
—. 2010, ApJ, 714, 758
Govoni, F. et al.. 2015, "Cluster magnetic fields through the study of polarized radio halos in the SKA era", in proceedings of "Advancing Astrophysics with the Square Kilometre Array", PoS(AASKA14)105
Hlavacek-Larrondo, J. et al.. 2012, MNRAS, 421, 1360
Hudson, D. S. et al.. 2010, A&A, 513, A37
Kale, R. et al.. 2013, A&A, 557, A99
Markevitch, M. & Vikhlinin, A. 2007, Physics Reports, 443, 1
Mazzotta, P. & Giacintucci, S. 2008, ApJ, 675, L9
McDonald, M. et al.. 2013, ApJ, 774, 23
McNamara, B. R. & Nulsen, P. E. J. 2012, New Journal of Physics, 14, 055023
McNamara, B. R. et al.. 2006, ApJ, 648, 164
Miley, G. K. et al.. 2006, ApJ, 650, L29
Mittal, R. et al.. 2009, A&A, 501, 835
Mullis, C. R. et al.. 2004, ApJ, 607, 175
Murgia, M. et al.. 2009, A&A, 499, 679
Panagoulia, E. K. et al.. 2014, MNRAS, 438, 2341
Peterson, J. R. & Fabian, A. C. 2006, Physics Reports, 427, 1
Piffaretti, R. et al.. 2011, A&A, 534, A109
Postman, M. et al.. 2012, ApJ Supplement Series, 199, 25
Prandoni, I. & Seymour, N. 2015, "Revealing the Physics and Evolution of Galaxies and Galaxy Clusters with SKA Continuum Surveys", in proceedings of "Advancing Astrophysics with the Square Kilometre Array", PoS(AASKA14)067

PoS(AASKA14)076

Rafferty, D. A. et al.. 2008, ApJ, 687, 899
Santos, J. S. et al.. 2010, A&A, 521, A64
—. 2012, A&A, 539, A105
Sun, M. 2009, ApJ, 704, 1586
van Weeren, R. J. et al.. 2014, ApJ, 786, L17
Zhuravleva, I. et al.. 2014, ArXiv e-prints
ZuHone, J. A. et al.. 2013, ApJ, 762, 78
—. 2010, ApJ, 717, 908

PoS(AASKA14)076

PROCEEDINGS OF SCIENCE

Morphological classification of radio sources for galaxy evolution and cosmology with the SKA

S. Makhathini[1], **O. M. Smirnov**[12], **M. J. Jarvis**[34] **and I. Heywood**[51]

[1] *Department of Physics & Electronics, Rhodes University, P.O. Box 94, Grahamstown 6140, South Africa*
[2] *SKA South Africa, 3rd Floor, The Park, Park Road, Pinelands, 7405, South Africa*
[3] *Astrophysics, Department of Physics, University of Oxford, Oxford OX1 3RH, UK*
[4] *University of the Western Cape, ZA-7535 Cape Town, South Africa*
[5] *CSIRO Astronomy & Space Science, P.O. Box 76, Epping, NSW 1710, Australia*
E-mail: sphemakh@gmail.com, o.smirnov@ru.ac.za, matt.jarvis@astro.ox.ac.uk, ian.heywood@csiro.au

Morphologically classifying radio sources in continuum images with the SKA has the potential to address some of the key questions in cosmology and galaxy evolution. In particular, we may use different classes of radio sources as independent tracers of the dark-matter density field, and thus overcome cosmic variance in measuring large-scale structure, while on the galaxy evolution side we could measure the mechanical feedback from FRII and FRI jets. This work makes use of a `MeqTrees`-based simulations framework to forecast the ability of the SKA to recover true source morphologies at high redshifts. A suite of high resolution images containing realistic continuum source distributions with different morphologies (FRI, FRII, starburst galaxies) is fed through an SKA Phase 1 simulator, then analysed to determine the sensitivity limits at which the morphologies can still be distinguished. We also explore how changing the antenna distribution affects these results.

Advancing Astrophysics with the Square Kilometre Array
June 8-13, 2014
Giardini Naxos, Italy

PoS(AASKA14)081

S. Makhathini

1. Introduction

The capabilities of the Square Kilometre Array (SKA) allow it to conduct experiments in areas of fundamental physics and cosmology with accuracies that are unprecedented in the field of radio astronomy (Cordes et al. 2004; Rawlings et al. 2004; Kramer et al. 2004, this volume).

One key experiment that forthcoming radio continuum surveys will be able to perform involves the investigation of large scale structure formation in the Universe. The inhomogeneous distribution of matter in the Universe is thought to be seeded by random perturbations in the density field imprinted shortly after cosmic inflation. The magnitude of these primordial fluctuations are typically investigated by measuring the angular two-point correlation functions (2PCF; e.g. Peebles 1980)[1] of both galaxy catalogues (e.g. Wang et al. 2013) and the temperature fluctuations in the Cosmic Microwave Background (e.g. Spergel et al. 2003). Evidence for non-Gaussianity in the density field has implications for inflationary models, and can be investigated by determining the bispectrum[2], specifically the non-linearity function f_{NL} (2.7 ± 5.8; Planck Collaboration et al. 2014).

One of the best methods for constraining f_{NL} involves the use of galaxy surveys to trace the dark matter distribution at more recent cosmic epochs. It is necessary for these surveys to cover very large areas in order trace the large-scale power. The SKA will have the sensitivity to detect a large number of very faint radio sources (which are typically all at cosmological distances) over large areas of the sky. However one advantage the radio wavelength has over optical surveys is the possibility of morphologically distinguishing different source populations.

Three such populations of sources are the two Fanaroff-Riley (FR; Fanaroff & Riley 1974) classes of jet-producing active galaxies, and regular star forming disks exhibiting synchrotron emission at radio wavelengths, and possibly hosting a weak active nucleus. Each of these sources has a distinct morphological appearance, and coupled with the correlation between the source type and the halo mass in which it resides, the uncertainty on f_{NL} could be conservatively halved by a plausible SKA continuum survey (Ferramacho et al. 2014). Characterising radio source morphology is also critical for the vast majority of galaxy evolution and AGN-related science. It is now clear that feedback from AGN is a critical mechanism in the evolution of massive galaxies over all redshifts. One of the few methods of identifying the sources responsible for the hot-mode, or radio-mode feedback is through radio continuum observations, as indications of such activity at other wavelengths are not widely observed (Best & Heckman 2012). Furthermore, radio morphologies can help distinguish AGN from star-forming galaxies, which will dominate the source counts at the flux-densities that the SKA will reach (Muxlow et al. 2005; McAlpine et al. 2015, this volume) This is crucial if we are to use the SKA to provide a robust, obscuration free, method of determining the evolution of the star-formation rate density in the Universe (Muxlow et al. 2005, this volume). However, one of the most crucial elements of good morphological information is to separate star formation and AGN activity (see e.g. McAlpine et al. 2015, this volume) in the same

[1]The Fourier inversion of which is the matter power spectrum

[2]The Fourier inversion of which is the three point correlation function

PoS(AASKA14)081

galaxy, thus allowing us to attempt to decouple the bolometric output from these two processes. Key to this experiment is the radio survey having sufficient spatial resolution and imaging fidelity in order to faithfully reproduce the source morphologies in the synthesised image. In this chapter we consider a limited class of radio sources in an attempt to forecast the ability of the SKA1-MID array to detect and morphologically distinguish between these sources. We concentrate on instrumental limitations to morphological classification (sensitivity, resolution, imaging fidelity); questions of the relative size of morphologically distinct source populations are outside the scope of this work. In other words, we attempt to answer the following question: if the sources are morphologically distinct in the radio, can we make this distinction with SKA1-MID, and how deeply? We use plausible SKA configurations and perform full imaging simulations of schematic representations of various source types. The redshift, signal to noise and resolution limits on reliable source classifications are determined.

2. Background on Layouts

The general scientific requirements for SKA1 (Braun 2013) suggests that (at least for SKA1-MID), an array with a maximum baseline of around 100 km is required. Therefore, we consider a layout with the shortest possible maximum baseline that does at least as well as the "second generation" baseline design in the resolution range 0.4-1″ over 650, 800 and 1000 MHz while not significantly compromising the performance at the larger angular scales. Moreover, having a layout which performs just as well as (or better than) the baseline layout but which covers significantly less space translates to a reduction in trenching and data transport costs, which presents an opportunity to re-invest the funds elsewhere. The following SKA1-MID layouts are under consideration here:

REF2A100B173 The "Second-generation" layout (254 dishes) produced by Robert Braun (September 2013)[3]. This layout has a maximum baseline of 173 km. In this chapter, we also refer to this layout as REF2.

W*i*-*j*A*k*B*l* This is the REF2 layout with the core "puffed up" by 10%, with i dishes moved from the outer core to the spiral arms and j extra dishes added to the spiral arms. The spacing in the arms is then optimised to get more sensitivity on the longer ($>$ 50 km) baselines (See baseline distribution histograms in Figure 2). Each spiral arm stretches out to k kilometres and the maximum baseline length is about l kilometres.

The natural sensitivity at specific angular scales for an interferometer can be determined by making noise maps using only visibilities corresponding to those angular scales. Table 1 shows the sensitivity on angular scales {0.4-1, 1-2, 2-3, 3-4, 600-3600} arcsec for the two layouts under consideration. It is evident from this table that the W9-0A72B120 layout (henceforth, referred to as W9) has more sensitivity at small angular scales, but we note that further optimisations are still possible – even for different angular scales. In fact, the sophistication of simulation packages like `MeqTrees` (Noordam & Smirnov 2010) coupled with new insights into fundamental limits on radio interferometric imaging and calibration (Wijnholds & van der Veen 2008) allow for the distribution of array elements to be optimised subject to a well defined set of science of goals. It is

[3]We assume this to be the baseline layout.

PoS(AASKA14)081

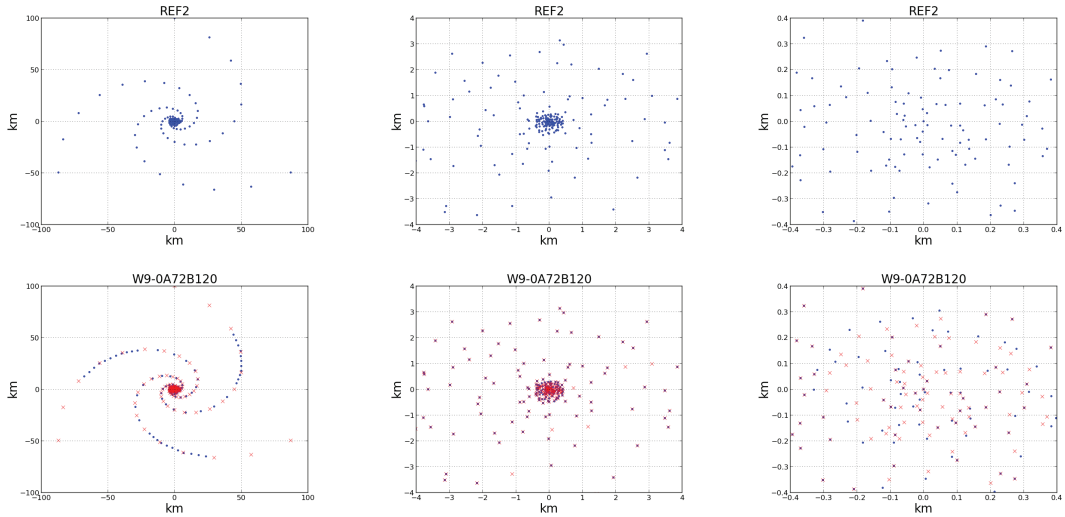

Figure 1: Antenna layouts on scales of ±100 km (left), ±4 km (centre) and ±400 m (right). The REF2 layout is plotted on the upper row, and as red crosses for direct comparison to the W9-0A7B120 configuration on the lower row.

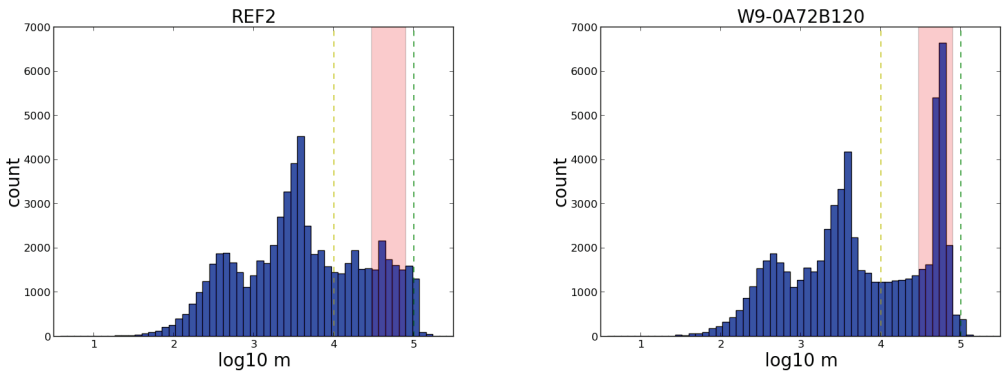

Figure 2: Baseline distribution with the uv-distance in $\log_{10}$ km . Yellow and green dashed lines mark 10 and 120 kilometres respectively, and the pink strip represents baselines from 30-80 km.

also worth noting that the optimisation can be further constrained by cost and engineering limitations. Figure 4 shows the PSF sizes (uniform weighting) for the two layouts under consideration. The figure shows that the 120km W9 layout has very similar resolving performance compared to the 173km REF2.

PoS(AASKA14)081

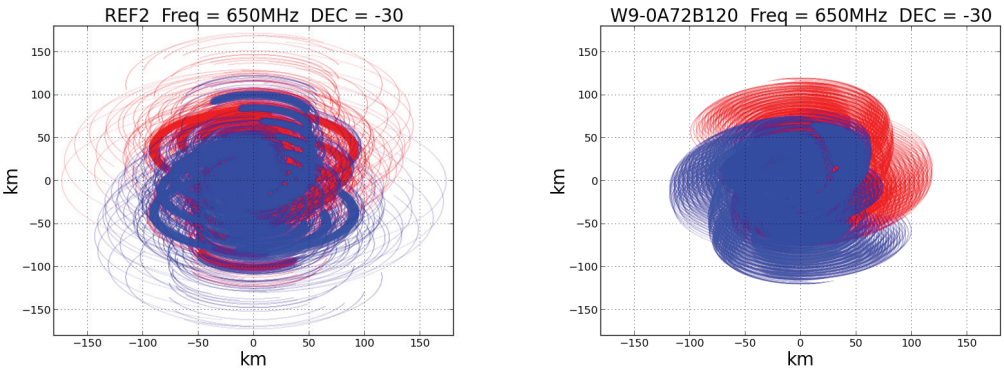

Figure 3: UV-Coverage for 8 hour tracks at 650 MHz (50 MHz wide channel) at declination -30 degrees for the different layouts. Blue indicates uv-points, red indicates conjugate uv-points.

Table 1: Relative (w.r.t REF2) RMS pixel noise for a 50MHz band after an 8hr synthesis with a 60s integration for the different layouts at different angular scales. These values are generated at 650, 800 and 1000 MHz, at angular scales {0.4-1, 1-2, 2-3, 3-4, 600-3600} arcsec and are labeled *resbin* {1, 2, 3, 4, 5} respectively. This is done for natural weighting at declination -30 degrees.

	650MHz					800MHz					1000MHz				
resbin	1	2	3	4	5	1	2	3	4	5	1	2	3	4	5
SKA1REF2	1.00	1.00	1.00	1.00	1.00	1.00	1.00	1.00	1.00	1.00	1.00	1.00	1.00	1.00	1.00
SKA1W9-0A72B120	0.77	0.81	1.12	1.06	1.00	0.72	1.05	1.06	1.17	1.06	0.72	1.05	1.08	1.26	1.05

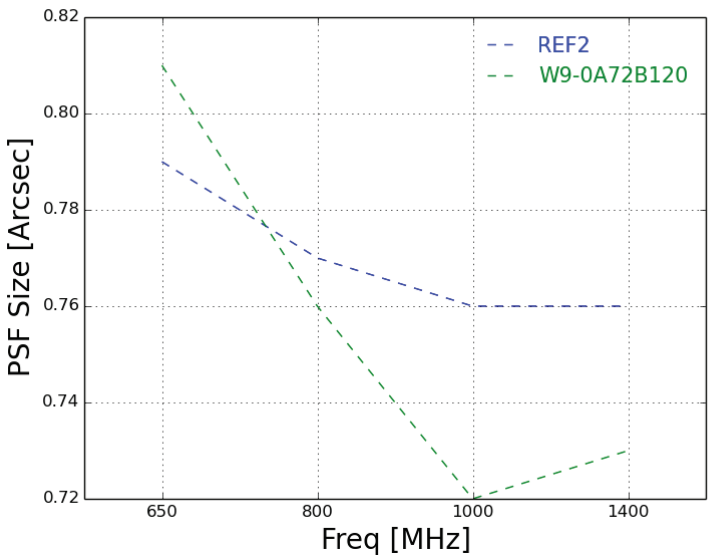

Figure 4: Uniformly weighted PSF sizes as a function of frequency for the REF2 (blue) and W9-0A72B120 (green) layouts.

PoS(AASKA14)081

3. The Experiment

Our aim is to gauge the sensitivity and resolution limits at which SKA1-MID can reliably detect and morphologically classify FRI, FRII and star forming galaxies (SFG). We note that we do not consider any evolution in the structure of the radio sources with redshift, or the effects of inverse Compton scattering, but note that such considerations would need quantifying in a more comprehensive study. We concentrate on SKA1-MID as it provides the best possibility of investigating source morphologies when compared to the very low resolution offered by SKA1-LOW and the factor of $\sim 2-3$ poorer resolution at a similar frequency for SKA1-SUR.

3.1 Telescope Simulations

We use the `MAKEMS` tool to make simulated measurement sets (MS) of 8 hour tracks centred at 700 MHz, with fifteen 50 MHz channels at a declination of -30 degrees. We then use the `MeqTrees` software to fill the MS with simulated visibilities. The noise per real and imaginary part for each visibility is calculated as

$$\sigma_{\rm vis} = {\rm SEFD}/\sqrt{2\Delta\nu\Delta t}, \tag{3.1}$$

where Δt is the integration time in seconds and $\Delta\nu$ is the channel width in Hertz. We use the baseline document's system equivalent flux density (SEFD) value of 637 Jy for band 1. Note, the noise is proportional to the square-root of the synthesis time, therefore since we have "full" uv-coverage at 8 hours, we can reasonably approximate a N hour synthesis for $N > 8$ by scaling the visibility noise as

$$\sigma^N_{\rm vis} \simeq \sigma_{\rm vis}\sqrt{8/N}. \tag{3.2}$$

We simulated a 10 hour synthesis using the REF2 and the alternative layout W9. The noise per visibility for both layouts is 8.69 mJy/beam, and the root mean square (RMS) of the pixel noise (uniform weighting) is 5.42 μJy/beam for REF2 and 5.29 μJy/beam for W9. Note that W9 is slightly more sensitive compared to REF2 due to the more complete uv-coverage over the scales of interest. Primary beam, calibration and atmospheric effects are beyond the scope of this chapter, however we note that significant progress has been (and continues to be) made in this area (see Smirnov, O. M. 2011; Grobler et al. 2014; Kazemi et al. 2011; Kazemi & Yatawatta 2013; Tasse, C. 2014).

3.2 Sky Models

Starting at redshift $z = 1$, we use `MeqTrees` to predict visibilities for realistic flux distributions (FRI, FRII, or SFG galaxies) and use the `LWIMAGER` (part of the `CASAREST` package) tool to make clean maps. The clean maps are then processed (see Section 3.4) to determine the morphology of the flux distributions. This process is repeated at incrementally higher (steps of $z = 0.5$) redshifts until detection or classification is no longer possible. For the FRI and FRII cases, we model a flat spectrum core with two hot-spots. The core has a luminosity of 7.94×10^{22} WHz^{-1}sr^{-1}, with each hot-spot having 90% of the core luminosity and a spectral index of -0.7. The core and the hot-spots are modelled as point sources and the lobes as Gaussians. For convenience we consider the favourable inclination angle of 45 degrees. The true size of these sources is 200 kpc. For the

PoS(AASKA14)081

SFG case we model a a Gaussian of luminosity 1.59×10^{24} WHz^{-1}sr^{-1} with a spectral index of -0.7, and a true size of 5 kpc.

3.3 Imaging Techniques

We make high resolution ($0.1''$) clean maps using Hogbom `CLEAN` (Högbom 1974); cleaning down to twice the rms pixel noise. Note that for uniform and Briggs weighting a crucial parameter is the size of the bin in the uv plane over which weights are "uniformised". By default this is determined from the full image size, but `LWIMAGER` allows one to uniformise the weights over bins corresponding to a user-defined FoV instead. For these simulations uv-bins corresponding to a FoV of $10'$ were used.

3.4 Morphological Classification

The classification is done in two main steps: (i) locate bright compact emission and (ii) determine the extent of the lobes. For the former, we use the `pyBDSM` source finding tool[4]. If there is one bright compact component the galaxy is classified as a SFG, while if more than one bright component is found the pixel statistics along the path joining the bright components are analysed in order to determine the extent of the lobes – see Figure 5 for an illustration. Finally, if lobes are detected, the galaxy can be classified as either FRI or FRII. This classification algorithm hinges on an accurate characterisation of the noise.

One crucial component in classifying these radio galaxies is an accurate characterisation of the jets, which is a major challenge at low SNR. This problem can be compounded by the inability to deconvolve the PSF at low SNR (this is particularly a problem for `CLEAN`). However a class of algorithms based on compressive sensing (CS) has recently emerged to tackle deconvolution issues in the context of the SKA and its precursor/pathfinder facilities (see section 4.4.2 in Norris et al. 2013), in particular `MORESANE` (Dabech *et al*. 2014, submitted) and `PURIFY` (Carrillo et al. 2014). Although not yet as well tested as `CLEAN`, these algorithms have been shown to be superior to `CLEAN` in detecting diffuse and compact emission, especially at low SNR (Ferrari et al., this volume). In addition to the CS-based algorithms, a Bayesian approach to radio interferometry imaging has led to the `RESOLVE` algorithm (Junklewitz et al. 2013), which has also been shown to produce better results compared to `CLEAN`. This progress in deconvolution algorithms will enhance the accuracy and depth of source characterisation algorithms.

4. Simulation Results

Before we present the simulations results, we first show in Figure 6 how the SNR varies with redshift assuming the sky models and the observation set up described in Section 3. From these figures it is clear that SKA1-MID will be able to probe radio emission at very high redshifts. For FR sources we expect an SNR (w.r.t the lobe surface brightness for FR sources) of 3 at redshifts around 5.5, and the same SNR at a redshift of 5 for SFGs after 10 hours of integration and after 100 hours of integration we expect an SNR of 3 at redshifts of 9.5 for FR sources and 8.5 for SFGs. On the other hand, morphological characterisation will be limited by the ability to resolve

[4] `https://dl.dropboxusercontent.com/u/1948170/html/installation.html`

PoS(AASKA14)081

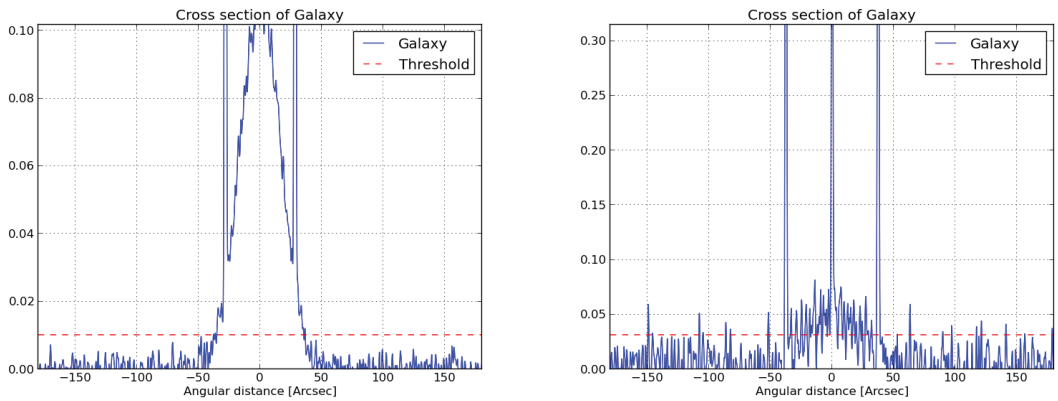

(a) High SNR, $z = 4$ (b) Low SNR, $z = 7$

Figure 5: Illustration of how the extent of the lobes is determined for an FR2 source. In both cases, having found the hot spots, the RMS of pixels within some box (20×20 pixels in this case) along the path connecting the hot spots is computed. If the RMS is above some threshold (red line), then the pixels are taken to be part of the lobes. Finally, the edges of the lobes can be determined by keeping track of where the RMS of the pixels within this box gets larger than the threshold.

these sources. SKA1-MID with a $\sim 0.5''$ PSF (uniform weighting) at 700 MHz, will not be able to resolve sources of sizes less than 5 kpc (see Figure 7).

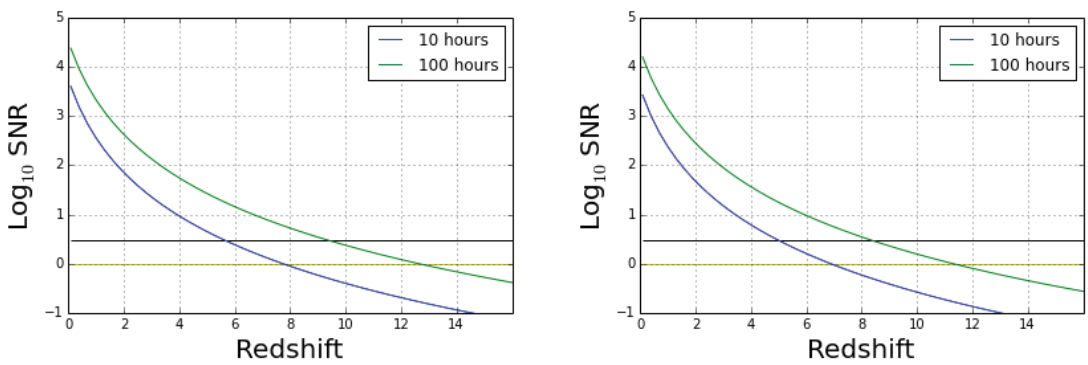

(a) FRI and FRII sources (b) SFGs

Figure 6: The SNR (relative to the surface brightness) from a 10 (blue) and a 100 (green) hour synthesis as a function of redshift for FRI and FRII sources (left) and the SFGs (right). Lines of constant SNR=1 (yellow) and SNR=3 (black) also plotted. These plots were generated using the REF2 layout.

In Figures 8-10 we show images of the galaxies under consideration as a function of redshift. For each galaxy type we show the sky model (row 1) and images from simulations using the REF2 and W9 layouts (rows 2 and 3 respectively). Our morphological classification algorithm was able to detect and distinguish FR sources up to a redshift of 8, and up to a redshift of 5 for the SFGs after 10

PoS(AASKA14)081

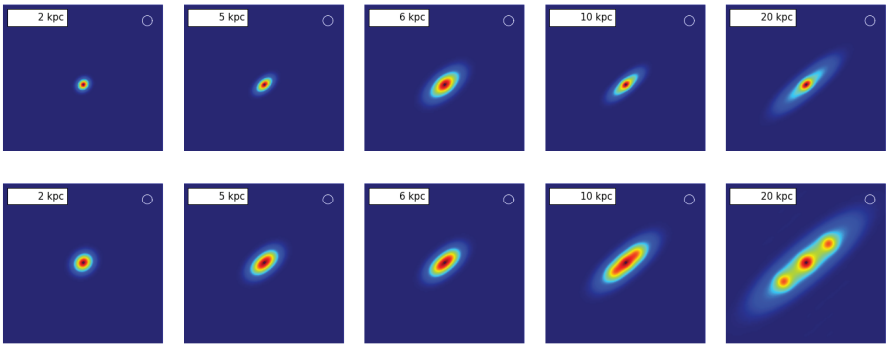

Figure 7: Model FR1 (row 1) and FR2 (row 2) sources of different sizes as seen by the REF2 layout at $z = 1$. The white circle on the top left corner gives an indication the PSF size ($0.51''$).

hours of integration. Note that in the SFG case, we set a 5σ threshold for the `pyBDSM` source finder to avoid false detections, however detection and classification of these sources can (potentially) still be done below the 5σ level if the false detections can be quantified using techniques such as described in Serra et al. (2012).

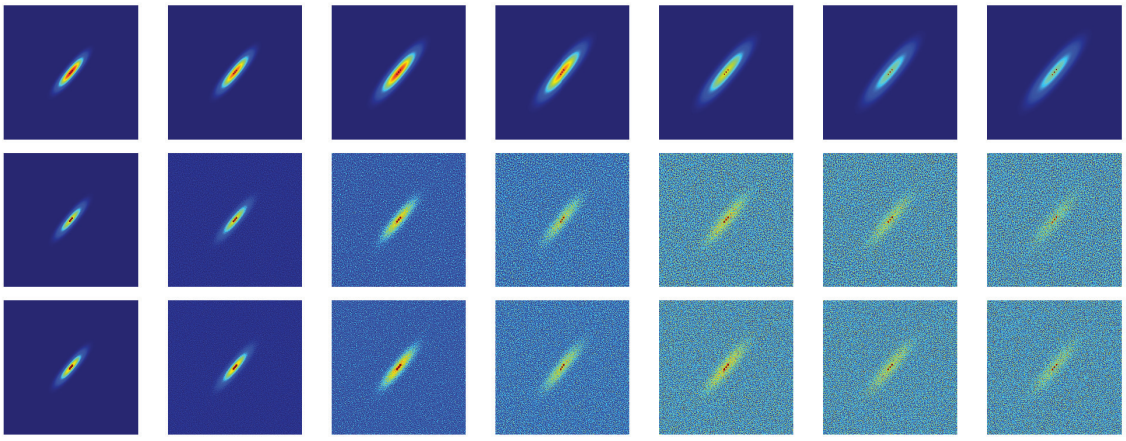

Figure 8: Model FRI galaxies (row 1) as a function of redshift {1, 2, 3, 4, 5, 6, 7, 7.5, 8, 8.5} as seen by the REF2 (row 2) and W9 (row 3) layouts after a 10 hour synthesis.

Now we consider three cases along the timeline that SKA1 may be built out: (i) a 50% SKA1-MID sensitivity, (ii) a 70% SKA1-MID in terms of sensitivity, and (iii) is the full SKA facility– with 10 times the sensitivity of SKA1-MID. Figure 11 shows how the SNR from a 10 hour synthesis varies with redshift for these three cases.

PoS(AASKA14)081

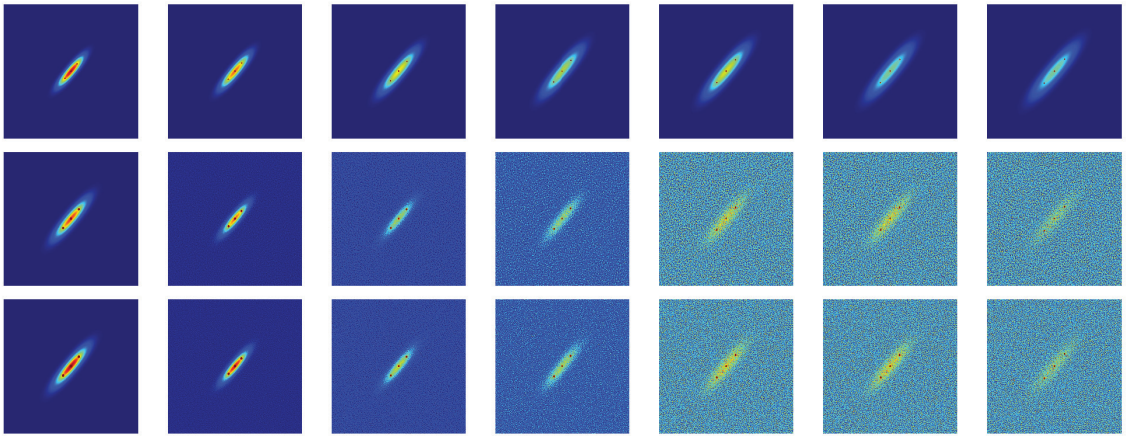

Figure 9: Model FRII galaxies (row 1) as a function of redshift {1, 2, 3, 4, 5, 6, 7, 7.5, 8, 8.5} as seen by the REF2 (row 2) and W9 (row 3) layouts after a 10 hour synthesis.

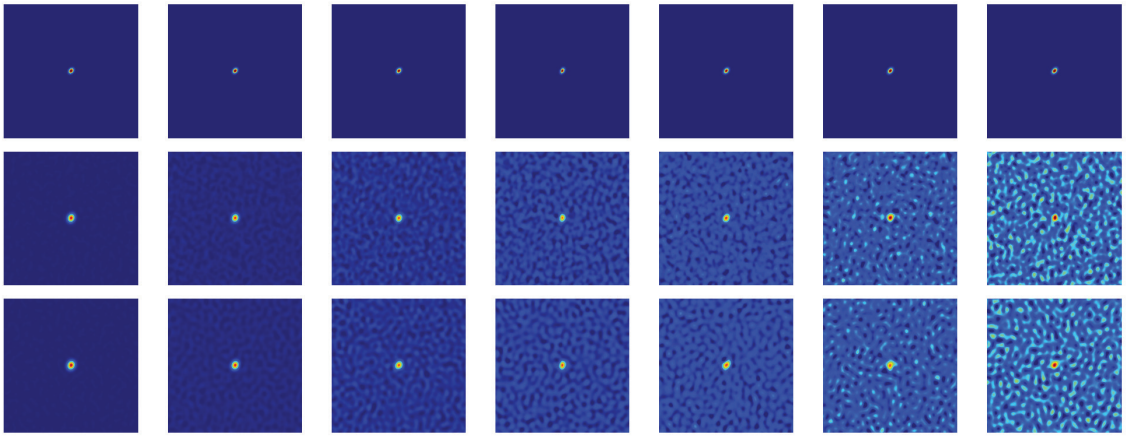

Figure 10: Model SF galaxies (row 1) as a function of redshift {1, 2, 3, 3.5, 4, 4.5, 5} as seen by the REF2 (row 2) and W9 (row 3) layouts after a 10 hour synthesis.

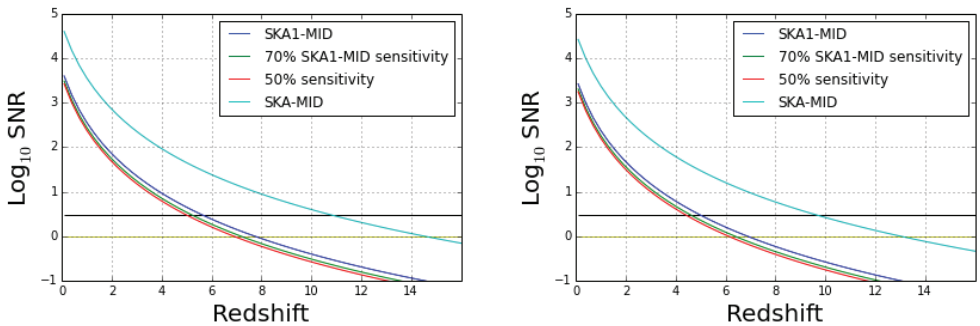

(a) FRI and FRII sources (b) SFGs

Figure 11: The SNR (relative to the surface brightness) from a 10 hour synthesis as a function of redshift for FRI and FRII sources (left) and the SFGs (right). The plots are for 4 cases: (i) SKA1-MID sensitivity (blue), (ii) 70% SKA1-MID sensitivity (green), (iii) 50% SKA1-MID (red) and (iv) full SKA-MID sensitivity (sky blue; assuming SKA-MID has 10 times the sensitivity of SKA1-MID). Lines of constant SNR=1 (yellow) and SNR=3 (black) are also plotted.

PoS(AASKA14)081

5. Conclusions

Our simulation results suggest that accurate morphological classification of these high redshift radio sources will be feasible even at the most extreme redshifts (up to $z \sim 8$ after 10 hours integration) in deep SKA1-MID images. These results also show that (at least for the case we have considered) an SKA1-MID layout with a maximum baseline length of 120 km does as well as the second generation baseline layout which has a maximum baseline length of around 170 km. In fact, the W9 layout is slightly more sensitive to our simulated galaxies as can seen in Figures 8 and 9. This would mean that for science cases where it is important to morphologically classify radio sources, e.g. for galaxy evolution (see Camera et al. 2015, this volume) the proposed 120 km layout has an advantage, and longer baselines are not necessary.

Morphological classification will be limited by resolution and not sensitivity. SKA1-MID will be able to resolve radio sources down to scales of ~ 5 kpc at cosmological distances. Morphological classification at smaller scales will require higher resolution. This is only available by going to higher frequencies (though impractical in a survey scenario due to the reduced field of view), or with substantially longer baselines, such as those provided by the full SKA dish array with stations in SKA partner countries.

It is also worth noting that model fitting techniques (Martí-Vidal et al. 2014; White et al. 1997; Reid 2006) have the capability to "super-resolve" multiple components within the PSF main lobe. Given the high sensitivity of SKA1-MID, the prospects of morphologically separating star formation and AGN activity are very good since the ability to infer the morphology of sub-resolution sources scales as $\sqrt{SNR}$ (Martí-Vidal et al. 2014). In particular, with SKA1-MID achieving an SNR of 10 to 100 in the range z=1 $\sim$ 4, this translates into the ability to resolve features of roughly one third to a 10th of the PSF size via model fitting, thus making morphological classification of kpc-scale sources possible.

A more general algorithm (compared to the one presented here) will be required to do this classification in deep field images with multiple sources. Such algorithms can be further improved by considering spectral and polarization information.

Acknowledgments

S. Makhathini acknowledges financial support from the National Research Foundation of South Africa. O. Smirnov's research is supported by the South African Research Chairs Initiative of the Department of Science and Technology and National Research Foundation.

References

Best, P. N. & Heckman, T. M. 2012, Monthly Notices of the Royal Astronomical Society, 421, 1569

Braun, R. 2013, SKA1 Level 0 Science Requirements., Document Number SKA-TEL.SCI-SKO-SRQ-001 Revision 1

Camera, S. *et al*. 2015, Eds. R. Braun et al., Proc. of the Conference held in Giardini Naxos, 8-13 June 2014, in press

PoS(AASKA14)081

Carrillo, R. E. *et al*. 2014, Mon. Not. Roy. Astron. Soc., 439, 3591
Cordes, J. *et al*. 2004, New Astronomy Reviews, 48, 1413 , science with the Square Kilometre Array Science with the Square Kilometre Array
Fanaroff, B. L. & Riley, J. M. 1974, Monthly Notices of the Royal Astronomical Society, 167, 31P
Ferramacho, L. D. *et al*. 2014, Monthly Notices of the Royal Astronomical Society, 442, 2511
Grobler, T. L. *et al*. 2014, Monthly Notices of the Royal Astronomical Society, 439, 4030
Högbom, J. A. 1974, A&A, 15, 417
Junklewitz, H. *et al*. 2013, preprint(arxiv:1311.5282)
Kazemi, S. & Yatawatta, S. 2013, Monthly Notices of the Royal Astronomical Society, 435, 597
Kazemi, S. *et al*. 2011, Monthly Notices of the Royal Astronomical Society, 414, 1656
Kramer, M. *et al*. 2004, New Astronomy Reviews, 48, 993 , science with the Square Kilometre Array Science with the Square Kilometre Array
Martí-Vidal, I. *et al*. 2014, Astronomy & Astrophysics, 563, A136
McAlpine, K. *et al*. 2015, "The SKA view of the Interplay between SF and AGN Activity and its role in Galaxy Evolution", in"Advancing Astrophysics with the SKA", PoS(AASKA14)083
Muxlow, T. W. B. *et al*. 2005, Monthly Notices of the Royal Astronomical Society, 358, 1159
Noordam, J. E. & Smirnov, O. M. 2010, A&A, 524, A61
Norris, R. P. *et al*. 2013, Publications of the Astronomical Society of Australia, 30, 20
Peebles, P. J. E. 1980, The large-scale structure of the universe (Princeton University Press), 435
Planck Collaboration *et al*. 2014, A&A, 571, A24
Rawlings, S. *et al*. 2004, New Astronomy Reviews, 48, 1013 , science with the Square Kilometre Array Science with the Square Kilometre Array
Reid, R. I. 2006, Monthly Notices of the Royal Astronomical Society, 367, 1766
Serra, P. *et al*. 2012, Publications of the Astronomical Society of Australia, 29, 296
Smirnov, O. M. 2011, A&A, 527, A107
Spergel, D. N. *et al*. 2003, The Astrophysical Journal Supplement Series, 148, 175
Tasse, C. 2014, A&A, 566, A127
Wang, Y. *et al*. 2013, Monthly Notices of the Royal Astronomical Society, 432, 1961
White, R. L. *et al*. 1997, The Astrophysical Journal, 475, 479
Wijnholds, S. & van der Veen, A.-J. 2008, Selected Topics in Signal Processing, IEEE Journal of, 2, 613

PoS(AASKA14)081

PROCEEDINGS OF SCIENCE

Radio Observations of Star Forming Galaxies in the SKA era

Claudia Mancuso[*1], **Andrea Lapi**[1,2], **Zhen-Yi Cai**[3], **Mattia Negrello**[4], **Gianfranco De Zotti**[1,4], **Francesca Perrotta**[1], **Luigi Danese**[1]

[1]*Astrophysics Sector, SISSA, Via Bonomea 265, I-34136 Trieste ;* [2]*Dipartimento di Fisica, Università 'Tor Vergata', Via della Ricerca Scientifica 1, I-00133 Roma, Italy ;* [3]*Center for Astrophysics, University of Science and Technology of China, Hefei, 230026, China;* [4]*INAF - Osservatorio Astronomico di Padova, Vicolo dell'Osservatorio 5, I-35122 Padova, Italy*
E-mail: cmancuso@sissa.it

We have combined determinations of the epoch-dependent star formation rate (SFR) function with relationships between SFR and radio (synchrotron and free-free) emission to work out detailed predictions for the counts and the redshift distributions of star-forming galaxies detected by planned Square Kilometer Array (SKA) surveys. The evolving SFR function comes from recent models fitting the far-infrared (FIR) to millimeter-wave luminosity functions and the ultraviolet (UV) luminosity functions up to $z = 10$, extended to take into account additional UV survey data. We used very deep 1.4 GHz number counts from the literature to check the relationship between SFR and synchrotron emission, and the 95 GHz South Pole Telescope (SPT) counts of dusty galaxies to test the relationship between SFR and free-free emission. We show that the SKA will allow us to investigate the SFRs of galaxies down to few $M_\odot$/yr up to z=10, thus extending by more than two orders of magnitude the high-z SFR functions derived from *Herschel* surveys. SKA1-MID surveys, down to μJy levels, will detect hundreds of strongly lensed galaxies per square degree; a substantial fraction of them will show at least two images above the detection limits.

Advancing Astrophysics with the Square Kilometre Array
June 8-13, 2014
Giardini Naxos, Italy

[*]Speaker.

PoS(AASKA14)082

1. Introduction

The huge amount of infrared (IR) to millimeter-wave data that has been accumulating in the last several years thanks to *Spitzer*, *Herschel*, SCUBA and South Pole Telescope (SPT) surveys has made possible spectacular advances in our understanding of galaxy evolution. In fact the interstellar dust absorbs and re-emits at IR wavelengths about half of the starlight of the Universe (Casey et al., 2014). Hence, the evolution of the IR luminosity function directly maps that of the dust-enshrouded star formation rate (SFR). *Herschel* data are particularly powerful in this respect as they probe the dust emission peak, thus providing the best estimates of the total IR luminosity.

However, the IR emission misses the starlight not absorbed by dust and therefore underestimates the SFR whenever the absorption optical depth is not very high. This is the case for the earliest phases of galaxy evolution when the metal enrichment of the interstellar medium is just beginning, as well as for dust-poor dwarf galaxies and metal-poor regions of more-massive galaxies (Kennicutt & Evans, 2012). A complete inventory of the SFR requires a combination of IR and UV photometry and thus suffers from limitations in both wavebands.

An important alternative tool for measuring the cosmic star formation history of the Universe is provided by deep radio continuum surveys. A tight relationship between low-frequency radio (synchrotron) and IR luminosity (hence SFR) has long been established (Helou, Soifer, & Rowan-Robinson, 1985; Condon, 1992; Yun, Reddy, & Condon, 2001; Ivison et al., 2010; Jarvis et al., 2010; Bourne et al., 2011; Mao et al., 2011). However the physical basis of this relationship is not yet totally clear. In fact many physical processes (propagation of relativistic electrons, strength and structure of the magnetic field, size and composition of dust grains) must conspire together to produce this relation (Bell, 2003; Helou et al., 1993; Niklas et al., 1997; Murphy, 2009; Lacki et al., 2010; Hippelein et al., 2003). Hence it is not granted that the relation also applies to redshift/luminosity ranges where the available data are insufficient to test it accurately. Moreover we cannot be sure that the observed synchrotron emission is not contaminated by faint nuclear activity.

There is a second process contributing to the radio emission of star-forming galaxies: the free-free emission from hot electrons, which is directly proportional to the production rate of ionising photon by young, massive stars. It shows up at rest frame frequencies of tens of GHz, where it is generally optically thin, and thus offers a clean way to quantify the current star formation activity in galaxies. This picture could be complicated by the presence of anomalous dust emission (Planck Collaboration XX, 2011, and references therein) which occurs at similar frequencies and is thought to arise from spinning dust grains (e.g., Draine & Lazarian, 1998). However there is currently no evidence that this component contributes significantly to globally integrated measurements (Murphy et al., 2012). Thus high frequency radio observations may be particularly powerful for precisely measuring the star formation history of the Universe.

Very deep radio surveys have shown that, at GHz frequencies, the counts below 100–200 μJy are dominated by star-forming galaxies (Padovani et al., 2011, and references therein). Current surveys only extend to a few tens of μJy, i.e. cover a flux density range where, at low radio frequencies, the detected radio emission is of synchrotron origin. Only with the advent of the Square Kilometer Array (SKA) we expect that the high-z star-forming galaxies can be seen via their free-free emission (see also Murphy, E. J., "The Astrophysics of Star Formation Across Cosmic Time at z $\geq$ 10 GHz with the Square Kilometre Array", PoS (AASKA14)085).

PoS(AASKA14)082

In this paper we carry out a thorough investigation of the radio counts of star forming galaxies. In Sect. 2 we present a short outline of the model, that builds on the work by Cai et al. (2013) and Cai et al. (2014). In Sect. 3 we discuss the calibration of the relation between radio emissions and SFR. The South Pole Telescope (SPT) surveys at mm wavelengths are especially useful to test the SFR/free-free relation; this motivated a re-analysis of the SPT 95 GHz sample of dusty galaxies. These relations allow us to extend to radio frequencies the Cai et al. (2013) model for the cosmological evolution of star forming galaxies and exploit it, in Sect. 4, to work out predictions for the counts of such galaxies in the range 1.4 – 30 GHz. We also compare the coverage of the SFR–z plane by *Herschel*, UV surveys and SKA. Finally, Sect. 5 summarizes our main conclusions. Predictions of number counts of galaxies based on a different approach are presented by Jarvis, M., "Radio Continuum Simulations for the SKA", PoS (AASKA14)080.

Throughout this paper we adopt a flat ΛCDM cosmology with matter density $\Omega_{\rm m} = 0.32$, $\Omega_{\rm b} = 0.049$, $\Omega_\Lambda = 0.68$, Hubble constant $h = H_0/100\,{\rm km\,s^{-1}\,Mpc^{-1}} = 0.67$, spectrum of primordial perturbations with index $n = 0.96$ and normalization $\sigma_8 = 0.83$ (Planck Collaboration XVI, 2013).

2. Outline of the model

A direct tracer of recent star formation is the UV emission of galaxies, coming from the photospheric emission of massive young stars. In recent years a great effort has been made to measure the UV luminosity functions up to high redshifts (Bouwens et al., 2008, 2011; Smit et al., 2012; Oesch et al., 2012, 2013a,b; Schenker et al., 2013; McLure et al., 2013), with the aim of reconstructing the history of cosmic re-ionization.

However, as the chemical enrichment of the ISM proceeds and, correspondingly, the dust abundance increases, a larger and larger fraction of starlight is absorbed and re-emitted at far-IR wavelengths. The most active star-formation phases of high-z galaxies indeed suffer by strong dust obscuration and are most effectively studied in the far-IR/sub-mm region.

A comprehensive investigation of the evolution of the IR luminosity functions has been recently carried out by Cai et al. (2013) based on a "hybrid" approach that reflects the observed dichotomy in the ages of stellar populations of early-type galaxies on one side and late-type galaxies on the other (cf. Bernardi et al., 2010, their Fig. 10). Early-type galaxies and massive bulges of Sa galaxies are composed of relatively old stellar populations with mass-weighted ages $\gtrsim$ 8–9 Gyr (corresponding to formation redshifts $z \gtrsim 1$–1.5), while the disk components of spirals and the irregular galaxies are characterized by significantly younger stellar populations. Thus the progenitors of early-type galaxies, referred to as proto-spheroidal galaxies or protospheroids, are the dominant star-forming population at $z \gtrsim 1.5$, while IR galaxies at $z \lesssim 1.5$ are mostly late-type "cold" (normal) and "warm" (starburst) galaxies.

The Cai et al. (2013) model accurately fits a broad variety of data[1]: multi-frequency and multi-epoch luminosity functions of galaxies and AGNs, redshift distributions, number counts (total and per redshift bins). Moreover, it accurately accounts for the recently determined counts and redshift distribution of strongly lensed galaxies detected by the South Pole Telescope (SPT; Mocanu et al., 2013; Weiß et al., 2013), published after the paper was completed (Bonato et al., 2014).

[1] See figures in http://people.sissa.it/∼zcai/galaxy_agn/.

PoS(AASKA14)082

In general the total (8–1000 μm) IR luminosity, $L_{\rm IR}$, is a good proxy of the obscured SFR when the dust heating is dominated by young stars. In disks of normal galaxies, however, the IR luminosity is the sum of a "warm" component heated by young stars and of a "cold" (or "cirrus") component, heated by the general radiation field that may be dominated by older stars. This issue was investigated by Clemens et al. (2013) using a complete sample of local star-forming galaxies detected by *Planck*. We adopt the relation between SFR and $L_{\rm IR}$ derived by these authors, for a Chabrier initial mass function (IMF).

As mentioned in Sect. 1, to get a complete census of the cosmic SFR we need to complement IR measurements with UV SFR tracers to measure the unattenuated starlight. For the high-z proto-spheroidal galaxies we adopted the accurately tested physical model for the evolution of the UV luminosity function worked out by Cai et al. (2014) in the framework of the scenario proposed by Granato et al. (2004) and further elaborated by Lapi et al. (2006, 2011), Mao et al. (2007), and Cai et al. (2013).

For the low-z galaxies we have supplemented the Cai et al. (2013) model for evolution of late-type galaxies in the IR with a parametric model for evolution in the UV. Briefly, the UV ($\lambda = 1500$ Å) luminosity function is described by:

$$\Phi(\log L_{1500}, z)\mathrm{d}\log L_{1500} = \Phi^* \left(\frac{L_{1500}}{L^*}\right)^{1-\alpha} \times \exp\left[-\frac{\log^2(1+L_{1500}/L^*)}{2\sigma^2}\right]\mathrm{d}\log L_{1500}. \quad (2.1)$$

A simple pure luminosity evolution model ($L^*(z) = L_0^*(1+z)^{\alpha_L}$ up to $z = 1$) turned out to provide a sufficiently good description of the data (Mancuso et al., in preparation). The best-fit values of the parameters are $\log(\Phi_0^*/[\mathrm{dex}^{-1}\,\mathrm{Mpc}^{-3}]) = -2.150 \pm 0.095$, $\log(L_0^*/L_\odot) = 9.436 \pm 0.119$, $\alpha = 1.477 \pm 0.050$, $\sigma = 0.326 \pm 0.035$, and $\alpha_L = 2.025 \pm 0.063$.

The Kennicutt & Evans (2012) calibrations were adopted to convert the UV luminosity functions into SFR functions. The total redshift-dependent SFR functions were then computed summing the IR-based and the UV-based ones.

3. Calibration of the relation between radio emission and SFR

A tight linear correlation between the 1.4 GHz luminosity, dominated by synchrotron, and the IR luminosity has been established since many years (Condon, 1992). A calibration of the relation between the SFR and the synchrotron emission was calculated by Murphy et al. (2011). In order to take into account electron ageing effects (Banday & Wolfendale, 1991) we have adopted a steepening by $\Delta\alpha = 0.5$ above a break frequency of 20 GHz. The relationship between synchrotron luminosity and SFR then writes:

$$L_{\rm sync} \simeq 1.9 \times 10^{28} \left(\frac{\mathrm{SFR}}{\mathrm{M}_\odot \mathrm{yr}^{-1}}\right) \left(\frac{\nu}{\mathrm{GHz}}\right)^{-0.85} \left[1 + \left(\frac{\nu}{20\mathrm{GHz}}\right)^{0.5}\right]^{-1} \mathrm{erg\,s^{-1}\,Hz^{-1}}. \quad (3.1)$$

Coupling this relation with the redshift dependent SFR functions yielded by the model outlined in Sect. 2 we get a good fit to the sub-mJy 1.4 GHz counts (Fig. 1, left panel) without any adjustment of the parameters. The high-frequency synchrotron emission is increasingly suppressed with increasing z, as the timescale for energy losses of relativistic electrons by inverse Compton scattering off the Cosmic Microwave Background photons decreases as $(1+z)^{-4}$ (Norris et al., 2013; Carilli

PoS(AASKA14)082

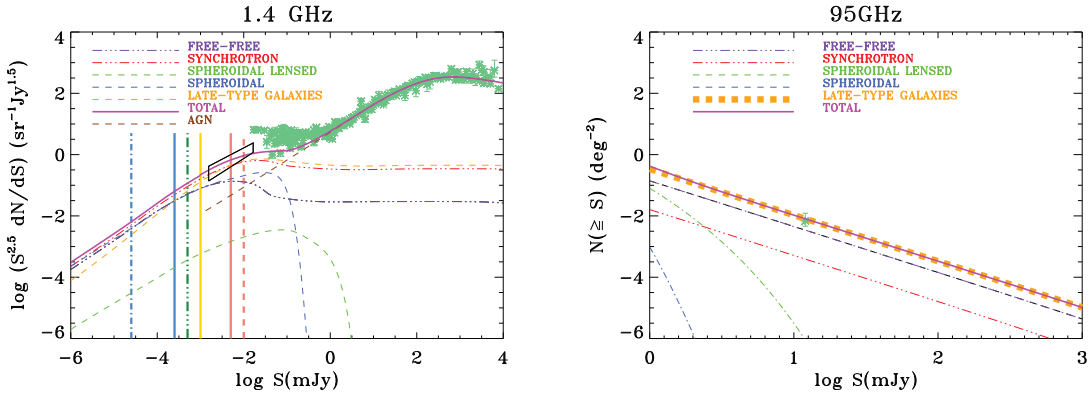

Figure 1: *left panel*: Euclidean normalized differential counts at 1.4 GHz compared with model predictions. The dashed brown line shows the best fit model for radio AGNs by Massardi et al. (2010). The other dashed lines show the contributions of the star-forming populations considered in this paper. The two triple-dot dashed lines show the total synchrotron and free-free emissions from these populations. The solid vertical lines correspond, from left to right, to three 5 σ detection limits of preliminarily planned SKA1-MID surveys. The vertical blue dash-dotted line and the pink dashed line are respectively the flux limits for Ultra-Deep SKA2 (MID) and for the 50% Wide SKA1-MID surveys, while the green dash-dot-dotted line is the limit for both 50% Deep SKA1-MID and Wide SKA2 (MID) surveys. *Right panel*: our re-assessment of the integral counts of dusty galaxies at ν=95 GHz (asterisks with error bars) compared with the expectations from the Cai et al. (2013) model.

et al., 2008; Murphy, 2009). This may lower the counts at the faintest flux densities, but not by a large factor since, as illustrated by Fig. 1 (left panel), below the limits of current surveys the free-free contribution is comparable to the synchrotron one.

A relationship between SFR and free-free emission was derived by Murphy et al. (2012). We have reformulated it as:

$$L_{\rm ff} = 3.75 \times 10^{26} \left(\frac{\rm SFR}{M_\odot/{\rm yr}}\right) \left(\frac{T}{10^4\,{\rm K}}\right)^{-0.5} {\rm g}(\nu,{\rm T}) \exp\left(-\frac{h\nu}{k{\rm T}}\right) {\rm erg\,s^{-1}\,Hz^{-1}} \qquad (3.2)$$

where T is the temperature of the emitting plasma and $g(\nu, T)$ is the Gaunt factor for which we adopt the approximation proposed by Draine (2011) which is more accurate than the one used by Murphy et al. (2012). The coefficient of eq. (3.2) was computed requiring that this equation equals that by Murphy et al. (2012) for $\nu = 33$ GHz (the frequency at which the relation was calibrated), $T = 10^4$ K and a pure hydrogen plasma.

We note that the calibrations of the above relationships are based on the Kroupa IMF while that between the IR emission and the SFR (Sect. 2) relies on the Chabrier IMF. However, as shown by Chomiuk & Povich (2011) the two IMFs give almost identical calibrations.

To test the $L_{\rm ff}$-SFR relation we used the South Pole Telescope (SPT) observations of dusty galaxies at 95 GHz (Mocanu et al., 2013), since we expect that, at this frequency, the free-free emission shows up clearly in local galaxies not hosting a radio loud AGN. To estimate the 95 GHz counts of dusty galaxies Mocanu et al. (2013) adopted a statistical approach. They choose the local minimum in the distribution of the α_{220}^{150} spectral indices, $\alpha_{220}^{150} = 1.5$, as the threshold for source classification and computed, for each source, the probability that their posterior α_{220}^{150} is greater

PoS(AASKA14)082

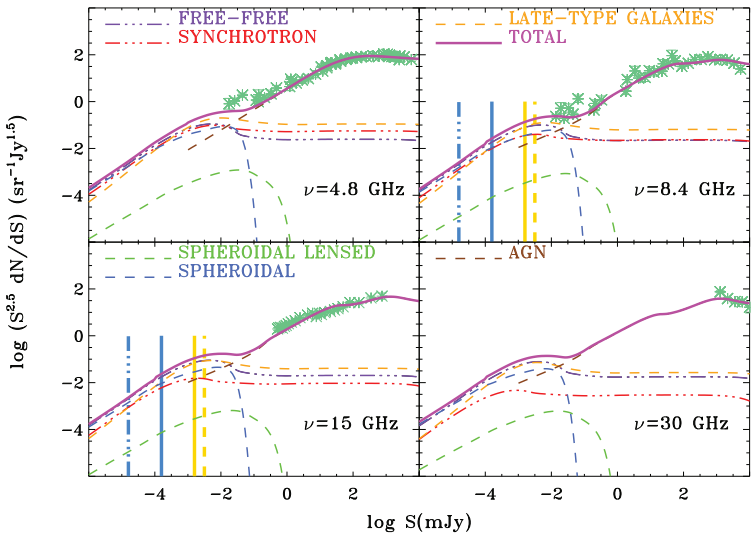

Figure 2: Predicted versus observed counts at 4.8, 8.4, 15 and 30 GHz. Dusty galaxies come up at sub-mJy flux density levels and their counts are accounted for by the model. At higher flux densities the counts are dominated by canonical, AGN powered radio sources; the models shown are from Massardi et al. (2010) at 4.8 GHz and from de Zotti et al. (2005) at 8.4, 15 and 30 GHz. The solid vertical lines show the limits for predicted deep (yellow) and ultra deep (blue) band 5 SKA1-MID surveys. The dash-dotted blue line and the dashed yellow line are the limits for an Ultra Deep SKA2 (MID) survey and a 50% SKA1-MID Deep survey respectively.

than the threshold value, $P(\alpha_{220}^{150} > 1.5)$. This quantity was interpreted as the probability that a source is dust-dominated. The 95 GHz differential counts were computed as the sum of probabilities $P(\alpha_{220}^{150} > 1.5)$. Since the fraction of dusty galaxies is much lower than that of synchrotron dominated sources, this statistical approach is endowed with large uncertainties and may strongly overestimate the counts of dusty galaxies.

We have then re-estimated the counts using a lengthier but safer approach, i.e. we have checked the SED of each 95 GHz source brighter than the 95% completeness limit of 12.6 mJy, collecting all the photometric data available in the literature. To model the SEDs we considered both synchrotron and free-free emission, as well as thermal dust emission. We found that only 4 sources, all with $P(\alpha_{220}^{150} > 1.5) \simeq 1$, are indeed dusty galaxies. This is a factor $\simeq 3$ below the number found by Mocanu et al. (2013). The corresponding integral count is shown in the right panel of Fig. 1.

Further tests and/or predictions of the model are provided by counts at 4.8, 8.4 ,15 and 30 GHz (Fig. 2). The relative importance of free-free compared to synchrotron obviously increases with increasing frequency. While at 1.4 GHz the free-free contribution is always below the synchrotron one, at 8.4 GHz it takes over at tens of μJy levels.

4. Predictions for surveys with the Square Kilometer Array

Preliminary plans for the phase 1 SKA-MID include a set of surveys at $\sim$ 1-1.4 GHz aimed at investigating the galaxy evolution: an Ultra-Deep survey over 1deg^2 with rms $\sim$ 50 nJy/beam, a Deep survey over 10-30 deg^2 with rms $\sim$ 0.2 μJy/beam, and a Wide survey over 1000-5000

PoS(AASKA14)082

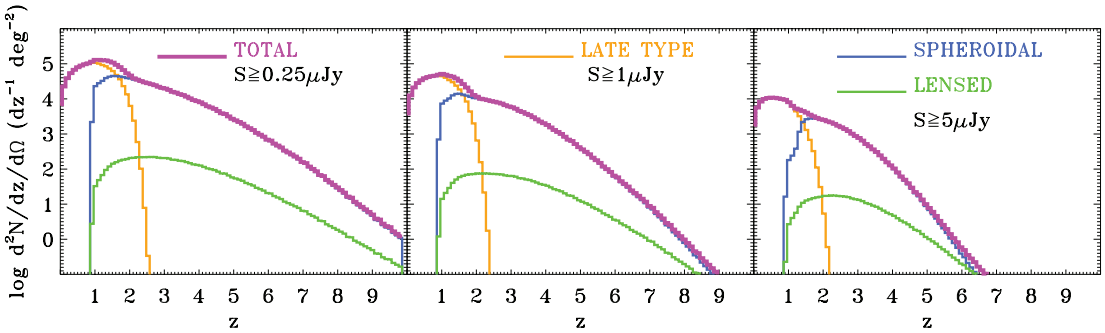

Figure 3: Predicted redshift distributions for 1.4 GHz surveys down to 0.25, 1 and 5 μJy, which are the 5 σ flux density limits of preliminarily planned SKA1-MID surveys.

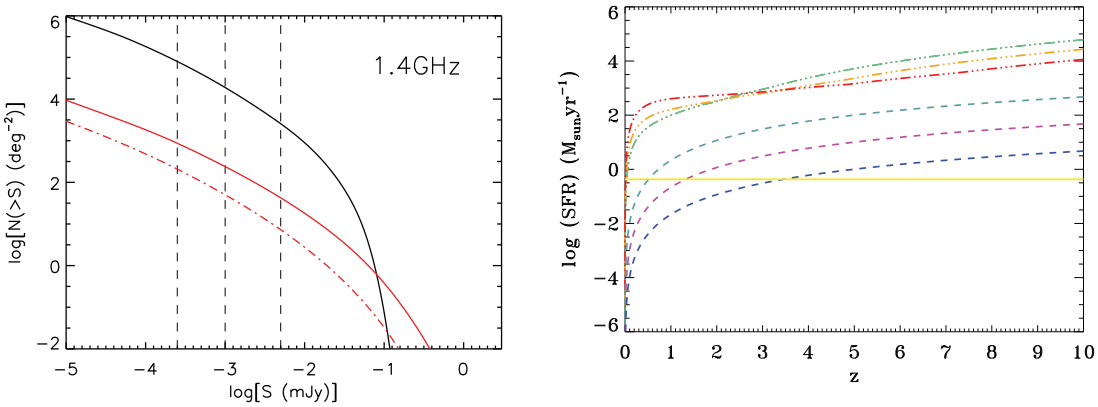

Figure 4: *left panel:* integral number counts of proto-spheroids at 1.4 GHz. Solid black line: unlensed proto-spheroids; solid red line: strongly lensed protospheroids as a function of the total flux density (sum of all images of a single source); dot-dashed red line: counts of strongly lensed proto-spheroids as a function of the flux density of the second brightest image. The vertical dashed lines mark the flux density limits of the possible surveys for SKA1-MID. *Right panel:* minimum SFR detectable by SKA1-MID (dashed magenta line), 50% SKA1-MID (dashed light blue line) and SKA2 (MID) (dashed blue line) Ultra-Deep surveys, as a function of z, compared with the minimum SFR detected by *Herschel* surveys (dashed-dot-dot-dot lines, green for 250 μm, orange for 350 μm and red for 500 μm) and by UV/Hα surveys (horizontal yellow line; see text).

deg^2 with rms $\sim$ 1 μJy/beam (see Dewdney et al. (2013), Braun (2013)). The corresponding 5 σ limits are indicated by vertical solid lines in the left panel of Fig. 1; the other vertical lines indicate the detection limits achievable with 50% of SKA1-MID Ultra-Deep and Wide surveys and (full) SKA2 (MID) Ultra-Deep and Wide surveys sensitivity. We also show the contributions to the 1.4 GHz Euclidean normalized differential number counts of the three populations of dusty galaxies considered by Cai et al. (2013). The main contributors to the "bump" at tens of μJy levels are late-type galaxies at $z \simeq$ 1–1.5. Higher z proto-spheroidal galaxies become increasingly important at lower flux densities, down to a few hundred nJy's.

The predicted redshift distributions for surveys at the SKA1-MID flux density limits are shown in Fig. 3. The fraction of galaxies at very high redshifts ($z \geq 6$) increases rapidly with decreasing flux density. At a few hundred nJy levels we expect detections of galaxies at z of up to 10, making

PoS(AASKA14)082

possible to investigate the cosmic SFR across the re-ionization epoch. Note that, although the deepest surveys with the HST are getting close to that, they inevitably miss the dust-obscured star formation, while dust obscuration does not affect SKA measurements.

The fraction of strongly lensed galaxies in flux-limited surveys increases with redshift, to the point that these sources are dominant at the highest redshifts (see Fig. 3). The predicted counts for magnifications $\mu \geq 2$ are illustrated in the left panel of Fig. 4, where the solid black line represents the unlensed proto-spheroidal galaxies, while the red lines represent the lensed galaxies as a function of the total flux density (solid) or of the flux density of the second brightest image (dot-dashed). The model predicts 655, 204 and 40 strongly lensed galaxies per deg^2 brighter than 0.25, 1 and 5 μJy, respectively; for 250, 100 and 20 of them, respectively, the SKA1-MID will directly detect at least two images. A more detailed discussion on the gravitational lens statistics with SKA is presented in McKean, J., "Strong Gravitational Lensing with the SKA", PoS (AASKA14)084.

The right panel of Fig. 4 compares the SKA potential in measuring the evolution of the cosmic SFR to the outcome of *Herschel* and of the deepest UV and Hα surveys. The minimum luminosities, hence the minimum SFRs, reached by the latter surveys vary little with redshift. The yellow horizontal line corresponds to their average. Planned SKA surveys can detect galaxies with SFRs from tens to hundred $M_\odot$/yr, up to the highest redshifts, extending the SFR functions by up to 3 orders of magnitude compared with *Herschel*, thus encompassing SFRs typical of $L_\star$ galaxies.

5. Conclusions

We have worked out detailed predictions of the counts and redshift distributions for planned SKA surveys, distinguishing the contributions of the different populations of star-forming galaxies: normal late-type, starburst and proto-spheroidal galaxies. The predictions are based on models by Cai et al. (2013) and Cai et al. (2014), that fit a broad variety of UV and far-IR/sub-mm data relevant to determine the epoch-dependent SFR function. These models, however, do not include the contribution to the SFR functions of moderate to low redshift late-type and starburst galaxies. We have upgraded them adding these populations. The upgraded models were combined with the relationships between SFR and radio (synchrotron and free-free) emission derived by Murphy et al. (2011, 2012). Such relationships has been checked exploiting the deepest 1.4 GHz counts and with data from the 95 GHz SPT survey, that we have re-analyzed finding that the published SPT counts of dusty galaxies are overestimated by a factor $\simeq 3$.

We have shown that the SKA will allow us to get information, not affected by dust extinction, on galaxy SFRs down to tens of $M_\odot$/yr up to the highest redshifts, thus extending by up to 3 orders of magnitude the high-z SFR functions derived from *Herschel* surveys.

Acknowledgements

We gratefully acknowledge many constructive comments by an anonymous referee, that helped us improving this paper. Work supported in part by ASI/INAF Agreement 2014-024-R.0 for the *Planck* LFI activity of Phase E2 and by PRIN INAF 2012, project "Looking into the dust-obscured phase of galaxy formation through cosmic zoom lenses in the Herschel Astrophysical Large Area Survey".

PoS(AASKA14)082

References

Banday, A. J., Wolfendale, A. W. 1991, MNRAS, 248, 705
Bell, E. F. 2003, ApJ, 586, 794
Bernardi, M., Shankar, F., Hyde, J. B., et al. 2010, MNRAS, 404, 2087
Bonato, M., Negrello, M., Cai, Z.-Y., et al. 2014, MNRAS, 438, 2547
Bourne, N., Dunne, L., Ivison, R. J., et al., 2011, MNRAS, 410, 1155
Bouwens, R. J., Illingworth, G. D., Franx, M., Ford, H. 2008, ApJ, 686, 230
Bouwens, R. J., Illingworth, G. D., Oesch, P. A., et al. 2011, ApJ, 737, 90
Braun, R. 2013, "SKA1 Imaging Science Performance", Document number SKA-TEL-SK0-DD-XXX Revision A Draft 2
Cai, Z.-Y., Lapi, A., Bressan, A., et al. 2014, ApJ, 785, 65
Cai, Z.-Y., Lapi, A., Xia, J.-Q., et al. 2013, ApJ, 768, 21
Carilli, C. L., Lee, N., Capack, P., et al. 2008, ApJ, 689, 883
Casey, C. M., Narayanan, D., Cooray, A. 2014, PhR, 541, 45
Chomiuk, L., Povich, M. S. 2011, AJ, 142, 197
Clemens, M. S., Negrello, M., De Zotti, G., et al. 2013, MNRAS, 433, 695
Condon, J. J. 1992, ARA&A, 30, 575
Dewdney, P., Turner, W., Millenaar, R., et al. 2013, "SKA1 System Baseline Design", Document number SKA-TEL-SK0-DD-001 Revision1
De Zotti, G., Ricci, R., Mesa, D., et al. 2005, A&A, 431, 893
Draine, B. T. 2011, Physics of the Interstellar and Intergalactic Medium by Bruce T. Draine. Princeton University Press, 2011. ISBN: 978-0-691-12214-4,
Draine, B. T. & Lazarian, A. 1998, ApJ, 494, L19
Granato, G. L., De Zotti, G., Silva, L., Bressan, A., Danese, L. 2004, ApJ, 600, 580
Helou, G., Soifer, B. T., Rowan-Robinson, M. 1985, ApJ, 298, L7
Helou, G., Bicay, M. D. 1993, ApJ, 415, 93
Hippelein, H., Haas, M., Tuffs, R. J., et al. 2003, A&A, 407, 137
Ivison, R. J., Swinbank, A. M.;,Swinyard, B., et al. 2010, A&A, 518, L31
Jarvis, M. J., Smith, D. J. B., Bonfield, D. G., et al. 2010, MNRAS, 409, 92
Kennicutt, R. C., & Evans, N. J. 2012, ARA&A, 50, 531
Lacki, B. C, Thompson, T. A., 2010, ApJ, 717, 196
Lapi, A., González-Nuevo, J., Fan, L., et al. 2011, ApJ, 742, 24
Lapi, A., Shankar, F., Mao, J., et al. 2006, ApJ, 650, 42
Mao, M. Y., Huynh, M. T., Norris, R. P., et al. 2011, ApJ, 731, 79
Mao, J., Lapi, A., Granato, G. L., De Zotti, G., Danese, L. 2007, ApJ, 667, 655
Massardi, M., Bonaldi, A., Negrello, M., et al. 2010, MNRAS, 404, 532
McLure, R. J., Dunlop, J. S., Bowler, R. A. A., et al. 2013, MNRAS, 432, 2696
Mocanu, L. M., Crawford, T. M., Vieira, J. D., et al. 2013, ApJ, 779, 61
Murphy, E. J., Bremseth, J., Mason, B. S., et al. 2012, ApJ, 761, 97
Murphy, E. J., Condon, J. J., Schinnerer, E., et al. 2011, ApJ, 737, 67
Murphy, E. J., 2009, ApJ, 706, 482
Niklas, S., Beck, R. 1997, A&A, 320, 54

PoS(AASKA14)082

Norris, R. P., Afonso, J., Bacon, D., et al. 2013, PASA, 30, 20
Oesch, P. A., Bouwens, R. J., Illingworth, G. D., et al. 2012, ApJ, 759, 135
Oesch, P. A., Bouwens, R. J., Illingworth, G. D., et al. 2013a, ApJ, 773, 75
Oesch, P. A., Bouwens, R. J., Illingworth, G. D., et al. 2013b, arXiv:1309.2280
Padovani, P., Miller, N., Kellermann, K. I., et al. 2011, ApJ, 740, 20
Planck Collaboration XX 2011, A&A, 536, A20
Planck Collaboration XVI 2013, arXiv:1303.5076
Schenker, M. A., Robertson, B. E., Ellis, R. S., et al. 2013, ApJ, 768, 196
Smit, R., Bouwens, R. J., Franx, M., et al. 2012, ApJ, 756, 14
Weiß, A., De Breuck, C., Marrone, D. P., et al. 2013, ApJ, 767, 88
Yun, M. S., Reddy, N. A., Condon, J. J. 2001, ApJ, 554, 803

PoS(AASKA14)082

PROCEEDINGS OF SCIENCE

The SKA view of the Interplay between SF and AGN Activity, and its role in Galaxy Evolution

Kim McAlpine[*1], **Isabella Prandoni**[2], **Matt Jarvis**[3,1], **Nick Seymour**[4], **Paolo Padovani**[5], **Philip Best**[6], **Chris Simpson**[7], **Daria Guidetti**[2], **Eric Murphy**[8], **Minh Huynh**[9], **Mattia Vaccari**[1], **Sarah White**[3], **Rob Beswick**[10], **Jose Afonso**[11,12], **Manuela Magliocchetti**[13] **and Marco Bondi**[2]

[1]*University of the Western Cape,Robert Sobukwe Road, Bellville, 7535, South Africa;* [2]*INAF - Istituto di Radioastronomia, via Gobetti 101, 40129 Bologna, Italy;* [3]*Oxford University, Astrophysics, Department of Physics, Keble Road, Oxford OX1 3RH;* [4]*CSIRO Astronomy and Space Science, P.O. Box 76, Epping, NSW 1710, Australia;* [5]*ESO,Karl-Schwarzschild-Str. 2, D-85748 Garching bei München, Germany;* [6]*Institute for Astronomy, University of Edinburgh, Royal Observatory Edinburgh, Blackford Hill, Edinburgh EH9 3HJ;* [7]*Astrophysics Research Institute, Liverpool John Moores University, Twelve Quays House, Egerton Wharf, Birkenhead CH41 1LD;* [8]*California Institute of Technology, IPAC, MC 220-6, Pasadena, CA 91125, USA;* [9]*ICRAR - University of Western Australia, M468, 35 Stirling Hwy, Crawley WA 6009, Australia;* [10]*University of Manchester,Macclesfield, Cheshire, SK11 9DL;* [11] *Instituto de Astrofísica e Ciências do Espaço, Universidade de Lisboa, OAL, Tapada da Ajuda, PT1349-018 Lisboa, Portugal;* [12] *Departamento de Física, Faculdade de Ciências, Universidade de Lisboa, Edifício C8, Campo Grande, PT1749-016 Lisbon, Portugal;* [13] *INAF-IAPS,Via Fosso del Cavaliere 100, I-00133 Roma, Italy;*

E-mail: kim.mcalpine at gmail.com

It has become apparent that active galactic nuclei (AGN) may have a significant impact on the growth and evolution of their host galaxies and vice versa but a detailed understanding of the interplay between these processes remains elusive. Deep radio surveys provide a powerful, obscuration-independent tool for measuring both star formation and AGN activity in high-redshift galaxies. Multiwavelength studies of deep radio fields show a composite population of star-forming galaxies and AGN, with the former dominating at the lowest flux densities ($S_{1.4GHz} < 100\ \mu$Jy). The sensitivity and resolution of the SKA will allow us to identify, and separately trace, the total star formation in the bulges of individual high-redshift galaxies, the related nuclear activity and any star formation occurring on larger scales within a disc. We will therefore gain a detailed picture of the apparently simultaneous development of stellar populations and black holes in the redshift range where both star-formation and AGN activity peak ($1 \leq z \leq 4$). In this chapter we discuss the role of the SKA in studying the connection between AGN activity and galaxy evolution, and the most critical technical requirements for such of studies.

Advancing Astrophysics with the Square Kilometre Array
June 8-13, 2014
Giardini Naxos, Sicily, Italy

[*]Speaker.

PoS(AASKA14)083

1. Introduction

A wide range of theoretical and observational considerations point to a close connection between star-formation and AGN activity and yet a clear understanding of this complex relationship and its true role in shaping galaxy evolution remains elusive. From a theoretical perspective galaxy formation models require a mechanism to prevent the formation of cooling flows and thereby inhibit star-formation in massive early-type galaxies, otherwise gas is channelled to the centre of the galaxy triggering star formation. Consequently the models predict overly massive and actively star-forming galaxies at low redshifts, in contrast to observations (e.g. White & Frenk 1991). A related, similar problem is encountered on a larger scale in observations of the intracluster medium (ICM) of galaxy clusters where the X-ray emitting gas at the centre of clusters is observed to be much hotter than expected given the radiative cooling times of the system (see Voit & Donahue 2005, for a review). A variety of semi-analytic (Granato et al. 2004; Bower et al. 2006; Croton et al. 2006; Somerville et al. 2008) and hydrodynamic simulations (Gabor & Bournaud 2014; Dubois et al. 2013; Puchwein & Springel 2013) have thus included 'feedback' from the central AGN as a means to disrupt the predicted cooling flows and are subsequently able to better reproduce the bright end of the galaxy mass function as well as the emergence of the red sequence. Observationally the existence of correlations between the mass of the central black hole and properties of the host galaxy such as the stellar mass of the central bulge (M_{BH}-M_{bulge}; Magorrian et al. 1998; Häring & Rix 2004; Scott et al. 2013) and its velocity dispersion (M_{BH}-σ; Gebhardt et al. 2000; Tremaine et al. 2002) seem to confirm the possibility of a link between AGN and star-formation activity.

1.1 'Quasar' Feedback

There are two proposed modes of AGN 'feedback', the first, often referred to as 'quasar' mode feedback, is associated with classical luminous quasars as well as less powerful optical and X-ray bright AGN. In this mode the AGN is powered by radiatively efficient accretion of cold gas via an accretion disk and emits powerfully across a wide range of the electromagnetic spectrum (UV through to X-ray). A dusty torus structure surrounding the black hole and accretion disk obscures the emission at some wavelengths at large polar angles (Antonucci 1993, and references therein). The majority of optically selected AGN are faint at radio wavelengths and are referred to as radio quiet (RQ) AGN, but a small fraction are radio-loud and emit large scale, relativistic radio jets. The radio-loud fraction depends on mass (Best et al. 2005, 2007), accretion type (Janssen et al. 2012) and redshift (Donoso, Best, & Kauffmann 2009). In the local universe ($0.03 < z < 0.3$) 'quasar' mode accretors increase their radio-loud fraction as a shallow function of host galaxy mass ($f_{RL}^{QSO} \propto M_*^{1.5}$), from approximately $\sim$0.002% at $10^{10.7} M_*$ to 0.1% at $10^{11.7} M_*$ (Janssen et al. 2012).

Feedback occurs as a result of high-velocity winds accelerated by the AGN, either as a result of thermal heating of gas or radiation pressure on dust, which remove gas from the galaxy. Star formation will cease abruptly once the available fuel supply is removed. It is typically assumed that the amount of energy supplied to this wind 'feedback' is proportional to the mass and luminosity of the central black hole, thus feedback will only become effective above a certain mass threshold, where the momentum of the outflow is large enough to overcome the gravitational potential of the black hole and halt accretion. Observationally there is little direct evidence that typical AGN, (e.g. Seyferts) in the local universe produce the required large-scale outflows. However, more

PoS(AASKA14)083

promisingly, high-velocity winds have been detected in a small number of very powerful AGN, $>10^{45}$ erg s^{-1}, in both ionised (Maiolino et al. 2012; Pounds & King 2013; Liu et al. 2013) and molecular gas (Sturm et al. 2011; Cano-Díaz et al. 2012; Cicone et al. 2014). These have typical speeds of 400–1000 km s^{-1} which, with some assumptions, translates to outflow rates of 700-1000's M$_\odot$ yr^{-1}, which may be capable of producing the required feedback effect. The inferred outflow rates in these more powerful AGN systems are very impressive but some recent simulations suggest that they may still have little overall effect on the gas in the galactic disk. This is due to the highly variable nature of AGN activity, such that the time-averaged outflow rates may be significantly lower than instantaneously observed outflow rates (Gabor & Bournaud 2014). More observations are thus required to understand the prevalence and/or longevity of these outflows, as they have only been detected in a small number of objects thus far, as well as to establish how their influence varies as a function of accretion rate, black hole mass, stellar mass and cosmic epoch.

1.2 'Radio' Feedback

A second model of feedback suggests that energy injected from AGN in the form of jets is responsible for switching off cooling at the centre of massive halos. A fairly large fraction, $\sim$ 10%, of massive galaxies (particularly galaxies near the centers of groups and clusters) are seen to emit radio synchrotron emission from lobes powered by jets (Best et al. 2005, 2007) . Most of these radio sources have characteristics which suggest they are experiencing a mode of accretion which is distinct from that powering traditional optical quasars. Specifically they do not have emission lines characteristic of classical optical or X-ray bright quasars (Best et al. 2005; Kauffmann et al. 2008), there is no evidence of accretion related X-ray or optical emission, nor any mid-infrared emission associated with a dusty, obscuring torus (Hardcastle et al. 2007). They are radiatively inefficient with accretion rates that are believed to be much lower than in typical quasar mode accretion, i.e. they typically accrete at $<$1% of Eddington compared to 1–10% of Eddington for efficient accretors. These AGN are often labelled 'radio' mode or 'jet' mode accretors. The fraction of 'radio' mode accretors increases very sharply with host galaxy mass ($f_{RL}^{Radio} \propto M_*^{2.5}$) and appears to saturate at $\sim$10% at $M_*^{11.5}$ (Best et al. 2005; Janssen et al. 2012). The total energy output from these AGN is lower than in the radiatively efficient case. However, depending on how efficiently the kinetic energy in the jets is converted to heat in the interstellar gas, these AGN may still have considerable potential to influence the star-formation properties of the galaxies they inhabit. Observationally the strongest direct evidence in support of 'radio' mode AGN feedback is the presence of bubbles and cavities in the diffuse X-ray halos of clusters, groups and individual elliptical galaxies (e.g. Pedlar et al. 1990; McNamara et al. 2000; Fabian et al. 2003; Bîrzan et al. 2004; Rafferty et al. 2006; Croston et al. 2008; Cavagnolo et al. 2010) which appear to be aligned with the axis of an AGN radio jet. Further evidence of the interaction between radio galaxies and their immediate environments is provided by radio polarization studies of such jet-cavity systems. These studies demonstrate that this interaction affects not only the density distribution of the ICM/IGM but also the magnetisation of the surrounding plasma, draping the magnetic field lines around the leading edge of the radio lobes. There is thus a clear response in the external medium linked to the direction of the radio source expansion (Guidetti et al. 2011, 2012).

Estimates of the amount of energy required to inflate these bubbles can be used to infer the mechanical heating power of radio jets. Best et al. (2006) demonstrated that the inferred time-

PoS(AASKA14)083

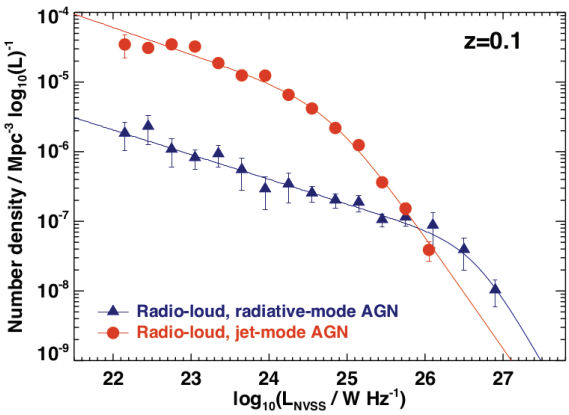

Figure 1: The local radio luminosity function (0.01<z<0.3) at 1.4 GHz derived separately for radio-loud 'quasar' (radiative) and 'radio' (jet) mode accretors. Figure from Heckman & Best (2014).

averaged energetic output of 'radio' mode accretors, from such cluster observations, should indeed be sufficient to counter cooling losses in massive, red galaxies. Simpson et al. (2013) find evidence to suggest that this balance is still in effect at z> 1, implying that 'radio' mode feedback is already suppressing star-formation at moderate redshifts.

1.3 'Quasar' versus 'Radio' mode

The reason for the fundamental differences between the two classes of AGN activity is still uncertain. It has been argued that it may arise from differences in the fuelling gas, where the radiatively inefficient 'radio' mode accretors are fuelled by hot gas found in the halos surrounding the galaxy or cluster either directly via Bondi accretion (Allen et al. 2006; Hardcastle et al. 2007), or via indirect chaotic accretion of molecular gas clumps which cool out of the hot gas phase (Pizzolato & Soker 2010; McNamara et al. 2011; Gaspari et al. 2013). In contrast 'quasar' mode accretors are fuelled predominantly by cold gas, supplied either by mergers or by non-axisymmetric structures within the galaxy which drive disk gas to the galaxy centre (Kormendy & Kennicutt 2004; Kim et al. 2012). Alternatively, the two modes may largely arise due to the differences in their Eddington-scaled accretion rate onto the black hole.

There are still many unanswered questions regarding the role of both 'radio' and 'quasar' mode accretors in galaxy evolution and their relative importance as a function of both epoch and environment. Current simulations suggest that 'quasar' mode accretion may be the dominant feedback mechanism at high redshifts (z >1) where the supply of cold gas for fuel is greater. 'Radio' mode feedback appears to be relatively more important at late times, where it is essential to suppress star-formation in massive elliptical galaxies in order to reproduce their observed colours in the local universe (e.g. Somerville et al. 2008).

2. The AGN, star-formation, merger connection

Many theoretical models suggest that radiatively efficient 'quasar' mode AGN are triggered by mergers which can drive rapid inflows of gas which fuel both intense star-formation and rapid black hole accretion (e.g. Barnes 1992; Barnes & Hernquist 1996; Springel et al. 2005; Di Matteo et al. 2005). However the majority of moderate luminosity AGN, with X-ray luminosities

PoS(AASKA14)083

$L_X < 10^{44}$ erg s^{-1}, show no evidence of merger activity and are associated with disk host morphologies (Cisternas et al. 2011; Schawinski et al. 2012; Kocevski et al. 2012). Several studies have concluded that AGN activity appears to increase in merging systems only as a result of underlying correlations between mergers and star formation activity and between star-formation and AGN activity. In other words AGN activity remains fixed at a given specific star-formation rate while star-formation activity generally increases as a result of mergers (Reichard et al. 2009; Li et al. 2008a,b). These results suggest that secular processes may be much more important in driving black hole growth than previously assumed, even at high redshifts (z$\sim$2) and that the only requirement for AGN triggering is an abundant supply of central cold gas, regardless of its origin. Recent simulations have successfully produced stochastic, secularly evolving AGN where accretion is triggered by random collisions of interstellar gas clouds with the central black hole, the accretion rate and lifespan of the AGN in this scenario is strongly influenced by the gas fraction of the galaxy (Gabor & Bournaud 2013).

Major mergers do appear to be important for triggering the highest luminosity AGN with the highest accretion rates. The majority of AGN with X-ray luminosities $L_X > 10^{44}$ erg s^{-1} are hosted in galaxies with evidence of disturbed morphologies (Urrutia et al. 2008; Treister et al. 2012). Furthermore post-starbust systems, whose starbursts are possibly induced by mergers, appear to host the highest luminosity AGN (Wild et al. 2007). As the incidence of mergers and detections of potential AGN 'quasar' feedback winds are both higher in more powerful AGN it has been speculated that merger triggered AGN may be associated with stronger AGN feedback effects than AGN accreting via secular processes (e.g. Heckman & Best 2014). The high sensitivity of the SKA to both obscured AGN and star-formation activity will allow us to investigate where, in terms of accretion and star-formation rate, this change in the dominant mode of black hole growth occurs and whether it is associated with a change in the interaction between star-formation and AGN activity.

3. Jet induced star-formation

The majority of theoretical models require that AGN activity results in an overall suppression of star-formation activity however there is observational evidence suggesting that AGN jets may in fact induce or enhance star-formation in some objects (i.e. positive 'feedback'). This jet induced star-formation has been observed directly in only a few objects, locally in Minkowski's object (Croft et al. 2006) and Centaurus A (Mould et al. 2000), at intermediate redshifts in PKS2250-41 (Inskip et al. 2008) and high redshifts in 4C 41.17 (Dey et al. 1997; Bicknell et al. 2000; Steinbring 2014) and can take place in both FRI and FRII objects. There is also some indirect evidence of young stellar populations and cold molecular gas being associated, and in some cases aligned, with radio jets (Klamer et al. 2004; Emonts et al. 2014).

Simulations suggest that shocks generated by the jet propagating through a clumpy, homogeneous medium can trigger the collapse of overdense clouds resulting in actively star-forming regions (Fragile et al. 2004; Gaibler et al. 2012). It has been suggested that particularly in the early Universe, when galaxies were still forming and gas densities were much higher, jet-induced star formation may have been more common. The resolution and sensitivity of the SKA, in combination with other instruments such as ALMA, will allow detailed studies of the interaction of radio jets

PoS(AASKA14)083

with the clumpy ISM and IGM of galaxies and clusters to gain clearer insights into this feedback mechanism and its relevance to galaxy evolution.

4. Jet induced outflows

An interesting object, which presents an alternative model of AGN feedback, is the ULtraluminous Infrared Galaxy (ULIRG) 4C12.50, which hosts a young AGN. In this object a very fast outflow, 1000 km s^{-1} has been detected in HI, as well as in ionized (Holt et al. 2011) and molecular gas (Dasyra & Combes 2012). High resolution VLBI observations of HI demonstate that the outflow is, in projection, cospatial with a bright, highly polarized, hotspot in radio continuum located at the edge of the radio AGN jet (Morganti et al. 2013). This argues that the outflow is driven by the interaction between the radio jet and a dense cloud in the ISM rather than by an AGN wind. The energy of this outflow is less than required by most 'quasar' feedback models, but may be consistent with a 'two-stage' model of feedback whereby an initially weak wind expands and dilutes dense gas clouds in the ISM making them more susceptible to secondary radiative feedback from the quasar (Hopkins & Elvis 2010).

5. The role of the SKA

Radio surveys in the SKA era are ideal tools to investigate the SF-AGN connection for four main reasons: i) radio surveys are sensitive to emission from star-forming galaxies (see e.g. Condon 1992), and the contribution from these star-forming galaxies increases significantly at μJy flux densities; ii) they can detect radio emission from both 'quasar' and 'radio' mode accretors, (see e.g. Best & Heckman 2012); iii) they can provide sub-arcsec resolution essential for disentangling emission from star-formation and AGN activity; iv) radio waves offer the advantage of being unaffected by dust extinction and obscuration by circumnuclear gas, thus they are able to detect star-formation and AGN activity which would be largely obscured at optical, near-infrared and X-ray wavelengths. The true prevalence of obscured AGN activity at moderate to high redshifts is still largely unclear. X-ray stacking of sources with excess mid-infrared *Spitzer* emission has revealed a population of largely unknown, heavily obscured AGN at z$\sim$2, indicating that obscured AGN activity may be much more common at high redshift than previously thought (Daddi et al. 2007). There is also evidence of a large contribution from obscured AGN activity in recent multiwavelength studies of *Herschel* sources (Delvecchio et al. 2014). The SKA will thus be extremely valuable in revealing the true incidence and relevance of such obscured AGN activity for 'feedback' models at a crucial epoch of massive galaxy formation.

At frequencies of $\sim$1 GHz radio emission can be used to provide a reasonably accurate measure of galaxy star-formation rate (SFR) via the Far-Infrared Radio Correlation (FIRC; Yun et al. 2001). The relation holds over nearly 5 orders of magnitude in star-formation rate, although both observations (Bell 2003; Jarvis et al. in prep) and theory (Lacki et al. 2010) suggest that the relationship between star-formation rate and both radio and far-infrared emission becomes non-linear at low stellar masses and/or low star-formation rates (see also Beswick et al. this volume). It has been confirmed that the correlation holds out to redshifts of z$\sim$1 (Garrett 2002; Appleton et al. 2004; Beswick et al. 2008; Mao et al. 2011; Murphy 2009), and even as high as z$\sim$2 (Sargent et al.

PoS(AASKA14)083

2010; Bourne et al. 2011; Thomson et al. 2014) there is little evidence of strong evolution in the relation. However, towards higher redshifts theory predicts that the non-thermal emission from radio galaxies will be suppressed due to inverse Compton (IC) losses off the cosmic microwave background (see e.g. Murphy et al. 2009; Lacki & Thompson 2010), reducing the reliability of the FIRC as a star-formation estimator.

The radio-loud AGN population, which dominates at flux densities greater than a few mJy, is comprised of both 'quasar' and 'radio' mode accretors. Radio jets are associated with a small fraction of optically selected, radiatively efficient AGN and radio emission is the most reliable way of selecting samples of 'radio' mode, radiatively inefficient AGN as their emission at UV and X-ray wavelengths is much weaker than in the radiatively efficient case. The 'quasar' and 'radio' mode AGN dominate the radio-loud AGN population at high and low luminosities respectively. However there appear to be examples of both types of objects at all radio luminosities; the local luminosity function for radio-loud 'quasar' and 'radio' mode accretors are presented in figure 1. Separating the contributions of the 'radio' and 'quasar' accretors will thus require data at other wavelengths as neither jet morphology nor luminosity are reliable discriminants in the radio.

At μJy levels, there is an increasing contribution to the radio population from radio-quiet (RQ) AGN (e.g. Simpson et al. 2006; Smolčić et al. 2008; Padovani et al. 2009; Bonzini et al. 2012). RQ AGN are 'quasar' mode accretors which don't display the large, kiloparsec scale radio jets detected in radio loud AGN. Hence they show the presence of AGN activity in one or more bands of the electromagnetic spectrum (e.g. optical, mid-infrared, X-ray), but their radio emission is much fainter, relative to the optical than in the traditional radio-loud case. There is intense debate regarding the dominant mechanism generating radio emission in these objects, as discussed in detail in Orienti et al. (this volume) and Smolčić et al. (this volume). The radio emission from most RQ AGNs is unresolved or barely resolved at few arcsec scales, indicating that the radio emission is confined in small regions (at most comparable to the host galaxy size). RQ AGNs may be scaled down versions of radio loud AGNs displaying mini radio jets, either associated to systems with very low accretion rates (e.g. Giroletti & Panessa 2009; Prandoni et al. 2010) or to efficiently accreting quasar-like systems (see modelling work by Jarvis & Rawlings 2004). In the local universe AGN core and jet structures have been observed at very high resolutions in a small number of RQ AGNs, while others find evidence to suggest that the radio emission is generated primarily by star formation in the host galaxy (e.g. Kimball et al. 2011; Padovani et al. 2011; Bonzini et al. 2013), particularly at high redshifts. In the local universe both radio-quiet and radio-loud 'quasar' mode accretors are associated with ongoing star-formation, making it difficult disentangle the contribution from star-formation and AGN activity in these objects. The SKA will enable us to establish whether/if radio-quiet AGN influence the gas of their host galaxy primarily via the 'quasar' wind mode of feedback, or whether small-scale radio jets in these systems also contribute some measure of 'radio' mode feedback.

5.1 Resolving AGN and SF with the SKA

The power of the SKA in unravelling the AGN/SF connections lies in its ability to trace the contribution from star-formation and AGN activity in individual galaxies out to high redshifts without any need to correct for poorly characterized selection effects induced by dust obscuration or orientation effects (e.g. Type 1 or Type 2 AGN). Morphological classification using high resolu-

PoS(AASKA14)083

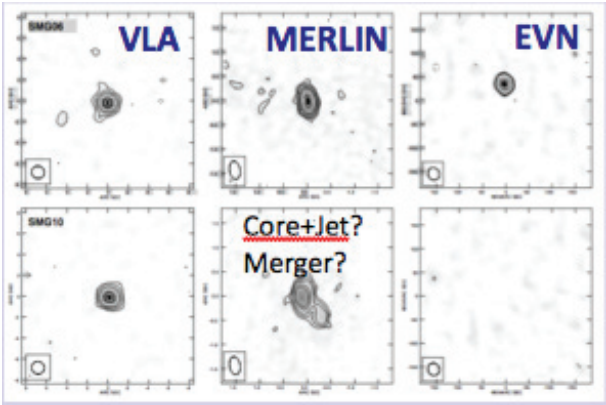

Figure 2: Radio emission at 1.4 GHz on arcsec scale (VLA, left), on 200 mas scale (MERLIN, middle) and mas scale (EVN, right) for two galaxies in the HDF North field, at $z \sim 2.7$ (top panels) and at $z \sim 1.2$ (bottom panels) respectively. An AGN core is detected in the upper object at VLBI scale, while no VLBI detection is found for the other, supporting a star-formation scenario, over a jet and core one. Figure from Biggs et al. (2010).

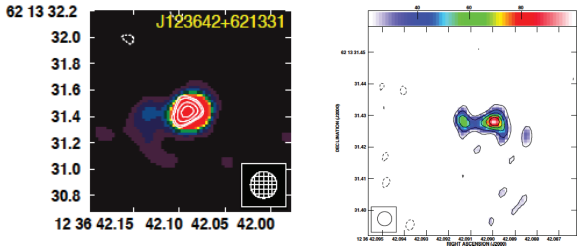

Figure 3: *Left panel:* Radio emission on 200 mas scale at 1.4 GHz (colors, VLA and MERLIN) and 5 GHz (white contours, eMERLIN) for an ultraluminous galaxy at $z \sim 4.4$ in the GOODS-N region. Figure from (Guidetti et al. 2013). *Right panel:* VLBI image of 1.6 GHz radio emission with 4 mas resolution (both colors and contours) from the same galaxy confirming the presence of an AGN. Figure from Chi et al. (2013).

tion radio observations is essential to determine the relative fraction of the emission generated by star-formation activity and nuclear activity. At faint, μJy levels the majority of radio AGN are unresolved thus reliably separating the SF and AGN contributions depends on our ability to distinguish compact AGN cores and inner jets at $\lesssim$kpc scales from star-forming disks and bulges with typical sizes ranging from 1–10's kpc. Figures 2 and 3 are examples which illustrate the exceptional potential of high resolution (mas) radio observations as a discriminant between AGN and star-formation activity. In figure 2 two intermediate/high redshift galaxies in the HDF North have been observed at 1.4 GHz from arcsec to mas scales. At VLBI scale an AGN core is detected in the first galaxy, while no VLBI detection is found for the second, supporting a merger scenario, over a core and jet one. This implies that in this object star formation processes are at work. Figure 3 shows a distant ($z \sim 4.4$) ultra-luminous infrared galaxy identified in the GOODS-N region, and interpreted as a dusty star-forming galaxy with an embedded weak AGN (Waddington et al. 1999). eMERLIN and global VLBI observations ($>$ 1000 km baselines) were ultimately able to confirm the presence of an embedded AGN by resolving a jet and core structure separated by $\sim$70 pc. This may be an example of a high redshift ultra luminous infrared galaxy in which the high star-formation rate and the efficiency are enhanced by AGN jet activity (e.g. Silk 2005). This radio morphological identification is particularly valuable in cases of highly obscured AGN activity which goes largely undetected at other wavelengths. High resolution radio observations have revealed highly compact AGN cores in submillimeter galaxies whose emission at near-infrared and X-ray wavelengths were completely devoid of AGN signatures (Casey et al. 2009).

PoS(AASKA14)083

While high resolution observations at mid frequency (e.g. 1 GHz) will detect the extended steep spectrum emission from star-forming regions in an unbiased manner, these frequencies are biased against detecting the contribution from AGN with inverted or Gigaherz Peaked Spectra (GPS) whose spectra turn-over at lower frequencies due to either synchrotron self absorption or free-free absorption from an inhomogenous screen (O'Dea 1998; Marr et al. 2014; Orienti & Dallacasa 2014). High resolution multifrequency observations are thus vitally important for unambiguously separating star-formation and AGN emission in the presence of absorption effects.

6. SKA surveys

The SKA continuum science reference surveys are outlined in Prandoni and Seymour (this volume), which have been designed to meet a wide variety of science goals. Of the four proposed reference surveys those which are most relevant to the goal of understanding the star-formation AGN interplay is the three tier survey in band 1/2 at $\sim$1 GHz at high resolution with SKA1-MID and the two tier survey at band 5 at 10 GHz. The three tiers at $\sim$1 GHz range in depth (1σ) from 1, 0.2 and 0.05 μJy over areas of 1000–5000, 10–30 and 1 square degrees with a resolution of 0.5$''$using SKA1-MID. The luminosity functions for star-forming galaxies and AGN for these surveys are presented in Jarvis et al., (this volume) and Smolčić et al. (this volume). The luminosity functions demonstrate that these three tiers will probe star-formation rates of 0.5 $M_\odot$ yr^{-1} at z$\sim$0.5 and 10 $M_\odot$ yr^{-1} at redshifts z$\sim$1–2 and z$\sim$3–4. They are also shown to be sensitive to both radio loud and radio quiet AGN with luminosities of 10^{22} W Hz^{-1} at z$\sim$0.5, 1–2 and 3–4 in tiers 1, 2 and 3 respectively, thus probing the co-evolution of AGN and galaxies from the local universe to the early stages of galaxy evolution. Furthermore the area surveyed is sufficiently large to study the variation in the AGN star-formation connection as a function of all the variables of interest which include the black hole and stellar mass, AGN accretion rate, star-formation rate, accretion mode, merger status and environment.

In the case of radio-quiet AGN the luminosity limits refer to the compact emission generated by nuclear activity. As discussed earlier, there is much debate as to the relative contributions of star-formation and AGN activity to the total radio flux in these objects, if the AGN core constitutes a very small fraction of the total emission this will have important implications for our ability to probe the star-formation AGN connection down to the limiting star-formation rates of the proposed surveys. However recent work by White et al. (2014) indicates that the AGN contributes a non-negligable radio flux in radio-quiet AGN.

With 200 km baselines the SKA1 should achieve a minimum angular resolution of between 0.3-0.5$''$ at 1.4 GHz (SKA1 band 2), which should be sufficient to resolve $\sim$ 4 kpc structures at z$\gtrsim$1. High resolution observations have already been used, with some success, to identify AGN and SF emission in the μJy radio population in the Hubble Deep Field North (Muxlow et al. 2005; Guidetti et al. 2013). MERLIN observations with resolutions of 0.2-0.5$''$ reveal that the majority of these sources have subgalactic sizes, typically $\sim$1-1.2$''$, and that very few, 2%, have double lobes surrounding a compact core (2/92). These sizes have now been confirmed for larger samples with recent e-MERLIN observations (Wrigley et al., in prep), while stacking experiments suggest similar size distributions down to levels of a few μJy (Muxlow et al. 2007). Unambiguous classification of the dominant emission mechanism (AGN/SF) at these resolutions still frequently relies on

PoS(AASKA14)083

infrared or spectral index information, thus even in the era of the SKA multiwavelength data will be essential to studies of continuum radio sources. Multiwavelength SED modelling, spectroscopy and information from X-ray, optical and infrared surveys will all aid in decoupling the contribution to the bolometric output from AGN and star-formation. These complementary datasets will enable us to fully exploit radio observations from SKA1. The key surveys at other wavelengths that will complement the radio continuum surveys with the SKA are thoroughly explored in Prandoni and Seymour (this volume), Jarvis et al. (this volume) and Ciliegi et al. (this volume).

The higher resolution and spectral index information provided by higher frequency observations by SKA1 in bands 3,4 and 5 would also be extremely valuable for identifying AGN activity either via the presence of flat spectrum compact core emission or compact emission whose brightness temperature exceeds that of starbursts. The two proposed tiers at higher frequencies are necessarily limited to small areas due to the smaller field of view and reduced sensitivity of the array in band 5. We are proposing a shallower, high resolution ($0.05''$) survey over 0.5 square degrees to 0.3 μJy/beam, and a deeper, lower resolution ($0.1''$) survey to 0.03 μJy beam^{-1} over 30 square arcminutes. The depths are chosen to match the two shallower 1 GHz surveys assuming sources with spectral indices $S_\nu \propto \nu^{-1}$. These high frequency observations provide a means to morphologically or spectrally identify AGN cores which may be obscured at other wavelengths and are difficult to distinguish from star-formation in lower resolution radio observations. The observations will also be able to resolve individual star formation and accretion-related emitting components to allow detailed investigations of their interactions. Higher frequency observations also probe the thermal (free-free) emission dominated region of the radio spectrum of high redshift galaxies ($z \geq 2$). This is a more direct indicator of SF activity than the synchrotron emission used at lower frequencies and can thus provide essential complementary information about high redshift star-formation activity and its relationship to AGN activity. The value of high frequency observations are discussed in more detail in Murphy et al. (this volume).

Our science goals require sufficient resolution to separate the AGN cores from star-forming disks and this will require much higher resolution, of the order of $<0.1''$, than currently planned with SKA1 at mid frequencies ($\sim$1 GHz). Only by combining high sensitivity with high (mas) resolution is it possible to disentangle the AGN and SF contributions at high redshifts. Studies along these lines will be conducted in the near future over small deep fields by combining deep μJy observations at sub-arcsec resolution carried out with the JVLA at 5 GHz (Guidetti et al. in prep) with e-MERLIN observations, allowing angular resolutions on spatial scales of 50-100 mas (eMERGE survey, Muxlow et al. 2008). Sub-μJy sensitivities will be routinely reached by SKA on similar spatial scales, as baselines up to $\sim$ 100 km (SKA1) and $\sim$ 1000 km (SKA) will be incrementally implemented, according to the current design. However, as shown in Figs. 2 and 3, only VLBI-like observations allow us to securely pinpoint AGN cores in sources at cosmological redshifts which calls for $10\times$ longer baselines ($\gg$ 1000 km) for the full SKA. In the interim, VLBI capability with SKA1 would greatly improve our ability to pinpoint embedded AGN emission in high resolution follow-up observations.

The increased resolution and sensitivity of the full SKA will vastly improve our abilities to morphologically separate the contributions from star-formation and accretion processes within individual galaxies. At 1.4 GHz a survey to 3 nJy (1σ) at $\sim 0.03''$ resolution could detect resolved star formation at 50 $M_\odot$ yr^{-1} out to $z\sim 2$. The increased sensitivity at higher frequencies will also

PoS(AASKA14)083

make it feasible to obtain high resolution spectral index information over larger areas of the sky, which can further aid in the AGN/SF decomposition. A deep SKA survey at 10 GHz to 3 nJy (1σ) could detect resolved star formation taking place at z$\sim$2 at 50 $M_\odot$ yr^{-1} at a resolution of 0.1$''$, or to 100 $M_\odot$ yr^{-1} at 0.07$''$. At 3 nJy we could detect low luminosity AGN cores of 10^{19} W Hz^{-1} at z$\sim$0.5, these luminosities are comparable to radio cores detected in faint Seyferts in the local universe (Nagar et al. 2002; Giroletti & Panessa 2009).

As resolution is key to the science goals laid out in this chapter, the usefulness of a 50% SKA1 depends strongly on its maximum available baseline. Earlier progress could thus be achieved by deploying some fraction of the longest baselines at an earlier stage of construction. Alternatively, if the 50% SKA1 has only maximum baselines of 50 km the resolution at 1 GHz is $\sim$1.5$''$, which is less than the planned resolution of the deep tier of the VLASS survey of 0.65$''$ at $\sim$3 GHz (Murphy et al, 2014). Greater scientific gains could be made by conducting a high frequency, band 5, counterpart to the VLASS deep tier which could provide resolved spectral index information at a matched, or slightly higher resolution. The planned VLASS depth is 1.5 μJy over 10 square degrees, a comparable depth at 10 GHz equates to 0.6 μJy $beam^{-1}$, assuming a spectral index of $S_\nu \propto \nu^{-0.7}$. A 50% sensitivity SKA1 could survey to this depth at 10 GHz over 1 square degree in $\sim$1000 hours.

Due its unique combination of high resolution imaging and sensitivity to obscured star-formation and AGN activity the SKA will be the leading facility to clarify the interplay between AGN and star-formation over a large fraction of cosmic time and thoughout the epoch of peak star formation and AGN activity.

References

Afonso, J., Mobasher, B., Koekemoer, A., Norris, R. P., & Cram, L. 2006, AJ, 131, 1216
Allen, S. W., Dunn, R. J. H., Fabian, A. C. et al., 2006, MNRAS, 372, 21
Antonucci, R. 1993, ARA&A, 31, 473
Appleton, P. N., Fadda, D. T., Marleau, F. R., et al. 2004, ApJS, 154, 147
Barnes, J. E. 1992, ApJ, 393, 484
Barnes, J. E. & Hernquist, L. 1996, ApJ, 471, 115
Bell, E. F. 2003, ApJ, 586, 794
Best, P. N. & Heckman, T. M. 2012, MNRAS, 421, 1569
Best, P. N., Kaiser, C. R., Heckman, T. M. et al., 2006, MNRAS, 368, L67
Best, P. N., Kauffmann, G., Heckman, T. M. et al., 2005, MNRAS, 362, 25
Best, P. N., von der Linden, A., Kauffmann, G. et al., 2007, MNRAS, 379, 894
Beswick R. J., Muxlow T. W. B., Thrall H., Richards A. M. S., Garrington S. T., 2008, MNRAS, 385, 1143
Beswick, R. J., et al., “SKA studies of nearby galaxies: star-formation & accretion processes across all environments”, in proceedings of “Advancing Astrophysics with the Square Kilometre Array", PoS(AASKA14)070
Bicknell, G. V., Sutherland, R. S., van Breugel, W. J. M. et al., 2000, ApJ, 540, 678
Biggs, A. D., Younger, J. D., & Ivison, R. J. 2010, MNRAS, 408, 342
Bîrzan, L., Rafferty, D. A., McNamara, B. R. et al., 2004, ApJ, 607, 800

PoS(AASKA14)083

Bonzini, M., Mainieri, V., Padovani, P. et al., 2012, ApJS, 203, 15
Bonzini, M., Padovani, P., Mainieri, V. et al., 2013, MNRAS, 436, 3759
Bourne, N., Dunne, L., Ivison, R. J. et al., 2011, MNRAS, 410, 1155
Bower, R. G., Benson, A. J., Malbon, R. et al., 2006, MNRAS, 370, 645
Cano-Díaz, M., Maiolino, R., Marconi, A. et al., 2012, A&A, 537, L8
Casey, C. M., Chapman, S. C., Muxlow, T. W. B. et al., 2009, MNRAS, 395, 1249
Cavagnolo, K. W., McNamara, B. R., Nulsen, P. E. J. et al., 2010, ApJ, 720, 1066
Chi, S., Barthel, P. D., & Garrett, M. A. 2013, A&A, 550, A68
Cicone, C., Maiolino, R., Sturm, E. et al., 2014, A&A, 562, A21
Ciliegi, P. et al., "Synergistic science with *EUCLID* and SKA: The nature and history of cosmic star formation", in proceedings of "Advancing Astrophysics with the Square Kilometre Array", PoS(AASKA14)150
Cisternas, M., Jahnke, K., Inskip, K. J. et al., 2011, ApJ, 726, 57
Condon, J. J. 1992, ARA&A, 30, 575
Croft, S., van Breugel, W., de Vries, W., Dopita, M. et al., 2006, ApJ, 647, 1040
Croston, J. H., Hardcastle, M. J., Birkinshaw, M. et al. 2008, MNRAS, 386, 1709
Croton, D. J., Springel, V., White, S. D. M. et al., 2006, MNRAS, 365, 11
Daddi, E., Alexander, D. M., Dickinson, M. et al., 2007, ApJ, 670, 173
Dasyra K. M., Combes F., 2012, A&A, 541, LL7
Delvecchio I., et al., 2014, MNRAS, 439, 2736
Dey, A., van Breugel, W., Vacca, W. D., & Antonucci, R. 1997, ApJ, 490, 698
Di Matteo, T., Springel, V., & Hernquist, L. 2005, Nature, 433, 604
Donoso E., Best P. N., Kauffmann G., 2009, MNRAS, 392, 617
Dubois, Y., Gavazzi, R., Peirani, S., & Silk, J. 2013, MNRAS, 433, 3297
Emonts, B. H. C., Norris, R. P., Feain, I. et al., 2014, MNRAS, 438, 2898
Fabian, A. C., Sanders, J. S., Allen, S. W. et al., 2003, MNRAS, 344, L43
Fragile, P. C., Murray, S. D., Anninos, P., & van Breugel, W. 2004, ApJ, 604, 74
Gabor J. M., Bournaud F., 2013, MNRAS, 434, 606
Gabor, J. M. & Bournaud, F. 2014, MNRAS, 441, 1615
Gaibler, V., Khochfar, S., Krause, M., & Silk, J. 2012, MNRAS, 425, 438
Garrett, M. A. 2002, A&A, 384, L19
Gaspari, M., Ruszkowski, M., & Oh, S. P. 2013, MNRAS, 432, 3401
Gebhardt, K., Bender, R., Bower, G. et al., 2000, ApJ, 539, L13
Giroletti, M. & Panessa, F. 2009, ApJ, 706, L260
Granato, G. L., De Zotti, G., Silva, L., et al., 2004, ApJ, 600, 580
Guidetti, D., Bondi, M., Prandoni, I. et al., 2013, MNRAS, 432, 2798
Guidetti, D., Laing, R. A., Bridle, A. H. et al., 2011, MNRAS, 413, 2525
Guidetti, D., Laing, R. A., Croston, J. H. et al., 2012, MNRAS, 423, 1335
Hardcastle, M. J., Evans, D. A., & Croston, J. H. 2007, MNRAS, 376, 1849
Häring, N. & Rix, H.-W. 2004, ApJ, 604, L89
Heckman, T. & Best, P. 2014, ARA&A, 52
Holt J., Tadhunter C. N., Morganti R., Emonts B. H. C., 2011, MNRAS, 410, 1527
Hopkins P. F., Elvis M., 2010, MNRAS, 401, 7

PoS(AASKA14)083

Inskip, K. J., Villar-Martín, M., Tadhunter, C. N. et al., 2008, MNRAS, 386, 1797
Janssen R. M. J., Röttgering H. J. A., Best P. N., Brinchmann J., 2012, A&A, 541, AA62
Jarvis, M. J. & Rawlings, S. 2004, New Astronomy Reviews, 48, 1173
Jarvis, M. J., et al., "The star-formation history of the Universe with the SKA", in proceedings of "Advancing Astrophysics with the Square Kilometre Array", PoS(AASKA14)068
Kauffmann, G., Heckman, T. M., & Best, P. N. 2008, MNRAS, 384, 953
Kim, W.-T., Seo, W.-Y., Stone, J. M. et al., 2012, ApJ, 747, 60
Kimball, A. E., Kellermann, K. I., Condon, J. J. et al., 2011, ApJ, 739, L29
Klamer, I. J., Ekers, R. D., Sadler, E. M., & Hunstead, R. W. 2004, ApJ, 612, L97
Kocevski, D. D., Faber, S. M., Mozena, M. et al., 2012, ApJ, 744, 148
Kormendy, J. & Kennicutt, Jr., R. C. 2004, ARA&A, 42, 603
Lacki, B. C. & Thompson, T. A. 2010, ApJ, 717, 196
Lacki, B. C., Thompson, T. A., & Quataert, E. 2010, ApJ, 717, 1
Li, C., Kauffmann, G., Heckman, T. M., Jing, Y. P., & White, S. D. M. 2008a, MNRAS, 385, 1903
Li, C., Kauffmann, G., Heckman, T. M. et al., 2008b, MNRAS, 385, 1915
Liu, G., Zakamska, N. L., Greene, J. E. et al., 2013, MNRAS, 436, 2576
Magorrian, J., Tremaine, S., Richstone, D. et al., 1998, AJ, 115, 2285
Maiolino, R., Gallerani, S., Neri, R. et al., 2012, MNRAS, 425, L66
Mao M. Y., Huynh M. T., Norris R. P. et al., 2011, ApJ, 731, 79
Marr J. M., Perry T. M., Read J. et al., 2014, ApJ, 780, 178
McNamara, B. R., Rohanizadegan, M., & Nulsen, P. E. J. 2011, ApJ, 727, 39
McNamara, B. R., Wise, M., Nulsen, P. E. J. et al., 2000, ApJ, 534, L135
Morganti R., Fogasy J., Paragi Z., Oosterloo T., Orienti M., 2013, Sci, 341, 1082
Mould, J. R., Ridgewell, A., Gallagher, III, J. S. et al., 2000, ApJ, 536, 266
Murphy, E. J. 2009, ApJ, 706, 482
Murphy, E. J., Chary, R.-R., Alexander, D. M. et al., 2009, ApJ, 698, 1380
Murphy, M., et al., "SKA Observations at >10 GHz : Fundamental Astrophysics of Star Formation at High-z", in proceedings of "Advancing Astrophysics with the Square Kilometre Array", PoS(AASKA14)085
Muxlow, T. W. B., Richards, A. M. S., Garrington, S. T. et al., 2005, MNRAS, 358, 1159
Muxlow T. W. B., Beswick R. J., Thrall H. et al., 2007, ASPC, 380, 199
Muxlow, T., Smail, I., McHardy, I. et al., & E-Merge Consortium. 2008, in The role of VLBI in the Golden Age for Radio Astronomy
Nagar N. M., Falcke H., Wilson A. S., Ulvestad J. S., 2002, A&A, 392, 53
O'Dea C. P., 1998, PASP, 110, 493
Orienti, M., et al., "The physics of the radio emission in the quiet side of the AGN population with the SKA", in proceedings of "Advancing Astrophysics with the Square Kilometre Array", PoS(AASKA14)087
Orienti M., Dallacasa D., 2014, MNRAS, 438, 463
Padovani, P., Mainieri, V., Tozzi, P. et al., 2009, ApJ, 694, 235
Padovani, P., Miller, N., Kellermann, K. I. et al., 2011, ApJ, 740, 20
Pedlar A., Ghataure H. S., Davies R. D. et al., 1990, MNRAS, 246, 477
Pizzolato, F. & Soker, N. 2010, MNRAS, 408, 961

PoS(AASKA14)083

Pounds, K. A. & King, A. R. 2013, MNRAS, 433, 1369
Prandoni, I., Gregorini, L., Parma, P., et al. 2001, A&A, 369, 787
Prandoni, I., de Ruiter, H. R., Ricci, R. et al., 2010, A&A, 510, A42
Prandoni, I., Seymour, N., "Revealing the Physics and Evolution of Galaxies and Galaxy Clusters with SKA Continuum Surveys", in proceedings of "Advancing Astrophysics with the Square Kilometre Array", PoS(AASKA14)067
Puchwein, E. & Springel, V. 2013, MNRAS, 428, 2966
Rafferty, D. A., McNamara, B. R., Nulsen, P. E. J. et al., 2006, ApJ, 652, 216
Reichard, T. A., Heckman, T. M., Rudnick, G. et al., 2009, ApJ, 691, 1005
Sargent, M. T., Schinnerer, E., Murphy, E. et al., 2010, ApJ, 714, L190
Schawinski, K., Simmons, B. D., Urry, C. M. et al., MNRAS, 425, L61
Scott, N., Graham, A. W., & Schombert, J. 2013, ApJ, 768, 76
Seymour, N., Dwelly, T., Moss, D., et al. 2008, MNRAS, 386, 1695
Silk, J. 2005, MNRAS, 364, 1337
Simpson, C., Martínez-Sansigre, A., Rawlings, S., et al., 2006, MNRAS, 372, 741
Simpson, C., Westoby, P., Arumugam, V. et al., 2013, MNRAS, 433, 2647
Smolčić, V., Schinnerer, E., Scodeggio, M. et al., 2008, ApJS, 177, 14
Smolčić, V., et al., "Exploring AGN Activity over Cosmic Time with the SKA", in proceedings of "Advancing Astrophysics with the Square Kilometre Array", PoS(AASKA14)069
Somerville, R. S., Hopkins, P. F., Cox, T. J., et al. 2008, MNRAS, 391, 481
Springel, V., Di Matteo, T., & Hernquist, L. 2005, ApJ, 620, L79
Steinbring, E. 2014, AJ, 148, 10
Sturm, E., González-Alfonso, E., Veilleux, S. et al., 2011, ApJ, 733, L16
Thomson, A. P., Ivison, R. J., Simpson, J. M. et al., 2014, ArXiv:1404.7128T
Treister, E., Schawinski, K., Urry, C. M. et al., 2012, ApJ, 758, L39
Tremaine, S., Gebhardt, K., Bender, R. et al., 2002, ApJ, 574, 740
Urrutia, T., Lacy, M., & Becker, R. H. 2008, ApJ, 674, 80
Voit, G. M. & Donahue, M. 2005, ApJ, 634, 955
Waddington, I., Windhorst, R. A., Cohen, S. H. et al., 1999, ApJ, 526, L77
White, S. D. M. & Frenk, C. S. 1991, ApJ, 379, 52
White S. V., Jarvis M. J., Häußler B. et al., 2014, arXiv, arXiv:1410.3892
Wild, V., Kauffmann, G., Heckman, T. et al., 2007, MNRAS, 381, 543
Yun, M. S., Reddy, N. A., & Condon, J. J. 2001, ApJ, 554, 803

PoS(AASKA14)083

PROCEEDINGS OF SCIENCE

Strong gravitational lensing with the SKA

J. P. McKean[*1,2], **N. Jackson**[3], **S. Vegetti**[4], **M. Rybak**[4], **S. Serjeant**[5], **L. V. E. Koopmans**[2], **R. B. Metcalf**[6], **C. D. Fassnacht**[7], **P. J. Marshall**[8], **M. Pandey-Pommier**[9]

[1]*Netherlands Institute for Radio Astronomy (ASTRON), P.O. Box 2, 7990 AA Dwingeloo, The Netherlands;* [2]*Kapteyn Astronomical Institute, University of Groningen, P.O. Box 800, 9700 AV Groningen, The Netherlands;* [3]*Jodrell Bank Centre for Astrophysics, School of Physics and Astronomy, University of Manchester, Turing Building, Oxford Road, Manchester M13 9PL, United Kingdom;* [4]*Max Planck Institute for Astrophysics, Karl-Schwarzschild-Strasse 1, D-85740 Garching, Germany;* [5]*Department of Physical Sciences, The Open University, Milton Keynes, MK7 6AA, United Kingdom;* [6]*Dipartimento di Fisica e Astronomia - Universita di Bologna, via Berti Pichat 6/2, 40127, Bologna, Italy;* [7]*Department of Physics, University of California Davis, 1 Shields Avenue, Davis, CA 95616, USA;* [8]*Kavli Institute for Particle Astrophysics and Cosmology, Stanford University, 452 Lomita Mall, Stanford, CA 94035, USA;* [9]*CRAL-l'Observatoire de Lyon, Universite de Lyon, 69561, France*

E-mail: mckean@astron.nl

Strong gravitational lenses provide an important tool to measure masses in the distant Universe, thus testing models for galaxy formation and dark matter; to investigate structure at the Epoch of Reionization; and to measure the Hubble constant and possibly w as a function of redshift. However, the limiting factor in all of these studies has been the currently small samples of known gravitational lenses ($\sim 10^2$). The era of the SKA will transform our understanding of the Universe with gravitational lensing, particularly at radio wavelengths where the number of known gravitational lenses will increase to $\sim 10^5$. Here we discuss the technical requirements, expected outcomes and main scientific goals of a survey for strong gravitational lensing with the SKA. We find that an all-sky (3π sr) survey carried out with the SKA1-MID array at an angular resolution of 0.25–0.5 arcsec and to a depth of 3 μJy beam^{-1} is required for studies of galaxy formation and cosmology with gravitational lensing. In addition, the capability to carryout VLBI with the SKA1 is required for tests of dark matter and studies of supermassive black holes at high redshift to be made using gravitational lensing.

Advancing Astrophysics with the Square Kilometre Array
June 8-13, 2014
Giardini Naxos, Italy

*Speaker.

PoS(AASKA14)084

1. Introduction

Gravitational lensing is the deflection of light from a distant background object (*the source*) by an intervening foreground mass distribution (*the lens*). If the surface mass density of the lens is sufficiently high, and if the source and lens are properly aligned, then multiple images of the background source are formed. The positions and distortions of these multiple images give important information about the mass distribution of distant lensing galaxies where velocity dispersions from spatially-resolved spectroscopy are either difficult or impossible. They also give a magnified view of the distant background source, probing a source population that is typically too faint to be detected with current instrument sensitivities.

After the discovery of the first gravitational lens system B0957+561 (Walsh et al. 1979), in the Jodrell Bank 966-MHz quasar survey, the early history of strong lensing was dominated by VLA-based surveys, including the MIT surveys (Hewitt et al. 1992) of mainly steep-spectrum sources and the JVAS/CLASS surveys (Myers et al. 2003; Browne et al. 2003) of flat-spectrum radio sources. The majority of the currently known 36 radio-loud gravitational lens systems were found in this period. Further radio-based surveys became limited by the survey speed of high-resolution telescopes; because the typical separation of multiple images in gravitational lens systems, where the deflector is a massive galaxy, is ~ 1 arcsec, gravitational lens discovery programmes require large amounts of time on relatively oversubscribed interferometer arrays. Even with the recently upgraded JVLA and e-MERLIN, the survey speed is insufficient for large-scale searches. During the last 10 years, the advent of large-area optical imaging and spectroscopy surveys (e.g. SDSS) have found hundreds of gravitationally lensed star-forming galaxies (Bolton et al. 2008) and quasars (Inada et al. 2012). The advent of wide-field surveys in the sub-mm with *Herschel* (Negrello et al. 2010) and the SPT (Vieira et al. 2013), coupled with the resolution and sensitivity of ALMA, is also expected to increase the numbers of strong gravitational lenses by a few hundred. In total, there are around 300–500 gravitational lenses known from galaxy, galaxy-group and galaxy-cluster lensing, with about 10 per cent having a radio-loud (-bright) background source.

Gravitational lenses have been of extraordinary astrophysical value in many fields: for determining the radial mass density profiles of galaxies (e.g. Koopmans et al. 2009); the direct detection of sub-galactic scale substructure predicted by dark matter models for galaxy formation (e.g. Vegetti et al. 2012); measuring the mass of supermassive black holes in distant quiescent galaxies (e.g. Winn et al. 2004); measuring the stellar initial mass function in external galaxies by a combination of lensing and stellar population modelling (e.g. Auger et al. 2010); and by providing a one-step measurement of cosmological parameters, most notably the Hubble constant using time-delays (e.g. Suyu et al. 2010). Furthermore, the lens also magnifies the background source by factors of ~ 5–100, which gives unique information about the structure of high redshift objects. This allows a source population that is intrinsically faint to be observed and studied, for example, the faintest known radio sources are currently gravitationally lensed objects (e.g. Jackson 2011). Also, the magnification from the gravitational lens provides a high resolution (sub-kpc) view of galaxies at cosmologically distant epochs ($z \sim 1$–5; e.g. Deane et al. 2013).

Most of these astrophysical applications have been limited by small-sample statistics, since only a minority of gravitational lenses are usually suitable for any particular study. However, we are on the verge of a huge increase in the number of gravitational lenses available for study in the

PoS(AASKA14)084

radio with the SKA and in the optical/infrared with missions such as *Euclid* and the LSST. In this review, we show that a lensing survey with the SKA, coupled with the synergy provided by *Euclid* and the LSST, will open up a new parameter space, both in terms of statistics and in the discovery of rare and valuable gravitational lenses for studying galaxy formation, the high redshift Universe and cosmology. This review builds upon the Radio All-sky SKA Lensing (RASKAL) survey proposed by Koopmans et al. (2004) during the first SKA Science Workshop.

2. Discovery space of SKA: The gravitational lensing statistics of continuum sources

Surveys such as those envisaged with the SKA will be capable of increasing the sample of radio-loud gravitational lens systems from a few tens to tens of thousands relatively straightforwardly. In order to determine the actual numbers that are expected to be found, we need to evaluate the lensing probability, $\tau(z_s)$, of a given radio source,

$$\tau(z_s) = \int_0^{z_s} n(z)\sigma_x \frac{cdt}{dz} dz, \tag{2.1}$$

where z_s is the source redshift, $n(z)$ is the number density of the lenses, σ_x is the cross-section of the gravitational lenses, and cdt is the path length to the background source (e.g. Turner et al. 1984). By integrating the lensing probability over all of the sources in the parent sample, we can determine the total number of sources that are gravitationally lensed. If we know the number counts of the parent sample as a function of flux-density and redshift, then we can calculate the number of gravitational lenses expected within a flux-limited survey. To zeroth order, gravitational lensing is a rare event; a high-redshift object has a $\sim 10^{-2}$–10^{-3} chance of lying within the Einstein radius of an intervening galaxy-scale mass distribution (depending on the source population redshift and magnification bias). For cluster lensing the probability is even smaller, at about $\sim 10^{-4}$. Therefore, surveys of a few hundred million high redshift objects should in principle give access to a few hundred thousand lenses, although recognition difficulties will mean that the actual number discovered will be a factor 10–100 less than this (see Section 3).

In order to estimate the lensing potential of the SKA surveys, we first require a model that describes the lens and source populations. To calculate the number density of lenses, we have used the light-cones generated by Kitzbichler & White (2007) coupled with semi-analytic prescriptions (De Lucia & Blaizot 2007) from the Millennium simulation (Springel et al. 2005). We have assumed that each potential lens has a velocity dispersion that is related to its luminosity via the Faber-Jackson relation, with a normalisation that gives for an L_* galaxy a velocity dispersion of $\sigma_* = 190$ km s^{-1}. We have then scaled the L_* luminosity using the lensing statistics from the CLASS survey (Myers et al. 2003); this is done by requiring that an initial sample of radio sources with flux densities > 1 mJy, and differential source counts with a slope of -2 (McKean et al. 2007) produces 22 gravitational lenses, as observed by CLASS (Browne et al. 2003). This has been done by assuming the CLASS selection criteria, namely that selected gravitational lenses should have flux ratios < 10:1 and an image separation > 300 mas. To first order, this calibration removes the effects of cosmic variance. The SKADS database (Wilman et al. 2008) was used to provide the population of background radio sources. This population is a best-guess extrapolation of known radio surveys down to the μJy level (e.g. Condon et al. 2012), and will almost certainly be superseded once the SKA surveys begin in earnest. The exact nature of the very faint (< 0.1 μJy)

PoS(AASKA14)084

population is important, because the magnification provided by lensing (factors 5–100) yields many more gravitational lens systems in populations with a steep source count, a phenomenon used to advantage in sub-mm surveys (e.g. Negrello et al. 2010).

In total, 4.56×10^5 radio sources from a 1 square degree area of SKADS and with a 1.4-GHz flux density > 1 μJy were extracted and randomly placed in the Millennium area. Any galaxy within 1 arcsec was considered to be a potential lens; the lensing status was then evaluated for each such pair. The results from the simulation are shown in Figure 1. In the 1 square degree of SKADS used, 440 radio sources with a total radio flux density > 1 μJy were found to be gravitationally lensed and have image separations > 0.3 arcsec. Of these lensed sources, 49 have total flux-densities > 10 μJy, and 10 have total flux-densities > 50 μJy. These calculations clearly show that for a fixed observing time it is most efficient to carry out a shallow, wide-field survey for gravitational lenses with the SKA. As we will demonstrate in Section 3, a survey with an rms of ~ 3 μJy beam^{-1} (2 year duration), and a detection threshold of about 15σ for lensing, yields about $\sim$5 lenses per pointing (0.5 square degrees) using the full 250 dish SKA1-MID array. These systems will contain lensed objects typical of the radio population at a slightly fainter flux density level of a few tens of μJy, in other words, approximately evenly distributed between lensed AGN and lensed starbursts.

The simulations also show the gravitational lenses that may be available from surveys with the SKA2, which will be up to a factor of 5–10 deeper than with SKA1-MID. These are potentially far more exotic objects, with the lensing galaxies at redshifts 1–4, extremely faint, very high redshift background sources, and in very large numbers despite the unfavourably flat faint radio source count of SKADS; the lensing rate approaches $\sim$ 1:150 due to the high redshifts (median $z \sim 3$) of the background source population. The details of these samples should be taken with caution because they rely on uncertain extrapolations. In particular, the likelihood of a large population of radio sources at $z > 10$ is low. What these simulations do illustrate, however, is the unique power of a gravitational lensing survey to probe any faint, high redshift radio source populations that may exist, if we know the detailed properties of the lensing galaxies. The latter is currently unknown, but is an area of very active study that will progress greatly over the next 5–10 years. For example, a deep (sub-μJy) small area continuum survey with the SKA1-MID array would directly detect this population of magnified and exotic high redshift objects, accessing the type of objects that will be seen routinely with the SKA2. Alternatively, if the predicted number of lenses is not found, then this would mean that the faint radio source population has a much different luminosity function than is currently expected. However, this assumes that the challenges related to the lens identification and confirmation process are well understood, which is typically the case for lens surveys are radio wavelengths where the lens selection function (resolution, sensitivity, flux-ratios; e.g. Myers et al. 2003) is well defined.

The major uncertainties in the number of gravitational lenses that will be potentially available for study in any SKA survey are the extrapolation of the radio source counts to very faint flux density levels and high redshifts, and the detection efficiency. The former uncertainty is negligible at the level of a few tens of μJy (which is most relevant for an SKA1 survey), but is very probably a factor of a few at the 1-μJy level, and likely an order of magnitude for the $z > 5$ radio source population. This uncertainty dominates the estimates for any SKA2 survey. The detection efficiency has an uncertainty that is likely to be of a factor of a few, although more detailed blind simulations

PoS(AASKA14)084

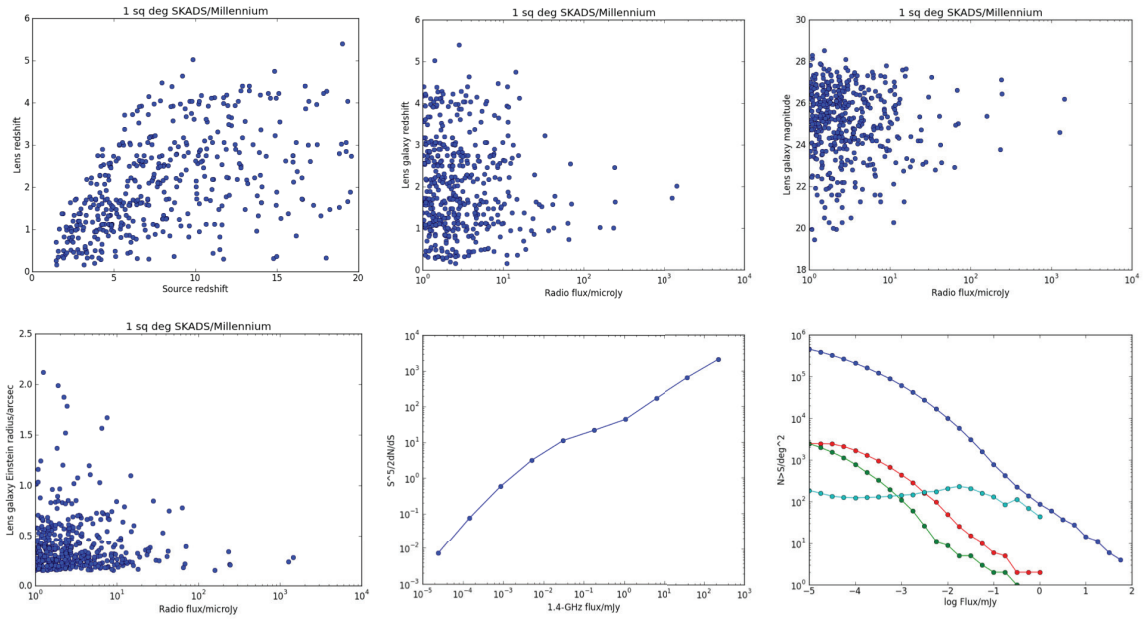

Figure 1: The results from the SKA gravitational lensing simulations. *Upper left*: Lens galaxy redshift versus source galaxy redshift. *Upper middle*: Lens galaxy redshift versus source galaxy flux density. *Upper right*: Lens galaxy magnitude versus source galaxy flux density. *Lower left*: Lens galaxy Einstein radius versus source galaxy flux density. *Lower middle*: The predicted differential number counts normalised to Euclidian from the SKADS simulation. *Lower right*: The total integrated number counts as a function of flux density for all sources (dark blue), the lensed sources (red), the lensed sources using the unlensed flux-density (green) and the lensing incidence (cyan).

are needed to reduce this uncertainty.

3. Gravitational lens candidate identification and confirmation techniques

The main observational challenge will be the recognition of genuine gravitational lenses among the large numbers of false positives corresponding to radio sources with intrinsic structure; the key criterion is angular resolution, although frequency coverage and image sensitivity also play a role. Known galaxy-scale gravitational lenses have image separations between $\sim$ 0.3–4.5 arcsec, with the typical image separation being $\sim$ 1 arcsec (e.g. McKean et al. 2005). From our SKA lensing simulations, the predicted image separation distribution for sources with a total flux-density > 50 μJy has a range between 0.3 and 1.4 arcsec. Therefore, an angular resolution of between 0.25–0.5 arcsec is required for identifying most of the lens candidates for follow-up imaging. It is for this reason that gravitational lensing surveys will only be possible with the SKA1-MID array.

To simulate the expected imaging quality for a gravitational lens search, we have taken the array configuration for SKA1-MID and generated mock gravitational lensing data based on an extended star-forming galaxy and a compact AGN; for both types of object, we have used *total* source flux-densities of 1, 0.25 and 0.05 mJy. From Figure 2, we see that sensitive observations (Briggs weighting; Robust = 0) with SKA1-MID have sufficient sensitivity (~ 3 μJy beam^{-1}) and angular resolution ($\sim$ 0.5 arcsec) to detect galaxy-scale gravitational lenses with extended sources.

PoS(AASKA14)084

We find that it is possible to achieve an angular resolution of 0.25 arcsec (for Robust = 2), but as expected, this increases the image rms by a factor of ~ 5, leading to the fainter extended radio sources having a surface brightness below the detection limit. Nevertheless, observations at Band 2 (0.95–1.76 GHz) with SKA1-MID can be used to select gravitational lensing candidates. An all-sky (3π sr) survey with SKA1-MID, reaching a sensitivity of 3 μJy beam^{-1} could potentially find $\sim 3 \times 10^5$ gravitational lens systems with image separations > 0.3 arcsec.

The resulting recognition problem (candidate to confirmed lens) will be considerable, but can be eased by adding additional information. The first is the large bandwidth to be used in the SKA1-MID survey, which will mean that some spectral index information will be available to discriminate between multiple images of the same object and, for example, a non-lensed source consisting of a flat-spectrum core and steep-spectrum jet or lobe emission. In addition, follow-up observations of candidates at Band 5 (4.6–13.8 GHz) will give a more robust measurement of the spectral index of the components and provide higher angular resolution imaging of the candidates (0.06–0.20 arcsec; Robust $= 0$ weighting) to determine if the surface brightness of the images is conserved, as is required by gravitational lensing. The second piece of information will come from surveys at other wavelengths, in particular those of *Euclid* and the LSST. Cross-correlating the SKA gravitational lens candidates with the high resolution optical data will determine whether there is a massive lensing galaxy at the expected position (see Figure 3) and provide a photometric redshift estimate of the gravitational lens. Even if neither the SKA1-MID and *Euclid*/LSST surveys are capable of detecting gravitational lenses on their own, experience from CLASS shows that the use of two surveys at different wavelengths (radio and optical) gives a very much greater discrimination between multiply-imaged sources and those that display intrinsic structure.

Using the predicted number counts and image separation distribution from our SKADS simulation, we have estimated the number of gravitational lenses that should be straightforwardly identified from the SKA1-MID survey presented above with minimum follow-up. Here, we only consider those lensed images with separations > 0.5 arcsec and total flux-densities > 1 mJy. We find a conservative estimate of about $\sim 10^4$ new radio-loud gravitational lens systems would be found (~ 1 per 3 square degrees), which is a factor of over 10^2 more than is currently known. We note that an initial pilot survey, that covers the same sky area as the *Euclid* deep fields (15000 deg^2) and to an rms of 6 μJy beam^{-1}, would conservatively identify around 2000 strong gravitational lenses in 3 months observing time. An SKA1-MID array that is only 50 per cent complete would still be useful for finding gravitational lenses, providing the sensitivity and length of the baselines remains unchanged and a wide area survey is carried out. The situation will improve dramatically with the SKA2, where the improved sensitivity, particularly on the long baselines will allow the potentially large population of $\sim 10^5$ faint lensed radio sources to be straightforwardly identified in the survey imaging data.

4. Searches for gravitationally lensed spectral line sources

An alternative method to efficiently find new gravitational lens systems with the SKA is to select candidates via magnification bias; here a specific property of the source results in very steep number counts. For example, Negrello et al. (2010) successfully used this technique to select a sample of strong gravitational lenses by using a 500 μm flux density limit and exploiting the

PoS(AASKA14)084

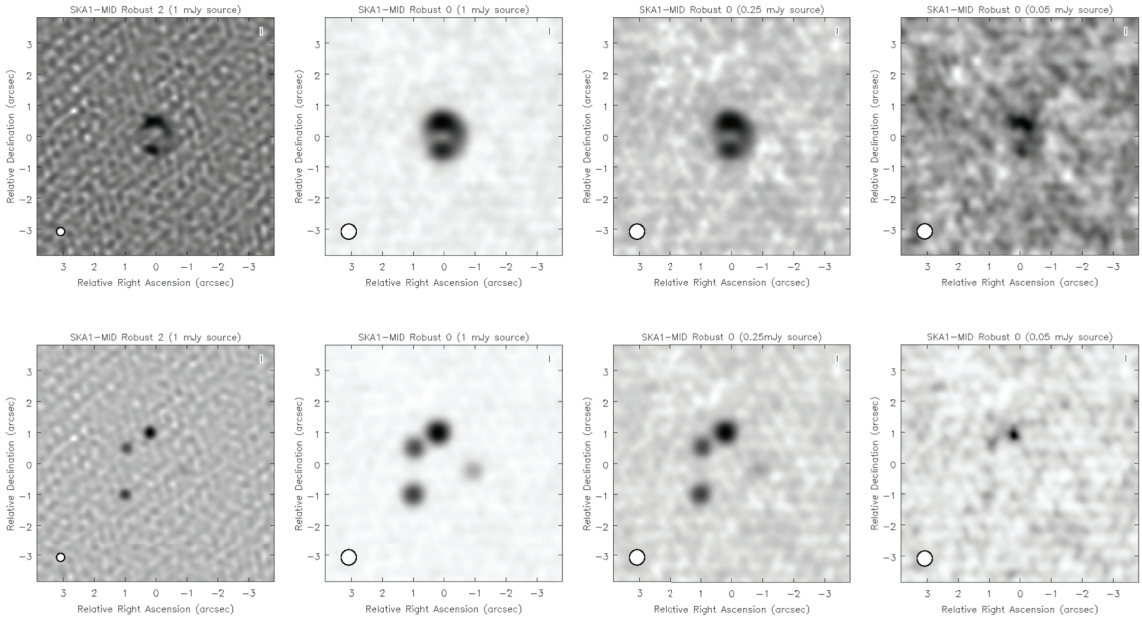

Figure 2: Simulations of an SKA1-MID snapshot observation of an extended radio galaxy (top) and an AGN (bottom) with total flux-densities of 1, 0.25 and 0.05 mJy (left middle, right middle, right) using Briggs weighing Robust = 0 (0.5 arcsec beam size) and for a total flux-density of 1 mJy (left) with Robust = 2 (0.25 arcsec beam size).

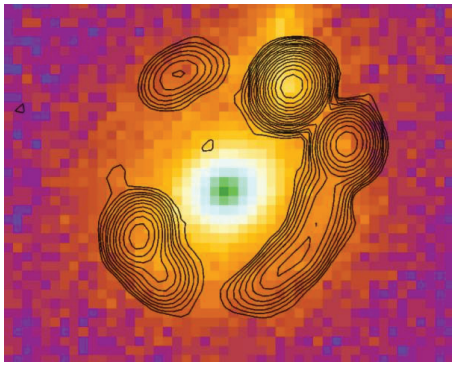

Figure 3: High resolution *HST* optical imaging of the gravitational lens CLASS B0631+519 with the MERLIN 1.7 GHz radio contours shown overlaid. The optical data only detect the two lensing galaxies, whereas the radio data are only sensitive to the emission from the background source. Together, these two datasets clearly show that CLASS B0631+519 is a gravitational lens (York et al. 2005).

steep slope of sub-mm number counts to obtain a $\sim$ 100 per cent reliable strong gravitational lens sample. González-Nuevo et al. (2012) extended this technique to the high-luminosity end of the sub-mm luminosity function. The HI mass function is expected to broadly follow its local form of a Schechter function (e.g. Abdalla et al. 2010). Therefore, a wide-field SKA HI survey, as proposed by Abdalla et al. (2010), should also be amenable to magnification bias at the high-mass end of the HI mass function.

For the detailed formalism used for calculating differential magnification probability distribu-

PoS(AASKA14)084

tions, $p(\mu,z)\mathrm{d}\mu$, for a strong gravitational lens with magnification $\mu > 2$, see Perrotta et al. (2002, 2003). It is expected that the high magnification tail has the form $p(\mu,z) = a(z)\mu^{-3}$ for some function $a(z)$, regardless of the lens population. The $a(z)$ function depends on the nature and evolving number density of the gravitational lenses. Blain (1996) and Perrotta et al. (2002, 2003) consider several options for galaxy lens populations. In the latter, the mass spectrum follows the Sheth & Tormen (1999) formalism. As for the continuum case (Section 2), we assume a singular isothermal sphere density profile for the lens population and assume a non-evolving model, but normalised to the Perotta et al. predictions at an arbitrary redshift of $z = 1$.

A more significant uncertainty in the lensing predictions is the maximum magnification caused by the finite source sizes. We follow Perrotta et al. (2002) in spanning the range of plausible maximum magnifications with $\mu \leq 10$ and $\mu \leq 30$, implying source characteristic radii of $\sim 1-10\ h^{-1}$ kpc; note that if the assumed source sizes are larger than this then the maximum magnifications will be lower, but it is expected that galaxies will be systematically more compact at higher redshifts (e.g. Gunn & Gott 1972) so our assumed sizes are likely fair. Several higher magnification events are known (e.g. Swinbank et al. 2010), but we conservatively neglect this more extreme population. Note that the surface density of strong gravitational lenses increases with maximum magnification. The choices of maximum magnification here is more conservative than that of, for example, Blain (1996) who used $\mu \leq 40$, and Lima et al. (2010) who used $\mu \leq 100$.

Figure 4 shows the results of applying this strong gravitational lensing formalism to a non-evolving HI mass function (Zwaan et al. 2003), and to the evolving mass function of Abdalla et al. (2010). Selecting gravitational lens candidates as those with HI masses of $> 12\ M_*$ in an HI spectral line survey, should yield a sample of between 0.5–5 gravitational lenses per square degree, but with a ~ 100 per cent selection efficiency and the key advantage that the source redshifts are known. Further details, and additional calculations for the Dark Energy Grism survey with *Euclid*, are presented by Serjeant (2014).

5. Science capabilities with SKA

In this Section, we review the main astrophysical results that will come from the strong gravitational lensing programme of the SKA. These will be a combination of results that will exploit the large statistical sample of gravitational lenses, or will use smaller samples of rare gravitational lenses for investigating galaxy formation and cosmology.

5.1 Galaxy formation studies

The hierarchical model for galaxy formation predicts that structure in the Universe formed through the mergers of smaller mass systems, resulting in the tapestry galaxies, clusters of galaxies and large-scale structure that we observe today. A crucial result of this model is that the stellar and gas components of these structures should be embedded within an extended dark matter halo (e.g. Navarro et al. 1996). The form of the radial mass-density profile of the resulting dark matter haloes and the level of low mass substructure within them are both sensitive to the galaxy formation model and the energy of the dark matter particle.

Over the last decade, gravitational lenses have been used to place important constraints on the mass distributions for galaxies at cosmological distances and have tested these predictions

PoS(AASKA14)084

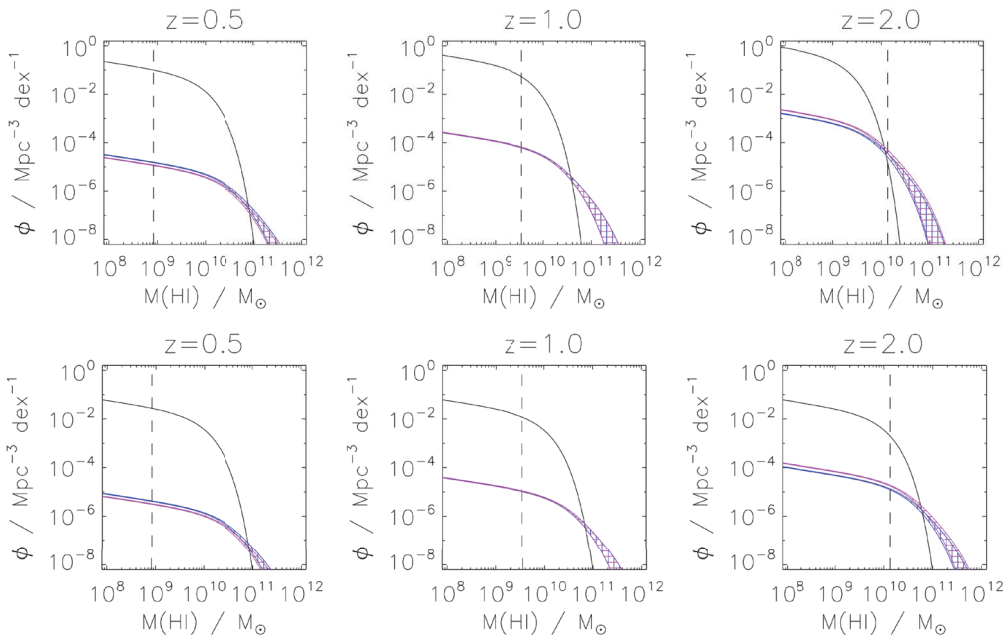

Figure 4: The HI mass function (black line) at redshifts $z = 0.5, 1, 2$, assuming no evolution from the $z = 0$ mass function (top) and assuming an evolving mass function (Bottom). The no-evolution lens population is shown in blue, and the singular isothermal sphere lenses of Perrotta et al. (2002, 2003) are in pink. The hatched regions show the range of maximum magnification $\mu \leq 10$ and $\mu \leq 30$. Note that at $> 12\ M_*$ the observed population is dominated almost entirely by gravitationally lensed HI galaxies.

from hierarchical galaxy formation models. At radio wavelengths, high resolution imaging of gravitationally lensed extended radio sources at mas-scales with VLBI have constrained the inner (within 5–20 kpc) radial mass density profiles for a handful of lens galaxies (e.g. Cohn et al. 2001; Wucknitz et al. 2004), finding that they are close to isothermal (i.e. $\gamma = 2$ where $\rho(r) \propto r^{-\gamma}$). However, the most significant results have come at optical wavelengths, where high resolution imaging with the *HST* of the Einstein rings and arcs of extended blue star-forming galaxies, coupled with stellar kinematics (velocity dispersions and velocity fields) for the lens, have determined radial mass density profiles for a homogenous sample of 58 early-type galaxies at $z \sim 0.2$ (Koopmans et al. 2009). Again, these results find that massive galaxies have on average isothermal density profiles ($\gamma = 2.09 \pm 0.02$).

An important constraint on galaxy formation models from gravitational lensing comes through the detection of low mass substructure around more massive galaxy-scale haloes. The cold dark matter model for galaxy formation predicts a substructure mass function, $dn \propto dm\, m^{-1.9}$ (e.g. Diemand et al. 2007), and a mass fraction in substructure of $< 1\%$. However, the lack of observed satellites found around our own Milky Way suggests that the mass function may be much flatter than thought, which could be due to our Milky Way being a unique case, the substructures being there in the expected abundance, but are dark, or due to a differing physics of the dark matter (e.g. warm dark matter; self-interacting dark matter). Gravitational lenses can be used to test galaxy formation models on these small-scales because the surface brightness distribution of the observed images depends on the form of the potential and they can be (very) sensitive to local perturbations

PoS(AASKA14)084

in the mass model due to small clumps of dark matter in the parent halo (or along the line-of-sight). There are two main applications of this technique. The first is *gravitational imaging* (Koopmans 2005; Vegetti & Koopmans 2009), which uses the information contained within extended arcs to detect the presence of individual substructures and measure their mass properties. This technique has been used to detect substructures with masses as low as $2 \times 10^8\ M_\odot$ out to redshift $z = 0.881$ from infrared adaptive optics imaging at ~ 65 mas resolution (Vegetti et al. 2012). The second method uses *flux-ratio anomalies* (e.g. Metcalf & Madau 2001; Dalal & Kochanek 2002), which occur when the flux-density of one or more point images are different from what is predicted by a smooth mass model. This method is sensitive to the total amount of substructure at the Einstein radius of the lens, and can be used to statistically detect a substructure population down to $\sim 10^4\ M_\odot$. Here, observations at radio wavelengths are important because the flux-ratios are less effected by microlensing from stars in the lensing galaxy (Koopmans et al. 2003) and extinction due to dust is not an issue.

The SKA, when combined with optical telescopes like *Euclid* and the LSST, will revolutionise studies of the mass distributions of galaxies by increasing the overall sample sizes and will allow measurements to be made for samples over a wide range of galaxy mass, type, redshift and environment. The main results that will come from the SKA strong gravitational lensing sample are as follows.

- The main constraints on the radial mass-density profiles of structure will come from high resolution imaging taken in Band 5 (4.6–13.8 GHz) with the SKA1-MID array, which can potentially be coupled with HI velocity field measurements of lenses at low redshift ($z < 0.4$) using spectral line observations in Band 2; combining the constraints from the lensing and dynamics breaks the degeneracies between mass models that are inherent in both methods individually (e.g. Barnabè et al. 2009). The completion of the SKA2 will allow a much larger population of lenses at higher redshift to be studied in this way, which will determine whether there is any evolution in the mass properties of galaxies with epoch and provide a key observational constraint to galaxy formation simulations.

- The very precise measurement of the projected mass within the Einstein radii of galaxies (~ 10 kpc) from strong lensing can be used, with optical and infrared measurements, to independently determine the stellar mass and place constraints on the stellar initial mass function (e.g. Auger et al. 2010). This requires both the redshift of the lens and source to be known, and the modelling of the SKA1-MID array data to determine the Einstein radii of the lenses. The SKA strong gravitational lenses will provide a large statistical sample to investigate variations of the stellar IMF with galaxy type and mass when coupled with the optical/IR imaging provided by *Euclid* and the LSST.

- The SKA1-MID array has the potential to provide important constraints at the low end of the dark matter halo mass function using strong gravitational lensing, which would independently test models for the dark matter particle. The main requirement for the gravitational imaging method is the angular resolution of the data (source structure and signal-to-noise ratio are also important). Follow-up observations with SKA1-MID in Band 5 of those lenses with extended radio sources will give an angular resolution of 0.03–0.1 arcsec, similar to the

PoS(AASKA14)084

resolution provided by the *HST* and ground based adaptive optics telecopes, and so should give detections of substructures down to $\sim 10^8\ M_\odot$ for a large sample of lens galaxies. However, the most important constraints to the dark matter halo mass function will come from observations on VLBI-scales since the mas angular resolution will be sensitive to structures at the $\sim 10^6\ M_\odot$ level (see Figure 5), a mass regime where various models for the dark matter particle strongly differ. Therefore, an SKA1-MID array that is capable of VLBI observations with, for example, the EVN, is required for this unique science goal of the strong gravitational lensing programme to be achieved.

- It will also be possible to place constraints on the substructure mass function with the SKA1-MID array using those gravitational lenses with compact (point) emission from AGN (see Figure 2). It is expected that there will be ~ 300 four image gravitational lens systems from the SKA1-MID survey that can be used for this; a factor of about 50 more than are currently known. This will require the precise measurement of the flux-ratios of the point-like images; this will be done through monitoring the systems with the SKA1-MID Band 5 to achieve the desired angular resolution and to determine if the fluxes have been changed by intrinsic variability and the gravitational lensing time-delay (the latter can be used to determine the cosmological parameters, see below).

- The sensitivity of the SKA will allow the routine detection of highly de-magnified core lensed images that are predicted to form at < 100 pc from the centre of the lensing galaxy (for shallower than isothermal lensing potentials). Such images probe the central mass distribution and can be used to constrain the central density profile where dark matter is insignificant, but the influence of both the central supermassive black hole (SMBH) and the central stellar cusp are important (e.g. Mao et al. 2001). Understanding the central regions of galaxies is important because they are directly relevant to the question of how the SMBH influences (and is influenced by) the process of galaxy formation. This central question has been debated since the discovery of the relation between the SMBH mass and the bulge stellar velocity dispersion on much larger scales (Ferrarese & Merritt 2000). However, the detection of core-lensed images is extremely rare due to their very high de-mganification ($\sim 10^{-4}$–10^{-5}) relative to the other lensed images. There is currently only one confirmed case (Winn et al. 2004).

  Targeted observations with SKA1-MID should allow the detection of core-lensed images in about 100 systems, compared to the 20–30 accessible to e-MERLIN, provided that an angular resolution of about < 100 mas can be achieved, as is expected from observations at Band 5 with the SKA1-MID. The large frequency coverage of Band 5 is also required to confirm that the emission is from the central image and not the lensing galaxy (see Figure 6). With the SKA2, measurements of the central-image properties of thousands of lens systems will be possible, and hence will provide a census of central potentials in many different lensing galaxies as a function of redshift, mass and environment. With these sensitivities, non-detections become just as interesting as detections because they typically indicate SMBH masses greater than the M–σ relation, unusually steep central density profiles, or both. Moreover, in combination with VLBI studies, as could be done if the SKA operated as part of a VLBI array, it may be possible to detect splitting of the central image on mas-

PoS(AASKA14)084

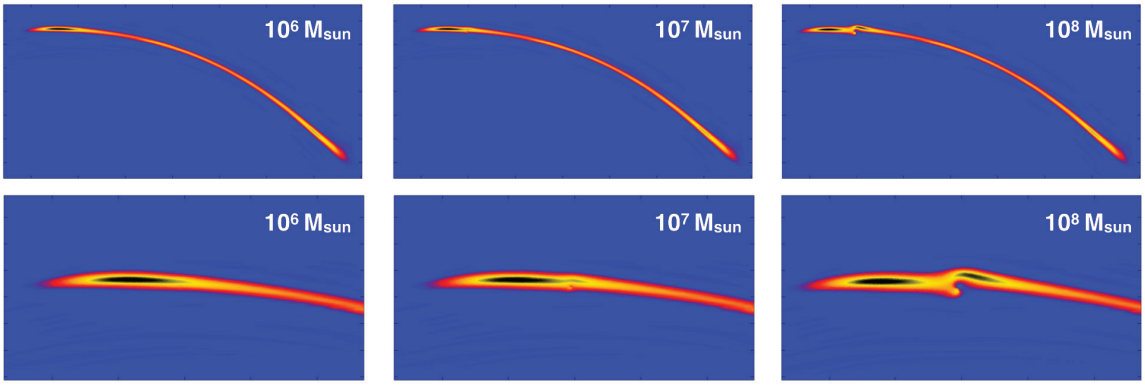

Figure 5: Simulations of the effect low mass dark matter haloes have on arc surface brightness distributions for a 10^6 $M_\odot$ (left), 10^7 $M_\odot$ (middle) and 10^8 $M_\odot$ (right) substructure. The top row of images show the full gravitational arc, detected on VLBI scales with an SKA1-MID+VLBI array, and the bottom row show a zoomed in view of the region most affected by the substructure. The 10^7 $M_\odot$ and 10^8 $M_\odot$ substructures can be seen directly in the data, whereas the 10^6 $M_\odot$ substructure would need to be detected using the gravitational imaging technique.

scales due to the combined effect of the black hole and central stellar cusp; in these cases all degeneracies can be broken and both components' masses can be measured separately.

5.2 Studies of the lensed source population

Although the SKA will transform our understanding of the high redshift Universe, the sensitivity and angular resolution of the telescope can be increased by orders of magnitude (at no additional cost) through using the magnification provided by gravitational lenses. In this respect, almost any high-redshift object science application with the SKA could benefit from the use of natural telescopes, providing a model for the lens (the optics) is well understood; there are now several sophisticated methods available for the reconstruction of the distorted sources behind gravitational lenses (e.g. Wucknitz 2004; Vegetti & Koopmans 2009; Hezaveh et al. 2013).

Here we briefly summarise some of the principle applications of the SKA strong gravitational lensing sample for studying the background source population.

- The increase in sensitivity (factors of 5–100) will allow a population of objects that could not otherwise be observed to be detected and studied in detail. For example, the faintest known continuum radio source ($S_{5\ \mathrm{GHz}} \sim 1$ μJy; Jackson 2011) is gravitationally lensed (see Figure 7). The first immediate result will be to study the parent population of sources that will be detected with the SKA2 using the SKA1-MID array. The form of the parent population luminosity function is sensitive to the number of gravitational lenses that will be detected in the deep continuum surveys to be carried out with SKA1-MID. For example, about 440 gravitational lenses should be detectable in the SKA1-MID ultra deep survey (1 deg^2; rms 0.05 μJy; see Prandoni & Seymour 2014). Furthermore, the magnification provided by the gravitational lenses (~ 10) will enable radio sources with star-formation rates of > 1 $M_\odot$ yr^{-1} at $z \sim 3$–4 and > 5 $M_\odot$ yr^{-1} at $z \sim 6$ to be detected. These sources would directly probe the

PoS(AASKA14)084

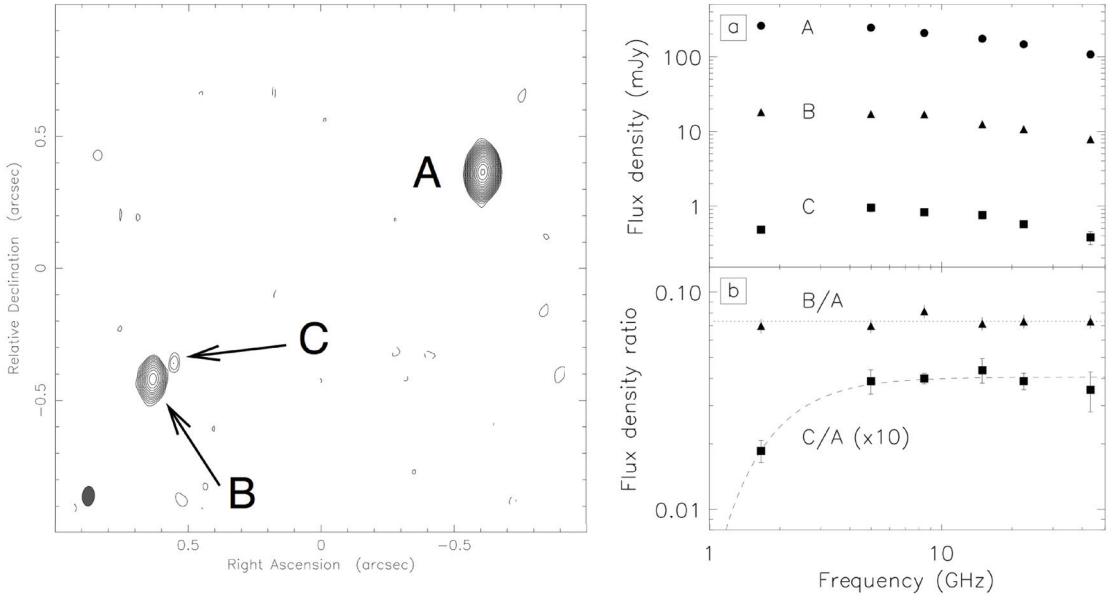

Figure 6: The gravitational lens system J1632-0033 is the first and only gravitational lens system to have a central lensed images for a galaxy-scale system. Images A and B are of the redshift 3.42 lensed radio sources, whereas image C is the core lensed image. The spectra of the three images are identical are high frequencies, since propagation effects (free-free absorption within the lensing galaxy) are less severe (Winn et al. 2004).

radio luminosity function in a regime that is around an order magnitude lower in luminosity than would be possible without the magnification from gravitational lensing.

- The magnification will be particularly important for studying spectral line sources for which the large observational bandwidths will not increase the detectability, but will increase the volume that can be searched. An example is presented in Figure 7, where the most distant radio spectral line in emission is shown (water maser at $z = 2.64$; Impellizzeri et al. 2008). Water maser systems are expected to be highly abundant at high redshift (McKean et al. 2011) and could be used to measure the masses of supermassive black holes in distant galaxies through observations of the maser line kinematics over time (e.g. see Kuo et al. 2013 for studies at low redshift). Coupled with high angular resolution imaging (see below) of highly magnified water maser lines, it could also be possible to measure geometric distances for radio sources at moderate redshifts ($z \sim 0.7$–1) and test models for dark energy. In addition, water maser emission is known to be highly variable and so could also provide an independent measurement of dark energy through measuring the time-delay due to gravitational lensing (see below). High resolution observations would be possible using the SKA1-MID array Band 5 (probing $z \sim 0.6$–4) for detection and variability monitoring, and with an SKA1-MID array that is part of a global VLBI array for imaging. Also, it may be possible to detect the HI absorption forrest from the Epoch of Reionization by targeting the population of high redshift objects that have had their intrinsic flux density boosted by

PoS(AASKA14)084

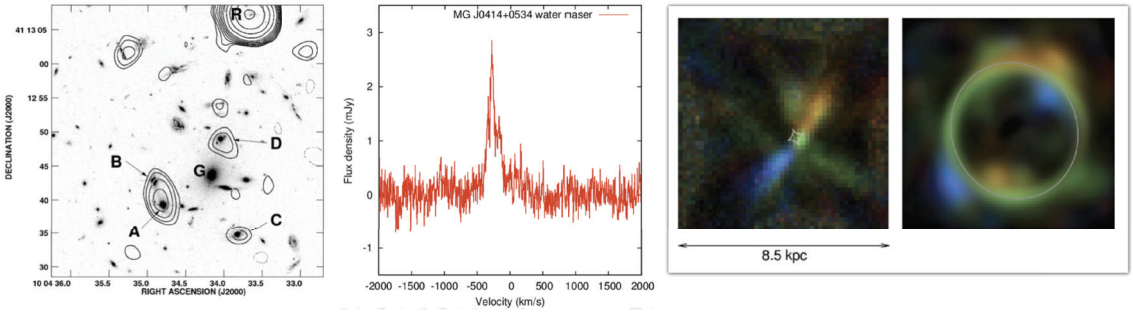

Figure 7: (left) JVLA imaging of the highly magnified radio source (images A, B, C, D) behind the lensing cluster SDSS J1004+4112 (Jackson 2011). (middle) The spectral line emission detected from the most distant known water maser galaxy, MG J0414+0534 at redshift 2.64 (Impellizzeri et al. 2008). (right) The CO (2–1) Einstein ring from the z = 4.12 quasar PSS J2322+1944 at 0.3 arcsec resolution with the VLA (right) and the reconstructed source (left) after lens modelling, which shows a rotation disk of gas (Riechers et al. 2008).

gravitational lensing. Such observations would use the SKA1-LOW array.

- The magnification provided by the lens increases the solid angle of the background source, which allows the object to be observed at high angular resolution. Such observations will be most useful for studying the morphology of radio sources at high redshifts and the structure of their various thermal and non-thermal components on pc to sub-kpc scales; e.g. star-formation, atomic and molecular gas distributions and AGN activity. An example of what can potentially be done is also shown in Figure 7, where the CO molecular gas distribution of a redshift ~ 4 quasar (Riechers et al. 2008) has been determined after correcting for the effect of the lens. This will require a high frequency capability (< 30 GHz) to investigate high redshift galaxies ($z > 3$), and the full collecting area of the SKA2 to study the formation of galaxies at the Epoch of Reionization ($z \sim 6$–10).

5.3 Studies of cosmology

Gravitational lenses can be used to measure distances at cosmological redshifts, and are therefore potentially important for cosmology. The most direct application of gravitational lensing for cosmology is the measurement of the Hubble constant, which can be achieved by monitoring gravitational lenses with background sources that are variable in flux-density. As the images result from multiple different light-paths, the measurement of time delays between image variations gives a measurement of the difference in angular diameter distance, and if the redshifts of the source and lens are known, this in turn measures the Hubble constant, together with a secondary dependence on other cosmological parameters such as Ω_m and Ω_Λ. The first H_0 measurements were conducted on gravitational lenses discovered in the radio, mainly using the VLA in the 1990s (e.g. Biggs et al. 1999; Fassnacht et al. 2002). Subsequent H_0 determinations were predominantly made using gravitational lens systems containing radio-quiet, optically-selected quasars, mainly due to the availability of dedicated small optical telescopes, for example, recent measurements of time-delays have been dominated by the COSMOGRAIL collaboration (e.g. Eulaers et al. 2013).

PoS(AASKA14)084

The major systematic problem with gravitational lens determinations of H_0 is that, as well as the time delays, accurate mass models of the lensing galaxies and the surrounding masses are needed. This process is subject to complex degeneracies (e.g. Schneider & Sluse 2013), and needs careful modelling and treatment of the systematics (e.g. Suyu et al. 2010) to achieve robust results. Nevertheless, two well-modelled gravitational lenses in which the systematics are under control give errors on H_0 (dominated by systematics) of about 5% ($H_0 = 75^{+2.4}_{-3.6}$ km s^{-1} Mpc^{-1}; Suyu et al. 2013), and further progress is likely in the next few years. Since H_0 is not determined by CMB measurements unless assumptions are made about other cosmological parameters (such as zero curvature or $w = -1$), very accurate standalone measurements of H_0 are capable of improving other cosmological constraints; for example, the dark energy figure of merit can be improved by factors of several (Linder 2011), and the more reliable gravitational lensing results already provide a constraint of $w = -1.52^{+0.19}_{-0.20}$ at the 68 per cent confidence level (Suyu et al. 2014).

The second major cosmological application of gravitational lensing uses the statistics of the numbers of gravitational lenses or the properties of gravitational lenses in well-selected samples. These are sensitive both to the numbers and masses of the potential lensing galaxies at particular redshifts (and hence to galaxy evolution), to the distribution and luminosity function of the sources, and to the cosmological world model. Thus, we can use any samples in which the lenses and sources are well understood to constrain cosmology, or use a world model, together with lens surveys to investigate galaxy evolution. In the early days, gravitational lensing statistics were used to confirm the existence of Λ-like terms in the world model (e.g. $\Omega_\Lambda = 0.69^{+0.14}_{-0.27}$; Chae et al. 2002); later, gravitational lensing statistics were used to provide evidence for (lack of) evolution in elliptical galaxies (Chae & Mao 2003). Recently Oguri et al. (2012) have argued that lens statistics constrain Ω_Λ more robustly, $\Omega_\Lambda = 0.79^{+0.06}_{-0.07}$ (stat.) $^{+0.06}_{-0.06}$ (syst.), and are consistent with a $w = -1$ equation of state, although the latter requires the combination with other cosmological probes.

The main cosmological applications of the SKA gravitational lens sample are as follows.

- Our simulations indicate that the SKA will provide a much more powerful probe of gravitational lenses in the high-redshift universe (see Figure 1). On the most optimistic assumption, that of isothermal potentials in low-mass, high-redshift lensing galaxies, vast numbers of high-redshift lenses will be produced. The likelihood that this assumption is false, and that such galaxies will be more dark-matter dominated and hence less efficient gravitational lenses, itself implies that statistics of an SKA lensing survey will contain information about mass distributions in high-redshift galaxies. Improvements in the cosmological world model, in particular in w, are likely to result from the discovery and followup of a large number of new lens systems. In particular, the lensing statistics of samples from CLASS and the SDSS are based on samples of just 13 and 19 gravitational lenses, respectively. Increasing such samples by orders of magnitude, will result in the uncertainties being dominated by the systematics related to the assumed galaxy evolution model.

- Increasing the samples of gravitational lenses by a factor of $> 10^2$ will allow us to monitor gravitational lenses for time delays and be more selective in using those gravitational lenses for which the systematics can be well controlled. This will require the AGN-dominated systems to be observed and monitored with the SKA1-MID array in Band 5 to provide better data for gravitational lens modelling and to determine time-delay light curves (observations

PoS(AASKA14)084

at 8.46 GHz at 0.2 arcsec resolution have been successfully applied in the past). Constraints on w are then possible by combining the gravitational lensing time-delay data (which are mainly sensitive to H_0) and the CMB data from *Planck* (e.g. Suyu et al. 2013). Time-delay measurements will become more powerful both with numbers, and with a larger range of redshifts of gravitational lenses for which information can be extracted, as the statistical uncertainties are dominated by the handful of currently known systems that are appropriate for such an analysis.

- Increasing samples by factors of $> 10^2$ will also yield rare and cosmologically important objects. The ideal lens for cosmology would be one in which two sources are present at different redshift (e.g. Collett & Auger 2014), but in which one is variable, such as a radio quasar. This allows an angular distance measurement without problems of mass degeneracy, providing kinematical information for the gravitational lens is known; a few such lenses give w essentially free of systematic errors (see Schneider 2014 for discussion of the systematics). Such systems will be a factor 500-1000 rarer than "standard" radio lenses, because the lensing probability on any one line-of-sight is 0.1-0.2%. This is within the likely yield of the SKA2 surveys.

6. Summary

The SKA era will transform our understanding of the Universe and strong gravitational lenses will play an important role in investigating galaxy formation and evolution over cosmic time, the properties of dark matter and the cosmological world model. This review has demonstrated that the SKA1-MID array is capable of detecting $\sim 10^5$ new radio-loud gravitational lenses, providing there is sufficient sensitivity on 0.25–0.5 arcsec baselines and a frequency coverage between 1–14 GHz. A more conservative estimate suggests that $\sim 10^4$ should be straightforwardly identified in an SKA1-MID array survey at ~ 3 μJy beam^{-1} sensitivity and with a 3π sr sky area, with the main uncertainties being dominated by the luminosity function of the background source population. Coupling the SKA1-MID data with optical and infrared surveys, and further high resolution radio imaging, will be needed to identify the remaining gravitational lenses in the expected wide-area sky surveys. An initial pilot survey, matched to the sky area covered with *Euclid* should find several thousand new gravitational lenses from only 3 months of observing with the SKA1-MID array. Such a pilot survey would test the lensing statistics and lens identification methods. Finally, we note that it is important for several of the unique science goals of the SKA strong gravitational lensing programme that there is the VLBI capability of the SKA.

References

Abdalla, F. B., Blake, C., & Rawlings, S. 2010, MNRAS, 401, 743
Auger, M. W., Treu, T., Gavazzi, R., et al. 2010, ApJL, 721, L163
Barnabè, M., Czoske, O., Koopmans, L. V. E., et al. 2009, MNRAS, 399, 21
Biggs, A. D., Browne, I. W. A., Helbig, P., et al. 1999, MNRAS, 304, 349
Blain, A. W. 1996, MNRAS, 283, 1340

PoS(AASKA14)084

Bolton, A. S., Burles, S., Koopmans, L. V. E., et al. 2008, ApJ, 682, 964
Browne, I. W. A., Wilkinson, P. N., Jackson, N. J. F., et al. 2003, MNRAS, 341, 13
Chae, K.-H., Biggs, A. D., Blandford, R. D., et al. 2002, Physical Review Letters, 89, 151301
Chae, K.-H. & Mao, S. 2003, ApJL, 599, L61
Cohn, J. D., Kochanek, C. S., McLeod, B. A., et al. 2001, ApJ, 554, 1216
Collett, T. E. & Auger, M. W. 2014, MNRAS, 443, 969
Condon, J. J., Cotton, W. D., Fomalont, E. B., et al. 2012, ApJ, 758, 23
Dalal, N. & Kochanek, C. S. 2002, ApJ, 572, 25
De Lucia, G. & Blaizot, J. 2007, MNRAS, 375, 2
Deane, R. P., Rawlings, S., Garrett, M. A., et al. 2013, MNRAS, 434, 3322
Diemand, J., Kuhlen, M., & Madau, P. 2007, ApJ, 657, 262
Eulaers, E., Tewes, M., Magain, P., et al. 2013, A&A, 553, A121
Fassnacht, C. D., Xanthopoulos, E., Koopmans, L. V. E., et al. 2002, ApJ, 581, 823
Ferrarese, L. & Merritt, D. 2000, ApJL, 539, L9
González-Nuevo, J., Lapi, A., Fleuren, S., et al. 2012, ApJ, 749, 65
Gunn, J. E. & Gott, III, J. R. 1972, ApJ, 176, 1
Hewitt, J. N., Turner, E. L., Lawrence, C. R., et al. 1992, AJ, 104, 968
Hezaveh, Y., Dalal, N., Holder, G., et al. 2013, ApJ, 767, 9
Impellizzeri, C. M. V., McKean, J. P., Castangia, P., et al. 2008, Nature, 456, 927
Inada, N., Oguri, M., Shin, M.-S., et al. 2012, AJ, 143, 119
Jackson, N. 2011, ApJL, 739, L28
Kitzbichler, M. G. & White, S. D. M. 2007, MNRAS, 376, 2
Koopmans, L. V. E. 2005, MNRAS, 363, 1136
Koopmans, L. V. E., Biggs, A., Blandford, R. D., et al. 2003, ApJ, 595, 712
Koopmans, L. V. E., Bolton, A., Treu, T., et al. 2009, ApJL, 703, L51
Koopmans, L. V. E., Browne, I. W. A., & Jackson, N. J. 2004, New Astronomy Reviews, 48, 1085
Kuo, C. Y., Braatz, J. A., Reid, M. J., et al. 2013, ApJ, 767, 155
Lima, M., Jain, B., & Devlin, M. 2010, MNRAS, 406, 2352
Linder, E. V. 2011, Phys. Rev. D, 84, 123529
Mao, S., Witt, H. J., & Koopmans, L. V. E. 2001, MNRAS, 323, 301
McKean, J. P., Browne, I. W. A., Jackson, N. J., et al. 2007, MNRAS, 377, 430
McKean, J. P., Browne, I. W. A., Jackson, N. J., et al. 2005, MNRAS, 356, 1009
McKean, J. P., Impellizzeri, C. M. V., Roy, A. L., et al. 2011, MNRAS, 410, 2506
Metcalf, R. B. & Madau, P. 2001, ApJ, 563, 9
Myers, S. T., Jackson, N. J., Browne, I. W. A., et al. 2003, MNRAS, 341, 1
Navarro, J. F., Frenk, C. S., & White, S. D. M. 1996, ApJ, 462, 563
Negrello, M., Hopwood, R., De Zotti, G., et al. 2010, Science, 330, 800
Oguri, M., Inada, N., Strauss, M. A., et al. 2012, AJ, 143, 120
Perrotta, F., Baccigalupi, C., Bartelmann, M., et al. 2002, MNRAS, 329, 445
Perrotta, F., Magliocchetti, M., Baccigalupi, C., et al. 2003, MNRAS, 338, 623
Riechers, D. A., Walter, F., Brewer, B. J., et al. 2008, ApJ, 686, 851
Schneider, P. 2014, A&A, 568, L2
Schneider, P. & Sluse, D. 2013, A&A, 559, A37

PoS(AASKA14)084

Serjeant, S. 2014, ApJL, 793, L10
Sheth, R. K. & Tormen, G. 1999, MNRAS, 308, 119
Springel, V., White, S. D. M., Jenkins, A., et al. 2005, Nature, 435, 629
Suyu, S. H., Auger, M. W., Hilbert, S., et al. 2013, ApJ, 766, 70
Suyu, S. H., Marshall, P. J., Auger, M. W., et al. 2010, ApJ, 711, 201
Suyu, S. H., Treu, T., Hilbert, S., et al. 2014, ApJL, 788, L35
Swinbank, A. M., Smail, I., Longmore, S., et al. 2010, Nature, 464, 733
Turner, E. L., Ostriker, J. P., & Gott, III, J. R. 1984, ApJ, 284, 1
Vegetti, S. & Koopmans, L. V. E. 2009, MNRAS, 392, 945
Vegetti, S., Lagattuta, D. J., McKean, J. P., et al. 2012, Nature, 481, 341
Vieira, J. D., Marrone, D. P., Chapman, S. C., et al. 2013, Nature, 495, 344
Walsh, D., Carswell, R. F., & Weymann, R. J. 1979, Nature, 279, 381
Wilman, R. J., Miller, L., Jarvis, M. J., et al. 2008, MNRAS, 388, 1335
Winn, J. N., Rusin, D., & Kochanek, C. S. 2004, Nature, 427, 613
Wucknitz, O. 2004, MNRAS, 349, 1
Wucknitz, O., Biggs, A. D., & Browne, I. W. A. 2004, MNRAS, 349, 14
York, T., Jackson, N., Browne, I. W. A., et al. 2005, MNRAS, 361, 259
Zwaan, M. A., Staveley-Smith, L., Koribalski, B. S., et al. 2003, AJ, 125, 2842

PoS(AASKA14)084

PROCEEDINGS OF SCIENCE

The Astrophysics of Star Formation Across Cosmic Time at $\gtrsim$10 GHz with the Square Kilometre Array

Eric J. Murphy[1], **Mark T. Sargent**[2*], **Rob J. Beswick**[3], **Clive Dickinson**[3], **Ian Heywood**[4,5], **Leslie K. Hunt**[6], **Minh T. Hyunh**[7], **Matt Jarvis**[8,9], **Alexander Karim**[10], **Marita Krause**[11], **Isabella Prandoni**[12], **Nicholas Seymour**[13], **Eva Schinnerer**[14], **Fatemeh S. Tabatabaei**[14], **Jeff Wagg**[15]

[1]*IPAC, Caltech, MC 220-6, Pasadena CA, 91125, USA;* [2]*Astronomy Centre, Department of Physics and Astronomy, University of Sussex, Brighton BN1 9QH, UK;* [3]*Jodrell Bank Centre for Astrophysics, The University of Manchester, Oxford Rd, Manchester M13 9PL, UK;* [4]*CSIRO Astronomy & Space Science, P.O. Box 76, Epping, NSW 1710, Australia;* [5]*RATT, Department of Physics and Electronics, Rhodes University, PO Box 94, Grahamstown 6140, South Africa;* [6]*INAF - Osservatorio Astrofisico di Arcetri, Largo E. Fermi 5, 50125, Firenze, Italy;* [7]*ICRAR, University of Western Australia, Stirling Highway, Crawley, Western Australia 6009, Australia;* [8]*Astrophysics, University of Oxford, Denys Wilkinson Building, Keble Road, Oxford, OX1 3RH, UK;* [9]*Department of Physics, University of the Western Cape, Bellville 7535, South Africa;* [10]*Argelander-Institut für Astronomie, Auf dem Hügel 71, 53121 Bonn, Germany;* [11]*Max-Planck-Institut für Radioastronomie, Auf dem Hügel 69, 53121 Bonn, Germany;* [12]*INAF - Istituto di Radioastronomia, Via Gobetti 101, Bologna, Italy;* [13]*CASS, P.O. Box 76, Epping, NSW, 1710, Australia;* [14]*Max-Planck-Institut für Astronomie, Königstuhl 17, 69117 Heidelberg, Germany;* [15]*Square Kilometre Array Organisation, Lower Withington, Cheshire, UK*
Email: emurphy@ipac.caltech.edu

In this chapter, we highlight a number of science investigations that are enabled by the inclusion of Band 5 (4.6 – 13.8 GHz) for SKA1-MID science operations, while focusing on the astrophysics of star formation over cosmic time. For studying the detailed astrophysics of star formation at high-redshift, surveys at frequencies $\gtrsim$10 GHz have the distinct advantage over traditional $\sim$1.4 GHz surveys as they are able to yield higher angular resolution imaging while probing higher rest frame frequencies of galaxies with increasing redshift, where emission of star-forming galaxies becomes dominated by thermal (free-free) radiation. In doing so, surveys carried out at $\gtrsim$10 GHz provide a robust, dust-unbiased measurement of the massive star formation rate by being highly sensitive to the number of ionizing photons that are produced. To access this powerful star formation rate diagnostic requires that Band 5 be available for SKA1-MID. We additionally present a detailed science case for frequency coverage extending up to 30 GHz during full SKA2 operations, as this allows for highly diverse science while additionally providing contiguous frequency coverage between the SKA and ALMA, which will likely be the two most powerful interferometers for the coming decades. To enable this synergy, it is crucial that the dish design of the SKA be flexible enough to include the possibility of being fit with receivers operating up to 30 GHz.

Advancing Astrophysics with the Square Kilometre Array
June 8-13, 2014
Giardini Naxos, Italy

PoS(AASKA14)085

1. Introduction

Currently, the SKA1 System Baseline Design (Dewdney et al. 2013) states that SKA1-MID dishes will be capable of operations up to at least 20 GHz, but only three out of five frequency bands (spanning a total range of $0.350 - 13.8$ GHz) will be populated. In this chapter, we discuss the scientific motivation for the inclusion of the highest-frequency band (i.e., Band 5; $4.6 - 13.8$ GHz) during SKA1-MID operations, as it opens up unique science unachievable with any other band. Observations at frequencies $\gtrsim$10 GHz have the distinct advantage over those at $\sim$1 GHz as they probe higher rest frame frequencies of galaxies with increasing redshift, where emission becomes dominated by *thermal* (free-free) radiation. Radio free-free emission is both largely extinction free and can be directly related to the ionizing photon rate arising from newly formed massive stars. Evidence for this has been indicated by detailed studies of star-forming regions in the Galaxy (e.g., Mezger & Henderson 1967), nearby dwarf irregulars (e.g. Klein & Graeve 1986), the nuclei of normal galaxies (e.g., Turner & Ho 1983, 1994) and starbursts (e.g., Klein et al. 1988; Turner & Ho 1985), Wolf-Rayet galaxies (e.g., Beck et al. 2000), as well as high resolution investigations of super star clusters within nearby blue compact dwarfs (e.g., Turner et al. 1998; Kobulnicky & Johnson 1999; Johnson et al. 2009). By *directly* measuring the ionizing photon rate from massive stars independent of dust, such observations provide an unbiased estimate of the massive star formation rate. With $\sim$200 km baselines, observations at $\gtrsim$10 GHz can achieve a maximum angular resolution of $\lesssim 0\farcs03$, sampling $\approx$250 pc scales within disk galaxies at $z \gtrsim 1$ and allowing for detailed investigations of galaxy energetics and distributed star formation during the peak of cosmic star formation activity.

In this chapter, we focus on a number of critical advancements in our understanding of *star formation* over cosmic time that can only be realized through observations at $\gtrsim$10 GHz with the SKA. The science goals presented here are largely based on the ultra-deep SKA1-MID/Band 5 reference survey outlined in Prandoni & Seymour (2015). We also focus on galaxies at large cosmological distances, and refer the reader to the chapter by Beswick et al. (2015) for a detailed discussion on studying the astrophysics of star formation within nearby galaxies. While Band 5 is also critical for studies of AGN, we only provide a few examples of such instances as a comprehensive overview of this topic is beyond the scope of the chapter. For example, by being in the Faraday-thin regime, observations at $\gtrsim$10 GHz allow for a clear view of the intrinsic polarization properties for detailed exploration of the internal physics, magnetic fields, and thermal plasma environments of AGN cores. Additionally, observations at $\gtrsim$10 GHz provide access to maser line emission that can be used to identify AGN.

We additionally present a detailed science case for frequency coverage extending up to 30 GHz (where ALMA Band 1 will begin) during full SKA2 operations, as this is critical for a proper accounting of the energetic processes powering galaxies; non-thermal (synchrotron), free-free (bremsstrahlung), and thermal dust emission all start to contribute at somewhat commensurate levels at such frequencies. The science that is enabled by the inclusion of this frequency range is highly diverse. For instance, this spectral window opens up the possibility for investigations of the star formation law, which relates the star formation rate and gas surfaces densities in galaxies, by providing access to the low-J rotational lines of CO $J = 1 \rightarrow 0$ and $J = 2 \rightarrow 1$ for galaxies in the redshift range of $z = 2.8 - 10.5$. Such a capability will be highly synergistic with ALMA

PoS(AASKA14)085

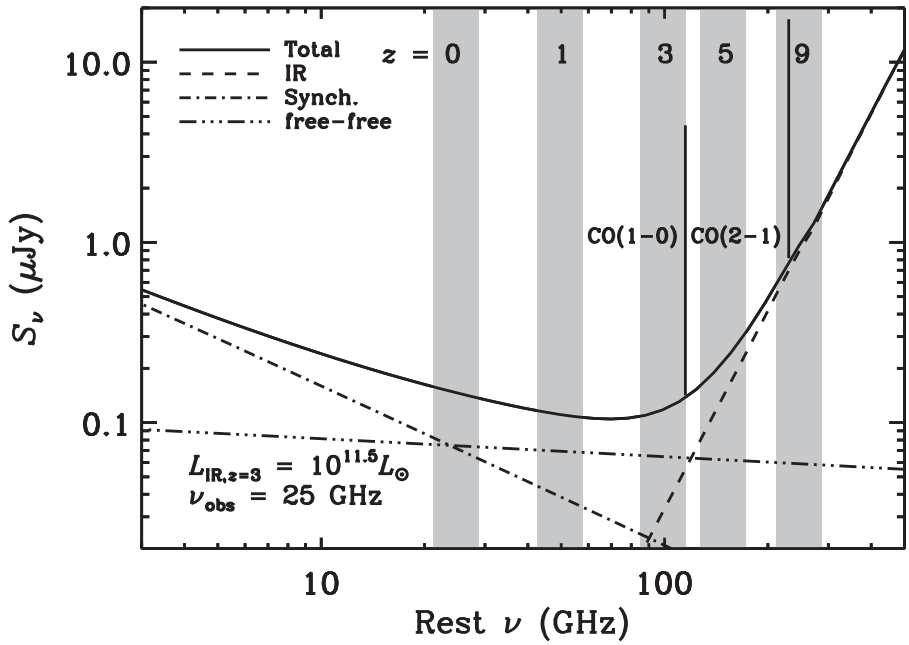

Figure 1: A rest frame model radio-to-infrared galaxy spectrum having an IR (8-1000μm) luminosity of $L_{\rm IR} = 10^{11.5} L_\odot$ at redshift 3. The shaded regions indicate where a 25 GHz observation (see §3), having 30% bandwidth in the observed frame, would redshift for $z = 0, 1, 3, 5$, and 9. Individual emission components (free-free, synchrotron, and thermal dust) are shown, indicating that at this frequency range between 30 and 100 GHz (in the rest frame) is most sensitive to free-free emission, making this spectral window extremely robust for accurately measuring the star formation rates of high-redshift galaxies. Additionally shown are CO ($J = 1 \rightarrow 0$) and CO ($J = 2 \rightarrow 1$) spectral lines having a line-to-IR flux ratio of M 82 and 1000 km s^{-1} widths. These lines, which are essential for accurately measuring the molecular gas content of galaxies as they trace the bulk of the cold molecular gas component, are accessible in the redshift range of $z = 2.8 - 10.5$ over the full $20 - 30$ GHz spectral window.

observations that map out the peak of the dust emission for galaxies in a similar redshift range.

2. Astrophysics Enabled by the Inclusion of Band 5 in SKA1-MID

2.1 Detailed Radio Spectral Analyses with Band 5

Synchrotron emission provides unique information on the most powerful phase of star formation (i.e., supernova), as well as the most energetic components of the interstellar medium (i.e., the magnetic fields and cosmic rays). The latter each contribute significantly to the total pressure of the interstellar gas, which is important for the onset of star formation, formation of galactic bubbles, and outflows (Parker 1966; Ferrière 2001; Cox 2005). To what extent cosmic rays and magnetic fields influence the energy balance, and thus the evolution of galaxies, remains an open and highly debated question. This, and the origins and energetics of the synchrotron emission in general, can be addressed especially well through detailed studies of the radio spectral energy distribution (SED). The fact that at radio wavelengths most surveys have targeted a single radio frequency/band (mainly 1.4 GHz) has prevented a proper radio-SED analysis both on galaxy-wide scales and lo-

PoS(AASKA14)085

cally within individual galaxies. However, star-formation timescales and histories (SFH) can shape radio spectral indices and lead to larger variations than currently known.

The combination of the various SKA1-MID reference surveys outlined in the overview chapter (Prandoni & Seymour 2015) will provide unprecedented information about the shape of the radio spectrum of low- and high-redshift sources. This, in turn, will yield a much better understanding of the relative contributions of thermal and non-thermal emission as the thermal fraction increases with frequency. For star-forming galaxies near the apparent peak epoch in the star formation rate density at $z \sim 2-3$, the emission observed in Band 5 at ~ 10 GHz arises at a rest-frame frequency of $30-40$ GHz, probing the spectral regime where free-free emission begins to dominate over synchrotron (e.g., see Figure 1). This means that it is crucial to examine how radio spectra evolve with time and whether they change significantly with SFH (e.g., Murphy 2009; Schleicher & Beck 2013). Young starbursts in the local Universe have flat thermal-like radio spectral indices (Deeg et al. 1993; Roussel et al. 2003; Hunt et al. 2004, 2005) and high star formation rate surface-density regions are fainter at low radio frequencies than more tenuous regions (Murphy et al. 2011; Heesen et al. 2014). At high redshift, there is currently no consensus on age-dependent spectral indices of starbursts: while some distant starbursts appear to have a flatter radio spectral index (Hunt & Maiolino 2005; Valtchanov et al. 2011) there is also evidence to the contrary (Bourne et al. 2011; Thomson et al. 2014).

The unprecedented sensitivity of SKA1-MID and SKA2 will open a wide window to the radio Universe, which is ideal for coherent multi-band surveys allowing for the first time robust radio-SED analyses for distinct galaxy building blocks such as central starbursts/AGNs, spiral arms, star forming regions/complexes and the diffuse interstellar media (see also §2.2.1). SKA1-MID capabilities at $\gtrsim$10 GHz will be fundamental for assessing truly how the star formation rate density evolves over cosmic time. Only with high-frequency observations can the SKA provide necessary constraints for any changes of radio spectral index with redshift, as expected for increased dominance of free-free emission in younger objects (Hunt et al. 2005; Hirashita & Hunt 2006).

There is growing evidence that starbursts deviate from the “star-forming main sequence" because of intense, spatially concentrated star formation activity, which is reflected by the increased dust temperature (Condon et al. 1991; Ciliegi et al. 2007; Melbourne et al. 2012; Hayward et al. 2012; Symeonidis et al. 2013; Magnelli et al. 2014) and by a flattening of the radio spectral index (Murphy et al. 2013). Radio spectral indices may also be important to help diagnose mergers (Murphy 2013), and estimate their contribution to the starburst fraction at high redshift, currently estimated to be about 10-15% (Rodighiero et al. 2011; Sargent et al. 2012). Radio-SED analysis with SKA1-MID will address the most pressing questions on: (a) the origin of the synchrotron emission in various galactic environments, (b) the change in the shape of the SEDs, reflecting changes in radiative processes due to varying physical conditions (e.g., synchrotron spectral index with redshift), and (c) the balance between the total energy budget of galaxies emitted in radio and infrared over cosmic time. Such investigations can only be conducted using Band 5 in combination with lower frequency observations to cover the necessary frequency range for a coherent radio-SED analysis.

2.2 Studying Star Formation in the High-Redshift Universe with Band 5

To date, deep field radio surveys aimed at measuring the star formation history of the Universe

PoS(AASKA14)085

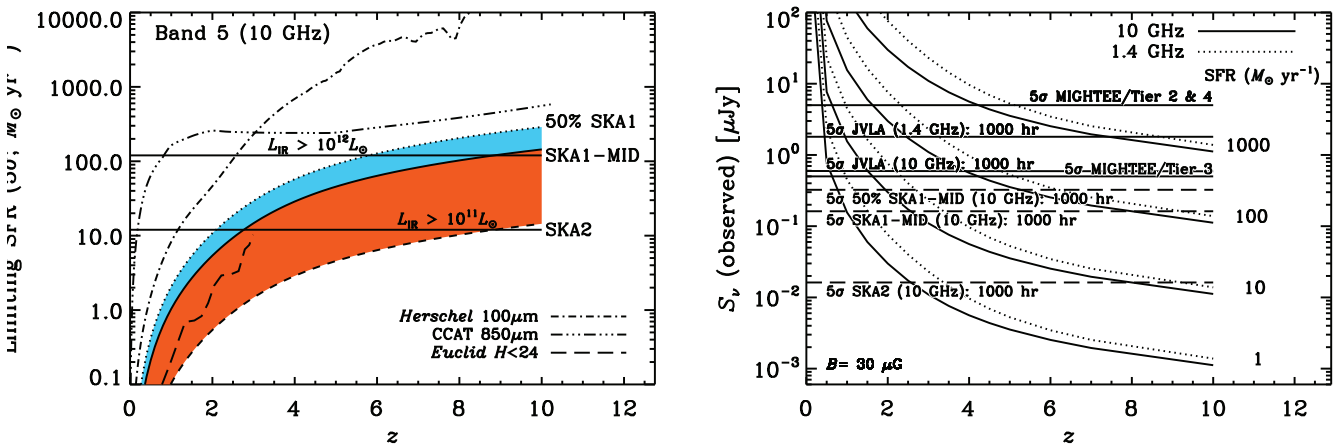

Figure 2: *Left:* The expected 10 GHz selection function (5 σ) for unresolved star-forming galaxies after a 1000 hr observation with SKA1-MID and SKA2 given in units of limiting star formation rate as described by the ultra-deep Band 5 reference survey in Prandoni & Seymour (2015). Sensitivities are taken from Braun (2013) assuming 5 GHz of usable bandwidth and a 0.″1 synthesized beam. The case of a 50% less sensitive SKA1-MID is also shown. For comparison, we superimpose the (5 σ) selection functions for ultra-deep GOODS-S *Herschel*100 μm data (dot-dashed line; Magnelli et al. 2013), which are the deepest *Herschel* far-infrared extragalactic survey data ever taken, the CCAT confusion limit at 850 μm (triple dot-dashed line; assuming a 30 m dish), and for a simulated *Euclid* wide survey limited at $H < 24$ mag (long-dashed line; Ciliegi et al. 2015). Even with optimistic far-infrared SED assumptions, SKA1-MID surveys should be nearly one and two orders of magnitude more sensitive than 850 μm CCAT observations and the deepest space-based far-infrared survey data at $z \gtrsim 4$, respectively, providing the most sensitive observations to obscured star formation at high redshifts. *Right:* The expected 10 GHz (solid line) and 1.4 GHz (dotted line) flux densities for galaxies of different star formation rate assuming an intrinsic magnetic field strength of 30 μG. The depths of possible future surveys taken by the JVLA, MeerKAT (MIGHTEE), and SKA are shown. Since the non-thermal emission from star-forming galaxies should be suppressed due to increased inverse-Compton scattering of cosmic-ray electrons off of the CMB, the discrepancy between the point source sensitivity requirements of surveys at 1.4 and 10 GHz falls below a factor of $\lesssim 2$ by $z \gtrsim 4$.

have been carried out almost exclusively at 1.4 GHz, and are thus most sensitive to non-thermal emission processes from galaxies. This exclusiveness of low frequency surveys has largely been because of primary beam and sensitivity considerations given the steep spectra ($S_\nu \propto \nu^{-0.7}$) of local star-forming galaxies. To then construct a picture for the star formation history of the Universe from these low frequency surveys requires an indirect conversion to a star formation rate based on the empirically derived far-infrared/radio correlation (Helou et al. 1985; Yun et al. 2001). However, as already stated above, surveys at frequencies ≳10 GHz have the distinct advantage of yielding higher angular resolution imaging while probing higher rest frame frequencies of galaxies with increasing redshift, where emission becomes dominated by *thermal* (free-free) radiation and *directly* provides a dust-unbiased measurement of the instantaneous rate of formation of massive stars.

The ability to measure free-free radiation directly becomes increasingly important at high redshifts given the increased uncertainties when using standard star formation rate diagnostics. Rest-frame FUV observations provide a direct measure of emission from the photospheres of young, massive stars, however it is often hampered by extinction effects that vary spatially within, and among, galaxies. Additionally, changes in metallicity and gas-to-dust ratios as a function of redshift may result in galaxies becoming increasingly dust-free at high-z, thus making conversions of

PoS(AASKA14)085

infrared dust emission to star formation rates difficult to interpret.

Observations carried out by SKA1-MID using Band 5 at $\approx$10 GHz will sample the rest frame $\approx$30 GHz emission from galaxies at $z \sim 2$, providing one of the most accurate measurements for star formation activity at high-z. Results from recent work using the Robert C. Byrd Green Bank Telescope (GBT) and the Karl G. Jansky Very Large Array (JVLA) find that 33 GHz thermal fractions on $\sim$kpc scales for a range of local galaxy nuclei and extranuclear star-forming regions are $\sim$80%, on average (Murphy et al. 2011, 2012). Additionally, global investigations of starburst radio spectra (M 82, NGC 253, and NGC 4945) similarly suggest $\gtrsim$80% thermal fractions at 33 GHz (Peel et al. 2011). As we push the detection of star-forming galaxies out to significantly higher redshifts, we anticipate even larger thermal fractions due to increased inverse-Compton losses to cosmic-ray electrons off of the CMB with redshift, whose energy density scales as $U_{\rm CMB} \sim (1+z)^4$; non-thermal emission from galaxies should become severely suppressed with increasing redshift, making this frequency range ideal for accurate estimates of star formation activity at high z, unbiased by dust (Carilli et al. 2008; Murphy 2009).

It is worth stressing that, independent of radio spectral index variations, observations at $\gtrsim$10 GHz are more easily interpreted at high redshift because they become dominated by free-free emission, yielding highly accurate star formation rate estimates even when the non-thermal spectral index is unknown. As a quantitative example, even in the absence of any information for the intrinsic non-thermal spectrum, other than the measured distribution for local galaxies (i.e., $\alpha^{\rm NT} = -0.83$; $\sigma_{\alpha^{\rm NT}} = 0.13$; Niklas et al. 1997), by having such a long lever arm over which to measure the radio spectral index using deep 10 GHz data ensures that a typical uncertainty on the thermal fractions, and thus estimated star formation rates, is *only* $\sim$*30%* for 20σ detections at both 1.4 and 10 GHz (40% for 5σ detections). This uncertainty is half of the dispersion measured for the far-infrared–radio correlation (used to convert 1.4 GHz data to a star formation rate), and is drastically smaller than the uncertainties associated with extinction correcting rest-frame UV data, as well as the factor of $\sim$2 uncertainty associated with IR luminosity star formation calibrations (e.g., Murphy et al. 2012). And, if the thermal fractions do increase as a function of redshift relative to what is measured for local galaxies, this uncertainty will only decrease.

In the left panel of Figure 2 the 10 GHz (5 σ) selection functions for star-forming galaxies are shown for SKA1-MID and SKA2 after a 1000 hr exposure as a function of redshift. Even with SKA1-MID observations alone, deep surveys will reach an untouched part of parameter space, being able to detect extremely faint galaxies hosting low levels of star formation at extremely high redshifts. This is exactly the population of star-forming galaxies for which synchrotron emission should become severely suppressed by CMB effects. At such a depth, SKA1-MID observations will be nearly two orders of magnitude more sensitive than the deepest far-infrared (i.e., 100 μm) survey carried out with the *Herschel* space telescope (Magnelli et al. 2013), as well as approximately an order of magnitude more sensitive than a 30 m CCAT confusion limited survey at 850 μm. Furthermore, if SKA1-MID is limited to 50% of its expected sensitivity, the impact on the Band 5 science described here will be minimal (e.g., see left panel of Figure 2).

Unlike observations at 1.4 GHz (e.g., Seymour et al. 2008; Smolčić et al. 2009; Morrison et al. 2010) those at 10 GHz are dominated by thermal emission beyond $z \sim 2$ even for large galaxy magnetic field strengths. Consequently, star-forming galaxies at increasing redshift should have increasingly flatter spectra due to the suppression of their synchrotron emission by inverse-Compton

PoS(AASKA14)085

scattering off the CMB, making higher frequency surveys nearly as sensitive to the same population of star-forming galaxies detected in lower frequency surveys. This is illustrated in right panel of Figure 2, where we plot the expected 1.4 and 10 GHz flux densities of star-forming galaxies for a range of star formation rates as a function of redshift. The ratio of 1.4 to 10 GHz (observed-frame) flux densities is expected to decrease significantly with increasing redshift. Also shown are the anticipated (5 σ) 10 GHz sensitivities for SKA1-MID and SKA2 after a single 1000 hr exposure compared to JVLA and MeerKAT capabilities. After such a deep integration at $\sim$10 GHz, SKA1-MID and SKA2 should be able to detect galaxies forming starts at $\sim$100 and 10 $M_\odot\,\mathrm{yr}^{-1}$, at all redshifts, respectively.

While the new WIDAR correlator on the JVLA is finally allowing users to investigate the high-z Universe with deep-field pointings at these higher frequencies, it is only with the SKA that such observations will yield source counts commensurate with current lower frequency surveys, opening up a completely new parameter space for galaxy evolution studies in the radio. This is illustrated in the left panel of Figure 3, where we show the expected cumulative 10 GHz source counts for 1000 hr exposures with SKA1-MID and SKA2 assuming a synthesized beam of $\theta_\mathrm{s} = 0\farcs1$ based on the S^3 simulated sky (Wilman et al. 2008). Such an observation corresponds to the ultra-deep SKA1-MID/Band 5 reference survey outlined in Prandoni & Seymour (2015). The anticipated source density at these 5σ surface brightness limits is $\approx$30 and $\approx$85 arcmin^{-2} with SKA1-MID and SKA2, respectively, resulting in a total of $\approx$840 and $\approx$2500 detections per each single pointing deep field, respectively. For the case of a 50% less sensitive SKA1-MID, the corresponding source density is $\approx$20 arcmin^{-2}, resulting in a total of $\approx$550 detections per each single pointing. Thus, even though the primary beam at $\gtrsim$1.4 GHz is $\approx$50 times larger than that at 10 GHz, deep Band 5 surveys with the SKA will yield statistically significant samples allowing for more complete (e.g., in frequency coverage) investigations on the radio properties of galaxies over cosmic time.

2.2.1 Resolving Star-Forming Disks During the Peak of the Cosmic Star Formation History

With $\sim$200 km baselines, observations at $\gtrsim$10 GHz will be able to achieve a maximum angular resolution of $\lesssim 0\farcs03$, sampling $\approx$250 pc scales within disk galaxies at $z \gtrsim 1$, providing an extinction-free view for the morphologies of dusty star-bursting galaxies that dominate the star formation activity between $1 \lesssim z \lesssim 3$. While probing such fine physical scales requires sources that are extremely bright, the SKA should still have the sensitivity to easily resolve sub-L* at high redshifts. In the right panel of Figure 3 we illustrate the expected brightness temperature sensitivity of the SKA for resolving sub-L* galaxies forming stars at a rate of $\sim$10 $M_\odot\,\mathrm{yr}^{-1}$ at $1 \lesssim z \lesssim 3$. For reference, L* galaxies at $1 \lesssim z \lesssim 3$ have corresponding total infrared (IR; $8-1000\,\mu$m) luminosities ranging between $10^{11}\,L_\odot \lesssim L_\mathrm{IR} \lesssim 10^{12}\,L_\odot$ (Gruppioni et al. 2013). We assume galaxy sizes of $0\farcs65$, which is similar to the Hα sizes of galaxies in this same redshift range (Nelson et al. 2013). Given that star-forming galaxies are likely to host clumpy star formation, the estimated brightness temperature requirements for detecting such galaxies are likely conservative. Even so, SKA1-MID will easily resolve such sources at $z \lesssim 2$, while also being able to map galaxies at $\lesssim 0\farcs1$ resolution that are forming stars at $\sim$100 $M_\odot\,\mathrm{yr}^{-1}$. Such high resolution imaging will be well matched to existing and forthcoming optical/NIR imaging (e.g., JWST) for detailed investigations of resolved star formation and stellar mass. Furthermore, resolving highly obscured star-bursting systems at $z \gtrsim 1$, with $\approx$500 pc resolution, will enable critical new investigations of their energetics and dis-

PoS(AASKA14)085

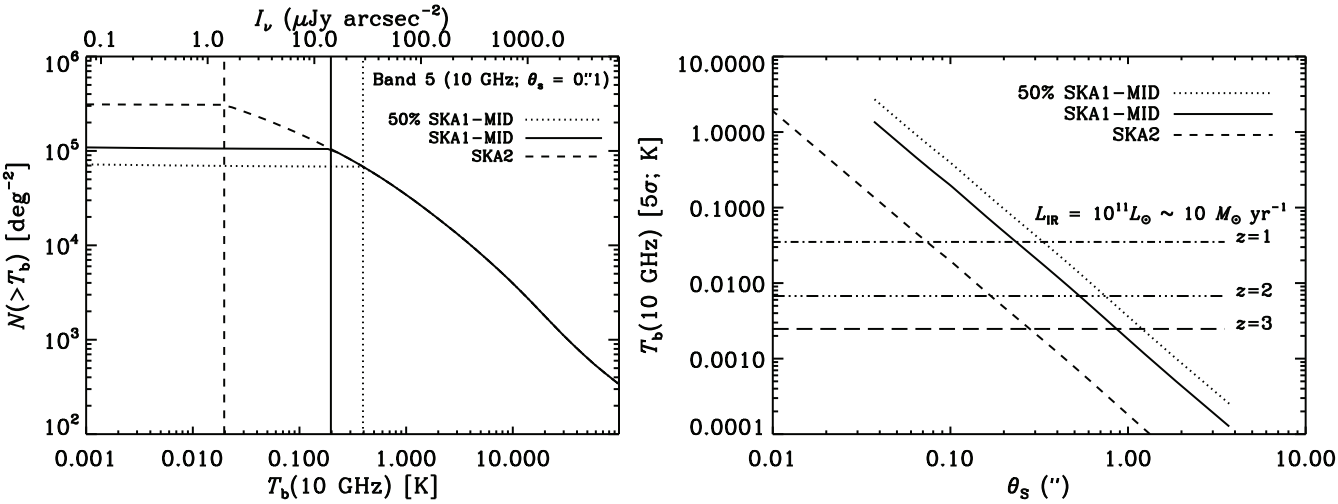

Figure 3: *Left:* The anticipated cumulative extragalactic source counts for a Band-5 deep field based on the S^3 simulated radio sky (Wilman et al. 2008). The vertical line indicates the 5σ surface brightness sensitivity for 1000 hr observations with SKA1-MID and SKA2. Brightness temperature sensitivies are taken from Braun (2013) assuming 5 GHz of usable bandwidth and a 0.″1 synthesized beam. The anticipated source density at these surface brightness limits is ≈30 and ≈85 arcmin^{-2}, respectively. The case of a 50% less sensitive SKA1-MID is also shown, for which the corresponding source density is ≈20 arcmin^{-2}. *Right:* The brightness temperature sensitivity (5 σ) of the SKA as a function of synthesized beam, assuming uniform sensitivity for baselines up to 200 and 2000 km baselines for SKA1-MID and SKA2, respectively. Additionally plotted is the expected brightness temperature of a $L_{\rm IR} = 10^{11}\,L_\odot$ galaxy assuming an intrinsic source size of 0.″65 (corresponding to a physical size of ∼5 kpc at $z = 1$, 2, and 3). Even with SKA1-MID, observations at 10 GHz should be able to resolve sources forming stars at $\sim 10\,M_\odot\,{\rm yr}^{-1}$ up to $z \sim 2$ under the conservative assumption of uniformly distributed emission.

tinguish between disks and mergers without being subject to spatially varying obscuration of the rest frame UV light. For instance, having angular sizes of each source measured will allow us to calculate brightness temperatures, which can be used to identify maximal starbursts (Murray et al. 2005) and AGN (Condon et al. 1991) for the brightest sources in the field.

2.3 Identifying AGN in the High-Redshift Universe with Band 5

2.3.1 Polarization in the Faraday-thin Regime

At $\nu \gtrsim 10$ GHz, Band 5 observations are well above frequencies at which internal or external Faraday rotation or depolarization effects are important, allowing for a clear view of the intrinsic polarization properties of the sources. This is an important complement to polarization observations at lower frequencies. By being in the Faraday-thin regime, joint statistical analyses with lower frequencies (e.g., Band 2) will directly measure the depolarization, hopefully shedding light on the outstanding mystery as to whether the faint source population has higher fractional polarization than stronger sources (Mesa et al. 2002; Taylor et al. 2007) or not (Hales et al. 2014). Disentangling the role of depolarization and the relation to luminosity and redshift are important keys to this puzzle. For example, knowing the statistics of frequency dependence of polarization will let us model the effect of redshift.

Very broad frequency bands permit modeling for multiple rotation measure components and exploration of the internal physics, magnetic fields and thermal plasma environments of the AGN

PoS(AASKA14)085

cores. This is something that can only be done at radio wavelengths and provides unique insights into AGN physics on the scales of the accretion disk. Polarization information can also be used to sort out cross-identifications of sources; i.e., this information can be used to distinguish radio lobes from completely separate galaxies. As already stated, for star-forming galaxies at increasingly high redshift, a significant fraction of the 10 GHz flux density will be thermal. In addition to having high angular resolution imaging for resolving disks versus AGN cores, polarization can play an important role for interpreting the thermal/non-thermal mix of the radiation and separating AGN from disks. It is only by including Band 5 in SKA1-MID that such polarization studies can be carried out.

2.3.2 Maser Lines

For a more general discussion of maser science that can be done during SKA1 operations, we refer the reader to the chapter by (Beswick et al. 2015), and only focus here on what is enabled by the inclusion of Band 5. The transition between the $6_{16} - 5_{23}$ rotational levels of H_2O can show in extragalactic sources as spectacularly strong maser emission at rest frame 22.235 GHz. The maser action results from the collisional excitation of water molecules in extremely dense gas clouds [$n(H_2) \geq 10^7$ cm^{-3}] with temperatures greater than 1000 K (Lo 2005). Thus, extragalactic water masers are associated with an AGN, originating in either the circumnuclear accretion disc (Greenhill et al. 1995) or circumnuclear molecular clouds that are excited by the impact of a jet or AGN outflow (Claussen et al. 1998; Peck et al. 2003; Greenhill et al. 2003). The most luminous of water masers, so called gigamasers, have isotropic line luminosities greater than 10,000 $L_\odot$ (Barvainis & Antonucci 2005; Impellizzeri et al. 2008). So far only 2 water masers have been discovered at $z > 0.5$, and one of those only because the AGN is lensed, but their discovery suggests the space density of luminous water masers was much higher at high redshift than in the local Universe (Impellizzeri et al. 2008). SKA1-MID will be able to detect gigamaser water emission to $z \sim 2$ in roughly 24 hr of integration (assuming 4 times the sensitivity of the JVLA), and megamaser emission to $z = 0.5 - 1$.

Finding water masers at higher redshifts has the potential to confirm whether the unified model for low luminosity AGN can be extended to the higher luminosity distant sources. We can attempt to address whether high QSO luminosities result in “gigamasers," or whether they destroy the warm dense molecular gas required to supply the water molecules for the maser emission. Finding masers in high redshift AGN may provide insight into the size and structure of their circumnuclear molecular clouds or accretion disks, and enable independent measurements of their black-hole masses. Even more importantly, it has the potential to constrain the nature of dark energy through accurate measurement of geometrical distances (Herrnstein et al. 1999; Braatz et al. 2010), and thus independently verify the results from Type 1A supernova experiments. Measuring a distance with water masers requires the long baselines of the SKA, but SKA1-MID could already make progress in this area with high fidelity very long baseline interferometry (VLBI) imaging.

3. Looking Towards a Completed SKA

Restricting SKA1-MID operations to frequencies < 20 GHz leaves a gaping hole between where the SKA frequency coverage ends, and ALMA Band 1 begins (i.e., at $\approx$31 GHz). Further-

PoS(AASKA14)085

more, given the technical demands required for achieving the core science goals at $\sim$GHz frequencies (e.g., dynamic range and pointing accuracy), having dishes that are able to operate efficiently at frequencies as high as $\sim$30 GHz may inevitably become a requirement for SKA1-MID. We therefore additionally present some fundamental science goals that are only achievable by keeping the SKA design flexible enough such that future receiver bands at $\gtrsim$20 GHz could be added to the facility as SKA2 becomes realized.

The frequency range between 20 and 30 GHz is currently under-explored in extragalactic astrophysics, largely because the emission from galaxies at these frequencies is intrinsically faint. However, this is a critical part of frequency space for proper modeling and accounting of the energetic processes powering galaxies, as this region samples the location where the microwave emission is powered by non-thermal (synchrotron), free-free (bremsstrahlung), and thermal dust emission at somewhat commensurate levels (see Figure 1). Thus, the ability to properly deconstruct radio spectra into its component parts, which is highly desirable for investigations focusing on the evolution of star-formation because of the need for a clean star formation rate diagnostic (i.e., free-free continuum), clearly relies on access to this spectral window.

Similar to the discussion above for observations at $\sim$10 GHz, in this $20-30$ GHz band, the sensitivity to free-free emission from a galaxy increases with redshift, as illustrated by the shaded regions in Figure 1. By redshift $z\sim 2$, where the star formation rate density of the Universe is dominated by extremely dusty starbursts that are essentially opaque at optical/UV wavelengths, a 25 GHz SKA2 observation samples the rest frame 75 GHz emission, which is completely dominated by free-free emission arising from young, massive star-forming regions independent of increased synchrotron suppression with redshift due to CMB effects. Unlike optical/UV, Hα, low-frequency radio (synchrotron), and infrared observations, free-free emission in the $\sim 30-100$ GHz range provides a direct measurement of the ionizing photon rate from massive stars independent of dust, making it one of the most robust measurements of a galaxy's star formation rate.

3.1 Resolving Individual Star-Forming Regions at $z\gtrsim 1$

With baselines of 200 km, observations at 25 GHz will be able to achieve angular resolutions of $\approx 0\farcs01$, probing $\approx$100 pc scales at $z\gtrsim 1$ (i.e., the size of giant molecular clouds and HII regions). Given a 1000 hr exposure, SKA2 should have the brightness temperature sensitivity to resolve such sources having star formation rates of $\sim 100\,M_{\odot}\,\mathrm{yr}^{-1}$ with $\approx 0\farcs02$ (150 pc) resolution at $z\sim 1$ (right panel of Figure 3). Assuming eventual baselines of $\sim$2000 km, the array will have the ability to resolve individual star-forming regions on the 10's of pc scales at $z\gtrsim 1$, which should be possible for strongly lensed sources. Accordingly, SKA2 will enable routine investigations on the distribution of star formation *within* galaxies at cosmological distances, when the Universe was forming stars at an order of magnitude higher rate than today. Such observations will be ideally complemented by targeted follow-up observations using ALMA to study the molecular gas distribution at similar scales. To date, such investigations must rely on chance gravitational lensing to achieve such high spatial resolution (e.g., Smith et al. 2009; Swinbank et al. 2011). Consequently, combining these datasets will yield new insight on the physics of star formation by providing a means to investigate whether the relatively constant gas depletion timescale in local galaxy disks persists in the underlying disks of galaxies during the peak of the cosmic star formation rate density at $z\sim 2$ (e.g., Bournaud et al. 2014). This is a transformational step in the studies of star

PoS(AASKA14)085

formation, as presently, such detailed ("high" resolution) investigations of the distributed ($\lesssim$sub-kpc-scale) star formation and molecular gas within galaxies can solely be achieved for objects in the nearby Universe (e.g., Bigiel et al. 2008, 2011; Leroy et al. 2008, 2013). At even higher redshifts, the observed frame 25 GHz emission will probe the cold dust emission of galaxies, pinning down the Raleigh-Jeans tail of dust spectral energy distributions, which is critical for dust modeling as the cold dust traces the bulk of the dust (and total ISM) mass within galaxies (e.g., Scoville et al. 2014). By a redshift of $z \sim 5$, such observations with SKA2 would be able to measure rest frame 2 mm emission. And, with only 200 km baselines, such observations would already be able to measure the cold dust emission on the scales of giant molecular clouds in galaxies just after (and during) the epoch of reionization.

3.2 Detecting Molecular Gas During the Peak of the Cosmic Star Formation Density

In addition to studying the radio-to-infrared continuum at these frequencies, there is a wealth of spectral line studies that can only be achieved through access to this spectral window. A detailed discussion of the full potential for molecular gas studies with the SKA is presented in this book by Wagg et al. (2015). Here we only briefly mention the synergies that can be achieved by combining ALMA and SKA observations for studying molecular gas and star formation at high redshift.

For investigations of the star formation law (Schmidt 1959; Kennicutt 1998), which relates the star formation rate and gas surfaces densities in galaxies, a key element is having an estimate of the total molecular gas content, which is well measured by low-J rotational lines of CO; higher J transitions, more easily measured with ALMA, trace the warm dense gas and are not as sensitive to the bulk of the molecular gas content in galaxies. Both CO ($J = 1 \rightarrow 0$) and CO ($J = 2 \rightarrow 1$) can be measured for galaxies in the redshift range of $z = 2.8 - 10.5$ over the full $20 - 30$ GHz spectral window (see Figure 1). Such a capability will have a strong synergy with ALMA, as targeted, high-frequency ALMA observations (e.g., Band 9) will be able to map out the peak of the dust emission in such galaxies (tracing star formation activity), which can be compared to maps of the low-J CO lines obtained using the SKA. The joint capability of these two interferometers to determine the full CO spectral line energy distribution of high-z galaxies, from the ground state to high-J transitions, would also facilitate insight into the relative importance of high- and low-excitation components, and hence into the causes for spatial variations of star-formation efficiency within high-z galaxies. While it is to be expected that the decreasing contrast between line emission and the warmer CMB makes line detections increasingly difficult at $z > 4$ (da Cunha et al. 2013), the SKA is uniquely positioned to detect this low-contrast emission from low rotational levels of molecules at high redshift. Investigations such as these will become routine, and greatly improve our models of star formation over cosmic time which, to date, are rather unsophisticated in their prescriptions for transforming gas into stars at early times.

The ability to measure the densest star-forming gas would also be possible via the HCN ($J = 1 \rightarrow 0$) and HNC ($J = 1 \rightarrow 0$) lines, which redshift to frequencies $\lesssim 30$ GHz for $z \gtrsim 2$. Additionally, the combination of molecular lines and their isotopologues (e.g., $J = 1 \rightarrow 0$ lines of ^{13}CO and ^{12}CO) can be used to investigate the physical conditions in galaxies at and beyond the peak of star formation (i.e., $3 \lesssim z \lesssim 5$). The ratio of these lines provides a robust measure for the temperature of dense, UV-shielded star-forming cores. Such observations can in fact be used to test for initial mass function (IMF) variations (e.g., Papadopoulos 2010), as it is currently thought that a transition

PoS(AASKA14)085

to a more top-heavy IMF at early times may be necessary to explain the epoch of reionization (e.g., Chary 2008). The same can also be said for ratios of free-free to rest-frame UV emission, which are highly sensitive to changes in the IMF. There are, of course, radio recombination lines at these frequencies that will also prove useful to redshift identification and for characterizing the conditions of star formation (e.g., radio recombination line-to-continuum ratios can be used to directly measure the electron temperature of HII regions).

4. Conclusions

The SKA is a major scientific investment that will provide the astronomical community with a *general use* facility having an expected lifetime of $\gtrsim$50 yr. The inclusion of high-frequency (i.e., $\gtrsim$10 GHz Band 5) capabilities during SKA1-MID operations, thereby limiting significant redundancy between SKA1-MID and SKA1-SUR capabilities, will yield the highest scientific return by delivering the most flexible telescope to the astronomical community.

Given these fundamental science goals, including detailed investigations on the evolution and distribution of the star formation and molecular gas content in galaxies into the epoch of reionization, it is crucial that the dish design of the SKA be flexible enough to include the possibility of being fit with receivers operating up to 30 GHz. While SKA1-MID should benefit from having some MeerKAT dishes that are fitted with receivers operating near between $8-14.5$ GHz, and therefore opening up a new window on some of the science topics outlined above, $20-30$ GHz capabilities are currently not included in the SKA1 System Baseline Design (Dewdney et al. 2013). Furthermore, having contiguous frequency coverage between the SKA and ALMA will ensure that future scientific opportunities, including the ones that we are currently not able to anticipate, will not be missed over the next half century.

References

Barvainis, R., & Antonucci, R. 2005, ApJ, 628, L89
Beck, S. C., Turner, J. L., & Kovo, O. 2000, AJ, 120, 244
Beswick, R. J. et al. 2015, “SKA Studies of Nearby Galaxies: Star-formation, Accretion Processes and Molecular Gas Across all Environments", in proceedings of "Advancing Astrophysics with the Square Kilometre Array", PoS(AASKA14)070
Bigiel, F., Leroy, A., Walter, F., et al. 2008, AJ, 136, 2846
Bigiel, F., Leroy, A. K., Walter, F., et al. 2011, ApJ, 730, LL13
Bournaud, F., Daddi, E., Weiss, A., et al. 2014, (arXiv:1409.8157)
Bourne, N., Dunne, L., Ivison, R. J., et al. 2011, MNRAS, 410, 1155
Braatz, J. A., Reid, M. J., Humphreys, E. M. L., et al. 2010, ApJ, 718, 657
Braun, R., “SKA1 Imaging Science Performance", Document number SKA-TEL-SKO-DD-XXX Revision A Draft 5
Carilli, C. L., & Rawlings, S. 2004, New Astronomy Reviews, 48, 979
Carilli, C. L., Lee, N., Capak, P., et al. 2008, ApJ, 689, 883
Chanial, P., Flores, H., Guiderdoni, B., et al. 2007, A&A, 462, 81
Chary, R.-R. 2008, ApJ, 680, 32

PoS(AASKA14)085

Ciliegi, P. et al. 2015, "Synergistic Science with *Euclid* and SKA : the Nature and History of Star Formation", in proceedings of "Advancing Astrophysics with the Square Kilometre Array", PoS(AASKA14)150
Claussen, M. J., Marvel, K. B., Wootten, A., & Wilking, B. A. 1998, ApJ, 507, L79
Condon, J. J., Huang, Z.-P., Yin, Q. F., & Thuan, T. X. 1991, ApJ, 378, 65
Cox, D. P. 2005, ARA&A, 43, 337
da Cunha, E., Groves, B., Walter, F., et al. 2013, ApJ, 766, 13
Deeg, H.-J., Brinks, E., Duric, N., Klein, U., & Skillman, E. 1993, ApJ, 410, 626
Dewdney, P. E., Turner, W., Millenaar, R., et al. 2013, "SKA1 System Baseline Design", Document number SKA-TEL-SKO-DD-001 Revision 1
Elbaz, D., Dickinson, M., Hwang, H. S., et al. 2011, A&A, 533, A119
Ferrière, K. M. 2001, Reviews of Modern Physics, 73, 1031
Greenhill, L. J., Henkel, C., Becker, R., Wilson, T. L., & Wouterloot, J. G. A. 1995, A&A, 304, 21
Greenhill, L. J., Booth, R. S., Ellingsen, S. P., et al. 2003, ApJ, 590, 162
Gruppioni, C., Pozzi, F., Rodighiero, G., et al. 2013, MNRAS, 432, 23
Hales, C. A., Norris, R. P., Gaensler, B. M., & Middelberg, E. 2014, MNRAS, 440, 3113
Hayward, C. C., Jonsson, P., Kereš, D., et al. 2012, MNRAS, 424, 951
Heesen, V., Brinks, E., Leroy, A. K., et al. 2014, AJ, 147, 103
Helou, G., Soifer, B. T., & Rowan-Robinson, M. 1985, ApJ, 298, L7
Herrnstein, J. R., Moran, J. M., Greenhill, L. J., et al. 1999, Nature, 400, 539
Hirashita, H., & Hunt, L. K. 2006, A&A, 460, 67
Hunt, L. K., Dyer, K. K., Thuan, T. X., & Ulvestad, J. S. 2004, ApJ, 606, 853
Hunt, L. K., Dyer, K. K., & Thuan, T. X. 2005, A&A, 436, 837
Hunt, L. K., & Maiolino, R. 2005, ApJ, 626, L15
Impellizzeri, C. M. V., McKean, J. P., Castangia, P., et al. 2008, Nature, 456, 927
Johnson, K. E., Hunt, L. K., & Reines, A. E. 2009, AJ, 137, 3788
Kennicutt, R. C., Jr. 1998, ApJ, 498, 541
Klein, U., & Graeve, R. 1986, A&A, 161, 155
Klein, U., Wielebinski, R., & Morsi, H. W. 1988, A&A, 190, 41
Kobulnicky, H. A., & Johnson, K. E. 1999, ApJ, 527, 154
Leroy, A. K., Walter, F., Brinks, E., et al. 2008, AJ, 136, 2782
Leroy, A. K., Walter, F., Sandstrom, K., et al. 2013, AJ, 146, 19
Lo, K. Y. 2005, ARA&A, 43, 625
Magnelli, B., Popesso, P., Berta, S., et al. 2013, A&A, 553, A132
Magnelli, B., Lutz, D., Saintonge, A., et al. 2014, A&A, 561, A86
Melbourne, J., Soifer, B. T., Desai, V., et al. 2012, AJ, 143, 125
Mesa, D., Baccigalupi, C., De Zotti, G., et al. 2002, A&A, 396, 463
Mezger, P. G., & Henderson, A. P. 1967, ApJ, 147, 471
Morrison, G. E., Owen, F. N., Dickinson, M., Ivison, R. J., & Ibar, E. 2010, ApJ, 188, 178
Murphy, E. J. 2009, ApJ, 706, 482
Murphy, E. J., Condon, J. J., Schinnerer, E., et al. 2011, ApJ, 737, 67
Murphy, E. J., Bremseth, J., Mason, B. S., et al. 2012, ApJ, 761, 97
Murphy, E. J., Stierwalt, S., Armus, L., Condon, J. J., & Evans, A. S. 2013, ApJ, 768, 2

PoS(AASKA14)085

Murphy, E. J. 2013, ApJ, 777, 58
Murray, N., Quataert, E., & Thompson, T. A. 2005, ApJ, 618, 569
Nelson, E. J., van Dokkum, P. G., Momcheva, I., et al. 2013, ApJ, 763, L16
Niklas, S., Klein, U., & Wielebinski, R. 1997, A&A, 322, 19
Papadopoulos, P. P. 2010, ApJ, 720, 226
Parker, E. N. 1966, ApJ, 145, 811
Peck, A. B., Henkel, C., Ulvestad, J. S., et al. 2003, ApJ, 590, 149
Peel, M. W., Dickinson, C., Davies, R. D., Clements, D. L., & Beswick, R. J. 2011, MNRAS, 416, L99
Prandoni I. & Seymour N. 2015 ,"Revealing the Physics and Evolution of Galaxies and Galaxy Clusters with SKA Continuum Surveys", in proceedings of "Advancing Astrophysics with the Square Kilometre Array", PoS(AASKA14)067
Rodighiero, G., Daddi, E., Baronchelli, I., et al. 2011, ApJ, 739, L40
Roussel, H., Helou, G., Beck, R., et al. 2003, ApJ, 593, 733
Sargent, M. T., Béthermin, M., Daddi, E., & Elbaz, D. 2012, ApJ, 747, L31
Schleicher, D. R. G., & Beck, R. 2013, A&A, 556, A142
Schmidt, M. 1959, ApJ, 129, 243
Scoville, N., Aussel, H., Sheth, K., et al. 2014, ApJ, 783, 84
Seymour, N., Dwelly, T., Moss, D., et al. 2008, MNRAS, 386, 1695
Smith, G. P., Ebeling, H., Limousin, M., et al. 2009, ApJ, 707, L163
Smolčić, V., Schinnerer, E., Zamorani, G., et al. 2009, ApJ, 690, 610
Swinbank, A. M., Papadopoulos, P. P., Cox, P., et al. 2011, ApJ, 742, 11
Symeonidis, M., Vaccari, M., Berta, S., et al. 2013, MNRAS, 431, 2317
Taylor, A. R., Stil, J. M., Grant, J. K., et al. 2007, ApJ, 666, 201
Thomson, A. P., Ivison, R. J., Simpson, J. M., et al. 2014, MNRAS, 442, 577
Turner, J. L., & Ho, P. T. P. 1983, ApJ, 268, L79
—. 1985, ApJ, 299, L77
—. 1994, ApJ, 421, 122
Turner, J. L., Ho, P. T. P., & Beck, S. C. 1998, AJ, 116, 1212
Valtchanov, I., Virdee, J., Ivison, R. J., et al. 2011, MNRAS, 415, 3473
Wagg, J. et al. 2015, "Enabling the Next Generation of cm-Wavelength Studies of High-Redshift Molecular Gas with the SKA", in proceedings of "Advancing Astrophysics with the Square Kilometre Array", PoS(AASKA14)161
Wilman, R. J., Miller, L., Jarvis, M. J., et al. 2008, MNRAS, 388, 1335
Yun, M. S., Reddy, N. A., & Condon, J. J. 2001, ApJ, 554, 803

PoS(AASKA14)085

PROCEEDINGS OF SCIENCE

The SKA Mid-frequency All-sky Continuum Survey: Discovering the unexpected and transforming radio-astronomy

Ray P. Norris[*1,7], **Kaustuv Basu**[2], **Michael Brown**[3], **Ettore Carretti**[1], **Anna D. Kapińska**[4,7], **Isabella Prandoni**[5], **Lawrence Rudnick**[6], **Nick Seymour**[1,4]

[1]*CSIRO Astronomy & Space Science, PO Box 76, Epping, NSW 1710, Australia;* [2]*Argelander Institute for Astronomy, University of Bonn, Auf dem Huegel 71, 53121 Bonn, Germany;* [3]*Michael J. I. Brown, School of Physics, Monash University, Clayton Vic 3800, Australia;* [4]*ICRAR, The University of Western Australia, 35 Stirling Hwy, Crawley, WA 6009, Australia;* [5] *INAF - Istituto di Radioastronomia, Via Gobetti 101, 40125 Bologna, Italy;* [6]*Minnesota Institute for Astrophysics, School of Physics & Astronomy, University of Minnesota, USA.* [7]*ARC Centre of Excellence for All-Sky Astrophysics (CAASTRO), Sydney, Australia.*

E-mail: Ray.Norris@csiro.au

SKA is an instrument, not an experiment (Phil Diamond, Stellenbosch, 17 Feb 2014)

We show that, in addition to specific science goals, there is a strong case for conducting an all-sky (i.e. the visible 3π steradians) SKA continuum survey which does not fit neatly into conventional science cases. History shows that the greatest scientific impact of most major telescopes (e.g., HST, VLA) lies beyond the original goals used to justify the telescope. The design of the telescope therefore needs to maximise the ultimate scientific productivity, in addition to achieving the specific science goals. In this chapter, we show that an all-sky continuum survey is likely to achieve transformational science in two specific respects:

- Discovering the unexpected
- Transforming radio-astronomy from niche to mainstream

Advancing Astrophysics with the Square Kilometre Array
June 8-13, 2014
Giardini Naxos, Sicily, Italy

*Speaker.

PoS(AASKA14)086

1. Introduction

Experience shows that when telescopes enter unexplored areas of observational phase space, they make unexpected discoveries, and these discoveries often outshine the specific goals for which the telescope was built. For example, only one of the top ten discoveries with the Hubble Space Telescope (*HST*) was listed amongst the key goals used to justify its funding. So while specific science goals are useful to focus SKA design, they are unlikely to appear amongst its greatest scientific achievements. So in addition to achieving **known** science goals, SKA must be designed to maximise its ability to discover the (potentially more important) **unknown** science goals. An all-sky survey maximises the chance of detecting rare unknown objects and phenomena.

An additional motivation for an all-sky survey is that radio-astronomy is currently something of a niche science, and major radio-astronomical surveys typically have about 10% of the impact of major optical and infrared surveys. This is set to change as next-generation radio surveys cross a threshold beyond which they are dominated by normal star-forming galaxies, as opposed to the much rarer radio-loud AGN which have dominated previous radio surveys.

Both these general goals, and other specific science goals, are best addressed by an all-sky radio continuum survey. For convenience in this paper, we abbreviate this proposed SKA1 All-Sky continuum Survey to SASS1, and designate as SASS2 the potential counterpart with SKA2.

White (2014) points out that large survey telescopes (e.g. *WISE, GALEX, Pan-STARRS, LSST*) go to extraordinary lengths to achieve near-all-sky coverage. The *2MASS* project even went to the trouble of building observatories in both hemispheres to achieve true all-sky coverage. SASS1 will open up the radio sky just as other large all-sky surveys are opening up the optical, infrared, and X-ray skies. SASS1 is an opportunity for SKA to join the multiwavelength all-sky astronomical renaissance which will occur in the next decade.

Here we show that SASS1 is likely to achieve transformational science in two specific respects:

- Discovering the unexpected
- Transforming radio-astronomy from niche to mainstream

In addition, we list the supporting science cases for which an all-sky survey is critical for achieving specific science goals:

- Cosmology (Dipole/low-l multipoles, low-l Planck anomalies, f_{NL}, etc.)
- Galaxy Clusters and Large-scale Structure
- Evolution of Galaxies
- The Magnetic Sky
- Nearby Galaxies

This paper is organised as follows: §2 describes the Science Background, §3 discusses the transformational science cases, and §4 discusses the supporting science cases. §§2 to 4 are written in the context of the SKA1 baseline design. This is summarised in §5, and then §§6 and 7 discuss the science in two alternative scenarios: a 50% SKA1, and SKA2.

2. Science Background

2.1 Radio Continuum Surveys

Radio continuum surveys have a rich and productive history, generating some of the most cited papers in radio-astronomy. Previous radio surveys have been dominated by AGN (Active

PoS(AASKA14)086

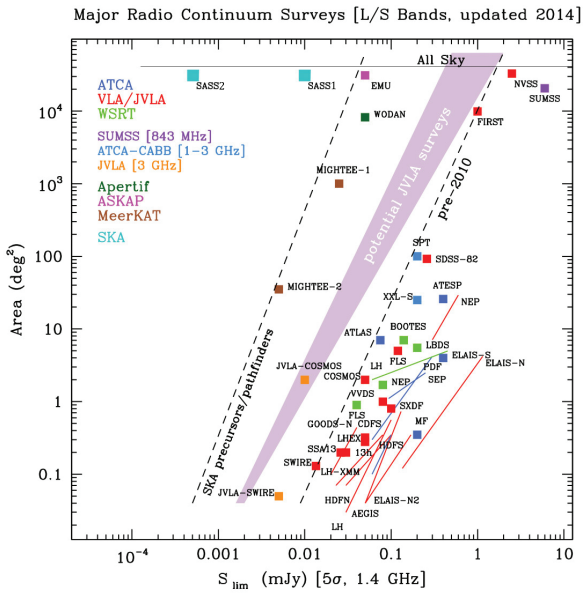

Figure 1: Comparison of existing and planned deep 20 cm radio continuum surveys. The horizontal axis shows the 5-σ sensitivity, and the vertical axis shows the sky coverage. The right-hand diagonal dashed line shows the approximate envelope of existing surveys, which is largely determined by the availability of telescope time. The squares in the top-left represent the new radio surveys discussed in this paper.

Galactic Nuclei) but radio surveys are now crossing a threshold where normal star-forming galaxies dominate the number counts. For example, the EMU (Evolutionary Map of the Universe) survey on the Australian SKA Pathfinder (ASKAP) is expected to detect about 70 million galaxies (compared to the current total of $\sim$ 2.5 million known radio sources), for most of which the radio emission is dominated by star formation rather than AGN.

Not only will next-generation radio surveys measure intensities to unprecedented levels, but they will also have better resolution, better sensitivity to extended emission, and will measure spectral index and polarisation for the strongest sources. For example, the ASKAP surveys will measure polarisation and spectral index for about 3 million sources, giving a 100-fold increase in the number of known polarised radio sources.

The predicted sensitivities and areas for the main 1.4 GHz surveys are shown in Figure 1. The largest existing radio survey, shown in the top right, is the wide but shallow NRAO VLA Sky Survey (NVSS: Condon et al., 1998). The most sensitive existing radio survey is the deep but narrow JVLA-SWIRE (Lockman hole) observation in the lower left (Condon et al., 2012). Current surveys are bounded by a diagonal line that roughly marks the limit of available telescope time of current-generation radio telescopes. The region to the left of this line is currently unexplored, and this area of observational phase space presumably contains as many potential new discoveries as the region to the right.

Wide-field survey radio astronomy in the next few years is likely to be dominated by ASKAP surveys, for which planning, funding, and construction is well advanced. For example, EMU (Norris et al., 2011) will survey 75% of the sky to a sensitivity of 10 μJy/beam rms. Only a total

PoS(AASKA14)086

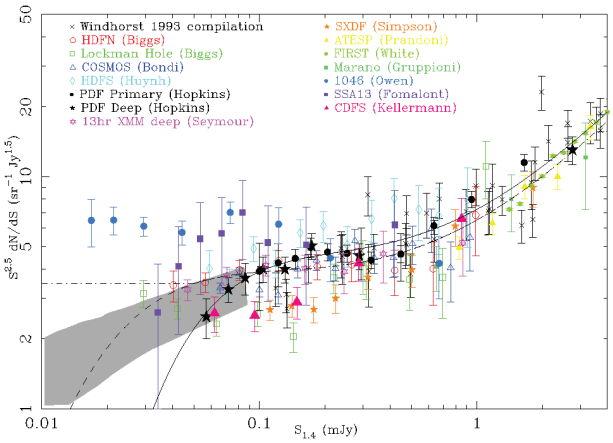

Figure 2: The Euclidean normalised differential radio source counts at 1.4 GHz (taken from Norris et al., 2013; Hopkins et al., 2003). The curves are alternative polynomial fits. The horizontal dot-dashed line represents a non-evolving population in a Euclidean universe. The shaded region shows the prediction based on fluctuations due to weak confusing sources ($P(D)$ analysis: Condon et al., 1974; Mitchell & Condon, 1985).

of about 10 deg^2 of the sky has been surveyed at 1.4 GHz to this sensitivity, in fields such as the *Hubble*, *Chandra*, ATLAS, COSMOS and Phoenix deep fields.

From the early 2020's, SASS1 and other SKA1 radio surveys will advance well beyond the limits reached by current telescopes. SASS1 will survey the sky to an rms of 2 μJy/beam with a resolution of 2 arcsec. SASS1 will take 2 years with SKA1-SUR, or would take 6 years with SKA1-MID, or 50 years with ASKAP, or 600 years with the JVLA. We consider it unlikely that SKA1-MID would be scheduled for 6 years integration time for an all-sky survey, so for the rest of this document we use the SKA1-SUR specifications, for which we consider a 2-year time allocation to be realistic, especially if commensal with HI and polarisation surveys.

2.2 The radio sky at μJy levels

Most extragalactic radio continuum surveys (e.g. Prandoni &Seymour, 2014) aim to understand the formation and evolution of galaxies over cosmic time, and the cosmological parameters and large-scale structures that drive it. Four generations of all-sky surveys are shown in Table 1.

At high flux densities, the source counts (Figure 2) are dominated by AGN. Below 1 mJy/beam, the normalised source counts flatten, suggesting an additional population consisting of a mixture of both SF galaxies and radio-quiet AGN. It is difficult to distinguish AGN from SF galaxies and techniques include radio morphology, spectral index, polarisation, variability, radio–infrared ratio, optical and IR colours and spectral energy distributions (SED's), optical line ratios, X-ray power and hardness ratio, and radio brightness on VLBI scales. None of these techniques is foolproof, and a combination of techniques is necessary to provide unambiguous classification.

Furthermore, there is growing recognition that high-luminosity galaxies, particularly at high redshift, are not simply "star-forming" or "AGN" but include a significant contribution from both (e.g. Norris et al., 2012). Such galaxies are sometimes labelled "composite" galaxies.

PoS(AASKA14)086

Table 1: Four generations of all-sky (i.e. $\sim 3\pi$ steradian) continuum surveys. Counts for EMU are based on source counts from ATLAS (Franzen et al., 2015; Banfield et al., 2015) and COSMOS (Schinnerer et al., 2007), and deeper counts are based on the $P(D)$ analysis by Vernstrom et al. (2014). SKA1 specifications are taken from the baseline design (i.e. FOV 18 sq deg.). SKA2 specifications assume FOV=360 sq deg, and ten times the SKA1 sensitivity.

Survey	Resolution (arcsec)	5σ Flux density limit (μJy/beam)	number of sources (millions)	number of pol. sources (millions)	Integration time years	reference
NVSS	45	2250	1.8	0	0.31	Condon et al.(1998)
EMU	10	50	70	3	1.5	Norris et al.(2011)
SASS1	2	10	500	10	2	this paper
SASS2	0.1	0.5	3500	70	0.5	this paper

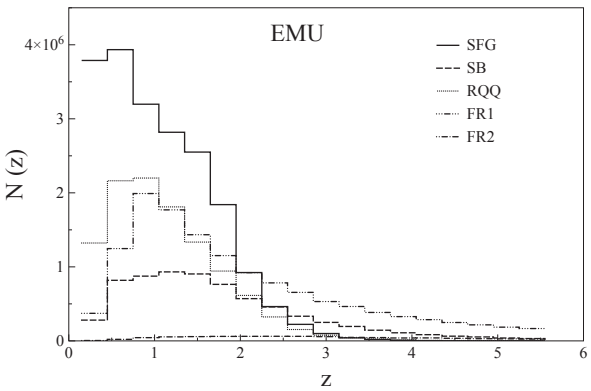

Figure 3: Expected redshift distribution of sources with $S_{1.4} > 50$ μJy/beam (the EMU $5-\sigma$ sensitivity), based on the SKADS simulations (Wilman et al., 2008). The five lines show the distributions for star-forming galaxies (SFG), starburst galaxies (SB), radio-quiet quasars (RQQ), and radio-loud galaxies of Fanaroff-Riley types I and II (Fanaroff & Riley, 1974).

2.3 Cross-Identification

Most science goals require cross-identification between radio sources and optical/infrared surveys. Surveys such as EMU have relatively large synthesised beamwidths ($\sim$ 10 arcsec) which make this challenging, but this is mitigated by the following factors:

- most radio sources at 50 μJy/beam have a 3.6 μm infrared counterpart, and so cross-identification between the radio and IR, and then cross-identification between IR and optical, produces a much better reliability than matching between radio and optical directly, and
- the accuracy of a radio source position is $\sim beamwidth/(2\times SNR)$, where SNR is the signal-to-noise ratio of the detection. So a 5-σ detection has a positional accuracy of $\sim$ 1 arcsec, and stronger sources even better accuracy, and
- using sophisticated Bayesian algorithms (e.g. Fan et al., 2014; Weston et al., 2014) which make full use of available photometric and morphological information, rather than using a simple nearest-neighbour or likelihood ratio algorithm.

As a result, cross-identifications with EMU are expected to achieve a high reliability.

PoS(AASKA14)086

For SASS1, the increased radio sensitivity implies that detected galaxies will be (a) optically fainter and (b) much more numerous. A higher spatial resolution is therefore needed, and the 2-arcsec synthesised beamwidth of SASS1 provides a 0.2 arcsec positional accuracy for a 5-σ detection, ensuring a high reliability of cross-identification.

2.4 Redshifts

Spectroscopic redshifts are currently known for about 100,000 extragalactic radio sources, and this will increase to about 1 million within the next five years. Thus most known radio sources do not have spectroscopic redshifts. However, many more non-radio galaxies (currently over 2 million, and expanding to tens of millions within a decade) have spectroscopic redshifts. As the sensitivity of radio surveys increases, the fraction of radio sources that have measured spectroscopic redshifts will increase, but will continue to be a small fraction.

About half the SASS1 sources will have good optical/IR identifications with multiwavelength data (e.g. *SDSS, VHS, SkyMapper*), enabling a photometric redshift to be determined. In some cases, with good data, photometric redshifts can be extremely reliable, whereas those obtained from poor data are less reliable.

The large numbers (hundreds of millions) of sources enable new approaches to be used, such as statistical redshifts, in which the redshift of an individual galaxy is poorly known, but the redshift distribution of a sample of galaxies can be used within a statistical framework.

Different science goals have different needs for redshifts. The cosmological tests described below yield significant constraints on cosmological parameters with no redshift knowledge whatsoever (Raccanelli et al., 2015), although even incomplete redshift information significantly improves the constraint (Camera et al., 2012; Rees et al., 2014). For goals such as measuring the evolution of cosmic star formation rate, photometric or statistical redshifts are adequate, provided the incompleteness and uncertainties are well-determined.

3. Transformational Science Cases

3.1 Discovering the unexpected

Ekers (2009) has shown that of 18 major astronomical discoveries in the last 60 years, only seven were planned. The remaining 11 were unexpected discoveries resulting from new technology or from observing the sky in an innovative way, exploring uncharted parameter space. In particular, the greatest science impact of new astronomical facilities often come not from the science goals listed in the proposal to build the telescope, but from unexpected discoveries; unexpected discoveries by a new instrument often outshine its original science goals. For example, Table 2 shows that only one of the top ten discoveries made with the *HST* was listed in the key science goals used to justify the project. While specific SKA science goals are necessary to focus the design of a scientifically productive facility, we must also recognise that the most significant discoveries from the SKA are unlikely to come from these science goals.

On the other hand, discovering the unexpected need not be a random or passive process. Recognising the importance of unexpected discoveries, the SKA should be designed to optimise the survey strategy and data-mining software, to maximise the probability of such discoveries. This is

PoS(AASKA14)086

Table 2: Major discoveries made by the Hubble Space Telescope (*HST*). Of the *HST*'s "top ten" discoveries (as ranked by National Geographic magazine), only one was a key project used in the *HST* funding proposal (Lallo, 2012). A further four projects were planned in advance by individual scientists but not listed as key projects in the *HST* proposal. Half the "top ten" *HST* discoveries were unplanned, including two of the three most cited discoveries, and including the only *HST* discovery (Dark Energy) to win a Nobel prize.

Project	Key Project?	Planned?	Nat Geo top ten?	Highly cited?	Nobel Prize?
Use cepheids to improve value of H_0	✓	✓	✓	✓	
UV spectroscopy of ig medium	✓	✓			
Medium-deep survey	✓	✓			
Image quasar host galaxies		✓	✓		
Measure SMBH masses		✓	✓		
Exoplanet atmospheres		✓	✓		
Planetary Nebulae		✓	✓		
Discover Dark Energy			✓	✓	✓
Comet Shoemaker-Levy			✓		
Deep fields (HDF, HDFS, GOODS, FF, etc)			✓	✓	
Proplyds in Orion			✓		
GRB Hosts			✓		

achieved by maximising the volume of virgin observational phase space, and developing software to mine the data for the unexpected. SKA1 will open up new swathes of observational phase space, with a high likelihood of making significant unexpected discoveries. Searching for the unexpected, and developing software to mine for the unexpected, must be a high priority of SKA1.

Figure 1 shows that SASS1 will open up a large area of virgin parameter space, to the left of the the dotted line, and should therefore plan for unexpected discoveries. We cannot rely on blind serendipity, because of the large data volumes, and the complexity of the instrument, but should plan to mine the data systematically for the unexpected. To maximise the scientific productivity, the SKA design process should:

- start by designing the telescope to address known science goals
- choose design parameters, observational parameters, and survey parameters to maximise the volume of new observational phase space
- ensure that processing techniques are not limited to answering known questions
- design software specifically to mine the data for unexpected discoveries.

Discoveries are thinly distributed through the observational phase space. We cannot predict where they lie, and it is difficult to quantify the volume of phase space being explored. Key elements to maximising the expected number of unexpected discoveries will include

- making an all-sky survey to discover rare objects,
- making a deep survey to discover faint objects,
- maximise the use of relatively unexplored parameters such as circular polarisation, time variability, sensitivity to diffuse emission, etc.

PoS(AASKA14)086

The last three items are already well addressed in other chapters. Here we emphasise the need for an all-sky survey to discover rare objects.

3.2 Transforming radio-astronomy from niche to mainstream

It is not widely appreciated by radio-astronomers that radio-astronomy is seen as a niche area of astronomy by the majority of non-radio astronomers, because existing radio measurements are not as intrinsically deep as existing optical data, and so $\sim 90\%$ of objects studied by a typical astronomer have no radio data. As a result, astronomers modelling the SED of a galaxy, or fitting a photometric redshift, will typically use optical and infrared data, but will rarely use radio data, because previous all-sky radio surveys were insufficiently sensitive to detect most galaxies. Similarly, developers of algorithms and templates don't bother including radio data in their code, making it even harder to use radio data. As a result, the most-cited radio surveys have only about 10% of the citations (and presumably only 10% of the impact) of the most-cited optical surveys (Table 3).

Next-generation radio continuum surveys with the SKA and its pathfinders are crossing a sensitivity threshold below which most galaxies detected in radio surveys are normal star-forming galaxies. For a star-forming galaxy in the SKADS simulation (Wilman et al., 2008), the 10 μJy/beam detection limit of SASS1 corresponds to a median I-band magnitude of ~ 21.5. Assuming typical R-I values of 0.5-1 (e.g. Smail et al., 1995), this corresponds to an R limit of 22.5-23, which is approaching the sensitivity limit of sky surveys such as *SDSS* and *SkyMapper*. The all-sky continuum survey with SKA2 will go several magnitudes deeper, approaching the survey limit of *LSST*. As a result, almost every galaxy found in optical/IR surveys will have radio photometry (and in many cases, polarisation and spectral index information). The high spatial resolution of SASS1 also ensures reliable cross-identifications with optical/IR hosts (see §2.3).

In 10 years time radio photometry is likely to be as commonplace in galaxy SED and photo-z estimation as IR photometry is now, leading to (a) better photometric redshifts and (b) a better distinction between star-forming and AGN components of the SED. This in turn will help address many other science goals such as the evolution of the cosmic star formation, assembly of galaxies, and the role of AGN in regulating galaxy formation.

The radio data will add information orthogonal to that currently available, since radio is unaffected by dust and is a sensitive tracer of both star formation and AGNs even in so-called radio-quiet AGNs. Surveying the entire sky ensures that most objects of interest in next generation surveys such as *LSST* have measured radio photometry.

In addition, polarisation and spectral index can be measured for tens of millions of stronger sources, to determine galaxy properties. For example, the detection of significant polarisation in anything but a very nearby galaxy demonstrates the presence of an AGN (and can be used to probe its properties) while spectral index can be used as an indicator of age in both star-forming galaxies (measuring the ratio of synchrotron to free-free emission) and in an AGN (by measuring the turnover frequency and energy loss by high-energy electrons).

Radio-astronomy is therefore set to take its place alongside optical and infrared as another tool in every astronomer's toolkit, and an indispensable part of every fitted spectral energy distribution or photometric redshift measurement. Next-generation radio surveys are expected to have as many citations (and as much scientific impact) as next-generation optical surveys. SASS1 will not only

PoS(AASKA14)086

Table 3: The six most highly cited optical/infrared extragalactic surveys and the six most highly cited radio extragalactic surveys, showing the number of refereed journal papers based on the survey, and the number of papers that cite the survey. These numbers were measured by searching ADS for refereed papers which contained (“galaxy" or “galaxies") and (“long survey name” or “short survey name”) in the abstract or title. Numbers for 3CR, and 4C are probably overestimates because they include papers which mention a source name starting with 4C etc. FIRST is not included because the name “FIRST" produced an unmanageable number of spurious results, and the long name of the FIRST survey does not make it into the top six.

Survey	# publications	# citations	Survey	# publications	# citations
	Optical/IR			**Radio**	
SDSS	4487	198454	4C	458	13831
HDF	601	52486	NVSS	355	11891
2MASS	1167	38129	3CR	323	15231
GOODS	608	36100	HIPASS	92	3441
2dFGRS	210	27364	PMN	90	2603
CfA	343	20929	WENSS	64	1580

Table 4: The four cosmological probes for which SASS1 is competitive. A high-z ISW detection would be inconsistent with standard ΛCDM but consistent with massive neutrinos.

	Technique	Physical effect
1.	Auto-correlations of radio data	spatial power spectrum
2.	Cross-correlation between ($z \leq 0.5$) optical foreground galaxies and ($\langle z \rangle \sim 1.5$) sources	cosmic magnification at low z
3.	Cross-correlation between sources and CMB ($\theta \leq 1^\circ$; no z needed)	cosmic magnification at high z
4.	Cross-correlation between source density and CMB ($\theta \sim 10^\circ$) in 2-3 z bins	Integrated Sachs-Wolfe effect

increase the number of known radio sources by nearly an order of magnitude, but will dominate international surveys, and move radioastronomy from niche science to mainstream.

4. Supporting Science Cases

In this Section we briefly discuss the specific science goals for which an all-sky survey delivers well-defined advantages over a smaller area survey.

4.1 Cosmology

SASS1 will make sensitive measurements of dark energy evolution, modified gravity and primordial non-Gaussianity, using a combination of probes listed in Table 4., placing significant constraints on cosmological (e.g. Dark Energy equation of state) and fundamental physical parameters (e.g. departures from General Relativity, and non-Gaussian inflation), even when redshifts for individual radio sources are unknown (e.g. Raccanelli et al., 2010; Camera et al., 2012; Raccanelli et al., 2015; Rees et al., 2014).

PoS(AASKA14)086

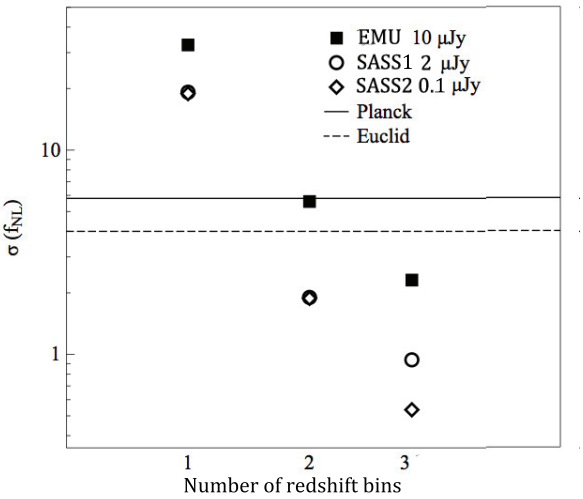

Figure 4: The uncertainty of the measurement of the non-Gaussianity parameter f_{NL} using the Integrated Sachs-Wolf effect on EMU, SASS1, and SASS2 data, compared to *Planck* and *Euclid*. Adapted from Raccanelli et al. (2015).

In such studies, an all-sky survey is essential to minimise cosmic variance and measure low-order spherical harmonics. For example, radio source counts have already been shown (Blake et al., 2002) to have a dipole signature, and SKA surveys will provide a measurement of that dipole signature that is independent of the dominant signal in WMAP/Planck. Furthermore, the Planck survey has shown a possible large-scale (low-l multipole) deviation from the standard ΛCDM model which can be tested with radio source counts over a survey covering a large fraction of the sky. The large sky area of the survey and the huge number of galaxies that will be detected, combined with their high mean redshift, will test parts of parameter space that are not accessible to other wavelengths.

While some of these cosmological tests require no redshifts, even limited redshift information can dramatically improve them (e.g. Raccanelli et al., 2010; Camera et al., 2012; Raccanelli et al., 2015; Rees et al., 2014). While obtaining individual redshifts for millions of radio sources is impossible in the next decade, dividing the radio source population into redshift bins is achievable with existing data. For example, selecting polarised radio sources without an optical identification in SDSS or Skymapper (i.e. $R > 23$) yields a population of AGNs at z $\gtrsim$1. This high redshift tail of the radio galaxy population can provide exquisite constraints on the evolution of dark energy. Separating the radio galaxy populations and measuring the bias on ultra-large scales will give unprecedented constraints on primordial non-Gaussianity.

4.2 Galaxy Clusters and Large-Scale Structure

Galaxy clusters are extremely sensitive probes of the growth rate of cosmic structures, but finding and characterising them is limited by selection bias. Traditionally, clusters have been found through optical galaxy counts, X-ray emission or the thermal Sunyaev-Zel'dovich (SZ) effect, resulting in several thousand detections.

The radio emission from clusters consists of (a) the halos, which are large (up to $\sim$ 1 Mpc)

PoS(AASKA14)086

diffuse regions of synchrotron emission found in galaxy cluster centres, (b) radio relics, which are diffuse areas of shock-excited synchrotron emission, (c) mini halos, found around the central AGN in some cluster cores, and (d) tailed galaxies, which are FRI sources whose jets and lobes are blown by ram pressure from the intra-cluster medium. Diffuse emission from halos and relics has so far been identified in only a few tens of clusters.

The radio halo power scales roughly as the third power of cluster mass (e.g. Sommer & Basu, 2014) so current surveys have been able to detect only the few most massive objects at relatively low redshifts. Radio halo luminosity is also strongly bimodal (Cassano et al., 2012) with radio haloes being detected almost exclusively in disturbed or merging clusters. The SKA's short baselines make SASS1 very sensitive to diffuse emission. SASS1 will therefore be able to detect even a 2×10^{14} solar mass cluster at $z = 0.5$, where its total flux density is ~ 30 μJy/beam, and will detect about 100,000 radio halos out to redshift $z = 0.5$. This mass limit will be comparable to numbers expected from the future X-ray (*eROSITA*) and optical (*Euclid*) missions. Such unprecedented numbers of radio selected clusters will enable the measurement of the dark matter halo merger rate with redshift, a key but untested component of the hierarchical structure formation model.

Other clusters will be detected from their peripheral relics or tailed radio galaxies. Based on ATLAS data, Dehghan et al. (2014) suggest SASS1 will detect $\sim$1 million tailed galaxies, perhaps making them the most widespread cluster diagnostic in the SASS1 era. Similarly, the number of high-redshift ($z > 1$) clusters is expected to grow to tens of thousands, Cross-identifying these objects with other probes (e.g. *eROSITA*) will provide a precise constraint on the dark energy equation of state.

Clusters of galaxies are not isolated regions, but are located at the intersection of filaments and sheets in the large-scale structure (LSS, or the "cosmic web"). The filaments themselves are expected to radiate radio synchrotron emission, powered by the infall shocks of baryons. The sensitivity and field-of-view of SASS1 will enable it to image this diffuse emission, thus mapping the cosmic web. An all sky survey will accurately map the energy distribution of the relativistic electrons in the warm hot intergalactic material (WHIM), and cross-correlate it with other LSS probes.

4.3 Evolution of Galaxies

Extragalactic radio astronomy tackles the origin, assembly, and evolution of galaxies, including regulation by feedback mechanisms, and the origin, growth, and evolution of supermassive black holes. Largely unstudied populations of starburst galaxies and low-power active galactic nuclei (AGN) are also being explored

Source counts at flux densities above 1 mJy/beam are dominated by radio-loud AGN, while below 1 mJy/beam they include significant contributions from radio-quiet AGN and star-forming galaxies. SASS1 will not only detect the underlying populations and dissect the lifecycles of AGN (Hopkins et al., 2003), but will also answer some of most debated questions in modern astrophysics such as the importance of AGN feedback in galaxy formation and evolution across cosmic time (Best et al., 2012). Radio-loud AGN also provide an obscuration-independent method of selecting the highest redshift AGN, which trace proto-clusters in the early Universe (Miley et al., 2008).

Some classes of radio AGN are rare, requiring an all-sky survey to obtain statistically significant sample sizes across a range of luminosities and redshifts. For example, CSS and GPS sources

PoS(AASKA14)086

(Fanti et al., 1990; Randall et al., 2011) represent an early stage of radio-loud AGN that are completely embedded in their host galaxies, and hence particularly important for investigations of the AGN feedback and AGN lifecycles (Kapinska, 2015). Even rarer are the radio-loud AGN in the brief phase as they cease jet activity, and their luminosity rapidly drops. The expected number density of dying radio sources is hard to estimate as few are known (Parma et al., 2007; Dwarakanath et al., 2009) and a high survey sensitivity to diffuse emission is required. Rarer still, at least in the local Universe, are the sources in which an FRII-luminosity jet has turned on inside a starburst galaxy, but has not yet bored its way through the dense molecular gas and dust to quench the star formation: only one has so far been found (Mao et al., 2014). Detection of a representative number of such rare radio sources will determine AGN duty cycles and large scale (cluster scale) feedback processes; only all-sky surveys will provide enough data to compile such samples.

4.4 The Magnetic Sky

Magnetic fields are important at all scales in the Universe, from small scales in the interstellar medium, to the vast scale of cosmic filaments. Yet, at all scales, we fail to understand the effect and magnitude of the magnetic contribution to the energy balance and evolution. High quality polarisation observations address diverse science goals, including the effect on the formation and evolution of galaxies and clusters, the magnitude of fields in the intra-cluster medium and their role in the cosmic web, and the question of the origin of cosmic magnetism. The key tool for analysing polarisation data from broadband radio surveys is Rotation Measure (RM) Synthesis (Brentjens & de Bruyn, 2005), which can detect faint polarised emission.

SASS1 will produce a detailed total intensity and polarization image of the entire sky, delivering an all-sky RM grid 300-1000 times denser than those currently available (Taylor et al., 2009), and 3-10 times denser than those produced in the ASKAP-POSSUM survey (Gaensler et al., 2010), and probing 10-100 times deeper than current polarisation surveys (see Fig. 5). RM Synthesis of SASS1 data will recover the polarised signal affected by internal depolarisation. These data will track the evolution of magnetic fields in the interstellar medium, in Active Galactic Nuclei, in the intracluster medium, at the boundary of galaxy clusters, in the bridges that join clusters, and in the filamentary cosmic web. There are even indications that the evolution of magnetic fields in normal galaxies at high redshifts can be traced by their Faraday effects when they are seen as MgII absorbers in front of polarized background quasars (Farnes et al., 2014).

A significant step forward would be the measurement of the redshift evolution of the Faraday rotation measure in clusters, as SASS1 will detect $\sim 10^5$ clusters with at least one background source in each (Krause et al., 2009). Compared to the few RMs known for a few nearby clusters today, this will revolutionize our understanding of the cosmic magnetic fields and their impact on the growth of large-scale structure.

4.5 Nearby Galaxies

SASS1 will measure star formation rates and AGN activity in thousands ($\sim$50000 galaxies at $z<0.01$) of nearby galaxies, each of which will have generous multiwavelength data. Hundreds of galaxies will have ground-based drift-scan/IFU spectroscopy, along with *WISE* mid-infrared images, enabling detailed spatial comparison of the radio star formation rate with H-alpha star

PoS(AASKA14)086

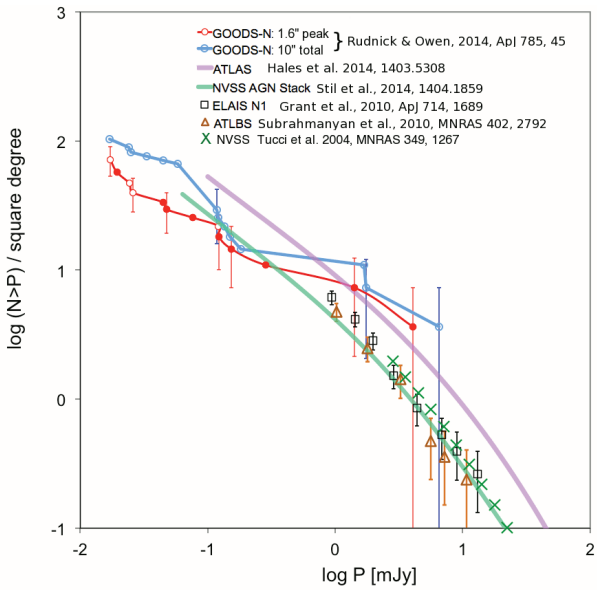

Figure 5: Recent determinations of polarised number counts, taken from (Rudnick & Owen, 2014; Hales et al., 2014; Stil et al., 2014; Grant et al., 2010; Subrahmanyan et al., 2010; Tucci et al., 2004). P is the total linearly polarised intensity. SKA will probe 10-100 times deeper than these surveys.

formation rate, with dust extinction correction. The 2-arcsec resolution of SASS1 corresponds to 400 pc at z=0.01, so that individual giant molecular clouds can be studied.

Virtually all spiral galaxies and high mass elliptical galaxies in this redshift range will be detected by SASS1 (Brown et al., 2011), so the radio duty cycle of galaxies can be directly measured. The shape of the radio luminosity function can thus be derived from the galaxy mass function and radio duty cycle, rather than being empirically modelled with broken power-laws.

Since the large-scale ($\sim$10 Mpc) clustering of dark matter halos is a function of their mass, the halo masses of radio source populations will be determined by measuring how optically selected galaxies cluster around radio sources. At fixed halo mass, the small-scale clustering of galaxies as a function of radio power will reveal the relative contribution of galaxy mergers and secular evolution in driving star formation and AGN activity. If secular evolution plays a dominant role in driving star formation rates in nearby galaxies, the $\leq$ 1 Mpc environments of galaxies (at fixed halo mass) with high and low star formation rates will be virtually identical.

5. Science outcomes in SKA1

§§2-4 were based on the baseline design specifications of SKA1, giving a continuum survey (SASS1) of 3π steradians (i.e. covering the declination range -90 to +30°) with an rms sensitivity of 2 μJy/beam. Table 1 shows that SASS1 increases the number of known radio sources by nearly an order of magnitude compared to EMU, or by a factor of 200 compared to the number ($\sim$ 2.5 million) of radio sources known in 2014, resulting in the following science outcomes:

- Discovering the unexpected: experience with previous major instruments (e.g. *HST*) shows that the most significant discoveries from SKA will not be those listed in the science goals.

PoS(AASKA14)086

SASS1 goes nearly an order of magnitude deeper than any other all-sky survey with all-sky coverage ensuring detection of even the rarest phenomena within that phase space.

- Transforming radio-astronomy from niche to mainstream: SASS1 sensitivity will detect most star-forming galaxies to $R \sim 23$, matching SDSS and SkyMapper, so SASS1 will supply radio data for most galaxies currently being studied by optical astronomers, and will be routinely used in constructing SEDs and photo-z's.
- Cosmology: SASS1 will place significant constraints on the parameters of dark energy, modified gravity, non-gaussianity, and neutrino mass, and will test low multipole isotropy of the Universe, giving measurements independent of those from optical and HI surveys.
- Galaxy Clusters and Large-scale Structure: SASS1 will detect about a million clusters, including about 100,000 radio halos. Together with *Euclid* and *eROSITA* data, this will transform our understanding of the physics of the large scale structure of the Universe.
- Evolution of Galaxies: SASS1 will detect about 500 million galaxies spanning all redshifts, and will trace the growth of black holes, the evolution of the cosmic star formation rate, and the interaction between these, to exquisite precision, finally nailing down the feedback mechanisms which regulate the growth and evolution of galaxies.
- The Magnetic Sky: SASS1 will measure the polarisation of about 10 million galaxies, determining not only the effect of magnetic fields on galaxies, but also providing a rotation measure grid nearly three orders of magnitude denser than currently available, measuring the intergalactic magnetic field as a function of redshift, giving clues to the origin of magnetism.
- Nearby Galaxies: SASS1 will provide detailed imaging of virtually all nearby ($z<0.01$) star-forming and high-mass elliptical galaxies, to a resolution of 400pc or higher, measuring the effect of both environment and AGN activity on the evolution of these galaxies.

6. Science outcomes from SKA1 early science operations

Here we estimate the scientific productivity of an "early science SKA1" all-sky-survey, with 50% of the sensitivity of SKA2. We assume the "50%" SKA1 still has the same resolution as the full SKA1, and is therefore able to deliver an-all-sky radio continuum survey with 4 μJy/beam rms, which is a factor 2.5 deeper than the deepest previous survey, ASKAP-EMU.

- Discovering the unexpected: Halving SKA1 sensitivity makes it only a factor of 2.5 deeper than EMU, reducing the amount of virgin observational space, reducing the likelihood of new discoveries compared to SKA1.
- Transforming radio-astronomy from niche to mainstream: Halving SASS1 sensitivity will detect all star-forming galaxies to $R \sim 22$ so will still supply radio data for most galaxies being studied optically, and will be increasingly used in constructing SEDs and photo-z's.
- Cosmology: A "half-SASS1" will still make important cosmological measurements, but they will be less competitive than those derived from optical or HI measurements.
- Galaxy Clusters and Large-scale Structure: Halving the sensitivity of SASS1 will result in about one quarter as many clusters detected, but this is still an enormous increase on what is currently available at present, or will be available from EMU.
- Evolution of Galaxies: Halving the sensitivity of SASS1 significantly reduces the redshift range at which star-forming galaxies and low power AGN can be detected. The study of

PoS(AASKA14)086

high-power AGN will be largely unaffected, but measuring the evolution of the cosmic star formation rate will be seriously affected.

- The Magnetic Sky: Halving the sensitivity of SASS1 will result in a reduction by one third in the number of galaxies for which polarisation can be measured. The increase compared to ASKAP-POSSUM is still valuable as the measurement of the intergalactic magnetic field depends critically on the sampling density.
- Nearby Galaxies: Halving SASS1 sensitivity reduces the number of nearby galaxies by a factor of $\sim$3, leaving $\sim$20,000 which can be studied in detail, far more than available now.

7. Science outcomes from SKA2

Assuming that SKA2 is ten times more sensitive and twenty times the FOV of SKA1-MID, then it can survey the whole sky in 83 12-hour observations. A 6-month survey (SASS2) can therefore observe each region of the sky four times, yielding an rms sensitivity 20 times deeper than SASS1. In 6 months, SASS2 will have rms $\sim$0.1 μJy/beam at $<$0.1arcsec (assuming the longer baselines planned for SKA2). The higher resolution will also provide low confusion and unambiguous cross-identifications to optical and infrared counterparts. Table 1 shows that SASS2 increases the number of known radio sources by nearly three orders of magnitude compared to current knowledge. This results in the following science outcomes:

- Discovering the unexpected: Figure 1 shows that SASS2 covers orders of magnitude more observational phase space than any other radio survey, almost certainly resulting in major science discoveries that are unlikely to feature in the current SKA science goals.
- Transforming radio-astronomy from niche to mainstream: SASS2 will detect all star-forming galaxies to $R \sim 27$, matching *LSST*, and will supply radio data for nearly all galaxies studied by optical astronomers, becoming an indispensable component of SEDs and photo-z's.
- Cosmology: SASS2 will probably measure the parameters of dark energy, modified gravity, non-gaussianity, and neutrino mass with lower uncertainties than other competing projects (*DES, Euclid*, etc) but this has yet to be established by careful modelling. Figure 5 gives on example of how SASS2 can measure non-gaussianity ten times better than *Euclid*, provided SASS2 sources can be placed into 3 redshift bins.
- Galaxy Clusters and Large-scale Structure: SASS2 could, in principle, detect about 30 million clusters from their radio emission, including about 2 million radio halos. However, this figure is extrapolated far beyond our current knowledge of cluster physics, and is unlikely to be accurate. Clearly, SASS2 will be venturing into uncharted territory in this field!
- Evolution of Galaxies: SASS2 will detect over 3 billion galaxies spanning all redshifts. It will trace the growth of black holes, the evolution of the cosmic star formation rate, and the interaction between these to high precision, and will discover new classes of galaxy. SASS2's high resolution will enable unambiguous identification with optical and IR sources.
- The Magnetic Sky: SASS2 will measure polarisation for about 70 million galaxies, measuring not only the effect of magnetic fields upon galaxies, but also providing a rotation measure grid nearly four orders of magnitude denser than currently available. It will measure the intergalactic magnetic field as a function of redshift and environment (sheet, string, void, etc.) giving vital clues to the origin and evolution of cosmic magnetism.

PoS(AASKA14)086

- Nearby Galaxies: SASS2 will not only provide detailed imaging of all nearby (z<0.05) star-forming and high-mass elliptical galaxies, but will do so at a resolution of 0.1 arcsec (100pc or higher), measuring the effect of both environment and AGN activity on the evolution and star formation in these galaxies.

Acknowledgment: We thank an anonymous referee for careful reading and helpful comments. ADK acknowledges financial support from the Australian Research Council Centre of Excellence for All-sky Astrophysics (CAASTRO), through project number CE110001020.

References

Banfield, J., et al., 2015, *The Third Data Release of the Australia Telescope Large Area Survey: 1.4 GHz Mosaics and Source Catalogue* to be submitted to MNRAS
Best, P. N., Heckman, T. M., 2012, MNRAS, 421, 1569
Blake, C., & Wall, J. 2002, Nature, 416, 150
Brentjens, M. A., & de Bruyn, A. G. 2005, A&A, 441, 1217
Brown, M. J. I., Jannuzi, B. T., Floyd, D. J. E., et al. 2011, ApJ, 731, L41
Camera, S., Santos, M. G., Bacon, D. J., et al. 2012, MNRAS, 427, 2079
Cassano, R., Brunetti, G., Norris, R. P., et al. 2012, A&A, 548, A100
Condon, J. J. 1974, ApJ, 188, 279
Condon, J. J., Cotton, W. D., Greisen, E. W., et al. 1998, AJ, 115, 1693
Condon, J. J., Cotton, W. D., Fomalont, E. B., et al. 2012, ApJ, 758, 23
Dehghan, S., Johnston-Hollitt, M., Franzen, T. M. O., et al. 2014, AJ, 148, 75
Dwarakanath, K. S., Kale, Ruta, 2009, ApJ, 698, 163
Ekers , R.D., 2009, *Big and Small* PoS(sps5)007
Fan, D-W., et al., 2014, *Matching Radio Catalogs using Geometrical Models with Application to SWIRE and ATLAS* in preparation
Fanaroff, B. L., & Riley, J. M. 1974, MNRAS, 167, 31
Fanti, R., Fanti, C., Schilizzi, R. T., et al. 1990, A&A, 231, 333
Farnes, J. S., O'Sullivan, S. P., Corrigan, M. E., & Gaensler, B. M. 2014, ApJ, 795, 63
Franzen, T., et al., 2015, *The Australia Telescope Large Area Survey I: 1.4 GHz Source Catalogue and Counts* to be submitted to MNRAS
Gaensler, B. M., Landecker, T. L., Taylor, A. R., & POSSUM Collaboration 2010, Bulletin of the American Astronomical Society, 42, #470.13
Grant, J. K., Taylor, A. R., Stil, J. M., et al. 2010, ApJ, 714, 1689
Hales, C. A., Norris, R. P., Gaensler, B. M., et al. 2014, MNRAS, 440, 3113
Hopkins, A. M. et al. 2003, AJ, 125, 465
Kapinska et al.(2015), *Unravelling lifecycles & physics of radio-loud AGN in the SKA era* in proceedings of "Advancing Astrophysics with the Square Kilometre Array", PoS(AASKA14)173
Krause, M., Alexander, P., Bolton, R., et al. 2009, MNRAS, 400, 646
Lallo, M. D. 2012, Optical Engineering, 51, 011011 (arXiv:1203.0002)
Mao, M. Y., Norris, R. P., Emonts, B., et al. 2014, MNRAS, 440, L31
Miley, George, De Breuck, Carlos, 2008, A&A, 15,67

PoS(AASKA14)086

Mitchell, K. J., & Condon, J. J. 1985, AJ, 90, 1957
Norris, R. P., Hopkins, A. M., Afonso, J., et al. 2011, *PASA*, 28, 215
Norris, R. P., Lenc, E., Roy, A. L., & Spoon, H. 2012, MNRAS, 422, 1453
Norris, R. P., Afonso, J., Bacon, D., et al. 2013, *PASA*, 30, 20
Parma, P., Murgia, M., de Ruiter, H. R., et al. 2007, A&A, 470, 875
Prandoni I. & Seymour N. 2015, *Revealing the Physics and Evolution of Galaxies and Galaxy Clusters with SKA Continuum Surveys*, in proceedings of "Advancing Astrophysics with the Square Kilometre Array", PoS(AASKA14)067
Raccanelli, A., Samushia, L., & Percival, W. J. 2010, MNRAS, 409, 1525
Raccanelli, A., Zhao, G.-B., Bacon, D. J., et al. 2012, MNRAS, 424, 801
Raccanelli, A., Doré, O., Bacon, D. J., et al. 2015, *Probing primordial non-Gaussianity via iSW measurements with SKA continuum surveys* arXiv:1406.0010
Randall, K. E., Hopkins, A. M., Norris, R. P., et al. 2011, MNRAS, 416, 1135
Rees, G., et al., 2015, *The cosmological sensitivity of next-generation radio continuum surveys* in preparation
Rudnick, L., & Owen, F. N. 2014, ApJ, 785, 45
Schinnerer, E., et al. 2007, ApJS, 172, 46
Smail, I., Hogg, D. W., Yan, L., & Cohen, J. G. 1995, ApJ, 449, L105
Sommer, M. W., & Basu, K. 2014, MNRAS, 437, 2163
Subrahmanyan, R., Ekers, R. D., Saripalli, L., et al. 2010, MNRAS, 402, 2792
Stil, J. M., Keller, B. W., George, S. J., et al. 2014, ApJ, 787, 99
Taylor, A. R., Stil, J. M., & Sunstrum, C. 2009, ApJ, 702, 1230
Tucci, M., Martínez-González, E., Toffolatti, L., et al. 2004, MNRAS, 349, 1267
Vernstrom, T., Norris, R.P., Scott, D., et al. 2014, MNRAS, in press, arXiv1408.4160
Weston, S., et al., 2014, *Likelihood Ratio cross-identification of ATLAS radio sources* in preparation
White, R.L., 2014, *In defense of all-sky surveys* VLA sky survey white paper
Wilman, R. J., et al. 2008, MNRAS, 388, 1335

PoS(AASKA14)086

PROCEEDINGS OF SCIENCE

The physics of the radio emission in the quiet side of the AGN population with the SKA

M. Orienti[*1†], **F. D'Ammando**[1,2], **M. Giroletti**[1], **G. Giovannini**[1,2], **F. Panessa**[3]

[1] *INAF – IRA, Bologna, Italy*
[2] *University of Bologna, Bologna, Italy*
[3] *INAF-IAPS, Roma, Italy*

Super massive black holes (SMBH) are thought to be ubiquitously hosted in massive galaxies. They may be either quiescent, like the case of Sgr A* in our Galaxy, or active, and they are at the basis of the phenomena known as Active Galactic Nuclei (AGN). In this case they often manifest their presence by releasing a huge amount of energy which usually overwhelms the star-related contribution of the entire host galaxy. Although they have been targets of many multiwavelength campaigns, the main physical processes at work in AGN are still under debate. In particular the origin of the radio emission and the mechanisms involved are among the open questions in astrophysics. The radio-loud AGN population and their radio emission is linked to the presence of bipolar outflows of relativistic jets. However, the large majority of the AGN population do not form powerful highly-relativistic jets on kpc scales, like those observed in radio galaxies and radio quasars. This does not mean that they are radio-silent objects. On the contrary, these systems are characterized by radio luminosity up to 10^{23} W/Hz at 1.4 GHz, challenging our knowledge on the physical processes at the basis of the radio emission in radio-quiet objects. The main mechanisms proposed so far are synchrotron radiation from mildly relativistic mini-jets, thermal cyclo-synchrotron emission by low-efficiency accretion flow (like ADAF or ADIOS), or thermal free-free emission from the X-ray heated corona or wind. The difficulty in understanding the main mechanism involved is related to the weakness of these objects, which precludes the study of non-local radio-quiet AGN. Multifrequency, high-sensitivity polarimetric radio observations are, thus, crucial to constrain the nature of the power engine, and they may help in distinguishing between the contribution from star formation and AGN activity. The advent of the Square Kilometer Array (SKA), with its sub-arcsecond resolution and unprecedented sensitivity will allow us to investigate these processes in radio-quiet AGN, even at high redshift for the first time. Both the broad-band radio spectrum and the polarization information will help us in disentangling between non-thermal and thermal origin of the radio emission. The jump in sensitivity of a few order of magnitudes at the (sub-)μJy level will enable us to detect radio emission from a large number of radio-quiet AGN at high redshift, providing a fundamental step in our understanding of their cosmological evolution.

Advancing Astrophysics with the Square Kilometre Array
June 8-13, 2014
Giardini Naxos, Italy

PoS(AASKA14)087

1. Introduction

Galaxies represent the majority of the observable matter in the Universe. Gravitationally bound gas, dust and stars are their basic constituents. In their centre a super massive black hole (SMBH) is usually found, and if it is in an "active" phase it is responsible for a significant contribution to the SED that cannot be attributed to other origins such as stars, gas and dust. In this case, the central region of the galaxy is termed an Active Galactic Nucleus (AGN) and is one of the most energetic phenomena in the Universe. Its emission is observed in a large range of the electromagnetic spectrum, from infrared (IR) to X-rays, by processes directly and indirectly related to the release of gravitational energy from matter falling onto the SMBH.

If the AGN is able to form a bipolar outflow of relativistic plasma, then its radio emission becomes comparable to or even stronger than the emission observed in the other energy bands. The presence, or lack, of relativistic jets is at the basis of the radio-loud and radio-quiet dichotomy. Only 10 per cent of the AGN population is radio-loud, while in the large majority the radio emission is a negligible part of the bolometric luminosity. The latter are termed radio-quiet AGN and their radio luminosity at 1.4 GHz does not exceed 10^{23} W/Hz (e.g. Condon et al. 1992).

Although the radio emission is a very marginal part of the energy released by radio-quiet AGN, it represents a unique way to investigate the high energy particle accelerators. Understanding the origin of the radio emission from radio-quiet AGN is not trivial. Usually radio-quiet AGN are hosted in late-type galaxies where star formation is responsible for the majority of the radio emission. For this reason, disentangling the AGN-related emission from the stellar contribution is a hard task to perform. The knowledge of the physical processes occurring in the nuclear region of radio-quiet AGN is a critical point for understanding differences and similarities with the radio-loud AGN population, as well as for investigating a possible link between the AGN and the star formation.

The advent of the Square Kilometer Array (SKA) will provide a jump forward in the observational capabilities reaching unexplored sensitivity levels, and thus allowing the study of faint and non-local objects, improving the statistics and providing a fundamental step forward in our understanding of the physical processes at work and their implications for the AGN feedback.

In this Chapter we briefly introduce the key issues about the radio emission in the radio-quiet AGN population and we discuss how the advent of the SKA will help in shedding a light on this hot topic. The Chapter is organized as follows: in Section 2 we present the state of the art of the radio emission in radio-quiet AGN; in Section 3 we indicate how SKA may address some open questions during the SKA1 phase, and the jump that is expected when the array will be fully operative. Concluding remarks are in Section 4.

2. Radio emission in radio-quiet AGN: state-of-the-art

2.1 The stellar contribution

A significant fraction of the radio emission in radio-quiet AGN comes from processes related to the stellar evolution, like synchrotron emitting cosmic rays accelerated by supernovae, and ther-

*Speaker.
†orienti@ira.inaf.it

PoS(AASKA14)087

mal free-free radiation from the ionized gas in star forming regions. The fact that the tight radio/far-infrared (FIR) correlation found for star-forming galaxies (SFG) holds in radio-quiet AGN supports the idea that the bulk of the radio emission in radio-quiet AGN is related to stellar processes, while the agreement is poor in radio-loud AGN due to the presence of relativistic jets (e.g. Padovani et al. 2011).

When observed with adequate angular resolution and sensitivity the radio emission is often spread across the host galaxy. A clear example is represented by the Seyfert galaxy NGC 1097. On arc-second scale the radio emission traces the profile of the host galaxy and its spiral arms (Hummel et al. 1987, Condon 1987), while on smaller scale the radio emission is organized in a spectacular circumnuclear starburst ring where several star forming regions are clearly identified.

Circumnuclear starburst emission enshrouding the central AGN is observed in many Seyfert galaxies, like Circinus (Elmouttie et al. 1998), NGC 7469 and NGC 7586 (e.g. Orienti & Prieto 2010). The co-spatial distribution of the AGN and starburst activity has suggested a connection between these two phenomena. A close link between star formation and radio emission in radio-quiet AGN is further supported by their evolution which is indistinguishable from that observed in SFG and their luminosity function (LF), which appears to be an extension of the SFG LF (Padovani et al. 2011).

2.2 The particle accelerators in the nuclei of radio-quiet AGN

The origin of the radio emission from the nucleus of radio-quiet AGN is a matter of debate. The fact that the FIR flux better correlates with the low-resolution kpc-scale radio flux density, rather than the high-resolution pc-scale emission disfavours a dominant stellar origin for the nuclear emission (Thean et al. 2000).

The main mechanisms proposed include 1) thermal emission/absorption from hot gas (Gallimore et al. 2004); 2) low-efficiency accretion/radiation flow (Narayan & Yi 1994, Blandford & Begelman 1999); 3) non-thermal synchrotron radiation from a mildly relativistic jet (Orienti & Prieto 2010), or 4) a combination of processes (Falcke & Markoff 2000, Ghisellini et al. 2004).

The study of a sample of local Seyfert nuclei pointed out an empirical correlation between radio and X-ray luminosities, suggesting that the accretion flow and the radio emission are strongly coupled (Panessa et al. 2007). Interestingly, this correlation seems the same as the one found for radio-loud radio galaxies, whose radio emission is related to relativistic jets. This may indicate a possible common mechanism between the two populations. However, this claim cannot be unambiguously proved due to the large difference in luminosity between Seyferts and radio galaxies.

Support for the presence of synchrotron emission from the Seyfert nuclei comes from the detection of radio structures similar to those observed in powerful radio source (i.e. jets, lobes and hot spots), like the case of Circinus (Elmouttie et al. 1998) and NGC 1068 (Ulvestad et al. 1987). In these two sources, evidence for AGN able to accelerate particles to high energy was claimed after the detection by the Large Area Telescope on board *Fermi* of γ-ray emission which seems to exceed the cosmic-ray contribution from the host galaxy (Hayashida et al. 2013, Lenain et al. 2010).

In Seyfert galaxies the radio emission is confined within the host galaxy, whereas radio galaxies have radio structures on scales up to hundred of kiloparsecs or even megaparsecs. Not all Seyfert nuclei behave in the same way. In particular, it has been found that flat-spectrum Seyfert nuclei

PoS(AASKA14)087

usually do not show extended morphology, and the radio emission comes from an unresolved (sub-)parsec-scale region (Anderson & Ulvestad 2005). On the contrary, in the steep-spectrum Seyfert nuclei the radio emission is not centrally concentrated, but rather is diffuse over a larger region (e.g. NGC 4151, Ulvestad et al. 1998). In some sources kpc-scale bubbles are observed (e.g. Mrk 6, Mingo et al. 2011). These bubbles may drive shocks in the interstellar medium of the host galaxy and may play a role in regulating the star formation in the hosts (e.g. Mingo et al. 2012). These differences may arise from different physical mechanisms: steep-spectrum nuclei may be able to produce extended, but slow jet structures, whereas in flat-spectrum nuclei the energy released by the AGN is mainly localized in the innermost region, without developing jets.

3. The role of SKA

Due to its weakness, the radio emission of radio-quiet AGN has been investigated mainly in nearby objects. If the resolution is not adequate, the nuclear component may be washed out by the stellar-related emission, and the radio properties may be contaminated by the contribution from different components.
VLBI observations have turned out to be an effective hunter of AGN by detecting compact, variable components with brightness temperatures above 10^6 K, and high core dominance (i.e. the ratio between the milliarcsecond and arcsecond flux density). Panessa & Giroletti (2013) studied a complete sample of local radio-quiet AGN by collecting heterogeneous VLBI observations, confirming the importance of deep high-resolution observations on more statistically complete samples and at different redshift. This issue becomes even more complicated when the sub-mJy population is taken into account due to observational limitations.
A correct determination of the stellar- and AGN-related emission is important for a comprehensive characterization of the radio emission from the AGN, its evolution and the possible interplay with the host galaxy. These key issues can be addressed by:

- determining the core dominance by comparing low-resolution and high-resolution radio observations, which provides information on the fraction of the radio emission concentrated in the central region,
- the study of the broad-band radio spectrum and the polarization properties of the nuclear region, which are important tools for testing whether the radio emission is synchrotron radiation.

The expected SKA performances will provide a jump forward in our understanding of the physics of these extraordinary celestial bodies.

3.1 Unveiling the nuclear emission with SKA1-MID

A primary requirement for the study of the AGN contribution to the radio emission is an adequate angular resolution. With a baseline of about 100 km, the SKA1-MID array has the potential to address this issue. The angular resolution that will be achieved ranges between $\sim$0.4 arcsec at

PoS(AASKA14)087

21 cm (band 2) and ∼0.07 arcsec at 3.6 cm (band 5). This resolution has already proved to be adequate for separating the AGN emission from the possible contribution of nuclear star forming regions. In fact, if we consider the bulk of the radio-quiet AGN at $z \sim 1.5-2$, a resolution of 0.07 arcsec corresponds to ∼0.6 kpc, while the host galaxy should have a total angular size of ∼2 arcsec. The separation of the nuclear emission becomes of course easier as we consider closer objects. In addition, a minimum baseline of ∼400 m will allow the detection of the diffuse emission in nearby objects up to ∼1.5 arcmin (band 2), enabling a proper spatial characterization of both star-forming processes and possible extended jet structures.

The availability of multifrequency polarimetric observations will be crucial for unveiling both the spectral index and polarization distribution. Assuming a continuum sensitivity (770-MHz band) of $\sim 0.57 \mu$Jy h$^{-1/2}$ (natural weight, Table 1 in Dewdney et al. 2013), it would be possible to study large sample of radio-quiet AGN with a 10σ sensitivity of ~ 10 μJy (uniform weight) in a reasonable time. The high resolution coupled with the deep sensitivity will allow one to reliably separate the AGN emission from the stellar contribution. This would allow the study of radio emission from AGN with luminosity $L \sim 10^{18}$ W/Hz, $L \sim 10^{20}$ W/Hz, $L \sim 5 \times 10^{22}$ W/Hz, and $L \sim 10^{23}$W/Hz at redshift 0.01, 0.1, 1, and 2, respectively. The two-tiered survey at Band 5 will be a starting point for this study.

The availability of a (quasi-)continuous radio spectrum will be a crucial tool for addressing this issue. In fact, thermal and synchrotron self-absorbed spectra are expected to show different properties, like the slope and the location of the peak frequency.

Observations covering a continuous frequency range from ~ 1 GHz to ~ 10 GHz will be crucial for discriminating between the thermal and non-thermal radio emission. This would require that band 2 (950-1760 MHz), 4 (2800-5180 MHz) and 5 (4600-13800 MHz) should be installed in SKA1-MID. A flat spectrum up to high frequency will be a clear evidence for thermal emission, while a turnover around a few GHz strongly supports the non-thermal synchrotron radiation. Furthermore, if the peak of the spectrum is due to synchrotron self-absorption, the frequency is strongly related to the physical properties of the emitting region: $\nu_p \propto H^{1/5}B^{2/5}$, where H is the magnetic field and B is the brightness. If the magnetic field computed from the observational parameter is unrealistically high, then it would prove that the peak in the spectrum is not due to synchrotron self-absorption, like in the case of NGC 4457 where the estimated magnetic field was $\sim 10^9$ G (Bontempi et al. 2012).

A spectral resolution of 100 MHz would be adequate for a proper characterization of the radio spectrum. Assuming the performances expected for the SKA1-MID (∼63 and 82 μJy h$^{-1/2}$ for a 100 kHz spectral resolution in band 2 and 5, respectively), it would be possible to easily achieve a 5σ sensitivity of ~ 20 μJy with a 100-MHz spectral resolution in about one hour (uniform weight). The broad-band radio spectrum may be combined with the polarization information for constraining the nature of the radio emission arising from different regions. For example, a jet structure is expected to show polarized steep-spectrum synchrotron emission, while the diffuse synchrotron emission from a star-forming region should be highly depolarized due to the tangled magnetic field caused by the supernovae explosions. However, low-resolution observations may cause beam depolarization in case of non-resolved jet structures.

A more complex issue will be understanding the physical processes at the basis of the nuclear, flat-spectrum emission from the core region. In principle one may expect that unpolarized emis-

PoS(AASKA14)087

sion may originate in thermal bremsstrahlung radiation from the gas of the hot corona, while some (very low) level of polarization may be observed in presence of synchrotron self-absorption. However, we must keep in mind that strong depolarization from the gas enshrouding the central region is likely to play a major role. Therefore, the lack of polarized emission cannot reliably discriminate between the two processes.

The SKA1-MID early-science capabilities

Important results on local AGN would be already achievable during the early-science operations. Assuming a maximum baseline of $\sim$ 50 km, and the availability of frequencies up to 5 GHz (band 4), the resolution would be 0.2 arcsec. This would preclude us from resolving the central kiloparsec region beyond redshift $z \sim$0.4. However, objects with $z < 0.1$ would be studied in excellent details and we should already be able to build the (quasi-)continuous spectrum of the different regions with a 5σ threshold of $\leq$60 μJy in a reasonable time. This would allow the study of objects with a luminosity of $L \sim 10^{21}$ W/Hz at redshift $z = 0.1$, down to luminosity $L \sim 10^{19}$ W/Hz at $z = 0.01$.

3.2 Towards the entire array: SKA

The advent of the full SKA array will provide a jump in the observational capabilities. The deployment of the receivers up to 24 GHz will provide a step forward in the study of the nuclear emission of either thermal or non-thermal origin. For a maximum baseline of 2000 km (i.e. 20 times longer than the SKA1-MID) the resolution at high frequency will be a few milliarcsecond, allowing the characterization of parsec-scale regions even at high redshift. This will be accompanied by an improvement of about one order of magnitude of the sensitivity, allowing the unprecedented detection of (sub-)μJy objects with largely affordable exposure time.
In addition to the study of the total intensity emission from the nuclear region, observations allowing the detection of circular polarization may be a fundamental tool for identifying cyclo-synchrotron emission from low-efficiency accretion/radiation flow.

4. Concluding remarks

The radio-quiet AGN population is expected to represent a large fraction of the faint radio sky that will be picked up by the Square Kilometer Array. Due to its weakness, the radio emission from these objects is not fully understood. Furthermore, the co-existence of both the AGN and star-formation activity makes the segregation of these two components a hard task. Constraining the radio properties of both contributions will be fundamental for determining the mechanisms at work, how they evolve, constraining the unbiased luminosity functions, and exploring a possible interplay between them.
The observational capabilities of SKA will be crucial for addressing these key issues:

PoS(AASKA14)087

- disentangling the contribution of the star-formation activity from the nuclear emission in nearby as well as in high redshift objects. This will be achieved by the availability of high angular resolution and deep sensitivity,
- understanding the nature of the radio emission from the central AGN. The quasi-continuous radio spectra covering a large range of frequencies will help in discriminating thermal bremsstrahlung radiation from hot gas, from non-thermal synchrotron radiation,
- determining the presence of extended jet-like structure related to the AGN activity by the analysis of the polarized emission.

The advent of the Square Kilometer Array will provide a substantial advance in our understanding of the radio-quiet AGN population, and the role that they play in the evolution of the host galaxy.

References

Anderson, J.M., Ulvestad, J.S. 2005, ApJ, 627, 674
Blandford, R.D.; Begelman, M.C. 1999, MNRAS, 303, L1
Bontempi, P., Giroletti, M., Panessa, F., Orienti, M., Doi, A. 2012, MNRAS, 426, 588
Condon, J.J. 1987, ApJS, 65, 485
Condon, J.J. 1992, ARA&A, 30, 575
Dewdney, P., Turner, W., Millenaar, R., McCool, R., Lazio, J., Cornwell, T., 2013, "SKA1 System Baseline Design", Document number SKA-TEL-SKO-DD-001 Revision1
Elmouttie, M. Haynes, R.F., Jones, K.L., Sadler, E.M., Ehle, M. 1998, MNRAS, 297, 1202
Fabian, A.C., Rees, M.J. 1995, MNRAS, 277, L55
Falcke, H., Markoff, S. 2000, A&A, 362, 113
Gallimore, J.F., Baum, S.A. O'Dea, C.P. 2004, ApJ, 613, 794
Ghisellini, G., Haardt, F., Matt, G. 2004, A&A, 413, 535
Hayashida, M., Stawarz, L., Cheung, C.C., et al. 2013, 779, 131
Ho, L.C., Ulvestad, J.S. 2001, ApJS, 133, 77
Hummel, E., van der Hulst, J.M., Keel, W.C. 1987, A&A, 172, 32
Lenain, J.-P., Ricci, C., Türler, M., Dorner, D., Walter, R. 2010, A&A, 524, 72
Mingo, B., Hardcastle, M.J., Croston, J.H., et al. 2011, ApJ, 731, 21
Mingo, B., Hardcastle, M.J., Croston, J.H., et al. 2012, ApJ, 758, 95
Nagar, N.M., Wilson, A.S., Falcke, H. 2001, ApJ, 559, 87
Narayan, R., Yi, I. 1994, ApJ, 428, 13
Orienti, M., Prieto, M.A. 2010, MNRAS, 401, 2599
Padovani, P., Miller, N., Kellermann, K.I., Mainieri, V., Rosati, P., Tozzi, P. 2011, ApJ, 740, 20
Panessa, F., Barcons, X., Bassani, L., et al. 2007, A&A, 467, 519
Panessa, F., Giroletti, M. 2013, MNRAS, 432, 1138
Thean, A., Pedlar, A., Kukula, M.J., Baum, S.A., O'Dea, C.P. 2000, MNRAS, 314, 573
Thean, A., Pedlar, A., Kukula, M.J., Baum, S.A., O'Dea, C.P. 2001, MNRAS, 325, 737
Ulvestad, J.S., Neff, S.G., Wilson, A.S. 1987, AJ, 93, 220
Ulvestad, J.S., Roy, A.L., Colbert, E.J.M., Wilson, A.S. 1998, ApJ, 496, 196

PoS(AASKA14)087

PROCEEDINGS OF SCIENCE

Radio investigation of Ultra-Luminous X-ray Sources in the SKA Era

Anna Wolter[1], **Anthony P. Rushton**[2,3], **Mar Mezcua**[4], **David Cseh**[5], **Fabio Pintore**[6], **Isabella Prandoni**[7], **Zsolt Paragi**[8], **Luca Zampieri**[9]

[1]*INAF-Osservatorio Astronomico di Brera;* [2]*University of Oxford;* [3]*University of Southampton;* [4]*Instituto de Astrofisica de Canarias (IAC);* [5]*Radboud University, Nijmegen;* [6]*Università degli Studi di Cagliari;* [7]*INAF-IRA Bologna;* [8]*JIVE, Dwingeloo;* [9]*INAF-Osservatorio Astronomico di Padova*

E-mail: anna.wolter@brera.inaf.it

A puzzling class of exotic objects, which have been known about for more than 30 years, is reaching a new era of understanding. We have discovered hundreds of Ultra Luminous X-ray sources (ULXs) - non-nuclear sources with X-ray luminosity in excess of the Eddington luminosity for "normal" size stellar Black Holes (BH) - and we are making progresses towards understanding their emission mechanisms. The current explanations imply either a peculiar state of accretion onto a stellar size BH or the presence of an intermediate mass BH, the long-sought link between stellar and supermassive BHs. Both models might co-exist and therefore studying this class of object will give insight into the realm of accretion in a variety of environments and at the same time find look-alikes of the primordial seed BHs that are thought to be at the origin of todays supermassive BHs at the centre of galaxies. The radio band has been exploited only scantily due to the relative faint fluxes of the sources, but we know a number of interesting sources exhibiting both extended emission (like bubbles and possibly jets) and cores, as well as observed transient behaviour. The new eras of the SKA will lead us to a major improvement of our insight of the extreme accretion within ULXs. We will both investigate in detail known sources and research new and fainter ones. When we have reached a thorough understanding of radio emission in ULX we could also use the SKA as a discovery instrument for new ULX candidates. The new array will give an enormous space to discovery: sources like the ones currently known will be detected in a snapshot up to 50 Mpc instead of at 5 Mpc with long, pointed observations.

Advancing Astrophysics with the Square Kilometre Array
June 8-13, 2014
Giardini Naxos, Sicily, Italy

PoS(AASKA14)091

1. Ultra Luminous X-ray Sources

X-ray observations of nearby galaxies show a population of point-like, off-nuclear sources with luminosities (if isotropic) in excess of the classical Eddington limit for accretion onto a 10 $M_\odot$ compact object, that we categorize as Ultra-Luminous X-ray sources (ULXs; see, e.g., Fabbiano, 2006; Feng & Soria, 2011, for reviews). Nowadays, hundreds of ULX candidates have been detected and many of them have been studied in detail (see e.g. Roberts & Warwick, 2000; Colbert & Ptak, 2002; Swartz et al., 2004; Liu & Bregman, 2005; Liu & Mirabel, 2005; Walton et al., 2011; Swartz et al., 2011). As the definition of ULX is purely empirical, the class is likely a mixed bag of sources, powered by different mechanisms. We already know that a fraction of candidates in the catalogs (see e.g. Swartz et al., 2011) are identified with known supernovae or background AGNs (see e.g. Mezcua et al., 2013b, for the correct identification of SNR4449-1). The ULX population is probably different in early- and late-type galaxies, due also to the different stellar population in the two classes of objects. In early-type galaxies, ULXs are consistent with being the luminous tail of the low-mass X-ray binary population (e.g. Plotkin et al., 2014). The largest sample of ULXs comes from late-type galaxies (see Swartz et al., 2011, and references therein), correlating in general with Star Forming regions (see e.g. Mineo et al., 2012).

The main questions that need to be answered can be summarised by: • How can we determine the fundamental properties of ULXs? • Can we infer the Black Hole (BH) masses and mass-function? • And can we determine the growth of intermediate-mass BHs?

The nature of the ULX engine is still puzzling and continues to provide us with a strong theoretical challenge, for instance how to grow massive BHs (Belczynski et al., 2010). In spiral galaxies, the number of ULXs has been found to correlate with the galaxy's global star formation rate, suggesting that they are mostly high-mass X-ray binaries (HMXBs; Swartz et al., 2004, 2011; Liu et al., 2006). This is consistent with studies that show good correlations of the star formation rate in a galaxy with its global hard X-ray luminosity (Ranalli et al., 2003; Persic & Rephaeli, 2007) and with the number of HMXBs (Grimm et al., 2003; Mineo et al., 2012), as confirmed by the study of the X-ray luminosity function in ULX-rich galaxies (e.g. Wolter & Trinchieri, 2004; Zezas et al., 2006). A significant fraction of ULXs may be fuelled by super-Eddington accretion onto stellar mass BHs (5-20 $M_\odot$; King et al., 2001; King, 2008), with non-negligible beaming effects. On the other hand, a few X-ray point sources in distant galaxies have extreme luminosities: $L_X > 10^{41}$ erg/s (the so-called HyperLuminous X-ray sources: HLX; Kaaret et al., 2001; Matsumoto et al., 2001; Wolter et al., 2006; Farrell et al., 2009; Sutton et al., 2011). Such extreme luminosities (and spectra, at least in the case of HLX-1 and M 82 X-1, Servillat et al., 2011; Feng & Kaaret, 2010) can be easily explained by sub-Eddington accretion onto an intermediate-mass black hole (IMBH). Black holes with stellar masses would need unreasonable beaming and/or super-Eddington accretion rates to produce such high luminosities (e.g. Swartz et al., 2011). It has also been proposed that bright persistent ULXs may contain the $\sim 20-80 M_\odot$ BH remnants of massive stars formed via direct collapse in a low metallicity environment (Mapelli et al., 2009; Zampieri & Roberts, 2009). A few observational results seem to confirm this scenario (Pizzolato et al., 2010; Prestwich et al., 2013; Cseh et al., 2014; Ripamonti et al., 2015). The tentative identification of the orbital modulation of a ULX optical counterpart (Liu et al., 2009; Zampieri et al., 2012), the discovery of a candidate IMBH of over 500 $M_\odot$ in the galaxy ESO 243-49 (Farrell et al., 2009, 2012), the detection of X-

PoS(AASKA14)091

ray quasi-periodic oscillations (QPOs) in a handful of ULX (e.g. Strohmayer & Mushotzky, 2003; Feng et al., 2010; Dewangan et al., 2006; Pasham & Strohmayer, 2013), and the first tentative dynamical measure of the BH mass in M101 X-1 (Liu et al., 2013) are only some examples of the fervid activity going on in the field.

The study of the timing properties of ULXs represents a promising way to better understand their nature by comparison with the properties of Galactic BH binaries (BHB). Galactic BHBs are among the brightest X-ray Galactic sources and have been extensively studied over the last decades by several large multi-wavelength campaigns (e.g. Remillard & McClintock, 2006; Fender et al., 2009). There are almost a hundred known BHBs, both persistent and transient sources, and we have acquired a fairly good knowledge of the physics underway in these systems, where a soft accretion disk covered by a comptonizing cloud of hot electrons, responsible for the hard emission, explains well the observed emission. Different states observed in BHBs are probably associated with different accretion regimes. Certain state transitions are associated with radio-emitting mass ejection events. This is supported by the observed correlation between aperiodic variability and X-ray flux (Belloni, 2010; Munoz-Darias et al., 2011). This type of relation can be used as a good tracer of the different accretion regimes in Galactic sources. In addition, a systematic analysis of spectral variability of ULXs in the X-ray band with the help of the hardness-intensity and colour-colour diagrams can provide a powerful tool to investigate the properties of their accretion flow also in comparison with the well-studied galactic BHBs. Studies in this direction were recently carried out by Pintore et al. (2014) and Sutton et al. (2013) for a few bright, nearby ULXs with the best quality data. By organizing sources according to mean spectral colours and intensity, they have shown that the behaviour of the sources can be divided in two/three different groups with homogenous properties. Furthermore, they suggested that the observed spectral and temporal variabilities can be related to the mass accretion rate and inclination angle to these sources. Understanding analogies and differences from Galactic BHBs is clearly important to shed light on the nature of ULXs, especially for very bright or hyper-luminous objects that may host IMBHs.

2. ULXs in the radio band

The radio band opens new possibilities not only by allowing a multiband approach to the investigation of the ULX central energy source, but also by determining the properties of the source and its environment. We can distinguish between compact radio emission, extended emission from a jet, and shell-like emission from SNRs. Radio spectral properties can help to distinguish between the various jet types and to reveal the nature of the emitting source (eg. thermal or synchrotron emission). Combined radio and X-ray data for a large sample of sources can be compared with known classes of emitters, like AGNs, supernova remnants, X-ray transients etc. Radio data also provide a means to estimate source lifetimes and the energy associated with the equipartition assumption.

Until now, only a handful of ULXs have been detected in the radio, due to the faintness of the sources relative to the sensitivity limits of the current telescopes. An observational VLA campaign aimed at detecting radio emission from a sample of 7 HLXs, that reached an rms of 0.01 mJy/beam yielded only one detection (Mezcua et al., 2013b). Typically, observed ULXs have luminosities in the radio band of the order $L_R = 10^{34-36}$ erg/s, from one to three orders of magnitude lower than

PoS(AASKA14)091

radio supernovae (Weiler et al., 2012). The radio to X-ray flux follows roughly a linear correlation, albeit with a large scatter, similar to that derived for interacting supernovae (Chevalier, 2003), but the difference in L_R supports the hypothesis the most ULXs are not supernovae. Furthermore, ULX bubbles do not resemble SNR: they carry at least two orders of magnitude more total energy, reach a size of hundreds of pc, have a different spectral shape, predominantly described by synchrotron emission (Pakull & Mirioni, 2002; Cseh et al., 2012; Mezcua et al., 2013b, 2014).

The detected sources are mostly closer than 15 Mpc. One notable exception is the radio counterpart of HLX-1 at 95 Mpc, which has a flux density of 50 μJy at cm wavelengths (Webb et al., 2012) and was targeted just because it is a very luminous object (but it may be the nucleus of a stripped dwarf or of a bulgeless satellite galaxy, Webb et al., 2010; Mapelli et al., 2013). A number of optical/UV nebulae have also been detected around nearby ULXs (Pakull & Mirioni, 2002; Pakull & Mirioini, 2003). Three famous nebulae have been studied in the radio, Holmberg II X-1 (Miller et al., 2004; Cseh et al., 2014), NGC 5408 X-1 (Kaaret et al., 2003) and IC 342 X-1 (Cseh et al., 2012): their radio spectra are consistent with optically thin synchrotron emission; the radio nebulae can be compared with optical results and allow an estimate of the energetics of the systems. All of these sources currently observed associated to a nebula are located within 5 Mpc (see also Wolter & Zampieri, 2013). However, as the nebulae are resolved only for nearby ULXs, with the present instruments it is still not known if the existence of the nebulae is ubiquitous in ULXs or if they can be categorized in different classes. Preliminary results seem to imply that if they are present they might be much fainter than the ones already observed (Mezcua et al., 2013b). In some cases a compact core or resolved jets are observed (Mezcua & Lobanov, 2011; Mezcua et al., 2013a,b, 2014; Cseh et al., 2014). Indeed a thorough investigating of a complete sample of ULXs in this respect is still lacking. Furthermore, by assuming the emission of ULXs is due to accretion in a sub-Eddington regime, similar to radiatively inefficient Galactic XRBs and AGNs, the radio detection allows us to locate the ULXs in the fundamental plane (FP) of sub-Eddington accreting black holes (Corbel et al., 2003; Gallo et al., 2003; Merloni et al., 2003; Falcke et al., 2004) as defined by a correlation between radio core (L_R) and X-ray (L_X) luminosity and black hole mass ($M_{\rm BH}$), recently revised by Plotkin et al. (2012) to $\log L_{\rm X} = 1.45 \times \log L_{\rm R} - 0.88 \times \log M_{\rm BH} - 6.07$. This could be one of the most viable option of determining or setting an upper limit to the mass of ULXs in the stated assumptions: we can apply this when the sources are in the hard state and the radio emission comes from the compact jet. For instance, by using the upper limits in the radio band and assuming a hard state in IC 342 X-1 with the FP plane, Cseh et al. (2012) derived an upper limit on $M_{\rm BH}$ of 1000 $M_\odot$ (see also Mezcua et al., 2013b). Further X-ray spectral studies confirmed this upper limit by setting more stringent mass constraints on the BH of 30-200 $M_\odot$ (Marlowe et al., 2014). More recent findings nevertheless seem to exclude that the sources are found in the hard state, except HLX-1, where a radiatively inefficient accretion flow (RIAF) was found (NuSTAR observations by Bachetti et al., 2013; Walton et al., 2013). If a hard state is more commonly found for sources that are not persistent in the radio band, then we should focus on repeated observations in order to find variable/transient sources (e.g. see review by Webb et al., 2014). Compact radio emission is observed in the hard state, while strong relativistic transient ejections are seen during state transitions, when the source goes from hard to soft state (see Fender et al., 2012; Zhang et al., 2013, and references therein).

Planned and future surveys at centimetre-wavelenghts will repeatedly observe the sky, offer-

PoS(AASKA14)091

ing thus the chance to study the variability of the sources and, possibly, even to detect new sources based on their variability patterns. Such surveys include The Hunt for Dynamic and Explosive Radio Transients conducted with Meerkat (a.k.a. Thunderkat [1]), and the Australian Square Kilometre Array Pathfinder (ASKAP) Survey for Variables and Slow Transients (Murphy et al., 2013) that will reach a continuum sensitivity of 47 μJy/beam in 1 hr. The resolution of the ASKAP survey ($10''$) will not allow the ULX to be resolved from the galaxy nucleus, while MeerKAT could in principle do this, if it reaches, as envisioned, a 50 mas resolution. Also the JVLA is planning an all sky survey: VLASS[2].

The SKA, due to its large survey speed will allow monitoring of known radio counterparts to determine both spectra and timing properties, and detection of both new counterparts to known ULXs and possibly new ULXs. In addition, radio measurements will permit the estimate of the minimum energy associated with equipartition in the bubble (see Kaaret et al. (2003); Miller et al. (2004) for Ho II X-1 and Mezcua et al. (2013a) for N5457-X9). In case a jet can be identified to large distances and for faint sources, we will be able to infer the mass of ULXs accreting at sub-Eddington rates.

3. Measuring ULXs in the new era of advanced radio telescopes

SKA observations of ULXs will study both the kinetic feedback of relativistic jets and the nebulous radio bubbles around their compact objects. Observations can be divided into measurements of either the steady extended structure or the possibly transient core emission. The former requires high-resolution observations to resolve the surrounding radio bubbles and to track the expansion of superluminal motion; the latter requires monitoring and rapid response measurements that will alert the community to new flaring events. As such, SKA-LOW is not a priority for studying ULXs, as the resolution is too low to resolve the bubbles and the transient decoherence time (period between recurrent events) may not be distinguishable due to the optical depth effect at long wavelengths. Therefore the discussion below will focus on the future GHz surveys from the SKA. The study of ULXs will in general benefit from analysis of all the other emission sources in the galaxy, which is described in depth in Beswick et al. (2015).

3.1 Detecting 'bubbles' surrounding ULXs

A few example ULXs that have known associated radio bubbles are N5457-X9 $L_{1.6\mathrm{GHz}} = 1 \times 10^{34}$ erg s^{-1} (Mezcua et al., 2013a), Holmberg II-X1 $L_{4.8\mathrm{GHz}} = 2.2 \times 10^{34}$ erg s^{-1} (Cseh et al., 2014), IC 342 X1 $L_{4.8\mathrm{GHz}} = 1.8 \times 10^{35}$ erg s^{-1} (Cseh et al., 2012), plus the candidate microquasars in NGC7793 (S26) $L_{5.5\mathrm{GHz}} = 2 \times 10^{35}$ erg s^{-1} (Soria et al., 2010) and in M83 (MQ1) $L_{5.5\mathrm{GHz}} = 2 \times 10^{35}$ erg s^{-1} (Soria et al., 2014). All have typical sizes of a few 10-100 pc across (corresponding to $\sim 1 - 10''$ at a distance of a few Mpc). These bubbles have some similarities with the W50 nebula surrounding the Galactic microquasar SS433, observed to have a total flux of 70 Jy at 1.4 GHz, and assuming to have a distance of 5.5 kpc, would have a slightly lower luminosity of 3.5×10^{33} erg s^{-1} compared to the ULX bubbles.

[1] http://www.ast.uct.ac.za/thunderkat/ThunderKAT.html
[2] https://science.nrao.edu/science/surveys/vlass

PoS(AASKA14)091

To measure all the ULX bubbles in the local universe, a reasonable luminosity limited survey should therefore reach a brightness of $L_{\rm radio} \leq 10^{33}$ erg s^{-1}, in order to detect all the currently known types of diffused radio bubbles. This would correspond to a required flux detection of $S_{\rm radio} < 835 \times \nu_{GHz} D_{\rm Mpc}^{-2}$ μJy bm^{-1} or $S_{1.5{\rm GHz}} < 550 \times D_{\rm Mpc}^{-2}$ μJy bm^{-1}. We also require a sub-arcsecond resolution to resolve the bubbles out to a distance of a few $\times$10 Mpc. In Figure 1 we show the distance at which the SKA can make a 7σ detection of this luminosity as a function of estimated integration time per field, for three different instances of SKA. The telescope parameters assume dual polarisation, with SEFD values of 391, 1630 and 16300 K m^{-2} and instantaneous bandwidths of 500, 700 and 700 MHz for SKA1-SUR, SKA1-MID and SKA2-MID respectively. As shown in Figure 1, both SKA1-SUR and SKA1-MID quickly reach this detection limit for our Local Group of galaxies, while SKA1-SUR requires significantly more telescope time to detect ULX radio bubbles much further than $\sim$ 5 Mpc away. Moreover, SKA1-MID will significantly detect all radio bubbles within $<$ 10 Mpc by integrating for $\sim$ 1 hr per field (assuming rms noise of $\sim$ 0.6 μJy bm^{-1}) and very deep SKA1-MID observations could detect ULXs bubbles out to $\sim$ 18 Mpc. Phase 2 of the SKA will double the distance of detecting ULX bubbles of a given luminosity with only modest telescope time per target. This will effectively increase the search volume by over an order of magnitude and very deep pointings could detect known radio bubbles out to $\sim$ 55 Mpc.

3.2 Monitoring core emission from ULXs

Whilst the steady radio emission from the surrounding ULX environment can be readily estimated from known sources, accreting sources (such as ULXs) may also produce core emission, directly related to the accretion process and possibly transient outbursts of varying luminosity and cadence. Outbursts from compact sources are associated with changes in the accreting conditions and a detailed coupling between the X-ray state (i.e. X-ray spectral hardness) and their radio producing jets has been well documented for X-ray binaries (Corbel et al., 2015). Hitherto, there are only a few extragalactic transient sources that might originate from a super-Eddington stellar-mass or a sub-Eddington IMBH. The best example of transient behaviour comes from the Hyper-Luminous X-ray source HLX-1 in the galaxy ESO 243-49. Webb et al. (2012) showed that HLX-1 goes through regular outbursts to a flux density of 50–80 μJy bm^{-1} (between 5–9 GHz) and assuming the host galaxy is at $\sim$ 95 Mpc, this gives a peak luminosity of $L_{5-9\ {\rm GHz}} \sim 2-8 \times 10^{36}$ erg s^{-1}. HLX-1 goes through a semi-recurrent outburst with a cadence of around 1 year and an outburst duration of 100–200 days (although the peak emission only last a few days). Similarly, a radio transient in M82 reaches a flux density of $\sim$ 1.5 mJy bm^{-1} (Muxlow et al., 2010) corresponding to a luminosity of $L_{5\ {\rm GHz}} \sim 1 \times 10^{35}$ erg s^{-1} for a distance of 3.5 Mpc, although no clear X-ray emission is associated with this source, hence this object is not strictly a ULX (although it shares similar radio properties). The Ultra Luminous Infra-Red Galaxy Arp 220 (at a distance of $\sim$ 77 Mpc) also shows multiple recurrent radio transients with a flux density around few 100 μJy bm^{-1} (Batejat et al., 2012) corresponding to an apparent luminosity of $\sim 7 \times 10^{36}$ erg s^{-1}. Finally, the radio emission associated with a ULX in NCG 2276 produces a radio flux at 5 GHz of 1.43 mJy, which assuming a distance of 33.3 Mpc gives a radio luminosity of $\sim 9.5 \times 10^{36}$ erg s^{-1} (Mezcua et al., 2013b); this emission could be either an extremely bright surrounding radio nebula or a very slowly evolving jet from an intermediate mass black hole, although we do not have yet a secure association with

PoS(AASKA14)091

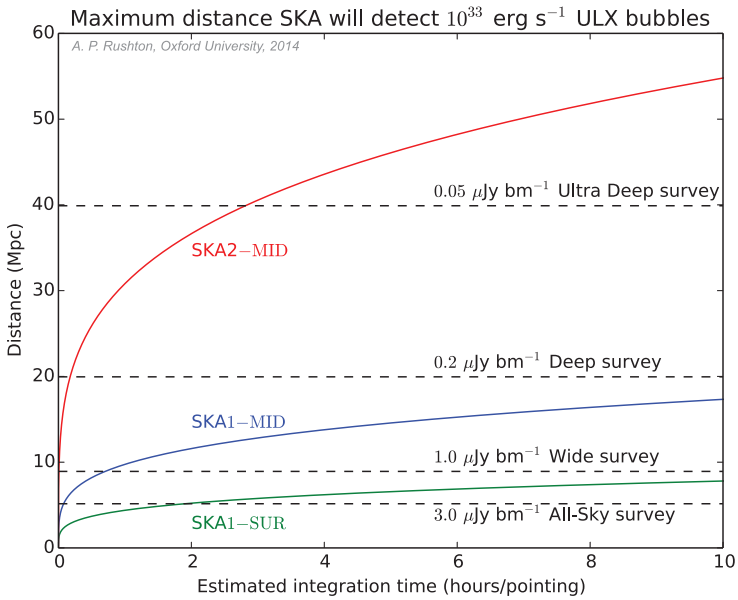

Figure 1: The maximum distance the SKA will detect ULX radio bubbles with a luminosity of 10^{33} erg s^{-1} as a function of integration time. The green, blue and red are the estimated integration time required to make a significant ($> 7\sigma$) detection using SKA1-SUR, SKA1-MID and SKA2-MID respectively. The horizontal dashed lines show the maximum distance to which the bubbles can be significantly detected with four different surveys being planned with some of the reference continuum surveys discussed in Prandoni & Seymour (2015). In particular we show the 1.4 GHz All-sky high resolution ($\leq 0.5''$) survey (3 μJy bm^{-1} rms), and the three tiers of the $0.5''$ resolution 1 GHz survey: 'Wide' (1000-5000 deg^2, 1 μJy bm^{-1} rms), 'Deep' (10-30 deg^2, 0.2 μJy bm^{-1} rms) and 'Ultra Deep' (1 deg^2, 0.05 μJy bm^{-1} rms).

the galaxy (Wolter et al., 2014). Therefore, the brightest radio counterparts of ULXs (or ULX-like sources like S26 in Soria et al., 2010) appear to have a luminosity of up to $L_{\rm radio} \sim 10^{37}$erg s^{-1}, hence can already be detected with current instruments out to $\sim$ 100 Mpc. Identifying more of these 'hyper-bright' off-nuclear radio sources may be a serendipitous by-product of the wide-field SKA surveys (Fender, 2015, and Sect. 3.3 here), however, high-resolution observations will be required to separate their locations from their galactic nuclei. Certainly, for target fields at >100 Mpc, SKA-VLBI will be needed as follow-up to resolve the few milli-arcsecond central core of the host galaxies (Paragi et al., 2015).

The high-sensitivity and fast survey speed of the SKA instruments will be particularly useful for finding slow transients and persistent core emission in the nearest galaxies. From observations of compact Galactic binaries (i.e. accreting neutron stars and stellar-mass black holes), we know that hard X-ray states produce a flat-spectrum radio jet. Transitions to softer X-ray states are associated with a steep spectrum radio flare (i.e. brighter at longer wavelengths), possibly due to the formation of a shock within the jet. We can therefore estimate the distance we will detect these outbursts if they are also associated with ULXs. For example, the brightest Galactic transient is Cygnus X-3, which can peak above 10 Jy bm^{-1} (Miller-Jones et al., 2004), and although the exact distance is uncertain (estimated between 7-10 kpc), this corresponds to around $L_{\rm radio} \approx 5 \times 10^{33}$

PoS(AASKA14)091

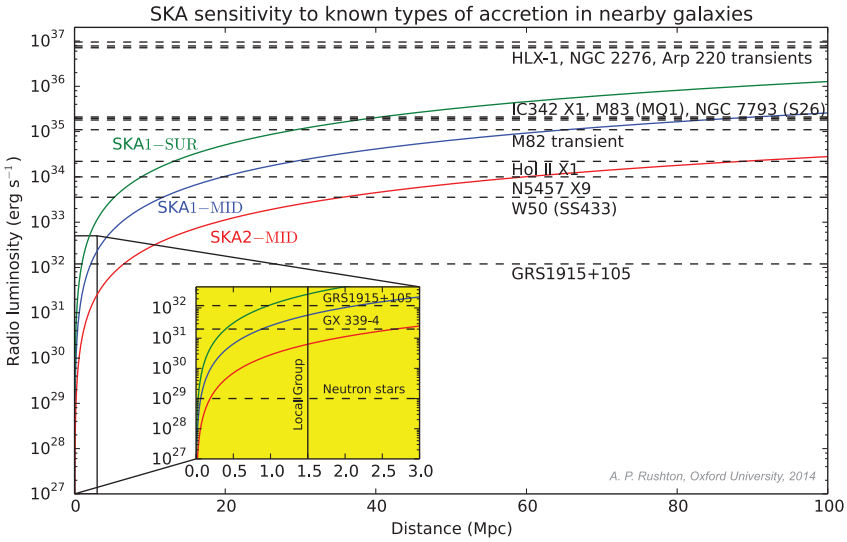

Figure 2: The sensitivity of the SKA to known transient sources in the nearby universe as function of distance. The green, blue and red are the estimated (7σ) flux density detection limit of SKA1-SUR, SKA1-MID and SKA-MID respectively assuming a 1 hour integration per target. The horizontal dashed lines are the luminosities of known radio emitting ULXs and Galactic compact stellar sources.

erg s^{-1} (peaking brighter than the entire W50/SS433 nebula!). GRS1915+105, the first superluminal source detected in the Galaxy, is also relatively bright with a peak flux of 250 mJy bm^{-1} (Rushton et al., 2010) and a distance of more than 10 kpc, which gives a $L_{\rm radio} \sim 10^{32}$ erg s^{-1}. Finally, the radio luminosity directly emitted from the jet in SS433 produces a near persistent flux that flares up to ~ 2.5 Jy bm^{-1}, although as the distance is only 5.5 kpc this is a corresponding luminosity of only $L_{1.0\ \rm GHz} \approx 9 \times 10^{31}$ erg s^{-1}. As an example of the detection limit of the SKA, we show in Figure 2 the estimated 7σ detection limit of SKA to these known transients out to a distance of 100 Mpc for integrations of 1 hour.

In case of radiatively inefficient accretion flow, which usually means accretion at low or very low Eddington rates, the Fundamental Plane method can be applied. Although it is questionable to use the FP as a general tool, in those cases in which it can be applied it yields an independent estimate of the BH mass. For instance, a 100 M$_\odot$ at low Eddington rate would produce $L_{\rm X} = 1 \times 10^{40}$ erg s^{-1} and consequently $L_{\rm R} \sim 1 \times 10^{33}$ erg s^{-1} according to Plotkin et al. (2012).

3.3 How to exploit the All-Sky Surveys for ULXs

The SKA will be used to make all-sky surveys and it is therefore interesting to quantify the ULX discovery potential of such surveys. Following Prandoni & Seymour (2015) we consider two 1.4 GHz all-sky (3π; the total sky visible to the SKA) radio-continuum reference surveys for SKA in its phase 1 (SKA1): one characterised by 2 μJy bm^{-1} rms, 2″ resolution; the other one by 3 μJy bm^{-1} rms and 0.5″ resolution. With such rms sensitivities we are able to detect the faintest ($> 10^{33}$ erg s^{-1}) ULX only in the very local Universe (only up to a distance of 5-6 Mpc), while the brightest ULX ($> 10^{35-36}$ erg s^{-1}) can be detected up to 50-150 Mpc. As far as angular resolution

PoS(AASKA14)091

is concerned, $2''$ is more than enough to be able to distinguish ULX candidates from other point sources at the galaxy center, in the majority of situations, as it allows us to resolve scales of the order of 50-500 pc at 5-50 Mpc.

Assuming a factor 10 increase in sensitivity, we can anticipate that SKA all-sky surveys will be able to push ULX blind searches up to distances of 150-200 Mpc for source luminosities of 10^{35} erg s^{-1}. Sub-arcsec angular resolutions will be needed to resolve physical scales of $\sim$ 500 pc.

The first and easiest task would be to identify radio counterparts or upper limits for the known ULXs in current and future lists. We emphasise that the ULXs with a detected radio counterpart are at this time only a small fraction of the ULX population. We envisage that after having measured a large enough number of radio data for ULXs we will be able to better characterise the sources properties and define a parameter space that will allow the detection of new objects directly from the radio observations. New accreting sources could be identified for instance from the recurrent ejection of jets, while the determination of their bolometric luminosity would come a-posteriori from multi-wavelength follow-up observations. Current X-ray facilities as XMM-Newton and Chandra are expected to last many years and are providing catalogs of X-ray sources to compare with the future radio sky. Athena has been selected by ESA in the framework of the Cosmic Vision 2015-2025 plan, and is currently planned to a launch in the late 2020s. Other instruments have been proposed to have either a sharper resolution (like Smart-X) or timing properties (like LOFT) and will be at work in synergy with the SKA if approved.

3.4 Searching for ULXs during the SKA early science phase

The estimated sensitivity of surveys presented in this chapter assume the completion of phase 1 and 2 of the SKA, in order to detect the maximum number of ULXs and produce the largest statistical sample of these compact objects in the radio band. Owing to the time-critical nature of these accreting sources, the early science phase of the SKA will be crucially important and will provide a longer monitoring period for the brightest sources. The cadence for decoherence between outbursts is typically months to years (and sometimes a few decades) and regular monitoring of the nearest galaxies should commence immediately.

Known and bright sources such as HLX-1 could be significantly detected within only a few minutes integration time with 50% of SKA1-MID and about 30 mins. using 50% of SKA1-SUR; therefore, 50% SKA1-MID could be used to regularly monitor the known transient ULXs and be triggered when outbursts are detected at other wavelengths, whilst 50% SKA1-SUR could blindly search for serendipitous events. Also, during the early science phase, the SKA will be the most sensitive radio telescope in the Southern hemisphere and can be used to make targeted searches for radio bubbles from the nearest ULXs.

Acknowledgments

It is a pleasure to acknowledge useful discussions with Robert Beswick and Sara Motta. F.P., A.W. and L.Z. acknowledge financial support from the INAF research grant PRIN-2011-1 (“Challenging Ultraluminous X-ray sources: chasing their black holes and formation pathways”) and financial contribution from the agreement ASI-INAF I/037/12/0.

PoS(AASKA14)091

References

Bachetti, M., et al., 2013, ApJ, 778, 163

Batejat, F., Conway, J. E., Rushton, A., et al. 2012, A&A, 542, L24

Belczynski, K., Builk T., Fryer, C.L., Ruiter, A., Valsecchi, F., Vink, J.S., Harley, J.R, 2010, ApJ, 714, 1217

Belloni, T.M., 2010 Proceedings of "X-ray Astronomy 2009: Present Status, Multi-Wavelength Approach and Future Perspectives", Bologna, Italy, September 7-11, 2009, AIP, eds. A. Comastri, M. Cappi, and L. Angelini, Volume 1248, pp. 107-110

R. J. Beswick, R.J., Brinks, E., Pérez-Torres, M.A., et al. “SKA studies of nearby galaxies: star-formation, accretion processes and molecular gas across all environments” in proceedings of “Advancing Astrophysics with the Square Kilometre Array”, PoS(AASKA14)070

Chevalier 2003 From Twilight to Highlight: The Physics of Supernovae: Proceedings of the ESO/MPA/MPE Workshop Held at Garching, Germany, 29-31 Juli 2002, ESO ASTROPHYSICS SYMPOSIA. ISBN 3-540-00483-1. Edited by W. Hillebrandt and B. Leibundgut. Springer-Verlag, 2003, p. 299

Colbert, E.J.M. & Ptak, A.F., 2002 ApJS, 143, 25

Corbel, S., Nowak, M. A., Fender, R. P., Tzioumis, A. K., and Markoff, S, 2003, A&A, 400, 1007

Corbel, S., Miller-Jones, J.C.A., Fender, R.P., Maccarone, T., O’Brien, T., Paragi, Z., Rupen M., Woudt, P.A., 2015, “Incoherent transient radio emission from stellar-mass compact objects in the SKA era”, in proceedings of “Advancing Astrophysics with the Square Kilometre Array”, PoS(AASKA14)053

Cseh, D., Corbel, S., Kaaret, P., et al. 2012, ApJ, 749, 17

Cseh, D., Kaaret, P., Corbel, S., et al. 2014, MNRAS, 439, L1

Dewangan, G. C., Griffiths, R. E., Rao, A. R., 2006, ApJ, 641, L125

Fabbiano, G., 2006, ARA&A, 44, 323

Falcke, H., Körding, E., Markoff, S. 2004, A&A, 414, 895

Farrell, S.A., Webb, N.A., Barret, D., Godet, O., Rodrigues, J.M., 2009, Nature, 460, 73

Farrell, S.A., et al. 2012, ApJ, 747, L13

Fender, R. P., Homan, J., Belloni, T. M., 2009, MNRAS, 396, 1370

Fender, R.P., & Belloni, T.M. 2012, Science, 337, 540

Fender, R. P. 2015, “The Transient Universe with the Square Kilometre Array”, in proceedings of “Advancing Astrophysics with the Square Kilometre Array”, PoS(AASKA14)051

Feng, H., & Kaaret, P., 2010, ApJ, 712, L169

Feng, H., Rao, F., Kaaret, P., 2010, ApJL, 710, L137

Feng H., & Soria R., 2011, New Astronomy Reviews, 55, 166

Gallo E., Fender. R.P., Pooley, G.G., 2003, MNRAS, 344, 60

Grimm H.-J., Gilfanov M., Sunyaev R., 2003, MNRAS, 339, 793

Kaaret, P., Prestwich, A. H., Zezas, A., Murray, S. S., Kim, D.-W., Kilgard, R. E., Schlegel, E. M., Ward, M. J., 2001, MNRAS, 321, L29

Kaaret, P., Corbel, S., Prestwich, A.H., Zezas, A., 2003 Science, 299, 365

King, A. R., Davies, M. B., Ward, M. J., Fabbiano, G., Elvis, M., 2001, ApJL, 552, L109

King, A.R., 2008, MNRAS, 385, L113

PoS(AASKA14)091

Liu J.-F. & Bregman J.N. 2005, ApJS, 157, 59
Liu & Mirabel 2005, A&A, 429, 1125
Liu, J.-F., Bregman, J.N., Irwin. J., 2006, ApJ. 642, 171
Liu, J.-F., Bregman, J.N., McClintock, J.E., 2009, ApJL, 690, L39
Liu J.-F., Bregman, J.N., Bai, Y., Justham, S., Crowter, P. 2013, Nature, 503, 500
Marlowe, H., Kaaret, P., Lang, C., Feng, H., Grisé, F., Miller, N., Cseh, D., Corbel, S., Mushotzky, R.F., 2014, MNRAS, 444, 642
Mapelli, M., Colpi, M., Zampieri, L., 2009, MNRAS, 395, L71
Mapelli, M., Annibali, F., Zampieri, L., Soria, R., 2013, A&A, 559, 124
Matsumoto, H., Tsuru, T.G., Koyama, K., Awaki, H., Canizares, C.R., Kawai, N., Matsushita, S., Kawabe, R., 2001, ApJL, 547 L25
Merloni, A., Heinz, S., diMatteo, T., 2003, MNRAS, 345, 1057
Mezcua, M., & Lobanov, A.P., 2011, AN, 332, 379
Mezcua, M., Farrell, S. A., Gladstone, J. C., Lobanov, A. P. 2013, MNRAS, 436, 1546
Mezcua, M., Lobanov, A.P., Martín-Vidal, I., 2013, MNRAS, 46, 2454
Mezcua, M., Roberts, T.P., Sutton, A.D., Lobanov, A.P. 2013, MNRAS, 436, 3128
Mezcua, M., Fabbiano, G., Gladstone, J.C., Farrell, S.A., Roria, R., 2014, ApJ, 785, 121
Miller, J.M., Fabian, A.C., Miller, M.C., 2004 ApJL, 614, L117
Miller-Jones, J.C.A., Blundell, K.M., Rupen, M.P., et al. 2004, ApJ, 600, 368
Mineo S, Gilfanov M., Sunyaev R., 2012, MNRAS, 419, 2095
Munoz-Darias, T., Motta, S., Belloni, T.M., 2011, MNRAS, 410, 679
Murphy, T., et al., 2013, PASA, 30, 6
Muxlow, T. W. B., Beswick, R. J., Garrington, S. T., et al. 2010, MNRAS, 404, L109
Paragi, Z., Godfrey, L., Reynolds, C., et al. 2015, "Very Long Baseline Interferometry with the SKA", in proceedings of "Advancing Astrophysics with the Square Kilometre Array", PoS(AASKA14)143
Pasham, D.R., & Strohmayer, T.E., 2013, ApJ, 753, 139
Pakull, M.W. & Mirioni, L., 2002, arXiv:astro-ph/0202488
Pakull M.W. & Mirioni, L., 2003, RMxAC, 15, 197
Persic, M., & Rephaeli, Y., 2007, A&A, 463, 481
Pintore, F., Zampieri, L., Wolter, A., Belloni, T.M., 2014, MNRAS, 439, 3461
Pizzolato F., Wolter A., Trinchieri G., 2010, MNRAS, 406, 1116
Plotkin, R.M., Markoff, S., Kell, B.C., Körding, E., Andreson, S.F., 2012 MNRAS, 419, 267
Plotkin, R.M., Gallo, E., Miller, B.P., Baldassare, V.F., Treu, T., Woo, J.-H., 2014, ApJ, 780, 6
Prandoni I. & Seymour N. 2015, "Revealing the Physics and Evolution of Galaxies and Galaxy Clusters with SKA Continuum Surveys", in proceedings of "Advancing Astrophysics with the Square Kilometre Array", PoS(AASKA14)067
Prestwich, A. H., Tsantaki, Maria, Zezas, A., Jackson, F., Roberts, T. P., Foltz, R., Linden, T., Kalogera, V., 2013, ApJ, 769, 92
Ranalli, P., Comastri, A., Setti. G., 2003, A&A, 399, 39
Remillard, R.A., & McClintock, J.E., 2006, ARA&A, 44, 49
Ripamonti, E., Wolter, A., Gomitoni, M., Mapelli, M., 2015, in prep.
Roberts, T.P., & Warwick, R.S., 2000, MNRAS, 315, 98

PoS(AASKA14)091

Rushton, A., Spencer, R.E., Pooley, G., & Trushkin, S. 2010, MNRAS, 401, 2611
Servillat, M., Farrell, S.A., Lin, D., Godet, O., Barret, D., Webb, N.A., 2011, ApJ, 743, 6
Soria, R., Pakull, M.W., Broderick, J.W., Corbel, S., & Motch, C. 2010, MNRAS, 409, 541
Soria, R., Long, K.S., Blair, W.P., et al. 2014, Science, 343, 1330
Strohmayer, T.E., & Mushotzky, R.F., 2003, ApJ, 586, 61
Sutton, A.D., Roberts, T.P., Walton, D.J., 2011, AN, 332, 362
Sutton, A.D., Roberts, T.P., Middleton, M.J., 2013, MNRAS, 435, 1758
Swartz D.A., Ghosh K.K., Tennant A.F., Wu K., 2004, ApJS, 154, 519
Swartz D.A., Soria R., Tennant A.F., Yukita M., 2011, ApJ, 741, 49
Walton, D.J., Gladstone, J.C., Roberts, T.P. Fabian, A.C., 2011, AN, 332, 354
Walton, D., et al., 2013, ApJ, 779, 148
Webb, N.A., Barret, D., Godet, O., Servillat, M., Farrell, S.A., Oates, S.R., 2010, ApJL, 712, L107
Webb, N., Cseh, D., Lenc, E., et al. 2012, Science, 337, 554
Webb, N., Cseh., D., Kirsten, F., 2014, PASA, 31, 9
Weiler, K.W., Panagia, N., Montes, M.J., Sramek, R.A., 2002, ARA&A, 40, 38
Wolter A., Trinchieri G., 2004, A&A, 426, 787
Wolter A., Trinchieri G., Colpi, M. 2006, MNRAS, 373, 1327
Wolter, A., & Zampieri, L. Black Hole (g)Astronomy, Brindisi, 2013, http://astro.u-strasbg.fr/~goosmann/gAstronomy_BH_Accretion/Session_6/session6_talk_wolter.pdf
Wolter A., Mapelli, M., Esposito, P., Pizzolato, F., Ripamonti, E., 2006, MNRAS, submitted
Zampieri, L. & Roberts, T.P., 2009, MNRAS, 400, 677
Zampieri, L., Impiombato, D., Falomo, R., Grisé, F., Soria, R., 2012, MNRAS, 419, 1331
Zezas A., Fabbiano G., Baldi A., Schweizer F., King A.R., Ponman T.J., Rots A.H., 2006, ApJS, 166, 211
Zhang, G, Mendez, M., Belloni, T.M., Homan, J., 2013, MNRAS, 436, 2276

PoS(AASKA14)091

PROCEEDINGS OF SCIENCE

The SKA and Galaxy Cluster Science with the Sunyaev-Zel'dovich Effect

Keith Grainge[1], **Stefano Borgani**[2,3], **Sergio Colafrancesco**[4], **Chiara Ferrari**[5], **Anna Scaife**[6], **Paolo Marchegiani**[4], **S. Emritte**[4]. **J. Weller**[7,8,9]

[1] *Jodrell Bank Centre for Astrophysics, School of Physics and Astronomy, The University of Manchester, Manchester, UK;*
[2] *Astronomy Unit, Department of Physics, University of Trieste, via G.B. Tiepolo 11, I-34131 Trieste, Italy;*
[3] *INFN-National Institute for Nuclear Physics, Via Valerio 2, I-34127 Trieste, Italy;*
[4] *School of Physics, University of the Witwatersrand, 1 Jan Smut Ave, WITS-2050 Johannesburg, South Africa;*
[5] *Laboratoire Lagrange, UMR 7293, Université de Nice Sophia-Antipolis, CNRS, Observatoire de la Côte d'Azur, 06300 Nice, France;*
[6] *School of Physics & Astronomy, University of Southampton, Southampton, SO17 1BJ, UK;*
[7] *University Observatory Munich, Department of Physics, Ludwig-Maximilians University, 81679 Munich, Germany;*
[8] *Excellence Cluster Universe, Boltzmannstr. 2, 85748 Garching bei Munchen, Germany;*
[9] *Max-Planck-Institute for Extraterrestrial Physics, Giessenbachstrasse, 85748 Garching, Germany*

E-mail: keith.grainge@manchester.ac.uk

Studying galaxy clusters through their Sunyaev-Zel'dovich (SZ) imprint on the Cosmic Microwave Background has many important advantages. The total SZ signal is an accurate and precise tracer of the total pressure in the intra-cluster medium and of cluster mass, the key observable for using clusters as cosmological probes. Band 5 observations with SKA-MID towards cluster surveys from the next generation of X-ray telescopes such as e-ROSITA and from Euclid will provide the robust mass estimates required to exploit these samples. This will be especially important for high redshift systems, arising from the SZ's unique independence to redshift. In addition, galaxy clusters are very interesting astrophysical systems in their own right, and the SKA's excellent surface brightness sensitivity down to small angular scales will allow us to explore the detailed gas physics of the intra-cluster medium.

Advancing Astrophysics with the Square Kilometre Array
June 8-13, 2014
Giardini Naxos, Sicily, Italy

PoS(AASKA14)170

1. Introduction

The Sunyaev-Zel'dovich (SZ) effect (Sunyaev & Zel'dovich 1970, 1972) is a secondary anisotropy introduced onto the Cosmic Microwave Background (CMB) through inverse Compton scattering of CMB photons from the electrons (thermal and non-thermal) contained the intra-cluster medium (ICM) of galaxy clusters (see e.g. Birkinshaw (1999); Carlstrom et al. (2002) for an overview of the SZ effect). On average this scattering leads to an increase in the energy of these photons, while conserving photon number, which results in a change in intensity ΔI_ν from that of the CMB

$$\Delta I_\nu = \frac{2(k_B T_0)^3}{(hc)^2} \frac{\sigma_T}{m_e c^2} \int P_e g(x) dl \tag{1.1}$$

where T_0 is the temperature of the CMB today, h is the Planck constant, k_B is the Boltzmann constant and c is the speed of light. P_e is the electron pressure in the cluster ICM (i.e. $P_e = k_B T_e \cdot n_e$ for a thermal plasma with temperature T_e and number density n_e of the scattering electrons); and $g(x)$ is the spectral shape of the SZ effect (see Figure 1), in the non-relativistic limit given by

$$g_{nr}(x) = \frac{x^4 e^x}{(e^x - 1)^2} \left[x \coth \frac{x}{2} - 4 \right] \tag{1.2}$$

in terms of the non-dimensional frequency x given by

$$x = \frac{h\nu}{k_B T_0} \tag{1.3}$$

SKA1-MID will have the capability to spectrally separate thermal and non-thermal components of the SZ effect.

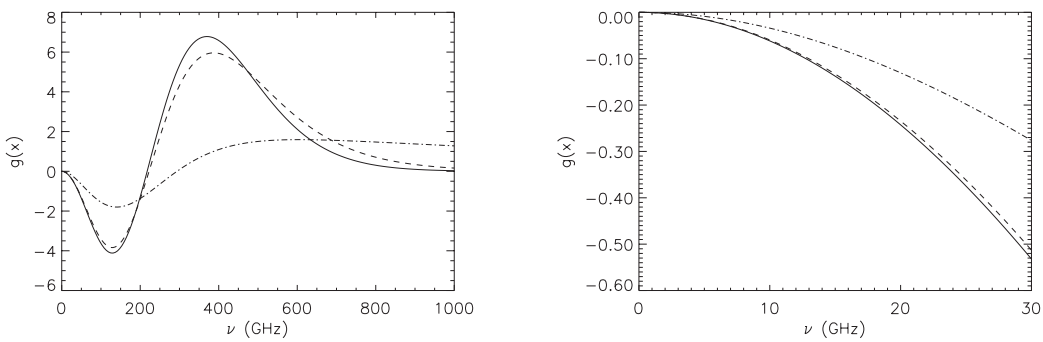

Figure 1: Left. The spectral function $g(x)$ calculated for a cluster with temperature $k_B T_e = 10$ keV (dashed) compare to the non-relativistic case (solid). We also show the spectral function for a relativistic, non-thermal plasma with spectrum $N_{e,rel} \propto E^{-3.5}$ and $E_{e,min} = 722.7$ keV (dot-dashed). Right. A zoom of the same plot in the frequency range up to 30 GHz, which is the most relevant for the SKA. (Colafrancesco et al. 2003)

Equation 1.1 shows the following key aspects which make the SZ effect a powerful probe of galaxy clusters:

- The surface brightness of the SZ effect is independent of redshift, z. The cosmological dimming of radiation by $(1+z)^4$ due to the expansion of the Universe is exactly cancelled

PoS(AASKA14)170

by the increased CMB energy density at the time of the scattering. It is therefore possible to see the SZ effect from clusters all the way back to the epoch of their formation, provided that they retain their ICM.

- The intensity of the SZ effect is proportional to the line-of-sight integral of the total pressure of the ICM. Therefore the integrated SZ flux over solid angle is proportional to the total thermal energy in the cluster, which is expected to be closely related to the overall cluster mass. This point will be returned to in Section 2.

At frequencies below the null of the SZ effect (which is found at 217 GHz in the non-relativistic limit) the SZ effect shows an intensity *decrement* towards the cluster, a very useful characteristic signature for discriminating the SZ signal from other emission mechanisms. At centimetre radio frequencies we are in the Rayleigh-Jeans regime and I_ν is well approximated as having a thermal ν^2 frequency dependence. Given that contaminating radio halo emission typically has a falling $\nu^{-\alpha_r}$ spectrum with $\alpha_r > 1$ (Feretti et al. 2012), it is often advantageous to perform SZ work at high frequency (e.g. SPT (Carlstrom et al. 2011); ACT (Swetz et al. 2011); Planck (Planck Collaboration XI 2011)). However, both the first reliable SZ detection (Birkinshaw et al. 1984) and the first SZ image (Jones et al. 1993) were made at 15 GHz; and this same frequency was used by one of the next generation of telescopes specifically designed for SZ work, AMI (Zwart et al. 2008), which has made follow-up detections of 99 Planck clusters (Perrott et al. 2014). Based on these observations, in this Chapter we explore the possibility of observing the SZ-effect from galaxy clusters using SKA operating in Band 5. We focus upon improving knowledge of cluster scaling relations, which are key to exploiting clusters as tracers for cosmology; and upon probing the detailed astrophysics of the intracluster plasma.

2. Cluster masses with SKA SZ observations

Clusters of galaxies are recognised as powerful cosmological probes (Allen et al. 2011; Kravtsov & Borgani 2012). Measurement of their number counts constrain cosmological parameters through the sensitive dependence of halo mass function to the linear growth rate of cosmic density perturbations. Furthermore, under the assumption that clusters are fair containers of cosmic baryons, measurements of the redshift dependence of their gas mass fraction provide tight constraints on cosmological parameters through the expansion history.

Both such cosmological applications of galaxy clusters necessarily require precise measurements of the total cluster mass and a precise characterisation of the physical properties of the intra-cluster medium. Since direct mass measurements are rather difficult to carry out for a large ensemble of galaxy clusters, a convenient approach for the cosmological exploitation of large cluster surveys should be based on the measurement of suitable mass proxies which are at the same time relatively easy to infer from observations and tightly related to cluster mass.

As already mentioned in the Introduction, the total SZ signal of a galaxy cluster is proportional to the total thermal energy content of the ICM. In fact, for a cluster at redshift z, the integrated SZ signal within an aperture angle θ can be written as

$$Y(\theta) = D_A(z)^{-2} Y(R) = 2\pi D_A(z)^{-2} \int_0^R y(r) r dr, \tag{2.1}$$

PoS(AASKA14)170

where $D_A(z)$ is the angular diameter distance and $y(r)$ is the profile of the Comptonisation parameter. This quantity is proportional to the line-of-sight integral of the electron pressure, which is $n_e T_e$ for a thermal plasma, according to

$$y = \int \sigma_T n_e \frac{k_B T_e}{m_e c^2} dl \,. \tag{2.2}$$

Therefore, as long as the ICM can be described as a plasma in hydrostatic equilibrium within the cluster potential well, we expect the integrated SZ signal to be tightly related to the total cluster mass. Under the further assumption that gas follows the DM distribution, the prediction of the self–similar model (see, e.g., Arnaud et al. (2010)) gives

$$Y_{\Delta_c} \propto E(z)^{2/3} M_{\Delta_c}^{5/3} \tag{2.3}$$

for the scaling relation between mass and integrated Y parameter, both computed within an aperture encompassing an overdensity of Δ_c times the critical density at the cluster redshift, $\rho_c(z)$. In the above equation, $E(z)$ describes the redshift dependence of the Hubble parameter.

As a consequence, the total SZ signal provides a rather precise and robust mass proxy. It is precise, since its scaling relation against cluster total mass is characterized by a small intrinsic scatter. It is robust, since this scaling relation has a quite weak dependence on the physical processes which determine the ICM thermodynamical properties. This is illustrated in Figure 2, which shows results on the Y–M scaling at $\Delta_c = 500$ from a set of hydrodynamical simulations of galaxy clusters (see also Kay et al. (1999); Sembolini et al. (2013); Le Brun et al. (2014)), compared to observational results (from Fabian et al. in prep). The results from simulations clearly show that the scaling relation between integrated SZ signal and mass has a low scatter, $< 10\%$, with slope and normalisation which are almost independent of the physical processes included in the simulations.

Future surveys, both in the X–rays (e.g. from eROSITA[1] (Pillepich et al. 2012)) or in optical/near-IR band (i.e. LSST[2] and Euclid[3]) will detect $\sim 10^5$ clusters and groups over an area of about 10^4 deg^2. Mass measurements in the X–rays will be limited to a small fraction (few thousands) of mostly nearby clusters from eROSITA, while weak lensing mass measurements in the Euclid survey will be mostly limited to $z < 1$ clusters.

Thanks to its sensitivity, SKA1-MID will allow targeted follow-up observation of clusters detected at high redshift in these future surveys, thereby providing mass measurements, through a calibration of the Y-M relation, for the $z > 1$ cluster population.

At the same time, the high angular resolution accessible by SKA1-MID will allow accurate measurement of ICM pressure profiles. The verification of the hydrostatic equilibrium condition to these pressure profiles will allow reconstruction of mass profiles in a robust way. It is worth pointing out that pressure profiles through X–ray observations (Arnaud et al. 2010; Sun et al. 2011) are obtained in an indirect way from the combination of surface gas mass and temperature profiles. Gas clumping is expected to bias the X-ray measurements of both gas mass profiles from surface brightness profiles and temperature profiles because the thermal bremsstrahlung X-ray emissivity

[1] http://www.mpe.mpg.de/eROSITA
[2] http://www.lsst.org/lsst/
[3] http://sci.esa.int/euclid/

PoS(AASKA14)170

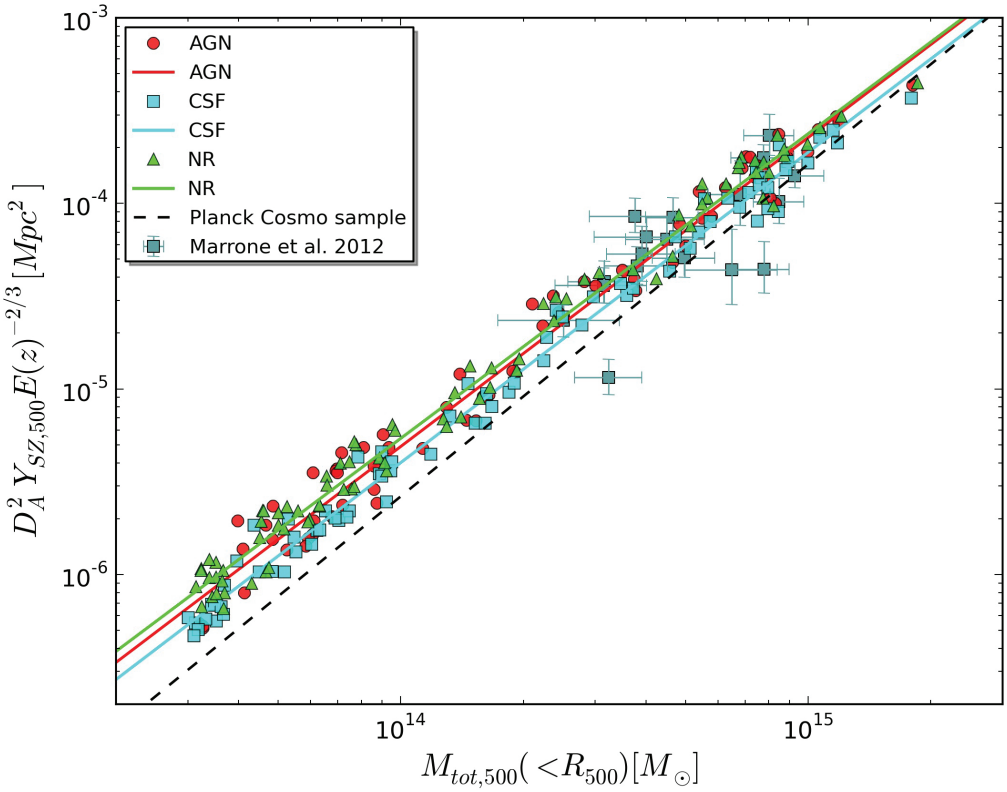

Figure 2: The relation between total mass and integrated SZ signal, both computed within an aperture encompassing at overdensity $\Delta_c = 500$ times the critical density, for both simulations and observational data (after Fabjan et al. 2014, in preparation). Points without errorbars refer to results from a set of cosmological hydrodynamical simulations of galaxy clusters (Planelles et al. 2014) (green triangles: non–radiative simulations; cyan squares: simulations including radiative cooling, star formation and supernova feedback; red circles: further including AGN feedback). Gray squares with errorbars are observational results from Marrone et al. (2012), while the dashed black line is the best-fit to the observational calibration presented in Planck Collaboration XX (2013).

$\varepsilon_{brem} \propto n_e^2 T^{1/2}$. On the other hand, the tendency of gas to sit in pressure equilibrium is such that gas clumping should have a minor impact on pressure profiles, that are directly measured by high-resolution SZ observations, in which the CMB temperature decrease is $\Delta T_{CMB} \propto n_e T_e$.

Thanks to the different dependencies of X–ray and SZ signals on gas density and temperature, their combination offers the possibility to measure these two quantities without resorting to challenging X–ray spectroscopy. This possibility is quite interesting in view of the all–sky X-ray survey to be provided by eROSITA. Owing to the relatively shallow flux limit of the eROSITA survey, only surface brightness profiles will be available for most of the clusters that will be detected in this survey at relatively high signal-to-noise ratio. The combination of these X-ray observations with SZ maps from SKA1-MID will allow one to recover electron pressure profiles and hence the temperature profiles deconvolved with information coming from the density profiles.

eROSITA is predicted to have a cluster mass detection limit of $M_{200} = 4 \times 10^{14} M_\odot$ at $z > 1$

PoS(AASKA14)170

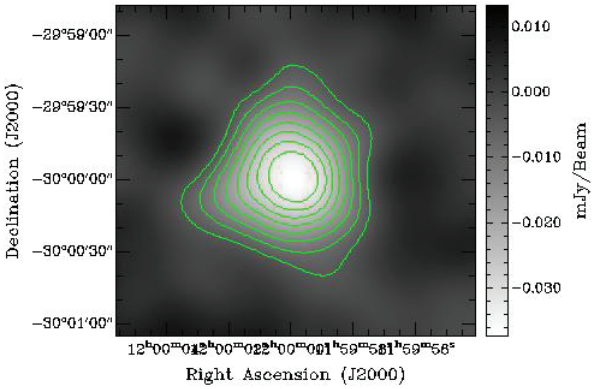

Figure 3: Simulated 1-hour observation with SKA1-MID of a cluster with $M_{200} = 4 \times 10^{14} M_O$ at $z = 1.83$ mapped with a 5 $k\lambda$ uv-taper. The cluster SZ effect is detected here at 14 σ c.l.

and will detect approximately 1000 clusters at z>1 and 10 at z>1.83 (Merloni et al. 2012). Figure 3 demonstrates the capability of SKA1-MID to follow-up these clusters in SZ; it shows a mock observation of a $M_{200} = 4 \times 10^{14} M_\odot$ cluster observed for one hour by SKA-MID in band 5 (8.8–13.8 GHz) and is able to detect the SZ effect at 14 σ. Since the SZ effect is an extended feature, we apply a 5 $k\lambda$ uv-taper as a crude matched filter. The data from the long SKA1-MID baselines are therefore effectively discarded, but as discussed further in Section 5 these data are used for the removal of contamination from radio point sources. This simulation demonstrates that a 1000-hour SKA1-MID programme can therefore follow up all of the high redshift sample that eROSITA will discover. In addition these additional observations of mass proxies will allow a better estimate of the scatter in the mass-observable relation for clusters detected with Euclid (Rozo et al. 2009).

3. Detailed investigations of the intra-cluster medium

Deep X-ray observations of galaxy clusters have revealed different kind of structures in the density and temperature distribution of the ICM, from central X-ray cavities filled with the radio emitting relativistic plasma ejected by active galaxies (e.g. Fabian et al. (2000)), to high surface brightness regions, such as shock and cold fronts related to cluster mergers (e.g. Markevitch (2008) and references therein). Detailed studies of the ICM pressure distribution are necessary to characterise the complex dynamical and feedback processes acting within galaxy clusters.

The SZ effect surface brightness provides a direct measure of the integrated pressure along the line of sight and is well suited to identifying ICM discontinuities (such as cold fronts or shocks) in the absence of resolved X-ray spectroscopy. High-sensitivity and high-resolution SZ observations are therefore an extremely valuable tool to study the evolutionary physics of the ICM.

In the 2030 horizon, SKA2 will be ideally complemented by the Athena X–ray satellite[4] for the study of high-redshift clusters. Thanks to its large collecting area and spectroscopic capability, Athena will open the possibility of studying the thermal and dynamical status of the ICM at

[4]http://www.the-athena-x-ray-observatory.eu

PoS(AASKA14)170

unprecedented precision for a significant number of galaxy clusters. A combination of X–ray observations from Athena with detailed electron pressure maps from SKA2 will shed light on the thermal structure of the ICM and on the dynamics of gas motions associated to the hierarchical build-up of galaxy clusters and by AGN feedback processes taking place in the cluster core regions.

In the last years increasing attention is being paid to the analysis of diffuse intracluster radio emission related to the presence of a non-thermal component in the ICM, with the main aim of studying its link with the complex evolutionary physics of galaxy clusters (e.g. Ferrari et al. (2008); Feretti et al. (2012); Brunetti & Jones (2014)). A joint analysis of synchrotron emission and SZ signal is emerging as a promising tool to study the interplay between the non-thermal and thermal component of the ICM (see, e.g., Basu (2012); Cassano et al. (2013); Colafrancesco et al. (2014) and references therein). In this context, combined GMRT observations (at 610 and 240 MHz) with high-resolution MUSTANG results on the galaxy cluster RXJ1347, (Ferrari et al. 2011) have pointed out a strong correlation between an excess in the radio surface brightness of the diffuse radio source at the centre of the cluster (a radio mini-halo already detected by Gitti et al. (2007)) and a high pressure region detected in the SZ map of RX J1347 and confirmed by X-ray observations (see Fig. 4). This result indicates that, in addition to the relativistic electrons ejected by the AGN and (possibly) re-accelerated by MHD turbulence in the central cluster region, the presence of cosmic rays in the excess emission of the radio mini-halo is most likely related to a shock front propagating into the ICM. Figure 5 shows a simulated 1-hour observation of cluster RXJ1347 with the SKA1-MID.

These examples aim at illustrating that, if Band 5 will be covered by the MID component, SKA will be the first telescope able to efficiently detect both synchrotron and SZ radiation, thus becoming an extremely powerful instrument for getting a complete view of the thermal and non-thermal physics of the ICM.

4. SKA1-MID observations of cluster SZ signals

Galaxy clusters typically have a size > 1 Mpc. The observed SZ signal will therefore be heavily resolved out on long SKA1-MID baselines. However, the compact core of SKA1-MID has a high filling factor and this is critical for measuring low surface brightness features such as the SZ effect.

The simulations presented in this chapter use only the SKA1-MID's cross-correlation visibilities. If, in addition, auto-correlation data are available, these will give the zero-spacing SZ flux and this will aid immensely in inferring an accurate reconstruction of the ICM properties. The expected statistical significance of the auto-correlation data corresponding to the 1-hour observation in Figure 3 is 40σ, while that in Figure 5 is 300σ.

5. Removal of contaminating signals

It is expected that there will be substantial contamination of the SZ signal from discrete radio sources in the field, but this contamination can be removed by a technique described in e.g. Grainge et al. (1993). The flux and positions of the point sources can be measured with high precision by mapping with the long SKA1-MID baselines, which are much more numerous than the short

PoS(AASKA14)170

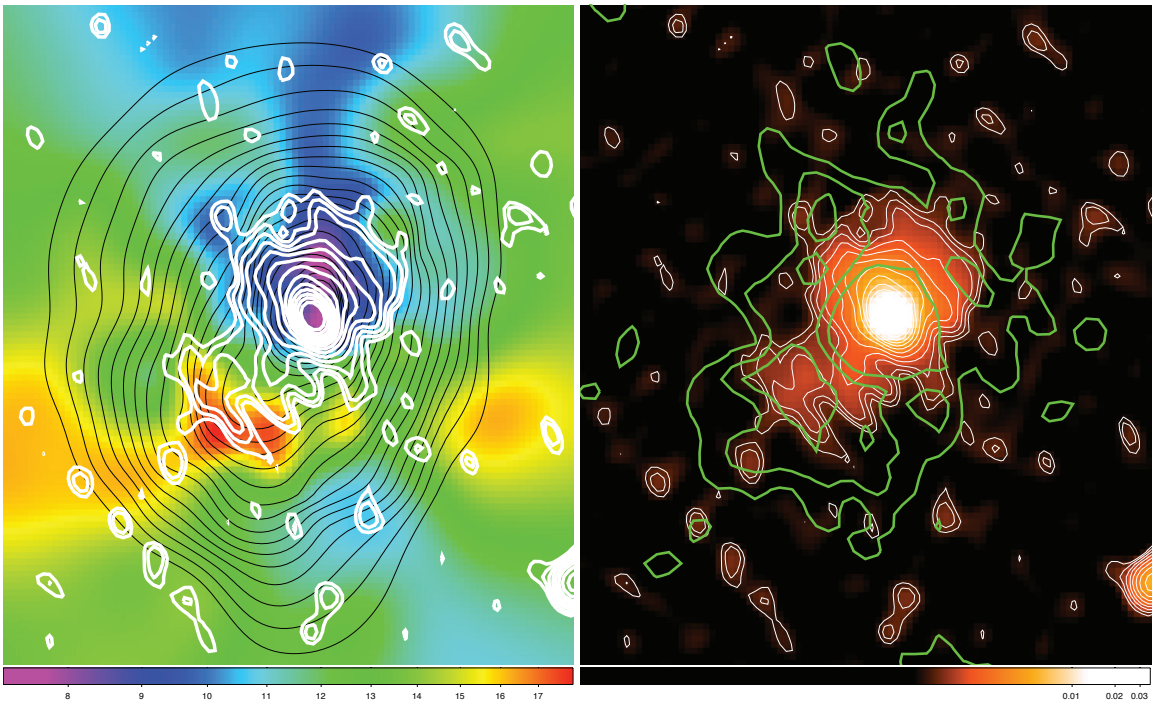

Figure 4: Left: XMM-Newton X-ray temperature map of the galaxy cluster RXJ1347 in keV. X-ray iso-contours from the Chandra [0.5, 2.5] keV band image are superimposed in black. Total intensity radio contours are overlaid in white. They start at 3 σ level and are spaced by a factor of $\sqrt{2}$. Right: total intensity 614 MHz map and contours (white) of RXJ1347. Contours of the MUSTANG SZE image of the cluster are overlaid in green (levels as in Fig. 6 in Mason et al. (2010)). The shock region correspond to the inner contour on the SZ map and to the hottest (red) structure in the X-ray temperature map. Extracted from Ferrari et al. (2011).

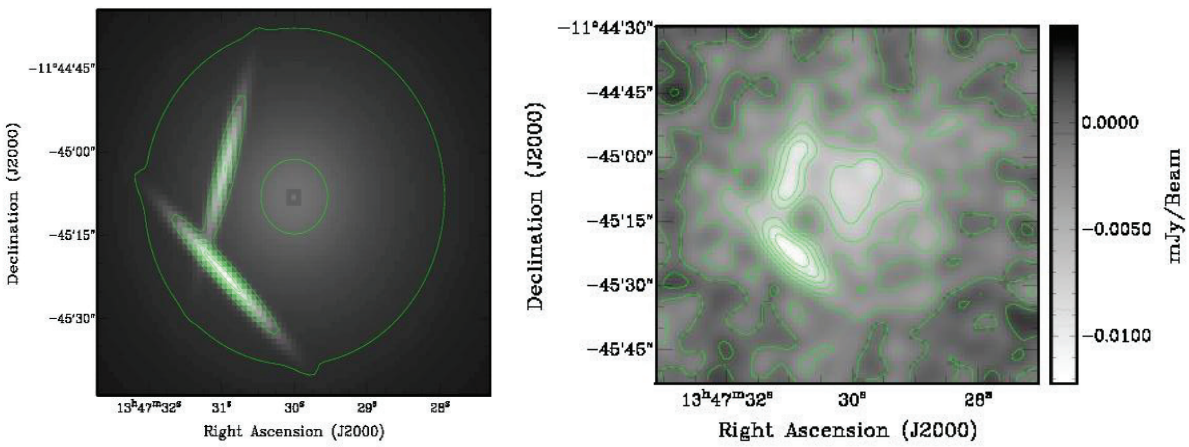

Figure 5: Left: Model of cluster RXJ1347 (z = 0.451) based on observations at 90 GHz with the MUSTANG camera on GBT (Mason et al. 2010). Right: Simulated 1 hour SKA1-MID observation with a 20 $k\lambda$ uv-taper; the southern shock heated gas region is detected at 20 σ. The detection of the bulk SZ effect from the cluster is at a significance of over 100 σ if mapped with a 5 $k\lambda$ taper.

PoS(AASKA14)170

baselines used for measure of the SZ. As a result, for the 1 hour simulation shown in Figure 3 the noise level from a map with a uv-taper chosen to give a psf of $1''$ is four times lower than that in the map which shows the SZ. Thus sources with flux $S \approx 3\mu$Jy and above will be able to be identified and subsequently subtracted from the short baselines that measure the SZ. Extrapolating from the 10C source counts (Davies et al. 2011) we expect to detect around 1 source per square arcminute at this level in the field and approximately ten times as many in the centre of the cluster. Source confusion is therefore not an issue. The SKA1 aims to have dynamic range of 70dB in order to address other science areas; since brightest cluster point sources are typically $S \approx 10$–100 mJy, for SZ work we will not need anything like this performance.

In addition to the extended radio halos and relics continuum emission (Ferrari et al. 2015), galaxy clusters host a variety of extended radio sources, such as tailed radio galaxies whose shape is determined by interaction with the ICM (e.g. Giacintucci and Venturi (2009)); radio bubbles that create holes in the ICM distribution and rise buoyantly through the thermal gas (e.g. Dunn et al. (2005)); and compact radio sources related to galaxy activity (either blazar and/or starburst like). In order to study the diffuse SZ effect signal in clusters, it is of course crucial to be able to separate the different kinds of radio sources in the cluster environment, i.e. to discriminate between SZ and the radio emission related to active galaxies or to other non-thermal processes in the ICM.
Although these different radio sources have a wide variety of spectral shapes, they are all very distinct from the approximately thermal spectrum of the SZ effect (see Figure 1). Radio halo synchrotron spectra are usually quite steep (spectral slopes $\alpha_r > 1$) and extended radio sources within the cluster (e.g., radiogalaxies with extended jets/lobes) also show quite steep spectra in their extended regions due to the effects of electron aging and radiative losses. Intra-cluster cavities have even steeper spectra ($\alpha_r \approx 0.7 - 2.3$, see Birzan et al. (2004)) being filled with the termination region of radiogalaxy lobes that are usually populated by old electrons. A spatially-resolved spectral analysis with the sensitivity and resolution offered by the SKA1-MID will greatly help in providing the component separation needed to study the extended SZ effect signal in galaxy clusters. In addition, such spectral capability may also be able to distinguish any thermal and non-thermal component of the SZ effect in clusters through careful analysis of the Band 5 data from SKA1-MID.

Simulated SKA1-MID observations of non-thermal emission in galaxy clusters (Ferrari et al. 2015) demonstrate that the study of extended radio emission features in clusters is feasible, thanks to developments in deconvolution and source detection algorithms optimised for the analysis of extended and diffuse radio sources. With these developments, the SKA1-MID will allow multi-frequency images of diffuse cluster radio sources to be made over large bands ranges (specifically Band 5), enabling detailed spectral index studies of galaxy clusters, which is essential for the component separation analysis and the detection of the SZ effect signal.

This analysis can be extended in the future to include i) a comparison between deconvolution results obtained using the new reconstruction algorithms based on compressed sensing and sparse representations (e.g. the MORESANE algorithm and the multi-scale version of CLEAN (Dabbech et al. 2014)), ii) polarisation studies for targeted observations, iii) an extended feasibility study taking into account the full SKA1 frequency range (including also SKA1-LOW), iv) a detailed analysis using the configuration of the full SKA array aimed at the study of the SZ effect in galaxy clusters.

PoS(AASKA14)170

6. SKA uniqueness and synergies for SZ observing

As mentioned in Section 1 there are several telescopes that have been specifically designed for SZ work; the SKA1-MID will provide useful complementary capabilities to these. The SPT and ACT telescopes are primarily designed for surveying, enabled by their large fields of view, but they are unattractive for pointed observational programmes. Their angular resolution of $\approx 1'$ is insufficient to image the detailed structure discussed in Section 3. SKA1-MID's resolution and sensitivity will be ideal for follow-up imaging of the cluster catalogues produced by these instruments. Similarly, Planck with its resolution of$\approx 5'$ is a survey instrument for SZ. Its cluster catalogue has 1227 entries (Planck Collaboration XXIX 2013), but its cluster selection function is weighted more heavily towards low redshift than either SPT and ACT.

The SZA (Carlstrom 2006) (now part of the CARMA array) and AMI are centimetre wavelength interferometric telescopes that are ideal for SZ follow-up observations. While they cannot match SKA1-MID's sensitivity, their access to shorter baselines than those available to SKA1-MID are a useful complement, especially for studies of low redshift clusters.

CCAT (Woody et al. 2012) has resolution of a few arc-seconds and will be capable of the same type of observations proposed in this chapter for the SKA1-MID. Golwala (2008) calculates that a 600 hour programme on CCAT could study 100 clusters in the mass range $M = 3.5 \times 10^{14} - 1 \times 10^{15} M_{\odot}$; for comparison, in Section 2 we describe a 1000-hour SKA1-MID programme to follow up the 1000 clusters with $M_{200} > 4 \times 10^{14} M_{\odot}$in the high redshift eROSITA sample. CCAT's great strength is its unique frequency coverage, from 90 GHz to above 1 THz, which give the potential for spectrally discriminating the thermal, kinematic and relativistic contributions to the SZ effect. Combining a low frequency 8.8-13.8 GHz measurement from SKA1-MID with the CCAT measurements can greatly help this discrimination (Knox et al. 2004).

ALMA (Brown et al. 2004) is potentially very powerful for SZ work. However, ALMA's field of view, even at Band 3, is small, less than $1'$, and so it resolves out the bulk of the cluster SZ signal. For high resolution imaging of the detailed ICM structure ALMA is, however, very complementary to the SKA1-MID. As discussed in Scaife & Grainge (2010), a possible future upgrade to ALMA through implementing Band 1 capabilities would greatly improve ALMA's utility as an SZ instrument.

7. Early SKA1 science and looking towards the full SKA

Pointed SZ observations are an attractive early SKA1-MID science goal; it has been shown that a great deal of good work could be performed with MeerKAT (Scaife et al. 2009). As has been discussed earlier, the SZ signal is detected primarily on the shorter SKA1-MID baselines, with some sensitivity required on longer baselines to remove radio contamination. So assuming a build-out from the centre, filling out the MeerKAT core to give good filling factor out to high radius greatly enhances the SKA1-MID's for SZ work. Also, the autocorrelations provided by the new SKA1-MID antennas give invaluable information about the zero-spacing flux.

Looking to SKA2, a possible increase in maximum observing frequency is extremely attractive for SZ measurements. Now that autocorrelations are an accepted part of the SKA Baseline, one can start to speculate whether the SKA2 will aim to fill the gap in uv-space between the auto-

PoS(AASKA14)170

and cross-correlations; following the solution adopted by ALMA, this could be achieved with the addition of a close-packed array of small ($\sim$ 7m) dishes.

Acknowledgments

Chiara Ferrari acknowledges financial support by the "*Agence Nationale de la Recherche*" through grant ANR-09-JCJC-0001-01, the "*Programme National Cosmologie et Galaxies (2014)*", the *BQR* program of Lagrange Laboratory (2014). Sergio Colafrancesco acknowledges support by the South African Research Chairs Initiative of the Department of Science and Technology and National Research Foundation and by the Square Kilometre Array (SKA). Stefano Borgani acknowledges financial support from the PRIN-MIUR 2009AMXM79 Grant, from the PRIN-INAF 2012 Grant "The Italian network for computational cosmology" and from the INDARK INFN Grant. We would like to thank Dunja Fabjan for providing Figure 2. We thank Malak Olamaie for cluster models.

References

Allen, S. W., Evrard, A. E., & Mantz, A. B. 2011, ARAA, 49, 409 [arXiv:1103.4829]

Arnaud, M., Pratt, G. W., Piffaretti, R., et al. 2010, A&A, 517, A92 [arXiv:0910.1234]

Basu, K., 2012, MNRAS, 421, 112, [arXiv:1111.2856]

Birkinshaw, M., Gull, S. F., and Hardebeck, H., 1984, Nature, 309, 34

Birkinshaw, M., 1999, Phys. Rept., 310, 97 [arXiv:astro-ph/9808050]

Birzan, L. et al. 2004, ApJ, 607, 800 [arXiv:astro-ph/0402348]

Brown, R. L., Wild, W., Cunningham C., 2004, Advances in Space Research, 34, 555

Brunetti, G., & Jones, T. W. 2014, International Journal of Modern Physics D, 23, 30007, [arXiv:1401.7519]

Carlstrom, J. E., Holder, G. P., and Reese, E. D., 2002, ARAA, 40, 643 [arXiv:astro-ph/0208192]

Carlstrom J. E., 2006, ASPC, 356, 35

Carlstrom, J. E. et al., Publications of the Astronomical Society of the Pacific, 2011, 123, 568 [arXiv:0907.4445]

Cassano, R. et el., 2013, ApJ, 777, 141, [arXiv:1306.4379]

Colafrancesco, S., Marchegiani, P. and Palladino, E. 2003, A&A, 397, 27 [arXiv:astro-ph/0211649)]

Colafrancesco, S. et al. 2014, A&A, 566, 42 [arXiv:1312.1846]

Dabbech, A., Ferrari, C., Mary, D., Slezak, E. and Smirnov, O., 2014, in preparation.

Davies, M. L. et al., 2011, MNRAS, 415, 2708, [arXiv:1012.3659]

Dunn, R. J. H., Fabian, A. C., & Taylor, G. B., 2005, MNRAS, 364, 1343 [arXiv:astro-ph/0510191]

Fabian, A.C., Sanders, J.S., Ettori, S., et al., 2000, MNRAS, 318, L65 [arXiv:astro-ph/0007456]

Ferrari, C., Govoni, F., Schindler, S., Bykov, A.M., Rephaeli, Y., 2008, SSRv, 134, 93, [arXiv:0801.0985]

PoS(AASKA14)170

Ferrari, C., Intema, H.T., Orrú, E., et al., 2011, A&A, 534, 12 [arXiv:1107.5945]
Ferrari, C., et al., 2015, "Non-thermal emission from galaxy clusters: feasibility study with SKA", in "Advancing Astrophysics with the Square Kilometre Array", PoS(AASKA14)075
Feretti, L., Giovannini, G., Govoni, F., and Murgia, M., 2012, A&ARv, 20, 54 [arXiv:1205.1919]
Gitti, M., Ferrari, C., Domainko, W., Feretti, L., and Schindler, S., 2007, A&A, 470, 25, [arXiv:0706.3000]
Giacintucci, S. and Venturi, T., 2009, A&A, 505, 55 [arXiv:0907.2306]
Golwala, S., 2008, "CCAT Feasibility Study – SZ Science" http://www.astro.caltech.edu/ golwala/talks/CCATFeasibilityStudySZScience.pdf
Grainge, K., Jones, M., Pooley, G., Saunders, R., Edge, A., 1993, MNRAS, 265, 57
Jones, M. E. et al., 1993, Nature, 365, 320
Kay, S. T., Peel, M. W., Short, C. J., et al. 2012, MNRAS, 422, 1999 [arXiv:1112.3769]
Knox, L., Holder, G. P., Church, S. E., 2004, ApJ, 612, 96 [arXiv:astro-ph/0309643]
Le Brun, A. M. C., McCarthy, I. G., Schaye, J., & Ponman, T. J. 2014, MNRAS, 441, 1270 [arXiv:1312.5462]
Kravtsov, A. V., & Borgani, S. 2012, ARAA, 50, 353 [arXiv:1205.5556]
M. Markevitch, *Intergalactic shock fronts*, *SSRv* **134** (2008) 93, [arXiv:1010.3660]
Marrone, D. P., Smith, G. P., Okabe, N., et al. 2012, ApJ, 754, 119 [arXiv:1107.5115]
Mason, B.S., Dicker, S.R., Korngut, P.M., et al., 2010, ApJ, 716, 739
Merloni, A. et al., 2012, "eROSITA Science Book"
Nagai, D., Kravtsov, A. V., Vikhlinin, A., 2007, *ApJ*, 668, 1 [arXiv:astro-ph/0703661]
Perrott, Y. C. et al., 2014, [arXiv1405.5013]
Pillepich, A., Porciani, C., & Reiprich, T. H. 2012, MNRAS, 422, 44, [arXiv:1111.6587]
Planck Collaboration: Ade, P. A. R. et al, Astronomy & Astrophysics, 2011, 536, 8 [arXiv:1101.2024]
Planck Collaboration, Ade, P. A. R., Aghanim, N., et al. 2013, [arXiv:1303.5080]
Planck Collaboration: Ade, P. A. R. et al., 2013, "Planck 2013 results. XXIX. Planck catalogue of Sunyaev-Zeldovich sources", [arXiv:1303.5089]
Planelles, S., Borgani, S., Fabjan, D., et al. 2014, MNRAS, 438, 195 [arXiv:1311.0818]
Rozo, E. et al., 2009, ApJ, 699, 768 [arXiv:0809.2794]
Scaife, A. M. M. et al., 2009, COSMOKatSZ science proposal.
Scaife, A. M. M., & Grainge, K. J. B., 2010, BASI, 38, 185 [arXiv:1002.1895]
Sembolini, F., Yepes, G., De Petris, M., et al. 2013, MNRAS, 434, 2718
Sun, M., Sehgal, N., Voit, G. M., et al. 2011, ApJ, 727, L49 [arXiv:1012.0312]
Sunyaev, R. A. and Zel'dovich, Y. B., 1970, Astroph. Sp. Sci., 7, 3
Sunyaev, R. A. and Zel'dovich, Y. B., 1972, Comments on Astrophysics and Space Physics, 4, 173
Swetz, D. S. et al., 2011, ApJS, 194, 41 [arXiv:1007.0290]
Woody, D. et al., 2012, in Ground-based and Airborne Telescopes IV, edited by L. M. Stepp, R. Gilmozzi, and H. J. Hall, vol. 8444 of Proc. SPIE, 84442M
Zwart, J. T. L. et al., 2008, MNRAS, 391, 1545 [arXiv:0807.2469]

PoS(AASKA14)170

PROCEEDINGS OF SCIENCE

Astronomy Below the Survey Threshold in the SKA Era

Jonathan Zwart[1], Jasper Wall[2], Alexander Karim[3], Carole Jackson[4], Ray Norris[5], Jim Condon[6], Jose Afonso[7,8], Ian Heywood[5], Matt Jarvis[9], Felipe Navarrete[3], Isabella Prandoni[10], Emma Rigby[11], Huub Rottgering[11], Mario Santos[1], Mark Sargent[12], Nick Seymour[4], Russ Taylor[1,13], Tessa Vernstrom[2]

[1] *University of the Western Cape, Department of Physics, Private Bag X17, Bellville 7035, South Africa*
[2] *University of British Columbia, Department of Physics and Astronomy, 6224 Agricultural Road, Vancouver, V6T 1Z1, Canada*
[3] *Max-Planck-Institut für Radioastronomie, Auf dem Hügel 69, D-53121 Bonn, Germany*
[4] *International Centre for Radio Astronomy Research, Curtin University, Bentley, WA 6102, Australia*
[5] *CSIRO Astronomy & Space Science, PO Box 76, Epping NSW 1710, Australia*
[6] *National Radio Astronomy Observatory, 520 Edgemont Road, Charlottesville, VA 22903, USA*
[7] *Instituto de Astrofísica e Ciências do Espaço, Universidade de Lisboa, OAL, Tapada da Ajuda, PT1349-018 Lisboa, Portugal*
[8] *Departamento de Física, Faculdade de Ciências, Universidade de Lisboa, Edifício C8, Campo Grande, PT1749-016 Lisbon, Portugal*
[9] *Astrophysics, Denys Wilkinson Building, Keble Road, University of Oxford, Oxford, Oxon, OX1 3RH, UK*
[10] *INAF, Istituto di Radioastronomia, Via P Gobetti 101, 40129 Bologna, Italy*
[11] *Leiden Observatory, Leiden University, P.O. Box 9513, 2300 RA Leiden, The Netherlands*
[12] *Astronomy Centre, Dept. of Physics and Astronomy, School of Maths and Physical Sciences, University of Sussex, Falmer, Brighton BN1 9QH, UK*
[13] *Astrophysics, Cosmology & Gravity Centre, Department of Astronomy, University of Cape Town, Private Bag X3, Rondebosch 7701, South Africa*
E-mail: jz@uwcastro.org

Astronomy at or below the *survey threshold* has expanded significantly since the publication of the original *Science with the Square Kilometer Array* in 1999 and its update in 2004. The techniques in this regime may be broadly (but far from exclusively) defined as *confusion* or *P(D)* analyses (analyses of one-point statistics), and *stacking*, accounting for the flux-density distribution of noise-limited images co-added at the positions of objects detected/isolated in a different waveband. Here we discuss the relevant issues, present some examples of recent analyses, and consider some of the consequences for the design and use of surveys with the SKA and its pathfinders.

Advancing Astrophysics with the Square Kilometre Array
June 8-13, 2014
Giardini Naxos, Sicily, Italy

PoS(AASKA14)172

1. Astronomy beneath the Survey Threshold

Since the publication of the original SKA science case (Taylor & Braun, 1999), and indeed since the 2004 publication of its update by Carilli & Rawlings, more has been understood about sub-threshold astronomy and numerous detailed analyses have shown how to extract astronomical and cosmological results. We look to summarize these developments, issues and techniques, as well as to note some implications for the SKA, its precursors and pathfinders. We largely restrict our discussion to the radio continuum, while noting that sub-threshold techniques are highly applicable (a) to other wavebands (e.g. Marsden et al. 2009, Bourne et al. 2012), (b) when using polarization to investigate cosmic magnetism (Stil 2015), and (c) for HI spectral-line work (Blyth et al. 2015).

Source surface densities generally rise steeply with decreasing source intensity — i.e. the *source count* is 'steep'. With this come two aspects of surveys now generally accepted. Firstly, it is very unwise to 'push' cataloguing and source-counting — the *survey threshold* — down to anywhere near the *confusion limit* or the *noise limit*; the combined effects of these plus *Eddington bias* require cataloguing to be limited to intensities $> 5\sigma$, σ representing the combined confusion (see below) and system noise. Second, there is much astronomy to be done with proper and rigorous statistical interpretation of survey data to levels well below this threshold.

Confusion analysis (*P(D)*, or single-point statistics) as first proposed by Scheuer (1957) is essentially single-frequency, extending our knowledge of the source count at that frequency to intensities below the threshold. Stacking on the other hand was a conscious product of multi-waveband astronomy, to investigate bulk properties of objects above thresholds and in catalogues in one waveband, but generally (not exclusively) below survey thresholds in another band. Stacking then implies adding images in the latter band at the positions of the catalogue in the former, to discover average faint intensities. It was perhaps pioneered in the X-ray regime (Caillault & Helfand 1985) for the average X-ray properties of G-stars. By the time of the SDSS survey, sophisticated analyses were carried out to examine radio properties of radio-quiet quasars (White et al., 2007), and indeed radio-quiet galaxies (Hodge et al., 2008). Chief requirements are absolute astrometry to better than 1 arcsec in both bands and good dynamic range in the sub-threshold band.

It is essential for galaxy-formation and evolution studies to be able to investigate both faint AGN and star-formation activity (see e.g. Smolčić et al. 2008, 2009a,b; Seymour et al. 2009; Bonzini et al. 2013; Padovani et al. 2014). This is particularly so in view of the now commonly accepted link between an AGN phase and the quenching of star formation (Begelman 2004; Croton et al. 2006) in order to effect cosmic downsizing. In addition, the statistical techniques discussed here bring within reach a wealth of extragalactic astrophysics considered further in Jarvis et al. (2015); Kapinska et al. (2015); McAlpine et al. (2015); Murphy et al. (2015); Smolčić et al. (2015). These make it possible to proceed from noisy flux measurements to source counts, luminosity functions, star-formation rates and their cosmic densities, all as a function of e.g. environment, stellar mass, redshift, but *only* when ancillary data are available. More comprehensive introductions to the science available via stacking and $P(D)$ analyses (together with comprehensive referencing) are provided in Glenn et al. (2010); Padovani (2011); Heywood et al. (2013); Zwart et al. (2014).

PoS(AASKA14)172

2. Beating the Survey Threshold

Before describing the methods of $P(D)$ and stacking — and their biases — in more detail, we set out some relevant definitions. Confusion and associated concepts are discussed in the following points, and these may be clearer on examination of Figs 1 and 2.

Confusion is integration or blending of the background of faint sources by either (a) the finite synthesized beam (spatial response) of a telescope, or (b) the intrinsic angular extents of the sources. The anisotropies of blended background sources become visible when instrumental noise is low enough.

Intrinsic (Natural) Confusion, also sometimes referred to as **Source Blending** (which has still other meanings), occurs if extended sources/objects in *any* image — at any wavelength — physically overlap on the sky. Note that this is independent of the resolution of the image, as it depends only on the intrinsic (distribution, angular-diameter and density) properties of the sources. For 1.4-GHz radio surveys, intrinsic confusion occurs at well below 1-μJy rms (Windhorst, 2003).

Instrumental Confusion occurs if the source density is so high that sources are likely to be detected in a 'significant' fraction of the resolution elements (PSFs/synthezised beams) in an image. This is the most commonly assumed form of confusion and it generally comes to mind when the term is used.

Sidelobe Confusion happens if bright sources are likely to appear in the sidelobes of the synthesized beam to the extent that the **Dynamic Range** of the image is compromised (Makhathini et al. 2015; Smirnov et al. in prep.).

Identification Confusion occurs when the combination of resolution and positional accuracy in the radio image and the density of sources at a cross-identification wavelength (e.g. optical or infra-red), are such that a 'significant' fraction of the sources cannot be reliably identified with objects seen at the other wavelength. The likelihood ratio is an example of a method that can be used to overcome this (see e.g. McAlpine et al. 2012).

Confusion Limit There are various meanings. If used in the context of surveys for discrete sources, the term is sometimes used to signify the flux-density depth to which discrete sources can be reliably detected and their intensities measured. In the foregoing we have referred to this as the *survey threshold*. At the brighter end of the source count with steep slope of about -2.7, a safe threshold is the flux density at which the surface density is perhaps 50 beam-areas per source; at faint flux densities where the count slope is less steep, say -1.7, it becomes $\approx$25 beam-areas per source (Condon, 2013). The confusion limit, the level at which the background is totally blended as depicted in Fig. 1, must occur at flux densities corresponding to source densities of $>$ one source per beam area. The confusion limit is also taken at times to mean the flux density at which the *confusion noise* is equal to system noise.

Confusion Noise is generally taken to be a single-point statistic describing the width of the distribution of single pixel values in a confusion-dominated image; see Figs 1 and 2. The

PoS(AASKA14)172

origin of this 'noise' depends on which type of confusion is in question. Since the single-point distribution is usually highly skewed and very non-Gaussian (Condon, 2013), a single descriptor of it is not suitable. Theoretically the distribution for a power-law source count has an infinite tail to the positive side so that the mean and variance are infinite. (With very 'steep' counts approaching -3 in slope, the distribution does approximate Gaussian.) 'Shallow' slopes result in a preponderance of brighter source intensities and a long positive tail. Despite the dangers, some approximation to the core width is generally made to compare with system noise or in rough calculations of attainable survey depth. Under some circumstances (e.g. Feroz et al. 2009) an estimate of the confusion noise per beam is taken to be the second moment of the residual differential source count up to some limiting threshold, where all sources with flux densities greater than that threshold have already been subtracted; one feature of/problem with this definition is that confusion noise is then a sensitive function of survey noise i.e. integration time. Fig. 3 shows a way to scale the instrumental confusion to different resolutions and/or frequencies near 1.4 GHz (see also Condon et al. 2012).

Eddington bias is the apparent steepening of the observed source count (Eddington, 1913) by the intensity-dependent over-estimation of intensities, due to either system noise or confusion noise or both. The process of over-estimating flux densities of faint sources is sometimes called flux boosting, a misleading term because no physical increase of observed intensity is taking place, as it is in the case of relativistic beaming. Jauncey (1968) first drew 'flux boosting' to our attention; it was the submm astronomers who identified it as leading to Eddington bias and grasped how to estimate unbiased flux densities (and hence counts) using a Bayesian Likelihood Analysis (BLA) and count estimates as priors (Wall & Jenkins 2003; Coppin et al. 2005).

Estimators and biases Flux densities measured by standard techniques, e.g. PSF fitting, or average pixel value near a map peak, are *not* flux densities, but like all measured quantities, are *estimators* of flux densities. If instrumental or confusion noise is significant and the source count strongly favours faint intensities, the usual case, then such an estimator will be *biased*. The flux density is not boosted — the measurement is wrong. De-biasing, deboosting or however it is termed, is simply stating that a better — possibly even unbiased — estimator is being used.

Probability of deflection, **P(D)**, or **P(D) distribution**, is the full distribution of single-pixel values. **P(D) analysis** is the analysis of this distribution (see Section 2.1) to deduce the underlying faint source count.

Stacking (Section 2.2) is the co-addition of maps at the positions of sources detected in another map or catalogue. In contrast to a $P(D)$ blind analysis, stacking is intrinsically prior-based source extraction, but can also be used to conquer confusion.

We now discuss strategies for analysing noise-limited data, be they confusion-limited or system-noise limited. The two prevailing techniques, which are complementary, are either blind ($P(D)$ analysis) or prior-based (stacking).

PoS(AASKA14)172

2.1 Probability of Deflection (*P(D)*) analysis

The technique was first applied by Hewish (1961) to estimate counts at 178 MHz by forward modelling, using the 4C survey data. *P(D)* has been adopted to estimate source counts (with subsequent constraints on luminosity functions) at a number of wavebands other than radio, e.g. X-ray (Toffolatti & Barcons, 1992; Barcons et al., 1994); infra-red (Jenkins & Reid, 1991; Oliver et al., 1992); far infra-red (Friedmann et al., 2002); and submm (Patanchon et al., 2009). Most recently (Vernstrom et al., 2014b) it has been applied to the confusion-limited data of the VLA single-pointing Condon et al. (2012) integration (Fig. 1). A Bayesian Likelihood Analysis was used, with a multi-node count model (Patanchon et al., 2009). The results are in Fig. 2, which demonstrates how the *P(D)* analysis has resolved the discrepant direct counts and has extended knowledge of the 3-GHz count to nanoJy levels.

$P(D)$ analysis in the face of extended source structures is highly problematic. P(D) analyses to date have assumed no effects of resolution, i.e. assume source angular sizes « beam sizes. It is possible to attempt such analyses on the basis of (risky) asumptions about angular structures. A different approach was adopted by Vernstrom et al. (2014a). Their analysis of ATCA data at 1.75 GHz obtained with a $\approx$ 1-arcmin beam suggested an excess of diffuse emission on scales of 1–2 arcmin. To carry out a correct $P(D)$ analysis in the face of source resolution generally requires detailed knowledge of the angular-size distribution of sources as a function of faint flux density. For example, SKA1 surveys could be used to deduce the angular-size distribution, which could then be extrapolated to fainter levels to aid the $P(D)$ analysis. But any population for which we had such detailed knowledge would probably not require data from $P(D)$ analyses. Moreover any tacit

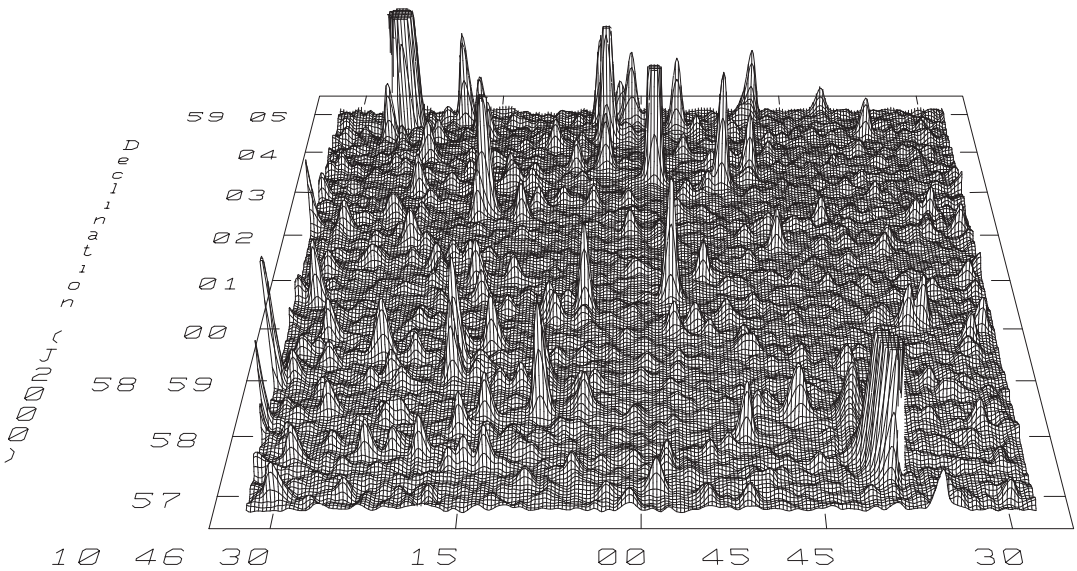

Figure 1: A 3-GHz image from a 57-hour integration with the Karl G. Jansky Very Large Array (VLA) in C-configuration (Condon et al., 2012), with synthesized beam 8-arcsec FWHM. The instrumental noise is 1.02 μJy beam^{-1}. All features in the image, positive and negative, are on beamwidth scales and these cover the image, indicating that the background of faint sources has been completely smoothed or integrated by the beam response. The large positive deflections represent discrete radio sources, producing the long positive tail of the $P(D)$ distribution (Condon et al. 2012; Vernstrom et al. 2014b; see Fig. 2).

PoS(AASKA14)172

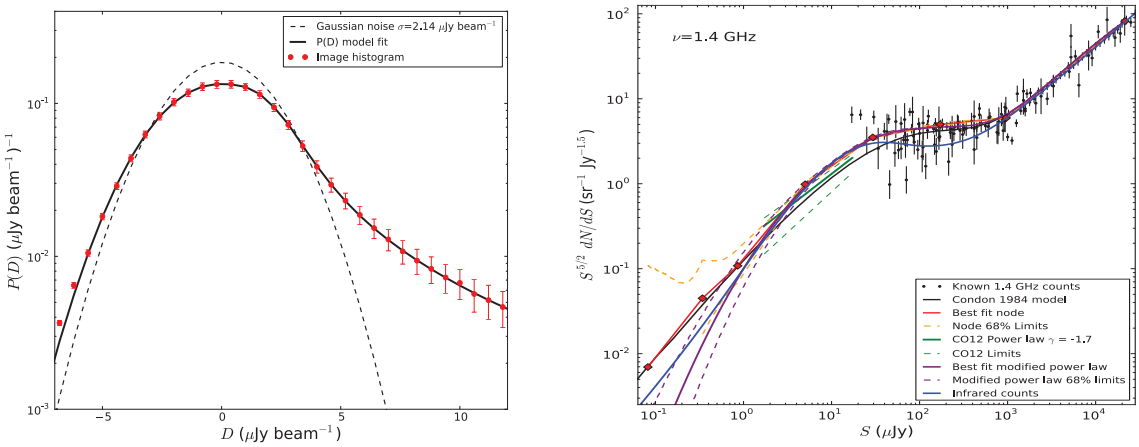

Figure 2: Left — Oversampled *P(D)* distribution (Vernstrom et al., 2014b) for the central 5-arcmin radius of the 3-GHz image of Fig. 1 (dots and $\sqrt{N}$ error bars), with the best-fitting 8-node model (solid curve). The dashed line represents a Gaussian of σ =1.255 μJy, accurately describing the instrumental noise. **Right** — Source counts at 1.4 GHz, shown in relative differential form. Points and error bars show previous estimates of the counts from the literature. The short straight (green) line plus dashed lines above and below it show results from Condon et al. (2012), the early interpretation of the current deep survey data. Joined points plus dashed error limits show the results from the $P(D)$ analysis of Vernstrom et al. (2014b), translated from 3.0 to 1.4 GHz with a spectral index of -0.7. Smooth curves represent counts calculated from models of radio and infra-red luminosity functions and cosmic evolution; see Vernstrom et al. (2014b) for references.

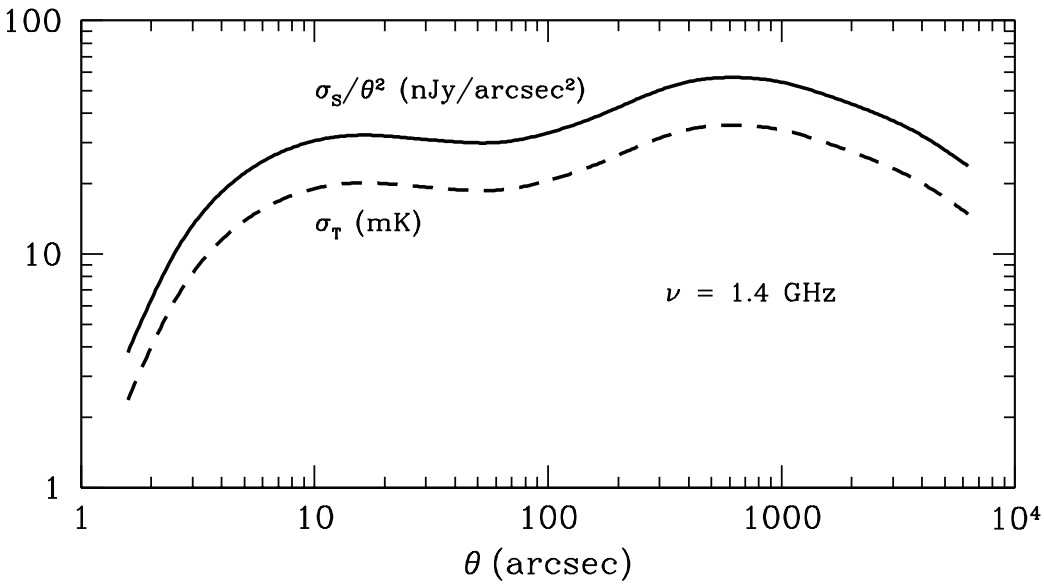

Figure 3: 1.4-GHz 'rms' confusion σ for point sources based on the Wilman et al. (2008) source count, as a function of FWHM resolution for a Gaussian beam in units of Jy beam^{-1} and K of brightness temperature. The 'rms' is defined in this diagram as half the Jy beam^{-1} or K range containing two thirds of the data points, making it a more stable statistic given the long tails of the $P(D)$ distribution. The curves can be rescaled to nearby frequencies by scaling $\sigma_S \propto \nu^{-0.7}$ or $\sigma_T \propto \nu^{-2.7}$.

PoS(AASKA14)172

assumption that we 'know' the composition of the faint-source populations to be star-forming, and that therefore we can infer faint radio-source structures from optical data, is premature.

2.2 Stacking

The literature is very ambiguous on the precise definition of stacking, perhaps the most succinct being "taking the covariance of a map with a catalogue" (Marsden et al., 2009). Having made some selection of sources in an often-deeper (in terms of raw surface density) catalogue, one measures the flux in a map, usually at another wavelength, building up a distribution of map-extracted fluxes for that sample. For example, one might select sources in the near infra-red (i.e. by stellar mass; e.g. Dunne et al. 2009; Karim et al. 2011; Zwart et al. 2014) and measure their 1.4-GHz fluxes, using photometric redshifts to convert those fluxes into star-formation rates via calibration to the far-infra-red–radio correlation (e.g. Yun et al. 2001; Condon et al. 2002). Or one might stack a total-intensity catalogue in polarization in order to investigate cosmic magnetism (Stil, 2015). The flux histogram thus obtained resembles the $P(D)$ of Fig. 2 (left-hand dotted line), and can be binned by some physical quantity, e.g. stellar mass and/or redshift.

Sufficiently rich surveys (with respect to areal coverage/depth) to-date routinely beat individual detection/confusion limits by an order of magnitude to recover the average (see below) properties of pre-selected source populations. The main complications arise if the angular resolution of the map to be stacked is much coarser than in the selection band. For coarse-resolution maps, signal from more than one source can contribute to the net flux in a given pixel in the stacking band (e.g. Webb et al. 2004, Greve et al. 2010) and due consideration must be given to this as a possible source of confusion noise. However, similar problems can in principle arise even at high angular resolution as the source density increases for deeper maps. One might hence conclude that a stacking experiment suffers under low-angular-resolution conditions as well as when survey sensitivity is increasing. The effects of source crowding are negligible if the source distribution is random, following a Poisson distribution at least at the scale of the beam (Marsden et al. 2009; Viero et al. 2012). Even if the latter condition were violated, efficient deblending algorithms have been proposed (e.g. Kurczynski & Gawiser 2010).

Which average? A key difficulty (see e.g. White et al. 2007) is what summary statistic to use to describe the flux distribution (as a whole or within each bin), if any. Since the brightest discrete sources generate a long tail to higher fluxes, the median is generally preferred over the mean. But there are a number of biases that can corrupt this estimator, including the flux limits and shape of the underlying intrinsic (to the population) distribution, as well as the magnitude of the map noise (Bourne et al., 2012). Indeed, much current work is focussed on the identification and elimination of sources of bias, and even circumventing entirely the difficult need for debiasing a single summary statistic.

One promising avenue is the development of algorithms for modelling the underlying source-count distribution (or other/intrinsic physical property) parametrically in the presence of measurement noise (see e.g. Condon et al. 2013), without the use of a single (usually biased) summary statistic. Mitchell-Wynne et al. (2014) demonstrated such a technique on a COSMOS catalogue and FIRST maps, recovering the COSMOS source counts correctly from the FIRST data using a Maximum-Likelihood method to reach 0.75σ with 500 sources.

PoS(AASKA14)172

Zwart et al. (in prep.) have extended this work to a fully-Bayesian framework, allowing model selection through the Bayesian evidence, to measure 1.4-GHz source counts for a near-infrared-selected sample. Early indications are that the survey threshold can be beaten by up to two orders of magnitude. Roseboom & Best (2014) also used a BLA to measure luminosity functions, as a function of redshift, right from stacked fluxes. And Johnston, Smith and Zwart (in prep.) are incorporating redshift evolution directly into the modelling process. We also note another stacking technique (Lindroos & Knudsen 2013; Knudsen et al. 2015; Lindroos et al. 2014) in which visibilities are calculated at the positions of known sources and then co-added, with the advantage over an image-plane analysis that it leads to reduced uncertainties.

Finally, stacking and $P(D)$ can take a role in the handling of systematics. For example, in the 1–5σ regime, *P(D)* has a strong signal in terms of the source count at least, and if nothing else, *P(D)* source-count analyses can show just what and when Eddington bias overwhelms the data, so that one can decide *a posteriori* whether to count discrete sources down to 6σ or 3.2σ (or at whichever threshold is suitable). It has played its part in the characterization of CLEAN bias in FIRST (see e.g. Stil 2015). Seymour (in prep.) has proposed stacking independent interferometer pointings in order to obtain the primary beam and total noise.

3. The Road to SKA

There are a number of systematics in $P(D)$ and stacking experiments that must be understood during the analysis of pathfinder data. Here we give a summary of the dominant systematics relevant to the sub-threshold regime about which we *currently* know.

1. CLEAN/snapshot bias; this pernicious effect occurs where instantaneous *uv* coverage is limited. This could therefore be a concern for wide-field snapshot surveys, but less of a problem for longer-integration targeted deep fields such as those envisaged for SKA1-MID. White et al. (2007) were able to correct for the bias with a simple scaling factor, *appearing* to be linear even to relatively faint flux densities.

2. Resolution bias; Stil et al. (2014) pointed out that a bias is introduced when the synthesized beam is undersampled. So for stacking SKA1 data, one may require higher-resolution images than allowed for by simply requiring the synthesized beam to be Nyquist-sampled. One must give due consideration to astrometry.

3. Instrumental calibration, e.g. primary beam model, will certainly be an issue for SKA1; as a sky-based phenomenon, characterization of the primary beam is critical for noise-regime analyses, especially as one wants to go to larger areas and/or mosaics and for polarization. Another example is time-dependent system temperatures (corresponding to spatially-varying map noise) for e.g. VLBI. Joint solution of sky and systematics is beginning to be investigated (Lochner et al., in prep.) but is not routine. See also Smirnov et al. (in prep.).

4. Sidelobe confusion (as opposed to classical confusion), is additional noise introduced into an image via imperfect source deconvolution within the image (i.e. by all sources below the source subtraction cut-off limit) and from the (asymmetric) array response to sources

PoS(AASKA14)172

outside the imaged field-of-view. Grobler et al. (2014) give an example of artifacts buried in the thermal noise. For instruments with a large field-of-view this is particularly challenging and the instrumental artifacts are hard to separate from classical confusion. This is where an accurate $P(D)$ and careful stacking analyses (section 2.2) will couple to fully exploit the imaging of the SKA surveys.

5. Noise characterization is an issue for any survey; understanding of the noise structure is critical for obtaining the correct result in a $P(D)$ or stacking experiment. Uncertainties on source intensities could vary by position in the map (e.g. the mosaicking eggbox sensitivity pattern), by depth (if the confusion noise begins to contribute in a stacking experiment, or if the dirty synthesized beam begins to enter the stack), or by resolution (confusion noise again). If one has some idea of the functional form of the noise, it can be fitted simultaneously with the physics quantities; debiasing a single-point average is rather harder. In a fully Bayesian analysis the likelihood function should be appropriate for the distribution of the measurement uncertainties.

6. Source clustering and sample variance, which Heywood et al. (2013) showed how to limit in the survey-design phase. This has also been tackled in the submillimetre by Viero et al. (2013).

7. Simulations are of crucial importance to all these analyses (for estimating biases due to clustering to give but one example). For radio-continuum studies we use the work of Wilman et al. (2008). Note that accounting for the (possible) background excess found by ARCADE2 (Fixsen et al., 2011) may require new sub-μJy populations (Seiffert et al., 2011; Vernstrom et al., 2011, 2014b). These in turn would require simulations differing from those available via the Wilman et al. prescription, not yet formulated as we move into the pathfinder phase.

The SKA pathfinders such as LOFAR, MWA, MeerKAT and ASKAP themselves will clearly play a key role both in allowing us to update our source-count constraints, as well as in improving statistical techniques that in turn can be adopted for SKA1 analyses, to which we now turn our attention.

4. Considerations for SKA

The integrated version of the count (Vernstrom et al., 2014a) provides important source-surface-density data for design of SKA pathfinder surveys and for development of the SKA. However, extrapolation to other survey wavelengths via a single spectral index must be restricted to a factor of 2 at most, to say 1.4 and 5.0 GHz, and even then over only a limited flux-density range. Counts outside this frequency range differ markedly, and these differences have been modelled by radio-source population syntheses, e.g. Jackson & Wall (1999); Wilman et al. (2008); Massardi et al. (2011).

While it would be speculatory at this stage to predict the confusion implications for the full SKA, various authors have made calculations for SKA1, including present authors, Prandoni & Seymour (2015), and Condon (2013). Illustrative calculations are shown in Figs 4 and 5 (for

PoS(AASKA14)172

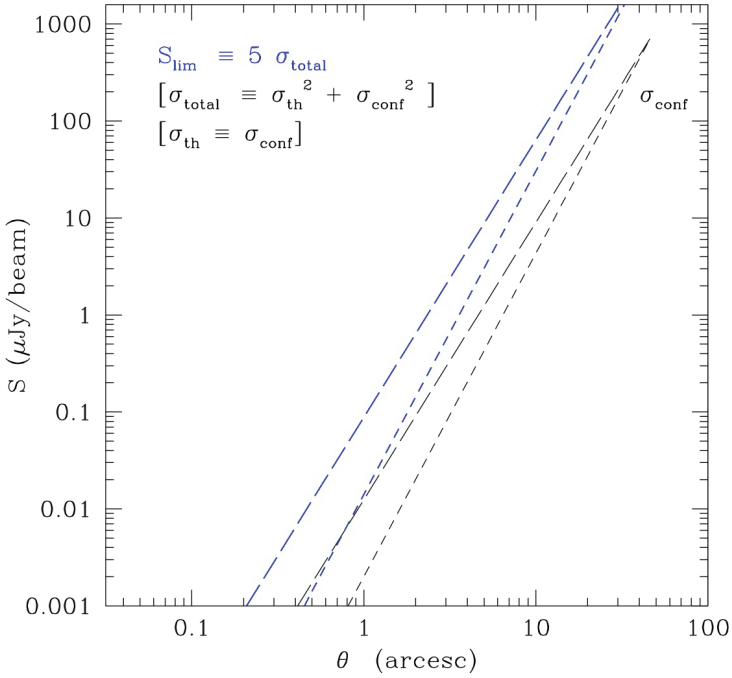

Figure 4: 1.4-GHz limits (dashed and dotted blue lines) of confusion-limited surveys, as a function of spatial resolution $\theta =$ HPBW. Two estimates of the confusion noise are considered. The first (dashed line) is the classical formulation, assuming the source counts derived by Condon et al. (2012), i.e. $N(S) \approx 9000S^{-1.7}$ Jy sr^{-1} at 3 GHz translating to $N(S) \approx 12000S^{-1.7}$ Jy sr^{-1} at 1.4 GHz. The second (dotted line) uses the approximation of Eq. 27 of Condon et al. (2012) assuming $\nu = 1.4$ GHz.

details of the reference surveys refer to Prandoni & Seymour 2015). Although the details remain to be calculated in the light of the newest deep count estimates (e.g. Vernstrom et al. 2014a,b), general statements can be made. We deal with SKA1-LOW then SKA1-MID/SUR.

Firstly, $P(D)$ experiments at full sensitivity are only anticipated for the lowest frequencies and possibly in the deepest fields, where SKA1(-LOW) will see true confusion-limited data. The SKA will be limited by dynamic range (see section 2), and maximizing this will require care in configuration design (Condon, 2013). Second, SKA1-LOW will obtain its confusion-limited data easily so that (a) survey design needs much consideration and (b) confusion or $P(D)$ experiments will be possible. These experiments may be of great significance, because of the unknown contribution of very steep-spectrum populations favoured at low frequencies. Such sources are hard to detect at faint intensities/large distances of ≈1.4-GHz surveys because of K-corrections. Their presence or otherwise in the low-frequency source count will be telling in terms of their presumed epoch-dependent luminosity function. Likewise there is likely to be unique potential to probe star-forming galaxies to higher redshifts than has previously been possible.

Estimates for the SKA1-LOW classical-confusion limit extrapolate higher-frequency source counts (e.g. 1.4 GHz) because of the paucity of deep ≈150-MHz source-count data. While there is a steep slope across the ≈100 mJy–1 Jy 150-MHz differential source count, this will flatten if there is a sizeable, fainter source population at $S_{150\,\mathrm{MHz}} < 10$ mJy. This behaviour is predicted by the flattening of the 1.4-GHz differential source count at $S_{1.4\,\mathrm{GHz}} \lesssim 2$ mJy. Previous work, which has adopted a standard spectral index to extrapolate from 1.4 GHz to 150 MHz in order to predict the low-frequency sky, could be naïve: it assumes that the fainter population observed at 1.4 GHz obeys a standard spectral index ($\alpha = -0.7$) and/or that there is no low frequency (only) very steep-spectrum faint population that is undetectable at 1.4 GHz.

For SKA1-MID, survey design needs careful consideration in terms of whether confusion is to

PoS(AASKA14)172

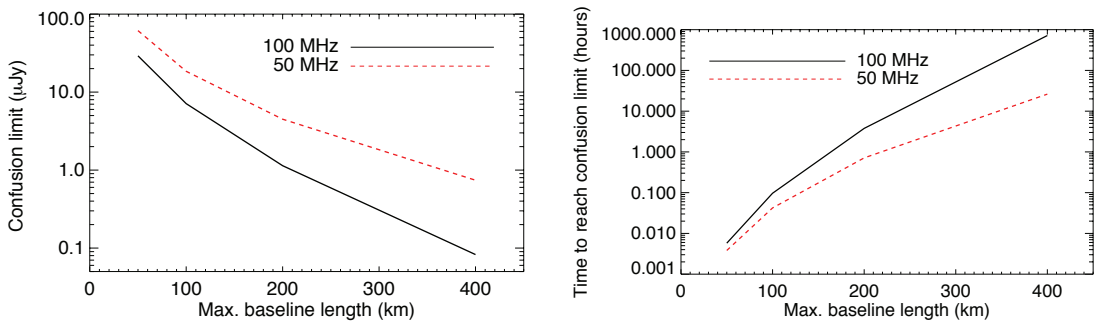

Figure 5: *Left* – the 1-σ flux density at which the survey threshold/confusion limit (here taken as depth at which there is one $> 3\sigma$ source per 20 beams) is reached for increasing maximum baseline. *Right* – integration time per pointing needed to reach this limit for increasing maximum baseline. A maximum baseline of > 100 km is needed for surveys deeper than 10 μJy.

be avoided, or whether it is the object of experiment (i.e. $P(D)$). The detection thresholds of SKA1-MID/SUR will be vastly lower than those of SKA1-LOW, mainly allowing for stacking probes of radio populations selected in the formers' higher-frequency all-sky surveys. But ultra-deep probes will demand an adequate handling of source-clustering biases despite the high angular resolutions the SKA will achieve at typical (GHz) survey wavelengths.

On the subject of panchromatic data, it is anticipated that stacking will be undertaken in both wide and deep surveys, and Euclid and LSST will almost certainly play a role here (**?**). If millions of sources are detected by EUCLID, for example, over a wide redshift range, and only (say) 20 per cent are directly detected in the radio, then stacking SKA1-MID data allows for the potential to capture a substantial fraction of the galaxy population in order to measure the luminosity functions of star-forming and AGN galaxies, and as a function of environment (see elsewhere in this volume).

Characterization of any SKA1-MID-detected diffuse emission (such as cluster halos and relics) that couples to shorter baselines will necessarily require a good understanding of confusion noise (see e.g. Feroz et al. 2009). Stacking itself is highly applicable for detecting such emission and constraining scaling relations (e.g. Sehgal et al. 2013).

References

Barcons, X., Raymont, G. B., Warwick, R. S., et al. 1994, *Mon. Not. R. Astr. Soc.*, 268, 833

Begelman, M. C. 2004, in Coevolution of Black Holes and Galaxies, 374

Blyth, S., et al. 2015, "Exploring Neutral Hydrogen and Galaxy Evolution with the SKA", in Proceedings of "Advancing Astrophysics with the Square Kilometre Array", PoS(AASKA14)128

Bonzini, M., Padovani, P., Mainieri, V., et al. 2013, *Mon. Not. R. Astr. Soc.*, 436, 3759

Bourne, N., et al. 2012, *Mon. Not. R. Astr. Soc.*, 421, 3027

Caillault, J.-P., & Helfand, D. J. 1985, *Astrophys. J.*, 289, 279

Carilli, C. L., & Rawlings, S. 2004, *New Astronomy Reviews*, 48, 979

Condon, J. 2013, Requirements for Continuum Surveys with SKA1, Tech. rep., NRAO

PoS(AASKA14)172

Condon, J. J., Cotton, W. D., & Broderick, J. J. 2002, *Astron. J.*, 124, 675
Condon, J. J., Kellermann, K. I., Kimball, A. E., Ivezić, Ž., & Perley, R. A. 2013, *Astrophys. J.*, 768, 37
Condon, J. J., Cotton, W. D., Fomalont, E. B., et al. 2012, *Astrophys. J.*, 758, 23
Coppin, K., Halpern, M., Scott, D., Borys, C., & Chapman, S. 2005, *Mon. Not. R. Astr. Soc.*, 357, 1022
Croton, D. J., Springel, V., White, S. D. M., et al. 2006, *Mon. Not. R. Astr. Soc.*, 365, 11
Dunne, L., Ivison, R. J., Maddox, S., et al. 2009, *Mon. Not. R. Astr. Soc.*, 394, 3
Eddington, A. S. 1913, *Mon. Not. R. Astr. Soc.*, 73, 359
Feroz, F., Hobson, M. P., Zwart, J. T. L., Saunders, R. D. E., & Grainge, K. J. B. 2009, *Mon. Not. R. Astr. Soc.*, 398, 2049
Fixsen, D. J., Kogut, A., Levin, S., et al. 2011, *Astrophys. J.*, 734, 5
Friedmann, Y., Bouchet, F., Blaizot, J., & Lagache, G. 2002, in EAS Publications Series, Vol. 4, EAS Publications Series, ed. M. Giard, J. P. Bernard, A. Klotz, & I. Ristorcelli, 357–357
Glenn, J., Conley, A., Bethermin, M., et al. 2010, *Mon. Not. R. Astr. Soc.*, 409, 109
Greve, T. R., et al. 2010, *Astrophys. J.*, 719, 483
Grobler, T. L., Nunhokee, C. D., Smirnov, O. M., van Zyl, A. J., & de Bruyn, A. G. 2014, *Mon. Not. R. Astr. Soc.*, 439, 4030
Hewish, A. 1961, *Mon. Not. R. Astr. Soc.*, 123, 167
Heywood, I., Jarvis, M. J., & Condon, J. J. 2013, *Mon. Not. R. Astr. Soc.*, 432, 2625
Hodge, J. A., Becker, R. H., White, R. L., & de Vries, W. H. 2008, *Astron. J.*, 136, 1097
Jackson, C. A., & Wall, J. V. 1999, *Mon. Not. R. Astr. Soc.*, 304, 160
Jarvis, M., et al. 2015, "The star-formation history of the Universe with the SKA", in Proceedings of "Advancing Astrophysics with the Square Kilometre Array", PoS(AASKA14)068
Jauncey, D. L. 1968, *Astrophys. J.*, 152, 647
Jenkins, C. R., & Reid, I. N. 1991, *Astron. J.*, 101, 1595
Kapinska, A., et al. 2015, "Unravelling lifecycles and physics of radio-loud AGN in the SKA Era", in Proceedings of "Advancing Astrophysics with the Square Kilometre Array", PoS(AASKA14)173
Karim, A., Schinnerer, E., Martínez-Sansigre, A., et al. 2011, *Astrophys. J.*, 730, 61
Knudsen, K., et al. 2015, "Stacking of SKA data: comparing uv-plane and and image-plane stacking", in Proceedings of "Advancing Astrophysics with the Square Kilometre Array", PoS(AASKA14)168
Kurczynski, P., & Gawiser, E. 2010, *Astron. J.*, 139, 1592
Lindroos, L., & Knudsen, K. K. 2013, in IAU Symposium, Vol. 295, IAU Symposium, ed. D. Thomas, A. Pasquali, & I. Ferreras, 94–94
Lindroos, L., Knudsen, K. K., Vlemmings, W., Conway, J., & Martí-Vidal, I. 2014, ArXiv e-prints, arXiv:1411.1410
Makhathini, S., et al. 2015, "Morphological classification of radio sources for galaxy evolution and cosmology with the SKA", in Proceedings of "Advancing Astrophysics with the Square Kilometre Array", PoS(AASKA14)081
Marsden, G., et al. 2009, *Astrophys. J.*, 707, 1729
Massardi, M., et al. 2011, *Mon. Not. R. Astr. Soc.*, 412, 318

PoS(AASKA14)172

McAlpine, K., et al. 2015, "The SKA view of the Interplay between SF and AGN Activity and its role in Galaxy Evolution", in Proceedings of "Advancing Astrophysics with the Square Kilometre Array", PoS(AASKA14)083

McAlpine, K., Smith, D. J. B., Jarvis, M. J., Bonfield, D. G., & Fleuren, S. 2012, *Mon. Not. R. Astr. Soc.*, 423, 132

Mitchell-Wynne, K., Santos, M. G., Afonso, J., & Jarvis, M. J. 2014, *Mon. Not. R. Astr. Soc.*, 437, 2270

Murphy, E., et al. 2015, "The Astrophysics of Star Formation Across Cosmic Time at >10 GHz with the Square Kilometre Array", in Proceedings of "Advancing Astrophysics with the Square Kilometre Array", PoS(AASKA14)085

Oliver, S. J., Rowan-Robinson, M., & Saunders, W. 1992, *Mon. Not. R. Astr. Soc.*, 256, 15P

Padovani, P. 2011, *Mon. Not. R. Astr. Soc.*, 411, 1547

Padovani, P., Bonzini, M., Miller, N., et al. 2014, in IAU Symposium, Vol. 304, IAU Symposium, 79–85

Patanchon, G., Ade, P. A. R., Bock, J. J., et al. 2009, *Astrophys. J.*, 707, 1750

Prandoni, I., & Seymour, N. 2015, "Revealing the Physics and Evolution of Galaxies and Galaxy Clusters with SKA Continuum Surveys", in Proceedings of "Advancing Astrophysics with the Square Kilometre Array", PoS(AASKA14)067

Roseboom, I. G., & Best, P. N. 2014, *Mon. Not. R. Astr. Soc.*, 439, 1286

Scheuer, P. A. G. 1957, *Proc. Camb. Phil. Soc.*, 53, 764

Sehgal, N., et al. 2013, *Astrophys. J.*, 767, 38

Seiffert, M., Fixsen, D. J., Kogut, A., et al. 2011, *Astrophys. J.*, 734, 6

Seymour, N., Huynh, M., Dwelly, T., et al. 2009, *Mon. Not. R. Astr. Soc.*, 398, 1573

Smolčić, V., et al. 2015, "Exploring AGN Activity over Cosmic Time with the SKA", in Proceedings of "Advancing Astrophysics with the Square Kilometre Array", PoS(AASKA14)069

Smolčić, V., Schinnerer, E., Scodeggio, M., et al. 2008, *Astophys. J. Suppl.*, 177, 14

Smolčić, V., Zamorani, G., Schinnerer, E., et al. 2009a, *Astrophys. J.*, 696, 24

Smolčić, V., Schinnerer, E., Zamorani, G., et al. 2009b, *Astrophys. J.*, 690, 610

Stil, J., & Keller, B., 2015, "Stacking for Cosmic Magnetism with SKA Surveys", in Proceedings of "Advancing Astrophysics with the Square Kilometre Array", PoS(AASKA14)112

Stil, J. M., Keller, B. W., George, S. J., & Taylor, A. R. 2014, *Astrophys. J.*, 787, 99

Taylor, A. R., & Braun, R., eds. 1999, Science with the Square Kilometer Array : a next generation world radio observatory, ed. A. R. Taylor & R. Braun

Toffolatti, L., & Barcons, X. 1992, in X-ray Emission from Active Galactic Nuclei and the Cosmic X-ray Background, ed. W. Brinkmann & J. Truemper, 358

Vernstrom, T., Norris, R. P., Scott, D., & Wall, J. V. 2014a, ArXiv e-prints, arXiv:1408.4160

Vernstrom, T., Scott, D., & Wall, J. V. 2011, *Mon. Not. R. Astr. Soc.*, 415, 3641

Vernstrom, T., Scott, D., Wall, J. V., et al. 2014b, *Mon. Not. R. Astr. Soc.*, 440, 2791

Viero, M. P., et al. 2013, *Astrophys. J.*, 779, 32

Wall, J. V., & Jenkins, C. R. 2003, Practical Statistics for Astronomers (CUP)

Webb, T. M. A., Brodwin, M., Eales, S., & Lilly, S. J. 2004, *Astrophys. J.*, 605, 645

White, R. L., Helfand, D. J., Becker, R. H., Glikman, E., & de Vries, W. 2007, *Astrophys. J.*, 654, 99

PoS(AASKA14)172

Wilman, R. J., Miller, L., Jarvis, M. J., et al. 2008, *Mon. Not. R. Astr. Soc.*, 388, 1335
Windhorst, R. A. 2003, *New Astronomy Reviews*, 47, 357
Yun, M. S., Reddy, N. A., & Condon, J. J. 2001, *Astrophys. J.*, 554, 803
Zwart, J. T. L., Jarvis, M. J., Deane, R. P., et al. 2014, *Mon. Not. R. Astr. Soc.*, 439, 1459

PoS(AASKA14)172

PROCEEDINGS OF SCIENCE

Unravelling lifecycles & physics of radio-loud AGN in the SKA era

Anna D. Kapińska[*,1,2], **Martin J. Hardcastle**[*,3], **Carole A. Jackson**[4], **Tao An**[5,6], **Willem A. Baan**[5], **Matt J. Jarvis**[7,8]

[1] *ARC Centre of Excellence for All-Sky Astrophysics (CAASTRO);* [2] *ICRAR, The University of Western Australia, M468, 35 Stirling Hwy, Crawley WA 6009, Australia;* [3] *School of Physics, Astronomy and Mathematics, University of Hertfordshire, College Lane, Hatfield AL10 9AB, United Kingdom;* [4] *ICRAR, Curtin University, GPO Box U1987, Perth WA 6845, Australia;*
[5] *Shanghai Astronomical Observatory, Chinese Academy of Sciences, 200030 Shanghai, China;*
[6] *Key Laboratory of Radio Astronomy, Chinese Academy of Sciences, 210008 Nanjing, China;*
[7] *Oxford Astrophysics, Department of Physics, Keble Road, Oxford OX1 3RH, United Kingdom;*
[8] *Department of Physics, University of Western Cape, Cape Town 7535, South Africa*
E-mail: anna.kapinska at uwa.edu.au

Radio-loud AGN ($> 10^{22}$ W Hz^{-1} at 1.4 GHz) will be the dominant bright source population detected with the SKA. The high resolution that the SKA will provide even in wide-area surveys will mean that, for the first time sensitive, multi-frequency total intensity and polarisation imaging of large samples of radio-loud active galactic nuclei (AGN) will become available. The unprecedented sensitivity of the SKA coupled with its wide field of view capabilities will allow identification of objects of the same morphological type (i.e. the entire FR I, low- and high-luminosity FR II, disturbed morphology as well as weak radio-emitting AGN populations) up to high redshifts ($z \sim 4$ and beyond), and at the same stage of their lives, from the youngest CSS/GPS sources to giant and fading (dying) sources, through to those with restarted activity radio galaxies and quasars. Critically, the wide frequency coverage of the SKA will permit analysis of same-epoch rest-frame radio properties, and the sensitivity and resolution will allow full cross-identification with multi-waveband data, further revealing insights into the physical processes driving the evolution of these radio sources. In this chapter of the SKA Science Book we give a summary of the main science drivers in the studies of lifecycles and detailed physics of radio-loud AGN, which include radio and kinetic luminosity functions, AGN feedback, radio-AGN triggering, radio-loud AGN unification and cosmological studies. We discuss the best parameters for the proposed SKA continuum surveys, both all-sky and deep field, in the light of these studies.

Advancing Astrophysics with the Square Kilometre Array
June 8-13, 2014
Giardini Naxos, Sicily, Italy

[*]Speaker.

PoS(AASKA14)173

1. Introduction

Large-scale radio surveys compiled over the past 50 years have revealed a multitude of source types that we term 'radio-loud AGN' (Peacock & Wall 1982; Wall 1994). These objects will be the dominant population of bright sources detected by the SKA. The deep SKA radio surveys will allow detailed and complete analysis of most, if not all, radio-loud AGN populations and provide the basis to resolve some of the most critical questions in this area.

The radio emission from radio-loud AGN is synchrotron emission produced by a population of electrons, transported in a relativistic outflow from the vicinity of the central supermassive black hole, and accelerated to high energies as the jet expands and decelerates to sub-relativistic speeds. This is the dominating source of radio emission from radio-loud AGN down to luminosity densities of $\sim 10^{22}$ W Hz^{-1} at 1.4 GHz; below this luminosity density AGN are referred to as weakly radio-emitting and it is under debate whether their radio emission is still dominated by an active nucleus rather than star formation. The subject of weakly radio-emitting AGN is covered elsewhere in this volume (Orienti et al. 2015, see also §6.1). Based on unification models (e.g. Barthel 1989; Urry & Padovani 1995; Jackson & Wall 1999), radio-loud AGN are often distinguished as radio galaxies, radio-loud quasars and BL Lac-type objects (dependent on the orientation to the observer). Radio galaxies and radio-loud quasars are further broadly divided into unresolved or compact symmetric objects, FR I and FR II type sources (including peculiar morphologies) and giant radio galaxies (see §2.1; classification of different life stages and radio morphologies). Here, we consider all of these radio-loud AGN, with no selection on multi-wavelength properties of their hosts.

The physics of, and physical conditions in, the radio-emitting plasma are of great interest in themselves, but radio-loud AGN are important for a number of other reasons. Firstly, they provide an obscuration-independent method of selecting AGN out to the highest redshifts, and in some cases, e.g. radiatively inefficient, low accretion-rate AGN radio emission gives us the *only* method of measuring the output and accretion rate of the system. Secondly, radio-loud AGN are now routinely invoked in models of galaxy formation and evolution, where they provide a so-called 'feedback' mechanism. AGN feedback is now thought to be one of the main mechanisms preventing the cooling of large-scale gas and the consequent growth of the host galaxies (Bower et al. 2006; Croton et al. 2006). Finally, we expect the SKA surveys to reach nJy levels, detecting statistically significant numbers of sources across the wide range of the radio luminosity function (RLF) *at all cosmic epochs*. When coupled with sufficient angular resolution and multi-waveband data, it will be possible to separate the contribution of radio emission due to an active nucleus from that due to ongoing or bursting star formation (SF; McAlpine et al. 2015).

In this Chapter we primarily focus on how the SKA will reveal the evolution of the radio-loud AGN populations characterised by their radio morphologies and luminosity densities, and at the same time directly provide the necessary radio data for studies of the radio source physics for the first time. There are a number of key questions that these deep samples can address.

- What is the RLF at all cosmic epochs?

  There is a huge range of radio AGN luminosity densities; in the local Universe this extends from 10^{22} to 10^{27} W Hz^{-1} at 1.4 GHz (Mauch & Sadler 2007). Due to the Malmquist effect, deep samples are highly biased towards high luminosity sources near to the limiting

PoS(AASKA14)173

magnitude at each epoch. The result is that RLFs derived from 'complete' small-area radio samples are limited in accuracy and fail to fully probe the breadth of the full RLF. Although it is well established that the RLF evolves steeply for the overall radio-loud AGN population (note the steepness is luminosity dependent, e.g. Dunlop & Peacock 1990; Sadler et al 2007; Donoso, Best & Kauffmann 2009; Rigby et al 2011; McAlpine, Jarvis & Bonfield 2013; Best et al. 2014, among many others), it is still not clear whether it is sources themselves or number of sources that become brighter.

- Is there a link between the evolving radio-loud AGN RLF and the evolution of galaxies and galaxy clusters? Are feedback processes inherent to all radio-loud AGN, or to just a subset of them, and what does this reveal about the physical processes within these populations?

  Although interaction between the radio lobes and the hot ambient medium is directly observable in X-rays in the local Universe, it is still an open question whether the physics of radio galaxies is consistent with the role they are thought to play in the models of galaxy formation and evolution (Cattaneo et al 2009; McNamara & Nulsen 2012). Studies of radio-loud AGN populations in the local Universe (e.g. Best & Heckman 2012) show that there is a fundamental dichotomy between hosts of high- and low-excitation radio galaxies, and that it is the low luminosity radio sources that drive the AGN activity at $z < 0.2$ (e.g. Shabala, Kaviraj, & Silk 2011). A number of authors attempted to implement AGN feedback into galaxy evolution models (e.g. Shabala & Alexander 2009), but deep radio-loud AGN samples of wide range of luminosity densities and at $z > 0.5$ are required to validate the models.

- What is the kinetic luminosity function (KLF) for AGN?

  The radio luminosity density is the detectable signature of a radio-loud AGN, but, as we will discuss in this paper, this bears only a weak relationship to the intrinsic kinetic luminosity (jet power) of AGN. By providing multi-frequency, high-resolution images for large samples of radio-loud AGN, the SKA will give us the best possible chance to break the luminosity density/kinetic power degeneracy and therefore understand the power input by AGN to their host environments and supermassive black hole growth over cosmic time (for population studies see e.g. Kapińska & Uttley 2013, for a case study see Hardcastle et al 2012).

- What drives the AGN evolution? Is the 'radio-loud AGN' activity a singular phase for a galaxy, either long- or short-duration, or is it cyclic? What triggers the fuelling cycle?

  At present we know of a number of radio-loud AGN that show signatures of previous activity episodes (Schoenmakers et al. 2000), but it is still not clear whether all radio sources are re-triggered or only some fraction of them (e.g. Saikia & Jamrozy 2009), or even what triggers radio activity. A number of authors have attempted to tackle this problem via both statistical population as well as case studies at low-redshifts (for recent works see e.g. Shabala et al. 2008; Janssen et al 2012; Kaviraj et al. 2014; Maccagni et al. 2014). However, deep radio-loud AGN samples of a wide range of luminosity densities at $z > 0.5$ are required to extend these studies to higher redshifts (e.g. Karouzos, Jarvis, & Bonfield 2014).

In what follows we assume that continued progress in wide and deep optical/IR imaging and spectroscopic surveys will be such that it will be possible to *identify* a large fraction of the observed

PoS(AASKA14)173

radio galaxy population and assign redshifts to the sources – a precondition for any study of a population and its physics. Further discussions of radio-loud AGN hosts must involve a discussion of the expected optical survey coverage by the start of SKA science operations – this is discussed elsewhere in this volume (Antoniadis et al. 2015; Bacon et al. 2015; Kitching et al. 2015).

The chapter is composed as follows. In Section 2 we present our current view of the lifecycle of a radio galaxy, and our current observational and theoretical understanding on the radio source evolution as it ages throughout its lifetime. In Sections 3 – 5 we separately discuss each stage of a radio-loud AGN life, from a radio galaxy birth, through its mid-life, to its death; in each of those sections we consider the necessary SKA1 and SKA receivers for each of the radio source class (i.e. life phase) observations. In Section 6 we take a broader view on the radio-loud AGN populations, and discuss them in terms of AGN duty cycles, AGN unification and cosmological studies. A brief summary of the SKA elements for this study is given in Section 7. We assume a flat Universe with the Hubble constant of $H_0 = 67$ km s^{-1} Mpc^{-1}, and $\Omega_{\rm M} = 0.685$ and $\Omega_\Lambda = 0.315$ (Planck Collaboration et al. 2013) throughout the paper.

2. Lifecycles of radio-loud AGN

The typical timescales of AGN radio activity are estimated to be ~ 0.1 Gyr (e.g. Wan, Daly, & Guerra 2000; Kapińska, Uttley & Kaiser 2012; Antognini, Bird, & Martini 2012). Once the radio activity is triggered, the launched jet expands through the host galaxy and ambient medium until the jet supply ceases and the radio source slowly fades radiating away the remaining energy stored in radio lobes. A series of these events is what we refer to as a 'lifecycle' of a radio source.

2.1 How complete is our current picture?

The observed populations of radio-loud AGN fall into reasonably well defined classes distinguished by radio morphology, luminosity density and physical size (the latter of which is generally interpreted to be proportional to age). The smallest size radio galaxies, the so-called Compact Symmetric Objects (CSO, < 500 pc; Wilkinson et al. 1994), Gigahertz Peaked Spectrum (GPS, < 1 kpc with turnover broadband radio spectra; Blake 1970; Stanghellini et al. 1990; O'Dea, Baum & Stanghellini 1991) and Compact Steep Spectrum (CSS, < 10 kpc; Peacock & Wall 1982; Fanti et al. 1990; O'Dea 1998) sources are compact radio sources completely embedded in the host galaxy. They are believed to be predominantly young, 'start-up' or 'baby radio-galaxies', approximately $10^3 - 10^5$ years old (Section 3). These sources may be resolved at VLBI angular resolutions, where they often reveal morphologies similar to those of more extended, of the order of 100-kpc, sources (e.g. Readhead 1995; Snellen, Schilizzi & van Langevelde 2000). At kiloparsec scales, the Fanaroff-Riley (1974) class I and II (FR I, FR II respectively) are distinguished (Section 4). According to unification models (Urry & Padovani 1995; Owen, Ledlow & Keel 1996; Wall & Jackson 1997; Jackson & Wall 1999), these can be observed at various angles disguising themselves at times as, for example, core-dominated quasar and blazar sub-populations. FR I and FR II type sources are found to be typically $\sim 10^7$ years old (Section 6).

A radio source is thought to evolve through these phases as it ages: from young, compact and luminous CSO/GPS and CSS sources, the jets of which strongly interact with dense interstellar medium (ISM) as they try to leave the host galaxy, to the large-scale FR I and FR II stage

PoS(AASKA14)173

at which the relativistic jets extend into the inter-galactic (IGM) and intra-cluster medium (ICM). This paradigm was first proposed by Phillips & Mutel (1982) and Carvalho (1985), and further refined by Readhead (1995), Readhead et al. (1996) and Snellen et al. (1999, 2000), and is based on high resolution observations of young radio sources. With the recent observational advances we can now extend these evolutionary tracks to the very late stages of radio source evolution which include giant ($>$ 1 Mpc; Komberg & Pashchenko 2009), dying (Parma et al. 2007), and re-started radio galaxies (Schoenmakers et al. 2000, Section 5).

Whilst simple and appealing, this widely accepted evolutionary path may represent just one of many possible evolutionary tracks of radio-loud AGN – perhaps the longest, main lifecycle path. Alternative paths may include sources that do not reach the giant phase stage, the FR I/FR II stage, or even the CSS stage (e.g. Marecki, Spencer & Kunert 2003). Recent observational evidence for such alternatives comes from the existence of so-called young faders (Kunert-Bajraszewska, Marecki & Spencer 2004; Kunert-Bajraszewska et al. 2010), a class of compact, low radio luminosity density and small-scale CSS sources that resemble large-scale dying radio galaxies. It is still not clear what causes the radio activity to cease and why it may happen on a wide range of timescales, with some radio sources becoming long-lived giants and others dying in their infancy. For example, in the discussion on why only some FR Is and FR IIs evolve to Mpc scales, longer lifetimes, more powerful engines, or under-dense environments have been suggested as a solution, but no consensus has yet been reached (Machalski & Jamrozy 2006; Jamrozy et al. 2008; Komberg & Pashchenko 2009; Kuźmicz & Jamrozy 2013).

A true over-abundance of a young class of radio sources would advocate the view that some radio activity is indeed terminated prematurely. Our current radio source population counts suffer from well-recognised selection biases. Deep, sensitive and complete $N(z)$ measurements of each, well defined radio source type are required. However, selection criteria for the samples must ensure inclusion of all types of radio source at the same time to allow for the lifecycle analyses. Such deep measurements have also a potential to help us to investigate the weakly radio-emitting source population (weak-radio AGN), analyses of which are pivotal in the investigations of AGN duty cycles (Section 6).

2.2 Our theoretical understanding of radio-loud AGN evolution

Building on the seminal work undertaken in the 1970s (Blandford & Rees 1974; Scheuer 1974), tremendous progress has been made especially in the past 20 years towards an analytical understanding of the physics and evolution of extragalactic radio sources. Semi-analytical approximations developed for classical double FR II radio sources (Kaiser & Alexander 1997; Kaiser, Dennett-Thorpe & Alexander 1997; Blundell, Rawlings & Willott 1999), are being extended to both young GPS/CSS (Snellen et al. 2000; Alexander 2000, 2006; An & Baan 2012; Maciel & Alexander 2014) and dying radio galaxy stages (Komissarov & Gubanov 1994; Kaiser & Cotter 2002). The latter has been supported by observations of cavities in X-ray brightness maps of galaxy clusters (considered to be signatures of radio source activity; Bîrzan et al. 2004; McNamara & Nulsen 2007), as well as the discovery of so-called double-double (re-started) radio galaxies (Schoenmakers et al. 2000). The most recent developments include analytical modelling of re-started radio sources (Kaiser, Schoenmakers & Röttgering 2000; Brocksopp et al. 2011) that can account for multiple activity episodes. Very few radio sources with signatures of re-started radio

PoS(AASKA14)173

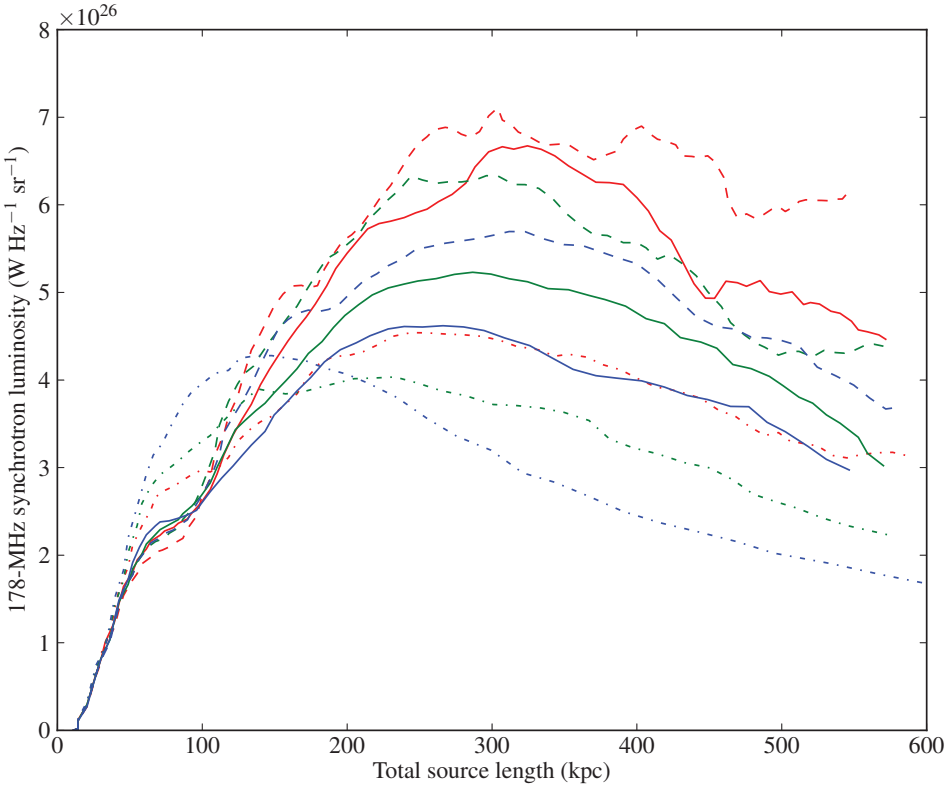

Figure 1: The evolution of radio luminosity density as a function of source physical size as seen in 3D MHD simulations. The different coloured lines show the evolution of a radio source of the *same* jet power (10^{38} W) in different plausible group/cluster environments, where dot-dashed lines represent poor environments, solid lines intermediate and dashed lines rich environments, and the colours denote the steepness of the density profile in the β-model (King 1962, blue represent the steepest and red the flattest profile). Note the wide scatter in the luminosity densities at late times and the significant difference between the early luminosity densities and those in the 'plateau' phase at a few hundred kpc. Standard estimates of jet kinetic power (based on scaling relations) would assign a wide range of different kinetic powers to the source simulated here, depending on the part of the lifecycle observed and the environment it inhabits. Figure adapted from Hardcastle & Krause (2014).

activity have been observed to date – the semi-analytical models are based on fewer than 30 known cases of re-started radio galaxies and on only one source with clear signatures of two episodes of previous activity (Brocksopp et al. 2007, 2011). However, the existence of these sources and understanding of the physics involved is crucial in identifying the radio AGN activity (re)triggering processes and determining duty cycles of radio sources. At the same time, numerical models involving realistic environments are now reaching the stage where they can be used to produce estimates of the evolution of integrated and resolved source properties that complement, and in some cases improve upon, those available from analytic modelling (e.g. Figure 1).

On the other hand, FR I sources are notoriously difficult to model analytically or numerically because of their complex, turbulent and often heavily disturbed radio structures. A number of

PoS (AASKA14) 173

attempts have been made (Laing, Canvin & Bridle 2003; Luo & Sadler 2010), but no general analytical model exists that can predict properties of the FR I class as a whole. This is particularly important, as FR Is are thought to be much more numerous at low luminosity densities; it is possible that they will comprise the majority of the radio-loud AGN population at high redshift, low luminosity density radio samples; however, evidence for their high numbers is currently limited to a few studies in deep fields (Simpson et al. 2012; McAlpine, Jarvis & Bonfield 2013). Numerical approaches to the problem of modelling FR I radio galaxies have been so far focusing predominantly on dynamical evolution of their radio structures (e.g. Perucho & Martí 2007; Perucho et al. 2014). Sensitive, deep SKA observations that will be available for a large number of such sources are required for further theoretical advances [detailed discussion on this subject is covered elsewhere in this volume; see Agudo et al. (2015); Laing (2015)].

However, analytical models investigating the plausible transition of FR II sources into FR Is have been developed (Wang et al. 2011; Turner & Shabala 2015), and it is also thought that all radio sources start off with the FR II morphology. Furthermore, we have also discovered a curious class of hybrid radio morphology objects, which show properties of both FR I and FR II sources (Gopal-Krishna & Wiita 2000; Kapińska et al. 2015). This has direct implications for studies of the AGN host types, environments and their evolution across cosmic time, especially in terms of the observed FR dichotomy (Saripalli 2012), and are already allowing us to statistically model young radio sources, FR IIs and the FR transition populations.

Clearly, observational advances drive our theoretical understanding of radio sources; only by combining both can we study the physical properties of radio-loud AGN that cannot be measured directly (Blundell, Rawlings & Willott 1999; Kapińska, Uttley & Kaiser 2012), but are crucial in the studies of galaxy and galaxy clusters evolution, and AGN feedback and activity.

3. The birth of radio galaxies

Young, compact radio sources are expected to be very numerous (Fanti et al. 1990), but are generally poorly studied in large samples. The observed complete, flux density limited parent samples often impose significant constraints on the population of radio galaxies that can be detected; most samples are biased towards middle-aged radio sources where the radio luminosity density is expected to be the highest for a given jet kinetic power (Figure 1). There is also a strong bias of GPS/CSS sources to higher redshifts as compared to 100-kpc scale radio galaxies (Snellen et al. 2000). In recent years, a number of faint GPS and CSS samples have been constructed probing lower intrinsic luminosities of these objects (Snellen et al. 1999; Tschager et al. 2003; Kunert-Bajraszewska et al. 2010); but it is important to bear in mind that such samples are often constructed in a very different way than typical, complete samples of extragalactic radio sources, thus making it difficult to compare them to larger, and more evolved radio galaxies.

CSO/GPS and CSS sources are considered to be predominantly young radio galaxies, with typical ages of $10^3 - 10^5$ years (Owsianik & Conway 1998; Murgia et al. 1999; Polatidis & Conway 2003). However, it is often difficult to distinguish truly young sources from objects whose expansion is 'frustrated' by interaction with a dense ISM (van Breugel, Miley & Heckman 1984; O'Dea, Baum & Stanghellini 1991; An & Baan 2012). There is also increasing evidence that young double radio sources can have a substantial effect on the ISM of their hosts (Croston, Kraft & Hard-

PoS(AASKA14)173

castle 2007; Croston et al. 2009; Heesen et al 2014); this seems to be also true for the small radio sources associated with canonically radio-quiet AGN (Mingo et al. 2012).

Estimation of the ratio of young to older, large radio galaxies gives crucial constraints on the lifetime distribution of such objects (i.e. what fraction of them survive to the ages of 10^7 years implied by dynamical and spectral ageing studies of 100-kpc scale radio galaxies), and hence on the accretion history of supermassive black holes that power them. It seems very plausible that there is substantial 'infant mortality' in radio galaxies, i.e. that many do not last long enough to reach the largest sizes and highest luminosity densities (Kunert-Bajraszewska, Marecki & Spencer 2004; Kunert-Bajraszewska et al. 2010; An & Baan 2012; Maciel & Alexander 2014). This has been theoretically discussed by Reynolds & Begelman (1997), and fading CSS as well as GPS sources with re-started activity have also been observed (Baum et al. 1990; Kunert-Bajraszewska et al. 2010). Deep and complete $N(z)$ measurements are crucial here to answer question whether all these small scale radio galaxies are progenitors of larger-scale FR I and FR II sources and to our overall understanding of the AGN lifecycles and the activity patterns of their central engines.

3.1 Required SKA elements and the SKA surveys

With the SKA1 baseline design (Dewdney et al 2013), survey depths will be such that we have a realistic chance of detecting the small-scale counterparts of all radio galaxies of even the lowest jet kinetic power (10^{35} W; Hardcastle, Evans & Croston 2006) out to $z \sim 0.6$ using all-sky surveys with SKA1-SUR or SKA1-MID (Band 2, 1.4 GHz) and deep field observations with high frequency receivers on SKA1-MID (Band 4 and 5, 4 GHz and 9.2 GHz respectively). Assuming the jet kinetic power – luminosity density scaling relation of Willott et al. (1999) holds, and scaling down the resulting luminosity density by a few orders of magnitude to account for evolution during the radio source growth (Figure 1) we estimate luminosity densities of $\sim 10^{22}$ W Hz^{-1} for young radio sources which could be progenitors of the weakest FR II radio galaxies. Given the numbers of FR IIs, we would expect at least of order one of these young sources per square degree on the sky, and possibly many more if many FR II-power jets turn off before they reach 100-kpc scales.

The main limitation of SKA1 for the study of CSS/GPS sources will be angular resolution; if we assume 0.05 arcsec resolution at the highest frequencies (SKA1-MID Band 5), then at $z = 0.3$ we will resolve only sources with linear sizes > 0.66 kpc, and > 1.35 kpc at higher redshifts (assuming source size at least $3\times$ the beam size). Lower frequencies (and especially SKA1-LOW) will not be useful for detailed radio morphology analyses. However, the high frequency capabilities will still allow an almost complete survey of the whole of the low- and mid-z radio galaxy population down to the smallest sizes and lowest powers. Using a combination of angular resolution and in-band spectral information we will be able to distinguish young objects (steep spectrum, double lobe structure) from beamed, core-dominated systems (flat spectrum). The broad-band spectral coverage of SKA1-MID, -SUR and -LOW, especially when combined with each other, is crucial for selection of the GPS sources and investigation of their physics (Callingham et al. 2015). Early science can be carried out by aiming to be complete to some less ambitious combination of jet kinetic power lower limit and redshift upper limit, which will still give valuable insights into the properties of the lower-power sources.

All of these observations will provide a large number of sources too small for the SKA1 to resolve but which can be followed up by longer-baseline instruments such as the EVN, which

PoS(AASKA14)173

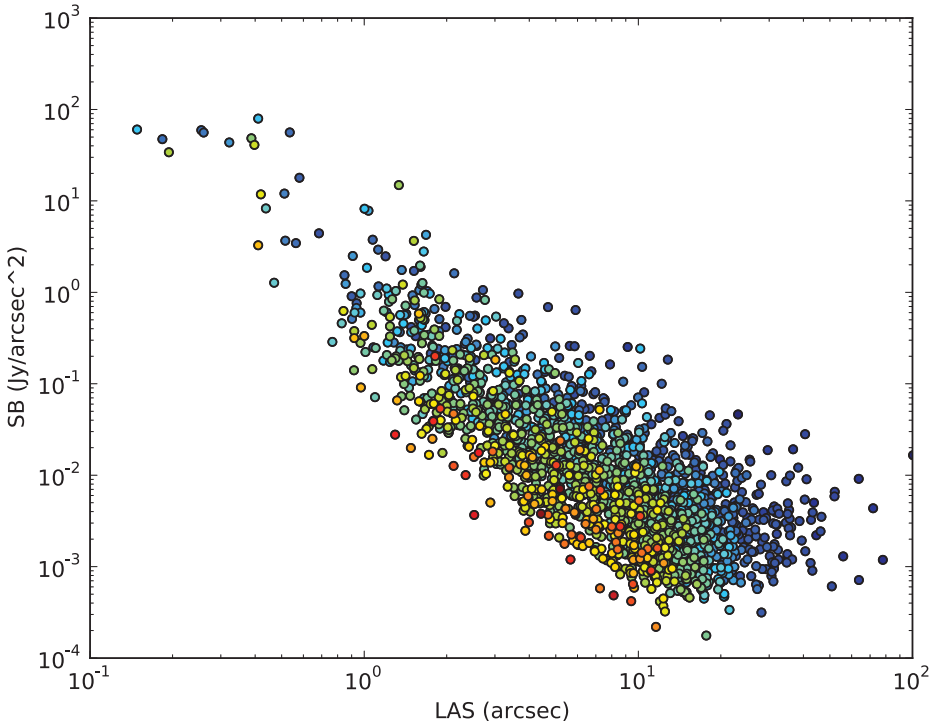

Figure 2: Largest angular size (LAS) and 151 MHz surface brightness (SB) for FR II radio galaxies from the SKADS SEX simulations (Wilman et al. 2008). Colour coding indicates redshift, from dark blue ($z = 0$) to red ($z \simeq 6$).

are expected to provide an important complementary facility in the SKA era, unless the SKA VLBI facility is incorporated from the beginning of the telescope operations. Furthermore, detailed polarimetric studies of individual objects remain crucial to both understanding the relativistic jet–ISM interaction on parsec scales (An et al. 2010; Agudo et al. 2015; Johnston-Hollitt et al. 2015), and establishing the fraction of young vs. frustrated CSO/GPS and CSS sources.

In the final SKA stage we would expect to be able to see essentially every source with jet kinetic power $> 10^{35}$ W, independent of its age except for sources less than a few hundred years old, out to $z = 0.5 - 1.0$ (Bands 2 and 5), and all FR II-power ($> 10^{36}$ W; Rawlings & Saunders 1991) start-up galaxies out to $z \sim 3$, well into the regime where cosmological evolution of the radio source population becomes important. Assuming the angular resolution will be improved to at least 0.005 arcsec, we will be able to resolve sources of linear sizes > 150 pc at all redshifts.

4. Radio galaxies in their mid-life: evolution, jet power and environmental impact

4.1 Detailed physics of jets and radio lobes

Large radio galaxies, with physical sizes of tens to hundreds of kpc, are the best-studied class of radio galaxy and have the best-understood effects on their ambient medium – the hot phase of the IGM/ICM; these are the sources generally thought to be responsible for the 'radio-mode feedback'

PoS(AASKA14)173

that prevents the hot phase from cooling out onto the most massive galaxies (Bîrzan et al. 2004; McNamara & Nulsen 2007). As shown in Figure 1, the brightness of the radio emission is expected to peak in this phase of a source's evolution, so these are the objects predominantly selected in large-scale flux density-limited surveys, and will be the easiest to detect and image with the SKA.

Traditionally, radio galaxies detected in surveys have been characterized on the basis of an integrated flux density, and thus an estimate of radio luminosity density – this can be directly used to construct RLFs of radio-loud AGN. However, for AGN feedback or radio source studies what one really wants to know is the jet kinetic power – the instantaneous or time-averaged rate at which radio-loud AGN are transferring energy to their environments. The relationship between the observed radio emission and the jet kinetic power is a long-standing problem (Rawlings & Saunders 1991; Willott et al. 1999; Kapińska, Uttley & Kaiser 2012, see also Section 2.2) and it is increasingly clear that the answer is not expected to be simple. At low radio luminosities, a substantial scatter in the relation between radio luminosity density and jet kinetic power is observed (Cavagnolo et al. 2010; Godfrey & Shabala 2013); this is expected on theoretical grounds, since the radio luminosity density should be a function of the jet kinetic power, the age of the source (Kaiser, Dennett-Thorpe & Alexander 1997), radio morphology, and, crucially, the source's environment (Barthel & Arnaud 1996; Hardcastle & Krause 2013) which we know to differ widely from source to source even at a fixed redshift (Ineson et al. 2013). In the case of weakly radio-emitting AGN, we can assess the interaction with their host environments just by measuring a luminosity density in some band and applying a bolometric correction. The problems described above mean that, for radio-loud AGN, no comparable correction exists.

The jet kinetic power-environment-age degeneracy can be broken with observations that characterize not just the radio luminosity density but also the physical size, aspect ratio and spectral age of the source; in principle, this can allow not just the jet kinetic power but also the properties of the environment (possibly including an estimate of the heating rate) to be determined directly from radio observations. Spectral age measurements can be made by fitting to the spatially resolved broad-band spectrum of the source (Harwood et al. 2013), and so to apply these techniques we need high spatial resolution (to image the lobes) as well as high spatial dynamic range (so that the largest scales are also well mapped). For this method to result in robust measurements, large samples of the order of hundred – thousand sources are required.

4.2 The role of SKA

To illustrate the potential of the SKA1 baseline design (Dewdney et al 2013) in this area we consider the FR II radio sources in the SKADS simulations of the extragalactic sky (Wilman et al. 2008). These simulations are probably not accurate enough to give reliable estimates for the properties of the young source population discussed in Section 3, but should be adequate to consider the well-resolved FR II population. We focus on the FR IIs here since the dynamics and particle content of these 'classical double' sources are (relatively) well understood (Kaiser & Alexander 1997; Celotti 2003). Figure 2 shows the mean 151 MHz surface brightness of all FR IIs in the simulation as a function of source largest angular size; their surface brightness at 5 GHz is expected to be a factor 6 to 30 lower. With 0.05 arcsec beam (SKA1-MID Band 5) we can achieve modest levels of resolution (at least 5 beams across these large-scale sources) for most FR IIs in the simulation, and do a lot better for the bulk of the population. While the μJy sensitivity and

PoS(AASKA14)173

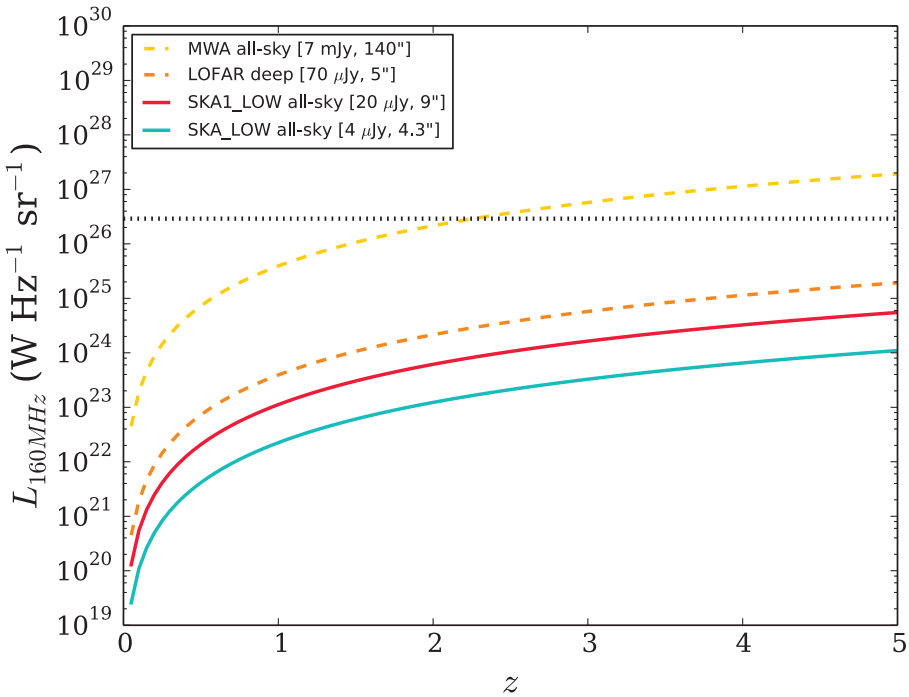

Figure 3: $L-z$ limits of planned SKA1-LOW and SKA-LOW continuum all-sky surveys (solid lines; deep field observations are not feasible, confusion limited). We assume SKA-LOW will reach 90 km baselines (arm-core, 2× SKA1-LOW) and angular resolution of 4.3 arcsec. For comparison, the current SKA-LOW pathfinders and precursors are plotted (dashed lines): the ongoing MWA all-sky survey (7 mJy rms) and deep LOFAR Surveys observations (expected 70μJy rms for Tier 1). The horizontal line (dotted, black) marks the traditional FR I/FR II divide (Fanaroff & Riley 1974) scaled to 160 MHz (assuming $S \propto \nu^{-0.75}$).

exceptional *uv*-coverage of the projected surveys will allow the typical surface brightness of all but the faintest lobes to be imaged. Although at lower resolution, the SKA1-SUR in Band 2 (1.4 GHz) will be also very useful for this application as it will provide us with large, wide-field surveys of FR Is and FR IIs compiled within only 2 years on-sky time (Figure 4); we will still be able to resolve over half a population of these sources.

Good constraints on spectral age require broad-band measurements, ideally including low-frequency observations which would measure the un-aged energy spectrum of the electrons, the so-called injection index, which is known to vary significantly across the source population (Konar & Hardcastle 2013). The reference design for SKA1-LOW (Dewdney et al 2013), with a beam at best a few arcsec, will not resolve the bulk of these sources, complicating the experiment. However, samples constructed from such low-frequency observations would be the base samples in our analyses of the AGN lifecycles and RLFs as they present the best probe of observing radio-loud AGN unbiased by the effects of relativistic beaming and orientation. At MHz frequencies, observations preferentially select jet and lobe emission due to its inherent injection spectral signature (i.e. very steeply rising spectra towards lower radio frequencies). The SKA1-LOW all-sky survey, completable within two years on-sky time, is expected to reach rms noise levels of 20μJy (confusion limited) at angular resolution of $\sim 9''$. This translates to luminosity densities of 5.7×10^{23} W Hz^{-1} at $z = 2$ (Figure 3) allowing us to detect the vast majority of CSS, FR I and FR II sub-

PoS(AASKA14)173

populations out to very high redshifts ($z \sim 4-5$ and beyond), but only at a modest spatial resolution of $20-75$ kpc depending on the redshift.

While the SKA1 reference design (Dewdney et al 2013) will allow many thousands of FR II sources to be imaged to high redshift at high-to-moderate resolution, providing an essential test-bed for this technique, the final stage of the SKA will be necessary to obtain well-resolved low-frequency images; this would require baselines of > 300 km. Such baselines will allow us to resolve ($3-5\times$ beam size of 1.3 arcsec) over half of the population of FR IIs at these low radio frequencies (Figure 2). This would also extend the study to the much fainter, high-redshift FR I population, and thus allow full analysis of the FR dichotomy at all epochs. Ideally, one would like to reach angular resolutions of 0.4 arcsec as this would allow us to resolve almost whole FR II population; this however, would require baselines as long as ~ 1000 km for SKA-LOW.

5. Death, relics and activity re-triggering

5.1 The population of relic radio galaxies

The prominent features of radio sources (core, jets, hotspots) are fed by the continuous supply of energy from the active nucleus; once the jet activity stops, these features will disappear relatively quickly, and the lobe plasma will continue to expand and to cool via synchrotron and inverse-Compton losses, leaving a 'relic' radio galaxy (Cordey 1987). During this fading phase very strong spectral evolution of the source occurs, with the high radio frequency part of the spectrum developing an ultra steep, exponential cut-off, and the spectral break shifting to lower radio frequencies. Although every galaxy must go through this stage, only a handful examples of true dying radio sources is currently known (Parma et al. 2007; Dwarakanath & Kale 2009). Reasons for the rarity of such sources may be their low surface brightness and relatively short time they spend in the fading phase as compared to the average lifetime of a radio source; at GHz frequencies a source will fade away within 10^4-10^5 years, while at MHz frequencies this may take $\sim 10^7$ years. Identification of genuinely dying radio galaxies will give important information about lifetimes and duty cycles of extragalactic radio sources. Fading radio galaxies have also implications for AGN feedback since large amounts of the energy supplied by the jet remains stored in the lobes at the end of the active jet phase, and it remains an open question whether, and on what time and spatial scales, that energy is imparted to the ICM.

As discussed in Section 2.1 the cessation of the jet energy supply seems to happen at any stage of radio source growth, and so we need to be searching for dying radio galaxies at all spatial scales, from pc to Mpc scales. Luminosity densities of lobes of fading radio galaxies are $0.3-40\times10^{23}$ W Hz^{-1} at 1.4 GHz (Parma et al. 2007; Dwarakanath & Kale 2009), while those of low-luminosity CSS sources, a significant number of which is believed to be in fading phase, to reach as low as 2×10^{23} W Hz^{-1} at 1.4 GHz (Kunert-Bajraszewska et al. 2010). With the currently available all-sky surveys (e.g. FIRST, NVSS; Becker, White & Helfand 1995; Condon et al. 1998) we are able to probe only the 'tip of the iceberg' of this population, at relatively low redshifts ($> 6\times10^{23}$ W Hz^{-1} up to $z \sim 0.3$ at 1.4 GHz) assuming the sources are not resolved out.

This is the biggest problem we are presently struggling with – very few instruments can detect such low surface brightness sources, radio structures of which are often spread over multiple

PoS(AASKA14)173

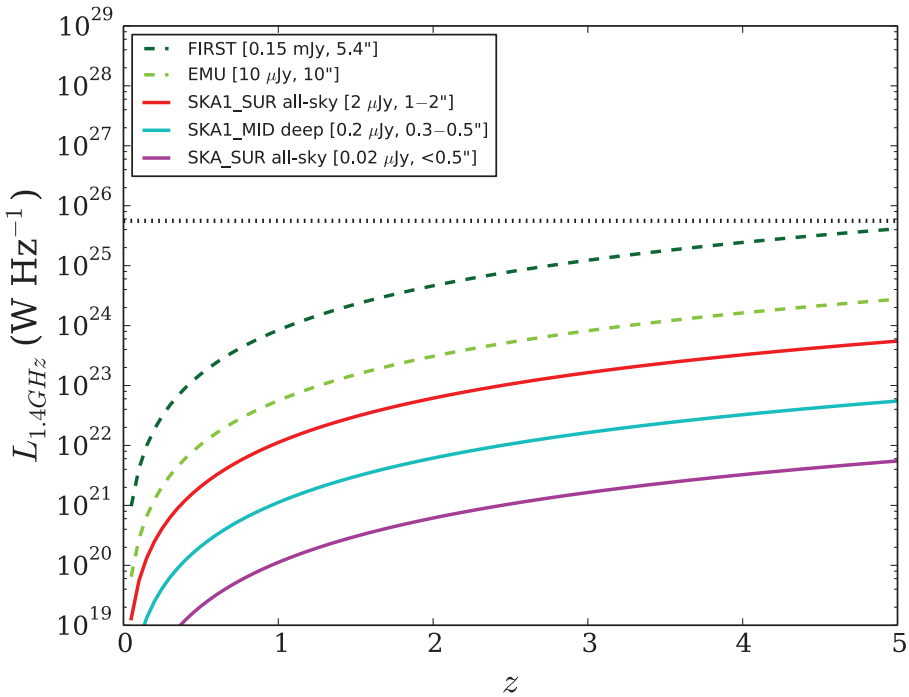

Figure 4: $L-z$ limits of planned SKA1-SUR and SKA1-MID (Band 2) continuum all-sky and deep surveys. We assume SKA-SUR will reach 10× the sensitivity of SKA1-MID. For comparison, the FIRST survey that have been serving us well over the past 20 years (0.15 mJy rms at 1.4 GHz) and the planned ASKAP-EMU all-sky survey (anticipated 10μJy) are plotted (dashed lines). The horizontal line (dotted, black) marks the traditional FR I/FR II divide (Fanaroff & Riley 1974) scaled to 1.4 GHz (assuming $S \propto \nu^{-0.75}$).

telescope's beams. One of the most spectacular recent examples of hidden imprints of previous activity (fading lobes) is 3C 452, which up to now was believed to be a classical FR II radio galaxy (Sirothia, Gopal-Krishna & Wiita 2013). How many radio sources have previous activity signatures hidden in such a way? Clearly, there is a hidden world of secret lives of radio-loud AGN we are just starting to uncover. Presently advances and new discoveries are being already made with the existing and new facilities such as Murchison Wide-field Array (MWA; e.g. Hurley-Walker et al. 2014), Giant Metrewave Radio Telescope (GMRT) and Low Frequency Array (LOFAR).

5.2 What will SKA see?

As an EoR driven instrument, SKA1-LOW will have tremendous surface brightness sensitivity capabilities, and so will be well adapted to searches for large, faint objects with little compact structure, although it may be difficult to identify them with their host galaxies. In principle, the number of large-scale fading radio galaxies should be comparable to the number of 'alive' large-scale FR Is and FR IIs, but the fading radio galaxies will have much steeper spectra and considerably lower radio luminosity density; surface brightness sensitivity is one of the crucial aspects of the new radio telescopes if we want to obtain large samples of this rare class of radio source.

To demonstrate capabilities of the SKA and its precursors, let us assume a fading radio source of an observed luminosity density 6×10^{23} W Hz^{-1} at 160 MHz and 500 kpc total physical size. This luminosity density and physical size can be easily translated to a brightness temperature per

PoS(AASKA14)173

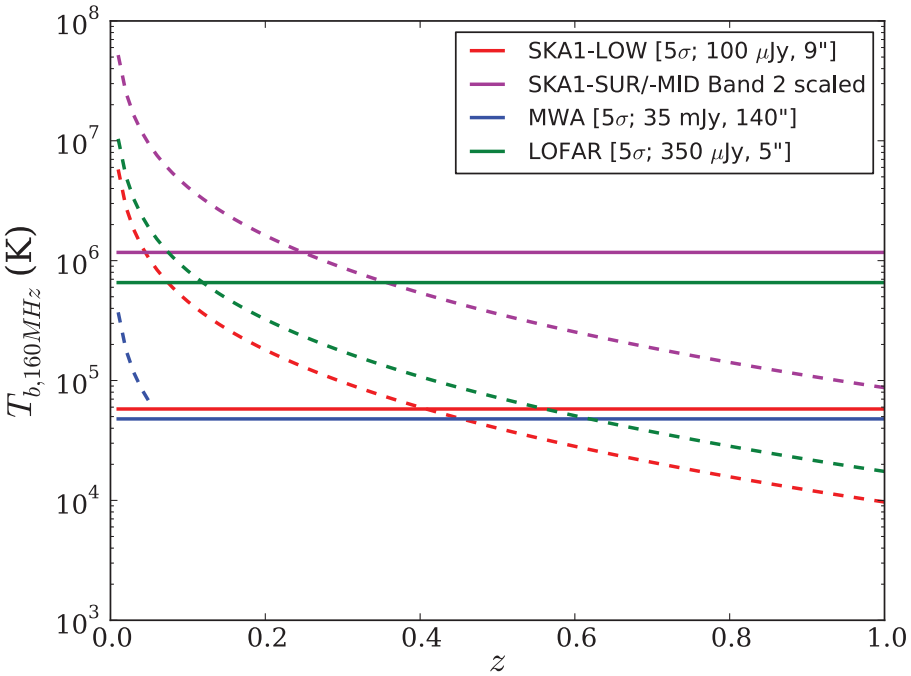

Figure 5: Brightness temperature capabilities of SKA1-LOW and its precursors (MWA, LOFAR) for detecting fading radio source of 500 kpc physical size and total luminosity density 6×10^{23} W Hz^{-1} at 160 MHz. Solid lines indicate the brightness temperature sensitivity of each instrument for a given set of flux density limit and angular resolution; 5σ values are plotted. Dashed lines indicate the observed surface brightness temperature per beam of the assumed source, as a function of z, and are drawn only to a point where the angular size of the source is $> 3\times$ the beam size of the instrument with which we want to detect the source. Both solid and dashed lines of the same colour refer to the same instrument. For a comparison, capabilities of SKA1-SUR/SKA1-MID Band 2 (1.4 GHz) in detecting such a source are plotted; predicted Band 2 all-sky survey sensitivity of 1μJy has been scaled to 160 MHz using an assumed steep spectral index of a fading radio source, $\alpha \sim 1.8$. For discussion see Section 5.2. Note that the surface brightness sensitivity of an instrument depends on both its sensitivity (flux density limit) and angular resolution.

telescope's beam and an angular size once a redshift is assigned. As shown in Figure 5, SKA1-LOW will be invaluable in searches for such radio sources, being able to detect and resolve them (at least with the modest $3\times$ beam size) up to $z \sim 0.4$. Furthermore, we attempted to verify capabilities of higher frequency receivers of SKA for this application. Assuming a steep spectral index of the considered fading radio source, $\alpha \sim 1.8$, its total luminosity density at 1.4 GHz would be 1.3×10^{22} W Hz^{-1} spread over many telescope's beams, but the high sensitivity of SKA1-SUR/-MID will still be able to detect such a source out to $z \sim 0.2$. Those higher frequency receivers will be able to detect less extreme sources at higher redshifts; for instance, a fading radio galaxy of a total luminosity density 6×10^{24} W Hz^{-1} at 1.4 GHz will be detectable out to $z \sim 1.6$, and although SKA1-LOW will detect sources of such luminosity density at 160 MHz $z \sim 2$ and beyond, the former receivers will provide us with much higher resolution. A combination of both arrays may provide us with versatile range of images of dying radio sources.

PoS(AASKA14)173

6. Evolution of the AGN population, radio-loud AGN unification and cosmology

6.1 Duty cycles of radio activity

Duty cycles, the relative times a radio source spends in its active and quiescent phases, is a crucial piece of information in our understanding of AGN lifecycles and their impact on the evolving Universe. To constrain these, we need to establish what causes radio sources to shut off and re-trigger, and whether all radio sources go through the re-triggering phase, or only a fraction of them. We need to construct representative RLFs not only of the radio-loud AGN in the midst of their activity (Sections 3–5), but also of those in quiescence that are composed of the weakly radio-emitting AGN; these samples need to be well defined in terms of black hole accretion levels (e.g. Falcke, Körding & Nagar 2004; Merloni & Heinz 2008).

It remains an open question as to whether there are underlying physical distinctions between the radio-loud/weak-radio AGN populations, or if there exists a continuum of radio activity which extends to the nuclear radio-quiescent galaxies, dominated by active or evolved star formation (see e.g. Broderick & Fender 2011; Kimball et al 2011; Mahony et al. 2012, for recent analyses). The sensitive SKA continuum surveys will, for the first time, provide us with large samples of the largely unexplored weakly radio-emitting AGN ($10^{20} - 10^{22}$ W Hz^{-1} at 1.4 GHz). During the SKA1 stage, with SKA1-SUR/SKA-MID (Band 2) all-sky surveys we will be able to detect the weak-radio AGN population down to luminosity densities of 5×10^{21} W Hz^{-1} (5σ detection) at $z = 0.5$. With deep SKA1-SUR/SKA1-MID (Band 2) and SKA1-MID (Band 5) surveys we will go much deeper reaching 1×10^{21} W Hz^{-1} at $z = 0.5$ and 4×10^{19} W Hz^{-1} in the local Universe ($z \sim 0.1$). SKA1-MID Band 5 receivers will also allow us to resolve these sources on linear scales of 0.3 kpc at $z \sim 0.5$. For detailed discussion on the physics of the weak-radio AGN and observations during the SKA era see Orienti et al. (2015).

6.2 Radio-loud AGN unification

The deep SKA surveys will sample all radio-loud AGN populations (Section 1) with a subset of these being resolved in suitable detail to model their detailed internal physical processes. However, another view of the radio-loud AGN lifecycles is to view them in terms of populations that manifest themselves as quasars, radio galaxies, and blazars, depending on their orientation on the sky. Clearly, the detailed studies of these sources as described in this paper will improve our view of the radio-loud AGN populations and provide direct tests of simple unification models which extrapolate sparse RLF information with evolutionary scenarios to fit deep source count data (e.g. Owen, Ledlow & Keel 1996; Wall & Jackson 1997; Jackson & Wall 1999). As discussed in Section 2.2 we model AGN lifecycles assuming that FR Is and FR IIs are physically distinct classes of radio source. This view is supported by simple unified models for radio-loud AGN where the FR I and FR II populations are the 'parent' populations of many other observed classes of sources (e.g. Urry & Padovani 1995; Jackson & Wall 1999). In adopting these unified models, we can probe both the gross evolution of these populations and disentangle the effects of the AGN lifecycle, as well as map the contribution from weakly radio-emitting AGN and SF sources at least up to $z \sim 0.5$. Angular resolutions of the order of arcsec are sufficient for these studies (e.g. McAlpine, Jarvis & Bonfield 2013).

PoS(AASKA14)173

Whilst testing the radio-loud AGN unification models we will obtain a simplified method to map the evolution of the radio-loud AGN population by exploiting the deep source counts, radio luminosity functions and populations under test. These analyses are best done from samples and source counts at low frequencies (<800 MHz); at these frequencies the sources are dominantly steep-spectrum and uncontaminated by relativistic beaming effects. For instance, following the methodology of e.g. Jackson & Wall (1999) or McAlpine, Jarvis & Bonfield (2013) we will be able to determine the evolution scenarios that fit best to the observed complete samples. These analyses may be used to provide insight into AGN duty cycles (Section 6.1), and the prevalence of certain types of sources such as GPS/CSS and dying radio galaxies. Using a range of deep counts at a range of observed frequencies (100 MHz – few GHz) we can test evolutionary and lifecycle scenarios as well as explore the radio-loud / radio-quiet AGN divide.

6.3 The SKA era precision cosmology

One of the important aspects of the science described here is that we will identify different populations of AGN, and as presented in Ferramacho et al. (2014) who showed that if one can separate out the various populations, which in turn sample the underlying dark-matter density distribution with a different bias, then the effects of cosmic variance may be overcome in determining the angular power spectrum. This is critical for studying the Universe on the largest scale (Camera et al. 2015). Powerful radio-loud AGN, provide a unique sampling of the underlying dark matter distribution as they are, generally, the most highly biased tracers of the density field, and are detected up to the highest redshifts ($z \sim 6$). Therefore, when combined with less biased tracers, e.g. star-forming galaxies (Jarvis et al. 2015), they may provide a unique way to understand the largest scales in the Universe, given that the ability to overcome the cosmic variance is dependent on the difference between the bias of the two populations under consideration. The key issue here is to separate AGN from star-forming galaxies, and the high-resolution of SKA1-MID can enable the separation of AGN and star-forming galaxies on either morphology for jet sources ($\gtrsim 0.5$ arcsec) or through pure brightness temperature measurements. Furthermore, knowledge of the $N(z)$ is also crucial and the detailed follow-up that would be carried out for this science case, in particular obtaining redshifts, will also be valuable for cosmological science.

7. Concluding remarks

A combination of the SKA arrays and their receivers at a wide range of frequencies and angular resolutions are necessary to address the science case discussed in this chapter. In particular, the SKA1-LOW array with its 300 MHz bandwidth, which we assumed here to be centered on 160 MHz, is an indispensable tool for searching for old, dying radio sources, and for the construction of complete, flux density and volume limited samples of radio-loud AGN unbiased by the effects of relativistic beaming. SKA1-SUR and SKA1-MID Band 2 (centered on 1.4 GHz, with 800 MHz bandwidth) will provide us with deep, wide-field surveys at a reasonable resolution of $1-2$ arcsec. This will allow for morphological identification of large radio-loud AGN samples, as well as it will provide us with large weak-radio AGN samples in the local Universe. SKA1-MID Band 2, with angular resolution $3-5\times$ better ($0.3-0.5$ arcsec), can be used as a follow up for a number of deep fields. Finally, SKA1-MID with its Band 4 and Band 5 (centered on 4 GHz and

PoS(AASKA14)173

9.2 GHz, with 2.4 GHz and 2×2.5 GHz bandwidths respectively) is particularly useful for high resolution (0.05 arcsec) imaging of jets and lobes of both young and evolved radio galaxies for detailed physics analyses. It will be also useful for distinguishing sources within our radio samples that are truly relativistically beamed. The SKA-VLBI facility, if incorporated from the beginning of the telescope operations, will be invaluable for detailed physics investigations of most of radio-loud AGN.

A combination of these SKA arrays and frequency bands will provide us with broad-band radio spectra of the sources – this is crucial for selecting certain types of radio source; e.g. GPS sources are distinguished by their turn-over spectra, while dying radio galaxies are extreme steep spectrum sources ($\alpha > 1.8$). Furthermore, such broad-band spectra will allow for spectral age estimates of the radio sources so important for the radio-loud AGN physics and lifecycle studies.

With such rich data sets we will be able to not only to investigate radio-loud AGN and their engine and model radio source detailed physics, but also to trace the AGN activity (triggering and feedback) up to the high-z Universe and advance the galaxy formation and evolution models. Progress in these crucial science areas is currently hindered by the lack of wide-field, deep radio-loud AGN samples that extend to high-z, and so is limited only to the local Universe.

Advances are now being made with the SKA pathfinders and precursors, such as MWA, LOFAR, MeerKAT and ASKAP. SKA1 will be much faster than any of these precursors and pathfinders, completing all-sky surveys (3π sr) within only 2 years on-sky time. It is, however, the full SKA that may revolutionise our understanding of the radio-loud AGN lifecycles and physics, by reaching the unexplored flux density depths of the radio sky.

Acknowledgements

ADK acknowledges financial support from the Australian Research Council Centre of Excellence for All-sky Astrophysics (CAASTRO), through project number CE110001020. CAJ is a West Australian Premier's Fellow and acknowledges support from the WA Government Department of Premier and Cabinet and from the Curtin University. TA acknowledges financial support from the China Ministry of Science and Technology (grant no. 2013CB837900). The authors thank the referee for detailed comments on the manuscript which improved completeness of this chapter.

References

Agudo I. et al., 2015, 'Studies of Relativistic Jets in Active Galactic Nuclei with SKA', in proceedings of 'Advancing Astrophysics with the Square Kilometre Array', PoS(AASKA14)093

Alexander P., 2000, MNRAS, 319, 8

Alexander P., 2006, MNRAS, 368, 1404

An T., & Baan W. A., 2012, ApJ, 760, 77

An T., Hong, X. Y., Hardcastle M. J., et al., 2010, MNRAS, 402, 87

Antognini J., Bird J., Martini P., 2012 ApJ, 756, 116

Antoniadis J. et al., 2015, 'Multi-wavelength, Multi-Messenger Pulsar Science in the SKA Era', in proceedings of 'Advancing Astrophysics with the Square Kilometre Array', PoS(AASKA14)157

PoS(AASKA14)173

Bacon D. et al., 2015, 'Large Synoptic Survey Telescope synergy with the Square Kilometre Array', in proceedings of 'Advancing Astrophysics with the Square Kilometre Array', PoS(AASKA14)145
Barthel P. D., 1989, ApJ, 336, 606
Barthel P. D., & Arnaud K. A., 1996, MNRAS, 283, L45
Baum S. A., O'Dea C. P., Murphy D. W., & de Bruyn A. G., 1990, A&A, 232, 19
Becker R. H., White R. L., & Helfand D. J., 1995, ApJ, 450, 559
Best P. N., Ker L. M., Simpson C., Rigby E. E., & Sabater, J., 2014, MNRAS, 445, 955
Best P. N., & Heckman T. M., 2012, MNRAS, 421, 1569
Bîrzan L., Rafferty D. A., McNamara B. R., Wise M. W., & Nulsen P. E. J., 2004, ApJ, 607, 800
Blake G. M., 1970, ApL, 6, 201
Blandford R. D., & Rees M. J., 1974, MNRAS, 169, 395
Blundell K. M., Rawlings S., & Willott C. J., 1999, AJ, 117, 677
Bower R. G., Benson A. J., Malbon R., et al., 2006, MNRAS, 370, 645
Brocksopp C., Kaiser C. R., Schoenmakers A. P., & de Bruyn A. G., 2007, MNRAS, 382, 1019
Brocksopp C., Kaiser C. R., Schoenmakers A. P., & de Bruyn A. G., 2011, MNRAS, 410, 484
Broderick J. W., & Fender R. P., 2011, MNRAS, 417, 184
Callingham J., Gaensler B., Ekers R., et al., 2015, *to be submitted*
Camera S. et al., 2015, 'Cosmology on the largest scales with the SKA', in proceedings of 'Advancing Astrophysics with the Square Kilometre Array', PoS(AASKA14)025
Carvalho J. C., 1985, MNRAS, 215, 463
Cattaneo A., Faber S. M., Binney J., et al, 2009, Nature, 460, 213
Cavagnolo K. W., McNamara B. R., Nulsen P. E. J., et al., 2010, ApJ, 720, 1066
Celotti A., 2003, NewAR, 47, 525
Condon J. J., Cotton W. D., Greisen E. W., et al., 1998, AJ, 115, 1693
Cordey R. A., 1987, MNRAS, 227, 695
Croston J. H., Kraft R. P., & Hardcastle M. J., 2007, ApJ, 660, 191
Croston J. H., Kraft R. P., Hardcastle M. J., et al., 2009, MNRAS, 395, 1999
Croton D. J., Springel. V., White S. D. M., et al., 2006, MNRAS, 365, 11
Johnston-Hollitt., M. et al., 2015, 'Using Tailed Radio Galaxies to Probe the Environment and Magnetic Field of Galaxy Clusters in the SKA Era', in proceedings of 'Advancing Astrophysics with the Square Kilometre Array', PoS(AASKA14)101
Dewdney P., Turner W., Millenaar R., et al., 2013, 'SKA1 System Baseline Design', Document no. SKA-TEL-SK0-DD-001 Revision 1
Donoso E., Best P. N., & Kauffmann G., 2009, MNRAS, 392, 617
Dunlop J. S. & Peacock J. A., 1990, MNRAS, 247, 19
Dwarakanath K. S., & Kale R., 2009, ApJL, 698, L163
Falcke H., Körding E., & Nagar N. M., 2004, NewAR, 48, 1157
Fanaroff B. L., & Riley J. M., 1974, MNRAS, 167, 31P
Fanti R., Fanti C., Schilizzi R. T., et al., 1990, A&A, 231, 333
Ferramacho L. D., Santos M. G., Jarvis M. J., & Camera S., 2014, MNRAS, 442, 2511
Godfrey L. E. H., & Shabala S. S., 2013, ApJ, 767, 12
Gopal-Krishna, & Wiita P. J., 2000, A&A, 363, 507

PoS(AASKA14)173

Hardcastle M. J., Evans D. A., & Croston J. H., 2006, MNRAS, 370, 1893
Hardcastle M. J., & Krause M. G. H., 2013, MNRAS, 430, 174
Hardcastle M. J., & Krause M. G. H., 2014, MNRAS, 443, 1482
Hardcastle M. J., Massaro F., Harris D. E., et al, 2012, MNRAS, 424, 1774
Harwood J. J., Hardcastle M. J., Croston J. H., & Goodger J. L., 2013, MNRAS, 435, 3353
Heesen V., Croston J. H., Harwood J. J., Hardcastle M. J., & Hota A., 2014, MNRAS, 439, 1364
Hurley-Walker N., Jonhston-Hollitt M., Ekers R., et al., 2015, MNRAS, *accepted*, arXiv:1412:3856
Ineson J., Croston J. H., Hardcastle M. J., et al., 2013, ApJ, 770, 136
Jackson C. A., & Wall J. V., 1999, MNRAS, 304, 160
Jamrozy M., Konar C., Machalski J., & Saikia D. J., 2008, MNRAS, 385, 1286
Jarvis M. et al., 2015, 'The star-formation history of the Universe with the SKA', in proceedings of 'Advancing Astrophysics with the Square Kilometre Array', PoS(AASKA14)068
Janssen R. M. J., Röttgering H. J. A., Best P. N., & Brinchmann, J., 2012, A&A, 541, 62
Kaiser C. R., & Alexander P., 1997, MNRAS, 286, 215
Kaiser C. R., & Cotter G., 2002, MNRAS, 336, 649
Kaiser C. R., Dennett-Thorpe J., & Alexander P., 1997, MNRAS, 292, 723
Kaiser C. R., Schoenmakers A. P., & Röttgering H. J. A., 2000, MNRAS, 315, 381
Kapińska A. D., Andernach H., Banfield J., et al., 2015, 'Radio Galaxy Zoo: Hybrid morphology radio galaxies', *to be submitted*
Kapińska A. D., & Uttley P., 2013, AN, 334, 408
Kapińska A. D., Uttley P., & Kaiser C. R., 2012, MNRAS, 424, 2028
Karouzos M., Jarvis M. J., & Bonfield D., 2014, MNRAS, 439, 861
Kaviraj S., Shabala S. S., Deller A. T., & Middelberg E., 2014, *submitted*, arXiv:1411.2028
Kimball A. E., Kellermann K. I., Condon J. J., Ivezic Z., & Perley R. A., 2011, ApJ, 739, 29
King I., 1962, AJ, 67, 471
Kitching T. et al., 2015, 'Euclid-SKA Synergies', in proceedings of 'Advancing Astrophysics with the Square Kilometre Array', PoS(AASKA14)146
Komberg B. V., & Pashchenko I. N., 2009, Astronomy Reports, 53, 1086
Komissarov S. S., & Gubanov A. G., 1994, A&A, 285, 27
Konar C., & Hardcastle M. J., 2013, MNRAS, 436, 1595
Kunert-Bajraszewska M., Gawroński M. P., Labiano A., & Siemiginowska A., 2010, MNRAS, 408, 2261
Kunert-Bajraszewska M., Marecki A., & Spencer R. E., 2004, in European VLBI Network on New Developments in VLBI Science and Technology, Bachiller R., Colomer F., Desmurs J.-F., de Vicente P., eds., pp. 73–76
Kuźmicz A., & Jamrozy M., 2013, Advances in Astronomy and Space Physics, 3, 42
Laing R. A., 2015, 'Kinematics and Dynamics of kiloparsec-scale Jets in Radio Galaxies with SKA', in proceedings of 'Advancing Astrophysics with the Square Kilometre Array', PoS(AASKA14)107
Laing R. A., Canvin J. R., & Bridle A. H., 2003, NewAR, 47, 577
Luo Q., & Sadler E. M., 2010, ApJ, 713, 398
Maccagni F. M., Morganti R., Oosterloo T. A., & Mahony E. K., 2014, A&A, 571, 67
Machalski J., & Jamrozy M., 2006, A&A, 454, 95

PoS(AASKA14)173

Maciel T., & Alexander P., 2014, MNRAS, 442, 3469
Mahony E. K., Sadler E. M., Croom S. M., et al., 2012, ApJ, 754, 12
Marecki A., Spencer R. E., & Kunert M., 2003, PASA, 20, 46
Mauch T., & Sadler E. M., 2007, MNRAS, 375, 931
McAlpine K., Jarvis M. J., & Bonfield D. G., 2013, MNRAS, 436, 1084
McAlpine K. et al., 2015, 'The SKA view of the Interplay between SF and AGN Activity, and its role in Galaxy Evolution', in proceedings of 'Advancing Astrophysics with the Square Kilometre Array', PoS(AASKA14)083
McNamara B. R., & Nulsen P. E. J., 2007, ARA&A, 45, 117
McNamara B. R., & Nulsen P. E. J., 2012, New Journal of Physics, 14, 055023
Merloni A., & Heinz S., 2008, MNRAS, 388, 1011
Mingo B., Hardcastle M. J., Croston J. H., et al., 2012, ApJ, 758, 95
Murgia M., Fanti C., Fanti R., et al., 1999, A&A, 345, 769
O'Dea C. P., 1998, PASP, 110, 493
O'Dea C. P., Baum S. A., & Stanghellini C., 1991, ApJ, 380, 66
Orienti M., D'Ammando F., Giroletti M., Giovannini G., & Panessa F., 2015, 'The physics of the radio emission in the quiet side of the AGN population with the SKA', in proceedings of 'Advancing Astrophysics with the Square Kilometre Array', PoS(AASKA14)087
Owen F. N., Ledlow M. J., & Keel W. C., 1996, AJ, 111, 53
Owsianik I., & Conway J. E., 1998, A&A, 337, 69
Parma P., Murgia M., de Ruiter H. R., et al., 2007, A&A, 470, 875
Peacock J. A., & Wall J. V., 1982, MNRAS, 198, 843
Perucho M., & Martí J. M., 2007, MNRAS, 382, 526
Perucho M., Martí J. M., Laing R. A., & Hardee P. E., 2014, MNRAS, 441, 1488
Phillips R. B., & Mutel R. L., 1982, A&A, 106, 21
Planck Collaboration et al., 2013, arXiv:1303.5076
Polatidis A. G., & Conway J. E., 2003, PASA, 20, 69
Rawlings S., & Saunders R., 1991, Nature, 349, 138
Readhead A. C. S., 1995, Proceedings of the National Academy of Science, 92, 11447
Readhead A. C. S., Taylor G. B., Pearson T. J., & Wilkinson P. N., 1996, ApJ, 460, 634
Reynolds C. S., & Begelman M. C., 1997, ApJL, 487, L135
Rigby E. E., Best P. N., Brookes M. H., et al., 2011, MNRAS, 416, 1900
Sadler E. M., Cannon R. D., Mauch T., et al., 2007, MNRAS, 381, 211
Saikia D. J., & Jamrozy M., 2009, Bull. Astr. Soc. India, 37, 63
Saripalli L., 2012, AJ, 144, 85
Scheuer P. A. G., 1974, MNRAS, 166, 513
Schoenmakers A. P., de Bruyn A. G., Röttgering H. J. A., et al., 2000, MNRAS, 315, 371
Shabala S. S., Ash S., Alexander P., & Riley J. M., 2008, MNRAS, 388, 625
Shabala S. S., & Alexander P., 2009, ApJ, 699, 525
Shabala S. S., Kaviraj S., & Silk J., 2011, MNRAS, 413, 2815
Simpson C., Rawlings S., Ivison R., et al., 2012, MNRAS, 421, 3060
Sirothia S. K., Gopal-Krishna, & Wiita P. J., 2013, ApJL, 765, L11
Snellen I. A. G., Schilizzi R. T., Miley G. K., et al., 1999, NewAR, 43, 675

PoS(AASKA14)173

Snellen I. A. G., Schilizzi R. T., Miley G. K., et al., 2000, MNRAS, 319, 445
Snellen I. A. G., Schilizzi R. T., & van Langevelde H. J., 2000, MNRAS, 319, 429
Stanghellini C., Baum S. A., O'Dea C. P., & Morris G. B., 1990, A&A, 233, 379
Tschager W., Schilizzi R. T., Röttgering H. J. A., et al., 2003, A&A, 402, 171
Turner R., & Shabala S. S., 2015, MNRAS, *submitted*
Urry, C. M., & Padovani P., 1995, PASP, 107, 803
van Breugel W., Miley G., & Heckman T., 1984, AJ, 89, 5
Wall J. V., 1994, Australian Journal of Physics, 47, 625
Wall J. V., & Jackson C. A., 1997, MNRAS, 290, L17
Wan L., Daly R. A., & Guerra E. J., 2000, ApJ, 544, 671
Wang Y., Knigge C., Croston J. H., & Pavlovski G., 2011, MNRAS, 418, 1138
Wilkinson P. N., Polatidis A. G., Readhead A. C. S., Xu W., & Pearson T. J., 1994, ApJL, 432, L87
Willott C. J., Rawlings S., Blundell K. M., & Lacy M., 1999, MNRAS, 309, 1017
Wilman R. J., Miller L., Jarvis M. J., et al., 2008, MNRAS, 388, 1335

PoS(AASKA14)173

Cosmology

PROCEEDINGS OF SCIENCE

Overview of Cosmology with the SKA

Roy Maartens[*1,2], **Filipe B. Abdalla**[3,4], **Matt Jarvis**[5,1], **Mario G. Santos**[1,6] – **on behalf of the SKA Cosmology SWG**

[1] *Department of Physics, University of Western Cape, Cape Town 7535, South Africa*
[2] *Institute of Cosmology & Gravitation, University of Portsmouth, Portsmouth PO1 3FX, UK*
[3] *Department of Physics & Astronomy, University College London, London WC1E 6BT, UK*
[4] *Department of Physics & Electronics, Rhodes University, Grahamstown 6140, South Africa*
[5] *Astrophysics, University of Oxford, Oxford OX1 3RH, UK*
[6] *SKA South Africa, The Park, Park Road, Cape Town 7405, South Africa*

E-mail: roy.maartens@gmail.com

The new frontier of cosmology will be led by three-dimensional surveys of the large-scale structure of the Universe. Based on its all-sky surveys and redshift depth, the SKA is destined to revolutionize cosmology, in combination with future optical/ infrared surveys such as Euclid and LSST. Furthermore, we will not have to wait for the full deployment of the SKA in order to see transformational science. In the first phase of deployment (SKA1), all-sky HI intensity mapping surveys and all-sky continuum surveys are forecast to be at the forefront on the major questions of cosmology. We give a broad overview of the major contributions predicted for the SKA. The SKA will not only deliver precision cosmology – it will also probe the foundations of the standard model and open the door to new discoveries on large-scale features of the Universe.

Advancing Astrophysics with the Square Kilometre Array
June 8-13, 2014
Giardini Naxos, Italy

[*] Speaker.

PoS(AASKA14)016

1. SKA cosmology – a new paradigm

It has often been assumed in the past that the SKA would only be competitive in cosmology when the 'billion galaxy survey' was completed – i.e., when the full SKA (SKA2) was constructed. Only SKA2 can deliver the capacity for a spectroscopic survey of ~ 1 billion HI galaxies.

Recently this view has been overturned. The billion galaxy survey will indeed be a game-changer in cosmology, in some senses the ultimate spectroscopic survey. However, well before this stage is reached, SKA1 will be able to deliver competitive and transformational cosmology. The main development that makes this possible is based on innovative ideas for deploying a new type of cosmological galaxy survey (Santos et al. 2015):

- All-sky neutral hydrogen (HI) intensity mapping surveys that do not detect individual galaxies but only the integrated HI emission of galaxies in each pixel, together with very accurate redshifts at each tomographic slice.

In addition, it has been recently realised that the radio continuum offers a novel probe of large-scale structure (Jarvis et al. 2015):

- All-sky radio continuum surveys that detect radio galaxies through their total emission out to very high redshift.

Together with the 'standard' HI galaxy redshift surveys, these radio surveys on SKA1 and then SKA2 are destined to revolutionize cosmology. As an illustration of this, Fig. 1 shows forecasts for errors on measurements of the radial and transverse baryon acoustic oscillation (BAO) feature. In SKA1, the HI intensity mapping surveys outperform the HI galaxy redshift survey – and also current-generation optical galaxy surveys. The power of the HI galaxy survey in SKA2 is also evident.

This chapter is a brief overview of the three chapters which review the science that the SKA can achive via three types of cosmological survey:

- HI galaxy redshift surveys (Abdalla et al. 2015)
- HI intensity mapping surveys (Santos et al. 2015)
- Radio continuum surveys (Jarvis et al. 2015).

These three review chapters highlight the main results in sixteen further chapters, which focus on specific science goals and techniques. The three review chapters also discuss the main technical challenges, which will not be covered here.

Recently, a re-baselining of the SKA phase 1 was decided, in order to fit the planned budget. This includes the reduction of the SKA1-MID number of dishes to 70% of what was originally planned (e.g. 133 dishes instead of 190) and deferral of SKA1-SUR. Overall, no major impact from this re-baselining is expected for the cosmology science cases with SKA1. In particular, deferral of SKA1-SUR should be accommodated by the fact that all proposed cosmology surveys should be doable with SKA1-MID. The cut in the number of SKA1-MID dishes will reduce the telescope sensitivity by about 20% (when including MeerKAT dishes). Note however, that improvements in

PoS(AASKA14)016

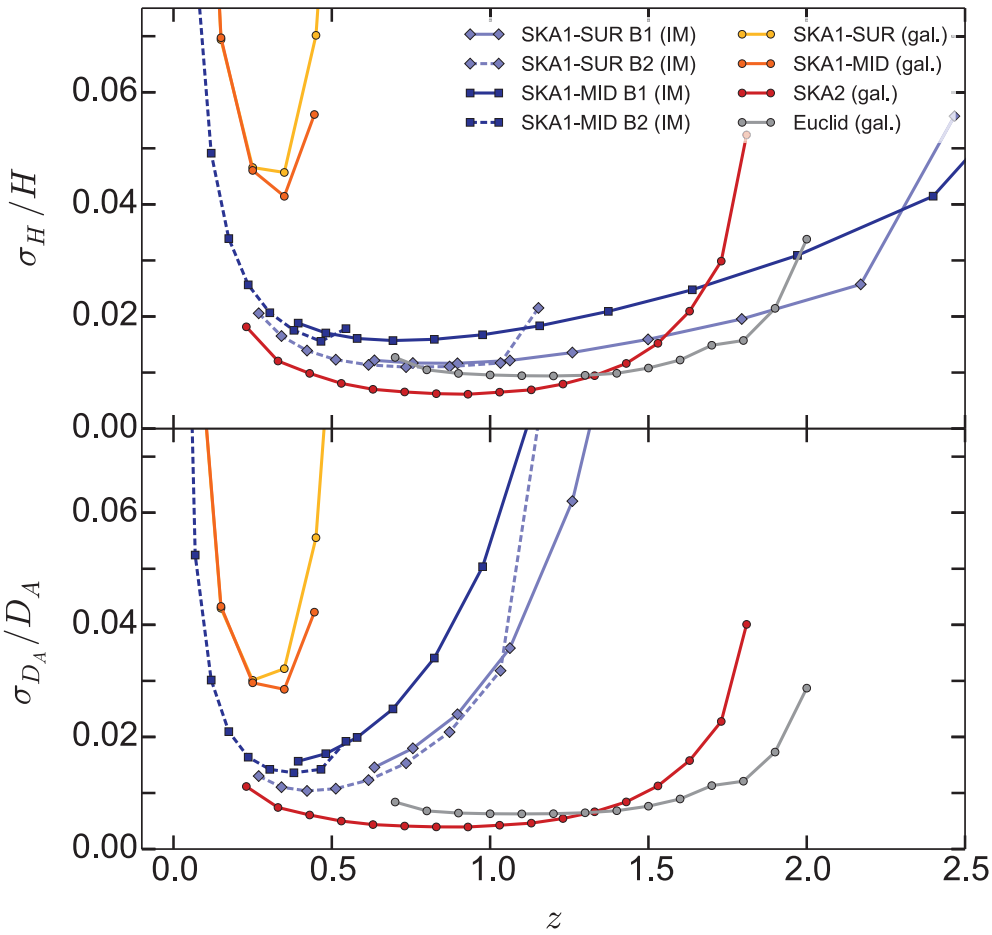

Figure 1: Error on the Hubble rate and angular diameter distance from radial and transverse BAO measurements, showing performance of SKA HI surveys – intensity mapping (IM) and galaxy redshift surveys (gal). Euclid spectroscopic survey shown for comparison. (Bull et al. 2015)

the receiver sensitivity could very well compensate for this reduction (besides the obvious option of increasing the survey time). Even if this cut indeed propagates to the final survey sensitivity, the main science cases will not be affected since they aim to probe very large scales, were cosmic variance is dominating. We can see this for instance in Fig. 3, where a curve with 50% of SKA1-MID can be compared to the full SKA1-MID or SUR. The effect on smaller scales (e.g. BAO measurements) will be more relevant, although it should not affect the main conclusions. Also, we have always included a 80% efficiency factor in our analysis, so any improvement on this efficiency could again compensate the cut. Given the expected small impact on the "cosmology science" and the overall uncertainty in efficiency parameters, we decided to keep the SKA Cosmology Chapters unchanged, since they already include a description of the science achieved with SKA1-MID and even consider a range of sensitivities.

PoS(AASKA14)016

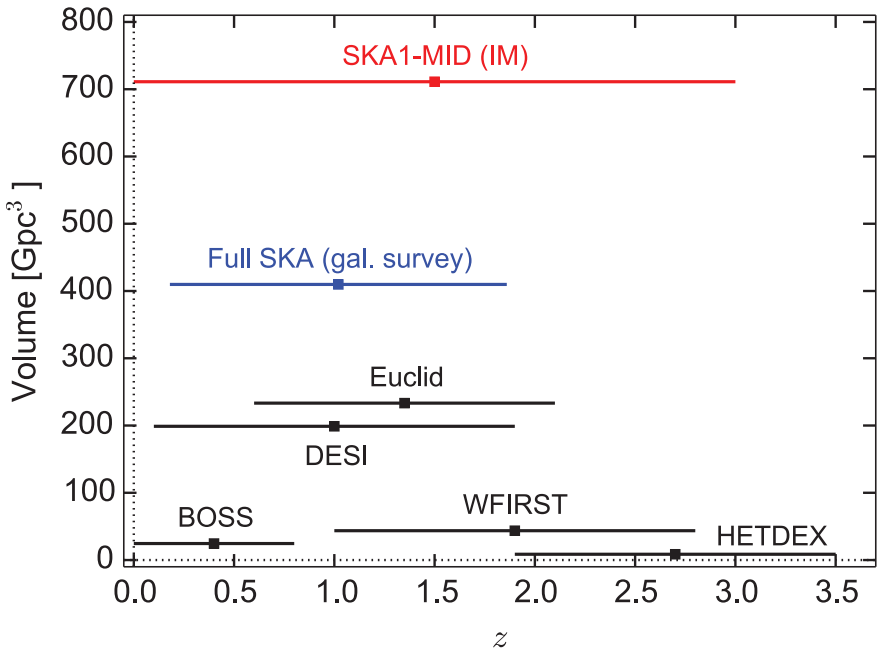

Figure 2: Survey volumes (at the midpoint of the redshift range) for various current and future surveys. (Santos et al. 2015)

2. The new frontier in cosmology

Modern cosmology rests on the twin pillars of cosmic microwave background (CMB) surveys and surveys of the large-scale structure (LSS) of the Universe, supplemented by distance measures from type Ia supernovae (SNIa). The CMB currently delivers the tightest constraints on the primordial Universe, since most of the information in CMB temperature and polarization anisotropies relates to the epoch of matter-radiation decoupling, $z \sim 1000$.

There are CMB constraints on the low redshift Universe, principally via the lensing of the CMB by large-scale structure. The CMB can also contribute through cross-correlation with large-scale structure data, in the form of the integrated Sachs-Wolfe effect. However, the main probe of the low-redshift Universe – and especially of the critical question of the late-time acceleration of the Universe – is the large-scale distribution of matter (together with SNIa surveys). Galaxy surveys have not reached the levels of precision of the CMB. But major advances have been made, especially in measurements of the BAO scale.

A new frontier of precision cosmology is emerging – three-dimensional surveys of the LSS in the Universe. Current galaxy surveys do not yet cover both a wide area of sky and a significant redshift depth. This is what is needed for a high enough volume – and thus a high enough number of modes – for next-generation precision cosmology. But future planned surveys, like Euclid, LSST and especially the SKA, will achieve both of these features. These LSS surveys will open up the new frontier of cosmology that can deliver precision at and beyond CMB levels. Indeed, the largest LSS surveys will be somewhat like performing the CMB survey over a range of redshifts.

The SKA will carry out higher volume surveys than ever before of the LSS of the Universe

PoS(AASKA14)016

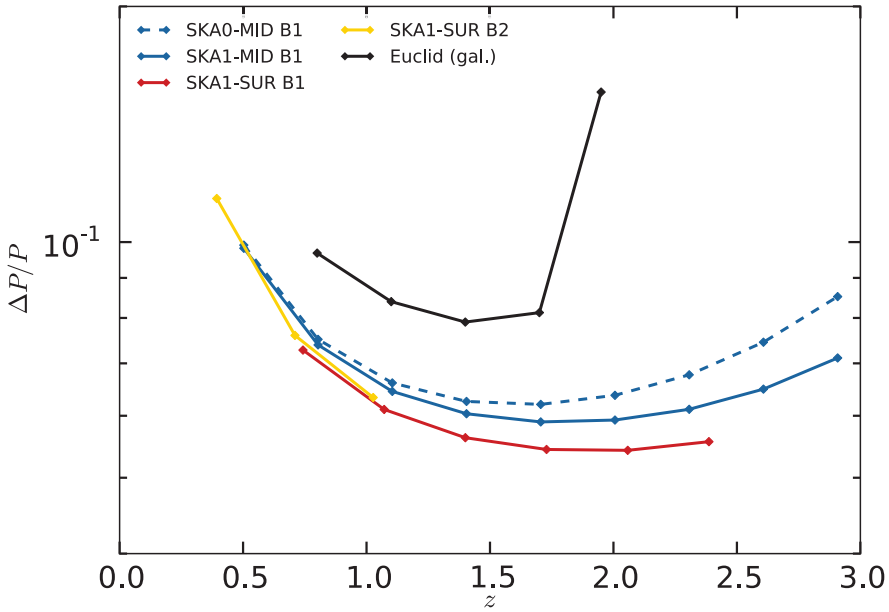

Figure 3: Errors on the power spectrum at very large scales, $k = 0.01h\,\mathrm{Mpc}^{-1}$, achievable with SKA1 HI intensity mapping. SKA0-MID denotes early science on MID at $\sim 50\%$ of the SKA1 specification. Euclid spectroscopic survey is also shown for comparison. (Santos et al. 2015)

(see Fig. 2). This will already be achieved in SKA1, with the HI intensity mapping surveys. With SKA2, the HI galaxy redshift survey will be the biggest ever spectroscopic galaxy survey. In more detail:

- HI intensity mapping surveys on SKA-MID and/ or SKA-SUR: $\sim$30,000 deg^2 out to $z \sim 3$ in SKA1. Even though individual galaxies are not detected, the resolution is more than adequate to measure the fluctuations needed for BAO and other large-scale features (such as primordial non-Gaussianity). Figures 2 and 3 show the enormous potential of these surveys for ultra-large-scale cosmology in SKA1.

- Radio continuum surveys on SKA-MID: $\sim$30,000 deg^2 out to $z \sim 6$, detecting $\sim 10^8$ galaxies in SKA1 and $\sim 10^9$ in SKA2. Although these are strictly two-dimensional surveys, they can be made partly three-dimensional by using redshift information from HI surveys or optical surveys. In addition, we can separate radio galaxy populations, leading to powerful applications of the multi-tracer technique.

- HI galaxy redshift surveys on SKA-MID and/ or SKA-SUR: $\sim$5,000 deg^2 out to $z \sim 0.7$, detecting $\sim 10^7$ galaxies (SKA1) and $\sim$30,000 deg^2 out to $z \sim 2$, detecting $\sim 10^9$ galaxies (SKA2 – the billion galaxy survey).

- Weak lensing surveys based on measuring the shapes of galaxies, starting with a $\sim$5,000 deg^2 survey on SKA1-MID and building up to a $\sim$30,000 deg^2 survey in SKA2. In SKA1, the lensing of the HI intensity mapping signal should also be detected (analogous to the detection by Planck of CMB lensing).

PoS(AASKA14)016

It is also possible to do some cosmology with SKA-LOW (see Pritchard et al. (2015); Santos et al. (2015)).

3. Precision and discovery

We often hear about the era of precision cosmology, in which observations are increasingly accurately tying down the handful of parameters that describe the standard 'concordance' model, i.e. a spatially flat Friedmann model with cold dark matter (CDM) and dark energy in the form of vacuum energy (the cosmological constant Λ). The CMB and the evolution of large-scale structure are described by perturbations of the background model, and the origin of these perturbations is usually taken to be primordial inflation, driven by a simple single-field inflaton.

The concordance model has been extremely successful – able to encompass a huge range of features and scales within in a single simple framework. It also has strong predictive power because of this simplicity. And so indeed a major part of cosmology is justifiably concerned with the precision determination of the parameters of the concordance model. The WMAP and Planck CMB surveys and the leading galaxy surveys, from 2dFGRS to WiggleZ, SDSS-III and DES, have laid the foundations for precision cosmology. The SKA is designed to make a significant contribution to precision cosmology, based on the statistical power delivered by ultra-large volumes.

But there is more to cosmology than precision. Firstly, there are unresolved issues affecting the concordance model, the most important of which concerns the nature of dark energy. There is no satisfactory explanation for dark energy (in the form of the vacuum or otherwise) from fundamental physics, and we are reduced to testing various phenomenological models. Secondly, no model in physics is ever complete. No matter how good the model and the theory are, both will inevitably be replaced as new data and theoretical inconsistencies come to light. So we need to understand precision in a relative, and not absolute, sense. In fact, we have to go further – physics involves also the testing of models with the aim of overturning them.

The limits of precision cosmology are also the beginnings of 'discovery cosmology'. We cannot predict what new discoveries will emerge, but we need to orient towards the unexpected. We should not plan all of our observational tests in the framework of our current understanding of the concordance model, but rather allow for the possibility that new effects and new physics may be involved. One way to promote this is to devise and implement tests of fundamental features of the concordance model, in addition to the more routine tasks of measuring standard parameters.

4. Key science goals and SKA forecasts

Cosmology requires LSS surveys that can accurately probe (a) the expansion history and geometry of the Universe, and (b) the growth of structure. The first are measured via the 'standard ruler' imprinted in the correlation function by the BAO, with comoving scale $\sim 100h^{-1}$ Mpc. The growth of structure is described by the power spectrum of the observed density (or HI brightness temperature) contrast δ, and observables derived from it, such as the growth rate $f = d\ln\delta/d\ln a$, which is measured via redshift space distortions (RSD). A weak lensing survey gives another independent probe of the LSS.

PoS(AASKA14)016

The growth of structure provides a test for deviations from general relativity on large scales. Using the growth rate, we can measure $\gamma = \ln f / \ln \Omega_m$, looking for deviations from the general relativity value ≈ 0.55. Using the density contrast and weak lensing measurements allows us in addition to test for 'gravitational slip', i.e. a mismatch between the Newtonian and curvature perturbations that may signal deviations from general relativity.

The density contrast and weak lensing are mainly probes of the late-time accelerating Universe. LSS surveys can also probe the primordial Universe through the curvature and though large-scale correlations, which carry the signature of primordial non-Gaussianity, of general relativistic effects, and of possible deviations from statistical isotropy and homogeneity.

Some of the key questions at the forefront of cosmology today, where forecasts indicate that the SKA can be transformational, are briefly described below. Further details are given in the three review chapters (Abdalla et al. 2015; Jarvis et al. 2015; Santos et al. 2015).

4.1 How were the primordial fluctuations generated?

This fundamental question in cosmology requires inter-related tests via CMB and LSS surveys. The level of primordial non-Gaussianity is one of the most important discriminators of the primordial mechanism that generates cosmological fluctuations. The Planck CMB survey has achieved an error of $\sigma(f_{\rm NL}) = 7.5$ (using the LSS convention), where $f_{\rm NL}$ is the primordial non-Gaussianity parameter. This is the current state of the art, and LSS surveys lag far behind. In the LSS power spectrum, the primordial non-Gaussian signal grows as k^{-2}, i.e. it is strongest on the largest scales. But these are also the scales where cosmic variance is an obstacle.

Ultra-large-volume surveys of the LSS are needed to surpass the CMB accuracy. Then we will be able to put pressure on the standard model (slow-roll single-field inflation), or give support to it. In the standard model, LSS surveys would see $f_{\rm NL} \simeq -2.2$, due to a nonlinear general relativistic correction (Camera et al. 2015). In order to implement this test, LSS surveys need to reach $\sigma(f_{\rm NL}) \lesssim 2$.

In SKA Phase 1, intensity mapping surveys will achieve enormous volumes with accurate redshifts. The galaxy redshift surveys will not be competitive in SKA1 but SKA2 will deliver the best constraints for a single-tracer LSS survey. Finally, the continuum survey can also be effective if radio galaxy populations can be separated, allowing for the application of the powerful multi-tracer method that beats down cosmic variance on the large scales where non-Gaussianity is strongest. In summary, the forecasts are as follows:
For single-tracer measurements with HI surveys, we find (Santos et al. 2015; Abdalla et al. 2015)

$$\sigma(f_{\rm NL}) = 2.3 \text{ (SKA1 IM)}, \;\; 1.5 \text{ (SKA2 GRS)}. \tag{4.1}$$

For multi-tracer measurements with continuum surveys (Jarvis et al. 2015),

$$\sigma(f_{\rm NL}) < 1 \text{ (SKA2 Cont} + z \text{ from HI/optical)}. \tag{4.2}$$

See Fig. 4 for the galaxy redshift and continuum surveys.

4.2 What is driving the acceleration of the Universe?

Perhaps the most fundamental question in cosmology is – what is driving the acceleration of the late-time Universe? Is it

PoS(AASKA14)016

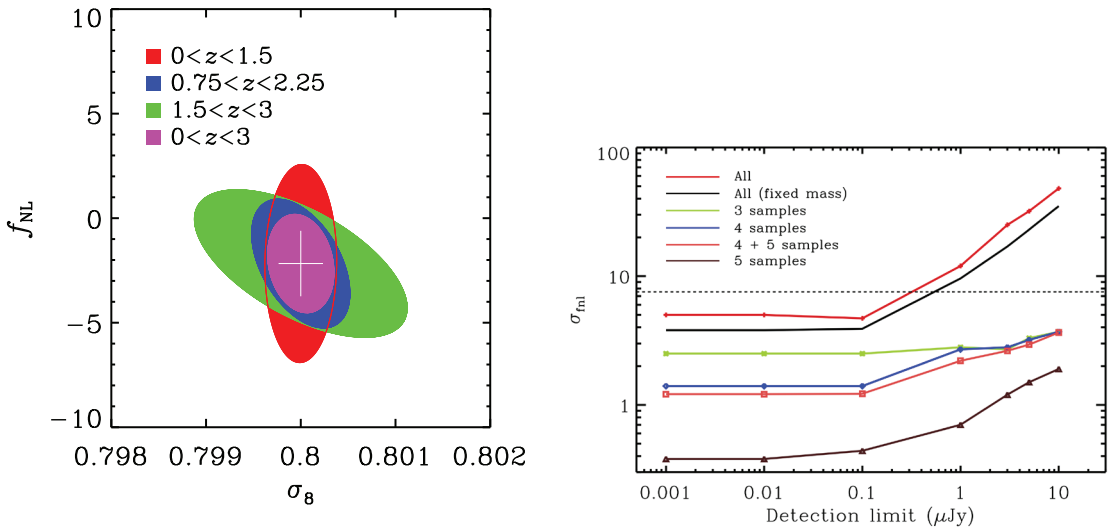

Figure 4: Forecast errors on f_{NL}. *Left:* With the SKA2 galaxy redshift survey. (Camera et al. 2015) *Right:* With continuum surveys at different sensitivities (including SKA1 and SKA2), using the multi-tracer method. (Jarvis et al. 2015)

- Vacuum energy (Λ, with $w = -1$) – the simplest option (concordance model)?
- Dynamical dark energy[1], with $w \neq -1$?
- A weakening of gravity on very large scales, i.e. a breakdown in general relativity ('modified gravity')?

Forecasts indicate that intensity mapping in SKA1 can outperform current-generation optical surveys, and is not far behind future optical spectroscopic surveys – see Figs. 1 and 5. The latter figure also shows the game-changing power of SKA2 on the question of dark energy/ modified gravity.

We are entering an era in which we can expect a definite answer to the acceleration question – and the answer will have profound implications for our understanding of the Universe. In order to succeed, we will need the combined power of the SKA and other LSS surveys like Euclid.

4.3 Is the Universe statistically isotropic and homogeneous?

The concordance model, as well as dynamical dark energy and modified gravity models, are all based on the fundamental assumption that the Universe is statistically isotropic and homogeneous – the 'Cosmological Principle'. This principle should be interrogated by carefully designed observational tests.

One critical feature of the standard assumption is that the dipole in the CMB – accurately measured by Planck – should match the dipole in the LSS, since both are predicted to originate from our motion relative to the common radiation/ matter frame in the background. Current contraints on

[1]Typically this is tested via the parametrization $w = w_0 + w_a(1-a)$ or by using principal component analysis.

PoS(AASKA14)016

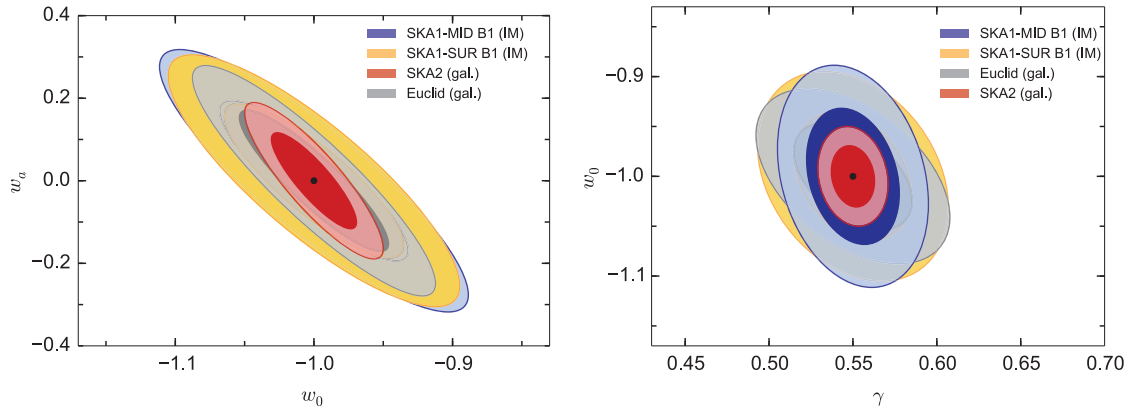

Figure 5: Constraints from RSD on the dark energy equation of state (*Left*) and on modified gravity (deviations from the GR growth rate) (*Right*), for SKA1 HI intensity mapping surveys, the SKA2 HI galaxy redshift survey and Euclid. (Planck and BOSS data inlcuded.) (Raccanelli et al. 2015)

the LSS dipole from the NVSS survey are too weak to answer the question of whether the dipoles agree. SKA all-sky continuum surveys will be able to constrain the LSS dipole at similar levels to Planck constraints on the CMB dipole. The error on the dipole direction θ is forecast to be (Schwarz et al. 2015)

$$\sigma(\theta) \sim 5^\circ \ \ (\text{SKA1}), \quad \sim 1^\circ \ \ (\text{SKA2}). \tag{4.3}$$

SKA2 is close to the Planck precision and improves on the NVSS constraints by a factor ~ 100. The outcome – whether it is a confirmation or an overturning of the fundamental assumption – will be a milestone for cosmology.

The angular two-point correlation function from SKA all-sky surveys can be used to probe the quadrupole and octupole of the LSS distribution. This will give a unique opportunity to test whether the anomalies in the low multipoles of the CMB are statistically significant or not.

In addition to tests of statistical isotropy, we can test whether the matter distribution shows the same nearly scale-invariant behaviour, $n_s \sim 1$, on super-Hubble scales, as seen in the CMB. Various tests of statistical homogeneity have been devised, based on relationships between distances and Hubble rates as functions of redshift. BAO meaurements with the SKA (see Fig. 1) will allow us to apply these tests at high enough accuracy to pose a real challenge to the standard model.

4.4 What is the distribution of matter on horizon scales and how does it evolve?

Up to now, LSS surveys have not yet been able to probe the matter power spectrum beyond the equality scale, $k \sim .01h\,\text{Mpc}^{-1}$. We have yet to confirm observationally the predicted turnaround in the power spectrum – an important consistency test of the standard model. In addition, we need to probe further, and measure the power spectrum near the Hubble horizon. At higher redshifts, we can in principle probe super-horizon modes. On this basis we can confirm the predictions of the concordance model, or discover deviations. These deviations could be due to primordial non-Gaussianity or modified gravity – or to some unexpected new feature.

PoS(AASKA14)016

There are two basic requirements in order to succeed. Firstly, we need all-sky surveys with spectroscopy and deep redshift reach. Secondly, we need the correct theoretical tools to analyse correlations on horizon scales and across large redshift distances – i.e., we need to incorporate all the relativistic effects that correct the Newtonian-Kaiser approximation at high redshift and at horizon scales (Camera et al. 2015).

SKA1 can deliver the all-sky spectroscopy via intensity mapping, up to $z \sim 3$, while the galaxy redshift survey in SKA2 will reach $z \sim 2$ with high angular resolution. Already in SKA1, we will be able to map for the first time the large-scale HI distribution in 3/4 of the universe, from today all the way back to redshifts where the concordance model predicts no effect of dark energy. SKA-LOW will allow us to probe even larger scales in the Epoch of Reionization, as the angular scale of the horizon becomes smaller and smaller at very high redshift.

We will then be able to test the concordance predictions at high z. Furthermore, we will be able for the first time, to extend the tests of general relativity to horizon scales.

4.5 What is the curvature of the Universe?

The concordance model has zero spatial curvature, $\Omega_K = 0$, but small nonzero curvature is allowed by current data. LSS surveys with huge volume are needed to move beyond CMB accuracy ($|\Omega_K| \lesssim 10^{-2}$ from Planck) and determine whether the curvature is above the perturbative level of $O(10^{-5})$. A detection of non-perturbative curvature could rule out many inflation models. SKA1 intensity mapping surveys have huge volume and accurate spectroscopy, and they reach well beyond the redshifts that are affected by acceleration, thus helping to break degeneracies arising from dark energy. This leads to a predicted accuracy of $|\Omega_K| < 10^{-3}$, using BAO measurements.

4.6 A revolution in weak lensing

The measurement of galaxy shapes provides a statistical estimate of the weak gravitational lensing shear due to the intervening LSS, and this gives a powerful probe of the total matter and its distribution. Cosmological weak lensing surveys have so far been in the optical, but in principle they can also be carried out in the radio. The SKA offers the possibility of the first ever weak lensing survey in the radio that can deliver cosmological precision. Such surveys would map the dark matter and dark energy/ modified gravity in an entirely new and independent way from their optical counterparts. A cross-correlation of radio and optical would offer a major reduction in sytematics that could significantly enhance the precision of weak lensing.

A continuum survey in SKA1, covering 5,000 deg^2, would provide the foundation to prepare for a 30,000 deg^2 survey with SKA2, which is predicted to have transformational potential in combination with Euclid – as shown in Fig. 6.

5. Conclusions

We have given a brief overview of the major science goals and capabilities of the SKA in cosmology. Further details on these science topics are to be found in the three review chapters, covering the three types of survey (Abdalla et al. 2015; Jarvis et al. 2015; Santos et al. 2015). Among the novel science goals described in those reviews and not covered here, are:

PoS(AASKA14)016

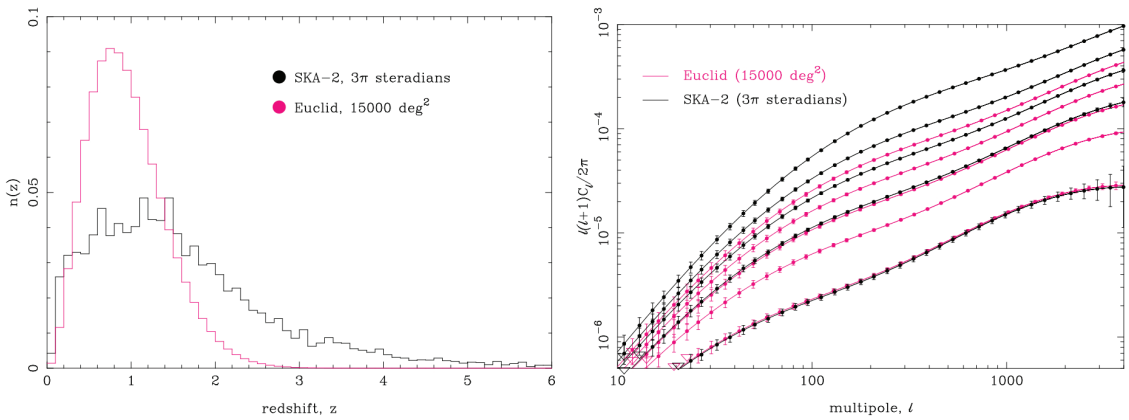

Figure 6: *Left:* Redshift distribution of sources for a 30,000 deg^2 weak lensing survey with SKA2, and for the 15,000 deg^2 survey with Euclid. *Right:* The corresponding constraints on a 5-bin tomographic auto-power spectrum analysis. (Jarvis et al. 2015)

- Using the topology of the HI distribution as a cosmological probe (SKA1 and SKA2);
- Constraining primordial non-Gaussianity through the HI bispectrum (SKA1 and SKA2);
- Measuring the redshift drift of sources – i.e. the real-time tracking of the change in redshift of a source – as a probe of acceleration (SKA2).

The review chapters also examine in detail the crucial technical issues which were not discussed here, such as foreground contamination and instrumental systematics.

SKA is a facility that is planned to have a ~ 50 year lifetime. It will be the premier facility for spectroscopy up to $z \sim 3$, and will not be surpassed by other spectroscopic surveys in volume, since HI is common up to high redshifts. On longer time-scales, one can envisage significant improvements to the forecasts described here. However, we have focused on the shorter term. In particular, we have shown that the SKA can deliver not only competitive, but transformational, science even in Phase 1 of the deployment, years before full deployment. With full deployment comes the ultimate 'billion galaxy survey'.

In this overview, we have focused on the potential of SKA itself, and have not discussed the additional power arising from combining the SKA with Euclid, LSST and other future optical/infrared surveys. Indeed, this combination will allow us to beat down experimental systematics and cosmic variance, delivering greater power than each survey on its own.

The science goals that we discussed included topics falling under the heading of 'precision cosmology', i.e. tying down with ever greater accuracy the key parameters of the concordance model. But in addition, there are other goals that probe the foundations of the concordance model, looking for deviations – both those theoretically foreseen and those that will be unexpected discoveries.

References

Abdalla, F. B., Bull, P., Camera, S., et al. 2015, "Cosmology from HI galaxy surveys with the SKA", in Advancing Astrophysics with the Square Kilometre Array, PoS(AASKA14)017

PoS(AASKA14)016

Bull, P., Camera, S., Raccanelli, A., et al. 2015, "Measuring baryon acoustic oscillations with future SKA surveys", in Advancing Astrophysics with the Square Kilometre Array, PoS(AASKA14)024

Camera, S., Raccanelli, A., Bull, P., et al. 2015, "Cosmology on the Largest Scales with the SKA", in Advancing Astrophysics with the Square Kilometre Array, PoS(AASKA14)025

Jarvis, M., Bacon, D., Blake, C., et al. 2015, "Cosmology with SKA Radio Continuum Surveys", in Advancing Astrophysics with the Square Kilometre Array, PoS(AASKA14)018

Pritchard, J., Ichiki, K., Mesinger, A., et al. 2015, "Cosmology from EoR/Cosmic Dawn with the SKA", in Advancing Astrophysics with the Square Kilometre Array, PoS(AASKA14)012

Raccanelli, A., Bull., P., Camera, S., et al. 2015, "Measuring redshift-space distortion with future SKA surveys", in Advancing Astrophysics with the Square Kilometre Array, PoS(AASKA14)031

Santos, M. G., Bull, P., Alonso, D., et al. 2015, "Cosmology from a SKA HI intensity mapping survey", in Advancing Astrophysics with the Square Kilometre Array, PoS(AASKA14)019

Schwarz, D., Bacon, D., Chen, S., et al. 2015, "Testing foundations of modern cosmology with SKA all-sky surveys", in Advancing Astrophysics with the Square Kilometre Array, PoS(AASKA14)035

PoS(AASKA14)016

PROCEEDINGS OF SCIENCE

Cosmology from HI galaxy surveys with the SKA

Filipe B. Abdalla[*1,2], **Philip Bull**[3], **Stefano Camera**[4], **Aurélien Benoit-Lévy**[1], **Benjamin Joachimi**[1], **Donnacha Kirk**[1], **Hans-Rainer Klöckner**[5], **Roy Maartens** [6,7], **Alvise Raccanelli**[8,9], **Mario G. Santos**[4,6,10], **Gong-Bo Zhao**[11,7] **on behalf of the Cosmology SWG.**

[1]*Department of Physics and Astronomy, University College London, London WC1E 6BT, UK* [2]*Department of Physics and Electronics, Rhodes University, PO Box 94, Grahamstown, 6140 South Africa;* [3] *Institue of Theoretical Astrophysics, University of Oslo, P.O. Box 1029 Blindern, N-0315 Oslo, Norway;* [4] *CENTRA, Instituto Superior Técnico, Universidade de Lisboa, Lisboa 1049-001, Portugal;* [5] *Max-Planck-Institut fur Radioastronomie, Auf dem Hügel 69, 53121 Bonn, Germany;* [6] *Department of Physics, University of Western Cape, Cape Town 7535, South Africa;* [7] *Institute of Cosmology & Gravitation, University of Portsmouth, Portsmouth PO1 3FX, UK;* [8] *Jet Propulsion Laboratory, California Institute of Technology, Pasadena CA 91109, USA;* [9] *California Institute of Technology, Pasadena CA 91125, USA;* [10] *SKA SA, 4rd Floor, The Park, Park Road, Pinelands, 7405, South Africa;* [11] *National Astronomy Observatories, Chinese Academy of Sciences, Beijing, 100012, P.R.China*
E-mail: fba@star.ucl.ac.uk

The Square Kilometer Array (SKA) has the potential to produce galaxy redshift surveys which will be competitive with other state of the art cosmological experiments in the next decade. In this chapter we summarise what capabilities the first and the second phases of the SKA will be able to achieve in its current state of design. We summarise the different cosmological experiments which are outlined in further detail in other chapters of this Science Book. The SKA will be able to produce competitive Baryonic Oscillation (BAOs) measurements in both its phases. The first phase of the SKA will provide similar measurements in optical and IR experiments with completely different systematic effects whereas the second phase being transformational in terms of its statistical power. The SKA will produce very accurate Redshift Space Distortions (RSD) measurements, being superior to other experiments at lower redshifts, due to the large number of galaxies. Cross correlations of the galaxy redshift data from the SKA with radio continuum surveys and optical surveys will provide extremely good calibration of photometric redshifts as well as extremely good bounds on modifications of gravity. Basing on a Principle Component Analysis (PCA) approach, we find that the SKA will be able to provide competitive constraint on dark energy and modified gravity models. Due to the large area covered the SKA it will be a transformational experiment in measuring physics from the largest scales such as non-Gaussian signals from f_{nl}. Finally, the SKA might produce the first real time measurement of the redshift drift. The SKA will be a transformational machine for cosmology as it grows from an early Phase 1 to its full power.

Advancing Astrophysics with the Square Kilometre Array
June 8-13, 2014
Giardini Naxos, Italy

*Speaker.

PoS(AASKA14)017

1. Introduction.

It has been over a decade since we entered an era of precision cosmology in which precise estimation of the key cosmological parameters is the ultimate goal of cosmological surveys. The advances in our ability to map out the Cosmic Microwave Background (CMB) have lead the way and culminated in the very accurate datasets which are available to us from the Planck mission Planck Collaboration et al. (2013a). The CMB is however limited in providing information about the nature of components in the late time Universe given that it is mainly probing the nature of the Universe, some 400,000 years after the Big Bang. The Planck mission is able to provide somewhat better constraints on Dark Energy given that it can also measure the lensing of the CMB, which other earlier missions did not have the capability of doing Planck Collaboration et al. (2013b). Even with the lensing of the CMB, Planck is not an ideal mission for obtaining information about the nature of dark energy.

It is with galaxy surveys that the way will be paved in the next decade in terms of improving our current knowledge on the accelerating Universe. Missions that probe both the geometrical nature of the late time Universe as well as the growth of structure will be the missions which, statistically speaking, have the best handle on Dark Energy. Missions such as the SKA and the Euclid Satellite will indeed measure both geometry and growth with galaxy redshift surveys by using techniques such as Baryonic Acoustic Oscillations and Redshift Space Distortion measurements of the Large Scale Structure. There are more novel optimal ways of probing the Large Scale Structure of the Universe with radio telescopes using Intensity Mapping which are summarized in Santos et al. (2015b). However in this chapter here we concentrate on the arguably more systematic-free experiment which aims at obtaining full galaxy redshift surveys with the SKA.

The outline of this summary chapter is as follows. In Section 2 we outline the basic assumptions used for the forecast we have made in the rest of the chapter. In Sections 3 and 4 we summarise the main cosmological probes, namely the Baryonic acoustic oscillations and Redshift space distortion measurements with SKA. In Section 5 we look at the power of an SKA galaxy redshift survey when used in conjunction with other SKA probes to measure Modified Gravity and to calibrate photometric redshifts. In section 6 we look at the science that can be done with an SKA at the largest possible scales by probing non-Gaussianity. In Section 7 we summarise the cosmological redsfhit drift science that is accessible to a future SKA2. We conclude in Section 8.

2. The SKA1 and SKA2 galaxy redshift surveys: Number counts and bias

Neutral hydrogen (HI) is the most abundant element in galaxies, making it a prime candidate to observe them and trace the underlying dark matter. Moreover, with a rest frequency of 1420 MHz, the HI (21 cm) line can be used by radio telescopes to measure the redshift of galaxies to high accuracy and across a large redshift range. The line is however quite weak, requiring highly sensitive telescopes such as the SKA in order to make large sky HI galaxy surveys (so far, only a few galaxies up to $z \sim 0.2$ have been detected Freudling et al. (2011)).

Predicting the number of HI galaxies one will be able to observe, as well as the associated bias with respect to the dark matter, are fundamental ingredients in order to forecast the constraining power for cosmology of future radio telescopes. Two components are essential for this prediction:

PoS(AASKA14)017

i) the HI content/luminosity of galaxies and ii) the expected sensitivity of the telescope. In chapter Santos et al. (2015a) we analysed explicitly the sensitivities for different SKA setups (both for phase 1 and the full SKA) and the corresponding number counts and bias. The HI luminosities were obtained using the SAX-sky simulation (Obreschkow et al. 2009). Translating this into a detection is not completely straightforward since it depends on the source detection algorithm. We assumed that at least two points across the HI line should be measured, in order to have some handle on the typical "two-horn" structure of the HI line and the combined measurement of all the points across the line should result in a signal to noise of 10σ or at least 5σ. To calculate the bias, galaxies from the SAX simulation for a given flux sensitivity and redshift were put in the box for which the power spectrum of the number counts was calculated and compared to the dark matter one. Due to the size limits of the simulation, shot noise can contaminate the measurement so that values at flux sensitivities above 20μJy or at very high-z, should be only indicative (this is however not a concern since the shot noise tends to dominate the measurements).

Given the required balance for cosmological applications between surveying a large sky area to beat cosmic variance and having high galaxy number densities to beat shot noise, we found that the optimal sky area for a SKA1 survey is around 5,000 deg^2, while SKA2 should probe the full available sky, $\sim$ 30,000 deg^2. Results show that we should find about 5×10^6 HI galaxies with SKA1 (for either MID or SUR) up to $z \sim 0.5$ and about 9×10^8 galaxies with the full SKA up to $z \sim 2$. Obviously results might change a little as the SKA specifications are tuned and different HI simulations are used. These numbers assumed a 10σ detection with the full SKA while for SKA1 we took a more relaxed requirement of 5σ in order to allow for a higher detection of galaxies. The bias is shown to have a value around 1 at $z \sim 0.7$, increasing with both redshift and assumed flux cut since we will be probing higher mass galaxies. The numbers required for the forecasting done throughout the chapters can be nicely summarised by the following equations:

$$dn/dz = 10^{c_1} z^{c_2} \exp(-c_3 z) \tag{2.1}$$

$$b(z) = c_4 \exp(c_5 z), \tag{2.2}$$

where dn/dz is the number of galaxies per square degree and per unit redshift. The c_i parameters for each survey should be taken from Table 4 in Santos et al. (2015a). The main conclusion is that although SKA1 will already detect a large number of galaxies if we compare to optical surveys, we can only use it for cosmological applications up to $z \sim 0.4$ due to the sharp decline of the HI galaxy density with redshift. This means that frequencies $\gtrsim 1$ GHz should be enough (i.e. Band 2). On the other hand, SKA2 will push this up to $z \sim 1.7$, requiring a significantly wider band down to ~ 500 MHz (or even higher redshifts with Band 1, down to 350 MHz). It will also be able to cover the full visible sky ($\sim$30,000 sq. deg.), making it a prime instrument for cosmological applications.

3. BAO and distance constraints.

Baryon acoustic oscillations (BAO) are the imprints of sound waves – formed when baryons and photons were coupled at early times – on the large-scale distribution of matter in the Universe. Because they constitute a preferred scale in the clustering distribution of galaxies, one can use the BAO as a statistical standard ruler, allowing accurate measurements of distances and the expansion

PoS(AASKA14)017

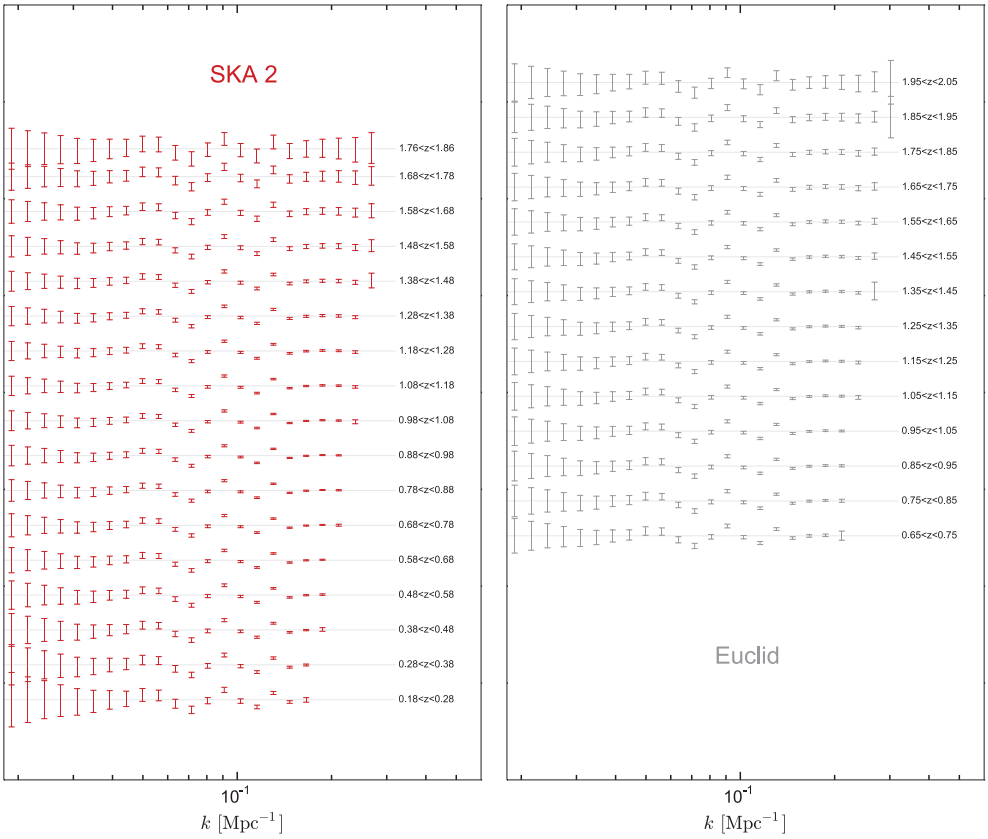

Figure 1: Constraints on the baryon acoustic oscillation feature in the power spectrum, as a function of scale and redshift, for SKA2 (left) and Euclid (right). Both the SKA and Euclid will be extremely competitive for such measurements, but the SKA2 survey will have a wider redshift range – extending to lower redshifts than Euclid – and will cover a larger survey area.

rate as a function of redshift, which in turn provide key information on the energy content of the Universe, and the nature of dark energy.

HI galaxy redshift surveys with the SKA will be capable of measuring the BAO in both the radial and tangential directions over an unprecedentedly large volume, taking in around three quarters of the sky out to high redshifts. For Phase 1, a survey with flux sensitivity $\sim 100\mu$Jy over 5,000 sq. deg. will reach $z \approx 0.5$, producing broadly comparable constraints to BOSS Anderson & et al. (2012). As several large planned galaxy surveys (e.g. Euclid) obtain spectra in the infrared part of the spectrum, they are unable to obtain significant numbers of galaxies at very low redshift. As such, a HI survey will be highly complementary, providing a useful low-redshift anchor to the Euclid galaxy redshift survey (which will cover 15,000 sq. deg. from $0.7 \lesssim z \lesssim 2$), for example (Fig. 1 and Fig. 2).

A Phase 2 survey down to a threshold of $\sim 5\mu$Jy over the same area will result in a dramatically extended redshift range, providing $\sim 0.3\%$-level constraints on both the angular diameter distance and expansion rate in the range $0.4 \lesssim z \lesssim 1.3$. This is sufficient to surpass the precision of a Euclid galaxy redshift survey. The galaxy selection function drops out at higher redshifts, though,

PoS(AASKA14)017

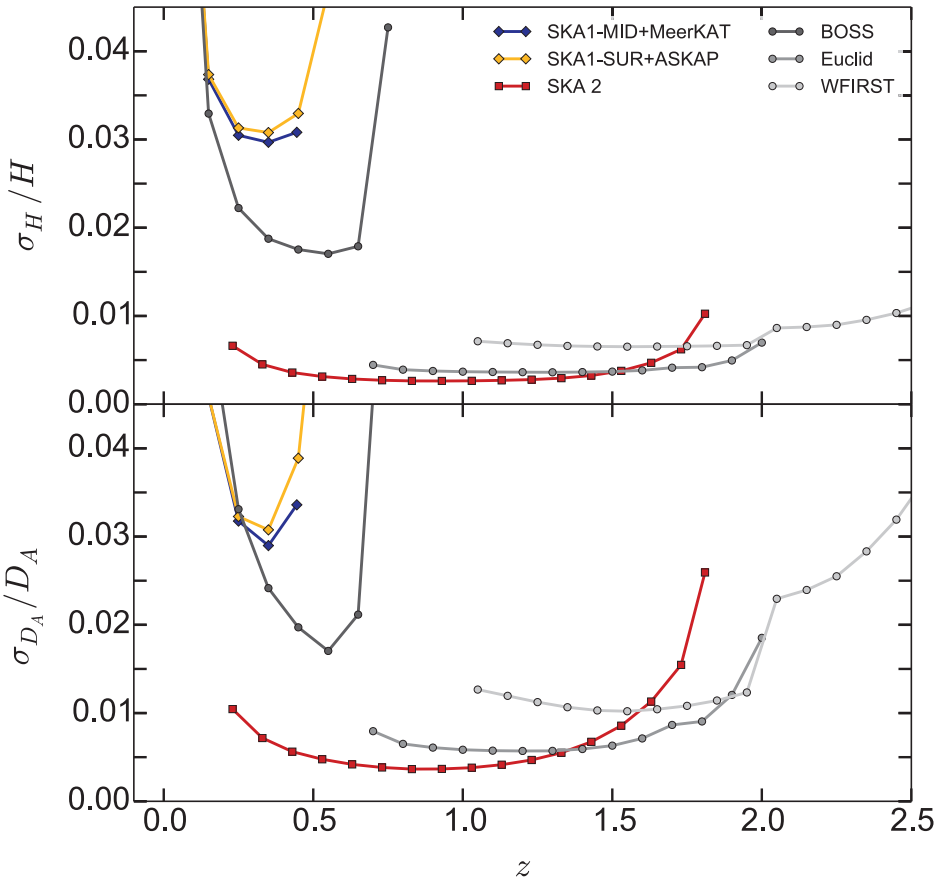

Figure 2: Forecast constraints on the angular diameter distance and expansion rate measured from the BAO, RSDs, and broadband shape of the power spectrum. While an SKA Phase 1 galaxy survey will not be competitive, Phase 2 will produce the best constraints of any planned survey on both quantities, up to $z \simeq 1.4$.

leaving intensity mapping as the SKA's principal BAO probe at $z \gtrsim 1.5$. Further details on BAO measurements, including potential systematic and results from existing surveys, can be found in Bull et al. (2015). We can see the full forecasts on the equation of state for dark energy in Fig.3 where the statistical power of SKA1 and SKA2 is compared to that of the Euclid mission in constraining dark energy. All the above assumes 10,000 hours of survey time; unlike Euclid, however, the SKA is a permanent facility that will be available for the best part of the next century, making it possible (in principle) to considerably improve on the above forecasts with longer surveys.

4. RSD constraints.

Baryonic Acoustic Oscillations can only provide information which relates to the geometry of the late time Universe. There are however several competing theories of Dark Energy which are degenerate in their prediction of the late time behavior of the accelerated expansion. It is possible however to distinguish such theories by looking at how structure grows in such models. The peculiar motion of galaxies can be an extremely good probe of gravitational collapse and hence

PoS(AASKA14)017

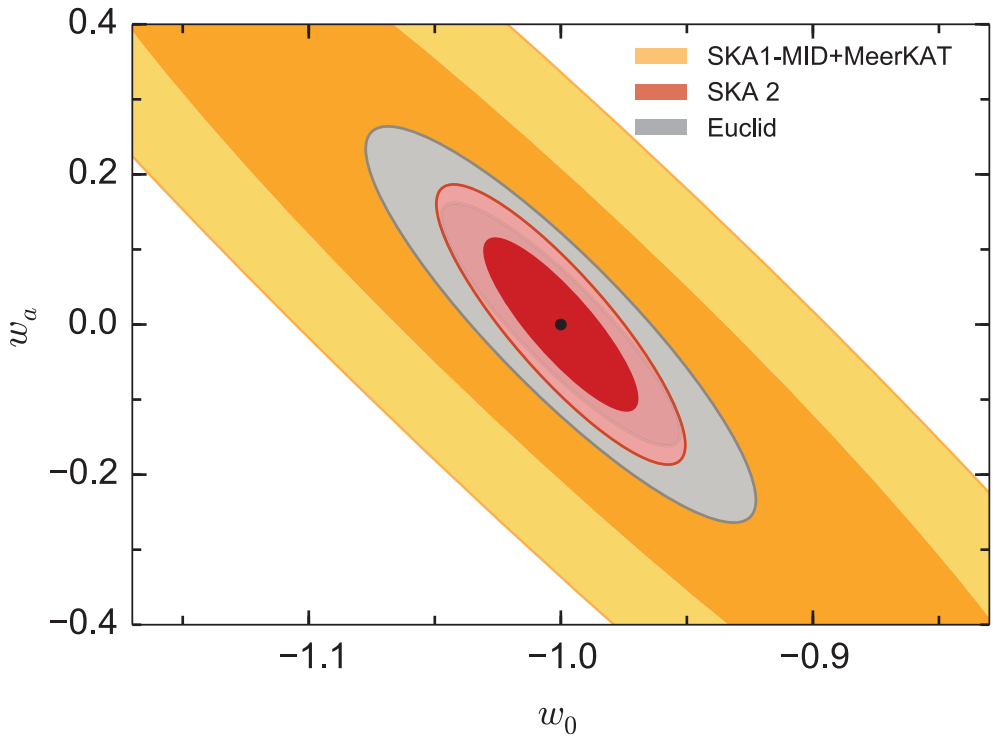

Figure 3: Constraints on the dark energy equation of state in the (w_0, w_a) parametrisation, using BAO measurements as well as Planck CMB and BOSS low-redshift BAO priors. A "billion galaxy" redshift survey with SKA2 will be significantly more powerful than the Euclid galaxy survey, mostly due to its extended redshift coverage and larger survey volume. Surveys with SKA1 will be complementary to optical and IR surveys, as they will cover a large area of the sky with high density at low redshift, but cannot compete in terms of raw dark energy constraints as they do not extend to high enough z.

growth. Hence if the dynamics of galaxy motions can be measured by looking at the statistical distribution of galaxies we can use such data to further constrain models of dark energy, by looking at modifications to the full shape of the power spectrum (or correlation function) of galaxies. This is usually expressed in terms of measurements of the linear growth rate, f, which denotes the logarithmic derivative of the matter density constrast with respect to the scale factor. Although there are complications with RSD measurements which include knowledge of the galaxy bias, and in some cases non-linear and large-scale modeling, RSDs remain one of the best ways of producing measurements of modified theories of gravity. Given that redshift space distortions manifest themselves in anisotropies in the measured power spectrum signal as a function of the angle we have with the line of sight, other effects such as the Alcock-Paczynski (AP) effect weakens the constraints that one may get from Redshift space distortions. However, by measuring the magnitude of this effect we may produce further geometrical measurements of the AP factor, F, which is a related to a ratio of the angular diameter distance and the Hubble factor.

The vast numbers of galaxies found in the SKA Phase 1 and 2 surveys will allow for a very accurate measurement of the redshift space distortion factor, f, as well as the AP distortion factor, F. As we can see from Fig.4, the SKA1 survey is competitive at low redshift, and can provide

PoS(AASKA14)017

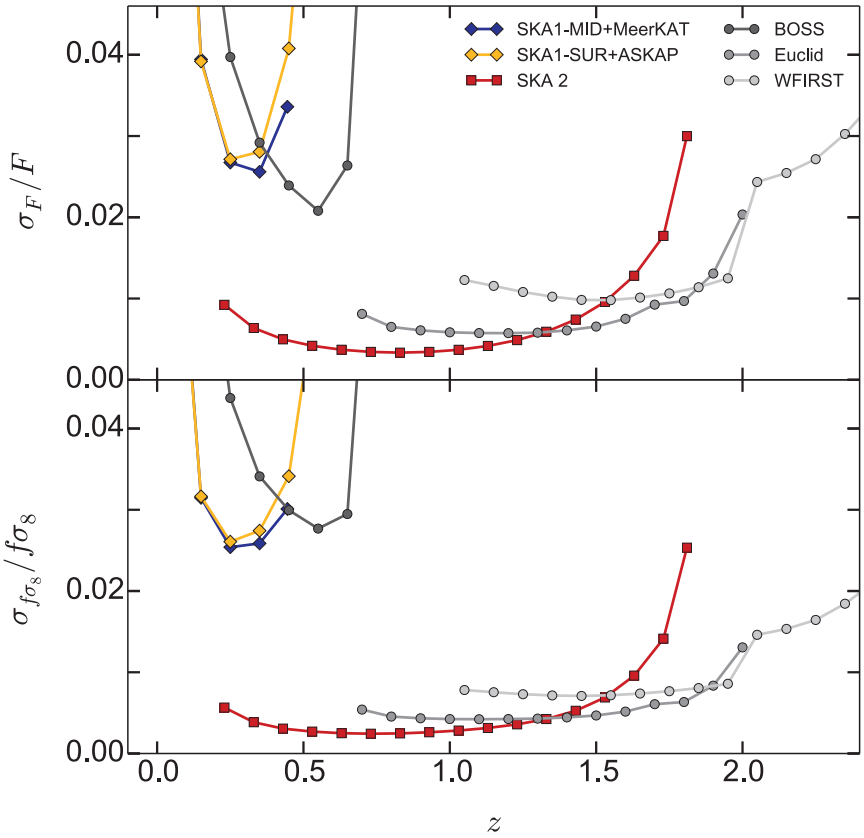

Figure 4: Sensitivity to redshift space distortions of HI galaxy surveys with Phase 1 and 2 of the SKA, compared with other galaxy surveys. The upper panel shows the Alcock-Paczynski parameter, $F(z) = (1+z)D_A(z)H(z)/c$, and the lower panel shows the growth rate observable $f\sigma_8$, which is the product of the linear growth rate, $f(z)$, and the normalisation of the power spectrum, $\sigma_8(z)$.

complementary constraints to the Euclid survey over a very large area in the sky. This is due to the fact that the Euclid mission is targeting Hα lines to secure redshifts and doing so at higher redshifts. We can also see that as we move on to a survey with SKA2, the constraints from the SKA are better than Euclid-type experiments for redshifts $z \lesssim 1.2$. A survey with SKA2 would be able to measure redshift space distortions to better than 0.5% precision in the range $0.4 < z < 1.3$. This "billion galaxy" survey can also measure the AP factor to a similar level over the same redshift range. An SKA1 survey would be able to measure both distortion parameters to a little over 2% accuracy out to $z \simeq 0.5$. Further details on RSD measurements from the SKA, including potential systematic and results from existing surveys, can be found in Raccanelli et al. (2015).

5. Cross correlation science with the SKA.

SKA will be able to deliver multiple surveys of the same large-scale structure (LSS) fields which makes it a perfect opportunity to benefit from the power of cross-correlating different cosmic probes. The combination of Intensity Mapping (IM), Weak Gravitational Lensing (WGL) of

PoS(AASKA14)017

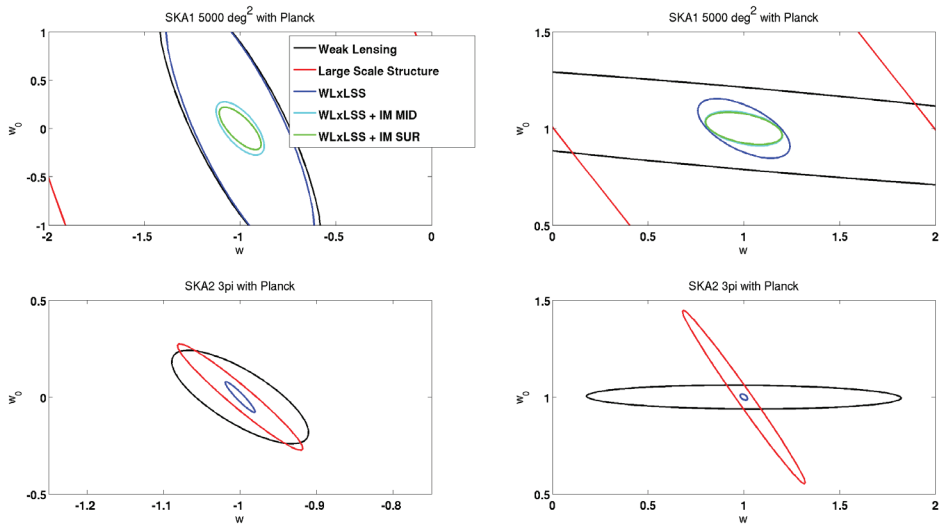

Figure 5: Improvement on the Figures of merit of dark energy and Modified gravity using the cross correlations of the spectrosocpic SKA sample with other SKA surveys. Constraints on dark energy [left panels] and deviations from GR [right panels] for SKA1 over 5,000deg^2 [top panels] and SKA2 over 30,000deg^2 [bottom panels] including Planck priors. Black ellipses show photometric WL constraints only. Red ellipses show spectroscopic LSS constraints only. Blue ellipses show the combination of WL and LSS including cross-correlations. Cyan ellipses show this WLxLSS constraint combined independently with an SKA intensity mapping (IM) survey using the MID instrument and the green contours the same but with the SUR instrument. All constraints are 68% confidence contours.

distant galaxies from the continuum survey and a HI galaxy survey which delivers precise redshift estimates makes SKA an incredibly exciting project for exploring cross-correlation science.

The combination of an SKA galaxy redshift survey with spectroscopic quality redshifts and an SKA WGL survey with photometric redshifts obtained from some external source is particularly powerful. The LSS survey has extremely high redshift resolution but uses galaxies which are biased tracers of the underlying dark matter distribution. The WGL survey has poor redshift discrimination but is unbiased and has a higher number density of sources than the galaxy survey. Together they comprise a joint data set with excellent redshift information and good control of galaxy bias.

The power of cross-correlation comes from the fact that the probes are both sensitive to the same underlying density field. The cross-correlation signal is immune to certain systematic effects that limit each autocorrelation, allowing them to be controlled. Each cosmological probe is sensitive to particular combinations of cosmological parameters. By accessing the underlying field in different ways the cross-correlation can help break degeneracies between those parameters, producing markedly tighter constraints.

In Fig. 5 we show an example of the powerful constraints that can be obtained from the cross-correlation of SKA LSS, WGL and IM surveys. We show constraints on dark energy in the left panels and deviations from GR in the right panels. The top panels show constraints from an SKA1-type survey and the bottom panels from a full SKA survey.

We show constraints from the photometric WGL and spectroscopic LSS surveys on their own.

PoS(AASKA14)017

We also show the combination of WGLxLSS including all cross-correlations and include IM priors for the SKA1 survey. The joint constraints on DE are several times tigther than any single probe. All constraints include priors from the Planck CMB temperature autocorrelation.

The constraints on gravity are particularly impressive, with the cross-correlation yielding measurements that are orders of magnitude more accurate than either probe alone. This is due to the combination of one probe that uses non-relativistic tracers (i.e. galaxies in the LSS survey) and one that uses relativistic tracers (WGL measures distortions due to the deflection of light). Relativistic tracers are sensitive to the sum of the metric potential, $\Phi+\Psi$, while non-relativistic tracers respond to the Newtonian potential, Ψ, alone. In GR these potentials are equal but Modified Gravity (MG) models generically produce different metric potentials. The combination of both types of probe breaks strong degeneracies in MG theories, producing dramatically improved sensitivity. Further details on the improvemnet are presented in detail in Kirk et al. (2015).

6. Model-independent constraints on Dark Energy and Modified Gravity

As a powerful redshift survey, the SKA HI galaxy survey will provide competitive constraint on the equation-of-state $w(z)$ of dark energy and the $\mu(k,z), \gamma(k,z)$ functions, which quantify the effect of the modification of gravity. In the ΛCDM model, $w=-1$ and $\mu=\gamma=1$. Any departure of these functions from these fiducial values would imply the dynamics of dark energy, or the breakdown of general relativity (GR), or both.

The easiest way to study the observational constraints on the w, μ, γ functions is to parameterise them first, and to constrain these parameters using observations. However, this approach might suffer from the *theoretical bias*, *i.e.*, the result can be biased if the *ad hoc* parametrisation is inappropriate. Nonparametric methods, *e.g.*, the Principle Component Analysis (PCA) approach, can not only minimise the theoretical bias, but also provide invaluable information on the detectability of dark energy dynamics and the modification of gravity. For a detailed study of the PCA forecast of dark energy and modified gravity using the SKA HI survey, we refer the readers to the SKA PCA chapter Zhao et al. (2015). Here we only summerise the main result in Figs 6 and 7.

Fig 6 shows the error of the eigenmodes of $w(z)$ using different data combinations. Combining with the simulated Planck and DES data, we find that SKA Phase 1 (SKA1) and SKA Phase 2 (SKA2) can well constrain 3 and 5 eigenmodes of $w(z)$ respectively. The errors of the best measured modes can be reduced to 0.04 and 0.023 for SKA1 and SKA2 respectively, making it possible to probe for dark energy dynamics.

Fig 7 is a similar plot for the $\mu(k,z)$ function, which quantifies the effect of modified gravity. As shown, SKA1 and SKA2 can constrain 7 and 20 eigenmodes of $\mu(k,z)$ respectively within the 10% sensitivity level. Especially 2 and 7 modes can be constrained within sub percent level using SKA1 and SKA2 respectively. This is a significant improvement compared to the combined datasets without SKA.

7. Cosmology on the largest scales with the SKA.

All-sky SKA surveys, in HI threshold and intensity mapping Santos et al. (2015b) and in

PoS(AASKA14)017

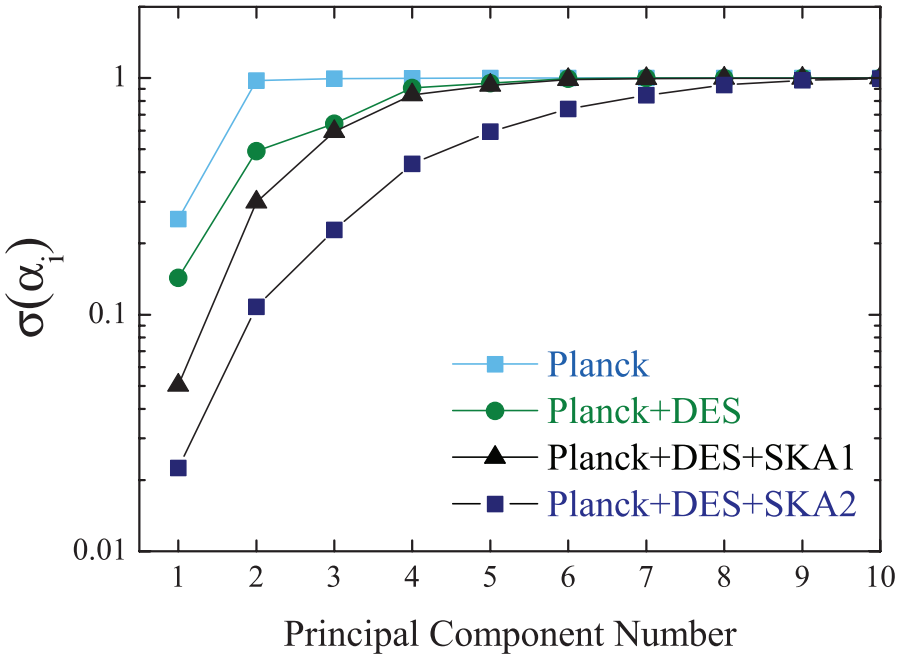

Figure 6: The forecasted 68% CL measurement error on α_i, the coefficiant of the ith principal components of $w(z)+1$, namely, $w(z)+1=\sum_i \alpha_i e_i(z)$, using different data combinations illustrated in the legend. A weak prior of $\sigma(w(z))<1$ was assumed.

continuum Jarvis et al. (2015) , will probe the biggest volumes ever of large-scale structure in the Universe. This will allow a major advance in tackling two of the main questions in cosmology: Are the fluctuations generated in the early Universe non-Gaussian? Does General Relativity (GR) hold on the largest scales?

The most stringent constraints currently available on primordial non-Gaussianity come from the Planck CMB experiment Planck Collaboration et al. (2013c). Future CMB data on polarization will improve these results, but probably not significantly. Surveys of the matter distribution are the new frontier for non-Gaussianity (see e.g. Giannantonio et al. (2012, 2014)), and the SKA has the potential to deliver game-changing constraints, given the ultra-large scales that it probes Camera et al. (2014). Indeed, non-Gaussian correction to the clustering of biased tracers of the underlying DM distribution occur on extremely large scales Dalal et al. (2008); Matarrese & Verde (2008). Since Planck detected no non-Gaussianity larger than $|f_{\rm NL}|\sim 10$, we need to probe huge volumes of the cosmic large-scale structure if we want to be able to detect such a tiny deviation from Gaussianity. This is because the larger the surveyed scale, the tighter the constraint on primordial non-Gaussianity Camera et al. (2013). This expectation is supported by recent forecasts of the constraining power of different SKA surveys Camera et al. (2015). Another advantage for SKA arises from the possibility of discriminating between different source types, allowing the use of the so-called multi-tracer technique to reduce cosmic variance and thus further increase the constraining capabilities on very large scales Seljak (2009); Abramo & Leonard (2013); Ferramacho

PoS(AASKA14)017

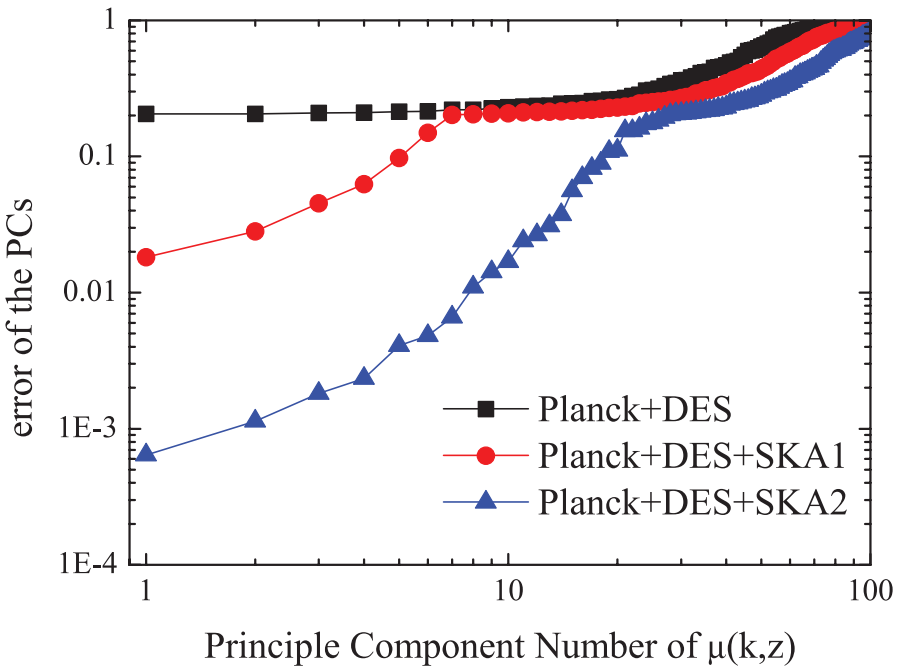

Figure 7: The forecasted 68% CL error on the coefficients of the principal components of $\mu(k,z)$ for different data combinations shown in the legend. The function μ quantifies the effect of modified gravity on structure formation on linear scales. Specifically, the Poisson equation reads $k^2\Psi = 4\pi G\mu(k,z)\delta\rho$.

et al. (2014).

Tests of GR on cosmological scales can only be based on a combination of observations of the large-scale structure. Current constraints are weak, but with its huge volumes and multiple probes, the SKA should lead the next generation of tests. In addition, we can strengthen the current tests of dark energy and modified gravity models by extending these tests to much larger scales, increasing the statistical power of the observations and improving constraints on any scale dependence of deviations from GR.

Probing ultra-large scales includes a theoretical challenge that has only been recently recognized. On very large scales, relativistic effects on the galaxy over-density also become important. (This is also true for the HI brightness temperature fluctuations, but the relativistic effects are suppressed in intensity mapping). They arise since we observe on the past lightcone and they can significantly change the predictions of the standard Kaiser approximation. In addition to the standard redshift-space distortions and the weak lensing magnification, there are Doppler, Sachs-Wolfe, integrated SW and time-delay contributions, which can become significant on horizon scales. It is therefore necessary to include these effects in predictions that will be tested against observations.

The SKA has the potential to detect these relativistic effects, thus providing a clear signal of GR—or an indication of its violation on the largest scales. Furthermore, the amplitude of the relativistic effects can be of the same order as primordial local non-Gaussianity that is consistent with Planck's constraints.

PoS(AASKA14)017

Primordial non-Gaussianity is a powerful test of inflationary models—and Planck has already ruled out those models that generate large non-Gaussianity. The key target is the simple single-field inflation models. These models generate negligible non-Gaussianity, but a nonlinear GR correction to the Poisson equation means that large-scale structure would measure $f_{\rm NL} \sim -2$. (We will discuss this and the new techniques to improve constraints on primordial non-Gaussianity via a proper accounting of the relativistic effects in detail in Camera et al. (2015).) SKA HI galaxy redshift surveys will greatly help on this effort. Indeed, Camera et al. (2014) showed that a HI galaxy redshift survey covering the range $0 < z \leq 3$ is able, thanks to the huge volume it probes, to put the currently most stringent constraint on $f_{\rm NL}$ from a single threshold tracer, i.e. $\sigma(f_{\rm NL}) = 1.54$. Moreover, their analysis has been performed for the first time by fully accounting for the GR effects above described. More specifically, the numbers used for the bias and galaxy redshift distribution for different flux cuts were taken directly from simulations. The other parameters required for the relativistic corrections were in turn directly derived from these parameters, which allowed for a fully consistent analysis of the fluctuations on ultra-large scales taking into account the GR corrections.

8. Time domain cosmology with SKA.

Real time cosmology will be possible with the SKA due to the superior survey capabilities and the ability to measure Milk-Way type galaxies up to redshifts of 1. The basic experiment is to detect the change in redshift of individual galaxies caused by the expansion of the Universe with two epochs of observations. Various observables can be used to describe the expansion history of the Universe (see e.g. Gudmundsson & Björnsson (2002)), but apart from the redshift most of these observables are out of reach by the current technical capabilities of the SKA. In order to measure the redshift drift caused by the acceleration of the "near-by" Universe the frequency resolution of the SKA needs to be adapted, which is a feasible task in synthesis interferometer such as the SKA and could be realised via a software solution.

The idea to measure the expansion rate of the Universe via redshifts has been explored in 1962 by Sandage Sandage (1962). At that time the technological limitations made these measurements out of reach. It took more than 30 years until the idea has been revisited Loeb (1998) in 1998, who proposed to use the Lyman-alpha forest absorption lines toward quasars to measure the expansion rate of the Universe. This paper was the basis to investigate these kind of measurements by optical facilities like the E-ELT and experiments like this are nowadays referred to as CODEX-like experiments (see e.g. Pasquini et al. (2005)). Unfortunately this test is greatly affected by the limitations introduced by the atmosphere, which is opaque for Lyman-alpha photons from redshifts $z \geq 1.7$. In comparison the redshift estimates performed by the SKA will not have such limitations and it has been realised that a statistical detection of the cosmic acceleration would be possible with the SKA at redshifts below a redsfhit of one using Milky-Way type galaxies Klöckner (2014). Based on the cosmological parameter measured by the WMAP and Planck (Hinshaw et al. (2013), Planck Collaboration et al. (2013b)) a maximum redshift drift of about $2 \cdot 10^{-10}$ can be expected after an observing period of 12 years (see Fig. 8). Furthermore, based on the current ΛCDM model of the Universe the contribution of the cosmic acceleration will change with redshift and the ultimate experiment to test different cosmological models would be to trace the redshift drifts

PoS(AASKA14)017

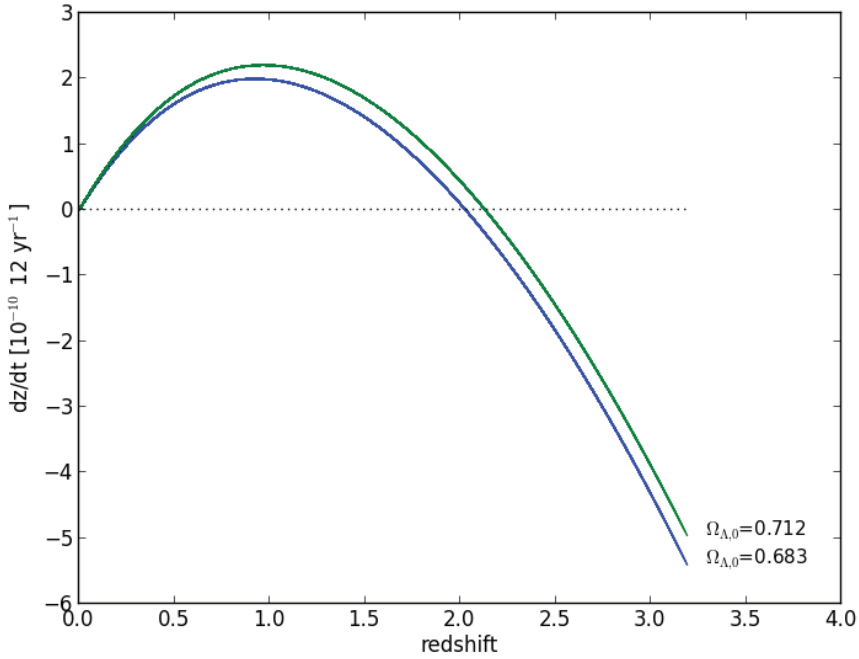

Figure 8: The expected redshift drift for various ΛCDM cosmologies ($\Omega_\Lambda = 0.712$ WMAP, $\Omega_\Lambda = 0.683$ Planck) assuming two epochs of observations within 12 years.

at various redshifts. Investigating the sensitivity estimates and the number counts of the expected HI galaxies, it could be shown that the number counts are sufficiently large to compensate for the uncertainties of the measurements and therefore permit a statistical detection of the redshift drift per redshift bin. These investigations also indicated that this experiment does not necessary require the full SKA sensitivity, it could be performed already by 2 shallow HI 3/4-sky surveys built up by 20 sqdeg pointed observed for 1 hour. Due to the relatively short survey duration of about a year per epoch and the anticipated life time of the SKA of about 50 years, the SKA offers the unique opportunity to perform this experiment five or even more times. Such experiments will open up a new path in precision cosmology enabling the direct and model independent measure of the jerk term of the acceleration. In addition, the combination of the measurements of the redshift drift in redshift space by the SKA and the E-ELT, both are sampling different redshift ranges, are the only experiments that will fully trace the evolution of the dark matter in the Universe in a completely model independent way.

9. Conclusions.

We have summarized the cosmological capabilities for the SKA to perform galaxy redshift surveys. The SKA phase one will be able to map millions of galaxies up to redshift of the order of $z \sim 0.5$ whereas the full SKA, will allow us to have a billion galaxy redshift survey over most of the sky. We have summarized the forecasts for BAO and RSD measurements and shown that the SKA1 is complementary to other state of the art facilities, while the full SKA provides transformational

PoS(AASKA14)017

science and greater accuracy than other space missions in the next decade. We have outlined how well the SKA can use its galaxy redshift surveys to provide Modified Gravity constraints as well as calibrating photometric redshifts using cross correlations with other SKA and optical samples. We have summerised how well SKA can do to constrain the dynamics of dark energy and modified gravity using the nonparametric method (the PCA approach). A full SKA survey will be able to yield cosmology at the largest scales providing measurements of f_{nl} to better accuracy than the Planck satellite, with different physical probes. We have also summarized the capabilities of the SKA over a ten year period to map out the redshift drift in real time. In summary the SKA will provide transformational science in cosmology.

References

Abramo, L. R., & Leonard, K. E. 2013, MNRAS, 432, 318

Anderson, L., & et al. 2012, MNRAS, 427, 3435

Bull, P., et al. 2015, "Measuring baryon acoustic oscillations with future SKA surveys", in Advancing Astrophysics with the Square Kilometre Array, PoS(AASKA14)024

Camera, S., Santos, M. G., Ferreira, P. G., & Ferramacho, L. 2013, Physical Review Letters, 111, 171302

Camera, S., Santos, M. G., & Maartens, R. 2014, arXiv:1409.8286

Camera, S., et al. 2015, "Cosmology on the Largest Scales with the SKA", in Advancing Astrophysics with the Square Kilometre Array, PoS(AASKA14)025

Dalal, N., Doré, O., Huterer, D., & Shirokov, A. 2008, PhRevD, 77, 123514

Ferramacho, L. D., Santos, M. G., Jarvis, M. J., & Camera, S. 2014, MNRAS, 442, 2511

Freudling, W., Staveley-Smith, L., Catinella, B., et al. 2011, ApJ, 727, 40

Giannantonio, T., Porciani, C., Carron, J., Amara, A., & Pillepich, A. 2012, MNRAS, 422, 2854

Giannantonio, T., Ross, A. J., Percival, W. J., et al. 2014, PhRevD, 89, 023511

Gudmundsson, E. H., & Björnsson, G. 2002, ApJ, 565, 1

Hinshaw, G., Larson, D., Komatsu, E., et al. 2013, ApJS, 208, 19

Jarvis, M. J., et al. 2015, "The star-formation history of the Universe with the SKA", in Advancing Astrophysics with the Square Kilometre Array, PoS(AASKA14)068

Kirk, D., et al. 2015, "Cross correlation surveys with the Square Kilometre Array", in Advancing Astrophysics with the Square Kilometre Array, PoS(AASKA14)020

Klöckner, H.-R. 2014, in Pathway to the SKA - The German White Paper, eds. H.-R. Klöckner,M. Kramer, H. Falcke, D. Schwarz, A. Eckart, G. Kauffmann,

Loeb, A. 1998, ApJL, 499, L111

Matarrese, S., & Verde, L. 2008, ApJL, 677, L77

Obreschkow, D., Klöckner, H.-R., Heywood, I., Levrier, F., & Rawlings, S. 2009, ApJ, 703, 1890

Pasquini, L., Cristiani, S., Dekker, H., et al. 2005, The Messenger, 122, 10

Planck Collaboration, Ade, P. A. R., Aghanim, N., et al. 2013a, ArXiv e-prints, arXiv:1303.5076

—. 2013b, ArXiv e-prints, arXiv:1303.5077

—. 2013c, ArXiv e-prints, arXiv:1303.5084

Raccanelli, A., et al. 2015, "Measuring redshift-space distortion with future SKA surveys", in Advancing Astrophysics with the Square Kilometre Array, PoS(AASKA14)031

PoS(AASKA14)017

Sandage, A. 1962, ApJ, 136, 319

Santos, M. G., et al. 2015a, "Cosmology from a SKA HI intensity mapping survey", in Advancing Astrophysics with the Square Kilometre Array, PoS(AASKA14)019

Santos, M. G., et al. 2015b, "HI galaxy simulations for the SKA: number counts and bias", in Advancing Astrophysics with the Square Kilometre Array, PoS(AASKA14)021

Seljak, U. 2009, Physical Review Letters, 102, 021302

Zhao, G. B., et al. 2015, "Model-independent constraints on dark energy and modified gravity with the SKA", in Advancing Astrophysics with the Square Kilometre Array, PoS(AASKA14)165

PoS(AASKA14)017

PROCEEDINGS OF SCIENCE

Cosmology with SKA Radio Continuum Surveys

Matt J. Jarvis[1,2,*], **David Bacon**[3], **Chris Blake**[4], **Michael Brown**[5], **Sam Lindsay**[1], **Alvise Raccanelli**[6,7], **Mario Santos**[8,9], **Dominik Schwarz**[10]

[1]*Astrophysics, University of Oxford, Keble Road, Oxford, OX1 3RH, UK;* [2]*Physics Department, University of the Western Cape, Bellville 7535, South Africa;* [3]*Institute of Cosmology and Gravitation, University of Portsmouth, Burnaby Road, Portsmouth PO1 3FX, UK;* [4] *Centre for Astrophysics & Supercomputing, Swinburne University of Technology, PO Box 218, Hawthorn, VIC 3122, Australia;* [5] *Jodrell Bank Centre for Astrophysics, Alan Turing Building, University of Manchester, Oxford Road, Manchester, M13 9PL, UK;* [6] *Jet Propulsion Laboratory, California Institute of Technology, Pasadena CA 91109, USA;* [7] *California Institute of Technology, Pasadena CA 91125, USA;* [8]*Physics Department, University of the Western Cape, Bellville 7535, South Africa;* [9]*SKA SA, 3rd Floor, The Park, Park Road, Pinelands, 7405, South Africa;* [10]*Fakultät fuür Physik, Universität Bielefeld, 33501 Bielefeld, Germany*

E-mail: matt.jarvis@astro.ox.ac.uk

Radio continuum surveys have, in the past, been of restricted use in cosmology. Most studies have concentrated on cross-correlations with the cosmic microwave background to detect the integrated Sachs-Wolfe effect, due to the large sky areas that can be surveyed. As we move into the SKA era, radio continuum surveys will have sufficient source density and sky area to play a major role in cosmology on the largest scales. In this chapter we summarise the experiments that can be carried out with the SKA as it is built up through the coming decade. We show that the SKA can play a unique role in constraining the non-Gaussianity parameter to $\sigma_{f_{NL}} \sim 1$, and provide a unique handle on the systematics that inhibit weak lensing surveys. The SKA will also provide the necessary data to test the isotropy of the Universe at redshifts of order unity and thus evaluate the robustness of the cosmological principle. Thus, SKA continuum surveys will turn radio observations into a central probe of cosmological research in the coming decades.

Advancing Astrophysics with the Square Kilometre Array
June 8-13, 2014
Giardini Naxos, Italy

*Speaker

PoS(AASKA14)018

1. Introduction

Over the past decade it has become clear that large-area radio surveys can play an important role in enhancing our understanding of the cosmological model. Various groups have used the NRAO VLA Sky Survey (NVSS; Condon et al. 1998) as a low-redshift tracer of the large-scale structure of the Universe by both cross-correlations with the Cosmic Microwave Background (CMB) to find evidence for the Integrated Sachs-Wolfe effect (Sachs & Wolfe 1967; Giannantonio et al. 2008), and by investigating the largest scales for signs of non-Gaussianity (e.g. Xia et al. 2010).

As we move into the SKA-era, then such wide-area surveys will reach much deeper levels, and begin to rival optical surveys in terms of source density. This is because the synchrotron emission that dominates the extragalactic radio background emission at < 10 GHz is emitted from all galaxies with any ongoing star formation or accretion activity. In addition, the wide area radio surveys will extend to substantially larger areas ($\simeq 30,000$ deg^2) than many of the forthcoming optical surveys.

Given that synchrotron radio emission from galaxies is unaffected by dust obscuration, and the $k-$corrections are relatively straightforward given the power-law nature of the synchrotron spectrum, then radio surveys offer a unique advantage for many cosmological applications. On the other hand, the generally featureless spectrum means that redshift information for individual sources can only be obtained with observations at other wavelengths, or through 21-cm spectral line observations (see e.g. Bull et al. 2015).

Like optical surveys, radio surveys are made up of sources that trace the underlying density field very differently, i.e. from highly biased tracers such as powerful AGN to low-bias populations such as star-forming galaxies. However, unlike the wide-field optical surveys, radio continuum emission is unaffected by dust, and in the age of the SKA, the star-forming galaxies, as well as the AGN, can be detected to high redshifts. These sources can then provide an important probe of the very largest scales in the universe.

In this chapter we review the different experiments and surveys that could be carried out with the SKA in phase 1, and in the longer term with the full SKA, for cosmology using radio continuum observations.

2. Assumptions

We base our estimates of the redshift distribution of various source populations on the luminosity functions that underpin the semi-empirical extragalactic sky simulations of Wilman et al. (2008, 2010). These simulations provide a very good description of the latest source counts from various deep field surveys with the JVLA (e.g. Condon et al. 2012). Although modifications may be required to accurately reproduce the most recent results from e.g. *Herschel*, the general trends and evolution prescribed are relatively well matched to our current understanding, and the extrapolations to flux-density levels yet to be reached in the radio band are constrained by observations at a range of other wavelengths. For example, in the chapter on weak lensing at radio wavelengths and testing the foundations of cosmology Brown et al. (2015) and Schwarz et al. (2015), both use an increase in the source density of the star-forming population by a factor of 2.5, in order to match the latest source counts from deep fields. In Table 1 we present the number count for each radio source

PoS(AASKA14)018

Table 1: Expected number density (deg^{-2}) of the various radio source populations in the simulations of Wilman et al. (2008) for a survey with detection threshold of $S_{1\ \mathrm{GHz}}$ = 100 nJy (*top-left*), 1μJy (*top-right*), 5μJy (*bottom-left*) and 10μJy (*bottom-right*). SFGs=star-forming galaxies; SBs=starburst galaxies; RQQs=radio-quiet quasars; FRIs=Fanaroff-Riley Class I sources; FRIIs=Fanaroff-Riley Class II sources. Note that the number density of SFGs and SBs in the table may be multiplied by a factor of 2.5 to match the latest observed source counts at the μJy level (see Brown et al. 2015, for further details).

	100 nJy						1 μJy					
Redshift	N/deg^2						N/deg^2					
	SFGs	SBs	RQQs	FRIs	FRIIs	Total	SFGs	SBs	RQQs	FRIs	FRIIs	Total
0.0< z <0.5	5892	35	4530	358	0.0	10815	3419	37	1710	279	0.0	5445
0.5< z <1.0	15366	191	7093	2833	0.2	25483	7759	260	1964	1004	0.2	10987
1.0< z <1.5	19353	731	4311	3191	0.8	27587	9181	666	1466	857	0.8	12171
1.5< z <2.0	18102	599	2478	1920	1.2	23100	8042	719	967	598	1.2	10327
2.0< z <2.5	16455	1103	1828	1706	1.0	21093	5844	697	664	449	1.0	7655
2.5< z <3.0	13572	888	1104	1198	1.6	16764	4141	525	438	328	1.6	5434
3.0< z <3.5	11582	925	787	895	0.8	14190	2970	369	281	249	0.8	3870
3.5< z <4.0	10298	887	613	848	0.3	12646	2213	302	204	209	0.3	2928
4.0< z <4.5	8144	790	414	579	0.3	9927	1676	232	145	163	0.3	2216
4.5< z <5.0	7026	649	306	481	0.2	8462	1259	184	102	130	0.2	1675
5.0< z <5.5	6037	720	233	415	0.0	7405	1005	154	75	110	0.0	1344
5.5< z <6.0	5257	638	182	319	0.0	6396	803	126	54	93	0.0	1076
Total	137084	8156	23879	14743	6.4	183868	48312	4271	8070	4469	6.4	65128

	5 μJy						10 μJy					
Redshift	N/deg^2						N/deg^2					
	SFGs	SBs	RQQs	FRIs	FRIIs	Total	SFGs	SBs	RQQs	FRIs	FRIIs	Total
0.0< z <0.5	1761	40	701	140	0.0	2642	1117	40	445	99	0.0	1701
0.5< z <1.0	2894	267	913	425	0.2	4499	1594	208	636	293	0.2	2731
1.0< z <1.5	2973	368	713	351	0.5	4405	1588	225	495	239	0.5	2548
1.5< z <2.0	2350	317	468	245	1.2	3381	1206	192	309	167	1.2	1875
2.0< z <2.5	1462	218	290	184	1.0	2155	693	129	179	124	1.0	1126
2.5< z <3.0	930	162	174	136	1.2	1403	405	95	97	92	1.2	690
3.0< z <3.5	605	118	103	105	0.7	932	239	67	53	71	0.7	431
3.5< z <4.0	407	91	66	84	0.3	648	145	50	31	56	0.3	282
4.0< z <4.5	274	69	39	66	0.4	448	87	38	17	44	0.4	186
4.5< z <5.0	185	53	26	53	0.1	317	53	28	9	35	0.1	125
5.0< z <5.5	130	42	17	42	0.0	231	34	21	5	28	0.0	88
5.5< z <6.0	91	35	10	36	0.0	172	21	17	3	24	0.0	65
Total	14062	1780	3520	1867	5.6	21235	7182	1110	2279	1272	5.6	11849

population for four flux-density thresholds at $\nu = 1$ GHz, which are representative of the typical surveys that could be conducted with the SKA1 and SKA2. However, we note that moving the frequency to around 700 MHz would lead to an increase in the field-of-view by factor of ~ 2 and an increase in the source density that scales with the spectral index, i.e. $S_\nu \propto \nu^\alpha$, with $\alpha = -0.7$ for a typical star-forming galaxy.

3. Evolution of bias for radio sources

One of the key measurements that can be extracted from surveys is knowledge of the bias of the population, i.e. how the light emitted traces the underlying dark-matter distribution. It will be very challenging to measure the evolution of the bias of radio sources from the large-scale surveys that will predominantly be used for measuring the cosmological signal, due to the lack of redshift information. However, assuming that the bias of a given source population is scale-invariant, then

PoS(AASKA14)018

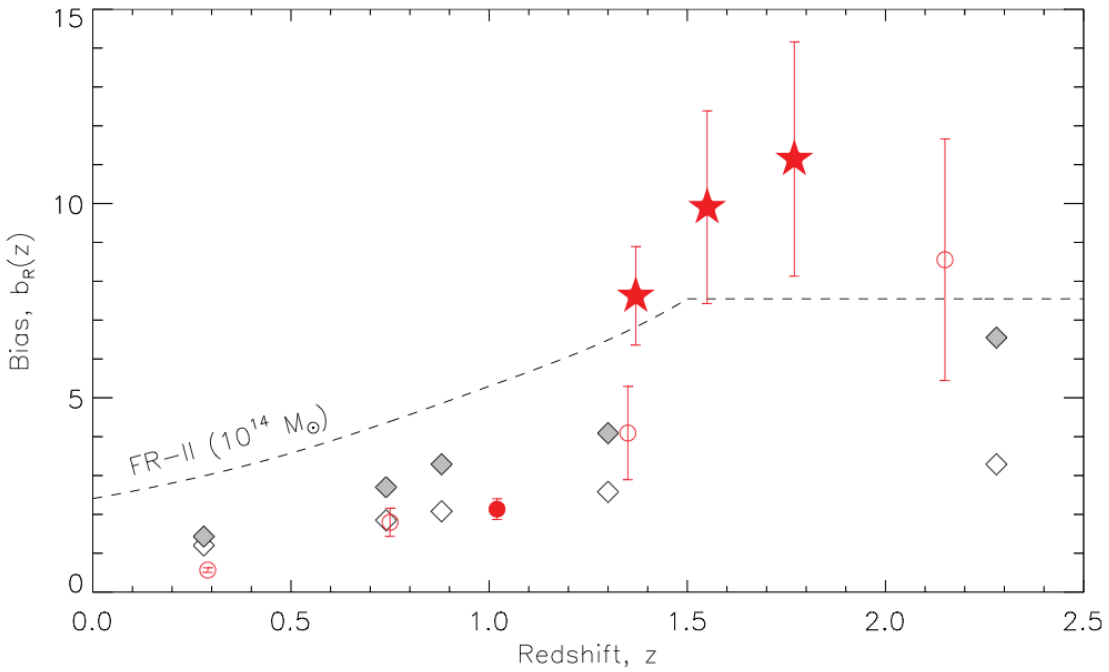

Figure 1: Linear bias of near-infrared identified radio sources as a function of median redshift. Open circles correspond to the four independent redshift bins used while the filled circle is the bias for the full sample of 766 radio sources with $Ks < 23.5$ and $S_{1.4} > 90\mu$Jy. Star symbols correspond to lower luminosity limits of 10^{23}, $10^{23.5}$ and 10^{24} W Hz^{-1} from low to high redshift. The dashed line shows the FR-II bias adopted by (Wilman et al. 2008) in the SKADS simulations, and the diamond symbols show the expected bias based on the SKADS prescriptions (open) and with the FR-I halo mass increased to 10^{14} $M_\odot$ (filled), matching the FR-IIs. Taken from Lindsay et al. (2014a).

deeper surveys with a greater degree of multi-wavelength information can be used to measure both the redshift distribution and the bias of the radio sources, in conjunction with measuring the large-scale structure for the wide-area surveys. Such data will also be important for understanding the effects that baryons have on the underlying dark matter, and how this in turn affects the clustering signal.

An initial attempt at constraining the bias of the radio source population was carried out by Lindsay et al. (2014a,b) who used a combination of wide-shallow and deep-narrow radio and optical/near-infrared survey data to determine the clustering of the radio source population in redshift shells (Figure 1). They found that the dominant AGN population, namely the low-luminosity (FRI-type sources as defined in the SKADS simulations) appear to have a higher bias than currently simulated. This provides an opportunity to use the multi-tracer technique to overcome the debilitating effects of cosmic variance on large-scale measurements of the power spectrum using various probes (Seljak 2009).

However, such work is not limited to small scales, where the ancillary data provides the radial information. With the SKA we will also be in a position to cross-correlate the radio source population with CMB-lensing maps from current (e.g. Planck Collaboration et al. 2013a; Das et al. 2014) and future CMB facilities. Some work along these lines has already been performed (Sherwin et al.

PoS(AASKA14)018

2012; Geach et al. 2013), providing a unique measurement of the bias for high-redshift quasars.

With information about the redshift distribution of the various sub-populations of radio sources (e.g. star-forming/AGN type) in any deep radio survey, then this information can inform the measurement of the bias from cross-correlating with CMB-lensing maps. This can provide a robust measurement of both the weighted bias of all populations, or if they can be morphologically distinguished (see Makhatini et al. 2015), the bias and its evolution for each individual source population.

4. Cosmological Probes

4.1 The Angular Power Spectrum

In the the absence of redshift information, the most straightforward experiment is to measure angular correlation function or power spectrum of the radio sources. Raccanelli et al. (2012) and Camera et al. (2012) have already shown that a measurement of the angular power spectrum, in combination with the CMB and supernovae Ia, can be a very useful tool to determine both the dark energy equation of state and departures from general relativity, even with the precursor surveys within reach of ASKAP, LOFAR and MeerKAT. However, to make radio surveys competitive with the largest surveys at other wavelengths then we require the combination of source density, sky area and morphological characterisation that is only feasible with the SKA.

Recently, Ferramacho et al. (2014) demonstrated that even without redshift information for the individual sources, or a subset of sources, the wide-area radio continuum surveys can play a unique role in constraining the level of non-Gaussianity. Utilising the multi-tracer technique (Seljak 2009), they showed that the different populations of radio sources, which trace the underlying dark-matter distribution with vastly different biases, can constrain the local non-Gaussian parameter f_{NL} with uncertainty $\sigma_{\mathrm{f_{NL}}} = 3.6$ for a galaxy detection flux limit of 10 μJy and $\sigma_{\mathrm{f_{NL}}} = 2.2$ for 1 μJy (Figure 2). The former survey is within reach of SKA1, but requires good resolution in order to morphologically distinguish the different classes of radio source, i.e. FRI/FRII from star-forming galaxies and radio-quiet quasars. As shown in Makhatini et al. (2015) this sort of classification is possible to very high redshift with SKA1-MID.

Therefore radio surveys with SKA1-MID, without any additional data, have the potential to constrain primordial non-Gaussianity to a factor of ~ 2 better than the present constraints obtained with Planck. This leads to the possibility of obtaining $\sigma_{\mathrm{f_{NL}}} = 2.2$ with SKA2 (Figure 2).

Furthermore, the late time ISW effect allows us to strongly constrain a class of models that can have w_0 and w_a very similar to a quintessence model, or even to ΛCDM, but that allows for viscous pressure. The set of models that are called unified dark sector models or similar (e.g. a single viscous dark fluid) could in principle resemble LCDM in w_a and w_0, and produce a much larger ISW effect (see e.g. Li & Barrow 2009; Velten & Schwarz 2011).

4.2 Cosmic Dipole, Isotropy and Homogeneity

All-sky continuum surveys with the SKA will probe large angular scales at a median redshift of order unity. This will allow tests of fundamental assumptions of modern cosmology, especially of statistical isotropy. Combined with spectroscopic redshifts, either from SKA HI surveys, or by means of other instruments, statistical homogeneity of the cosmos will be tested. SKA will allow

PoS(AASKA14)018

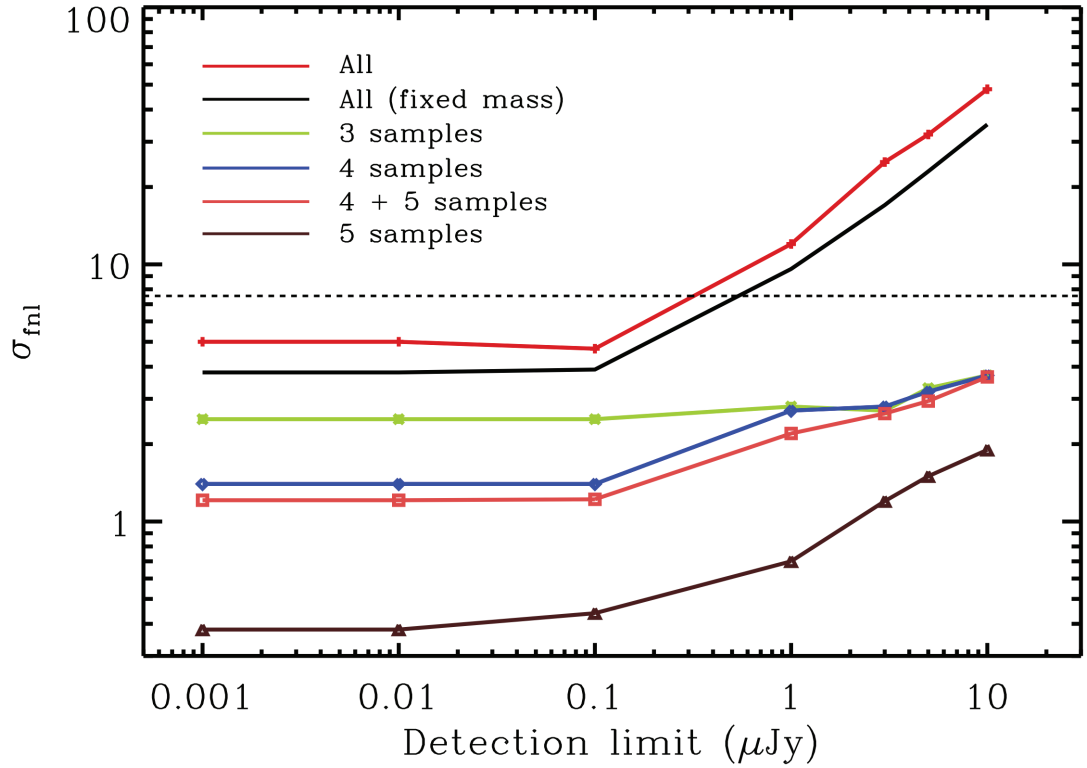

Figure 2: Forecast constraints on f_{NL} obtained with the multi-tracer method as a function of the flux-density threshold used to detect galaxies. The various populations considered are FR-I and FR-II radio galaxies, radio-quiet quasars, star-forming galaxies and starburst galaxies, with different biases, as described in both Wilman et al. (2008) and Ferramacho et al. (2014). We present the results obtained using the full sample of objects with an averaged effective bias and those obtained using the combination of 3 populations of radio galaxies (where SRG, SB and RQQ correspond to one population group), using 4 populations (where only SFG and SB are undifferentiated) and with a selection of 5 populations for $z < 1$ and 4 populations for $z > 1$ (again with undifferentiated SFG and SB). We also show the result for the ideal case where all 5 populations could be differentiated over the entire redshift range of the survey. The horizontal line represents the best constraint obtained by the Planck collaboration (Planck Collaboration et al. 2013c). Taken from Ferramacho et al. (2014).

us to study scales at $z \sim 1$ that have not been in causal contact since the first horizon crossing during inflation, and therefore contain information that was frozen in during cosmological inflation.

SKA all-sky surveys will allow the measurement of the cosmic radio dipole almost as precisely as the CMB dipole. SKA1 will constrain the cosmic radio dipole direction with an accuracy better than 5 degrees (Fig. 3), and SKA2 within a degree (at 99 per cent C.L.). Compared to todays best estimate based on NVSS data, this will be an improvement of a factor of 100 in the accuracy of the cosmic radio dipole direction for SKA1. This measurement could firmly establish or refute the commonly adopted assumption that the CMB and the overall large-scale structure frames agree.

The CMB exhibits unexpected features at the largest angular scales, among them a lack of angular correlation, alignments between the dipole, quadrupole and octopole, hemispherical asymmetry, a dipolar power modulation, and parity asymmetries (Planck Collaboration et al. 2013b;

PoS(AASKA14)018

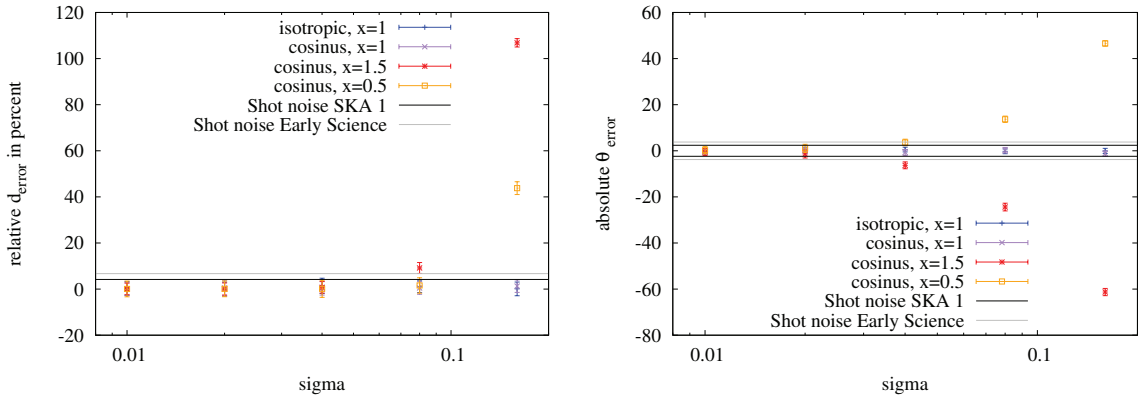

Figure 3: Left: Accuracy (in per cent) of the measurement of the dipole amplitude as function of fractional error on flux density calibration on individual point sources (sigma). All points are based on 100 simulations. Right: Accuracy (in degrees) of the measurement of the dipole direction. The horizontal lines denote the error due to shot noise for a dipole estimate based on 8×10^7 sources (SKA Early Science) and 2×10^8 sources (SKA1). See Schwarz et al. (2015) for further details.

Copi et al. 2013a,b). Understanding the statistical significance of these anomalies is crucial, as a lack of statistical isotropy or Gaussianity could rule out the standard cosmological model.

The precision of these CMB measurements is limited by our understanding of the foregrounds, and observational uncertainties are already much smaller than the cosmic variance at such scales. Therefore, it is very difficult to identify the cause of these anomalies without an independent probe at the same scales.

The angular two-point correlation at angles > 60 degrees from SKA continuum surveys, as well as the reconstruction and cross-correlation of low multipoles will offer further insight into these puzzles, see Schwarz et al. (2015).

Supplemented with spectroscopic information, several tests of homogeneity can be envisaged. One possibility is to probe a consistency relation of Friedmann-Lemaître models, which involves the dimensionless comoving distance, the Hubble rate, and their derivatives (Clarkson et al. 2008).

Thus, studying the large-angular scales in SKA continuum surveys might help resolve the puzzle of CMB anomalies and test the cosmological principle.

4.3 BAO and RSDs with spectroscopic follow-up of emission-line sources

Although not a primary case for the SKA, radio continuum sources are, by definition, active and exhibit emission lines in their optical spectra. This property can be utilised to perform efficient follow-up spectroscopy with the next generation of optical and near-infrared spectrographs, in much the same way that the WiggleZ survey targeted UV-bright sources (e.g. Blake et al. 2012). Such follow-up would provide an efficient method for extracting precise redshift information for a very large number of sources over a large fraction of the sky. This could provide new and robust measurements of the Baryon Acoustic Oscillations up to high-redshift (potentially targeting emission line objects at $z > 2$), as well as redshift-space distortions.

Rather than a key driver for the SKA, this demonstrates a unique synergy, and something that is planned to be tested by combining the LOFAR extragalactic surveys with the new multi-object

PoS(AASKA14)018

spectrographs (MOS) that are currently in development (see Section 5).

4.4 Integrated Sachs-Wolfe Effect

The ISW effect (Sachs & Wolfe 1967) manifests itself in the correlation between large-scale structure and CMB temperature. In an Einstein-de Sitter universe, the energy gained by a photon falling into a gravitational potential well is exactly cancelled out by the energy lost upon climbing out of the well. In a universe with a dark energy component or modified gravity to the same effect, the local gravitational potential varies with time, and potential wells are stretched throughout the crossing time of the photons. This disparity between the potential on entry and exit imparts a net blueshift on the incident photon and, equivalently, an increase in photon temperature. Specifically, this effect is important at late times ($z \lesssim 1$), once the Universe had begun its transition towards a dominant dark energy component and accelerated expansion. The ISW signal is small, compared to the intrinsic temperature anisotropies in the CMB, acting on large scales where cosmic variance most affects CMB uncertainties, and so cross-correlation with local large-scale structure, with extensive sky coverage, is required in order to produce a significant result. Giannantonio et al. (2012) discuss the current state of ISW measurements, and potential problems. While several detections of the ISW effect had been made previously, cross-correlating the CMB maps from the Wilkinson Microwave Anisotropy Probe (WMAP) with radio, infrared, optical, and X-ray surveys (for results using radio surveys see e.g. Nolta et al. 2004; Raccanelli et al. 2008), these were all at rather low significance. Giannantonio et al. (2008) reached an increased significance of $\sim 4.5\sigma$ by combining surveys to develop a fuller catalogue of local large-scale structure. With the latest CMB measurements from the Planck satellite, and corresponding all-sky surveys of massive, low-redshift galaxies (and an understanding of their relationship to the underlying dark matter distribution), the ISW could be a powerful cosmological tool (Figure 4; Raccanelli et al. 2014).

4.5 Cosmic Magnification Bias

The presence of mass alters the geodesic followed by light rays, causing the deflection of those rays along the line of sight when passing by intervening large-scale structure. This causes distortions and magnification in the observed images of distant astronomical sources, and is known as gravitational lensing. The shape distortion of the background galaxies ('cosmic shear') can be used to constrain some cosmological parameters (see below, section 4.6), as can the magnification of background sources by foreground lensing structures ('cosmic magnification').

This magnification is governed by two effects. The increased flux received from distant sources due to lensing has the effect of bringing into the survey sources which would otherwise have been too faint to be detected. The lensing also stretches the solid angle, reducing the apparent surface density of the lensed background sources. Gravitational lensing should, therefore, leave a cosmic magnification signal in the angular cross-correlation function of two samples of sources with non-overlapping redshift distributions, since the foreground sample lenses the background sample. This signal, the magnification bias, is dependent on the balance struck between the loss of sources due to dilution, and the gain due to flux magnification.

Using the galaxy-quasar cross-correlation function, Scranton et al. (2005) made an 8σ detection of the cosmic magnification signal of quasars lensed by foreground galaxies, both selected

PoS(AASKA14)018

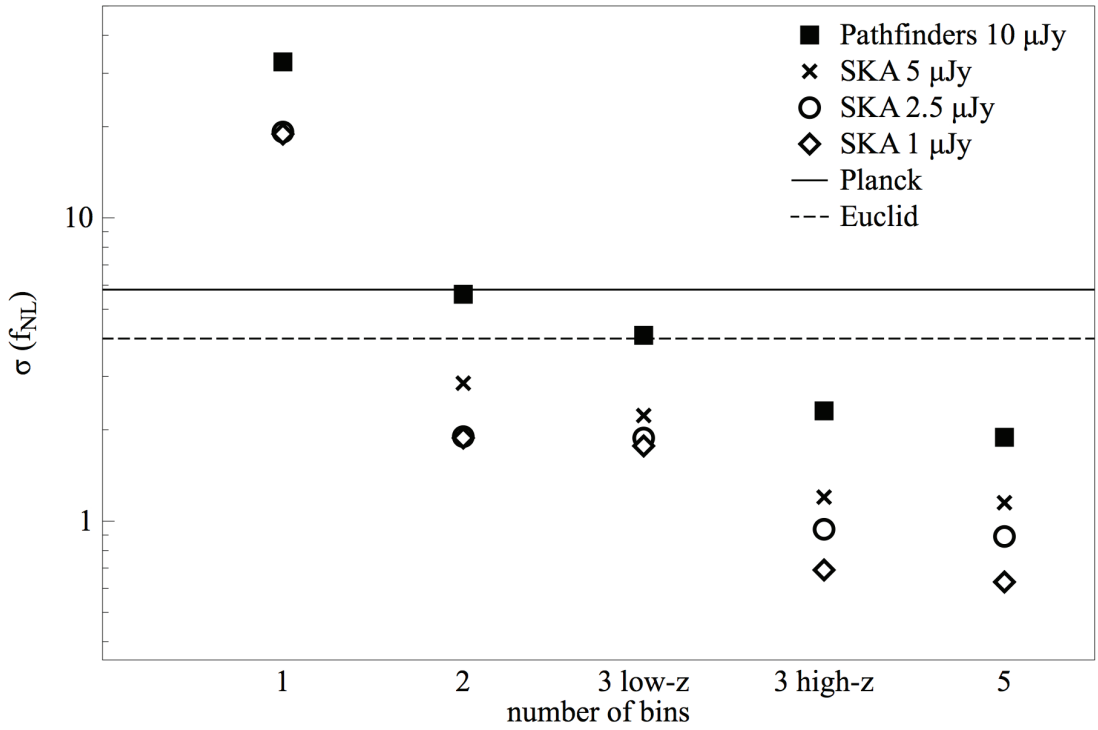

Figure 4: Constraints on ($f_{\rm NL}$) with integrated Sachs-Wolfe measurements using SKA continuum surveys. The effect of having several redshift bins for the measurements of the $f_{\rm NL}$ parameter for different flux-density limits that will be possible for various stages of the SKA. For full details see Raccanelli et al. (2014).

from the Sloan Digital Sky Survey (SDSS). They found that bright quasars, with steep source counts, exhibited an excess around foreground structure, and faint quasars, with shallow source counts were in deficit. Since this first success, Hildebrandt, van Waerbeke & Erben (2009) have made detections with normal galaxies from the Canada-France-Hawaii Telescope Legacy Survey (CFHTLS), and Wang et al. (2011) have done likewise in the far-infrared with *Herschel*.

Raccanelli et al. (2012) have shown that the cosmic magnification signal in SKA pathfinders can contribute to cosmological constraints; the cross-correlations envisioned there are between radio surveys (for the background sample) and optical surveys such as SDSS (for the foreground sample, and removal of radio foreground). With SKA1 and SKA2, the continuum survey can provide the background sample, while the HI survey can provide the foreground sample and removal of radio foreground (in combination with optical surveys such as Euclid and/or LSST). This will allow us to provide constraints on bias, dark energy and gravity parameters, with a method quite different from lensing autocorrelation of source shapes; this affords an important check on systematic effects which could enter into shape measurement.

4.6 Weak Lensing

Weak gravitational shear is the coherent distortion in the shapes of distant galaxies due to the deflection of light rays by intervening mass distributions. Measurements of the effect on large scales is termed "cosmic shear" and has emerged as a powerful probe of late-time cosmology over

PoS(AASKA14)018

the last 15 years (e.g. Heymans et al. 2012). Since gravitational lensing is sensitive to the *total* (i.e. dark plus baryonic) matter content of the Universe, it has great potential as a very robust cosmological probe, to a large degree insensitive to the complications of galaxy formation and galaxy bias. One of the most promising aspects of weak lensing measurements is their combination with redshift information: such measurements are then a sensitive probe of both the geometry of the Universe and the evolution of structure over the course of cosmic time. In turn, these latter effects are dependent on the nature of the dominant dark energy component in the Universe and/or on modifications to the theory of General Relativity on large scales.

To date, the field of weak lensing has largely been the preserve of optical surveys due to the much larger number densities of background galaxies achieved in such surveys. However, this will change with the advent of the Square Kilometre Array, which will reach galaxy number densities of up to ~ 10 galaxies arcmin^{-2} with SKA1 and ~ 75 galaxies arcmin^{-2} with SKA2 (Figure 5). In addition, as described in the weak lensing chapter in this volume (Brown et al. 2015), the radio offers truly unique approaches to measuring weak lensing that are (i) not available to optical surveys and (ii) potentially extremely powerful in minimising the most worrying systematic effects in weak lensing cosmology. In particular, the PSF of an interferometer is completely deterministic (at least at the mid frequencies of the SKA), and the intrinsic synchrotron spectrum is smooth and featureless, thus the colour-dependent PSF should be far more straightforward to account for, cf. broad-band optical imaging. Moreover, using complementary radio shape information, along with polarisation information, which will be measured by default in the SKA continuum surveys, will help to control shape measurement systematics and the impact of intrinsic alignments. For SKA1 the radio continuum surveys will therefore be very complementary to the next generation of optical weak-lensing surveys from both the ground (e.g. DES) and space (e.g. *Euclid*).

In the longer term, surveys with SKA2 will extend the reach of weak lensing beyond that of the optical mega-surveys of LSST and *Euclid*. First, the typical redshifts probed by SKA surveys will go beyond that of optical surveys. In addition, the size of survey which SKA will be capable of achieving will by $\simeq 30,000$ deg^2, twice that of Euclid and only rivalled (or complemented) by LSST (see Figure 5).

However, as highlighted in (e.g. Patel et al. 2015) shape measurement at radio wavelengths need a similar effort to that spent in extracting shear estimates from ground-based optical surveys.

5. The multi-wavelength requirements

5.1 Spectroscopic redshifts

As with most cosmological measurements, greater accuracy can be achieved if higher precision redshifts can be obtained. In particular, using radio sources as targets for next generation MOS facilities could make such surveys highly efficient due to the higher likelihood of obtaining redshifts from emission lines.

As detailed in Jarvis et al. (2015) the future MOS facilities such as MOONS (Cirasuolo et al. 2012, 2014), Prime Focus Spectrograph (PFS; Takada et al. 2014) and the Maunakea Spectroscopic Explore [1] (MSE) will provide a very good complement to SKA surveys, albeit only over around

[1] http://mse.cfht.hawaii.edu

PoS(AASKA14)018

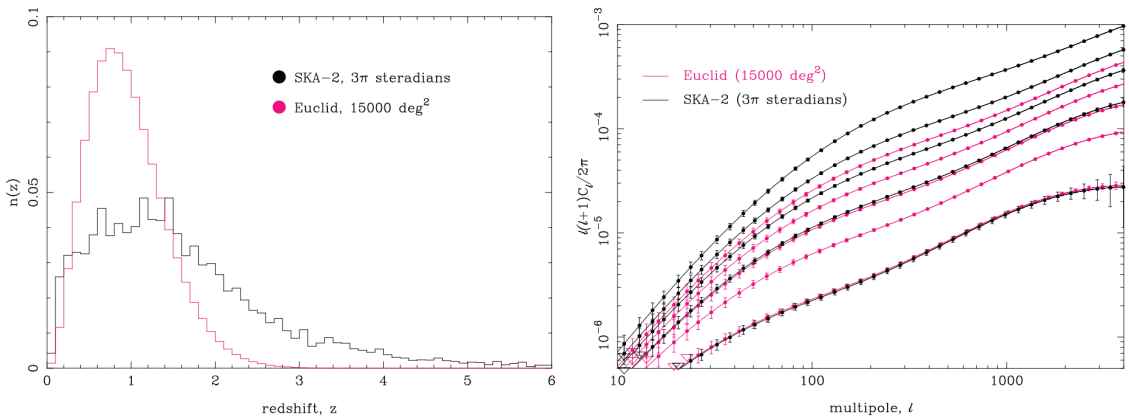

Figure 5: Left panel: The redshift distribution of source galaxies for a 3π steradian weak lensing survey with the full SKA. Also shown is the redshift distribution for the 15,000 deg^2 survey with *Euclid* . The n(z) extends to higher redshifts in the radio survey and probes a greater range of cosmic history. Right panel: The corresponding constraints on a 5-bin tomographic power spectrum analysis. For both experiments, an RMS dispersion in ellipticity measurements of $\gamma_{\rm rms} = 0.3$ is assumed, and the tomographic bins have been chosen such that the bins are populated with equal numbers of galaxies. Open triangles denote 1σ upper limits on a bandpower. Note that only the auto power spectra in each bin are displayed though much cosmological information will also be encoded in the cross-correlation spectra between the different $z-$bins. See Brown et al. (2015) for more information.

half of the SKA sky for both PFS and MSE due to them being sited in Hawaii. For the wider surveys, 4MOST (de Jong et al. 2012) would provide a basis for obtaining redshifts for the brighter star-forming galaxies, predominantly in the low-redshift Universe.

5.2 Photometric redshifts

The bulk of the radio sources detected at these faint levels will be too faint at optical wavelengths to obtain spectroscopic redshifts. We will therefore be reliant on photometric redshifts. In the early phases this will be from surveys that are currently underway (e.g. McCracken et al. 2012; Jarvis et al. 2013; de Jong et al. 2013; Edge et al. 2013; Banerji et al. 2014).

As we move to the full operation of SKA1 then we should also have LSST (see Bacon et al. 2015) and *Euclid* (see Kitching et al. 2015), which will provide very deep imaging from the g-band through to H-band across a large swathe of the southern sky.

6. Survey requirements for SKA1

6.1 Deep

Although the main cosmological science will come from large-area surveys with the SKA, it is also important to conduct a deep survey with the best ancillary data available. As outlined in various chapters (e.g. Jarvis et al. 2015; McAlpine et al. 2015; Takahashi et al. 2015; Bacon et al. 2015), deep fields covered with the LSST will be prime candidates for undertaking a deep radio-continuum survey. Such data will allow accurate photometric redshifts, and therefore the $N(z)$ of the radio sources to be determined to a flux-density limit much fainter than possible over the wider

PoS(AASKA14)018

area. Using these data will act as a benchmark for the assumptions needed for fully exploiting the wide-area surveys. The key issue is that the cosmic volume surveyed should be representative and not suffer significantly from sample variance, which could act to skew the redshift distribution if large-scale structures dominate certain redshift slices. Moreover, such deep-fields provide us with the necessary information to understand how the radio sources trace the dark-matter distribution as we move from the single-halo term to the two-halo term at a few Mpcs.

In order to reach the requisite depth, to gain insights into the source population as a function of redshift from morphological classification, and to conduct the most efficient deep survey, SKA1-MID would be the facility of choice for this tier. This is because SKA1-SUR has a field-of-view much larger than the individual deep-drilling fields that will be targeted by the LSST, which are of order 10 deg^2. Furthermore, the resolution required, at the relatively low frequency that such a survey needs to be conducted to reach the requisite source density/depth, in order to classify objects morphologically, would be extremely difficult to achieve with SKA1-SUR (for details see Jarvis et al. 2015).

6.2 Medium-deep

In practice, it will be necessary to add to the deep surveys to overcome sample variance, particular for the most highly-biased populations at moderate redshifts. However, the key driver for a medium-deep survey with SKA1 is to undertake the first wide-area weak lensing survey at radio wavelengths. As detailed in Brown et al. (2015), a survey covering ~ 5000 deg^2 to ~ 1 μJy rms in Band 2, will provide excellent constraints on the power spectrum that are very complementary to weak-lensing surveys being conducted at optical wavelengths on a similar timescale.

6.3 Wide

The key survey for measuring the largest scales in the Universe is obviously a survey that can cover as much cosmological volume as possible. First, given that distant radio sources can be found in relatively shallow surveys due to their extreme brightness, then area is initially more important than extreme depth, and conducting an all-sky survey very early in the expansion up to SKA1 would be extremely beneficial for cosmology applications.

In terms of which element of SKA1 is the best for such a survey, then the question is more open than for the deep and medium-deep tiers, as the areal coverage benefits from the large field-of-view offered by SKA1-SUR, allowing in principle the survey to be conducted on a shorter timescale. However, the resolution of ~ 1 arcsec at 1 GHz for SKA1-SUR precludes the science that requires the morphological characterisation of radio sources (see e.g. McAlpine et al. 2015; Makhatini et al. 2015), which is needed to exploit the multi-tracer technique and overcome the inhibiting effects of cosmic variance on the largest scales (Section 4.1), or the different redshift distributions of different populations. Given that the cosmic variance is the dominant source of uncertainty on measurements of the power spectrum on the largest scales, then this is a crucial issue.

Although the large scales can be probed efficiently by SKA1-SUR, the additional benefits of high-resolution imaging, which pave the way for using the multi-tracer method using SKA1-MID, provide a unique probe of the largest scales. Given that SKA1-MID is required to conduct the weak lensing survey, and the expansion to all sky for SKA1-MID does not present a large increase in

PoS(AASKA14)018

survey time compared to SKA1-SUR (a SKA1-MID survey can be carried out at lower frequency, < 1 GHz, thus increasing the size of the primary beam, while still retaining the requisite resolution for morphological characterisation of the radio sources), then it would make sense to conduct even the widest of surveys with SKA1-MID.

7. Towards SKA2

As we move towards SKA2 then the ability to conduct a world-leading weak lensing survey with completely different systematics to any optical survey becomes very compelling. A source density of ~ 75 sources per arcmin^2 over 3π steradians is within reach (assuming a detection threshold of $S_{1\ \mathrm{GHz}} \geq 100$ nJy), eclipsing the source density from current surveys, such as the Dark Energy Survey (e.g. Banerji et al. 2014), and is higher density than *Euclid* will have. Furthermore, the PSF at radio wavelength is analytically predictable, and the additional information from polarisation (and HI rotation curves) means that the major source of uncertainty from intrinsic alignments may be overcome. Thus, SKA continuum surveys will turn radio observations into a central probe of cosmological research in the coming decades. As shown above, SKA1 may already lead to transformational findings.

8. Acknowledgments

MJJ and MGS acknowledges support by the South African Square Kilometre Array Project, the South African National Research Foundation. MGS also acknowledges support from FCT grant PTDC/FIS-AST/2194/2012.

References

Bacon, D. et al.. 2015, “Synergy between the Large Synoptic Survey Telescope and the Square Kilometre Array”, in Advancing Astrophysics with the SKA, PoS(AASKA14)145

Banerji, M. et al.. 2014, ArXiv.1407.3801

Blake, C. et al.. 2012, MNRAS, 425, 405

Brown, M. et al.. 2015, “Weak gravitational lensing with the Square Kilometre Array”, in Advancing Astrophysics with the SKA, PoS(AASKA14)023

Bull, P., Camera, S., Raccanelli, A., et al.. 2015, “Measuring baryon acoustic oscillations with future SKA surveys”, in Advancing Astrophysics with the SKA, PoS(AASKA14)024

Camera, S., Santos, M. G., Bacon, D. J., Jarvis, M. J., McAlpine, K., Norris, R. P., Raccanelli, A., & Röttgering, H. 2012, MNRAS, 427, 2079

Cirasuolo, M. et al.. 2012, in Society of Photo-Optical Instrumentation Engineers (SPIE) Conference Series, Vol. 8446, Society of Photo-Optical Instrumentation Engineers (SPIE) Conference Series

Cirasuolo, M. et al.. 2014, in Society of Photo-Optical Instrumentation Engineers (SPIE) Conference Series, Vol. 9147, Society of Photo-Optical Instrumentation Engineers (SPIE) Conference Series, 0

Clarkson, C., Bassett, B., & Lu, T. H.-C. 2008, Physical Review Letters, 101, 011301

PoS(AASKA14)018

Condon, J. J., Cotton, W. D., Fomalont, E. B., Kellermann, K. I., Miller, N., Perley, R. A., Scott, D., Vernstrom, T., & Wall, J. V. 2012, ApJ, 758, 23
Condon, J. J., Cotton, W. D., Greisen, E. W., Yin, Q. F., Perley, R. A., Taylor, G. B., & Broderick, J. J. 1998, AJ, 115, 1693
Copi, C. J., Huterer, D., Schwarz, D. J., & Starkman, G. D. 2013a, ArXiv.1310.3831
—. 2013b, ArXiv.1311.4562
Das, S. et al.. 2014, JCAP, 4, 14
de Jong, J. T. A. et al.. 2013, The Messenger, 154, 44
de Jong, R. S. et al.. 2012, in Society of Photo-Optical Instrumentation Engineers (SPIE) Conference Series, Vol. 8446, Society of Photo-Optical Instrumentation Engineers (SPIE) Conference Series
Edge, A., Sutherland, W., Kuijken, K., Driver, S., McMahon, R., Eales, S., & Emerson, J. P. 2013, The Messenger, 154, 32
Ferramacho, L. D., Santos, M. G., Jarvis, M. J., & Camera, S. 2014, MNRAS, 442, 2511
Geach, J. E. et al.. 2013, ApJL, 776, L41
Giannantonio, T., Crittenden, R., Nichol, R., & Ross, A. J. 2012, MNRAS, 426, 2581
Giannantonio, T., Scranton, R., Crittenden, R. G., Nichol, R. C., Boughn, S. P., Myers, A. D., & Richards, G. T. 2008, Phys. Rev. D, 77, 123520
Heymans, C. et al.. 2012, MNRAS, 427, 146
Jarvis, M. J. et al.. 2013, MNRAS, 428, 1281
Jarvis, M. J. et al.. 2015, "The star-formation history of the Universe with the SKA", in Advancing Astrophysics with the SKA, PoS(AASKA14)068
Kitching, T. et al.. 2015, "Euclid-SKA Synergies", in Advancing Astrophysics with the SKA
Li, B. & Barrow, J. D. 2009, Phys. Rev. D, 79, 103521
Lindsay, S. N., Jarvis, M. J., & McAlpine, K. 2014a, MNRAS, 440, 2322
Lindsay, S. N. et al.. 2014b, MNRAS, 440, 1527
Makhatini, S., Smirnov, O., Jarvis, M., & Heywood, I. 2015, "Morphological classification of radio sources for galaxy evolution and cosmology with the SKA", in Advancing Astrophysics with the SKA, PoS(AASKA14)081
McAlpine, K. et al.. 2015, "The SKA view of the Interplay between SF and AGN Activity and its role in Galaxy Evolution", in Advancing Astrophysics with the SKA, PoS(AASKA14)083
McCracken, H. J. et al.. 2012, A&A, 544, A156
Nolta, M. R. et al.. 2004, ApJ, 608, 10
Patel, P., Harrison, I., Makhatini, S., et al.., 2015, "Weak Lensing Simulations for the SKA", in Advancing Astrophysics with the SKA, PoS(AASKA14)083
Planck Collaboration et al.. 2013a, ArXiv.1303.5077
—. 2013b, ArXiv.1303.5083
—. 2013c, ArXiv.1303.5084
Raccanelli, A., Bonaldi, A., Negrello, M., Matarrese, S., Tormen, G., & de Zotti, G. 2008, MNRAS, 386, 2161
Raccanelli, A. et al.. 2014, ArXiv.1406.0010
—. 2012, MNRAS, 424, 801
Sachs, R. K. & Wolfe, A. M. 1967, ApJ, 147, 73

PoS(AASKA14)018

Schwarz, D. et al.. 2015, "Testing foundations of modern cosmology with SKA all-sky surveys", in Advancing Astrophysics with the SKA, PoS(AASKA14)032
Seljak, U. 2009, Physical Review Letters, 102, 021302
Sherwin, B. D. et al.. 2012, Phys. Rev. D, 86, 083006
Takada, M. et al.. 2014, PASJ, 66, 1
Takahashi, K. et al.. 2015, "Overview of Complementarity and Synergy with Other Wavelengths in Cosmology in the SKA era", in Advancing Astrophysics with the SKA, PoS(AASKA14)159
Velten, H. & Schwarz, D. J. 2011, JCAP, 9, 16
Wilman, R. J., Jarvis, M. J., Mauch, T., Rawlings, S., & Hickey, S. 2010, MNRAS, 405, 447
Wilman, R. J. et al.. 2008, MNRAS, 388, 1335
Xia, J.-Q., Viel, M., Baccigalupi, C., De Zotti, G., Matarrese, S., & Verde, L. 2010, ApJL, 717, L17

PoS(AASKA14)018

PROCEEDINGS OF SCIENCE

Cosmology with a SKA HI intensity mapping survey

Mario G. Santos[*,a,b] **Philip Bull,**[c] **David Alonso,**[d] **Stefano Camera,**[e] **Pedro G. Ferreira,**[d] **Gianni Bernardi,**[b] **Roy Maartens,**[a,f] **Matteo Viel,**[g,h] **Francisco Villaescusa-Navarro,**[g,h] **Filipe B. Abdalla,**[i,j] **Matt Jarvis,**[d,a] **R. Benton Metcalf,**[k] **A. Pourtsidou,**[k,f] **Laura Wolz,**[i]

[a] *Department of Physics, University of Western Cape, Cape Town 7535, South Africa*
[b] *SKA SA, The Park, Park Road, Cape Town 7405, South Africa*
[c] *Institute of Theoretical Astrophysics, University of Oslo, 0315 Oslo, Norway*
[d] *Astrophysics, University of Oxford, Oxford OX1 3RH, UK*
[e] *CENTRA, Instituto Superior Técnico, Universidade de Lisboa, Lisboa 1049-001, Portugal*
[f] *Institute of Cosmology & Gravitation, University of Portsmouth, Portsmouth PO1 3FX, UK*
[g] *INAF, Astronomical Observatory of Trieste, 34131 Trieste, Italy*
[h] *INFN, Sezione di Trieste, 34100 Trieste, Italy*
[i] *Department of Physics & Astronomy, University College London, London, WC1E 6BT, U.K.*
[j] *Department of Physics and Electronics, Rhodes University, PO Box 94, Grahamstown, 6140, South Africa*
[k] *Dipartimento di Fisica e Astronomia, Universitá di Bologna, 40127 Bologna, Italy*

E-mail: mgrsantos@uwc.ac.za

HI intensity mapping (IM) is a novel technique capable of mapping the large-scale structure of the Universe in three dimensions and delivering exquisite constraints on cosmology, by using HI as a biased tracer of the dark matter density field. This is achieved by measuring the intensity of the redshifted 21cm line over the sky in a range of redshifts without the requirement to resolve individual galaxies. In this chapter, we investigate the potential of SKA1 to deliver HI intensity maps over a broad range of frequencies and a substantial fraction of the sky. By pinning down the baryon acoustic oscillation and redshift space distortion features in the matter power spectrum – thus determining the expansion and growth history of the Universe – these surveys can provide powerful tests of dark energy models and modifications to General Relativity. They can also be used to probe physics on extremely large scales, where precise measurements of spatial curvature and primordial non-Gaussianity can be used to test inflation; on small scales, by measuring the sum of neutrino masses; and at high redshifts where non-standard evolution models can be probed. We discuss the impact of foregrounds as well as various instrumental and survey design parameters on the achievable constraints. In particular we analyse the feasibility of using the SKA1 autocorrelations to probe the large-scale signal.

Advancing Astrophysics with the Square Kilometre Array
June 8-13, 2014
Giardini Naxos, Italy

[*] Speaker.

PoS(AASKA14)019

1. Introduction

The cosmic microwave background (CMB) has been one of the main observational tools for cosmology in recent years. Although basically only giving 2-dimensional information, we were able to constrain the standard cosmological model with great accuracy (Planck Collaboration 2013). This "high precision cosmology" is particularly true for the “vanilla" model with 6 parameters. More parameters or non-standard models can lead to degeneracies and limit the constraining power of the CMB (for instance the w_0/w_a non-flat model). The next step towards precision cosmology and exploring novel models will need to use extra information. In particular, due to its huge information content, measurements of the 3-dimensional large-scale structure of the Universe across cosmic time will be an invaluable tool. One of the most accessible methods to probe this is through large galaxy surveys to trace the underlying dark matter distribution. Several surveys are now under way or in preparation, such as BOSS (SDSS-III), DES, eBOSS, DESI, 4MOST, LSST, and the Euclid satellite. These surveys are based on imaging of a large number of galaxies at optical or near-infrared wavelengths combined with redshift information to provide a 3-dimensional position of the galaxies.

The new generation of radio telescopes now under construction will provide even larger and deeper radio continuum surveys, capable of detecting galaxies above redshift 3. This is particularly true for the SKA, as discussed in Jarvis et al. (2015). Although they can provide important constraints on cosmological parameters, they still lack redshift information from the radio that would provide further improvements on the constraints, in particular for the dark energy evolution. A solution is to use the hydrogen 21cm line to provide the redshift information. Telescopes probing the sky between a rest frequency of 1420 MHz and 250 MHz would be able to detect galaxies up to redshift 5. The problem is that this emission line is usually quite weak: at $z = 1.5$, most galaxies with a HI mass of $10^9\,M_\odot$ will be observed with a flux density of $\sim 1\,\mu$Jy using the HI line.

In order to obtain “game changing" cosmological constraints, we showed in Santos et al. (2015) that experiments with sensitivities better than $10\,\mu$Jy over 10 kHz channels will then be required to provide enough galaxies to beat shot noise and become cosmic variance dominated. Although “near term" radio telescopes such as ASKAP and MeerKAT should be able to achieve such sensitivities on deep single pointings, it will require a much more powerful telescope such as SKA Phase 2, to integrate down to the required sensitivity over the visible sky in a reasonable amount of time. This would imply that one would need to wait until then to use radio telescopes for cosmology.

Galaxy surveys are threshold surveys in that they set a minimum flux above which galaxies can be individually detected. Instead we could consider measuring the integrated 21cm emission of several galaxies in one angular pixel on the sky and for a given frequency resolution. For a reasonably large 3d pixel we expect to have several HI galaxies in each pixel so that their combined emission will provide a larger signal. Moreover we can use statistical techniques, similar to those that have been applied for instance to CMB experiments, to measure quantities in the low signal to noise regime. By not requiring the detection of individual galaxies, the specification requirements imposed on the telescope will be much less demanding. This is what has been commonly called an “intensity mapping" experiment. It is similar to what is being planned for experiments aimed at probing the Epoch of Reionization (at $z > 6$), such as the ones using the radio telescopes

PoS(AASKA14)019

LOFAR, MWA and PAPER. By not requiring galaxy detections, the intensity mapping technique transfers the problem to one of foreground cleaning: how to develop cleaning methods to remove everything that is not the HI signal at a given frequency. This in turn also impacts on the calibration requirements of the instrument.

This chapter describes the HI intensity mapping surveys that are feasible with the SKA, listing the assumed telescope specifications as well as the corresponding sensitivity and the different cosmological constraints that can be achieved. A discussion of foreground contamination and calibration requirements is also included. For a summary of the expected cosmological constraints with SKA1 intensity mapping surveys, we refer the reader to section 7 and in particular Fig. 5.

2. The signal

After reionization, most neutral hydrogen will be found in dense systems inside galaxies, e.g. Damped Lyman-alpha Absorbers (DLAs). In terms of the brightness temperature, the average signal over the sky can be written as:

$$\overline{T}_b(z) \approx 566h \left(\frac{H_0}{H(z)}\right)\left(\frac{\Omega_{\rm HI}(z)}{0.003}\right)(1+z)^2\ \mu{\rm K}, \tag{2.1}$$

where the neutral hydrogen density fraction is given by

$$\Omega_{\rm HI}(z) \equiv (1+z)^{-3}\rho_{\rm HI}(z)/\rho_{c,0}, \tag{2.2}$$

$\rho_{\rm HI}(z)$ is the proper HI density and $\rho_{c,0}$ the critical density of the Universe at redshift zero. Figure 1 shows constraints on $\Omega_{\rm HI}(z)$ from different experiments. At low redshifts, it is measured using 21 cm observations directly from galaxies (except the GBT point which uses intensity mapping). At high redshifts, $\Omega_{\rm HI}$ is estimated by computing the HI associated with Damped Lyman-α systems observed in absorption in quasar spectra. These systems are easy to identify, given their prominent damping wings in both high-resolution and low-resolution data even at low signal-to-noise, and a HI column density is inferred by Voigt profile fitting. This is in turn easily translated into a value for $\Omega_{\rm HI}$. Present constraints infer a constant $\Omega_{\rm HI}$ at $z = 2-4$, while at higher redshift this value is expected to increase, as the Universe is becoming more neutral. For a recent summary of observed trends we refer to Padmanabhan et al. (2014)

Assuming the signal is linear with respect to the underlying dark matter fluctuations, the total brightness temperature at a given position on the sky and frequency will be

$$T_b(\nu,\Omega) \approx \overline{T}_b(z)\Big[1 + b_{\rm HI}\delta_m(z) - \frac{1}{H(z)}\frac{dv}{ds}\Big]. \tag{2.3}$$

The signal will then be completely specified once we find a prescription for the HI density and bias function ($b_{\rm HI}$). This can be obtained by making use of the halo mass function, $\frac{dn}{dM}$ and relying on a model for the amount of HI mass in a dark matter halo of mass M, e.g. $M_{\rm HI}(M)$, so that

$$\rho_{\rm HI}(z) = \int_{M_{\rm min}}^{M_{\rm max}} dM \frac{dn}{dM}(M,z)\, M_{\rm HI}(M,z), \tag{2.4}$$

$$b_{\rm HI}(z) = \rho_{\rm HI}^{-1}\int_{M_{\rm min}}^{M_{\rm max}} dM \frac{dn}{dM}(M,z)\, M_{\rm HI}(M,z)\, b(z,M), \tag{2.5}$$

PoS(AASKA14)019

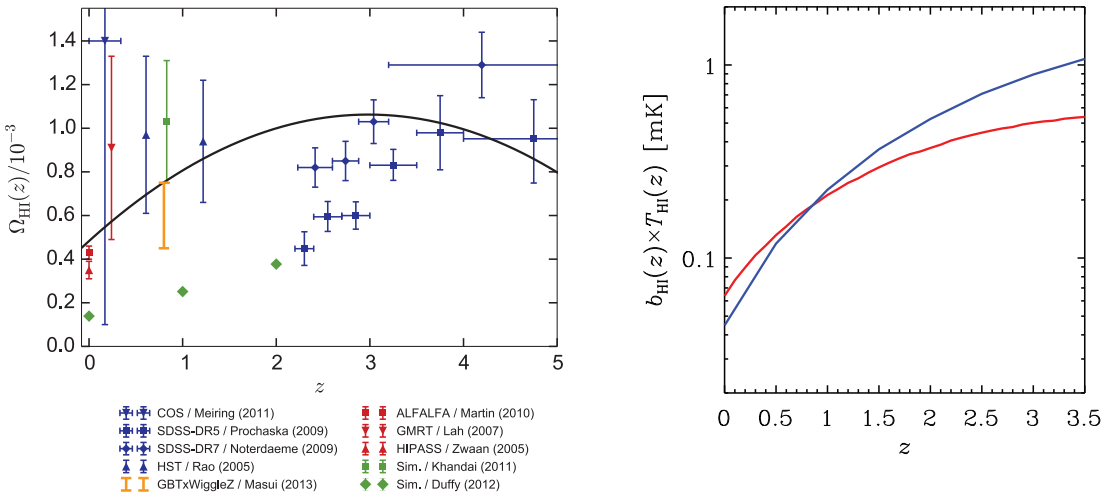

Figure 1: Left: Current constraints on the HI density fraction as a function of redshift (Meiring et al. 2011; Prochaska & Wolfe 2009; Noterdaeme et al. 2009; Rao et al. 2006; Martin et al. 2010; Lah et al. 2007; Zwaan et al. 2005; Khandai et al. 2011), partially based on the compilation in Duffy et al. (2012). DLA observations are shown in blue, cross-correlations in orange, other observations in red, and simulations in green. The thick black line shows $\Omega_{\rm HI}(z)$ from the fiducial model power law used throughout this chapter. Right: Evolution of the brightness temperature times bias with redshift for the linear (red curve) and our fiducial power-law model (blue).

where the halo mass function, $\frac{dn}{dM}$, should be in proper units and $b(z,M)$ is the halo bias.

Some concerns might arise due to the possible stochastic behaviour of the function $M_{\rm HI}(M)$ or its dependence with the environment (so that it would be a function of position also). However, given the low resolution pixels used in HI intensity mapping experiments, we expect a large number of HI galaxies per pixel, which should average-down any fluctuations and allow us to take the above deterministic relation for the mass function. For example, for the typical scales we are interested in Cosmology, one needs angular/frequency resolutions of around 1 degree and 5 MHz respectively, which translates into a comoving volume of $\sim 10^5$ Mpc^3. In each volume element, we expect a total of around 10^6 dark matter halos with mass between $10^8 - 10^{15} M_\odot$, and $\sim 31,000$ with masses between 5×10^9 and $1\times 10^{12} M_\odot$ (where the latter range corresponds to halos expected to contain most of the HI mass). This supports our assumption of a position-independent HI mass function due to the averaging over many halos. Some level of stochasticity could still increase the shot noise of the signal, but this is expected to be quite small.

For the mass function, the most straightforward "ansatz" would be to assume that it is proportional to the halo mass – the constant of proportionality can then be fitted to the available data. Even in this case however, we need to take into account the fact that not all halos contain galaxies with HI mass. Following Bagla et al. (2010), we can assume that only halos with circular velocities between $30 - 200$ kms^{-1} are able to host HI. This translates into a halo mass through

$$v_{\rm circ} = 30\sqrt{1+z}\left(\frac{M}{10^{10}M_\odot}\right)^{1/3} \text{kms}^{-1}. \tag{2.6}$$

PoS(AASKA14)019

Unfortunately this option fails to fit well the HI density measurements at high-z. A more evolved option would be to consider the proportionality to the mass as a function of redshift. This would at least guarantee the fit to the density measurements by construction. Throughout this chapter, we decided to consider instead a simple power law model of the halo mass (M):

$$M_{\rm HI}(M) = AM^{\alpha}, \tag{2.7}$$

which is independent of redshift. We found that a value of $\alpha \sim 0.6$ fits both the low z and high z data reasonably well. This can be seen in figure 1 (left), that shows the $\Omega_{\rm HI}(z)$ measurements and the evolution obtained from this model (solid line). The constant A is normalised to the results from Switzer et al. (2013) at $z \sim 0.8$. The right panel shows the redshift evolution for both the linear and power law model of the temperature multiplied by the bias, which is the figure of merit for the strength of the power spectrum used in the forecasts.

Another issue is whether we can assume that the bias is scale dependent. Again, as long as we restrict ourselves to large scales, this should be a reasonable assumption since we are averaging over many galaxies. Results from simulations show that the bias can be safely assumed constant for $k < 1$ h/Mpc at high redshifts (while at $z < 1$, it should be safe for $k < 0.1$ h/Mpc). Note that this bias can also be modelled using a variety of relatively simple prescriptions on top of the outputs of large volume and high resolution hydrodynamic or N-body simulations (Villaescusa-Navarro et al. 2014). These models capture the essential features of the HI distribution and aim at mimicking more complex physical effects (e.g. radiative transfer) by assigning HI to each (dark matter or gas) particle of the simulated volume. Although less sophisticated than the framework presented in Obreschkow et al. (2009), these models work remarkably well, allowing us to quantitatively address the scale dependence of the bias. They show that at $z > 2$ the HI bias steepens for scales $k > 1$ Mpc^{-1} in a way which depends on the actual HI modelling as can be seen in Fig. 2. A summary of how uncertainties in the bias signal propagate into the 21 cm HI power spectrum has been recently provided by Padmanabhan et al. (2014).

3. Simulations

There exists a number of practical challenges to intensity mapping, for instance the problem of foregrounds (see section 4 below), that must be addressed in order to maximize the amount and quality of the scientific information that can be extracted. Quantifying the exact statistical and systematic uncertainties for a practical experiment analytically can be an unsurmountable task, and as is now the trend in most cosmological observations, simulations must be used, which must describe both the cosmological signal we expect to measure and all other processes (e.g. foregrounds, instrumental effects, etc.) that may have a significant effect on the recovered data. Ideally we would want these simulations to yield the most realistic state-of-the-art description possible, however this is not always feasible if a large number of independent realizations need to be generated in order to quantify the aforementioned uncertainties. A compromise between computational speed and complexity must be met, so that enough simulations can be run, while correctly reproducing the relevant physics.

In the case of the cosmological signal for intensity mapping it is possible to accomplish this by using simplified methods to generate realizations of the matted density field that follow the correct

PoS(AASKA14)019

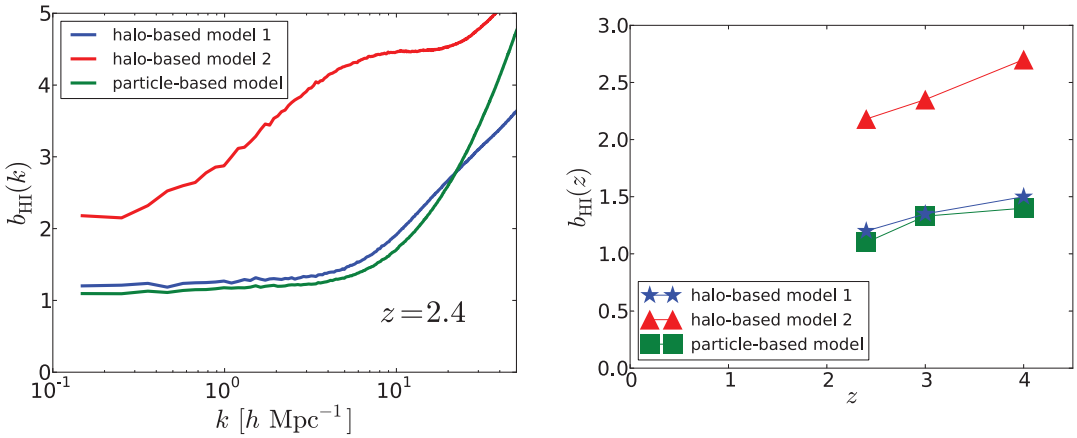

Figure 2: HI simulations from Villaescusa-Navarro et al. (2014). Left: HI bias as a function of the wavenumber at $z = 2.4$ for three different ways of modelling the HI within and outside haloes. Halo-based model 1 refers to a modification of the modelling performed by Bagla et al. (2010); halo-based model 2 is built in order to fit the recent BOSS constraints on the Damped Lyman-α systems; particle-based model is inspired by the work of Davé et al. (2013) which assigns HI both within and outside haloes and fits constraints of intergalactic medium data. Note the different scale dependence of the three models and the large bias of the halo-based model 2. Right: for the same three models we show the evolution of the HI bias with redshift in the range probed by the simulations.

distribution on large scales. Along these lines, a lot of work has been done in the last years within the community of galaxy redshift surveys on producing fast but accurate methods to generate mock simulations of the galaxy distribution (Tassev et al. 2013; White et al. 2014). One of the goals of such models is to populate dark matter haloes with a realistic distribution of neutral hydrogen. To do this, N-body or hydrodynamic simulations need to be performed at relatively high resolution to properly resolve the smallest haloes that can host HI. This framework has the following features: *i*) it is simple – we refer to Villaescusa-Navarro et al. (2014) for a comprehensive review in which three different methods based on Bagla et al. (2010) (halo based) and on Davé et al. (2013) (particle based); *ii*) it can be easily complemented by a Halo Occupation Distribution model in order to cross-correlate HI properties with those of a realistic galaxy population; *iii*) it allows us to address quantitatively the bias scale dependence (as we discussed above) and the amount of HI which could reside outside haloes; *iv*) it is bound to reproduce basic observable quantities of the HI distribution at high and low redshift (like for example Lyman-α forest absorption lines); *v*) it can be translated promptly into realistic observed HI maps, once the noise/instrumental properties are known. One recent potentially interesting finding by Font-Ribera et al. (2012) with the SDSS-BOSS survey, and using the properties of Damped Lyman-α systems, have demonstrated that HI is hosted in relatively high mass haloes. If we require the simulations to reproduce this, then the HI bias will be larger by a factor of two compared to models for which we disregard these observations (this is the halo-based model 2 of Fig. 2).

The case of the foregrounds is, however, more complicated. While it is possible to use a few datasets and certain empirical models to produce conservative realizations of the radio foregrounds (de Oliveira-Costa et al. 2008; Shaw et al. 2013; Alonso et al. 2014b), the lack of full-sky multi-frequency data prevents us from developing truly realistic simulations of the radio sky. This

PoS(AASKA14)019

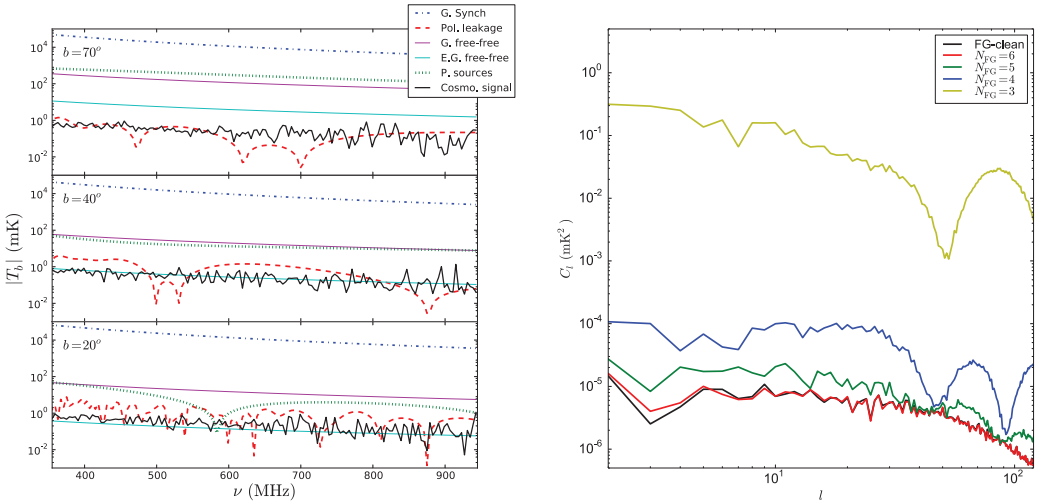

Figure 3: Left: Frequency-dependence of the different foregrounds and the cosmological signal at different galactic latitudes (given in the top right corner of each panel), according to the simulations of Alonso et al. (2014b). A 1% polarization leakage was assumed for this simulation. Right: Angular power spectrum of the foreground-cleaned temperature map at 600 MHz for different numbers of foreground degrees of freedom ($N_{\rm FG}$), using a PCA approach. The method converges to the true cosmological signal for $N_{\rm FG} = 6$.

situation will improve in the future as better quality data is obtained by the new radio observatories, which will occur at the same time as the first intensity mapping observations. Alonso et al. (2014b) have recently created a publicly available code to generate fast IM mock observations, including the cosmological signal, foregrounds and some simple instrumental effects. This code can be used, for example, to study the influence of foreground subtraction on the recovered cosmological signal, or to analyse the effects of different instrumental configurations (see figure 3).

4. Foregrounds

One of the most important challenges facing HI intensity mapping is the presence of foregrounds (both galactic and extra-galactic) with amplitudes several orders of magnitude larger than the signal to be measured. Because the frequency structure as well as other statistical properties of the foregrounds are significantly different from those of the cosmological signal, it is not unreasonable to hope that they can be successfully subtracted (Di Matteo et al. 2002; Oh & Mack 2003; Santos et al. 2005; Morales et al. 2006; Wang et al. 2006; Gleser et al. 2008; Jelić et al. 2008; Liu et al. 2009; Bernardi et al. 2009, 2010; Jelić et al. 2010; Moore et al. 2013; Wolz et al. 2014; Shaw et al. 2013). Although a lot of work in terms of simulations and testing cleaning techniques has already been done, we still face huge challenges ahead, in particular if we want to use this signal for high precision cosmology. Increasingly realistic large simulations should be developed to try to test the limitations of the intensity mapping measurements. This should include as many instrumental effects as possible in order to account for possible contamination from the calibration process. Ultimately, we will need to start analysing real data in order to improve and build up our knowledge towards the SKA.

PoS(AASKA14)019

4.1 Foreground classification

Foregrounds for intensity mapping can essentially be classified as being extragalactic (caused by astrophysical sources beyond the Milky Way) or galactic in nature.

The most relevant galactic foregrounds are galactic synchrotron emission (GSE) and galactic free-free emission. GSE is caused by high-energy cosmic-ray electrons accelerated by the Galactic magnetic field, and is by far the dominant foreground for HI intensity mapping, being up to five orders of magnitude larger than the cosmological signal. For the relevant radio frequencies it should be possible to describe GSE as a power-law in frequency with a spectral index $\beta \sim -2.8$ (Dickinson et al. 2009; Delabrouille et al. 2013). Furthermore, GSE is partially linearly polarised. Its polarised part will be affected by the Faraday effect, a rotation of the polarization angle caused by the Galactic magnetic field and the optically thick interstellar medium (Rybicki & Lightman 1986; Waelkens et al. 2009). Since the dependence of this effect on frequency is quite strong for the frequency range that pertains to intensity mapping, any leakage from the polarized part into the unpolarized measurements of the cosmological signal would generate a very troublesome foreground to subtract (Jelić et al. 2010; Moore et al. 2013). On the other hand, free-free emission is caused by free electrons accelerated by ions, and thus traces the warm ionised medium. As in the case of GSE, free-free emission is predicted to be spectrally smooth in the relevant range of frequencies (Dickinson et al. 2003).

Extragalactic radio sources can be classified into two different categories: bright radio galaxies, such as active galactic nuclei, and "normal" star-forming galaxies. The spatial distributions of these two types should be qualitatively different, the former being less dominated by gravitational clustering and more by Poisson noise. This has an impact on the degree of smoothness across frequency of the observed intensity when considering the combined contribution of all the galaxies in a given direction of the sky (Santos et al. 2005; Zaldarriaga et al. 2004).

Other possible foreground sources are atmospheric noise, radio frequency interference and line foregrounds, caused by line emission from astrophysical sources in other frequencies. Due to the spectral isolation of the 21cm line, together with the expected low intensity of the most potentially harmful lines (such as OH at $\nu_{\rm OH} \sim 1600\,$MHz), the HI signal should be very robust against line confusion.

4.2 Foreground subtraction

The problem of foregrounds has been addressed in the literature mainly within the EoR regime. The different algorithms that have been proposed to date can be classified into *blind* (Wang et al. 2006; Switzer et al. 2013; Chapman et al. 2012) and *non-blind* (Liu & Tegmark 2011; Shaw et al. 2013, 2014) methods, depending on the kind of assumptions made about the nature of the foregrounds (e.g. whether only generic properties such as spectral smoothness and degree of correlation are assumed or whether a more intimate knowledge of the foreground statistics is required). The poor observational constraints on the foregrounds in the relevant range of frequencies justifies considering the use of blind methods. Recently Wolz et al. (2014) studied the effectiveness of independent component analysis (in particular the implementation of FastICA, e.g. Hyvärinen 1999) for intensity mapping. By propagating the foreground removal residuals into the cosmological analysis, they showed that, while foreground cleaning may induce a residual bias on large

PoS(AASKA14)019

angular scales, which could prevent a full analysis based on the shape of the temperature power spectrum, robust features like the BAO scale should remain unaffected. This result is reasonable: most relevant foregrounds are (fortunately) exceptionally smooth and therefore it should be possible to distinguish them from the much "noisier" cosmological signal. Any foreground residual will probably be dominated by galactic synchrotron emmission, which is most relevant on large angular scales. In the same context, Alonso et al. (2014a) studied the efficiency of different blind cleaning methods (see figure 3), showing that foreground removal can be successful over a wide range of scales provided the foregrounds are sufficiently smooth, and that all blind methods yield quantitatively similar results.

In the realm of non-blind methods, the parametric eigenvalue algorithm developed by Shaw et al. (2013) for the CHIME experiment decomposes the data with help of statistical models for both foregrounds and 21cm signal. This algorithm leaves minor foreground residuals in the large modes of the power spectrum. Instrumental errors such as polarization leakage, beam deformations and calibration uncertainties can significantly affect the foreground removal by mode mixing effects. Shaw et al. (2014) advanced their description to polarized data considering a number of instrumental errors in their tests. For future SKA experiments, detailed studies including varying instrumental settings and the impact of the residuals on the power spectrum are required in order to minimize bias on cosmological results. Foreground subtraction for the SKA is treated in detail in Wolz et al. (2015) including realistic simulations.

4.3 Polarisation leakage

Although the cosmological signal is unpolarized, sky polarization can represent an additional foreground source due to imperfect calibration. The problem can be described by using the measurement equation formalism (Hamaker et al. 1996; Smirnov 2011) that describes the propagation of the signal through an interferometric array. A pedagogical view can be presented by using the scalar form of the measurement equation (Sault et al. 1996), which relates the measured visibilities to the (I,Q,U,V) Stokes parameters that describe the true sky brightness distribution:

$$\begin{aligned} V_{ij}^{pp} &= \frac{1}{2} g_i^p g_j^p (I+Q) \\ V_{ij}^{pq} &= \frac{1}{2} g_i^p g_j^q (U+iV) \\ V_{ij}^{qp} &= \frac{1}{2} g_i^q g_j^p (U-iV) \\ V_{ij}^{qq} &= \frac{1}{2} g_i^q g_j^q (I-Q). \end{aligned} \tag{4.1}$$

Here, V represents the visibility between antennas (i,j) and polarisations (p,q), e.g. it represents the cross-correlation of the electric fields measured by each antenna (the output of the correlator). The case of "single dish" observations can be simply represented by putting $i=j$. The actual response of the telescope to the input sky is represented here by g, usually referred as the "gain" of the system. More instrumental effects can be included in these equations but the simple approach above is enough to show the effect.

If we can calibrate the instrument perfectly, then we can effectively renormalise the gains above (i.e. set $g^p = g^q = 1$) and obtain the measured intensity as $\tilde{I}_{i,j} \equiv V_{ij}^{pp} + V_{ij}^{qq} = I$ (again this is

PoS(AASKA14)019

also valid for $i = j$). However, in the presence of calibration errors, there will be an uncertainty in these gains, e.g. $g^{p,q}_{i,j} = 1 + dg^{p,q}_{i,j}$. This will effectively translate into an error in the estimated total intensity: $\tilde{I}_{i,j} = I + dI + dQ$ where $dI = \frac{I}{2}(dg^p_i + dg^p_j + dg^q_i + dg^q_j)$ is the usual assumed error due to inaccurate calibration and $dQ = \frac{Q}{2}(dg^p_i + dg^p_j - dg^q_i - dg^q_j)$ is the polarization term that leaks to the total intensity (in the expressions above we assumed small calibration errors). Concentrating in the auto-correlations we have $dI = I(dg^p + dg^q)$ and $dQ = Q(dg^p_i - dg^q_i)$. We then see that even if there is the usual calibration error, the leakage will be zero as long as the error is the same for both polarizations.

Although the polarization leakage is different for different instruments, typical values for leakages are below 1% and they tend to be reasonably stable over time scales of hours. In this case, the greatest contamination could come from off-axis leakage, i.e. signals entering the telescope from directions other than the pointing one. Their magnitude can be far greater (i.e. up to 30%), depending upon the observing frequency and their time variability. All the algorithms for foreground subtraction rely on the frequency smoothness of the total intensity spectrum. This smoothness is theoretically well motivated (Santos et al. 2005; Petrovic & Oh 2011; Bernardi et al. 2014) but no longer holds for polarization as the Stokes Q,U parameters are Faraday rotated when the radiation goes through an ionized medium. The emerging scenario is that intrinsically smooth synchrotron radiation can be contaminated by non-smooth polarized emission due to imperfect calibration. This additional foreground seems to be the limiting factor of current HI mapping measurements (Switzer et al. 2013). Note however that we can in principle model this contamination from the leakage of faraday rotated polarisation by "looking" at polarised point sources with the telescope.

Unlike the EoR case, both point-like and diffuse Galactic polarized emission may be problematic for intensity mapping at $z \sim 1-2$. The average polarization fraction of extragalactic radio sources is $\sim$5% at 1.4 GHz (Tucci et al. 2004)) with RM values up to a few tens of rad m^{-2} at high Galactic latitude where HI intensity mapping is carried out (Simard-Normandin et al. 1981; Taylor et al. 2009). The properties of Galactic synchrotron polarization are much less known at the frequencies relevant to HI intensity mapping. It is fairly observationally established that the spatial distribution of polarized intensity poorly correlates with total intensity at 1.4 GHz due to small scale structure present in the ionized interstellar medium (i.e. Gaensler et al. 2001; Bernardi et al. 2003; Sun et al. 2011). Observations of supernova remnants also show that objects further away than a few kpc are completely depolarized at 1.4 GHz, indicating the presence of a polarization horizon beyond which diffuse polarization is no longer observable (Sun et al. 2011). The distance of such polarization horizon decreases at lower frequencies, down to a few hundreds pc at 150-300 MHz (Haverkorn et al. 2004; Bernardi et al. 2013), indicating that relativistic and thermal plasma are co-located in the interstellar medium (Burn 1966). Typical RM values for Galactic polarization also decrease with decreasing frequencies. Given the complex spatial and frequency properties of Galactic polarization, extrapolations to the frequencies relevant for HI intensity mapping observations are fairly uncertain, although we expect that a significant improvement will happen in the next years due to new surveys.

PoS(AASKA14)019

5. Experimental considerations

5.1 Noise

Most cosmological applications with HI intensity mapping will rely on the use of statistical quantities, in particular the power spectrum or its equivalent in real space - the 2-point correlation function. To that effect, the noise power spectrum is a prime quantity to access the sensitivity of a given experiment (and associated survey) to detect the cosmological signal. Two main setups can be considered: surveys using single dish observations where the auto-correlation signal from one or more dishes is used, or surveys using interferometers where the cross-correlation signal from the array elements is used.

5.1.1 Auto-correlations

For single dish observations, the noise temperature rms is given by

$$\sigma_T \approx \frac{\lambda^2 T_{\rm sys}}{A_{\rm e}\Delta\Omega\sqrt{2\delta\nu t_p}} \approx \frac{T_{\rm sys}}{\varepsilon\sqrt{2\delta\nu t_p}} \tag{5.1}$$

where $\Delta\Omega$ is the beam area of the telescope, $A_{\rm e}$ its effective collecting area, $\delta\nu$ the frequency resolution, t_p the observing time per pointing, λ the wavelength of the observation and $T_{\rm sys}$ the total system temperature. The factor of $1/\sqrt{2}$ takes into account the fact we have 2 polarisations. The second approximation takes $\Delta\Omega$ to be the square of the FWHM of the beam and uses a fudge factor $\varepsilon \approx 1$ to factor in the efficiency of the telescope. Pointings need to be packed so that the measurement is reasonably continuous across the sky. Usually this means pixels of size $\theta_{\rm B}^2 \approx (\pi/8)(1.3\lambda/D)^2$ [sr] or smaller. Given a total observing time $t_{\rm tot}$, the time per pointing is then $t_p = t_{\rm tot}(\theta_{\rm B})^2/S_{\rm area}$ where $S_{\rm area}$ is the survey area. The 3D noise power spectrum is just $P_N = \sigma_T^2 V_{\rm pix}$, where $V_{\rm pix} = (r\theta_{\rm B})^2 \times (y\delta\nu)$ is the 3D comoving volume of each volume element, r is the comoving distance to the redshift of the signal and $y = cH(z)^{-1}(1+z)^2/\nu_{21}$. Therefore, the $\theta_{\rm B}^2$ cancels in the power spectrum and we finally get

$$P_N = r^2 y \frac{T_{\rm sys}^2 S_{\rm area}}{2\varepsilon^2 t_{\rm tot}}. \tag{5.2}$$

As we can see, the dish size drops out of the final expression - it is only relevant for the angular resolution which should match what is required for the signal we are trying to measure (to summarise, the dish collecting area and beam size are connected and will cancel out and the way we "pack" the beams for mosaicking is connected to the assumed pixel resolution in the map and will cancel out in the power spectrum). For a fixed total observation time, the survey area should also be chosen to match the required angular scales. If the noise power spectrum is similar to the signal, one also gains by increasing the survey area since this will increase the number of independent measurements for a given scale.

If we have N_d dishes, the combined noise power spectrum will be $P_N = r^2 y T_{\rm sys}^2 S_{\rm area}/(2\varepsilon^2 N_d t_{\rm tot})$. For a single dish with N_b beams, we can cover the same sky area in less time, so that the noise power spectrum will go as $P_N = r^2 y T_{\rm sys}^2 S_{\rm area}/(2\varepsilon^2 N_d N_b t_{\rm tot})$. With Phased Array Feeds (PAFs) the situation is slightly more complicated as the feeds are packed in order to allow for a large number of beams.

PoS(AASKA14)019

This will imply some amount of beam overlap below a given critical frequency

$$P_N = r^2 y \frac{T_{\rm sys}^2 S_{\rm area}}{2\varepsilon^2 N_d N_b t_{\rm tot}} \times \begin{cases} 1 & \nu > \nu_{\rm crit} \\ \left(\frac{\nu_{\rm crit}}{\nu}\right)^2 & \nu \leq \nu_{\rm crit} \end{cases}, \tag{5.3}$$

where $\nu_{\rm crit}$ is the PAF critical frequency. Note that $S_{\rm area} > N_b \theta_B^2$ (with $\theta_B^2 \propto 1/\nu^2$ as usual).

5.1.2 Interferometer

For observations with interferometers, we start by considering the noise rms in the uv plane for a "uv" pixel of size $(\Delta u)^2$:

$$\sigma_T(\mathbf{u}, \nu) = \frac{\lambda^2 T_{\rm sys}}{A_e \sqrt{2\delta\nu\, n(\mathbf{u})\, (\Delta u)^2 t_p}}, \tag{5.4}$$

where A_e is the effective collecting area of one element (dishes or stations), t_p the time per pointing and $n(\mathbf{u})$ is the average number density of baselines (averaged over a 24h period), usually only a function of $|\mathbf{u}|$.

For interferometers, we are going to assume that mosaicking different pointings will not allow the recovery of angular scales larger than the telescope field of view (the primary beam), which is basically set by the size of the array elements, e.g. $\theta_{\rm B}^2 \sim \lambda^2/D^2$ $[sr]$, where D is the dish or station diameter. Usually, the total observing time $t_{\rm tot}$ and time per pointing t_p are then the same. On the other hand, we can use different pointings to increase the number of independent measurements on scales smaller than the telescope field of view. The time per pointing should then be decreased as $t_p = t_{\rm tot}/N_p$, where N_p is the number of pointings. The 3d noise power spectrum is then given by

$$P_N(\mathbf{k}, \nu) = \frac{\lambda^4 r^2 y T_{\rm sys}^2 N_p}{2A_e^2 n(u) t_{\rm tot}} = \frac{\lambda^4 r^2 y T_{\rm sys}^2 S_{\rm area}}{2A_e^2 \theta_{\rm B}^2(\nu) n(u) t_{\rm tot}}. \tag{5.5}$$

with $u = r(z)k_\perp/(2\pi)$ and $N_p \equiv S_{\rm area}/\theta_{\rm B}^2$. Note that if we assume that $n(u)$ is constant on the uv plane between some minimum $D_{\rm min}$ and maximum $D_{\rm max}$ baseline, then we can write

$$n(u) = \frac{N_a(N_a - 1)\lambda^2}{2\pi(D_{\rm max}^2 - D_{\rm min}^2)}. \tag{5.6}$$

where N_a is the number of elements of the interferometer contributing to that baseline range. The expression follows by noting that the integration over $n(u)$ should give the total number of baselines. In the analysis below, we considered the full $n(u)$ distribution[1].

For PAFs, each of the beams will be cross-correlated with the corresponding beam from a different dish (e.g., the field of view of the interferometer is set by the size of one of these beams). The total number of beams per dish, N_b, will allow to survey a target area more quickly and thus increase $t_p = t_{tot} N_b \theta_{\rm B}^2/S_{\rm area}$. However, we need to consider again the beam overlap below the critical frequency so that

$$P_N = \frac{\lambda^4 r^2 y T_{\rm sys}^2 S_{\rm area}}{2A_e^2 N_b n(u) \left[\theta_{\rm B}(\nu_{\rm crit})\right]^2 t_{\rm tot}} \times \begin{cases} \left(\frac{\nu}{\nu_{\rm crit}}\right)^2 & \nu > \nu_{\rm crit} \\ 1 & \nu \leq \nu_{\rm crit} \end{cases}. \tag{5.7}$$

[1] files with n(u) for the different telescope setups are available at https://gitorious.org/radio-fisher/bao21cm.git

PoS(AASKA14)019

Note that the collecting area of one element of a dish array, A_e can be written as $A_e \approx \pi D^2 \varepsilon/4$ with $\varepsilon \lesssim 1$.

If we consider aperture arrays such as what is used for SKA-LOW, the situation is slightly different. In that case, above a given critical frequency, the area of a station will go as $1/\nu^2$, being constant below that (when the array becomes dense). On the other hand, the array beam $\theta_{\rm B}$ should go as $1/\nu$ at any frequency (set by the size of the array) so that

$$P_N = \frac{\lambda^4 r^2 y T_{\rm sys}^2 S_{\rm area}}{2\left[A_e(\nu_{\rm crit})\right]^2 \theta_{\rm B}^2(\nu) N_b n(u) t_{\rm tot}} \times \begin{cases} \left(\frac{\nu}{\nu_{\rm crit}}\right)^4 & \nu > \nu_{\rm crit} \\ 1 & \nu \leq \nu_{\rm crit} \end{cases}, \tag{5.8}$$

where we are already considering the possibility of multiple beams (N_b) with SKA-LOW.

5.1.3 Total error

Computation of the total error in the measurement of the power spectrum at a given scale, $P(k)$, will require knowledge of both the noise and the number of independent modes used to measure that scale, since the error is $\sim (P(k)+P_N(k))/\sqrt{N_{\rm modes}}$. These number of modes will be related to the volume of the survey and optimisation will depend on the balance between reducing noise and increasing the number of modes. Moreover, issues such as the large k cutoff along the angular and frequency directions need to be factored in due to the resolution of the experiment. All these details have been taken into account in the forecasting and fully described in Bull et al. (2014a).

5.2 Target scales

The scales we want to probe for cosmology will impose requirements on the telescope specifications (or the other way around). In terms of probing baryon acoustic oscillations (BAO - see Bull et al. 2015), the relevant scales can be translated to:

- Angular scales between 30 arcminutes and 4 degrees.
- Frequency scales between 2 MHz and 35 MHz
- Surveys covering large areas of the sky are required in order to increase the statistical detection.
- A large bandwidth is required in order to maximize the redshift range covered. Ideally: $\gtrsim 350$ MHz $(0 < z \lesssim 3)$. Though a split in bands is probably required: the low frequency part will be important for large scale physics and "non-standard" cosmological constraints while the high frequency/low z part will be useful to probe the more standard "vanilla" models. Since there will be other surveys probing this low z region we suggest to focus on the < 1000 MHz region if a split in bands needs to be made.

For GR corrections and non-Gaussianity, we are interested on ultra-large scales, e.g. modes $k \lesssim 0.01$ Mpc^{-1}. This should allow high precision measurements to be made of the turn over scale in the power spectrum. These scales will correspond to angular sizes > 10 deg (at $z \sim 1$) and frequency intervals of order 100 MHz which should be easily achievable (but note that the

PoS(AASKA14)019

Redshift	Frequency (MHz)	Average Signal (μK)	Angular scale (deg)	Signal rms (μK - 1 MHz)	Signal rms (μK - 10 MHz)
0.5	947	156.5	1.4	36.2	29.0
1.0	710	254.8	1.9	29.8	24.7
1.5	568	351.0	2.4	25.9	21.5
2.0	473	427.8	2.8	23.2	19.1

Table 1: Average of the signal as a function of redshift/frequency as well as the signal rms (square root of the variance) for scales relevant for BAO ($\sim$ 150 Mpc) assuming single dish observations with $\sim$ 15 m dishes. The variance of the signal is calculated for a 3d smoothing window corresponding to the given angular and frequency scale (frequency in parentheses).

foreground cleaning scale will require even larger bandwidths). These angular requirements mean that we will not be able to use interferometers to probe these large scales since their primary beam is usually smaller than this (and we are assuming that mosaicking cannot be used to recover the large scales with the interferometer).

The signal we are looking for fluctuates both in frequency and across the sky. We are not looking for the average intensity. In table 1 we show the expected signal rms fluctuations for scales related to the dish FoV and a couple of frequency intervals.

5.3 Current and planned experiments

First attempts at using intensity mapping have been promising, but have highlighted the challenge of calibration and foreground subtraction. The Effelsberg-Bonn survey (Kerp et al. 2011) has produced a data cube covering redshifts out to $z = 0.07$, while the Green Bank Telescope (GBT) has produced the first (tentative) detection of the cosmological signal through IM by cross-correlating with the WiggleZ redshift survey (Chang et al. 2010; Switzer et al. 2013; Masui et al. 2013). As probes to constrain cosmological parameters these measurements are, as yet, ineffective, but they do point the way to a promising future.

As described above, we can divide the intensity mapping experiments into two types: single dish surveys and interferometers. In single dish surveys (e.g. using auto-correlations) each pointing of the telescope gives us one single pixel on the sky (though more dishes or feeds can be used to increase the field of view). This has the advantage of giving us the large scale modes by scanning the sky. Since brightness temperature is independent of dish size we can achieve the same sensitivity with a smaller dish although that will in turn limit the angular resolution of the experiment (a 30 arc min resolution at $z \sim 1$ would require a dish of about 50 m in diameter). One example is the GBT telescope as described above. BINGO (Battye et al. 2013) is a proposed 40m multi-receiver single-dish telescope to be situated in South America and aimed at detecting the HI signal at $z \sim 0.3$.

Interferometers basically measure the Fourier transform modes of the sky. They have the advantage of easily providing high angular resolution as well being less sensitive to systematics that can plague the auto-correlation power. On the other hand, the minimum angular scale they can probe is set by their shortest baseline which can be a problem when probing the BAO scales. One example of a purpose built interferometer for intensity mapping is CHIME, a proposed array, aimed

PoS(AASKA14)019

at detecteding BAO at $z \sim 1$, made up of 20×100m cylinders, based in British Columbia, Canada. The pathfinder has 2 half-length cylinders, and the full experiment has 5 (CHIME Collaboration 2012).

The next generation of large dish arrays can also potentially be exploited for HI intensity mapping measurements. Such is the case of MeerKAT and ASKAP. However, these interferometers do not provide enough baselines on the scales of interest (5m to 80m) so that their sensitivity to BAO will be small. The option is to use instead the auto-correlation information from each dish, e.g. make a survey using the array in single dish mode. The large number of dishes available with these telescopes will guarantee a large survey speed for probing the HI signal. The great example of this approach will be SKA1, the first phase of the SKA telescope, to be built in 2018. A HI intensity mapping survey will turn SKA phase 1 into a state of the art cosmological probe and we discuss its use in the next sections.

6. Surveys with the SKA

A recent re-baselining decision has changed the setup assumed in this chapter. In particular, SKA1-SUR has been deferred. However, in the interest of completeness, it was decided to keep the SKA1-SUR sensitivity calculations for future reference, although the discussed science should be doable with just SKA1-MID. In terms of HI intensity mapping surveys with SKA, several factors need to be considered:

- The initial plan for SKA phase 1 (SKA1) included 3 different instruments and all of them could in principle provide an intensity mapping survey at redshifts below 5 (after reionization). This includes SKA1-LOW which is planned to operate at frequencies below 350 MHz (so $z \gtrsim 3$). SKA1-MID (and initially SKA1-SUR) is on the other hand planned to work down to 350 MHz, although the deployment of the required bands might not happen at the same time.

- SKA1-MID can be used in "single dish mode" where the auto-correlations are used to probe the large cosmological scales, or in "interferometer mode" better at resolving the smaller scales. For SKA-LOW we will only consider the interferometer mode. In principle one can also consider a survey with SKA-LOW using the auto-correlation of the beam from each station (from the beam-former). This could be useful for probing large scales with a full sky survey but wouldn't be optimised for BAO since at ~ 350 MHz the beam would be around 3 deg^2. Other option would be to consider the dipoles as the correlation elements instead of stations. These are possibilities that need to be further explored, but since SKA-LOW is more focused on high redshifts where reionization effects need to be factored in, for the current analysis we decided to concentrate only on the standard interferometer case as an example for SKA-LOW.

- SKA1-MID will have several bands and, according to the current design, we will need to use two bands to cover the full redshift range from $z = 0$ to $z = 3$.

- The SKA is probably going to be built in 3 phases (or even 4 if we consider the SKA precursors, MeerKAT and ASKAP). We should therefore consider in the analysis two more phases

PoS(AASKA14)019

besides SKA1: SKA Phase 0 - An "early science" phase of deployment for each SKA1 component, where sensitivity has grown to about 50% of its fully specified level and the full SKA (SKA Phase 2), with 10x the sensitivity and 20x the field of view of SKA1.

The baseline design for SKA1 was described in Dewdney et al. (2013) and further updated in Braun (2014). The setup we consider here as being the full SKA1-MID setup, corresponds to 254 single pixel feed dishes (including MeerKAT 64 dishes), to be built in South Africa. SKA1-SUR would be 96 dishes (including ASKAP 36 dishes) fitted with 36 beam PAFs to increase the field of view to be set in Australia. SKA1-LOW was initially planned to have 911 aperture array stations each with 35 m diameter. Following the details in table 1 of Santos et al. (2015) we list in table 2 the different surveys that are considered in this chapter. Note however that with the new setup recently announced, SKA1-MID is supposed to only have 70% of the dishes (e.g. 133 instead of 190) which will give a total of 197 dishes instead of 254 when including MeerKAT. This will impact on the overall sensitivity, although the final value can range from about a 20% reduction in sensitivity to no reduction at all depending on the efficiency achieved by the system and the final receiver sensitivity. As can be seen from the figures below, sensitivities achieved with MID or SUR are similar, so that no major impact is expected at this level by deferring SUR. To access the effect of a 70% cut on MID, we can look at the curves corresponding to SKA0 (50% cut) in Fig. 5. In particular, on very large scales, we see that the impact of this reduction will be small and still allow SKA1 to perform transformational measurements.

7. Cosmological constraints

7.1 Dark energy and spatial curvature

Surveys of large-scale structure are a rich source of information about the geometry and expansion history of the Universe. The baryon acoustic oscillations (BAO) are a preferred clustering scale imprinted in the galaxy distribution, originating from the time when photons and baryonic matter were coupled together in the early Universe. By using them as a statistical 'standard ruler', one can obtain constraints on the expansion rate, $H(z)$, and (angular) distance-redshift relation, $D_A(z)$, as functions of redshift, as has been done successfully with recent large galaxy redshift surveys such as BOSS and WiggleZ. Measuring these functions is vital for testing theories of dark energy which seek to explain the apparent acceleration of the cosmic expansion, as they constrain its equation of state, $w = P/\rho$, and thus its physical properties. Shedding light on the behaviour of dark energy – especially whether w deviates from -1 and whether it varies in time – is one of the foremost problems in cosmology.

To precisely measure the BAO feature in the matter correlation function, which appears as a 'bump' at comoving separations of $r \approx 100h^{-1}$ Mpc, one needs to detect many galaxies (in order to reduce shot noise), and to cover as large a survey volume as possible (in order to reduce sample variance). Intensity mapping has a few major advantages over conventional galaxy surveys for this task. IM surveys can map a substantial fraction of the sky with low angular resolution in a short period of time. Combined with the wide bandwidths of modern radio receivers, this makes it possible to cover extremely large survey volumes and redshift ranges in a relatively short time, helping to beat down sample variance (see Fig. 4).

PoS(AASKA14)019

Telescope [(a)]	Band [MHz] [(b)]	z	Target freq.	$T_{\rm inst}$ [K]	N_d	D [m] [(c)]	$A_{\rm eff}$ [m^2] [(d)]	θ_B^2 [deg^2] [(e)]	N_b
SKA0-MID	900 - 1760	(0) - 0.58	1310 [MHz]	20	127	15	140	0.51	1
SKA0-SUR [(f)]	650 - 1800 [(g)]	(0) - 1.19	1300	30	48	15	140	0.51	36 [(h)]
SKA1-MID	350 - 1050	0.35 - 3.06	700	28	254	15	140	1.78	1
SKA1-MID	900 - 1760	(0) - 0.58	1310	20	254	15	140	0.51	1
SKA1-SUR	350 - 900 [(g)]	0.58 - 3.06	710	50	60	15	140	1.71	36 [(h)]
SKA1-SUR [(f)]	650 - 1800 [(g)]	(0) - 1.19	1300	30	96	15	140	0.51	36 [(h)]
SKA1-LOW	50 - 350 [(i)]	3.06 - 27	110	40	911	35	925 [(j)]	28	3 [(k)]
SKA2 [(l)]	300 - 1000	0.42 - 3.73	500	15	4000	10	63	8.0	10

Table 2: Assumed telescope/survey configurations. For frequency dependent quantities, the values are calculated at the indicated target frequency. In order to compare between different setups, a total of 10,000 hours is assumed for each survey. Both single dish and interferometer data are considered for each survey when possible. Survey area is chosen to optimise detection at the required cosmological scale. For all surveys we take the total temperature to be $T_{\rm sys} = T_{\rm rcvr} + T_{\rm sky}$ with $T_{\rm rcvr} = 0.1 T_{\rm sky} + T_{\rm inst}$ and $T_{\rm sky} \approx 60\,(300\,{\rm MHz}/\nu)^{2.55}$ K.
Notes: (a) MID and SUR telescopes are already assumed to include MeerKAT (64 dishes) and ASKAP (36 dishes) respectively. **(b)** For MID and SUR the largest band of the combined telescopes is indicated assuming that outside the overlapping band only the corresponding dishes are used in the sensitivity calculations. **(c)** Diameter of dish or station. **(d)** Effective collecting area of the dish or stations. **(e)** Primary beam or instantaneous field of view of the telescope at the target frequency - assumed to go as $1/\nu^2$ unless stated otherwise. For the combined telescopes, the smallest beam of the two telescopes is used. **(f)** Assuming that all ASKAP PAFs will be replaced to meet the SKA1-SUR band and instrument temperature of 30K. **(g)** Only 500 MHz instantaneous bandwidth. **(h)** The combined PAF beam ($N_b \times \theta_B^2$) is assumed constant below the target (critical) frequency as explained in the text. **(i)** Note that band$\times$ N_b is fixed at 300 MHz. **(j)** Assumed to be constant below the target frequency and going as $1/\nu^2$ above it. **(k)** Beams can point in different directions so no overlap is assumed. **(l)** Values here are completely indicative. We choose to consider an interferometer type experiment, targeting the high ($z > 1$) redshift region and a FoV large enough for BAO scales. We only fix the sensitivity to be about 10 times what is assumed for SKA1 and the total field of view (including number of beams) to be about 20 times SKA1 at the target frequency.

While individual galaxies cannot in general be resolved, each telescope pointing measures the integrated emission from many galaxies, making the total signal easier to detect and reducing the shot noise. All that is required is to obtain sufficient flux sensitivity to detect the integrated 21cm emission and to have sufficient resolution to resolve the required scales at a given redshift. Figure 5 summarises the expected constraints from the SKA HI IM surveys for two relevant target scales: the BAO scale at $k \sim 0.074$ Mpc^{-1} and a very large scale, past the equality peak at $k \sim 0.01$ Mpc^{-1}. We see the huge constraining power of these surveys. In particular, due to the large volumes probed, they will be unmatched on ultra-large scales. Even at BAO scales, both SKA1-MID and SUR present constraints not far from Euclid while only using a ~ 2 year survey (the full Euclid requires about 5 years). Moreover, SKA1-LOW will be able to make a detection at $z \sim 4$ which again will be an unique feature.

For the BAO scales (see Table 1 and Fig. 5, left panel), the angular resolution of the Phase 1 SKA dishes is such that these scales are best matched to an autocorrelation survey at low redshift, and an interferometric survey at higher redshift. Measurements of the equation of state are most critical at lower redshifts, $z \lesssim 1.5$, where dark energy begins to dominate the cosmic expansion.

PoS(AASKA14)019

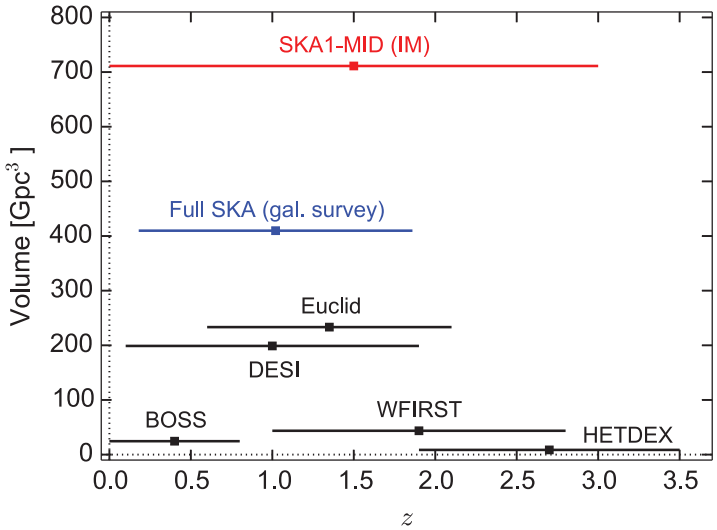

Figure 4: Survey volumes and redshift range for various current and future surveys (volume calculated at the central redshift).

Bull et al. (2015) show that a 10,000 hour and 25,000 deg^2 autocorrelation survey on either SKA1-MID or SUR will be capable of producing high-precision constraints on w, bettering all existing surveys due to its large survey area (see Fig. 6). While the resulting dark energy 'figure of merit' is a factor of ~ 3 worse than forecasts for a future Euclid galaxy redshift survey when combined with Planck CMB data and BOSS low-redshift BAO measurements (since Euclid cannot probe redshifts below 0.7), a phase 1 IM survey will nevertheless be of great utility in superseding other low-z measurements in the joint analyses that will produce the best constraints on w.

Another important quantity that can be derived from BAO measurements is the spatial curvature, Ω_K, which describes the global geometry of the observable Universe. A key prediction of the prevailing inflationary theory of the early Universe is that the spatial curvature should be extremely small. Current constraints (e.g. Planck Collaboration 2014) find $|\Omega_K| \lesssim 10^{-2}$, but a precision measurement at the $\sim$ few $\times\ 10^{-4}$ level is needed to really put pressure on inflationary models (e.g. Kleban & Schillo 2012). In combination with Planck CMB data, an SKA IM survey would be able to approach this value, measuring

$$|\Omega_K| < 10^{-3} \tag{7.1}$$

with 68% confidence (Bull et al. 2014a).

7.2 Growth of structure

Viewed in redshift space, the matter distribution is anisotropic due to the distorting effect of peculiar velocities in the line of sight direction. Coherent peculiar velocities on large scales encode information about the history of the growth of structure in the Universe through their dependence on the linear growth rate, $f(z)$, which can be measured from the degree of anisotropy of the redshift-space correlation function. The growth rate is directly related to the strength of gravity, and so is an extremely useful tool for probing possible deviations from general relativity that have been invoked as an alternative to dark energy to explain cosmic acceleration.

Intensity mapping and galaxy surveys do not measure the linear growth rate directly, but are instead sensitive to simple combinations of $f(z)$, the bias $b(z)$, and the overall normalisation of

PoS(AASKA14)019

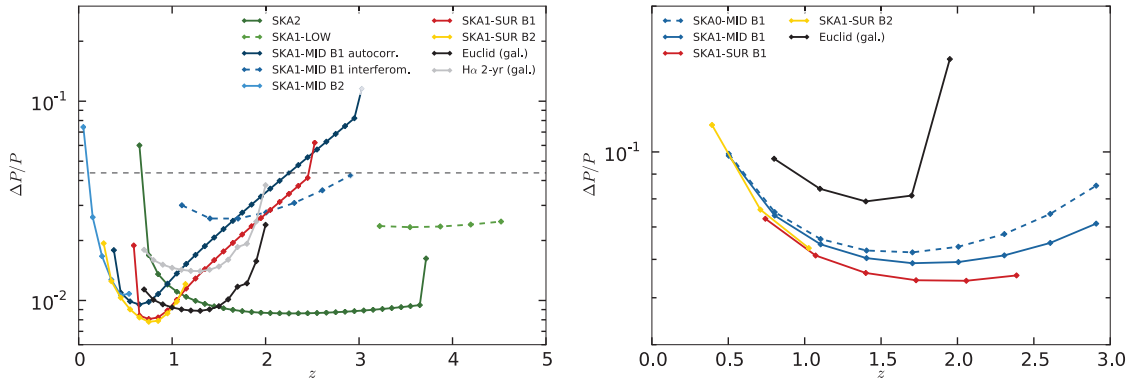

Figure 5: Left: Constraints (noise over signal) from SKA HI IM surveys for BAO scales ($k \sim 0.074$ Mpc^{-1}) as a function of redshift. Dashed line shows the BAO detection threshold. Assumptions: 10,000 hours observation, 25,000 deg^2 survey and bins of $dz = 0.1$, except for SKA1-MID in interferometer mode and SKA-LOW where 1,000 deg^2 and $dz = 0.3$ was taken. The results for SKA0 band 2 (low z), where only 50% of the dishes are used, was not shown as the results are very similar to SKA1. The lower green curve shows what would be expected from a SKA2 IM survey (in interferometer mode) optimised for high-z. The grey curve shows what can be expected for a two-year H$_\alpha$ galaxy survey with similar depth as Euclid but over a smaller sky area. **Right:** Constraints (noise over signal) from SKA HI IM surveys for large scales, past the equality peak ($k \sim 0.01$ Mpc^{-1}) as a function of redshift. A value below 1 would imply a detection. For SKA1-SUR band 2, the available 500 MHz bandwidth was chosen at the low end of the band in order to probe higher redshifts. SKA1-MID band 2 is not shown as it is constrained to low redshifts ($z < 0.5$) with the current band specs. Dashed line indicates what can be achieved with SKA0 (50% of SKA1) which is quite similar to SKA1. Note that, in order to be as generic as possible, we did not include the foreground contamination in this analysis since the results will depend on the cleaning method adopted. The foreground residuals should degrade these constraints, specially on scales of the order of the frequency band.

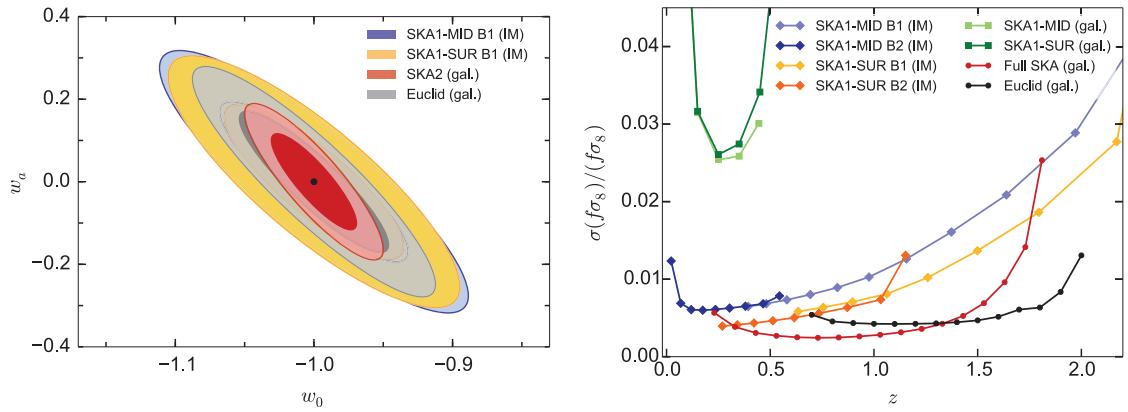

Figure 6: Left: Predicted constraints from SKA on dynamical dark energy parameters. We show predicted constraints from SKA1 IM and SKA2 galaxy, compared with predictions for Euclid. **Right:** Predicted constraints from SKA on the unparameterized growth function $f\sigma_8$ from the SKA1 (galaxy and IM) and the SKA2 galaxy survey, compared with predicted constraints coming from the Euclid galaxy survey. Both constraints include Planck+BOSS priors.

PoS (AASKA14) 019

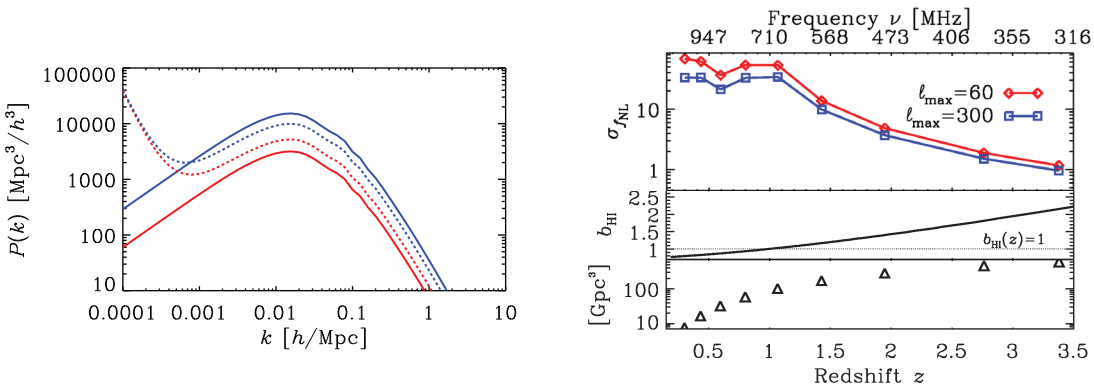

Figure 7: *Left:* Power spectrum of dark matter (solid) and HI (dashed) at $z = 0.4$ (blue, top) and $z = 2.5$ (red, bottom), with $f_{\rm NL} = 10$. *Right:* Forecast 1σ error on $f_{\rm NL}$ (top); HI Gaussian bias (middle); effective IM survey volume (bottom). From Camera et al. (2013).

the power spectrum $\sigma_8(z)$. A reasonable choice of parametrisation is to take the combinations $(f\sigma_8, b\sigma_8)$. As shown in Raccanelli et al. (2015), a 10,000 hour and 25,000 deg^2 SKA phase 1 intensity mapping autocorrelation survey will be capable of measuring $f\sigma_8$ with high precision over a wide redshift range, obtaining sub-1% constraints in the range $0.05 \lesssim z \lesssim 1.0$ with Band 2 of SKA1-MID or SUR, and reaching out to $z \approx 2.0$ with $\sim 4\%$ precision using Band 1 of MID/SUR (see Fig. 6).

At low redshifts, these figures are highly complementary to (e.g.) a Euclid galaxy redshift survey, which should obtain $\sim 0.5\%$ measurements of $f\sigma_8$ in the interval $0.7 \lesssim z \lesssim 2.0$. By comparison, SKA1-MID/SUR will have $\sim 0.5\%$ measurements for $z \approx 0.3 - 0.7$.

7.3 Probing ultra-large scales

As briefly mentioned above, there is important information that can be extracted from the ultra-large scale modes of order and above the cosmological horizon (see Fig. 5, right panel). We refer the reader to Camera et al. (2015) and references therein for an extensive description of the ultra-large scale effects briefly mentioned here, as well as to the ways by which the SKA will be able to tackle successfully the technical problems arising when trying to access those scales.

One of the most important features on horizon scales is primordial non-Gaussianity. Many models of inflation predict a small amount of non-Gaussianity in the statistical distribution of primordial fluctuations. This produces a signal in the bispectrum, but also in the power spectrum – since primordial non-Gaussianity induces a scale-dependent correction to the Gaussian bias: $b \to b + \Delta b$. This correction grows on large scales as $\Delta b \propto f_{\rm NL} k^{-2}$ for primordial non-Gaussianity of the local type, where $f_{\rm NL}$ is the non-Gaussian parameter.

In Camera et al. (2013), an analysis is given of the constraining power of IM surveys over non-Gaussianity; their results are summarised in Fig. 7. This shows that the forecast errors on $f_{\rm NL}$ can be taken down towards $\sigma_{f_{\rm NL}} \lesssim 3$ for a deep enough survey with sufficient dishes. We recast their analysis according to the updated specifics of Table 2, and adopt a SKA1-MID IM survey operating for 10,000 hours at a system temperature of 20 K. The chosen bandwidth is

PoS(AASKA14)019

therefore $350-1050$, where we keep the last, high-frequency bins between 1000 and 1050 MHz for foreground removal. The bandwidth is further subdivided into constant frequency bins of 10 MHz width, collected into 'chunks' of 20 by 20 bins in order to construct a 65 by 65 tomographic matrix. (To deal with the large number of bins, we use a block diagonal tomographic matrix where we correct for the overlapping, as described in Camera et al. 2013.) Such a configuration eventually yields a constraint on the primordial non-Gaussianity parameter

$$\sigma_{f_{\rm NL}} = 2.3, \tag{7.2}$$

namely more than three times better than the current constraint from Planck (using the large-scale structure convention).

SKA IM surveys will also allow us to test Einstein's theory of general relativity for the first time on horizon scales. One of the most interesting effects predicted by general relativity is the correction to the standard Newtonian approximation for the observed galaxy overdensity. The Kaiser redshift-space distortion term is a relativistic correction that is significant on small scales. Further relativistic corrections include other redshift terms (Doppler and gravitational), Sachs-Wolfe (SW) type terms, and integrated contributions – from weak lensing magnification, time-delay and ISW terms (see Camera et al. (2015)):

$$\delta_{T_b}^{\rm obs} = (b_{\rm HI} + \Delta b)\delta - \frac{(1+z)}{H} n^i \partial_i (\mathbf{n}\cdot\mathbf{v}) + \delta_{\rm GR}, \tag{7.3}$$

The terms in $\delta_{\rm GR}$ grow on ultra-large scales and need to be accounted for.

It turns out that for IM, some of these corrections are strongly suppressed; e.g. the weak lensing magnification and the integrated time-delay terms are zero for IM (Hall et al. 2013; Duniya et al. 2013). However, the Doppler terms and the ISW contribution remain and need to be incorporated.

At the same time as testing general relativity, one can also test specific modified gravity theories which deviate from general relativity on large scales. SKA IM surveys should enhance considerably the current constraints on parameters that describe modified gravity solutions; this is an area for future work.

7.4 Weak Lensing

HI intensity mapping can also be used to measure weak gravitational lensing. Gravitational magnification will have an effect on the clustering properties of galaxies that is coherent over a large range in redshift. The effect can be detected by applying a quadratic estimator to the brightness temperature maps. HI intensity mapping with SKA would allow for weak lensing measurements at higher redshifts than are possible with more traditional weak lensing methods based on the shearing of galaxy images in the visible. The technique is more fully described in the Weak Lensing chapter of this proceeding and in Pourtsidou & Metcalf (2014a,b).

The signal-to-noise of such a measurement is strongly dependent on the HI density at $z \sim 2-3$ which is not yet strongly constrained by observations (see figure 1). For a conservative assumption of no evolution in $\Omega_{\rm HI}(z)$, we find that SKA-MID phase 2 should be able to measure the shape of lensing power spectrum and its evolution between $z = 2$ and 3 (see Fig. 8, left panel). This assumes a 20,000 sq.deg. survey.

PoS(AASKA14)019

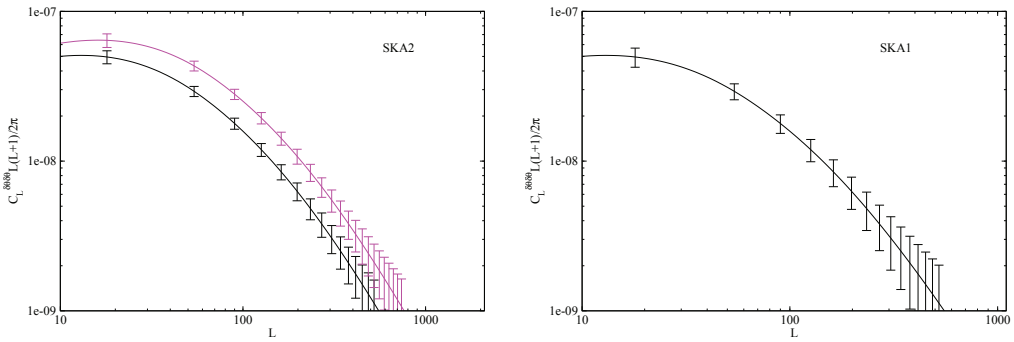

Figure 8: *Left*: Displacement field power spectrum for $z_s = 2$ (solid black line) and $z_s = 3$ (solid magenta line) and the corresponding measurement errors using the SKA2 specifications and assuming no redshift evolution in the HI density. *Right*: Displacement field power spectrum for $z_s = 2$ and the corresponding measurement errors using the SKA1 specifications and an increasing $\Omega_{\rm HI}(z)$ with redshift.

If $\Omega_{\rm HI}(z)$ increases by a factor of ~ 5 by redshift 3, as seen in the DLA observations from Peroux et al. (2003), significantly higher signal-to-noise can be achieved and SKA phase 1 should be capable of measuring the lensing power spectrum and its evolution with high accuracy, as shown in Fig. 8, right panel. This would be a unique probe of the expansion history of the universe and gravity at this range in redshift.

8. Technical challenges

The idea of using intensity mapping to reconstruct the large scale structure of the universe bring radio astronomy back to what has been one of its greatest successes – mapping out cosmological diffuse emission. Indeed, tremendous progress has been made in mapping out the cosmic microwave background (CMB) and the hope is that many of the techniques developed there may inform us on how best to proceed. We will now briefly address some of the problems that need to be tackled if we are to move forward with this technique.

For a start it is clear that different redshift ranges will require different observation "modes": at high redshift it is preferable to use interferometers while at low redshifts it should be more efficient to work with single dishes (or "auto-correlation" mode in the parlance of radio astronomers). This is not a watertight rule. For example, with the clever use of phase arrays or cylindrical arrays, it should be possible to construct interferometers with short baselines and large fields of view hence accessing larger wavelengths at lower redshifts. But, for now, this separation of scales/redshift is useful in guiding us through the issues.

At low redshifts one needs to perform a classic CMB-like observation which is to raster scan the sky building up a rich set of cross-linked scans that cover as much area as possible with as much depth as is necessary. The key problems are then dealing with the long term drifts in the noise (the $1/f$ noise which is ubiquitous in such experiments) and accurately calibrating the overall signal. Usually, the first problem can be dealt with sufficiently fast scan speed (such that the bulk of the signal is concentrated in frequency in the regime where the $1/f$ has died off and the noise is

PoS(AASKA14)019

effectively uncorrelated) but this can be difficult to achieve with large dishes such as the ones that are envisaged in current and future experiments. For some setups, the fortuitous configuration of elevation and location mean that drift scanning may lead to a fast enough scan speed.

With regards to calibrating single dish experiments, this is a source of major concern. Major systematic effects to be tackled are spillover and sidelobe pickup as well as gain drifts. Again, these are issues that have been tackled successfully in the analysis of CMB data although novel approaches can be envisaged. So, for example, the BINGO experiment (Battye et al. 2013) propose to use a partially illuminated aperture and a fixed single dish, minimising the problems that arise from moving parts. Another intriguing possibility is, for a cluster of single dishes working in autocorrelation mode, to use the cross correlation data for calibrating off known sources. This means that in principle, calibrating the gains should be straightforward using the interferometer data since the high resolution will allow access to a good sky model.

In the case of interferometric measurements, the challenge is to capture as much of the long wavelength modes as possible. The largest wavelength is set by the smallest baseline which implies that arrays with large dishes will not adequately sample BAO scales at low redshifts in interferometer mode. To mitigate this problem, one can work with dense aperture arrays which can be a possible design for SKA2 (or just use smaller dishes and pack them closer together). This results in smaller baselines and a larger field of view for the interferometer, but reduces its total effective collecting area (and thus its sensitivity) if we want to maintain the number of correlations low. Alternatively, reflector designs have been proposed – for example, long cylindrical reflectors with many closely-spaced receivers installed along the cylinder (Shaw et al. 2014). This provides a large number of short baselines, and a primary beam that is $\sim 180^\circ$ in one direction but much narrower along the orthogonal direction.

9. Conclusions

Neutral hydrogen (HI) intensity mapping is set to become a leading cosmology probe during this decade. Intensity mapping at radio frequencies has a number of advantages over other large-scale structure surveys methodologies. Since we only care about the large-scale characteristics of the HI emission, there is no need to resolve and catalogue individual objects, which makes it much faster to survey large volumes. This also changes the characteristics of the data analysis problem: rather than looking at discrete objects, one is dealing with a continuous field, which opens up the possibility of using alternative analysis methods similar to those applied (extremely successfully) to the CMB. Thanks to the narrow channel bandwidths of modern radio receivers, one automatically measures redshifts with high precision too, bypassing one of the most difficult aspects of performing a galaxy redshift survey.

These advantages, combined with the rapid development of suitable instruments over the coming decade, should turn HI intensity mapping into a highly competitive cosmological probe. One of the key instruments that can be used for this purpose is phase I of the SKA. A large sky survey with this telescope should be able to provide stringent constraints on the nature of dark energy, modified gravity models and the curvature of the Universe. Moreover, it will open up the possibility to probe Baryon Acoustic Oscillations at high redshifts as well as ultra-large scales, beyond the horizon size,

PoS(AASKA14)019

which can be used to constrain effects such as primordial non-Gaussianity or potential deviations from large-scale homogeneity and isotropy.

Several challenges will have to be overcome, however, if we want to use this signal for cosmological purposes. In particular, cleaning of the huge foreground contamination, removal of any systematic effects and calibration of the system. Foreground cleaning methods have already been tested with relative success taking advantage of the foreground smoothness across frequency but novel methods need to be explored in order to deal with more complex foregrounds. Other contaminants, such as some instrumental noise bias that shows up in the auto-correlation signal, can in principle be dealt with the same methods. Ultimately, we should deal with the cleaning of the signal and the map making at the same time. This will require even more sophisticated statistical analysis methods and it will be crucial to take on such an enterprise in the next few years in order to take full advantage of this novel observational window for cosmology.

Acknowledgments: — MGS and RM are supported by the South African SKA Project and the National Research Foundation. PB is supported by European Research Council grant StG2010-257080. RM is supported by the UK Science & Technology Facilities Council (grant ST/K0090X/1).

References

Alonso, D., Bull, P., Ferreira, P. G., & Santos, M. G. 2014a, arXiv:1409.8667
Alonso, D., Ferreira, P. G., & Santos, M. G. 2014b, MNRAS, 444, 3183
Bagla, J., Khandai, N., & Datta, K. K. 2010, Mon. Not. Roy. Astron. Soc., 407, 567
Battye, R. A., Browne, I. W. A., Dickinson, C., et al. 2013, MNRAS, 434, 1239
Bernardi, G., Carretti, E., Fabbri, R., et al. 2003, MNRAS, 344, 347
Bernardi, G., de Bruyn, A. G., Brentjens, M. A., et al. 2009, A & A, 500, 965
Bernardi, G., de Bruyn, A. G., Harker, G., et al. 2010, A & A, 522, A67
Bernardi, G., Greenhill, L. J., Mitchell, D. A., et al. 2013, ApJ, 771, 105
Bernardi, G., McQuinn, M., & Greenhill, L. J. 2014, ArXiv e-prints
Braun, R. 2014, Document number SKA—TEL—SKO—DD—XXX Revision A Draft 2
Bull, P., Ferreira, P. G., Patel, P., & Santos, M. G. 2014a, ArXiv e-prints
Bull, P., et al. 2015, "Measuring baryon acoustic oscillations with future SKA surveys", in Advancing Astrophysics with the Square Kilometre Array, PoS(AASKA14)024
Burn, B. J. 1966, MNRAS, 133, 67
Camera, S., Santos, M. G., Ferreira, P. G., & Ferramacho, L. 2013, Phys.Rev.Lett., 111, 171302
Camera, S., et al. 2015, "Cosmology on the Largest Scales with the SKA", in Advancing Astrophysics with the Square Kilometre Array, PoS(AASKA14)025
Chang, T.-C., Pen, U.-L., Bandura, K., & Peterson, J. B. 2010, Nature, 466, 463
Chapman, E., Abdalla, F. B., Harker, G., et al. 2012, MNRAS, 423, 2518
CHIME Collaboration. 2012, CHIME Overview, http://chime.phas.ubc.ca/CHIME_overview.pdf
Davé, R., Katz, N., Oppenheimer, B. D., Kollmeier, J. A., & Weinberg, D. H. 2013, MNRAS, 434, 2645
de Oliveira-Costa, A., Tegmark, M., Gaensler, B. M., et al. 2008, MNRAS, 388, 247
Delabrouille, J., et al. 2013, A & A, 553, A96

PoS(AASKA14)019

Dewdney, P., Turner, W., Millenaar, R., et al. 2013, Document number SKA—TEL—SKO—DD—001 Revision 1
Di Matteo, T., Perna, R., Abel, T., & Rees, M. J. 2002, ApJ, 564, 576
Dickinson, C., Davies, R. D., & Davis, R. J. 2003, MNRAS, 341, 369
Dickinson, C., Eriksen, H. K., Banday, A. J., et al. 2009, ApJ, 705, 1607
Duffy, A. R., Kay, S. T., Battye, R. A., et al. 2012, MNRAS, 420, 2799
Duniya, D. G. A., Bertacca, D., & Maartens, R. 2013, JCAP, 10, 15
Font-Ribera, A., Miralda-Escudé, J., Arnau, E., et al. 2012, JCAP, 11, 59
Gaensler, B. M., Dickey, J. M., McClure-Griffiths, N. M., et al. 2001, ApJ, 549, 959
Gleser, L., Nusser, A., & Benson, A. J. 2008, MNRAS, 391, 383
Hall, A., Bonvin, C., & Challinor, A. 2013, Phys.Rev., D87, 064026
Hamaker, J. P., Bregman, J. D., & Sault, R. J. 1996, Astronomy & Astrophysics, Supplement, 117, 137
Haverkorn, M., Katgert, P., & de Bruyn, A. G. 2004, A & A, 427, 169
Hyvärinen, A. 1999, IEEE Trans. on Neural Network, 10, 626
Jarvis, M., et al. 2015, "Cosmology with SKA Radio Continuum Surveys", in Advancing Astrophysics with the Square Kilometre Array, PoS(AASKA14)018
Jelić, V., Zaroubi, S., Labropoulos, P., et al. 2010, MNRAS, 409, 1647
Jelić, V., et al. 2008, MNRAS, 389, 1319
Kerp, J., Winkel, B., Ben Bekhti, N., Flöer, L., & Kalberla, P. M. W. 2011, Astronomische Nachrichten, 332, 637
Khandai, N., Sethi, S. K., Di Matteo, T., et al. 2011, Mon.Not.Roy.Astron.Soc., 415, 2580
Kleban, M., & Schillo, M. 2012, JCAP, 1206, 029
Lah, P., Chengalur, J. N., Briggs, F. H., et al. 2007, MNRAS, 376, 1357
Liu, A., & Tegmark, M. 2011, PRD, 83, 103006
Liu, A., Tegmark, M., Bowman, J., et al. 2009, MNRAS, 398, 401
Martin, A. M., Papastergis, E., Giovanelli, R., et al. 2010, Astrophys.J., 723, 1359
Masui, K. W., et al. 2013, Ap. J. L., 763, L20
Meiring, J. D., Tripp, T. M., Prochaska, J. X., et al. 2011, Astrophys.J., 732, 35
Moore, D. F., Aguirre, J. E., Parsons, A. R., Jacobs, D. C., & Pober, J. C. 2013, ApJ, 769, 154
Morales, M. F., Bowman, J. D., & Hewitt, J. N. 2006, ApJ, 648, 767
Noterdaeme, P., Petitjean, P., Ledoux, C., & Srianand, R. 2009, A & A, 505, 1087
Obreschkow, D., Klöckner, H.-R., Heywood, I., Levrier, F., & Rawlings, S. 2009, ApJ, 703, 1890
Oh, S. P., & Mack, K. J. 2003, MNRAS, 346, 871
Padmanabhan, H., Choudhury, T. R., & Refregier, A. 2014, ArXiv e-prints
Peroux, C., McMahon, R. G., Storrie-Lombardi, L. J., & Irwin, M. J. 2003, MNRAS, 346, 1103
Petrovic, N., & Oh, S. P. 2011, MNRAS, 413, 2103
Planck Collaboration. 2013, ArXiv e-prints
Planck Collaboration. 2014, Astron.Astrophys.
Pourtsidou, A., & Metcalf, R. B. 2014a, submitted to MNRAS
—. 2014b, MNRAS, 439, L36
Prochaska, J. X., & Wolfe, A. M. 2009, ApJ, 696, 1543
Raccanelli, A., et al. 2015, "Measuring redshift-space distortion with future SKA surveys", in

PoS(AASKA14)019

Advancing Astrophysics with the Square Kilometre Array, PoS(AASKA14)031
Rao, S. M., Turnshek, D. A., & Nestor, D. 2006, Astrophys.J., 636, 610
Rybicki, G. B., & Lightman, A. P. 1986, Radiative Processes in Astrophysics (Wiley-VCH)
Santos, M. G., Cooray, A., & Knox, L. 2005, ApJ, 625, 575
Santos, M. G., et al. 2015, "HI galaxy simulations for the SKA: number counts and bias", in Advancing Astrophysics with the Square Kilometre Array, PoS(AASKA14)021
Sault, R. J., Hamaker, J. P., & Bregman, J. D. 1996, Astronomy & Astrophysics, Supplement, 117, 149
Shaw, J. R., Sigurdson, K., Pen, U.-L., Stebbins, A., & Sitwell, M. 2013, ApJ, 781, 57
Shaw, J. R., Sigurdson, K., Sitwell, M., Stebbins, A., & Pen, U.-L. 2014, ArXiv e-prints
Shaw, J. R., Sigurdson, K., Sitwell, M., Stebbins, A., & Pen, U.-L. 2014, Astrophys.J.
Simard-Normandin, M., Kronberg, P. P., & Button, S. 1981, ApJS, 45, 97
Smirnov, O. M. 2011, A & A, 527, A106
Sun, X. H., Reich, W., Han, J. L., et al. 2011, A & A, 527, A74
Switzer, E. R., Masui, K. W., Bandura, K., et al. 2013, MNRAS, 434, L46
Tassev, S., Zaldarriaga, M., & Eisenstein, D. J. 2013, JCAP, 6, 36
Taylor, A. R., Stil, J. M., & Sunstrum, C. 2009, ApJ, 702, 1230
Tucci, M., Martínez-González, E., Toffolatti, L., González-Nuevo, J., & De Zotti, G. 2004, MNRAS, 349, 1267
Villaescusa-Navarro, F., Viel, M., Datta, K. K., & Choudhury, T. R. 2014, ArXiv e-prints
Waelkens, A., Jaffe, T., Reinecke, M., Kitaura, F. S., & Enßlin, T. A. 2009, A & A, 495, 697
Wang, X., Tegmark, M., Santos, M. G., & Knox, L. 2006, ApJ, 650, 529
White, M., Tinker, J. L., & McBride, C. K. 2014, MNRAS, 437, 2594
Wolz, L., Abdalla, F. B., Blake, C., et al. 2014a, MNRAS, 441, 3271
Wolz, L., et al. 2015, "Foreground Subtraction in Intensity Mapping with the SKA", in Advancing Astrophysics with the Square Kilometre Array, PoS(AASKA14)035
Zaldarriaga, M., Furlanetto, S. R., & Hernquist, L. 2004, ApJ, 608, 622
Zwaan, M. A., Meyer, M., Staveley-Smith, L., & Webster, R. 2005, MNRAS, 359, L30

PoS(AASKA14)019

PROCEEDINGS OF SCIENCE

Cross correlation surveys with the Square Kilometre Array

Donnacha Kirk[1], **Aurélien Benoit-Lévy**[1], **Filipe B. Abdalla**[*1,2], **Philip Bull**[3], **Benjamin Joachimi**[1]

[1] *Department of Physics and Astronomy, University College London, London WC1E 6BT, UK*
[2] *Department of Physics and Electronics, Rhodes University, PO Box 94, Grahamstown, 6140 South Africa;*
[3] *Institue of Theoretical Astrophysics, University of Oslo, P.O. Box 1029 Blindern, N-0315 Oslo, Norway*
E-mail:
drgk@star.ucl.ac.uk
benoitl@star.ucl.ac.uk
fba@star.ucl.ac.uk

By the time that the first phase of the Square Kilometre Array is deployed it will be able to perform state of the art Large Scale Structure (LSS) as well as Weak Gravitational Lensing (WGL) measurements of the distribution of matter in the Universe. In this chapter we concentrate on the synergies that result from cross-correlating these different SKA data products as well as external correlation with the weak lensing measurements available from CMB missions. We show that the Dark Energy figures of merit obtained individually from WGL/LSS measurements and their independent combination is significantly increased when their full cross-correlations are taken into account. This is due to the increased knowledge of galaxy bias as a function of redshift as well as the extra information from the different cosmological dependences of the cross-correlations. We show that the cross-correlation between a spectroscopic LSS sample and a weak lensing sample with photometric redshifts can calibrate these same photometric redshifts, and their scatter, to high accuracy by modelling them as nuisance parameters and fitting them simultaneously cosmology. Finally we show that Modified Gravity parameters are greatly constrained by this cross-correlations because weak lensing and redshift space distortions (from the LSS survey) break strong degeneracies in common parameterisations of modified gravity.

Advancing Astrophysics with the Square Kilometre Array
June 8-13, 2014
Giardini Naxos, Italy

[*]Speaker.

PoS(AASKA14)020

1. Introduction

The Square Kilometre Array is a facility which will be able to provide huge advances in several areas of astronomy and cosmology. It will be able to map the large scale distribution of galaxies as well as measure the weak gravitational lensing signal from far away objects. The information from these probes is not fully independent as both the LSS and WGL signals depend on the large scale distribution of matter in our Universe.

The combination of the information encoded in the large scale distribution of galaxies and in the signal from weak gravitational lensing can significantly increase our knowledge of the Universe we live in. Weak Gravitational Lensing (WGL) does not respond to the bias of galaxies and hence the combination of the signal from WGL and LSS can help constrain the bias of galaxies tracing the Large Scale Structure. Furthermore WGL usually requires photometric redshifts to yield an estimate of the redshift distribution of such galaxies. The cross correlation between WGL samples with a spectroscopic redshifts samples can help calibrate the redshift distribution of WGL galaxies. Finally if we consider theories of modified gravity, WGL combined with the Redshift Space Distortion (RSD) signal in the LSS survey can together probe potential modifications to the Poisson equation as well as the equation which determines how light bends in the presence of matter in separate ways. This breaks a very powerful degeneracy in the common parameterisations of deviations from GR, hence their joint constraints are orders of magnitude more powerful than individual constraints.

In this chapter we take surveys equivalent to those possible with SKA phase 1 as well as SKA phase 2 and estimate how well the combination of probes can calibrate photometric redshifts and improve the figures of merit for Dark Energy and Modified Gravity. We consider several scenarios, notably we describe as SKA 1 early scenarios which are surveys which will be available during a construction phase of the SKA before phase 1 is completed. We assume that there is both a continuum and a line survey for the Weak Lensing and the Large Scale Structure respectively. The Continuum survey would have longer baselines and would be focused on weak lensing and is similar to the survey outlines in the Weak Lensing chapter in this science book. The redshifts for these galaxies would come from matching to optical galaxies with photometric redshifts. The LSS surveys are assumed to be galaxies found in line emission mainly from the signal present in the core of the SKA. We make little distinction between the technologies needed for such surveys but note that a proper UV distribution is needed for a Weak lensing survey and some necessary sensitivity is needed for the line survey. These SKA1 early surveys are effectively 1000 and 5000 sq degree surveys assuming two thirds of the SKA phase 1 sensitivity. We also assume two SKA phase 1 surveys which would reach signals of around 100 μJy in the case of a line survey. The Weak lensing survey is assumed not to be larger than 5000 sq degrees in the case of phase 1 as anything more would be infeasible given the sensitivity of the instrument. We assume a larger LSS survey of 30000 sq degs with phase 1 obtaining galaxies and redshifts. For phase 2 we assume both WGL and LSS surveys covering the same amount of the sky with 5000 and 30000 square degrees respectively where increased area trades off with decreased depth.

These surveys are summarised in Table 1 and 2 and their respective redshift distribution is the same assumed in other chapters of this science book.

PoS(AASKA14)020

2. Formalism for Cross-Correlations

In the following we will provide forecasts for various cross-correlations of cosmological probes using the Fisher Matrix formalism (see Heavens (2009) for an overview). The Fisher matrix is defined as

$$F_{\alpha\beta} \equiv \langle H_{\alpha\beta} \rangle = \left\langle -\frac{\partial^2 \ln L}{\partial p_\alpha \partial p_\beta} \right\rangle , \tag{2.1}$$

where L is the likelihood and where p_α are cosmological parameters. Assuming a Gaussian likelihood for the data and a cosmology-independent data covariance, the Fisher matrix is given by Tegmark et al. (1997),

$$F_{\alpha\beta} = \sum_{\ell=\ell_{min}}^{\ell_{max}} \sum_{(i,j),(m,n)} \frac{\partial D^{(ij)}(\ell)}{\partial p_\alpha} \mathrm{Cov}^{-1}\left[D^{(ij)}(\ell), D^{(mn)}(\ell)\right] \frac{\partial D^{(mn)}(\ell)}{\partial p_\beta} . \tag{2.2}$$

For any unbiased estimator the Fisher matrix provides a lower bound on the marginalised error of a parameter p_α, via the Cramer-Rao inequality, $\Delta p_\alpha \geq \sqrt{(F^{-1})_{\alpha\alpha}}$. The data vector, $D^{(ij)}(\ell)$, consists of angular power spectra, $C_{XY}^{(ij)}(\ell)$ as a function of multipole ℓ, for a given combination of probes, X and Y, and a pair of redshift bins i and j. The covariance matrix in Eq. (2.2) is assumed to be Gaussian and takes into account shot noise as well as cosmic variance contributions, see e.g. Takada & Jain (2004) for the weak lensing case.

Following the notations of Joachimi & Bridle (2010), the angular power spectra of the cross-correlations between the various quantities related to the gravitational potential or the matter density can be written in a generic way using the Limber approximation,

$$C_{XY}^{(ij)}(\ell) = \int_0^{\chi_{\rm hor}} d\chi \, \frac{w_X^{(i)}(\chi)\, w_Y^{(j)}(\chi)}{f_K^2(\chi)} \, P_\delta(\ell/f_K(\chi), \chi) , \tag{2.3}$$

where χ is comoving distance, and $\chi_{\rm hor}$ the comoving horizon. The matter power spectrum is denoted by P_δ and the comoving angular diameter distance by $f_K(\chi)$. The kernels for the different cosmological probes are given by the following equations,

$$w_\varepsilon^{(i)}(\chi) = \frac{3\Omega_m H_0^2}{2c^2} \frac{f_K(\chi)}{a(\chi)} \int_\chi^{\chi_{\rm hor}} \mathrm{d}\chi' p^{(i)}(\chi') \frac{f_K(\chi'-\chi)}{f_K(\chi')} \quad \text{(galaxy weak lensing)} ; \tag{2.4}$$

$$w_n^{(i)}(\chi) = b_g(\ell/f_K(\chi), \chi)\, p^{(i)}(\chi) \quad \text{(galaxy clustering)} ; \tag{2.5}$$

$$w_{\rm CMB}(\chi) = \frac{3\Omega_m H_0^2}{2c^2} \frac{f_K(\chi)}{a(\chi)} \frac{f_K(\chi_* - \chi)}{f_K(\chi_*)} \quad \text{(CMB lensing)} . \tag{2.6}$$

Here, a denotes the scale factor, $p^{(i)}$ the redshift probability distribution for a galaxy sample i (either a broad tomographic bin or a narrow range defined via spectroscopic redshift), and b_g the galaxy bias which can vary as a function of scale and redshift. CMB lensing has a single source distance, χ_*, to the last scattering surface.

Note that the Limber approximation assumes that the kernels involved are broad in the line-of-sight direction, which breaks down in the case of spectroscopic clustering information. In this case we replace the formalism outlined above with the exact calculation as detailed in Padmanabhan et al. (2007).

PoS(AASKA14)020

Survey	Area [deg^2] Photo-z	Area [deg^2] Spec-z	n_g [arcmin^{-2}] Photo-z	n_g [arcmin^{-2}] Spec-z	DE FoM inc. Planck WGL	LSS	WGLxLSS
SKA1 early	1,000	1,000	4.8	-	3.0	-	-
SKA1 early	5,000	5,000	1.6	-	3.6	-	-
SKA1	5,000	5,000	4.2	1.8	16	0.05	19.2
SKA1	5,000	30,000	4.2	4.7	16	1.8	956
SKA2	5,000	5,000	44	22	182	320	6362
SKA2	30,000	30,000	20	10	425	1042	13150

Survey	Area [deg^2] Photo-z	Area [deg^2] Spec-z	MG FoM inc. Planck WGL	LSS	WGLxLSS
SKA1 early	1,000	1,000	1.9	-	-
SKA1 early	5,000	5,000	2.0	-	-
SKA1	5,000	5,000	8.0	4.7	415
SKA2	5,000	5,000	69	257	7429
SKA2	30,000	30,000	118	583	29947

Table 1: (Top) Summary of SKA survey forecasts and Dark Energy Figure of Merit results including Planck priors.(Bottom) Summary of survey forecasts For the modified gravity Figure of Merit from SKA phases one and two. The MG FOM here is defined in the same way as the DE FOM with the parameters of interest being the constants modifying the relation between the potentials.

We forecast constraints for our weak lensing (WGL) surveys alone, $\{C_{\varepsilon\varepsilon}^{(ij)}(\ell)\}$, large-scale structure (LSS) surveys alone (galaxy clustering including redshift-space distortions), $\{C_{nn}^{(ij)}(\ell)\}$, and the joint WGLxLSS analysis including cross-correlations, $\{C_{\varepsilon\varepsilon}^{(ij)}(\ell), C_{n\varepsilon}^{(ij)}(\ell), C_{nn}^{(ij)}(\ell)\}$. We also provide an assessment of the constraining power of CMB lensing with SKA LSS, $\{C_{\mathrm{SKA}\,nn}^{(ij)}(\ell), C_{\mathrm{CMB}\,\varepsilon\varepsilon}^{(ij)}(\ell)\}$, and CMB lensing with SKA WGL probes, $\{C_{\mathrm{SKA}\,\varepsilon\varepsilon}^{(ij)}(\ell), C_{\mathrm{CMB}\,\varepsilon\varepsilon}^{(ij)}(\ell)\}$.

3. Weak lensing - galaxy position cross correlations

The SKA survey will provide very competitive measurements of multiple cosmological probes. Combination of different probes allows the breaking of degeneracies between parameters which provides better control of systematics and better constraints on parameters of cosmological interest than any individual probe can achieve.

In this section we consider the combination of an SKA Weak Lensing (WGL) survey (with photometric redshifts provided externally) and an SKA galaxy position i.e. Large-Scale Structure (LSS) survey with spectroscopic quality redshifts.

Fig. 1 shows the headline constraints on dark energy (left panel) and deviations from General Relativity (right panel). Table 1 gives details of the assumed area and number density of sources for the different surveys we forecast.

The WGL surveys have photo-z quality redshifts. SKA1 early is assumed to get these from a DES-like survey so we assume photo-z error, $\delta_z = 0.07(1+z)$ and 5 tomographic bins of equal number density out to $z = 2$. SKA1 and SKA2 are assumed to get redshifts from a Euclid-like survey with $\delta_z = 0.05(1+z)$ and 10 tomographic bins of equal number density out to $z = 2$.

PoS(AASKA14)020

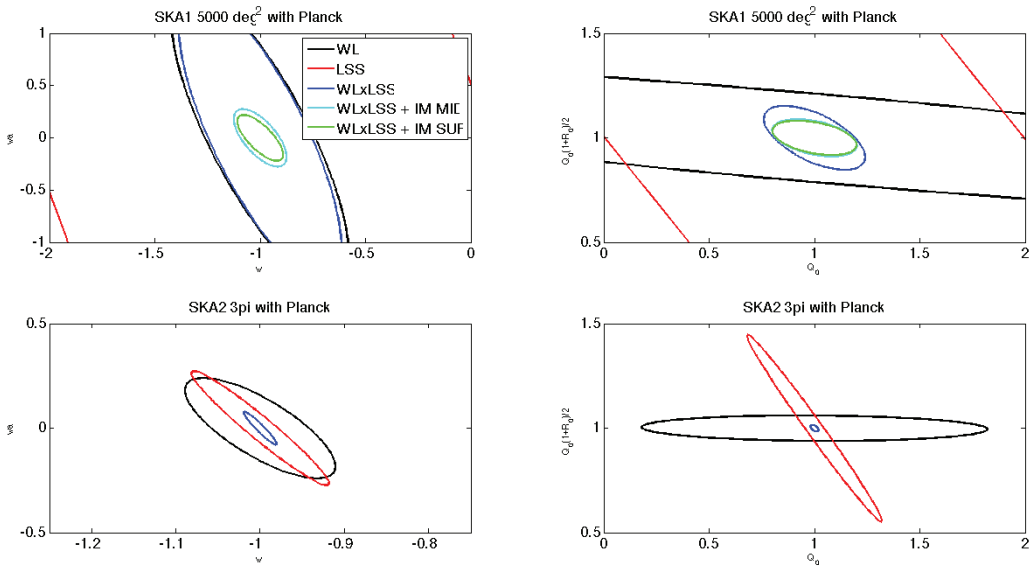

Figure 1: Constraints on dark energy [left panels] and deviations from GR [right panels] for SKA1 over 5,000deg^2 [top panels] and SKA2 over 30,000deg^2 [bottom panels] including Planck priors. Black ellipses show photometric WGL constraints only. Red ellipses show spectroscopic LSS constraints only. Blue ellipses show the combination of WGL and LSS including cross-correlations. Cyan ellipses show this WGLxLSS constraint combined independently with an SKA intensity mapping (IM) survey using the MID instrument and the green contours the same but with the SUR instrument. All constraints are 68% confidence contours.

The LSS surveys have galaxy redshift distributions described in the HI bias and simulations chapter of this book. Our forecasts assume 20 tomographic bins up to $z = 0.6$ for SKA1 and 40 tomographic bins up to $z = 2.0$ for SKA2. We use the exact $C(\ell)$ formalism (not the limber approximation) and include the effects of Redshift Space Distortions (RSDs) according to the formalism of Kaiser (1987). Both these effects are neglected in the WGL forecasts because the broad tomographic bins make their impact negligible.

Our FM analysis forecasts constraints for a set of cosmological parameters: $\{\Omega_m, \Omega_b, \Omega_{DE}, w_0, w_a, h, \sigma_8, n_s, b, Q_0, Q_0(1+R_0)/2\}$. As well as the standard wCDM parameters, b is a free amplitude on galaxy bias for each shell and $Q_0, Q_0(1+R_0)/2$ are parameterisations of deviations to General Relativity that modify the Poisson equation and the ratio of metric potentials, our ability to constrain these parameters quantifies our ability to test gravity on cosmic scales, see Kirk et al. (2013) for more detail. When quoting constraints on dark energy we marginalise over the cosmological parameters and galaxy bias but keep the modified gravity parameters fixed. When quoting constraints on modified gravity we marginalise over cosmology, including w_0 and w_a, and galaxy bias. Priors consistent with the latest Planck temperature constraints are included and the same used in the BAO chapter in this science book.

It is worth remarking that our forecasting approach is not the only method that has been used to estimate the joint power of a photometric WGL survey and a spectroscopic LSS survey. We treat all our observables as projected angular power spectra, $C(\ell)$s. The alternative is to model the

PoS(AASKA14)020

LSS survey with a full 3D $P(k,z)$ analysis then combine with WGL $C(\ell)$s. Our projection over the line-of-sight width of a tomographic bin throws away information compared to a full 3D analysis. For a photo-z WGL survey the photo-z scatter and the broad lensing kernel combine to produce a redshift resolution floor, below which precision cannot be pushed. This means our relatively coarse redshift binning captures all the available information. The spectroscopic survey has no such limitation, this is why we use a very large number of narrow tomographic bins to capture equivalent redshift-evolution information as contained in a full 3D analysis. The advantage of our approach is that all observables are in the same form and cross-correlations arise naturally. Mixing a 2D and 3D analysis leads to some rather ad-hoc formalisms to combine different observables.

Our results finding significant improvement from cross-correlation agree with Gaztañaga et al. (2012) who use a mixed 2D and 3D formalism. However, both Cai & Bernstein (2012) and de Putter et al. (2013) adopt a similar mixed approach but see little improvement from cross-correlation. This is an active area of research and discussion on the correct formalism or even how to accurately compare results is continuing.

DE Figure of Merit (FoM, see Albrecht et al. (2006)) for our various survey combinations are shown in Table 1. The joint WGLxLSS constraints are extremely strong. While the LSS surveys for both SKA1 and SKA2 favour large areas over depth, the joint WGLxLSS constraint for SKA2 prefers the deeper but smaller 5,000deg^2 survey over the shallower 30,000 deg^2 survey. The Modified Gravity constraint shown in the right panel of Fig. 1 has a WGLxLSS constraint that is orders of magnitude stronger than either probe alone. This is due to pronounced degeneracy breaking from the combination of a probe using light (WGL, sensitive to the sum of metric potentials $\Psi+\Phi$) and a probe using galaxies as non-relativistic tracers (LSS, sensitive to the Newtonian potential Ψ).

SKA1 WL + LSS represents a formidable dataset but it will of course not be the only one available. Dedicated optical surveys such as DES and eBOSS will be available and relatively mature by the completion of SKA1. In terms of number density and area a representative SKA1 survey configuration is comparable to DES+eBOSS with perhaps marginally better photo-z accuracy achieved with SKA1. We find that SKA1 (WGL+LSS+IM) provides comparable constraints on DE to a representative DES+eBOSS forecast while SKA1 significantly outperforms (more than a factor of five improvement) DES+eBOSS in constraining deviations from GR, probably driven by wider sky coverage for the spec-z survey. The fact that both probes are collected by the same instrument offers benefits for the understanding and control of systematics. Of course having datasets of comparable statistical power from both optical and radio surveys is of considerable scientific value of itself. It is with SKA2 that the project becomes definitively world-leading with much higher WL source density than the Euclid mission and a spectroscopic quality LSS survey covering the full area and depth of the WL measurement.

4. Cross correlations for redshift calibration.

Photometric redshifts are less accurate but much faster and cheaper to gather than spectroscopic redshifts. SKA will allow a large number of spectroscopic-quality redshifts to be gathered as it measures both galaxy position and redshift via the 21cm line for low redshift galaxies. For higher redshift galaxies used for example in the WGL survey it will require photometric-quality redshifts gathered by other surveys like Euclid.

PoS(AASKA14)020

A photometric redshift from a Euclid-like experiment can have a random scatter compared to the true redshift of order $\delta_z \sim 0.05(1+z)$. As well as this Gaussian scatter on the true redshift (which can lead to objects being assigned to the incorrect tomographic bin). We note that the true redshift distribution can become much broader than the extent of the corresponding tomographic bin. There are problems estimating the true mean redshift of a certain tomographic bin and what are known as "catastrophic outliers", galaxies whose redshift has been severely misidentified due to failures in the photo-z estimation pipeline, usually these are defined as estimates more than 3σ away from the true redshift, which e.g. can occur at optical wavelengths if the the Lyman and Balmer breaks are confused. Systematic shifts in the redshift distribution of tomographic bins can induce significant biases in cosmological analysis, so that the mean of these distributions needs to be known to better than a few parts in a thousand.

Cross-correlation with a spectroscopic survey which covers some or all of the same galaxy distribution as the photometric survey can be used to identify and mitigate these errors and calibrate the photometric redshift distribution.

We repeat the WGLxLSS forecasts made above but include now a range of nuisance parameters, $\{\delta_{z,i}, \Delta b_{z,i}\}$, which quantify our uncertainty on the photometric redshifts. Here $\delta_{z,i}$ is the Gaussian uncertainty on the photo-z estimate in each photo-z bin, i, with fiducial values 0.05 and $\Delta b_{z,i}$ is the bias on the mean redshift of bin i due to photo-z mis-estimation with mean values 0. We ignore catastrophic outliers in this analysis. Each of these parameters is allowed to vary in our FM analysis and the inclusion of the WGLxLSS cross-correlation allows them to be constrained.

See Fig 2 for constraints on these nuisance parameters for the SKA2 3π survey. Cross-correlation of the WGL survey with the spectroscopic LSS survey improves our estimate of the photo-z distribution by up to factor of 10. We emphasise that this is a cross-correlation between photometric WGL and spectroscopic LSS, in future we intend to study the cross-correlation between a LSS analysis using the photometric WGL galaxies and the spectroscopic LSS survey. This should prove even more effective at calibrating the photo-z errors because it is not hindered by the broad geometric kernels which restrict redshift resolution in WGL.

5. Cross-correlations with CMB lensing

The gravitational potential of the large scale structure generates a deflection of the trajectories of the Cosmic Microwave Background (CMB) photons. This effect, known as CMB lensing consists of a remapping of the underlying unlensed temperature and polarization fields. Mathematically, CMB lensing is described as follows: We introduce a vector field $\mathbf{d}(\hat{\mathbf{n}})$ (the deflection field) such that the lensed temperature $T(\hat{\mathbf{n}})$ and unlensed temperature $\tilde{T}(\hat{\mathbf{n}})$ are related by

$$T(\hat{\mathbf{n}}) = \tilde{T}(\hat{\mathbf{n}} + \mathbf{d}(\hat{\mathbf{n}})) \tag{5.1}$$

and analogously for the Stokes parameters $Q(\hat{\mathbf{n}})$, $U(\hat{\mathbf{n}})$ which describe linear CMB polarization.

To lowest order in perturbation theory, the deflection field $\mathbf{d}(\hat{\mathbf{n}})$ is the gradient of a scalar lensing potential (i.e. $\mathbf{d}(\hat{\mathbf{n}}) = \nabla\phi(\hat{\mathbf{n}})$) which can be written as a line-of-sight integral:

$$\phi(\hat{\mathbf{n}}) = -2\int d\eta \, \frac{\chi(\eta - \eta_{\rm rec})}{\chi(\eta_{\rm rec})\chi(\eta)} \Psi(\chi\hat{\mathbf{n}}, \eta), \tag{5.2}$$

PoS(AASKA14)020

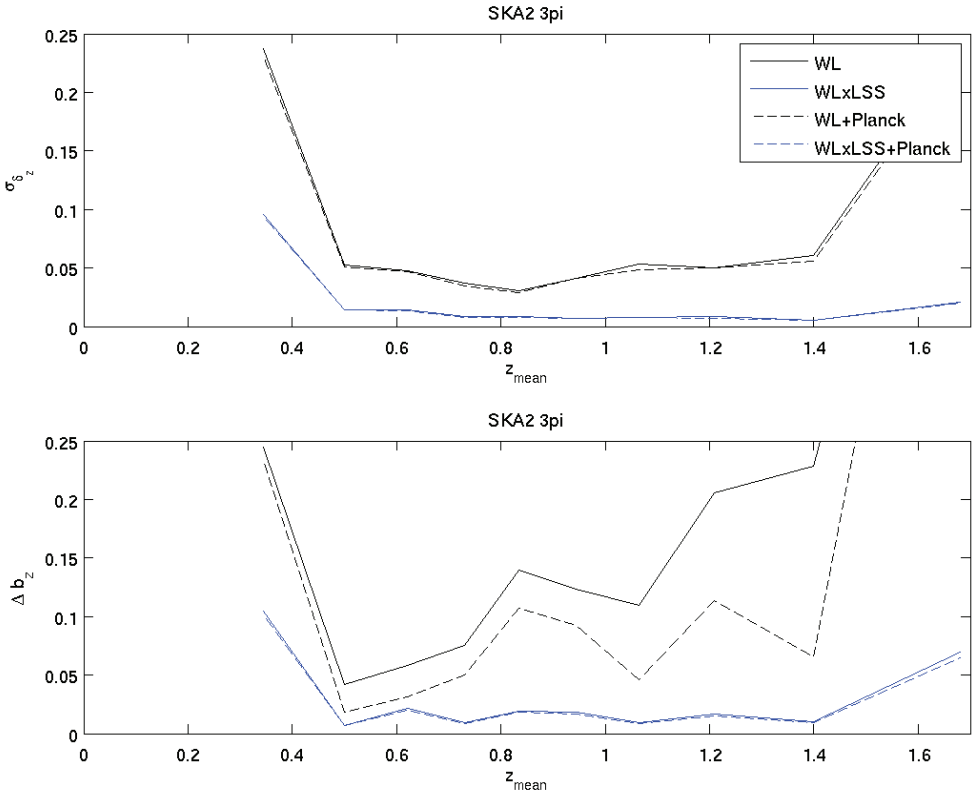

Figure 2: Constraints on photometric redshift error [top] and bias on mean redshift [lower] as a function of mean redshift of each tomographic bin for SKA2 over 30,000deg^2. WGL- only constraints are shown in black, WGLxLSS constraints in blue. Constraints including Planck priors are shown as dashed lines.

where Ψ is the Newtonian potential, η is conformal time, $\eta_{\rm rec}$ is the epoch of last scattering, and χ is the angular diameter distance in comoving coordinates, see Lewis & Challinor (2006) for a review).

CMB lensing modifies the Gaussian structure of the primary anisotropies and generates a correlation between the temperature and its gradient (Hu (2000)). These couplings can efficiently be used to construct an estimator, quadratic in the observed temperature, that can be applied to data to recover the lensing potential (Okamoto & Hu (2003)).

High resolution and high sensitivity CMB experiments can therefore provide a new cosmological probe of the large-scale structure of the Universe that is complementary to that obtained from galaxy surveys. Indeed CMB lensing is mostly sensitive to structure located in the $1 \leq z \leq 5$ range.

The lensing potential reconstructed from CMB lensing can be thought of as the projection on the sky of all the mass distribution up to the last scattering surface. As such we expect significant angular cross-correlation with the large-scale structure observables of radio surveys. The redshift dependence of the CMB lensing kernel means that, to ensure a strong cross-correlation, we ideally want a LSS survey with many galaxies at $z \gg 1$ and a WGL survey with many galaxies at $Z \gg 2$. SKA will produce very useful surveys in this respect, more useful than Euclid for example when

PoS(AASKA14)020

Survey	Area [deg^2] Photo-z	Planck WGL	Planck LSS	SPT3G WGL	SPT3G LSS
SKA1 early	5,000	5.7%	4.1%	2,8%	1.7%
SKA1	5,000	4.8%	3.4%	2.2%	1.3%
SKA1	3π	3.8%	2.2%	4.3%	1.9%
SKA2	5,000	2.9%	2.4%	0.9%	0.7%
SKA2	3π	1.6%	1.3%	1.1%	0.9%

Table 2: Constraints on the amplitude of the cross-correlation between the Planck and SPT3G lensing potential and the SKA surveys observables: weak lensing (WGL) and galaxy clustering (LSS).

considering this cross-correlation with CMB lensing.

The first reported detection of the gravitational lensing of the Cosmic Microwave Background was made by correlating WMAP data with the radio galaxy counts from the NRAO VLA sky survey (NVSS) (Smith et al. (2007), Hirata et al. (2008)). With the advent of arcminute scale CMB experiments (ACT, SPT), and full-sky CMB data from Planck, prospects for cross-correlation between CMB lensing and future radio data are extremely encouraging.

SKA will provide both precise measurement of the position and the shape of galaxies. In the following we use the same redshift distributions assumed in the Weak lensing chapter from this science book, and consider a value constant for the bias $b = 1$.

On the CMB lensing side, we consider the following surveys:

- Planck. We consider the Planck lensing potential from the Planck 2013 results (Planck Collaboration (2013)). The current Planck lensing map should be replaced in October 2014 and will include the full Planck data. We thus multiply the 2013 lensing noise levels by a factor 0.8 to account for this added data.

- South Pole Telescope (SPT). The SPT collaboration will observe the CMB polarization anisotropies to arcminute resolution on a 2500 sq. deg. patch in the southern hemisphere. The resulting lensing map will then be of a much better quality than the Planck one, but on a smaller area on the sky. The forecasted noise levels were provided by G.Holder and G. Simard (private communication).

In the following we quantify the level of detection of the cross-correlation between CMB lensing and the SKA observables. We use the values indicated in table 1 for the different incarnations of the SKA surveys. Since we are considering cross-correlations with external data set, we need to restrict the sky fraction to the maximum common area between SKA surveys and Planck/SPT data. We therefore restrict the SKA surveys to 2500 sq. deq. when correlating with the SPT lensing map. For the correlation between SKA surveys and the Planck lensing map we consider a maximum area of 15000 sq. deg.

Constraints on the amplitude of the cross-correlation between the SKA surveys observables (weak-lensing and galaxy clustering) and the CMB lensing potential are summarized in table 2. Some examples of those cross-correlations are shown in fig. 3.

PoS(AASKA14)020

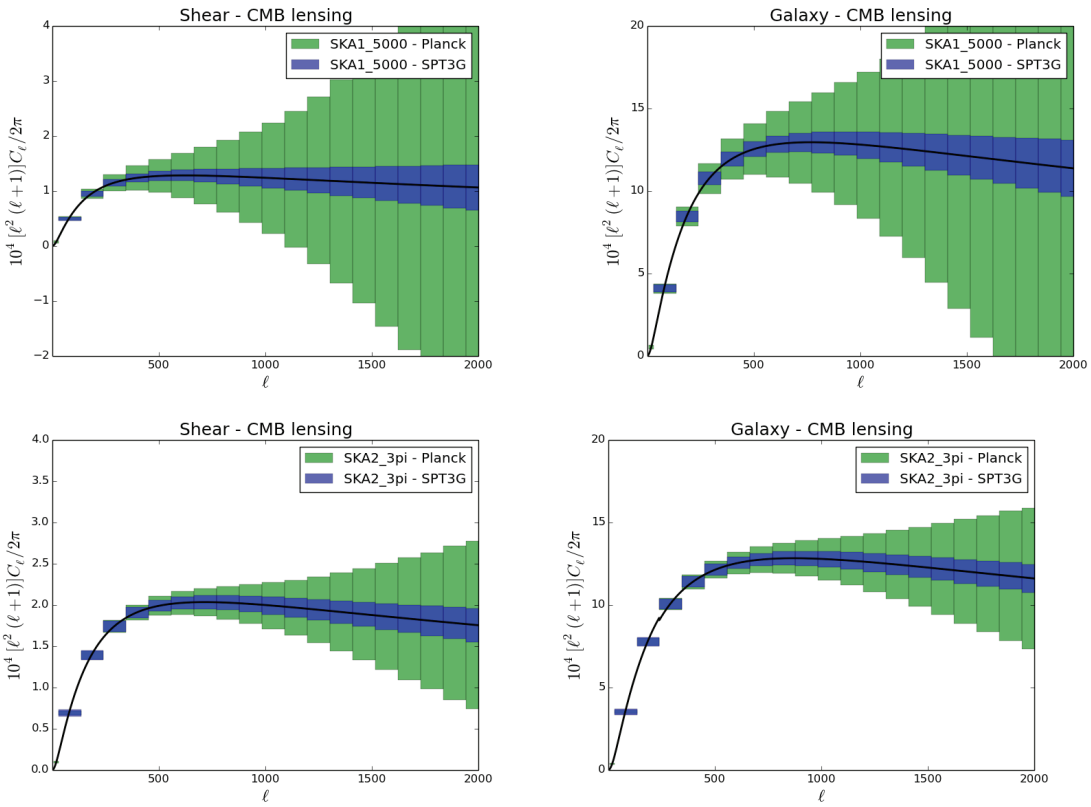

Figure 3: Weak-lensing (left column) and galaxy clustering (right column) for SKA1-5000 (top row) and SKA2-3π (bottom row) cross-correlations with the CMB lensing potential. Errors bars correspond to the Planck (green) and SPT3G (blue) noise levels.

Prospects for cross-correlations between SKA and CMB lensing are very encouraging. As can be seen from the plots in fig. 3, most of the signal will come from the use of high resolution, small scale CMB data such as SPT3G (similar results would hold using the Atacama Cosmology Telescope (ACT) specifications). This can be seen as the blue errors bars being much smaller than the green ones, which represent the correlation with Planck. However, thanks to its large sky coverage, Planck will dominate on the largest scale, despite being intrinsically noisier than arcminute scale CMB data.

The cross-correlation of SKA probes with CMB-lensing will improve our control of systematics and our ability to measure cosmology. CMB-lensing is sensitive to the integrated matter density between the observer and last-scattering without the mediation of biased tracers, helping us to control galaxy bias in a similar way to WGL but because the measurement of CMB-lensing is independent it can also calibrate important WGL systematics including shear measurement bias and intrinsic alignments, see Vallinotto (2013) for an example of the kinds of improvements that are possible.

PoS(AASKA14)020

6. Conclusions.

We have investigated the synergies from cross-correlating different SKA datasets as well as cross-correlation with CMB lensing datasets from other missions. We conclude that, using internal cross-correlation, the SKA will be able to calibrate the redshift inaccuracies present in its weak lensing sample, optimising the possible statistical measurements of cosmology. We see from our results that LSS measurements with galaxies from the SKA are not very competitive during phase 1 but they are still important as they help with the aforementioned redshift calibration, particularly the planned $\sim$100 deg^2 deep survey which will overlap fully in redshift with the WGL survey source population. We estimate this calibration to be possible at the sub-per cent level with SKA2.

We have shown that these cross-correlations provide huge gains for our Dark Energy analysis with SKA phase 2, but the largest gains come when we study Modified Gravity where, for SKA1 and SKA2, gains of several orders of magnitude are possible from combining WGL and LSS datasets.

We also present constraints on the amplitude of the cross correlations between the lensing signal of future CMB experiments and the SKA and a sub present level constraint on the amplitude is possible. This would impose stringent constraints on the bias of SKA galaxy samples, calibrate systematic uncertainties in our WGL measurement and help constrain other cosmological parameters.

References

Albrecht, A., Bernstein, G., Cahn, R., et al. 2006, Arxiv e-prints, astro-ph/0609591

Cai, Y. C. & Bernstein, G. 2012, MNRAS, Volume 422, Issue 2, pp. 1045-1056

Gaztañaga, E., Eriksen, M., Crocce, M., et al. 2012, MNRAS, Volume 422, Issue 4, pp. 2904-2930

Heavens, A 2009, ArXiv e-prints, 0906.0664

Hirata, C. M., Ho, S., Padmanabhan, N., et al. 2012, Physical Review D, vol. 78, Issue 4, id. 043520, 2008

Hu, W 2000, Physical Review D (Particles, Fields, Gravitation, and Cosmology), Volume 62, Issue 4, 15 August 2000, id.043007

Kaiser, N 1987, MNRAS, 227, 1

Kirk, D., Lahav, O., Bridle, S., et al. 2013, ArXiv e-prints, 1307.8062

Joachimi, B. & Bridle, S. L. 2010, Astronomy and Astrophysics, Volume 523, id.A1, 21 pp. , 2010

Lewis, A. & Challinor, A. 2006, Physics Reports, Volume 429, Issue 1, p. 1-65.

Okamoto, T. & Hu, W. 2003, Physical Review D, vol. 67, Issue 8, id. 083002

Padmanabhan, M., Schlegel, D. J., Seljak, U., et al. 2007, MNRAS, Volume 378, July 2007, pp. 852-872

Planck Collaboration, 2013, Astronomy and Astrophysics, Volume 571, id.A17, 39 pp.

de Putter, R., Doré, O., & Takada, M. 2013, Arxiv e-prints, 1308.6070

Smith, K. M., Zahn, O., & Doré, O. Physical Review D, vol. 76, Issue 4, id. 043510, 2007

Takada, M. & Jain, B. 2004, MNRAS, Volume 348, Issue 3, pp. 897-915

Tegmark, M., Taylor, A. N., & Heavens, A. F. ApJ, 480, 22, 1997

Vallinotto, A 2013, ApJ, Volume 778, Issue 2, article id. 108, 4 pp. (2013)

PoS(AASKA14)020

PROCEEDINGS OF SCIENCE

HI galaxy simulations for the SKA: number counts and bias

Mario G. Santos[1,2], **David Alonso**[3], **Philip Bull**[4], **Marta Silva**[5,1], **Sahba Yahya**[1]

[1] *Department of Physics, University of Western Cape, Cape Town 7535, South Africa*
[2] *SKA SA, 4rd Floor, The Park, Park Road, Pinelands, 7405, South Africa*
[3] *Astrophysics, University of Oxford, DWB, Keble Road, Oxford OX1 3RH, UK*
[4] *Institute of Theoretical Astrophysics, University of Oslo, PO Boks 1029 Blindern, 0315 Oslo, Norway*
[5] *CENTRA, Instituto Superior Técnico, Universidade de Lisboa, Lisboa 1049-001, Portugal*
E-mail: mgrsantos@uwc.ac.za

This chapter describes the assumed specifications and sensitivities for HI galaxy surveys with SKA1 and SKA2. It addresses the expected galaxy number densities based on available simulations as well as the clustering bias over the underlying dark matter. It is shown that a SKA1 HI galaxy survey should be able to find around 5×10^6 galaxies over 5,000 deg^2 (up to $z \sim 0.8$), while SKA2 should find $\sim 10^9$ galaxies over 30,000 deg^2 (up to $z \sim 2.5$). The numbers presented here have been used throughout the cosmology chapters for forecasting.

Advancing Astrophysics with the Square Kilometre Array
June 8-13, 2014
Giardini Naxos, Italy

PoS(AASKA14)021

1. Introduction

Large scale structure surveys have so far relied on imaging of a large number of galaxies at optical or near-infrared wavelengths combined with redshift information to obtain the 3-dimensional galaxy distribution (e.g. DES, BOSS, Euclid). Hydrogen is the most abundant baryon in the Universe, making it a prime candidate for a tracer of the underlying dark matter distribution and an invaluable probe of the energy content of the Universe and the evolution of large-scale structure. In order to use hydrogen as a tracer at radio wavelengths, we need to rely on radio observations of the neutral hydrogen (HI) 21cm line. With a rest frequency of 1420 MHz, telescopes probing the sky between this and 250 MHz would be able to detect galaxies up to redshift 5. Although we expect most galaxies to contain HI, since the spin-flip transition responsible for the 21cm signal is highly forbidden, the emission is quite weak: at $z = 1.5$ most galaxies with a HI mass of 10^9 $M_\odot$ will be observed with a flux density of ~ 1 μJy. This implies that for low sensitivity surveys, only the closest or HI-richest galaxies will be observed, and therefore massive telescopes will be required in order to detect sufficient numbers of HI galaxies at a level capable of providing competitive constraints in Cosmology. This chapter analyses the expected number density of HI galaxies as a function of redshift as well as its clustering bias taking into account the flux sensitivities for HI galaxy surveys using the planned SKA telescopes. We discuss the process by which we obtain these numbers - using a set of state of the art simulations - identify inherent limitations in the current set up and suggest a series of improvements. Although we focus on SKA1 and 2, the sensitivity calculations presented here allow us to easily consider other configurations such as an early deployment of SKA1 (corresponding to about 50% of its expected sensitivity).

2. Sensitivity calculations

The noise associated to the flux density (flux per unit frequency) measured by an interferometer can be assumed to be Gaussian with a rms given approximately by

$$\sigma_S \approx \frac{2k_B T_{\rm sys}}{A_{\rm eff}\sqrt{2\delta\nu\, t_p}}, \tag{2.1}$$

for an array with total effective collecting area $A_{\rm eff}$, frequency resolution $\delta\nu$ and observation time per pointing t_p (k_B is the Boltzmann constant). The extra factor of $1/\sqrt{2}$ comes from assuming dual polarised systems. Telescope sensitivities are sometimes quoted in terms of the "System Equivalent Flux Density": SEFD $\equiv 2k_{\rm B}T_{\rm sys}/A_{\rm eff}$ or just "A over T": $A_{\rm eft}/T_{\rm sys}$. The effective collecting area depends on the efficiency of the system which is expected to be in the range of 70 to 80% for the SKA1 dishes.

Note that the expression above gives the flux density sensitivity per resolution beam (not to be confused with the dish primary beam or telescope field of view). Moreover, this is the sensitivity if the full array is used without constraints on the psf (point spread function or resolution beam). This is what is usually called the natural array sensitivity. Although angular resolution is not a crucial issue in a HI galaxy survey, some weighting of the visibilities might be required in order to obtain a better behaved psf. In that case, the sensitivity of the telescopes will be further reduced. The required shape and resolution of the psf will depend on the source detection algorithm for

PoS(AASKA14)021

HI galaxies which is still a subject of active research. For SKA1, using uniform weighting plus Gaussian tapering of the visibilities can produce "well behaved" Gaussian beams at 10 arc-seconds resolution with flux sensitivities that are 30% to 80% worse than what is quoted here (see Braun 2013). However, new source extraction algorithms might be able to deal with more complex psfs (for instance, by working in the visibility space directly) and approach the natural array sensitivity. Therefore in this chapter we decided to quote values using the full array, underlining that in reality the situation might be less optimistic.

The equivalent brightness temperature uncertainty is

$$\sigma_T = \frac{\sigma_S c^2}{2k_B \nu^2 (\delta\theta)^2}, \tag{2.2}$$

where $\delta\theta$ is the angular resolution of the interferometer. The total temperature is

$$T_{\rm sys} = T_{\rm inst} + T_{\rm sky} \tag{2.3}$$

with $T_{\rm sky} \approx 60\left(\frac{300\,{\rm MHz}}{\nu}\right)^{2.55}$ K and $T_{\rm inst}$ the instrument temperature, which is usually higher than the sky temperature above 300 MHz. For typical instrument specifications, the array noise flux rms can be written as:

$$\sigma_S = 260\,\mu{\rm Jy}\left(\frac{T_{\rm sys}}{20\,{\rm K}}\right)\left(\frac{25{,}000\,{\rm m}^2}{A_{\rm eff}}\right)\left(\frac{0.01{\rm MHz}}{\delta\nu}\right)^{1/2}\left(\frac{1{\rm h}}{t_{\rm p}}\right)^{1/2}. \tag{2.4}$$

For a given survey area, $S_{\rm area}$ we will need approximately $S_{\rm area}/(\theta_{\rm B})^2$ pointings where $(\theta_{\rm B})^2$ is the telescope primary beam (instantaneous field of view) with the full width at half maximum of the beam, given by (in radians)

$$\theta_{\rm B} \approx 1.22\lambda/\sqrt{A_{\rm dish}}, \tag{2.5}$$

where $A_{\rm dish}$ is the effective area of each dish. The time per pointing t_p is then related to the total integration time $t_{\rm tot}$ through

$$t_p = t_{\rm tot}\frac{(\theta_{\rm B})^2}{S_{\rm area}}. \tag{2.6}$$

This will increase the time per pointing at the lowest frequencies (for a fixed $t_{\rm tot}$). Note however that when doing a survey some overlap of the beams is expected in order to achieve uniformity on the noise across the sky map. Following the SKA1 imaging performance memo, we assume that the mosaicked beams will correspond to a size of:

$$\theta_{\rm B}^2 \approx \frac{\pi}{8}\left(\frac{1.3\lambda}{D}\right)^2\ [{\rm sr}]. \tag{2.7}$$

The situation is slightly more complicated for PAFs (Phased Array Feeds) as below a certain critical frequency (usually taken as the middle of the band), the beams will remain constant. Therefore, for a PAF with a certain number of beams, N_b, we will assume that above the critical frequency, the full beam will be $N_b \times$ SPF, where SPF is the single pixel feed beam as above (eq. 2.7) and below that critical frequency, it will remain constant.

Following the current baseline design (Dewdney et al. 2013), table 1 summarises the specifications for each telescope, while table 2 contains the specifications assumed for the target HI

PoS(AASKA14)021

Telescope	Band [MHz]	z	$T_{\rm inst}$ [K]	$N_{\rm dish}$	$D_{\rm dish}$ [m]	$A_{\rm eff}$ [m^2]	beam [deg^2] [a]	Flux rms [μJy] [b]
SKA1-MID	350 - 1050	0.35 - 3.06	28	190	15	21,824	1.78	417
SKA1-MID	950 - 1760	(0) - 0.50	20	190	15	26,189	0.48	247
MeerKAT	580 - 1015	0.40 - 1.45	29	64	13.5	6,413	1.68	1015
MeerKAT	900 - 1670	(0) - 0.58	20	64	13.5	5,955	0.64	1093
MID + MK	580 - 1015	0.40 - 1.45	28.5	254	–	28,237	1.37	328
MID + MK	950 - 1670	(0) - 0.50	20	254	–	32,144	0.51	202
SKA1-SUR	350 - 900 [c]	0.58 - 3.06	50	60	15.0	8,482	61 (710) [d]	1918
SKA1-SUR	650 - 1670 [c]	(0) - 1.19	30	60	15.0	8,482	18 (1300) [d]	1151
ASKAP	700 - 1800	(0) - 1.03	50	36	12.0	3,257	30 (1250) [d]	4996
SUR + ASKAP	650 - 1670 [e,f]	(0) - 1.19	30 [e]	96	–	11,740	18 (1300) [d]	832
SKA2 [g]	480 - 1290	0.1 - 2.0	20	250 [h]	50	400,000	30	16

Table 1: Telescope configurations.
Notes: [a] This is the primary beam (FoV) calculated at the center of the band unless stated otherwise. It is proportional to λ^2 (except for PAFs). For the combined telescopes, the smallest beam of the two telescopes is used. [b] Flux density rms at the centre of the band (or the frequency shown in parenthesis) for a frequency interval of 0.01 MHz and 1 hour integration using Eq. 2.4. This is the natural array sensitivity. Requirements on the shape of the psf can increase this value by about 50%. [c] Only 500 MHz instantaneous bandwidth. [d] PAF beams assumed constant below the critical frequency (shown in parenthesis in MHz) and going as $1/\nu^2$ above that. [e] Assuming that all ASKAP PAFs will be replaced to meet the SKA1-SUR frequency band and instrument temperature of 30K. [f] Assuming that only band 2 will be initially deployed. [g] Values only indicative - can be changed. Both beam and flux rms are assumed constant across the band. [h] These should be stations (dense aperture arrays).

galaxy surveys. Note that, in order for the sensitivities to be proportional to ν, we assume that the mosaicking is done at the highest frequency used for the HI survey (i.e. telescope pointings are packed side by side at the highest frequency). This way, at lower frequencies, the beams will overlap, since their size varies as $1/\nu^2$, which will increase the time per pointing with the corresponding improvement in sensitivity. Of course, for PAFs, this sensitivity will remain constant below the critical frequency. Table 2 shows that both SKA1 instruments (MeerKAT+MID and ASKAP+SUR) have comparable performance for a HI galaxy survey at the highest frequency band considered here (band 2). Note however that this assumes that all ASKAP PAFs will have to be replaced with new generation receivers at some point. On the other hand, at the lowest frequencies (band 1), SKA1-SUR seems to perform better.

3. HI galaxy surveys

To calculate the HI galaxy number density and bias as a function of flux rms, we used the SAX-sky simulation[1]. The SAX-Sky simulation consists of a galaxy catalogue containing the position and several astrophysical properties for each object in a mock observing cone. It was produced by Obreschkow et al. (2009) by adding HI and CO properties to the galaxies obtained by De Lucia

[1] `http://s-cubed.physics.ox.ac.uk/s3_sax`

PoS(AASKA14)021

Telescope	Band [MHz]	beam [deg^2]	Survey area [deg^2]	t_p [hours]	$S_{\rm rms}^{\rm (ref)}$ [μJy]
SKA1-MID [a] (Band 1)	350 - 1050	0.88	5,000	1.76	315
SKA1-MID [a] (Band 2)	950 - 1760	0.88	5,000	1.76	187
MeerKAT [a] (Band 1)	580 - 1015	1.06	5,000	2.13	696
MeerKAT [a] (Band 2)	900 - 1670	1.06	5,000	2.13	750
SKA1-MID + MeerKAT [a] (Band 1)	580 - 1015	0.88	5,000	1.76	247
SKA1-MID + MeerKAT [a] (Band 2)	950 - 1670	0.88	5,000	1.76	152
SKA1-SUR [b] (Band 1)	350 - 900	61 (710)	5,000	122	174
SKA1-SUR [b] (Band 2)	650 - 1670	18 (1300)	5,000	36	192
ASKAP [b]	700 - 1800	30 (1250)	5,000	6	645
SKA1-SUR + ASKAP [b]	700 - 1670	18 (1300)	5,000	36	140
SKA2 [c]	480 - 1290	30	30,000	10	5.14

Table 2: Survey specifications. We assume a total observation time of 10,000 hours. The corresponding flux density rms ($S_{\rm rms}^{\rm (ref)}$) is calculated for a frequency interval of 0.01 MHz using the natural array sensitivity.
Notes: [a] Values calculated at the target frequency of 1.0 GHz unless stated otherwise. The beam and time per pointing (t_p) are assumed to change as $(\frac{1.0\,\rm GHz}{\nu})^2$ across the band. The flux density rms is assumed to change as $\frac{\nu}{1.0\,\rm GHz}$ across the band. [b] Values calculated at the PAF critical frequency (in parentheses, in MHz). Below that frequency, values are assumed constant. Above it, the beam and t_p are assumed to go as $1/\nu^2$, and the flux density rms as ν. [c] Indicative values. The beam and flux density rms are assumed constant across the band.

& Blaizot (2007) through the post processing of the Millennium dark matter simulation (Springel et al. 2005).

The Millennium simulation is a large dark matter simulation with a box size of 500 h^{-1} Mpc and a spatial resolution of 5 h^{-1} kpc. It was run in order to study the formation of dark matter halos and their evolution with time and therefore comoving snapshots are available at 64 fixed time steps from redshifts 127 to 0. The simulation was run using a WMAP1-compatible cosmology and a mass resolution of $8.6 \times 10^8\, h^{-1}{\rm M}_\odot$. The halos were identified as Friends-of-Friends groups containing more than 20 particles, and merger trees were built to link each halo with its substructures throughout time. In De Lucia & Blaizot (2007) the simulation was post-processed in order to populate the halos with simple models of galaxies and used a semi-analytical scheme to evolve the galaxies properties independently unless a merger occurs. The properties of each of these galaxies includes the mass of the different constituents, such as the mass of the cold and hot gas components, as well as the galaxy star formation rate (SFR), Hubble type, etc.

The atomic and molecular gas components of each galaxy were then obtained by Obreschkow et al. (2009) from the cold gas component based on properties of nearby regular spiral galaxies. Assuming that the cold gas of these galaxies resides in flat, approximately symmetric disks, it follows that the local gas pressure is connected to the molecular gas fraction by a known physically based prescription, which is also compatible with observations (at least for the more HI massive galaxies). The hydrogen mass of the cold gas component was assumed to be 0.74% of the total

PoS(AASKA14)021

mass. In order to properly emulate the light cone, the SAX-sky simulation used only part of each snapshot of the Millennium simulation as is described in Obreschkow et al. (2009). Therefore, the boxes at fixed redshifts with HI properties which can be obtained from the SAX-sky simulation are considerably smaller than $500\,h^{-1}$ Mpc along the line of sight. This can undermine the estimation of statistical quantities such as the galaxy bias (the number densities, on the other hand, can be easily obtained from the queries in the s-cubed web site).

3.1 Galaxy number counts

For the detection of a galaxy, we required that at least two points on the HI line are measured, that is, the width of the line has to be larger than twice the assumed frequency resolution of the survey. The idea is to obtain information on the typical line double peak expected from HI galaxies due to their rotation. This in principle will remove any galaxy that is seen "face on" since it would show just a narrow peak. More evolved source detection methods can (and should) be explored, to avoid spurious detections due to RFI, but we will keep this simple approach for now. A signal to noise of 10 is then usually required for the detection of a galaxy. We used the following variables and prescription to detect HI galaxies in the SAX database:

- `zapparent` – Apparent redshift (including Doppler correction).
- Experiment spectral resolution set to $dV = 2.1(1 + \texttt{zapparent})$ at the galaxy rest frame (in Km/s). This corresponds to an observed frequency resolution of 0.01 MHz which is what has been assumed for the sensitivity calculations.
- `hiwidthpeak` [Km/s] – Line width between the two horns of the HI-line profile in the galaxy rest frame (already corrected for the galaxy inclination).
- Following what has been discussed, we take only galaxies where $\texttt{hiwidthpeak}/2 > dV$.
- `hiintflux` [Jy Km/s] – Velocity-integrated line flux of the HI-line (in the observers frame).
- For each galaxy the observed sensitivity in terms of flux density (flux per frequency) is then $\text{flux}_\text{d} = \texttt{hiintflux}/\texttt{hiwidthpeak}$. Note that this already factors in the relation between velocity integrated flux and the frequency integrated flux as well as the relation between the velocity line width in the rest frame and the corresponding observed frequency.
- Finally, we take only galaxies where flux $> N_\text{cut} S_\text{rms}/\sqrt{(\texttt{hiwidthpeak}/dV)}$ (we took $N_\text{cut} = 10$ for a "10-sigma" cut).

In order to be as general as possible we did not try to match completely the flux rms used in the query to the survey specifications given in table 2. Instead we give results for different values so that a simple interpolation can be used for different surveys. In particular, if we decide to use a 5σ cut instead of 10σ, it is just a question of looking for the numbers corresponding to the flux rms that is half the survey value (since the obtained number counts all assumed a 10-sigma cut).

PoS(AASKA14)021

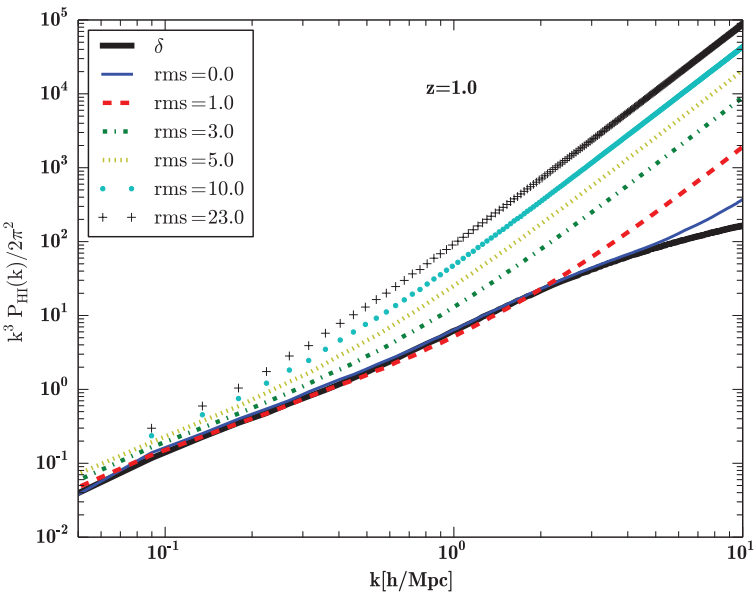

Figure 1: The dimensionless HI galaxy power spectrum for different flux cuts using the prescription described above for each flux rms. Black solid line shows the dark matter power spectrum from CAMB. The straight lines at high k indicate shot noise.

3.2 Galaxy bias

To obtain the bias, the "detected" galaxies were put in a box, for which the power spectrum of the number counts was calculated. The bias squared was then taken as the ratio of that power spectrum to the dark matter one at $k = 0.2$ h/Mpc. To perform this study we used boxes with different sizes from $L_{\parallel} = 58h^{-1}$ Mpc and $L_{\perp} = 100h^{-1}$ Mpc for redshift 0.06 to $L_{\parallel} = 162h^{-1}$ Mpc and $L_{\perp} = 398h^{-1}$ Mpc for redshift 2.07. This makes the bias extraction problematic, since we cannot efficiently probe modes below $k \sim 0.1$ h/Mpc, where we can safely neglect non-linear effects. For high flux rms, the number of galaxies is low and the shot noise dominates up to very small wave numbers. The conclusion is that for high flux/redshift values the results should be taken as only an indication, in particular for bias above $\sim 20\mu$Jy flux rms. As an example we show in Figure 3.1 the dimensionless HI galaxy power spectrum at $z = 1$ for different sensitivities. Also note that the Millennium simulation only has galaxies with masses $\gtrsim 2 \times 10^{10} M_{\odot}$ and therefore the bias and number density for rms=1 might be affected by the lack of smaller galaxies. However this should not affect the statistics for higher rms values. The cosmological analysis should compare results for different fiducial values and fully marginalise over the bias and number counts.

4. Fitting functions for galaxy number counts and bias

In this section we describe fitting functions for the galaxy number counts, dn/dz, and bias, $b(z)$, as a function of redshift. At a constant flux rms, these are well described by the functions

PoS(AASKA14)021

(Yahya et al. 2014)

$$dn/dz = 10^{c_1} z^{c_2} \exp(-c_3 z) \tag{4.1}$$

$$b(z) = c_4 \exp(c_5 z), \tag{4.2}$$

where c_i are free parameters. dn/dz is the number of galaxies per square degree, per unit redshift. Best-fit values of the parameters are given in Table 3, and Fig. 2 compares the fitted curves with data points from the simulations.

Note that for a redshift bin of width Δz, the observed number of galaxies in a 1 deg^2 patch is $\approx \frac{dn}{dz}\Delta z$, and the comoving galaxy number density is $n(z) = \frac{dn}{dz}\frac{1}{dV/dz}$, where $\frac{dV}{dz} = \frac{dr}{dz}(\pi/180)^2 r(z)^2$, $r(z)$ is the coming distance to redshift z and $dr/dz = c/H(z)$.

As explained above, the flux sensitivities for the telescopes listed in Table 2 are taken to either evolve with frequency, $S_{\rm rms} \propto \nu$, or are assumed constant across the band. For the non-PAF receivers (SKA1-MID and MeerKAT), the flux rms as a function of redshift is

$$S_{\rm rms}(z) = S_{\rm rms}^{\rm (ref)} \left(\frac{N_{\rm cut}}{10}\right) \frac{\nu_{21}}{1\ {\rm GHz}} (1+z)^{-1}, \tag{4.3}$$

where $S_{\rm rms}^{\rm (ref)}$ is the reference flux rms at 1 GHz listed in Table 2, $N_{\rm cut}$ is the detection threshold in multiples of the flux rms, and $\nu_{21} \simeq 1.42$ GHz is the rest frame frequency of the HI line. For the PAF receivers (SKA1-SUR and ASKAP), the flux rms is

$$S_{\rm rms}(z) = S_{\rm rms}^{\rm (ref)} \left(\frac{N_{\rm cut}}{10}\right) \times \begin{cases} 1 & \nu \leq \nu_{\rm crit} \\ \frac{\nu_{21}}{\nu_{\rm crit}}(1+z)^{-1} & \nu > \nu_{\rm crit} \end{cases}, \tag{4.4}$$

where $\nu_{\rm crit}$ is the PAF critical frequency listed in Table 2, and $S_{\rm rms}^{\rm (ref)}$ is the reference flux at the critical frequency. The full SKA has $S_{\rm rms}(z) = $ const. We take $N_{\rm cut} = 5$ for all but the full SKA, to which we apply a more stringent 10σ threshold. To obtain the number counts and bias for a given telescope, we interpolate Eqs. 4.1 and 4.2 as a function of flux rms using the values given in Table 2, and evaluate them as a function of redshift using the appropriate $S_{\rm rms}(z)$ function. We then fit the same fitting functions to the results – best-fit parameters are given in Table 4. Note that while the frequency-corrected number counts are all satisfactorily fitted by Eq. 4.1, four of the bias functions are not well described by Eq. 4.2; these are flagged in the table.

5. Limitations of current simulations and future improvements

Although the SAX-Sky is a state-of-the-art simulation in terms of cosmological radio surveys, it suffers from a number of shortcomings that would be desirable to address in the future, in order to improve the quality of the forecasts for the SKA.

Probably the most challenging problem for this type of simulations is finding a compromise between the enormous volume that experiments like the SKA are expected to probe, and the complexity necessary to simulate the type of objects that will be observed with sufficient precision. In our case, we would ideally need a simulation with a box of size $L_{\rm box} \sim 15\,h^{-1}$Gpc and resolving haloes down to $\sim 10^9\,h^{-1}M_\odot$, which is simply out of the question given the present typical

PoS(AASKA14)021

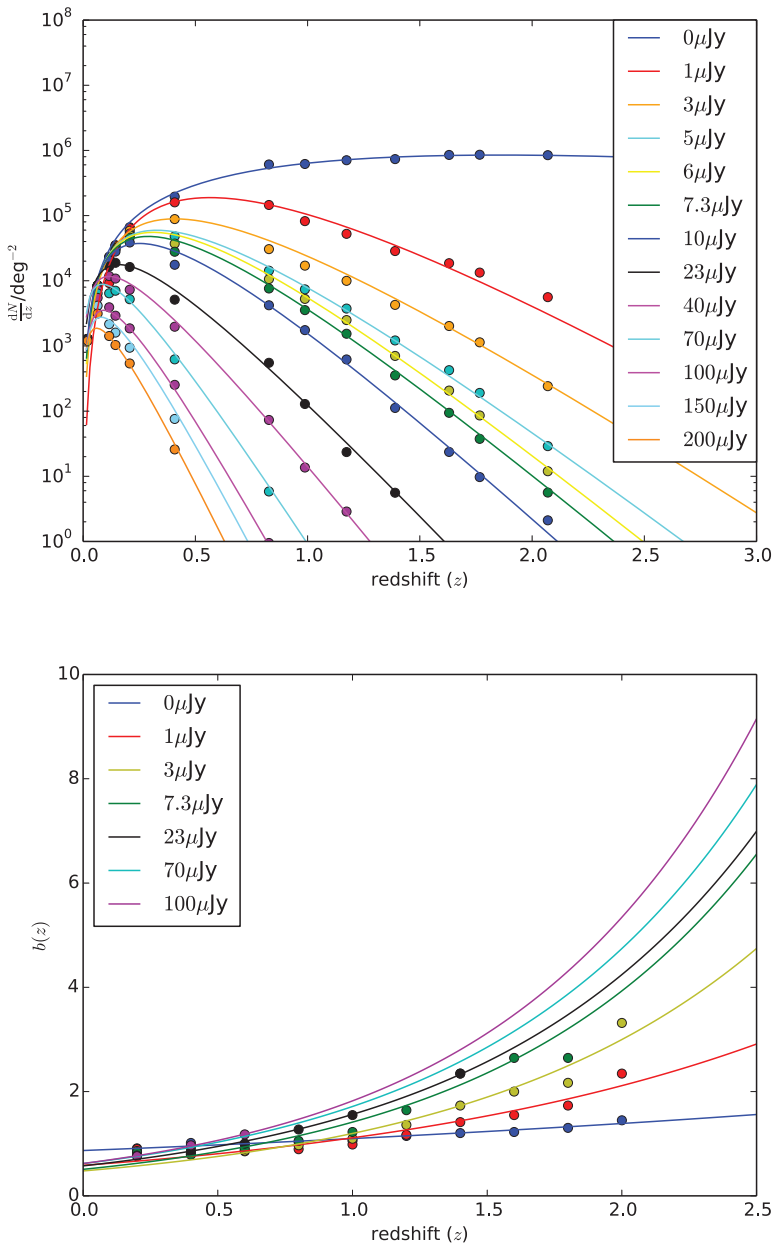

Figure 2: Upper panel: Dependence of the HI galaxy redshift distribution dn/dz (units: deg^{-2}). Note that the numbers are for different flux rms which will in turn correspond to a given galaxy flux cut according to the source detection procedure described in the text (which assumed a 10-sigma cut). Curves follow the fits according to Eq. 4.1 and dots are from the S^3-SAX simulation. Lower Panel: HI galaxy bias for different $S_{\rm rms}$. Note that above 70 μJy values for high redshifts are purely extrapolations. However, this has little impact as at high z, shot noise will dominate for these sensitivities.

PoS(AASKA14)021

$S_{\rm rms}$ [μJy]	c_1	c_2	c_3	c_4	c_5
0	6.23	1.82	0.98	0.8695	0.2338
1	7.33	3.02	5.34	0.5863	0.6410
3	6.91	2.38	5.84	0.4780	0.9181
5	6.77	2.17	6.63	0.5884	0.8076
6	6.84	2.23	7.13	0.5908	0.8455
7.3	6.76	2.14	7.36	0.5088	1.0222
10	6.64	2.01	7.95	0.4489	1.2069
23	6.02	1.43	9.03	0.5751	0.9993
40	5.74	1.22	10.58	0.5125	1.1842
70	5.62	1.11	13.03	0.6193	1.0179
100	5.63	1.41	15.49	0.6212	1.0759
150	5.48	1.33	16.62	–	–
200	5.00	1.04	17.52	–	–

Table 3: Values of the fitted parameters for Eqs. 4.1 and 4.2. For higher flux cuts we suggest taking $b(z)$=1, as only galaxies below $z \sim 0.5$ are relevant anyway.

Telescope	c_1	c_2	c_3	c_4	c_5	$N_{\rm gal}$
SKA1-MID (Band 1)	4.6399	0.8577	13.402	0.8675*	0.4767*	7.40×10^4
SKA1-MID (Band 2)	5.3662	1.2611	13.979	0.7038*	0.8616*	3.39×10^6
MeerKAT (Band 1)	4.9849	1.8010	17.359	1.0000	0.0000	6.27×10^3
MeerKAT (Band 2)	7.6813	4.5740	28.067	1.0000	0.0000	1.22×10^5
SKA1-MID + MeerKAT (Band 1)	5.1667	1.1585	14.170	0.8116*	0.7163*	7.76×10^4
SKA1-MID + MeerKAT (Band 2)	5.4381	1.3315	11.836	0.6343	0.9708	4.96×10^6
SKA1-SUR (Band 1)	5.1814	1.1668	14.208	0.8108*	0.7174*	9.95×10^3
SKA1-SUR (Band 2)	5.9023	1.5879	16.149	0.6232	1.0636	4.25×10^6
ASKAP	4.8577	1.1551	17.499	1.0000	0.0000	8.08×10^5
SKA1-SUR + ASKAP	5.8611	1.4742	15.344	0.6206	1.0559	5.55×10^6
SKA2	6.7767	2.1757	6.6874	0.5887	0.8130	9.12×10^8

Table 4: Values of the best-fit number count/bias parameters (Eqs. 4.1 and 4.2) for individual telescopes, after scaling the flux rms with frequency and interpolating. Some of the resulting bias functions are not fit very well by Eq. 4.2; these are flagged. The total number of galaxies expected for each survey is also shown (with 5,000 deg^2 except for SKA2).

PoS(AASKA14)021

computational resources. One must therefore accept a number of approximations, which simplify the problem while preserving the accuracy of the relevant physical processes. Recently there has been significant progress, sparked by the computational needs of the cosmological redshift surveys community, in finding alternative numerical methods, such as the production of faster simulations of the matter distribution that are reliable on cosmological scales (e.g. Tassev et al. 2013; White et al. 2014).

Even using these methods, it would still be difficult to reach the required mass resolution. However, a number of methods have been proposed to extend the mass range in a consistent way (Sousbie et al. 2008; de la Torre & Peacock 2013). Also, once a simulation has been performed using a particular cosmological model, it can be efficiently modified to any alternative model in order to study the cosmological dependence of different observables (Mead & Peacock 2014). This kind of methods can also be used to generate not just one, but a large number of realisations, which can be used, for instance to compute uncertainties in a rigorous way.

Furthermore, while the galaxy population contained in the SAX-Sky simulation was created applying a semi-analytical model to the dark matter distribution of the Millennium simulation, it would be of interest (if only for comparison) to use a prescription based on fundamental principles, using results from hydrodynamical N-body simulations (Davé et al. 2013).

6. Conclusions

Simulations calculating the HI content of galaxies will be crucial to predict the number of galaxies that will be observed with future HI surveys. Both the number counts and bias will be fundamental ingredients in order to forecast the constraining power for cosmology of telescopes such as the SKA. In this chapter we analysed explicitly the expected flux sensitivities for the different SKA setups (both for phase 1 and 2) as well as the number counts and bias. Calculations show similar noise rms for SKA1-SUR and SKA1-MID. Numbers were obtained using the SAX-simulations and following a prescription for detecting the HI sources. The bias is shown to have a value around 1 at $z \sim 0.7$, increasing with both redshift and assumed flux cut (dependence on redshift is more prominent for high flux cuts). Assuming a 5-sigma cut, a 5,000 deg^2 survey with MID or SUR, should find around 5×10^6 galaxies. This can already have interesting applications for cosmology, but only at low redshifts, $z \sim 0.5$. SKA2 should be able to detect about 10^9 galaxies over 30,000 deg^2 with a 10-sigma cut. This will make it the ultimate "cosmological machine". Further work is still required in order to improve the numbers. In particular: i) source detection algorithms should be compared using real sky and instrument simulations to address the efficiency of HI galaxy detection; ii) larger simulations need to be done in order to account for cosmological scales and in particular provide a better calculation of the bias; iii) full hydrodynamical simulations should be used in order to calibrate the larger simulations and confirm the HI content evolution of galaxies with redshift. Nevertheless, the numbers obtained in this chapter should already give a reasonable forecast of the expected measurements, in particular for the galaxy number counts.

Acknowledgments: — MGS and SY are supported by the South African SKA Project and the National Research Foundation. PB is supported by European Research Council grant StG2010-257080.

PoS(AASKA14)021

References

Braun, R. 2013, Document number SKA-TEL-SKO-DD-XXX, REV A DRAFT 2

Davé, R., Katz, N., Oppenheimer, B. D., Kollmeier, J. A., & Weinberg, D. H. 2013, MNRAS, 434, 2645

de la Torre, S. & Peacock, J. A. 2013, MNRAS, 435, 743

De Lucia, G. & Blaizot, J. 2007, M.N.R.A.S., 375, 2

Dewdney, P., Turner, W., Millenaar, R., McCool, R., Lazio, J., & Cornwell, T. 2013, Document number SKA—TEL—SKO—DD—001 Revision 1

Mead, A. J. & Peacock, J. A. 2014, MNRAS, 440, 1233

Obreschkow, D., Klöckner, H.-R., Heywood, I., Levrier, F., & Rawlings, S. 2009, ApJ, 703, 1890

Sousbie, T., Courtois, H., Bryan, G., & Devriendt, J. 2008, ApJ, 678, 569

Springel, V., White, S. D. M., Jenkins, A., Frenk, C. S., Yoshida, N., Gao, L., Navarro, J., Thacker, R., Croton, D., Helly, J., Peacock, J. A., Cole, S., Thomas, P., Couchman, H., Evrard, A., Colberg, J., & Pearce, F. 2005, Nat., 435, 629

Tassev, S., Zaldarriaga, M., & Eisenstein, D. J. 2013, JCAP, 6, 36

White, M., Tinker, J. L., & McBride, C. K. 2014, MNRAS, 437, 2594

Yahya, S., Bull, P., Santos, M. G., Silva, M., Maartens, R., Okouma, P., & Bassett, B. 2014, arXiv:1412.4700

PoS(AASKA14)021

PROCEEDINGS OF SCIENCE

Weak gravitational lensing with the Square Kilometre Array

M. L. Brown[*,1] **D. J. Bacon**,[2] **S. Camera**,[1] **I. Harrison**,[1] **B. Joachimi**,[3] **R. B. Metcalf**,[4] **A. Pourtsidou**,[2] **K. Takahashi**,[5] **J. A. Zuntz**,[1] **F. B. Abdalla**,[3,6] **S. Bridle**,[1] **M. Jarvis**,[7] **T. D. Kitching**,[3] **L. Miller**,[7] **P. Patel**[8]

[1] *Jodrell Bank Centre for Astrophysics, School of Physics and Astronomy, University of Manchester, Oxford Road, Manchester M13 9PL, UK*
[2] *Institute of Cosmology and Gravitation, University of Portsmouth, Burnaby Road, Portsmouth PO1 3FX, UK*
[3] *Department of Physics and Astronomy, University College London, Gower Street, London, WC1E 6BT, UK*
[4] *Dipartimento di Fisica e Astronomia, Universitá di Bologna, viale B. Pichat 6/2 , 40127, Bologna, Italy*
[5] *Faculty of Science, Kumamoto University, 2-39-1 Kurokami, Kumamoto 860-8555, Japan*
[6] *Department of Physics and Electronics, Rhodes University, PO Box 94, Grahamstown, 6140, South Africa*
[7] *Astrophysics, Department of Physics, University of Oxford, Oxford OX1 3RH, UK*
[8] *Department of Physics, University of Western Cape, Cape Town 7535, South Africa*

Email: m.l.brown@manchester.ac.uk

We investigate the capabilities of various stages of the SKA to perform world-leading weak gravitational lensing surveys. We outline a way forward to develop the tools needed for pursuing weak lensing in the radio band. We identify the key analysis challenges and the key pathfinder experiments that will allow us to address them in the run up to the SKA. We identify and summarize the unique and potentially very powerful aspects of radio weak lensing surveys, facilitated by the SKA, that can solve major challenges in the field of weak lensing. These include the use of polarization and rotational velocity information to control intrinsic alignments, and the new area of weak lensing using intensity mapping experiments. We show how the SKA lensing surveys will both complement and enhance corresponding efforts in the optical wavebands through cross-correlation techniques and by way of extending the reach of weak lensing to high redshift.

Advancing Astrophysics with the Square Kilometre Array
June 8-13, 2014
Giardini Naxos, Italy

[*] Speaker.

PoS(AASKA14)023

1. Background

1.1 Cosmology with weak lensing surveys

Weak gravitational lensing is the coherent distortion in the shapes of distant galaxies due to the deflection of light rays by intervening mass distributions. Measurements of the effect on large scales is termed "cosmic shear" and has emerged as a powerful probe of late-time cosmology over the last 15 years (see e.g. Heymans et al. 2013 for recent results from the CFHTLenS survey). Since gravitational lensing is sensitive to the *total* (i.e. dark plus baryonic) matter content of the Universe, it has great potential as a very robust cosmological probe, to a large degree insensitive to the complications of galaxy formation and galaxy bias. One of the most promising aspects of weak lensing measurements is their combination with redshift information: such measurements are then a sensitive probe of both the geometry of the Universe and of the evolution of structure over the course of cosmic time. In turn, these latter effects are dependent on the nature of the dominant dark energy component in the Universe and/or on modifications to the theory of General Relativity on large scales.

The observed distortions in the shapes of distant galaxies yields an estimate of the lensing shear field, γ. Since gravity is a potential theory, the shear at angular position θ can be related to a lensing potential (ψ) as

$$\gamma_{ij}(\theta) = \left(\delta_i\delta_j - \frac{1}{2}\delta^K_{ij}\delta^2\right)\psi(\theta), \tag{1.1}$$

where $\delta_i \equiv r(\delta_{ij} - \hat{r}_i\hat{r}_j\nabla_i)$ is a dimensionless, transverse differential operator, and $\delta^2 = \delta_i\delta^j$ is the transverse Laplacian. The indices (i,j) each take the values $(1,2)$. In equation (1.1) we have assumed a flat sky which is an excellent approximation for the scales of interest (i.e. from ~ 100 h^{-1}kpc to ~ 100 h^{-1}Mpc). The lensing potential can in turn be related to the 3-d gravitational potential, $\Phi(\mathbf{r})$ by (e.g. Kaiser 1998; Hu 2000)

$$\psi(\theta) = \frac{2}{c^2}\int_0^r dr'\left(\frac{r-r'}{rr'}\right)\Phi(\mathbf{r}'), \tag{1.2}$$

where r is the comoving distance to the sources.

In the limit of weak lensing ($\gamma << 1$), and in the absence of intrinsic correlations in galaxy ellipticities, one can form an unbiased estimator for the shear field at a given sky position from the average of the observed galaxy ellipticities at that position. Since the shear field induced by large scale structure is small (typically $\sim$ a few %) compared to the intrinsic dispersion in galaxy ellipticities ($\sigma_\varepsilon \sim 0.3$) one needs to average over many background galaxies in order to obtain a precise measurement. Measurements of cosmic shear can be affected by a number of instrumental and astrophysical systematic effects. The primary insturmental effect of concern is anisotropies in the point spread function (or beam) of the telescope which can mimic a cosmic shear signal. On the astrophysical side, alignments in the *intrinsic* shapes of galaxies can also mimic a cosmic shear signal. Consequently a great deal of effort is currently focused on careful instrument design for the next generation of weak lensing surveys as well as theoretical modelling and numerical simulations of intrinsic alignment effects.

Observationally, to date the field of weak lensing has largely been the preserve of optical surveys due to the much larger number densities of background galaxies achieved in such surveys.

PoS(AASKA14)023

However, this will change with the advent of the Square Kilometre Array which will reach number densities of well-detected and well-resolved galaxies of up to ~ 5 galaxies arcmin^{-2} over several thousand deg^2 in Phase 1, and ~ 10 galaxies arcmin^{-2} over 3π steradians in Phase 2. In addition, as described in this chapter, the radio offers truly unique approaches to measuring weak lensing that are (i) not available to optical surveys and (ii) potentially extremely powerful in minimizing the most worrying systematic effects in weak lensing cosmology.

SKA surveys will also extend the reach of weak lensing beyond that of the optical mega-surveys of LSST and Euclid. First the typical redshifts probed by SKA surveys will go beyond that of optical surveys. Secondly the SKA offers the prospects of measuring the weak lensing distortion in 21cm HI intensity maps. Such an intensity mapping lensing survey will not only extend to the high-redshifts inaccessible to optical surveys but will also include precise redshift information to accompany the distortion signal. This signal will fill the gap between traditional galaxy lensing signal (where the sources are typically located at $z \sim 1$) and the CMB lensing signal originating at $z = 3000$. It thus holds the promise of yielding very precise cosmological constraints on the evolution of structure during early times where structures are better described with linear physics and can provide unique insight into so-called "early dark energy" models which exhibit observable signatures at early times.

1.2 Radio weak lensing studies to date

To date, the application of weak lensing analyses to radio data has been rather limited due to the relatively low number density of background galaxies achieved in large scale radio surveys. The only major weak lensing analysis of a radio survey was performed in Chang et al. (2004) who detected a cosmic shear signal in the Faint Images of the Radio Sky at Twenty cms (FIRST) survey (Becker et al. 1995), conducted with the Very Large Array (VLA). Although the number density of sources in FIRST was low by optical standards (FIRST contains ~ 90 sources deg^{-2} compared with typically ~ 10 sources arcmin^{-2} in deep optical lensing surveys), a detection of cosmic shear on large scales was achieved by virtue of the large survey area covered ($\sim$ 10,000 deg^2).

The analysis of Chang et al. (2004) made use of the shapelets method (Chang & Refregier 2002; Refregier & Bacon 2003) to measure the shapes of the FIRST sources directly from the *uv* interferometric data and included a thorough treatment of the possible systematics that can affect radio-based lensing shear estimates in particular.

More recently, Patel et al. (2010) revisited the idea of radio-based lensing shear estimation through a re-analysis of the combined VLA + MERLIN observations of the Hubble Deep Field North (Muxlow et al. 2005). This work presented an implementation of image-based shapelets for shear estimation and also highlighted the advantages of cross-correlating radio-based and optical-based shear estimates obtained over the same area of sky.

1.3 The path to SKA weak lensing

A great deal of algorithm development and new analysis techniques are required in order to develop the field of radio weak lensing beyond the initial studies mentioned above. Key areas where work is required are the development of shape and/or shear estimation techniques that are well suited to radio interferometer datasets, the development of cross-correlation techniques for

PoS(AASKA14)023

combining optical and radio-based shear estimates and the development and demonstration of novel radio-specific lensing approaches making use of polarization and rotational velocity information. A number of SKA pathfinder and precursor telescopes lend themselves naturally to developing several of these areas.

A key pathfinder telescope for demonstrating the long-baseline high resolution observations suited for weak lensing is the e-MERLIN interferometer based in the UK. A number of e-MERLIN legacy programs are well-suited to pathfinding the techniques for SKA weak lensing. Of particular note are the e-MERGE[1] and SuperCLASS[2] projects. e-MERGE is a multi-tiered project that (amongst other things) will image the GOODS-N field to 0.5 μJy rms in the central 100 arcmin^2 and to 1 μJy rms in the surrounding 800 arcmin^2. The SuperCLASS project complements e-MERGE. Its primary science driver is to detect the weak lensing effects of a supercluster of galaxies located at $z = 0.2$. SuperCLASS will image a 1.75 deg^2 field to 4 μJy rms. Both e-MERGE and SuperCLASS will perform their primary observations at 1.4 GHz with a resolution of 200 mas. Both will therefore act as training experiments for demonstrating shape measurement and shear extraction algorithms on high-resolution radio data, on the path to the SKA.

A further opportunity exists to refine and test radio lensing analyses with the upgraded JVLA. A series of sky surveys (VLASS[3]) are currently being discussed for the JVLA and these will potentially include a deep fields component. If conducted with an array configuration that includes long baselines, these could be extremely powerful for pathfinding weak lensing techniques in the radio over larger survey areas, approaching 10 deg^2 (Brown et al. 2013).

Other opportunities for demonstrating weak lensing techniques in the run up to the SKA include LOFAR surveys[4] (when the international baselines are included) and the CHILES[5] and CHILES con Pol[6] surveys on the JVLA. The LOFAR surveys will be critical for testing weak lensing techniques at low frequencies while the CHILES and CHILES con Pol surveys will prove useful for testing novel ideas for radio lensing including the use of polarization information and HI rotational velocity measurements (see Section 2.4).

2. Cosmic shear with radio continuum surveys

2.1 Accessing the largest scales and the highest redshifts

One of the potentially most exciting aspects of weak lensing surveys with the SKA will be the extra reach in terms of accessing the largest scales in the Universe and going beyond the reach of other weak lensing surveys in terms of the redshifts that are probed. We illustrate this in Figs. 1–3 where the redshift distributions of weak lensing source galaxies and the corresponding forecasted errors on a set of tomographic shear power spectra are presented. We present these forecasts for a 2-year continuum survey with the SKA at three different stages of development – an early phase of SKA1 comprising 50% of the envisaged sensitivity targeting a survey area of 1000 deg^2; the

[1] http://www.e-merlin.ac.uk/legacy/projects/emerge.html
[2] http://www.e-merlin.ac.uk/legacy/projects/superclass.html
[3] https://science.nrao.edu/science/surveys/vlass
[4] http://lofar.strw.leidenuniv.nl
[5] http://www.mpia-hd.mpg.de/homes/kreckel/CHILES/index.html
[6] http://www.aoc.nrao.edu/∼chales/chilesconpol/

PoS(AASKA14)023

Table 1: Observational parameters used to produce the power spectrum and cosmological parameter forecasts in Figs. 1–4.

Survey	A_{sky} (deg^2)	n_{gal} (arcmin^{-2})	z_m
SKA1-early	1000	3.0	1.0
VST-KiDS	1500	7.5	0.6
SKA1	5000	2.7	1.0
DES	5000	6.0	0.6
SKA2	30940	37	1.6
Euclid	15000	30	0.9

full SKA1 surveying 5000 deg^2, and a SKA2 survey covering 3π steradians. To generate these forecasts, we have adopted the performance specifications for SKA1 outlined in Braun (2013). In particular, we have modeled the performance of Band 2 of the SKA-Mid facility as under the current baseline design, this telescope and frequency band combination provides the most powerful survey speed for the high angular resolution observations required for weak lensing. We have further assumed an object detection threshold of $S/N > 10$ and an angular resolution requirement of $\theta_{\rm res} = 0.5$ arcsec. To model the redshift and flux dependence of the source population, we have made use of the SKA Design Studies (SKADS) simulations of Wilman et al. (2008), updated to match the galaxy number counts observed in the deepest radio surveys performed to date (Muxlow et al. 2005; Morrison et al. 2010; Schinnerer et al 2010). We have also assumed an RMS dispersion in intrinsic galaxy ellipticities of $\gamma_{\rm rms} = 0.3$

For comparison on these plots, we also show the corresponding forecasts for optical weak lensing surveys that will be conducted over similar survey areas and on comparable timescales. Specifically, we consider the VST-KiDS (de Jong et al. 2013), the Dark Energy Survey[7] and the Euclid satellite mission (Laureijs et al. 2011). The observational parameters adopted to produce these forecasts are summarized in Table 1. In all cases, the radio surveys extend to higher redshift than the corresponding optical probes. They thus hold the potential to probe the power spectrum at higher redshift providing a more sensitive lever arm with which to constrain the growth of structure over cosmic time.

Fig. 4 presents forecasted constraints on the matter density (Ω_m) and matter power spectrum normalization (σ_8) cosmological parameters for the same envisaged SKA surveys as were adopted to generate Figs. 1–3. Note that these forecasts are presented for the case of the standard 6-parameter ΛCDM model and no prior information is assumed – that is the projected constraints are coming solely from the envisaged SKA weak lensing survey.

To generate the constraints, we have computed a simple shear power spectrum covariance matrix from Takada & Jain (2004), and we use the CosmoSIS cosmological parameter estimation code (Zuntz et al. 2014) to compute power spectra, parameter constraints, and marginalised contours. Note that no systematic errors are included in the analysis; errors are purely statistical. However, we have attempted to take into account anticipated knowledge and uncertainties regard-

[7] http://www.darkenergysurvey.org

PoS(AASKA14)023

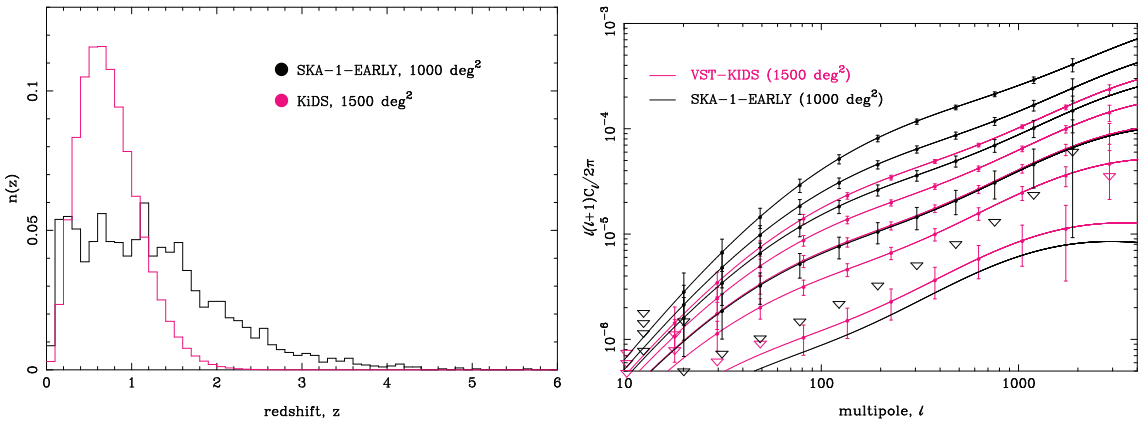

Figure 1: *Left panel:* The redshift distribution of source galaxies for a 1000 deg^2 weak lensing survey requiring 2 years observing time on the SKA1-early facility. Also shown is the redshift distribution for the 1500 deg^2 VST-KiDS optical lensing survey. The $n(z)$ extends to higher redshifts in the radio survey and probes a greater range of cosmic history. *Right panel:* The corresponding constraints on a 5-bin tomographic power spectrum analysis. For both experiments, we assumed an RMS dispersion in ellipticity measurements of $\gamma_{\rm rms} = 0.3$ and the tomographic bins have been chosen such that the bins are populated with equal numbers of galaxies. Note how the radio survey extends to higher redshifts where the lensing signal is stronger and therefore easier to measure. Open triangles denote 1σ upper limits on a bandpower. Note that only the auto power spectra in each bin are displayed though much cosmological information will also be encoded in the cross-correlation spectra between the different z-bins.

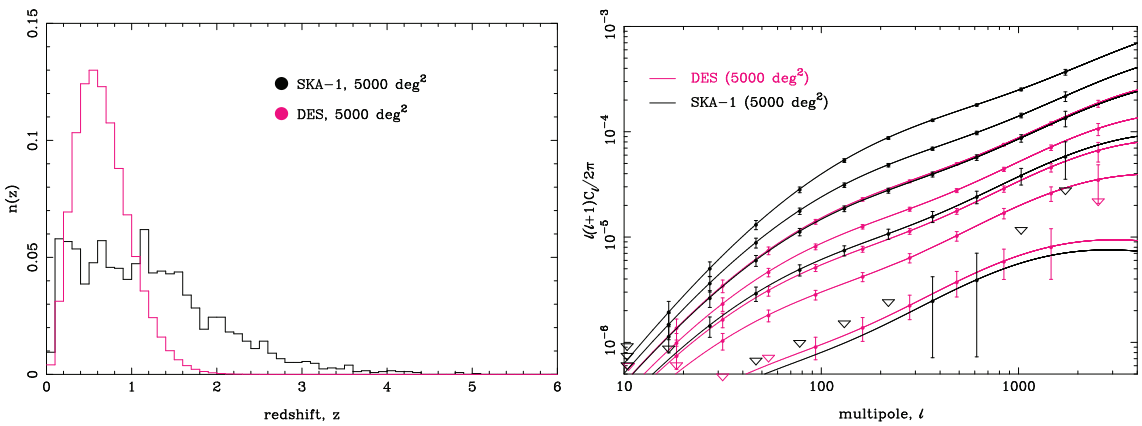

Figure 2: As Fig. 1 but for a 5000 deg^2 weak lensing survey requiring 2 years observing time on the full SKA1 facility. Also shown for comparison are the $n(z)$ distribution and forecasted power spectrum constraints for the 5000 deg^2 Dark Energy Survey.

ing photometric and spectroscopic redshift estimates for the background galaxy population. For SKA1-early, we have assumed that we have no spectroscopic redshift information and that we have photo-z estimates from overlapping optical surveys with errors $\sigma_z = 0.05(1+z)$ up to a limiting redshift of 1.5. To model the much larger uncertainties expected for the high-z radio galaxies, we adopt $\sigma_z = 0.3(1+z)$ so that a $z = 2$ galaxy has a redshift uncertainty of $\pm \sim 1$. For SKA1, we additionally assume that we will have spectroscopic redshifts from overlapping HI observations for 15% of the $z < 0.6$ population. Finally for SKA2, we assume we have spectroscopic redshifts

PoS(AASKA14)023

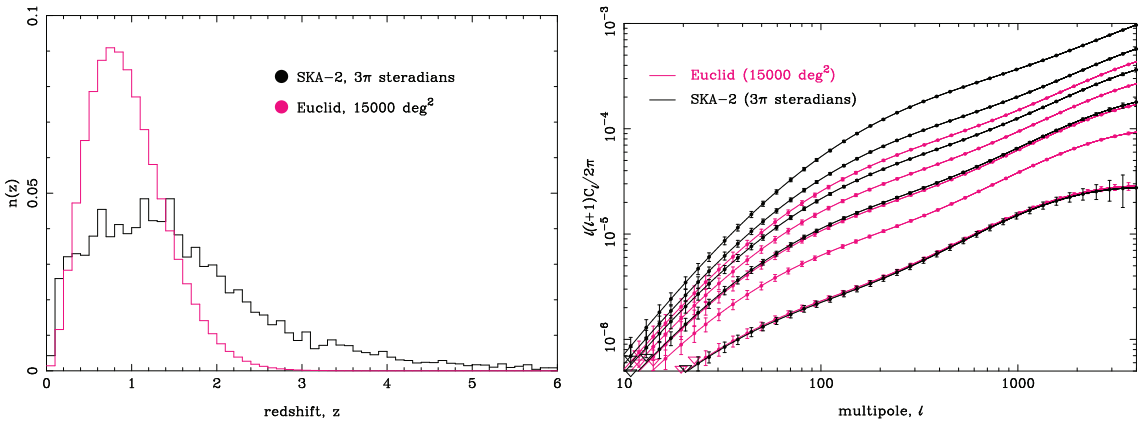

Figure 3: As Fig. 1 but for a 3π steradian weak lensing survey requiring 2 years observing time on SKA2. Also shown for comparison are the $n(z)$ distribution and forecasted power spectrum constraints for the 15000 deg^2 Euclid satellite mission.

for 50% of the $z < 2.0$ population. The forecasts presented in Fig. 4 account for these redshift uncertainties.

We see from Fig. 4 that even the SKA1-early survey targeting the smallest sky area can provide competitive constraints on cosmological parameters — the forecasted constraints for the 1000 deg^2 SKA1-early survey are a factor of $\sim$5 better than the tomographic weak lensing analysis of the current state-of-the-art CFHTLenS data (Heymans et al. 2013). We also see large improvements in the constraints obtainable with each subsequent stage of the SKA — the constraints obtainable with SKA1 are broadly comparable with the KiDS and DES optical surveys while SKA2 is competitive with Euclid.

Fig. 4 also demonstrates that our nominal choice of target survey areas for the three stages of the SKA are, broadly speaking, optimal choices from the point of view of constraining these cosmological parameters — for SKA1-early the 1000 deg^2 survey provides the strongest constraints, for SKA1 the 5000 deg^2 survey performs the best while for SKA2, the 3π steradian survey provides the best constraints.

2.2 The promise of radio observations to suppress weak lensing systematics

Optical and radio surveys, such as Euclid and/or LSST and the SKA, have a particularly useful synergy in reducing and quantifying the impact of systematic effects which may dominate each survey alone on some scales. By cross-correlating the shear estimators from one of these surveys with those of the other, several systematic errors are mitigated.

We can see this by writing the contributions to an optical (o) or radio (r) shear estimator:

$$\gamma^{(o)} = \gamma_{\rm grav} + \gamma_{\rm int}^{(o)} + \gamma_{\rm sys}^{(o)} \tag{2.1}$$

$$\gamma^{(r)} = \gamma_{\rm grav} + \gamma_{\rm int}^{(r)} + \gamma_{\rm sys}^{(r)}, \tag{2.2}$$

where $\gamma_{\rm grav}$ is the gravitational shear we are seeking, $\gamma_{\rm int}$ is the intrinsic ellipticity of the object, and $\gamma_{\rm sys}$ are systematic errors induced by the telescope. If we correlate optical shears with optical

PoS(AASKA14)023

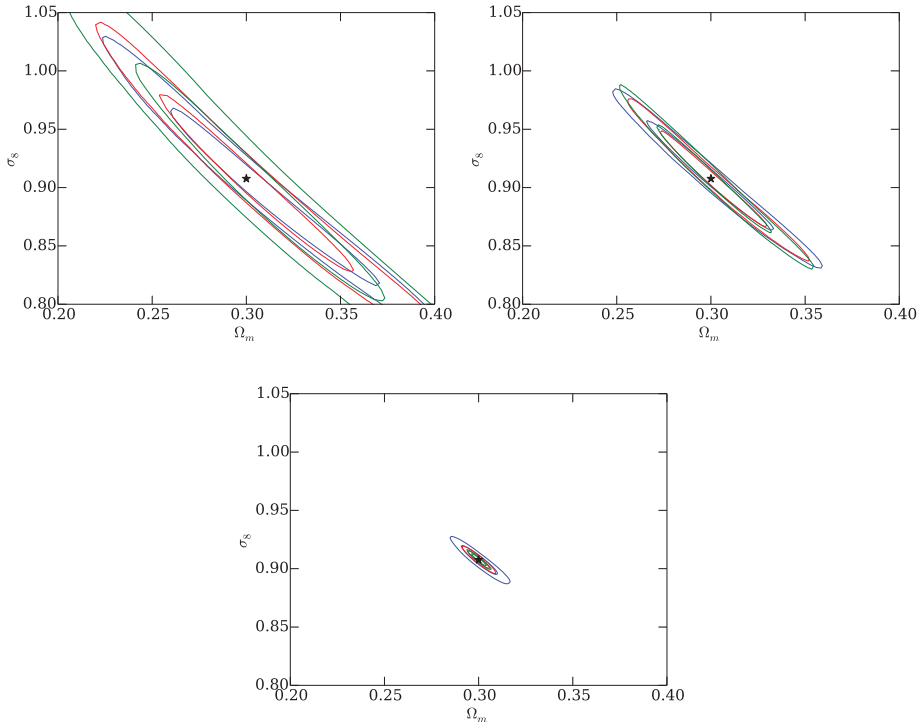

Figure 4: Forecasted constraints in the $\sigma_8 - \Omega_m$ parameter space for 2-year continuum surveys using SKA-Mid/Band 2 with SKA1-early (*upper left panel*), SKA1 (*upper right panel*) and SKA2 (*lower panel*) performance parameters. For each of these cases, we present the constraints for survey areas of 1000 deg^2 (blue) 5000 deg^2(red) and 3π steradians (green).

shears, or radio shears with radio shears, we obtain terms like

$$\langle\gamma\gamma\rangle = \langle\gamma_{\rm grav}\gamma_{\rm grav}\rangle + \langle\gamma_{\rm grav}\gamma_{\rm int}\rangle + \langle\gamma_{\rm int}\gamma_{\rm int}\rangle + \langle\gamma_{\rm sys}\gamma_{\rm sys}\rangle, \tag{2.3}$$

where the first term is the gravitational signal we seek, the second term is the GI intrinsic alignment (Hirata & Seljak 2004), the third term is the II intrinsic alignment (e.g. Heavens et al. 2000), and the final term is the contribution from systematics. All of these terms could be similar size on certain scales, which is of damage to cosmological constraints. On the other hand, if we cross-correlate the optical shears with radio shears, we obtain

$$\langle\gamma^{(o)}\gamma^{(r)}\rangle = \langle\gamma_{\rm grav}\gamma_{\rm grav}\rangle + \langle\gamma_{\rm grav}\gamma^{(o)}_{\rm int}\rangle + \langle\gamma_{\rm grav}\gamma^{(r)}_{\rm int}\rangle + \langle\gamma^{(o)}_{\rm int}\gamma^{(r)}_{\rm int}\rangle + \langle\gamma^{(o)}_{\rm sys}\gamma^{(r)}_{\rm sys}\rangle. \tag{2.4}$$

The second and third terms are the GI alignment (Hirata & Seljak 2004), which still survives. However, the fourth term involves the correlation between optical and radio shapes, which will be less than that between one frequency alone as the emission mechanisms are different (c.f. Patel et al. 2010 where no correlation at zero lag was found). This term is therefore reduced. Most importantly, the fifth term involving systematics is expected to be zero, as the systematics in these two telescopes, which are of completely different design and function, are not expected to be correlated at all. We are therefore able to remove the dangerous systematics correlation from our shear analysis – and to gain an estimate of its magnitude in the autocorrelation case.

PoS(AASKA14)023

Table 2: Requirements on multiplicative and additive biases on ellipticity measurement for proposed SKA weak lensing surveys to be dominated by statistical rather than systematics uncertainties. Q is a global "quality factor" which we calculate from m and c following Voigt et al. (2010).

Experiment	A_{sky}	n_{gal}	z_m	$m <$	$c <$	$Q >$
SKA1-early	1000	3.0	1.0	0.014	0.0012	62
SKA1-early	5000	1.2	0.8	0.012	0.0011	79
SKA1-early	30940	0.35	0.5	0.011	0.0011	80
SKA1	1000	6.1	1.2	0.0090	0.00095	103
SKA1	5000	2.7	1.0	0.0067	0.00082	140
SKA1	30940	0.9	0.7	0.0058	0.00076	164
SKA2	1000	37	1.6	0.0031	0.00055	318
SKA2	5000	23	1.4	0.0019	0.00043	523
SKA2	30940	10	1.3	0.0012	0.00035	825

A further systematic that is potentially problematic for weak lensing surveys are color-gradients (Voigt et al. 2012). However, galaxies typically have smooth spectral dependence at radio frequencies. This, combined with the ability to measure the spectral dependence of the beam very accurately, means that radio weak lensing surveys will be insensitive to this systematic.

2.3 Shear measurement

In order to extract the weak lensing science from the SKA, we will need to make highly accurate measurements of the shearing of background sources in real, noisy data. In optical experiments, this shear measurement process has typically consisted of measuring the ellipticity of individual galaxies and combining these measurements to form an estimate of the cosmic shear. A wide variety of galaxy shape measurement algorithms have been developed for this task and tested through the STEP and GREAT programmes (see e.g. Mandelbaum et al. 2014 and references therein) and experience with real data, honing the techniques and focusing research on areas which require improvement. As a consequence, shape measurement from optical data is a well-established field and techniques already developed are sufficiently advanced that shape measurement-induced systematics are likely to be sub-dominant to statistical errors in current and near future optical lensing surveys. These shape measurement systematics are often parameterised in terms of the additive bias c and multiplicative bias m on the ellipticity e^{obs} recovered from an input source with known true ellipticity e^{true}:

$$e^{obs} = (1+m)e^{true} + c. \tag{2.5}$$

A formalism is provided in Amara & Refregier (2008) for calculating the m and c necessary for systematic errors to be sub-dominant, with requirements for a selection of SKA surveys shown in Table 2. However, these algorithms have almost solely been motivated by optical and NIR data, meaning their robustness to issues peculiar to radio data, in particular potential systematics from the non-linear deconvolution process necessary for imaging (and removal of sidelobe artifacts), is unclear. Of the two radio weak lensing studies so far performed, both measure shear by modeling data using the orthonormal shapelets basis set (Refregier & Bacon 2003). Patel et al. (2010) use

PoS(AASKA14)023

shapelets to model images reconstructed using the CLEAN algorithm, while Chang et al. (2004) take advantage of the fact that shapelets remain localised analytic functions under Fourier transformation to directly model the visibility plane and were able to make a 3.6σ detection of cosmic shear. More recently, Patel et al. (2013) have applied image plane shapelets to simulations, allowing them to quantify the efficacy of the method, achieving values $m = 0.176$ and $c = 0.006$ for a simulated e-MERLIN observation. For SKA1, Patel *et al.* in this volume achieve $m = 0.28$ and $c = 0.001$ for image plane shapelets, comparable to requirements of $m < 0.0054$, $c < 0.0073$ for the SKA1 5000 deg^2 survey, as well as providing an initial comparison of the relative performance of visibility plane shapelets.

A number of open problems still remain. Although initial steps have been taken, only a small part of the space of possible radio shear measurement techniques has so far been explored. Future work may be expected to take place with two main themes:

- Investigation of the ability of image reconstruction algorithms to produce images with the level of fidelity necessary for weak lensing cosmology and subsequent adaptation of known methods from optical/NIR weak lensing to radio data. High-fidelity image reconstruction is an active research topic in its own right, with many extensions and alternatives to traditional CLEAN and Maximum Entropy methods under development (e.g. Sutter et al. 2014; Carrillo et al. 2014 and references therein).

- Investigation of techniques which measure shear directly from interferometer visibilities. Such techniques have the advantage of avoiding systematics introduced by the non-linear deconvolution necessary for the imaging process and a visibility plane technique (shapelets in Chang et al. 2004) has been the only technique so far to successfully detect weak lensing in radio data. However, for the datasets produced by the SKA, computational challenges for visibility plane techniques will be great. Simultaneously fitting $\sim$5 parameter models to large numbers of sources over large numbers of visibilities is likely to be unfeasible, though averaging and novel methods such as *uv*-stacking (Lindroos et al. 2014) have the potential to help. There also remains the open question as to whether resources to store the raw visibilities from SKA observations for later analysis will be available.

In the near-term, we expect to begin addressing these issues by extending previous Gravitational LEnsing Accuracy Testing (GREAT) challenges (e.g. Mandelbaum et al. 2014) to radio data with a radioGREAT challenge[8]. This will aim to better quantify the current status of shape measurement techniques for radio weak lensing, assess their behaviour across changing data parameters and spur new interest and developments in the field.

2.4 Polarization and rotation velocities as indicators of intrinsic alignments

One unique advantage of radio telescopes for weak lensing is the polarization information which can provide information on the intrinsic (unlensed) shapes of background galaxies. As described in Brown & Battye (2011), the position angle of the integrated polarized emission from a background galaxy is unaffected by gravitational lensing. If the polarized emission (which is

[8]http://radiogreat.jb.man.ac.uk

PoS(AASKA14)023

polarized synchrotron emission sourced by the galaxy's magnetic field) is also strongly correlated with the disk structure of the galaxy then measurements of the radio polarization position angle can be used as estimates of the galaxy's intrinsic (unlensed) position angle.

Such an approach could potentially have two key advantages over traditional weak lensing analyses. Firstly, the polarization technique can be used to effectively remove the primary astrophysical contaminant of weak lensing measurements – intrinsic galaxy alignments (Heavens et al. 2000; Catelan et al. 2001; Hirata & Seljak 2004; Brown et al. 2002) – which are a severe worry for ongoing and future precision cosmology experiments based on weak lensing. Secondly, depending on the polarization properties of distant background disk galaxies, the polarization technique has the potential to reduce the effects of noise due to the intrinsic dispersion in galaxy shapes.

The power of the polarization technique in practice will depend on two key observational parameters: the scatter in the relationship between the observed polarization position angle and the intrinsic structural position angle of the galaxy ($\alpha_{\rm rms}$) and the number of galaxies for which one can obtain accurate polarization measurements ($n_{\rm pol}$). These parameters depend on the details of the polarization properties of background galaxies (e.g. the mean polarization fraction, $\Pi_{\rm pol}$) which are currently not well known. There are some existing measurements for a sample of local spiral galaxies (Stil et al. 2009) which suggest $\alpha_{\rm rms} < 15^\circ$ and $\Pi_{\rm pol} < 20\%$ although the sample is small. Note that it may be possible to select sub-samples of the total galaxy population to have particular polarization properties. For example, one could imagine that selecting only galaxies with high fractional polarization would yield a galaxy sub-sample with highly ordered magnetic fields which would consequently have a very tight correlation (low $\alpha_{\rm rms}$) between the polarization orientations and the intrinsic structural position angles of the galaxies. Of course, such a sub-sample would also have a very low surface number density of galaxies. The polarization technique may therefore be better suited to probing the shear power spectrum on large scales where high number densities are not required.

A second novel idea that is well suited to radio observations is to use rotational velocity measurements to provide information about the intrinsic shapes of galaxies. The idea, first suggested by Blain (2002) and Morales (2006), is to measure the axis of rotation of a disk galaxy and to compare this to the orientation of the major axis of the galaxy disk image. In the absence of lensing, these two orientations should be perpendicular and measuring the departure from perpendicularity directly estimates the shear field at the galaxy's position. Such an analysis would require commensal HI line observations which could in principle be done at no extra cost in terms of telescope time. The rotation velocity technique shares many of the characteristics of the polarization approach described above – in the limit of perfectly well-behaved disk galaxies, it is also free of shape noise and it can also be used to remove the contaminating effect of intrinsic galaxy alignments. In practice, the degree to which the rotational velocity technique improves on standard methods will be dependent on observational parameters analogous to the ones for polarization discussed above. Recently, Huff et al. (2013) have proposed to extend this technique using the Tully-Fisher relation to calibrate the rotational velocity shear measurements and thus reduce the residual shape noise even further.

Both the polarization technique and the rotation velocity approach are currently being tested as part of the SuperCLASS, CHILES and CHILES con Pol projects. They offer great promise for reducing the impact of shape noise and intrinsic alignments in radio weak lensing surveys.

PoS(AASKA14)023

3. Weak lensing with HI Intensity Mapping

Weak gravitational lensing of high redshift 21cm emission has been the subject of several studies focusing on the Epoch of Reionization (EoR) observations. In Zahn & Zaldarriaga (2006) and Metcalf & White (2009) it was shown that if the EoR is at redshift $z \sim 8$ or later, a large telescope like the SKA could measure the lensing power spectrum and constrain the standard cosmological parameters. The authors extended the Fourier-space quadratic estimator technique, which was first developed in Hu (2001) for CMB lensing observations to three dimensional observables, i.e. the 21 cm intensity field $I(\theta, z)$. These studies did not consider 21 cm observations from redshifts after reionization when the average HI density in the Universe is much smaller.

HI intensity mapping is a technique that has been proposed for measuring the distribution of HI gas before and during reionization (see Pritchard *et al.* in this volume) and measuring the BAO at redshifts of order unity (Chang et al. 2008, 2010; Seo et al. 2010; Masui et al. 2010; Ansari et al. 2012; Battye et al. 2013; Chen 2012; Pober et al. 2013). In this technique, no attempt is made to detect individual objects. Instead the 21 cm emission is treated as a continuous three dimensional field. The angular resolution of the telescope need not be high enough to resolve individual galaxies which makes observations at high redshift possible with a reasonably sized telescope.

A recent study (Pourtsidou & Metcalf 2014) extended the 21cm-intensity-mapping-lensing method further, taking into account the discreteness of galaxies, and investigated the possibility of measuring lensing at intermediate redshifts without resolving (in angular resolution) or even identifying individual sources. Here we present an improved analysis of the signal-to-noise expected from an SKA-like telescope array, and demonstrate the performance of the SKA-Mid facility for SKA1 and for SKA2.

One of the first objectives of a 21cm lensing survey will be to measure the two-point statistics of the convergence field $\kappa(\vec{L}, z_s)$ or, equivalently, the displacement field $\delta\theta(\vec{L}, z_s)$, averaged over z_s. That is,

$$C_L^{\delta\theta\delta\theta} = \frac{9\Omega_m^2 H_0^3}{L(L+1)c^3} \int_0^{z_s} dz P(k = L/r(z), z)[W(z)]^2/E(z), \tag{3.1}$$

where $W(z) = (r(z_s) - r(z))/r(z_s)$, $E(z) = H(z)/H_0$. The expected error in the power spectrum $C_L^{\delta\theta\delta\theta}$ averaging over $\vec{L}$ directions in a band of width ΔL is given by

$$\Delta C_L^{\delta\theta\delta\theta} = \sqrt{\frac{2}{(2L+1)\Delta L f_{\rm sky}}} \left(C_L^{\delta\theta\delta\theta} + N_L \right). \tag{3.2}$$

Here, N_L is the derived $\delta\theta$ estimate reconstruction noise which involves the underlying dark matter power spectrum, the HI density $\Omega_{\rm HI}(z)$ as well as the HI mass moments up to 4th order and, of course, the thermal noise of the telescope (see Pourtsidou & Metcalf 2014 for details). For the HI mass function we will first assume the most conservative scenario, i.e. a no evolution model using the results from the HIPASS survey (Zwaan et al. 2003), giving $\Omega_{\rm HI} \simeq 4.9 \times 10^{-4}$ (Model A). We will also consider a more realistic evolution scenario from Zhang & Pen (2006) where $\Omega_{\rm HI}(z) = 4.9 \times 10^{-4}(1+z)^{2.9}\exp(-z/1.3)$. This is expressed through an evolution of the normalization of the Schechter function $\phi^\star$ (Model B).

Here we will concentrate on source redshift $z_s \sim 2$. The SKA1-Mid array operates in the frequency range $\sim 350 - 3050$ MHz divided in three bands (Dewdney et al. 2013). Our chosen

PoS(AASKA14)023

z_s corresponds to frequency $\nu_s = 473\,\mathrm{MHz}$ (Band 1). The power spectrum of the thermal noise of a SKA-like interferometer core array (using the uniform distribution approximation) is $C_\ell^{\mathrm{N}} = \frac{(2\pi)^3 T_{\mathrm{sys}}^2}{B t_{\mathrm{obs}} f_{\mathrm{cover}}^2 \ell_{\mathrm{max}}(\nu)^2}$, where the system temperature $T_{\mathrm{sys}} = (40 + 1.1 T_{\mathrm{sky}})\,\mathrm{K}$ with $T_{\mathrm{sky}} = 60\lambda^{-2.55}$, B is the chosen frequency window, t_{obs} the total observation time, D_{tel} the diameter (maximum baseline) of the array, $\ell_{\mathrm{max}}(\lambda) = 2\pi D_{\mathrm{tel}}/\lambda$ is the highest multipole that can be measured by the array at frequency ν (wavelength λ), and f_{cover} is the total collecting area of the telescopes A_{coll} divided by $\pi(D_{\mathrm{tel}}/2)^2$. For SKA-Mid we can consider a 2 yr observation time, $f_{\mathrm{sky}} \sim 0.7$ (corresponding to $\sim 30,900\,\mathrm{deg}^2$ survey area), and we further choose $B = 20\,\mathrm{MHz}$ and $\Delta L = 36$. Keeping these values constant, in Fig. 5 we present forecasts for the displacement field power spectrum for source redshifts $z_s = 2$ and $z_s = 3$. For the Model A HI mass function, SKA1 does not have the sensitivity to measure the signal. However, for Model B we see a great improvement in the signal-to-noise ratio, such that the lensing signal can be well measured by SKA1 (Fig. 5, left panel). For SKA2, a precise characterization of the power spectrum is possible at multiple redshifts even in the conservation no-evolution scenario (Model A, Fig. 5, right panel).

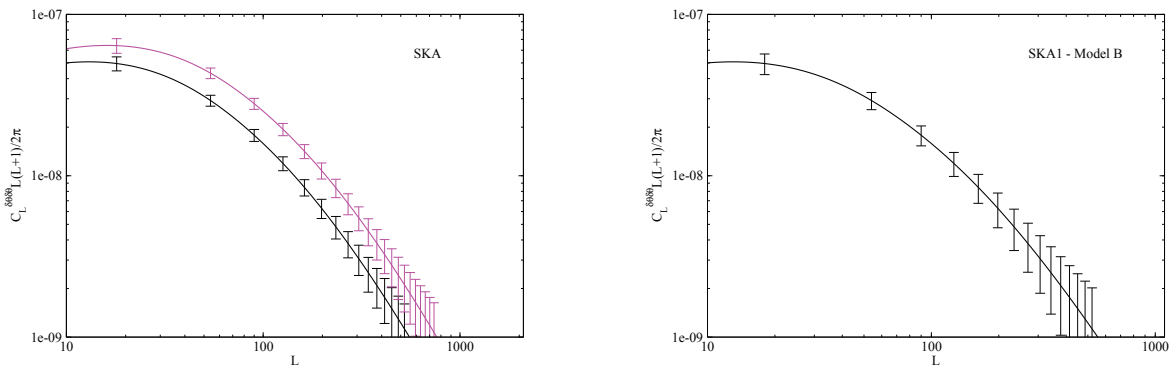

Figure 5: *Left*: Displacement field power spectrum for $z_s = 2$ and the corresponding measurement errors using the SKA1-Mid specifications and Model B for the HI mass function. *Right*: Displacement field power spectrum for $z_s = 2$ (solid black line) and $z_s = 3$ (solid magenta line) and the corresponding measurement errors using the SKA2 specifications and Model A (no evolution) for the HI mass function. See the main text of Section 3 for details of the HI mass function adopted for Models A and B.

This technique should enable us to measure the lensing power spectrum at source redshifts well beyond those accessible with more traditional weak lensing surveys based on the shearing of individual galaxy images. This is a promising approach to investigating the possible evolution of dark energy or modified gravity at high redshift. In addition to measuring the power spectrum, the SKA-Low array should be able to map the dark matter distribution with high fidelity in a 5-by-5 degree field using this technique (see Pritchard *et al.* in this volume for details).

4. Galaxy and cluster weak lensing

In addition to probing large-scale structure, weak lensing can be used to measure the distribution of mass (both dark and bright) around individual galaxies, as well as other structures such as galaxy pairs, groups and clusters, or voids (Mandelbaum et al. 2006; Gillis et al. 2013; Melchior

PoS(AASKA14)023

et al. 2014). Since the signal from an individual lens is too weak to be detectable, except for massive clusters, such "galaxy-galaxy" measurements are usually stacked to produce an average mass distribution around a certain type of lens objects. On large, linear scales galaxy-galaxy lensing constrains galaxy bias (e.g. Hoekstra et al. 2002). Moreover, interpreted as a galaxy position-shear cross-correlation it can provide additional cosmological constraints and valuable calibration of astrophysical systematics (Bernstein 2009; Joachimi & Bridle 2010) and Kirk *et al.*, this volume). On smaller scales galaxy-galaxy lensing is sensitive to the radial matter density profile of galaxy haloes as well as the abundance and distribution of substructure in its outskirts, all as a function of galaxy properties such as type, stellar mass, or velocity dispersion (van Uitert et al. 2013).

The SKA surveys will provide a unique angle to galaxy-galaxy weak lensing studies, with key contributions in the following areas:

- **Competitive or superior statistical errors**: These errors are driven by the number density of both lens and source galaxies (particularly on small scales) and the sample variance due to a finite sky coverage (particularly on large scales).
- **Spectroscopic redshifts for new galaxy samples**: To obtain unbiased measurements, a clean separation of lens and source samples is paramount. Spectroscopic redshifts for foreground objects allow for a clean and precise definition of lens samples and lens properties. Accurate redshifts for a subset of the source sample characterise the redshift distribution of background objects.
- **Novel lens galaxy sample definitions**: The information from radio wavelengths can be used to define new lens samples e.g. in terms of their radio luminosity, AGN activity, or gas abundance. This allows for the measurement of the relation between these properties and matter halo characteristics, e.g. the HI gas mass to halo mass ratio as a function of redshift.

To quantify this performance, we forecast expected errors on a one-parameter radial matter profile constrained via the average tangential shear measured in the range of 0.1 Mpc/h to 1 Mpc/h transverse separation from the lenses. We use a singular isothermal sphere (SIS) as a simple profile,

$$\rho_{\rm SIS}(r) = \frac{\sigma_v^2}{2\pi G r^2} \,, \tag{4.1}$$

where r denotes three-dimensional distance, and where σ_v is the velocity dispersion, which is the single free parameter. To facilitate comparison, we set $\sigma_v = 250$ km/s for all calculations. The tangential shear signal for this profile is given by (assuming a spatially flat Universe, Bartelmann & Schneider 2001)

$$\langle \gamma_+ \rangle (r_p) = 2\pi \left(\frac{\sigma_v}{c}\right)^2 \frac{\chi_{\rm L}}{r_p} \left(1 - \frac{\chi_{\rm L}}{\chi_{\rm S}}\right) \,, \tag{4.2}$$

where $\chi_{\rm L}$ is the comoving distance to the lens, and $\chi_{\rm S}$ the comoving distance to the source galaxy used to estimate the gravitational shear.

In Fig. 6 we show the forecasted relative error on the SIS free parameter σ_v for a selection of lens and source sample combinations. We have divided the lens samples into redshift bins of width 0.1 and 0.2, respectively. It is possible to explore new terrain in galaxy-galaxy lensing already with early SKA1 data by selecting lens samples using spectroscopic redshifts from an HI survey.

PoS(AASKA14)023

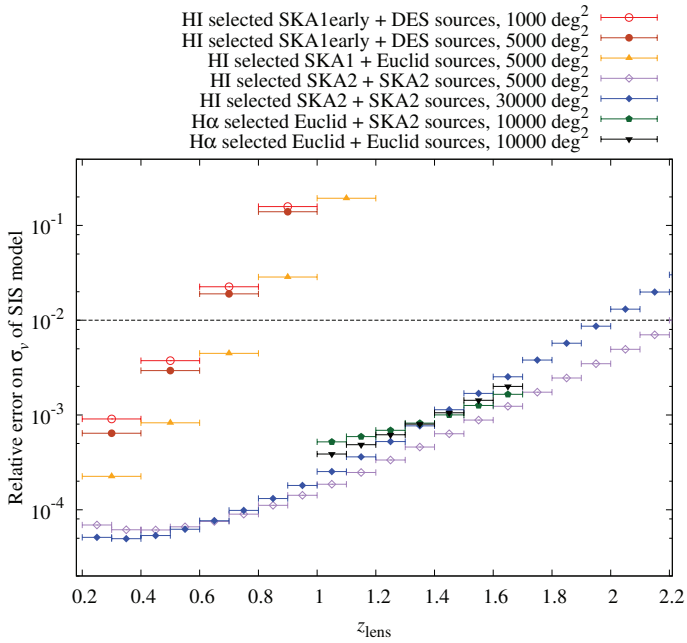

Figure 6: Relative 1σ error on the velocity dispersion, σ_v, of a singular isothermal sphere (SIS) profile as a function of the redshift of the lensed objects, constrained via the average tangential shear signal in the transverse separation range $r_p \in [0.1; 1]\,\mathrm{Mpc}/h$. The legend lists the lens sample selection, the source sample from which the shear signal is measured, and the assumed overlap in survey area. The error bars show the assumed width of the redshift bins. A 1 % constraint is indicated by the horizontal dashed line.

Combining this with a source sample from an optical survey such as the Dark Energy Survey (DES), one can obtain percent-level constraints out to $z \sim 0.6$ for a few subsamples (e.g. selected on gas abundance). The full SKA1 in combination with Euclid imaging for a source sample will decrease errors further by about a factor of five and extend the range where lenses can be studied to $z = 0.8$.

SKA2 will enable unique and powerful galaxy-galaxy lensing measurements without the need to rely on optical counterparts. As Fig. 6 shows, it will generate an unprecedented redshift baseline to study halo properties with a single facility. Out to $z \sim 1.5$ constraints are below the per mil level, which allow for tight constraints on complex models and/or the division into several subsamples. SKA2 will also be on par with Euclid in measuring the galaxy-galaxy lensing signal of emission-line (mostly Hα) galaxies detected in the Euclid spectroscopic survey, providing independent corroboration for this high-redshift measurement. Note finally that the very deep SKA2 surveys will allow the application of the novel techniques described in Section 2.4 as well as magnification analyses (e.g. Morrison et al. 2012) in a galaxy-galaxy lensing context.

5. Concluding remarks

The field of weak lensing with radio surveys is currently in its infancy but the prospect of SKA surveys coming online at the end of this decade presents a huge opportunity for opening a new wavelength window on the dark Universe. We have argued in this Chapter that the radio band

PoS(AASKA14)023

and the SKA in particular offer exciting prospects for enhancing and extending the reach of weak lensing studies beyond the limits of what is possible using their traditional optical approaches.

The SKA surveys will probe the galaxy population to higher redshift where the lensing signal is larger and potentially easier to measure. There is huge potential to exploit the cross-correlation of lensing shear measurements obtained from overlapping optical and radio surveys which can be powerful in mitigating a number of systematic effects.

Moreover, the radio band offers the exciting possibility of applying new techniques to measure weak lensing signals. One can make use radio polarization and/or rotational velocity information (from HI observations) to mitigate against intrinsic galaxy alignments which are the most worrying systematics for future precision weak lensing measurements. The opportunity to analyze HI Intensity Mapping surveys for the effects of weak lensing will open a new window on the dark Universe at redshifts that are well beyond the reach of traditional cosmic shear techniques.

The SKA also offers a new route to performing galaxy-galaxy lensing where spectroscopic redshifts from HI observations and the extra diagnostics coming from the radio band will allow for the precise definition of new lens samples.

As with other future large-scale survey instruments, weak lensing studies with the SKA will facilitate the auto- and cross-correlation of galaxy clustering and cosmic shear measurements within the same experimental set up. Generally speaking, the joint exploitation of clustering and lensing is extremely useful as the two probes are highly complementary. Constraints from baryonic acoustic oscillations and/or redshift space distortions are "orthogonal" to weak lensing, especially in the presence of uncertainties in photometric redshifts and inaccurate knowledge of galaxy clustering bias (Zhan 2006; Abate et al. 2012; Laureijs et al. 2011; Amendola et al. 2013).

In terms of constraining power for dark energy and/or modified gravity, galaxy clustering data measure the "dark fluid" equation of state at higher redshift than other standard candles like type Ia supernovae. Furthermore, clustering probes the evolution of matter fluctuations, which means that, through the Poisson equation, it is a proxy for the Newtonian potential Φ. In the case of modified gravity, clustering is sensitive to modifications occurring to the Newtonian gravitational constant. On the other hand, the deflection potential is proportional to the sum of the two metric potentials – which are equal in GR but not in more general gravity theories. Through this dependence, lensing effects represent a direct probe of non-standard gravity behaviours. As a consequence, the sensitivity to beyond-GR growth parameters comes in its greatest part from weak lensing, which provides the only direct measurements of growth (without biasing), e.g. Weinberg et al. (2013).

In order to realise the significant and exciting potential that radio weak lensing has to offer, a great deal of development work on analysis techniques, and demonstrating those techniques on real radio data from precursor surveys will be required. A key challenge will be to develop the field of galaxy shape estimation for radio observations to the level of maturity that is currently enjoyed by the optical lensing community. Work has already started in this direction and will gain further momentum through the ongoing "radioGREAT" challenge during the coming year. At the same time, surveys with e-MERLIN, LOFAR and the JVLA are starting to produce the high-resolution, wide-field data suitable for demonstrating radio weak lensing techniques on real observations. The planned program of algorithm development work coupled with the successful application of the developed radio lensing tools to the SKA pathfinder and precursor surveys will position the community favourable to fully exploit the tremendous opportunity for radio weak

PoS(AASKA14)023

lensing that will be afforded by the commissioning of the SKA at the end of this decade.

References

Abate A. et al. (LSST Dark Energy Science Collaboration), 2012, arXiv:1211.0310
Amara A., Refregier A., 2008, MNRAS, 391, 228, arXiv:0710.5171
Amendola L. et al., 2013, Living Rev. Relativity 16, 6
Ansari R., Campagne J. E., Colom P., Magneville C., Martin J. M., Moniez M., Rich J., Yeche C., 2012, C. R. Phys., 13, 46
Bartelmann M., Schneider P., 2001, Phys. Reports, 340, 291
Battye R. A., Browne I. W. A., Dickinson C., Heron G., Maffei B., Pourtsidou A., 2013, MNRAS, 434, 1239
Becker R. H., White R. L., Helfand D. J., 1995, ApJ, 450, 559
Bernstein G. M., 2009, ApJ, 695, 652
Blain A. W., 2002, ApJL, 570, L51
Braun R., 2013, "SKA1 Imaging Science Performance", Document number SKA-TEL-SKO-DD-XXX, Revision A Draft 2
Brown M. L., Battye R. A., 2011, MNRAS, 410, 2057
Brown M. L., Taylor A. N., Hambly N. C., Dye S., 2002, MNRAS, 333, 501
Brown M. L. et al., 2013, arXiv:1312.5618
Carrillo R. E., McEwen J. D., Wiaux Y., 2014, MNRAS, 439, 3591, arXiv:1307.4370
Catelan P., Kamionkowski M., Blandford R. D., 2001, MNRAS, 320, L7
Chang T.-C., Pen U.-L., Bandura K., Peterson J. B., 2010, Nature, 466, 463
Chang T., Pen U.-L., Bandura K., Peterson J. B., McDonald P., 2008, Phys. Rev. Lett., 100, 091303
Chang T.-C., Refregier A., 2002, ApJ, 570, 447
Chang T., Refregier A., Helfand D. J., 2004, ApJ, 617, 794
Chen X., 2012, Int. J. Mod. Phys., 12, 256
de Jong J. T. A., Verdoes Kleijn G. A., Kuijken K. H., Valentijn E. A., 2013, Exp. Astronomy, 35, 25
Dewdney P., Turner W., Millenaar R., McCool R., Lazio J., Cornewll T., 2013, "SKA1 System Baseline Design", Document number SKA-TEL-SKO-DD-001 Revision 1
Gillis, B. et al., 2013, MNRAS, 431, 1439
Heavens A., Refregier A., Heymans C., 2000, MNRAS, 319, 649
Heymans C. et al., 2013, MNRAS, 432, 2433
Hirata C. M., Seljak U., 2004, Phys Rev D, 70, 063526
Hoekstra H., van Waerbeke L., Gladders M. D., Mellier Y., Yee H. K. C., 2002, ApJ, 577, 604
Hu W., 2000, Phys. Rev. D., 62, 3007
Hu W., 2001, ApJ, 557, L79
Huff E. M., Krause E., Eifler T., George M. R., Schlegel D., 2013, arXiv:1311.1489
Joachimi B., Bridle S. L., 2010, A&A, 523, A1
Kaiser N., 1998, ApJ, 498, 26
Laureijs R. et al., 2011, arXiv:1110.3193

PoS(AASKA14)023

Lindroos L., Knudsen K. K., Vlemmings W., Conway J., Martí-Vidal I., 2014, MNRAS accepted, arXiv:1411.1410
Mandelbaum R., Seljak U., Cool R. J., Blanton M., Hirata C. M., Brinkmann J., 2006, MNRAS, 372, 758
Mandelbaum R. et al., 2014, ApJS, 212, 5, arXiv:1308.4982
Masui K. W., McDonald P., Pen U.-L., 2010, Phys. Rev. D, 81, 103527
Melchior P., Sutter P. M., Sheldon E. S., Krause E., Wandelt B. D., 2014, MNRAS, 440, 2922
Metcalf R. B., White S. D. M., 2009, MNRAS, 394, 704
Morales M. F., 2006, ApJL, 650, L21
Morrison C. B. et al., 2012, MNRAS, 426, 2489
Morrison G. et al., 2010, ApJS, 188, 178
Muxlow T. W. B. et al., 2005, MNRAS, 358, 1159
Patel P., Bacon D. J., Beswick R. J., Muxlow T. W. B., Hoyle B., 2010, MNRAS, 401, 2572
Patel P., Abdalla F. B., Bacon D. J., Rowe B., Smirnov O., Beswick R. J., 2013, arXiv:1303.4650
Pober J. C. et al., 2013, AJ, 145, 65
Pourtsidou A., Metcalf R. B., 2014, MNRAS, 439, L36
Refregier A., Bacon D. J., 2003, MNRAS 338 48
Schinnerer E. et al., 2010, ApJS, 188, 384
Seo H. J., Dodelson S., Marriner J., Mcginnis D., Stebbins A., Stoughton C., Vallinoto A., 2010, ApJ, 721, 164
Stil J. M., Krause M., Beck R., Taylor A. R., 2009, ApJ, 693, 1392
Sutter P. M. et al., 2014, MNRAS, 438, 768, arXiv:1309.1469
Takada M., Jain B., 2004, MNRAS, 348, 897
van Uitert E., Hoekstra H., Franx M., Gilbank D. G., Gladders M. D., Yee H. K. C., 2013, A&A, 549, A7
Voigt L. M., Bridle, S. L., 2010, MNRAS, 404, 458, arXiv:0905.4801
Voigt L. M., Amara A., Cropper M., Kitching T. D., Massey R., Rhodes J., Schrabback T., 2012, MNRAS, 421, 1385
Weinberg, D. H. et al., 2013, Phys. Rep. 530, 87
Wilman R. J. et al., 2008, MNRAS, 388, 1335
Zhan H., 2006, J. Cosmol. Astropart. Phys., 08, 008
Zahn O., Zaldarriaga, M., 2006, ApJ, 653, 922
Zhang P., Pen, U. L., 2006, MNRAS, 367, 169
Zuntz J. et al., 2014, arXiv:1409.3409
Zwaan M. A. et al., 2003, Astron.J., 125, 2842

PoS(AASKA14)023

PROCEEDINGS OF SCIENCE

Measuring baryon acoustic oscillations with future SKA surveys

Philip Bull[*1], **Stefano Camera**[2,3], **Alvise Raccanelli**[4,5,6], **Chris Blake**[7], **Pedro G. Ferreira**[8], **Mario G. Santos**[9,3], **Dominik J. Schwarz**[10]

[1]*Institute of Theoretical Astrophysics, University of Oslo, PO Boks 1029 Blindern, 0315 Oslo, Norway;* [2]*Physics Department, University of the Western Cape, Cape Town 7535, South Africa;* [3]*CENTRA, Instituto Superior Tecnico, Universidade de Lisboa, Av. Rovisco Pais 1, 1049-001, Lisboa, Portugal;* [4]*Department of Physics & Astronomy, Johns Hopkins University, 3400 N. Charles St., Baltimore, MD 21218, USA;* [5]*Jet Propulsion Laboratory, California Institute of Technology, Pasadena CA 91109, USA;* [6]*California Institute of Technology, Pasadena CA 91125, USA;* [7]*Centre for Astrophysics & Supercomputing, Swinburne University of Technology, PO Box 218, Hawthorn, VIC 3122, Australia;* [8]*Astrophysics, University of Oxford, UK;* [9]*Physics Department, University of the Western Cape, Cape Town 7535, South Africa;* [9]10*Fakultät für Physik, Universität Bielefeld, Postfach 100131, D-33501 Bielefeld, Germany*
E-mail: p.j.bull@astro.uio.no

The imprint of baryon acoustic oscillations (BAO) in large-scale structure can be used as a standard ruler for mapping out the cosmic expansion history, and hence for testing cosmological models. In this chapter we briefly describe the scientific background to the BAO technique, and forecast the potential of the Phase 1 and 2 SKA telescopes to perform BAO surveys using both galaxy catalogues and intensity mapping, assessing their competitiveness with current and future optical galaxy surveys. We find that a 25,000 deg^2 intensity mapping survey on a Phase 1 array will preferentially constrain the radial BAO, providing a highly competitive 2% constraint on the expansion rate at $z \simeq 2$. A 30,000 deg^2 galaxy redshift survey on SKA2 will outperform all other planned experiments for $z \lesssim 1.4$.

Advancing Astrophysics with the Square Kilometre Array
June 8-13, 2014
Giardini Naxos, Italy

*Speaker.

PoS(AASKA14)024

1. Introduction

The Baryon Acoustic Oscillations (BAO) are a relic from the time when photons and baryons were coupled in the early Universe, and constitute a preferred clustering scale in the distribution of matter on cosmological scales. Since the physical scale of the oscillations can be inferred from observations of the cosmic microwave background (CMB), one can use the measured apparent size of the BAO as a 'standard ruler' in the late-time Universe. Used as a distance measure in this way, the BAO are one of the most powerful cosmological observables that can be derived from large-scale structure (LSS) surveys – making it possible to accurately reconstruct the geometry and expansion history of the Universe, while being remarkably robust to systematic errors. In combination with the CMB and other observations, precision BAO measurements are able to decisively answer fundamental questions about the nature of dark energy (especially its possible evolution with redshift), possible modifications to General Relativity, and the spatial curvature of the Universe.

The SKA will be able to measure the BAO in two ways (Fig. 1). The first, using the intensity mapping (IM) technique, seeks to reconstruct the cosmological density field in three dimensions over unprecedentedly large volumes, using the 21cm spin-flip transition of neutral hydrogen to trace the density field in redshift space. The second is a more conventional galaxy redshift survey, which will detect many millions of discrete sources over a wide range of redshifts, with accurate redshift determinations coming from the 21cm line. Of the two, IM is the newer and less-tested method – galaxy surveys have been used to great effect as probes of LSS over the past several decades, whereas the first IM experiments are only just coming online, and are subject to a number of potential foregrounds and systematics that are yet to be fully quantified. Nevertheless, an IM survey is the best prospect for doing transformative cosmology with Phase 1 of the SKA – surpassing all existing BAO constraints at low redshift, and strongly complementing future surveys at higher redshift.

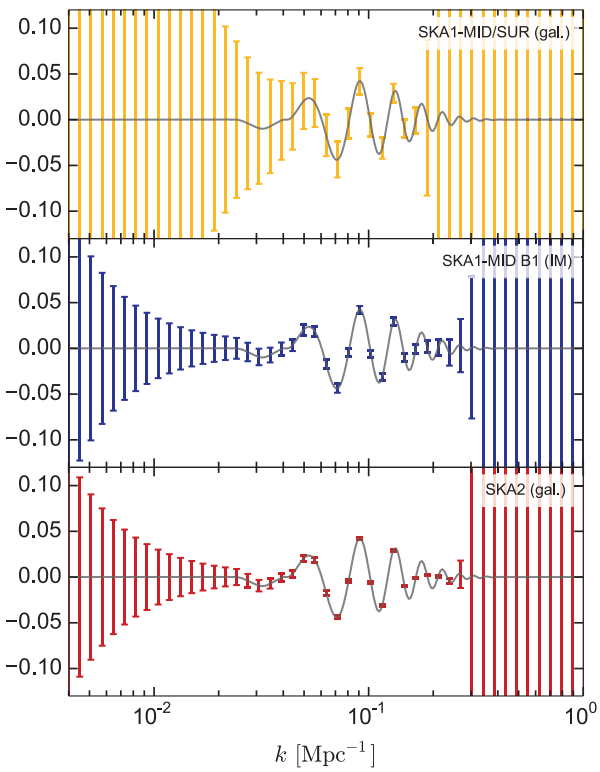

Figure 1: Constraints on the BAO 'wiggles', $f_{\rm BAO}(k) = P(k)/P_{\rm ref}(k) - 1$ (where $P_{\rm ref}(k)$ is a BAO-free reference spectrum), combined over all available redshift bins for three SKA galaxy/IM surveys. Full forecasts are given in Section 4.

In this chapter, we will review the physics of the BAO, its suitability for use as a standard ruler, and the current state of the art in BAO measurements from optical and Lyman-α surveys. We will then describe two possible methods for reconstructing the BAO with large surveys on the SKA, and present forecasts of the capabilities of SKA Phase 1 and 2 for each.

PoS(AASKA14)024

2. BAO as a standard ruler

In the early Universe, baryons and radiation were tightly coupled together via interactions with free electrons, by Coulomb attraction and Thomson scattering respectively. The tendency of overdensities in the baryon distribution to collapse under gravity was resisted by the increase in radiation pressure of photons collapsing along with them, setting up acoustic oscillations in the coupled photon-baryon plasma. The speed of sound in the fluid gives rise to a preferred scale – the *sound horizon*, r_s – corresponding to the distance a sound wave could have travelled since the Big Bang. As the Universe cooled and the relative proportion of radiation to matter fell, Thomson scattering became inefficient and the photons and electrons decoupled, allowing the radiation to stream away. With the radiation pressure gone, the sound waves stalled, and the pattern of over- and under-densities that they had set-up were left frozen into the baryon distribution with a typical correlation length corresponding to the sound horizon at this time. Cold dark matter, being coupled to the baryonic matter gravitationally, was drawn into the same pattern of fluctuations, leaving a preferred distance scale in the total matter distribution.

One can measure this distance scale in a statistical manner by reconstructing the matter correlation function, $\xi(\mathbf{r}) = \langle \delta_M(\mathbf{x})\delta_M(\mathbf{x}+\mathbf{r})\rangle$, from surveys of large-scale structure using galaxies or other tracers of the matter density field. The BAO scale appears as a relatively broad 'bump' feature on ~ 150 Mpc scales, and so large survey volumes are needed to measure it well. One only measures a *relative* distance scale from the correlation function; retrieving physical distances depends on knowing the comoving sound horizon (i.e. the physical scale of the oscillations) as well. This can be calibrated from the CMB angular power spectrum, for example.

The BAO can be measured separately in the radial and tangential directions. If one makes no attempt to separate the two (i.e. by taking an angular average), the distance measured is $d(z) = r_s(z_d)/D_V(z)$, where z_d is the redshift of the baryon drag epoch, and the *dilation scale* is given by

$$D_V(z) = \left((1+z)^2 D_A^2(z) \frac{cz}{H(z)} \right)^{\frac{1}{3}}. \tag{2.1}$$

The expansion rate, $H(z)$, and angular diameter distance, $D_A(z)$, describe the geometry of the Universe, so measurements of $D_V(z)$ over a range of redshift can be used to constrain the evolution of the equation of state of dark energy, $w(z)$, for example. As shown by Eq. (2.1), however, one only measures a combination of $H(z)$ and $D_A(z)$, and so model degeneracies can arise. The degeneracy can be broken by separating the BAO in each direction; the quadrupole of the correlation function is sensitive to the combination

$$F(z) = (1+z)D_A(z)H(z)/c, \tag{2.2}$$

and the combination of D_V and F uniquely determines D_A and H. In practise, one can separate out the tangential and radial directions by marginalising over the shape of the clustering pattern, without needing to understand the effects of redshift space distortions (Anderson et al. 2013).

2.1 Constraining dark energy with distance measurements

A measurement of $H(z)$ and $D_A(z)$ can be directly related to the dynamics and geometry of space time. Specifically, the Friedmann equations relate the expansion rate to the energy content and

PoS(AASKA14)024

curvature of the universe via

$$H^2(z) = \frac{8\pi G}{3}\left[\rho_M(1+z)^3 + \rho_R(1+z)^4 + \rho_{\rm DE}(z)\right] - \kappa(1+z)^2$$

where ρ_M and ρ_R are the energy density in matter and radiation today, κ is the curvature of space and $\rho_{\rm DE}(z)$ encapsulates all the unaccounted "dark" energy which may be contributing to the expansion of the universe. This dark energy can take a wide range of different forms: scalar fields (or quintessence) which are analogous to the Higgs field of the standard model (Copeland et al. 2006), gravitational degrees of freedom that are a remnant from higher dimensions, or even more radical modifications to Einstein's General Theory of Relativity (Clifton et al. 2012). Given its exotic nature and the fact that we cannot account for the dark energy with any of the other, known forms of energy, this is a unique opportunity to explore physics beyond the standard model and learn something qualitatively new about the fundamental laws of nature.

To learn about dark energy using BAO, we attempt to pin down its time evolution. Given that we are solely focusing on the dynamics and geometry of the background spacetime, $\rho_{\rm DE}(z)$ is completely determined by its value today, $\rho_{\rm DE}(0)$, and its equation of state, $w(z)$, such that $d\ln\rho_{\rm DE}/d\ln z = 3[1+w(z)]$. It is by characterising $w(z)$ that we hope to learn about the underlying physics that is driving the expansion of the Universe at late times. In theory $w(z)$ can have a wide range of behaviours, but in practice it is useful to consider simpler parametrizations. A particularly popular and useful parametrisation is to – effectively – Taylor expand the equation of state in terms of the scale factor $a \equiv (1+z)^{-1}$ so that

$$w \simeq w_0 + w_a(1-a), \tag{2.3}$$

where w_0 and w_a are constants. While clearly oversimplifying the time evolution of $w(z)$ and in principle only accurate for $z \ll 1$, this parametrisation turns out to capture the behaviour of a very broad class of models for dark energy. Furthermore, it can be shown that, under general conditions, there are reasonably tight consistency relations between w_0 and w_a that can be used to select out particular types of physical model. In this paper we will use w_0 and w_a to quantify the precision of our constraints, although more general approaches have been used which involve decomposing the full history of $w(z)$ into suitable functional components (Zhao et al. 2015).

A precise measurement of w_0 and w_a can lead to profound insights. Current constraints are weak – especially from $z \gtrsim 1$ – but are consistent with $w_0 = -1$ and $w_a = 0$, which is what one might expect from a cosmological constant, in itself quite a remarkable result. If future constraints show that $w_0 \neq -1$ and $w_a \neq 0$ then it would correspond to the discovery of a new degree of freedom in the Universe: a new fundamental field or modifications to general relativity on cosmological scales. If one were to find $w_0 < -1$ (that is, if the equation of state were to cross the "phantom divide" at late times (Caldwell et al. 2003)), then the consequences would be quite dramatic and one would have to consider a substantial revision of the current rules of field theory and gravitation.

2.2 Systematic effects and density field reconstruction

One of the major advantages of using the BAO to measure distances is their robustness to systematic effects. Since the distance information is primarily contained in the *location* of a feature in the correlation function (or equivalently the power spectrum), rather than its amplitude or detailed

PoS(AASKA14)024

shape, there is little dependence on difficult-to-calibrate quantities like the overall normalisation of the matter power spectrum. Nevertheless, the non-linear growth of structure and scale-dependent effects can blur and bias the measured location of the BAO feature, so must be taken into account.

Consider how galaxies respond to the growth of large-scale structure, for example. As they fall toward their local clusters and superclusters, the large-scale galaxy pairs which encode the pristine baryon acoustic scale are shifted to smaller or larger separations, broadening the baryon acoustic peak and decreasing the accuracy with which it can be recovered. The technique of "density-field reconstruction" (Eisenstein et al. 2007) performs an approximate computation of these motions using the observed distribution of galaxies, and hence restores objects to the near-original position in the linear density field. This has the effect of sharpening the acoustic peak and significantly improving distance measurements.

The potential level of improvement depends on the number density of the tracer, as well as the individual noise of the realisation, but for sample variance-limited surveys can be a factor of ~ 2 (Seo & Eisenstein 2007). The reconstruction technique has been applied with success to BAO measurements in the largest galaxy redshift surveys at intermediate redshifts: the Sloan Digital Sky Survey (SDSS) Luminous Red Galaxy sample (Padmanabhan et al. 2012), the Baryon Oscillation Spectroscopic Survey (BOSS) (Anderson et al. 2013) and the WiggleZ Survey (Kazin et al. 2014).

Non-linear structure formation can also introduce scale-dependent effects. One typically thinks of the present-day density field becoming significantly non-linear only on scales below ~ 30 Mpc, far below the BAO scale at ~ 150 Mpc. Mode coupling on small scales, and the fact that the observed correlation function is a convolution over all Fourier modes, means that non-linear effects have an impact on considerably larger scales, however. Galaxy bias also affects the shifts introduced by non-linearities. While non-linear effects that change the shape of the clustering pattern can be marginalised without biasing the location of the BAO feature, the combination of all effects can introduce a modest (but non-negligible) $\sim 0.1-0.2\%$ bias after reconstruction (Seo et al. 2010; Mehta et al. 2011).

2.3 Previous measurements

Since the first significant detection of the baryon acoustic peak in the SDSS Luminous Red Galaxy (LRG) sample by (Eisenstein et al. 2005), BAO measurements have improved along with the increasing volume mapped by galaxy redshift surveys, and now provide per-cent level distance and expansion measurements at various cosmic epochs. The most precise current measurements derive from BOSS (DR11, (Anderson et al. 2013)), which now offers 2% and 1% distance measurements at $z = 0.32$ and $z = 0.57$ respectively, using nearly one million galaxies covering 8,500 deg^2 of sky and a volume of 13 Gpc^3. BOSS has also measured BAOs in the structure of the Lyman-α forest on the sightlines to quasars, providing a 2% distance measurement at $z = 2.34$ (Delubac et al. 2015).

Measurements at lower precision have previously been reported by the WiggleZ Dark Energy Survey ($\sim 4\%$ measurements in two independent bins at $z = 0.44$ and $z = 0.73$, (Kazin et al. 2014)), the 6-degree Field Galaxy Survey (4.5% measurement in the local Universe at $z = 0.1$, effectively serving as an independent determination of H_0 (Beutler et al. 2011)), and the final SDSS LRG sample (Padmanabhan et al. 2012). BAOs have also been detected in photometric redshift surveys at intermediate redshifts (Seo et al. 2012).

PoS(AASKA14)024

Upcoming optical and near-infrared redshift surveys enabling BAO measurements include the extended BOSS project (eBOSS), which will provide precision distance measurements in the range $z < 1$, the Hobby-Eberly Telescope Dark Energy Experiment (HETDEX), targeting $2 < z < 4$, the Euclid and WFIRST satellites, and proposed ground-based projects such as the Dark Energy Survey Instrument (DESI) and the VISTA/4MOST telescope. Ref. (Font-Ribera et al. 2014) describe how a combination of these facilities should provide percent-level distance constraints over the range $0 < z < 4$. In this chapter we discuss whether SKA surveys are able to compete in this landscape.

3. Experiment and survey design

There are two main methods that can be used to measure the BAO with the SKA: a galaxy redshift survey and an intensity mapping survey. In this section, we describe the relative merits of the two methods, and define baseline specifications for both types of survey on the Phase 1 and 2 configurations.

3.1 HI galaxy redshift survey

Galaxies are biased tracers of the cosmological density field. By detecting many individual galaxies and measuring their redshifts, one can constrain the matter correlation function (or equivalently, the power spectrum). As discussed above, redshift surveys at optical wavelengths have been used to great effect for cosmology, and with the SKA one will be able to do the same in the radio.

Most important is the choice of target galaxy population. In particular, one requires galaxies with an easily measurable emission/absorption feature for measuring redshifts – the most appropriate for the SKA being HI (Santos et al. 2015b). The high spectral resolution of SKA receiver systems rivals the redshift resolution of optical spectroscopic surveys, and their large bandwidths allow a wide redshift range to be covered in principle. The Phase 1 arrays have insufficient sensitivity to yield competitively-sized samples of HI galaxies, however – even with optimistic assumptions, a 10,000 hour survey over 5,000 deg^2 with SKA1-MID or SUR will achieve an RMS flux sensitivity of $S_{\rm rms} \approx 70 - 100\ \mu$Jy, equating to roughly 5×10^6 galaxies out to $z \approx 0.5$ for a 5σ detection threshold. This is worse than the expected yield from the full 10,000 deg^2 BOSS survey, which will be completed long before Phase 1 sees first light. SKA2, on the other hand, will be far more sensitive, reaching $S_{\rm rms} \approx 5\ \mu$Jy for a 10,000 hour survey over 30,000 deg^2, even with a more stringent 10σ threshold. The expected yield for such a survey is $\sim 10^9$ galaxies between $0.18 < z < 1.84$, far surpassing any planned optical or near-infrared survey for $z \lesssim 1.4$. The predicted number density and bias of HI galaxies for SKA1-MID (including MeerKAT dishes), SKA1-SUR (including ASKAP dishes), and SKA2 are given in Table 1; more details on the sensitivity calculation are given in Santos et al. (2015b).

There are a number of potential systematic effects that can affect galaxy redshift surveys. In large optical galaxy surveys at least, stars are a major contaminant – while one can distinguish stars from galaxies by their colour, bright stars effectively mask galaxies behind them, leading to a complicated angular selection function on the sky. This is less of an issue in the radio, although other contaminants, such as diffuse galactic synchrotron emission and non-galaxy point sources, can also cause problems for the source-finding algorithms used to compile the galaxy catalogue. Source-

PoS(AASKA14)024

SKA1-MID		
z_c	$n(z)$ [Mpc^{-3}]	$b(z)$
0.05	2.92×10^{-2}	0.678
0.15	6.74×10^{-3}	0.727
0.25	1.71×10^{-3}	0.802
0.35	4.64×10^{-4}	0.886
0.45	1.36×10^{-4}	0.975

SKA1-SUR		
z_c	$n(z)$ [Mpc^{-3}]	$b(z)$
0.05	4.14×10^{-2}	0.664
0.15	8.00×10^{-3}	0.724
0.25	1.56×10^{-3}	0.802
0.35	3.39×10^{-4}	0.890
0.45	7.86×10^{-5}	0.989
0.55	1.91×10^{-5}	1.099
0.65	4.77×10^{-6}	1.221
0.75	1.23×10^{-6}	1.357
0.85	3.21×10^{-7}	1.507

SKA2		
z_c	$n(z)$ [Mpc^{-3}]	$b(z)$
0.23	4.43×10^{-2}	0.713
0.33	2.73×10^{-2}	0.772
0.43	1.65×10^{-2}	0.837
0.53	9.89×10^{-3}	0.907
0.63	5.88×10^{-3}	0.983
0.73	3.48×10^{-3}	1.066
0.83	2.05×10^{-3}	1.156
0.93	1.21×10^{-3}	1.254
1.03	7.06×10^{-4}	1.360
1.13	4.11×10^{-4}	1.475
1.23	2.39×10^{-4}	1.600
1.33	1.39×10^{-4}	1.735
1.43	7.99×10^{-5}	1.882
1.53	4.60×10^{-5}	2.041
1.63	2.64×10^{-5}	2.214
1.73	1.51×10^{-5}	2.402
1.81	9.66×10^{-6}	2.566

Table 1: Predicted number density and bias of HI galaxies as a function of redshift, for SKA1-MID (including MeerKAT, Band 2), SUR (including ASKAP), and SKA2 ($\Delta z = 0.1$ bins). All assume 10,000 hour surveys, over 5,000 deg^2 (SKA1-MID and SUR) and 30,000 deg^2 (SKA2). The detection thresholds are chosen to be 5σ, 5σ, and 10σ respectively. See Santos et al. (2015b) for more details.

finding in radio data is also made more challenging by needing to search through 3D datacubes resolved in angle and frequency, rather than just sets of discrete 2D images.

One should also be careful of source evolution effects. For example, the luminosity function of the tracer population is expected to change with redshift, modifying the number of galaxies that can be detected. Depending on the tracer, this limits the useful redshift range of a survey, and complicates its selection function. This evolution is commonly parametrised as an evolution of the galaxy bias, $b(z)$, and the principal effect on the BAO is to change the shot noise by changing the effective galaxy number density, $n(z)$. It is also possible that the bias can become scale-dependent, however, which introduces the possibility of systematically biasing the BAO scale.

As discussed in Section 2.2, redshift space distortions and effects on non-linear scales also affect the measured power spectrum. A simple model for the impact of RSDs and non-linearities on the galaxy power spectrum is given by (Kaiser 1987; Seo & Eisenstein 2007),

$$P_{\rm tot}(\mathbf{k}) \;=\; (b(z)+f(z)\mu^2)^2 e^{-\frac{1}{2}k^2\sigma^2_{\rm NL}(z,\mu)} P(k,z), \tag{3.1}$$

$$\sigma_{\rm NL}(z,\mu) \;=\; \sigma_{\rm NL} D(z)\left(1+f(z)\mu^2[2+f(z)]\right)^{\frac{1}{2}} \tag{3.2}$$

where $D(z)$ is the growth factor, $f(z) = d\log D/d\log a$ is the linear growth rate of structure, and $P(k,z)$ is the isotropic matter power spectrum. The leading term of Eq. (3.1) is the anisotropy due

PoS(AASKA14)024

to RSDs ($\mu \equiv \cos\theta$), and the exponential term models the "washing-out" of redshift information due to incoherent non-linear velocities, characterised by the velocity dispersion, $\sigma_{\rm NL}$. These effects are discussed in more detail in Raccanelli et al. (2015).

3.2 Intensity mapping survey

If one is only interested in measuring the matter distribution on large scales, there is not strictly any need to resolve individual galaxies. Instead, one can perform a survey with relatively low angular resolution that detects only the integrated intensity from many unresolved sources. This is called intensity mapping (IM), and allows extremely large volumes to be surveyed very efficiently.

The SKA will be capable of performing large IM surveys over $0 \lesssim z \lesssim 3$ using the redshifted neutral hydrogen 21cm emission line (Santos et al. 2015a). Neutral hydrogen is ubiquitous in the late universe, residing principally in dense regions inside galaxies that are shielded from the ionising UV background, and the 21cm line is narrow and relatively unaffected by absorption or contamination by other lines. It is thus an excellent tracer of the matter density field in redshift space. The background brightness temperature of the HI emission is (Bull et al. 2015)

$$\overline{T}_b = \frac{3}{32\pi}\frac{hc^3 A_{10}}{k_B m_p \nu_{\rm HI}^2}\frac{(1+z)^2}{H(z)}\Omega_{\rm HI}(z)\rho_{c,0}, \tag{3.3}$$

where A_{10} is the Einstein coefficient for emission, and $\Omega_{\rm HI}(z)$ is the fraction of the critical density today, $\rho_{c,0}$, in neutral hydrogen. Assuming that HI is a linearly-biased tracer of the total matter density field, we can relate fluctuations in the brightness temperature to the (Fourier-transformed) redshift-space matter density perturbation,

$$\delta T_b = \overline{T}_b \delta_{\rm HI}(\mathbf{k}) = \overline{T}_b (b_{\rm HI} + f\mu^2) e^{-\frac{1}{4}k^2\sigma_{\rm NL}^2(z,\mu)}\delta_M(k), \tag{3.4}$$

where the anisotropic terms are due to RSDs and non-linear growth (Eq. 3.1). One can then measure the 3D redshift-space matter power spectrum, $\langle \delta_M(\mathbf{k})\delta_M^*(\mathbf{k}')\rangle = (2\pi)^3\delta^{(3)}(\mathbf{k}-\mathbf{k}')P(\mathbf{k})$, by mapping out the brightness temperature distribution in angle and frequency, $\nu = \nu_{\rm HI}/(1+z)$.

	SKA1-MID		SKA1-SUR	
	Band 1	Band 2	Band 1	Band 2
$T_{\rm inst}$ [K]	28	20	50	30
$z_{\rm min}$	0.35	0.00	0.58	0.00
$z_{\rm max}$	3.05	0.49	3.05	1.18
$\nu_{\rm min}$ [MHz]	350	950	350	650
$\nu_{\rm max}$ [MHz]	1050	1760	900	1670
$D_{\rm dish}$ [m]	15	15	12	12
$\delta\nu$ [kHz]	50	50	50	50
$\Omega_{\rm sur}$ [10^3 deg^2]	25	25	25	25
$N_{\rm dish} \times N_{\rm beam}$	254×1	254×1	60×36	60×36

Table 2: Baseline IM survey specifications for the Phase 1 SKA configurations. SUR is equipped with PAFs; the assumed scaling of the PAF FOV with frequency is explained in Santos et al. (2015b).

PoS(AASKA14)024

Example survey specifications for Phase 1 of the SKA are shown in Table 2. One of the key decisions in designing an IM survey for the SKA will be whether to use the array in autocorrelation (single-dish) or cross-correlation (interferometer) mode. As one is interested in mapping out extended structure on comparatively large angular scales rather than detecting individual galaxies that subtend only small angles, the angular sensitivity is an important factor. Roughly speaking, single-dish experiments are sensitive to angular scales between the field of view (FOV) of a single dish and the full area of the survey, whereas interferometers can only see between the scales corresponding to their minimum and maximum baseline lengths. Since the minimum baseline can be no smaller than the diameter of a single dish, the maximum possible angular scale that interferometers are sensitive to is set by the single-dish FOV (i.e. the primary beam). The two modes are therefore in some sense complementary (Fig. 2).

For the $\sim$ 15m dishes of the SKA, the physical scales corresponding to the BAO are best matched to an autocorrelation survey for $z \lesssim 1$, and an interferometric survey at higher z. Having the BAO features fall somewhere within an instrument's resolution window is only a minimum requirement, however – ideally, one should maximise its sensitivity at the relevant angular scales too. This is trivial in the single-dish case, which has an essentially flat response over its full range of angular scales, but for interferometers there is a strong dependence on the detailed baseline distribution. For IM with the SKA, a high density of short baselines is optimal, suggesting an array configuration with highly-clustered stations. For the currently-proposed SKA1 configurations, however, the density of short baselines is not high enough, and autocorrelation mode always wins out on sensitivity at low redshift. An interferometric survey would be better suited to BAO detections at high redshift, $z > 1.5$, but this is a less interesting range for constraining dark energy. A proposed dense aperture array component of SKA2 would likely be better suited to intensity mapping; aperture arrays have the large FOV and high density of short baselines necessary for sensitivity to the angular scales of the BAO at lower z.

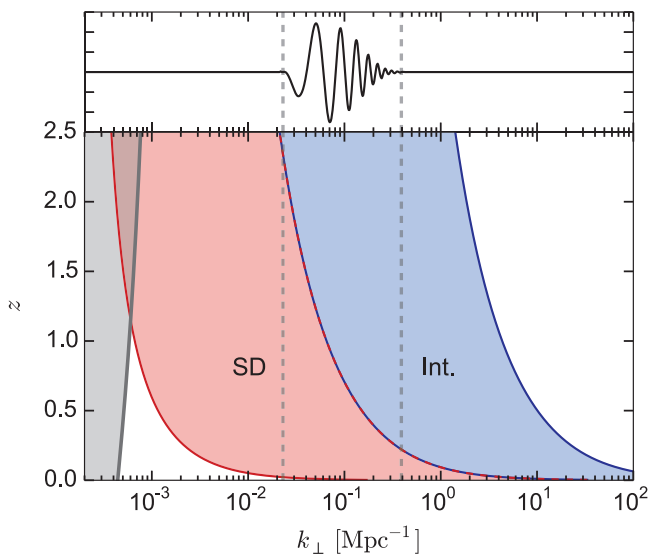

Figure 2: Maximum and minimum transverse (angular) scales that can be probed as a function of redshift in single-dish (autocorrelation) and interferometer modes, for a representative SKA array (15m dishes with baselines restricted to a 1 km core, and 25,000 deg^2 survey area). The BAO (dashed vertical lines) and comoving horizon scale (grey band) are shown for comparison. (N.B. the array will also be sensitive to structure in the radial (frequency) direction.)

Though promising, the intensity mapping methodology is not yet mature, and it remains to be seen whether a number of potentially serious issues can be overcome. The most obvious of these is the presence of foreground emission from the galaxy and extragalactic point sources, which strongly contaminates the HI signal. Fortunately, despite being several orders of magnitude brighter, most of the foregrounds are spectrally smooth and so can be readily distinguished from all

PoS(AASKA14)024

but the largest-scale modes of the fluctuating cosmological signal. More insidious is the leakage of polarised foreground emission into the total intensity channel; this is not spectrally smooth because of frequency-dependent Faraday rotation caused by the partially-incoherent magnetic field of the galaxy (Alonso et al. 2014). The issue of foreground contamination is explored in more detail in Wolz et al. (2015).

Another significant issue for single-dish surveys in particular is correlated ("$1/f$") noise. A well-known problem in CMB analysis, correlated noise from the receiver system and elsewhere dominates the uncorrelated white noise component on long timescales. This causes the signal-to-noise ratio to grow more slowly as a function of integration time, and introduces striping artefacts into maps of the emission, seriously hindering the recovery of large-scale modes of the signal. For the CMB, this is handled by using receivers with low knee frequencies (< 1 Hz), scanning rapidly across the sky, and filtering out timescales longer than $1/f_{\rm knee}$ from the time-ordered data. An SKA autocorrelation survey would have to adopt similar strategies to make a wide-angle survey viable. Finally, ground pickup/spillover is also an issue for autocorrelation surveys, and must be suppressed (e.g. with ground shielding), or mapped out and subtracted.

4. Forecasts for the SKA

In this section we present forecasts for BAO distance measurements – and the resulting constraints on cosmological parameters – for several SKA configurations, and compare them with what will be possible with other methods in around the same timeframe. The forecasts are based on the Fisher forecasting formalism developed in (Bull et al. 2015), using the number counts from Table 1 (galaxy survey), and experimental specifications set out in Table 2 (IM survey). Complementary forecasts for redshift space distortions are given in Raccanelli et al. (2015).

While there are a number of possible combinations of arrays, frequency bands, and survey modes for both Phase 1 and 2, for compactness we have chosen to concentrate on the best-performing configurations. For example, for Phase 1 we neglect Band 1 of SUR and MID for galaxy surveys, as they will detect comparatively few HI galaxies, and we consider only autocorrelation mode for intensity mapping, since the angular resolution of an interferometric IM survey on the SKA is poorly matched to the BAO for $z \lesssim 1$. We present forecasts only for a galaxy survey for SKA2, although it should be noted that an IM survey on a mid-frequency aperture array should be able to provide similar constraints on the BAO out to $z \approx 2$.

4.1 Fisher forecasting

To accurately characterise the expected performance of a given experiment, one would ideally perform a full simulation, incorporating a variety of potential systematic and instrumental effects, and running the simulated data through the actual analysis pipeline. This is computationally intensive, and detailed aspects of the hardware and signal may not yet be known, as is the case here. Fisher forecasting takes a simpler approach, instead using the expected properties of the signal and noise for an experiment to derive a Gaussian approximation to the likelihood for a set of parameters to be measured. Though clearly not definitive, Fisher forecasts at least take into account important effects like correlations between parameters, and are sufficiently accurate for understanding the relative performance of different experiments.

PoS(AASKA14)024

The key procedure in Fisher forecasting is to construct the Fisher matrix, F, for a set of parameters, θ. When inverted, this yields an estimate of the covariance matrix for the Gaussianised likelihood. The Fisher matrices for both IM and galaxy redshift surveys can be written in the form

$$F_{ij} = \frac{1}{2}\int \frac{d^3k}{(2\pi)^3} V_{\rm eff}(\mathbf{k}) \left[\frac{\partial}{\partial\theta_j}\log C^T \cdot \frac{\partial}{\partial\theta_j}\log C^T\right], \tag{4.1}$$

where $C^T = C^S + C^N$ is the total covariance of the measured signal, consisting of the true signal (S) and noise (N), and $V_{\rm eff}(\mathbf{k}) = V_{\rm phys}\left(C^S/C^T\right)^2$ is the effective volume of the survey (which covers a physical volume $V_{\rm phys}$). Only C^S is a function of the cosmological parameters of interest, $\{\theta\}$. For a galaxy survey, the total signal is the galaxy power spectrum plus shot noise, $C^T = P_{\rm tot}(\mathbf{k}) + 1/n(z)$. For intensity mapping, the expression is more complicated: $C^S \propto T_b^2 P_{\rm tot}(\mathbf{k})$ and $C^N \propto T_{\rm sys}^2 S_{\rm area}/t_{\rm tot} B(\mathbf{k})$, where B is a window function that depends on the angular and frequency resolution of the radio telescope (full expressions for both interferometer and autocorrelation experiments are given in Bull et al. (2015)). We have neglected the effects of foreground subtraction here.

To calculate the Fisher matrix, we must specify a fiducial cosmology and a set of parameters to be measured (including nuisance parameters). We adopt the Planck best-fit ΛCDM model (Planck Collaboration 2014),

$$h = 0.67,\ \Omega_\Lambda = 0.684,\ \Omega_K = 0,\ \Omega_b = 0.049, w = -1,\ n_s = 0.962,\ \sigma_8 = 0.834,\ N_{\rm eff} = 3.046, \tag{4.2}$$

and in the first instance forecast for the parameters

$$\left\{\alpha_\perp = D_A(z)|_{\rm fid.}/D_A(z), \alpha_\parallel = H(z)/H(z)|_{\rm fid.}, \sigma_8 f(z), \sigma_8 b(z), n_s, \sigma_{\rm NL}\right\}, \tag{4.3}$$

where 'fid.' denotes evaluation in the fixed fiducial cosmology. Since we are only interested in the BAO here, we discard information on the distance parameters $\{\alpha_\perp, \alpha_\parallel\}$ from all other sources. In practise, this means that we only keep the terms with derivatives of the BAO part of the power spectrum with respect to α, i.e. $\partial f_{\rm BAO}(k)/\partial\alpha$, where we have split the isotropic power spectrum into a smooth part and an oscillating part, $P(k) = [1 + f_{\rm BAO}(k)]P_{\rm smooth}(k)$. We also assume that no reconstruction of the density field is performed.

Finally, one can project from this set of parameters into another that corresponds directly to the parameters of a cosmological model. We will consider the projection of the distance/growth functions, $\{\alpha_\perp, \alpha_\parallel, f\}$, into the parameters

$$\{h, n_s, \Omega_\Lambda, \Omega_K, w_0, w_a, \sigma_{\rm NL}, \sigma_8, b(z)\}. \tag{4.4}$$

This corresponds to fitting a cosmological model to the distance measurements extracted from the BAO, and the growth rate measured from the anisotropy of the correlation function.

4.2 BAO forecasts for the SKA

Predicted constraints on the BAO feature in the power spectrum for three different SKA surveys were shown in Fig. 1, as a function of scale. For Phase 1, it is clear that an intensity mapping survey will have much better overall sensitivity to the BAO than a galaxy survey when constraints

PoS(AASKA14)024

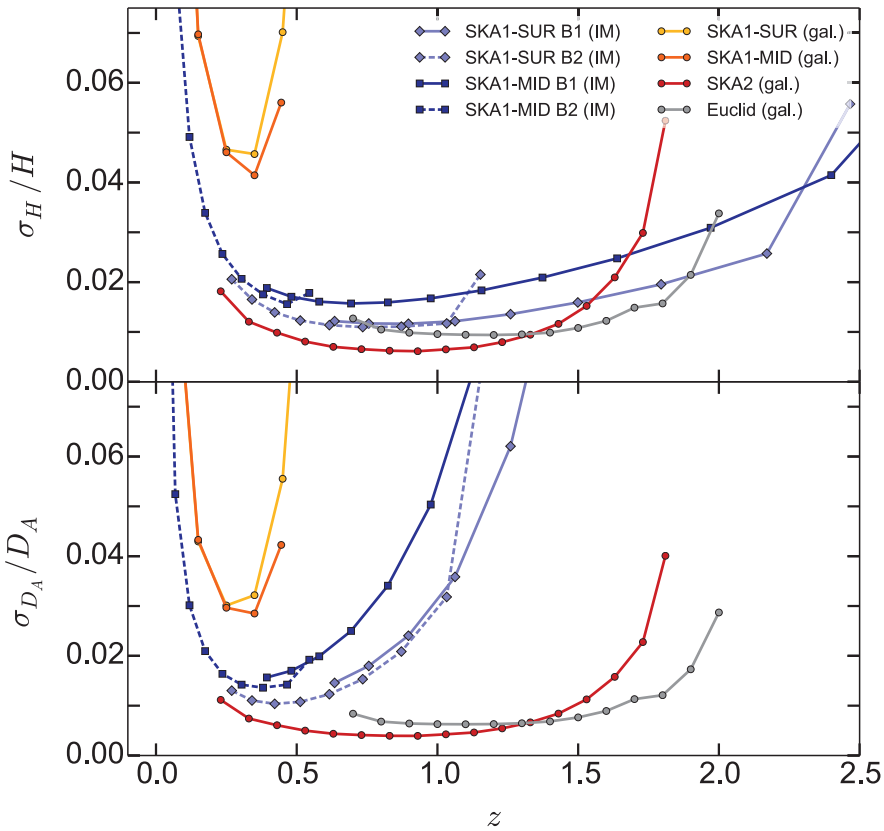

Figure 3: BAO-only fractional constraints (68% CL) on the expansion rate (top panel) and angular diameter distance (bottom panel) for SKA IM and galaxy redshift surveys. The bias has been marginalised as a free parameter in each redshift bin. The degradation of the D_A constraints at higher z for the IM experiments is caused by their falling angular resolution (c.f. Fig. 2).

are combined over the full redshift range. A galaxy survey with SKA2 will far surpass both of these (subject to various systematic effects).

Fig. 3 shows forecast constraints on the expansion rate and angular diameter distance for the proposed SKA surveys, in bins of width $\Delta z = 0.1$ (galaxy surveys) or $\Delta\nu = 60$ MHz (IM surveys). Forecasts for a Euclid galaxy survey are also shown for comparison, based on the predicted number counts and bias in Amendola et al. (2013). For Phase 1, a galaxy survey will not be competitive with other BAO measurements owing to insufficient sensitivity. An IM autocorrelation survey will be significantly more powerful, providing constraints on $H(z)$ that are similar to the (sample variance-limited) Euclid experiment, but over a significantly wider redshift range – Band 2 of both SUR and MID will yield sub-2/3% constraints beyond $z \simeq 2$. Constraints on the angular diameter distance will be considerably worse at higher redshift due to the limited angular resolution in autocorrelation mode, however (c.f. Fig. 2). A galaxy survey with SKA2 will be sample variance-limited over 30,000 deg^2 for $0.4 \lesssim z \lesssim 1.3$, surpassing all other planned surveys over that range.[1]

[1] An IM survey on a Phase 2 dense mid-frequency aperture array operating from 450 MHz upwards could provide similarly tight constraints on D_A and H all the way out to $z = 2$ if a large enough collecting area could be built.

PoS(AASKA14)024

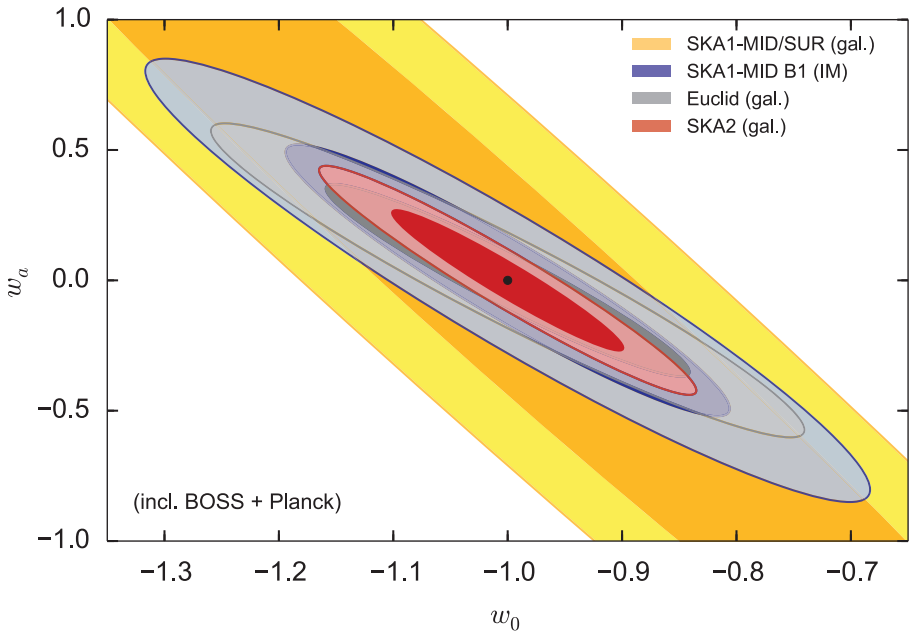

Figure 4: Forecast constraints on (w_0, w_a) for several SKA configurations and Euclid, in combination with Planck and BOSS. All other parameters have been marginalised, including Ω_K, and the bias is free per z bin.

Expected constraints on the dark energy equation of state parameters (Eq. 2.3) are shown in Fig. 4 for a subset of these configurations, combined with forecast Planck CMB and BOSS low redshift BAO constraints.[2] Forecasts for a future Euclid galaxy survey are shown for comparison, also with Planck+BOSS included. While unable to match Euclid on raw figure of merit[3] (FOM = 69, versus 129 for Euclid), the Phase 1 IM survey has a highly complementary redshift range and wide survey area (with potentially $\sim 100\%$ overlap), and should be completed in the early 2020's, making it the low redshift dataset of choice for joint analyses with Euclid and other high redshift experiments like WFIRST and DESI. Combining surveys will be important for pinning-down the nature of dark energy in the medium term, as "Stage IV" galaxy surveys may not offer sufficient precision on their own to discriminate between most dark energy models (Marsh et al. 2014). In the longer term, the galaxy survey with SKA2 will be able to achieve a substantially larger FOM of around 310.

5. Conclusions

The Baryon Acoustic Oscillations imprint a distance scale into the distribution of matter on large scales that can be used to constrain the expansion history and geometry of the Universe. In turn, this can be used to constrain key cosmological parameters, potentially allowing us to answer fundamental questions about the nature of dark energy such as whether it evolves with time. The BAO

[2]We have assumed that the BOSS sample is statistically independent from the surveys that we combine it with.

[3]The dark energy figure of merit is defined as $\mathrm{FOM} = 1/\sqrt{\det(F^{-1}|_{w_0,w_a})}$ (Albrecht et al. 2006).

PoS(AASKA14)024

are remarkably robust to systematic effects, and have been successfully measured to high precision by a number of optical galaxy redshift surveys and Lyman-α forest observations.

The SKA will be able to measure the BAO through two different types of survey: HI galaxy redshift surveys, where millions of individual galaxies are detected and their redshifts measured from the HI emission line; and HI intensity mapping surveys, where the integrated HI emission from many unresolved galaxies is used to reconstruct the cosmological density field on large scales. Redshift surveys are a tried and tested technique, but require high sensitivity to capture enough galaxies. Intensity mapping has yet to mature, but is potentially a much more efficient way of detecting the BAO. Both suffer from a number of potential systematics, such as those associated with the non-linear evolution of the cosmological density field on small scales.

Phase 1 of the SKA will be able to produce competitive constraints on the (mostly radial) BAO at redshifts relevant for dark energy if a large IM autocorrelation survey can be performed. The Phase 1 arrays lack the sensitivity to detect enough galaxies to produce interesting constraints from a redshift survey, and there are an insufficient number of short baselines to make an interferometric IM survey worthwhile (unless higher redshifts are targeted). Note that an IM autocorrelation survey on an early deployment (pre-Phase 1) system may also be able to produce useful constraints on the expansion rate so long as sufficient survey time ($\sim$10,000 hours) can be obtained.

SKA2, on the other hand, will have the sensitivity to produce an immense galaxy redshift survey over almost $3/4$ of the sky, surpassing all other planned BAO measurements at $0.4 \lesssim z \lesssim 1.3$. This should allow it to pin down the equation of state of dark energy with unprecedented precision, assuming various systematic effects can be overcome. A mid-frequency aperture array could achieve similar precision at higher redshift (out to $z \simeq 2$) if a sufficiently large and dense collecting area can be used, but we have not considered this possibility in detail here.

Finally, while we have concentrated on the BAO as the most robust distance measure, redshift space distortions and even the overall shape of the power spectrum contain a great deal of extra information that can be used to constrain dark energy. In this sense, the forecasts here represent the most conservative estimates of the cosmological constraints that can be achieved with the SKA. If sufficient control over systematics can be achieved, considerably tighter measurements of $w(z)$ and the growth of structure can be expected by using these other probes too (Raccanelli et al. 2015).

References

Albrecht, A., Bernstein, G., Cahn, R. et al., 2006, arXiv:astro-ph/0609591.

Alonso, D., Ferreira, P. G. & Santos, M. G., 2014, MNRAS, 444, 3183 [arXiv:1405.1751]

Amendola, L. et al. [Euclid Theory Working Group Collaboration], 2013, Living Rev. Rel., 16, 6

Anderson, L., Aubourg, E., Bailey, S. et al., 2013, MNRAS, 427, 3435.

Bacon, D. et al., 2015, "Synergy between the Large Synoptic Survey Telescope and the Square Kilometre Array", in proceedings of "Advancing Astrophysics with the Square Kilometre Array", PoS(AASKA14)145

Beutler, F., Blake, C., Colless, M. et al., 2011, MNRAS, 416, 3017.

Bull, P., Ferreira, P. G., Patel, P. & Santos, M. G., ApJ, 803, 21 [arXiv:1405.1452]

Caldwell, R. R., Kamionkowski, M. & Weinberg, N. N., 2003, Phys. Rev. Lett., 91, 071301

Clifton, T., Ferreira, P. G., Padilla, A. & Skordis, C., 2012, Phys. Rept., 513, 1

PoS(AASKA14)024

Copeland, E., Sami, M. & Tsujikawa, S., 2006, Int. J. Mod. Phys., D15, 1753

Delubac, T. et al. [BOSS Collaboration], 2015, A&A, 574, A59 [arXiv:1404.1801]

Eisenstein, D. J. et al. [SDSS Collaboration], 2005, ApJ, 633, 560

Eisenstein, D. J., Seo, H. -J., Sirko, E. & Spergel, D., 2007, ApJ, 664, 675

Font-Ribera, A., McDonald, P., Mostek, N. et al., 2014, JCAP, 1405, 023 [arXiv:1308.4164].

Kaiser, N., 1987, MNRAS, 227, 1

Kazin, E. A., Koda, J., Blake, C. & Padmanabhan, N., 2014, MNRAS, 441, 3524 [arXiv:1401.0358].

Kitching, T. et al., 2015, "Euclid & SKA Synergies", in proceedings of "Advancing Astrophysics with the Square Kilometre Array", PoS(AASKA14)146

Marsh, D. J. E., Bull, P., Ferreira, P. G. & Pontzen, A., 2014, Phys. Rev. D, 90, 105023 [arXiv:1406.2301].

Mehta, K. T., Seo, H. -J., Eckel, J. et al., 2011, ApJ, 734, 94

Padmanabhan, N., Xu, X., Eisenstein, D. J. et al., 2012, MNRAS, 427, 2132

Planck Collaboration, 2014, A&A, 571, A16 (2014)

Raccanelli, A. et al., 2015, "Measuring redshift-space distortions in future SKA surveys", in proceedings of "Advancing Astrophysics with the Square Kilometre Array", PoS(AASKA14)031

Santos, M. et al., 2015a,"Cosmology with a SKA HI intensity mapping survey", in proceedings of "Advancing Astrophysics with the Square Kilometre Array", PoS(AASKA14)019

Santos, M. et al., 2015b, "HI galaxy simulations for the SKA: number counts and bias", in proceedings of "Advancing Astrophysics with the Square Kilometre Array", PoS(AASKA14)021

Seo, H. -J. & Eisenstein, D. J., 2007, ApJ, 665, 14

Seo, H. -J., Eckel, J., Eisenstein, D. J. et al., 2010, ApJ, 720, 1650

Seo, H. -J., Ho, S., White, M. et al., 2012, ApJ, 761, 13

Wolz, L. et al., 2015, "Foreground Subtraction in Intensity Mapping with the SKA", in proceedings of "Advancing Astrophysics with the Square Kilometre Array", PoS(AASKA14)035

Zhao, G. -B. et al., 2015, "Model-independent constraints on dark energy and modified gravity with the SKA", in proceedings of "Advancing Astrophysics with the Square Kilometre Array", PoS(AASKA14)165

PoS(AASKA14)024

PROCEEDINGS OF SCIENCE

Cosmology on the Largest Scales with the SKA

Stefano Camera[*,a] **Alvise Raccanelli,**[bcd] **Philip Bull,**[e] **Daniele Bertacca,**[f] **Xuelei Chen,**[g] **Pedro G. Ferreira,**[h] **Martin Kunz,**[ij] **Roy Maartens,**[fk] **Yi Mao,**[l] **Mário G. Santos,**[fma] **Paul R. Shapiro,**[n] **Matteo Viel**[op] **and Yidong Xu**[g]

[a]CENTRA, IST, Universidade de Lisboa, 1049-001 Lisboa, Portugal; [b]Department of Physics & Astronomy, Johns Hopkins University, Baltimore, MD 21218, USA; [c]Jet Propulsion Laboratory, California Institute of Technology, Pasadena, CA 91109, USA; [d]California Institute of Technology, Pasadena, CA 91125, USA; [e]Institute of Theoretical Astrophysics, University of Oslo, 0315 Oslo, Norway; [f]Department of Physics, University of the Western Cape, Cape Town 7535, South Africa; [g]National Astronomical Observatories, Chinese Academy of Sciences, Beijing 100012, China; [h]Astrophysics, Physics Department, University of Oxford, Oxford OX1 3RH, UK; [i]Département de Physique Théorique and Center for Astroparticle Physics, Université de Genève, CH 1211 Genève 4, Switzerland; [j]African Institute for Mathematical Sciences, Cape Town 7945, South Africa; [k]Institute of Cosmology & Gravitation, University of Portsmouth, Portsmouth P01 3FX, UK; [l]Institut d'Astrophysique de Paris, Institut Lagrange de Paris, CNRS, UPMC Univ. Paris 06, UMR7095, F-75014 Paris, France; [m]SKA SA, 4th Floor, The Park, Park Road, Pinelands 7405, South Africa; [n]Department of Astronomy and Texas Cosmology Center, University of Texas at Austin, Austin, TX 78712, USA; [o]INAF, Astronomical Observatory of Trieste, via Tiepolo 11, 34131 Trieste, Italy; [p]INFN, Sezione di Trieste, 34100 Trieste, Italy
E-mail: stefano.camera@tecnico.ulisboa.pt

The study of the Universe on ultra-large scales is one of the major science cases for the Square Kilometre Array (SKA). The SKA will be able to probe a vast volume of the cosmos, thus representing a unique instrument, amongst next-generation cosmological experiments, for scrutinising the Universe's properties on the largest cosmic scales. Probing cosmic structures on extremely large scales will have many advantages. For instance, the growth of perturbations is well understood for those modes, since it falls fully within the linear régime. Also, such scales are unaffected by the poorly understood feedback of baryonic physics. On ultra-large cosmic scales, two key effects become significant: primordial non-Gaussianity and relativistic corrections to cosmological observables. Moreover, if late-time acceleration is driven not by dark energy but by modifications to general relativity, then such modifications should become apparent near and above the horizon scale. As a result, the SKA is forecast to deliver transformational constraints on non-Gaussianity and to probe gravity on super-horizon scales for the first time.

Advancing Astrophysics with the Square Kilometre Array
June 8-13, 2014
Giardini Naxos, Italy

[*]Speaker.

PoS(AASKA14)025

1. Introduction

An uncharted area of physical and observational cosmology is the physics of ultra-large scales. By this we mean length scales which are near or beyond the cosmic horizon. Most large-scale surveys have been limited to sampling length scales of order hundreds of megaparsecs, whilst deeper surveys (i.e. higher redshift surveys) are not yet good enough to accurately measure modes which are of order the horizon. Yet, the cosmological information hidden in the extremely large scales is of great importance for our comprehension of the Universe. For a start, the growth of cosmological perturbations is well within the linear regime on those ultra-large scales. This allows for better checks of our theoretical model, since we can there safely disregard the non-linear growth of structures—which always requires some degree of *ad hoc* modelling. Furthermore, on very large scales the most relevant physics is simply given by the gravitational interaction, thus freeing us from the necessity of taking astrophysical processes into account.

Theoretical knowledge of the Universe on the largest cosmic scales can be very precise, but ultra-large scales have been most difficult to access. This is mainly due to two observational issues. Firstly, if we want to probe very large scales—i.e. very large wavelengths or very small Fourier momenta—a wide field of view is not sufficient. For a wide-field, shallow survey the transverse components, $\mathbf{k}_\perp$, of the physical wavevector $\mathbf{k}$ may be arbitrarily small, but the smallest measured wavenumber, $k \equiv |\mathbf{k}| = \sqrt{\mathbf{k}_\perp^2 + k_\parallel^2}$, is limited by the fact that the survey probes only a thin shell—thus providing us with a large parallel component, $k_\parallel$. In other words, we need to observe a very large 'cube' of Universe. This is a challenging task for conventional galaxy redshift surveys, for it is extremely hard to achieve the required sensitivity at high redshift over a large area of the sky. Closely related to this is the second observational problem, namely cosmic variance. Even though the full SKA will be able to detect HI galaxies as far away as $z \simeq 2$ over roughly three quarters of the celestial dome—thus actually observing a huge cosmic cube—the relatively small number of sources with ultra-large separation can heavily limit the constraining potential of the survey.

The SKA is in a unique position to change this state of affairs and push forward the study of ultra-large scale modes. To tackle successfully the two observational issues described above, the SKA will employ two newly developed techniques, one being HI intensity mapping (IM) and the other the so-called multi-tracer approach. Since we can exploit IM both during and after the epoch of reionisation (EoR), the SKA will be able to probe exceptionally large redshifts. When mapping large-scale structure after the EoR, it is possible to efficiently collect information on large wavelengths without having to worry about resolving small-scale features or individual galaxies. When mapping the EoR, one can effectively sample a large number of horizon-size volumes at the time.

In addition, the multi-tracer technique will allow us to beat down cosmic variance. This approach is based on galaxies being biased but not stochastic tracers of the underlying density field. Thus, by observing different galaxy populations—namely, different tracers—we can construct several realisations of the clustered halo distribution. Although measurements of global cosmological properties like the total matter density Ω_m or the Hubble constant H_0 will still be affected by cosmic variance, we will be able to constrain halo properties to a much higher degree of accuracy.

In this Chapter, we outline the science to be done by using the SKA to map the matter distribution on the largest cosmic scales. We first make the case for why ultra-large scales are interesting,

PoS(AASKA14)025

focussing on relativistic effects, modified gravity (MG) and scale-dependent biasing arising from primordial non-Gaussianity (PNG). Then, we address how different methods will constrain these various physical phenomena, showing that indeed the SKA will be transformational for constraining PNG, and unique for probing gravity on super-horizon scales. Lastly, we discuss the issues that need to be faced when trying to probe the largest scales. We refer the reader to chapters by Santos et al. (2015), Abdalla et al. (2014) and Jarvis et al. (2014) for details on the phases of the SKA, its observation modes and the different methods we are discussing here.

2. The Importance of Probing Ultra-Large Cosmic Scales

The study of the biggest volumes ever of cosmic large-scale structure will allow a major advance in tackling two of the most fundamental questions in contemporary cosmology: What is the physical mechanism that generated the inflationary expansion in the early Universe? Does general relativity (GR) hold on the largest scales?

Most models of inflation do predict some degree of non-Gaussianity in the distribution of primordial density fluctuations, but the simplest models predict negligible PNG. A detection of PNG will be vital for ruling out classes of models and advancing our understanding of inflation. Currently, the most stringent constraints on PNG come from the Planck satellite, but future cosmic microwave background (CMB) experiments are unlikely to improve these results significantly. The new frontier of constraining PNG is large-volume surveys of the matter distribution.

Similarly, tests of GR on cosmological scales are based on observations of the large-scale structure. Current constraints are weak, but with its huge surveyed volumes and multiple probes, the SKA will take the lead in the next generation of tests. Additionally, we can tighten the current constraints on dark energy (DE) and MG models by including much larger scales, thus increasing the statistical power of the observations and improving the sensitivity to any scale-dependent deviation from GR.

In this Section we review such ultra-large scale phenomena, highlighting their importance for our understanding of the Universe.

2.1 General Relativistic Effects

Probing ultra-large scales involves a theoretical challenge that has been recognised only recently. GR effects arise from observing on the past light-cone, which distorts the number counts and brightness temperature fluctuations on very large scales. So far, most analyses have been performed using a Newtonian approximation, with the flat-sky redshift-space distortions (RSDs) grafted on as a special relativistic effect. This is the 'standard' relativistic correction to the Newtonian approximation, which is significant on sub-horizon scales. Sometimes, the effect of lensing convergence is also included. This is adequate for past and present surveys, which analyse galaxy clustering on scales well below the horizon. Sometimes this Newtonian-like approach also includes the contribution of weak lensing magnification to the matter over-density. The lensing effects can be significant on small scales. But future wide and deep surveys will need to employ a more precise modelling, accounting not only for RSDs and lensing, but for all geometric and relativistic corrections. The full relativistic analysis includes terms that are suppressed on sub-horizon scales such as velocity (or Doppler) terms, Sachs-Wolfe (SW) and integrated SW (ISW) type terms, and

PoS(AASKA14)025

time-delay contributions (e.g. Yoo 2010; Jeong et al. 2012; Bonvin & Durrer 2011; Challinor & Lewis 2011; Bruni et al. 2012).

One can work with the redshift-space correlation functions and include all GR and wide-angle contributions (Bertacca et al. 2012; Raccanelli et al. 2014a, 2013; Bonvin et al. 2014). By analysing this, we can potentially extract more information about the structure of galaxy clustering. For instance, the odd Legendre multipoles of the correlation function vanish in the Newtonian flat-sky approximation, whereas they are in general non-zero for wide-angle separations and in the full GR analysis (Raccanelli et al. 2014a; Bonvin et al. 2014). Alternatively, the use of the angular power spectrum also avoids the flat-sky assumption, which is important for full-sky surveys with many wide-angle correlations (Bonvin & Durrer 2011; Challinor & Lewis 2011; Di Dio et al. 2013).

To give a flavour of how GR corrections alter the Newtonian prediction, we show in Fig. 1 the ratio between a galaxy clustering angular power spectrum in which some GR effect has been switched on and the simple Newtonian result. We factorise the various corrections as follows: RSDs (top, left panel); velocity (top, right panel), where we include terms proportional to the velocity along the line of sight; weak lensing convergence (bottom, left panel); and potentials (bottom, right panel), which account for the effect of gravitational potentials at the source, SW, ISW and time-delay terms (see e.g. Challinor & Lewis 2011). The two sets of curves refer to different surveys, all of them assumed to observe a certain population of galaxies with constant bias 1.5, distributed according to a Gaussian window centred at redshift z_m and with width σ_w. Specifically, we compare a shallow survey with $z_m = 0.5$ (red curves) to a deep survey with $z_m = 2.0$ (blue curves). Moreover, we consider both the cases of a narrow (solid lines) and a broad (dashed lines) window, viz. $\sigma_w = 0.01$ and 0.1 for the shallow survey and $\sigma_w = 0.05$ and 0.5 for the deep survey. From Fig. 1, it is apparent that, although RSDs and lensing are the dominant, the other terms can also become important, particularly for as deep a survey as the SKA.

The GR corrections to the power spectrum should be observable for certain SKA surveys, using the multi-tracer technique—the task of forecasting this capacity is under way. Even if these corrections are not directly detectable, it is essential to include them in theoretical analysis of the power spectrum, for two related reasons:

1. to avoid biasing parameter estimations through a theoretical systematic of incorrect modelling;

2. to correctly extract maximal information from the largest scales.

2.2 Primordial Non-Gaussianity

The largest cosmic scales are a crucial source of information about the physical processes at play during the early stages of the Universe's evolution. The standard model of inflation and its generalisations predict seed primordial density fluctuations with some level of non-Gaussianity in the probability distribution (e.g. Bartolo et al. 2004). We can parameterise the non-Gaussianity in Bardeen's gauge invariant potential Φ as the sum of a linear Gaussian term ϕ and a quadratic correction (Verde et al. 2000; Komatsu & Spergel 2001), i.e.

$$\Phi = \phi + f_{\rm NL}\left(\phi^2 - \langle\phi^2\rangle\right). \tag{2.1}$$

PoS(AASKA14)025

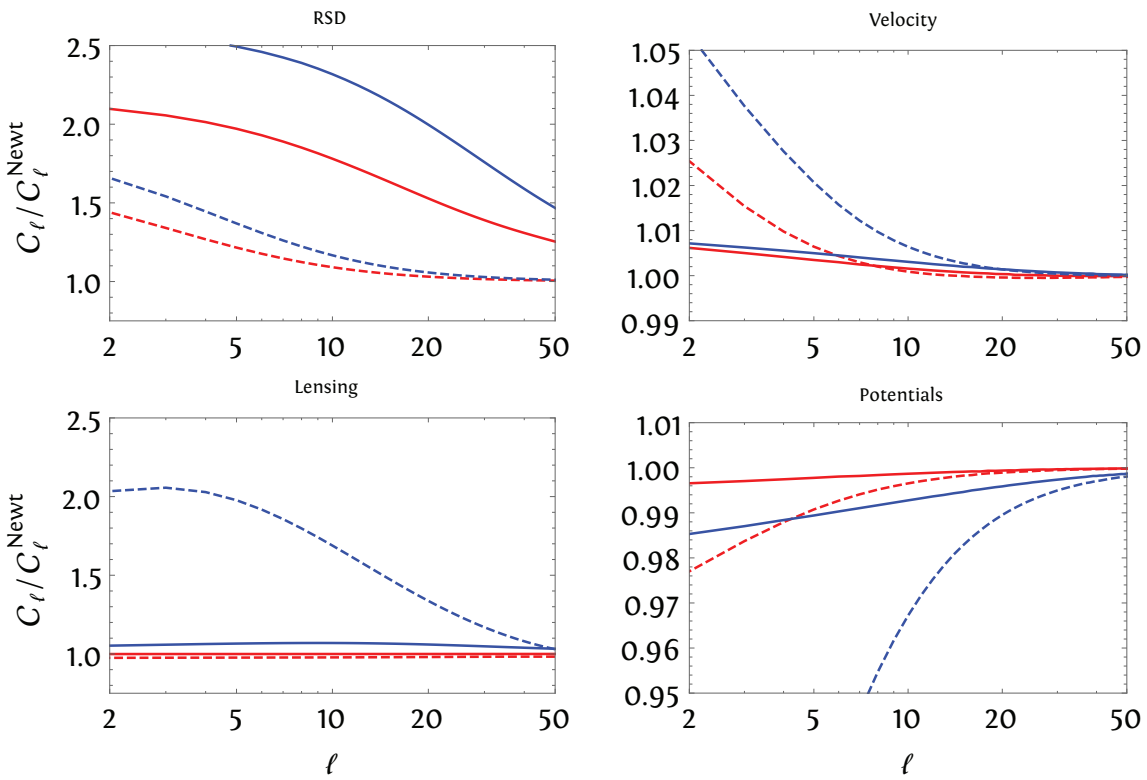

Figure 1: Ratios of angular power spectra including some kind of GR corrections to the standard Newtonian approximation, $C_\ell^{\rm Newt}$. Red (blue) curves refer to a shallow (deep) survey, while solid (dashed) lines to narrow (broad) source redshift distributions. (See text for details.)

If the distribution of primordial density perturbations is not Gaussian, it cannot be fully described by a power spectrum; we rather need higher-order moments such as the bispectrum. In particular, different models of inflation give rise to different bispectrum shapes, thus making the study of PNG valuable for obtaining a deeper knowledge of the physics of inflation.

The standard single-field inflationary scenario generates negligibly small deviations from Gaussianity. These deviations are said to be of the local shape, and the related bispectrum of Bardeen's potential is maximised for squeezed configurations, where one of the three wavenumbers has a much smaller magnitude than the other two. In this case, the PNG parameter, $f_{\rm NL}$, is expected to be of the same order as the slow-roll parameters, namely very close to zero (Falk et al. 1993). However, this does not mean that $f_{\rm NL} \approx 0$. Due to the inherent non-linearity of GR, it is not possible for Gaussianity in the primordial curvature perturbation to be reflected exactly in the density perturbation. A non-linear GR correction to the initial conditions leads to an effective $f_{\rm NL}^{\rm GR} = -5/3$ in large-scale structure (Verde & Matarrese 2009).

Local-shape PNG can also be generated when an additional light scalar field other than the inflaton contributes to the observed curvature perturbations (Bartolo et al. 2004). This happens for instance in curvaton models (Sasaki et al. 2006; Assadullahi et al. 2007) or in multi-field models (Bartolo et al. 2002; Bernardeau & Uzan 2002; Huang 2009). Other than local-type PNG, there are inflationary models in which the kinetic term of the inflaton Lagrangian is non-standard,

PoS(AASKA14)025

containing higher-order derivatives of the field itself. One significant example of this is the 'DBI' model (Alishahiha et al. 2004; Arkani-Hamed et al. 2004; Seery & Lidsey 2005), where the primordial bispectrum is maximised for configurations where the three wavevectors have approximately the same amplitude—the so-called equilateral-type PNG (Creminelli et al. 2007). Otherwise, for deviations from Gaussianity evaluated in the regular Bunch-Davies vacuum state, the primordial potential bispectrum is of local or equilateral shape, depending on whether or not higher-order derivatives play a significant rôle in the evolution of the inflaton field. If the Bunch-Davies vacuum hypothesis is dropped, the resulting bispectrum is maximal for squashed configurations (Chen et al. 2007; Holman & Tolley 2008). Lastly, another shape of the bispectrum can be constructed that is nearly orthogonal to both the local and equilateral forms (Senatore et al. 2010).

The best probe of PNG up to now has relied on measuring the CMB temperature anisotropy bispectrum (see Ade et al. 2014, for the latest results). However, it has been demonstrated that PNG also induces an additional, peculiar scale and redshift dependence in a biased tracer of the underlying matter distribution (Dalal et al. 2008; Matarrese & Verde 2008; Schmidt & Kamionkowski 2010; Desjacques et al. 2011). The modification $\Delta b_X(z,k)$ to the Gaussian large-scale bias b_X of a biased tracer X induced by local-type PNG is

$$\Delta b_X(z,k) = b_X(z) + 3[b_X(z)-1]\frac{\Omega_m H_0^2 \delta_c}{k^2 T(k) D_+(z)} f_{\rm NL}, \tag{2.2}$$

where $b_X(z)$ is assumed scale-independent, δ_c is the critical value of the matter over-density at collapse, the transfer function $T(k) \to 1$ on large scales, and $D_+(z)$ is the linear growth factor of density perturbations normalised to unity today.[1]

It is clear from this equation that the effect of PNG on the power spectrum grows on large scales, as k^{-2}. These are the same scales on which GR corrections are becoming significant. Therefore, one needs to incorporate the GR corrections in theoretical analysis in order to make accurate (and non-biased) predictions and estimates of PNG.

2.3 Modified Gravity

Einstein's theory of GR has been tested to exquisite precision on 'small' scales, namely in the laboratory, the Solar System and with the help of pulsars. On the contrary, tests on scales approaching the cosmological horizon are still rather weak. However, there is great interest in testing GR on very large scales in the context of DE, as the cosmological constant suffers from a plethora of theoretical problems. Since the accelerated expansion of the Universe is a late-time phenomenon, it is natural to look for hints concerning the physical nature of the underlying mechanism on very large scales.

The landscape of MG theories is rather heterogeneous, and there is little reason to prefer any one model over the others. Attempts to parameterise this landscape in a suitably generic way have been only partially successful (Hu & Sawicki 2007; Linder & Cahn 2007; Baker et al. 2013; Battye & Pearson 2012) although methods based on effective field theory approaches provide a possible avenue for the large class of scalar field models with second-order equations of motion, like

[1] Note that we adopt the large-scale structure (LSS) convention, which implies $f_{\rm NL}^{\rm LSS} \approx 1.3 f_{\rm NL}^{\rm CMB}$ (see e.g. Dalal et al. 2008; Afshordi & Tolley 2008, for more details).

PoS(AASKA14)025

Horndeski-type theories (Piazza & Vernizzi 2013; Bellini & Sawicki 2014). Phenomenological parameterisations can in principle describe the full range of deviations from GR relevant for cosmology and thus fully exploit the information contained in the data by effectively modelling the metric perturbations (see Kunz 2012, and references therein). However, phenomenological models are mostly useful to capture the evolution of linear perturbations, which effectively limits them to large scales.

Many MG theories modify the expansion history of the Universe—often by construction, as they are intended as alternatives to DE. However, it has been shown that many DE models are also able to produce arbitrary $w(z)$, and MG models can be tuned to mimic the cosmological constant value of $w(z) = -1$. Therefore, the expansion history is not a smoking gun for MG. On the other hand, MG theories in general also alter the growth history of the Universe, i.e. the evolution of the metric perturbations and thus the growth of the matter density contrast too. Many MG models modify the effective strength of gravity as a function of scale and/or redshift, break the equivalence principle and so forth, thus yielding a number of possible observational signatures. On large (linear) scales, the linear growth rate, $f(z)$, is the most sensitive probe of the growth history, and can be well-measured using RSDs from galaxy redshift surveys and IM (see Hall et al. 2013, for IM). Another important quantity in this context is the scalar anisotropic stress (or gravitational slip), which is generally non-zero in MG theories, especially on very large scales (Saltas & Kunz 2011). The anisotropic stress is an attractive test for deviations from the standard model because it is measurable without any assumptions on the initial power spectrum or the bias by combining peculiar velocities (e.g. RSDs from IM) with weak lensing measurements (Motta et al. 2013). Its presence appears to be also linked directly to a modification of the propagation of gravitational waves, which can be used as a way to define what MG means (Saltas et al. 2014; Camera & Nishizawa 2013).

Going to very large scales is important for many reasons. Generally speaking, the small scales where perturbations are highly non-linear tend to be less useful for cosmological tests of GR, as MG theories generically need to be screened on small scales to avoid violating the strong Solar System constraints (although the mildly non-linear region is interesting). In addition, accurate predictions on non-linear scales require dedicated N-body simulations for each theory, and as mentioned above, it is unclear how to use the unifying phenomenological framework on non-linear scales. Baryonic effects on small scales are also badly understood and add a systematic error which effectively renders these scales unusable for precision cosmology for the time being. Then, as the effects that we are looking for are small, we need as many modes as we can get, which also pushes us to large volumes. Last but not least, the scale dependence of deviations from GR is a crucial observable to distinguish between different models, and first we need a wide range of scales to be able to observe a scale dependence, and secondly the horizon scale is a natural place where to look for this effect.

Eventually, another way to probe MG at early times provides a link to PNG. According to Bartolo et al. (2014), modifications of GR during inflation can create a non-zero quasi-local bispectrum with a non-negligible amplitude that can be probed with the methods described in this Chapter. Furthermore, the GR effects that become relevant on very large scales are actually beneficial for testing gravity on those scales, as they contain additional information about the evolution of perturbations. How to extract this additional information best is currently an active research topic, but the SKA is uniquely suited to take advantage of this new source of constraints.

PoS(AASKA14)025

3. Accessing Ultra-Large Cosmic Scales

In this Section, we review the two envisaged techniques that the SKA will exploit to tackle the difficult problem of accessing the largest cosmic scales, viz. IM (both from and after the EoR) and galaxy multi-tracing. In Sec. 3.4, we also discuss the most important systematics that we shall have to deal with for a fruitful exploitation of such methods. As a figure of merit, we adopt the achievable accuracy $\sigma(f_{\rm NL})$ on a forecast measurement of the PNG parameter. However, the techniques presented here will in general enable us to investigate all the peculiar phenomena which occur on extremely large cosmic scales. For example, dedicated analyses aiming at studying other ultra-large scale effects such as GR corrections are being performed at the time of the editing of this Chapter.

3.1 Intensity Mapping After the Epoch of Reionisation

IM is an alternative approach for probing the density field of the large-scale structure (Battye et al. 2004; Wyithe & Loeb 2008; Chang et al. 2008; Peterson et al. 2009). It involves mapping out the combined emission of the 21 cm, or HI, line from unresolved galaxies. In doing so, the large-scale structure is detected in three dimensions. If one foregoes identifying individual galaxies, one can greatly speed up the observation and detection of the large-scale structure. IM experiments are sensitive to structures at a redshift range that is observationally difficult to span for ground-based optical surveys (Seo et al. 2010). SKA IM surveys will cover a large fraction of the sky (around 25,000 sq. deg.) over an extremely broad redshift range, making it possible to access the largest cosmic scales in the late Universe. Here, we outline the basics of late-time IM, but refer to Santos et al. (2015) for a more detailed description.

In order to model the 21 cm power spectrum, it is crucial to quantify the bias function between the matter and HI power spectra, $b_{\rm HI}(k,z)$, which allows us to write

$$P^{\rm HI}(k,z) = b_{\rm HI}^2(k,z)\,P^{\delta}(k,z), \tag{3.1}$$

where $P^{\delta}(k,z)$ is the underlying matter power spectrum. Several techniques can be adopted in order to extract mock HI power spectra from realistic hydrodynamic or N-body simulations of the cosmic large-scale structure. In one of the simplest approaches (Bagla et al. 2010; Guha Sarkar et al. 2012; Bharadwaj et al. 2001), the HI is assigned to particles that belong to dark matter haloes as identified in the simulated cosmological volume and the HI content of each halo of mass M, $M_{\rm HI}(M)$, needs to be characterised. Other, more recent approaches are instead based on a particle-by-particle method where the HI is assigned to gas particles according to more refined physical prescriptions which take into account self-shielding effects and the conversion to molecular hydrogen (e.g. Davé et al. 2013; Popping et al. 2009; Rahmati et al. 2013; Duffy et al. 2012; Mao et al. 2012). A comprehensive comparison of several different methods in terms of 21 cm power spectrum is redshift space, performed in the post-reionisation era at $z \simeq 2-4$, has been recently presented by Villaescusa-Navarro et al. (2014), who used high resolution cosmological hydrodynamic simulations. They show that the $b_{\rm HI}(k,z)$ approaches a constant value to a good approximation at scales $k \lesssim 1h\,{\rm Mpc}^{-1}$, that galactic feedback in the form of winds is not affecting the signal on the largest scales and that the signal is dominated at least at $z < 6$ by HI residing in haloes. Although a full characterisation of the bias function in the (k,z)-plane is difficult to make, it is reassuring

PoS(AASKA14)025

that on extremely large scales the overall HI bias is flat, thus allowing us to perform cosmological studies of MG and PNG. It is also worth mentioning that the other key quantity is the total HI fraction, $\Omega_{\rm HI}$ (see Padmanabhan et al. 2014), which is in fact measured by observations of quasar absorption lines of the Lyman-α forest and damped Lyman-α systems at $z > 2$ (Tescari et al. 2009; Zafar et al. 2013). By means of this data we can then constrain the HI bias.

3.1.1 Primordial Non-Gaussianity Probed by Scale-Dependent Bias

Camera et al. (2013) explored this method for constraining the PNG of primordial fluctuations. IM experiments seem ideally suited for this goal (see Joudaki et al. 2011; Hazra & Sarkar 2012; D'Aloisio et al. 2013; Lidz et al. 2013; Mao et al. 2013, for proposals for doing so in the EoR). As argued before, the tightest constraints on $f_{\rm NL}$ will be obtained for large and deep surveys. Therefore, the volume of the survey determines the ability to probe below $f_{\rm NL}$ of $\mathscr{O}(1)$. For such a method to be successful, we need a deep survey with a large bandwidth accessing frequencies of 400 MHz and below. Assuming that line-of-sight scattering and self-absorption phenomena can be neglected, the HI line radiation can be related to the differential number counts of halo objects (e.g. Challinor & Lewis 2011), from which we can estimate $b_{\rm HI}$. Crucially, given our fundamental ignorance about the redshift evolution of the bias, we need to span a wide range of redshifts to capture $b_{\rm HI}(k,z) \neq 1$. This is because, as it is clear from Eq. (2.2), no PNG effect is to be detected if the tracer we are looking at is unbiased with respect to the underlying matter density distribution.

Fig. 2 shows $\sigma(f_{\rm NL}^{\rm loc})$ contours in the plane of the surveyed area and total observation time obtained with an HI IM experiment with bandwidth between 250 and 1000 MHz, corresponding to $0.5 \lesssim z \lesssim 4.5$, subdivided into 75 frequency bins of width $\Delta\nu = 10$ MHz (Camera et al. 2013). Abscissas roughly cover from a $15 \times 15\,{\rm deg}^2$ survey to half sky. The three top panels stand for the dish survey case, where the y-axis actually shows total observation time, $t_{\rm TOT}$, multiplied by the number of dishes, N_d. Three maximum angular modes are presented, $\ell_{\rm max} = 25$, 60, and 300, corresponding to dish diameters of 5, 15 and 80 m at $z \approx 3$. For higher angular resolution, interferometers may be a better option. In the bottom panels of Fig. 2, we show $\sigma(f_{\rm NL}^{\rm loc})$ for such a possibility using 1, 10 and 100 pointings. Choosing $D_a \simeq 80$ m as the diameter for the array, the resolution is set at $\ell_{\rm max} \simeq 300$. Here, the main design parameter is the field of view, FoV, which sets $\ell_{\rm min} = 2\pi/\sqrt{\rm FoV}$ and is fixed by the effective size of each element, $d_{\rm eff} \sim \lambda/\sqrt{\rm FoV}$. For a 'dense array', this is related to the number of elements, $N_e \sim D_a^2/d_{\rm eff}^2$. Given that the maximum angular scale is set by the FoV, by adding more pointings, we simply diminish the signal variance by N_p, though the noise increases too, because the observation time $t_{\rm obs} \to t_{\rm obs}/N_p$.

SKA1 would use 15 m dishes, viz. $\ell_{\rm max} \simeq 60$. Specifically, 254 dishes of SKA1-MID, 10,000 hours and a survey area around 30,000 sq. deg. will correspond to $\sigma(f_{\rm NL}^{\rm loc}) \sim 2$, as can be seen in Fig. 2. On the one hand, SKA1-MID will only go down to 350 MHz, whereas the minimum frequency assumed in Fig. 2 is 250 MHz. On the other hand, Camera et al. (2013) adopted a more conservative value for the system temperature, i.e. 30 K, whilst SKA1-MID will do better, with a system as cold as 20 K. Otherwise, SKA1-SUR will have a band from 900 to 350 MHz ($0.58 < z < 3.06$) and another from 1400 MHz to 700 MHz ($0 < z < 1.1$). Temperature will be slightly higher, at 50 K, for the former and 30 K for the latter. The effective number of dishes would be redshift dependent, most likely $64 \times \nu$ for the first band with $(z,\nu) = (0.6,30)$, $(1.0,20)$, $(2.0,9)$ and $(3.0,5)$, whereas for the second band it would be $94 \times \nu$ with $(z,\nu) = (0.0,23)$, $(0.5,10)$ and

PoS(AASKA14)025

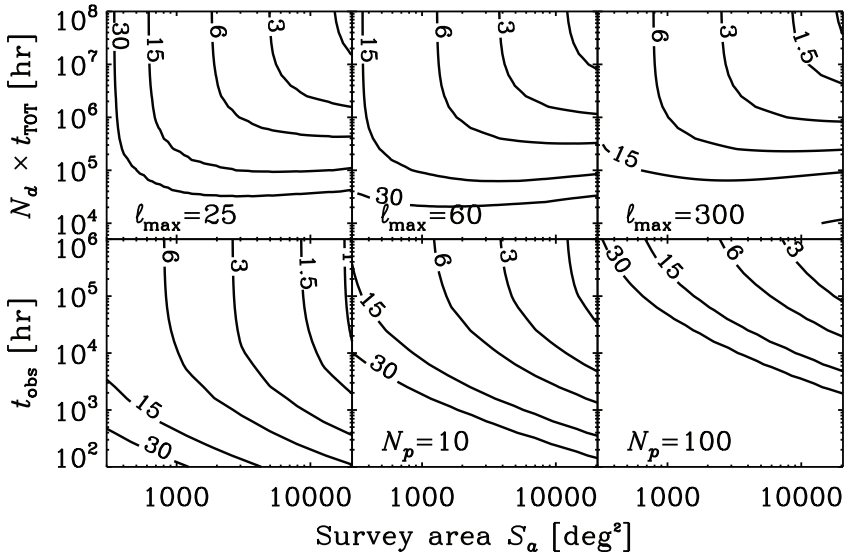

Figure 2: Forecast 1σ marginal error contours on $f_{\rm NL}^{\rm loc}$ as a function of surveyed sky and total observation time, for a dish survey with N_d dishes (upper panels) and an interferometer making N_p pointings (lower panels) (from Camera et al. 2013).

$(1.0, 6)$. For interferometric surveys, we would need to wait for SKA phase 2, with the proposed 'aperture array' system working below 1 GHz. It should be possible to achieve FoV $\sim 1000\,{\rm deg}^2$, thus reaching the $\sigma(f_{\rm NL}^{\rm loc}) \lesssim 1$ limit. See Santos et al. (2015) for a detailed description of SKA IM specifics.

3.1.2 Primordial Non-Gaussianity Probed by the Bispectrum

Compared to observable galaxies, HI is a weaklier biased tracer of the underlying matter distribution, except for the largest scales where the scale-dependent correction due to PNG dominates. Therefore, on moderately large scales, we may model the HI bispectrum as the tree-level matter bispectrum modified by linear and non-linear bias factors, $b_{\rm HI,1}$ and $b_{\rm HI,2}$. Here, we focus on the reduced HI bispectrum in redshift space, $Q_s^{\rm HI}$, which is much less sensitive to other cosmological parameters (Sefusatti & Komatsu 2007). We have

$$Q_s^{\rm HI}(k_1,k_2,k_3) = \frac{a_0^{\rm B}(\beta)}{\left[a_0^{\rm P}(\beta)\right]^2}\left[\frac{1}{b_{\rm HI,1}}Q^{\rm tree}(k_1,k_2,k_3) + \frac{b_{\rm HI,2}}{(b_{\rm HI,1})^2}\right], \tag{3.2}$$

where $Q^{\rm tree}$ is the reduced matter bispectrum predicted by the second-order perturbation theory, $a_0^{\rm P}(\beta) = 1 + 2\beta/3 + \beta^2/5$ and $a_0^{\rm B}(\beta) = 1 + 2\beta/3 + \beta^2/9$, with $\beta \equiv f(z)/b_{\rm HI,1}$ the linear Kaiser factor.

The relative importance of PNG in the HI bispectrum increases towards higher redshifts. This is very promising for measuring the primordial component from the HI bispectrum with SKA1-MID, which covers the whole redshift range from $z \sim 0$ to $z \sim 3$ ($350 - 1420$ MHz). In addition, the large survey volume enabled by IM would result in a much better constraint on $f_{\rm NL}$. The full SKA, with its lower system temperature, better u-v coverage, and broader frequency band (hence

PoS(AASKA14)025

broader redshift coverage and larger survey volume) will provide us with more stringent constraints on PNG than those achievable by other experiments such as the Tianlai project.

For SKA1-MID, IM may be conducted with the dishes used individually in auto-correlation mode, being calibrated using interferometry. In this case, $k_{\rm max}$ is limited by the Nyquist frequency, as well as the smallest scale above which we could trust the tree-level matter bispectrum. We adopt a non-linear scale cutoff, $k_{\rm nl}$, for the tree-level matter bispectrum, by requiring the variance in the density contrast field at $\pi/(2k_{\rm nl})$ to equal 0.5 in each redshift bin. With $N_d = 254$ 15 m diameter dishes, a survey area of 20,000 deg^2, and a total integration time of 5,000 hr, we find $\sigma(f_{\rm NL}^{\rm loc}) = 45.7$ and $\sigma(f_{\rm NL}^{\rm eq}) = 214.3$ when we marginalise over the HI bias factors $b_{\rm HI,1}$ and $b_{\rm HI,2}$ at each redshift bin, while $\sigma(f_{\rm NL}^{\rm loc}) = 15.3$ and $\sigma(f_{\rm NL}^{\rm eq}) = 61.8$ if we assume a constant bias factors. Otherwise, by using interferometry with the full SKA, $k_{\rm max}$ is set by the non-linear scale $k_{\rm nl}$, and we find much accurate marginalised errors $\sigma(f_{\rm NL}^{\rm loc}) = 6.6$ and $\sigma(f_{\rm NL}^{\rm eq}) = 55.4$, or $\sigma(f_{\rm NL}^{\rm loc}) = 2.2$ and $\sigma(f_{\rm NL}^{\rm eq}) = 10.9$.

3.2 Intensity Mapping from the Epoch of Reionisation

The PNG affects the clustering of the early star-forming galactic haloes responsible for creating a network of ionised patches in the surrounding intergalactic medium during the EoR. This leaves a PNG imprint on the HI tomographic mapping in the intergalactic medium using its redshifted 21 cm radiation. On large scales, where the typical size of ionised regions is much smaller than the scale of interest, we can neglect the non-linear effects of reionisation patchiness on the 21 cm power spectrum. Then the 21 cm temperature power spectrum during the EoR can be written as

$$P^{\Delta T}(\mathbf{k},z) = \widetilde{\delta T}_b^2 \bar{x}_{\rm HI}^2 \left[b_{\rm HI}(k,z) + \mu_{\mathbf{k}}^2\right]^2 P^{\delta}(k,z), \tag{3.3}$$

where $\widetilde{\delta T}_b(z) = 23.88\,(\Omega_{\rm b}h^2/0.02)\sqrt{0.15/(\Omega_m h^2)(1+z)/10}$ mK, $\bar{x}_{\rm HI}(z)$ is the global neutral hydrogen fraction, and $\mu_{\mathbf{k}} \equiv \mathbf{k}\cdot\hat{\mathbf{n}}/k$, i.e. the cosine of angle between the line-of-sight $\hat{\mathbf{n}}$ and wave vector $\mathbf{k}$ of a given Fourier mode.

The ionised density bias $b_{\rm HII}$ is the fundamental quantity derived from reionisation models, related to the neutral density bias $b_{\rm HI}$ by $b_{\rm HI} = (1 - \bar{x}_{\rm HII}\, b_{\rm HII})/\bar{x}_{\rm HI}$. The reionisation in the presence of PNG can be modelled using two independent methods as follows (D'Aloisio et al. 2013):

1. *Excursion-set model of reionisation (ESMR)* – We can use a parameter $\zeta_{\rm ESMR}$ to characterize the efficiency of the local collapsed fraction of mass in luminous sources above some mass threshold in releasing ionising photons into the intergalactic medium (Furlanetto et al. 2004). The full functions $\bar{x}_{\rm HI}(z)$ and $b_{\rm HII}(k,z)$ are set by two parameters, $f_{\rm NL}^{\rm loc}$ and $\zeta_{\rm ESMR}$.

2. *Phenomenological model* – Similar to the scale-dependent halo bias, D'Aloisio et al. (2013) derived a scale-dependent non-Gaussian correction to the ionised density bias, $\Delta b_{\rm HII}(k,z)$, analogous to Eq. (2.2). It depends upon the scale-independent Gaussian ionised density bias $b_{\rm HII}(z)$. Therefore, we can marginalise $f_{\rm NL}$ over two phenomenological parameters, $\bar{x}_{\rm HI}(z_i)$ and $b_{\rm HII}(z_i)$, in each redshift bin z_i.

Both methods can be used to constrain PNG with the 21 cm power spectrum from the EoR. Mao et al. (2013) demonstrated that for a single frequency bin measurement, their constraints on $f_{\rm NL}^{\rm loc}$

PoS(AASKA14)025

are just as good. However, a model such as the ESMR can be used to combine multiple frequency bin measurements because it fixes the reionisation history (and therefore $P^{\Delta T}$) for a given value of $f_{\rm NL}$ and $\zeta_{\rm ESMR}$. Thus, it appears more promising.

For a numerical evaluation, we assume that residual foregrounds can be neglected for $k_\parallel \geq k_{\parallel,\rm min} = 2\pi/(yB)$, e.g. $k_{\parallel,\rm min} = 0.055\,{\rm Mpc}^{-1}$ at $z = 10.1$. The minimum $k_\perp$ is set by the minimum baseline, $k_{\perp,\rm min} = 2\pi L_{\rm min}/(\lambda D_a)$. We focus on the 21 cm signal on large scales $k_{\rm max} = 0.15\,{\rm Mpc}^{-1}$, so that linearity conditions are met. We assume we can combine information from 7 frequency bins, each of 6 MHz bandwidth, covering the evolution of ionised fraction $\bar{x}_{\rm HII} \approx 0.06 - 0.70$, corresponding to $z \approx 9.5 - 13.4$ in the ESMR method. Using the Fisher matrix formalism, we forecast that the SKA1-LOW can constrain the local-type PNG, $\sigma(f_{\rm NL}^{\rm loc}) = 7.4$, using the ESMR method. Furthermore, if the sensitivity can be improved by 4 times better, then the full SKA can put as tight a constraint as $\sigma(f_{\rm NL}^{\rm loc}) = 4.7$ by using the 21 cm power spectrum from the EoR alone.

3.3 Multi-Tracer Technique

Measuring clustering statistics on large scales has the major advantage of probing non-Gaussian effects on halo/galaxy bias where they are stronger. Unfortunately though, those same scales are limited by cosmic variance, i.e. the lack of enough independent measurements for the scales we are trying to probe, given the limited size of the volume that is observed. Seljak (2009) proposed a way to get around cosmic variance limitation by using different biased tracers of the underlying matter distribution. The main idea is that with at least two differently biased tracers, one can measure the ratio of these two biases to a level that is only limited by shot noise, hence beating cosmic variance. This is particularly sensitive when the bias of one tracer is much larger than that of the other. In order to understand this, let us assume that we measure two density maps at a given redshift, one for a biased tracer and another for the dark matter itself. Due to cosmic variance, there will be several cosmologies that are consistent with the dark matter map. However, the ratio of the two maps should give a direct measurement of the bias, with an uncertainty just given by the shot noise of the tracer (see also e.g. Abramo & Leonard 2013).

Ferramacho et al. (2014) developed this in the context of radio continuum surveys for SKA and its pathfinders. They explored the strong correlation that exists between radio galaxy types and their bias, which can be at first order linked to a single halo mass for each type. This seems to hold true for most types of radio galaxies, such as radio-quiet and radio-loud active galactic nuclei, including FRI and FRII galaxies, and also star-forming galaxies, including starbursts. Using simulated catalogues, and taking into account all the statistical information from continuum galaxy surveys—namely the combined auto- and cross-correlation angular power spectra of multi-tracer galaxies—Ferramacho et al. (2014) showed that it is possible to strongly reduce the impact of cosmic variance at large scales. By employing the Fisher matrix formalism, they forecast that this method will constrain the local-type PNG parameter up to an amazing accuracy of $\sigma(f_{\rm NL}^{\rm loc}) \sim 0.7$, in the most optimal case where all the galaxy populations may be distinguished over the whole redshift range, and $\sigma(f_{\rm NL}^{\rm loc}) \sim 2.9$, in a much more conservative framework accounting for realistic limitations to the observational identification of each galaxy population.[2] Note that the improve-

[2]For more insight about the impact of redshift information for radio continuum surveys in the context of the SKA, see also Camera et al. (2012) and Raccanelli et al. (2014b), where in the latter work they used the ISW effect and redshift

PoS(AASKA14)025

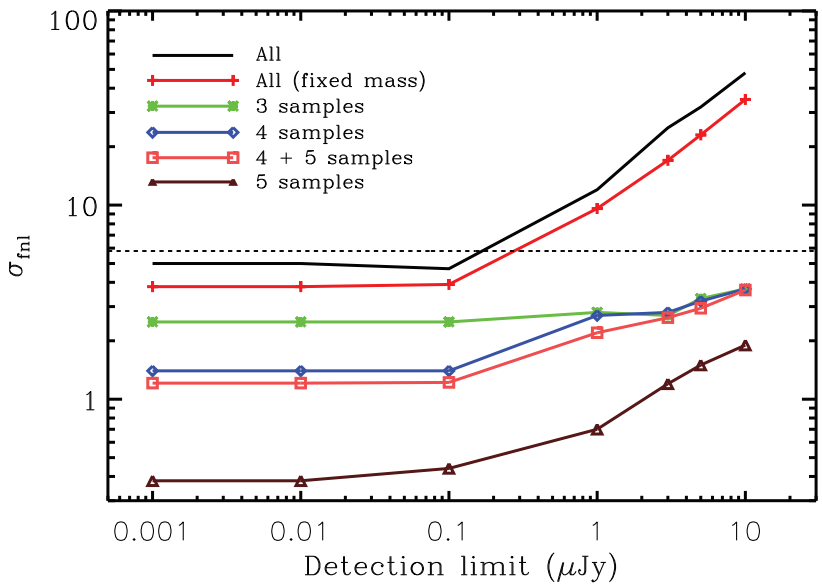

Figure 3: Constraints on $f_{\rm NL}^{\rm loc}$ obtained with the multi-tracer method as a function of the flux cut used to detect galaxies (from Ferramacho et al. 2014). The horizontal line represents the best constrain obtained by the Planck collaboration.

ment obtained through the multi-tracer analysis is indeed significant, as the whole galaxy catalogue without any galaxy type differentiation only allows for constraints on $f_{\rm NL}$ with an error of $\sigma(f_{\rm NL}^{\rm loc}) = 32$ in the realistic scenario. Fig. 3 resumes the forecast constraints as a function of flux cut limit (see Ferramacho et al. 2014, for details).

3.4 Systematics Occurring on the Largest Scales

The SKA should be able to provide a statistical detection of large scale effects due to its high sensitivity and large volumes probed, it will thus be crucial to control the systematics which will occur on these same scales. For the measurements we have been discussing, the following contaminants will need to be considered:

- *Masks* – Several systematic effects related to partial sky coverage can result in biases and spurious large-scale signals. This is an issue for both galaxy surveys as well as IM. This effect can in principle be dealt with by means of inversion methods, as has been done by the CMB community for instance to address the masking of our own galaxy.

- *Foreground subtraction* – For IM experiments, most foreground removal algorithms subtract out modes that are smoothly-varying in frequency, since this is how most galactic and extragalactic foregrounds behave. In the process, some fraction of large scale cosmological modes along the line of sight will also be subtracted. The effect should be most important for scales around the total bandwidth, but there will be a contamination on smaller scales too (Alonso et al. 2014).

measurements from other experiments to constrain $\sigma(f_{\rm NL}^{\rm loc}) \sim 1$. Comparable, encouraging results for SKA HI galaxy redshift surveys have recently been obtained by Camera et al. (2014).

PoS(AASKA14)025

- *Correlated noise* – Auto-correlation observations are needed to access the largest angular scales with IM using the SKA. There is a noise term that has correlations in time, e.g. a non-white noise behaviour, with a drift that depends on the receiver design. This term cancels out in interferometric observations but is present in the auto-correlation signal from each dish. Therefore, strategies will have to be designed to remove this contribution. The situation can be particularly critical for large scale modes since this contamination shows up on time scales larger than the typical "1/f" knee of the receiver, which can translate into striping artefacts on large angular scales. The usual solution is to design fast survey strategies capable of probing the required angles over a period that is shorter than the typical time-scale of the receiver. This will impose strong constraints on the receiver design that need to be accessed. Nevertheless other techniques should be explored. For instance the fact that the noise can also be a smooth function of frequency may allow for a solution in dealing with this effect.

- *Mosaicking* – Large scale surveys will require several pointings (observations in different directions) in order to cover the required sky area—the so called 'mosaicking'. This is true for any of the surveys, either continuum, HI galaxy or HI intensity mapping (the situation with SKA1-LOW is different due to its large field of view). Careful design of the scanning strategy needs to be made so that the noise is sufficiently uniform across the sky, in particular when overlapping the pointings. For example, fluctuations of this noise can generate different flux sensitivities across the sky and affect the number of detected galaxies in a threshold survey. This could in turn generate spurious fluctuations on angular scales (the situation is less of a concern if we consider a high flux cut in the galaxy survey, such as 10σ). The same issue can arise if there are non-negligible fluctuations on the calibrated signal. These problems can in principle be dealt with through the mosaicking approach as well as an accurate calibration process. Moreover, these fluctuations should be uncorrelated on large angular scales which should allow them to be distinguished from the signal.

4. Conclusions

The access to observations on ultra-large scales that are possible with the SKA enables a range of unique science goals at the forefront of cosmology. They include constraints on DE and MG, amongst the key science goals identified by the Committee for a Decadal Survey of Astronomy and Astrophysics (National Research Council, 2010). The constraints possible with the SKA will rival those the Euclid satellite will deliver (Laureijs et al. 2011; Amendola et al. 2013), but will be complementary especially where the systematic effects are concerned. The SKA will also be able to use relativistic effects to test GR on the largest scales, and it will surpass the constraints on PNG obtained by the Planck satellite. The SKA will probe the inflationary dynamics that took place in the Universe just fractions of a second after the Big Bang, and it will also test whether gravity was modified during that epoch.

This Chapter, together with others in this review, clearly shows that the SKA will be able to probe the foundations of our cosmological models, the evolution of the Universe and the nature of its constituents. Moreover, as we have described, this will be accessed by a range of SKA surveys which will probe the underlying signal in different ways. The SKA will contribute in unique

PoS(AASKA14)025

ways to broaden our understanding of the cosmos, and the SKA data will become a key tool for cosmology in the 21st century.

References

Abdalla, F. et al. 2014, Advancing Astrophysics with the Square Kilometre Array
Abramo, L. R. & Leonard, K. E. 2013, Mon. Not. Roy. Astron. Soc., 432, 318
Ade, P. et al. 2014, Astron. Astrophys., 571, A24
Afshordi, N. & Tolley, A. J. 2008, Phys. Rev., D78, 123507
Alishahiha, M., Silverstein, E., & Tong, D. 2004, Phys. Rev., D70, 123505
Alonso, D., Ferreira, P. G., & Santos, M. G. 2014, Mon. Not. Roy. Astron. Soc., 444, 3183
Amendola, L. et al. 2013, Living Rev. Rel., 16, 6
Arkani-Hamed, N., Creminelli, P., Mukohyama, S., & Zaldarriaga, M. 2004, JCAP, 0404, 001
Assadullahi, H., Valiviita, J., & Wands, D. 2007, Phys. Rev., D76, 103003
Bagla, J. S., Khandai, N., & Datta, K. K. 2010, Mon. Not. Roy. Astron. Soc., 407, 567
Baker, T., Ferreira, P. G., & Skordis, C. 2013, Phys. Rev., D87, 024015
Bartolo, N., Cannone, D., Jimenez, R., Matarrese, S., & Verde, L. 2014, Phys. Rev. Lett., 113, 161303
Bartolo, N., Komatsu, E., Matarrese, S., & Riotto, A. 2004, Phys. Rept., 402, 103
Bartolo, N., Matarrese, S., & Riotto, A. 2002, Phys. Rev., D65, 103505
Battye, R. A., Davies, R. D., & Weller, J. 2004, Mon. Not. Roy. Astron. Soc., 355, 1339
Battye, R. A. & Pearson, J. A. 2012, JCAP, 1207, 019
Bellini, E. & Sawicki, I. 2014, JCAP, 1407, 050
Bernardeau, F. & Uzan, J.-P. 2002, Phys. Rev., D66, 103506
Bertacca, D., Maartens, R., Raccanelli, A., & Clarkson, C. 2012, JCAP, 1210, 025
Bharadwaj, S., Nath, B. B., & Sethi, S. K. 2001, Journal of Astrophysics and Astronomy, 22, 21
Bonvin, C. & Durrer, R. 2011, Phys. Rev., D84, 063505
Bonvin, C., Hui, L., & Gaztanaga, E. 2014, Phys. Rev., D89, 083535
Bruni, M., Crittenden, R., Koyama, K., Maartens, R., Pitrou, C., et al. 2012, Phys. Rev., D85, 041301
Camera, S. & Nishizawa, A. 2013, Phys. Rev. Lett., 110, 151103
Camera, S., Santos, M. G., Bacon, D. J., Jarvis, M. J., McAlpine, K., et al. 2012, Mon. Not. Roy. Astron. Soc., 427, 2079
Camera, S., Santos, M. G., Ferreira, P. G., & Ferramacho, L. 2013, Phys. Rev. Lett., 111, 171302
Camera, S., Santos, M. G., & Maartens, R. 2014, eprint arXiv:1409.8286
Challinor, A. & Lewis, A. 2011, Phys. Rev., D84, 043516
Chang, T.-C., Pen, U.-L., Peterson, J. B., & McDonald, P. 2008, Phys. Rev. Lett., 100, 091303
Chen, X., Huang, M.-x., Kachru, S., & Shiu, G. 2007, JCAP, 0701, 002
Committee for a Decadal Survey of Astronomy and Astrophysics. National Research Council, 2010, New Worlds, New Horizons in Astronomy and Astrophysics (The National Academies Press)
Creminelli, P., Senatore, L., Zaldarriaga, M., & Tegmark, M. 2007, JCAP, 0703, 005
Dalal, N., Dore, O., Huterer, D., & Shirokov, A. 2008, Phys. Rev., D77, 123514

PoS(AASKA14)025

D'Aloisio, A., Zhang, J., Shapiro, P. R., & Mao, Y. 2013, Mon. Not. Roy. Astron. Soc., 433, 2900
Davé, R., Katz, N., Oppenheimer, B. D., Kollmeier, J. A., & Weinberg, D. H. 2013, Mon. Not. Roy. Astron. Soc., 434, 2645
Desjacques, V., Jeong, D., & Schmidt, F. 2011, Phys. Rev., D84, 061301
Di Dio, E., Montanari, F., Lesgourgues, J., & Durrer, R. 2013, JCAP, 1311, 044
Duffy, A. R., Kay, S. T., Battye, R. A., Booth, C. M., Dalla Vecchia, C., & Schaye, J. 2012, Mon. Not. Roy. Astron. Soc., 420, 2799
Falk, T., Rangarajan, R., & Srednicki, M. 1993, Astrophys. J., 403, L1
Ferramacho, L. D., Santos, M. G., Jarvis, M. J., & Camera, S. 2014, Mon. Not. Roy. Astron. Soc., 442, 2511
Furlanetto, S., Zaldarriaga, M., & Hernquist, L. 2004, Astrophys. J., 613, 16
Guha Sarkar, T., Mitra, S., Majumdar, S., & Choudhury, T. R. 2012, Mon. Not. Roy. Astron. Soc., 421, 3570
Hall, A., Bonvin, C., & Challinor, A. 2013, Phys. Rev., D87, 064026
Hazra, D. K. & Sarkar, T. G. 2012, Phys. Rev. Lett., 109, 121301
Holman, R. & Tolley, A. J. 2008, JCAP, 0805, 001
Hu, W. & Sawicki, I. 2007, Phys. Rev. D, 76, 104043
Huang, Q.-G. 2009, JCAP, 0906, 035
Jarvis, M. J. et al. 2014, Advancing Astrophysics with the Square Kilometre Array
Jeong, D., Schmidt, F., & Hirata, C. M. 2012, Phys. Rev., D85, 023504
Joudaki, S., Dore, O., Ferramacho, L., Kaplinghat, M., & Santos, M. G. 2011, Phys. Rev. Lett., 107, 131304
Komatsu, E. & Spergel, D. N. 2001, Phys. Rev., D63, 063002
Kunz, M. 2012, Comptes Rendus Physique, 13, 539
Laureijs, R., Amiaux, J., Arduini, S., Augueres, J.-L., et al. 2011, ESA-SRE, 12
Lidz, A., Baxter, E. J., Adshead, P., & Dodelson, S. 2013, Phys. Rev., D88, 023534
Linder, E. V. & Cahn, R. N. 2007, Astropart.Phys., 28, 481
Mao, Y., D'Aloisio, A., Zhang, J., & Shapiro, P. R. 2013, Phys. Rev., D88, 081303
Mao, Y., Shapiro, P. R., Mellema, G., Iliev, I. T., Koda, J., & Ahn, K. 2012, Mon. Not. Roy. Astron. Soc., 422, 926
Matarrese, S. & Verde, L. 2008, Astrophys. J., 677, L77
Motta, M., Sawicki, I., Saltas, I. D., Amendola, L., & Kunz, M. 2013, Phys. Rev., D88, 124035
Padmanabhan, H., Choudhury, T. R., & Refregier, A. 2014, eprint arXiv:1407.6366
Peterson, J. B., Aleksan, R., Ansari, R., Bandura, K., Bond, D., et al. 2009, astro2010: The Astronomy and Astrophysics Decadal Survey
Piazza, F. & Vernizzi, F. 2013, Class.Quant.Grav., 30, 214007
Popping, A., Dave, R., Braun, R., & Oppenheimer, B. D. 2009, Astron. Astrophys., 504, 15
Raccanelli, A., Bertacca, D., Dore, O., & Maartens, R. 2014a, JCAP, 1408, 022
Raccanelli, A., Bertacca, D., Maartens, R., Clarkson, C., & Dore, O. 2013, eprint arXiv:1311.6813
Raccanelli, A., Dore, O., Bacon, D. J., Maartens, R., Santos, M. G., et al. 2014b, eprint arXiv:1406.0010
Rahmati, A., Pawlik, A. H., Raicevic, M., & Schaye, J. 2013, Mon. Not. Roy. Astron. Soc., 430, 2427

PoS(AASKA14)025

Saltas, I. D. & Kunz, M. 2011, Phys. Rev., D83, 064042
Saltas, I. D., Sawicki, I., Amendola, L., & Kunz, M. 2014, Phys. Rev. Lett., 113, 191101
Santos, M. G. et al. 2015, Advancing Astrophysics with the Square Kilometre Array
Sasaki, M., Valiviita, J., & Wands, D. 2006, Phys. Rev., D74, 103003
Schmidt, F. & Kamionkowski, M. 2010, Phys. Rev., D82, 103002
Seery, D. & Lidsey, J. E. 2005, JCAP, 0506, 003
Sefusatti, E. & Komatsu, E. 2007, Phys. Rev., 76, 083004
Seljak, U. 2009, Phys. Rev. Lett., 102, 021302
Senatore, L., Smith, K. M., & Zaldarriaga, M. 2010, JCAP, 1001, 028
Seo, H.-J., Dodelson, S., Marriner, J., Mcginnis, D., Stebbins, A., et al. 2010, Astrophys.J., 721, 164
Tescari, E., Viel, M., Tornatore, L., & Borgani, S. 2009, Mon. Not. Roy. Astron. Soc., 397, 411
Verde, L. & Matarrese, S. 2009, Astrophys. J., 706, L91
Verde, L., Wang, L.-M., Heavens, A., & Kamionkowski, M. 2000, Mon. Not. Roy. Astron. Soc., 313, L141
Villaescusa-Navarro, F., Viel, M., Datta, K. K., & Choudhury, T. R. 2014, eprint arXiv:1405.6713
Wyithe, J. S. B. & Loeb, A. 2008, Mon. Not. Roy. Astron. Soc., 383, 606
Yoo, J. 2010, Phys. Rev., D82, 083508
Zafar, T., Peroux, C., Popping, A., Milliard, B., Deharveng, J.-M., et al. 2013, Astron. Astrophys.,, A141

PoS(AASKA14)025

PROCEEDINGS OF SCIENCE

Real time cosmology - A direct measure of the expansion rate of the Universe with the SKA

Hans-Rainer Klöckner[*1], **Danail Obreschkow**[2], **Carlos Martins**[3], **Alvise Raccanelli**[4], **David Champion**[1], **Alan Roy**[1], **Andrei Lobanov**[1], **Jan Wagner**[1,5], **Reinhard Keller**[1]

[1]*Max-Planck-Institut für Radioastronomie (MPIfR), Germany;* [2]*The University of Western Australia, ICRAR, Australia;* [3]*Centro de Astrofísica da Universidade do Porto, Portugal;* [4]*Department of Physics & Astronomy, Johns Hopkins University, Caltech, & JPL, USA;* [5]*KASI KVN, Korea*

E-mail: hrk@mpifr-bonn.mpg.de

In recent years cosmology has undergone a revolution, with precise measurements of the microwave background radiation, large galaxy redshift surveys, and the discovery of the recent accelerated expansion of the Universe using observations of distant supernovae. All these groundbreaking observations have boosted our understanding of the Cosmos and its evolution. Because of this detailed understanding, more detailed tests of cosmological models require unprecedented precision that is only available with the next generation of astronomical observatories. Radio observations in particular will be able to access more independent modes than optical, infrared or X-ray facility and will show very different systematics compared to these other wavebands.

The SKA enables us to do an ultimate test in cosmology by measuring the expansion rate of the Universe in real time. This can be done by a rather simple experiment of observing the neutral hydrogen (HI) signal of galaxies at two different epochs. The signal will encounter a change in frequency imprinted as the Universe expands over time and thus monitoring the drift in frequencies will provide a real time measure of the cosmic acceleration. Over a period of 12 years one would expected a frequency shift of the order of 0.1 Hz assuming a standard ΛCDM cosmology. However, monitoring such changes would require some modifications to the current baseline design of the SKA. In particular, the design needs to be adapted to achieve higher spectral resolution, at least within sub-bands (strong requirement), and to allow for a well monitored distribution of the local oscillator signal, preferably at milli-Hz accuracy over a period of 12 years (weaker requirement, which could be circumvented by pulsar observations). Based on the sensitivity estimates of the SKA and the number counts of the expected HI galaxies, it is shown that the number counts are sufficiently high to compensate for the observational uncertainties of the measurements and hence allow a statistical detection of the frequency shift. In addition, depending on the observational setup, it is shown that the evolution of the frequency shift in redshift space can be estimated to a precision of a percent.

Although technically challenging, the direct measurement of the frequency shift and hence the cosmic acceleration can provide a model independent confirmation of dark energy. At highest precision it can distinguish between some competing cosmological models and combined with probes at other wavelength can break degeneracies and improving the figure of merit of cosmological parameters.

Advancing Astrophysics with the Square Kilometre Array
June 8-13, 2014
Giardini Naxos, Italy

PoS(AASKA14)027

1. Introduction

The Big Bang concept of our Universe is well established as "the standard model of cosmology", but currently the observational data cannot tighten constraints on the physics at work at the very earliest phase in its evolution. In this picture, shortly after the big bang, 13.8 billion years ago, the Universe was dominated by an energy field with negative pressure that drove a period of accelerated expansion, "the inflation" phase. Since then the Universe has expanded, cooled down, and changed from a radiation- to a matter-dominated composition. If its content is dominated by a composition of baryonic and cold dark matter one would expect a decelerated expansion of the Universe. However by using type Ia supernovae (SNIa), as standard candles, a surprising discovery has been made, that the expansion of the Universe is undergoing a second epoch of acceleration (Riess et al. 1998, Perlmutter et al. 1999, this research was awarded a the Nobel prize in physics 2011). The reason for this recent accelerated expansion is still a mystery and points to an additional phase of negative pressure contribution of the mass-energy field and a possible modification of Einstein's general relativity. Thus measuring the recent acceleration will provide an additional route to probe the equation of state and the interplay of dark energy.

Techniques to measure expansion rates in the Universe were already explored in 1962 by Sandage (Sandage 1962), but the technological limitations at these time kept these measurements out of reach. It took more than 30 years for this idea to be revisited and Loeb proposed in 1998 to use Lyman-alpha forest absorption lines toward quasars for this measurement. The author concluded that the signal might be marginally detectable with a 10-m class telescope (Loeb 1998). Now with the E-ELT, a 40-m class telescope, to be built in the near future it seems possible to perform the "Loeb' test" with a specially designed spectrograph (for more information on the CODEX[1]-like experiments see e.g. Pasquini et al. 2005; Liske et al. 2008a, Liske et al. 2008b, Maiolino et al. 2013). Unfortunately this test is greatly affected by the cut-off restriction of ground based observations introduced by the atmosphere. Due to this cut-off, Lyman-alpha photons can only trace redshifts ($z \geq 1.65$) at which most of the cosmological models describe the expansion rate of the Universe by deceleration only. SKA observations in contrast, of the neutral hydrogen (HI) signals of Milky Way-type galaxies up to redshifts of unity, are not greatly affected by the atmosphere or ionosphere. This redshift regime is the one at which most of the "nearby" acceleration takes place and therefore is the most promising to investigate the influence of dark energy in the Universe.

The real time measurements of the cosmic acceleration its a very appealing experiment that promises a model independent confirmation of dark energy and a test to distinguish between cosmological models. Despite the technical challenges this experiment may face, is there a feasible SKA experiment in the radio regime that could measure the frequency shift caused by the evolving Universe?

2. The basic experiment

The basic experiment is to detect the changes over time of properties of individual galaxies caused by the expansion of the Universe. Generally various observables could be used to constrain the parameters needed to describe the expansion history of the Universe which are the source brightness,

*Speaker.

[1] "Cosmic Dynamics Experiment"

PoS(AASKA14)027

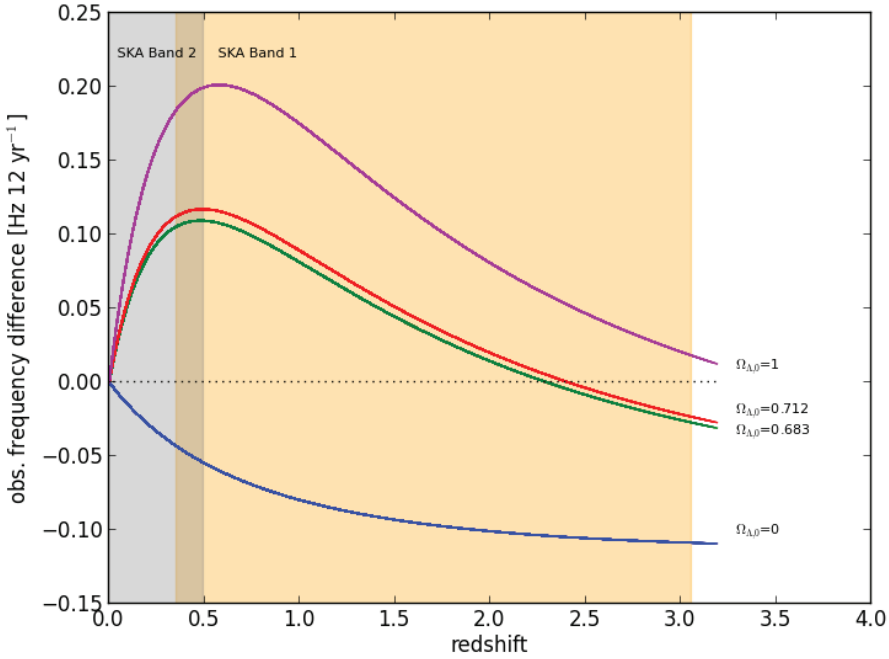

Figure 1: The expected redshift drift introduced by the cosmic acceleration against the redshift regime covered by the SKA. The redshift drift in 12 years is shown as a change in frequency of the neutral hydrogen signal for various ΛCDM cosmologies ($\Omega_m = 0.27$; $\Omega_\Lambda = 0.0$, WMAP, Planck, 1). The characteristic frequency shift shows a maximun shift of about 0.1 Hz, this translates into $dz/dt \sim 10^{-10}$ or ∼3 cm in redshift- and velocity-space, respectively. The coloured background indicates the frequency regimes of band 1 and 2 of the SKA basic design that are used to measure neutral hydrogen signals from galaxies (350 – 1050 MHz, 950 MHz – HI rest frame frequency).

the apparent angular size, the cosmic parallax, or the redshift (see e.g. Gudmundsson & Björnsson 2002, Quercellini et al. 2012). However to measure the changes of the first three observables seem to be out of reach to the current technical capabilities of the SKA. But it seems feasible for the SKA to trace the change of redshifts of individual galaxies and, compared to the CODEX-like experiment, a different approach is envisaged to measure the cosmic acceleration. The basic experiment would make use of the fast survey capabilities and the sensitivity to observe a billion of HI galaxies up to redshift 1. Based on two HI surveys the task is to combine the individual HI-line signals of a galaxy and statistically merge up to a billion of these measurements. The high number counts of galaxies will compensate the uncertainties of the measurements and therefore permit a statistical detection of the redshift drift (the initial setup of the experiment has been described in Klöckner 2012).

The redshift measurements are in general independent of a cosmological model and rely only on the knowledge of the rest frame frequency and the assumption that the fundamental constants do not change over the evolution of the Universe (Kanekar 2012). In a theoretical framework the change of redshifts can be described by $\dot{z} = \mathrm{H(z)} - (1+z)\mathrm{H_0}$ and the fraction $\mathrm{H(z)/H_0}$ is used to relate

PoS(AASKA14)027

the acceleration to different kinds of cosmological models. Therefore measuring the redshift drift at various redshifts provides a unique test of different cosmologies (Balbi & Quercellini 2007). In the following a ΛCDM cosmology is assumed and the Hubble parameter is described as

$$\mathrm{H(z)} = H_0[\Omega_\mathrm{m} \times (1+z)^3 + \Omega_\lambda + \Omega_\mathrm{k}(1+z)^2]^{\frac{1}{2}}, \tag{2.1}$$

with $\Omega_\mathrm{k} = 1 - (\Omega_\mathrm{m} + \Omega_\lambda)$. Note that the first equation has been written in such a way that the acceleration is positive ($\dot{\mathrm{v}} > 0$) and the deceleration is negative ($\dot{\mathrm{v}} < 0$) defined in the velocity frame. Figure 1 displays the expected frequency shift at different redshifts for various values of the cosmological parameter, Ω_λ, and a fixed Ω_m of 0.27. Depending on Ω_λ an acceleration of the Universe is expected up to redshifts of 3 (positive frequency shift), after this the expansion of the Cosmos will slow down (decelerate, negative frequency shift). Furthermore, depending on Ω_λ the frequency shift shows a distinct relationship with redshift and a pronounced signature with a maximum at 0.4 and 0.6 in redshift. In the case of the cosmological parameter measured by the WMAP and Planck mission (Hinshaw et al. 2013, Planck Collaboration 2013) a maximum frequency shift of 0.1 Hz can be expected after an observing period of 12 years.

The direct measurement of the frequency shift and the capability to distinguish between competing cosmological models requires a precisions of up to a few percent (e.g. 1% = 0.001 Hz). In order to reach this kind of accuracy the main task of this experiment is to utilise the HI line signals of a galaxy at 2 epochs and statistically combine up to a billion of these measurements. In this light the feasibility of this experiment depends on the projected sensitivity estimates and the number counts of HI galaxies up to cosmological redshifts. The expected number counts and the properties of individual HI galaxies are based on the SAX-SKA sky simulation (Obreschkow et al. 2009) and the image sensitivity can be determined via the following equations (see e.g. Klöckner et al. 2009):

$$\Delta\mathrm{I} = \frac{\mathrm{SEFD}}{\eta_s \sqrt{\mathrm{t}\Delta\nu}}, \tag{2.2}$$

with $\eta_s = 0.9$ is the system efficiency, t integration time [s], and $\Delta\nu$ is the channel width or bandwidth [Hz]. The system equivalent flux density (SEFD) is determined via

$$\mathrm{SEFD} = \frac{2\mathrm{kT_{sys}}}{\mathrm{A_{eff}}}, \tag{2.3}$$

where $\mathrm{T_{sys}}$ is the system temperature [K], k is the Boltzmann constant, $\mathrm{A_{eff}}$ is the effective collecting area [m^2].

In order to investigate if the SKA is capable of detecting the global signal of the redshift drift shown in Figure 1 a generic observational setup is assumed. The experiment would based on two-"all-sky" HI surveys with the following system parameters: SKA ($\mathrm{A_{eff}}$ / $\mathrm{T_{sys}}$ = 13.000 $\mathrm{m^2\ K^{-1}}$), 1 hour integration per pointing, 20 sq. degrees field of view, survey coverage of 30.000 sq. degrees. This setup will result in a sensitivity of about 45 μJy for the system channel width of 3.9 kHz and 28 mJy for 0.01 Hz wide channels (10% accuracy). Based on the sensitivity limit of 45 μJy the expected number count of HI galaxies in the redshift range z = 0.2-1 is of the order of 10^7 sources (#N). To derive the frequency shift from the observed HI line spectra of two epochs two

PoS(AASKA14)027

approaches can be applied. Either combining the cross-correlation spectrum of each source or fitting signal components to line spectra and determine their statistical means.

In the first case one would use the high-resolution spectra of the two epochs and stack the power spectrum of the cross-correlation spectra of all galaxies. Assuming that the noise properties of these spectra are independent, the noise of the resulting averaged power-spectrum will drop as $\sim 1/\sqrt{\#\mathrm{N}}$ to 2.8 μJy and therefore allowing the detection of the global signal of the redshift drift at a significance of $\sim 15\sigma$.

In the second case one would use the low-resolution spectra and determine the line properties by fitting a analytic function to the line profile (e.g. using a busy function Westmeier et al. 2013). In this way one assumes that all the observational parameters (the space velocity vector of the observatory) can be modeled with such precision that the residual data do not show any systematic effects above millimeter accuracy. The difference of the modelled centre frequencies determines the cosmic signal and its uncertainty will drop with $\sim 1/\sqrt{\#\mathrm{N}}$. Reversing the arguments, based on the assumption that the uncertainties need to match some fraction of cms^{-1}, this experiment is only possible if the redshifts or the velocities of 10^7 galaxies can be estimated at the observatory to a precision of 10 ms^{-1}.
Based on the generic observational setup both methods indicates that in general the SKA would be capable to measure the global signal of the redshift drift.

3. A feasible experiment with the SKA

Tracing the signature of the cosmic acceleration at various redshifts would be the ultimate experiment to test cosmological models. In the case of a ΛCDM cosmology the redshift drift shown in Figure 1 indicates a characteristic feature up to redshift of unity. The anticipated system performance of the SKA is an ideal match to one of the key requirements of this experiment. In particular the sensitivity figures of the SKA will be optimised to trace the HI line (in emission) of Milky Way-like galaxies up to a redshift of unity and therefore will produce the most complete HI/redshift surveys in this redshift range.

The main aim of this experiment is to measure a shift in frequency of about 0.1 Hz over a period of about 12 years (2.9 cms^{-1} in velocity space and 10^{-10} in redshift space). However these measurements may suffer from various systematic effects influencing the accuracy of the experiment. The potential contributions to the uncertainties of the redshift drift can be grouped as follows: (a) The probe of the redshift drift at cosmological distances show intrinsic variations. (b) The model of the Earth position in space and the observatory is insufficient for the accuracy needed. (c) The technical hardware of the observatory.

Case (a): Probing redshifts via the neutral hydrogen signal seems to be one of the most promising probes in the radio regime, even if our current knowledge of HI selected galaxies is limited up to redshifts of 0.2. Generally these galaxies do not show any evidence for clustering or a preference to populate over-dense regions in the Universe and hence their redshift estimates are less affected than optically selected galaxies (Papastergis et al. 2013; Klöckner & Romano-Diaz in prep.). The contribution of the peculiar motion to the apparent redshift has been estimated using the SAX-SKA- and the millenium-simulations (Obreschkow et al. 2009, De Lucia & Blaizot 2007). For the individual galaxies, with redshifts larger than z=0.2, the peculiar motion in redshift space has been

PoS(AASKA14)027

estimated to $d(z+z_{pec})/dt \sim 10^{-14}$. This effect is a factor 10 smaller than the cosmological signal at the percent level and can be neglected in the future.

Case (b): The most challenging step in observing an extragalactic redshift at the needed precision is to relate this measurement to an accurate reference system in time and celestial direction (e.g. Barycentre see Lindegren & Dravins 2003). Furthermore, the astrometry, the time standard, and the pointing accuracy can influence the modelling of the line-of-sight doppler shift contribution of the observatory. To match the precision requirements of the redshift-drift estimates the pointing accuracy need to be of the order of 1 arcsec. The accuracy in astrometry and the distribution of the time standard is related to the accuracy of the correlator model, including an Earth model and the JPL ephemeris. However changes in the position of the observatory e.g. due to tides (Solid-Earth: 30 cm, B. Campbell private comm.), ocean- or atmospheric-loading (2 cm, B. Campbell private comm.) etc. need to be taken into account in the post-processing of the full-sky survey.

Case (c): The major technical challenge to overcome is the constraint on the long time stability of the SKA system. The key is to reduce or handle systematic effects of the observatory in timing precision and frequency stability. Such requirements are difficult to evaluate and need to be assessed in more detail in future discussions. Nevertheless, it is assumed that pulsar observations will be used to monitor the long time stability of the system. These observations are sensitive enough to detect systematic effects within the observatory like time drifts or global changes of the observatory's 3-d velocity vector in the JPL ephemeris. Modelling of the arrival time of the pulse of a network of pulsars should enable us to correct for such systematics effects (Champion et al. 2010, Hobbs et al. 2012).

An additional technical limitation is the number of correlator channels in order to fully trace the neutral hydrogen signal of the galaxy. Generally the signal properties of the HI emission depends on the rotational velocity and the inclination of the galaxy. Assuming that the majority of the surveyed galaxies are Milky Way-type galaxies with a rotational velocity of 300 kms^{-1} a spectral window of 500 kms^{-1} would be sufficient to trace the entire signal. Tracing such a spectral window with the precision needed to estimate the redshift drift $\sim 10^{8-9}$ correlator channels are needed. Such a high number of channels could be realised by a dedicated pipeline, streaming the data from the predefined spectral window into a software correlator. The setup of the spectral windows and how the observations would be organised to set the frequency standard needs to be investigated in the future.

3.1 The experiments

In order to investigate the feasibility of tracing the signature of cosmic acceleration at various redshifts two approaches with low- and high-spectral resolution datasets are discussed.

In case of low-spectral resolution datasets and an observing precision of 10 ms^{-1}, the main constraint is to measure redshifts of $\sim 10^7$ galaxies per redshift interval. In general these high number counts can be achieved using an integration time of about 6 hours per pointing, assuming the same observational setup as used in the following discussion for the high-spectral-resolution case. The survey time for this experiment would be of the order of one year with a 10% precision on the redshift drift measurement. In order to archive higher precision the observing precision and hence the channel resolution in frequency space needs to be adapted.

PoS(AASKA14)027

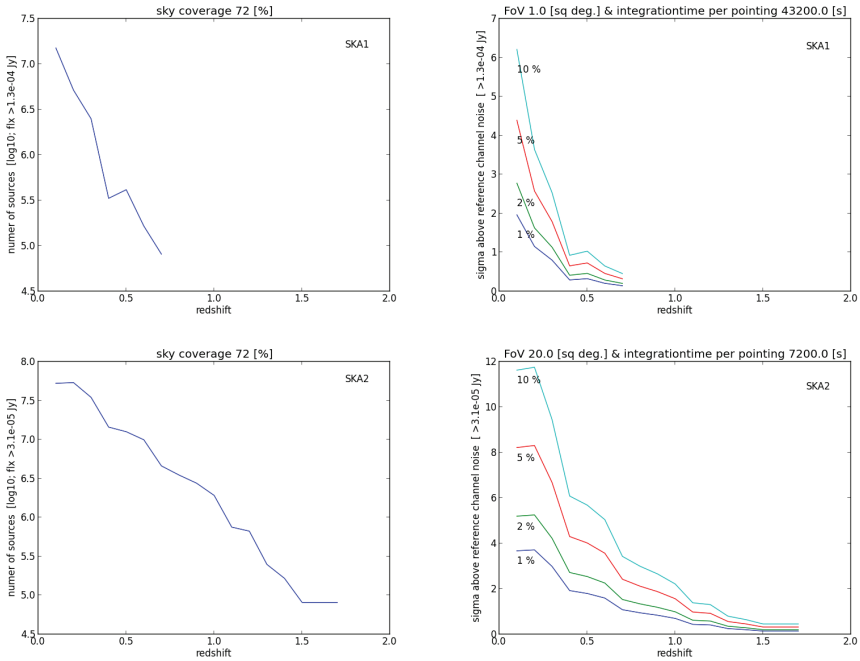

Figure 2: The basic ingredient of this experiment is the high number counts of galaxies and the sensitivity. The figures show the number counts and the significance per channel precision of detection versus redshift. The top panel show the results for a hypothetical SKA_1 with increased channel resolutions and the bottom displays the results for the full SKA.

In the following the feasibility of this experiment is explored by high-spectral resolution datasets ($\Delta\nu = 0.001, 0.002, 0.005, 0.01$ Hz). This discussion will address both phases of the SKA, the SKA and a SKA_1 with hypothetically channel width of this order.

SKA Phase 1 (SKA_1)

For the SKA_1 a generic observational setup is assumed with the following system parameters: SKA_1 (A_{eff} / T_{sys} = 1300 m^2 K^{-1}), various channel resolutions, 12 hours integration per pointing, 1 sq. degrees field of view, survey coverage of 30000 sq. degrees. The results are shown in the top panels of Figure 2. The results indicate that the number counts would be sufficient to detect a redshift drift at redshifts less than 0.3 with 5% to 10% precision. These results are somewhat misleading because to survey the entire sky with this setup would require 42 years which is not feasible, but it shows the importance of survey speed to this experiment.

In summary, the redshift drift experiment with the SKA_1 or 30% of the SKA is not possible. Despite the fact that the cosmological redshift drift can not be observed, a pathfinder experiment could be initiated to aim for 10 ms^{-1} accuracy to test the "low spectral resolution" case of the SKA_2 experiment. The anticipated accuracy of 10 ms^{-1} is already a factor 10 better with respect to the radial velocity measurements of nearby standart stars and may provide already some clues to the systematics and the ephemeris (Chubak et al. 2012).

SKA Phase 2 (SKA)

PoS(AASKA14)027

For the SKA a generic observational setup is assumed with the following system parameters: SKA (A_{eff} / T_{sys} = 13000 m^2 K^{-1}), various channel resolutions, 2 hour integration per pointing, 20 sq. degrees field of view, survey coverage of 30000 sq. degrees. The observations would take 125 days and the results are shown in the bottom panel of Figure 2 . The results show that the number counts would be sufficient enough to trace the functional dependency of the frequency shift caused by the cosmological expansion up to redshift of unity. The level of precision reached is a few percent and may even reach the percent level if the integration time per pointing is 12 hours.
Due to the relatively short survey duration this experiment could even be done several times within the life time of the SKA of 50 years.

4. Discussion & Summary

Measuring the expansion history of the Universe includes distances and the linear growth of density perturbations, and a combination of both observed at different epochs. The observations at different epochs allows for a direct measure of the expansion history, whereas SNIa surveys, weak lensing (Heavens 2003) and Baryon Acoustic Oscillations in the galaxy power spectrum (BAO; Wang 2006) are generally considered to be indirect probes of the acceleration. Their results rely on a priori knowledge of the cosmological model and even simple parameterisations of dark energy properties can result in misleading conclusions (e.g. Bassett et al. 2004, Shapiro & Turner 2006). In this light redshift-drift measurements are direct probes and rely only on the knowledge of the rest frame frequency of the measured signal. Its uncertainty in testing cosmological models is the knowledge of H_0. Compared to other probes with many more systematic uncertainties in parameterisation and calibration (e.g. cosmic chronometers; Moresco et al. 2012), the HI measurements offer less biased measurement and can be assumed to be a model-independent consistency test of cosmological theories. In addition, redshift drift measurements are sensitive to different combinations of cosmological parameters and thus combined with other probes can break degeneracies and will place stronger constrains on cosmologies (e.g. CMB, BAO, weak lensing). This complementarity nature of the redshift drift has been shown e.g. for the E-ELT case improving the CMB constraint by a factor of 2-3 and even has the potential to constrain new physics (Martinelli et al. 2012, Vielzeuf & Martins 2012).

The SKA will be able to measure the redshift drift to levels of a few percent precision up to redshifts of unity. The quoted measurement accuracy can be used to derive first constrains on cosmological model and detailed forecasting on the accuracy of cosmological parameters will be addressed in future investigations. However these precision enables us to compare the SKA experiment already to a study of optical redshift-drift measurements. This study indicates for a dynamical dark energy wCDM cosmology the greatest leverage on figure of merit (FOM) of the dark energy properties. In particular, an excess of 100 of FOM for dark energy at 1% precision and 1000, if combined with the CMB. For a lower precision of 5% the FOM is 290 if combined with the CMB and the Hubble constant (Kim et al. 2015).

Real time cosmology is possible with the SKA. The SKA is the only experiment that enables us to trace the nature of the “close by” acceleration and may provide essential information on possible mechanisms in place during the inflation phase and the evolution of the Universe. However the

PoS(AASKA14)027

proposed experiment does need the full sensitivity of the SKA array, the survey speed to detect a billion galaxies, and its technical requirements might imply some minor changes of the SKA baseline design. In addition, this experiment would benefit from a larger field of view of about 40 sq. deg. per pointing to allow for more sensitive observations per pointing. Nevertheless, the already relatively short survey time of the SKA allows for a even more ambitions experiment, measuring the cosmic jerk term. Such measurement might be feasible if the redshift drift experiment is performed several times within the life time of the SKA of 50 years.

Assuming the observational systematics can be modeled to $1^{-3}\mathrm{ms}^{-1}$ accuracy, the required spectral resolution of 10% (0.01 Hz) can be sufficiently reduced by a factor of hundred or more. In case the correlator can not provide the spectral resolution needed for this experiment, raw-data of individual galaxies of Band 1 or Band 2, or a part of it, could to be streamed to a dedicated software-correlator pipeline. In both cases the SKA will be able to detect the global signal of the redshift drift and with a dedicated observational setup the SKA will measure the redshift dependency of the redshift drift.

Even though this is a full SKA experiment; there are precursor observations possible with the SKA in Phase 1 to investigate the systematic effects within the ephemeris. These experiments would aim to investigate the properties of the 3-dimensional velocity vector of the Earth at resolutions of meter/s using the HI signal of nearby galaxies and HI in absorption toward quasars. Measurements of the 3-dimensional velocity vector will not only have cosmological applications they may also have the potential to model the Earth's gravitational field and could open up new synergies between the SKA and lunar ranging experiments.

Finally, the measurements of the redshift drift in redshift space by the SKA and the E-ELT (both sampling different redshift ranges) and the combination of their measurements are the only experiments that will fully trace the real-time evolution of the dark energy in the Universe.

References

Balbi A., Quercellini C., 2007, MNRAS, 382, 1623;
Bassett B.A., Corasaniti P.S., Kunz M., 2004, ApJL, 617, 1;
Chubak C., et. al., 2012, astro-ph\1207.6212;
Champion D. J., et. al., 2010, ApJ, 720, 201;
De Lucia G., Blaizot J., 2007, MNRAS, 375, 2;
Gudmundsson E.H., Björnsson G., 2002, ApJ, 565, 1;
Heavens A., 2003, MNRAS, 343, 1327;
Hobbs G., et. al., 2012, MNRAS, 427, 2780;
Hinshaw G., et al., 2013, ApJS, 208, 19;
Kanekar N., et. al., 2012, ApJ, 746, 16;
Kim A.G., Linder E.V., Edelstein J., Erskine D., 2015, Astroparticle Physics, 62, 195;
Klöckner H.-R., 2012, in "Pathway to the SKA - The German White Paper", eds. H.-R. Klöckner,M. Kramer, H. Falcke, D. Schwarz, A. Eckart, G. Kauffmann, A. Zensus, astro-ph\1301.4124;
Klöckner H.-R., Auld R., Heywood I., Obreschkow D., Levrier F., Rawlings S., 2009, PoS(SKADS 2009)009;
Lindegren L., Dravins D., 2003, A&A, 401, 1185;
Loeb A., 1998, ApJL, 499, 111;

PoS(AASKA14)027

Liske J., et. al., 2008a, The Messenger, 133, 10;
Liske J., et. al., 2008b, MNRAS, 386, 1192;
Maiolino R., et. al., 2013, in "The White Paper for the E-ELT HIRES", astro-ph\1310.3163;
Martinelli M., Pandolfi S., Martins C.J.A.P., Vielzeuf P.E. 2012, Physical Review D, 86, 123001;
Obreschkow D., Klöckner H.-R., Heywood I., Levrier F., Rawlings S., 2009, ApJ, 703, 1890
Pasquini L., et. al., 2005, The Messenger, 122,10;
Perlmutter S., et. al., 1999, ApJ, 517, 565;
Planck Collaboration, et al., 2013, astro-ph\1303.5076;
Quercellini C., Amendola L., Balbi A., Cabella P., Quartin M., Physics Reports, 2012, 521-3, 95;
Riess A.G., et. al., 1998, AJ, 116, 1009;
Sandage A., 1962, ApJ, 136, 319;
Shapiro C., Turner M.S., 2006, ApJ, 649, 563;
Vielzeuf P.E., Martins C.J.A.P. 2012, Physical Review D, 85, 087301;
Wang Y., 2006, ApJ, 647, 1
Westmeier T., Jurek R., Obreschkow D., Koribalski B. S., Staveley-Smith L., 2013, MNRAS, 438, 1176;

PoS(AASKA14)027

PROCEEDINGS OF SCIENCE

Weak Lensing Simulations for the SKA

Prina Patel[*a,b], **Ian Harrison**[c], **Sphesihle Makhathini**[d,b], **Filipe Abdalla**[e,d], **David Bacon**[f], **Michael L. Brown**[c], **Ian Heywood**[g,d], **Matt Jarvis**[h,a], **Oleg Smirnov**[d,b]

[a] *University of the Western Cape,* [b] *SKA South Africa,* [c] *Jodrell Bank,* [d] *Rhodes University,*
[e] *University College London,* [f] *ICG,* [g] *CSIRO,* [h] *University of Oxford,*
E-mail: prina83@gmail.com

Weak gravitational lensing is a very promising probe for cosmology. Measurements are traditionally made at optical wavelengths where many highly resolved galaxy images are readily available. However, the Square Kilometre Array (SKA) holds great promise for this type of measurement at radio wavelengths owing to its greatly increased sensitivity and resolution over typical radio surveys. The key to successful weak lensing experiments is in measuring the shapes of detected sources to high accuracy. In this document we describe a simulation pipeline designed to simulate radio images of the quality required for weak lensing, and will be typical of SKA observations. We provide as input, images with realistic galaxy shapes which are then simulated to produce images as they would have been observed with a given radio interferometer. We exploit this pipeline to investigate various stages of a weak lensing experiment in order to better understand the effects that may impact shape measurement. We first show how the proposed SKA1-Mid array configurations perform when we compare the (known) input and output ellipticities. We then investigate how making small changes to these array configurations impact on this input-outut ellipticity comparison. We also demonstrate how alternative configurations for SKA1-Mid that are smaller in extent, and with a faster survey speeds produce similar performance to those originally proposed. We then show how a notional SKA configuration performs in the same shape measurement challenge. Finally, we describe ongoing efforts to utilise our simulation pipeline to address questions relating to how applicable current (mostly originating from optical data) shape measurement techniques are to future radio surveys. As an alternative to such image plane techniques, we lastly discuss a shape measurement technique based on the shapelets formalism that reconstructs the source shapes directly from the visibility data. We end with a discussion of extensions to the out current simulations and concluding remarks.

Advancing Astrophysics with the Square Kilometre Array
June 8-13, 2014
Giardini Naxos, Italy

[*] Speaker.

PoS(AASKA14)030

1. Introduction

Weak gravitational lensing is a promising probe for cosmology. Light rays from distant sources are bent by the gravitational potential of objects on the path to an observer, leading to a coherent ellipticity or shear on images of galaxies near each other on the sky. We can measure statistics of this shear for galaxies in the Universe, at different redshifts and angular separations. These statistics are sensitive to the growth history of density fluctuations in the Universe (and therefore the matter power spectrum), and to the expansion history of the Universe (and hence for instance, dark energy parameters).

Weak shear measurements are already maturing at optical frequencies (e.g. Kilbinger et al., 2013), and a range of future optical experiments are planned to provide tight constraints on cosmological parameters using this probe (for instance the ground based Large Synoptic Survey Telescope (LSST), (LSST Science Collaboration et al., 2009), and Euclid space telescope, (Laureijs et al., 2012). See also Bacon et al. (2015) and Kitching et al. (2015)). In addition, shear can be measured at radio frequencies (e.g. Chang et al., 2004; Patel et al., 2010), and as shown in Brown et al. (2015) SKA will be able to provide competitive gravitational lensing measurements.

In order to demonstrate this, it is necessary to simulate realistic images which could be obtained using particular SKA measurement sets, including the effects of realistic gravitational lensing and telescope effects. Shear measurement techniques should be carried out on these images, and we should verify that we can obtain faithful estimates of the true shear. In this chapter, we describe our efforts to make such simulations and confirm that SKA configurations which are being considered by the community are suitable for making the SKA a powerful gravitational lensing telescope.

2. Simulation Pipeline

The simulations we utilise are based on a pipeline built in two parts which we briefly describe here and refer to Patel et al. (2014) for further details. The pipeline works by taking input images that contain realistic galaxy shapes and running them through a simulator. Within the simulator we can define the interferometer to use and other observation details such as the frequency, bandwidth, integration time etc. The simulator then predicts the visibilities for the given image and observation. The last part of the simulation then takes these visibilities and images them as would be done with real observed data and a restored image is produced. Once the simulation has produced a final restored image we then re-analyse these images with our chosen shape measurement technique and compare the input and out ellipticities.

2.1 Simulation

We firstly describe the input images we have created that are used throughout this work. The input images are based on a shapelet (see §4.2) based method that is described in detail in Refregier (2003) and Refregier & Bacon (2003). Briefly, the shapelets method decomposes a galaxy image into a series of localised basis functions called shapelets. The shapelets are a complete and orthonormal set of basis functions consisting of weighted Hermite polynomials, corresponding to perturbations around a circular Gaussian. The process of generating these input images is described

PoS(AASKA14)030

in detail in (Rowe et al., 2013), resulting in shapelet models that represent simulated, but realistic, (known) galaxy shapes as would have been observed with the Hubble Space Telescope (HST). Although these are simulated optical galaxies we make use of them as there exists no large enough sample of highly resolved galaxy images in the radio. In Patel et al. (2010) it was found that on a case-by-case basis the intrinsic shapes of radio and optical sources were only weakly correlated, but that the overall distribution of ellipticities were very similar at the two wavelengths. To keep computation time low we have created 100 such images that are 0.85×0.85 arcminutes^2 with a pixel scale of 0.05 arc seconds, that each contain $\simeq 100$ sources each. This gives a resulting input number density of $n \simeq 140$ arcminutes^{-2}, which is far larger than any current lensing survey.

These images are then fed into the simulator which in combination with the chosen interferometer and observation particulars, predicts the visibilities. If desired we are then able to include affects that would effect the visibilities in a variety of ways using the Radio Interferometer Measurement Equation (RIME) formalism (e.g. Smirnov, 2011), which relates the propagation of the signal from the source to detector via various observational effects. We are also able to include Gaussian measurement noise on the visibilities. Note in our simulations we do not currently employ any observation effects but we do include Gaussian measurement noise. These visibilities are then imaged using standard techniques (e.g. CLEAN) that we are again able to control, generating the output restored image.

2.2 Shape Measurement

We take the restored images produced by the simulation and then analyse them using the image based shapelet method described in §4.2 and compare the input and output ellipticities. Note, that in producing the restored image using CLEAN, a convolution is performed between the model image and the main lobe of the synthesised beam (PSF). We simulate this PSF as well and perform a deconvolution within the shapelet analysis, further details on deconvolution with shapelets can be found in Rowe et al. (2013), and further details about the image plane shapelet analysis can be found in Patel et al. (2014). We are then left with shapelet models (i.e. shapelet coefficients $f_{n,m}$) both before simulation and post, from which we estimate a 2-component (complex) ellipticity according to

$$\varepsilon = \frac{\sqrt{2} f'_{2,2}}{\langle f_{0,0} - f_{4,0} \rangle}, \tag{2.1}$$

(Massey et al., 2007). This ellipticity estimator is the Gaussian weighted quadrupole moment cast into shapelet space. We then follow Heymans et al. (2006) and fit a linear model to our data points

$$\varepsilon_i - \varepsilon_i^t = m_i \varepsilon_i^t + c_i, \tag{2.2}$$

where ε_i^t is the true input ellipticity and ε_i is the measured ellipticity. In all the follows the relative merit of each experiment can be compared through the calculated values of m_i and c_i. For a perfect experiment where we fully recover exactly all the shapes in the images $m_i = 0, c_i = 0$. A non-zero m_i is indicative of a calibration bias resulting from poor correction of factors that circularise images, poor PSF correction for example. $c_i \neq 0$ suggests a systematic where even circular objects appear elliptical. We have made no attempt to optimise any of our analyses to reduce the biases in anyway, neither have we looked for the origin of these biases. As such, the bias values presented here are

PoS(AASKA14)030

only meaningful in a comparative sense and should not be taken to represent the final performance that any such experiment might achieve. In a full analysis one would hope to understand the nature and origin of such biases to high precision in order to correct for them. One clear use of our pipeline is to asses the levels of bias that may be introduced by observation effects (e.g. Direction Dependant Effects (DDEs)).

The key to making a weak lensing measurement requires accurate measurements of many galaxy shapes. Our simulation pipeline offers a way in which all parts of the data processing pipeline, from raw visibilities to restored images, can be explored. In the rest of this document we present investigations that have been carried out to address some of the key questions most relevant to weak lensing studies with the SKA.

3. SKA Baselines Configurations

Since the configuration for SKA1-Mid is yet to be completely finalised we explore how changing the array configuration as proposed by a small amount would effect the ability to accurately measure the shapes of galaxies. We generated many different SKA1-Mid array configurations and ran them through our pipeline. In this section we describe what impact minor changes had on the calculated calibration and additive biases.

3.1 Baselines Changes and Impact on Weak Lensing

We initially calculated the bias values for the two proposed SKA1-Mid configurations. The first is that proposed by the SKAO (referred to as SKAM) and the other, a short time after, by Robert Braun (SKAM12), both are shown in Figure 1. Both these arrays contain 254 dishes with 197 of them within a 4 km core, and the other 57 divided into 3 logarithmically spaced spiral arms extending out to 100 km. For all simulations run in this section we have adopted an 8 hour observation at 700MHz and 10 50 MHz channels pointing at declination $\delta = -40^\circ$. We add Gaussian measurement noise to the visibilities resulting in the sources in the output images having a signal-to-noise of $\simeq 10$. We have also adopted a uniform weighting scheme through this work. Also shown in Figure 1 are the recovered ellipticity distributions derived for both configurations. Unsurprisingly, both these two configurations produce similar calibration values, with $m_i \simeq -0.261$ and very small additive bias. We use these recovered values of m_i and c_i as our base values to which we can compare the values derived from modified SKA1-Mid configurations. Note that all the calculated bias values for all considered arrays are given in Table 1.

The changes we explored were: changing the spacing in the arms, taking dishes from the core and redistributing them into the 3 spiral arms and adding new dishes to the spiral arms. In the former case, we looked at changing the arm distribution from logarithmic to equidistant and linear. In the case of the latter two, 9, 21, 30, 39, 51, and 60 dishes were added to the arms while keeping the maximum extent of the arms the same. In Table 1 we show the ellipticity recovery performance of these other SKA1-Mid configurations described above. The first two entries in blue and magenta correspond to the SKAO and Robert Braun configurations respectively. The cyan rows correspond to the configurations with equidistant and linear arms spacing. Entries in green and yellow are those where either dishes were redistributed from the core (green), or new dishes (yellow) were added to the spiral arms.

PoS(AASKA14)030

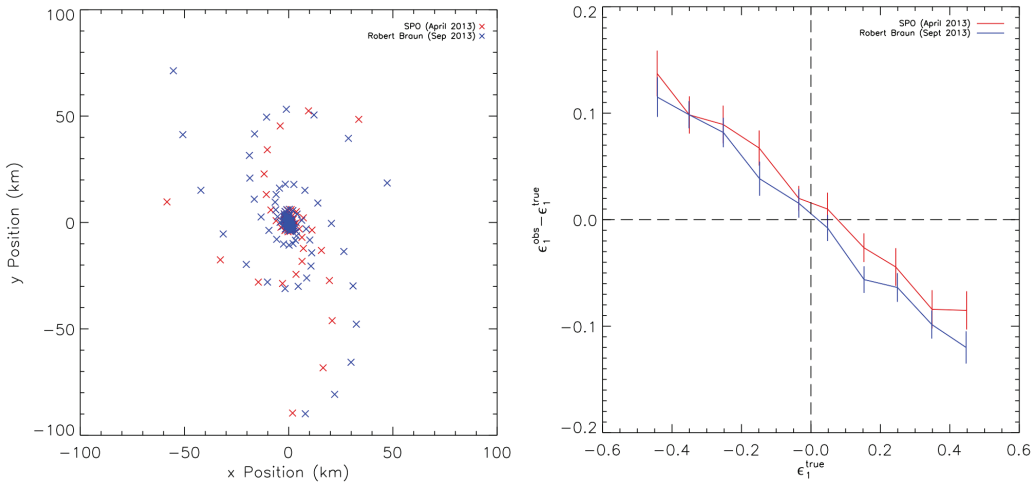

Figure 1: *Left panel:* Array configurations for SKA1-Mid as proposed by the SKAO (April 2013) and Robert Braun (September 2013). *Right Panel:* Recovered ellipticity (only component 1 of the ellipticity is shown) distributions for these SKA1-Mid arrays.

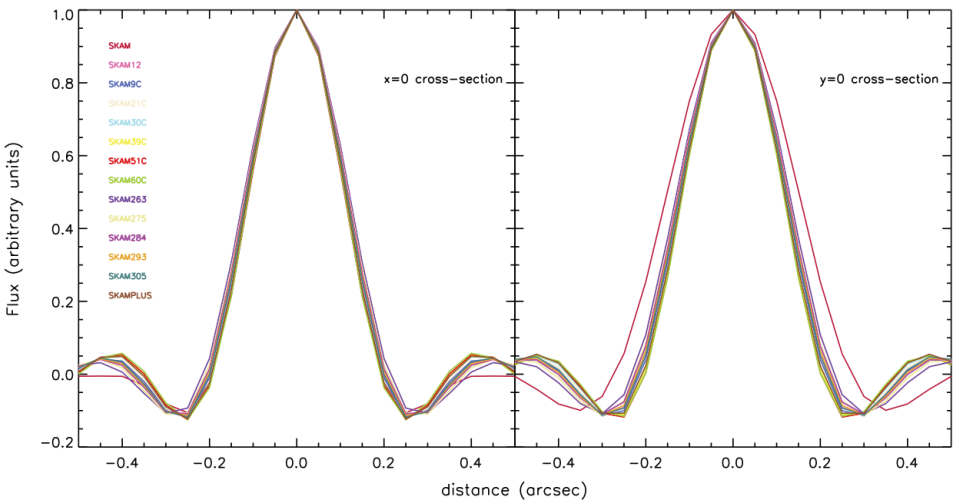

Figure 2: Cross-sections through the PSFs obtained from configurations described in § 3.

Since these are only modest changes to the configuration (i.e. $\sim 20\%$ movement/addition of dishes) we see no significant improvements in performance of the recovered ellipticity distributions. Since the deconvolution of the PSF in known to be one of the major causes of systematic error in shear measurement, in Figure 2 we show cross-sections of the PSFs for all the considered configurations. As can be seen, the change in the PSF is small and so reaffirms the result of consistent calibration values in the absence of any other potential causes of noise.

3.2 Alternative Configurations

For weak lensing the main aspect of the baselines configuration is concerned with achieving high sensitivity at scales where we can measure the shapes of sources in the continuum. This

PoS(AASKA14)030

Table 1: SKA1-Mid ellipticity recovery performance results. The first two entries in blue and magenta correspond to the SKAO and Robert Braun configurations respectively. The cyan rows correspond to the configurations with equidistant and linear arms spacing. Entries in green and yellow are those where either dishes were redistributed from the core (green), or new dishes (yellow) were added to the spiral arms. [a] quoted relative to the SKAO and Robert Braun configurations.

Name	N_{total} Dishes	N_{core} Dishes	N_{arms} Dishes	Arm Spacing	[a]Sensitivity for SNR = 10	Number Density n arcminute^{-2}	m_i	c_i
SKAM (SKAO)	254	197	19	Logarithmic	1.0	21.97	-0.278 ± 0.021 -0.258 ± 0.020	0.001 ± 0.005 0.017 ± 0.005
SKAM12 (Robert Braun)	254	197	19	Logarithmic	1.0	30.43	-0.227 ± 0.015 -0.280 ± 0.016	$-5 \times 10^{-4} \pm 0.004$ 0.001 ± 0.004
SKAM12EQ	254	197	19	Equidistant	1.25	19.32	-0.319 ± 0.015 -0.301 ± 0.015	-0.006 ± 0.004 0.010 ± 0.004
SKAM12LIN	254	197	19	Linear	1.0	30.69	-0.297 ± 0.015 -0.282 ± 0.016	-0.006 ± 0.004 0.004 ± 0.004
SKAM9C	254	188	22	Logarithmic	1.0	32.20	-0.292 ± 0.019 -0.264 ± 0.017	-0.006 ± 0.005 0.002 ± 0.005
SKAM21C	254	176	26	Logarithmic	1.0	32.33	-0.307 ± 0.018 -0.278 ± 0.019	-0.002 ± 0.005 0.001 ± 0.005
SKAM30C	254	167	29	Logarithmic	1.0	30.67	-0.308 ± 0.015 -0.286 ± 0.017	-0.006 ± 0.004 0.001 ± 0.005
SKAM39C	254	158	32	Logarithmic	1.0	25.41	-0.333 ± 0.014 -0.293 ± 0.015	-0.006 ± 0.004 0.011 ± 0.004
SKAM51C	254	146	36	Logarithmic	1.13	31.21	-0.314 ± 0.016 -0.285 ± 0.015	-0.005 ± 0.005 0.008 ± 0.004
SKAM60C	254	137	39	Logarithmic	1.13	25.72	-0.318 ± 0.015 -0.297 ± 0.015	-0.005 ± 0.004 0.005 ± 0.004
SKAM263	263	197	22	Logarithmic	1.13	33.52	-0.234 ± 0.016 -0.264 ± 0.016	-0.007 ± 0.004 -0.003 ± 0.004
SKAM275	275	197	26	Logarithmic	1.13	29.61	-0.256 ± 0.017 -0.256 ± 0.018	-0.004 ± 0.005 -0.009 ± 0.005
SKAM284	284	197	29	Logarithmic	1.13	29.79	-0.256 ± 0.017 -0.268 ± 0.017	-0.002 ± 0.005 0.002 ± 0.005
SKAM293	293	197	32	Logarithmic	1.25	29.87	-0.260 ± 0.018 -0.269 ± 0.016	-0.003 ± 0.005 -0.001 ± 0.004
SKAM305	305	197	36	Logarithmic	1.25	30.09	-0.272 ± 0.016 -0.281 ± 0.016	-0.005 ± 0.004 0.002 ± 0.005
SKAMPLUS	314	197	39	Logarithmic	1.38	31.42	-0.322 ± 0.015 -0.289 ± 0.017	-0.006 ± 0.004 0.005 ± 0.005

translates roughly to having significant sensitivity at scales corresponding to 0.5 - 1 arcseconds. For this reason increasing the the number of antennas in the spiral arms out to 70-80 km is beneficial for weak lensing while the lack of these baselines makes such a survey unfeasible.

To accommodate the other 3 cosmology science cases (cosmology with continuum and HI galaxy surveys and intensity mapping) as well as weak lensing alternative configurations have been proposed such that the *uv* coverage is as full as possible out to baselines of 70 - 80 km. In order to achieve a smooth transition between the three sections of the array (inner core, outer core and the spiral arms), the core is 'puffed' up slightly while the total number of dishes in the (inner+outer) core is preserved. The two proposed configurations are referred to using the following convention SKA1W*i*-*j*A*k*B*l*, where i refers to the number of dishes moved from the outer core to the spiral arms, j is the number of new dishes added to the arms, k is the maximum extent of the spiral arms and l the maximum baseline. The latter two are fixed in both cases to k= 72km and l= 120km. We shall refer to the two configurations, SKA1W9-0A72B120 and SKA1W9-12A72B120, as A and B respectively.

PoS(AASKA14)030

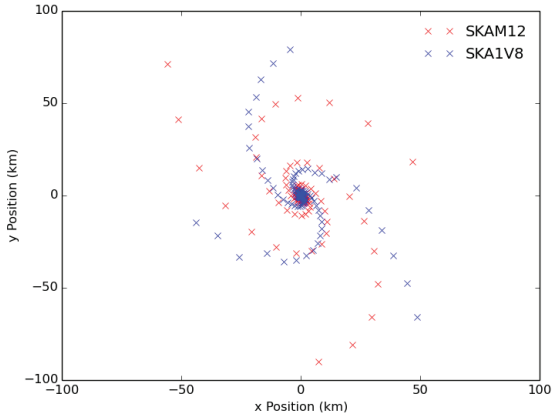

Figure 3: SKA1-Mid configurations proposed by Robert Braun (blue) and also one that is smaller in extent and takes into consideration the site geography (red). Results for both these configurations are compared in Table 2.

To assess the capabilities of these alternative configurations we run a new set of simulations at 600 MHz, 800 MHz and 1000 MHz with 1 50 MHz channel observing at declination $\delta = -30°$. To compare we also run the same simulation using the Robert Braun SKA1-Mid configuration discussed above, the results are presented in Table 2.

We notice immediately that as we increase the frequency of the observation, the calibration values decrease. This is because the resolution is $\propto \lambda/D$, where λ is the wavelength of observation and D the maximum baseline. In this case, our PSF is effectively becoming smaller, and so the higher the frequency, the more accurate our shape measurement. Also, as described in Makhathini et al. (2015) these arrays have optimised the distribution of dishes in the spiral arms such that the sensitivity at angular scales of $0.4-1$ arc second at 650 MHz can be enhances without significantly compromising the larger scales, so we expect them to perform best at the lower part of the frequency space explored here.

Also shown in Table 2 is the same simulation ran for the so-called SKA1V8 configuration. This is a slightly altered configuration of SKA1-Mid that also has a smaller extent than the two originally proposed configurations (maximum baseline of $\simeq$ 150km opposed to $\simeq$ 170km), it also takes into account the geography of the site. This configuration is plotted (along with SKAM12 from above) in Figure 3. Encouragingly, even with site topology incorporated this configuration produces similar calibration values to the one originally proposed that did not take this into account, while also bringing down the maximum extent of the spiral arms.

3.3 SKA Capabilities

In this Section we compute the performance of SKA and compare it to SKA1-Mid. In order to do this we have created a SKA configuration that consists of 5 spiral arms extending out too 150 km (each spiral arm has 50 dishes logarithmically spaced), but we have neglected all the dishes within the 1 km core. This is due to the very large number of baselines involved in a full SKA simulation (and hence massive computation time). Instead, since weak lensing is primarily concerned with

PoS(AASKA14)030

Table 2: Weak lensing simulations results for SKAM12 proposed by Robert Braun and also 2 alternatives (SKA1W9-0A72B120 and SKA1W9-12A72B120) that give a fuller *uv* coverage to baselines between 70 - 80 km. SKA1V8 is the SKA1-Mid configuration with a smaller extent and with site geography considered.

Array Configuration	600 MHz		800 MHz		1000 MHz	
	m_i	c_i	m_i	c_i	m_i	c_i
SKA1 REF2 (Robert Braun)	-0.560 ± 0.039	0.028 ± 0.011	-0.508 ± 0.031	0.052 ± 0.008	-0.424 ± 0.021	0.021 ± 0.005
	-0.491 ± 0.040	-0.004 ± 0.010	-0.434 ± 0.033	-0.007 ± 0.008	-0.400 ± 0.021	-0.001 ± 0.005
SKA1W9-0A72B120	-0.655 ± 0.027	0.033 ± 0.007	-0.604 ± 0.020	0.034 ± 0.005	-0.533 ± 0.020	0.016 ± 0.005
	-0.639 ± 0.025	-0.006 ± 0.006	-0.557 ± 0.021	-0.006 ± 0.005	-0.530 ± 0.021	0.003 ± 0.005
SKA1W9-12A72B120	-0.582 ± 0.043	0.038 ± 0.011	-0.563 ± 0.020	0.008 ± 0.005	-0.530 ± 0.018	0.002 ± 0.004
	-0.596 ± 0.040	-0.006 ± 0.010	-0.532 ± 0.020	-0.007 ± 0.005	-0.530 ± 0.017	-0.008 ± 0.004
SKA1V8	-0.545 ± 0.042	0.026 ± 0.011	-0.519 ± 0.037	0.071 ± 0.010	-0.458 ± 0.023	0.052 ± 0.006
	-0.506 ± 0.046	0.016 ± 0.011	-0.480 ± 0.036	-0.003 ± 0.009	-0.428 ± 0.024	0.004 ± 0.020

the longer baselines anyway, and also at this stage we are only interesting gaining some idea as to what SKA might be able to achieve, we adopt this simplification. The resultant SKA configuration is shown in the left hand panel of Figure 4.

To compare appropriately to the SKA1-Mid simulations discussed in §3 we again run the SKA simulation with an 8 hour observation at 700MHz and 10 50 MHz channels pointing at declination $\delta = -40°$. We have also again corrupted the visibilities by an amount that results in sources being at a SNR $\simeq 10$. The received ellipticity distribution is shown in the right hand panel of Figure 4, the resulting calibration values are:

$$\begin{aligned} m_1 &= -0.357 \pm 0.005 \\ c_1 &= 3 \times 10^{-4} \pm 0.001 \\ m_2 &= -0.354 \pm 0.005 \\ c_2 &= -0.002 \pm 0.001. \end{aligned} \tag{3.1}$$

We see that the multiplicative bias values recovered from SKA seem to be worse than for SKA1-Mid. We note at this stage that this is only a notional SKA configuration that we have simulated and so can not be completely relied upon when comparing to the more sophisticated SKA1-Mid configurations. Since our SKA configuration has some dishes missing, we are invariably missing many short and intermediate length baselines, that also carry shape information of scales that are relevant. We also see that error bars on m_i are a factor of 10 smaller than for SKA1-Mid. This is due to the many more sources that reach our final catalogue as SNR ~ 10 sources, meaning this is a more precise measurement.

3.4 Calibration Requirements for SKA

To provide some context for the obtained calibration values, we calculate the requirements on m and c for stages of SKA1-Mid and SKA and also for comparison, current and future optical surveys such as the Dark Energy Survey (The Dark Energy Survey Collaboration, 2005), Euclid and LSST. We adopt the requirements as computed in Amara & Réfrégier (2008), which are based upon the parameters: sky area, galaxy median redshift and galaxy number density. The requirements are set such that the statistical error is equal to the systematic error and thus provides an upper limit on the level of bias allowed.

PoS(AASKA14)030

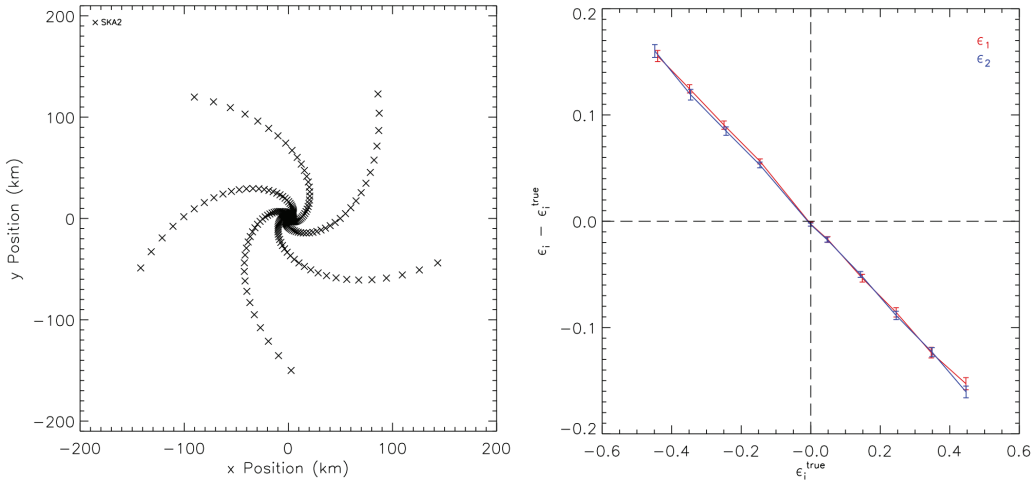

Figure 4: *Left panel:* A mock SKA configuration with 5 spiral arms extending to 150 km, but no dishes within the inner 1km of the core. *Right panel:* Recovered ellipticity distribution for SKA.

In addition, we follow the convention of converting the multiplicative and additive biases into a single *quality factor Q*, computed here as in Voigt & Bridle (2010) with an assumed rms cosmic shear of $\sigma_\gamma = 0.03$. In Table 3 we show the requirements for notional surveys conducted with an early phase of SKA1-Mid (SKA1-Mid early), SKA1-Mid and SKA, along with corresponding numbers for DES-like and Euclid/LSST-like surveys for comparison.

The values quoted for the number density and median redshifts are derived for an envisaged 2 year (net) continuum survey over 3 possible survey areas. The specification used are those given in Braun (2014), which in turn use the SKA1-Mid baseline design and the SKADS simulations of Wilman et al. (2008). The sensitivity levels have been chosen appropriately for weak lensing angular scales of 0.5 arc seconds at Band 2 and the galaxy number densities correspond to $> 10\sigma$ detections. SKA1-Mid early is defined to be such that it has 50% of the sensitivity of SKA1-Mid.

We note how these requirements are orders of magnitude smaller than those derived in the preceding section. In our simulations we have not attempted to optimise any of the parameters (either in the simulation or the shape measurement analysis) to seek out the smallest calibration values, e.g. we have made no attempt to optimise the imaging of the simulated data by investigating other imaging methods other than CLEAN. The requirements quoted represent the levels that need to be achieved in order for the error budget to be equal between the systematics and statistics. We hope that we can utilise our pipeline further to understand the various systematics and explore different imaging techniques etc. to provide more robust values of for the calibration biases.

4. Shear Measurement Techniques

As discussed above, the signal in weak gravitational lensing is the small shearing of galaxy images by foreground matter. The smallness of this shearing (typically of order 1%) and its sensitivity to change in cosmological parameters (typically of order 0.01% for a 1% change in the dark energy equation of state w) means that any effect which is capable of biasing results must be carefully controlled. One place in which such a bias may enter is in the translation from real, noisy data

PoS(AASKA14)030

Table 3: Requirements on multiplicative and additive biases on ellipticity measurement for proposed SKA weak lensing surveys to be dominated by statistical rather than systematics uncertainties, and for DES-like and Euclid/LSST-like for comparison. Q is calculated from m and c as in Voigt & Bridle (2010).

Experiment	A_{sky}	n_{gal}	z_m	$m <$	$c <$	$Q >$
DES-like	5000	12	0.8	0.004	0.0006	260
Euclid/LSST-like	20000	35	0.9	0.001	0.0005	990
SKA1-Mid early	1000	3.0	1.0	0.014	0.0012	62
SKA1-Mid early	5000	1.2	0.8	0.012	0.0011	79
SKA1-Mid early	30940	0.35	0.5	0.011	0.0011	80
SKA1-Mid	1000	6.1	1.2	0.0090	0.00095	103
SKA1-Mid	5000	2.7	1.0	0.0067	0.00082	140
SKA1-Mid	30940	0.9	0.7	0.0058	0.00076	164
SKA	1000	37	1.6	0.0031	0.00055	318
SKA	5000	23	1.4	0.0019	0.00043	523
SKA	30940	10	1.3	0.0012	0.00035	825

to a map of shear measurements across the field-of-view. Typically this is done by measuring the ellipticity of galaxies identified in the data, which is changed by shear. The preponderance of optical data of the quality necessary for weak lensing has led to the development of a large number of different techniques for performing this shape measurement process which take imageplane data as their inputs. Among the first derived (and subsequently most widely used) are methods which use weighted quadropole moment of combined galaxy-PSF images to measure ellipticities directly in a non-parametric way (KSB Kaiser et al. (1995); KSB+ Hoekstra et al. (1998); Re-Gaussianization Hirata & Seljak (2003)). Another popular approach is to assert that the galaxy images may be modelled with some analytic brightness distribution (such as a Gaussian or Sersic profile) and find the best fitting parameters, including ellipticity parameters, for each source (IM3SHAPE Zuntz et al. (2013), lensfit Miller et al. (2007)).

In the radio regime the approach which has found most application is that of shapelets, which reconstructs the data using an orthonormal set of basis functions. How these basis functions transform with shear is known, meaning the best-fitting coefficients for an image may be used to form an unbiased estimator for the shearing it has undergone through comparison with coefficents from some 'unlensed' sample. Shapelets also have the advantage of having similarly simple and analytic Fourier transformations which also remain localised, facilitating their use in directly modelling visibility data rather than reconstructed images.

As demonstrated above, using simulations with known ellipticity distributions provides a way of probing different aspects of the weak lensing pipeline. Most notably in the optical community simulations have been used for testing shape measurement techniques. Over the previous 10 years, the Shear TEsting Programme (STEP) and GRavitational lEnsing Accuracy Testing (GREAT) (see Mandelbaum et al. (2014) and references therein for a brief history) initiatives have simulated large optical weak lensing datasets and invited participants to (blindly) measure the shear in those images. This has allowed relative proficiency of different shear measurement methods and how they react to changes in data parameters, such as source size, S/N and simulated galaxy model

PoS(AASKA14)030

complexity, to be quantified. These investigations have given insight into the behaviour of shear measurement algorithms in optical data, but we may expect the challenges of radio data to be significantly different.

The production of images from interferometer data via deconvolution using algorithms such as CLEAN is a highly non-linear process and has the potential to produce spurious cosmic shear signals in addition to (and in convolution with) any introduced by a particular shape measurement algorithm. The noise in radio images is highly correlated (though optical methods have experience with this in dealing with multi-epoch data). The ability of presently available techniques to deal with these challenges is currently unclear, motivating a systematic evaluation along the model of STEP and GREAT programmes. A direct follow-on from these efforts may evaluate the ability of optical shape measurement algorithms to be extended to radio images, but a worthwhile comparison may also be done of the image reconstruction algorithms themselves, either in separation or in conjunction with shear estimation; in addition to long-established algorithms such as CLEAN and Maximum Entropy approaches, several new methods are under active research (e.g. Sutter et al. (2014), Carrillo et al. (2014) and references therein).

If image-reconstruction algorithms are unable to perform to the low level of systematics necessary for weak lensing science, it may be necessary to perform shear measurement directly using the visibilities produced by the telescope. Indeed, the only current detection of a shear signal in radio sources was performed in the visibility plane with shapelets. Notionally, being able to avoid the deconvolution process necessary for imaging is an important strength of visibility-plane shear measurement methods. The deterministic nature of instrumental effects in radio astronomy is often touted as a key advantage of radio weak lensing and it manifests here through the ability to forward convolve sky models in a well-defined way when searching for the best fitting parameters. However, the computational challenges of such a procedure are potentially great. Information from each individual source is no longer localised in the visibility plane, meaning all sources must be fitted simultaneously, rather than simply taking cut-outs of images around a single source as is done in image-plane methods. Starting with a naive model-fitting approach, if we attempt to fit 5 parameters per source (as is typically done in mainstream optical methods) for large numbers of sources over (extremely) large numbers of visibilities, this quickly becomes computationally unfeasible. There are various potential ways of alleviating these problems: data volumes could be reduced with averaging of visibilities on a grid, the number of necessary simultaneous fits could be reduced by averaging around a single source at the phase centre or by employing methods such as visibility-stacking (Lindroos et al., 2014) and we may also expect other, novel techniques to be developed. In addition to the computational problems involved in the analysis, the sheer volume of storage necessary to maintain access to unaveraged visibilities from the SKA may also be prohibitive.

4.1 radioGREAT

In order to investigate the issues discussed above, the radioGREAT[1] programme has been initiated, with three key goals:

- What are the requirements on shape measurement for cosmology with weak gravitational lensing in the radio band?

[1] http://radiogreat.jb.man.ac.uk

PoS(AASKA14)030

- Can we make images of the necessary fidelity to measure shapes of radio star-forming galaxies to the level of these requirements?
- Can we measure shapes of radio star forming galaxies to the level of these requirements whilst leaving our data in the visibility plane?

For an initial challenge, the task should be kept as simple as possible, with complications introduced individually in order to evaluate their effect on shape measurement. We may expect to follow closely the structure of the GREAT08 optical/NIR challenge, with a fiducial branch consisting of non-overlapping, simple Sersic galaxy models with identical, high signal-to-noise values ($>\sim 100$) and constant radii. Other branches may then consist of datasets containing individual modifications, to systematically evaluate the effect of e.g. altering galaxy size, reducing signal-to-noise, altering dynamic range and altering bandwidth and time smearing.

4.2 Shapelets in Real and Fourier Space

In contrast to traditional telescopes interferometers do not provide a direct image of the observed sky, but instead measure its Fourier transform at a finite number of *uv* points that correspond to each antenna pair in the array. The real space image must then be reconstructed from this discretely sampled visibility data, while also deconvolving the effective beam that arises from the finite sampling. Several methods exist to perform this task, e.g. CLEAN, MEM. These methods are well tested and are appropriate for various applications; however, these methods are non-linear and do not necessarily converge in a well defined manner.

The Hermite polynomials that form the shapelet basis set have some remarkable properties which greatly facilitate the modelling of the source shapes. Of particular interest here is the property that they are invariant (up to a rescaling) under of Fourier transform and thus are naturally suited for interferometric imaging. In optical surveys, shapelets have been little utilised after some conceptual concerns were raised with the approach (of shapelets like methods), however, similar conceptual problems were also raised with the KSB method although this method continued to be popular in the literature, see Melchior et al. (2011) for more details.

In the real space (or image plane) application of the shapelets technique the surface brightness $f(\mathbf{x})$ of an object is decomposed as

$$f(\mathbf{x}) = \sum_{\mathbf{n}} f_{\mathbf{n}} B_{\mathbf{n}}(\mathbf{x};\beta); \tag{4.1}$$

where

$$B_{\mathbf{n}}(\mathbf{x};\beta) = \frac{H_{n_1}(\beta^{-1}x_1)H_{n_2}(\beta^{-1}x_2)e^{-\frac{|x|^2}{2\beta^2}}}{\left[2^{(n_1+n_2)}\pi\beta^2 n_1! n_2!\right]^{\frac{1}{2}}} \tag{4.2}$$

are the two-dimensional orthonormal basis functions with a characteristic scale β, $H_m(\eta)$ is the Hermite polynomial of order m, $\mathbf{x} = (x_1, x_2)$ and $\mathbf{n} = (n_1, n_2)$. The basis functions are complete and if β and $\mathbf{x}$ are chosen to be close to the size and location of the galaxy, then the expansion will yield a quick convergence.

The Fourier transform of an objects intensity can be written as

$$\tilde{f}(\mathbf{k}) = (2\pi)^{-\frac{1}{2}} \int_{-\infty}^{\infty} f(\mathbf{x}) e^{i\mathbf{k}\cdot\mathbf{x}} d^2x \tag{4.3}$$

PoS(AASKA14)030

and decomposed as

$$\tilde{f}(\mathbf{k}) = \sum_{\mathbf{n}} f_{\mathbf{n}} \tilde{B}_{\mathbf{n}}(\mathbf{k};\beta), \tag{4.4}$$

where $\tilde{B}_{\mathbf{n}}(\mathbf{k};\beta)$ obey the dual property

$$\tilde{B}_{\mathbf{n}}(\mathbf{k};\beta) = i^{(n_1+n_2)} B_{\mathbf{n}}(\mathbf{k};\beta). \tag{4.5}$$

The invariance (unto a rescaling) under Fourier transform makes this basis set a natural choice for interferometric imaging.

As mentioned above, an interferometer correlates the signals measured by antenna pairs into a complex visibility. Each of these visibilities occupies a point on the *uv* plane which corresponds to the projected baseline formed between the antenna pair. In practice, the visibilities are not exactly a two-dimensional Fourier transform of the sky brightness. The visibility measured for an antenna pair (i, j) at a time and frequency of t and ν respectively is given by

$$V_{ij}(\nu,t) = \int \frac{A(\mathbf{l},\nu) f(\mathbf{l},\nu,t)}{\sqrt{1-|\mathbf{l}|^2}} e^{-2\pi i\left[u\ell+vm+w(\sqrt{1-|\mathbf{l}|^2}-1)\right]}, \tag{4.6}$$

where $f(\mathbf{l},\nu,t)$ is the surface brightness of the sky at location $\mathbf{l} = (\ell, m)$ with respect to the phase centre and $A(\ell,\nu)$ is the frequency dependent primary beam. The (u,v,w) coordinates are given by

$$\begin{pmatrix} u \\ v \\ w \end{pmatrix} = \begin{pmatrix} \sin H_0 & \cos H_0 & 0 \\ -\sin\delta_0 \cos H_0 & \sin\delta_0 \sin H_0 & \cos\delta_0 \\ \cos\delta_0 \cos H_0 & -\cos\delta_0 \sin H_0 & \sin\delta_0 \end{pmatrix} \frac{1}{\lambda} \begin{pmatrix} L_x \\ L_y \\ L_z \end{pmatrix}, \tag{4.7}$$

where λ is the wavelength of the observation, H_0 is the hour angle and δ_0 the declination. $L_{x,y,z}$ are the coordinate differences between the two antennas measured in a fixed-Earth coordinate system in which the sky rotates about the $\hat{L}_z$ axis. We also note that locus that is traced by the (u,v,w) coordinates also define the synthesised beam pattern (or PSF). Since these coordinates are entirely determined from the antenna and source positions and the time and frequency of the observation, the synthesised beam is entirely known for interferometers. Only for observations at the zenith $(z \simeq 0)$, in the absence of a primary beam $(A \simeq 1)$ and for small displacements from the phase center $(\ell, m << 1)$ does the relationship between the measured visibilities and the desired sky brightness reduce to an extact Fourier transform.

Since visibility datasets can be large $(> 10^5)$, directly fitting the shape parameters to all the *uv* data can be very computationally expensive. Instead one can apply a binning scheme to reduce the size of the data but without losing any information. In the *uv* plane we can grid the data using a cell size $\Delta u = 0.5\Delta\ell^{-1}$, and average the data in each cell and similarly for Δv. $\Delta\ell$ is chosen to be one half of the intended field-of-view and the 0.5 factor accounts for the Nyquist frequency. This choice of $\Delta u, v$ is designed to minimise the number of cells but also to avoid smearing at large scales which mimic primary beam attenuation.

In our implementation of this technique we model the intensity $f_s(\ell,m)$ of each source s as a sum of the shapelet basis functions $B_{\mathbf{n}}(\mathbf{l}-\mathbf{l}_s;\beta_s)$, centred on the source centroid $\mathbf{l}_s(\ell_s,m_s)$ with scale β_s, by estimating the shapelet coefficients $f_{\mathbf{n}s}$ of the sources given the binned visibility data described above. In principle, a fully sampled *uv* plane provides all the shape information about

PoS(AASKA14)030

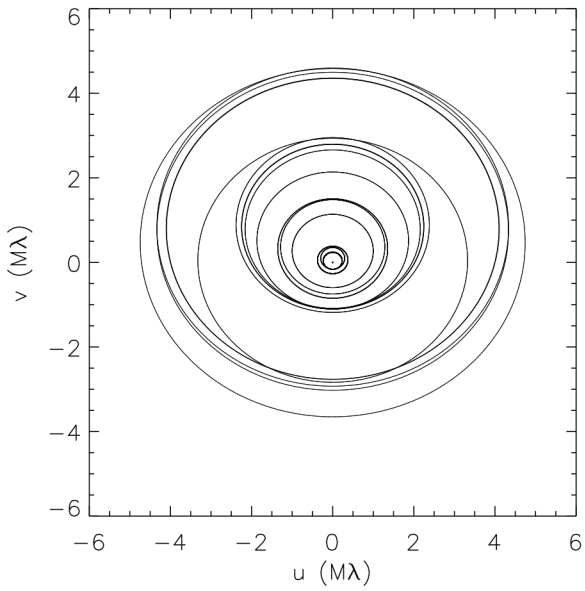

Figure 5: *uv* coverage of the eMERLIN experiment used to demonstrate shape measurement using shapelet fitting in the *uv* plane.

the sources and a linear decomposition similar to the image domain described above could be performed. However, given the finite sampling in the *uv* plane this is not possible here. To alleviate this problem we make a linear fit to the *uv* plane with the shapelet coefficients as free parameters.

4.3 *uv* Plane shapelet Fitting

To illustrate the technique we have performed simple simulations. We have taken a sample of the source models used in the studies discussed previously and made very simple sky patches containing a grid of 10×10 sources. In order to keep the simulations small (i.e. the number of visibilities) we have adopted the eMERLIN array for this experiment. The observation configuration is as follows: the fields are all observed at $\delta = +60^\circ$, at 1.4 GHz with a single 125 kHz channel, and for 24 hours and 20 second integration. The resulting *uv* coverage on which the following results are based is shown in Figure 5. We produce ~ 50 tiles that have a grid of 100 sources each, each tile consists of sources with the same n_{max}, the range of n_{max} is $0-20$. We simulate the visibilities for each of these sources, bin and fit for the shapelet coefficients as described above. As in the previous Sections we then compare the input and output ellipticities. Our current implementation of this technique fits all source with the same number of coefficients (i.e. for the same n_{max}), hence our motivation to tile sources according to n_{max}. In practice, we would want to fit all sources based on some guess or estimate for the what the n_{max} for each source in our field should be. Likewise, we currently input the source positions and β parameters into the code when we do the shape fitting. We are working towards an implementation where the n_{max} and β parameters are also fir for.

As an initial study, in Figure 6 we show the comparison of input and output ellipticities having fit all tiles with an $n_{max} = 4$, this is the lowest n_{max} we can chose for our adopted ellipticity estimator. We see that the bias we achieve in this (simplified) scenario is much less than anything we achieved

PoS(AASKA14)030

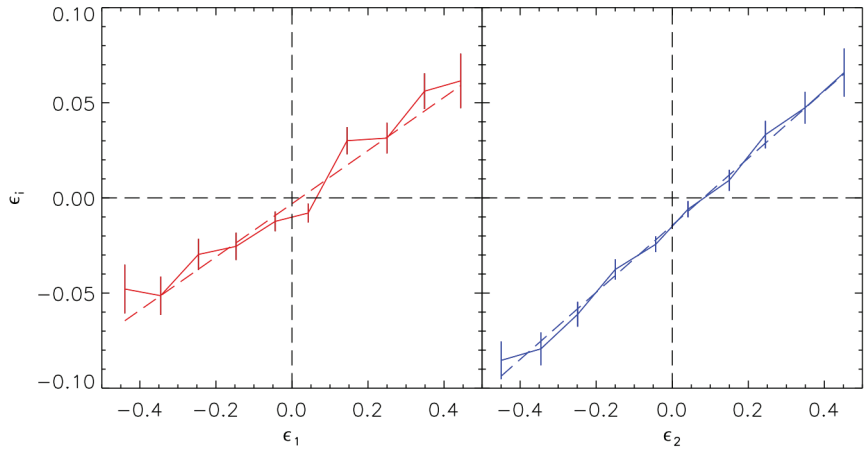

Figure 6: Ellipticity comparison based on shapelet fitting in the *uv* plane. The solid curves are show the binned data and the dashed curves are the best linear fits. The red lines are for ε_1 and the blue for ε_2.

in the image plane analyses of the previous Sections, the calculated bias values are

$$\begin{aligned} m_1 &= 0.140 \pm 0.012 \\ c_1 &= -0.003 \pm 0.002 \\ m_2 &= 0.176 \pm 0.010 \\ c_2 &= -0.014 \pm 0.002 \end{aligned} \tag{4.8}$$

Once again we find very little additive bias while a much smaller multiplicative bias than we have encountered elsewhere in this chapter. Although this in not a meaningful comparison as the input images and simulations are fundamentally different in both cases. We aim to expand these *uv* plane simulations considerably in order to make much better comparison between the performance of shapelet fitting in the *uv* and image planes. Ultimately we hope to extend this to real data that has already been analysed in the the image plane in Patel et al. (2010).

5. Discussion/Conclusion

Over recent times weak lensing has emerged as a very promising tool for cosmology. Making weak lensing measurements requires the measurement of very many galaxy shapes to high precision, while also carefully controlling systematics. Due to the involved nature of making radio images making use of simulated data provides a important way to probe such systematic effects in the system while also being key to testing current and new techniques.

In this chapter we have provided details of the ongoing efforts carried out to address the feasibility of weak lensing experiments with SKA1-Mid and SKA in the context of practical shape measurement. We have implemented a pipeline that allows us to explore many aspects of the data gathering and reduction processes, allowing us to asses if these are able to meet the high demands on data quality that weak lensing measurements require.

We have explored how small changes to the proposed SKA1-Mid array configuration has little impact on ones ability to accurately measure the shapes of galaxies. We have introduced alternative

PoS(AASKA14)030

configurations that are smaller in overall extent that give similar performance to those originally proposed and which have a better survey speed. Also, demonstrated was the performance of SKA1-Mid with the site geography taken into consideration and this provides encouraging results.

Using a notional SKA configuration we find slightly diminished calibration biases in comparison to SKA1-Mid but this result requires further investigation as it is unlikely this can truly be the case. A more complete configuration without missing baselines should give a much clearer idea of how SKA will perform in comparison on SKA1-Mid.

In our present studies we have not tried to optimise the simulations or shape measurement analysis in order to achieve the optimal calibration biases. However, we did present the requirements that will be required for constraining cosmology with real SKA surveys. We can make use of the pipeline that we have developed to determine where these biases originate.

We introduced the forthcoming radioGREAT challenge that will investigate current and new methods of shape measurement and their applicability to radio data. Starting with simple simulations we hope to emulate the successes of the STEP and GREAT challenges in the optical to address the difficulties that radio data gathering and reduction will most likely pose. We also demonstrate the shapelet shape measurement technique as applied directly to simple visibility data. In due course, we hope to further develop these simulations to more realistic scenarios and to properly compare the technique applied in both image and visibility plane, before eventually applying to real data.

Acknowledgements

PP is funded by a SKA South Africa Postdoctoral Fellowship. IH and MLB are supported by an ERC Starting Grant (Grant no. 280127). MLB is a STFC Advanced/Halliday fellowship. SM acknowledges financial support from the National Research Foundation of South Africa. OS research is supported by the South African Research Chairs Initiative of the Department of Science and Technology and National Research Foundation. FBA acknowledges the support of the Royal society via an RSURF. MJJ acknowledges support by the South African Square Kilometre Array Project and the South African National Research Foundation. DB is supported by UK Science and Technology Facilities Council, grant ST/K00090X/1.

References

Amara, A. & Réfrégier, A. 2008, MNRAS, 391, 228

Bacon, D. J., Bridle, S., Michael, B. L., et al. 2015, “Synergy between the Large Synoptic Survey Telescope and the Square Kilometre Array", in Advancing Astrophysics with the SKA, PoS(AASKA14)145

Braun, R. 2014, SKA1 Imaging Science Performance, Document number SKA-TEL-SKO-DD-XXX Revision A Draft, SKA Organisation

Brown, M., Bacon, D., Camera, S., et al. 2015, “Weak gravitational lensing with the Square Kilometre Array”, in Advancing Astrophysics with the SKA, PoS(AASKA14)023

Carrillo, R. E., McEwen, J. D., & Wiaux, Y. 2014, MNRAS, 439, 3591

Chang, T.-C., Refregier, A., & Helfand, D. J. 2004, ApJ, 617, 794

PoS(AASKA14)030

Heymans, C., Van Waerbeke, L., Bacon, D., et al. 2006, MNRAS, 368, 1323
Hirata, C. & Seljak, U. 2003, MNRAS, 343, 459
Hoekstra, H., Franx, M., Kuijken, K., et al. 1998, ApJ, 504, 636
Kaiser, N., Squires, G., & Broadhurst, T. 1995, ApJ, 449, 460
Kilbinger, M., Fu, L., Heymans, C., et al. 2013, MNRAS, 430, 2200
Kitching, T. D., Bacon, D. J., Brown, M., et al. 2015, Advancing Astrophysics with the SKA
Laureijs, R., Gondoin, P., Duvet, L., et al. 2012, in Society of Photo-Optical Instrumentation Engineers (SPIE) Conference Series, Vol. 8442, Society of Photo-Optical Instrumentation Engineers (SPIE) Conference Series
Lindroos, L., Knudsen, K. K., Vlemmings, W., et al. I. 2014, in prep.
LSST Science Collaboration, Abell, P. A., Allison, J., Anderson, S. F., et al. 2009, ArXiv e-prints
Makhathini, S., Smirnov, O., Jarvis, M., et al. 2015, "Morphological classification of radio sources for galaxy evolution and cosmology with the SKA", in Advancing Astrophysics with the SKA, PoS(AASKA14)081
Mandelbaum, R., Rowe, B., Bosch, J., et al. 2014, ApJS, 212, 5
Massey, R., Rowe, B., Refregier, A., et al. 2007, MNRAS, 380, 229
Melchior, P., Viola, M., Schäfer, B. M., et al. 2011, MNRAS, 412, 1552
Miller, L., Kitching, T. D., Heymans, C., et al. 2007, MNRAS, 382, 315
Patel, P., Abdalla, F. B., Bacon, D. J., et al. 2014, MNRAS, 444, 2893
Patel, P., Bacon, D. J., Beswick, R. J., et al. 2010, MNRAS, 401, 2572
Refregier, A. 2003, MNRAS, 338, 35
Refregier, A. & Bacon, D. 2003, MNRAS, 338, 48
Rowe, B., Bacon, D., Massey, R., et al. 2013, MNRAS, 435, 822
Smirnov, O. M. 2011, Astron. & Astrophys., 527, A106
Sutter, P. M., Wandelt, B. D., McEwen, J. D., et al. 2014, MNRAS, 438, 768
The Dark Energy Survey Collaboration. 2005, ArXiv Astrophysics e-prints, 0510346
Voigt, L. M. & Bridle, S. L. 2010, MNRAS, 404, 458
Wilman, R. J., Miller, L., Jarvis, M. J., et al. 2008, MNRAS, 388, 1335
Zuntz, J., Kacprzak, T., Voigt, L., et al. 2013, MNRAS, 434, 1604

PoS(AASKA14)030

PROCEEDINGS OF SCIENCE

Measuring redshift-space distortions with future SKA surveys

Alvise Raccanelli[1,2,3], **Philip Bull**[4], **Stefano Camera**[5,6], **David Bacon**[7], **Chris Blake**[8], **Olivier Doré**[2,3], **Pedro Ferreira**[9], **Roy Maartens**[5,7], **Mario Santos**[5,10,6], **Matteo Viel**[11,12], **Gong-bo Zhao**[13,7]

[1] *Department of Physics & Astronomy, Johns Hopkins University, 3400 N. Charles St., Baltimore, MD 21218, USA*
[2] *Jet Propulsion Laboratory, California Institute of Technology, Pasadena CA 91109, USA*
[3] *California Institute of Technology, Pasadena CA 91125, USA*
[4] *Institute of Theoretical Astrophysics, University of Oslo, P.O. Box 1029 Blindern, N-0315 Oslo, Norway*
[5] *Physics Department, University of the Western Cape, Cape Town 7535, South Africa*
[6] *CENTRA, Instituto Superior Técnico, Universidade de Lisboa, Lisboa 1049-001, Portugal*
[7] *Institute of Cosmology & Gravitation, University of Portsmouth, Portsmouth PO1 3FX, UK*
[8] *Centre for Astrophysics & Supercomputing, Swinburne University of Technology, PO Box 218, Hawthorn, VIC 3122, Australia*
[9] *Astrophysics, University of Oxford, DWB, Keble Road, Oxford OX1 3RH, UK*
[10] *SKA SA, 4rd Floor, The Park, Park Road, Pinelands, 7405, South Africa*
[11] *INAF - Osservatorio Astronomico di Trieste, Via Tiepolo 11, 34143, Trieste, Italy*
[12] *INFN sez. Trieste, Via Valerio 2, 34127 Trieste, Italy*
[13] *National Astronomy Observatories, Chinese Academy of Science, Beijing, 100012, P.R.China*

E-mail: alvise@jhu.edu

The peculiar motion of galaxies can be a particularly sensitive probe of gravitational collapse. As such, it can be used to measure the dynamics of dark matter and dark energy as well the nature of the gravitational laws at play on cosmological scales. Peculiar motions manifest themselves as an overall anisotropy in the measured clustering signal as a function of the angle to the line-of-sight, known as redshift-space distortion (RSD). Limiting factors in this measurement include our ability to model non-linear galaxy motions on small scales and the complexities of galaxy bias. The anisotropy in the measured clustering pattern in redshift-space is also driven by the unknown distance factors at the redshift in question, the Alcock-Paczynski distortion. This weakens growth rate measurements, but permits an extra geometric probe of the Hubble expansion rate. In this short chapter we will briefly describe the scientific background to the RSD technique, and forecast the potential of the SKA phase 1 and the SKA2 to measure the growth rate using both galaxy catalogues and intensity mapping, assessing their competitiveness with current and future optical galaxy surveys.

Advancing Astrophysics with the Square Kilometre Array
June 8-13, 2014
Giardini Naxos, Italy

PoS(AASKA14)031

1. Introduction

One of the biggest challenges of modern cosmology is to understand the accelerated expansion rate of the Universe. A number of proposals have been put forward, the most notable of which are the presence of dark energy or, alternatively, a modification to general relativity on cosmological scales. Radio surveys have been used to test these different hypotheses in the past, mainly using the integrated Sachs-Wolfe effect and the galaxy angular power spectrum (see e.g. Nolta et al. 2004; Raccanelli et al. 2008; Xia et al. 2010). With the new generation of radio arrays such as LOFAR (Rottgering et al. 2011) and ASKAP (Johnston et al. 2008), and in preparation to the SKA, there is a growing interest in understanding how future radio surveys can constrain cosmological parameters, and maybe discriminate between the two scenarios described above. Some examples of these investigations can be found in Raccanelli et al. (2012); Camera et al. (2012); Raccanelli et al. (2015). Here we focus on how the proposed SKA surveys will be able to provide measurements of Redshift-Space Distortions (RSD), allowing in this way measurements of cosmological parameters, and in particular the growth of structures.

In this chapter, we will briefly review the physics of Redshift-Space Distortions and how we model their effect on the power spectrum. We investigate potential issues and systematics and then we present forecasts for the measurements we can perform using the different proposed SKA surveys, focusing in particular on models describing the growth of structures. In two complementary chapters (Bull et al. 2014a; Camera et al. 2014) are presented forecasts for the BAO and large-scale measurements, investigating how those can constrain dark energy models and primordial non-Gaussianity.

2. The physics of the growth rate

The presence of a dark energy component in the energy-density of the Universe (or the fact that our theory of gravity needs to be modified on large scales), modifies the gravitational growth of large-scale structures. The large-scale structure we see traced by the distribution of galaxies arises through gravitational instability, which amplifies primordial fluctuations that originated in the very early Universe. The rate at which structure grows from small perturbations offers a key discriminant between cosmological models, as different models predict measurable differences in the growth rate of large-scale structure with cosmic time (e.g. Jain & Zhang 2008; Song & Percival 2008; Song & Koyama 2008). For instance, dark energy models in which general relativity is unmodified predict different large-scale structure formation compared to Modified Gravity models with the same background expansion (e.g. Dvali et al. 2000; Carroll et al. 2004; Brans 2000; Yamamoto et al. 2008, 2010).

The growth rate, $f(a)$, as a function of scale factor a is defined as:

$$f(a) \equiv \frac{d\ln\delta_M(a)}{d\ln a}\,, \tag{2.1}$$

where $\delta_M(a)$ is the amplitude of the growing mode of matter density perturbations. In the conformal Newtonian gauge the evolution equations for the velocity potential θ and δ_M are:

$$\dot{\delta}_M = 3(\dot{\Phi}+\mathscr{H}\Psi) - \left[k^2+3(\mathscr{H}^2-\dot{\mathscr{H}})\right]\theta_M\,, \tag{2.2}$$

$$\dot{\theta}_M = -\mathscr{H}\theta_M + \Psi\,. \tag{2.3}$$

PoS(AASKA14)031

We use dots to denote derivatives with respect to conformal time, and our conventions for the metric potentials are displayed in the perturbed line element: $ds^2 = a^2(\eta)\left[-(1+2\Psi)d\eta^2 + (1-2\Phi)dx^i dx_i\right]$ which satisfy (in the quasi-static regime) the field equations: $2\nabla^2\Phi = \kappa a^2\,\mu(a,k)\,\bar{\rho}_M\Delta_M$ and $\Phi/\Psi = \gamma(a,k)$. The parameters μ and γ encapsulate all the information about deviation from GR for metric theories of gravity (Baker et al. 2011).

Again, in the quasi static regime, the evolution equation for δ_M simplifies to:

$$\ddot{\delta}_M + \mathscr{H}\dot{\delta}_M - \frac{3}{2}\mathscr{H}^2\Omega_M\xi\,\delta_M = 0\,, \tag{2.4}$$

where we have defined $\xi \equiv \mu/\gamma$ (which is equal to 1 in GR). Using $x = \ln a$ as the independent variable we have:

$$\delta_M'' + \left(1 + \frac{\mathscr{H}'}{\mathscr{H}}\right)\delta_M' - \frac{3}{2}\Omega_M\xi\,\delta_M = 0\,. \tag{2.5}$$

Primes denote derivatives with respect to x. We can convert this into an evolution equation for f :

$$f' + q(x)\,f + f^2 = \tfrac{3}{2}\Omega_M\xi\,, \tag{2.6}$$

where $q(x) = \frac{1}{2}[1 - 3\,\omega(x)(1-\Omega_M(x))]$. The effect of the expansion rate (via $q(x)$) and modified gravity (via ξ) are explicit in the time evolution of f.

3. Redshift Space Distortions

Measurements of RSD played an important role in developing the current cosmological model, and it will be a fundamental part of several future cosmological experiments, because observations of RSD in galaxy surveys are a powerful way to study the pattern and the evolution of the Large Scale Structure of the Universe (Kaiser 1987; Hamilton 1997), as they provide constraints on the amplitude of peculiar velocities induced by structure growth, thereby allowing tests of the theory of gravity governing the growth of those perturbations. RSD have been measured using techniques based on both correlation functions and power-spectra (e.g. Peacock et al. 2001; Percival et al. 2004; Tegmark et al. 2006; Guzzo et al. 2008; Samushia et al. 2012; Samushia et al. 2013; Reid et al. 2010; Reid et al. 2012; Sánchez et al. 2012; Blake et al. 2010, 2011, 2012); the most recent analyses come from BOSS DR11 and GAMA (Samushia et al. 2014; Blake et al. 2013).

3.1 Formalism

RSD arise because we infer galaxy distances from their redshifts using the Hubble law: the radial component of the peculiar velocity of individual galaxies will contribute to each redshift and will be misinterpreted as being cosmological in origin, thus altering our estimate of the distances to them. The correction due to peculiar velocities can be used to set constraints on cosmological models and parameters, as it depends on the coherent large scale infall of matter toward overdense regions. The relation between the redshift-space position $\mathbf{s}$ and real-space position $\mathbf{r}$ is:

$$\mathbf{s}(\mathbf{r}) = \mathbf{r} + v_r(\mathbf{r})\hat{\mathbf{r}}, \tag{3.1}$$

PoS(AASKA14)031

where v_r is the velocity in the radial direction.

The Redshift-Space Distortions (RSD) corrections come from the fact that the real-space position of a source in the radial direction in modified by peculiar velocities due to local overdensities; this effect can be modeled as (Kaiser 1987; Hamilton 1997):

$$\delta^s(k) = \left(1+\beta\mu^2\right)\delta^r(k)\,, \tag{3.2}$$

where, in the linear regime, β is the quantity that solves the linearized continuity equation:

$$\beta\delta + \bar{\nabla}\cdot\bar{v} = 0\,. \tag{3.3}$$

Here $\beta = f/b$, where b is the bias relating the visible to the underlying matter distribution (see Section 3.3 for more details on it).

For this reason, measuring f from RSD allows us to set constraints on cosmological models and parameters.

3.2 The power spectrum

The matter power spectrum depends on a variety of cosmological parameters, and for this reason its measurement has been used (together with its Fourier transform, the correlation function) to constrain e.g. dark energy parameters (Samushia et al. 2012), models of gravity (Raccanelli et al. 2013), neutrino mass (de Putter et al. 2012; Zhao et al. 2012), dark matter models (Cyr-Racine et al. 2014; Dvorkin et al. 2014), the growth of structures (Samushia et al. 2013; Reid et al. 2012), and non-Gaussianity (Ross et al. 2013).

We define the power spectrum as:

$$P_g^s(k,\mu,z) = \left[b(z)+f(z)\mu^2\right]^2 P_m^r(k,z) + P_{shot}(z)\,, \tag{3.4}$$

where the superscripts ^{r} and ^{s} indicate real and redshift-space, respectively, and the subscripts $_m$ and $_g$ stands for matter and galaxies; μ is the angle with the line of sight. The shot noise contribution is taken to be:

$$P_{shot}(z) = \frac{1}{\bar{n}_g(z)}\,. \tag{3.5}$$

The standard analysis of RSD makes use of the so-called Kaiser formalism (Equation 3.4), that relies on several simplifying assumptions, including considering only the linear regime and the distant observer approximation; in Section 3.4 we briefly mention some possible extensions of this model. In this Chapter we will make use of the Kaiser formula, but for a detailed data analysis some further investigations will be needed.

3.3 Bias

While the distribution of galaxies is the observed quantity, the cosmological model directly predicts the statistical distribution of (dark) matter. The simplest assumption is that the galaxy distribution is a biased version of the underlying matter field, the so-called linear bias model, at position $\mathbf{x}$:

$$\delta_{\text{galaxies}}(\mathbf{x}) = b\,\delta_{\text{matter}}(\mathbf{x})\,, \tag{3.6}$$

PoS(AASKA14)031

with b a constant bias factor independent of a given smoothing scale R over which the density fields are calculated. This model is motivated by the fact that rare peaks in the density field (e.g. clusters of galaxies) have to be more strongly clustered (i.e. biased) than matter itself (e.g. Kaiser 1984). This is a simplifying assumption and the relationship between galaxies and matter is more complex: in fact, clustering properties of galaxies do depend on galaxies' intrinsic features. For example the relation could be scale-dependent, nonlinear, stochastic, non-local, a function of the particular sample of galaxies chosen, a function of cosmic time or dependent on many other physical quantities (such as the gas temperature, environment, merging history, etc.). Thus, the above equation can be generalized to a more complex form:

$$\delta_{\rm galaxies}(\mathbf{x}) = f(\delta_{\rm matter}(\mathbf{x}) + \varepsilon)\,, \tag{3.7}$$

with ε embedding all the dependencies on physical quantities other than dark matter density.

Currently, analytical efforts to model the bias are first attempting to model the halo-matter bias by relying on: the peak background split formalism in a coarse grained perturbation theory framework (e.g. Schmidt et al. 2013, and references therein); the excursion set approach also for non gaussian initial conditions as in Musso et al. (2012); perturbation theories (Bernardeau et al. 2001). Particular emphasis is also put on unveiling the scale dependence of the bias, out to the largest scales, that can be a powerful probe for testing initial conditions and/or the nature of gravity and it has been recently shown that also in the standard cosmological model (ΛCDM) the halo bias is scale dependent due to general relativitistic effects and not only to non-gaussianities (e.g. Baldauf et al. 2011).

A comprehensive analysis of halo bias is presented in Smith et al. (2006) by comparing the results of N-body simulations with semi-analytical prescriptions based on perturbation theory and the halo model, also relying on the cross-spectrum between matter and haloes. In the work above, it is shown that the non-linearities of the bias are determined not only by the non-linear evolution of the power spectrum but also by the fact that haloes of different masses are biased in a different way. In a recent study based on N-body simulations complemented by a galaxy formation model, Crocce et al. (2013) found a nearly scale independent bias at the level of $\sim 2-5$ % at scales larger than 20 Mpc$/h$ for a mock Luminous Red Galaxies sample.

Overall, simulations show that on scales larger than ≈ 30 Mpc/h the simplest linear parameterization works reasonably well, so for the purposes of this Chapter, we will assume the bias to be linear and constant at the scales of interests for SKA forecasts as in Equation 3.6; however, this assumption should be carefully tested in the future.

3.4 Beyond the Kaiser model

Equation 3.4 is valid only on linear scales, assumes the plane-parallel approximation and is derived using Newtonian physics; this approximation is valid when considering pair separations in a limited range of scales, large enough to avoid non-linear effect (i.e. $\gtrsim 30$ Mpc) and are relatively small (up to ~ 200 Mpc). If one wants to extend analyses of RSD to smaller and larger scales, there are modifications to the standard formalism to take into account.

PoS(AASKA14)031

3.4.1 Non-linearities

Within dark matter haloes, peculiar velocities of galaxies are highly non-linear, and these velocities can induce RSD that are larger than the real-space distance between galaxies within the halo. For this reason, on small scales we observe the so-called Fingers of God (FOG) effect – strong elongation of structures along the line of sight (Jackson 1972). This results in a damping of the power spectrum on small scales compared to the predictions of the linear model, and is usually modeled by multiplying the linear power-spectrum by a function $F(\sigma_v, k, \mu)$, where σ_v is the average velocity dispersion of galaxies within the relevant haloes.

Modeling of non-linearities has been investigated numerous times (e.g. Scoccimarro 2004; Taruya et al. 2009, 2010; Reid et al. 2010; Anselmi et al. 2010; Anselmi & Pietroni 2012; Kwan et al. 2011; Neyrinck et al. 2009, 2011; Jennings 2012; Carron & Szapudi 2013).

In this Chapter we look only at linear scales; extensions to the quasi- and non- linear regimes will help giving more constraining power, but they require investigations that are beyond the scope of this paper.

3.4.2 Large scale effects

When considering wide surveys and galaxy pairs with large separation, a more precise analysis involving wide-angle and GR corrections should be used (see e.g. Szalay et al. 1997; Matsubara 1999; Szapudi 2004; Papai & Szapudi 2008; Raccanelli et al. 2010; Samushia et al. 2012; Montanari & Durrer 2012; Bertacca et al. 2012; Raccanelli et al. 2013; Raccanelli et al. 2013a)). Moreover, on very large scales, the modeling for the power spectrum needs to take into account General Relativity (GR) effects general relativistic corrections will be important (see e.g. Yoo 2010; Bonvin & Durrer 2011; Challinor & Lewis 2011; Yoo et al. 2012; Jeong et al. 2011; Bertacca et al. 2012; Raccanelli et al. 2013b; Dio et al. 2014).

However, including wide-angle and GR corrections in the power spectrum is beyond the scope of this Chapter. A mode detailed analysis of large scale effects for the SKA is carried out in the SKA Chapter "Cosmology on the Largest Scales" (Camera et al. 2014).

3.5 Alcock-Paczynski Effect

Positions of galaxies are given in terms of angular positions and redshifts; angular diameter distances and Hubble expansion rates as functions of redshift are required in order to convert angular and redshift separations into physical distances. Those functions depend on the adopted cosmological model. If the real cosmology is significantly different from the fiducial one, this difference will introduce additional anisotropies in the correlation function through the Alcock-Paczynski effect. This can significantly bias the measurements of growth (see e.g. Ballinger et al. 1996; Simpson & Peacock 2010; Samushia et al. 2012; Montanari & Durrer 2012).

In the presence of Alcock-Paczynski effect, the redshift-space power-spectrum is:

$$P^{\rm s}(k', \mu', \alpha_\perp, \alpha_{||}, \mathbf{p}) = \frac{(b+\mu'^2 f)^2}{\alpha_\perp^2 \alpha_{||}} P^{\rm r}\left[\frac{k'}{\alpha_\perp}\sqrt{1+\mu'^2\left(\frac{1}{F^2}-1\right)}\right], \tag{3.8}$$

where $\mathbf{p}$ are standard cosmological parameters determining the shape of the real-space power-spectrum, k' and μ' are the observed wavevector and angle, related to the real quantities by $k'_{||} =$

PoS(AASKA14)031

$\alpha_{||}k_{||}$, $k'_{\perp} = \alpha_{\perp}k_{\perp}$, $\mu' = \frac{k'_{||}}{\sqrt{k'^2_{||}+k'^2_{\perp}}}$, where $F = \alpha_{||}/\alpha_{\perp}$, with $\alpha_{||}$ and $\alpha_{\perp}$ being the ratios of angular and radial distances between fiducial and real cosmologies, $\alpha_{||} = \frac{H^{\rm fid}}{H^{\rm real}}$, $\alpha_{\perp} = \frac{D^{\rm real}}{D^{\rm fid}}$.

Ignoring the AP effect is equivalent to assuming that α factors are equal to unity in Eq. (3.8).

4. SKA Surveys

The Square Kilometre Array (SKA) project is an international effort to build the world's largest radio telescope, several times more sensitive than any existing radio telescope and capable of addressing fundamental questions about the Universe (Carilli & Rawlings 2004). The SKA will be developed in two stages. The first stage currently encompasses two mid-frequency facilities ($\sim$ 1 GHz) operating within South Africa (SKA1-MID) and Australia (SKA1-SUR). A low frequency array (SKA1-LOW $\sim$ 100 MHz) will also be set in Australia. We refer to Dewdney et al. (2009) for a description of the setups. In the second stage of the SKA, the plan is to extend the array by about a factor of 10, both in collecting area and primary beam (field of view), thus significantly increasing the survey power of the facility. In the following sections, we consider two types of surveys that can be used to probe the redshift space distortions.

4.1 HI surveys

The most straightforward way to go after the RSD signal is through a line galaxy survey. In the radio, the solution is to use the HI 21cm line which, by measuring its characteristic shape, will allow determination of very accurate redshifts ($\delta z < 1.0 \times 10^{-4}$). The advantage of such threshold surveys is that we can be confident to be free of any foreground contamination. The disadvantage is that it requires high sensitivities to detect HI galaxies at non-local redshifts (the highest redshift HI galaxies detected up to date was at $z \sim 0.14$ with Arecibo (Freudling et al. 2011)).

Cosmological applications will require detecting enough galaxies to beat shot noise and over a large enough area to reduce cosmic variance. With the sensitivities for SKA1 and taking 10,000 hours of observation time, the optimal survey area will be around 5,000 deg^2. This will allow the detection of about 10^7 galaxies using band 2 from SKA1-MID or SKA1-SUR, while SKA1-MID band 1 should detect less galaxies ($\sim 10^4$) since it will be constrained to higher redshifts ($0.4 \lesssim z \lesssim 3$). SKA2, on the other hand, should be capable of detecting about 10^9 galaxies over a 30,000 deg^2 area, up to $z \sim 2.0$, making it the largest galaxy redshift survey ever. The noise calculations and parameters for this HI galaxy survey can be found in the HI simulations chapter (Santos et al. 2015a). In Figure 1 we plot the redshift distributions and bias for the different SKA configurations described above.

4.2 Late-time HI intensity mapping

A relatively new alternative to large galaxy redshift surveys is 21 cm *intensity mapping*. Galaxy surveys need high signal-to-noise detections of many millions of individual sources, requiring high flux sensitivity and long, dedicated surveys to reach $z \sim 1$. Intensity mapping (IM) attempts to circumvent these requirements by performing fast, low angular resolution surveys of the redshifted 21 cm emission line from neutral hydrogen (HI) integrated over many unresolved galaxies. For a more extensive discussion on HI intensity mapping, particularly in the context of

PoS(AASKA14)031

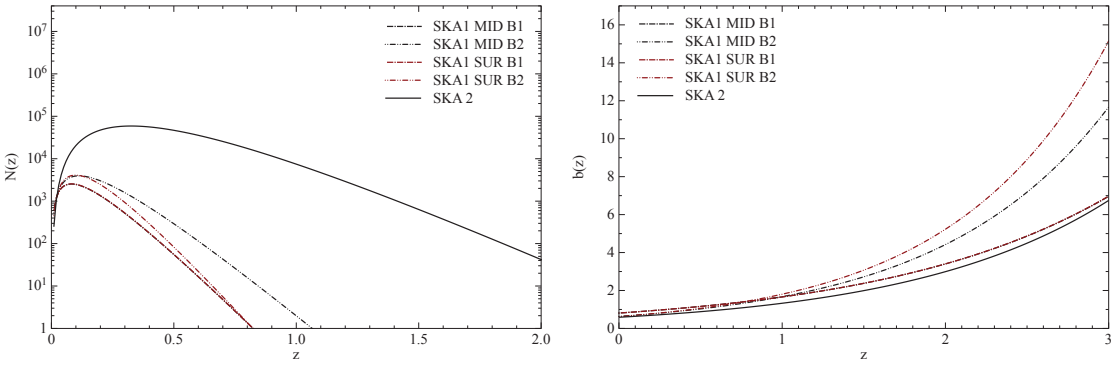

Figure 1: Redshift distributions (*left panel*) and bias (*right panel*) for the SKA1 and SKA2 surveys used in this work.

the SKA, we refer to Santos et al. (2015b). If we assume that, after reionisation, all the neutral hydrogen is contained within galaxies, as host galaxies are biased tracers of the cosmological large scale structure, so too is the integrated HI emission. Much of the cosmological information of interest (e.g. RSDs and BAOs) is found at large scales, so the lack of resolution is tolerable, and as the signal is from an emission line, redshift information is automatically provided as well. This allows large surveys to be performed extremely rapidly, efficiently recovering the 3D redshift-space matter power spectrum on large scales. An intensity mapping survey on SKA1-MID or SUR will be able to measure BAOs and RSDs over 25,000 deg^2 on the sky from $0 \lesssim z \lesssim 2.5$, for example (Santos et al. 2015b).

One way of thinking about an IM survey, then, is as a galaxy survey with the small angular scales averaged out. Information in the radial direction is mostly preserved, as modern radio receivers have sufficiently narrow frequency channel bandwidths that high redshift resolution can be obtained. The model for the RSD signal in intensity maps is therefore quite similar to that for a galaxy survey, except that the observable is the power spectrum of HI brightness temperature fluctuations, $\langle \delta T_b^* \delta T_b \rangle \propto T_b^2 P(\mathbf{k})$, where T_b is the mean HI brightness temperature. Note that the shot noise contribution has to be replaced by a more complicated direction-dependent noise term (see e.g. Bull et al. 2014b). In this chapter we will focus on the RSD constraints that can be achieved by measuring the anisotropic power spectrum with IM surveys on SKA1-MID and SUR. Our forecasts are for 10,000 hour autocorrelation surveys over 25,000 deg^2 on bands 1 and 2 of both arrays.

5. Forecast

In this Section we forecast the cosmological measurements that will be performed using the SKA using the configuration presented in Section 4; we present forecasts on parameters describing models for the growth of structures mentioned in Section 5.2.

5.1 Fisher Analysis

In order to predict the precision in the measurements of cosmological parameters, we perform a Fisher matrix analysis (Fisher 1935; Tegmark et al. 1997); we write the curvature or Fisher matrix

PoS(AASKA14)031

for the power spectrum in the following way:

$$F_{\alpha\beta} = \int_{z_{\rm min}}^{z_{\rm max}} dz \int_{k_{\rm min}}^{k_{\rm max}} dk \int_{-1}^{+1} d\mu \left[\frac{\bar{n}_g(z) P(k,\mu,z)}{1+\bar{n}_g(z) P(k,\mu,z)} \right]^2 \frac{V_s(z) k^2}{8\pi^2 \left[P(k,\mu,z)\right]^2} \frac{\partial P(k,\mu,z)}{\partial \vartheta_\alpha} \frac{\partial P(k,\mu,z)}{\partial \vartheta_\beta} B_{nl}\,, \tag{5.1}$$

where $\vartheta_{\alpha(\beta)}$ is the $\alpha(\beta)$-th cosmological parameter, V_s is the volume of the survey and $\bar{n}_g$ is the mean comoving number density of galaxies. The last term accounts for the non-linearities induced by the BAO peak (Seo & Eisenstein 2007):

$$B_{nl} = e^{-k^2\Sigma_\perp^2 - k^2\mu^2\left(\Sigma_{||}^2 - \Sigma_\perp^2\right)}, \tag{5.2}$$

and $\Sigma_\perp = \Sigma_0 D$, $\Sigma_{||} = \Sigma_0(1+f)D$, where Σ_0 is a constant phenomenologically describing the nonlinear diffusion of the BAO peak due to nonlinear evolution. From N-body simulations its numerical value is 12.4 h^{-1}Mpc and seems to depend linearly on σ_8, but only weakly on k and cosmological parameters. The integral in k is performed in each redshift bin using (Smith et al. 2003):

$$k_{\rm min} = \frac{2\pi}{V_{\rm bin}^{1/3}}\,; \tag{5.3}$$

$$k_{\rm max} = k_{\rm NL,0}(1+z)^{2/(2+n_s)}\,. \tag{5.4}$$

In the rest of this Section we present the models we investigate: we focus on ways to explain the cosmic acceleration, either via dynamical dark energy or modifications of the model for gravity.

5.2 Growth of structures

We study how the SKA could constrain parameters describing the growth of structures. There are several models for it based on different explanations for the accelerated expansion of the Universe; they can be divided into two main categories: dark energy and modified growth. Measuring RSD allows us to test different cosmological models and provides a good discriminant between modified gravity and dark energy models (see e.g. Linder 2005, 2007; Guzzo et al. 2008).

5.2.1 Dark Energy Models

In the standard ΛCDM model, the accelerated expansion of the universe is caused by a dark energy component that behaves like a cosmological constant, but alternative models have been proposed and are still allowed by data.

Dynamical models can be distinguished from the cosmological constant by considering the evolution of the equation of state of dark energy, $w = p/\rho$, where p and ρ are the pressure density and energy density of the fluid, respectively. In the cosmological constant model, $w = -1$, while for dynamical models $w = w(a)$. It is the useful to consider a Taylor expansion of the equation of state (Linder 2003):

$$w(a) = w_0 + w_a(1-a)\,; \tag{5.5}$$

in the ΛCDM model we have $w_0 = -1$ and $w_a = 0$. If a deviation from these values will be detected (in particular if $w_a \neq 0$), then this would suggest that the correct model is one where the dark energy component of the universe is evolving with time.

PoS(AASKA14)031

In Figure 2 we plot constraints on the parameters $\{w_0, w_a\}$ (including Planck+BOSS priors), for the different SKA1 and SKA2 surveys, comparing results with predictions for the Euclid experiment.

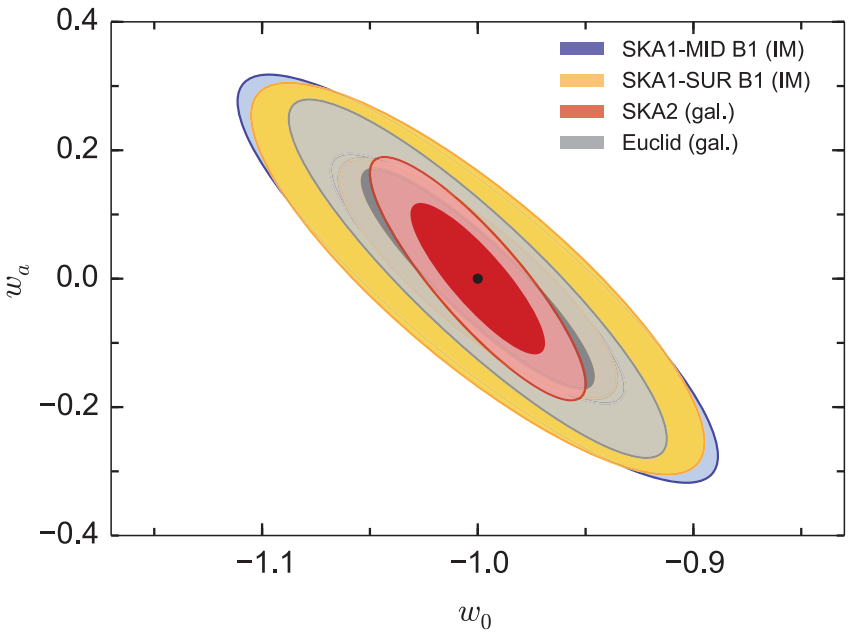

Figure 2: Predicted constraints from SKA on dynamical dark energy parameters. We show predicted constraints from SKA IM and SKA2, compared with predictions for Euclid.

SKA1 HI surveys will not be able to provide competitive constraints on these parameters, so we don't show them, but results form the IM surveys will be competitive, and the SKA2 galaxy survey should be able to allow improvements on measurements of dynamical dark energy parameters over the predicted Euclid galaxy survey.

5.2.2 Modified Growth Models

Measuring the matter velocity field at the locations of the galaxies gives an unbiased measurement of $f\sigma_{8\mathrm{m}}$, provided that the distribution of galaxies randomly samples matter velocities, where f is given by Equation 2.1 and $\sigma_{8\mathrm{m}}$ quantifies the amplitude of fluctuations in the matter density field. The growth factor is sometimes parameterized as (Linder 2005):

$$D(a) = a \exp\left[\int_0^a \left[\Omega_m^\gamma(a') - 1\right] \frac{da'}{a'}\right], \tag{5.6}$$

which leads to the following expression for f:

$$f = [\Omega_m(a)]^\gamma, \tag{5.7}$$

where:

$$\Omega_m(a) = \frac{\Omega_m a^{-3}}{\sum_i \Omega_i \exp\left[3\int_a^1 [w_i(a') + 1]\frac{da'}{a'}\right]}, \tag{5.8}$$

PoS(AASKA14)031

where the summation index goes over all the components of the Universe (i.e. dark matter, dark energy, curvature, radiation). Within this formalism, γ is a parameter that is different for different cosmological models: for example, in the standard ΛCDM+GR model it is constant, $\gamma \approx 0.55$, while it is ≈ 0.68 for the self-accelerating DGP model (see e.g. Linder 2005). In some other cases, it is a function of the cosmological parameters or redshift (see e.g. Raccanelli et al. 2013). It should be noted, however, that the parameterization given by Equation 5.6 does not necessarily describe the growth rate in non-standard cosmologies (see e.g. Schmidt 2009).

In this paragraph we study how the SKA will be able to constrain the growth of structures in two different cases; we investigate constraints on the growth of structures for models with:

- **Parameterized growth**:
  $\{\mathrm{h}, \Omega_\lambda, \Omega_\mathrm{K}, \Omega_\mathrm{m}, \Omega_\mathrm{b}, \mathrm{n_s}, \mathrm{w_0}, \mathrm{w_a}, \sigma_8, \mathrm{b}, \gamma, \mathrm{f_{NL}}\}$

  For the parameterized case we assume a model for the redshift evolution of f, the bias and σ_8 (and assume we have some independent measurements of them from e.g. the CMB), and we constrain the growth rate parameter γ. Our results show that, while predictions for SKA1 HI galaxies are not competitive, the IM case is competitive with current optical surveys and comparable to future surveys such as Euclid. Constraints coming from the SKA2 galaxy survey are predicted to considerably improve forecasted results from Euclid.

  In Figure 3 we plot constraints on the growth rate parameter γ and the effective w_0 (including Planck+BOSS priors) for some SKA1 IM surveys and for the SKA2, comparing results with predictions for Euclid.

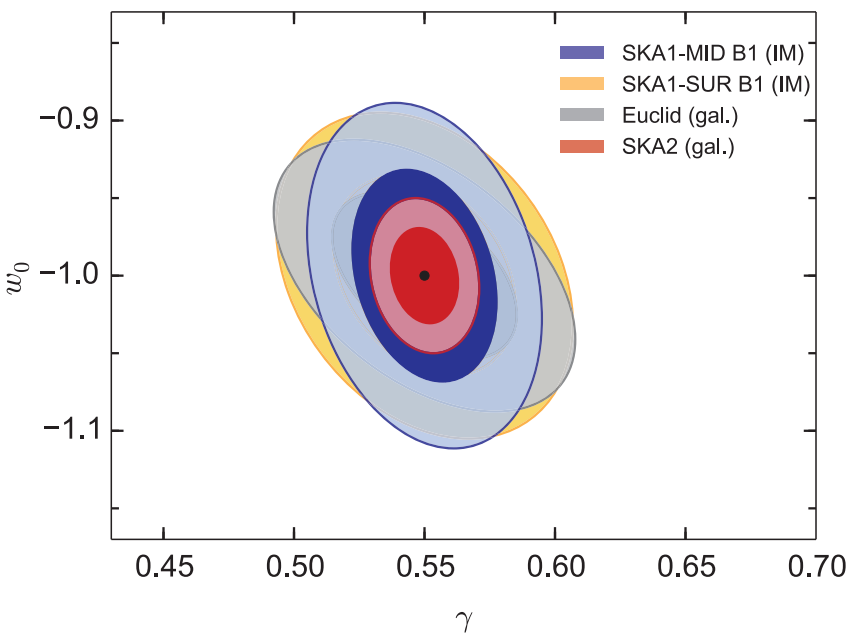

Figure 3: Predicted constraints from SKA on parameterized growth. We show predicted constraints from SKA IM and the SKA2, compared with predictions for Euclid.

- **Unparameterized growth function**:

PoS (AASKA14) 031

$\{h, \Omega_\lambda, \Omega_K, \Omega_m, \Omega_b, n_s, w_0, w_a, f\sigma_8, b\sigma_8\}$

In this case we assume we have no prior knowledge on the above parameters, and we constrain the combination $\{f\sigma_8, b\sigma_8\}$.

Again our predictions show that SKA1 HI galaxy surveys are not competitive, while the IM case is competitive with current optical surveys and comparable to future surveys such as Euclid, at low redshift. Constraints coming from the SKA2 galaxy survey are predicted to be the best ones at low-z and comparable to Euclid at medium z. This can be seen in Figure 4, where we plot constraints on the fractional precision on measurements of $f\sigma_8$ in different redshift bins.

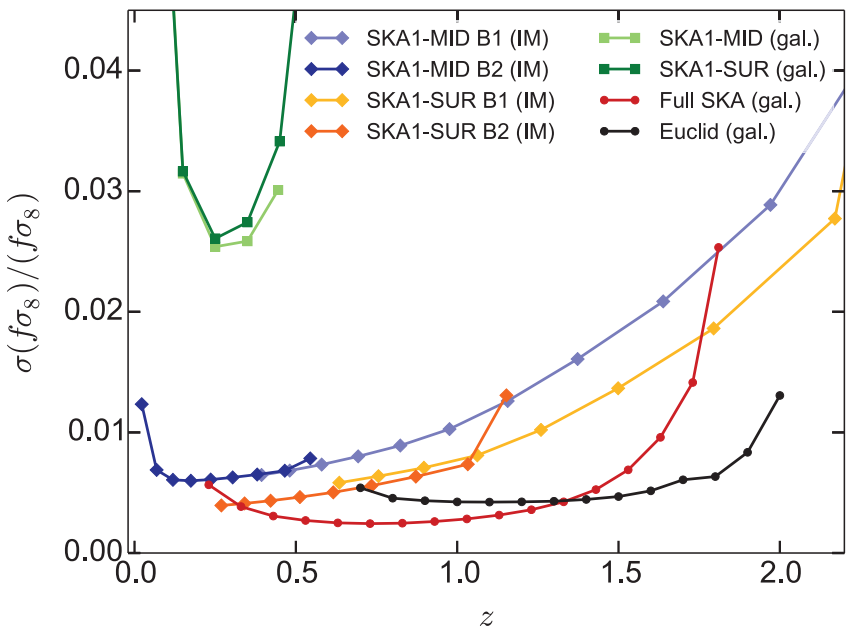

Figure 4: Predicted constraints from SKA on $f\sigma_8$ from the SKA1 (galaxy and IM) and the SKA2, compared with predicted constraints coming from the Euclid galaxy survey.

6. Discussion

In this Chapter we presented forecasts for the measurements on the growth that will be possible to obtain by measuring the full shape of the galaxy power spectrum with the SKA. We investigated how the different proposed SKA1 (both in the IM and HI cases) and SKA2 surveys will enable measurements of parameters describing models for the growth of structures.

In all cases analyzed, our results show that the SKA1 HI surveys will not be competitive with future galaxy surveys on the same time-scale. However, the IM case will give constraints, at low-z, at the same level of constraints provided from Euclid at medium-z. SKA2, on the other hand, should provide the best constraints on low-redshift, and constraints that are comparable to the predicted Euclid ones up to redshift $\sim$1.5.

In this work we haven't considered systematic effects that could bias the measurements and decrease their precision; on the other hand, in our results we haven't included a proper modeling

PoS(AASKA14)031

of non-linear effects, which would allow including many more modes, nor a modeling of the ultra-large-scale effects. Both would improve the constraining power of galaxy clustering measurements. Further improvements could be enabled by the use of the so-called multi-tracer technique. Another technique that will be worth investigating derives from measuring peculiar velocities of galaxies using the Tully-Fisher relation.

Overall our results show that the SKA promises to provide the best constraints on models for the growth for the next generation of galaxy surveys.

References

Anselmi, S., Matarrese, S., & Pietroni, M. 2010, arXiv:1011.4477
Anselmi, S. & Pietroni, M. 2012, arXiv:1205.2235
Baker, T., Ferreira, P. G., Skordis, C., & Zuntz, J. 2011, Phys. Rev. D, 84, 124018
Baldauf, T., Seljak, U., Senatore, L., & Zaldarriaga, M. 2011, arXiv:1106.5507
Ballinger, W. E., Peacock, J. A., & Heavens, A. F. 1996, astro-ph/9605017
Bernardeau, F., Colombi, S., Gaztañaga, E., & Scoccimarro, R. 2001, arXiv.org, 1
Bertacca, D., Maartens, R., Raccanelli, A., & Clarkson, C. 2012, JCAP10(2012)025
Blake, C. *et al.* . 2013, arXiv:1309.5556
—. 2012, arXiv:1204.3674
—. 2011, arXiv:1104.2948
—. 2010, arXiv:1003.5721
Bonvin, C. & Durrer, R. 2011, Phys.Rev.D, 84, 063505
Brans, C. H. 2000, arXiv:0506063
Bull, P., Camera, S., Raccanelli, A., Blake, C., Ferreira, P. G., Santos, M. G., & Schwarz, D. J. 2014a
Bull, P., Ferreira, P. G., Patel, P., & Santos, M. G. 2014b, arXiv:1405.1452
Camera, S. *et al.* . 2014
Camera, S., Santos, M. G., Bacon, D. J., Jarvis, M. J., McAlpine, K., Norris, R. P., Raccanelli, A., & Röttgering, H. 2012, MNRAS, 427, 2079
Carilli, C. L. & Rawlings, S. 2004, New Astron.Rev.
Carroll, S. M., Duvvuri, V., Trodden, M., & Turner, M. S. 2004, Phys.Rev.D, 70, 043528
Carron, J. & Szapudi, I. 2013, arXiv: 1306.1230
Challinor, A. & Lewis, A. 2011, Phys.Rev.D, 84, 043516
Crocce, M., Castander, F. J., Gaztanaga, E., Fosalba, P., & Carretero, J. 2013, arXiv:1312.2013
Cyr-Racine, F.-Y., de Putter, R., Raccanelli, A., & Sigurdson, K. 2014, Phys. Rev. D, 89, 063517
de Putter, R. *et al.* . 2012, arXiv:1201.1909
Dewdney, P., Hall, P., Schilizzi, R., & Lazio, J. 2009, Proceedings of the IEEE, 97
Dio, E. D., Montanari, F., Durrer, R., & Lesgourgues, J. 2014, JCAP, 01, 042
Dvali, G., Gabadadze, G., & Porrati, M. 2000, Phys.Lett., B484, 112
Dvorkin, C., Blum, K., & Kamionkowski, M. 2014, Phys.Rev.D, 89, 023519
Fisher, R. A. 1935, J. Roy. Stat. Soc., 98
Freudling, W., Staveley-Smith, L., Catinella, B., Minchin, R., Calabretta, M., Momjian, E., Zwaan, M., Meyer, M., & O'Neil, K. 2011, APJ, 727, 40

PoS(AASKA14)031

Guzzo, L. *et al.* . 2008, Nature, 451, 541
Hamilton, A. J. S. 1997, astro-ph/9708102, astro-ph
Jackson, C. J. 1972, MNRAS, 156
Jain, B. & Zhang, P. 2008, Phys.Rev.D, 78, 063503
Jennings, E. 2012, 2012MNRAS.427L..25J
Jeong, D., Schmidt, F., & Hirata, C. M. 2011, 2012, PRD 85, 023504
Johnston, S. *et al.* . 2008, arXiv:0810.5187
Kaiser, N. 1984, Astrophysical Journal, 284, L9
—. 1987, Royal Astronomical Society, 227, 1
Kwan, J., Lewis, G. F., & Linder, E. V. 2011, ApJ, 2012, 748, 78
Linder, E. V. 2003, Physical Review Letters, 90, 91301
—. 2005, astro-ph/0507263, astro-ph
—. 2007, arXiv:0709.1113, astro-ph
Matsubara, T. 1999, astro-ph/9908056
Montanari, F. & Durrer, R. 2012, Phys. Rev., D86, 063503
Musso, M., Paranjape, A., & Sheth, R. K. 2012, Monthly Notices of the Royal Astronomical Society, 427, 3145
Neyrinck, M. C., Szapudi, I., & Szalay, A. S. 2009, Astrophys.J., 698, L90
—. 2011, Astrophys. J., 731, 116
Nolta, M. R. *et al.* . 2004, Astrophys.J., 608, 10
Papai, P. & Szapudi, I. 2008, arXiv:0802.2940, astro-ph
Peacock, J. A. *et al.* . 2001, Deep Fields: Proceedings of the ESO Workshop Held at Garching, 221, iSBN: 3-540-42799-6 (c) 2001: Springer-Verlag
Percival, W. J. *et al.* . 2004, Monthly Notices of the Royal Astronomical Society, 353, 1201
Raccanelli, A., Bertacca, D., Dore, O., & Maartens, R. 2013a, arXiv:1306.6646
Raccanelli, A., Bertacca, D., Maartens, R., Clarkson, C., & Doré, O. 2013b, arXiv:1311.6813
Raccanelli, A., Bertacca, D., Pietrobon, D., Schmidt, F., Samushia, L., Bartolo, N., Doré, O., Matarrese, S., & Percival, W. J. 2013, MNRAS
Raccanelli, A., Bonaldi, A., Negrello, M., Matarrese, S., Tormen, G., & Zotti, G. D. 2008, Mon.Not.Roy.Astron.Soc., 386, 2161
Raccanelli, A. *et al.* . 2015, arXiv:1406.0010
Raccanelli, A., Samushia, L., & Percival, W. J. 2010, MNRAS, 409, 1525
Raccanelli, A. *et al.* . 2012, MNRAS, 424
Reid, B. A. *et al.* . 2010, MNRAS, 404, 60
Reid, B. A. *et al.* . 2012, arXiv:1203.6641
Ross, A. J. *et al.* . 2013, MNRAS, 428, 1116
Rottgering, H. *et al.* . 2011, arXiv:1107.1606
Samushia, L., Percival, W. J., & Raccanelli, A. 2012, MNRAS, 420, 2102
Samushia, L. *et al.* . 2013, Monthly Notices of the Royal Astronomical Society, Volume 429, Issue, 2, p.1514
—. 2014, Monthly Notices of the Royal Astronomical Society, Volume 439, Issue, 4, p.3504
Sánchez, A. G. *et al.* . 2012, MNRAS, 425, 415
Santos, M., Silva, M., & Yahya, S. 2015a

PoS(AASKA14)031

Santos, M. *et al.* . 2015b
Schmidt, F. 2009, Phys.Rev.D, 80, 123003
Schmidt, F., Jeong, D., & Desjacques, V. 2013, Physical Review D, 88, 23515
Scoccimarro, R. 2004, astro-ph/0407214, astro-ph
Seo, H.-J. & Eisenstein, D. J. 2007, Astrophys.J., 665, 14
Simpson, F. & Peacock, J. A. 2010, Phys Rev D,, 81, 043512
Smith, R. *et al.* . 2003, Mon.Not.Roy.Astron.Soc., 341, 1311
Smith, R. E., Scoccimarro, R., & Sheth, R. K. 2006, astro-ph/0609547
Song, Y.-S. & Koyama, K. 2008, arXiv:0802.3897, astro-ph
Song, Y.-S. & Percival, W. J. 2008, arXiv:0807.0810, astro-ph
Szalay, A. S., Matsubara, T., & Landy, S. D. 1997, astro-ph/9712007, astro-ph
Szapudi, I. 2004, The Astrophysical Journal, 614, 51
Taruya, A., Nishimichi, T., & Saito, S. 2010, arXiv:1006.0699
Taruya, A., Nishimichi, T., Saito, S., & Hiramatsu, T. 2009, arXiv:0906.0507
Tegmark, M. *et al.* . 2006, Phys.Rev.D, 74, 123507
Tegmark, M., Taylor, A., & Heavens, A. 1997, Astrophys.J., 480, 22
Xia, J.-Q., Viel, M., Baccigalupi, C., Zotti, G. D., Matarrese, S., & Verde, L. 2010, Astrophys. J., 717, L17
Yamamoto, K., Nakamura, G., Huetsi, G., Narikawa, T., & Sato, T. 2010, Phys.Rev.D, 81, 103517
Yamamoto, K., Sato, T., & Huetsi, G. 2008, Prog.Theor.Phys., 120, 609
Yoo, J. 2010, Phys.Rev.D, 82, 083508
Yoo, J., Hamaus, N., Seljak, U., & Zaldarriaga, M. 2012, Phys.Rev.D, 86, 063514
Zhao, G.-B. *et al.* . 2012, arXiv:1211.3741

PoS(AASKA14)031

PROCEEDINGS OF SCIENCE

Testing foundations of modern cosmology with SKA all-sky surveys

Dominik J. Schwarz[*,1] **David Bacon**,[2] **Song Chen**,[1] **Chris Clarkson**,[3] **Dragan Huterer**,[4] **Martin Kunz**,[5,6] **Roy Maartens**,[7,2] **Alvise Raccanelli**,[8,9,10] **Matthias Rubart**,[1] **Jean-Luc Starck**[11]

[1] *Fakultät für Physik, Universität Bielefeld, 33501 Bielefeld, Germany;* [2] *Institute of Cosmology & Gravitation, University of Portsmouth, Portsmouth PO1 3FX, United Kingdom;* [3] *Centre for Astrophysics, Cosmology & Gravitation and Department of Mathematics & Applied Mathematics, University of Cape Town, Cape Town 7701, South Africa;* [4] *Department of Physics, University of Michigan, Ann Arbor, MI 48109-1040, USA;* [5] *Université de Genève, Département de Physique Théorique and CAP, CH-1211 Genève 4, Switzerland;* [6] *African Institute for Mathematical Sciences, Cape Town 7945, South Africa;* [7] *Physics Department, University of the Western Cape, Cape Town 7535, South Africa;* [8] *Jet Propulsion Laboratory, California Institute of Technology, Pasadena CA 91109, USA;* [9] *California Institute of Technology, Pasadena CA 91125, USA;* [10] *Department of Physics & Astronomy, Johns Hopkins University, 3400 N. Charles St., Baltimore, MD 21218, USA* [11] *Laboratoire AIM, UMR CEA-CNRS-Paris, Irfu, SAp, CEA Saclay, F-91191 Gif-sur-Yvette CEDEX, France*

E-mail: dschwarz@physik.uni-bielefeld.de

Continuum and HI surveys with the Square Kilometre Array (SKA) will allow us to probe some of the most fundamental assumptions of modern cosmology, including the Cosmological Principle. SKA all-sky surveys will map an enormous slice of space-time and reveal cosmology at super-horizon scales and redshifts of order unity. We illustrate the potential of these surveys and discuss the prospects to measure the cosmic radio dipole at high fidelity. We outline several potentially transformational tests of cosmology to be carried out by means of SKA all-sky surveys.

Advancing Astrophysics with the Square Kilometre Array
June 8-13, 2014
Giardini Naxos, Italy

[*]Speaker.

PoS(AASKA14)032

1. Introduction

The Square Kilometre Array (SKA) will allow us to test fundamental assumptions of modern cosmology at redshifts of order unity and at an accuracy level matching and complementing the high fidelity observations of the cosmic microwave background (CMB).

The Cosmological Principle states that the Universe is spatially isotropic and homogeneous. This holds on sufficiently large scales and needs to be interpreted in a statistical sense. Historically, it provided a very powerful motivation to single out the Friedmann-Lemaître models despite a lack of knowledge regarding the initial conditions of the Universe. Cosmological inflation, proposed in the 1980s, allowed the Universe to start from a reasonably small patch of almost homogeneous and isotropic space. According to the idea of cosmological inflation, suddenly at least one small patch is inflated to contain today's observable Universe. In the course of inflation, any previously existing anisotropy or inhomogeneity is exponentially diluted. However, unavoidable quantum fluctuations are squeezed by the rapid expansion during inflation and become the seeds for large scale structure. The result is a statistically isotropic and homogeneous Universe (at least locally).

These ideas are confirmed by the observed high degree of isotropy of CMB radiation, which enables us to define a CMB frame by measuring a temperature monopole, $T_0 = 2.2755 \pm 0.0006\,\mathrm{K}$ and dipole, $T_1 = 3.355 \pm 0.008\,\mathrm{mK}$ towards $(l,b) = (263.99^\circ \pm 0.14^\circ, 48.26^\circ \pm 0.03^\circ)$ (Hinshaw et al. 2009). The concept of a spatially homogeneous Universe allows us to speak about a cosmic time or an age of the Universe. By measuring the CMB temperature T_0 and the present expansion rate of the Universe H_0 we can anchor the thermal history of the Universe to its expansion history.

Radio surveys played an important role to establish that the Universe extends to redshifts beyond unity and that it is almost isotropic [see e.g. Ryle & Clarke (1961)]. Today, observations of the CMB confirm the predictions of cosmological inflation impressively (Planck collaboration 2014a; 2014b). However, it is unknown for how long (or how many e-foldings) inflation took place. In order to explain the observed spatial flatness of the Universe, about 50 to 60 e-foldings could be enough, but in many models it took much longer, i.e. the domain in which the statistical cosmological principle applies is expected to be much larger than the observable Universe. The quest to determine the duration of inflation, as well as the related question of the topology of the Universe, can only be answered by observing the biggest scales.

Interestingly enough, the CMB exhibits unexpected features at the largest angular scales, among them a lack of angular correlation, alignments between the dipole, quadrupole and octupole, hemispherical asymmetry, a dipolar power modulation, and parity asymmetries (Planck collaboration 2014c; Copi et al. 2013a; 2013b). Understanding the statistical significance of these anomalies is a hot topic (Bennett et al. 2013; Starck et al. 2013; Rassat et al. 2014) since lack of statistical isotropy or Gaussianity could rule out the standard cosmological model. As the precision of these CMB measurements is limited by our understanding of the foregrounds and observational uncertainties are already much smaller than the cosmic variance at those scales, it is very hard to identify the cause of these anomalies without an independent probe at the same scales.

However, based on the observed CMB anisotropies and despite of these anomalies, deviations from statistical isotropy have to be small. The observational situation is less clear for the case of statistical homogeneity, as testing the assumption of isotropy is much simpler than testing homogeneity (Maartens 2011; Clarkson 2012).

PoS(AASKA14)032

SKA will probe an enormous number of independent modes when studying the large-scale structure of the Universe and will measure superhorizon sized modes at redshifts of order unity (better than any existing or planned infrared, optical, or X-ray campaign). This will enable us to probe scales that have not been in causal contact since the first horizon crossing during inflation and that contain information that was frozen in during cosmological inflation. In contrast to the CMB, the radio sky provides a probe of those largest scales at a redshift of order unity (2D for continuum surveys and 3D for HI surveys).

SKA would enable several tests of the fundamental cosmological principles. For example, the rest frames of the CMB and large scale structure (LSS) may not coincide due to novel superhorizon physics — for example, presence of isocurvature modes (Erickcek et al. 2008). SKA's width and depth will enable a measurement of the kinematic dipole with respect to the LSS reference frame via the relativistic aberration and Doppler shift ("bunching up" of SKA sources in the direction of the dipole). This, when combined with the CMB's own measurement of the kinematic dipole would, for the first time, enable the test of whether the two reference frames — that of the CMB and the LSS — are one and the same, as demanded by the Cosmological Principle.

Here we describe how to use all-sky (3π) SKA continuum surveys to test statistical isotropy and to measure the cosmic dipole and other low-ℓ multipole moments. These issues are tightly connected to tests of non-Gaussianity and the topology of the Universe, the former aspect is described in Camera et al. (2015). All-sky SKA HI threshold surveys will additionally allow us to test the homogeneity of the Universe at superhorizon scales – a test that has never before been performed. Statistical homogeneity and isotropy are assumed to hold true in other cosmology-related contributions to this book (Bull et al. 2015; Raccanelli et al. 2015). Tests of statistical isotropy and homogeneity will also allow (and force) us to dig deep into the systematics of SKA surveys and thus help to put all cosmological and non-cosmological results of SKA surveys on firm grounds.

The conceptually simplest probe of cosmology is differential number counts (de Zotti et al. 2010). If no redshift information is available, one can count the number of (extragalactic) radio sources per solid angle and flux density. Besides flux calibration issues, the cosmological information contained in differential number counts is limited by the diversity of radio sources and their luminosity and density evolution. Radio sources fall into two principal classes, active galactic nuclei (AGN) and star forming galaxies (SFG). The exquisite angular resolution of SKA surveys will allow us to resolve most of the AGNs and thus to obtain an extra handle based on morphology. Another possibility to overcome the restrictions from evolution is to study the directional fluctuations of differential number counts (Raccanelli et al. 2012; Chen & Schwarz 2014), as we do not expect that the properties of radio sources would single out preferred directions in the Universe.

All SKA forecasts presented in this work assume the baseline design and imaging capabilities as presented in Dewdney et al. (2013); Braun (2014).

2. Cosmic radio dipole (Early Science, SKA1 & SKA2)

The CMB dipole is generally assumed to be due to our peculiar motion and thus defines a cosmic reference frame. However, the observation of the dipole in the microwave sky alone does not allow us to tell the difference between a motion-induced CMB dipole and dipole contributions from other physical phenomena [e.g. the model in Erickcek et al. (2008)].

PoS(AASKA14)032

SKA 3π surveys (centr. frequency, ang. res.)	Early Science	SKA1	SKA2
LOW (151 MHz, 10")	1.0×10^8 (20 μJy)	2.4×10^8 (10 μJy)	2.2×10^9 (1 μJy)
MID/SUR B1 (610 MHz, 1")	7.8×10^7 (10 μJy)	1.9×10^8 (5 μJy)	1.8×10^9 (0.5 μJy)
MID/SUR B2 (1.4 GHz, 0.5")	3.8×10^7 (10 μJy)	9.7×10^7 (5 μJy)	1.2×10^9 (0.5 μJy)

Table 1: Expected total number of radio sources (10 σ) in various frequency bands and survey instruments, assuming the SKA baseline design and the cosmology and differential number counts as simulated in Wilman et al. (2008). In order to match observations at 1.4 GHz, the number of SFG has been multiplied by a factor of 2.5 compared to the simulations for all frequency bands. The numbers in brackets denote the assumed rms noise levels.

Due to the effects of aberration and Doppler shift, the kinetic dipole must also be present in radio observations (Ellis & Baldwin 1984). Besides the kinetic dipole, we also expect contributions from the large-scale structure and from Poisson noise. Such a radio dipole has been looked for in radio source catalogues, such as NVSS (Blake & Wall 2002; Singal 2011; Gibelyou & Huterer 2012; Rubart & Schwarz 2013) and WENSS (Rubart & Schwarz 2013) and was found within large error bars. While the direction of the observed radio dipole is consistent with the CMB dipole direction, its amplitude exceeds the theoretical expectations by a factor of a few. SKA will enable us to measure the radio dipole with high accuracy and to extract other low-ℓ multipole moments. Recently, the Planck mission reported a first detection of the effects of aberration and Doppler shift at high multipole moments (Planck collaboration 2014d). However, this observation is less precise than the reported measurements of the radio dipole and allows for a primordial contribution to the CMB dipole of comparable size.

The SKA will allow us to compare $\vec{d}_{\rm radio}$ to $\vec{d}_{\rm cmb}$, since SKA will test a super-horizon sized volume. Any statistically significant deviation will be exciting, while finding a match would put the concordance model on firmer grounds.

SKA continuum surveys at low frequencies ($< 1\,$GHz) should be ideal to probe the cosmic radio dipole already in the Early Science phase for two reasons. First, it is not necessary to cover the full area of the 3π surveys, since a sparse sampling spread out over all of the accessible sky should be sufficient for a first estimate. And second, a focus on low frequencies and bright sources will pick primarily AGNs which have a much higher mean redshift than the SFG.

Figure 1 illustrates the accuracy that we can hope to achieve for a measurement of the radio dipole based on a linear estimator (Crawford 2009; Rubart & Schwarz 2013). Our estimates are based on differential number counts from surveys in small and deep fields and simulations (Wilman et al. 2008). Our expectations for all-sky continuum surveys are summarized in Table 1. We find that the cosmic radio dipole can be measured at high statistical significance, even taking realistic data cuts into account (e.g. masking the galaxy and very bright extragalactic sources, or morphology, spectral index or flux cuts).

A major concern might be the effect of flux calibration errors on the dipole estimation. This has been studied by means of simulations. The results of this study are shown in figure 2. We assume Gaussian flux density errors with variance $\sigma(\delta)S$, where S denotes the expected flux density of a particular source and δ its declination. We consider the isotropic case in which $\sigma(\delta) = \sigma$ is isotropic and a declination dependent situation with $\sigma(\delta) = \sigma/\cos(\delta - \delta_*)$, δ_* being fixed by

PoS(AASKA14)032

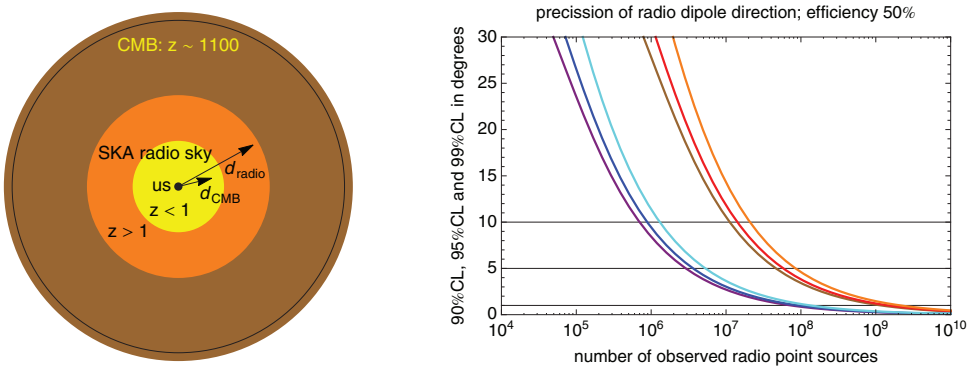

Figure 1: *Left:* All-sky (3π) SKA surveys (yellow and orange) will measure the cosmic radio dipole of differential source counts. Selecting AGNs will result in a sample with median redshift $z > 1$ (orange) and thus allow us to measure the peculiar velocity of the solar system with respect to the large scale structure on superhorizon scales. These measurements will be compared to the CMB dipole and thus test for the existence of a bulk flow of our Hubble volume compared to the CMB rest frame. *Right:* Angular accuracy at 90, 95 and 99 % C.L. of the measurement of the cosmic radio dipole as a function of observed point sources. The blue set of curves assumes $d_{\rm radio} = 4d_{\rm cmb}$, the red set assumes $d_{\rm radio} = d_{\rm cmb}$. It is assumed that only 50% of all detected radio sources survive all quality cuts (e.g. masking fields that contain very bright sources). Combined with Table 1 we find that SKA Early Science allows detection of a possible deviation from the CMB expectation at high significance. SKA1 will constrain the cosmic radio dipole direction with an accuracy better than 5 degrees, SKA2 within a degree (at 99% C.L.).

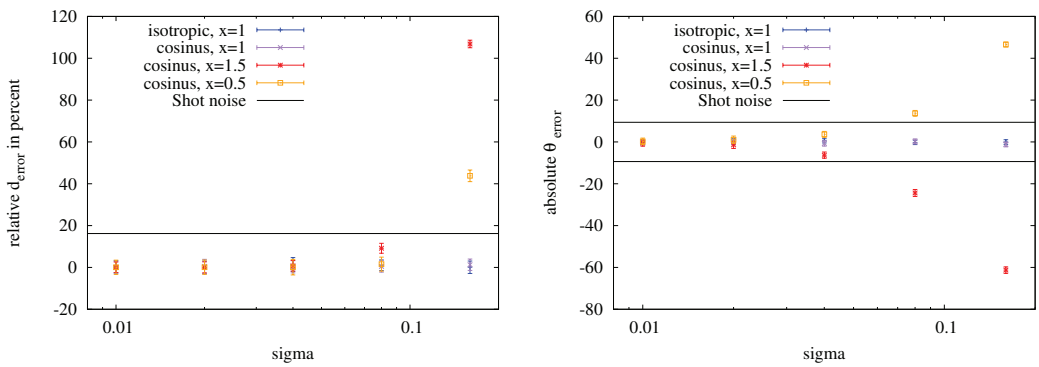

Figure 2: *Left:* Accuracy (in per cent) of the measurement of the dipole amplitude as function of fractional error on flux density calibration on individual point sources. All points are based on 100 simulations. *Right:* Accuracy (in degrees) of the measurement of the dipole direction. The horizontal lines denote the error due to shot noise for a dipole estimate based on 10^7 sources (SKA Early Science).

the latitude of the SKA site and $|\delta - \delta_*| < 70$ deg. For two cases we find negligible influence of calibration errors: If the flux calibration error is completely isotropic or if the slope x of the number counts $[N(>S) \propto S^{-x}]$ is equal to one. It turns out that $x = 1$ is a special value, where calibration errors at the lower flux density limit have no influence on the dipole estimator. We conclude that direction dependent calibration effects must not exceed certain limits as shown figure 2.

Another significant contaminant of the kinetic radio dipole is the local structure dipole. We can turn a disadvantage of continuum surveys, namely that we observe several source populations, into an advantage as follows: The lower mean redshift of SFGs compared to AGNs allows us to change

PoS(AASKA14)032

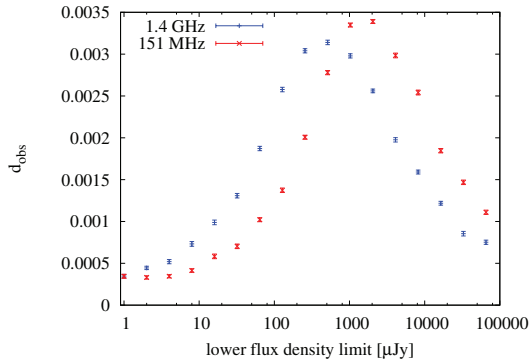

Figure 3: Amplitude of structure dipole due to a local void, affecting the measurements of the cosmic radio dipole as a function of lower flux density limit and for two wavebands centered on 151 MHz and 1.4 GHz (from Rubart et al. (2014)).

the mean depth of the survey by scanning different fluxes density limits and frequencies. This in fact allows for a tomographic survey of the radio dipole. For the example of a huge ($\sim$ 100 Mpc) local void this was studied recently (Rubart et al. 2014). Figure 3 illustrates this effect.

3. Large angular scales (SKA1 & SKA2)

It is not obvious that the isotropic distribution of light implies also the isotropy of space-time itself. The vanishing of the quadrupole and octopole moments of the CMB would imply the isotropy of space-time along the world line of the observer (Maartens 2011). While those low-ℓ multipoles are small compared to the monopole and dipole, they do not vanish exactly. We thus we can at best speak about an almost isotropic Universe. The radio sky offers another independent probe at $z > 1$ and at the largest angular scales.

Recent work has revealed the existence of CMB “anomalies" [for a review, see Copi et al. (2010)]. In brief, the angular correlation function in the WMAP and Planck temperature maps vanishes on scales larger than 60 degrees, contrary to theoretical expectation; moreover, the CMB quadrupole and octopole anisotropy patterns are aligned both mutually and with respect to the Solar System geometry. These anomalies have been widely studied and discussed, but their origin remains unexplained.

SKA will provide a deep and wide large-scale structure dataset that will enable separating the effects of the early and late universe on the observed CMB anisotropy. For example, the SKA data could be used to reconstruct the late-time contribution to the CMB anisotropy via the integrated Sachs-Wolfe effect, and thus provide information about the temporal evolution of the CMB anomalies.

3.1 Low-ℓ multipole moments

The analysis of low-ℓ multipoles from SKA continuum surveys can benefit from the methods developed for the study of the CMB. Missing sky area is always a problem for low-ℓ mode measurements. For CMB studies, many methods were proposed to deal with a mask of missing data for both power spectrum estimation and phase recovery. For the power spectrum, one of the

PoS(AASKA14)032

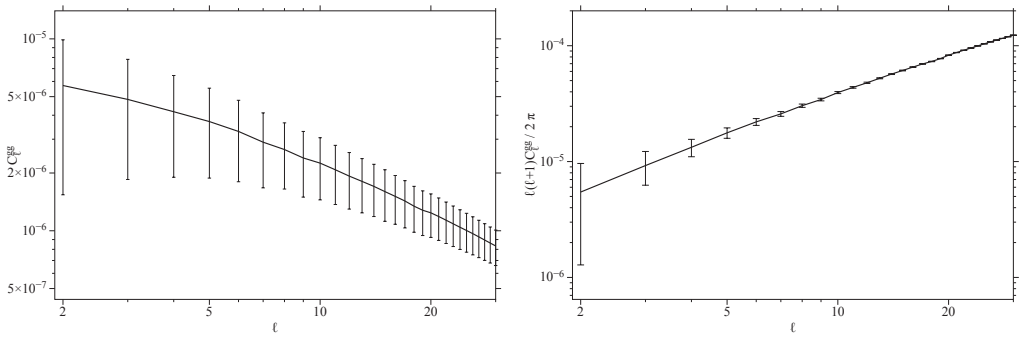

Figure 4: *Left:* Low-ℓ multipoles of the angular power spectrum as expected for a SKA1 continuum survey. *Right:* The corresponding band power. The errors contain shot noise and cosmic variance. The figures illustrate that statistically significant measurements of multipole moments can be expected.

most used methods is MASTER (Hivon et al. 2002). It consists in first building a matrix which captures the coupling between the modes induced by the mask, and then inverting this matrix. In Figure 4 we plot the angular power spectrum of SKA galaxies for low-ℓ mulitpoles with error bars corresponding to a SKA1 continuum survey.

For phase recovery, or more generally for large scale map reconstruction, many methods have been proposed based on Wiener filtering, l_2 or l_1 norm regularization, constraint realizations or diffusion [see Starck et al. (2013) and references therein]. Based on these new methodological idea, Planck data were analyzed with a mask removing 27% of the sky (Planck collaboration 2014c; Rassat et al. 2014). For a given observed sky area, the shape of the mask will also be important. The importance of random sampling is also described in Paykari et al. (2013), and many small missing parts, randomly distributed, will always be much better for large scale studies than a compact big missing part.

As for the dipole, SKA will tremendously improve the precision and quality of low-ℓ multipole moments and thus allow us to probe statistical isotropy, scale invariance and gaussianity.

3.2 Angular 2-point correlation function

The angular two point correlation is a powerful tool to measure the projected large-scale structure distribution of the Universe. It allows us to probe certain fundamental assumptions like scale-invariance of the primordial perturbations, Gaussianity and the isotropy of the Universe (by comparing two-point correlations on sub-samples of the observed sky).

The two-point correlation at large angular scales contains many interesting aspects: Firstly, the matter fluctuations at large scales are in the linear regime. Secondly, general relativistic effects and cosmological evolution prefer large scales. AGNs are very good candidates to probe this, since they are isotropically distributed on the sky and most of them have a significant ($z > 1$) cosmological distance. In order to accurately investigate ultra-large scale correlations, the theoretical frame work of differential number counts based on general relativity will be needed (Maartens et al. 2013; Raccanelli et al. 2014, 2013; Chen & Schwarz 2014).

In contrast to galaxy redshift surveys within the local Universe ($z \ll 1$), all linear order relativistic corrections, which include the Doppler effect, lensing, and generalized Sachs-Wolfe contri-

PoS(AASKA14)032

butions, are of relevance. The spread of luminosities of radio sources in continuum surveys washes out much of the clustering signal, and the general relativistic corrections are also suppressed. However, SKA HI surveys in which the source redshifts will be known will resolve these effects.

With the assistance of Lyman alpha data, one can model the luminosity function and evolution. With the SKA morphology data we expect to be able to identify different type of sources. This will allow us to study cross correlations between star forming galaxies and AGNs. We could also cross correlate with the CMB and different types of radio sources, which have different redshift distributions.

These aspects are treated in more detail in other contributions to this volume (Camera et al. 2015; Bull et al. 2015; Raccanelli et al. 2015). Let us just stress here the importance of re-establishing the almost scale-invariant power spectrum at superhorizon scales at $z \sim 1$, which will be possible by means of SKA all-sky surveys.

4. Copernican Principle and homogeneity (SKA1 & SKA2)

The Copernican Principle is the assumption that we are not distinguished observers in the Universe. If we observe an isotropic cosmos, then distant observers should also see a similarly isotropic cosmos. This implies that the Universe satisfies the Cosmological Principle and is homogeneous on large scales. A violation of homogeneity in principle offers an alternative explanation to the acceleration of the Universe (Célérier 2000), but simple inhomogeneous models without dark energy are incompatible with current data (Bull et al. 2012). However, radial homogeneity is only weakly constrained in ΛCDM (Valkenburg et al. 2014). Any deviations would imply a radical change to the standard model and scale-invariant initial conditions, making it a vital constraint on the standard model.

SKA HI intensity mapping on super-Hubble scales offers powerful new ways to test homogeneity. By comparing the radial and transverse scale of baryon acoustic oscillations we can test isotropy of the expansion rate around distant observers (Maartens 2011; February et al. 2013; Clarkson 2012). This places direct constraints on radial inhomogeneity about us, when redshift-space distortions, lensing and other large-scale GR effects are accounted for. Anisotropic expansion rates act on the sound horizon at decoupling so that by redshift z it has evolved into an ellipsoid with semi-axes

$$L_{\parallel}(z) = \frac{\delta z(z)}{(1+z)H_{\parallel}(z)}\,, \quad L_{\perp}(z) = d_A(z)\delta\theta(z), \tag{4.1}$$

given the observed radial and angular scales $\delta z(z), \delta\theta(z)$. $L_{\parallel}(z) = L_{\perp}(z)$ in a homogeneous universe. In an inhomogeneous universe $d_A(z)$ depends on the transverse Hubble rate along the line of sight, which will be different from the radial Hubble rate $H_{\parallel}(z)$, providing a test of homogeneity.

When combined with accurate distance data from SNIa, consistency relations can be used to check deviations from homogeneity in a completely model independent way (Clarkson et al. 2008). In a homogeneous universe, irrespective of dark energy or theory of gravity, the Hubble rate $h(z) = H(z)/H_0$ and dimensionless comoving distance $D(z) = (1+z)H_0 d_A(z)$ satisfy ($' = d/dz$)

$$\mathscr{C}(z) = 1 + h^2\left(DD'' - D'^2\right) + hh'DD' = 0\,, \tag{4.2}$$

PoS(AASKA14)032

so that $\mathscr{C}(z) \neq 0$ implies violation of the Copernican Principle. We expect that SKA1 will be able to constrain $\mathscr{C}(z)$ to 0 ± 0.05 for $z < 1.5$, based on a naive error propagation from Bull et al. (2014). A more careful forecast has yet to be done. Direct constraints on radial inhomogeneity can be given combining with all available data sets which will significantly improve current constraints which are much weaker than those for isotropy (Valkenburg et al. 2014).

Finally, the Copernican Principle allows for the possibility of a fractal universe, but this is not predicted by the concordance model – which predicts a fractal dimension of 3 on large scales – any deviations would imply new physics. It is therefore important to measure the fractal dimension of the distribution of radio sources at superhorizon scales. Such a test has been performed using the SDSS and the WiggleZ surveys, finding an approach to a three-dimensional distribution at ~ 100 Mpc scales (Hogg et al. 2005; Scrimgeour et al. 2012). A dramatic improvement will be possible based on SKA HI threshold surveys.

5. Summary

The Cosmological Principle provides the foundation for modern cosmology, and our understanding of the evolution of the Universe as well as all parameter constraints from the CMB, supernovae or large scale structure rely on this assumption. Testing the Cosmological Principle is thus of fundamental importance for cosmology generally as well as for the cosmological interpretation of the SKA data itself. As this chapter shows, SKA will be able to greatly increase our confidence that our cosmological framework makes sense (or lead to a scientific revolution if not).

We argue that SKA all-sky surveys will allow us to measure the cosmic radio dipole almost as precisely as the CMB dipole. SKA1 will constrain the cosmic radio dipole direction with an accuracy better than 5 degrees, SKA2 within a degree (at 99% C.L.). This measurement could finally firmly establish or refute the commonly adopted assumption that the CMB and the overall LSS frames agree, and will have impact on a variety of cosmological observations, from the local measurement of H_0 to the calibration of CMB experiments. A tomography of the cosmic radio dipole might reveal a detailed understanding of local LSS.

In addition, studying the large-angular scales in SKA continuum and HI surveys might help resolve the puzzle of CMB anomalies and test the cosmological principle, including tests of statistical homogeneity. Further large-scale structure issues, especially non-Gaussianity and relativistic corrections, are discussed in Camera et al. (2015).

The ideas presented in this work only provide a flavor of SKA's potential to answer fundamental cosmological questions. Some of those ideas can already be tested by means of the SKA pathfinder experiments ASKAP, MeerKAT and LOFAR, but they cannot compete with SKA's survey speed and sensitivity. Thus SKA will be a unprecedented discovery and precision machine for modern cosmology.

References

Bennett, C. L., Larson, D., Weiland, J. L., et al. 2013, ApJS, 208, 20
Blake, C., & Wall, J. 2002, Nature, 416, 150

PoS(AASKA14)032

Braun, R. 2014, "SKA1 Imaging Science Performance", Document number SKA-TEL-SKO-DD-XXX Revison A Draft 2
Bull, P., Camera, S., Raccanelli, A., et al. 2015, in "Advancing Astrophysics with the Square Kilometre Array", PoS(AASKA14)024
Bull, P., Clifton, T., & Ferreira, P. G. 2012, Phys. Rev. D, 85, 024002
Bull, P., Ferreira, P. G., Patel, P., & Santos, M. G. 2014, ArXiv e-prints, arXiv:1405.1452
Camera, S., Raccanelli, A., Bull, P., et al. 2015, in "Advancing Astrophysics with the Square Kilometre Array", PoS(AASKA14)025
Célérier, M.-N. 2000, A&A, 353, 63
Chen, S., & Schwarz, D. J. 2014, ArXiv e-prints, arXiv:1407.4682
Clarkson, C. 2012, Comptes Rendus Physique, 13, 682
Clarkson, C., Bassett, B., & Lu, T. H.-C. 2008, Physical Review Letters, 101, 011301
Copi, C. J., Huterer, D., Schwarz, D. J., & Starkman, G. D. 2010, Adv. Astron., 2010, 92
—. 2013a, ArXiv e-prints, arXiv:1310.3831
—. 2013b, ArXiv e-prints, arXiv:1311.4562
Crawford, F. 2009, ApJ, 692, 887
de Zotti, G., Massardi, M., Negrello, M., & Wall, J. 2010, A&A Rev., 18, 1
Dewdney, P., Turner, W., Millenaar, R., et al. 2013, "SKA1 System Baseline Design", Document number SKA-TEL-SKO-DD-001 Revision 1
Ellis, G. F. R., & Baldwin, J. E. 1984, MNRAS, 206, 377
Erickcek, A. L., Carroll, S. M., & Kamionkowski, M. 2008, Phys. Rev. D, 78, 083012
February, S., Clarkson, C., & Maartens, R. 2013, JCAP, 3, 23
Gibelyou, C., & Huterer, D. 2012, MNRAS, 427, 1994
Hinshaw, G., Weiland, J. L., Hill, R. S., et al. 2009, ApJS, 180, 225
Hivon, E., Górski, K. M., Netterfield, C. B., et al. 2002, ApJ, 567, 2
Hogg, D. W., Eisenstein, D. J., Blanton, M. R., et al. 2005, ApJ, 624, 54
Maartens, R. 2011, Roy. Soc. Lond. Phil. Trans. A, 369, 5115
Maartens, R., Zhao, G.-B., Bacon, D., Koyama, K., & Raccanelli, A. 2013, JCAP, 2, 44
Paykari, P., Pires, S., Starck, J.-L., & Jaffe, A. H. 2013, ArXiv e-prints, arXiv:1306.3035
Planck Collaboration, Ade, P. A. R., Aghanim, N., et al. 2014a, A&A, 571, A16
—. 2014b, A&A, 571, A22
—. 2014c, A&A, 571, A23
Planck Collaboration, Aghanim, N., Armitage-Caplan, C., et al. 2014d, A&A, 571, A27
Raccanelli, A., Bertacca, D., Doré, O., & Maartens, R. 2014, JCAP, 8, 22
Raccanelli, A., Bertacca, D., Maartens, R., Clarkson, C., & Doré, O. 2013, ArXiv e-prints, arXiv:1311.6813
Raccanelli, A., Zhao, G.-B., Bacon, D. J., et al. 2012, MNRAS, 424, 801
Raccanelli, A., Bull, P., Camera, S., et al. 2015, in "Advancing Astrophysics with the Square Kilometre Array", PoS(AASKA14)031
Rassat, A., Starck, J.-L., Paykari, P., Sureau, F., & Bobin, J. 2014, JCAP, 8, 6
Rubart, M., Bacon, D., & Schwarz, D. J. 2014, A&A, 565, A111
Rubart, M., & Schwarz, D. J. 2013, A&A, 555, A117
Ryle, M., & Clarke, R. W. 1961, MNRAS, 122, 349

PoS(AASKA14)032

Scrimgeour, M. I., Davis, T., Blake, C., et al. 2012, MNRAS, 425, 116
Singal, A. K. 2011, ApJL, 742, L23
Starck, J.-L., Fadili, M. J., & Rassat, A. 2013, A&A, 550, A15
Valkenburg, W., Marra, V., & Clarkson, C. 2014, MNRAS, 438, L6
Wilman, R. J., Miller, L., Jarvis, M. J., et al. 2008, MNRAS, 388, 1335

PoS(AASKA14)032

PROCEEDINGS OF SCIENCE

Topology of neutral hydrogen distribution with the Square Kilometer Array

Yougang Wang[1], **Yidong Xu**[1], **Fengquan Wu**[1], **Xuelei Chen**[*1], **Xin Wang**[2], **Juhan Kim**[3], **Changbom Park**[3], **Khee-Gan Lee**[4], **Renyue Cen**[4]

[1]*National Astronomical Observatory, Chinese Academy of Sciences, Beijing, China;*
[2]*Department of Physics and Astronomy, The Johns Hopkins University, Baltimore, USA;*
[3]*School of Physics, Korean Institute for Adavanced Studies, Seoul, Korea;*
[4]*Department of Astrophysical Sciences, Princeton University, Princeton, USA*
E-mail: wangyg@bao.ac.cn, xuelei@cosmology.bao.ac.cn

Morphology of the complex HI gas distribution can be quantified by statistics like the Minkowski functionals, and can provide a way to statistically study the large scale structure in the HI maps both at low redshifts, and during the epoch of reionization (EoR). At low redshifts, the 21cm emission traces the underlying matter distribution. Topology of the HI gas distribution, as measured by the genus, could be used as a "standard ruler". This enables the determination of distance-redshift relation and also the discrimination of various models of dark energy and of modified gravity. The topological analysis is also sensitive to certain primordial non-Gaussian features. Compared with two-point statistics, the topological statistics are more robust against the nonlinear gravitational evolution, bias, and redshift-space distortion. The HI intensity map observation naturally avoids the sparse sampling distortion, which is an important systematic in optical galaxy survey. The large cosmic volume accessible to SKA would provide unprecedented accuracy using such a measurement. During the EoR, topology can be a powerful and intuitive tool to distinguish among the different evolutionary stages of reionization, where the ionized regions make up a significant fraction of the volume. Furthermore, it can also discriminate among various reionization models. The genus curves evolve during cosmological reionization, and for different reionization scenarios, the topology of the HI gas distribution can be significantly different even if the global ionization fractions are the same. It can provide clear and intuitive diagnostics for how the reionization takes place, and indirectly probes the properties of radiation-sources. In this brief chapter we will describe the scientific background of the topology study, and forecast the potential of the SKA for measuring cosmological parameters and constraining structure formation mechanism through the study of topology of HI gas distribution.

Advancing Astrophysics with the Square Kilometre Array
June 8-13, 2014
Giardini Naxos, Italy

[*]Speaker.

PoS(AASKA14)033

1. Topology study of HI distribution

Topology has been introduced in cosmology to describe the properties of the large-scale structure (LSS), and to test the non-Gaussianity of the primordial density fluctuations (Gott et al. 1986; Hamilton et al. 1986; Park et al. 2013). Application of LSS topology study has been extended to measurement of cosmological parameters and constraining galaxy formation mechanism (Park et al. 2005; Choi et al. 2010, 2013). The LSS topology is also a cosmological invariant that can be used to reconstruct the expansion history of the universe (Park & Kim 2010; Zunckel et al. 2011; Wang et al. 2012; Speare et al. 2013; Blake et al. 2014). Mathematically, geometry of the excursion regions with density above a threshold can be characterized by the Minkowski Functionals (MFs) [1] (Mecke et al. 1994; Pratten & Munshi 2012; Hikage et al. 2006, 2008). The genus, related to one of the Minkowski functionals, is given by the number of holes minus the number of isolated regions in the iso-density contour surfaces of the smooth density field, and is a measure of topology that quantifies the connectivity of the contour surfaces (Park et al. 2013). All the MFs are analytically known for Gaussian fields, the genus per unit volume as a function of the threshold density $\nu = \delta/\sigma$ is given by

$$G(\nu) = A(1-\nu^2)e^{-\nu^2/2}, \qquad A = \frac{1}{4\pi^2}\left(\frac{\langle k^2\rangle}{3}\right)^{3/2} \tag{1.1}$$

The topology of the isodensity contours is insensitive to the systematic effects such as redshift-space distortion, non-linear evolution, sparse sampling (Park et al. 2005; Park & Kim 2010). Therefore, any deviation from the Gaussian prediction is evidence for non-Gaussianity, and can constrain the mechanism for primordial non-Gaussianity. The deviation can be caused not just by the three-point function but by all the high-order moments of the density field. Therefore, the study of non-Gaussianity using MFs is complementary to the approach of using three-point correlation function or bispectum, and is in principle able to detect general forms of non-Gaussianity. The Minkowski functionals measured from the HI 21cm map can characterize the complex distribution of the neutral hydrogen, both in the large-scale structure at low redshifts, and during the epoch of reionization (EoR) at high redshifts.

1.1 Primordial non-Gaussianity

The primordial perturbation may deviate from the Gaussian random field during the cosmological phase transition triggered by the spontaneous breakdown of symmetry creating topological defects such as the cosmic monopole, string, wall, and textures. Various non-standard inflationary scenarios which violate the single-field and slow-rolling condition may also produce significant primordial non-Gaussianity. It is usual to parameterize the non-Gaussian features generated by the inflation model as $\Phi(x) = \phi_G(x) + f_{\rm NL}\left[\phi_G^2(x) - \left\langle\phi_G^2\right\rangle\right]$ where ϕ_G is the Gaussian distribution of potential. For this form of primordial non-Gaussianity, the genus curve deviates from the Gaussian

[1] In three dimensions, the four Minkowski functionals for the isodensity contours are the volume fraction $V_0(\nu)$, surface area $V_1(\nu)$, mean curvature $V_2(\nu)$ and Euler characteristics $V_3(\nu) = \chi(\nu)$, which is related to the genus by $\chi = 2-2g$.

PoS(AASKA14)033

model, and up to second order perturbations it is given by Hikage et al. (2006, 2008).

$$\Delta(\nu) \equiv \delta\left(\frac{G}{A}\right) = -e^{-\nu^2/2} \times f_{\rm NL}\left[(S^{(1)}_{\rm pri} - S^{(0)}_{\rm pri})H_3(\nu_f) + (S'^{(2)}_{\rm pri} - S'^{(0)}_{\rm pri})H_1(\nu)\right]\sigma_0 \tag{1.2}$$

where $S^{(a)}_{\rm pri}$ is the skewness parameter (Matsubara 2003). The measured genus curve can then be used to constrain f_{NL}. However, even if the non-Gaussianity can not be parameterized in this form, it would still affect the genus curve, so the topology can be used to probe more general forms of primordial non-Gaussianity.

1.2 Dark Energy and Modified Gravity

The LSS topology is relatively stable with the growth of structure. Eq. (1.1) shows that A measures the slope of the power spectrum around the smoothing scale R_G, and for linear growth A would be conserved (Park et al. 2005), so as long as the same smoothing scale is used, the same comoving volume at different redshifts would enclose nearly the same amount of structures, as illustrated in the left panel of Fig.1 This fact can be used to measure the redshift-distance relation $r(z)$ (Park & Kim 2010). Since the topology of the structure is not scale-free, the genus enclosed in a wrongly sized volume and smoothed with a wrong scale would lead to deviation from the actual one,

$$A_Y(z, R_{G,Y})R^3_{G,Y} = A_X(R_{G,X})R^3_{G,X}, \tag{1.3}$$

where R is the volume, Y is the adopted cosmology parameters while X is the true cosmology. The smoothing scale R_G for different cosmologies are related by $(R_{G,X}/R_{G,Y})^3 = (D_A^2/H)_X/(D_A^2/H)_Y$, where D_A, H are the angular diameter distance and Hubble expansion rate respectively. Utilizing this effect, topology of the large scale structure can serve as a standard ruler in cosmology. This technique has been applied to constrain dark energy model (Blake et al. 2014; Zunckel et al. 2011).

For modified gravity models, the growth rate is different from the general relativity, and in some cases it is scale-dependent. This will induce changes in the genus curve. In the right panel of Fig.1 the redshift evolution of the genus amplitude for the $f(R)$ theory and some phenomenological modified gravity models are shown. Here the modified gravity model parameter B_0 is the present day value of the function $B(a)$, which is the square of the Compton scale given by $B(a) \equiv \frac{f_{RR}}{1+f_R}R'\frac{H}{H'}$, where f_R and f_{RR} are the first and second derivatives of $f(R)$, with R being the Ricci scalar.

So the topological measurements can also be used to constrain the modified gravity models (Wang et al. 2012). Compared with direct measurement using the growth factor, the topological measurement may be more robust, as they suffer less from the effect of bias, redshift distortion, and non-linearity.

1.3 Reionization

The topology analysis provides a direct and sensitive probe for the detailed process of cosmic reionization (Lee et al. 2008; Hong et al. 2014). Using the genus of HI density contours as a quantitative measure of topology, the reionization process of the intergalactic medium (IGM) can be divided into four distinct topological phases for the standard scenario of reionization: (1) pre-reionization, before the formation of any HII bubbles, the HI distribution reflects the primodial

PoS(AASKA14)033

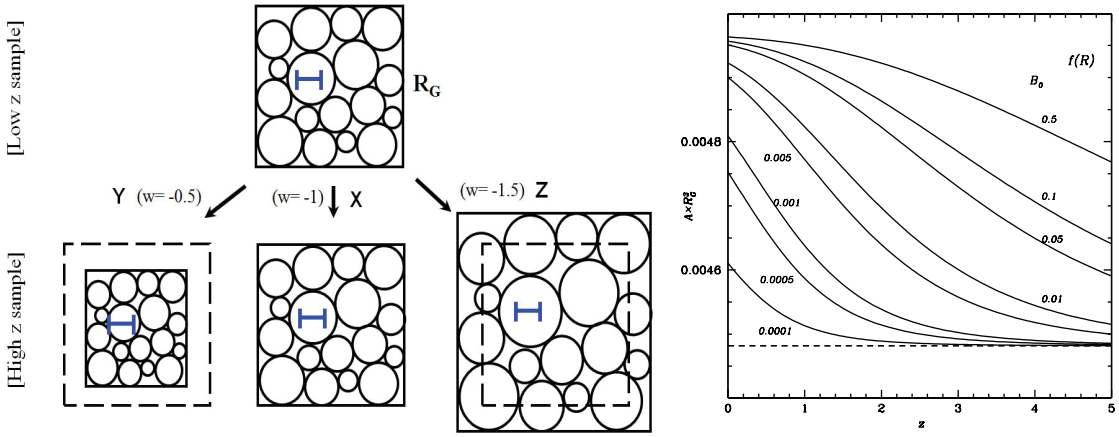

Figure 1: Left: The number of structures as cosmic standard ruler. Right: the redshift evolution of genus amplitude for $f(R)$ and phenomenological modified gravity models with different B_0 values.

density fluctuations, the genus curve is consistent with a Gaussian density distribution, and topology remains unchanged as the HI density evolves linearly; (2) pre-overlap, characterized by a topology dominated by isolated HII bubbles. At the earlier stages of this phase, the number of HII bubbles increases gradually with time, resulting in an increase in the amplitude of the genus curve, while at the later stages when HII bubbles start to merge, the genus curve goes through a turnover and subsequently decreases in amplitude. (3) overlap, during which the amplitude of the genus curve drops significantly as the HII bubbles rapidly merge; (4) postoverlap, when the IGM is almost ionized, and the evolution of the genus curve is consistent with an decreasing number of isolated neutral islands. The measurement of the genus curve can be used to characterize the evolutionary stages of the neutral topology and to identify the redshifts at which the different stages of reionization occur, thus distinguishing different reionization scenarios. This in turn provides information on the nature and properties of the early luminous sources.

2. The SKA performance

The observation of HI emission is presently limited to $z < 0.2$ by the sensitivity of existing telescopes. The SKA, with its great increase in sensitivity, will allow us to observe the HI at much higher redshifts, and probe the topology of HI distribution with unprecedented capability. The SKA will be built in two stages (Dewdney et al. 2013; Braun), the SKA-1 will consist of three arrays: SKA1-mid, SKA1-sur and SKA1-low, the features are listed in Table.1; The SKA2 is to be designed in the future, but should be about 10 times larger in mid-frequency and 4 times larger in the low frequencies.

The SKA1-low is designed for observation of the high redshifts of the EoR, while SKA1-mid for the low-to-mid-redshifts of post-reionization Universe, and SKA1-sur with its larger FoV is suitable for survey of large area. All of these can be used for HI topology study. The topological analysis can be applied on data from all HI surveys. We expect that large HI surveys will be one of

PoS(AASKA14)033

Table 1: The three SKA1 arrays.

Array	configuration	relevant band
SKA1-mid	190×15m dish + 64 MeerKAT 13.5m dish	band 1(0.35-1.05GHz), band 2(0.95-1.76GHz)
SKA1-sur	60×15m dish + 36 ASKAP 12m dish (PAF)	band 1 (0.35-0.5) and band 2 0.65-1.67 GHz.
SKA1-low	250,000 log periodic antenna in 866 stations	50-350 MHz

the key science projects of SKA, being carried out with multiple applications, and the HI topology can be studied in conjunction with the other projects.

A classic approach is the HI galaxy survey where the individual galaxies are observed as objects whose HI content exceeds the detection threshold:

$$S_{lim} = N_{th} \frac{kT_{sys}}{A_{eff}\sqrt{\Delta\nu t}} = N_{th} \frac{\mathrm{SEFD}}{\sqrt{\Delta\nu t}} \tag{2.1}$$

where N_{th} is a preset threshold value, e.g. 5 or 10. The SKA is potentially capable of surveying a billion of galaxies, with SKA-1 it is capable of surveying 10^{7-8} galaxies(Abdalla & Rawlings 2005; Myers et al. 2009) at z up to ~ 1.5. But even smaller surveys, e.g. those conducted with SKA-1 early science, or for small deep field, would for the first time reveal the HI distribution at redshifts much beyond our current limit, and the topological analysis will help us to understand quantitatively the characteristics of HI distribution and redshift evolution, as has been down for low redshift optical galaxies (Choi et al. 2010, 2013).

Another approach is intensity mapping (IM): the sky is mapped at low angular resolution, such that individual galaxies can not be distinguished, but data of HI large scale distribution can still be obtained (Chang et al. 2008). For the EoR experiments, including that of the SKA-low, due to the low angular resolution, this will also be the mode of observation. A few dedicated experiments, such as the CHIME[2] and Tianlai [3] are designed to conduct IM observations. While the SKA1-mid or SKA1-sur are not designed for this, it has been proposed that IM surveys may be conducted with the dishes used individually with output autocorrelation, while being calibrated using the interferometry (Santos 2015). Whether this would work still needs to be tested in the field, but if successful, it would allow higher sensitivity on interested scales at the price of lower angular resolution.

In Table2 we list both the HI galaxy and IM survey parameters we adopted for our forecast on dark energy and modified gravity. For SKA-low, as the design is still very uncertain, we do not make a full forecast here, but only discuss the potential of the measurement.

3. Large Scale Structures

After EoR, with the IGM highly ionized, the neutral hydrogen resides mainly in galaxies, and the HI topology traces out the LSS. We can use this observation to constrain the primordial non-Gaussianity, dark energy, and modified gravity.

[2]http://chime.phas.ubc.ca/

[3]http://tianlai.bao.ac.cn/

PoS(AASKA14)033

Table 2: SKA survey parameters utilized in this paper.

galaxies surveys	survey area (deg^2)	integration time (h)	flux limit (mJy)
SKA1-Mid	1,000 (5,000)	5,000 (25,000)	0.13
SKA2-Mid	1,000 (5,000)	5,000 (25,000)	0.05
SKA1-Sur	30,000	7,500 (50,000)	0.4 (0.15)
SKA2-Sur	30,000	7,500	0.05
HI intensity mapping	survey area (deg^2)	integration time (h)	frequency band (MHz)
SKA1-Mid-SD	30,000	10,000	350 – 1050
SKA1-Mid-Int	30,000	10,000	350 – 800
SKA2-Mid-Int	30,000	10,000	350 – 950

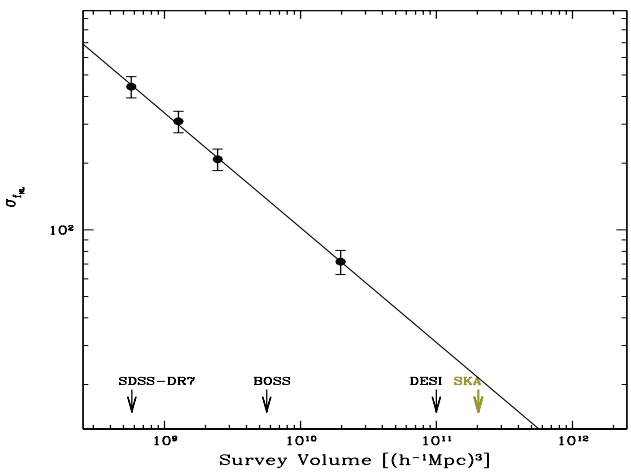

Figure 2: The measurement error of $f_{\rm NL}$ from genus curves. We mark the survey volumes of previous (SDSS-DR7, BOSS) and forth-coming (DESI & SKA) surveys.

For primordial non-Gaussianity, Fig.2 shows the $f_{\rm NL}$ constraints from measurement of genus curve in the Horizon Run III simulation, which has a volume of $10.8^3 h^{-3}$Gpc^3. We employed a Gaussian smoothing of $R_G = 22h^{-1}$Mpc to build a density field from subcubes, and compare the result for four survey volumes: SDSS, BOSS, DES and SKA. If the SKA-2 will observe galaxy distribution out to $z = 3$ with a solid angle of 20,000 deg^2, then using the genus-curve we can measure $f_{\rm NL}$ with an error, $\sigma(f_{\rm NL}) = 20$. We should note that this is comparable to the CMB limits, and the genus measurement can detect more general forms of non-Gaussianity.

Using the genus curve as standard ruler, dark energy equation of state parameters w_0, w_a can be constrained. As shown in Table (2), we consider a relatively deep survey using SKA1-Mid compared with shallow but wider surveys for SKA1-Sur.

The HI galaxies survey constraints are plotted in Fig. (3), and IM survey constraints are plotted in the right panel of Fig.4. With a conservative assumption of the survey parameters that require

PoS(AASKA14)033

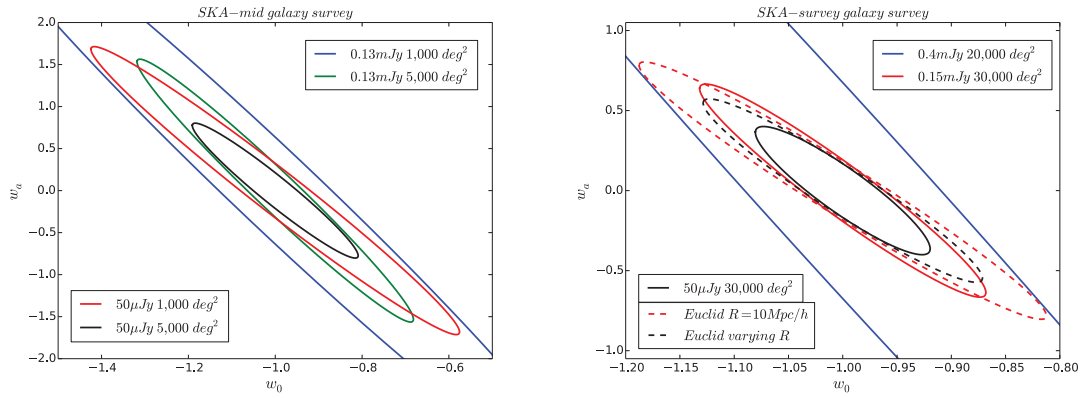

Figure 3: Constraint on dark energy with HI galaxy survey. *Left*: HI galaxy survey with SKA1-mid, Right: HI galaxy survey with SKA1-survey. The dashed contours indicate the constraints from Euclid.

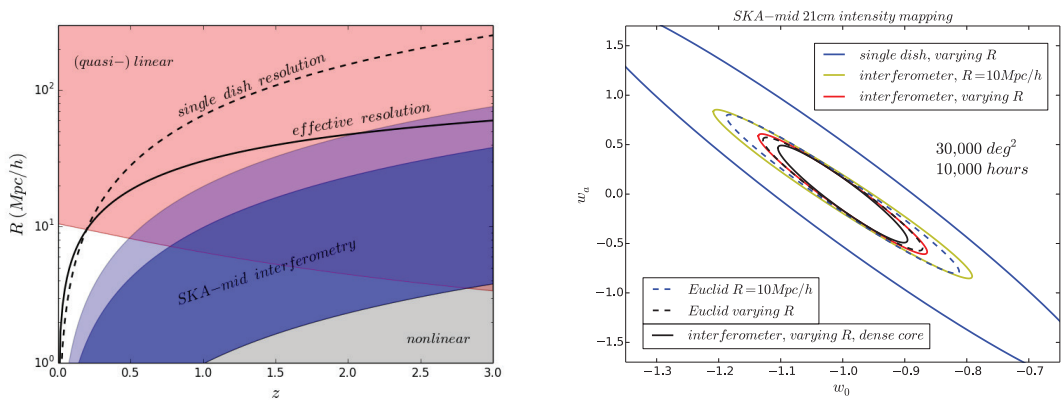

Figure 4: SKA-mid HI intensity mapping. *Left:* Various comoving scales as a function of redshift. The upper red region denotes the quasi-linear regime where the systematics of genus statistics are well-controlled. Blue bands are most sensitive scales that would be observed by the core of SKA-mid interferometer, where we assume the baseline range from 100m (50m for lighter blue band) to 1000m. The grey region at bottom-right corner are scales available with the SKA spiral arm baselines. The black dashed line indicates the physical angular resolution of single dish. The solid black line is the effective resolution $(R_{ang}^2 R_{freq})^{1/3}$, where we utilize the minimum quasilinear scale, i.e. the boundary of red region, as R_{freq}. *Right:* Constraints on dark energy equation of state w_0 and w_a. In the calculation, 'varying R' means the smoothing length is selected using smallest quasi-linear scale. The dashed contours indicate the constraints from Euclid.

PoS(AASKA14)033

5,000 hours integration time, neither constraint is very stringent for SKA1, but it is independent of other techniques, and strong constraints can be achieved with SKA2. As we already know that BAO gives better constraints than genus for dark energy, we just give the constraints of our calculation, and refer the interested reader to the chapter written by Bull et al. (this edition).

For the IM, there is certain complications. Unlike the BAO technique, where the physical scale is fixed, the topological standard ruler measure the scale around the smoothing length. To achieve better statistics, smaller smoothing length is desirable, though the systematics such as nonlinear growth put limits on the usable scale. In the left panel of Fig.4), we illustrate various physical scales for SKA1-mid. The quasi-linear region where systematics is well controlled is indicated by the upper red region.

For the single dish observing mode, the angular resolution by the $15m$ dish is poor (black dashed-line), varying from $30\mathrm{Mpc}/h$ at $z = 0.5$ to above $200\mathrm{Mpc}/h$ at $z = 3$. However, in the line-of-sight direction the resolution is good, the effective R_{eff},

$$R_{\mathrm{eff}} = (R_{\mathrm{ang}}^2 R_{\mathrm{freq}})^{1/3} \tag{3.1}$$

becomes much smaller. Assuming a reasonable R_{freq} as indicated by the lower edge of the red region, the effective smoothing length varies from $10\mathrm{Mpc}/h$ to $60\mathrm{Mpc}/h$. The cosmological constraints of this observation mode is shown as the blue contour in the right panel.

If sufficient number of short baselines is available, it may be possible to make an IM survey in the interferometric mode. We assume a compact core in the center of SKAmid, the blue belt in the left panel illustrates the most sensitive physical scale of this core, where we assume baselines distributed from 100m (50m for lighter blue region) to 1000m. With the systematic limit from nonlinear scale, one would be able to observe higher redshift volume from $z = 0.78$ ($z = 0.5$) at much smaller smoothing length and therefore a better statistical accuracy. As shown in the right panel, such observation mode improve the constraints significantly.

For modified gravity models, we consider specifically the $f(R)$ theory with a single model parameter B_0 characterizing the present value of Compton scale. HI galaxy survey by SKA2 will be able to constrain B_0 to 5×10^{-5} at 1-σ level for a fiducial value of $B_0 = 10^{-4}$, while the best constraints from intensity mapping is 8×10^{-5}. This is much better than the current strongest constraints of 1.1×10^{-3} at 95% C.L..

4. Reionization

The genus curve can be used to distinguish the different phases of reionization (Lee et al. 2008; Hong et al. 2014) discussed in §1.3. In Fig. 5 we show the genus curve from an EoR simulation (Trac et al. 2008), for four redshifts during the EoR. As expected, at the highest redshift($z = 19.7, x_i \approx 0$), the genus curve has the shape for that of a Gaussian distribution. The amplitude of the curve increases in the pre-overlap phase ($z = 9, x_i = 0.14$), but retains the shape for Gaussian distribution. The shape of the genus curve is drastically different during the overlap phase ($z = 6.97, x_i = 0.65$). Finally, the curve returns to the shape of Gaussian distribution in the post-reionization phase ($z = 5.99, x_i = 0.99$). From Eq.1.1 we see the amplitude of genus curve $A \propto k_e^3$, k_e first increases as the HII bubbles grows in number, and then decreases as the bubbles merge and overlap. Measuring k_e from A can provide information on the bubble sizes.

PoS(AASKA14)033

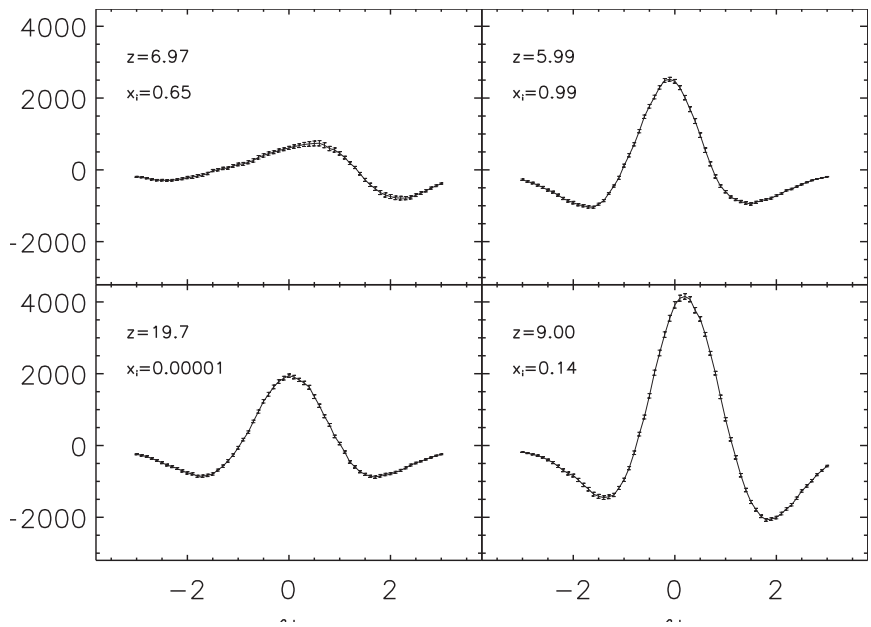

Figure 5: Genus curve and statistical error of δT_b at different redshifts from a simulation (Trac et al. 2008), the simulation box has a side length of 100Mpc h^{-1}, and smoothing length is 1Mpc h^{-1}

These curves are obtained with a smoothing length of 1Mpc$/h$. Along with the genus curves, the statstical error obtained from a 100Mpc$/h$ simulation box is plotted. The design of the SKA-low (Dewdney et al. 2013; Braun 2013) is still very uncertain, but it is agreed that there should be a compact core within 1km which provides high sensitivity observation on scales of a few arcmin for redshift 10. This is roughly sufficient for the measurement. The observation of SKA1-low for a deep field should be able to yield data which can be compared with such simulations.

5. Conclusion

Topology can be very useful at characterizing random fields. The SKA, with its high sensitivity, can observe the HI distribution much beyond the current limits. We can apply the topological analysis method to the SKA HI survey data. Such analysis can also be used to test or constrain primordial non-Gaussianity, dark energy and modified gravity. The constraints for the model parameters from the topological method are not as tight as the traditional methods, e.g., dark energy constraints from BAO measurements (See Bull et al. chapter) and primordial non-Gaussianity from scale-dependent bias and bispectrum measurements (See Camera et al. chapter), but it is very robust against non-linearity, bias and redshift distortion in the evolution of large scale structure. During the EoR, it can also distinguish different evolution phases and characters of reionization model. We made forecasts for some of these applications, in both HI galaxy survey and HI intensity mapping survey, and obtained constraints for different survey parameters. For SKA1, the precision of the measurement with the genus curve is moderate, but we anticipate that the addition of other Minkowski functionals would help improve these constraints, and for SKA2 the result is competitive. More importantly, the genus curve is capable of probing non-Gaussian features which

PoS(AASKA14)033

are not parameterized in the standard form, so with SKA it would be an important tool for probing and discovering non-Gaussianity in unexplored regimes.

References

Abdalla, F. B. & Rawlings, S. 2005, MNRAS, 360, 27
Blake, C., James, J. B., & Poole, G. B. 2014, MNRAS, 437, 2488
Chang, T.-C., Pen, U.-L., Peterson, J. B., & McDonald, P. 2008, Physical Review Letters, 100, 091303
Choi, Y.-Y., Kim, J., Rossi, G., Kim, S. S., & Lee, J.-E. 2013, ApJS, 209, 19
Choi, Y.-Y., Park, C., Kim, J., et al. 2010, ApJS, 190, 181
Gott, III, J. R., Dickinson, M., & Melott, A. L. 1986, ApJ, 306, 341
Hamilton, A. J. S., Gott, III, J. R., & Weinberg, D. 1986, ApJ, 309, 1
Hikage, C., Coles, P., Grossi, M., et al. 2008, MNRAS, 385, 1613
Hikage, C., Komatsu, E., & Matsubara, T. 2006, ApJ, 653, 11
Hong, S. E., Ahn, K., Park, C., et al. 2014, Journal of Korean Astronomical Society, 47, 49
Lee, K.-G., Cen, R., Gott, III, J. R., & Trac, H. 2008, ApJ, 675, 8
Matsubara, T. 2003, ApJ, 584, 1
Mecke, K. R., Buchert, T., & Wagner, H. 1994, A&A, 288, 697
Myers, S. T., Abdalla, F. B., Blake, C., et al. 2009, in ArXiv Astrophysics e-prints, Vol. 2010, astro2010: The Astronomy and Astrophysics Decadal Survey, 219
Park, C., Kim, J., & Gott, III, J. R. 2005, ApJ, 633, 1
Park, C. & Kim, Y.-R. 2010, ApJ, 715, L185
Park, C., Pranav, P., Chingangbam, P., et al. 2013, Journal of Korean Astronomical Society, 46, 125
Pratten, G. & Munshi, D. 2012, MNRAS, 423, 3209
Speare, R., Gott, J. R., Kim, J., & Park, C. 2013, ArXiv e-prints
Trac, H., Cen, R., & Loeb, A. 2008, ApJ, 689, L81
Wang, X., Chen, X., & Park, C. 2012, ApJ, 747, 48
Zunckel, C., Gott, J. R., & Lunnan, R. 2011, MNRAS, 412, 1401

PoS(AASKA14)033

PROCEEDINGS OF SCIENCE

Cosmology with galaxy clusters: studying the Dark Ages and the Epoch of Reionization in the SKA era

Sergio Colafrancesco[*1], **Paolo Marchegiani**[1], **M. Shehzad Emritte**[1]

[1] *School of Physics, University of the Witwatersrand, 1 Jan Smuts Ave, WITS-2050 Johannesburg, South Africa*

E-mail: sergio.colafrancesco@wits.ac.za

The cosmological evolution during the Dark Ages (DA) and the Epoch of Reionization (EoR) marks an important transition in the history of the universe that it is not yet fully understood. We study here a new technique to probe the history and the physics of the DA and EoR which makes use of the Comptonization of the cosmic microwave background (CMB) spectrum, modified by the physical effects occurring during this epoch related to the 21-cm radiation background, as induced by thermal and non-thermal electrons residing in the atmospheres of cosmic structures like galaxy clusters, radiogalaxy lobes and galaxy halos: we refer to this effect as SZE-21cm. The spectral features of the thermal and non-thermal SZE-21cm depend on the history and on the physical mechanisms occurring during the DA and EoR. We find that the redshift location of the main physical mechanisms occurring during the DA and EoR leave an imprint on the spectral shape of the SZE-21cm that is observable mainly in the 70-350 MHz range. We also prove that two different kinds of SZE-21cm are observable, the thermal and non-thermal SZE-21cm, and have different spectral shapes and frequency location, depending on the gas temperature (for the thermal SZE-21cm) and electrons minimum momentum (for the non-thermal SZE-21cm). The spectral imprint of the DA and EoR is maximized for clusters with high plasma temperature and optical depth, thus making rich clusters the optimal laboratories to study the SZE-21cm. We show that the global SZE-21cm signal can be detected by SKA1-LOW in the range $\nu \gtrsim 70-90$ MHz for clusters with temperature $\gtrsim 20-5$ keV respectively, and that we can separate the SZE-21cm from the standard SZE with SKA2 at $\nu \sim 100$ MHz for clusters with temperature $\gtrsim 15$ keV.

Advancing Astrophysics with the Square Kilometre Array,
June 8-13, 2014
Giardini Naxos, Sicily, Italy

[*] Speaker.

PoS(AASKA14)034

1. Probing the Dark Ages with galaxy clusters

Clusters of galaxies have been recognized since several decades as powerful cosmological tools and invaluable astrophysical laboratories (see, e.g., Kravtsov & Borgani 2012, Colafrancesco 2010). We will discuss here the role of the SKA to provide another fascinating possibility in using galaxy clusters as direct probes of the Dark Ages (DA) and of the Epoch or Reionization (EoR).
The most promising method to study the content of the universe during the DA and the beginning of the EoR (see, e.g., Koopmans 2015) is to search for signatures of the (highly redshifted) 21-cm hyperfine transition line of neutral hydrogen in the radio background spectrum (Pritchard & Loeb 2012). The 21-cm signal from the DA appears as a faint, diffuse background detectable at radio frequencies below 200 MHz (for redshift $z > 6$). Great opportunities for studying the EoR and the DA through the observations of the 21-cm background are offered by the SKA (Koopmans 2015).
During the DA and EoR the CMB radiation spectrum is modified by various physical mechanisms. Subsequent to recombination, the temperature of neutral gas is coupled to that of the CMB, and no changes in the CMB spectrum can be observed. At redshifts below ≈ 200 the gas cools adiabatically, its temperature drops below that of the CMB, and neutral Hydrogen resonantly absorbs CMB flux through the spin-flip transition (Field 1959, Scott & Rees 1990, Loeb & Zaldarriaga 2004). Heating effects of the neutral gas may also occur at high z. As the first Dark Matter (DM) clumps form in the universe, the WIMP DM annihilation can then produce a substantial heating of the surrounding IGM (Valdes et al. 2013). At much lower redshifts $z \lesssim 20$, gas temperature is also expected to heat up again as luminous sources turn on and their UV and soft X-ray photons reionize and heat the gas (Chen & Miralda-Escude 2004). An additional spectral signature is also expected from the Lyman-α radiation field produced by first sources (Barkana & Loeb 2005) through the Wouthuysen-Field effect (Wouthuysen 1952, Field 1959).
Such CMB spectral distortions offer an alternative and/or complementary method to study the DA and EoR by using the modification induced by the inverse Compton scattering of the CMB photon background, modified by the cosmic 21-cm background frequency spectrum, on intervening electrons in the atmospheres of various cosmic structures, like galaxy clusters, radiogalaxy lobes and galactic halos. We refer here to this effect as the SZE-21cm (Colafrancesco & Marchegiani 2014). Observations of the SZE-21cm can be carried out with interferometers since the modification associated with low-redshift scattering can be established from differential observations towards and away from galaxy clusters and other cosmic structures containing diffuse thermal and non-thermal plasmas. Unlike an experiment to directly establish the cosmic 21-cm frequency spectrum at low radio frequencies involving a total intensity measurement on the sky, differential observations with radio interferometers are less affected by the exact calibration of the observed intensity using an external source and by the confusion from Galactic foregrounds that are uniform over angular scales larger than those of a typical cluster, as the Galactic synchrotron background at low radio frequencies. Also, since the SZE does not depend on the redshift of the scattering cloud (e.g. clusters, radiogalaxy lobes), it is more suitable to study sources located at high-z, allowing to reduce the importance of the intrinsic radio emission of the source with respect to the SZE, and hence allowing to detect a larger number of sources, thus increasing the possibility to obtain more precise results by studying this effect in many sources at cosmological scales.
For this purpose, it is crucial to study the properties of the SZE-21cm in detail, by using a full

PoS(AASKA14)034

relativistic formalism suitable to study the SZE in a wide range of cosmic structures, including high-temperature gas in galaxy clusters as well as non-thermal and relativistic plasmas therein contained or associated with other cosmic structures like radio galaxy lobes (Colafrancesco et al. 2003, Colafrancesco 2008, Colafrancesco & Marchegiani 2014). Our general and complete approach is hence necessary to replace the simple and incorrect description of the SZE-21cm provided by Cooray (2006) that is performed in a non-relativistic approximation, considers a single thermal electron population and a single benchmark model for the CMB modified by the 21-cm background, and yields estimates of the SZE-21cm which are a factor from $\approx 40\%$ to $\gtrsim 3$ in disagreement with the correct calculation at the frequencies where the effect can be observed (Colafrancesco & Marchegiani 2014). The approach we present here provides a correct estimate of the SZE-21cm signals in various cosmic structures and thus allows to increase the number of objects that can be studied in this framework, including galaxy clusters with different properties, as radio halos, cooling flows and complex morphologies, and other extragalactic sources as radio galaxies. Moreover, in order to have a complete description of the CMB spectrum modified by the 21-cm background, we will also discuss models that include the effects of the DM annihilation heating.

2. The SZE-21cm

The input radiation field used here to calculate the SZE-21cm considers a general model taking into account three main sources: i) absorption and collision effects at $z \sim 200-30$; ii) Ly-α radiation field at $z \sim 30-20$, and iii) X-ray photon heating at $z \sim 20-6$ (details are given in Colafrancesco & Marchegiani 2014, Cooray 2006). We use this modified CMB radiation field scheme as a benchmark case for the sake of a general discussion of the SZE-21cm and its ability to probe the DA and EoR. We then use the results of the 21cm-fast code, with the addition of DM annihilation heating effects (Evoli and Ferrara, private communication, Valdes et al. 2013), in order to explore more detailed physical effects occurring during the DA and EoR. The modified CMB spectrum due to the 21-cm radiation, for both the benchmark case and the specific models of Valdes et al. (2013), is shown in Fig.1. The modified CMB spectrum emerging from the DA and EoR (see Fig.1) is then scattered by electrons (thermal and non-thermal) residing in the atmospheres of various cosmic structures (e.g., galaxy clusters, radiogalaxy lobes, galactic halos) and can be then measured by using a differential observing strategy on and off the specific cosmic structure and produce the specific SZE-21cm we discuss here. The spectral distortion due to the SZE of the CMB that is modified and emerged from the DA and EoR is given by

$$I_{mod}(x) = \int_{-\infty}^{+\infty} I_{0,mod}(xe^{-s})P(s)ds \tag{2.1}$$

(see Colafrancesco et al. 2003, Colafrancesco & Marchegiani 2014 for a general derivation), where $x = h\nu/(k_B T_0)$ is the normalized photon frequency, T_0 is the CMB temperature, h in the Planck constant and k_B the Boltzmann constant, $P(s)$ is the photon redistribution function (yielding the probability of a logarithmic shift $s = \ln(\nu'/\nu)$ in the photon frequency) that depends on the electrons spectrum producing the CMB Comptonization, and $I_{0,mod}(x)$ is the specific intensity of the incident CMB radiation field as modified during the DA and EoR. The function $P(s)$ can be calculated at the desired approximation order in the plasma optical depth τ or via a general relativistic

PoS(AASKA14)034

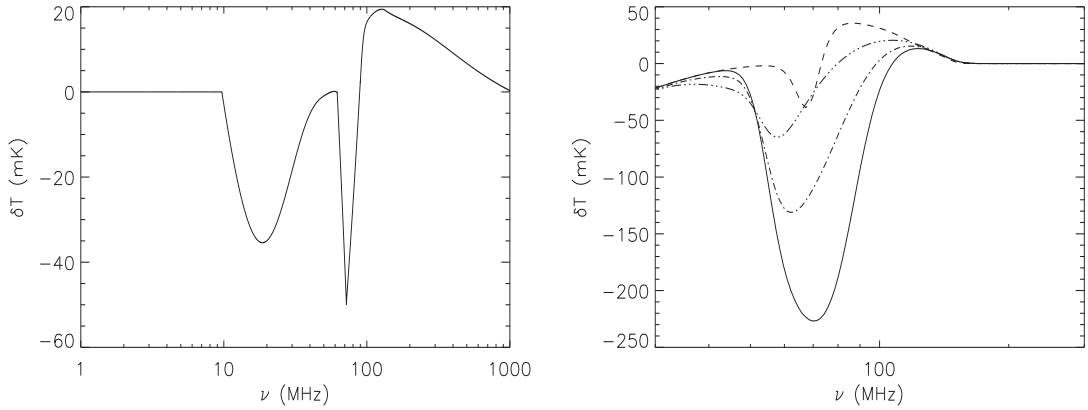

Figure 1: Modified CMB spectrum due to the 21-cm radiation (in units of brightness temperature relative to the CMB) for the benchmark case (left, from Cooray 2006), and for the models with DM heating (right, from Valdes et al. 2013). The right panel shows a fiducial model without DM (solid line), an extreme model without DM (dashed line), a fiducial model with DM with $M_{min} = 10^{-3}$ $M_\odot$ (dot-dashed line), where M_{min} is the mass of the smallest DM subhalo, and a fiducial model with DM with $M_{min} = 10^{-6}$ $M_\odot$ (three dots-dashed line).

method by using Fourier transform properties (see Colafrancesco et al. 2003 for details). Once the Comptonized spectrum in eq.(2.1) is calculated, the SZE is given by the difference:

$$\Delta I_{mod}(x) = I_{mod}(x) - I_{0,mod}(x) \ , \tag{2.2}$$

where $I_{0,mod}(x)$, written as a function of the frequency ν, is given by

$$I_{0,mod}(\nu) = I_0(\nu) + \delta I(\nu). \tag{2.3}$$

The modification to the CMB spectrum, $\delta I(\nu)$, can be expressed in terms of brightness temperature change relative to the CMB, defined as:

$$\delta T(\nu) = \frac{c^2}{2k_B\nu^2}\delta I(\nu). \tag{2.4}$$

In the following we discuss the results obtained for the specific case of the SZE-21cm produced by thermal electron populations, that provide the dominant contribution to the SZE observed in galaxy clusters, and by non-thermal electrons populations, that are present in clusters that show non-thermal activity (i.e. radio halos or relics) and in the extended lobes of radiogalaxies. We find that: *i)* the variations of the SZE-21cm w.r.t. the standard SZE with the non-modified CMB spectrum are more relevant for high-T clusters and for non-thermal electron plasmas with high values of minimum momentum p_1 (see Fig.2); *ii)* studying the spectrum of the SZE-21cm allows to derive precise information on the epoch at which the CMB has been modified and on the physical mechanism that produced such modifications. Specifically, the negative peak at ~ 60 MHz reflects the transition epoch between the collision/absorption and the Lyman-α interactions (at $z \sim 20-30$), while the positive peak at ~ 70 MHz reflects the effect of the Lyman-α deep absorption in the CMB spectrum ($z \sim 20$), and the negative peak at ~ 100 MHz shows the effect of the X-rays and UV reionization produced by first bright sources ($z < 20$). These spectral features in the SZE-21cm

PoS(AASKA14)034

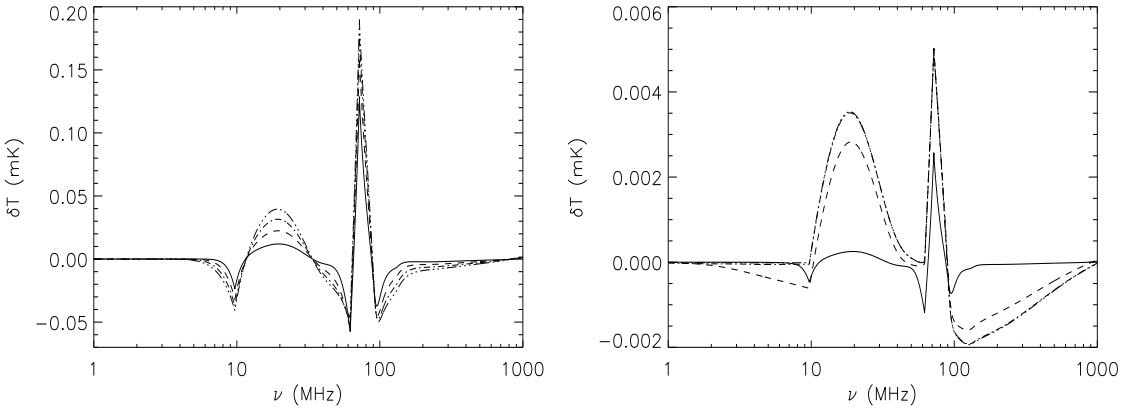

Figure 2: Left. Difference between the SZE-21cm and the standard SZE (in units of brightness temperature relative to the CMB) for clusters with thermal plasma at temperature k_BT =5, 10, 15 and 20 keV as shown by the solid, dashed, dot-dashed and dash-three dots lines, respectively. A constant value of the thermal electrons optical depth, $\tau = 5 \times 10^{-3}$, has been used in the calculations. Right. Difference between the SZE-21cm and the standard SZE (in units of brightness temperature relative to the CMB) for non-thermal electrons with a power-law spectrum with spectral index $s = 3.5$ and minimum momentum $p_1 = 0.1$, 1, 5 and 10, shown by the solid, dashed, dot-dashed and dash-three dots lines, respectively. A constant value of the non-thermal electrons optical depth, $\tau = 1 \times 10^{-4}$, has been used in the calculations.

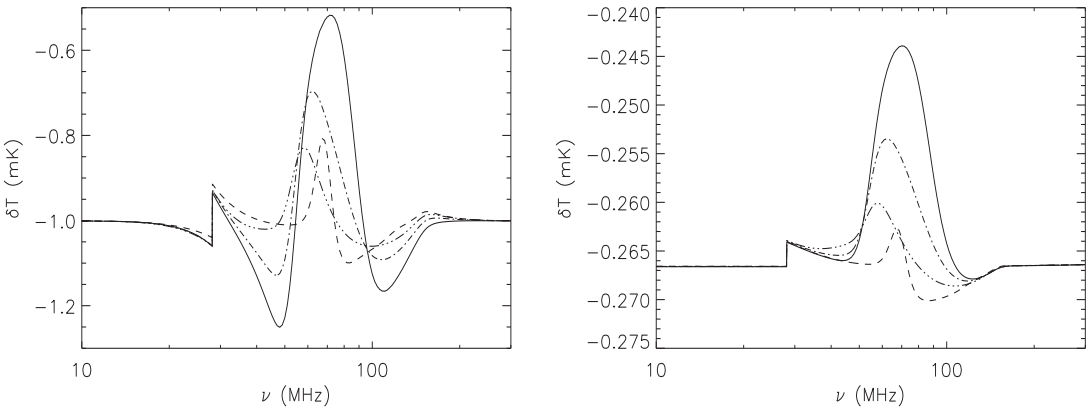

Figure 3: The SZE-21cm (in units of brightness temperature relative to the CMB) for a thermal plasma with $k_BT = 20$ keV and $\tau = 5 \times 10^{-3}$ (left panel) and for a non-thermal plasma with $s = 3.5$ and $p_1 = 10$ and with $\tau = 1 \times 10^{-4}$ (right panel). Both figures are calculated using the models of Valdes et al. (2013) for a modified CMB spectrum with a fiducial model without DM (solid line), an extreme model without DM (dashed line), a fiducial DM model with $M_{min} = 10^{-3}$ $M_\odot$ (dot-dashed line), and a fiducial DM model with $M_{min} = 10^{-6}$ $M_\odot$ (three dots-dashed line).

reflect hence the frequency location (i.e., the redshift occurrence) of the three main physical effects modifying the CMB spectrum. The SZE-21 cm calculated with the specific models in Fig.3 shows similar features in respect to the benchmark case, especially for the fiducial model without DM, where similar assumptions are made. In the extreme model, the effect of reionization by astrophysical sources is stronger, and this produces a damping in the modification to the CMB spectrum and to the SZE-21 cm. Similar effects can be produced also by DM annihilation heating, and in this case the damping is stronger in models with smaller values of minimum DM halo mass, since the

PoS(AASKA14)034

effect of smaller halos is more effective in heating the gas (Valdes et al. 2013); *iii)* the thermal and non-thermal SZE-21cm have quite different spectral shapes. Thus, it is possible, in principle, to derive information also on the existence and the properties of the electron populations in cosmic structures also from low-ν observations of the SZE-21cm. This property is complementary with the results of previous studies, according to which the properties of non-thermal electrons can be derived from the study of the SZE at higher frequencies (see, e.g., Colafrancesco et al. 2011, Colafrancesco 2013).

3. SKA observations of the SZE-21cm

Our analysis shows that most of information on the measurements of the SZE-21cm will come from the SKA1-LOW, for $\nu \lesssim 300$ MHz and additional/complementary information can also be obtained from SKA1-MID. The range of frequencies at which the SZE-21cm can be observed is from 10 to 300 MHz and the SKA1-LOW band 50-350 MHz is optimally suited to observe the thermal SZE-21cm. The SKA1-MID Band 1 (350-1050 MHz) is also interesting to address the observability of the tail in the non-thermal SZE-21cm. In Figure 4 we compare the flux calculated for the modified CMB and the one calculated for the non-modified CMB with the sensitivity of SKA1-LOW for 100 kHz bandwith, 1000 hrs of integration, 2 polarizations, no taper, no weight, and with the sensitivities of SKA-50% and SKA2 in the same conditions, by assuming a collecting area respectively 50% and 400% than SKA1. We find that the SZE-21 cm can be detected with SKA1 at frequencies $\nu \sim 70$ MHz for clusters with temperature $kT \approx 20$ keV and at $\nu \sim 90$ MHz even for relatively low temperature clusters $kT \approx 5$ keV.
Disentangling between the SZE-21cm and the standard SZE signals is more difficult: the difference between the two signals is always at most of the order of few μJy (see Figure 4, right panel), so this requires to measure the signal with high precision and at frequencies where the differences are larger. Good frequency channels for this purpose can be found at 62 MHz (where the SZE-21cm is stronger than the standard SZE because of the transition between collisions effect and Lyman-α interactions), 72 MHz (where the SZE-21cm is lower because of the Lyman-α peak), and at 96 MHz (where the SZE-21cm is stronger because of the X-ray heating effect). Because of the better sensitivity of SKA1-LOW at high frequencies, the best frequency range where we can obtain information on the SZE-21cm is $\nu \geq 96$ MHz. However, also in this frequency range the difference between the two signals is of the order of μJy, so very deep observations, and very accurate data analysis are required, together with the use of clusters with high values of temperature and optical depth. An appropriate strategy could be to select the SZE clusters at higher (mm. and sub-mm.) frequencies to derive precise information on the parameters of the ICM, and then use these constraints to obtain a better estimate of the properties of the SZE-21cm with SKA1-LOW. Instead, the goal to detect the difference between the standard and 21 cm-SZE can be achieved more easily with SKA2, for integration times of 1000 hrs. The detection of the non-thermal SZE-21cm in e.g. radiogalaxy lobes or cluster radio halos is more challenging being this signal a factor ~ 40 or more lower than the thermal SZE-21cm. However, the different spectral features of the non-thermal and thermal SZE-21cm (see Fig.2) can allow, in principle, a detection of this signal and hence an estimate of non-thermal cluster or radiogalaxy lobe properties independently of measurements in other spectral bands. In fact, it is possible to strategize the search of this signal in objects where

PoS(AASKA14)034

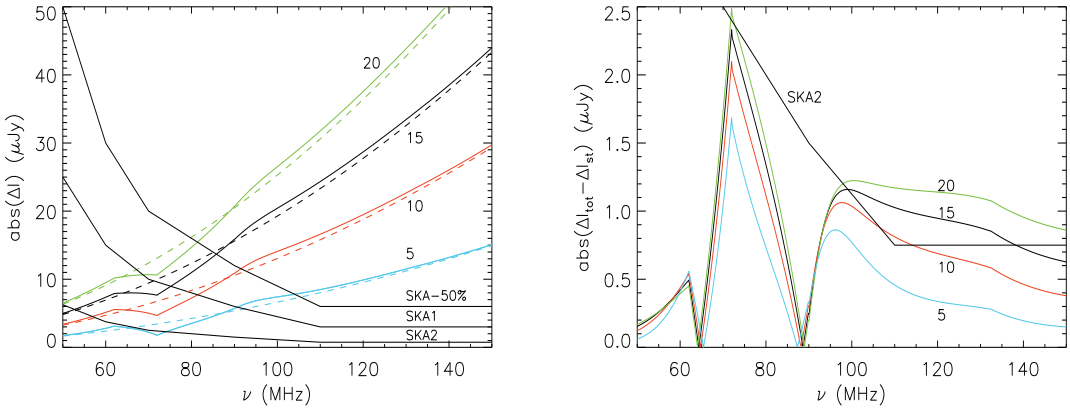

Figure 4: Left: spectra of the fluxes of the SZE-21cm (in units of μJy and in absolute value with the solid lines) and the SZE for a non-modified CMB (dashed lines) compared with the SKA1-LOW sensitivity for 100 kHz bandwith, 1000 hrs of integration, 2 polarizations, no taper, no weight, and the corresponding sensitivities for SKA-50% and SKA2 (thick lines). Right: absolute value of the difference between the SZE-21cm and the standard SZE for a non-modified CMB compared with the SKA2 sensitivity for 100 kHz bandwith, 1000 hrs of integration (thick line), 2 polarizations, no taper, no weight. Both figures refer to thermal plasma with temperatures $k_BT = 20$ (green), 15 (black), 10 (red) and 5 (cyan) keV, and are calculated for $\tau_0 = 5 \times 10^{-3}$, and a spatial profile given by a beta model with $\theta_c = 300$ arcsec, $\beta = 0.75$, $\theta_{max} = 10\theta_c$ (see Colafrancesco & Marchegiani 2014 for details).

the non-thermal components are dominant, such as in the case of radio galaxies lobes with more energetic electrons (i.e. with harder radio spectra), large optical depth (for which a good indication could be a strong radio luminosity) and high redshift, and to adopt a stacking analysis to derive information on the non-thermal SZE-21cm.

We stress here that the probe of the DA and EoR with the SZE-21cm technique we propose here would necessitate, in principle, of only one very deep observation of a hot massive cluster and one observation of a high optical depth radiogalaxy lobe, because the spectral features of the SZE-21cm are unique and not depending on the redshift of the source. However, observing a sample of galaxy clusters in the temperature range $10-20$ keV and a sample of radiogalaxy lobes with various spectra will provide a better characterization of the SZE-21cm spectral shape and hence a more precise determination of the DA and EoR spectral (redshift) features. A possible observational strategy for studying the SZE-21cm with the SKA is to observe *i)* a sample of high temperature and optical depth clusters in the souther hemisphere with high values of the Compton parameter $Y_{SZ} \propto \int d\ell P_e$ from Planck, SPT and ACT SZE source catalogs, and *ii)* a sample of radiogalaxies with extended lobes from existing catalogs of giant radio galaxies (GRG).
The range of frequencies at which the SZE-21cm can be observed is from 10 to 300 MHz and the SKA1-LOW band 50-350 MHz is optimally suited to observe the thermal SZE-21cm. The SKA1-MID Band 1 (350-1050 MHz) is also interesting to address the observability of the tail in the non-thermal SZE-21cm.
The reference resolution of SKA1-LOW at 110 MHz, corresponding to a minimum baseline of 50 km, is $\theta_{min} \sim 11$ arcsec. For an isothermal galaxy cluster, with a gas density profile given by a β-profile (Cavaliere & Fusco-Femiano 1976), the optical depth at a projected distance θ from the

PoS(AASKA14)034

center of the cluster is given by the expression:

$$\tau(\theta) = \tau_0 \left[1 + \left(\frac{\theta}{\theta_c} \right)^2 \right]^{\frac{1}{2} - \frac{3}{2}\beta} \tag{3.1}$$

(Colafrancesco et al. 2003). By assuming values typical of a near and rich galaxy cluster like Coma, i.e. $\tau_0 = 5 \times 10^{-3}$, $\beta = 0.75$, $\theta_c = 300$ arcsec, we can calculate the flux up to $\theta_{max} = 10\theta_c$, and we can estimate that the lack of sensitivity to scales $\theta < \theta_{min}$ implies a relative signal loss of the order of $\sim 1.1 \times 10^{-4}$ (Colafrancesco & Marchegiani 2014). Since the signal we aim to detect is of the order of tens of μJy at these frequencies (see Fig.4), the loss of signal is of the order of $\sim$ nJy, so it does not affect our results.

We note that the differential observations of the SZE-21cm are less affected by issues such as the exact calibration of the observed intensity using an external source and the confusion from galactic foregrounds that are uniform over angular scales larger than a typical cluster, as the Galactic synchrotron background at low radio frequencies. In addition, since the SZE does not depend on redshift, this technique is more suitable to study sources located at relatively large distances, allowing also to reduce the importance of their intrinsic radio emission with respect to the SZE-21cm, and allowing hence to detect a larger number of sources, thus increasing the possibility to obtain more precise results by studying this effect in many sources at cosmological scales. We also emphasize here that a particular attention must be dedicated to the subtraction of extended clumps of low-ν radio emission affecting the SKA1-LOW band.

Figure 4 shows that an early science study of the SZE-21cm with a 50% SKA1 performance can be obtained with a limited sample of very high-T clusters that maximize the probability of the SZE-21cm detection by producing the largest signals in the SKA1-LOW band. This project will benefit from the expected increase in sensitivity of SKA2 (see Fig.4), but will not depend on the SKA2 frequency coverage extension because the optimal ν range is still around $\nu \gtrsim 100$ MHz.

4. Conclusions and future outline

The SKA offers the unique possibility to probe the DA and the EoR also by using local structures as probes of this remote epoch. The SZE-21cm has the potential to provide precise studies of the DA and EoR, and its detection with the coming SKA can yield unique information on the history and physical mechanisms occurring during the DA and EoR. One of the advantages of using the SZE-21cm is the nature of its differential measurement and our knowledge of the cluster medium from local observations in the X-rays, radio and mm. frequency ranges. Observations have to be carried out towards high-temperature and high-optical depth (i.e., high Compton parameter Y_{SZ}) clusters to maximize both the amplitude of the signal and the spectral difference between the SZE-21cm and the standard SZE. The best frequency range of observations is between ≈ 70 and 110 MHz, where the difference between the SZE-21cm and the standard SZE is maximum, and the sensitivity of SKA1-LOW is sufficient to detect the overall signal with ≈ 1000 hours of integration. Together with such deep observations, a very accurate theoretical analysis is required, where the full formalism to calculate the SZE-21cm and detailed models for the cosmological 21-cm background must be used. It is also important to perform a detailed study of the SZE at higher

PoS(AASKA14)034

frequencies from existing (e.g., SPT, ACT) and future (e.g., Millimetron, SPT-3G) cluster observations in order to estimate the cluster plasma parameters to be used as prior constraints for the study of the SZE-21cm at the low radio frequencies covered by the SKA. Finally, the independence of the SZE from the redshift of the source allows the study of the SZE-21cm in a larger number of objects distributed over a wider redshift range, therefore producing statistical studies aimed at maximizing the detectable signal that will allow hence a better understanding of the cosmic history of the physical processes occurring during the DA and the EoR.

References

Barkana, R. and A. Loeb, 2005, Astrophys. J. 626, 1
Cavaliere, A. & Fusco-Femiano, R, 1976, A&A, 49, 137
Chen, X.L. and J. Miralda-Escude, 2004, Astrophys. J. 602, 1
Colafrancesco, S., 2008, MNRAS, 385, 2041
Colafrancesco, S. 2010, MmSAIt, 81, 104
Colafrancesco, S. 2013, Acta Pol., 53, 560
Colafrancesco, S., Marchegiani, P. and Palladino, E., 2003, A&A, 397, 27-52
Colafrancesco, S., Marchegiani, P. & Buonanno, R., 2011, A&A, 527, L1
Colafrancesco, S. and Marchegiani, P. 2014, A&A, submitted
Cooray, A., 2006, Phys. Rev. D, 73, 103001
de Oliveira-Costa, A. et al., 2008, MNRAS, 388, 247
Field, G.B. 1959, Astrophys. J. 129, 536
Koopmans, L. 2015, in proceedings of "Advancing Astrophysics with the Square Kilometre Array", PoS(AASKA14)001
Kravtsov, A.V. and Borgani, S., 2012, ARA&A, 50, 353
Loeb, A. and Zaldarriaga, M. 2004, Phys. Rev. Lett. 92, 211301
Paciga, G. et al., 2013, MNRAS, 433, 639
Pritchard, J.R., & Loeb, A. 2012, Rep. Progr. Phys., 75, 086901
Scott, D. and Rees, M.J. 1990, Mon. Not. R. Astr. Soc. 247, 510
Valdes, M., et al., 2013, MNRAS, 429, 1705
Wouthuysen, S.A., 1952, Astron. J., 57, 31

PoS(AASKA14)034

PROCEEDINGS OF SCIENCE

Foreground Subtraction in Intensity Mapping with the SKA

Laura Wolz[*1,2], **Filipe B. Abdalla**[1,3], **David Alonso**[2], **Chris Blake**[4], **Philip Bull**[5], **Tzu-Ching Chang**[6], **Pedro G. Ferreira**[2], **Cheng-Yu Kuo**[6], **Marios G. Santos**[7,8] **and Richard Shaw**[9]

[1] *Department of Physics and Astronomy, University College London, London WC1E 6BT, UK*
[2] *Astrophysics, University of Oxford, DWB, Keble Road, Oxford OX1 3RH, UK*
[3] *Department of Physics and Electronics, Rhodes University, PO Box 94, Grahamstown, 6140 South Africa*
[4] *Centre for Astrophysics & Supercomputing, Swinburne University of Technology, P.O. Box 218, Hawthorn, VIC 3122, Australia*
[5] *Institute of Theoretical Astrophysics, University of Oslo, P.O. Box 1029 Blindern, N-0315 Oslo, Norway*
[6] *Academia Sinica Institute of Astronomy and Astrophysics, P.O. Box 23-141, Taipei, 10617 Taiwan*
[7] *Department of Physics, University of Western Cape, Cape Town 7535, South Africa*
[8] *SKA SA, 4rd Floor, The Park, Park Road, Pinelands, 7405, South Africa*
[9] *Canadian Institute for Theoretical Astrophysics, 60 St. George Street, Toronto, ON M5S 3H8, Canada*

E-mail: lwolz@star.ucl.ac.uk

21 cm intensity mapping experiments aim to observe the diffuse neutral hydrogen (HI) distribution on large scales which traces the Cosmic structure. The Square Kilometre Array (SKA) will have the capacity to measure the 21 cm signal over a large fraction of the sky. However, the redshifted 21 cm signal in the respective frequencies is faint compared to the Galactic foregrounds produced by synchrotron and free-free electron emission. In this article, we review selected foreground subtraction methods suggested to effectively separate the 21 cm signal from the foregrounds with intensity mapping simulations or data. We simulate an intensity mapping experiment feasible with SKA phase 1 including extragalactic and Galactic foregrounds. We give an example of the residuals of the foreground subtraction with a independent component analysis and show that the angular power spectrum is recovered within the statistical errors on most scales. Additionally, the scale of the Baryon Acoustic Oscillations is shown to be unaffected by foreground subtraction.

Advancing Astrophysics with the Square Kilometre Array
June 8-13, 2014
Giardini Naxos, Italy

[*] Speaker.

PoS(AASKA14)035

1. Introduction

Intensity mapping of neutral hydrogen (HI) is a very promising, efficient tool to measure the large-scale structure of the Universe (Battye et al. 2004; Vujanovic et al. 2009; Lidz et al. 2011; Peterson & Suarez 2012). The HI gas with spectral emission of $\lambda = 21$cm caused by the spin-flip of the valence electron is assumed to linearly trace the Dark Matter distribution. In intensity mapping, the entire HI flux is measured in large resolution elements which still allow observations of structure on the Baryon Acoustic Oscillation scale (BAO) (Wyithe et al. 2008; Chang et al. 2008; Bull et al. 2014). These experiments are optimally conducted by telescopes with a large field-of-view (FoV) through, for instance, multi-pixel feeds. The Green Bank telescope (GBT) has pioneered the detection of the large scale structure with the 21 cm signal (Chang et al. 2010; Masui et al. 2013; Switzer et al. 2013). Near future experiments include single dish telescope such as BINGO (Battye et al. 2012) and interferometric designs such as CHIME (Bandura et al. 2014) or Tianlai (Chen 2012). The SKA will be able to carry out various intensity mapping experiments at different redshifts either in auto-correlation mode, i.e. single dish observations, or interferometric mode. For a more detailed discussion of intensity mapping with the SKA, we refer to the chapters by Santos et al. (2015) and Bull et al. (2015).

The drawback of intensity mapping observations are the foregrounds mainly due to the high radio emission of our own Galaxy caused by synchrotron and free-free electron radiation. In the considered frequency range, the Galactic foregrounds significantly dominate the acquired maps by several orders of magnitude. The only full-sky observation of the Galactic radio emission is at frequency $\nu = 408$MHz (Haslam et al. 1982). This map combined with smaller surveys is the basis of most studies to understand and fully model the Galactic radio emission, i.e. de Oliveira-Costa et al. (2008); Jelic et al. (2008); Alonso et al. (2014). The varying spectral index with latitude and the lack of small-scale observations impede the comprehension of the Galactic foregrounds. The missing observational constraints on the Galactic foregrounds make the subtraction a crucial, highly sensitive step in the intensity mapping analysis pipeline. Foreground residuals can cause serious systematic effects which bias the cosmological analysis and therefore require careful consideration (Wolz et al. 2014). Most statistical methods employed for this task are based on the spectral smoothness of the Galactic foregrounds whereas the cosmological signal is expected to have low correlations between frequency bins. Extragalactic foregrounds caused by bright point source emission are expected to show different spatial structure due to gravitational clustering and be far less dominant than Galactic sources. Extragalactic contaminations are yet to be fully incorporated in realistic simulations, however, not considered to cause any significant systematic effects.

In this article, we review three different foreground subtraction approaches: the Karhunen-Loève transform (KL, see Shaw et al. 2014a,b), the singular value decomposition (SVD, see Masui et al. 2013) and the independent component analysis (FASTICA, see Wolz et al. 2014). The SVD and FASTICA are blind search methods which decompose the data in principal or independent components, respectively, whereas the KL transform separates foregrounds and 21 cm signal by modeling their statistical properties. For the KL transform, we reconsider the foreground residuals of the power spectrum of an earlier study. We give an example of foreground removal by applying the FASTICA to an SKA phase 1 simulation for auto-correlation mode where we chose the settings

PoS(AASKA14)035

for SKA1-MID band 1. We emphasize that an SKA1-SUR band 2 experiment would have very similar prospects in terms of foreground removal and results are transferable to such an experiment. For SKA2 the foreground subtraction for experiments in the low redshift regime $z \approx 1$ will be less challenging due to higher signal-to-noise ratio. Intensity mapping of structure in higher redshifts $z \approx 3$, (which is of particular interest), is expected to be similarly challenging due to the increased sensitivity of the SKA2 experiment. We present the expected level of foreground residuals and BAO scale measurements in the angular power spectrum for FASTICA. In this work, we focus on methods which have been recently applied to intensity mapping simulations or data. In Chapman et al. (2015), foreground subtraction methods are presented in the context of SKA experiments on the epoch of reionization which potentially can be transferred to the intensity mapping framework.

The article is structured as follows. In Sec. 2, we describe the 21 cm signal, Galactic foregrounds and telescope noise properties including the simulation details. We also review the effect of instrumental errors on the foreground subtraction. In Sec. 3, the removal techniques are established and in the following Sec. 4, the performance of the FASTICA in foreground subtraction is evaluated by the considering the systematic errors. The conclusions are presented in Sec. 5.

2. Description of the Signal Components

In this section, we describe the nature of the cosmological signal we expect to observe and how we simulate it. We briefly outline the expected instrumental noise levels and review possible instrumental errors.

2.1 21cm Signal

The intensity in a frequency bin $\delta\nu$ coming from the 21cm emission of an object at redshift z with neutral hydrogen mass $M_{\rm HI}$, subtending a solid angle $\delta\Omega$ is given by Abdalla & Rawlings (2005)

$$I(\nu,\hat{\mathbf{n}}) = \frac{3\,h_p A_{12}}{16\pi\, m_{\rm H}} \frac{1}{((1+z)\,r(z))^2} \frac{M_{\rm HI}}{\delta\nu\,\delta\Omega} \nu_{21}, \tag{2.1}$$

where A_{12} is the Einstein coefficient corresponding to the emission from the 21 cm hyperfine transition, h_p is Planck's constant and $m_{\rm H}$ is the hydrogen atom mass. Here, $r(z)$ is the comoving curvature distance $r(z) = c\,\sinh(H_0\sqrt{|\Omega_k|}\,\chi(z)/c)/(H_0\sqrt{|\Omega_k|})$ and $\chi(z)$ is the radial comoving distance $\chi(z) = \int_0^z dz'/H(z')$.

This intensity $I(\nu,\hat{\mathbf{n}})$ can be written in terms of a black-body temperature in the Rayleigh-Jeans approximation $T = I\,c^2/(2k_B\nu^2)$, where k_B is Boltzmann's constant. Using this we can estimate the mean brightness temperature coming from redshift z and its fluctuations in terms of the neutral hydrogen density:

$$T_{21}(z,\hat{\mathbf{n}}) = (0.19055\,{\rm K})\,\frac{\Omega_{\rm b}\,h\,(1+z)^2\,x_{\rm HI}(z)}{\sqrt{\Omega_{\rm M}(1+z)^3+\Omega_\Lambda}}\,(1+\delta_{\rm HI}). \tag{2.2}$$

Here $x_{\rm HI}(z)$ is the neutral hydrogen fraction (i.e. fraction of the total baryon density in HI) and $\delta_{\rm HI}$ is the HI overdensity field in redshift space (smoothed over the volume defined by $\delta\nu$ and $\delta\Omega$).

We simulated the cosmological signal by generating a three-dimensional realization of the neutral hydrogen density in the lightcone using a lognormal field as described in section 3 of Alonso

PoS(AASKA14)035

et al. (2014). This was done using generic ΛCDM cosmological parameters $(\Omega_M, \Omega_b, \Omega_k, h, w_0, w_a, \sigma_8, n_s) = (0.3, 0.049, 0, 0.67, -1, 0, 0.8, 0.96)$, and we further assumed a redshift dependence for the neutral hydrogen fraction of $x_{\rm HI} = 0.008\,(1+z)$ and a clustering bias of 1 ($\delta_{\rm HI} = \delta$). Redshift-space distortions were included using the radial velocity field inferred from the Gaussian overdensity field used for the lognormal realization. The simulation box used is large enough to encompass a full-sky volume to redshift 2.5 (with the observer placed at the centre), and has a spatial resolution of about $2.65\,{\rm Mpc}/h$.

We interpolated the density field into spherical temperature maps at different frequencies using Eq. 2.2. These maps were generated using the HEALPix package (Gorski et al. 2005) with a resolution parameter `n_side` $= 512$ ($\delta\theta \sim 0.11^o$), at frequency intervals of $\delta\nu = 0.7\,$MHz between $405\,$MHz ($z \sim 2.5$) and $945\,$MHz ($z \sim 0.5$), making up a total of 770 frequency bands.

2.2 Galactic Foregrounds

For the simulation used in this analysis we generated foreground realizations for Galactic synchrotron emission and free-free emission (both Galactic and extragalactic). We used the method described in section 4 of Alonso et al. (2014) and did not include any leakage of the polarized synchrotron radiation.

The free-free foregrounds were generated as a Gaussian random realization of the corresponding power spectra modelled in Santos et al. (2005). This models these foregrounds as isotropic processes, which is obviously not a good approximation for the Galactic case. However, due to their exceptionally smooth frequency dependence and subdominant amplitude, we do not believe a more sophisticated modelling is required at this stage.

Galactic synchrotron is by far the largest foreground for intensity mapping, and a more complex method was used to simulate it. The method is largely based on that of Shaw et al. (2014b), and is also similar to those used in other studies (Jelić et al. 2010; Shaw et al. 2014a). The method starts by extrapolating the 408 MHz Haslam map (Haslam et al. 1982) to other frequencies using a given model for the direction-dependent synchrotron spectral index (for which we used the Planck Sky Model, see Delabrouille et al. 2013). Smaller-scale structure and frequency-decorrelation is then added on top of this through a Gaussian realization of the power spectra in Santos et al. (2005). Further details can be found in section 4.2 of Alonso et al. (2014).

2.3 Instrumental Noise

The noise RMS (flux sensitivity) for a single-pointing observation with a single-dish radio telescope is given by

$$\sigma_S = \frac{2k_B T_{\rm sys}}{A_e\sqrt{\delta\nu t_p}}, \tag{2.3}$$

where A_e is the effective collecting area of the dish, t_p is the duration of the observation, and we have assumed that the noise is Gaussian and uncorrelated. The total system temperature is $T_{\rm sys} = T_{\rm inst} + T_{\rm sky}$, where $T_{\rm inst} \sim$ few $\times$ 10K depends on the noise characteristics of the receiver system, and $T_{\rm sky} \approx 60{\rm K}(\nu/300\,{\rm MHz})^{-2.55}$ accounts for the temperature of the sky due to background radio emission. Converting Eq. (2.3) into a brightness temperature sensitivity gives $\sigma_T = T_{\rm sys}/\sqrt{\delta\nu t_p}$ in the Rayleigh-Jeans limit.

PoS(AASKA14)035

In our simulations, we assume that the various SKA configurations will be able to perform 10,000 hour auto-correlation surveys over an area of 30,000 sq. deg[1]. For an instrument with $N_{\rm dish}$ independent dishes, the total survey area $\Omega_{\rm tot}$ can be covered with an observation time per pointing of $t_p = t_{\rm tot}(N_{\rm dish}\Omega_B/\Omega_{\rm tot})$, where $\Omega_B \approx \lambda^2/A_e$ is the beam solid angle of a single dish. Assuming no overlap between survey pointings, the brightness temperature sensitivity per pointing becomes

$$\sigma_T = \frac{T_{\rm sys}}{\sqrt{\delta\nu t_{\rm tot}}}\sqrt{\frac{\Omega_{\rm tot}}{N_{\rm dish}\Omega_B}}. \tag{2.4}$$

The noise RMS per pixel in our simulations is then given by $\sigma_{\rm px} = \sigma_T\sqrt{\Omega_B\delta\nu/\Omega_{\rm pix}\delta\nu_{\rm pix}}$.

We simulate an intensity mapping experiment which can be performed by an SKA1-MID survey with band 1. We assume $T_{\rm inst} = 28$K for $N_{\rm dish} = 190$ with a dish diameter of $D_{\rm dish} = 15$m.

2.4 Instrumental Effects

In theory, the spectrally smooth foregrounds can be very well extracted by presented methods, however, instrumental effects significantly complicate the subtraction. Most of the foreground subtraction methods are not capable of dealing with varying beams which is required for auto-correlation observations. The issue can be mitigated by deconvolving the data to the lowest resolution, as has been done for our simulation and for example in Wolz et al. (2014). Scale-dependent foreground removal methods are required for future experiments in order to not lose spatial information.

The most prominent instrumental systematics are polarization leakage and frequency-dependent beam distortions which cause spatial and spectral modes to mix. In Alonso et al. (2014), a first step is taken to include polarization leakage in the intensity mapping simulation such that future studies can test the mode mixing effects. Additionally, calibration errors, telescope pointing errors and RFI adulterate signal processing. Existing methods need to be advanced to include these instrumental effects in the foreground removal step.

3. Review of Foreground Removal Methods

In the following section, we review selected foreground removal methods, the SVD, KL transform and FASTICA. Each of these methods have been designed and applied to different types of intensity mapping data types and are part of power spectrum estimator pipelines. The KL transform is part of a detailed interferometer simulation for CHIME (Shaw et al. 2014a,b). The SVD is a more empirical approach utilized to subtract the foregrounds of GBT observations (Masui et al. 2013; Switzer et al. 2013). The FASTICA has been tested on SKA-like simulations in Wolz et al. (2014). Each of these methods work in a different mathematical and experimental framework and we refer the reader to the respective articles for more details on the background description.

3.1 Karhunen-Loève Transform

The Karhunen-Loève transform has a long history in Cosmology (Bond 1995; Vogeley & Szalay 1996), but was first suggested as a method for 21 cm foreground removal in Shaw et al. (2014a). It

[1]We focus on auto-correlation surveys here because of their better sensitivity to relevant cosmological scales for the SKA Phase 1 configurations; see Santos et al. (2015) for a discussion of the relative merits of auto-correlation and interferometric surveys.

PoS(AASKA14)035

has also been used for the analogous problem of E/B mode separation for polarisation of the CMB (Lewis et al. 2002; Bunn et al. 2003). In this section, we give an overview of the technique, and discuss its practical implementation in Shaw et al. (2014a,b).

Ultimately foreground cleaning is simply a matter of finding a subset of our data within which there is significantly more 21 cm signal than there are astrophysical foregrounds. However, in the presence of mode mixing there is no immediately apparent representation which separates these signals. The Karhunen-Loève transform (often called the Signal-to-Noise eigendecomposition), gives an automated way of deriving this basis from the two-point statistics of each component.

This method requires models for the two-point statistics of both the signal and the foregrounds on the sky. We denote the matrix representation of the signal power spectrum as $\mathbf{C}_{21}$, whereas the foreground model, which includes both the synchrotron emission from our galaxy, and the contribution from a background of extragalactic point sources, is written as $\mathbf{C}_f$. Appropriate models are described in Shaw et al. (2014b)

The Karhunen-Loève transform seeks to find a linear transformation of the data $\mathbf{d}' = \mathbf{Pd}$ such that the covariance matrices of the 21 cm signal $\mathbf{S} = \mathbf{BC}_{21}\mathbf{B}^\dagger$ and foregrounds $\mathbf{F} = \mathbf{BC}_f\mathbf{B}^\dagger$ are jointly diagonalised. That is

$$\mathbf{S} \to \mathbf{S}' = \mathbf{PSP}^\dagger = \mathbf{\Lambda}\,, \tag{3.1}$$

and

$$\mathbf{F} \to \mathbf{F}' = \mathbf{PFP}^\dagger = \mathbf{I}\,, \tag{3.2}$$

where $\mathbf{\Lambda}$ is a diagonal matrix, and $\mathbf{I}$ is the identity. In this diagonal basis we can simply compare the amount of power expected in each mode by the ratio of the diagonal elements (this is given by the corresponding entries of $\mathbf{\Lambda}$), and identify the regions of the space with low foreground contamination (large entries in $\mathbf{\Lambda}$).

This transformation can be found by solving the generalised eigenvalue problem $\mathbf{Sx} = \lambda\mathbf{Fx}$. This gives a set of eigenvectors $\mathbf{x}$, and corresponding eigenvalues λ. Writing the eigenvectors in a matrix $\mathbf{P}$, row-wise, gives the transformation matrix to diagonalise the covariances. The eigenvalues λ corresponding to each eigenvector give the diagonal matrix $\mathbf{\Lambda}$. To isolate the 21 cm signal, we can simply select modes with eigenvalue (signal-to-foreground power) greater than some threshold. In Fig. 1 we show the effect of foreground cleaning on the power spectrum errors of simulated cylinder telescope similar to Bandura et al. (2014).

The Karhunen-Loève transform is a general and very effective scheme for the component separation. Unfortunately, the full covariance matrices are dense, and very large, $O(N_{\rm pix}N_{\rm freq}) \sim 10^8$–$10^9$ on a side, making the diagonalisation, which is an $O(N^3)$ operation, impossible in the general case. However, this technique can still be applied to the restricted domain of *transit telescopes*, where the symmetries of the system allow the problem to be broken up into many smaller problems which are significantly more tractable. This decomposition is known as the *m*-mode formalism, and was first demonstrated in Shaw et al. (2014a). Overall the complexity is reduced to $O(N_{\rm pix}^2 N_{\rm freq}^3)$ saving a factor of $\sim 10^6$ in computation.

3.2 Singular Value Decomposition

In this section, we present the foreground cleaning formalism in Switzer et al. (2013) for the redshifted HI survey with the Green Bank Telescope (GBT). It is based on the idea that the 21 cm sig-

PoS(AASKA14)035

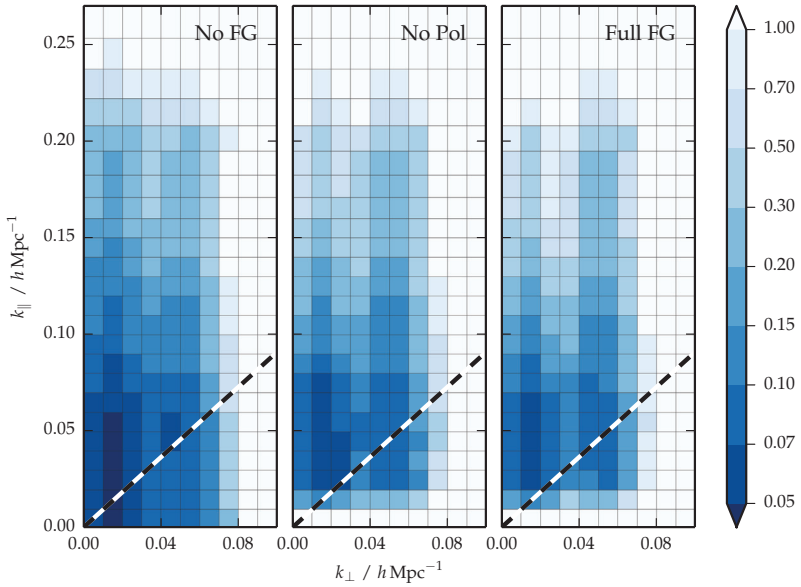

Figure 1: Forecast errors on the power spectrum as a fraction of its fiducial value for a 40 m × 40 m cylinder telescope similar to Bandura et al. (2014), observing between 400–500 MHz. The three panels show the predicted errors without foregrounds (left), with unpolarised foregrounds (centre), and with fully polarised foregrounds (right). We can see that we lose sensitivity to the large scale line of sight mode. The dashed line indicates the predicted bound of the 'foreground wedge', showing that with perfect knowledge of our instrument, foregrounds can be successfully cleaned well into this region.

nal is a line emission and has structure in the frequency/redshift domain, while the foregrounds are smooth on those scales. One can thus separate the two components in a model independent way by making use of principal component analysis. In this case, we arrange the three-dimensional maps into a frequency-frequency covariance matrix and use singular value decomposition to identify the dominant frequency modes. We label them as "foregrounds" and project out their contribution to obtain foreground cleaned maps.

Specifically, we rearrange the three-dimensional map into an $N_\nu \times N_\theta$ matrix $\mathbf{M}$, where N_θ includes all two-dimensional spatial pixels. For the purpose of this comparison, we ignore thermal noise in the map. The empirical $\nu - \nu$ covariance of the map is $\mathbf{C} = \mathbf{M}\mathbf{M}^{\mathrm{T}}/N_\theta$, which contains both foregrounds and 21 cm signal. Making use of the component separation idea, the matrix can be factored as $\mathbf{C} = \mathbf{U}\mathbf{\Lambda}\mathbf{U}^{\mathrm{T}}$, where $\mathbf{\Lambda}$ is diagonal and contains the eigenvalues in descending order. We tag the first few modes as 'foregrounds', and from each line of sight, we can then subtract a subset of the modes $\mathbf{U}$ that describe the largest components of the frequency variance through the operation $(1 - \mathbf{U}\mathbf{S}\mathbf{U}^{\mathrm{T}})\mathbf{M}$, where $\mathbf{S}$ is a selection matrix with 1 along the diagonal for modes to be removed and 0 elsewhere.

In practice, the separation of foreground and signal modes is not perfect due to the imperfect characterization of instrumental response. The choice of the selection matrix $\mathbf{S}$ is a compromise between maximal foreground removal and minimal signal loss. To estimate the latter, we inject simulated 21 cm signal to the data stream to determine the transfer function T which describes

PoS(AASKA14)035

loss of 21 cm signal due to foreground removal. As a rule of thumb, $T = P_{\mathrm{sig.\,out}}/P_{\mathrm{sig.\,in}} \sim [(1 - N_{\mathrm{m}}/N_{\nu})(1 - N_{\mathrm{m}}/N_{\mathrm{res}})]^2$, where N_{m} is the number of modes removed, N_{ν} is the number of frequency channels and N_{res} is the number of angular resolution elements. A limited number of resolution elements can greatly reduce the efficacy of the foreground cleaning at the expense of signal. The details of foreground transfer function calculation and the signal compensation can be found in Switzer et al. (2013).

Our approach to foreground removal is limited by the amount of information in the maps. The fundamental limitation here is not simply from the number of degrees of freedom along the line of sight, but instead is limited by the smaller of independent angular or frequency resolution elements in the map (Nityananda 2009). To see why this is the case, notice that in the absence of noise, our cleaning algorithm is equivalent to taking the SVD of the map directly: $\mathbf{M} = \mathbf{U\Sigma V}^{\mathrm{T}}$ and thus $\mathbf{C} \propto \mathbf{MM}^{\mathrm{T}} = \mathbf{U\Sigma}^2\mathbf{U}^{\mathrm{T}}$, with the same set of frequency modes $\mathbf{U}$ appearing in both decompositions. The rank of $\mathbf{C}$ coincides with the rank of $\mathbf{M}$ and is limited by the number of either angular or frequency degrees of freedom.

3.3 Independent Component Analysis

In the following subsection, the basic principles of the fast independent component analysis FASTICA method (Hyvärinen 1999) are outlined. FASTICA has been successfully used for foreground removal in the astrophysical framework, see for example Maino et al. (2002); Bottino et al. (2010); Chapman et al. (2012).

FASTICA is a method designed to decompose mixed signals into their independent constituents. Statistical independence is measured by the use of the Central Limit theorem which states that the probability distribution density (pdf) of a sum of independent variables is always more Gaussian than the pdf of one single component. The inverse application of that theorem implies that a single component can be extracted from the mixture by maximizing the non-Gaussianity of the pdf. This is turn implies that FASTICA can not be applied to Gaussian variables. We can formulate the problem in the linear equation $\mathbf{x} = \mathbf{As}$, where $\mathbf{x}$ is the signal, $\mathbf{A}$ the mixing matrix and $\mathbf{s}$ the independent components (IC). FASTICA blindly solves the inverted problem

$$\mathbf{s} = \mathbf{Wx} \tag{3.3}$$

where the weighing matrix $\mathbf{W}$ defined as the inverse of $\mathbf{A}$ is unknown. As a measure of the non-Gaussianity of the ICs, FASTICA maximizes a proxy for the negentropy.

FASTICA has been employed to subtract foregrounds in intensity mapping simulations in Wolz et al. (2014). Since the foregrounds are highly correlated between frequencies, FASTICA incorporates them into the ICs. The 21 cm signal has a very low correlation which is close to Gaussian. Hence, FASTICA blindly reconstructs the foregrounds and the residuals of this analysis are cosmological signal plus the receiver noise. In Wolz et al. (2014), it has been shown that foreground subtraction with FASTICA does not affect cosmological distance measures such as the BAO scale. An residual analysis of the SKA simulations with FASTICA is demonstrated in the following sections.

PoS(AASKA14)035

4. Residual Errors and BAO recovery

In this section, we present the foreground residuals and systematic errors when applying FASTICA to the described SKA1-MID simulation.

4.1 Experimental Set-up

The SKA1-MID band 1 simulation is based on the 21 cm and Galactic foregrounds simulation presented in Alonso et al. (2014), where the frequency range is 406MHz $< \nu <$ 945MHz with a frequency width of $\delta\nu = 0.7$MHz per channel. The beam is approximated by a Gaussian beam with constant solid angle $\Omega_{\text{beam}} = 1.6\text{deg}^2$. The instrumental noise is simulated according to Equ. 2.4 for an SKA-MID band 1 like observation. We mask out the sky above 63deg latitude in equatorial coordinates which results in a coverage of $30,000\text{deg}^2$. The intensity maps are stacked into constant redshift bins with width $\delta z \approx 0.05$ after the foreground removal to increase the signal-to-noise in the systematics analysis.

4.2 Results

We evaluate the foreground subtraction by estimating the angular power spectrum $C(\ell)$ of the original 21 cm intensity maps and the reconstructed maps. We correct for the partial sky coverage with the Peebles approximation, as described in Wolz et al. (2014). In Fig. 2(a), we show the relative error $C_{\text{ICA}}(\ell)/C_{\text{orig}}(\ell)$ of the FASTICA-cleaned maps for different number of ICs. The black error bars indicate the statistical variance of the measurements given by sampling error and instrumental noise. It can be seen that for a number of ICs higher than 4 the reconstruction converges towards the original input $C(\ell)$ for scales $\ell > 100$. For smaller scales, the broadband spectrum is slightly distorted and we observe deviations of $C_{\text{ICA}}(\ell)$ outside the statistical errors.

In Fig. 2(b), the relative systematic error $\delta(\ell, z_i)$ is depicted for all redshift bins z_i on the x-axis and for multipole bins $\delta\ell = 20$ in the y-direction. The systematic error is defined as $\Delta_{\text{sys}} = |C_{\text{orig}}(\ell) - C_{\text{ICA}}(\ell)|$. We divide that error by the statistical uncertainty on the measurements $\sqrt{\sigma(C(\ell))}$ composed of sampling variance and instrumental noise. The relative errors are pictured in a logarithmic scale such that values larger than zero imply insignificant systematic errors and smaller than zero indicate scales where systematics dominate the statistical errors. We see that the foregrounds at the edges of the redshift bins are poorly subtracted due to incomplete frequency information and those regions should be neglected in subsequent analysis.

Furthermore, we present BAO scale measurements of the SKA1 simulation in Fig. 3, the details of the methods can be found in Wolz et al. (2014). In Fig. 3(a), the BAO wiggles in the power spectrum produced by dividing by a BAO-featureless power spectrum model are shown for 4 different redshift bins. The lines represent the fitted models to the estimated data points. The black measurements mark the simulation without any foreground contaminations and the red lines include systematic errors. We see that there is no significant shift of the BAO features induced by the foreground subtraction. Fig. 3(b) presents the scale distortion parameter α as a function of redshift where $\alpha = D_A(z_i)/D_{A,\text{fid}}(z_i)$. The BAO recovery is not significantly affected by the foreground subtraction for most redshifts z_i.

PoS(AASKA14)035

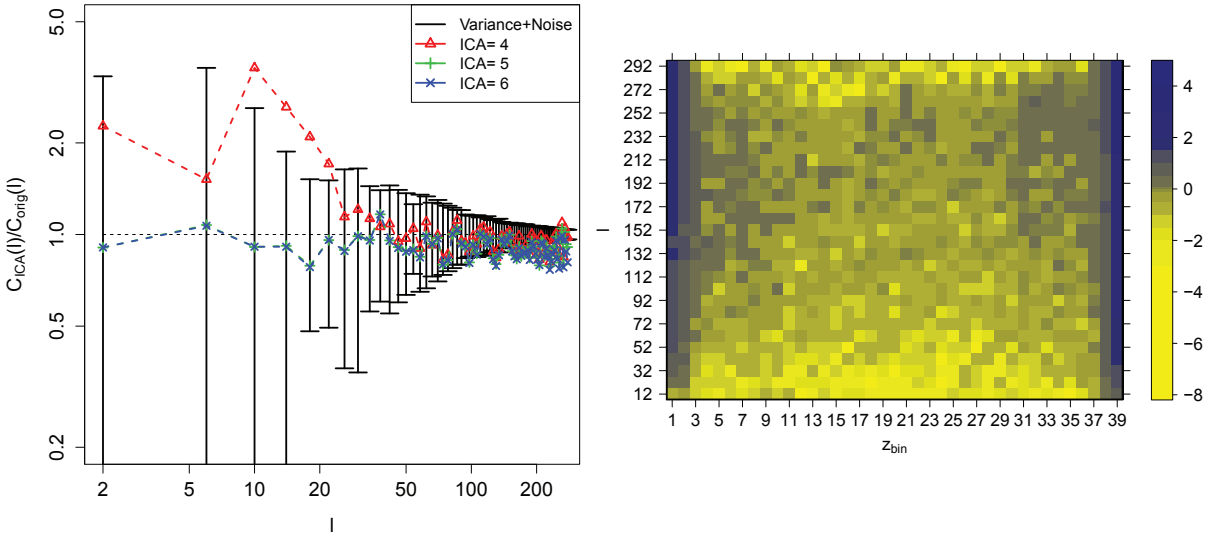

(a) Relative error on $C(\ell)$ for $1.45 < z < 1.50$

(b) Relative systematic errors; FASTICA with IC=5

Figure 2: The relative errors of the foreground subtraction with FASTICA on the angular power spectrum as a function of scale. On the left side, we present the fraction $C_{\mathrm{ICA}}(\ell)/C_{\mathrm{orig}}(\ell)$ for different numbers of ICA for an example redshift bin. The relative systematic errors $\delta(\ell, z_i)$ are given on a natural logarithmic scales in the right panel.

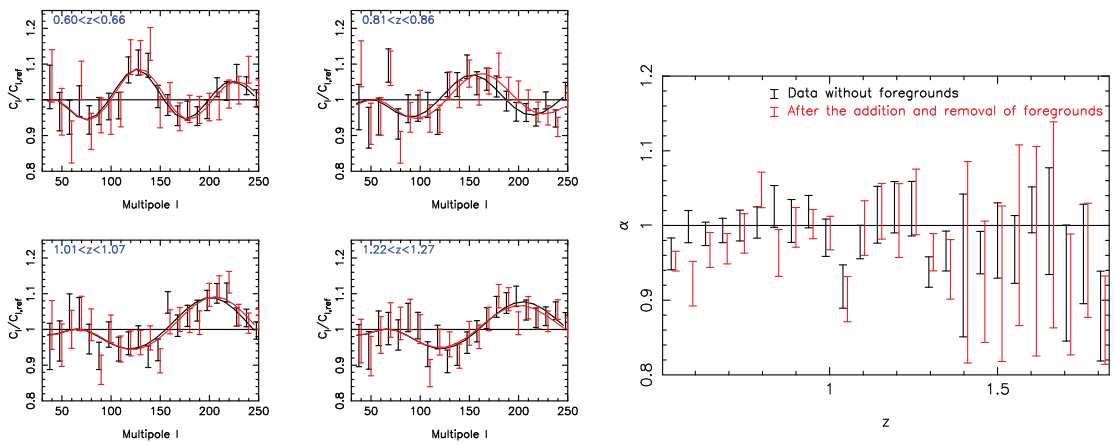

(a) BAO scale in angular power spectrum; FASTICA with IC=5

(b) BAO fit; FASTICA with IC=5

Figure 3: The BAO measurements of the original simulations without foregrounds (black) are compared to the measurements including foregrounds (red). In the left panel, we present the BAO wiggles in the angular power spectrum divided by a featureless fiducial model. The lines are produced by fitting a model to the measurements. The right panel shows the BAO scale distortion parameter α without and with foregrounds as a function of redshift.

PoS(AASKA14)035

5. Conclusions

In this article, we have presented a review of three effective methods for subtracting foregrounds in intensity mapping experiments. We have simulated a future SKA1 intensity mapping experiment with special focus on realistic foreground modeling. We presented a detailed residual analysis of the foreground-removed 21 cm signal with FASTICA. We conclude the article as follows.

- **Method comparison:** The KL transform is based on a-priori knowledge on the properties of foregrounds and 21 cm signal. SVD and FASTICA blindly decompose the observed data such that foregrounds are removed by subtracting an empirically chosen number of principal/independent modes. The blind methods are excellent in dealing with unexplored foregrounds or foreground fluctuations, however, prone to remove 21 cm signal or leave foreground residuals in the data. By detailed, realistic simulations and residual analysis such as presented in this work, the errors can be significantly reduced and systematics well-understood. The KL transform has the advantage of separating the components based on their covariances which reduces described errors. This method is less versatile to experimental settings due to its high computational costs and can possibly be affected by poor foreground modeling.

- **Systematic errors:** All presented methods have been shown to effectively clean intensity maps from high Galactic foregrounds in either simulations or observations such as the SVD method on the GBT data. Figs. 1 and 2 show that the systematic errors mostly affect the very large scales perpendicular to the line-of-sight. KL transform and FASTICA have been shown to not significantly bias the BAO detection in the cleaned data. We emphasize the importance of comprehensive and detailed simulations of intensity mapping experiments to ensure the reliability of the cosmological analysis.

- **Future requirements:** Instrumental errors can influence the data analysis significantly by mode-mixing effects. The foreground removal can be corrupted by telescope errors such as polarization leakage, telescope pointing and calibration errors. Shaw et al. (2014b) has included detailed instrumental effects in their simulation pipeline and studied the influence of each error on the power spectrum. Such effects require careful simulations for each individual experimental set-up in order to understand the systematic effects and how they interact with the foreground removal.

In this article, we outlined some of the latest efforts to subtract foregrounds from intensity mapping data. We showed that the 21 cm power spectrum can be successfully recovered via a wide range of scales and the BAO scale measurements are not biased by foreground subtraction. Within the next decade, those methods need to be advanced to the requirements of SKA1 and SKA2 experiments with special attention to include polarization effects and instrumental errors into the systematic analysis.

Acknowledgments

LW is supported by the IMPACT fund. FBA acknowledges the support of the Royal Society via a University Research Fellowship. DA is supported by European Research Council grant 259505.

PoS(AASKA14)035

CB acknowledges the support of the Australian Research Council through the award of a Future Fellowship. PB is supported by European Research Council grant StG2010-257080. PGF acknowledges support from the Higgs centre, STFC, BIPAC and the Oxford Martin School. MGS acknowledges support by the South African Square Kilometre Array Project, the South African National Research Foundation and FCT grant PTDC/FIS-AST/2194/2012.

References

Abdalla, F. B. & Rawlings, S. 2005, Mon.Not.Roy.astron.Soc., 360, 27

Alonso, D., Ferreira, P. G., & Santos, M. G. 2014, Mon.Not.Roy.astron.Soc., 444, 3183

Bandura, K., Addison, G. E., Amiri, M., et al. 2014, ArXiv e-prints

Battye, R. A., Brown, M. L., Browne, I. W. A., et al. 2012, ArXiv e-prints

Battye, R. A., Davies, R. D., & Weller, J. 2004, Mon.Not.Roy.astron.Soc., 355, 1339

Bond, J. R. 1995, Phys.Rev.Lett., 74, 4369

Bottino, M., Banday, A. J., & Maino, D. 2010, Mon.Not.Roy.astron.Soc., 402, 207

Bull, P., Ferreira, P. G., Patel, P., & Santos, M. G. 2014, ArXiv e-prints

Bull, P. et al. 2015, in Advancing Astrophysics with the Square Kilometre Array, PoS(AASKA14)024

Bunn, E. F., Zaldarriaga, M., Tegmark, M., & de Oliveira-Costa, A. 2003, Phys. Rev. D, 67, 023501

Chang, T.-C., Pen, U.-L., Bandura, K., & Peterson, J. B. 2010, Nature, 466, 463

Chang, T.-C., Pen, U.-L., Peterson, J. B., & McDonald, P. 2008, Phys.Rev.Lett., 100, 091303

Chapman, E., Abdalla, F. B., Harker, G., et al. 2012, Mon.Not.Roy.astron.Soc., 423, 2518

Chapman, E. et al. 2015, in Advancing Astrophysics with the Square Kilometre Array, PoS(AASKA14)005

Chen, X. 2012, Int.J.Mod.Phys.Conf.Ser., 12, 256

de Oliveira-Costa, A., Tegmark, M., Gaensler, B. M., et al. 2008, Mon.Not.Roy.astron.Soc., 388, 247

Delabrouille, J. et al. 2013, A.&A., 553, A96

Gorski, K., Hivon, E., Banday, A., Wandelt, B., Hansen, F., et al. 2005, astrophys.J., 622, 759

Haslam, C., Salter, C., Stoffel, H., & Wilson, W. 1982, astron.astrophys.Suppl.Ser., 47, 1

Hyvärinen, A. 1999, IEEE Transactions on Neural Networks, 10, 626

Jelic, V., Zaroubi, S., Labropoulos, P., et al. 2008, Mon.Not.Roy.astron.Soc., 389, 1319

Jelić, V., Zaroubi, S., Labropoulos, P., et al. 2010, Mon.Not.Roy.astron.Soc., 409, 1647

Lewis, A., Challinor, A., & Turok, N. 2002, Phys. Rev. D, 65, 023505

Lidz, A., Furlanetto, S. R., Oh, S. P., et al. 2011, astrophys.J., 741, 70

Maino, D., Farusi, A., Baccigalupi, C., et al. 2002, Mon.Not.Roy.astron.Soc., 334, 53

Masui, K. W., Switzer, E. R., Banavar, N., et al. 2013, astrophys.J.Lett., 763, L20

Nityananda, R. 2009, in Astronomical Society of the Pacific Conference Series, Vol. 407, The Low-Frequency Radio Universe, 389

Peterson, J. B. & Suarez, E. 2012, ArXiv e-prints

Santos, M. G., Cooray, A., & Knox, L. 2005, astrophys.J., 625, 575

Santos, M. G. et al. 2015, in Advancing Astrophysics with the Square Kilometre Array, PoS(AASKA14)019

PoS(AASKA14)035

Shaw, J. R., Sigurdson, K., Pen, U.-L., Stebbins, A., & Sitwell, M. 2014a, astrophys.J., 781, 57
Shaw, J. R., Sigurdson, K., Sitwell, M., Stebbins, A., & Pen, U.-L. 2014b, ArXiv e-prints
Switzer, E. R., Masui, K. W., Bandura, K., et al. 2013, Mon.Not.Roy.astron.Soc., 434, L46
Vogeley, M. S. & Szalay, A. S. 1996, astrophys.J., 465, 34
Vujanovic, G., Staveley-Smith, L., Pen, U.-L., Chang, T.-C., & Peterson, J. 2009, ATNF Proposal, 2491
Wolz, L., Abdalla, F. B., Blake, C., et al. 2014, Mon.Not.Roy.astron.Soc., 441, 3271
Wyithe, J. S. B., Loeb, A., & Geil, P. M. 2008, Mon.Not.Roy.astron.Soc., 383, 1195

PoS(AASKA14)035

PROCEEDINGS OF SCIENCE

Model-independent constraints on dark energy and modified gravity with the SKA

Gong-Bo Zhao [1, 2], **David Bacon** [2], **Roy Maartens** [3, 2], **Mario Santos** [3, 4], **Alvise Raccanelli** [5, 6, 7]

[1] *National Astronomy Observatories, Chinese Academy of Science, Beijing, 100012, People's Republic of China*
[2] *Institute of Cosmology and Gravitation, University of Portsmouth, Portsmouth, PO1 3FX, United Kingdom*
[3] *Department of Physics, University of the Western Cape, Cape Town 7535, South Africa*
[4] *SKA SA, 4th Floor, The Park, Park Road, Pinelands, 7405, South Africa*
[5] *Department of Physics & Astronomy, Johns Hopkins University, 3400 N. Charles St., Baltimore, MD 21218, USA*
[6] *Jet Propulsion Laboratory, California Institute of Technology, Pasadena CA 91109, USA*
[7] *California Institute of Technology, Pasadena CA 91125, USA*

Employing a nonparametric approach of the principal component analysis (PCA), we forecast the future constraint on the equation of state $w(z)$ of dark energy, and on the effective Newton constant $\mu(k,z)$, which parameterise the effect of modified gravity, using the planned SKA HI galaxy survey. Combining with the simulated data of Planck and Dark Energy Survey (DES), we find that SKA Phase 1 (SKA1) and SKA Phase 2 (SKA2) can well constrain 3 and 5 eigenmodes of $w(z)$ respectively. The errors of the best measured modes can be reduced to 0.04 and 0.023 for SKA1 and SKA2 respectively, making it possible to probe dark energy dynamics. On the other hand, SKA1 and SKA2 can constrain 7 and 20 eigenmodes of $\mu(k,z)$ respectively within 10% sensitivity level. Furthermore, 2 and 7 modes can be constrained within sub percent level using SKA1 and SKA2 respectively. This is a significant improvement compared to the combined datasets without SKA.

Advancing Astrophysics with the Square Kilometre Array
June 8-13, 2014
Giardini Naxos, Italy

PoS(AASKA14)165

1. Introduction

The physical origin of the acceleration of the universe remains unknown since its discovery in 1998 using supernovae (SN) observations (Riess et al. 1998; Perlmutter et al. 1999). It might imply that there exists a repulsive 'dark energy' component dominating the universe, or that we need a better understanding of the law of gravity, *i.e.*, the general relativity (GR) might need to be modified on cosmological scales (For a recent review of modified gravity theories, see Clifton et al. 2012). Although dark energy (DE) and modified gravity (MG) can accelerate the universe at the background level in the same way after the required tuning, the degeneracy can be broken when the cosmic structure formation is investigated.

In this era of precision cosmology, a combination of multiple observation probes including SN, cosmic microwave background (CMB), and large scale structure (LSS) surveys is key to unveil the mystery of the cosmic acceleration (Weinberg et al. 2013). This is because different kinds of surveys can be highly complementary, *e.g.*, the weak lensing (WL) and redshift surveys are able to probe $\gamma(k,z)$, quantifying the deviation of photon's trajectory from the geodesics, and $\mu(k,z)$, the time and spatial variation of the Newton's constant respectively, which are two different effects predicted by a wide range of MG models, making the combination of WL with redshift surveys robust for GR tests, as well as for the dark energy studies.

Given that the CMB and WL surveys of Planck (Planck Collaboration et al. 2014) and Dark Energy Survey (DES) [1] are accumulating data, we need large redshift surveys to complement. The BOSS spectroscopic survey (Anderson et al. 2014) of SDSS-III is currently the largest redshift survey worldwide, mapping the 10,000 square degree sky up to $z = 0.7$ by tracing 1.5 million luminous galaxies. It will be succeeded by eBOSS [2], a multi-tracer spectroscopic survey of SDSS-IV, which will focus on a smaller patch of the sky (7500 square degree) but going deeper. According to the forecast, it will achieve 1-2% distance measurement from the baryon acoustic oscillations (BAO) between $0.6 < z < 2.5$. The Square Kilometre Array (SKA) [3] HI galaxy redshift survey can provide us with accurate redshifts (using the 21cm line) of millions of sources over a wide range of redshifts, making it an ideal redshift survey for cosmological studies (Bull et al. 2015; Raccanelli et al. 2015; Bacon et al. 2015; Kitching et al. 2015; Santos et al. 2015; Abdalla et al. 2015).

Traditionally, observational constraints on DE or MG using either current or future data are usually performed in a parameterised fashion, *i.e.*, the equation of state of DE, $w(z)$, or the $\mu(k,z)$ and $\gamma(k,z)$ functions quantifying the effect of MG (Zhao et al. 2009b) [4], are parameterised using assumed function forms, and then the observational constraints on these parameters are worked out. Simple as it is, this approach has its drawbacks,

- It may cause *theoretical bias*: the result largely depends on the functional form used for the parametrisation, which is *a priori*. The functional forms are usually chosen for the purpose of simplicity, or for the assumed theoretical consistency, or for both;

[1] More details of the Dark Energy Survey are available at http://www.dark-energysurvey.org/
[2] More details of the eBOSS survey are available at http://www.sdss.org/sdss-surveys/eboss/
[3] More details of the SKA survey are available at https://www.skatelescope.org/
[4] There are other ways to parameterise the effect of MG, *e.g.*, see Baker et al. (2013).

PoS(AASKA14)165

- The number of parameters are usually minimised, *e.g.*, the CPL parametrisation (Chevallier & Polarski 2001; Linder 2003) of $w(z)$ has 2 parameters, while the BZ parametrisation (Bertschinger & Zukin 2008) for MG has 5 parameters. This can yield a reasonably good constraint on the reconstructed $w(z)$, or the MG functions even when data is weak, but it might under fit the data when data is excellent.

However, in nonparametric methods, including the principal component analysis (PCA), it is the assumption, rather than the number of parameters, that is minimised, hence it can largely avoid the theoretical bias.

In this chapter, we use the PCA method to perform the forecast of $w(z)$ and $\mu(k,z)$ using a SKA HI redshift galaxy survey.

2. Methodology

In this section, we employ a standard Fisher matrix technology (Tegmark et al. 1997) to perform the future forecast.

2.1 The Fisher matrix formulism

For a redshift survey, the Fisher matrix formalism reads (Seo & Eisenstein 2007) [5],

$$F_{ij} = \int_{-1}^{1} \mathrm{d}\mu \int_{k_{\min}}^{k_{\max}} \mathrm{d}k \, \frac{\partial \ln \tilde{P}(k,\mu)}{\partial p_i} \frac{\partial \ln \tilde{P}(k,\mu)}{\partial p_j} V_{\mathrm{eff}}(k,\mu) \frac{k^2}{8\pi^2} \tag{2.1}$$

$$\tilde{P}(k,\mu) = (b + f\mu^2)^2 P(k) e^{-k^2\mu^2\Sigma^2} \tag{2.2}$$

$$V_{\mathrm{eff}}(k,\mu) = \left[\frac{nP(k)(1+\beta\mu^2)^2}{nP(k)(1+\beta\mu^2)^2 + 1} \right]^2 V_{\mathrm{sur}} \tag{2.3}$$

where $\tilde{P}(k,\mu), V_{\mathrm{eff}}$ denote the power spectrum in redshift space and the effective volume respectively, and V_{sur} is the actual volume of the redshift survey. We have used the Kaiser formula, *i.e.*, Eq (2.2) to evaluate $\tilde{P}(k,\mu)$, where $P(k)$ is the linear matter spectrum calculated using `CAMB` (Lewis et al. 2000), b and f are the linear bias and the growth function respectively. To account for the Finger of God (FoG) effect, we have chosen Σ to be 4 Mpc, which is consistent with simulations.

The Fisher matrix formulae for CMB and WL surveys are elaborated in Zhao et al. (2009b).

2.2 Specifications of future SKA HI surveys

A future SKA HI redshift survey will trace the galaxies at radio wavelengths, and the redshifts will be measured precisely using the emission lines. In this work, we consider Phase 1 and Phase 2 of SKA HI surveys (dubbed SKA1 and SKA2 respectively). SKA1 will achieve an RMS flux sensitivity of $S_{\mathrm{rms}} \simeq 70 - 100\mu$Jy with SKA1-MID or SUR, surveying over 5000 deg^2 in 10,000 hours. The expected total number of galaxies in Phase 1 is roughly 5 million at redshift $z \lesssim 0.5$ with a 5σ detection. In Phase 2, a 10,000 hours survey over $30,000$ deg^2 will detect one billion galaxies

[5] Note that this is the Fisher matrix for a given redshift bin. The final Fisher matrix is the sum over the Fisher matrices of individual redshift bins.

PoS(AASKA14)165

at a 10σ detection level. The expected galaxy distribution and bias for SKA1 (SKA2) is shown in Fig 1. For more details of the survey specifications, see Santos et al. (2015). Although SKA1 is not able to compete with the BOSS survey, SKA2 will surpass any planned spectroscopic surveys in the optical bands at $z \lesssim 1.4$.

2.3 Cosmological parameters

To be generic, we parameterise the universe using parameters

$$P = \{\Omega_b h^2, \Omega_c h^2, h, \tau, n_s, A_s, w_i, \mu_{ij}, \gamma_{ij}\} \tag{2.4}$$

where $\Omega_b h^2$ and $\Omega_c h^2$ are energy density of baryons and cold dark matter respectively, h is the Hubble constant, τ is the optical depth, n_s and A_s are the spectral index and the amplitude of the primordial power spectrum respectively. w denotes the equation-of-state of dark energy. In general, we treat $w(z)$ as a unknown function and determine how many degrees of freedom of it can be constrained using the PCA method (Huterer & Starkman 2003; Crittenden et al. 2009, 2012; Zhao et al. 2009a; Asaba et al. 2013; Hall et al. 2013). To do this, we bin w in the late-time universe, namely, $0 \leq z \leq 30$ using $M+1$ z-bins, and consider the value of w in each bin as an independent parameter. Since the surveys we consider in this work will not be able to probe $z > 3$ in detail, we use M bins linear in z for $0 \leq z \leq 3$ and a single bin for $3 \leq z \leq 30$.

The μ and γ's are modified gravity parameters and they are defined as follows.

In Newtonian gauge, the linear scalar perturbations to the flat Friedmann-Robertson-Walker metric read,

$$ds^2 = -a^2(\eta)[(1+2\Psi(\vec{x},\eta))d\eta^2 - (1-2\Phi(\vec{x},\eta))d\vec{x}^2], \tag{2.5}$$

where η is the conformal time and $a(\eta)$ the scale factor. In Fourier space, one can write (Hu & Sawicki 2007; Bertschinger & Zukin 2008),

$$k^2\Psi = -\mu(k,a)4\pi G a^2 \rho \Delta \tag{2.6}$$

$$\Phi/\Psi = \gamma(k,a) \tag{2.7}$$

where Δ is the comoving matter density perturbation. The function γ describes anisotropic stresses, while μ describes a time- and scale-dependent rescaling of Newton's constant G, as well as the effects of DE clustering or massive neutrinos. In ΛCDM, the anisotropic stress due to radiation is negligible during matter domination, thus $\mu = \gamma = 1$.

Similar to $w(z)$, we treat $\mu(k,a)$ and $\gamma(k,a)$ as unknown functions and forecast how well we can constrain the eigenmodes of them using PCA. Since they are 2-variable functions in both k and a, we have to *pixelise* them in the (k,z) plane. We pixelise the late-time and large-scale universe ($0 \leq z \leq 30, 10^{-5} \leq k \leq 0.2\,\mathrm{h\,Mpc^{-1}}$) into $M+1$ z-bins and N k-bins, with each of the $(M+1)\times N$ pixels having independent values of μ_{ij} and γ_{ij}. We consider $w(z)$ as another unknown function, allowing each of the $M+1$ z-bins to have an independent value of w_i. We use M bins linear in z for $0 \leq z \leq 3$ and a single bin for $3 \leq z \leq 30$. We choose $M = N = 20$ and have checked that this pixelisation is fine enough to ensure the convergence of the results. We use logarithmic k-bins on superhorizon scales and linear k-bins on subhorizon scales, to optimize computational efficiency. As in Zhao et al. (2009b), we only consider information from scales well-described by linear perturbation theory, which is only a fraction of the (k,z)-volume probed by future surveys. Since the

PoS(AASKA14)165

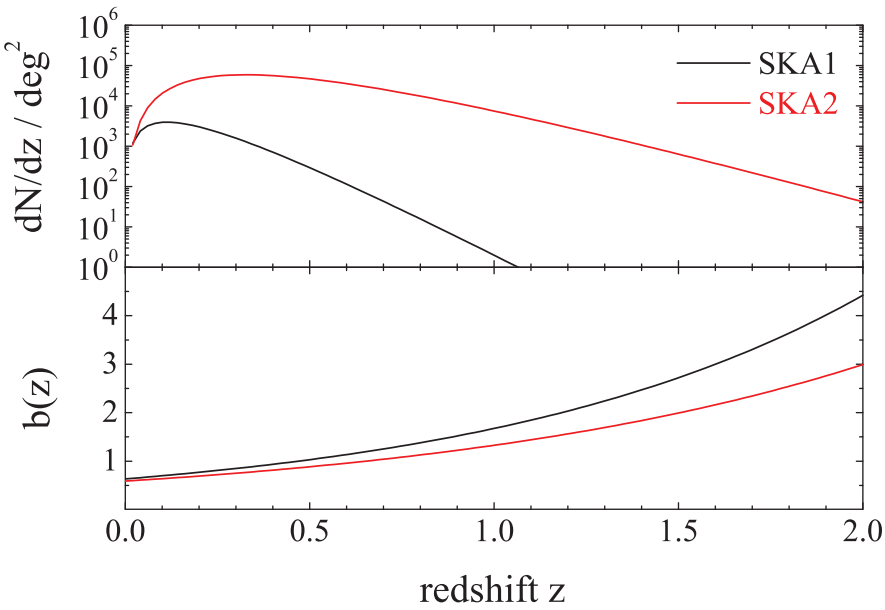

Figure 1: Upper panel: The expected galaxy distribution for SKA1 and SKA2; Lower panel: the corresponding bias as a function of redshift.

evolution equations (Zhao et al. 2009b) contain time-derivatives of $\mu(k,z)$, $\gamma(k,z)$ and $w(z)$, we follow Crittenden et al. (2009) and Zhao et al. (2009a) and use hyperbolic tangent functions to represent steps in these functions in the z-direction, while steps in the k-direction are left as step functions. The total number of free parameters in our forecast is therefore $(M+1)(2N+1)+17 = 878$.

2.4 The principal component analysis (PCA) method

The PCA method is a traditional method in data analysis. It helps to identify the *principal components* (PCs) of data by maximising the data covariance matrix. In cosmology, PCA has been used in determining the well-constrained combinations [6] of cosmological parameters, *e.g.*, the binned equation of state $w(z)$ of dark energy (Huterer & Starkman 2003; Crittenden et al. 2009, 2012) and the pixelised 2-variable functions of $\mu(k,z)$ and $\gamma(k,z)$ (Zhao et al. 2009a; Asaba et al. 2013; Hall et al. 2013), which quantify the deviation from general relativity on cosmological scales.

Generically, the PCA method can be formulated as follows. Let F be an $N \times N$ Fisher information matrix for a parameter set $P = \{p_1, p_2, ..., p_N\}$. We can find the *eigenmodes* of F by matrix diagonalisation, namely,

$$F = W^T \Lambda W, \tag{2.8}$$

where $\Lambda = \mathrm{diag}(\lambda_1, \lambda_2, ..., \lambda_N)$, and W is the transformation matrix relating P to Q, which is a set

[6] The PCA method discussed here identifies the best measured *linear* combinations of cosmological parameters, although extensions exist, *e.g.*, the kernel PCA method (Schölkopf et al. 1998) can optimise the constraint on *nonlinear* combinations of parameters.

PoS(AASKA14)165

of new parameters $Q = \{q_1, q_2, ..., q_N\}$. P and Q are related via,

$$Q = WP \tag{2.9}$$

The matrices Λ and W store the eigen-values and eigen-vectors of F: W tells how to map the old correlated parameters, the p's, to the new orthogonal ones, the q's, and Λ quantifies the uncertainty on the q's. The best measured parameter is the q with the minimal error (the one corresponding to the maximum entry in matrix Λ).

For dark energy, the p's are the binned $w(z)$ in redshift z. W helps to locate the 'sweet-spots' (the redshifts where the error on $w(z)$ get minimised), and Λ quantifies how 'sweet' they are (the size of errors when measuring these modes). For modified gravity, the p's are the pixelised functions of $\mu(k,z)$ and $\gamma(k,z)$ in the (k,z) plane, and the eigen-vectors in this case are 2D surfaces.

3. Results

For a given set of parameter values, we use MGCAMB (Zhao et al. 2009b; Hojjati et al. 2011) to compute the observables. We generate numerical derivatives of observables with respect to parameters, and use the specifications for the experiments to compute the Fisher information matrix, which defines the sensitivity of the experiments to these parameters (see Zhao et al. 2009b for computational details). Our fiducial values are in all cases ΛCDM: $\gamma_{ij} = \mu_{ij} = -w_i = 1$ for all i and j, and the fiducial values of the other parameters are those of Planck.

Besides the SKA HI surveys, we consider the two-point correlations (both auto- and cross-) between weak lensing shear (WL), and cosmic microwave background (CMB) temperature anisotropy, plus the CMB E-mode polarization and its correlation with the CMB temperature. Detailed descriptions of our assumptions for each measurement are found in Zhao et al. (2009b). WL is sourced by the sum of the potentials $(\Psi+\Phi)$. CMB data probe the Integrated Sachs-Wolfe effect (ISW) which depends on $\partial(\Phi+\Psi)/\partial\eta$. Thus, measuring WL over multiple redshift bins, along with CMB data, yields information about the relation between Ψ and Φ and their response to matter density fluctuations. For our forecasts, we assume the following probes: Planck (Planck Collaboration et al. 2014) for CMB, and DES for WL.

In what follows in the section, we shall present the results of our forecast for dark energy and modified gravity respectively.

3.1 Dark Energy constraints

In this section, we focus on DE constraints in the framework of general relativity. Therefore we fix the μ and γ pixels to be unity, but vary the remaining parameters in Eq (2.4) simultaneously. After marginalising over other parameters, we perform a PCA on the w bins.

The result is shown in Figs 2 and 3. In Fig 2, we show the 68% CL forecasted error on the part of the principal components (PCs) for four different data combinations. As shown, within the level of $\sigma(\alpha_i) < 0.5$, Planck alone can only constrain 1 mode (the distance to the last scattering surface); Planck + DES can constrain 2 modes, while adding in SKA1 or SKA2 can constrain 3 and 5 eigenmodes to this level. In particular, the best measured modes using SKA1 and SKA2 (combined with Planck and DES) can be determined at the level of $\sigma(\alpha_1) = 0.04$ and $\sigma(\alpha_1) =$

PoS(AASKA14)165

0.023 respectively. This is a significant improvement given that $\sigma(\alpha_1) = 0.25$ (Planck alone) and $\sigma(\alpha_1) = 0.13$ (Planck + DES).

The eigenvectors for the best constrained modes are shown in Fig 3. Roughly speaking, the nth best measured mode has $n-1$ nodes, corresponding to the $(n-1)$th time derivative of w. Having SKA helps determining the higher derivatives of $w(z)$, which is key to probe dark energy dynamics.

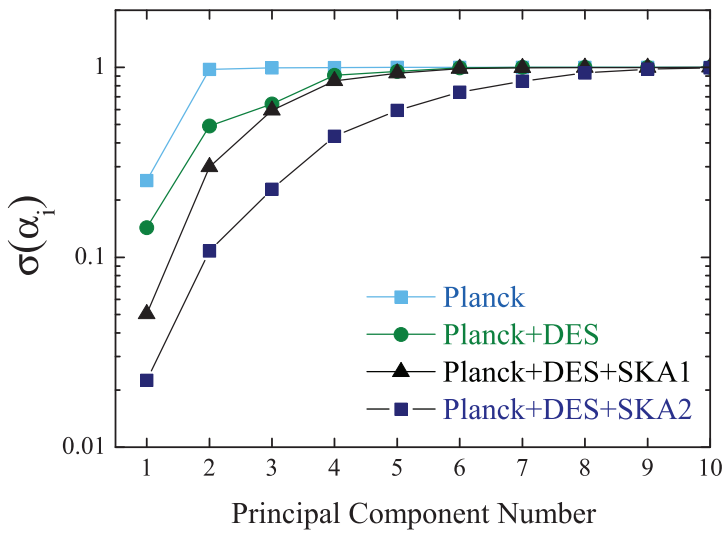

Figure 2: The forecasted 68% CL measurement error on α_i, the coefficient of the ith principal components of $w(z)+1$, namely, $w(z)+1 = \sum_i \alpha_i e_i(z)$, using different data combinations illustrated in the legend. A weak prior of $\sigma(w(z)) < 1$ was assumed.

3.2 Modified Gravity constraint

Here we consider the most general case, in which we drop the assumption of general relativity. Therefore we vary all the parameters in Eq (2.4) simultaneously and focus on the constraint on the μ and γ.

Let us study the expected errors on $\mu(k,z)$ [7]. The error on any μ_{ij} is large, and the pixels have highly correlated errors. We take only the μ_{ij} block of the covariance matrix, thus marginalizing over all other parameters, including the w_i and γ_{ij}. We invert this block to obtain the Fisher matrix for our μ values, $F_{(\mu)}$, and diagonalize $F_{(\mu)}$ by writing $F_{(\mu)} = W^T \Lambda W$. We expect, from existing data, that variations in μ larger than $\mathcal{O}(1)$ are unlikely. We enforce this by applying a prior $\lambda_m > 1$ to the matrix $F_{(\mu)}$. This procedure does not affect the well-measured modes, but gives a reference point with respect to which we define poorly constrained modes. Since we compute the full covariance matrix, then marginalize over all but the parameter(s) of interest, our procedure yields the results that we would get for μ if we simultaneously measured w, γ, and μ. This analysis can be repeated for γ or w.

[7] We don't show the γ constraint here since redshift surveys don't constrain γ directly.

PoS(AASKA14)165

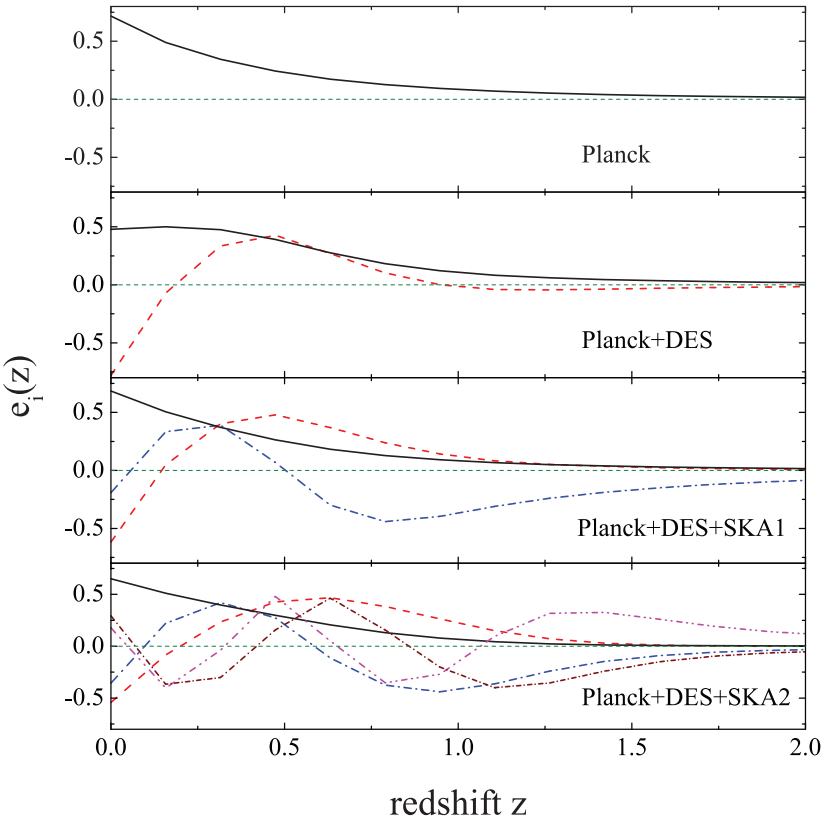

Figure 3: The best determined eigenvectors (with errors less than 0.5) of $w(z)$ for different data combinations shown in the legends. The modes are shown, in the order from better constrained to worse, as black solid, red dashed, blue dash-dot, purple dash-dot-dot and brown short dash-dot curves.The short dashed green horizon line shows $e_i(z) = 0$.

Measurements of WL and CMB probe combinations of Φ and Ψ, so the effects of γ, which affects only Φ, are mixed with those of μ, which affects both potentials. This yields degeneracy between μ and γ. But this degeneracy can be broken when SKA is combined since it only measures Ψ through the RSD.

From Fig. 4, we see that Planck + DES could not constrain any modes within 10% level, but adding in SKA1 can easily help to constrain 7 modes to this level. SKA2 can further increase this number to 20. In particular 2 and 7 modes can be constrained within sub percent level using SKA1 and SKA2 respectively.

Fig. 5 shows three best constrained eigenmodes for μ for different data combinations. A first observation is that the modes with more nodes (a node appears when eigensurfaces cross zero) are less constrained. This is intuitive: noisy modes are worse constrained than the smooth modes. The best modes are mainly functions of k and not z. This is partly because the total observable volume

PoS(AASKA14)165

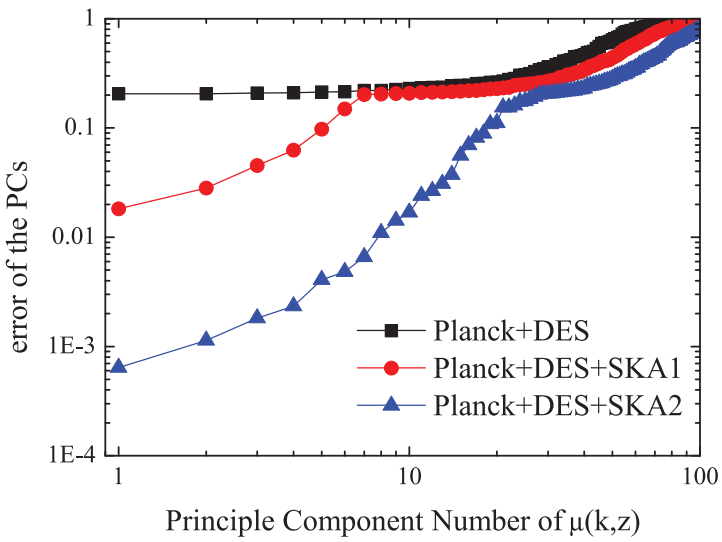

Figure 4: The forecasted 68% CL error on the coefficients of the principal components of $\mu(k,z)$ for different data combinations shown in the legend.

in the radial (z) direction is limited by the dimming of distant objects and, ultimately, the fact that structures only exist at relatively low z. Also, it is related to us considering only linear perturbations in our analysis, since at small z the observable volume is too small to fit the small k-modes that are still in the linear regime. Hence, there is more volume available for studying the spatial distribution of structure than the radial distribution.

For Planck+DES, we see a clear degeneracy in the k and z dependences of the modes. This is because changing μ at some point (k,z) should have the same impact on the observables as a change at a larger scale but later time. Interestingly, this k and z dependence goes away when SKA is combined. This is simply because SKA constrains μ very well via the RSD effect, which means that data can well distinguish the effect between the variation of μ in k and in z.

4. Conclusion and Discussions

In this work we apply the PCA method to investigate the constraint on dark energy and modified gravity using the future SKA HI redshift surveys, combined with CMB (Planck) and WL (DES) surveys. The PCA method is ideal to investigate dark energy and modified gravity in a non-parametric way, which efficiently minimises the theoretical bias stemming from choosing *ad hoc* functional forms for unknown functions.

We study dark energy and modified gravity separately. For dark energy equation-of-state, we find that SKA Phase 1 (2) can well constrain 3 and 5 eigenmodes of $w(z)$ respectively. The errors on the best measured modes can be reduced to 0.04 and 0.023 for SKA1 and SKA2 respectively, making it possible to probe dark energy dynamics (Zhao et al. 2012). On the other hand, for modified gravity constraints, SKA1 (2) can constrain 7 (20) eigenmodes of $\mu(k,z)$ respectively within

PoS(AASKA14)165

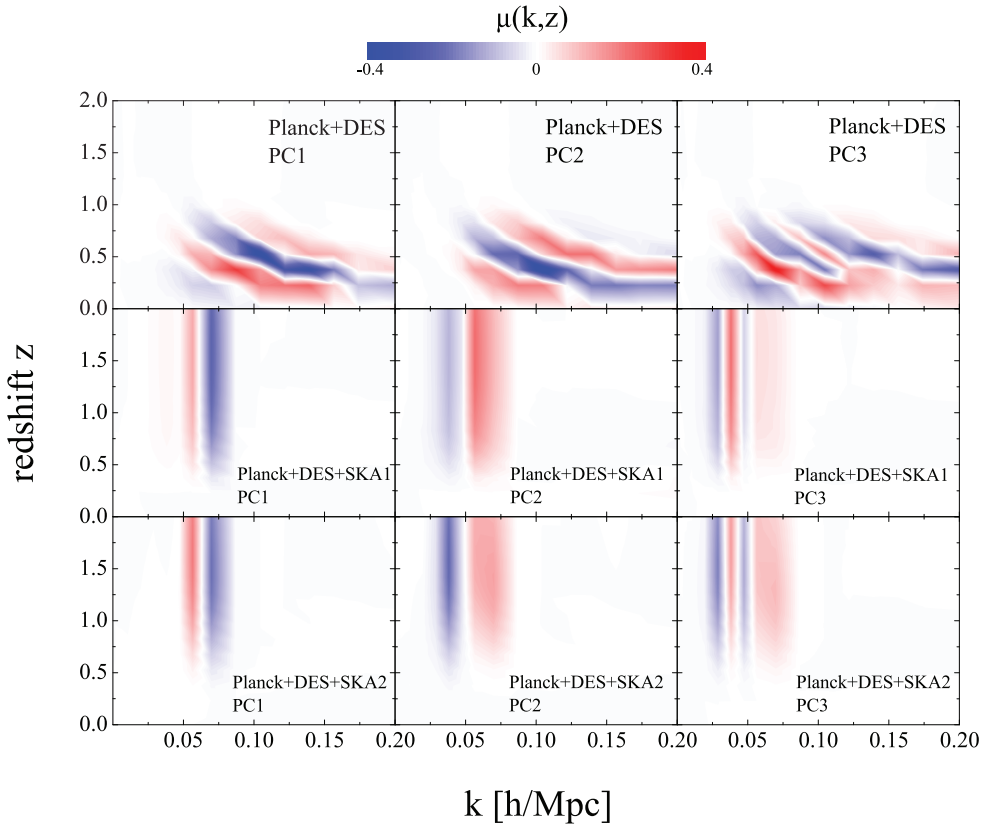

Figure 5: Eigensurfaces for the first three best constrained modes of μ after marginalisation over all other cosmological parameters. Top row: Planck + DES; Middle: Planck + DES + SKA1; Bottom: Planck + DES + SKA2.

10% sensitivity level. In particular 2 and 7 modes can be constrained within sub percent level using SKA1 and SKA2 respectively.

Imaging and redshift surveys are highly complementary when constraining cosmological parameters, especially for modified gravity models (Guzik et al. 2010; Song et al. 2011; Gaztañaga et al. 2012). The method developed in this work can be directly applied to future surveys of LSST (LSST Science Collaboration et al. 2009) and Euclid (Laureijs et al. 2011). For synergy between SKA and LSST and Euclid, see Bacon et al. (2015) and Kitching et al. (2015).

Acknowledgement:
GBZ is supported by Strategic Priority Research Program "The Emergence of Cosmological Structures" of the Chinese Academy of Sciences, Grant No. XDB09000000, by the 1000 Young Talents program in China, and by the 973 Program grant No. 2013CB837900, NSFC grant No. 11261140641, and CAS grant No. KJZD-EW-T01. All numeric calculations were performed on the SCIAMA2 supercomputer at University of Portsmouth. RM and MS are supported by the South African SKA Project and the National Research Foundation. DB and RM are supported by the UK Science & Technology Facilities Council (grant No. ST/K0090X/1).

PoS(AASKA14)165

References

Abdalla, F. *et al.*. 2015, Proceedings of "Advancing Astrophysics with the Square Kilometre Array", PoS(AASKA14), 017

Anderson, L. *et al.*. 2014, MNRAS, 441, 24

Asaba, S., Hikage, C., Koyama, K., Zhao, G.-B., Hojjati, A., & Pogosian, L. 2013, JCAP, 8, 29

Bacon, D. *et al.*. 2015, Proceedings of "Advancing Astrophysics with the Square Kilometre Array", PoS(AASKA14), 145

Baker, T., Ferreira, P. G., & Skordis, C. 2013, Phys. Rev. D, 87, 024015

Bertschinger, E. & Zukin, P. 2008, Phys. Rev. D, 78, 024015

Bull, P. *et al.*. 2015, Proceedings of "Advancing Astrophysics with the Square Kilometre Array", PoS(AASKA14), 024

Chevallier, M. & Polarski, D. 2001, International Journal of Modern Physics D, 10, 213

Clifton, T., Ferreira, P. G., Padilla, A., & Skordis, C. 2012, Phys. Rept., 513, 1

Crittenden, R. G., Pogosian, L., & Zhao, G.-B. 2009, JCAP, 12, 25

Crittenden, R. G., Zhao, G.-B., Pogosian, L., Samushia, L., & Zhang, X. 2012, JCAP, 2, 48

Gaztañaga, E., Eriksen, M., Crocce, M., Castander, F. J., Fosalba, P., Marti, P., Miquel, R., & Cabré, A. 2012, MNRAS, 422, 2904

Guzik, J., Jain, B., & Takada, M. 2010, Phys. Rev. D, 81, 023503

Hall, A., Bonvin, C., & Challinor, A. 2013, Phys. Rev. D, 87, 064026

Hojjati, A., Pogosian, L., & Zhao, G.-B. 2011, JCAP, 8, 5

Hu, W. & Sawicki, I. 2007, Phys. Rev. D, 76, 104043

Huterer, D. & Starkman, G. 2003, Physical Review Letters, 90, 031301

Kitching, T. *et al.*. 2015, Proceedings of "Advancing Astrophysics with the Square Kilometre Array", PoS(AASKA14), 146

Laureijs, R. *et al.*. 2011, arXiv1110.3193

Lewis, A., Challinor, A., & Lasenby, A. 2000, ApJ, 538, 473

Linder, E. V. 2003, Physical Review Letters, 90, 091301

LSST Science Collaboration *et al.*. 2009, arXiv0912.0201

Perlmutter, S. *et al.*. 1999, ApJ, 517, 565

Planck Collaboration *et al.*. 2014, A & A, 571, A16

Raccanelli, A. *et al.*. 2015, Proceedings of "Advancing Astrophysics with the Square Kilometre Array", PoS(AASKA14), 031

Riess, A. G. *et al.*. 1998, AJ, 116, 1009

Santos, M. *et al.*. 2015, Proceedings of "Advancing Astrophysics with the Square Kilometre Array", PoS(AASKA14), 021

Schölkopf, B., Smola, A. J., & Müller, K. R. 1998, Neural Computing, 10, 1299

Seo, H.-J. & Eisenstein, D. J. 2007, ApJ, 665, 14

Song, Y.-S., Zhao, G.-B., Bacon, D., Koyama, K., Nichol, R. C., & Pogosian, L. 2011, Phys. Rev. D, 84, 083523

Tegmark, M., Taylor, A. N., & Heavens, A. F. 1997, ApJ, 480, 22

Weinberg, D. H., Mortonson, M. J., Eisenstein, D. J., Hirata, C., Riess, A. G., & Rozo, E. 2013, Phys. Rept., 530, 87

PoS(AASKA14)165

Zhao, G.-B., Crittenden, R. G., Pogosian, L., & Zhang, X. 2012, Physical Review Letters, 109, 171301

Zhao, G.-B., Pogosian, L., Silvestri, A., & Zylberberg, J. 2009a, Physical Review Letters, 103, 241301

—. 2009b, Phys. Rev. D, 79, 083513

PoS(AASKA14)165

PROCEEDINGS OF SCIENCE

Stacking of SKA data: comparing uv-plane and image-plane stacking

Kirsten K. Knudsen[*1], **Lukas Lindroos**[1], **Wouter Vlemmings**[1], **John Conway**[1], **Iván Martí-Vidal**[1]

[1] *Chalmers University of Technology*

E-mail: kirsten.knudsen@chalmers.se, lindroos@chalmers.se

Stacking as a tool for studying objects that are not individually detected is becoming popular even for radio interferometric data, and will be widely used in the SKA era. Stacking is typically done using imaged data rather than directly using the visibilities (the *uv*-data). We have investigated and developed a novel algorithm to do stacking using the uv-data. We have performed extensive simulations comparing to image-stacking, and summarize the results of these simulations. Furthermore, we disuss the implications in light of the vast data volume produced by the SKA. Having access to the uv-stacked data provides a great advantage, as it allows the possibility to properly analyse the result with respect to calibration artifacts as well as source properties such as size. For SKA the main challenge lies in archiving the uv-data. For purposes of robust stacking analysis, it would be strongly desirable to either keep the calibrated uv-data at least in an average form, or implement a *stacking queue* where stacking positions could be provided prior to the observations and the uv-stacking is done almost in real time.

Advancing Astrophysics with the Square Kilometre Array
June 8-13, 2014
Giardini Naxos, Italy

[*]Speaker.

PoS(AASKA14)168

1. Introduction

Stacking is known as a tool to average together data for a given set of objects. In most cases, this is done for imaging and photometry where the sources in question are not individually detected (though have known positions). In that case, stacking the data yields an average detection or upper limit. This is done for data across the whole electromagnetic spectrum ranging from X-rays to radio (e.g. Nandra et al. 2002; Worsley et al. 2005; Knudsen et al. 2005; Dole et al. 2006; Carilli et al. 2008).

A large part of the imaging produced in radio comes from interferometric observations, with many large surveys available or planned (e.g., VLA-COSMOS, Schinnerer et al. 2007, and the VLA 1.4 GHz Survey of the Extended Chandra Deep Field South, Miller et al. 2013). The success of stacking using the interferometric images depends on how well the image reconstruction and deconvolution process has been. For example, as interferometric observations act as a spatial filter, flux could be missing or very bright sources can have caused increased noise and/or artifacts in the imaging.

The SKA will offer access to so much data and large surveys, that stacking will become a frequently used tool to study the fainter sources. This naturally gives rise to the question, what are efficient stacking tools? We have investigated stacking directly in the uv-plane on the visibilities rather than in the image-plane. We have developed a novel algorithm and compared this to image-stacking. In this chapter we discuss some of the implications of the results for stacking of SKA data.

While the scientific motivation for our work is studying faint, high-redshift galaxies with star formation rates below a few $M_{\odot}$/yr, galaxies, the algorithm analysed here would also find application in other fields of astronomy, and both for spectral line and continuum studies.

2. A novel *uv*-stacking algorithm

We have developed a new stacking algorithm for radio inteferometric data. The algorithm works directly on the uv-data and is applicable to any radio interferometric data. The algorithm has been tested on simulated data mimicking JVLA and ALMA observations and compared to image-stacking, i.e. stacking on the reconstructed and deconvolved images. This is presented in the paper Lindroos et al. (2015).

In summary, the algorithm works as follows: For sources (i.e. given positions) within a single pointing the visibilities are recalculated using

$$V_{\rm stack}(u,v,w) = V(u,v,w)\frac{\Sigma_{k=1}^{N} w_k \frac{1}{A_N(\hat{\mathbf{S}}_\mathbf{k})} e^{\frac{2\pi}{\lambda} i\mathbf{B}\cdot\left(\hat{\mathbf{S}}_\mathbf{0}-\hat{\mathbf{S}}_\mathbf{k}\right)}}{\Sigma_{k=1}^{N} w_k} \tag{2.1}$$

where $\hat{\mathbf{S}}_\mathbf{0}$ is the unit vector pointing to the phase centre, $\hat{\mathbf{S}}_\mathbf{k}$ is the unit vector pointing to the stacking positions, $A_N(\hat{\mathbf{S}}_\mathbf{k})$ describes the primary beam attenuation in the direction $\hat{\mathbf{S}}_\mathbf{k}$, $\mathbf{B}$ is the baseline of the visibility, λ is the wavelength, and w_k is the weight of the stacking position. This means, that the visibilities are not duplicated, yielding the important advantage that the size of the data set is not increased and kept managable. Furthermore, as the computation for each visilibity is done independently, the code can be parallellized and thus run quickly for large sets.

PoS(AASKA14)168

The whole algorithm is designed to be able to handle the effects from e.g. mosaics and wide-field observations. For mosaics, the algorithm is run for each pointing individually, and subsequently concatenated into one data set. Weights are recalculated to include the relative weights between pointings.

In the design of the algorithm, wide-field effects (for example, stretching of the *uv*-coordinates local to the stacked position) do not pose any restrictions on point-sources. In the case of extended sources, we estimate that the baseline re-projection effects should not be larger than at most a few per cent in the recovered size when using the JVLA, though larger for the longer SKA1-mid baselines.

In order to test the algorithm, we have carried out extensive simulations of JVLA and ALMA type of data. These data represent both the GHz and 100's GHz regime. The JVLA like simulations provide the closest representation to the SKA data, in particular SKA-MID. The simulations have systematically covered different aspects. The sources input to the simulations were defined as 'bright foreground sources' and 'target sources'. The former represent the bright sources across the sky and typically contribute to the noise. The latter are the sources of interest to be stacked. We have investigated several effects, in particular: sub-pixel sampling, wide-field effects, bright foreground sources, extended sources, and mosaiced fields. Below we focus on the extended foreground and target sources.

2.1 Extended bright foreground sources

The presence of bright sources in the data impacts on the dynamic range. While this is already a challenge for present-day interferometric arrays such as the JVLA, this will be even more pronounced for the SKA.

Bright sources present in data need to be removed, and this is generally the case both for image- and uv-stacking. Typically, bright sources are removed using the best available model, however, there will always be residuals left depending on the depth of the deconvolution, the quality of the data, and how well the sources can be modeled. In the GHz range, many radio sources have complex morphology, e.g. jets and lopes of radio galaxies, and this makes it difficult to completely model the flux distribution.

We have run extensive simulations, where bright, extended foreground sources were introduced. The size of the sources varied between a FWHM of 0.5" to 5" and the flux varied following a log-polynomial distribution derived from the COSMOS field (Bondi et al. 2008). After imaging (using Multi-Frequency Synthesis, Conway et al. 1990, combined with *w*-projection, Cornwell et al. 2008) and deconvolution (using CLEAN, Högbom 1974), a residual measurement set is produced and the noise in the centre of the deconvolved image is twice that of the thermal noise limit. Simulations were run in a Monte Carlo setup with typically 100 realisations to reduce statistical variations. Here we focus on the setup of a JVLA A-array configuration with a central frequency of 1.4 GHz and a bandwidth of 250 MHz (for further details, see Lindroos et al. 2015).

As an example, in Fig. 1, we show the amplitude as function of uv-distance for a uv-stacked source from a simulation with extended bright foreground sources; the bright foreground sources were removed from the simulated data using the Clean algorithm. We find that the short baselines of the stacked source suffer from imperfect bright source removal. Because the stacking was performed in the uv-plane we were able to measure the stacked flux reliably when selecting the

PoS(AASKA14)168

baselines not, or less affected by the bright source residuals, and thus determine the stacked flux to the level of the input model. For comparison, the fluxes measured in with image-stacking were about 10 per cent lower than the input model. As a check, we have carried out a similar simulation but without the bright foreground sources, and the resulting stacked source has no visible problems at the short baselines.

2.2 Extended target sources

Expanding the simulations, we have simulated target sources that are slightly extended with a size of 1.5" for the JVLA A-array configuration. The aim of this was to determine the performance of *uv*-stacking vs image-stacking in terms of estimating an average size. In Fig. 2, we show the amplitude as function of uv-distance for the stacked source. Again, as discussed above, the shortest baselines suffer from imperfect removal of the bright sources in the field. The uncertainty of size-estimate done using the uv-stacked data is half that of the same estimate done with image-stacked data.

The uv-stacking has the advantage of allowing for the possibility to ignore the shortest baselines. In comparison the image-stacked source could be subject to the high dynamic range issues, e.g. this could result in the presence of an extended component. It is possible to deal with this to some extent by using a low-spatial-frequency filter, however, a more direct way would be to do this directly on the uv-data.

Additionally, in comparison with the uv-stacked source, the image-stacked source is convolved with the beam, therefore it is best fitted with a model of the convolved dirty beam. Many large surveys currently are done as mosaics with several pointings. This means that the beam will not be the same for each pointing, and this is a complication for image-stacking and e.g. modelling a dirty beam.

We have applied the stacking algorithm to real data. As presented in Lindroos (2014), using both VLA and ALMA data from the Extended Chandra-Deep-Field South (VLA data: Miller et al. 2013, ALMA data: Hodge et al. 2013), initial results yield source sizes of about $1''$ for optically/near-infrared selected high-z galaxies. More importantly is, however, the fact that we can use the stacked uv-data for further interpretation. In Fig. 3, we show the averaged amplitude vs baseline length, and find that there is a rise towards the shortest baselines possibly caused by an extended component, and a plateau towards the longer baselines possibly indicating a point-like component. Among the possible interpretations of this, is that the stacked sources represent a mixture of extended and compact galaxies, or that the star-forming regions are compact but distributed over an extended region. We show this here, not to draw immediate conclusions about the distribution of the radio or mm emission from high-z, star-forming galaxies, but to illustrate the vast potential for further analysis of for example structural parameters when having the stacked uv-data available.

3. Discussion: Consequences for stacking of SKA data

The tests of our new stacking algorithm, shows that the uv-stacking provides a more robust result relative to the image-stacking. The algorithm is tested both in the GHz range, where currently the JVLA is the most sensitive array, and in the 100's GHz range, where ALMA is the most

PoS(AASKA14)168

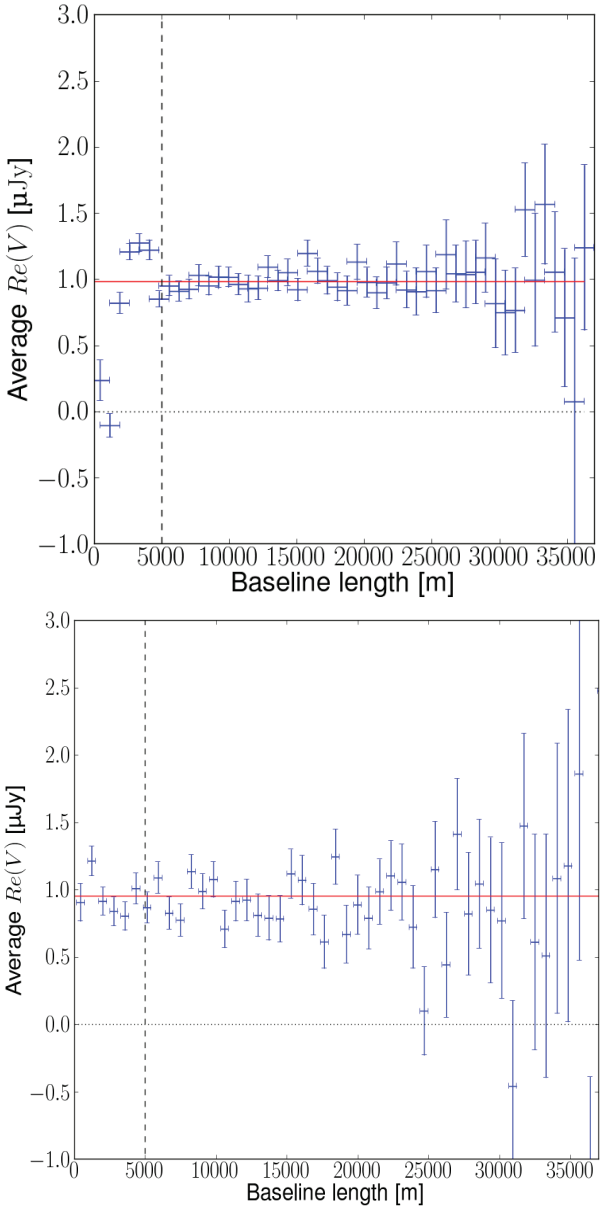

Figure 1: Simulations, representative of a JVLA A-array setup at 1.4 GHz Top: including bright extended source, which have been removed using clean from the data prior to stacking. Included here are the results of 100 Monte Carlo simulations. Bottom: Similar simulation, however without any bright foreground sources; 50 MC realisations. The artefacts seen at the short baselines, < 5000, are most likely caused by the imperfect removal of the bright, extended foreground sources. In real data, the removal of the bright sources cannot be controlled beyond our best knowledge, and therefore having the uv-stacked data available means that we can select which baselines we use in the analysis of e.g. average flux. The red line represent the best fit for point source flux with the short baselines < 5000 are excluded. From Lindroos et al. (2015).

PoS(AASKA14)168

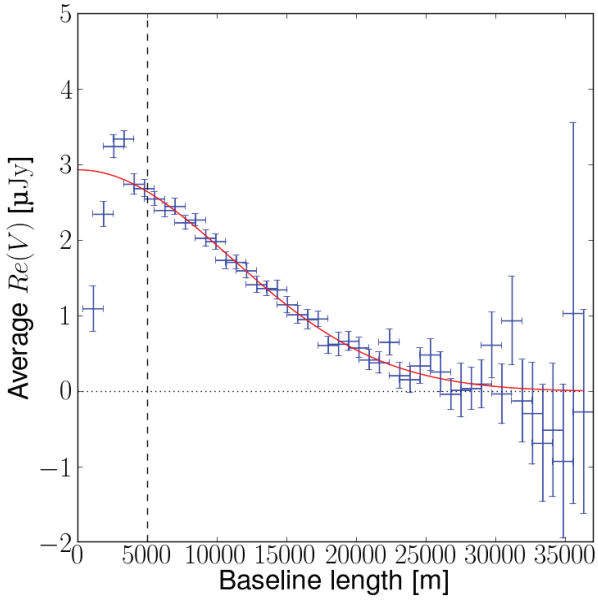

Figure 2: Simulations, representative of a JVLA A-array setup at a frequency of 1.4 GHz. Similar to Fig. 1, top panel, however, here the stacked target sources have extended emission of $\sim 1.5''$. The red line represent the best fit for an extended source with the short baselines < 5000 excluded. From Lindroos et al. (2015).

sensitive array. This means that our findings are applicable to the SKA-MID design and frequency range. The algorithm is designed to be applicable to radio interferometry in general, so also for lower frequencies such as SKA-LOW. The access to the stacked uv-data provides possibilities for a more robust analysis, in particular it enables reliable filtering at different spatial frequencies as well as means for detailed analysis of the stacked sizes.

Stacking is mentioned by many different future projects for the SKA, and therefore it is important to make available the tools that provide the most optimized stacking tools. We argue that uv-stacking is such a powerful tool, that it should be standard for future facilities. However, for future facilities such as the SKA, this also means facing a significant challenge, as it is expected that most raw and even calibrated SKA uv-data will not be archived, at least not for long-term storage. Consequently, one could argue that uv-data should also be stored long-term, unless the stacking is restricted to the image plane. In that case one needs to be aware that the results are less robust and more prone to additional uncertainties.

We consider three different options:

1. Design a *stacking queue*, which will be executed in almost real-time with the observations. The uv-stacking would be carried out after calibration, during a 'buffering' time before the uv-data is removed. In the case where the processed and calibrated uv-data will not be stored for long term archive access, but only kept for a short period needed for processing of (large) surveys, one could imaging that the SKA should offer an 'observing mode' where stacking lists are submitted, and then processed in parallel with the rest of the survey. This compromise would enable the stacked uv-data to be available for readily defined positions,

PoS(AASKA14)168

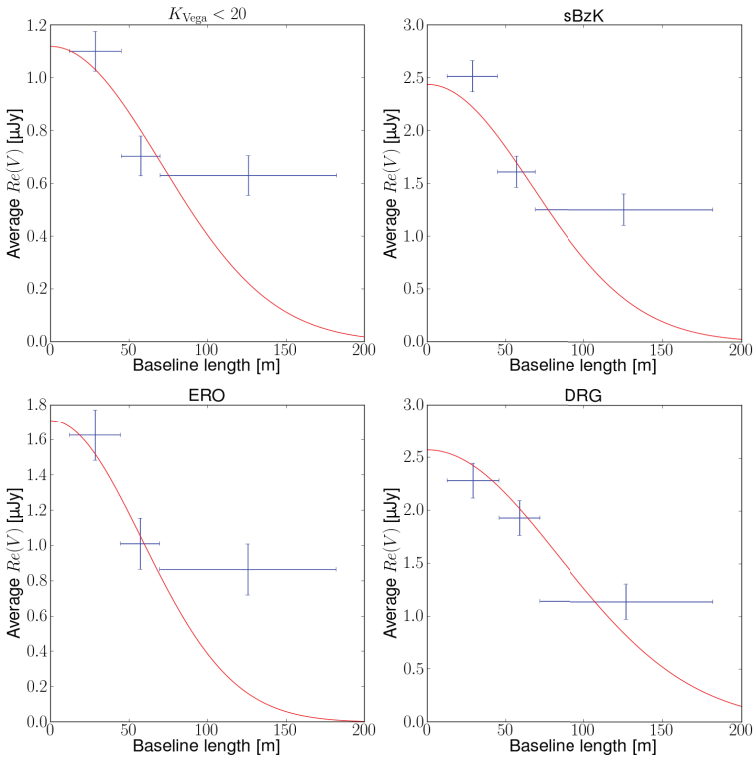

Figure 3: Stacking of ALMA data for high-z galaxies using four different selection criteria (following that of Decarli et al. 2014), $K < 20$, sBzK, EROs, and DRGs. For each uv-stacked data set, we plot the amplitude vs baseline length (binned). From Lindroos (2014), where similar results for VLA data are found.

as such a data set will be significantly reduced in size. The Lindroos et al (2015) algorithm is designed so that it could easily be tailored to such a purpose.

2. Ensure that calibrated uv-data is archived, if not all, then at least in some averaged format and at least for large surveys. This would enable the most flexible processing of the data in terms of stacking, also for astronomers not directly involved in the surveys.

3. Only stacking in the image-plane: Accepting potentially less reliable and less robust results in favour of not have to archive uv-data. However, this also means limitation for a number of different aspects, e.g. measuring sizes of stacked sources. Probably most importantly, it would mean no access to baseline info and thus limited possibility to filter out short baselines as illustrated in Figs. 1 and 2.

4. Summary

In this chapter we have discussed stacking of uv-data vs image-data from the perspective of the SKA. We describe our novel algorithm for stacking of visibilities, which we have compared to image-stacking. The uv-stacking algorithm has been developed for application to any type of radio interferometric data. The comparison was done primarily using simulated data based on JVLA and ALMA.

PoS(AASKA14)168

We have found in a detailed comparison that uv-stacking is a more robust method than image-stacking. The results produced from uv-stacking are either similar or more reliable than the image-stacked results. Having access to the stacked uv-data provides means it will be possible to remove or at least treat artefacts such as imperfect removal of bright sources, which can signficantly affect the stack results. Furthermore, having the stacked uv-data in hand enables a more detailed analysis of the properties of the stacked source, in particular size measurements.

It is therefore our conclusion that in the design of the SKA it should be carefully considered to allow for uv-stacking, either through the means of making (averaged) calibrated uv-data available in archives (at least for selected surveys), or as an alternative provide a specially designed *stacking queue* for large/deep surveys. Having access to the uv-data after stacking will be invaluable in ensuring that the desired signal can be optimally extracted from the data.

References

Bondi, M., Ciliegi, P., Schinnerer, E., et al., 2008, ApJ, 2681, 1129

Carilli, C.L., Lee, N., Capak, P., et al., 2008, ApJ, 689, 883

Conway, J.E., Cornwell, T.J., Wilkinson, P.N., 1990, MNRAS, 246, 490

Cornwell, T.J., Golap, K., Bhatnagar, S., 2008, IEEE Journal of Selected Topics in Signal Processing, 2, 647

Decarli, R., Smail, I., Walter, F., et al., 2014, ApJ, 780, 115

Dole, H., Lagache, G., Puget, J.-L., et al., 2006, A&A, 451, 417

Hodge, J.A., Karim, A., Smail, I., et al., 2013, ApJ, 768, 91

Högbom, J.A., 1974, A&AS, 15, 417

Knudsen, K.K., van der Werf, P.P., Franx, M., et al., 2005, ApJ, 632, L9

Lindroos, L., Knudsen, K.K., Vlemmings, W., Conway, J., Martí-Vidal, I., 2015, MNRAS, 446, 3502 (arXiv:1411.1410)

Lindroos, L., 2014, Licentiate thesis, Chalmers University of Technology, link: http://publications.lib.chalmers.se/publication/194419-stacking-of-interferometric-data-at-sub-millimeter-and-radio-wavelengths

Miller, N.A., Bonzini, M., Fomalont, E.B., et al., 2013, ApJS, 205, 13

Nandra, K., Mushotzky, R.F., Arnaud, K., et al., 2002, ApJ, 576, 625

Schinnerer, E., et al., 2007, ApJS, 172, 46

Worsley, M.A., Fabian, A.C., Bauer, F.E., et al., 2005, MNRAS, 357, 1281

PoS(AASKA14)168

Epoch of Reionisation

PROCEEDINGS OF SCIENCE

The Cosmic Dawn and Epoch of Reionization with the Square Kilometre Array

L.V.E. Koopmans[*†1], **J. Pritchard**[‡], **G. Mellema**[§], **F. Abdalla, J. Aguirre, K. Ahn, R. Barkana, I. van Bemmel, G. Bernardi, A. Bonaldi, F. Briggs, A.G. de Bruyn, T.C. Chang, E. Chapman, X. Chen, B. Ciardi, K.K. Datta, P. Dayal, A. Ferrara, A. Fialkov, F. Fiore, K. Ichiki, I. T. Illiev, S. Inoue, V. Jelić, M. Jones, J. Lazio, U. Maio, S. Majumdar, K. J. Mack, A. Mesinger, M.F. Morales, A. Parsons, U.-L. Pen, M. Santos, R. Schneider, B. Semelin, R.S. de Souza, R. Subrahmanyan, T. Takeuchi, C. Trott, H. Vedantham, J. Wagg, R. Webster, S. Wyithe**

[1] *Kapteyn Astronomical Institute, University of Groningen, The Netherlands*
Other author institutions are listed in the appendix
E-mail: koopmans@astro.rug.nl

Concerted effort is currently ongoing to open up the *Epoch of Reionization* ($z \sim$15-6) for studies with IR and radio telescopes. Whereas IR detections have been made of sources (Lyman-α emitters, quasars and drop-outs) in this redshift regime in relatively small fields of view, no direct detection of neutral hydrogen, via the redshifted 21-cm line, has yet been established. Such a direct detection is expected in the coming years, with ongoing surveys, and could open up the entire universe from $z \sim$6-200 for astrophysical and cosmological studies, opening not only the *Epoch of Reionization*, but also its preceding *Cosmic Dawn* ($z \sim$30-15) and possibly even the later phases of the *Dark Ages* ($z \sim$200-30). All currently ongoing experiments attempt statistical detections of the 21-cm signal during the *Epoch of Reionization*, with limited signal-to-noise. Direct imaging, except maybe on the largest (degree) scales at lower redshifts, as well as higher redshifts will remain out of reach. The *Square Kilometre Array* (SKA) will revolutionize the field, allowing direct imaging of neutral hydrogen from scales of arc-minutes to degrees over most of the redshift range $z \sim$6-28 with SKA1-LOW, and possibly even higher redshifts with the SKA2-LOW. In this SKA will be unique, and in parallel provide enormous potential of *synergy* with other upcoming facilities (e.g. JWST). In this chapter we summarize the physics of 21-cm emission, the different phases the universe is thought to go through, and the observables that the SKA can probe, referring where needed to detailed chapters in this volume. This is done within the framework of the current SKA1 baseline design and a nominal CD/EoR straw-man survey, consisting of a shallow, medium-deep and deep survey, the latter probing down to $\sim$1 mK brightness temperature on arc-minute scales at the end of reionization. Possible minor modifications to the design of SKA1 and the upgrade to SKA2 are discussed, in addition to science that could be done already during roll-out when SKA1 still has limited capabilities and/or core collecting area.

Advancing Astrophysics with the Square Kilometre Array
June 8-13, 2014
Giardini Naxos, Italy

PoS(AASKA14)001

1. Context and Layout

In this review chapter the impact of the *Square Kilometre Array* (hereafter SKA1 and SKA2 for the first and second phases of construction) in the field of high-redshift 21-cm observations of neutral hydrogen during the EoR and CD is outlined, building partly on the white paper of Mellema et al. (2013) and referring to more than a dozen related science chapters in this volume that discuss particular aspects in much greater detail. In Section 2 an overview of processes occurring during the *Dark Ages*, *Cosmic Dawn* and *Epoch of Reionization* (hereafter DA/CD/EoR) eras are given. In Section 3 the main physical processes that take place during these eras are discussed, with reference to the relevant accompanying chapters in this volume. In Section 4 observables of the redshifted 21-cm line are discussed, whereas in Section 5 we discuss the relevant parameters for any 21-cm survey design. In Section 6, we discuss a three-tiered survey with the SKA of the redshifted 21-cm emission from the CD/EoR. In Section 7 we discuss what can be done with a half (50% collecting area) and a full SKA1 and with SKA2 (nominally 4 times SKA1), during the rollout and build-out of SKA1 to SKA2. In Section 8 we draw some general conclusions and provide suggestions. Throughout this chapter when referring to SKA1/2, we mean SKA1/2-LOW.

2. A Short History of Neutral Hydrogen from Recombination to Reionization

This section shortly summarizes the main events that occurred in the Universe between recombination and reionization (see Fig.1), focussing on those aspects that are relevant to interferometric measurements of the 21-cm hyperfine transition line of neutral hydrogen with the SKA. We refer to Barkana & Loeb (2001); Furlanetto & Briggs (2004); Lewis & Challinor (2007); Pritchard & Loeb (2008); Morales & Wyithe (2010); Loeb & Furlanetto (2013); Fialkov et al. (2014a) for many more details.

2.1 Emission and absorption at 21-cm from z$\sim$1100 to z$\sim$6

Just after recombination at $z \sim 1100$, the spin temperature of neutral hydrogen coupled very effectively to the neutral gas temperature, which itself coupled to the *Cosmic Microwave Background* (CMB hereafter) photons via Compton heating because of a small trace density of electrons, making it impossible to observe 21-cm radiation either in emission or absorption. This period can truly be regarded as an "Age of Ignorance" in cosmology with no known directly observable tracer of either dark matter or baryons. Around $z \sim 200$, the neutral gas temperature decoupled from the CMB and adiabatically cooled in an expanding Universe. During this period (lasting to $z \sim 30$), called the *Dark Ages*, the 21-cm line can be seen in absorption and the physics of this period is relatively well-understood. At the end of the *Dark Ages*, the spin-temperature coupling to the CMB started to dominate over its coupling to the cold gas, increasing the spin-temperature such that its differential brightness temperature approached zero once more. Around the same time, at $z \sim 30$,

*Speaker.
†Chair CD/EoR SWG
‡Vice-Chair CD/EoR SWG
§Vice-Chair CD/EoR SWG

PoS(AASKA14)001

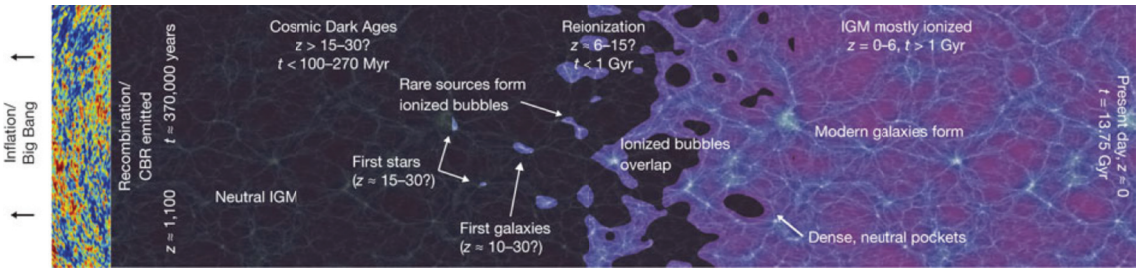

Figure 1: A graphical overview of the main phases of neutral and ionized hydrogen in the Universe. From Robertson et al. (2010).

haloes of $\sim 10^6$ solar masses started to form in sufficiently large numbers. Gas could cool sufficiently in to their potential wells to form the first (Pop-III) stars. These stars both radiated and heated their surrounding gas. Via the *Wouthuysen-Field* (W-F) effect, the spin-temperature was able to couple to the cold gas temperature, creating a second period (the *Cosmic Dawn*) where the 21-cm line was seen in absorption. While star-formation continued, it is thought that the first X-ray emitting sources appeared, heating the neutral gas and thereby (again via the *Wouthuysen-Field* effect) raising the overall spin-temperature to a level at or above the CMB temperature. Consequently, the 21-cm line became visible in emission around $z \sim 15$. While radiating and heating, these first sources (possibly including mini-quasars) also ionized the gas around them and a period of *Reionization* started that is thought to have lasted until $z \sim 5-6$. During the latter phase most of the neutral hydrogen became ionized and is thought to still reside in the IGM today. During the same period the gas was metal enriched and seed black-holes grew to super-massive black holes already seen at redshifts as high as $z \sim 7$. As discussed in the accompanying chapters in this volume, observing the *Dark Ages*, *Cosmic Dawn* and *Epoch of Reionization* is crucial for our understanding of the Universe which we see from the present day up to high redshifts and provide an enormous potential for synergy with other IR to sub-mm facilities (e.g. Euclid, ELT/TMT/GMT, JWST, ALMA, etc). As such, their study features high on nearly all future science and instrumental roadmaps, including that of the SKA, and is one of the main science drivers for a range of SKA precursors and pathfinders (e.g. LOFAR, MWA, PAPER and GMRT, and the planned HERA[1]).

2.2 Current constraints on the Cosmic Dawn and Epoch of Reionization

Even though the history of neutral hydrogen is crucial to our understanding of the high-redshift Universe, very little is known about it. There is only a handful of observations that currently constrains physical models of the evolution of neutral hydrogen:

- the Gunn-Peterson trough at/near the end of reionization from which (a limit on) the HI optical depth can be inferred (e.g. Becker et al., 2001; Fan et al., 2002, 2006),
- the discovery of Gamma-Ray Bursts (GRB) during and after reionization (e.g. Ruiz-Velasco et al., 2007; Sparre et al., 2014) from which the high-mass star-formation rate (SFR) can be inferred,

[1] http://reionization.org/

PoS(AASKA14)001

- the metal abundances and old stellar populations (e.g. Simcoe et al., 2012) possibly in Damped Lyman Absorbers (DLAs),
- the evolution of the IGM temperature after reionization from which a nominal reionization redshift can be inferred, if the IGM cooled adiabatically and did not re-heat (e.g. Theuns et al., 2002; Bolton et al., 2010),
- the polarization of the CMB due to ionized gas (basically electrons) integrated along the line-of-sight to the present day from which a median reionization redshift and duration can be inferred (see e.g. Robertson et al., 2015),
- the integrated IR and X-ray backgrounds setting limits on the emission from the first (Population III & II) stars, X-ray sources and quasars (e.g. Zemcov et al., 2014; Fernandez & Zaroubi, 2013; Helgason et al., 2014)
- the observations of the first galaxies through drop-out techniques, currently out to $z \sim 12$ already (e.g. Ellis et al., 2013), or Lyman-α emission (e.g. Matthee et al., 2014), providing limits on ionizing (stellar) sources, and the HI content in the IGM from Lyman-α emitters.

Although theoretical models are highly degenerate especially at increasingly larger redshifts, it does appear from these observations that reionization is roughly half-way at $z \sim 10$, followed by a rapid increase in the SFR-density below this redshift (e.g. Lorenzoni et al., 2011; Bouwens et al., 2012; Ellis et al., 2013). Around $z \sim 5-7$ potentially 10% of hydrogen could still be in neutral patches (e.g. Mesinger, 2010), although most of it was (re)ionized by then, making most of the the universe transparent to *uv*-radiation all the way to the present day. Beyond $z \sim 10$ even less is known and most of what we think was happening is actually based on theory (e.g. Pop-III stars) and simulations that are constrained by physical models extrapolated from lower redshifts (e.g. X-ray heating via XRBs; Fialkov et al., 2014b). It it therefore crucial that new observational avenues are explored to open up these early phases in the Universe for observational studies. The redshifted 21-cm emission of neutral hydrogen provides just such a possibility. Neutral hydrogen is all-pervasive until its (re)ionization completes and it complements (i.e. anti-correlates) with sources of ionization, with the CMB and with the IR/X-ray background (although see Fialkov et al., 2015). Moreover due to the line-nature of the 21-cm hyperfine transition, redshift (and velocity) information can be gained directly from 21-cm emission by fine-tuning observations to different radio frequencies [i.e. to $1420/(1+z)$ MHz]. Hence tomography of (redshifted) 21-cm emission can be done by covering a wide range of frequencies.
In the case of the SKA, frequencies of 50 MHz (during phase 1) and higher allow HI mapping at redshifts below $z \sim 27$ ($\sim$ 120 Myr after the Big Bang) all the way to the end of reionization $z \sim 5-6$ ($\sim$ 1 Gyr after the Big Bang). Especially the highest redshifts are extremely hard to reach with other instruments, even with the *James Webb Space Telescope* (JWST) in the next decade.

2.3 Current 21-cm detection experiments

There are two general approaches to observe HI emission via the 21-cm line: (i) its spatially-averaged global signal and (ii) its spatial fluctuations, both as function of frequency (i.e. redshift,

PoS(AASKA14)001

time, distance). In the former case the average redshifted 21-cm emission[2] at a given redshift is measured over a very large (possibly global) area of the sky such that spatial fluctuations are averaged away, in general via single dipoles or fully-filled antennae (e.g. dish, aperture arrays with near unity filling factor). The global signal can vary between a few mK brightness temperature near the end of reionization and around those redshift where the HI spin temperature and the CMB were almost same, to as much as +30 mK when the spin temperature was well above the CMB temperature, and to as low as -100 mK or even less during the *Cosmic Dawn* when HI was seen in absorption against the CMB and the spin-temperature coupled to the cold neutral gas. Whereas in principle these signals could be detected in a few hours to a few days based purely on thermal noise limits, such a detection turns out to be extremely difficult to the high dynamic range that is needed in band-pass calibration (i.e. $> 10^6$), in the presence of RFI and the complex spatially-temporal-frequency varying sky that couples to a generally polarized and frequency-dependent receiver beam. Whereas many global experiments are ongoing (e.g. EDGES, CORES, SARAS, LEDA, etc; see Subrahmanyan et al. 2015) none have reached the few to tens of mK level yet required for a solid detection although bandpass stability of ~ 1 K has now been reached (Patra et al., 2013, 2015).

An alternative/complementary approach to detect the redshifted 21-cm emission is via an interferometer, which is insensitive to the global signal (which is detectable on the (near)zero spacings only), but can only detect fluctuations in the 21-cm brightness temperature. Although these fluctuations can be considerable, they are far smaller in amplitude than the global signal hence requiring long ($\sim$1000 hrs) of integration time to detect. At lower redshifts during the *Epoch of Reionization*, however, ionized bubbles could be -30 mK in depth and detectable on somewhat longer baselines with arcmin resolution. Apart from the ionized bubbles, brightness temperature fluctuations are sourced by density fluctuations in the time-evolving dark-matter distribution and via the spin-temperature coupling to the neutral gas and/or the CMB, though the *Wouthuysen-Field* effect and through heating. In addition, fluctuations are sourced by peculiar and bulk-flow velocities that Doppler-shift the 21-cm line, affecting its brightness temperature. Whereas this complex astrophysics make interpretation of the 21-cm signal harder, it also provides a wealth of information on sources and physical process occurring during that period. In combination with the global signal and other observables (e.g. galaxies, CMB polarization, etc) these brightness-temperature fluctuations provide a treasure trove of information. The second advantage of using an interferometer is to reduce the levels of foreground emission from the Milky Way (several Kelvin versus several hundred Kelvin) that could potentially contaminate the feeble 21-cm signal, as well as the fact that interferometers are often easier to calibrate than total-power experiments. At the moment each of these approaches are pursued by multiple teams and valuable in their own right and targeting different parameter spaces, thereby complementing each other. Current HI detection experiments are ongoing with the GMRT (e.g. Paciga et al., 2011), LOFAR (e.g. Yatawatta et al., 2013; van Haarlem et al., 2013), PAPER (e.g. Ali et al., 2015; Pober et al., 2015), MWA (e.g. Dillon et al., 2014) and observations with the LWA (i.e. LEDA) (e.g. Greenhill et al., 2014), as well as with NenuFAR[3], under construction, are planned.

[2]More precisely its brightness temperature.

[3]http://nenufar.obs-nancay.fr/Argumentaire-scientifique.html

PoS(AASKA14)001

2.4 Planned high-redshift 21-cm arrays

Despite great strides forward over the last decade, no high-redshift 21-cm detection has yet been successfully claimed, neither of the global HI signal nor of its fluctuations. Even if successful, all current observational programs (except for those targeting the global signal) aim for a *statistical* detection via power-spectra (and high-order statistics) and only on the very largest angular scales (degrees) could one potentially reach a S/N$\sim$few in a few MHz frequency bin, comparable to the first CMB maps with COBE (Smoot et al., 1992). To overcome the current S/N$\sim$1 barrier substantially more collecting area is required, especially on short baselines corresponding to a few to tens of arc minute scales, by an order of magnitude over the current LOFAR-core collecting area, the latter being the largest low frequency array currently aiming to detect high-z 21-cm emission. Such a collecting area is foreseen in the current baseline design of SKA1 and might evolve in to SKA2 with four times the SKA1 collecting area (see this volume), allowing one to move from upcoming statistical detections to tomographic (i.e. direct imaging) measurements of HI in the next decade. A similar US-lead effort called HERA[4] is also planned extending the current PAPER project in South-Africa, and NenuFAR in France that aims for a nearly fully filled low-frequency (10-80MHz) array of 400-m diameter.

3. Some relevant physics during the CD/EoR eras

Radio-telescopes measure the sky's intensity distribution (more precisely its Fourier transform), which traditionally is expressed in terms of a brightness temperature $T_{\rm b}$ in the Rayleigh-Jeans regime. It can be shown that the brightness temperature of neutral hydrogen as function of redshift z, seen against the CMB, can be written as (e.g. Madau et al., 1997):

$$\delta T_{\rm b} = 27 x_{\rm HI}(1+\delta)\sqrt{\frac{1+z}{10}}\left(\frac{T_{\rm s}-T_{\rm CMB}}{T_{\rm s}}\right)\left(\frac{\Omega_{\rm b}}{0.044}\frac{h}{0.7}\right)\sqrt{\frac{\Omega_m}{0.27}} \times\left(\frac{1-Y_{\rm p}}{1-0.248}\right)\left(1+\frac{1}{H(z)}\frac{dv_{||}}{dr_{||}}\right)^{-1}\ \text{mK}. \tag{3.1}$$

This equation contains several terms set by cosmology (i.e. the global baryonic density and spatial density fluctuations, $\Omega_{\rm b}$ and δ, respectively; the total mass density and the Hubble constant $\Omega_{\rm m}$ and $H(z)$ or h, respectively), by (g)astro-physics (i.e. the spin-temperature $T_{\rm s}$ of HI, the CMB temperature $T_{\rm CMB}$) and by Doppler effects ($dv_{||}/dr_{||}$; e.g. due to peculiar motions and bulk-flows of the gas). Via the brightness temperature and different measures of it, e.g. variance, higher-order statistics, power-spectra, n-point correlations, tomographic cubes (i.e. images), HI-absorption spectra, cross-correlation, etc., one can address questions about the physics and sources responsible for processes during the CD/EoR such as heating (changing $T_{\rm gas}$), Lyman-α emission and the Wouthuysen-Field effect (changing $T_{\rm s}$ via $T_{\rm gas}$; Wouthuysen (1952); Field (1958, 1959)), reionization (changing $x_{\rm HI}$) and the growth of density fluctuations and peculiar velocities (changing δ and $dv_{||}/dr_{||}$).

[4] http://reionization.org/papers/

PoS(AASKA14)001

3.1 Phases of 21-cm emission and absorption

Largely due to the expansion of the universe and within it the gravitational collapse of matter, the universe at some point becomes non-linear in its (evolving) density structures producing the first stars, stellar remnants, black holes, and galaxies. These objects in turn will impact the IGM/HI surrounding them, leading to a host of observational effects that can be used to assess their properties. Below we shortly summarize the main phases of HI after recombination ($z \sim 1100$) and before complete reionization ($z \sim 5-6$). We again refer to Barkana & Loeb (2001); Furlanetto & Briggs (2004); Lewis & Challinor (2007); Pritchard & Loeb (2008); Morales & Wyithe (2010); Loeb & Furlanetto (2013); Fialkov et al. (2014a) for many more details.

- **Age of Ignorance (z∼1100-200):** Just after recombination the spin-temperature of neutral hydrogen tightly coupled to the CMB temperature, indirectly via the gas temperature (via Compton scattering), making the 21-cm line invisible against the CMB temperature. At the moment no known observational technique is able to probe this era, even if it were possible at these high redshifts. Observing these high redshift using the 21-cm line would first of all have to be carried out in space to avoid the ionospheric plasma frequency, but most likely would be limited by self-absorption in the MW (Novaco & Brown, 1978). In case of dark-matter annihilation (see e.g. Valdés et al., 2013) or other heating sources (Lyman-α photons from recombination; (see Fialkov & Loeb, 2013)) could one conceivably have the spin-temperature decouple from the CMB temperature. However, it is likely that this period in the history of the Universe will remain out of reach till far in the future, and remain a true *Age of Ignorance*.

- **Dark Ages (z∼200-30):** About five million years after recombination the spin-temperature of hydrogen coupled – via trace electrons – to the colder-than-the-CMB gas-temperature. Neutral hydrogen became visible in absorption again the CMB during that era. At the end of the *Dark Ages* the density of trace electrons, however, dropped sufficiently (through expansion of the Universe) to make the coupling of the spin and gas temperature inefficient. The spin temperature started to follow the CMB temperature again and $T_{\rm b}$ approached zero from below. However, this phase just preceded the formation of the first radiating sources and probably only lasted briefly or might not even have been fully reached (i.e. $T_{\rm b} \sim 0\,{\rm mK}$). *Processes that can be studied through measurements of $T_{\rm b}$ during the Dark Ages are the dark-matter power-spectrum evolution and its annihilation physics, baryonic bulk-flows (Tseliakhovich & Hirata, 2010) and the physics of gravity and general relativity.* The physics during this era can largely be understood through linear theory (Lewis & Challinor, 2007), or linear corrections thereof (e.g. Ali-Haïmoud et al., 2014) and deviations of observation from CDM predictions will immediately indicate new physics. Studying HI deep in to the *Dark Ages* however will remain out of reach in the near future and requires space-based radio telescopes because 21-cm emission will have been redshifted to near or below the ionospheric plasma frequency.

- **Cosmic Dawn (z∼30-15):** The *Cosmic Dawn* is typically defined as the time when the first stars (or other radiating sources) were formed. Lyman-α emission from these sources efficiently coupled the spin temperature to that of the cold gas (via the Wouthuysen-Field

PoS(AASKA14)001

effect), again leading to neutral hydrogen seen in absorption. At the same time, however, the gas itself was heated supposedly via X-ray heating or, possibly, via the hot ISM and Lyman-α photons (Pacucci et al. 2014). This gas-heating and the parallel process of coupling the spin and gas temperature led to a rapid rise in the brightness temperature of neutral hydrogen until it is finally seen in emission around $z \sim 15$. One should note that many of these processes are still ill-understood and all these effects (heating, coupling, etc) could shift around in redshift substantially, especially between the *Cosmic Dawn* and the *Epoch of Reionization*. Hence when these processes exactly occurred is not known and redshifts indicated here are merely indicative numbers currently expected from nominal models. *Processes that can be studied during the CD are the formation of the first (pop-III) stars, the first BHs, X-ray heating sources, W-F coupling, bulk-flows, etc.*

- **Epoch of Reionization (z$\sim$15-6):** While heating together with the W-F effect change the spin-temperature of the neutral hydrogen, the same radiation field (i.e. *uv*-radiation) starts to ionize hydrogen leading to the percolation of bubbles around the first mini-haloes containing (Pop-III) stars and possible intermediate mass black holes, i.e. mini-quasars. As time progresses and the universe becomes increasingly more non-linear (on small scales), more stars and quasars are formed. Although recombination can have some impact (see e.g. Sobacchi & Mesinger, 2014), it can not stop or balance ionization in an expanding universe and by $z \sim 6$ the entire universe, apart from pockets of neutral hydrogen (mostly in galaxies), will be ionized once more. *Processes that can be studied during the Epoch of Reionization are the physics of the ionizing sources, such as pop-III and II stars, mini-quasars, feedback to the IGM and the transition to the currently visible universe.*

- **Post-Reionization (z<6):** Whereas most neutral hydrogen will have been ionized, pockets of neutral hydrogen might remain even at lower redshifts and in galaxies (e.g. Mesinger, 2010), which could be studied though intensity mapping and via cross-correlations with other e.g. IR surveys (see this volume).

3.2 Sources of heating, radiation, feedback and ionization

Whereas the above situation delineates general eras during which certain physical processes (e.g. Lyman-α emission, heating, ionization, etc) might dominate, the understanding of these processes is far from certain and depends strongly on the types of sources responsible for *uv*- and X-ray emission. Via their imprint on the brightness temperature of neutral hydrogen one can gain insight in to these first radiating sources, which is one of the main reasons to study high-z 21-cm emission. Below a range of sources is listed that are currently thought to play a role. We refer to the accompanying chapter in this volume for more details.

- **Population-III and -II Stars**

  The first stars presumably formed just after the *Dark Ages* from relatively pristine gas (primordial abundances), and will soon be detectable by upcoming missions, such as JWST, through their supernova explosions (de Souza et al. 2013, 2014). These first stars (Pop-III) are thought to have been of high mass, although recent work suggests they fragmented

PoS(AASKA14)001

possible into stars of several tens of solar masses (e.g. Stacy & Bromm, 2013). It is the *uv*-radiation of these stars that is thought to couple the hydrogen spin temperature to that of the cold gas. Emission from resulting X-ray binaries (XRB) could subsequently lead to X-ray heating. In addition, the first and second generation (Pop-II) stars are thought to be responsible for the ultimate (re)ionization of nearly all neutral hydrogen during the *Epoch of Reionization*. What the relative roles of Pop-III and Pop-II stars exactly are in these processes, i.e. W-F coupling, heating and ionization, is currently ill-understood and the processes involved in the formation of Pop-III stars and whether they form the seeds for SMBHs is also not clear. At lower redshifts where the first galaxies can be observed, however, it is clear that stars responsible for reionization must be in mini-haloes and in galaxies $\sim$500 times fainter ($\sim$7 mag.) than current observational limits (e.g. Davé et al., 2006). Hence enormous extrapolations are needed to make any inference from current observations, let alone to redshifts even higher. Redshifted 21-cm emission observations clearly are important in setting limits on star formation and the types of stars (or AGN) that partake in the early phases of the CD/EoR eras.

- **Mini-Quasars and AGN**

  A second source of ionization and heating can be intermediate-mass black holes (IMBHs) and resulting mini-quasars due to accretion discs or Bondi accretion (e.g. Dijkstra, 2006). Whereas it is thought that mini-quasars are not the dominant source of ionizing photons, they can still play a secondary role and possibly be a source of harder X-ray photons that can more uniformly heat the IGM well above the CMB temperature. These IMBHs are also thought to be the seed-BHs of present-day SMBHs and AGN, although the process of accretion appears to be super-Eddington to have them grow from 100 solar masses (expected from massive Pop-III stars) to 10^9 solar masses in the AGN seen already at $z \sim 7$ (Mortlock et al., 2011).

- **X-ray Binaries**

  Great uncertainty also remains whether X-ray binaries are sources of heating at high redshifts and whether heating takes place on global scales. If heating is inefficient some IGM patches could remain very cold and below the CMB temperature causing the redshifted 21-cm brightness temperature to remain in absorption substantially impacting the level of strength of the total-intensity and fluctuation signals from neutral hydrogen. This could lead to considerable effects even at very low redshifts during the *Epoch of Reionization* (e.g. Pritchard & Loeb, 2008).

- **Dark-Matter Annihilation**

  Literately a "Dark Horse"[5] is whether dark matter could be a source of ionization or heating at very high redshifts during the Dark Ages, already influencing the evolution of the IGM well before the Cosmic Dawn (e.g Taoso et al., 2008; Ripamonti et al., 2010).

Having outlined a number of important eras as well as the physics and source responsible for the brightness temperature evolution of neutral hydrogen (both spatially and in time), we now

[5]Benjamin Disraeli, in "The Young Duke" (1831)

PoS(AASKA14)001

continue to discuss which observables the SKA can obtain and use to constrain these processes and from it learn about the sources responsible. We also shortly mention possible synergies with other (planned) facilities.

4. Observables via the redshifted 21-cm brightness temperature

Redshifted 21-cm emission from neutral hydrogen manifests itself in multiple ways and various methods and techniques can be used to extract information from it. In the following section we discuss a number of such approaches, whereas in the subsequent section a short summary is given of other observables (and facilities) that the 21-cm brightness temperature could be cross-correlated with. We refer to Mellema et al. (2013), as well as to Chang et al. (2015) and Jelic et al. (2015) in this volume, for more details on the synergy between the SKA and other observatories.

4.1 Measures of the brightness temperature field

All of the information one hopes to gain from the physics occurring during the Dark Ages, Cosmic Dawn and Epoch of Reionization from neutral hydrogen is obtained via its redshifted 21-cm brightness temperature. As shown in Section 3, this temperature is set by a combination of many different physical processes which need to be disentangled. As of yet, it is not fully clear whether this can be done completely or not. In addition, it is likely that in the first experiments, also with the SKA1, only limited measurements of the brightness temperature will be made. Below we summarize some of the standard measures of $T_{\rm b}$:

- **Total Intensity** Redshifted 21-cm emission of neutral hydrogen averaged inside "shells" of common redshift (or observed frequency) are close to impossible to measure with interferometers since they measure intensity differences (Subrahmanyan et al. 2015). However, as seen in Section 3, the total expected brightness temperature is of order $\sim 27 x_{\rm HI}(1+\delta)$ mK at $z \sim 10$ if $T_{\rm s} \gg T_{\rm CMB}$. When averaging over large areas of the sky ($\gg 1$ degree) $\langle \delta \rangle \approx 0$ and assuming no reionization (i.e. $x_{\rm HI} = 1$), one can determine the total intensity of the signal. This is "most easily" achieved with single receiver/dipole measurements and is discussed in much greater detail in Subrahmanyan et al. (2015). Measuring this signal as function of redshift allows one to learn about different physical processes such as Lyman-α coupling by the first stars, heating by (X-ray) sources, reionization, etc. At this point it is not clear whether the SKA will be capable of measuring this signal since it requires a very accurately calibrated instrument.

- **Variance or second moment** The second-order effect comes from variations in the brightness temperature due to variations of δ, $x_{\rm HI}$, $T_{\rm s}$ and $v_{||}$. These variations lead to a spatial variance in $T_{\rm b}$ as function of observed frequency or redshift (see Mellema et al. 2015 and Wyithe et al. 2015) which can be measured in interferometric images, assuming that systematics and thermal noise are under control and/or known (although thermal noise can be removed via cross-variance techniques over small time-frequency steps). By measuring the variance one can again learn how HI evolved over cosmic time, in particular when reionization peaked (the contrast between HI and bubbles is very large and leads to a large variance).

PoS(AASKA14)001

However, the shape of PDF(T_b) also teaches us about its moment (skewness and/or kurtosis) again revealing information about reionization (e.g. Harker et al., 2009). In particular the skewness of the PDF might be a tell-tale signature of reionization that would be hard to mimic by systematic effects (which often are strongly correlated between frequency and scale smoothly with frequency as well).

- **(Anisotropic-)Power-spectra** One step further would be the analysis of T_b in the Fourier domain in terms of the variance as function of spatial (or angular) scales, i.e. the power-spectrum. The power-spectrum depends on the spatially varying parameters in Equation 3.1, being x_{HI}, δ, T_s and $v_{||}$. All other parameters can be assumed constant and only enter via the general FRW metric. The power-spectrum is directly related to the underlying local physical processes and sources of reionization (governing x_{HI}), heating (governing T_s), as well as to the evolution of the density field (governing δ and $v_{||}$). To first order one can Taylor expand equation 3.1 in these parameters, Fourier transform the result, from which the power-spectrum can be formed. Since the parameters are not independent (e.g. an over-density can also lead to extra heating and ionization), the resulting 21-cm power-spectrum becomes a rather complex function of these parameters and their cross-correlations, and can become anisotropic. These can either be determined via simplified schemes or via direct numerical simulations (which also contain simplified sub-grid physics). Disentangling all effects from the power-spectrum as function of redshift is nontrivial and remains an ongoing and active research field. To first order, the power-spectrum is isotropic and can be spherically averaged (where the frequency direction over some limited bandwidth is a proxy for comoving distance, hence inverse wavenumber), although in the case of SKA (possibly even before) the sensitivity if sufficient to measure anisotropy in the power-spectrum which can be an exciting measure of underlying physics (e.g. Fialkov et al., 2015). Hence it is often better to express the power-spectrum in two dimensions, separating the wave vector in a component perpendicular to the line of sight and a component parallel to it, in particular to study peculiar velocities, the light-cone effect, as well as potentially identify still-remaining systematic errors in the data-processing.

- **Higher-order statistics/n-point correlations:** Already touched up on above, the brightness temperature field after the *Dark Ages* will start to deviate from a Gaussian random field. This means that the power-spectrum or two-point correlation function will become an increasingly more incomplete description. The brightness temperature difference between two points will deviate from a Gaussian distribution, and the three and high-point statistics will become non-zero (Pillepich et al., 2007; Cooray et al., 2008). Studying these statistics can therefore provide additional information about physical processes, even if direct imaging might still be infeasible.

- **Tomography/Images:** The ultimate goal of any HI observation is make direct images and determine the brightness temperature with high significance for each spatial-frequency cell (see Mellema et al. 2015 and Wyithe et al. 2015 this volume). This clearly contains the maximum amount of information obtainable from the data-set, but interpretation is not always straightforward and the analysis of images has been a sorely neglected topic in the litera-

PoS(AASKA14)001

ture. In fact, even from direct numerical simulations, results are often presented in limited statistical measures such as the power-spectrum. Developing new ideas on how to analyze brightness temperature images is therefore crucial before the SKA comes online since it will be the first instrument capable of imaging/tomography on scales of several arc minutes to degrees. Only in exceptional cases might one expect to do this pre-SKA.

- **Bubbles and HI topology:** Whereas initially imaging of HI brightness temperature fluctuations at the level of several mK might not be feasible (e.g. in roll-out, etc), the stark contrast of 20-30mK and size (ten(s) of Mpc) of ionized bubbles will probably allow them to be seen relatively easy on during the roll-out and later phases of SKA1 imaging. Their distribution as function of size, shape, etc. will likely reveal swiftly how reionization proceeded (i.e. inside-out, or otherwise). It might also reveal the nature of the sources causing reionization, in particular if (mini-)quasar play a role. Although some of this information is encoded in the power-spectra (which forms from a combination of the non-ionized HI field times a mask where HI has disappeared) their precise sizes, shapes, etc. will provide a far richer source of information. In addition it might be possible to study the local velocity field structure around bubbles which might reveal additional information that the power-spectra do not.

- **21-cm absorption:** Whereas all the above measures of neutral hydrogen are based on its brightness temperature contrast with the CMB, there could be radio sources (mJy or brighter) present at sufficiently high redshift that the 21-cm line could be see in absorption against such source (e.g. Carilli et al. (2002) and Ciardi et al. 2015). A mJy source (e.g. AGN or GRB) of a few arcmin resolution at say 150MHz would already be sufficient to measure the HI forest and from it (equivalent to the Lyman-α forest) measure the line-of-sight power-spectrum of neutral hydrogen. Although success depends on the (still unknown) presence of radio sources at redshifts well beyond the end of reionization, it would provide a unique opportunity to measure $P_{21}(k)$ on k-modes far larger (i.e. scales far smaller) than accessible via imaging/tomography or power-spectra as discussed above. As such SKA1 and 2 could provide the first measures of mini-haloes during the *Epoch of Reionization* something that even *JWST* will find difficult to do.

4.2 Synergy with other surveys/Cross-correlations

Whereas SKA will characterize the brightness temperature in detail via either power-spectra, direct imaging or 21-cm absorption possible to redshifts of $z \sim 27$ during the Cosmic Dawn, and will be unique at this, complementary observations can further enhance the capability to extract information from this rich data-set. Among these are: (1) the Planck (or future) CMB maps, (2) the Far-Infrared background or emitters, (3) surveys of high-z Lyman-α emitters, (4) high-z Lyman-break Galaxies/Dropouts, (5) high-z SNae/GRB transients, (6) CO/CII emitters and (7) DLAs. We refer to Chang et al. (2015) and Vibor et al. (2015) in this volume for details.

5. Survey Design

In this section we outline a potential observational survey with SKA1 (and 2) to characterize the redshifted 21-cm brightness temperature of HI between $z = 27$ (ν=50MHz) and z$\sim$6 (end the EoR),

PoS(AASKA14)001

via its two main observable: power-spectra and tomography. We assume throughout that calibration and foreground subtraction is done to a level accurate enough that it does not affect the resulting residual data-cubes (containing both the 21-cm signal as well as noise). For more details on the latter we refer to Mellema et al. (2013). Hence thermal noise and sample variance (in the case of power-spectra) are assumed to dominate the error budget in the power-spectra and thermal noise dominates the error-budget in the images.

5.1 Scaling Relations for power-spectrum sensitivity

To understand the choices of survey specifications we need some guidance. This is most easily understood by assuming a uniform *uv*-coverage in an interferometric experiment. As shown in Mellema et al. (2013) and based on McQuinn et al. (2006), the power-spectrum error due to thermal noise is then given by:

$$\Delta^2_{\rm Noise} = \left(\frac{2}{\pi}\right) k^{3/2} \left[D_{\rm c}^2 \Delta D_{\rm c} \Omega_{\rm FoV}/N_{\rm b}\right]^{1/2} \left(\frac{T_{\rm sys}}{\sqrt{B\,t_{\rm int}}}\right)^2 \left(\frac{A_{\rm core}A_{\rm eff}}{A^2_{\rm coll}}\right) \tag{5.1}$$

The total error is obtained by adding the sample variance to this, which depends on the power-spectrum of the signal itself and the number of independent samples per volume. Whereas this equation gives a reasonable idea of the level of thermal noise variance on 21-cm power-spectra, it can be tilted as function of $k = 2\pi/L$, depending on the *uv*-density as function of baseline length. In this equation, the co-moving distance to the survey redshift is $D_{\rm c}$, the depth of the survey for a bandwidth B is $\Delta D_{\rm c}$ and the field-of-view of the survey is $\Omega_{\rm FoV}$. In case of multi-beaming, the number of independent beams is $N_{\rm b}$. A system temperature of $T_{\rm sys}$ is assumed and an integration time $t_{\rm int}$. Each station/antenna is assumed to have an effective collecting area $A_{\rm eff}$, that corresponds to the field-of-view as $\Omega_{\rm FoV} \equiv \lambda^2/A_{\rm eff}$, where λ is the wavelength at the center of the frequency band. The antennae are distributed over a core area $A_{\rm core}$ in such a way that the *uv*-density is uniform and the total collecting area (the sum of all effective collecting areas of each receiver) is assumed to be $A_{\rm coll}$. The equation has been shown to be correct via numerical integration, using the method outlined in McQuinn et al. (2006). Regardless the assumption of a uniform *uv*-density (which affect the exponent in $k^{3/2}$ and the normalization), the scaling with the layout of the array follows

$$\Delta^2_{\rm Noise} \propto \left(\frac{A_{\rm core}\sqrt{A_{\rm eff}}}{A^2_{\rm coll}}\right) \propto \left(\frac{A_{\rm core}}{N^2_{\rm stat}A^{3/2}_{\rm eff}}\right) \propto \left(\frac{A_{\rm core}}{\sqrt{N_{\rm stat}}A^{3/2}_{\rm coll}}\right) \tag{5.2}$$

where we assume $A_{\rm coll} = N_{\rm stat}A_{\rm eff}$ with $N_{\rm stat}$ stations/receivers. Given the above equation and scaling relations, a number of conclusions can be drawn for the power-spectrum sensitivity at a given *k*-mode scale: (i) sensitivity scales most rapidly with collecting area, (ii) increasing field-of-view helps, but only with the square root of the field of view, and (iii) more compact arrays (still covering the *k*-modes of interest) are more sensitive. All current arrays (i.e. MWA, LOFAR and PAPER) follow strategies that optimize (or maximize within budgetary limits) these three parameters. SKA1 and 2 will both increase $A_{\rm coll}$ by 1-2 order of magnitude over all current arrays and minimize $A_{\rm core}$ by maximizing the filling factor and placing much of the collecting area in a rather small core area. Finally, based largely on computational limitations, the field of view of SKA is at least of order five degrees at 100 MHz, but during later phases (e.g. SKA2) could be increased through either

PoS(AASKA14)001

multi-beaming or through reducing the beam-formed number of receivers. Although in considering optimizing an array for CD/EoR science, one should not forget that the system also needs to be calibrated for instrumental and ionospheric errors, and foregrounds (compact and extended, in all Stokes parameters) need to be removed, which might require the use of long baselines. Any array, also SKA1 and later 2, therefore preferably would consist of a compact core with "arms" extending to many tens of kilometer.

5.2 Scaling relations for tomography/imaging

Similar to the power-spectrum sensitivity, one can also obtain a scaling relation for imaging or tomography. One readily finds that the thermal noise inside a resolution element corresponding to a scale $k_\perp$ scales as:

$$\begin{aligned}\Delta T &= \left(\frac{k_\perp}{2\pi}\right)\left[D_{\rm c}^2\times\Omega_{\rm FoV}\right]^{1/2}\left(\frac{T_{\rm sys}}{\sqrt{B\,t_{\rm int}}}\right)\sqrt{\left(\frac{A_{\rm core}A_{\rm eff}}{A_{\rm coll}^2}\right)}\\ &= \left(\frac{k_\perp}{2\pi}\right)\left[D_{\rm c}^2\times\Omega_{\rm core}\right]^{1/2}\left(\frac{T_{\rm sys}}{\sqrt{B\,t_{\rm int}}}\right)f_{\rm fill}^{-1},\end{aligned} \tag{5.3}$$

assuming a *sinc*-function as model for the sky-components (i.e. a top-hat in uv-space). In this case $A_{\rm eff}$ drops out of the equation, although we leave it in to retain a similar form to the equation for the power-spectrum. We also see that on larger angular scales (i.e. smaller $k_\perp$), the noise decreases and that a more compact array helps to reduce the thermal noise per resolution element, by increasing the number density of visibilities per *uv*-cell. The latter form of the equation expresses this through the filling factor ($f_{\rm fill}$) of the core area in terms of collecting area and the field-of-view in a resolution element of the core. Filtering longer baselines (or smoothing of the image) to a resolution corresponding to $k_\perp$ averages down the noise and lowers the brightness temperature error, hence $k_\perp$ does not necessarily correspond to the largest baseline afforded by the core area. The latter simply sets the *uv*-density. For example for the inner part of SKA1 the core of 400m diameter has $f_{\rm fill}\sim 1$ and on scales $k_\perp = 0.1$ cMpc^{-1} ($\sim 20'$) one expect an error of ~ 0.2 mK per MHz in 1000 hrs of integration time at 150MHz, assuming $T_{\rm sys} = 400$ K, which is below the expected brightness temperature fluctuations on that scale. However, with increasing resolution the filling factor of the core decreases and $k_\perp$ increases, both leading to a rapidly increasing brightness temperature error ultimately limiting the angular scale where imaging can still be done. For SKA1 and 2 this limits occurs on an angular scale of a few to about ten arc minutes in a reasonable ($\sim$1000 hr) integration time.

5.3 Current SKA1-LOW Baseline Design and its Relevant Design Specifications

In the following we assume the current SKA1 baselines design (BLD), based on the station layout provided in Braun (2014). Although the latter is not necessarily the ultimate layout, it represents a "close-enough" description of the array that no major differences are expected in the resulting sensitivity calculations, except if the array is (i) substantially thinned out (i.e. reducing the total collecting area), (ii) dramatic changes in antenna layout are introduced (i.e. changing the filling factor) or (iii) substantially reducing the instantaneous field of view (i.e. through beam forming larger numbers of receiver elements). We refer to other chapters in this volume for a full description

PoS(AASKA14)001

of the current BLD. Using these antenna positions (or radial distribution) we calculate full 12-hr *uv*-tracks in the direction of the South Galactic pole and average the *uv*-density within radial bins. Similar densities are obtained for tracks at lower elevations. We assume a nominal 35m beam-formed "station" as well, which leads to a frequency-dependent field-of-view, being around 5 degrees FWHM at 100 MHz.

The fiducial layout that we assume in this review is listed below. We emphasize that this is not necessarily the most optimal observing strategy, although in some cases (e.g. freq. coverage) full use of the capabilities of SKA1 and 2 are made. As we will discuss below, *multi-beaming can dramatically improve the return of a single CD/EoR survey*. Also integration times can be increased[6]. Finally we assume for the nominal survey that phase-tracking of a single field is done, rather than drift-scans although we come back to that in this Section and Section 6.3.

1. **Antenna layout:** We assume for SKA1 the layout as (generically) specified the BLD, assuming that for SKA2 the collecting area is increased by a factor of four. The latter is implemented here via a scaling of all baselines by a factor of two and quadrupling the number of stations at each SKA1 station position. This ensures that the filling factor in the core remains of order unity and decreases in a scale-invariant manner to SKA1. Other choices are possible and will be investigated in the future.

2. **Frequency range:** Based on the current baseline design of SKA1, we assume a full instantaneous frequency coverage of 50–350 MHz (i.e. z=27-3). This range is thought to encompass the full *Cosmic Dawn* and *Epoch of Reionization* (see Mellema et al., 2013). We assume that during SKA1 the bandwidth can at least be split in two beams of 150-MHz, increasing the survey speed by a factor two. We note again that more beams can reduce on-sky time significantly. In the future one might consider extending SKA1 to lower frequencies (below 50 MHz) during the upgrade/extension to SKA2, although this will not be considered in this chapter.

3. **Survey FoV**: The field of view of a single primary beam is assumed to be FWHM$\approx 5^\circ$ at 100 MHz[7]. At a redshift of $z \sim 10$, the comoving distance is ~ 9700 cMpc, hence the comoving scales covered by the primary beam extend up to $\sim$1 cGpc, about ten times larger than the scale where the dark-matter power-spectrum peaks (~ 100 cMpc). For a bandwidth of 10 MHz (see below), the volume depth is ~ 170 cMpc. This means that sample variance on scales of a few hundred cMpc is $\sim 10\%$ and less on smaller scales. On larger scales, sample variance rapidly increases and only a larger survey volume (i.e. increased field-of-view via multi-beaming or drift-scanning) can further reduce this source of variance. One might consider increasing the FoV by beam forming a smaller number of log-periodic elements. We discuss the effect of multi-beaming/increased FoV below.

[6]We note that largely only winter-nights can be used during which the Sun and Milky Way center are below the horizon *and* the ionospheric effect are milder. Hence for deep pointed integrations, accumulating a thousand hours of on-sky time might take multiple years as experience with current pathfinder/precursors of the SKA already shows. Leeway to offset collecting area against integration time might therefore not save costs since it can lead to extremely long project lifetimes.

[7]We assume a D=35m beam-formed primary beam at 100 MHz, although not necessarily physical stations of 35m.

PoS(AASKA14)001

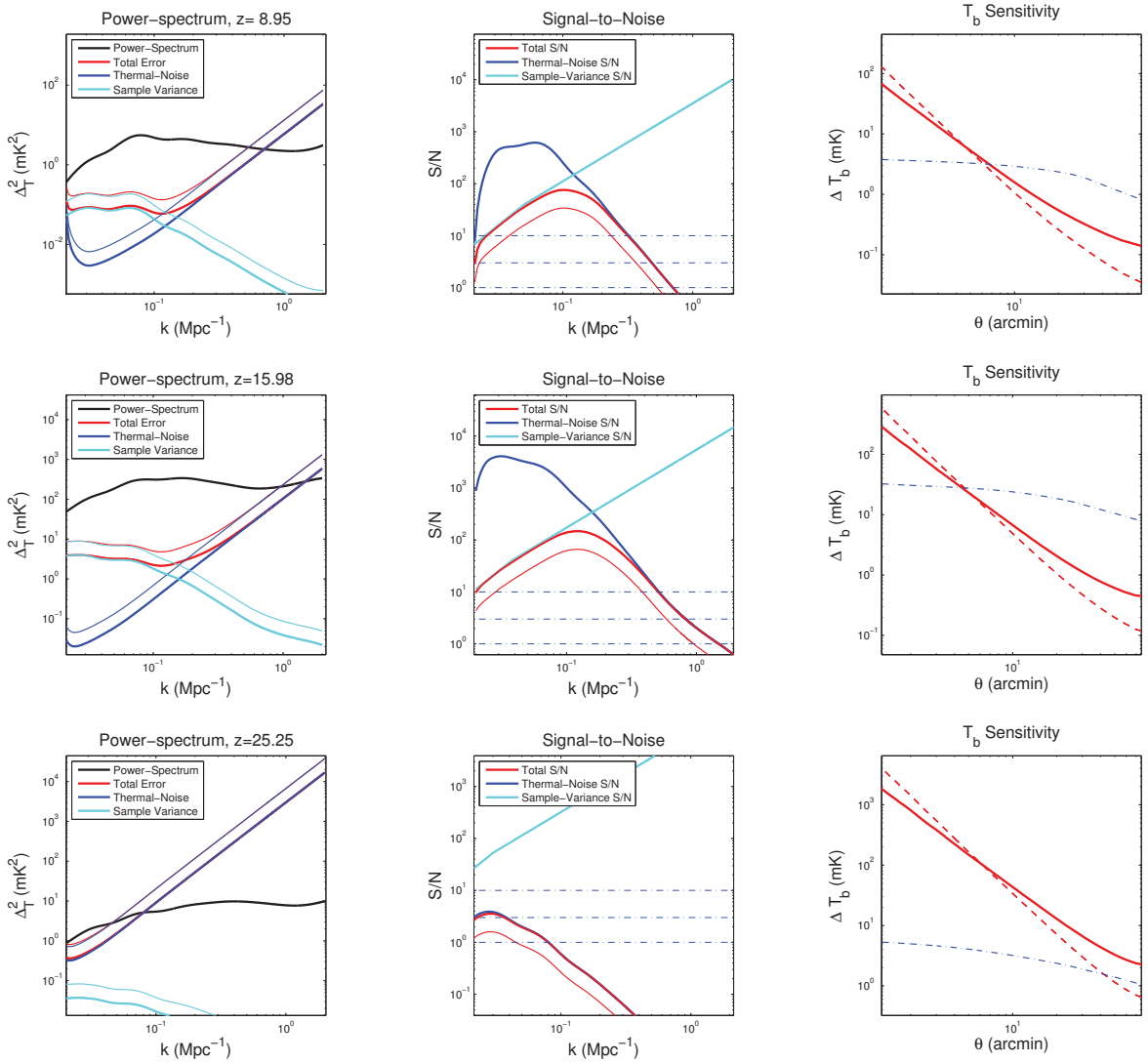

Figure 2: Deep Survey: Shown are the expected brightness temperature power-spectra from Mesinger et al. (2014) and the expected thermal-noise and cosmic-variance errors (following McQuinn et al., 2006) for the fiducial deep-survey parameters outlined in the text for SKA1-LOW. The thick/thin curves are for 5 versus 1 beam. The middle-column panels (red curves) indicate the expected total S/N ratio in such a deep survey, reaching a peak S/N$\sim$ 70, in good agreement with the results in Mesinger et al. (2014). The right column panels show the brightness temperature sensitivity as function of resolution, where the k-scale is transformed directly to angular scale at the corresponding redshift. The latter does not depend on the number of beams. The dashed line is for a BW that matches the angular scale rather than being fixed to 10MHz. The blue dot-dashed line is the expected variance on that scale by integrating over the power-spectrum.

4. **Integration times**: In this review, we assume an integration time of 10, 100 and 1000 hrs, for the different levels in a three-tiered survey with decreasing survey area, respectively. The reason for this choice is that SKA1 can reach levels of $\sim$1 mK in 1000-hrs integration time (per 1-MHz bandwidth) over a wide range of angular scales. However, this integration should only be thought of as a reference, since the level of brightness temperature can vary between models. This integration time is also often used in the literature as a reference, making comparison between models easier. The overall on-sky time of the assumed (three-tiered) survey, however, will be larger (see Section 6).

5. **Frequency Bandwidth/Redshift Binning:** We assume a bandwidth of 10 MHz, per redshift bin (not in total!), to maximize sensitivity but minimize light-cone effects, i.e. the impact of the evolution of the hydrogen brightness temperature with redshift mixed with the assumption that redshift can be regarded as a third spatial dimension of the data volume. The assumed bandwidth is a reasonable compromise. We note that bandwidth enters both in the survey depth (via $\Delta D_{\rm c}$) and in the sensitivity per visibility.

6. **Multi-Beaming:** We assume a single primary beam ($N_{\rm b} = 1$) for a 35m station in SKA1 for the full bandwidth (BW), possible two when split in to two 150-MHz bands, increasing for SKA2 potentially to covering the full log-period dipole beam ($N_{\rm b} \gg 1$). The latter would require an increase in correlator capacity beyond the currently envisioned SKA1 correlator. Below we will show the impact of multi-beaming, in particular in dramatically reducing sample variance on large angular scales.

7. **System Temperature:** We assume $T_{\rm sys} = 100 + 400 \times (\nu/150\,{\rm MHz})^{-2.55}$ K. Although this can change from field to field and can increase/decrease towards/away from the Galactic plane, we assume it to hold to reasonable order and is typical for assumptions in the literature.

8. **Inner-Cut uv-plane:** Finally we assume a 30-λ inner cut to the *uv*-plane (i.e. the sky-projected baselines in units of wavelength) to reduce the impact for foreground leakage in to the power-spectrum. This starts limiting scales $k < 0.02\,{\rm cMpc}^{-1}$ in the power-spectrum (See Fig.2) corresponding to scales of about 2 degrees or $\sim$ 300 cMpc at 150MHz. Since these scales already well exceed the peak of the DM and brightness temperature power spectra, they provide some information about cosmology, but far less information of the physics of CD/EoR. This cut is not needed if bright and large scale foregrounds can be controlled.

Whereas these assumptions, based on the BLD of SKA1 and 2 should not be regarded as definitive, they are a guide to typical observations specification, also currently used e.g. by MWA, LOFAR and PAPER, and thus serve as a reference.

6. A Three-tiered Cosmic Dawn and Epoch of Reionization Survey

Having specified our assumed nominal observational settings, in this section, we introduce an outline for a three-tiered survey of redshifted 21-cm emission during the CD/EoR that can address the wide range of physics questions posed in Section 3.

PoS(AASKA14)001

6.1 Main Observation Targets:

It should be stressed that observations of HI emission from the CD/EoR have thus far not been made (although upper limits are currently being set) and any present-day expectations are based on relatively sparse observations in different wavelength regimes or through very different observables(see Section 2.2). *Any CD/EoR-HI observational strategy should therefore cover as much of parameter space as possible (e.g. redshift, angular and frequency scales, field of view, etc), providing for surprises that the Universe might put up on us, obviously bounded by any reasonable estimate of what is possible.* Overall there are three general approaches to detecting and characterizing neutral hydrogen:

- via **direct imaging (i.e. tomography)** of neutral hydrogen down to the $1\sigma \approx 1$ mK brightness temperature level on >5-arcmin scales at $z \approx 6$, rising to degree scales at z=28.
- via **statistical (including power-spectrum) methods** to variance levels $1\sigma \approx 0.01 - 1$ mK^2 over the redshift regime z=6-28, respectively, at k<0.1 Mpc^{-1} and to k<1 Mpc^{-1} at $z < 15$.
- via **21-cm absorption line observations** against high-z radio sources, if present, with 1-5 kHz spectral resolution (2-10 km/s at z=10) with S/N>5 on 1 mJy.
- Although SKA2 can attain SKA1's limits 4× faster or, in the same integration time go 16× deeper (for power-spectra), new discoveries with SKA1 are expected to guide SKA2 observations, leading to new observational targets. SKA2 can also image smaller ionized bubbles and sub-mK brightness-temperature fluctuations during the Cosmic Dawn, unfeasible with SKA1. An extension of the frequency range from SKA1 to SKA2 could also enable one to probe the late Dark Ages at $z \sim$30-40.

The general target can be reached in a set of surveys and target fields in three tiers (depth versus area), which we will discuss in the following three sub-sections.

6.2 Deep Survey

The direct science goals of a Deep CD/EoR survey are to detect and characterize ionized structures and HI brightness temperature fluctuations on 5–300 arcmin scales (varying) over the EoR/CD redshift range $z = 6 - 28$ to 1-mK brightness temperature level and from it derive the state, thermal history and chemistry of the IGM, study the first stars, black holes and galaxies and constrain cosmology, the physics of dark matter and gravity. To reach this goal, deep 1000hr integrations are considered on 5 separate 20-square degree windows covering a total of 100 square-degree on-sky area, using the 50-200MHz frequency range with 0.1 MHz spectral resolution (for science), using the full SKA1-LOW array, using multi-beaming with $N_{\rm b} = 2$ lowering the on-sky time from 5000 to 2500 hrs. This will not be feasible with any current (or funded) array with S/N>1 and is unique to SKA1-LOW. This survey lowers the (expected) thermal noise $\sim 10\times$ over LOFAR and allows direct imaging with S/N$\gg$1. The Cosmic Dawn remains inaccessible to current/funded instruments, until this deep survey with SKA1-LOW. The sensitivities for power-spectra and imaging are shown in Fig. reffig:powerspectra1.

PoS(AASKA14)001

6.3 Medium+Shallow Survey

The direct science goals of a Medium+Shallow CD/EoR survey are to detect and characterize the 21-cm power-spectrum with a peak S/N$\sim$70 measured over $k = 0.02 - 1.00\,\mathrm{Mpc}^{-1}$ over the CD/EoR redshift range $z \sim 6 - 28$ and from it derive the state, thermal history and chemistry of the IGM, study the first stars, black holes and galaxies and constrain cosmology, the physics of dark matter and gravity. A medium-deep pointed survey of 50 times 100-hr integrations would cover 1,000 square degrees, and a preceding shallow pointed/drift-scan survey of 500 times 10-hr integrations would cover 10,000 square degrees, using the 50-200 MHz frequency range with 0.1 MHz spectral resolution (for science) and using the full SKA1-LOW array. Both survey can be carried out in 2500 hours each, assuming two beams of 150 MHz. Again multi-beaming could reduce the on-sky time substantially. A gain in power-spectrum sensitivity would be 1-2 orders of magnitude over current arrays (i.e. MWA, PAPER, LOFAR) in the sample-variance limited S/N regime ($k < 0.2\,\mathrm{Mpc}^{-1}$), but scales $k = 0.2 - 1\,\mathrm{Mpc}^{-1}$ are likely to remain inaccessible until SKA1-LOW is build, because of severe thermal-noise limitations. Again the Cosmic Dawn remains inaccessible to current/funded instruments, until SKA1-LOW is realized. The sensitivities for power-spectra and imaging are shown in Fig.3.

6.4 Absorption at 21-cm

The science goal is to obtain 21-cm absorption line spectra from (rare) radio sources at $z > 6$ to probe very small scales (i.e. $k \sim 1000\,\mathrm{Mpc}^{-1}$) or virialized structures (mini-haloes) and from it derive the state, thermal history and chemistry of the IGM, study the first stars, black holes and galaxies and constrain cosmology, the physics of dark matter and gravity. This can be done through deep 1000-hrs integrations on selected sources with a flux of > 1 mJy (possibly in the Deep Survey fields; see Ciardi et al. 2015) with a spectral resolution of a few km/s (1-5 khz at 150 MHz) over the 50-200 MHz frequency range ($z \sim 6 - 28$). We note also here, that no observations of this kind have ever been done and are not expected to be feasible before SKA1-LOW is build, because of the same severe thermal noise limitations that currently limit direct imaging.

6.5 Deep to Shallow Surveys: Multi-beaming and/or Drift-Scans

Optimal observing strategies will depend on many variables: ionospheric conditions, minimization of side-lobe leakage of strong sources, field in the zenith, low galactic brightness temperatures and polarization, optimal *uv*-coverage, multi-beaming versus frequency coverage, inclusion of long baseline information, monitoring of the station beams, RFI excision, drift-scans versus tracking, etc. For SKA1-LOW the field of view is typically 5-10 degrees and hence the sky drifts (see Trott, 2014, for details) though a stationary beam (i.e. non-tracking) in about 0.5-1 hr. Deep integrations of 1000+ hrs would therefore require 1000-2000 nights for every single deep field, which is prohibitively long. Tracking the field over N hrs, would allow the same integration time to be accumulated in N times fewer nights. Hence it appears that drift-scans would only be useful for larger scale shallow surveys, where the total integration per field can be small. On the other hand, because SKA1-LOW allows for two beams in the baseline design, one could conceive of a combination of tracking-drift-scan, where the field drifts from one stationary beam to a second stationary beam and only every 0.5-1 hr would one switch the phase center of the trailing beam to a new phase-center.

PoS(AASKA14)001

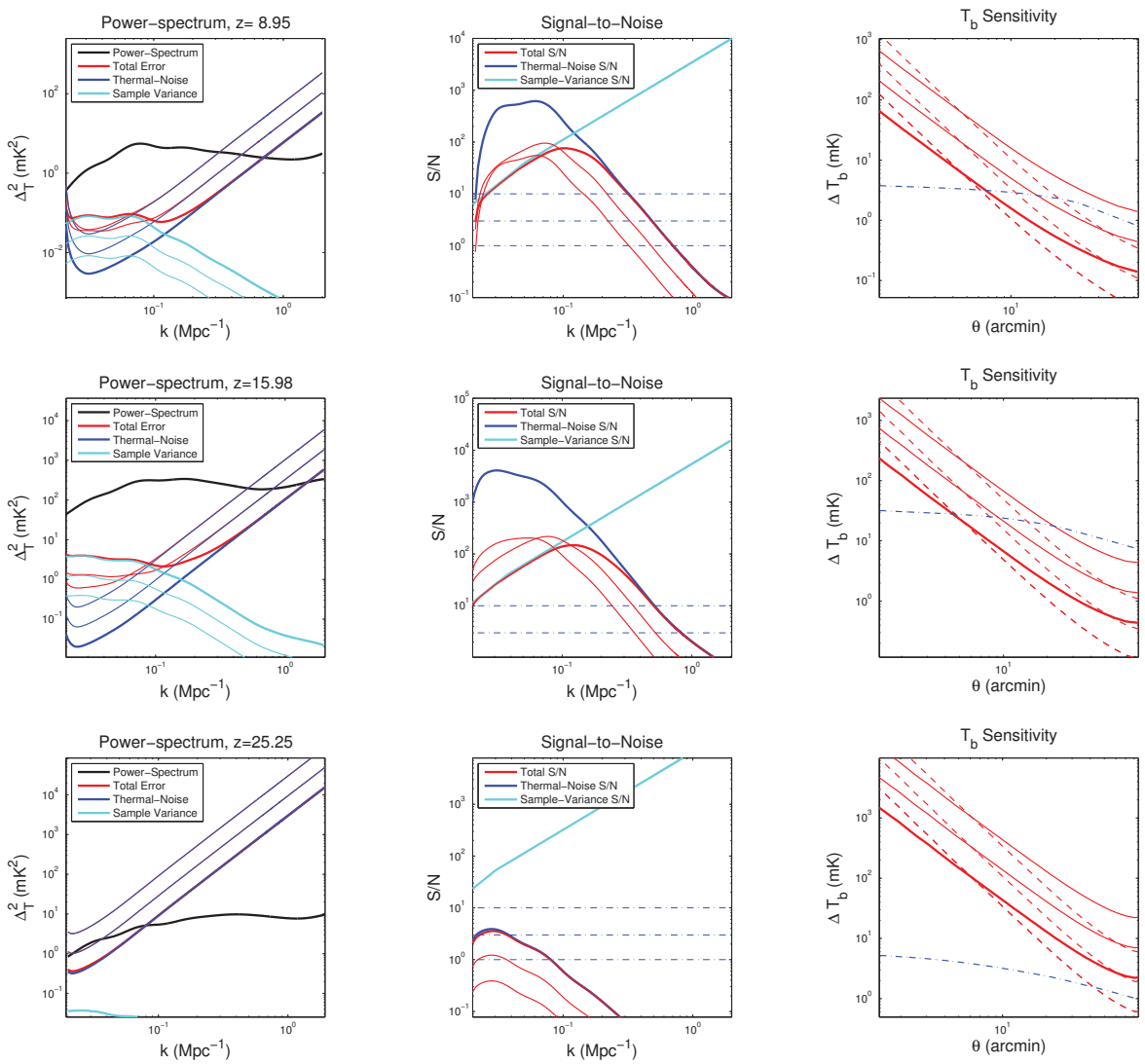

Figure 3: Deep-Medium-Shallow Surveys: Shown are the expected brightness temperature power-spectra from Mesinger et al. (2014) and the expected thermal-noise and cosmic-variance errors (following McQuinn et al. 2006) for the fiducial survey parameters outlined in Section 6 for SKA1. The middle panels (thick red curve) indicate the expected total S/N ratio in such a survey, reaching a peak S/N$\sim$ 70, in good agreement with the results in Mesinger et al. (2014). From top to bottom, the red curves for the deep, medium and shallow surveys are shown, clearly showing an increased gain in sensitivity at the larger k modes in the deep survey due to low thermal noise, and an increased gain in sensitivity at the smaller k modes in the medium+shallows surveys due to lower sample variance, leading to a relatively flat S/N curve over one dex in k space. For completeness, the right column show the brightness temperature sensitivity as function of resolution, where k-scale is transformed directly to angular scale at the corresponding redshift. From bottom to top are the deep, medium and shallow surveys. The dashed line is for a BW that matches the angular scale rather than being fixed to 10MHz. The blue dot-dashed line is the expected variance on that scale by integrating over the power-spectrum.

Since these ideas have not been worked out in detail (but see Trott, 2014), the precise observing strategy remains an open question and will depend on a combination of nights available, sensitivity, resolution in the image, calibration errors, etc.

7. Role-out of SKA1 and expansion to SKA2.

A great advantage of radio interferometers is that it can observe even if incomplete in its number of receiver elements and/or stations/dishes. To enable high-impact science even with an incomplete array it is important to think about rollout from an incomplete SKA1 to a fully complete SKA2.

7.1 Role-out from SKA1 to SKA2: 0.5, 1, 2 and 4 times SKA1

In this section we shortly discuss three stages: (i) roll-out of half of SKA1, (ii) SKA1 and (iii) rollout to a full SKA2, being four times the collecting area of SKA1. We only compare these stagesca assuming a scaling in the number of stations (i.e. collecting area) and no other specification (e.g. frequency coverage, multi-beaming, etc.). The ratio of the number of stations is assumed to be $f_{\rm s}$ where $f_{\rm s} = 1$ for SKA1. Since neither half of SKA1 nor SKA2 have any specified baseline designs, we have to make an assumption. Based on the scaling relations in Sections 5, a high filling factor is critical to reach surface brightness levels of $\sim$1 mK. The simplest assumption is therefore to take the current SKA1 BLD and scale the number of visibilities (i.e. the voltage/electric-field coherence between two receivers) by $f_{\rm s}^2$, but keeping the radial uv-density profile scale-invariant. The above scalings ensure that the filling factor at the center of the array remains the same during rollout which ensure maximum sensitivity on large angular scales. In Fig.4 we show the impact of $f_{\rm s} = 0.5, 1.0, 4.0$ on the power-spectra and brightness temperature sensitivity for tomography. We conclude a few things in comparison to the SKA1 baseline design:

- For $k < 0.1\,{\rm Mpc}^{-1}$ there is no power-spectrum sensitivity loss in a single beam ($\sim$ 20 square degrees) because one is sample-variance limited. Above $k > 0.1\,{\rm Mpc}^{-1}$, however thermal noise dominates the error budget and one quickly gains S/N. Hence SKA1 in roll-out could already carry out a shallow wide-field survey focussed on $k < 0.1\,{\rm Mpc}^{-1}$.

- During the EoR and especially during the CD, SKA1 to SKA2 start to reach $k > 1\,{\rm Mpc}^{-1}$ with good S/N, which is the region where the power-spectrum can rise quickly due to physics on small angular scale (mini-haloes) and where small ionized bubble will exhibit features in the power-spectrum. We note an almost order of magnitude increase in sensitivity from SKA1 to SKA2 at k-modes beyond $k \sim 0.2\,{\rm Mpc}^{-1}$

- Whereas half SKA1 will enable tomography on $\sim$ 5 arcmin scale during the EoR, during the CD this ability is lost and only with some luck scales larger than half a degree might be imaged. SKA1 and in particular SKA2, however, will enable tomography during the EoR, CD and late Dark Ages (the latter only for SKA2). As shown in Sections 5 & 6, sheer collecting area and its resulting instantaneous sensitivity is needed. This can only partly be compensated by integrating longer, but at the expensive of substantially increasing the project duration (possibly to a decade or more).

PoS(AASKA14)001

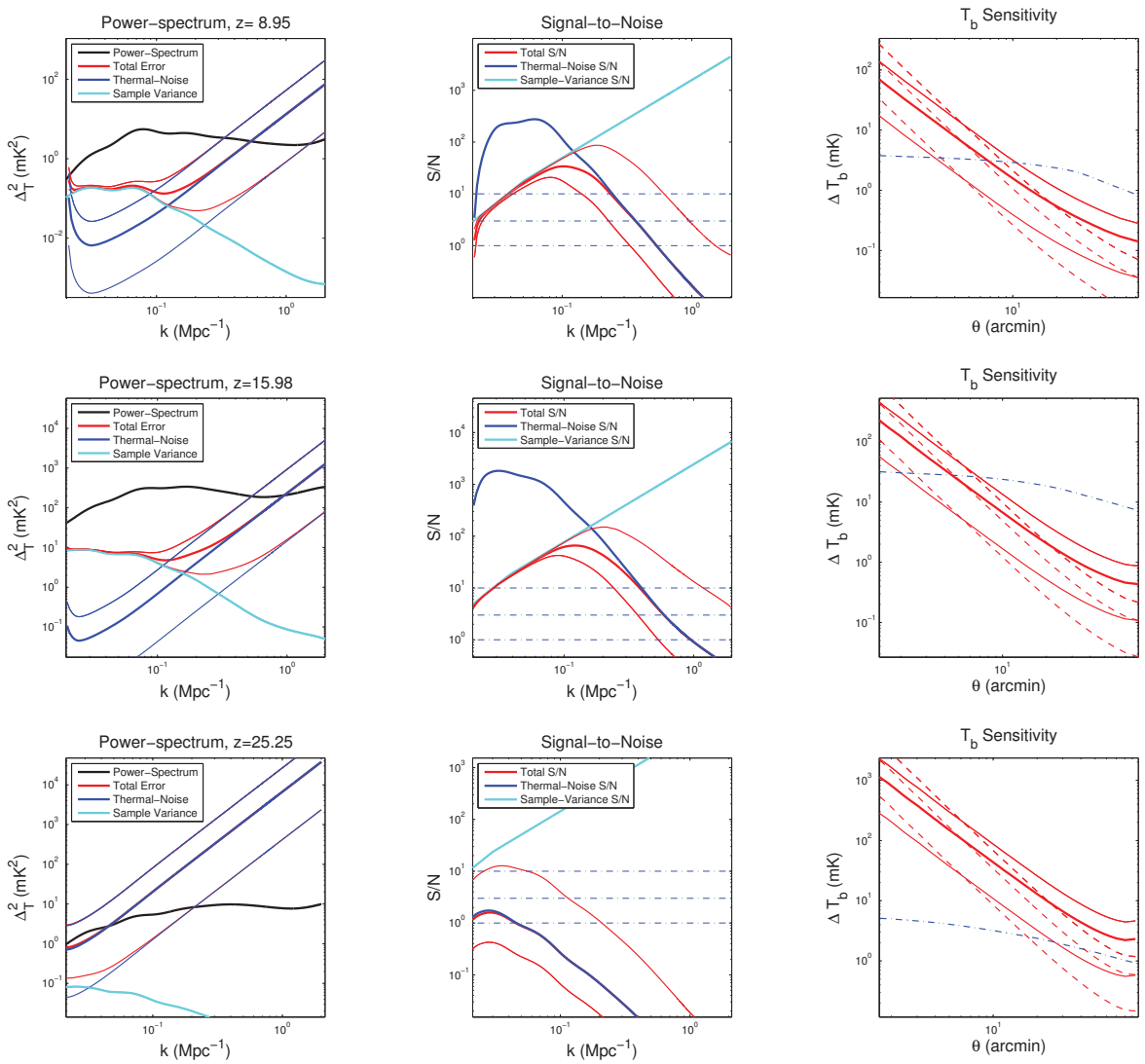

Figure 4: Rollout from half to four times SKA1: Idem to Fig.2 & 3. The solid red lines from bottom to top (middle column) show the S/N for a deep survey for $f_s = 0.5, 1.0, 4.0$. In the right column the brightness temperature (from bottom to top) is given for SKA2, SKA1 and half SKA1.

A remarkable result is that for most of the redshift regime ($z \approx 9-15$) cosmic variance limits the survey below $k \approx 0.2\mathrm{Mpc}^{-1}$. We note that because both the thermal and cosmic-variance errors scale identically with number of beams (see text), this transition scale is invariant under increasing the number of beams (i.e. multi-beaming), despite that the S/N increases as $\sqrt{N_{\rm beam}}$.

8. Summary, Conclusions and Highlights

SKA1-LOW and finally SKA2-LOW will be a transformational instrument in the study of the physics of the first stars, galaxies and black holes, dark-matter, the IGM, cosmology and possibly gravity during the first one billion years of the Universe, via statistical and direct measurements (e.g. power-spectra and tomography) of the redshifted 21-cm line from neutral hydrogen.

SKA1 will enable brightness temperature levels of $\sim$1 mK to be reached in 1000 hrs of integration (BW=1 MHz) from $z \sim 6$ to $z \sim 28$ (>50 MHz) over increasing angular scales ranging $\sim$5–300 arcminutes. SKA2 could potentially enable even higher redshift observations, starting to probe the late Dark Ages, as well as probe a much larger area of the sky (via multi-beaming) to a much greater depth in less time, reducing the thermal noise variance that will still limit SKA1 on the small scales where the dominant source population (e.g. mini-haloes) have their largest impact on neutral hydrogen (both via ionization and spin-temperature effects). The impact of SKA2 is expected in pushing tomography (i.e. direct imaging) to higher redshifts and to greater S/N (e.g. to probe redshift space distortions, higher order statistics, specific regions in the cubes, etc) where the sensitivity of SKA1 will still be insufficient. Although the *Cosmic Dawn* will be opened by SKA1, SKA2 will allow it to be studied in much great detail similar to the impact of SKA1 on the study of neutral hydrogen during the *Epoch of Reionization*.

We have outlined a three-tiered survey (deep and shallow/medium-deep and 21-cm absorption line measurements) with SKA1 that allow one to reach the goals of measuring the HI brightness temperature to a level of around 1 mK for tomography (a genuinely unique capability of SKA1 and SKA2) over a range of a few arc minutes up to a degree (depending on redshift), reduce sample variance and reach power-spectrum measurements up to one arcmin scales. Such a three tiered survey (assuming 21-cm absorption measurements can piggy-back on the deep survey) can be carried out in 3×2500 hrs[8] assuming that the full 300 MHz BW of SKA1 can be split in to two beams of 150 MHz. Such a survey is expected to take of order five years, assuming an efficiency of 50% of all night-time data (assuming 8-hr tracks) over such a period by selecting the best observing times and minimizing the impact of the ionosphere *and* emission from the Milky Way. This is not a project that can be carried out in a few months of full-time observations. Experience with the low-frequency SKA precursors and pathfinders confirms that good "observing conditions" are necessary for a successful CD/EoR projects.

Finally, a three-tiered survey with SKA1-LOW is expected to generate strong synergy with other major (future) facilities such as JWST, ALMA, Euclid, as well as with (CO/CII) intensity-mapping arrays and large ground-based IR facilities such as the ELT. Many of the details can be found in the accompanying CD/EoR chapters in this volume.

8.1 SKA1 and 2 Science High-lights

Some high-light science results, in random order, expected to be largely unique for SKA1 (and 2) are given below. For each bullet point we refer to the first author of the related chapters in this volume:

[8] We note that collecting 2500 hrs of "good" deep pointed data might take up to $\sim$5 years since winter-nights where the MW and Sun are below the horizon and the ionosphere is mild might only allow up to 500 hrs on-sky time to be accumulated per calendar year. Multi-beaming can significantly speed this up.

PoS(AASKA14)001

- Direct imaging of ionized regions and HI fluctuations on scales of arcminutes and larger during the *Epoch of Reionization* and *Cosmic Dawn* — *Mellema et al. 2015; Wyithe et al. 2015*
- Probing many aspects of cosmology/cosmography out to the highest possible redshifts (i.e. $z = 27$ in case of SKA1) — *Pritchard et al. 2015*
- Enabling one to probe $k \sim 1000\,\mathrm{Mpc}^{-1}$ scales via 21-cm absorption, probing mini-halos even out of reach of JWST — *Ciardi et al. 2015*
- Direct study of the state and chemistry of the IGM in the first billions years of the Universe – *Ahn et al. 2015; Subrahmanyan et al. 2015*
- Unique studies (i.e. CD) beyond the *Epoch of Reionization* which will remain out of reach of most of not all other (planned) facilities in particular of the first (Pop-III stars and X-ray heating sources) – *Mesinger et al. 2015; Semelin et al. 2015*
- Probing the impact of bulk-flows during the later *Dark Ages* and the *Cosmic Dawn* allowing physics during the *Dark Ages* and CMB to be probed in a unique manner – *Maio et al. 2015*
- Strong synergy with intensity mapping of the CO, CII, Lyman-α lines, possible molecular lines from primordial collapsing gas (e.g. H_2 and HD), as well as the kS-Z effect and NIR/X-ray mission, as well as with many other (planned) facilities in space and on the ground — *Chang et al. 2015; Jelic et al. 2015*

We conclude to say that direct detection of neutral hydrogen at high redshift, beyond the statistical approaches of current experiments, as well as probing the *Cosmic Dawn* will be defining abilities of the SKA (1 and 2). SKA can probe the universe back to 100 Myr after the Big Bang, well beyond even the limitations of JWST[9]. This unique science can be carried out in a three-tiered survey of 7500 hrs or total on-sky time.

References

Ahn, K., et al., 2015, “Probing the First Galaxies and Their Impact on the Intergalactic Medium through 21-cm Observations of the Cosmic Dawn with the SKA”, in proceedings of “Advancing Astrophysics with the Square Kilometre Array", PoS(AASKA14)003

Ali, Z. S., Parsons, A. R., Zheng, H., et al. 2015, ArXiv e-prints

Ali-Haïmoud, Y., Meerburg, P. D., & Yuan, S. 2014, Phys Rev D, 89, 083506

Barkana, R., & Loeb, A. 2001, Physics Reports, 349, 125

Becker, R. H., Fan, X., White, R. L., et al. 2001, AJ, 122, 2850

Bolton, J. S., Becker, G. D., Wyithe, J. S. B., Haehnelt, M. G., & Sargent, W. L. W. 2010, MNRAS, 406, 612

Bouwens, R. J., Illingworth, G. D., Oesch, P. A., et al. 2012, ApJL, 752, L5

[9] A single resolution element of SKA1 and 2 will be as large as the entire field of view of the JWST, placing "complementarity" in a different footlight. It is likely, if the two instruments have overlapping lifetimes that JWST will follow-up limited target regions selected by the SKA.

PoS(AASKA14)001

Braun, R., 2014, "SKA1 Array Configurations", Document Number SKA-OFF.AG.CNF-SKO-TN-001 Revision 1, SKA Organisation
Carilli, C. L., Gnedin, N. Y., & Owen, F. 2002, ApJ, 577, 22
Cooray, A., Li, C., & Melchiorri, A. 2008, Phys Rev D, 77, 103506
Chang, T.C., et al., 2015, "Synergy of CO/[CII]/Lya Line Intensity Mapping with the SKA", in proceedings of "Advancing Astrophysics with the Square Kilometre Array", PoS(AASKA14)004
Chapman, E., et al., 2015, "Cosmic Dawn and Epoch of Reionization Foreground Removal with the SKA", in proceedings of "Advancing Astrophysics with the Square Kilometre Array", PoS(AASKA14)005
Ciardi, B., et al., 2015, "21-cm forest with the SKA", in proceedings of "Advancing Astrophysics with the Square Kilometre Array", PoS(AASKA14)006
Davé, R., Finlator, K., & Oppenheimer, B. D. 2006, MNRAS, 370, 273
de Souza, R. S., Ishida, E. E. O., Johnson, J. L., Whalen, D. J., & Mesinger, A. 2013, MNRAS, 436, 1555
de Souza, R. S., Ishida, E. E. O., Whalen, D. J., Johnson, J. L., & Ferrara, A. 2014, MNRAS, 442, 1640
Dijkstra, M. 2006, New Astronomy Reviews, 50, 204
Dillon, J. S., Liu, A., Williams, C. L., et al. 2014, Phys Rev D, 89, 023002
Ellis, R. S., McLure, R. J., Dunlop, J. S., et al. 2013, ApJL, 763, L7
Fan, X., Narayanan, V. K., Strauss, M. A., et al. 2002, AJ, 123, 1247
Fan, X., Strauss, M. A., Becker, R. H., et al. 2006, AJ, 132, 117
Fernandez, E. R., & Zaroubi, S. 2013, MNRAS, 433, 2047
Fialkov, A., Barkana, R., & Cohen, A. 2015, Physical Review Letters, 114, 101303
Fialkov, A., Barkana, R., Pinhas, A., & Visbal, E. 2014a, MNRAS, 437, L36
Fialkov, A., Barkana, R., & Visbal, E. 2014b, Nature, 506, 197
Fialkov, A., & Loeb, A. 2013, Journal of Cosmology and Astroparticle Physics, 11, 66
Field, G. B. 1958, Proceedings of the IRE, 46, 240
—. 1959, ApJ, 129, 536
Furlanetto, S. R., & Briggs, F. H. 2004, New Astronomy Reviews, 48, 1039
Greenhill, L. J., Kocz, J., Barsdell, B. R., Clark, M. A., & LEDA Collaboration. 2014, in Exascale Radio Astronomy, 10301
Harker, G. J. A., Zaroubi, S., Thomas, R. M., et al. 2009, MNRAS, 393, 1449
Helgason, K., Cappelluti, N., Hasinger, G., Kashlinsky, A., & Ricotti, M. 2014, ApJ, 785, 38
Iliev, I., et al., 2015, "Epoch of Reionization modelling and simulations for SKA", in proceedings of "Advancing Astrophysics with the Square Kilometre Array", PoS(AASKA14)007
Jelic, V., et al., 2015, "SKA - EoR correlations and cross-correlations: kSZ, radio galaxies, and NIR background", in proceedings of "Advancing Astrophysics with the Square Kilometre Array", PoS(AASKA14)008
Lewis, A., & Challinor, A. 2007, Phys Rev D, 76, 083005
Loeb, A., & Furlanetto, S. R. 2013, The First Galaxies in the Universe
Lorenzoni, S., Bunker, A. J., Wilkins, S. M., et al. 2011, MNRAS, 414, 1455
Madau, P., Meiksin, A., & Rees, M. J. 1997, ApJ, 475, 429
Maio, U., et al., 2015, "Bulk Flows and End of the Dark Ages with the SKA", in proceedings of

PoS(AASKA14)001

"Advancing Astrophysics with the Square Kilometre Array", PoS(AASKA14)009
Matthee, J. J. A., Sobral, D., Swinbank, A. M., et al. 2014, MNRAS, 440, 2375
McQuinn, M., Zahn, O., Zaldarriaga, M., Hernquist, L., & Furlanetto, S. R. 2006, ApJ, 653, 815
Mellema, G., Koopmans, L. V. E., Abdalla, F. A., et al. 2013, Experimental Astronomy, 36, 235
Mellema, G., et al., 2015, "HI tomographic imaging of the Cosmic Dawn and Epoch of Reionization with SKA", in proceedings of "Advancing Astrophysics with the Square Kilometre Array", PoS(AASKA14)010
Mesinger, A. 2010, MNRAS, 407, 1328
Mesinger, A., Ewall-Wice, A., & Hewitt, J. 2014, MNRAS, 439, 3262
Mesinger, A., et al., 2015, "Constraining the Astrophysics of the Cosmic Dawn and the Epoch of Reionization with the SKA", in proceedings of "Advancing Astrophysics with the Square Kilometre Array", PoS(AASKA14)011
Morales, M. F., & Wyithe, J. S. B. 2010, *Ann. Rev. Astron.& Astrophys.* , 48, 127
Mortlock, D. J., Warren, S. J., Venemans, B. P., et al. 2011, Nature, 474, 616
Novaco, J. C., & Brown, L. W. 1978, ApJ, 221, 114
Paciga, G., Chang, T.-C., Gupta, Y., et al. 2011, MNRAS, 413, 1174
Pacucci, F., Mesinger, A., Mineo, S., & Ferrara, A. 2014, MNRAS, 443, 678
Patra, N., Subrahmanyan, R., Raghunathan, A., & Udaya Shankar, N. 2013, Experimental Astronomy, 36, 319
Patra, N., Subrahmanyan, R., Sethi, S., Udaya Shankar, N., & Raghunathan, A. 2015, ApJ, 801, 138
Pillepich, A., Porciani, C., & Matarrese, S. 2007, ApJ, 662, 1
Pober, J. C., Ali, Z. S., Parsons, A. R., et al. 2015, ArXiv e-prints
Pritchard, J. R., & Loeb, A. 2008, Phys Rev D, 78, 103511
Pritchard, J., et al., 2015, "Cosmology from EoR/Cosmic Dawn with the SKA", in proceedings of "Advancing Astrophysics with the Square Kilometre Array", PoS(AASKA14)012
Ripamonti, E., Iocco, F., Ferrara, A., et al. 2010, MNRAS, 406, 2605
Robertson, B. E., Ellis, R. S., Dunlop, J. S., McLure, R. J., & Stark, D. P. 2010, Nature, 468, 49
Robertson, B. E., Ellis, R. S., Furlanetto, S. R., & Dunlop, J. S. 2015, ApJL, 802, L19
Ruiz-Velasco, A. E., Swan, H., Troja, E., et al. 2007, ApJ, 669, 1
Semelin, B., et al., 2015, "The physics of Reionization: processes relevant for SKA observations", in proceedings of "Advancing Astrophysics with the Square Kilometre Array", PoS(AASKA14)013
Simcoe, R. A., Sullivan, P. W., Cooksey, K. L., et al. 2012, Nature, 492, 79
Smoot, G. F., Bennett, C. L., Kogut, A., et al. 1992, ApJL, 396, L1
Sobacchi, E., & Mesinger, A. 2014, MNRAS, 440, 1662
Sparre, M., Hartoog, O. E., Krühler, T., et al. 2014, ApJ, 785, 150
Stacy, A., & Bromm, V. 2013, MNRAS, 433, 1094
Subramanyan, R., et al., 2015, "All-sky signals from recombination to reionization with the SKA", in proceedings of "Advancing Astrophysics with the Square Kilometre Array", PoS(AASKA14)014
Taoso, M., Bertone, G., Meynet, G., & Ekström, S. 2008, Phys Rev D, 78, 123510
Theuns, T., Zaroubi, S., Kim, T.-S., Tzanavaris, P., & Carswell, R. F. 2002, MNRAS, 332, 367

PoS(AASKA14)001

Trott, C. M. 2014, PASA, 31, 26
Tseliakhovich, D., & Hirata, C. 2010, Phys Rev D, 82, 083520
Valdés, M., Evoli, C., Mesinger, A., Ferrara, A., & Yoshida, N. 2013, MNRAS, 429, 1705
van Haarlem, M. P., Wise, M. W., Gunst, A. W., et al. 2013, *A.&A*, 556, A2
Wouthuysen, S. A. 1952, AJ, 57, 31
Wyithe, S., et al., 2015, "Imaging HII Regions from Galaxies and Quasars During Reionisation with SKA", in proceedings of "Advancing Astrophysics with the Square Kilometre Array", PoS(AASKA14)015
Yatawatta, S., de Bruyn, A. G., Brentjens, M. A., et al. 2013, *A.&A*, 550, A136
Zemcov, M., Smidt, J., Arai, T., et al. 2014, Science, 346, 732

A. Author Institutions

L.V.E Koopmans, Kapteyn Astronomical Institute, University of Groningen, The Netherlands
J. Pritchard, Imperial College, U.K.
G. Mellema, Dept. of Astronomy and Oskar Klein Centre, Stockholm Univ., Sweden
F. Abdalla, University College London, U.K.
J. Aguirre, University of Pennsylvania, USA
K. Ahn, Dept. of Earth Science, Chosun University, Korea
R. Barkana, Tel Aviv University, Israel
I. van Bemmel, Joint Institute for VLBI in Europe, The Netherlands
G. Bernardi, SKA South Africa & Rhodes University, South Africa
A. Bonaldi, Jodrell Bank Centre for Astrophysics, University of Manchester, U.K.
F. Briggs, Research School of Astronomy & Astrophysics, Australian National University
A.G. de Bruyn, Netherlands Institute for Radio Astronomy (ASTRON), The Netherlands
T.C. Chang, Academia Sinica Institute of Astronomy & Astrophysics, Taiwan
E. Chapman, Department of Physics & Astronomy, University College London, U.K.
X. Chen, National Astronomical Observatories, Chinese Academy of Science, Beijing, China
B. Ciardi, Max Planck Institute for Astrophysics, Garching, Germany
K.K. Datta, Dept. of Physics, Presidency University, Kolkata, India
P. Dayal, Institute for Computational Cosmology, Durham University, U.K.
A. Ferrara, Scuola Normale Superiore, Pisa, Italy
A. Fialkov, Ecole Normale Superieure, Paris, France
F. Fiore, INAF Osservatorio Astronomico di Roma, Italy
K. Ichiki, Nagoya University, Japan
I. T. Iliev, Astronomy Centre, Department of Physics & Astronomy, University of Sussex, U.K.
S. Inoue, Max Planck Institute for Astrophysics, Germany
V. Jelić, Kapteyn Astronomical Institute, University of Groningen, and ASTRON, The Netherlands
M. Jones, Oxford University, U.K.
J. Lazio, Jet Propulsion Laboratory, California Institute of Technology, USA
K. J. Mack, University of Melbourne, Australia
U. Maio, INAF-Trieste, Italy & Leibniz Institute for Astrophysics, Germany

PoS(AASKA14)001

S. Majumdar, Stockholm University, Sweden
A. Mesinger, Scuola Normale Superiore, Pisa, Italy
M.F. Morales, Dark Universe Science Center, University of Washington, USA
A. Parsons, University California Berkeley, USA
U.-L. Pen, Canadian Institute for Theoretical Astrophysics, Toronto, Canada
M. Santos, University of Western Cape, South Africa
R. Schneider, INAF/Osservatorio Astronomico di Roma, Italy
B. Semelin, LERMA, Observatoire de Paris, France
R.S. de Souza, MTA Eotvos University, Hungary
R. Subrahmanyan, Raman Research Institute, Bangalore 560080, India
T. Takeuchi, Nagoya University, Japan
C. Trott, International Centre for Radio Astronomy Research, Curtin University, Australia
H. Vedantham, Kapteyn Astronomical Institute, University of Groningen, The Netherlands
J. Wagg, Square Kilometre Array Organisation
R. Webster, School of Physics, University of Melbourne, Australia
S. Wyithe, School of Physics, University of Melbourne, Australia

PoS(AASKA14)001

PROCEEDINGS OF SCIENCE

Probing the First Galaxies and Their Impact on the Intergalactic Medium through 21-cm Observations of the Cosmic Dawn with the SKA

Kyungjin Ahn*
Department of Earth Sciences, Chosun University, Gwangju 501-759, Korea
E-mail: kjahn@chosun.ac.kr

Andrei Mesinger
Scuola Normale Superiore, Piazza dei Cavalieri 7, 56126 Pisa, Italy
E-mail: andrei.mesinger@sns.it

Marcelo A. Alvarez
Canadian Institue for Theoretical Astrophysics, 60 St. George St., Toronto, ON. M5S 3H8, Canada
E-mail: malvarez@cita.utoronto.ca

Xuelei Chen
National Astronomical Observatory of China, 20A Datun Road, Chaoyang District, Beijing, China, 100012
E-mail: xuelei@cosmology.bao.ac.cn

We present an overview of the theory of high-redshift star and X-ray source formation, and how they affect the 21-cm background. Primary focus is given to Lyα pumping and X-ray heating mechanisms at cosmic dawn, opening a new observational window for high-redshift astrophysics by generating sizable fluctuations in the 21-cm background. We describe observational prospects for power spectrum analysis and 3D tomography (imaging) of the signature of these early astrophysical sources by SKA1-LOW and SKA2.

Advancing Astrophysics with the Square Kilometre Array
June 8-13, 2014
Giardini Naxos, Italy

*Speaker.

PoS(AASKA14)003

1. Introduction

The early phase of the Epoch of Reionization (EoR) or Cosmic Dawn (CD) is, by definition, believed to have started with the formation of the first stars, even though the EoR may also have been fuelled initially by somewhat unconventional radiation sources such as annihilating dark matter clumps (e.g. Spolyar et al. 2009). The first stars are believed to have formed within minihalos (halos with $T_{\rm vir} \lesssim 10^4$ K, or $10^4 \lesssim M/M_\odot \lesssim 10^{7-8}$) and to have been massive, emitting a sufficient amount of UV radiation to ionize the surrounding hydrogen and helium. These stars were born at zero metallicity, with their formation predominantly regulated by H_2 cooling, and thus they are also Population III (Pop III) stars. Until recently the conventional view, from high-resolution numerical simulations, was of massive ($\gtrsim 100 M_\odot$) stars forming in isolation (e.g. Abel et al. 2002; Bromm et al. 2002; Yoshida et al. 2006): one Pop III star per minihalo. This paradigm has undergone recent revision due to newer simulations in which smaller-mass ($\sim 10-40 M_\odot$) stars form binary systems (Turk et al. 2009; Stacy et al. 2010; Greif et al. 2011a), although the universality of this result is unclear (see Hirano et al. 2014 for a wide spectrum of Pop III stars in ~ 100 minihalos). At any rate, a change in the initial mass function (IMF) of Pop III stars affects the hardness of the spectral energy distribution (SED) of these stars, and thus the CD and EoR modelling as well. Stellar binaries may evolve into X-ray binaries that may, if efficient, result in a smoother ionization structure of the intergalactic medium (IGM) than that by UV sources, due to a much longer mean free path than that of typical UV photons (e.g. Haiman 2011; Mesinger et al. 2013 and references therein). Furthermore, the interstellar medium heated by supernova explosions can cool through a combination of Bremsstrahlung and metal line cooling, producing soft ($\lesssim$keV) X-rays that can efficiently heat the high-redshift IGM (Pacucci et al. 2014).

The theory of the formation and evolution of the first stars, therefore, is crucial in modelling CD and even the EoR, because the metallicity built up after the death of Pop III stars will give way to the formation of Population II (Pop II) stars, believed to be the main drivers of reionization. A major feedback that affects their formation is the dissociation of H_2 molecules – cooling agents – inside minihalos by Lyman-Werner band radiation (e.g. Haiman et al. 2000; for recent simulations with this effect in a $\gtrsim 100$ Mpc box see e.g. Ahn et al. 2012 and Fialkov et al. 2013). Stars would not have formed either in minihalos that were embedded in photoionized gas ($T \gtrsim 10^4$ K), since the increase in pressure would have suppressed minihalo gas accretion (Jeans-mass filtering).

There also appeared a noteworthy discovery having to do with the nature of large scale fluctuations. Tseliakhovich & Hirata (2010) used a peak-background split scheme to study the nonlinear evolution of the baryon/dark-matter velocity offset, which was seeded at the recombination epoch, and found that hydrodynamics at scales relevant to minihalo formation should have been affected (see more details of its astrophysical impact in the subchapter by Maio). The typical offset is found to be e.g. ~ 1 km/s at $z \sim 20$, corresponding to $M_{\rm halo} \sim 1.5 \times 10^5 M_\odot$, when minihalos were already abundant. While determination of the halo mass and environmental dependence of this effect awaits more detailed study, simulations already show an increase in the threshold mass for star formation and a delay in halo collapse (Stacy et al. 2011; Greif et al. 2011b; O'Leary & McQuinn 2012). More importantly, this nonlinear effect may shock-heat the gas globally, introducing a new feature into the power spectrum that corresponds to the relative velocity fluctuations (McQuinn & O'Leary 2012). When the global shock-heating is efficient, this new feature could even dominate

PoS(AASKA14)003

over the power spectrum of linear density perturbations and amplify the baryon acoustic oscillation (BAO) feature. Due to the uncertainties in the efficiency of this shock-heating, however, the actual amplitude of the power spectrum due to relative velocity fluctuations is still uncertain.

From an observational perspective on CD and the EoR, especially in terms of 21-cm power spectrum analysis, it is convenient to mark three prominent epochs: (1) the Lyα-pumping epoch, when the IGM is strongly coupled to $T_{\rm K}$ through Wouthysen-Field effect with a high Lyα intensity, (2) the X-ray heating epoch, when the IGM is gradually heated to beyond $T_{\rm CMB}$ by X-ray heating and (3) the EoR, when H II bubbles in cosmological scales form in a patchy way. It is generally believed that CD commences with the Lyα-pumping epoch, followed by the X-ray heating epoch, and finally the EoR occurs, whose sequence is rather robust unless 1-2 order-of-magnitude changes in the fiducial astrophysical parameters are allowed (Furlanetto 2006; McQuinn & O'Leary 2012; Mesinger et al. 2014). Very conveniently, the early phase of each epoch boosts the spatial fluctuation of δT_b, sequentially dominated by the patchiness in the Lyα intensity, the IGM temperature, and the ionized fraction, respectively, extending the observational window to very high redshifts.

While challenging, it should be possible to observe individual objects via tomography, which may be as small as the first galaxies. When UV sources are embedded in an IGM colder than the CMB, a "Lyα sphere" forms around the radiation source and a strong 21-cm absorption trough forms. When UV sources are accompanied by X-ray sources, the central, heated region is seen in emission, which is still surrounded by an absorption trough or an absorption plateau (e.g. Tozzi et al. 2000; Cen 2006; Chuzhoy et al. 2006; Chen & Miralda-Escudé 2008; Alvarez et al. 2010). A simulation of the formation and evolution of Pop III and II stars in a rare density peak, together with the X-ray binaries, shows that this ubiquitous feature will be observable by SKA2-LOW with 1000-hour integration, and marginally by SKA1-LOW (Ahn et al. 2014) with very aggressive integration at $z \lesssim 15$ (Section 3).

2. Power Spectrum Analysis

Because many independent modes with similar wavenumbers ($k \equiv |\mathbf{k}|$) are averaged over to form the 3D power spectrum, $P(k)$, power spectrum analysis has higher sensitivity than imaging in general. In addition, nature cooperates in such a way that three important physical processes – Lyα pumping, X-ray heating and patchy reionization – may sequentially boost 21-cm fluctuations to give a roughly constant S/N ratio over redshift, even though the foreground increases rapidly towards high redshift (e.g. Mesinger et al. 2014). Overall, the signal and the foreground noise grow roughly at a similar rate to yield S/N$\sim 10^{-5}$, although the S/N ratio should eventually become very small ($\sim 10^{-7}$) at $z \sim 30$ (Pritchard & Loeb, 2008).

The very first light from astrophysical sources to which the IGM is exposed is the stellar continuum below the hydrogen Lyman limit, or photons with energy $h\nu < 13.6\,\mathrm{eV}$, because ionizing photons (photons above the Lyman limit) are quickly absorbed by the neutral hydrogen and helium around while continuum photons are not. However, there is always some fraction of this continuum that is absorbed in Lyman series resonances as photons redshift over cosmological distances (e.g. Ahn et al. 2009). After absorption, cascades over the energy levels and multiple scattering of reemitted photons will convert about $\sim 30\%$ of those absorbed photons to Lyman-α photons (Hirata 2006; Pritchard & Furlanetto 2006). Even in the presence of density inhomogeneities, a point

PoS(AASKA14)003

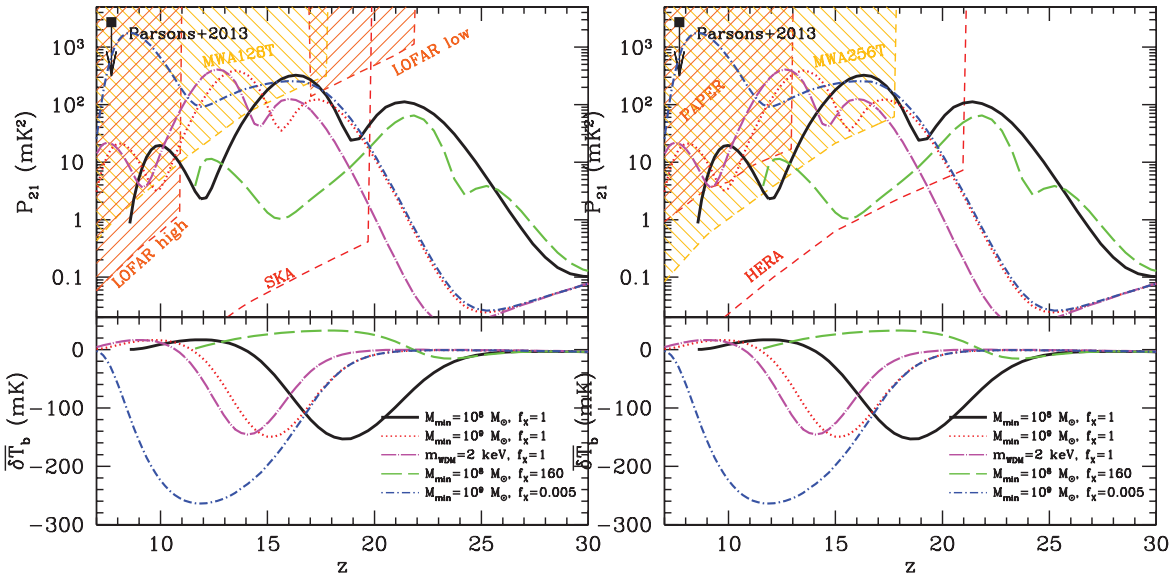

Figure 1: (top subpanels) Evolution of $D^2(k)$ at $k = 0.1/\mathrm{Mpc}$ and sensitivity of various planned observations including SKA1-LOW (We note that the apparent SKA1-LOW sensitivity cut at $z \approx 20$ is due to the particular choice of instantaneous bandwidth, $\Delta z = 0.5$, which limits the number of available $k_{||} = 0.1/\mathrm{Mpc}$ modes; we stress that bandwidth choices are arbitrary and that SKA1-LOW's planned bandpass extends out to $z = 28$.). Three peaks appear when fluctuations in δT_b are boosted due to the efficient Lyα-pumping, the X-ray heating and the patchy reionization, subsequently from high to low redshifts (Mesinger et al. 2014).

source produces a nearly spherical profile (Vonlanthen et al. 2011) that shows a step-wise feature decreasing more steeply than $1/r^2$ (Pritchard & Furlanetto 2006). As usually assumed, the IGM is still much colder than the CMB, and thus the regions where the Lyα pumping becomes strong ($N_\alpha \gtrsim N_{\alpha,\mathrm{th}} \simeq 10^{-10}\left(\frac{20}{1+z}\right)\ \mathrm{s^{-1}cm^{-2}Hz^{-1}sr^{-1}}$) will show strong absorption, or $\delta T_b \sim -100\,\mathrm{mK}$. Source clustering and the steep radial profile of the Lyα intensity around each source are the dominant sources of fluctuations in δT_b at earliest times. Soon thereafter, saturation occurs, and fluctuations decrease as sources grow in abundance and $N_\alpha \gg 1$ everywhere (Fig. 1). Changes in the spectral energy distribution (SED) of sources can affect the resulting power spectrum as demonstrated by Santos et al. (2011) (Fig. 2), while other systematic effects such as the star formation efficiency might make the prediction somewhat degenerate.

In many models, the Lyα pumping epoch is followed by the X-ray heating epoch. X-ray photons have a much longer mean free path than UV photons, and partially ionize the IGM by leaving behind energetic electrons as they traverse cosmological distances. These electrons can then ionize, excite, and heat the IGM. During the early phase of the X-ray heating epoch, the overall ionization level caused by X-rays is usually very small unless the X-ray emissivity is very high (see e.g. Mesinger et al. 2013). Thus the dominant contribution from X-rays to fluctuations in δT_b is inhomogeneous heating, which will boost the power spectrum again (Fig. 1). Another contribution to fluctuations is due to inhomogeneous Lyα pumping from excited hydrogen atoms (see e.g. Chen & Miralda-Escudé 2008), though its contribution is usually subdominant compared to the Lyα pumping induced by stellar UV photons (but see e.g. Ahn et al. 2014 for a significant contribution

PoS(AASKA14)003

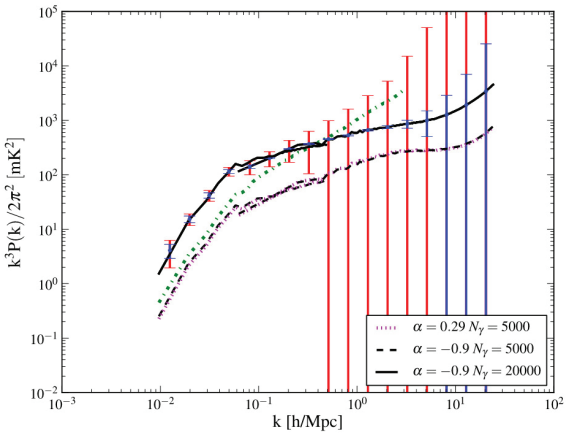

Figure 2: 21-cm temperature power spectrum at $z \simeq 20.3$ for a few Lyα emission models, based on the simulation results by Santos et al. (2011). Power-law SEDs are used: the number of photons per frequency emitted per stellar baryon $\varepsilon_\nu = A\nu^\alpha$, where A is tuned to produce the assumed integrated number of photons between Lyα (10.2 eV) and the Lyman limit (13.6 eV), or N_γ (legends are self-explanatory). $\alpha = -0.9$ and $\alpha = 0.29$ roughly represent Pop-II and Pop-III type SEDs, respectively. Cases with identical N_γ (black solid and black dashed curves) are almost degenerate. Pushing the minimum halo mass hosting stars down to $M_{\rm min} = 10^6 M_\odot$, with $\alpha = 0.25$ and $N_\gamma = 5000$, renders the overall shape of the power spectrum different from the other three cases, which all have $M_{\rm min} = 10^8 M_\odot$. Error bars in blue corresponds to the full SKA2-LOW collecting area, and the ones in red to the 10% of the collecting area (Santos et al. 2011).

when X-ray source formation is very efficient). It is usually expected that X-ray heating epoch produces the highest peak in the large-scale power spectrum in its redshift evolution (Fig. 1). Later, X-ray heating will become very efficient everywhere in the Universe such that $\delta T_b > 0$ and $T_{\rm IGM} \gg T_{\rm CMB}$ but with the ionization state still low, once again saturating the fluctuations and resulting in a significant decrease in the amplitude of the power spectrum (Fig. 1). This rise, peak and fall in the power spectrum amplitude results in the second "bump" seen in figure 1. Note that this provides the best window for high-z cosmology, because δT_b becomes proportional to the baryon density and nearly insensitive to other fluctuations. In addition, separating the matter power spectrum from that of the radiation fields, utilizing the impact by the peculiar motion (or the so-called μ-decomposition scheme which is very similar to that used in galaxy survey programs), may be possible (McQuinn et al. 2006; Mao et al. 2012; see also the subchapter by Pritchard).

Finally comes the main EoR, in most models. The power spectrum is boosted again, due to the patchiness of H II regions where $\delta T_b = 0$ and neutral regions where δT_b is proportional to the baryon density. Final saturation and power spectrum suppression occurs as bubbles overlap and the EoR approaches its final phase (e.g. Iliev et al. 2012), to generate the final bump in the power spectrum evolution (Fig. 1). Of course, one should allow more model variants. Currently, the X-ray emissivity at CD and during the EoR is still largely unknown, other than the weak constraint coming from the soft X-ray background (e.g. Dijkstra et al. 2004; McQuinn 2012), the $z \sim 2.5$ QSO absorption lines and the reionization histories of H I and He II (McQuinn 2012). This allows a wide model variation in the X-ray heating epoch, and thus the 3-bump feature in the power spectrum (Fig. 1) is not ubiquitous among reionization models if extreme cases are allowed (Pritchard &

PoS(AASKA14)003

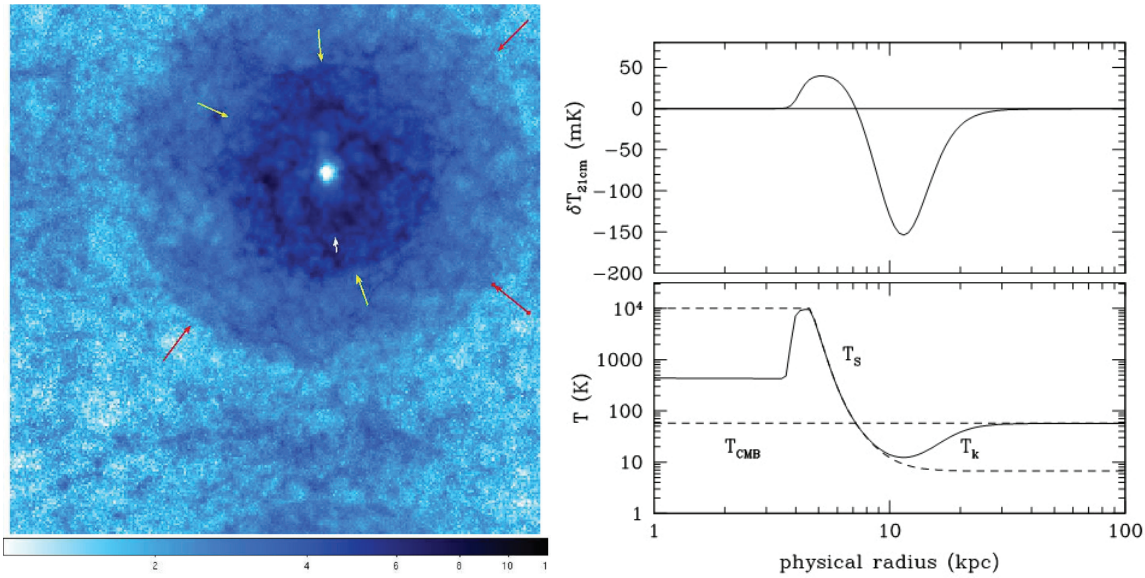

Figure 3: (a:left) Distinct ring structure due to the step-wise Lyα pumping around a point source. $-\delta T_b \times r^2$ at $z = 13.42$ is plotted with an arbitrary unit, to show these distinct rings (pointed by arrows) as boundaries of sudden change in color: each annulus bound by adjacent rings, where Lyα flux decreases as $1/r^2$, shows about the same color. The box size is 137 Mpc coming and the angular size is $51'$ (Vonlanthen et al. 2011). (b:right) Radial profile of an isolated radiation source of the UV and the X-ray. From inside out, $\delta T_b = 0$ (H II region), $\delta T_b > 0$ (X-ray heated region), $\delta T_b < 0$ (Lyα-pumped region).

Loeb 2012). The halo mass spectrum responsible for reionization is not well constrained either, allowing models with a significant contribution from minihalos (e.g. Wyithe & Cen 2007; Ahn et al. 2012).

The sweet spot for power spectrum analysis exists around $k \sim 0.1/\mathrm{Mpc}$, guaranteeing a large S/N over a wide range of redshifts while being mostly unaffected by the filtering of low-k foreground modes. SKA1-LOW (and the 50% capability of SKA1-LOW as well) has a large enough S/N ratio for observing $P(k \sim 0.1/\mathrm{Mpc})$ for $z \lesssim 20$ with 1000-hour integration, and SKA2-LOW will allow one to achieve similar S/N ratio for even larger k's with more extended redshift coverage, $z \lesssim 28$ (Fig. 1; see also Baek et al. 2010 for the evolution of other wavemodes). As is usually the case for CD and the EoR, pushing the observable redshift to $z \sim 28$ or $\nu \sim 50$MHz is strongly favored, in order to probe their early phases.

3. Tomography

As mentioned in Section 2, imaging is more difficult than power spectrum analysis. While the power spectrum contains a lot of information on the underlying astrophysics and cosmology, one should note that the 3D tomography (imaging) is indeed a more direct observation because one cannot invert $P(k)$ to obtain the actual image unless the 21cm field is Gaussian (see also the subchapter by Mellema).

Imaging can probe physical properties of radiation sources. One interesting feature is that due to the step-wise decrease of Lyα intensity (or Lyα pumping) in addition to the geometrical

PoS(AASKA14)003

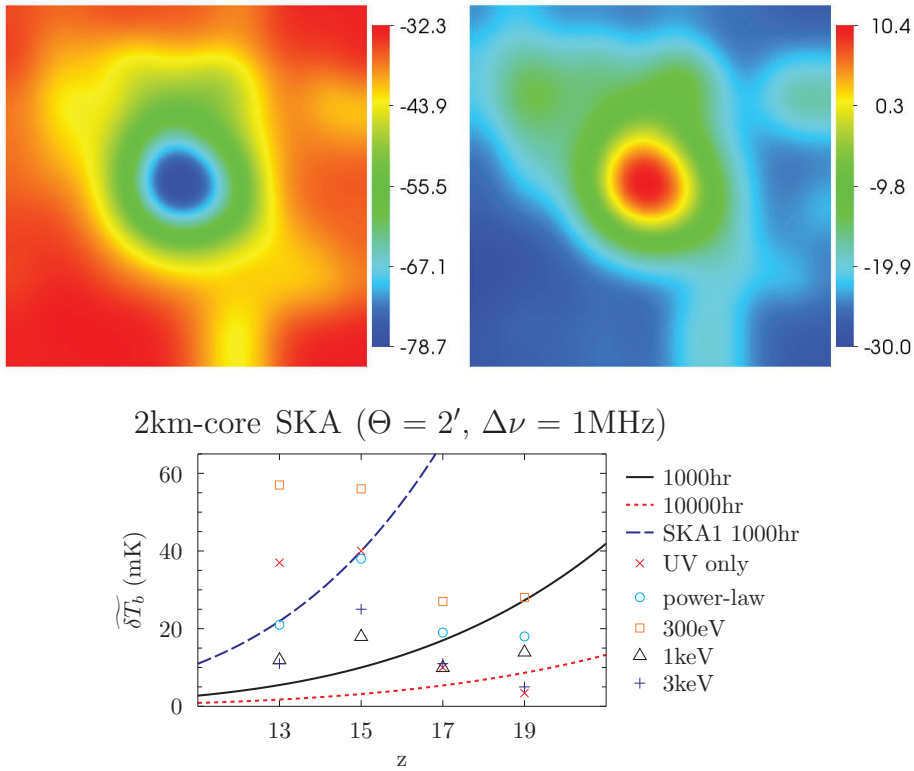

Figure 4: Realistic imaging forecast of the early objects with the first stars (Population III stars), Population II stars and Population III X-ray binaries, (Ahn et al. 2014). (a:top left) 21cm map (mK) from a simulated model of Pop III stars+Pop II stars *without* X-ray sources in a rare density peak inside a 40 Mpc (comoving) box at $z = 15$, smoothed with $\Theta = 2'$ and $\Delta\nu = 1$ MHz. The angular size of the box shown is $13'$ at this redshift. (b:top right) 21cm map (mK) from a simulated model of Pop III stars+X-ray binaries+Pop II stars in a rare density peak inside the same box as (a) at $z = 15$, smoothed with $\Theta = 2'$ and $\Delta\nu = 1$ MHz. (c:bottom) Imaging sensitivity of the 2-km core SKA2-LOW (Mellema et al. 2013) with $\Theta = 2'$ and $\Delta\nu = 1$ MHz, for integration times of 1000 hours (black, solid curve) and 10000 hours (red, dotted curve), against varying X-ray binary model predictions (points). It is difficult to image individual objects by SKA1-LOW unless nature cooperates: a few models are marginally observable at $z \lesssim 15$, as seen by the sensitivity of SKA1-LOW with the same smoothing filters and a 1000-hour integration time (blue, dashed curve).

dilution, $1/r^2$, the radial profile of the 21-cm signal around an isolated source will also exhibit a step-wise variation, or multiple "rings" (Vonlanthen et al. 2011; Fig. 3a). Detecting the multiple-ring feature from one radiation source remains, however, very difficult even with SKA2-LOW, and while stacking many such profiles might allow the detection of the rings, one should know the source redshift accurately, because stacking sources from other redshift planes will quickly smear out the ring feature.

A more notable and traceable feature from an isolated source is (unless the IGM is saturated $T_S \gg T_{CMB}$ due to strong X-ray heating) δT_b varying even more steeply than $1/r^2$. This is due to the step-wise variation of Lyα pumping rate, resulting in strong absorption nearby and weak absorption further away. This "Lyα blob" should be ubiquitous around isolated sources before the full saturation of Lyα pumping occurs everywhere, which is analogous to individual H II regions

PoS(AASKA14)003

in the patchy reionization process before the full overlap occurs (Fig. 3a).

It becomes even more interesting when the UV source is accompanied by an X-ray source. Typical emissivity of X-ray sources associated with UV (stellar) sources is relatively small (compared to proposed Population III X-ray binaries), and the corresponding X-ray heating zone (where $T_{\rm S} > T_{\rm CMB}$) is smaller than the Lyα blob when the IGM were colder than the CMB before exposure. In addition, the central region will be ionized mostly by UV sources, such that δT_b is zero at the center, positive outside, and negative even further outside (Fig. 3b). Note that probing the signature of individual objects is likely to be possible in only a relatively narrow range of frequency (redshift), since rapid growth in the abundance of galaxies will soon wash out such a signature.

This can occur even when there is a strongly clustered set of sources: Xu et al. (2014) simulated the formation of Population III and II stars and X-ray binaries inside a high-density peak ("Rarepeak") in the early Universe, and Ahn et al. (2014) postprocessed the simulated data and obtained a 21-cm map which shows a much more extended δT_b profile than that of a single object (Fig. 4a, b). A similar prediction for the spatially extended profile also exists for high-z QSO systems, very sparsely spaced in the Universe (Tozzi et al. 2000). In case of the Rarepeak, SKA2-LOW performing 1000-hour integration of a tracked field with the $\Theta = 2'$ and $\Delta\nu = 1$MHz smoothing filter will enable its (their) detection regardless of the model variation, ranging from the all-absorption trough case (without X-ray binaries) to the fully X-ray heated case (with efficient X-ray heating) with a high S/N ratio (Fig. 4c).

As it is easy to estimate the number density of such peaks a priori, one can forecast the odds to find those objects inside a dedicated field of observation. For Rarepeak, which is a $3.5\,\sigma$ density peak when the linear density field is filtered at $R \sim 3$ Mpc comoving scale, its number density is roughly $10^{-6}\,{\rm Mpc}^{-3}$. A tracking volume of FOV(SKA1-LOW)$\times(110-75)$ MHz $\simeq 5^\circ \times 5^\circ \times 35$ MHz (where FOV denotes the field of view), which covers the redshift range $z = [12-17]$, will host about 600 of those high-density peaks. Thus detecting the Lyα-blob feature of these objects at $z \lesssim 15$ through the SKA2-LOW 1000-hour integration is bound to succeed, while with the SKA1-LOW array configuration, about a 16000-hour integration is required to achieve the same sensitivity. Alternatively, we may target the few cases which can be marginally detected by SKA1-LOW with a 1000-hour integration with the same smoothing scheme (Fig. 4). While lower-redshift detections become much easier, at that time the distinct isolated feature may be erased by signals from other, more abundant density peaks if similar emissivity is assumed. In either case, since the exact epoch when this occurs is model-dependent, it is necessary to explore a wider range of the astrophysical parameter space than has been investigated by Ahn et al. (2014) and still consider the possibility to observe individual objects at lower redshifts by SKA1-LOW. It is also advisable to carry out imaging with SKA1-LOW even when it has reached 50% capability of its final phase, because again there may exist objects whose size and signal strength are large enough to be successfully imaged. For example, AGN+galaxy systems (Tozzi et al., 2000) or even rarer peaks than have been studied by Ahn et al. (2014) may appear in such an imaging observation, although a relatively low-redshift range, $z \simeq 13$, may be adequate due to the low sensitivity expected.

Aside from the high-redshift nature of these early stars/galaxies, the unique feature of the composite H II region + X-ray heated region + Lyα blob is not something one expects from the main EoR imaging. The main EoR imaging will focus mostly on large H II bubbles ($R \gtrsim 20$ Mpc) with $\delta T_b = 0$ before filtering, and the neutral region will simply fluctuate according to the underlying

PoS(AASKA14)003

density fluctuation. If so, tomography will tell us about source properties during the peak of EoR (see the subchapter by Mellema and the subchapter by Iliev), and cosmological information during the early phase of EoR (see the subchapter by Pritchard).

4. Conclusion

We have briefly reviewed theories of high-redshift astrophysics and their observational aspects during CD, when the first galaxies formed. The first galaxies significantly affect the IGM, leading to signatures that will be detectable through the observation of the 21-cm background. With new developments in the theory of first-star formation, the number of feasible models of this early epoch is ever increasing. These new developments include the initial mass function of Pop III stars, the spectral energy distribution of stars and X-ray sources, the byproduct of stars, and dynamical/radiative feedback effects, to name a few. SKA1-LOW and SKA2-LOW have the capability of probing first galaxies and their impact on the IGM through power spectrum analysis and imaging.

SK1-LOW will be able to observe the signature of these objects mostly through the 21-cm power spectrum, with better sensitivity and thus deeper target-redshift than most SKA precursors. Three prominent epochs, which are the Lyα pumping epoch, X-ray heating epoch, and the main EoR will be observed as three distinct evolutionary phases in the amplitude of the 21-cm power spectrum in the wavenumber range around $k \sim 0.1/\mathrm{Mpc}$. The shape of the power spectrum in a wide dynamic range of k might be able to tell us about the properties of the early objects, such as their SED.

SKA2-LOW will be able to carry out imaging, as well as the power spectrum analysis at higher sensitivity than SKA1-LOW. Imaging will help to constrain source properties much better than power spectrum analysis, because of model degeneracy and loss of information are inherent in the power spectra. Clustered sources of UV and X-ray sources may show their unique signature of the composite absorption and emission of 21-cm lines against the CMB, as long as their angular scale becomes large enough to achieve high S/N with SKA2-LOW. For serendipity, however, it is advised to carry out imaging also with SKA1-LOW.

There exists tension between high-redshift astrophysics and cosmology. Even at CD, the 21-cm signal of an astrophysical origin may swamp that of a cosmological origin. Nevertheless, there exists the possibility that the cosmological signal may be boosted significantly, if mechanical energy conversion occurs on cosmological scales (McQuinn & O'Leary, 2012). In either case, the best window for cosmology lies at the highest redshift range planned for SKA ($z \sim 28$).

References

Abel, T., Bryan, G. L., & Norman, M. L. 2002, Science, 295, 93
Ahn, K., Iliev, I. T., Shapiro, P. R., Mellema, G., Koda, J., & Mao, Y. 2012, ApJL, 756, L16
Ahn, K., Shapiro, P. R., Iliev, I. T., Mellema, G., & Pen, U. 2009, ApJ, 695, 1430
Ahn, K., Xu, H., Norman, M. L., Alvarez, M. A., & Wise, J. H. 2014, ArXiv e-prints 1405.2085
Alvarez, M. A., Pen, U.-L., & Chang, T.-C. 2010, ApJL, 723, L17
Baek, S., Semelin, B., Di Matteo, P., Revaz, Y., & Combes, F. 2010, A&A, 523, A4

PoS(AASKA14)003

Bromm, V., Coppi, P. S., & Larson, R. B. 2002, ApJ, 564, 23
Cen, R. 2006, ApJ, 648, 47
Chen, X., & Miralda-Escudé, J. 2008, ApJ, 684, 18
Chuzhoy, L., Alvarez, M. A., & Shapiro, P. R. 2006, ApJL, 648, L1
Dijkstra, M., Haiman, Z., & Loeb, A. 2004, ApJ, 613, 646
Fialkov, A., Barkana, R., Visbal, E., Tseliakhovich, D., & Hirata, C. M. 2013, MNRAS, 432, 2909
Furlanetto, S. R. 2006, MNRAS, 371, 867
Greif, T. H., Springel, V., White, S. D. M., Glover, S. C. O., Clark, P. C., Smith, R. J., Klessen, R. S., & Bromm, V. 2011a, ApJ, 737, 75
Greif, T. H., White, S. D. M., Klessen, R. S., & Springel, V. 2011b, ApJ, 736, 147
Haiman, Z. 2011, Nature , 472, 47
Haiman, Z., Abel, T., & Rees, M. J. 2000, ApJ, 534, 11
Hirata, C. M. 2006, MNRAS, 367, 259
Hirano, S., Hosokawa, T., Yoshida, N., Umeda, H., Omukai, K., Chiaki, G., & Yorke, H. W. 2014, ApJ, 781, 60
Iliev, I. T., Mellema, G., Shapiro, P. R., Pen, U.-L., Mao, Y., Koda, J., & Ahn, K. 2012, MNRAS, 423, 2222
Mao, Y., Shapiro, P. R., Mellema, G., Iliev, I. T., Koda, J., & Ahn, K. 2012, MNRAS, 422, 926
McQuinn, M. 2012, MNRAS, 426, 1349
McQuinn, M., & O'Leary, R. M. 2012, ApJ, 760, 3
McQuinn, M., Zahn, O., Zaldarriaga, M., Hernquist, L., & Furlanetto, S. R. 2006, ApJ, 653, 815
Mellema, G., Koopmans, L. V. E., Abdalla, F. A., et al., 2013, Experimental Astronomy, 36, 235
Mesinger, A., Ewall-Wice, A., & Hewitt, J. 2014, MNRAS, 439, 3262
Mesinger, A., Ferrara, A., & Spiegel, D. S. 2013, MNRAS, 431, 621
O'Leary, R. M., & McQuinn, M. 2012, ApJ, 760, 4
Pacucci, F., Mesinger, A., Mineo, S., & Ferrara, A. 2014, MNRAS, 443, 678
Pritchard, J. R., & Furlanetto, S. R. 2006, MNRAS, 367, 1057
Pritchard, J. R., & Loeb, A. 2008, Phys. Rev. D , 78, 103511
Pritchard, J. R., & Loeb, A. 2012, Reports on Progress in Physics, 75, 086901
Santos, M. G., Silva, M. B., Pritchard, J. R., Cen, R., & Cooray, A. 2011, A&A, 527, A93
Spolyar, D., Bodenheimer, P., Freese, K., & Gondolo, P. 2009, ApJ, 705, 1031
Stacy, A., Bromm, V., & Loeb, A. 2011, ApJL, 730, L1+
Stacy, A., Greif, T. H., & Bromm, V. 2010, MNRAS, 403, 45
Tozzi, P., Madau, P., Meiksin, A., & Rees, M. J. 2000, ApJ, 528, 597
Tseliakhovich, D., & Hirata, C. 2010, Phys. Rev. D , 82, 083520
Turk, M. J., Abel, T., & O'Shea, B. 2009, Science, 325, 601
Vonlanthen, P., Semelin, B., Baek, S., & Revaz, Y. 2011, A&A, 532, A97
Wyithe, J. S. B., & Cen, R. 2007, ApJ, 659, 890
Xu, H., Ahn, K., Wise, J. H., Norman, M. L., & O'Shea, B. W. 2014, ApJ, 791, 110
Yoshida, N., Omukai, K., Hernquist, L., & Abel, T. 2006, ApJ, 652, 6

PoS(AASKA14)003

PROCEEDINGS OF SCIENCE

Synergy of CO/[CII]/Lyα Line Intensity Mapping with the SKA

Tzu-Ching Chang[*1], **Yan Gong**[2], **Mario Santos**[3,4,5], **Marta Silva**[4], **James Aguirre**[6], **Olivier Doré**[7,8], **Jonathan Pritchard**[9], **on behalf of the EoR/CD-SWG**

[1]*Academia Sinica Institute of Astronomy and Astrophysics, P.O. Box 23-141, Taipei, 10617 Taiwan*
[2]*Department of Physics & Astronomy, University of California, Irvine, CA 92697, USA*
[3]*Department of Physics, University of Western Cape, Cape Town 7535, South Africa*
[4]*CENTRA, Instituto Superior T ÌĄecnico, Technical University of Lisbon, Lisboa 1049-001, Portugal*
[5]*SKA SA, 3rd Floor, The Park, Park Road, Pinelands, 7405, South Africa*
[6]*Department of Physics & Astronomy, University of Pennsylva- nia, 209 South 33rd Street, Philadelphia, PA 19104, USA*
[7]*NASA Jet Propulsion Laboratory, California Institute of Technology, 4800 Oak Grove Drive, MS 169-215, Pasadena, CA, 91109, U.S.A.*
[8]*California Institute of Technology, MC 249-17, Pasadena, California, 91125 U.S.A.*
[9]*Department of Physics, Blackett Laboratory, Imperial College, London SW7 2AZ, UK*
E-mail: tcchang@asiaa.sinica.edu.tw

This subchapter describes the science enabled by cross-correlations of the SKA1-LOW 21-cm EoR surveys with other line mapping programs. In particular, we identify and investigate potential synergies with planned programs, such as the line intensity mapping of redshifted CO rotational lines, [CII] and Ly-α emissions during reionization. We briefly describe how these tracers of the star-formation rate at $z \sim 8$ can be modeled jointly before forecasting their auto- and cross-power spectra measurements with the nominal 21cm EoR survey. After discussing the measurement prospect, we discuss how reionization parameters can be better constrained using these new measurements.

Advancing Astrophysics with the Square Kilometre Array
June 8-13, 2014
Giardini Naxos, Italy

*Speaker.

PoS(AASKA14)004

1. Introduction

While the distribution of neutral hydrogen mapped by SKA1-LOW provides an excellent and unique view of the reionization process over a large range of redshifts, detecting the sources responsible for reionization directly sheds light on the crucial stage of galaxy formation and complements our understanding of EoR. Extremely deep imaging with the Hubble Space Telescope (HST) has begun to probe the very bright end of the UV luminosity functions at z > 6 (Bouwens et al. 2014; Robertson et al. 2013), with improvements expected with the James Webb Space Telescope (JWST). In the sub-mm, the Atacama Large Millimeter Array (ALMA) has detected individual high redshift, luminous objects known from existing surveys (e.g., Ouchi et al. (2013)). However, observations that are aimed at detecting individual galaxies at z > 6 are difficult and time consuming, and neither of these space-borne facilities nor ALMA is expected to resolve the bulk of low luminosity sources responsible for reionization (Salvaterra et al. 2011). Approaches which can access the entire luminosity function of reionizing sources are needed.

Line Intensity Mapping has emerged as a promising technique that is sensitive to the integrated light produced by faint galaxies: instead of resolving individual sources, one measures on larger spatial scales the collective emission from an ensemble of sources, while retaining the spectral–thus redshift–information. This allows efficient redshift surveys that probe the integrated luminosity function of sources and provide three-dimensional information to study star formation activities during EoR.

A few spectral lines are currently being considered as promising tracers for high-redshift star formation activities in the intensity mapping regime. Among them, the most promising ones are the rotational transitions from carbon monoxide (CO) (Righi et al. 2008; Visbal & Loeb 2010; Carilli 2011; Gong et al. 2011; Lidz et al. 2011; Pullen et al. 2013; Breysse et al. 2014), the 158μm emission from singly ionized carbon ([CII]) (Gong et al. 2012; Uzgil et al. 2014; Silva et al. 2014), and the Lyman-α transition line from hydrogen (Silva et al. 2013; Pullen et al. 2014). Such large-scale surveys will not only reveal early star formation history but also measure the clustering of ionizing sources. These line intensity maps mark the three-dimensional distribution of ionized regions and probe different gas phases that complements the 21cm EoR surveys which trace neutral hydrogen. Together, they draw a complete view of the reionization process in the high-redshift Universe. In addition, on scales larger than the ionized regions, these line tracers anti-correlate with the 21cm emission. By measuring the shape of the cross-power spectrum of the two surveys, one can determine the characteristic scale of ionized regions, by marking the scale where the cross-correlation becomes negative, and be able to constrain statistically the characteristic size scale of ionized regions as a function of redshifts (Righi et al. 2008; Lidz et al. 2009).

Below we discuss each of these tracers in detail, and present forecasts on the measurements of power spectra and cross-correlation signals with the SKA1-LOW 21cm EoR survey. Due to the short emission wavelengths, it is not possible to observe [CII] and Lyα with the SKA, thus we present the results assuming other future surveys. For CO, however, the proposed highest-frequency band of SKA1-MID can potentially cover the redshifted CO(1-0) transition at $z > 7.3$. We discuss such possibilities in the next sections.

PoS(AASKA14)004

2. CO Intensity Mapping

The CO(1-0) rotational line has a rest frequency of 115 GHz. The proposed highest frequency band of SKA1-MID, 4.6-13.8GHz, will have a chance of capturing the redshifted CO(1-0) at $z > 7.3$. For intensity mapping purposes, where we aim to measure the large-scale distribution of redshifted CO at low-angular resolution, only the inner few kilometer core of SKA1-MID will be relevant. The uncertainty in the theoretical modelling of CO brightness temperature at high redshifts is still large, but most predict the amplitude to be about 10^{-6}K or smaller on quasi-linear scales. Large collecting area and high sensitivity are required, and a densely packed antenna configuration at the central core is desired, much like the requirement for SKA1-LOW for the 21cm EoR survey. Currently, however, the designed filling factor of SKA1-MID at the core is relatively small, only about 10^{-5} in the inner 1 km core in diameter, making the prospect of detecting redshifted CO very challenging.

Here we instead use SKA1-MID as a collection of single dishes, where each antenna records the total power while the cross products between antenna pairs are ignored. We note that performing the CO survey in the single dish mode lifts the compact antenna configuration requirement and enables a survey in the intensity mapping regime, but imposes constraints on the stability of the auto-correlation spectrum which would not be present if it were done interferometrically. We consider a narrow redshift range at $z = 8 \pm 0.5$, the lowest possible redshift allowed by SKA1-MID which should be more CO-rich. The specification is listed in Table 1, which also specifies the assumed SKA1-LOW 21cm survey parameters. Note that the assumed survey areas for CO auto-power spectrum and CO-HI cross-power spectrum calculations are chosen to be 0.1 and 10 deg^2, respectively, in order to optimize the signal-to-noise ratio in each case.

The amplitude of predicted CO brightness temperature fluctuations is rather uncertain, differing by orders of magnitude at $z = 8$ from model to model. This is currently one of the most challenging aspects for CO intensity mapping work. Figure 1 shows the forecasted CO power spectrum and the COx21cm cross-power spectrum measurements with the survey parameters listed in Table 1. Here we demonstrate the model uncertainties by plotting three of them: the middle solid curve with error bars is based on the models in Righi et al. (2008), while the upper dashed curve is based on Lidz et al. (2011) and lower dashed curve from Gong et al. (2011). The error bars include contributions from thermal noise and cosmic variance. The predicted total signal-to-noise ratio (SNR), summed over all accessible scales, of the upper, central and lower power spectra with SKA1-MID in single dish mode are 20.7, 4.0 and 0.1; for the CO and 21cm cross-power spectra with SKA1-MID and SKA1-LOW, the corresponding SNRs are 26.1, 6.0 and 0.7. The CO(1-0) signals and the cross power spectrum between 21cm and CO(1-0) emissions would be detectable at statistically significant level in more optimistic scenarios. The CO model uncertainties, however, exceed the measurement errors, thus making it difficult to plan a survey. On the other hand, a detection of CO power spectrum can be very discriminating against models and guide our theoretical understandings. Observational efforts for mapping CO at modest redshifts ($z = 2-3$) with existing instruments have only reached initial results, probing the high-end of CO luminosity functions (Decarli et al. 2014; Walter et al. 2014; Hodge et al. 2014). It is essential to improve our theoretical modelling and advance observational measurements of CO brightness temperature fluctuations across redshifts, which is currently an active area of research. In addition, one may

PoS(AASKA14)004

need to worry about foreground contaminations from synchrotron and free-free radiations coming from the Galaxy and other extragalactic sources. The severity depends on the observing frequencies (or the redshifted CO rotational lines of interest) and the CO signal strengths. However, these foregrounds are expected to be spectrally smooth and can be separated from the line emissions (Angelakis et al. 2009; Keating et al. 2014). At a few tens of gigahertz frequency range, spinning dust may also be a potential contamination, although its spectrum and strength are not well known (Ali-Haïmoud 2013). It will likely require a dedicated experiment with both a larger field-of-view and greater surface brightness sensitivity to make a strong CO detection, or a significantly more compact SKA-MID core than currently envisaged.

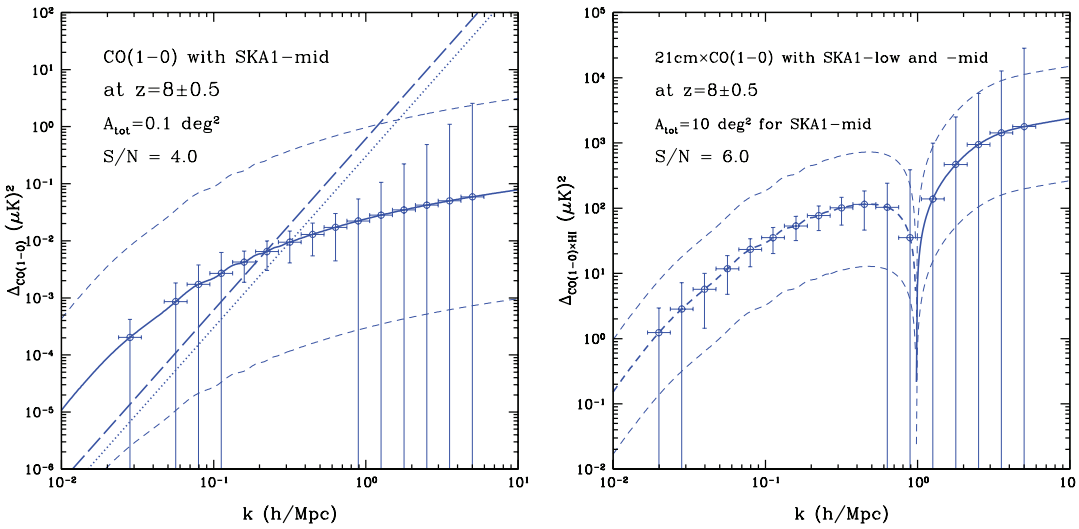

Figure 1: *Left:* SKA1-MID CO power spectrum at $z = 8$. *Right:* SKA1-LOW 21cm x SKA1-MID CO at $z = 8$. The upper, central, and lower curves indicate predicated CO signal strengths from three different models (see texts), whose uncertainties are larger than the predicted error bars. The survey areas for CO auto-power spectrum and CO-HI cross-power spectrum calculations are assumed to be 0.1 and 10 deg^2, respectively, to optimize the signal-to-noise ratios.

3. CII Intensity Mapping

Carbon is one of the most abundant elements in the Universe and it becomes singly ionized [CII] with an ionization energy of 11.26 eV, less than that of hydrogen. With a splitting of the fine-structure level at 91 K, [CII] is easily excited resulting in a line emission at 157.7 μm through the $^2P_{3/2} \rightarrow ^2 P_{1/2}$ transition. It is well established that the bulk of [CII] emission comes from photodissociation regions (PDRs), and provides a major cooling mechanism for the neutral interstellar medium (ISM). It is generally the brightest emission line in star-forming galaxy spectra and contributes to about 0.1% to 1% of the total far-infrared (FIR) luminosity in low redshift galaxies. Since carbon is naturally produced in stars, [CII] emission is expected to be a good tracer of the gas distribution in galaxies. ALMA high-resolution observations have revealed [CII] in high-redshift

PoS(AASKA14)004

Table 1: Parameters for SKA1-LOW and -MID at z=8±0.5. For SKA1-MID, single dish observation mode using 254 antennae is assumed. The survey areas for CO auto-power spectrum and CO-HI cross-power spectrum calculations are assumed to be 0.1 and 10 deg^2, respectively, in order to optimize the signal-to-noise ratios.

	SKA1-LOW	SKA1-MID auto/cross	unit
ant. diameter $D_{\rm ant}$	35	15	m
survey area $A_{\rm s}$	13	0.1/10	deg^2
FoV per ant.	13	0.01	deg^2
effective area per ant. A_e	925	170	m^2
freq. resolution $d\nu$	3.9	9.7	kHz
bandwidth (z=8±0.5) BW	18	1427	MHz
tot. int. time $t_{\rm int}$	1000	10,000	hr
min. baseline $D_{\rm min}$	30	-	m
max. baseline $D_{\rm max}$	1	-	km
uv$_{\rm min}$	16	-	
uv$_{\rm max}$	526	-	
T$_{\rm sys}$	400	25	K
effective num. ant.	433	254	
num. density of baselines $n_{\rm base}$	0.8	-	

galaxies, e.g, (Riechers et al. 2014; De Breuck et al. 2014), although no detections have been made for [CII] associated with galaxies at $z >\sim 7$ (González-López et al. 2014; Ota et al. 2014)

Even if the angular resolution to resolve the [CII] emission from individual galaxies at high redshift is not available, the brightness variations of the [CII] line intensity can be used to map the underlying distribution of galaxies and dark matter (Basu et al. 2004; Visbal & Loeb 2010; Gong et al. 2012).

Here we follow Gong et al. (2012) to calculate the expected CII line fluctuations at $6 < z < 9$, assuming that [CII] emission mainly originates in the hot gas in galaxies and that it is proportional to the gas metallicity, based on both analytical arguments and numerical models. Alternatively, [CII] emission can be estimated using observational relations, such as the empirical relation between [CII] luminosity and star formation rate (SFR) in low redshift galaxies from Sargsyan et al. (2012). This has the advantage of including [CII] emission from several media, since [CII] is emitted not only from hot ionized gas but also from cold, mostly neutral gas in PDRs, and also in minor proportion from other regions. The connection between [CII] emission and SFR can be easily understood both in PDRs, where the emission of radiation is proportional to the strength of the far UV radiation field thus to the SFR, and in ionized regions since their size is proportional to the ionization rate and thus to the SFR.

For redshifted [CII] line, the redshift range corresponds to observing frequencies of $\sim 200-300$ GHz. We assume a future [CII] intensity mapping instrument, based on a grating spectrometer and 20,000 bolometer array detectors for spectral line measurements. The instrument is assumed

PoS(AASKA14)004

to be on a telescope with a 10-m aperture. The details specifications are listed in Table 2. The forecasted cross-power spectrum of 21cm and [CII] surveys at $z = 8$ is shown in Figure 2. The red curve is the predicted amplitude of cross-correlation based on [CII] models in Gong et al. (2012), while the green curves indicate the theoretical uncertainties. Note the cross-correlation is negative at $k <\sim 1$ (h/Mpc), a signature from the anti-correlation of [CII] and 21cm on scales larger than the typical bubble size, as the former traces star formation activities thus the ionized region, while 21cm traces the neutral part of the Intergalactic Medium (IGM). A 4.7-σ detection is expected with this particular setup. At these frequencies, however, contributions from different CO rotational line emissions coming from different redshifts may confuse the redshifted [CII] emissions. One may apply bright-source masking or template fitting techniques to extract the redshifted [CII] signals. A pilot [CII] intensity mapping experiment, Time-Pilot, is currently underway to map out the redshifted [CII] emissions from high redshifts (Crites et al. 2014).

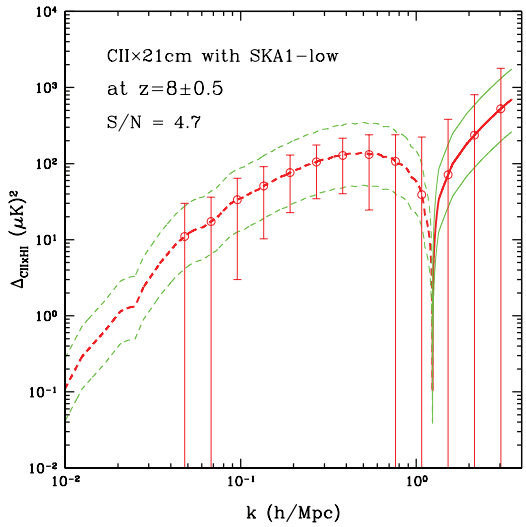

Figure 2: The cross-power spectrum of SKA1-LOW 21cm with a potential [CII] line mapping program at $z = 8$. The expected signals are plotted in red, while the theoretical uncertainties of the models are indicated by the green curves. The error bars are calculated based on parameters listed in Tables 1 and 2.

4. Lyα Intensity Mapping

Lyα photons have a rest-frame wavelength of 1216 $\AA$ and so Lyα emission during the EoR will redshift to the near-infrared regime today, making it potentially detectable by narrow-band infrared detectors. Lyα photons emitted by galaxies are mostly absorbed and reemitted by the neutral hydrogen in the galaxy which causes a scatter of the radiation greatly decreasing the Lyα flux detected by direct observations of Lyα emitters. Therefore, galaxy surveys are not able to fully measure all of the intrinsic Lyα emission. Intensity mapping is however a low resolution technique and so by not attempting to resolve the sources of Lyα photons we can in principle detect all of the Lyα radiation emitted both from galaxies and from the IGM.

PoS(AASKA14)004

Table 2: Experimental Parameters for a Possible [CII] Mapping Instrument.

Aperture diameter (m)	10
Survey Area (A_S; deg^2)	16
Total integration time (hours)	4000
Free spectral range (B_ν; GHz)	185−310
Freq. resolution (δ_ν; GHz)	0.4
Number of bolometers	20,000
Number of spectral channels	312
Number of spatial pixels	64
Beam size[a] ($\theta_{\rm beam}$; FWHM, arcmin)	0.4
Beams per survey area[a]	2.6×10^5
$\sigma_{\rm pix}$: Noise per detector sensitivity[a] (Jy$\sqrt{\rm s}$/sr)	2.5×10^6
$t_{\rm pix}^{\rm obs}$: Integration time per beam[a] (hours)	1.0
$z=8$ $V_{\rm pix}$ (Mpc/h)^3	4.8
$z=8$ $P_N^{\rm CII}$ (Jy/sr)^2 (Mpc/h)^3	4.3×10^9

[a] values computed at 238 GHz, corresponding to [CII] at $z=7$.

Recent work by Silva et al. (2013); Pullen et al. (2014) describes the process of Lyα emission in the EoR and post-EoR and shows estimates for intensity mapping of the Lyα signal at redshifts $7<z<11$. Lyα emission from galaxies is mainly sourced by stellar ionizing radiation since stars emit photons which ionize neutral hydrogen, which then emits Lyα photons upon recombination, and also because the heating of the gas by stellar UV radiation gives rise to e-HI collisions causing further Lyα emission. During the EoR stellar populations can also source emission in the dense and ionized IGM surrounding the galaxies through e-p recombinations and e-HI collisions. In addition, diffuse Lyα emission is also important. It can originate either from e-p recombinations sourced by X-ray radiation or from stellar continuum photon redshifted into the Lyα line of the IGM.

The intensity of the contributions from galaxies and from the IGM is dependent on several key astrophysical parameters such as: the star formation efficiency, the stellar spectrum, the escape fraction of ionizing photons from galaxies to the IGM, the gas temperature and clumping, the minimum mass of Lyα halos and the ionization state of the IGM. The relative contribution from galaxies and from the IGM to the Lyα photons budget is highly dependent on the ionization history and on the local heating of the IGM and so it is very difficult to estimate.

Observational maps of Lyα emission will be contaminated by extragalactic continuum emission and line foregrounds and also by emission from our galaxy. Continuum contamination can in principle be removed from intensity maps taking into account the smooth evolution of this radiation with frequency compared to the evolution of the Lyα line; however, zodiacal light emitted from our galaxy will bring confusion to the observational maps making it possible to only extract the Lyα power spectra at small scales where zodiacal light is spatially smooth. Foreground lines from lower redshifts, namely the 6563 $\AA$ Hα, the 5007 $\AA$ [OIII] and the 3727 $\AA$ [OII] lines will strongly affect Lyα observational maps however their contamination can be removed by masking the contaminated observational pixels as was shown in Gong et al. (2014).

Below we illustrate the cross-correlation signature of Lyα and 21cm emissions during EoR,

PoS(AASKA14)004

Table 3: Experimental Parameters for a Possible Lyα Mapping Instrument.

Aperture diameter (m)	0.2
Survey Area (A_S; deg^2)	13
Total integration time (hours)	2900
Free spectral range (B_λ; μ m)	0.85−1.1
Freq. resolution (λ/δ_λ)	220
Number of pixels in 2D array	72900
FOV per pointing; deg^2	0.6
Observational time per pointing (hours)	129.5
Survey volume (Mpc/h)^3	8.5×10^7

from an assumed Lyα intensity mapping experiment which consists of an aperture array with the parameters described in table 3. The parameters of the 21cm intensity mapping observation with SKA1-LOW are described in Table 1 for $z=8$, and the assumed frequency dependence of instrument system temperature T_{sys} and the collecting area A_e are as follows: $T_{sys}=T_{sky}+T_{rec}$, where $T_{sky}=60\left(\frac{300MHz}{\nu}\right)^{2.55}K$ is the sky temperature in Kelvin, and $T_{rec}=0.1*T_{sky}+40K$ is the instrument receiver temperature. $A_e=925\left(\frac{110}{\nu}\right)^2 m^2$. The Ly$\alpha$ intensity mapping calculation is from Silva et al. (2013). The forecast shows that the 21cm and Lyα cross-power spectra can be detected at high SNR values of (789, 442, 273, 462) for $z=(7,8,9,10)$, respectively, and is shown in Figure 3.

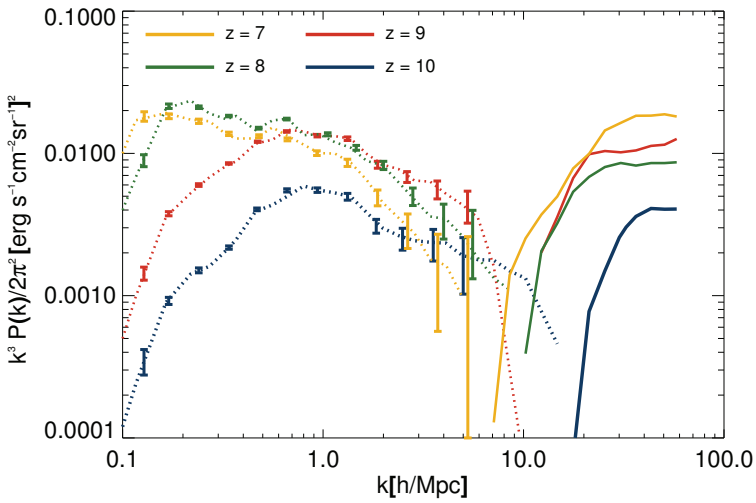

Figure 3: The SKA1-LOW 21cm and Lyα cross-power spectra at $z=(7,8,9,10)$. The Lyα models are based on Silva et al. (2013). The cross-power spectra are predicted to be detectable at >100 SNR significance level, given the assumed survey parameters

.

PoS(AASKA14)004

5. Discussion

The strength of the correlation between HI and molecular line emission depends on multiple factors and in particular, the sign of the correlation will depend on whether the emission comes mostly from the galaxies or the IGM. When cross-correlating CO with HI, the cross-correlation signals are expected to be associated with the clustering of galaxies (CO) and the IGM (HI), thus there is a strong and easy to interpret anti-correlation. When cross-correlating [CII] with HI, the bulk of the [CII] emissions are expected to come from galaxies, with some small contributions from the IGM, and we expect a strong anti-correlation. At the high redshifts of interest (z>6), a small amount of metals may reside in the IGM, however, the [CII] spin temperature is expected to follow the CMB temperature (Gong et al. 2012) thus little [CII] emission from the IGM is expected. For cross-correlations of HI with Lyα emissions, the situation is more complicated since the Lyα emission from the IGM can be very high and is very uncertain. Depending on the model considered, the emission from the IGM can even be higher than the emission from galaxies at some redshifts. In this case, Lyα and HI would be positively correlated on large scales; on the other hand, if no Lyα-HI cross-correlation signals are found, we can place constraints on the Lyα sources of emission.

6. Summary

In this chapter we motivated a novel use of SKA1-LOW 21cm to probe the epoch of reionization. By cross-correlating the 21cm line with other atomic and molecular lines observed in the intensity mapping regime, we can not only validate a potential 21cm EoR detection but also learn more about the EoR itself. On the one hand, the 21cm line traces neutral regions, the yet to be ionized universe while the other atomic lines trace star formation activities. The combination thus forms a potent, complete and unique picture of the reionization process.

We focus our study on CO, [CII] and Lyα transition lines currently identified as the most promising tracers. For CO, we study the possibility of using directly SKA1-MID at appropriate frequencies to map the EoR at z>7.5. For [CII] and Lyα, we assume the successful deployment of relevant instruments currently being planned. In all cases, we find that the strength of our detection strongly varies with theoretical model. For example, in the case of CO, according to the particular models considered, we could go from a strong detection (greater than 6 σ) to a non-detection. The same holds for CII, and it appears more promising for Lyα to be detected at high SNRs . While this situation might be worrisome, it simply reflects the fact that we are probing a totally new territory for astrophysics. Besides, these line tracers have different sources of astrophysical contamination which are in general much less severe than the ones plaguing the redshifted 21 cm line. A cross-correlation measurement can thus serve as an independent confirmation of the cosmological origin of the measured signals. The use of multiple line tracers would thus be invaluable to validate and enrich our understanding of the EoR, and it will open up a huge discovery space.

References

Ali-Haïmoud, Y. 2013, Advances in Astronomy, 2013, 2

PoS(AASKA14)004

Angelakis, E., Kraus, A., Readhead, A. C. S., et al. 2009, A & A, 501, 801
Basu, K., Hernández-Monteagudo, C., & Sunyaev, R. A. 2004, A & A, 416, 447
Bouwens, R. J., Illingworth, G. D., Oesch, P. A., et al. 2014, arXiv1403.4295
Breysse, P. C., Kovetz, E. D., & Kamionkowski, M. 2014, MNRAS, 443, 3506
Carilli, C. L. 2011, ApJ, 730, L30
Crites, A. T., Bock, J. J., Bradford, C. M., et al. 2014, in Society of Photo-Optical Instrumentation Engineers (SPIE) Conference Series, Vol. 9153, Society of Photo-Optical Instrumentation Engineers (SPIE) Conference Series, 1
De Breuck, C., Williams, R. J., Swinbank, M., et al. 2014, A & A, 565, A59
Decarli, R., Walter, F., Carilli, C., et al. 2014, ApJ, 782, 78
Gong, Y., Cooray, A., Silva, M., et al. 2012, ApJ, 745, 49
Gong, Y., Cooray, A., Silva, M. B., Santos, M. G., & Lubin, P. 2011, ApJ, 728, L46
Gong, Y., Silva, M., Cooray, A., & Santos, M. G. 2014, ApJ, 785, 72
González-López, J., Riechers, D. A., Decarli, R., et al. 2014, ApJ, 784, 99
Hodge, J., Riechers, D. A., Walter, F., et al. 2014, in American Astronomical Society Meeting Abstracts, Vol. 223, American Astronomical Society Meeting Abstracts #223, #246.34
Keating, G. K., Bower, G. C., DeBoer, D. R., Heiles, C. E., & Marrone, D. P. 2014, in American Astronomical Society Meeting Abstracts, Vol. 223, American Astronomical Society Meeting Abstracts #223, #133.03
Lidz, A., Furlanetto, S. R., Oh, S. P., et al. 2011, ApJ, 741, 70
Lidz, A., Zahn, O., Furlanetto, S. R., et al. 2009, ApJ, 690, 252
Ota, K., Walter, F., Ohta, K., et al. 2014, ArXiv e-prints
Ouchi, M., Ellis, R., Ono, Y., et al. 2013, ApJ, 778, 102
Pullen, A. R., Chang, T.-C., Doré, O., & Lidz, A. 2013, ApJ, 768, 15
Pullen, A. R., Doré, O., & Bock, J. 2014, ApJ, 786, 111
Riechers, D. A., Carilli, C. L., Capak, P. L., et al. 2014, ArXiv e-prints
Righi, M., Hernández-Monteagudo, C., & Sunyaev, R. A. 2008, A & A, 489, 489
Robertson, B. E., Furlanetto, S. R., Schneider, E., et al. 2013, ApJ, 768, 71
Salvaterra, R., Ferrara, A., & Dayal, P. 2011, MNRAS, 414, 847
Sargsyan, L., Lebouteiller, V., Weedman, D., et al. 2012, ApJ, 755, 171
Silva, M. B., santos, M. G., Cooray, A., & Gong, Y. 2014, ArXiv e-prints
Silva, M. B., Santos, M. G., Gong, Y., Cooray, A., & Bock, J. 2013, ApJ, 763, 132
Uzgil, B. D., Aguirre, J. E., Bradford, C. M., & Lidz, A. 2014, ApJ, 793, 116
Visbal, E., & Loeb, A. 2010, JCAP, 11, 16
Walter, F., Decarli, R., Sargent, M., et al. 2014, ApJ, 782, 79

PoS(AASKA14)004

PROCEEDINGS OF SCIENCE

Cosmic Dawn and Epoch of Reionization Foreground Removal with the SKA

Emma Chapman[*a], **Anna Bonaldi**[b], **Geraint Harker**[a], **Vibor Jelić**[cd], **Filipe B. Abdalla**[ae], **Gianni Bernardi**[feh], **Jérôme Bobin**[i], **Fred Dulwich**[j], **Benjamin Mort**[j], **Mario Santos**[fkl], **and Jean-Luc Starck**[i]

[a]Department of Physics & Astronomy, University College London; [b]Jodrell Bank Centre for Astrophysics, University of Manchester; [c]Kapteyn Astronomical Institute, University of Groningen; [d]ASTRON - the Netherlands Institute for Radio Astronomy; [e]Rhodes University, South Africa; [f]SKA South Africa; [h]Harvard-Smithsonian Center for Astrophysics; [i]CEA, IRFU, Service d'Astrophysique, France; [j]Oxford e-Research Centre, University of Oxford [k]Physics Department, University of the Western Cape, South Africa; [l]CENTRA, Instituto Superior Tecnico, Universidade de Lisboa, Portugal

E-mail: eow@star.ucl.ac.uk

The exceptional sensitivity of the SKA will allow observations of the Cosmic Dawn and Epoch of Reionization (CD/EoR) in unprecedented detail, both spectrally and spatially. This wealth of information is buried under Galactic and extragalactic foregrounds, which must be removed accurately and precisely in order to reveal the cosmological signal. This problem has been addressed already for the previous generation of radio telescopes, but the application to SKA is different in many aspects. We summarise the contributions to the field of foreground removal in the context of high redshift and high sensitivity 21-cm measurements. We use a state-of-the-art simulation of the SKA Phase 1 observations complete with cosmological signal, foregrounds and frequency-dependent instrumental effects to test both parametric and non-parametric foreground removal methods. We compare the recovered cosmological signal using several different statistics and explore one of the most exciting possibilities with the SKA — imaging of the ionized bubbles. We find that with current methods it is possible to remove the foregrounds with great accuracy and to get impressive power spectra and images of the cosmological signal. The frequency-dependent PSF of the instrument complicates this recovery, so we resort to splitting the observation bandwidth into smaller segments, each of a common resolution. If the foregrounds are allowed a random variation from the smooth power law along the line of sight, methods exploiting the smoothness of foregrounds or a parametrization of their behaviour are challenged much more than non-parametric ones. However, we show that correction techniques can be implemented to restore the performances of parametric approaches, as long as the first-order approximation of a power law stands.

Advancing Astrophysics with the Square Kilometre Array
June 8-13, 2014
Giardini Naxos, Italy

[*]Speaker.

PoS(AASKA14)005

1. Introduction

The statistical detection of the 21-cm reionization signal depends on an accurate and robust method for removing the foregrounds from the total signal. The first attempts to address this problem focused on exploiting the angular fluctuations of the 21-cm signal, e.g. Di Matteo et al. (2002); Oh & Mack (2003); Di Matteo, T. and Ciardi, B. and Miniati, F. (2004), but the 21-cm signal was found to be swamped by various foregrounds. The focus then moved on to the frequency correlation of the foregrounds, with the cross-correlation of pairs of maps used as a cleaning step (Zaldarriaga et al. 2004; Santos et al. 2005). This naturally evolved into methods which exploited the correlation of the foreground across whole segments of, or the entire bandwidth of, the observation: line of sight (LOS) fitting. This LOS fitting (to be discussed in much greater detail in Sec. 2) has been numerically shown to be the optimal method for power spectrum recovery (Liu & Tegmark 2011).

For this Chapter, we choose to concentrate on comparing the major LOS methods in the field, alongside the much more recent idea of avoiding the foregrounds altogether (e.g., Dillon et al. 2014) by focusing analysis on the area of Fourier space where the foregrounds are sub-dominant to the cosmological signal (see Sec. 2.3).

One of the 'saving graces' of foreground contamination is its smoothness over frequency space. While the foregrounds are expected to be highly correlated on the order of MHz, the cosmological signal in comparison is expected to be highly uncorrelated, e.g. Di Matteo et al. (2002); Gnedin & Shaver (2004). LOS methods can be divided into subcategories of parametric and non-parametric methods. Both aim to find the form of the smooth foreground function along frequency for each line of sight and subtract this from the total signal leaving residuals of noise, fitting errors and the cosmological signal.

The majority of early line of sight methods in the literature can be termed parametric as at some point they assume a specific form for the foregrounds, for example a polynomial (see Sec. 2.1). Despite the successes of the parametric methods, the fact remains that the form of the foregrounds is not definitively known across the frequency range and resolution of interest. Too great an assumption of their spectral form risks introducing a large element of uncertainty into the cosmological signal detection. It is with this argument that, more recently, 'blind' methods have been investigated. These allow the data to determine the form of the foregrounds, without assuming any particular shape beforehand (see Sec. 2.2). This has obvious advantages for a cosmological era so far not directly observed, but results are often not as promising as parametric results when applied to simulations. Arguably this is common sense, since in parametric methods one has modelled the foregrounds based on the simulation knowledge. If these methods were applied to foregrounds of different shape to the accepted form, they would risk suffering a large drop in accuracy.

Though there are now multiple proof-of-principle papers relating to LOS fitting for the EoR signal recovery, there has been little consideration given to which method aids the recovery of CD/EoR information most efficiently, accurately or precisely. Though the comparison of polynomial-fitting methods to any new method introduced is fairly common, the comparison between more complicated parametric, non-parametric methods and indeed foreground avoidance, is rare, with the exception of brief comparisons in Gu et al. (2013); Patil et al. (2014); Chapman et al. (2014). In this Chapter we aim to compare non-parametric and parametric methods on a SKA Phase 1 CD/EoR simulation, comparing the recovered signals both in terms of statistics and imaging.

PoS(AASKA14)005

In Sec. 2 we introduce the five methods used in this chapter to mitigate the simulated foreground contamination. In Sec. 3 we describe the state-of-the-art SKA Phase 1 simulation, consisting of cosmological signal, foregrounds and instrumental noise, used in this chapter. We show the results of applying the methods to these simulations in Sec. 4 before making our conclusions in Sec. 5.

2. Comparing Foreground Removal Methods

In this section we describe the methods of LOS foreground removal applied in this chapter. We divide the methods into those which assume a functional form for the foreground signal (parametric) and those which loosen the constraints on this form somewhat (non-parametric).

2.1 Parametric Methods

2.1.1 Polynomial fitting

The simplest method for foreground removal in total intensity is polynomial fitting in frequency or log frequency, e.g. McQuinn et al. (2006); Morales et al. (2006); Gleser et al. (2008); Jelić et al. (2008); Bowman et al. (2006); Liu et al. (2009); Petrovic & Oh (2011).

The usual method of polynomial fitting is to fit the total observed spectrum along the line of sight with a smooth function such as a n-th order polynomial: $\log T_{b,fg}(\nu) = a_0 + \sum_{i=1}^{n} a^i \log \nu^i$. The order of polynomial varies slightly between different papers, for example Wang et al. (2006) set $n = 2$ while Jelić et al. (2008) sets $n = 3$.

One should be careful in choosing the order of the polynomial to perform the fitting. If the order of the polynomial is too small, the foregrounds will be under-fitted and the EoR signal could be dominated and corrupted by the fitting residuals. If the order of the polynomial is too big, the EoR signal could be fitted out. For this work we will follow Jelić et al. (2008) and perform the fitting in log space using a 3rd order polynomial.

2.1.2 CCA (Correlated Component Analysis)

In this section we describe the main principles of operation of the Fourier-domain Correlated Component Analysis (CCA) method. More details on the method and on its application to the HI signal can be found in Ricciardi et al. (2010) and Bonaldi & Brown (2015), respectively. The CCA is a "model learning" algorithm, which estimates the frequency spectrum of the foreground components from the data exploiting second-order statistics. This method was developed for the Cosmic Microwave Background (CMB); its ability to improve the modelling of the poorly known anomalous microwave emission has been demonstrated in Bonaldi et al. (2007), Bonaldi & Ricciardi (2012) and Planck Collaboration (2013).

We start by modelling the data in the uv plane as a linear mixture of the foreground components. For each point in the uv plane we write

$$\vec{x} = \mathbf{BA}\vec{s} + \vec{n}. \tag{2.1}$$

The vectors $\vec{x}$ and $\vec{n}$ contain the data and the noise in Fourier space, respectively; the vector $\vec{s}$ contains the astrophysical foregrounds; the diagonal matrix $\mathbf{B}$ contains the instrumental dirty beams

PoS(AASKA14)005

in Fourier space and the matrix **A**, called the mixing matrix, contains the intensity of the foreground components at all frequencies. The 21-cm signal is modelled as a noise term, contributing to $\vec{n}$ together with the instrumental noise.

The additional assumptions made by the CCA are that the mixing matrix is constant within the considered area of the sky, and that its unknown elements can be reduced by adopting a suitable parametrization $\mathbf{A} = \mathbf{A}(\vec{p})$. For example, in the following, a power law is assumed for the synchrotron component with unknown, spatially constant, spectral index. For the free-free, we adopt a power-law behaviour with fixed spectral index of -2.08. When necessary, we can adopt other parametric models having more degrees of freedom. Though CCA allows the data to estimate the parameters of the model, it does exploit a parametrization, and therefore it is classified as a parametric method.

Once we have an estimate of the mixing matrix, using a relation between the cross-spectra of the data, we can invert eq. (2.1) and reconstruct the foreground components as $\vec{\hat{s}} = \mathbf{W}\vec{x}$ directly in the Fourier domain.

The cleaning of the HI signal consists of subtracting the estimated foreground components $\vec{\hat{s}}$ at all frequencies. We perform the subtraction as:

$$\vec{x} - \mathbf{R}\hat{\mathbf{H}}\vec{\hat{s}} \tag{2.2}$$

where **R** is a diagonal matrix whose elements are chosen to improve the subtraction by minimizing the power of the residuals at each frequency. This step compensates for small errors in the parametric model adopted by the CCA, which result in a slight over/underestimation of the amplitude of the foregrounds at a given frequency. The effectiveness of this approach is tested with the simulation R2 (see Sections 3.4 and 4.4). It is important to note that this minimization approach could be applied to all methods, and as such is a way of mitigating the weaknesses of the parametric method as opposed to the inherent ability for the non-parametric method to deal with foregrounds differing from our models.

2.2 Non-Parametric Methods

2.2.1 Wp smoothing

Wp smoothing is a technique, introduced to 21-cm work by Harker et al. (2009), to fit the foregrounds LOS-by-LOS. The aim is to directly exploit the physical expectation that the foregrounds are smooth, so in this sense the foreground separation is not completely blind. It does not, however, assume a specific parametric form for the foregrounds, or anything about their spatial structure. Wp penalises changes in curvature, with roughness measured 'apart from inflection points (IPs)', hence the name 'Wendepunkt' (Wp), the German word for 'inflection point'.

In the i-th LOS, we have a set $\{(\nu_1^i, s_1^i), (\nu_2^i, s_2^i), \ldots, (\nu_n^i, s_n^i)\}$ of observations in n frequency channels, which we wish to fit with a smooth function $f(\nu)$. Since Wp smoothing always applies to one LOS, from now on we will drop the superscript for clarity. Wp smoothing takes as its measure of roughness the integrated change of curvature. If κ is the radius of curvature, the standardized change of curvature is $\kappa'/\kappa \approx f'''/f''$, where the approximation, which we adopt here, holds exactly at local extrema ($f' = 0$) and becomes singular at IPs ($f'' = 0$).

PoS(AASKA14)005

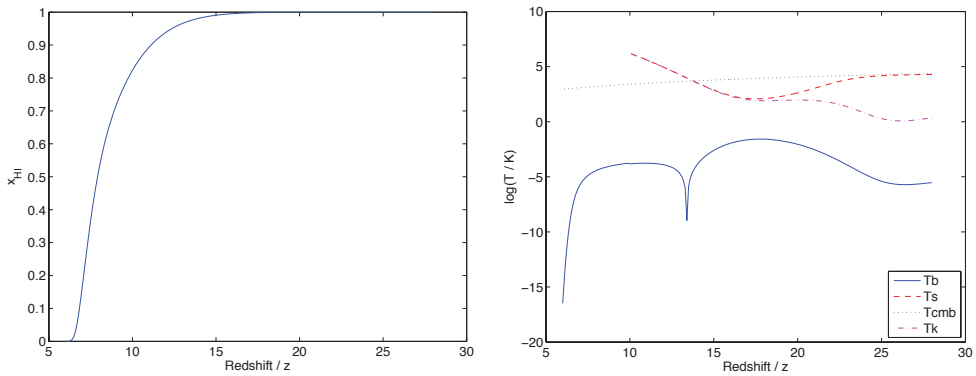

Figure 1: Left: The evolution of neutral hydrogen fraction with redshift. Right: The evolution of T_s, T_{cmb}, T_K and T_b with redshift. The absolute log is taken of T_b.

We therefore separate out the IPs, writing f'' as a smooth function $g(\nu)$ multiplied by a polynomial with the IPs as its roots. With the IPs specified, we find f by performing a penalised fit to the data, where the penalty term is given by a measure of the integrated change in curvature of g multiplied by a smoothing parameter, λ.

This formulation of Wp smoothing is given by Mächler (1993, 1995), who derived a boundary value problem, the solution of which is the function f we seek. Different algorithms have been proposed to solve this system (Mächler 1989; Gu et al. 2013), but we use that outlined by Harker et al. (2009). Unfortunately, these methods currently take $\sim 1\,\mathrm{s}$ to solve for a single sightline, depending on the value of λ, making Wp smoothing relatively slow for large data cubes.

In principle, the choice of a value for λ should be determined by the level of smoothness we expect in our foregrounds. In the limit of $\lambda \to 0$, f becomes the best-fitting function with the given inflection points, while for $\lambda \to \infty$ it becomes the best-fitting polynomial of degree $n_w + 2$. Here, we fix $n_w = 0$ and choose λ based on the performance of the method in simulations. The quality of the fit is quite insensitive to the value of λ up to at least a factor of 2, however.

2.2.2 GMCA

Blind source separation (BSS) uses a mixing model $\vec{x} = \mathbf{A}\vec{s} + \vec{n}$, where $\vec{x}$ is the observed data $\mathbf{A}$ is the mixing matrix, $\vec{s}$ is the unmixed data components and $\vec{n}$ is the noise. What defines a BSS problem is the need to estimate both $\mathbf{A}$ and $\vec{s}$ with no prior knowledge of either (note the difference to CCA, where a prior form for $\mathbf{A}$ was assumed). Methods differ in their approach to this estimation with, for example, the independent component analysis technique FastICA (Hyvärinen (1999),Hyvärinen et al. (2001) and applied to EoR data by Chapman et al. (2012)) assuming statistical independence of the components $\vec{s}$. Here we utilise another BSS technique, Generalized Morphological Component Analysis (GMCA), which assumes morphological diversity and sparsity of the foregrounds in order to model them. This approach originated with Zibulevsky & Pearlmutter (2001) who suggested that one could find a basis set in which the components to be found would be sparsely represented, i.e. a basis set where only a few of the coefficients would be non-zero. With the components being unlikely to have the same few non-zero coefficients one could then use this sparsity to more easily separate the mixture. We attempt to recover the cosmological signal as a residual of the process, i.e. it is actually part of $\vec{n}$. We can expand the data $\vec{x}$ in a

PoS(AASKA14)005

wavelet basis and seek an unmixing scheme, through the estimation of **A**, which yields the sparsest components $\vec{s}$ in the wavelet domain.

For more technical details about GMCA, we refer the interested reader to Bobin et al. (2007, 2008a,b, 2013), where it is shown that sparsity, as used in GMCA, allows for a more precise estimation of the mixing matrix **A** and more robustness to noise than ICA-based techniques such as FastICA. For a previous application of GMCA to EoR data see Chapman et al. (2013).

This component separation method has been applied to the Planck PR1 data to estimate a low-foreground CMB map (Bobin et al. 2014). In this context, sparsity is well adapted to remove naturally non-Gaussian and heterogeneous components such as foregrounds.

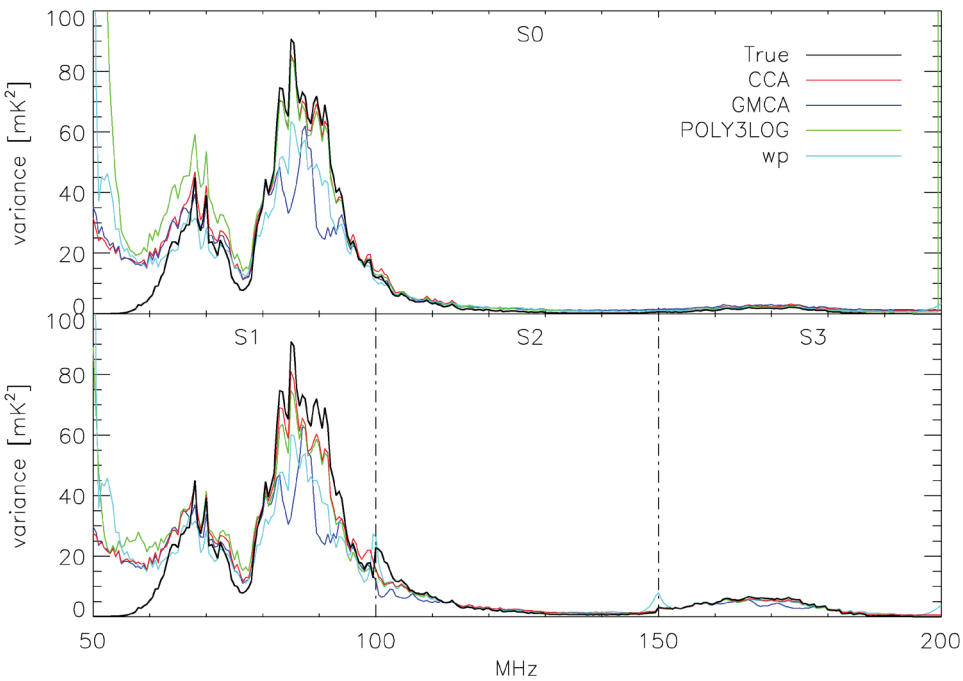

Figure 2: Variance of the simulated cosmological signal (black line) and of the reconstructed cosmological signals for the 4 foreground removal methods (coloured lines) for the S0 cube (top) and the S1, S2 and S3 cubes (bottom).

2.3 Foreground Avoidance

While the methods so far introduced have been focused on removing the foreground from the total signal, there has recently been discussion of avoiding the foregrounds instead. The coupling between the expected frequency smoothness of foregrounds and the unavoidable frequency dependent response of an interferometer leaves a characteristic footprint in k-space, separating an area over which foreground dominates, from a region which is virtually foreground free — a so-called 'EoR window'. The boundaries of this EoR window have been discussed at length in the literature (Datta et al. 2010; Vedantham et al. 2012; Morales et al. 2012; Trott et al. 2012; Parsons et al. 2012; Liu et al. 2014a; Liu et al. 2014b) as well as seen in early results from low frequency observations

PoS (AASKA14) 005

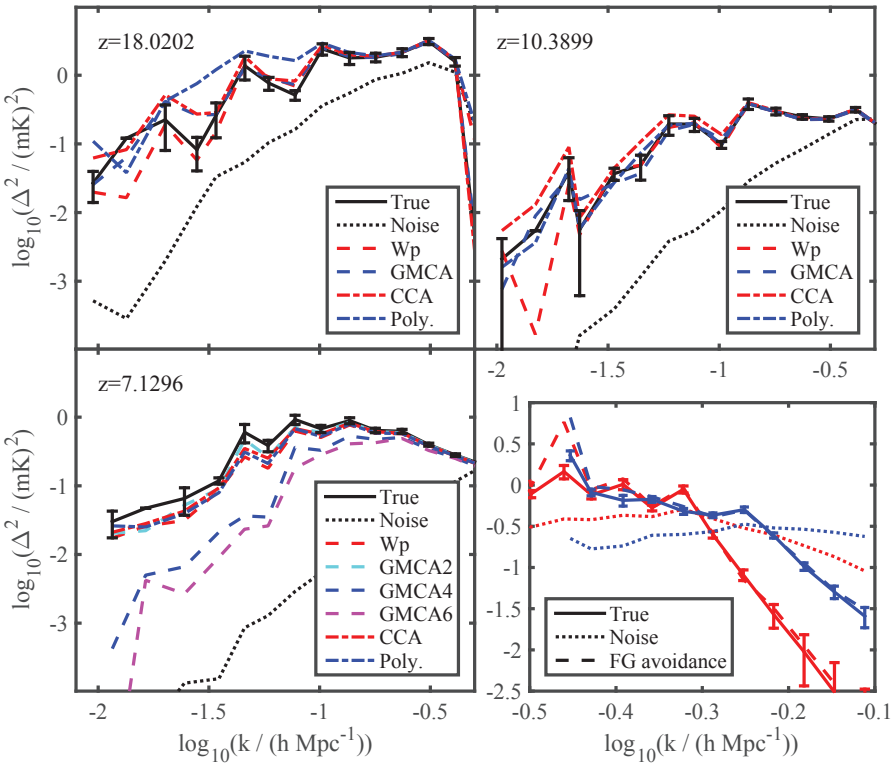

Figure 3: Spherically averaged power spectrum of the simulated cosmological signal, reconstructed cosmological signal, and noise. The top left, top right and bottom left panels show, respectively, power spectra computed in an 8 MHz slice in the centre of S1, S2 and S3. The central redshift of each slice is shown in the panel. Different line styles and colours show the true (input) signal, the noise, and the reconstructed signal for the four different foreground removal methods, as described in the legend. The axes are the same in each of these panels. Note that we show two extra GMCA lines according to foreground models with 2 and 6 components in the bottom left panel. We do not show the highest k points since they are strongly affected by the point spread function. The bottom right panel shows the application of foreground avoidance. Here, the different line styles show the true signal, the noise and the recovered signal, with the different colours used for the data at different redshifts (red for S2, blue for S3), with cutoffs in $k_{\rm los}$ as described in the text. The result for S1 is poorer, and is not shown in order to avoid compressing the scale of the plot; note that the scale in this panel is different from the other three. In all cases, the power spectra are computed after applying a Hanning taper in the frequency direction to avoid ringing: this is particularly important for foreground avoidance, since it mitigates the aliasing of unsubtracted foreground power to high $k_{\rm los}$.

(Bernardi et al. 2013; Dillon et al. 2014; Pober et al. 2013). The largest extent of the EoR window happens to be at low $k_{\rm perp}$ where the frequency dependent response of the instrument is smooth, excluding the low $k_{\rm los}$ mode that are likely to be dominated by foregrounds. When constructing other statistics such as a spherical power spectrum, one can then simply ignore all the foreground-dominated modes and use the k modes inside the EoR window alone. While this will result also in the loss of any cosmological signal outside the EoR window, the remaining region should be free of foreground contamination, if the foregrounds are indeed so well-defined even in the face of instrumental calibration errors. In comparison, while foreground removal allows the possibility of recovering the cosmological signal in all modes, there is also the possibility of foreground fitting

PoS(AASKA14)005

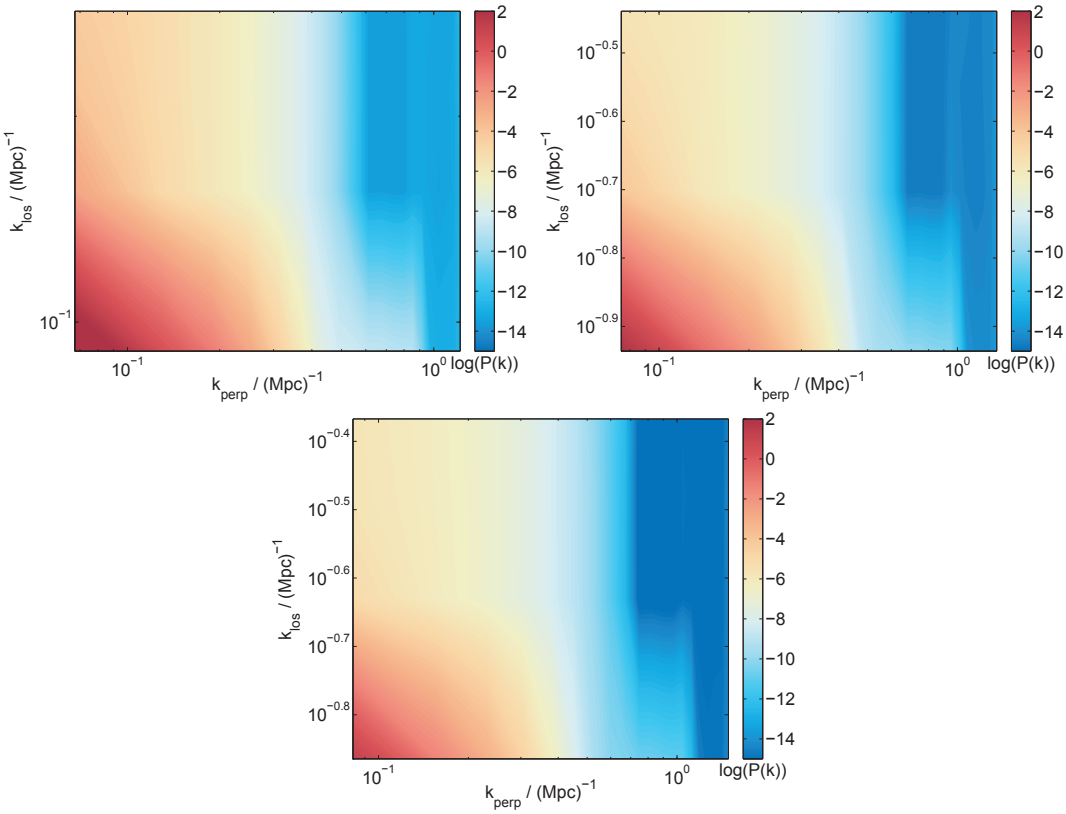

Figure 4: Cylindrical power spectrum of the S0 cube at 75 MHz, 125 MHz and 175 MHz (in reading order). The foreground contamination can be clearly seen for $k_{\rm los} < 10^{-0.93}$, $k_{\rm los} < 10^{-0.7}$ and $k_{\rm los} < 10^{-0.63}\,{\rm Mpc}^{-1}$ respectively, along with the action of the PSF at high $k_{\rm perp}$.

bias being introduced on all modes.

3. SKA Phase 1 Simulations

3.1 Cosmological Signal

We simulate the cosmological signal using the semi-numerical reionization code SIMFAST21 (Santos et al. 2010).

We create initial conditions boxes on a grid of 1024^3 cells before producing ionization and brightness temperature boxes on a grid of 256^3. The boxes are a constant 1 Gpc in side length and are output between redshifts 6 and 28 at separations of $dz = 0.1$. As the aim of this chapter is to assess the effectiveness of foreground removal methods, as opposed to studying a particular model of reionization, we have simply used the default options for SIMFAST21, for example a minimum halo mass of 1.0e8 $M_\odot$. When calculating the brightness temperature, T_b, it is usual to assume that $T_s >> T_{cmb}$ where T_s is the spin temperature and T_{cmb} is the CMB temperature. However, this assumption breaks down at high redshift due to the increasing effect of the gas temperature (T_K) and Lyman-alpha coupling on the spin temperature. We calculate the full spin temperature for all

PoS(AASKA14)005

redshifts above 10. We plot the evolution of the neutral hydrogen fraction, x_{HI}, and T_s, T_{cmb}, T_K and T_b in Fig. 1.

From the real space T_b boxes we create an observation cube, or 'light cone', with the LOS axis evolving in redshift and a constant 5 degree field of view.

3.2 Foregrounds

Though there have been foreground observations at frequencies relevant to LOFAR using WSRT (Bernardi et al. 2009; Bernardi et al. 2010) the foreground contamination at the frequencies and resolution of LOFAR remains poorly constrained. As a result, foreground models directly relevant for this paper rely on using constraints from observations at different frequency and resolution ranges. These constraints are used to normalize the necessary extrapolations made from observations to create a model relevant for LOFAR-EoR observations.

In general, the foreground components are modelled as power laws in 3+1 dimensions (i.e. three spatial and frequency) such that $T_\mathrm{b} \propto \nu^\beta$.

The foreground simulations used in this paper are obtained using the foreground models described in Jelić et al. (2008); Jelić et al. (2010). The foreground contributions considered in these simulations are Galactic synchrotron emission, Galactic free-free emission and extragalactic foregrounds.

3.3 Instrumental Effects

The instrumental effects were modelled using the OSKAR simulator[1] and a list of preliminary station positions for the SKA1-LOW.

The images of the SKA-low PSF were produced by assuming full correlation between all 866 core stations, where the maximum baseline length is 5.29 km. The telescope was located at 52.7 degrees latitude. Baseline coordinates were generated for a 12-hour synthesis observation, with a phase centre on the sky at apparent equatorial coordinates $(\alpha, \delta) = (218, 34.5)$ degrees. A 5-minute sampling interval was used to give 144 snapshots each of 374545 baselines. PSF images were then generated in CASA across a 5-degree field-of-view using 256 w-projection planes. The noise is then normalized according to a 1000 hour integration time using the prescription described in e.g. Thompson et al. (2001).

3.4 Cubes for Analysis

In order to simulate an observation, one normally constructs a 'dirty' cube whereby the cosmological signal and foregrounds are convolved with the same frequency-dependent PSF used to construct the instrumental noise. However, the standard foreground removal methods require the channels to have common resolution in order to work optimally. In which case we use five cubes, all with channels separated by 0.5 MHz, in our analysis:

- S0: A cube running from 50–200 MHz consisting of the clean foregrounds and cosmological signal convolved with the PSF at 50 MHz and the instrumental noise constructed with a sampling equivalent to the 50 MHz sampling in each channel.

[1] http://www.oerc.ox.ac.uk/ ska/oskar

PoS(AASKA14)005

- S1: A cube running from 50–99.5 MHz consisting of the clean foregrounds and cosmological signal convolved with the PSF at 50 MHz and the instrumental noise constructed with a sampling equivalent to the 50 MHz sampling in each channel.

- S2: A cube running from 100–149.5 MHz consisting of the clean foregrounds and cosmological signal convolved with the PSF at 100 MHz and the instrumental noise constructed with a sampling equivalent to the 100 MHz sampling in each channel.

- S3: A cube running from 150–200 MHz consisting of the clean foregrounds and cosmological signal convolved with the PSF at 150 MHz and the instrumental noise constructed with a sampling equivalent to the 150 MHz sampling in each channel.

- R2: We multiply each channel of the clean foreground cube by a random number drawn from a Gaussian distribution with standard deviation of 0.05, simulating a 5% random wiggle along the line of sight. This foreground cube is then convolved and used to construct a cube as described in S2.

The adjustment of the entire frequency range to a common resolution in S0 results in the loss of a lot of high resolution information at high frequency. There is a balance to be made between the amount of information lost and the amount of data the methods need to provide an optimal foreground estimate. We therefore test S1, S2 and S3 in order to assess whether the methods are able to make good signal recoveries of the higher resolution information at higher frequencies, despite a third of the data being available to constrain the foregrounds.

We construct R2 (R - rough) in order to test the reliance of the methods on the smoothness of the foregrounds. We expect methods with strong constraints on the smoothness such as polynomial, CCA and, to some degree, Wp smoothing to be more affected than GMCA which places no explicit prior on the smoothness. This roughness could be interpreted as an inherent roughness of the foregrounds themselves or as a simple approximation of an instrumental calibration error such a leakage of polarized foregrounds.

4. Results

4.1 Variance

We computed the variance of the true input cosmological signal and of the reconstructed cosmological signals for each of the 4 foreground removal methods. The variance has been computed for a pixel size of 2.3 arcmins. Given the low noise, the results are stable for changes of the pixel size. The results are shown in Fig. 2 for both the S0 cube and the collated S1, S2 and S3 cubes.

All methods show an excess variance at $\nu < 60$ MHz which is due to foreground residuals. The results are good for the other frequencies. GMCA and Wp smoothing somewhat underestimate the variance in the 80–90 MHz frequency range. For all methods the variance is correctly recovered over a broad frequency range.

There is not an apparent major disadvantage to any of the methods by splitting the cube into three segments and so we pursue analysis of only the S1, S2 and S3 cubes in the following, in

PoS(AASKA14)005

order to retain as much spatial information as possible while conforming to the common resolution requirements of the methods.

One might wonder at the two peaks in variance below 100 MHz. While the clean signal does not show such clear peaks, the action of the realistic SKA PSF on the clean cosmological signal induces this effect.

4.2 Power Spectrum

The spherically-averaged 21-cm power spectrum is one of the quantities most readily computed from theory and is a rich source of information on cosmology and on the nature of high-redshift sources (e.g. Barkana & Loeb 2005, and many subsequent works). It is expected that the SKA will be able measure it with high signal-to-noise across a broad range of scales. Moreover, k-space might be considered a natural space in which to study the 21-cm signal, since interferometers natively measure Fourier modes in the plane of the sky, while smooth foregrounds are likely to be more isolated in k-space (residing mainly at low $k_{\rm los}$) than in real space. The quality of power spectrum recovery has therefore become a popular metric when comparing foreground removal methods as well as instruments.

Fig. 3 shows the spherically averaged power spectrum for a slice in frequency in the centre of S1, S2 and S3. In a given frequency range, this is computed simply by finding the power (magnitude squared of the visibility) in each cell in Fourier space, and then binning this power in spherical shells, i.e. shells with a given $k = \sqrt{k_{\rm perp}^2 + k_{\rm los}^2}$. Following convention, we plot $\Delta^2(k) = k^3 P(k)/2\pi^2$, which traces the contribution to the variance of a unit interval in $\log(k)$ at k.

In each case, the noise power spectrum has been subtracted from the residual power to recover an estimate of the cosmological signal power. Foreground removal mostly yields a reasonable estimate of the cosmological signal, with the possible exception of GMCA in the lowest-redshift slice (in S3). It is not immediately clear why GMCA as opposed to any other method would not perform as well in this frequency segment. The fiducial four-component model of GMCA was chosen rather arbitrarily and ideally all methods should undergo a full Bayesian model selection in order to select the various input parameters (such as the smoothing parameter in Wp smoothing and number of components in the GMCA foreground model). In the S3 panel we have also plotted the power spectrum for GMCA with two and six components in the foreground model. We can see that by changing the number of components in the GMCA foreground model we can achieve a similar fit to the other methods which is perhaps indicative that a more robust method of model selection is needed. It is also worth remembering that the CCA results have undergone an in-built residual minimization which allow it to perform much better than if the minimization were not carried out. This minimization could equally be applied to any method.

We also include in Fig. 3 the result of implementing foreground avoidance. By constructing a cylindrical power spectrum in $k_{\rm perp}, k_{\rm los}$ we can define a $k_{\rm los}$ bound, below which modes are considered contaminated by foregrounds and above which lies what is termed the 'EoR window'. We can then construct a spherical power spectrum as described above but ignoring all modes below this bound. This is the 'foreground avoidance' line. We find this bound to be at $k_{\rm los} < 10^{-0.93}$, $k_{\rm los} < 10^{-0.7}$ and $k_{\rm los} < 10^{-0.63}$ Mpc^{-1} for the data at 75, 125 and 175 MHz respectively (see Fig. 4). As one can see, this severely limits the range of scales which can be recovered; however, there are

PoS(AASKA14)005

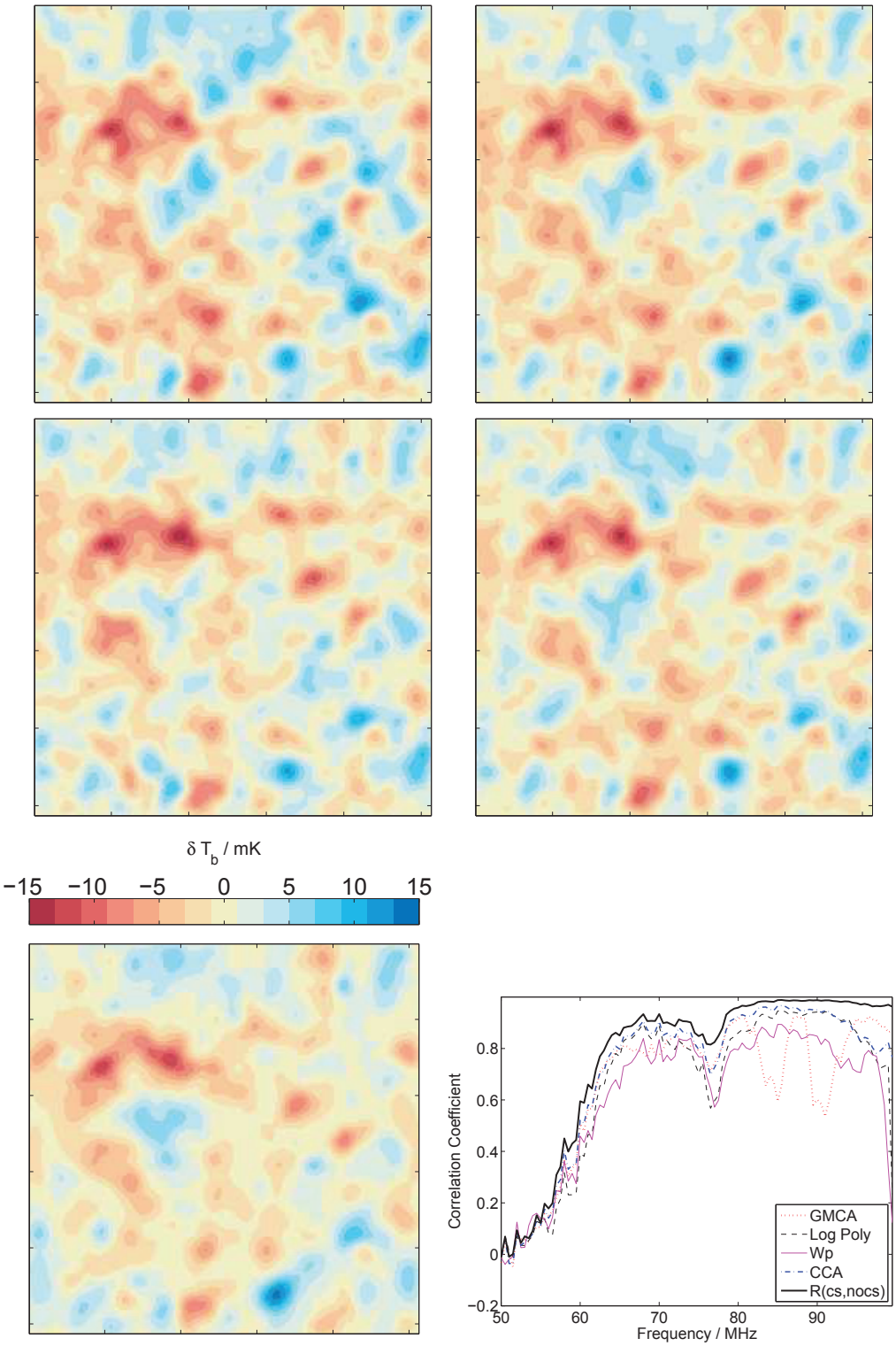

Figure 5: Top two rows, reading order: the smoothed residual maps of S1 at 75 MHz from the Polynomial, CCA, Wp and GMCA methods. Bottom row, left to right: The smoothed cosmological signal at 75 MHz and the correlation coefficient relating to residuals vs. cosmological signal. The best theoretical recovery possible, whereby foreground fitting errors are zero, is shown by the correlation between noise plus simulated cosmological signal vs. simulated cosmological signal in solid black.

PoS(AASKA14)005

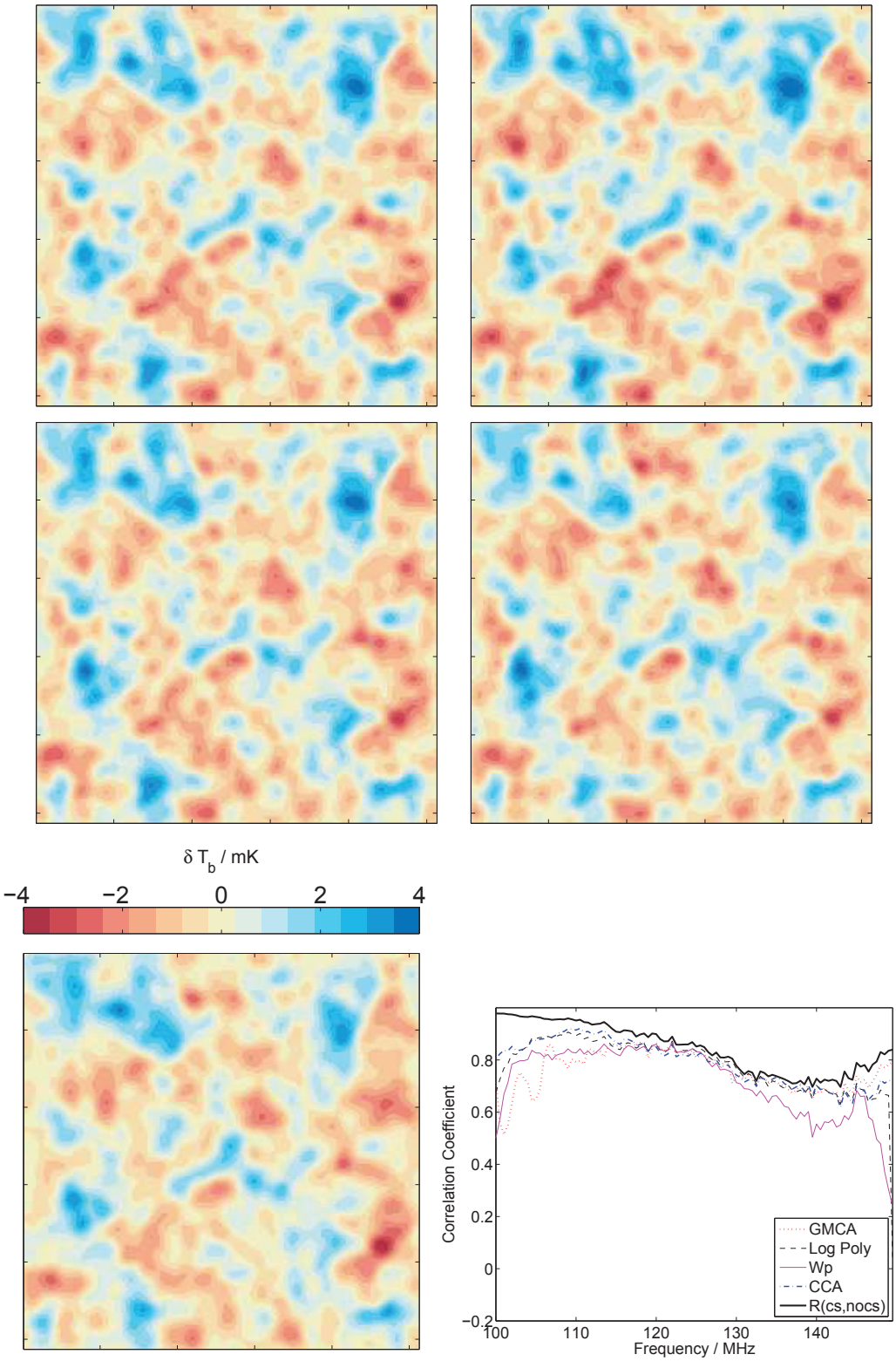

Figure 6: Top two rows, reading order: the smoothed residual maps of S2 at 125 MHz from the Polynomial, CCA, Wp and GMCA methods. Bottom row, left to right: The smoothed cosmological signal at 125 MHz and the correlation coefficient relating to residuals vs. cosmological signal.

PoS(AASKA14)005

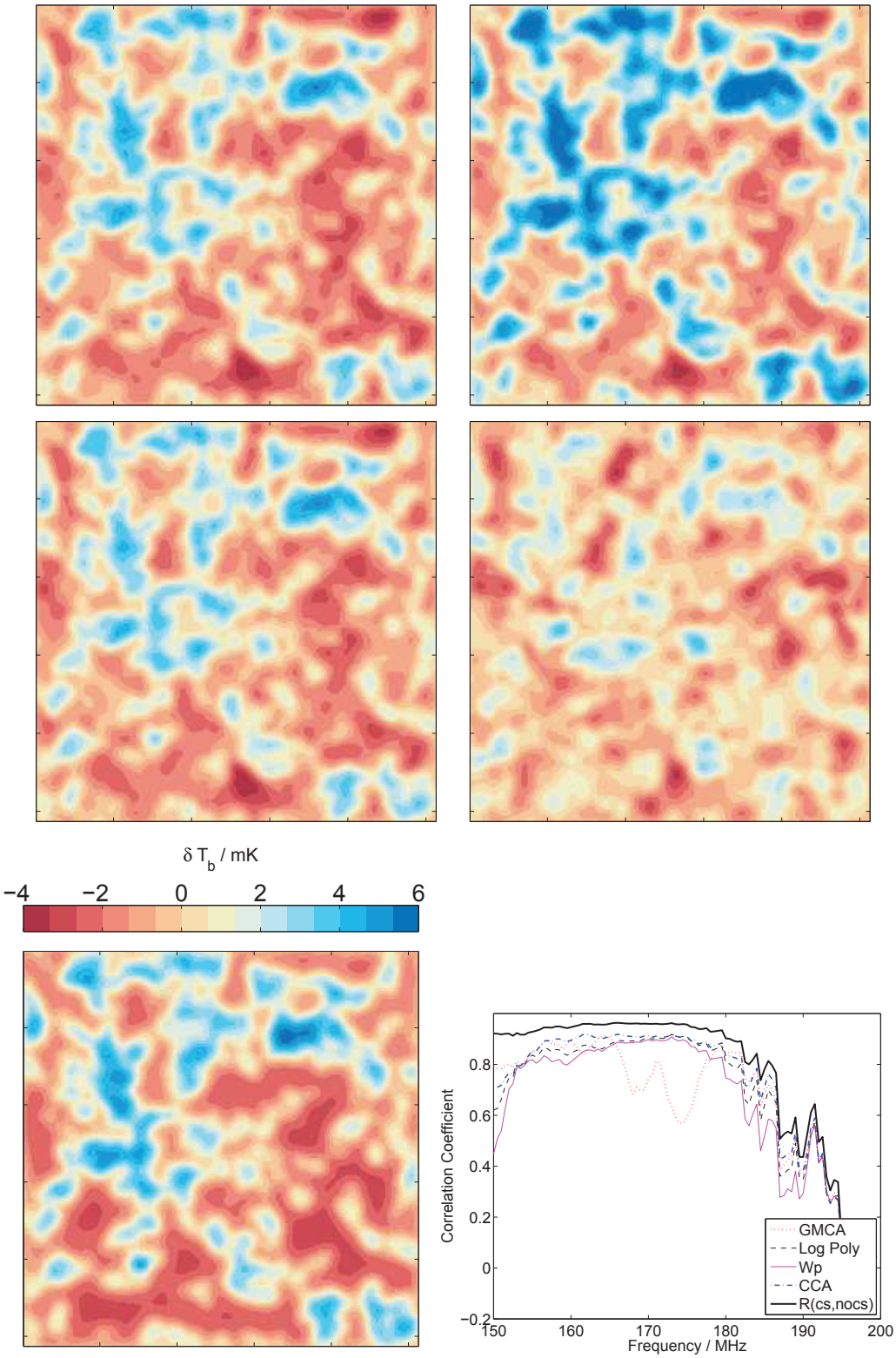

Figure 7: Top two rows, reading order: the smoothed residual maps of S3 at 175 MHz from the Polynomial, CCA, Wp and GMCA methods. Bottom row, left to right: The smoothed cosmological signal at 175 MHz and the correlation coefficient relating to residuals vs. cosmological signal.

PoS (AASKA14) 005

values of z and k for which it performs very well. An optimal power spectrum estimation strategy will likely combine removal and avoidance in some way, with some attempts in this direction having been made by Liu et al. (2014b).

4.3 Images

One of the most exciting scientific outcomes of the SKA is the ability to image the EoR and Cosmic Dawn. We now review how the foreground removal methods affect this capability. We present slices from the residual cubes for three different scenarios. In Fig. 5 we take S1 and show the residual slices at 75 MHz; in Fig. 6 we take S2 and show the residual slices at 125 MHz and in Fig. 7 we take S3 and show the residual slices at 175 MHz. Note that, for all images shown, the residual cube has been smoothed with a Gaussian kernel of FWHM eight pixels, which is equivalent to 9.36 arcminutes, in order to mitigate the effect of the instrumental noise. In each figure we also show the correlation coefficient between the smoothed residual cube and the smoothed simulated cosmological signal for the different methods. As we will only have statistical knowledge of the noise, we would not be well motivated in correlating the reconstructed and simulated cosmological signal, and instead also plot an 'envelope' in the form of a correlation between the simulated cosmological signal and the simulated cosmological signal combined with the instrumental noise. This provides an upper bound for the best correlation we can expect to see in the data if zero foreground fitting errors were present. We see that an impressive image recovery is apparent for all methods, though the extent of that recovery is highly variable with frequency.

4.4 Relaxation of foreground smoothness

We now demonstrate how the methods fare when analysing a cube containing foregrounds which have a random 5% deviation from the smooth power law along the line of sight. We show the correlation coefficient between the residuals of cube R2 and the cosmological signal in the top-left panel of Fig. 8. It is interesting to see the failure of the polynomial method compared to the ability of CCA to recover from a similar failure using the correction method mentioned in Section 2.1.2. This correction method could be applied to all approaches and relies on the first order approximation (i.e. that the wiggle is superimposed on a power law) of the foreground being accurate enough. The crucial point to take away is that non-parametric methods, such as GMCA, which do not have a prior on the foreground smoothness, are able to model the foreground accurately with no extra modelling input by the user. In comparison, the parametric (and indeed non-parametric methods like Wp smoothing which require, as opposed to assume, smoothness of foregrounds) need some form of 'extra modelling' such as correction factors or tweaking of the fitting parameters. It is likely that Wp fitting would see a similar improvement to CCA with such correction factors, as the same first-order approximation of smoothness applies.

4.5 Other SKA configurations

We now look at how one of our results is affected in the case of an early-SKA implementation where the sensitivity is halved and an SKA2 implementation where the sensitivity is quadrupled. We do this for only one method, GMCA, for clarity and conciseness. We show the correlation coefficient between the recovered maps in the three remaining panels of Fig. 8.

PoS(AASKA14)005

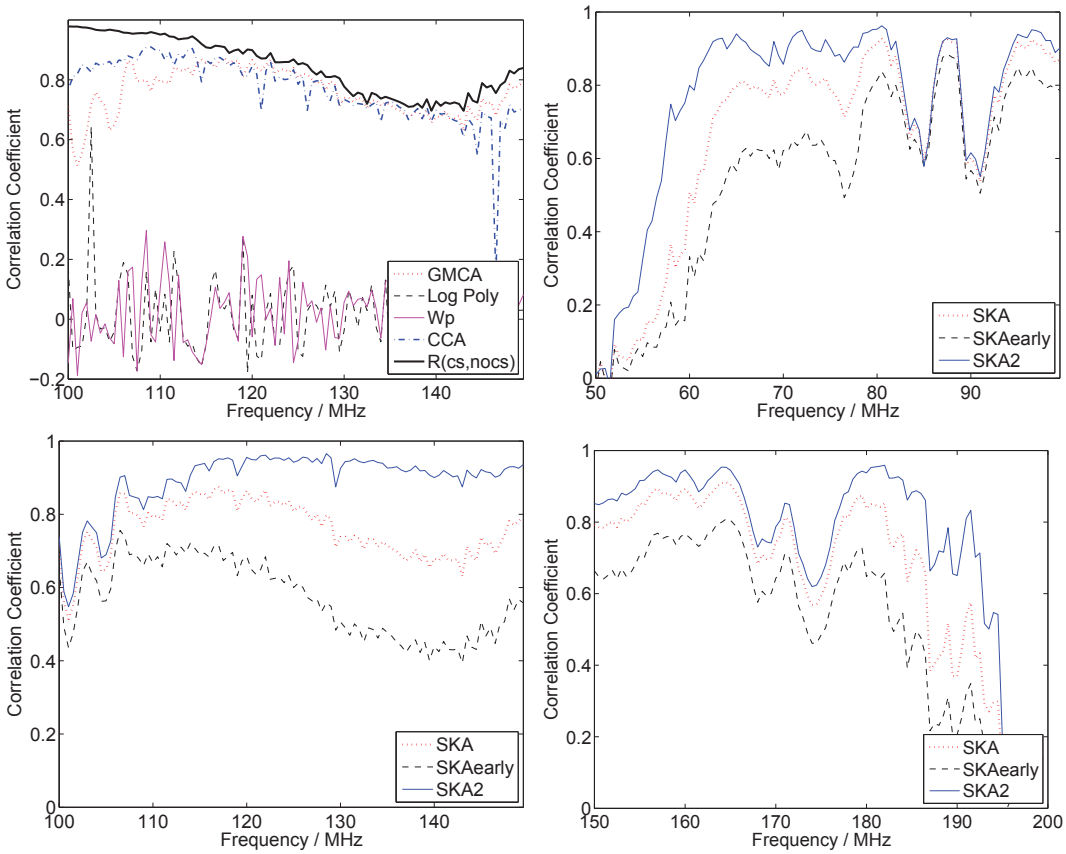

Figure 8: In reading order: The correlation coefficient relating to the R2 cube residuals and the cosmological signal. The correlation coefficient relating to the GMCA residuals for the different SKA scenarios vs. cosmological signal for the S1, S2 and S3 cubes.

As the instrumental noise level decreases, the recovery is greatly improved. The general shape of the curves remains similar, suggesting that there is significant contribution by foreground fitting errors which affect the correlation from slice to slice. There are indeed slices in the S1 cube, for example at 85 MHz, which produce the same correlation independent of noise level, suggesting foreground leakage is the dominant cause of error at those frequencies.

5. Conclusions

- We have applied a suite of foreground removal methods to a state-of-the-art simulation of SKA Phase 1 observations and analysed the recovered cosmological signal by using different statistics.
- The variance of the 21-cm signal is well recovered over a broad range of frequencies by all methods. While setting the entire bandwidth to a common resolution results in the loss of a lot of spatial information at high frequency, there is no obvious advantage in the accuracy of the recovered variance. We therefore opt for a compromise of setting several segments to common resolution.

PoS(AASKA14)005

- Foreground removal methods generally yield a reasonable estimate of the spherical power spectrum of the cosmological signal. Foreground avoidance severely limits the range of scales for which the power spectrum can be recovered, however in such a limited range the results are good.
- We obtain an impressive recovery of the images for all methods, the quality of which however varies with frequency.
- The relaxation of the hypothesis of foreground smoothness does not affect the performance of GMCA, which is non-parametric, while it affects polynomial fitting and Wp smoothing. However, as shown by the CCA, the quality of the results can be restored with some extra modelling, at least as long as the smooth model adopted is a reasonable approximation of the foreground spectrum.
- As the instrumental noise level decreases, the recovery of the signal is greatly improved. For some frequencies (85 MHz for example) the results are much more similar, which suggests that foreground subtraction errors in these cases are dominant.

6. Acknowledgments

EC would like to thank Jonathan Pritchard and the SKA-EoR working group for useful discussions. GH acknowledges funding from the People Programme (Marie Curie Actions) of the European Union's Seventh Framework Programme (FP7/2007-2013) under REA Grant Agreement No 327999. AB acknowledges support from the European Research Council under the EC FP7 grant number 280127.

References

Barkana, R., & Loeb, A. 2005, ApJL, 624, L65
Bernardi, G., de Bruyn, A. G., Brentjens, M. A., et al. 2009, A&A, 500, 965
Bernardi, G., de Bruyn, A. G., Harker, G., et al. 2010, A&A, 522, A67
Bernardi, G., Greenhill, L. J., Mitchell, D. A., et al. 2013, ApJ, 771, 105
Bobin, J., Moudden, Y., Starck, J.-L., Fadili, J., & Aghanim, N. 2008a, Statistical Methodology, 5, 307
Bobin, J., Starck, J.-L., Fadili, J., & Moudden, Y. 2007, IEEE Transactions on Image Processing, 16, 2662
Bobin, J., Starck, J.-L., Moudden, Y., & Fadili, M. J. 2008b, in "Advances in Imaging and Electron Physics", 152, 221
Bobin, J., Starck, J.-L., Sureau, F., & Basak, S. 2013, A&A, 550, A73
Bobin, J., Sureau, F., Starck, J.-L., Rassat, A., & Paykari, P. 2014, A&A, 563
Bonaldi, A., & Brown, M. L. 2015, Monthly Notices of the Royal Astronomical Society, 447, 1973
Bonaldi, A., & Ricciardi, S. 2012, Advances in Astronomy
Bonaldi, A., Ricciardi, S., Leach, S., et al. 2007, MNRAS, 382, 1791
Bowman, J. D., Morales, M. F., & Hewitt, J. N. 2006, ApJ, 638, 20

PoS(AASKA14)005

Chapman, E., Abdalla, F., Harker, G., et al. 2012, MNRAS, 423, 2518
Chapman, E., Abdalla, F. B., Bobin, J., et al. 2013, MNRAS, 429, 165
Chapman, E., Zaroubi, S., & Abdalla, F. 2014, preprint (astro-ph/1408.4695)
Datta, A., Bowman, J. D., & Carilli, C. L. 2010, ApJ, 724, 526
Di Matteo, T., Perna, R., Abel, T., & Rees, M. 2002, ApJ, 564, 576
Di Matteo, T. and Ciardi, B. and Miniati, F. 2004, MNRAS, 355, 1053
Dillon, J. S., Liu, A., Williams, C. L., et al. 2014, Phys. Rev. D, 89, 023002
Gleser, L., Nusser, A., & Benson, A. J. 2008, MNRAS, 391, 383
Gnedin, N. Y., & Shaver, P. A. 2004, ApJ, 608, 611
Gu, J., Xu, H., Wang, J., An, T., & Chen, W. 2013, ApJ, 773, 38
Harker, G., Zaroubi, S., Bernardi, G., et al. 2009, MNRAS, 397, 1138
Hyvärinen, A. 1999, Neural Networks, IEEE Transactions on, 10, 626
Hyvärinen, A., Karhunen, J., & Oja, E. 2001, *Independent Component Analysis* (John Wiley and Sons)
Jelić, V., Zaroubi, S., Labropoulos, P., et al. 2010, MNRAS, 409, 1647
Jelić, V., Zaroubi, S., Labropoulos, P., et al. 2008, MNRAS, 389, 1319
Liu, A., Parsons, A. R., & Trott, C. M. 2014a, Phys. Rev. D, 90, 023018
Liu, A., Parsons, A. R., & Trott, C. M. 2014b, Phys. Rev. D, 90, 023019
Liu, A., & Tegmark, M. 2011, Phys. Rev. D, 83, 103006
Liu, A., Tegmark, M., Bowman, J., Hewitt, J., & Zaldarriaga, M. 2009, MNRAS, 398, 401
Mächler, M. 1989, PhD thesis, ETH Zürich
—. 1993, *Very smooth nonparametric curve estimation by penalizing change of curvature*, Research report 71, Seminar für Statistik ETH Zürich
—. 1995, Annals of Statistics, 23, 1496
McQuinn, M., Zahn, O., Zaldarriaga, M., Hernquist, L., & Furlanetto, S. R. 2006, ApJ, 653, 815
Morales, M. F., Bowman, J. D., & Hewitt, J. N. 2006, ApJ, 648, 767
Morales, M. F., Hazelton, B., Sullivan, I., & Beardsley, A. 2012, ApJ, 752, 137
Oh, S. P., & Mack, K. J. 2003, MNRAS, 346, 871
Parsons, A. R., Pober, J. C., Aguirre, J. E., et al. 2012, ApJ, 756, 165
Patil, A. H., Zaroubi, S., Chapman, E., et al. 2014, ArXiv e-prints
Petrovic, N., & Oh, S. P. 2011, MNRAS, 413, 2103
Planck Collaboration. 2013, A&A, 557, A53
Pober, J. C., Parsons, A. R., Aguirre, J. E., et al. 2013, ApJL, 768, L36
Ricciardi, S., Bonaldi, A., Natoli, P., et al. 2010, MNRAS, 406, 1644
Santos, M. G., Cooray, A., & Knox, L. 2005, ApJ, 625, 575
Santos, M. G., Ferramacho, L., Silva, M. B., Amblard, A., & Cooray, A. 2010, MNRAS, 406, 2421
Thompson, A. R., Moran, J. M., & Swenson, Jr., G. W. 2001, *Interferometry and Synthesis in Radio Astronomy* (John Wiley and Sons)
Trott, C. M., Wayth, R. B., & Tingay, S. J. 2012, ApJ, 757, 101
Vedantham, H., Shankar, N. U., & Subrahmanyan, R. 2012, ApJ, 745, 176
Wang, X., M.Tegmark, Santos, M. G., & Knox, L. 2006, ApJ, 650, 529
Zaldarriaga, M., Furlanetto, S. R., & Hernquist, L. 2004, ApJ, 608, 622
Zibulevsky, M., & Pearlmutter, B. A. 2001, Neural Computation, 13, 863

PoS(AASKA14)005

PROCEEDINGS OF SCIENCE

21cm Forest with the SKA

Benedetta Ciardi
Max Planck Institute for Astrophysics, Garching, Germany
E-mail: ciardi at mpa-garching.mpg.de

Susumu Inoue
Institute for Cosmic Ray Research, University of Tokyo, Tokyo, Japan
E-mail: sinoue at icrr.u-tokyo.ac.jp

Katherine J. Mack
University of Melbourne, Melbourne, Australia
E-mail: kmack at unimelb.edu.au

Yidong Xu
National Astronomical Observatories, Chinese Academy of Sciences, Beijing, China
E-mail: xuyd at nao.cas.cn

Gianni Bernardi*
SKA SA, Cape Town, South Africa
Rhodes University, Grahamstown, South Africa
E-mail: giannibernardi at ska.ac.za

An alternative to both the tomography technique and the power spectrum approach is to search for the 21cm forest, that is the 21cm absorption features against high-z radio loud sources caused by the intervening cold neutral intergalactic medum (IGM) and collapsed structures. Although the existence of high-z radio loud sources has not been confirmed yet, SKA-low would be the instrument of choice to find such sources as they are expected to have spectra steeper than their lower-z counterparts. Since the strongest absorption features arise from small scale structures (few tens of physical kpc, or even lower), the 21cm forest can probe the HI density power spectrum on small scales not amenable to measurements by any other means. Also, it can be a unique probe of the heating process and the thermal history of the early universe, as the signal is strongly dependent on the IGM temperature. Here we show what SKA1-low could do in terms of detecting the 21cm forest in the redshift range $z \sim 7.5 - 15$.

Advancing Astrophysics with the Square Kilometre Array
June 8-13, 2014
Giardini Naxos, Italy

*Speaker.

PoS(AASKA14)006

1. Introduction

An alternative to both the tomography technique and the power spectrum approach is to search for the 21cm forest, that is the 21cm absorption features against high-z radio loud sources caused by the intervening cold neutral IGM and collapsed structures (e.g. Carilli, Gnedin & Owen 2002; Furlanetto & Loeb 2002; Furlanetto 2006; Carilli et al. 2007; Xu et al. 2009; Xu, Ferrara & Chen 2011; Mack & Wyithe 2012; Ciardi et al. 2013; Ewall-Wice et al. 2014). In fact the 21cm forest is more than a complement to tomography or power spectrum analysis. Since the strongest absorption features arise from small scale structures, the 21cm forest can probe the HI density power spectrum on small scales not amenable to measurements by any other means (e.g. Shimabukuro et al. 2014). Also, it can be a unique probe of the heating process and the thermal history of the early universe, as the signal is strongly dependent on the IGM temperature.

The photons emitted by a radio loud source at redshift z_s with frequencies $\nu > \nu_{21\mathrm{cm}}$, will be removed from the source spectrum with a probability $1-e^{-\tau_{21\mathrm{cm}}}$, absorbed by the neutral hydrogen present along the line of sight (LOS) at redshift $z = \nu_{21\mathrm{cm}}/\nu(1+z_s)-1$. The optical depth $\tau_{21\mathrm{cm}}$ can be written as (e.g. Madau, Meiksin & Rees 1997; Furlanetto, Oh & Briggs 2006):

$$\tau_{21\mathrm{cm}}(z) = \frac{3}{32\pi}\frac{h_p c^3 A_{21\mathrm{cm}}}{k_B \nu_{21\mathrm{cm}}^2}\frac{x_{\mathrm{HI}} n_{\mathrm{H}}}{T_s(1+z)(dv_{\parallel}/dr_{\parallel})}, \tag{1.1}$$

where n_{H} is the H number density, x_{HI} is the mean neutral hydrogen fraction, T_s is the gas spin temperature (which quantifies the relative population of the two levels of the $^2S_{1/2}$ transition), $A_{21\mathrm{cm}} = 2.85\times10^{-15}$ s^{-1} is the Einstein coefficient of the transition and $dv_{\parallel}/dr_{\parallel}$ is the gradient of the proper velocity along the LOS (in km s^{-1}), which takes into account also the contribution of the gas peculiar velocity. The other symbols appearing in the equation above have the standard meaning adopted in the literature.

Analogously to the case of the Ly-α forest, this could result in an average suppression of the source flux (produced by diffuse neutral hydrogen), as well as in a series of isolated absorption lines (produced by overdense clumps of neutral hydrogen), with the strongest absorption associated with high density, neutral and cold patches of gas. This suggests that the absorption features due to collapsed structures with no or very small star formation (to maximize the amount of HI available for absorption), such as minihalos or dwarf galaxies (Furlanetto & Loeb 2002; Meiksin 2011; Xu, Ferrara & Chen 2011) would be easier to detect than those due to the diffuse neutral IGM. However, this does strongly depend on the feedback effects acting on such objects. Because of the large uncertainties in the nature and intensity of high-z feedback effects (for a review see Ciardi & Ferrara 2005 and its updated version arXiv:astro-ph/0409018), it is not straightforward to estimate the relative importance of the absorption signals from the diffuse IGM and from collapsed objects.

While gas which has been (even only partially) ionized has a temperature of $\sim 10^4$ K, gas which has not been reached by ionizing photons has a temperature which can be even lower that of the CMB. This neutral gas can be heated by Ly-α or X-ray photons, thus reducing the optical depth to 21cm. While Ly-α heating is not extremely efficient, heating due to X-ray photons could easily suppress the otherwise present absorption features (e.g. Mack & Wyithe 2012; Ciardi et al. 2013). This seems to suggest that with observations of the 21cm forest it would be possible to discriminate between different IGM reheating histories, in particular if a high energy component in the ionising spectrum were present (Ewall-Wice et al. 2013).

PoS(AASKA14)006

2. Observed spectra

In this Section we describe the process used to simulate an observed spectrum. The simulated absorption spectrum, $S_{\rm abs}$, is calculated from a full 3D radiative transfer simulation of IGM reionization which resolves scales of $\sim$ 1 kHz (corresponding to $\sim$50 kpc comoving; Ciardi et al. 2012; Ciardi et al. 2013). In the simulation used here, the contribution to ionization and heating from x-rays and/or Ly-α photons is not included (although see Ciardi et al. 2013 for examples of spectra which include such effects), i.e. the gas which is not reached by UV ionizing photons remains cold.

The instrumental effects are estimated using the pipeline of the LOFAR telescope. More specifically, the equation giving the observed visibilities is:

$$V_\nu(\mathbf{u}) = \sum_i^{N_{sources}} I_\nu(\mathbf{s}) e^{-2\pi i \mathbf{u}\cdot\mathbf{s}} + n_s, \tag{2.1}$$

where $\mathbf{u} = (u, v, w)$ are the coordinates of a given baseline at a certain time t, I_ν is the observed source intensity, $\mathbf{s} = (l, m, n)$ is a vector representing the direction cosines for a given source direction and n_s represents additive noise. The noise is given by the radiometer equation:

$$n_s = \frac{1}{\eta_s} \frac{SEFD}{\sqrt{2 t_{\rm int} \Delta\nu}}, \tag{2.2}$$

where η_s is the system efficiency, $\Delta\nu$ is the bandwidth and t_{int} is the integration time. Because of our experience with the LOFAR telescope, we will make predictions based on its characteristics, and we will then scale the noise to match the one expected from SKA. We thus assume that $\eta_s = 0.5$ and $N_{st} = 48$. The system equivalent flux density is given by:

$$SEFD = \frac{2\kappa_B T_{\rm sys}}{N_{\rm dip} \eta_\alpha A_{\rm eff}}, \tag{2.3}$$

where κ_B is Boltzmann's constant, $A_{\rm eff} = min(\frac{\lambda 2}{3}, 1.5626)$ is the effective area of each dipole in the dense and sparse array regimes respectively, $N_{\rm dip}$ is the number of dipoles per station (24 tiles times 16 dipoles per tile for a LOFAR core station) and η_α is the dipole efficiency which we assume to be 1. The system noise $T_{\rm sys}$ has two contributions: *(i)* from the electronics and *(ii)* from the sky. We assume that the sky has a spectral index of -2.55, obtaining $T_{\rm sys} = [140 + 60(\nu/150\,{\rm MHz})^{-2.55}]$ K. The complete Fourier plane sampling can be done by evaluating the above equation for every set of baseline coordinates. The predicted visibilities are then gridded and transformed via inverse Fourier transforms in order to obtain the dirty images. For the purpose of the 21 cm forest, fine spectral resolution ($\sim$1 kHz, see later for further discussion) is needed, which means that the spectra need to be predicted for a large number of channels ($\sim$ 10000). After assembling the full image cube, the LOS spectrum is extracted. In principle, the effect of the Point Spread Function (PSF) side lobes running through the source of interest can be taken into account by including more sources at different positions, with or without absorption features. Here, we have ignored the effect of side lobe noise. In fact, as the SKA will have a very dense uv coverage and the expected 21cm absorption lines will be narrower than a few tens of kHz, we expect the side lobe noise to play a marginal role.

Figure 1 shows the 21cm absorption spectrum due to the diffuse IGM along a random LOS for a bright radio source at $z = 10$ (i.e. $\nu \sim 129$ MHz). For an easy comparison to existing work

PoS(AASKA14)006

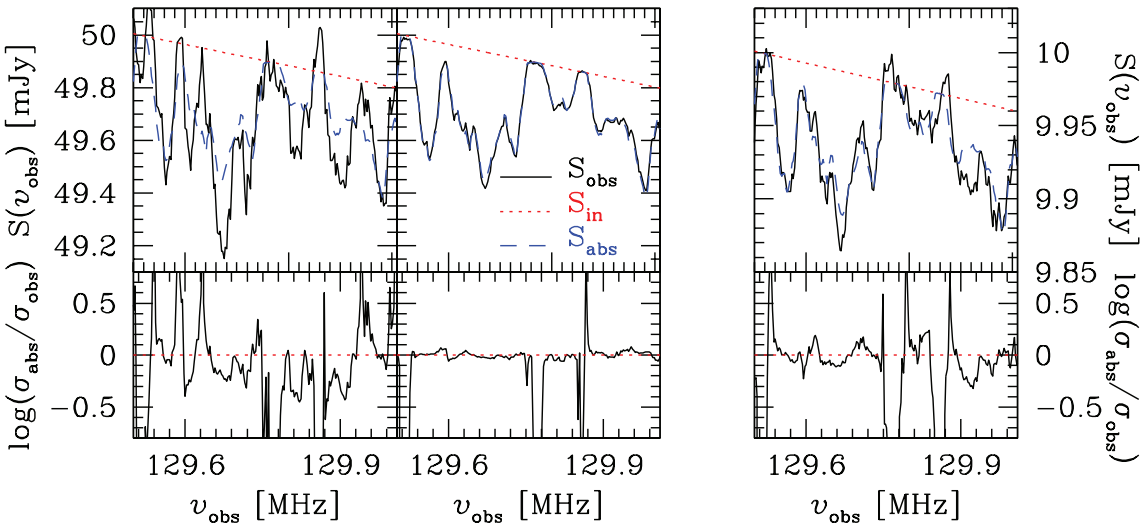

Figure 1: *Upper panels:* Spectrum of a radio source positioned at $z = 10$ ($\nu \sim 129$ MHz), with a power-law index $\alpha = 1.05$ and a flux density $J = 50$ mJy (left hand panels) and 10 mJy (right hand panel). The red dotted lines refer to the instrinsic spectrum of the radio source, $S_{\rm in}$; the blue dashed lines to the simulated spectrum for 21cm absorption, $S_{\rm abs}$ (in a universe where neutral regions remain cold); and the black solid lines to the spectrum for 21cm absorption as it would be seen with an observation time $t_{\rm int} = 1000$ h and a frequency resolution $\Delta\nu = 10$ kHz. The first panel to the left corresponds to a case with the LOFAR noise, while the other two panels have 1/10th of the LOFAR noise, roughly expected for SKA1-low. *Lower panels:* The ratio $\sigma_{\rm abs}/\sigma_{\rm obs}$ corresponding to the upper panels.

on the 21cm forest (e.g. Carilli, Gnedin & Owen 2002; Mack & Wyithe 2012; Ciardi et al. 2013), the intrinsic radio source spectrum, $S_{\rm in}$, is assumed to be similar to Cygnus A, with a power-law with index $\alpha = 1.05$ and a flux density $J = 50$ mJy and 10 mJy. The simulated absorption spectrum, $S_{\rm abs}$, is calculated from the simulations mentioned above. The observed spectrum, $S_{\rm obs}$, is calculated assuming an observation time $t_{\rm int} = 1000$ h with the LOFAR and SKA1-low telescopes and a bandwidth $\Delta\nu = 10$ kHz. A clear absorption signal is observed. This is more evident in the lower panels of Figure 1, which show the quantity $\sigma_{\rm abs}/\sigma_{\rm obs}$, where $\sigma_i = S_i - S_{\rm in}$ and i=abs, obs. As already mentioned above, the inclusion of Ly-α or x-ray heating could suppress or reduce the absoprtion features, with the extent of the effect being highly dependent on the source model (see e.g. Mack & Wyithe 2012; Ciardi et al. 2013).

Very strong absorption features could be easily detected also at lower redshift, when most of the IGM is in a high ionization state, if we were lucky enough to intercept high density cold pockets of gas (with $\tau_{\rm 21cm} > 0.1$; these cells are found in $\sim 0.1\%$ of the LOS in the simulation), as shown in Figure 2.

Moving towards higher redshift, when most of the gas in the IGM is still neutral and relatively cold, would offer the chance of detecting a stronger average absorption (rather than the single absorption features observed at lower redshift). If a radio source with characteristics similar to the ones described above were found, SKA1-low would easily detect the global absorption as shown in Figure 3, although it would not be straightforward to distinguish whether the suppression of the

PoS(AASKA14)006

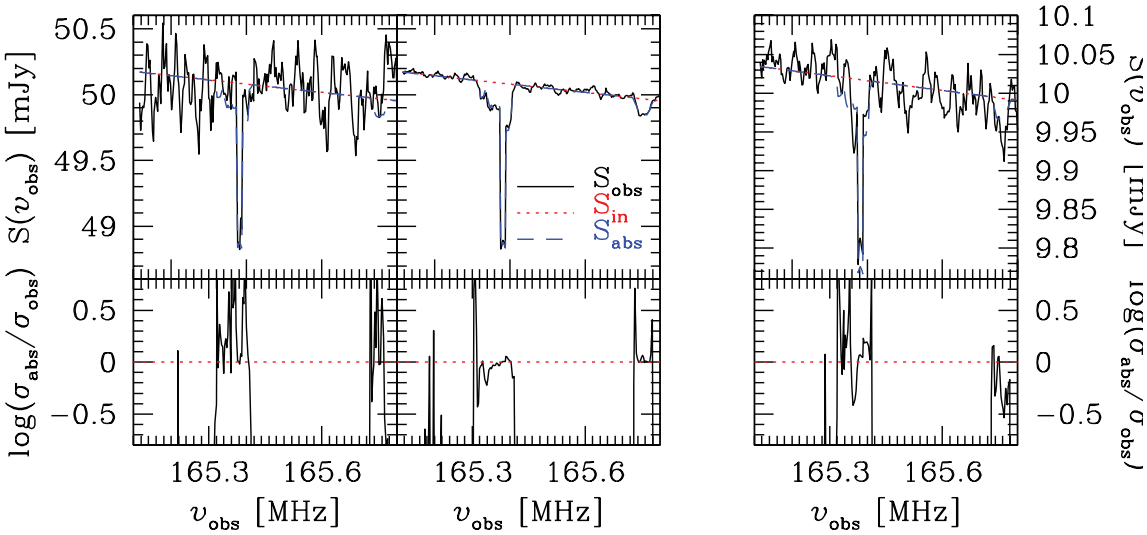

Figure 2: *Upper panels:* Spectrum of a radio source positioned at $z = 7.6$ ($\nu \sim 165$ MHz), with a power-law index $\alpha = 1.05$ and a flux density $J = 50$ mJy (left hand panels) and 10 mJy (right hand panel). The red dotted lines refer to the instrinsic spectrum of the radio source, $S_{\rm in}$; the blue dashed lines to the simulated spectrum for 21cm absorption, $S_{\rm abs}$ (in a universe where neutral regions remain cold); and the black solid lines to the spectrum for 21cm absorption as it would be seen with an observation time $t_{\rm int} = 1000$ h and a frequency resolution $\Delta\nu = 5$ kHz. The first panel to the left corresponds to a case with the LOFAR noise, while the other two panels have 1/10th of the LOFAR noise, roughly expected for SKA1-low. *Lower panels:* The ratio $\sigma_{\rm abs}/\sigma_{\rm obs}$ corresponding to the upper panels.

source flux were due to the intervining neutral IGM or an intrinsically lower flux.

3. Challenges

The most challenging aspect of the detection of a 21cm forest remains the existence of high-z radio loud sources. Although a QSO has been detected at $z = 7.085$ (Mortlock et al. 2011), it is radio quiet (Momjian et al. 2014), and the existence of even higher redshift quasars is uncertain. To observe the absorption features in the spectrum, this has to be observed with a certain precision, which depends on the brightness of the quasar and the sensitivity of the instruments. The minimum detectable flux density of an interferometer can be written as:

$$\Delta S_{\rm min} = \frac{2\,\kappa_B\,T_{\rm sys}}{A\sqrt{\Delta\nu\,t_{int}}}\,\frac{S}{N}, \tag{3.1}$$

where A is the collecting area of the array and S/N is the signal-to-noise ratio. As one may not be able to distinguish whether the flux decrement were due to the diffuse IGM or an intrinsically lower flux, we will probably only detect the additional absorptions with respect to the absorption by the IGM. Therefore, the minimum flux density of the background source required to observe the absorption lines is:

$$S_{\rm min} = 10.3{\rm mJy}\left(\frac{S/N}{5}\right)\left(\frac{0.01}{e^{-\tau_{\rm IGM}} - e^{-\tau}}\right)\left(\frac{5{\rm kHz}}{\Delta\nu}\right)^{1/2}\left(\frac{1000\,{\rm m^2K^{-1}}}{A/T_{\rm sys}}\right)\left(\frac{1000\,{\rm hr}}{t_{\rm int}}\right)^{1/2}. \tag{3.2}$$

PoS(AASKA14)006

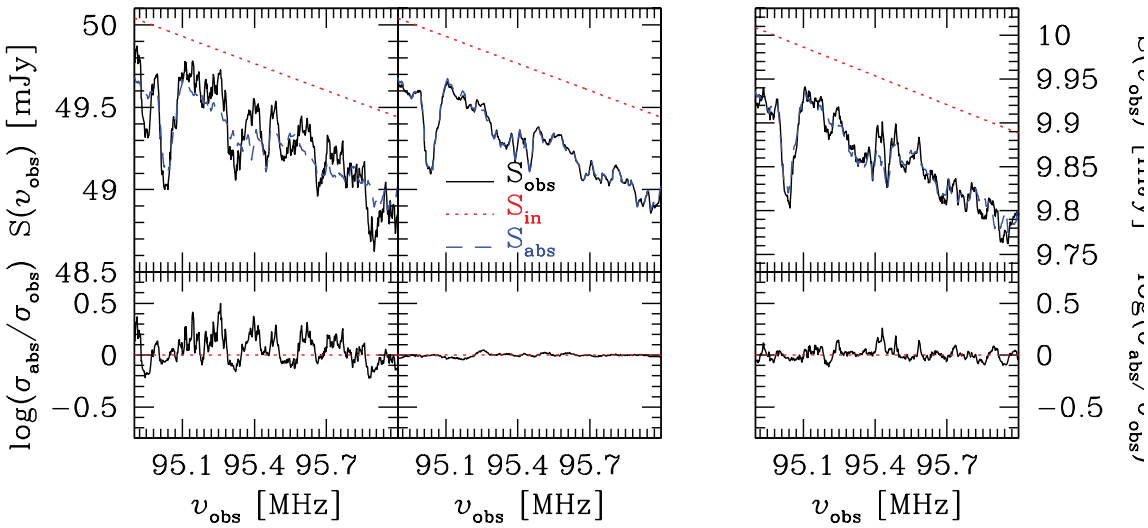

Figure 3: *Upper panels:* Spectrum of a radio source positioned at $z = 14$ ($\nu \sim 95$ MHz), with a power-law index $\alpha = 1.05$ and a flux density $J = 50$ mJy (left hand panels) and 10 mJy (right hand panel). The red dotted lines refer to the instrinsic spectrum of the radio source, $S_{\rm in}$; the blue dashed lines to the simulated spectrum for 21cm absorption, $S_{\rm abs}$ (in a universe where neutral regions remain cold); and the black solid lines to the spectrum for 21cm absorption as it would be seen with an observation time $t_{\rm int} = 1000$ h and a frequency resolution $\Delta\nu = 20$ kHz. The first panel to the left corresponds to a case with the LOFAR noise, while the other two panels have 1/10th of the LOFAR noise, roughly expected for SKA1-low. *Lower panels:* The ratio $\sigma_{\rm abs}/\sigma_{\rm obs}$ corresponding to the upper panels.

The SKA1-low will have $A/T_{\rm sys} \sim 1000{\rm m}^2{\rm K}^{-1}$, and we expect $A/T_{\rm sys} \sim 4000{\rm m}^2{\rm K}^{-1}$ for SKA2-low.

Extrapolating the observed number density of radio sources at $z = 4$ (Jarvis et al. 2001) to higher redshift and lower luminosity, one can calculate the number of quasars with flux density at the observed frequency $\nu_{obs} = 1420.4/(1+z)$ MHz larger than the lower limit described above, for a flat evolution model and a steep evolution model respectively (Xu et al. 2009). Using the planned SKA sensitivities, the predicted numbers of qualified radio sources are plotted in Fig.4.

The predicted number of radio sources which can be used for 21cm forest studies in the whole sky per unit redshift at $z = 10$ varies in the range $8 \times 10^2 - 2 \times 10^4$. This expected number, which is based on observations at redshift lower than reionization, is very uncertain. The exact number depends on the model adopted for the luminosity function of such sources and the instrumental characteristics (e.g. Carilli, Gnedin & Owen 2002; Xu et al. 2009), making such a detection an extremely challenging task. As a reference, the estimated quasar number per unit redshift at $z = 10$ for the 3-tiered survey is reported in Table 1.

If a sufficiently bright radio loud quasar were found beyond the redshift of reionization, then the absorption lines generated from early non-linear structures could be easily detected, as the spectral resolution of the SKA will not be a problem. Assuming the minimum halo mass hosting cold neutral gas to be $10^6{\rm M}_\odot$, about one absorption line in every 8.4kHz is expected at redshift $z \sim 10$. The absorption line density is lower for lower redshift and higher minimum mass. On

PoS(AASKA14)006

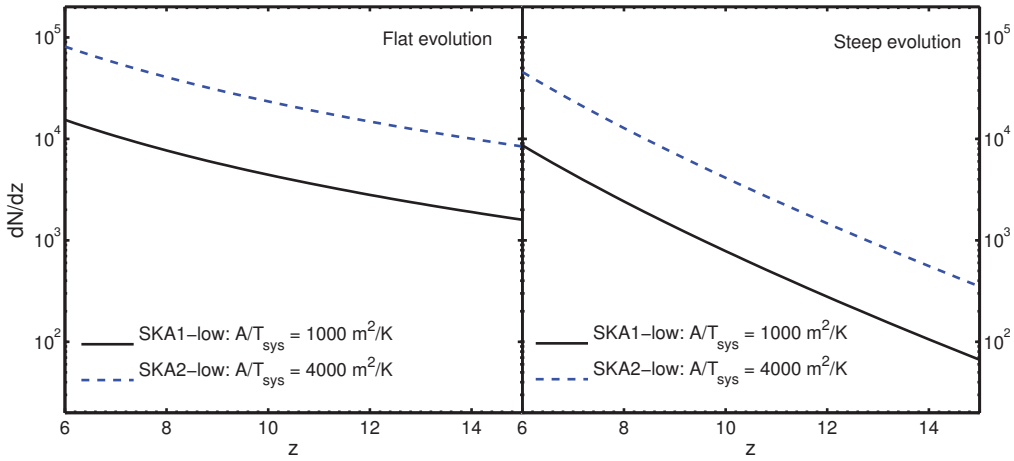

Figure 4: The number of quasars in the whole sky that can be used to detect signals with $e^{-\tau_{\rm IGM}} - e^{-\tau} \geq 0.01$ per redshift interval. The sensitivity of the radio array is taken to be $A/T_{\rm sys} = 1000$ m^{2}K^{-1} (black solid lines) and 4000 m^{2}K^{-1} (blue dashed). The integration time is assumed to be 1000 hours. *Left panel*: the number of qualified quasars in the flat evolution model. *Right panel*: the number of qualified quasars in the steep evolution model.

dN/dz	Model	Ω [sqd]	$t_{\rm int}$ [h]	$A/T_{\rm sys}$ [m^{2}K^{-1}]
11	Flat	100	1000	1000
27	Flat	1000	100	1000
68	Flat	10000	10	1000
57	Flat	100	1000	4000
142	Flat	1000	100	4000
358	Flat	10000	10	4000
2	Steep	100	1000	1000
5	Steep	1000	100	1000
12	Steep	10000	10	1000
10	Steep	100	1000	4000
25	Steep	1000	100	4000
63	Steep	10000	10	4000

Table 1: Estimated quasar number at $z = 10$ for the 3-tiered survey. The columns refer to: number per unit redshift, source model, survey area, observation time, $A/T_{\rm sys}$.

PoS(AASKA14)006

the other hand, the line width from non-linear structures ranges mostly from $\sim$ 1kHz to $\sim$ 5kHz. Given that the SKA1-low will have a spectral resolution of 1kHz, the line counting is feasible as long as sufficiently bright radio sources are available at high redshift. Especially, if one stacks together several lines to get an average profile, it will hopefully reveal the physical status of the early non-linear structures.

An alternative possibility is the radio afterglows of certain types of gamma-ray bursts (GRBs). GRBs have already been observed up to $z \sim 8-9$, and it is plausible that they occur up to the earliest epochs of star formation in the universe at $z \sim 20$ or higher. In addition, they have a simple power-law spectrum at low frequencies, making the signal extraction easy. However, if such GRBs are similar to those seen at lower redshifts, their radio afterglows are not expected to be bright enough at the relevant observed frequencies $\nu_{\rm obs} \lesssim 100$ MHz due to strong synchrotron self-absorption (Ioka & Meszaros 2005; Inoue, Omukai & Ciardi 2007). On the other hand, it has been recently proposed that GRBs arising from Population (Pop) III stars forming in metal-free or very metal poor environments may be much more energetic compared to ordinary GRBs, leading to blastwaves expanding to much larger radii, and consequently much brighter low-frequency radio afterglows, exceeding tens of mJy (Toma, Sakamoto & Mészáros 2011). This occurs over timescales of up to $\sim$ 1000 yr, making them virtually steady radio sources, differently from more standard, lower redshift GRBs which, on the other hand, offer relatively short integration times and a limited spectral length between the location of the GRB and the end of reionization (e.g. Xu et al. 2011). In Figure 5 we show an example of absorption spectra in high-z GRBs, from both Pop III and Pop II stars (Ciardi et al., in prep).

If the rate of Pop III GRBs with sufficiently bright radio emission is 0.1 yr^{-1} or roughly 10^{-4} of all GRBs, one may expect $\sim$ 100 such sources all sky at a given time. A practical question that remains is how we can observationally identify such sources. One possibility of using GRB afterglows as the background radio source is the broad-band observation, measuring the mean flux decrement in each band without resolving individual absorption lines (Xu et al. 2011).

4. Discussion and Summary

As explained above, absorption features due to small collapsed objects can be much stronger than those due to the diffuse neutral IGM. Since their cross-sections are small, the best conditions for detecting them would be when Ly-α coupling pushes the spin temperature in their lower density outskirts to the gas temperature before these regions have been affected by any heating (see Fig. 22 in Meiksin 2011), conditions expected above $z \sim 10$. However, even after heating has started to suppress the 21cm absorption signal, some weak features due to collapsed structures may remain. Interestingly, even when it may not be possible to detect these weak features individually, the presence of absorption may be detected statistically. Weak absorption would produce an increase in the variance of brightness fluctuations, as an addition to the telescope noise, resulting in an apparently noisier spectrum blue-ward of the 21cm transition (see Fig. 29 in Meiksin 2011; Fig. 8 in Mack & Wyithe 2012). The possibility to have a statistical detection of the 21cm forest (rather than the detection of single absorption features), is intriguing as the signature of the forest would be observed in the 21cm power spectrum (see also Ewall-Wice et al. 2013). By integrating the signal from many high redshift sources within the field of view, would reduce the sensitivity requirements

PoS(AASKA14)006

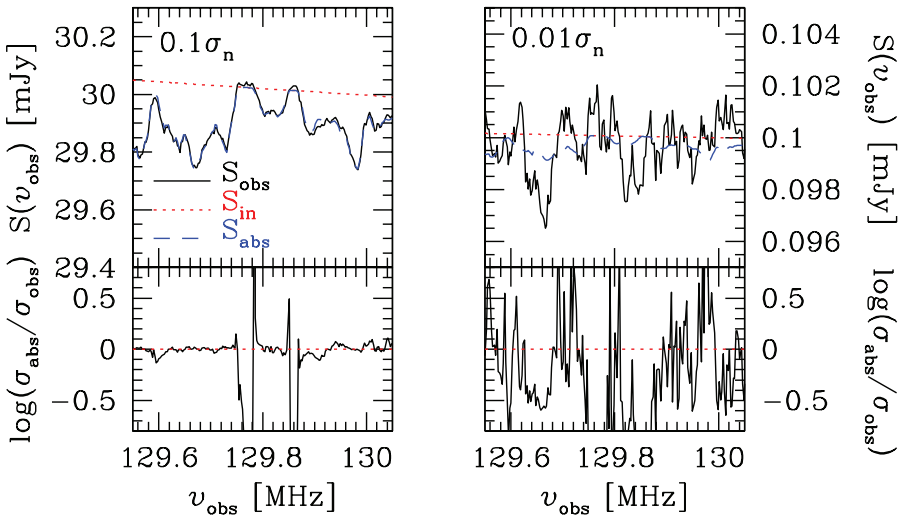

Figure 5: *Upper panels:* Spectrum of a GRB positioned at $z = 10$ ($\nu \sim 129$ MHz), with a power-law index $\alpha = 0.5$ and a flux density $J = 30$ mJy (GRB from Pop III stars; left hand panel) and 0.1 mJy (GRB from Pop II stars; right hand panel). The red dotted lines refer to the instrinsic spectrum of the source, $S_{\rm in}$; the blue dashed lines to the simulated spectrum for 21cm absorption, $S_{\rm abs}$ (in a universe where neutral regions remain cold); and the black solid lines to the spectrum for 21cm absorption as it would be seen with an observation time $t_{\rm int} = 1000$ h and a frequency resolution $\Delta\nu = 10$ kHz. The panel to the left (right) corresponds to a case with 1/10th (1/100th) of the LOFAR noise, roughly expected for SKA1-low (SKA2-low). *Lower panels:* The ratio $\sigma_{\rm abs}/\sigma_{\rm obs}$ corresponding to the upper panels.

of the instrument. On the other hand, the main problem of the paucity of high-z radio sources would persist.

The attempt to detect the 21cm forest has the potential to provide unprecedented information about the large-scale evolution of the intergalactic medium as well as the growth of small-scale structures. Different information can be gleaned depending on the nature of the observation. An attempt to detect the presence of the 21cm forest via a statistical analysis of the power spectrum (Ewall-Wice et al. 2013) will allow us to put constraints on the presence of high-redshift radio-loud sources at high wavenumbers ($k \gtrsim 0.5$ Mpc^{-1}), and to study the IGM thermal history at low wavenumbers ($k \lesssim 0.1$ Mpc^{-1}). Assuming high-redshift radio-loud sources are identified, and we are able to observe them directly in targeted observations, detailed study of the source spectra can reveal the mean thermal properties of the IGM via the flux decrement (Furlanetto 2006) or variance in the flux (Carilli et al. 2004; Mack & Wyithe 2012). If individual absorption features are identified in the spectrum, this could allow us to put constraints on the clumping factor at early times (Xu, Ferrarra & Chen 2011) and to map structure along the line of sight (IGM and/or the first collapsed structures and mini-halos), thus significantly extending our understanding of the process of reionization and the hierarchical growth of structure in the Universe.

Finally, we would like to comment on the fact that as observations of the 21 cm forest require very high frequency resolution, they are demanding both in terms of data storage and processing. However, when a bright continuum radio source is identified after an all-sky survey or deep EoR

PoS(AASKA14)006

observations, it is possible to significantly average in time after phasing up to the source. The maximum amount of data compression will be dictated by the need to identify and subtract bright, far away sources that may generate sidelobe noise in the measurement of the 21 cm forest. However, if bright sources are measured a priori from a sky survey they can be subtracted from the high time resolution visibilities and, afterwards, data can be easily compressed by an order of magnitude or more.

References

Carilli, C. L., Wang, R., van Hoven, M. B., et al. 2007, AJ, 133, 2841
Carilli, C. L., Gnedin, N. Y., Owen, F. 2002, ApJ, 577, 22
Ciardi, B., Bolton, J. S., Maselli, A., Graziani, L. 2012, MNRAS, 423, 558
Ciardi, B. et al. 2013, MNRAS, 428, 1755
Ciardi, B., Ferrara, A. 2005, Space Science Reviews, 116, 625
Ewall-Wice, A., Dillon, J. S., Mesinger, A., Hewitt, J. 2014, arXiv:1310.7936
Furlanetto, S. R. 2006, MNRAS, 370, 1867
Furlanetto, S. R., Oh, S. P., Briggs, F. H. 2006, Phys. Rep., 433, 181
Furlanetto, S. R., Loeb, A. 2002, ApJ, 579, 1
Inoue, S., Omukai, K., Ciardi, B. 2007, MNRAS, 380, 1715
Ioka, K., Mészáros, P. 2005, ApJ, 619, 684
Jarvis, M. J., Rawlings, S., Willott, C. J., et al. 2001, MNRAS, 327, 907
Mack, K. J., Wyithe, J. S. B. 2012, MNRAS, 425, 2988
Madau, P., Meiksin, A., Rees, M. J. 1997, ApJ, 475, 429
Meiksin, A. 2011, MNRAS, 417, 1480
Momjian, E., Carilli, C. L., Walter, F., Venemans, B. 2014, arXiv:1310.7960
Mortlock, D. J., et al. 2011, Nature, 2011, 1106
Shimabukuro, H., Ichiki, K., Inoue, S., Yokoyama, S. 2014, arXiv:1403.1605
Toma, K., Sakamoto, T., Mészáros, P. 2011, ApJ, 731, 127
Xu, Y., Chen, X., Fan, Z.,Trac, H., Cen, R. 2009, ApJ, 704, 1396
Xu, Y., Ferrara, A., Chen, X. 2011, MNRAS, 410, 2025

PoS(AASKA14)006

PROCEEDINGS OF SCIENCE

Epoch of Reionization modelling and simulations for SKA

Ilian T. Iliev*
Astronomy Centre, Department of Physics & Astronomy, Pevensey II Building, University of Sussex, Falmer, Brighton BN1 9QH, United Kingdom
E-mail: I.T.Iliev@sussex.ac.uk

Mario G. Santos
Department of Physics, University of Western Cape, Cape Town 7535, South Africa
SKA SA, 4rd Floor, The Park, Park Road, Pinelands, 7405, South Africa
CENTRA, Instituto Superior Técnico, Universidade de Lisboa, Lisboa 1049-001, Portugal
E-mail: mgrsantos@uwc.ac.za

Andrei Mesinger
Scuola Normale Superiore, Pisa, Italy
E-mail: andrei.mesinger@sns.it

Suman Majumdar, Garrelt Mellema
Department of Astronomy & Oskar Klein Centre, AlbaNova, Stockholm University, SE-106 91 Stockholm, Sweden
E-mail: smaju@astro.su.se,garrelt@astro.su.se

In this chapter we provide an overview of the current status of the simulations and modelling of the Cosmic Dawn and Epoch of Reionization. We discuss the modelling requirements as dictated by the characteristic scales of the problem and the SKA instrumental properties and the planned survey parameters. Current simulations include most of the relevant physical processes. They can follow the full nonlinear dynamics and are now reaching the required scale and dynamic range, although small-scale physics still needs to be included at sub-grid level. However, despite a significant progress in developing novel numerical methods for efficient utilization of current hardware they remain quite computationally expensive. In response, a number of alternative approaches, particularly semi-analytical/semi-numerical methods, have been developed. While necessarily more approximate, if appropriately constructed and calibrated on simulations they could be used to quickly explore the vast parameter space available. Further work is still required on including some physical processes in both simulations and semi-analytical modelling. This hybrid approach of fast, approximate modelling calibrated on numerical simulations can then be used to construct large libraries of reionization models for reliable interpretation of the observational data.

Advancing Astrophysics with the Square Kilometre Array
June 8-13, 2014
Giardini Naxos, Italy

*Speaker.

PoS(AASKA14)007

1. Introduction

The Cosmic Dark Ages, Cosmic Dawn and Epoch of Reionization, span altogether about a billion years between the CMB last scattering surface at redshift $z \sim 1100$ and the complete ionisation of hydrogen in the inter-galactic medium (IGM) at $z \sim 6$. This phase is quite distant from us and difficult to study, remaining one of the last poorly understood epochs of the Universe. During this time, the very first stars and galaxies formed, then gradually ionized the intergalactic medium and enriched it with metals, thereby laying the foundations for the cosmic structures we see today. Better knowledge of these epochs is therefore of key importance for understanding galaxy formation and evolution.

The main obstacle to further progress is the scarcity of observational data, which currently mostly probes the tail-end of reionization (both Ly-α source surveys and IGM absorption lines probe low neutral fractions, due to the high optical depth to resonant scattering of such radiation by even small amounts of neutral hydrogen) or are integral measures of its history (Cosmic Microwave Background, CMB, optical depth and polarization; kinetic Sunyaev-Zel'dovich effect, kSZ; Near Infrared Background, NIRB). The redshifted 21-cm signal promises to provide full 3D tomographic observations of the intergalactic medium throughout, and possibly even before reionization. The first generation of experiments, currently ongoing, will most likely provide just a statistical detection of the signal, e.g. power spectra, variance and/or probability distribution functions (PDFs) and their higher moments. In contrast, SKA should be able to also perform imaging and 3D mapping, as well as go much deeper in redshift, due to its far superior sensitivity, thereby completely transforming reionization research.

The shortage of observational constraints has meant that simulations have played and continue to play a larger role than in other areas, since we need to rely on modelling to understand even the basic properties of the expected signals. This in turn steers the design of the observational experiments targeted at this science. Furthermore, better understanding of the expected 21-cm signatures and their cross-correlations with other observations is important for reliably confirming any detection, since the signal is weak compared to the foregrounds which are several orders of magnitude stronger. Separating the signal and the foregrounds will not be trivial (see e.g. Chapman et al. 2015, reference: PoS(AASKA14)005) and subtraction may leave contaminating residuals mimicking the signal. The simulations will have a further important role to play in the interpretation of any detections. The reason for this is the disconnect in scales between the objects we want to study, i.e. the first galaxies, which are very small and faint, thus largely impossible to observe directly, and the actual 21-cm and other signals we will detect, which typically relate to large-scale patterns such as the reionization patchiness. The latter are caused by large number of clustered, individually dim sources. Therefore, the interpretation of any signals in terms of the nature and properties of the first galaxies is non-trivial and requires detailed modelling.

In recent years two basic approaches emerged in modelling the reionization patchiness - either by direct numerical simulations (e.g. Gnedin & Ostriker, 1997; Ciardi et al., 2000; Gnedin, 2000a; Ricotti, Gnedin & Shull, 2002; Iliev et al., 2006, 2014) or through semi-analytical/semi-numerical modelling (e.g. Furlanetto, Zaldarriaga & Hernquist, 2004; Zahn et al., 2007; Alvarez et al., 2009; Mesinger & Furlanetto, 2007a; Choudhury, Haehnelt & Regan, 2009; Santos et al., 2010; Battaglia et al., 2013), along with some intermediate methods involving simplified simula-

PoS(AASKA14)007

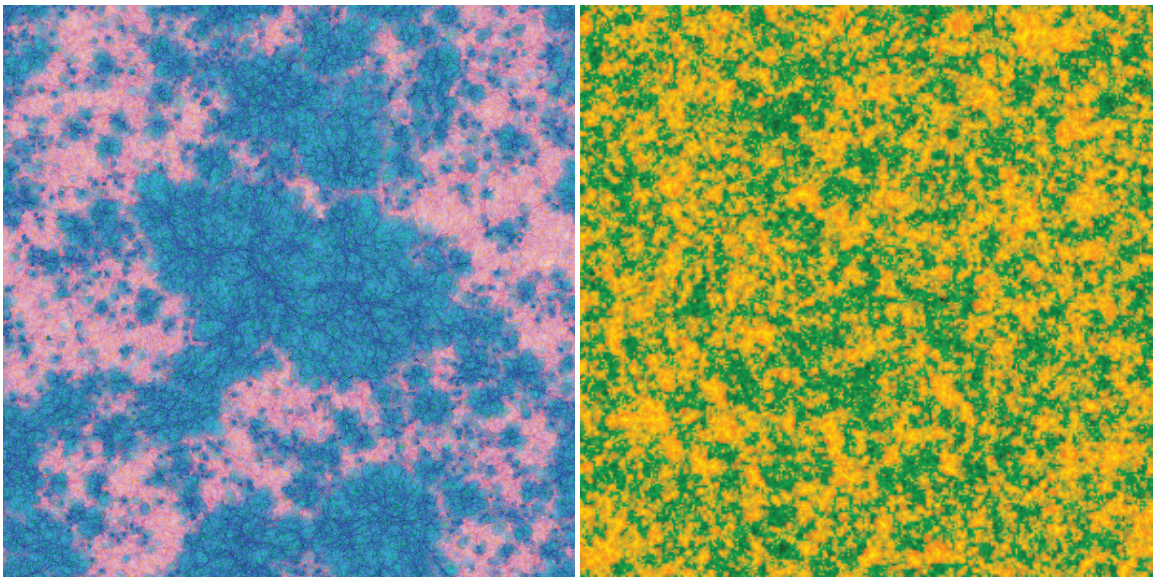

Figure 1: Spatial slices from radiative transfer simulations of reionization. Shown are the ionized (orange/blue) and neutral gas density (green/pink) at box-averaged ionized fractions by mass of $x_m \sim 0.4$ for (left) a small, high resolution volume ($47\,Mpc/h$, 612^3 radiative transfer grid) and a very large volume, comparable to the expected full FOV for SKA1-LOW ($500\,Mpc/h$, corresponding to $\sim 5^\circ \times 5^\circ$ on the sky, 250^3 grid) (Dixon et al., in prep.).

tions (Kohler, Gnedin & Hamilton, 2007; Thomas & et al., 2009). These different lines of attack are in practice highly complimentary and each has its advantages as well as disadvantages, as discussed in more detail in the next section.

2. Overview of current modelling

2.1 Radiative transfer simulations

The simulations of cosmic reionization fall in two broad types, as a consequence of the huge range of scales involved, which in practice cannot be covered in a single simulation on current computer hardware. The first type consists of small volume, high-resolution simulations which can be used to study in detail the formation of early galaxies and their radiative and supernova feedback on the gas with fully-coupled radiative hydrodynamic simulations. Such simulations cannot capture a large enough volume to represent the global reionization process or its observational signatures (e.g. Gnedin & Ostriker, 1997; Ciardi et al., 2000; Gnedin, 2000a; Ricotti, Gnedin & Shull, 2002). The second type consists of large-scale simulations, which instead follow volumes sufficiently large to study the global evolution, but lack resolution to directly resolve the small-scale physics (e.g. Iliev et al., 2006; Trac & Cen, 2007; Iliev et al., 2014) (see Figs. 1 and 2). This type of simulations decouple the radiative transfer, star formation and feedback processes from the underlying structure formation. The latter is done first, typically using large-scale N-body simulations, which is then followed up by detailed radiative transfer and non-equilibrium chemistry simulations. This approach allows for much larger dynamic range, and thus the larger volumes required for understanding the global reionization process and its observational signatures. In this

PoS(AASKA14)007

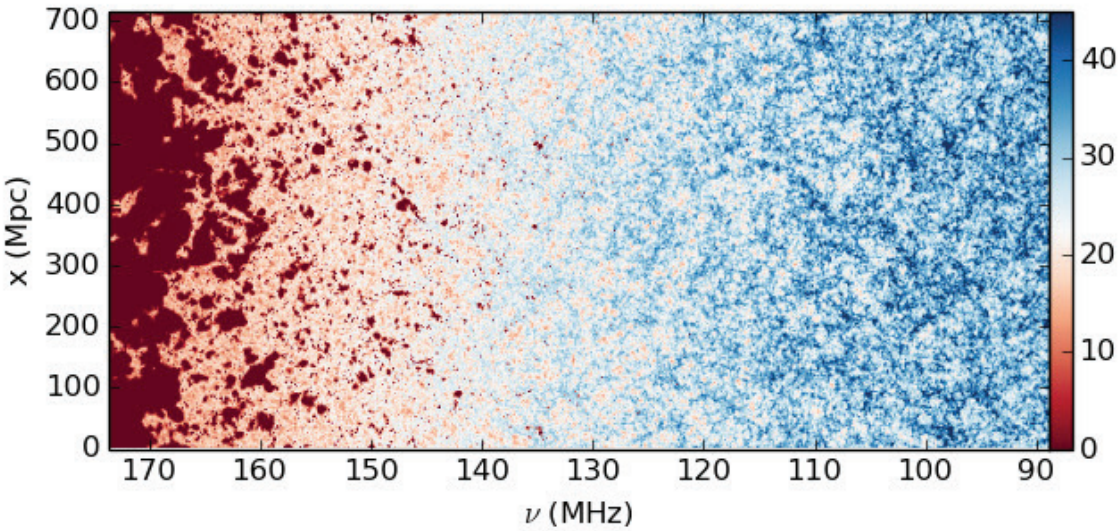

Figure 2: Space-frequency slice of the 21-cm emission from the intergalactic medium showing the evolution of the reionization geometry over time, from fully-neutral (blue) to mostly ionized (green). This is based in a radiative transfer simulation with 500 Mpc/h volume and 300^3 cells. The color shows the differential brightness temperature in mK at the full simulation resolution. (Dixon et al., in prep.)

case the detailed physical processes at unresolved scales have to be included using subgrid recipes, which are themselves based on high-resolution simulations or other modelling (e.g. Iliev et al., 2007; McQuinn et al., 2007; Ahn et al., 2012, 2014). Both types of simulations have played a major role in the significant recent advances in this area. We now have a good understanding of the characteristic scales of the process (Friedrich et al., 2011; Iliev et al., 2014), the physical processes affecting the patchiness and the various observational features which might help to discriminate between different EoR models (e.g. Wise & Abel, 2008; Baek et al., 2009; Ahn et al., 2012; Iliev et al., 2012; Alvarez & Abel, 2012; O'Leary & McQuinn, 2012; Park et al., 2013; Jensen et al., 2013; Sobacchi & Mesinger, 2014).

2.2 Semi-numerical simulations

Some of the early approaches to characterise the 21cm signal from the epoch of reionization have relied on more simple analytical models, mostly based on the excursion-set approach. These can be very useful to quickly generate the signal, in particular the power spectrum of 21-cm brightness temperature fluctuations (Furlanetto, Zaldarriaga & Hernquist, 2004; Furlanetto, McQuinn & Hernquist, 2006; Sethi, 2005). The speed and ease of use, allows for straightforward tests of the ability of a given experiment to constraint cosmological and astrophysical parameters (Santos & Cooray, 2006; McQuinn et al., 2006; Mao et al., 2008) and more generally to rapidly explore the vast parameter space available. The analytical models have also been useful to understand the possible contributions to the 21 cm signal at high redshifts (Barkana & Loeb, 2005; Pritchard, 2007), although it is at low redshifts ($z \lesssim 10$) that they seem to provide a better description of the 21-cm 2-point correlation function (Santos et al., 2008). However, these models have several issues in properly dealing with the spatial distribution of the reionization process, such as bubble overlap

PoS(AASKA14)007

and ignore complicated astrophysics during reionization. Such complexities are better handled in full (but expensive) numerical simulations, as was discussed above.

An intermediate approach that has become more popular are the so called semi-numerical 21cm simulations which try to merge the speed and ease of use of analytical models with the ability to follow the spatial evolution of reionization in more detail as provided by numerical simulations. The basic feature of these semi-numerical simulations is that they start from a random Gaussian field realization of the cosmological density field, or a full N-body simulation data, but then replace the time-consuming radiative transfer (RT) with an excursion-set approach (Furlanetto, Zaldarriaga & Hernquist, 2004) that determines if a region is ionized by comparing the number of ionizing photons to the number of atoms (plus recombinations) inside it. As in conventional cosmological RT simulations, this algorithm can be applied to discrete halo source fields, obtained either from traditional N-body simulations (e.g. Zahn et al., 2007; Choudhury, Haehnelt & Regan, 2009; Zahn et al., 2011) or through faster methods involving excursion-set formalism and perturbation theory (Mesinger & Furlanetto, 2007a; Santos et al., 2010; Mesinger, Furlanetto & Cen, 2011; Alvarez et al., 2009; Geil & Wyithe, 2008). The latter approach results in some reduction in accuracy (see Fig. 3; Zahn et al., 2011; Majumdar et al., 2014), but substantially increases the achievable dynamic range. Some of these approaches have also been extended to simulating the earlier epochs of the 21cm signal: the Cosmic Dawn/Dark Ages (Mesinger, Furlanetto & Cen, 2011; Santos et al., 2010). During the Dark Ages, the 21cm signal is governed by soft UV and X-ray photons, which can have mean free paths of hundreds of Mpc, requiring large volumes, which makes it a challenge to implement this in a complete radiative transfer/gas dynamics algorithm.

Semi-numerical simulations of reionization have been extensively tested against numerical simulations, with good agreement on moderate to large scales (>Mpc), relevant for most SKA science (Mesinger, Furlanetto & Cen, 2011; Zahn et al., 2011; Majumdar et al., 2014). The approximations start to break down however on non-linear scales, and care should be taken by comparing against more accurate methods when extending their application to any non-standard problems. Nevertheless, their speed and efficiency allows for rapid exploration of the large-parameter space of uncertainties, ushering in an exciting era of 21cm astrophysical parameter studies (e.g. Mesinger, Ewall-Wice & Hewitt, 2014; Pober et al., 2013).

The analysis of Zahn et al. (2011) has been largely focused on the comparison of the spherically average power spectrum of the 21-cm signal from different simulations. Their study suggested that these semi-numerical techniques can mimic the 21-cm power spectrum from that of a radiative transfer simulation with $\geq 70\%$ accuracy at length scales relevant for the present and future surveys. This study was extended in more recent works (Mesinger, Furlanetto & Cen, 2011; Majumdar et al., 2014) to include the comparison of EoR history, the redshift space anisotropies in the power spectrum and the morphology of the ionization fields (Fig. 3). Those analyses suggest that the halo based semi-numerical simulations can predict the history of EoR with an accuracy of $\geq 90\%$ when compared with radiative transfer simulations for length scales $k \leq 1.0\,\mathrm{Mpc}^{-1}$, whereas the same accuracy for the Press-Schechter based technique is $\geq 40\%$ at same length scale range. They have also shown that the anisotropies in the power spectrum of the 21-cm signal due to redshift space distortions can also be mimicked by both type of the semi-numerical simulations with an accuracy of 85% or more, which is well within the noise uncertainties of ~ 2000 hr LOFAR or ~ 1000 hr SKA1-LOW observation at 150 MHz, provided that the actual peculiar velocities are

PoS(AASKA14)007

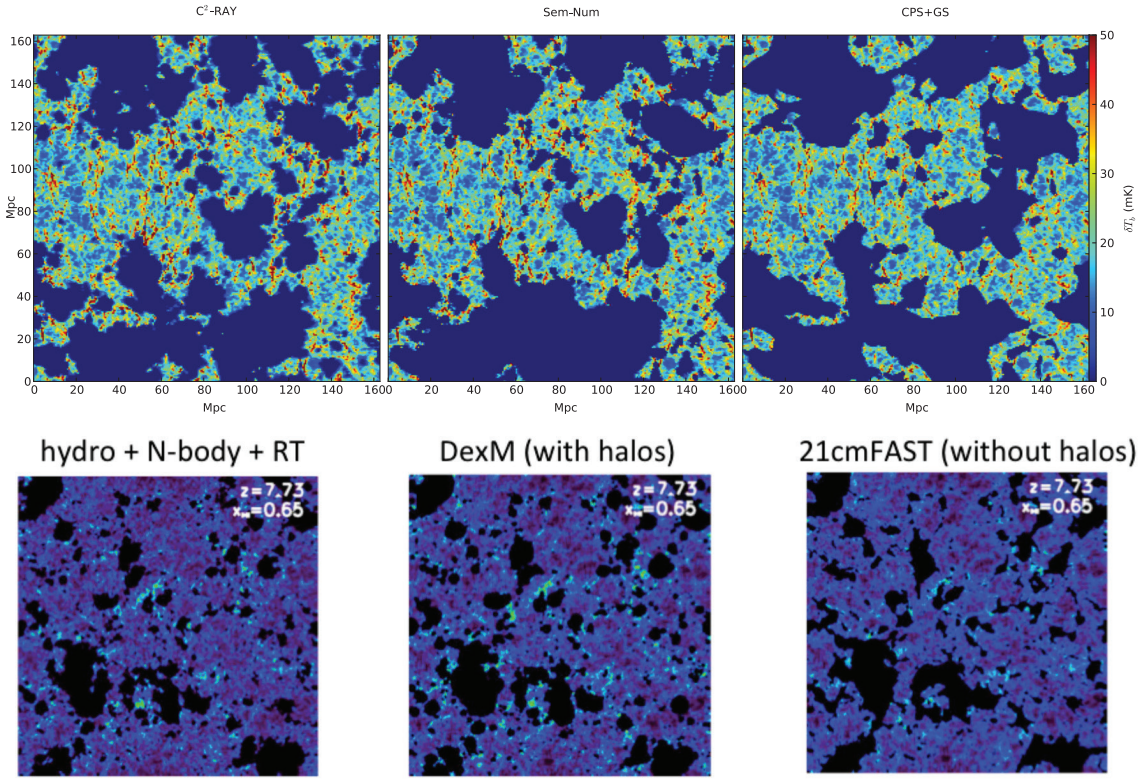

Figure 3: Reionization morphology through brightness temperature maps in redshift space for radiative transfer simulation (left) vs. two semi-numerical approaches - one which takes the halo positions into account (middle) and one that does not (right). For details see the original papers Majumdar et al. (2014) (top) and Mesinger, Furlanetto & Cen (2011) (bottom).

used to introduce the redshift space distortions rather than using a perturbative technique. It is also found that the cross-correlation between the ionization fields from the halo based semi-numerical technique and the radiative transfer simulations is more than 85% during almost the entire period of EoR, for length scales $k \leq 1.0\,\mathrm{Mpc}^{-1}$, whereas the same correlation between the conditional Press-Schechter formalism and the radiative transfer simulations, while good in some regimes, can reach values as low as $\sim 10\%$, specifically at late stages of EoR for the same length scale range.

These comparisons however, are also limited as the reionization scenario/model that has been compared in these cases is relatively simplistic in nature. The reionization history and the nature of the 21-cm signal from this epoch may differ depending on various other factors. One such important factor is the effect of radiative feedback on the star formation in low mass halos ($\leq 10^9\,\mathrm{M}_\odot$ in mass). This will most likely affect their star formation efficiency, although the details remain unclear (Couchman & Rees, 1986; Rees, 1986; Efstathiou, 1992; Thoul & Weinberg, 1995, 1996; Gnedin, 2000b; Kitayama et al., 2000; Dijkstra et al., 2004; Hoeft et al., 2006; Okamoto, Gao & Theuns, 2008). There has been some effort to include this in numerical (Iliev et al., 2007, 2012; Ahn et al., 2014) as well as in semi-numerical simulations (Sobacchi & Mesinger, 2013). Similarly, another such important issue is the effect of enhanced recombination in the Lyman Limit Systems and other small-scale structures, which are not resolvable in any of these simulations and

PoS(AASKA14)007

thus require detailed sub-grid modelling (Ciardi et al. 2006; Choudhury, Haehnelt & Regan 2009; Sobacchi & Mesinger 2014, Koda et al. in prep., Shukla et al., in prep.). Also, the effect of X-ray heating on the spin temperature evolution at the very early stages of reionization (Mesinger, Ferrara & Spiegel, 2013; Ghara, Choudhury & Datta, 2014) is another important factor which has not been included in these comparison studies.

3. SKA simulations

3.1 Basic Simulation Requirements

The volume and resolution required for proper numerical modelling of the reionization process are dictated by both its intrinsic characteristic scales (especially the typical sizes of ionized and neutral patches) and the instrumental parameters (FOV, beam size and bandwidth). The simulation volume should be large enough to faithfully sample all relevant scales, while the numerical resolution should be such that every beam/bandwidth is sampled with a sufficient number of elements so as to avoid discretization effects and other numerical artifacts.

The nominal SKA1-LOW Epoch of Reionization survey at the frequencies relevant for reionization is proposed to have FOV (FWHM) of ~ 3 (at $\nu = 200$ MHz) to 10 degrees (at $\nu = 50$ MHz), which corresponds to $\sim$ 500 Mpc-1.5 Gpc, with maximum resolution of $\sim$ 1 arcmin, or roughly 0.5 Mpc. Therefore simulations of the full SKA1-LOW FOV with sufficient resolution should have volume of at least 500 Mpc and grid sizes of at least several thousand cells per side. These simulation parameters are now just becoming achievable on current hardware. These are of course only very rough estimates and they only relate to the 21-cm sky maps and statistical studies (e.g. power spectra, or PDFs). For other purposes, for example 21-cm absorption studies against bright radio galaxies (see e.g. Ciardi et al. (2015) reference: PoS(AASKA14)006), a much higher simulation resolution will be required, corresponding to frequency channels of $\sim$ kHz, or cells of $\sim$ 10 kpc comoving. This is unrealistic when combined with $\sim$ 500 Mpc volumes unless adaptive-mesh refinement (AMR) techniques are employed, or else smaller simulation volumes have to be used for such work.

Apart from the purely instrumental requirements discussed above, the simulation parameters are also dictated by the characteristic scales of the reionization itself and the various processes that occur at different stages and will be of interest to study. Before the first UV sources form, the 21-cm fluctuations are dictated by the underlying density fluctuations, the temperature of the IGM, as well as additional effects like baryon-dark matter displacement (Tseliakhovich & Hirata, 2010, see also Maio et al. 2015, reference: PoS(AASKA14)009) and star formation suppression in minihaloes due to Lyman-Werner bands photons. Once the first ionizing sources appear, they propagate ionization fronts into the IGM initially forming small, local HII regions, which then quickly percolate and merge locally into larger ones. The same first sources also produce copious amounts of soft-UV radiation and likely some X-rays, which heat the IGM gas and decouple its spin temperature from the CMB, making it detectable. Outside dense regions/very high redshifts, the 21-cm line decoupling from the CMB also requires sufficiently strong Lyman-α background. All these different processes impose some characteristic scales on the 21-cm fluctuations. These are typically long-range modulations ranging from tens of Mpc (Lyman-α), to $\sim$ 100 Mpc (baryon-dark matter displacement

PoS(AASKA14)007

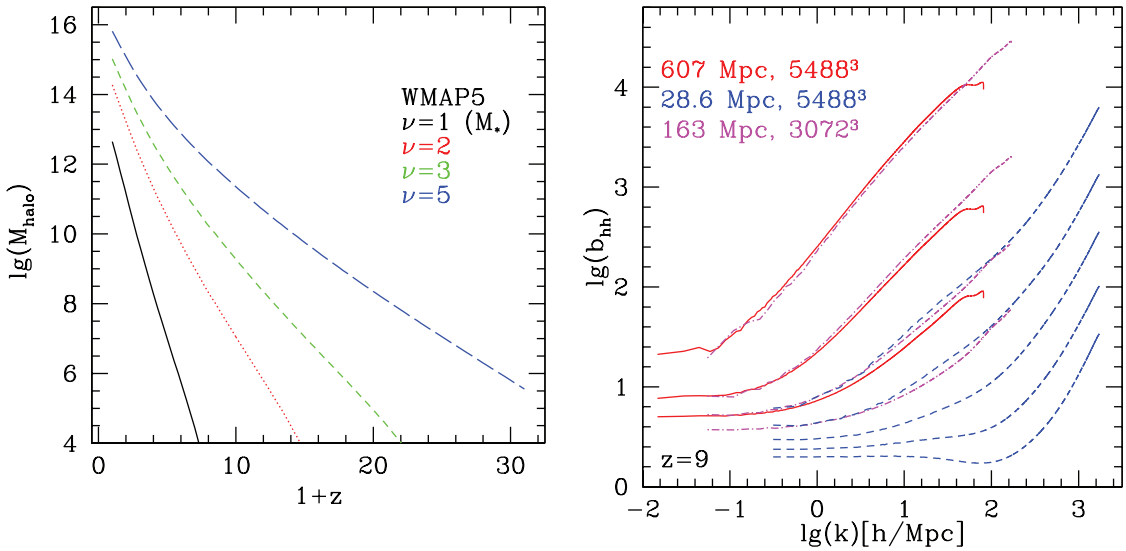

Figure 4: (left) How common are halos of different mass at high redshift? The lines show the mass vs redshift for $\nu - \sigma$ fluctuations in the Gaussian statistics, where $\nu = \delta_c/\sigma(z = 0, M) = 1$ (i.e. M*, typical halo; black, solid), $\nu = 2$ (red, dotted), $\nu = 3$ (green, short-dashed) and $\nu = 5$ (blue, long-dashed) (Iliev et al., 2012). (right) The halo bias, $b^2_{\rm hh} = \Delta_{\rm hh}/\Delta_\rho$, at redshift $z = 9$ for three cosmological volumes at different resolution, as labeled. Lines are for haloes binned by decades of mass (bottom to top curve) $10^5 M_\odot \leq M_{\rm halo} < 10^6 M_\odot$, $10^6 M_\odot \leq M_{\rm halo} < 10^7 M_\odot$, $10^7 M_\odot \leq M_{\rm halo} < 10^8 M_\odot$, $10^8 M_\odot \leq M_{\rm halo} < 10^9 M_\odot$, $10^9 M_\odot \leq M_{\rm halo} < 10^{10} M_\odot$, $10^{10} M_\odot \leq M_{\rm halo} < 10^{11} M_\odot$, $10^{11} M_\odot \leq M_{\rm halo} < 10^{12} M_\odot$, and $10^{12} M_\odot \leq M_{\rm halo}$.

and Lyman-Werner) and up to hundreds of Mpc (X-rays). Later-on, likely below redshift ~ 10 when the reionization becomes more widespread and is driven by larger, atomically-cooling halos, the 21-cm fluctuations due to these early backgrounds become less significant, baryon-dark matter displacement decreases and the dominant process determining the 21-cm fluctuations become the ionization patchiness. Its typical scales and geometry depend on the abundance and clustering of the main sources driving the process. Low-mass galaxies are exponentially more abundant, but are also liable to get their star formation suppressed by the Jeans mass filtering due to photoheating, as well as other radiative and mechanical feedback mechanisms. The details of these processes are still not firmly established and are currently the subject of active research.

The ionized regions growth continues throughout reionization (see Fig. 2 for an example). The characteristic patch sizes are dictated by the abundance, clustering and typical luminosities of the dominant ionizing sources, as well as various effects which modify the growth like recombinations in the IGM gas, Lyman-limit systems and other photon sinks. The intrinsic source clustering results from the statistics of the initial Gaussian random noise density fluctuations and depends strongly on redshift and the typical mass of the halos hosting the dominant sources. In ΛCDM the cosmological structures form hierarchically, with the smallest ones forming first and then growing and merging over time to form larger ones. Consequently, low-mass galaxies likely dominated the ionizing photon output throughout reionization. Figure 4 (left) shows the relative abundance of halos of different mass vs. redshift. At very high redshifts all halos are rare ($\nu \gg 1$) and only below redshift $z \sim 15$ the low-mass galaxies ($M = 10^8 - 10^{10} M_\odot$) become somewhat more common ($\nu = 2 - 3$).

PoS (AASKA14) 007

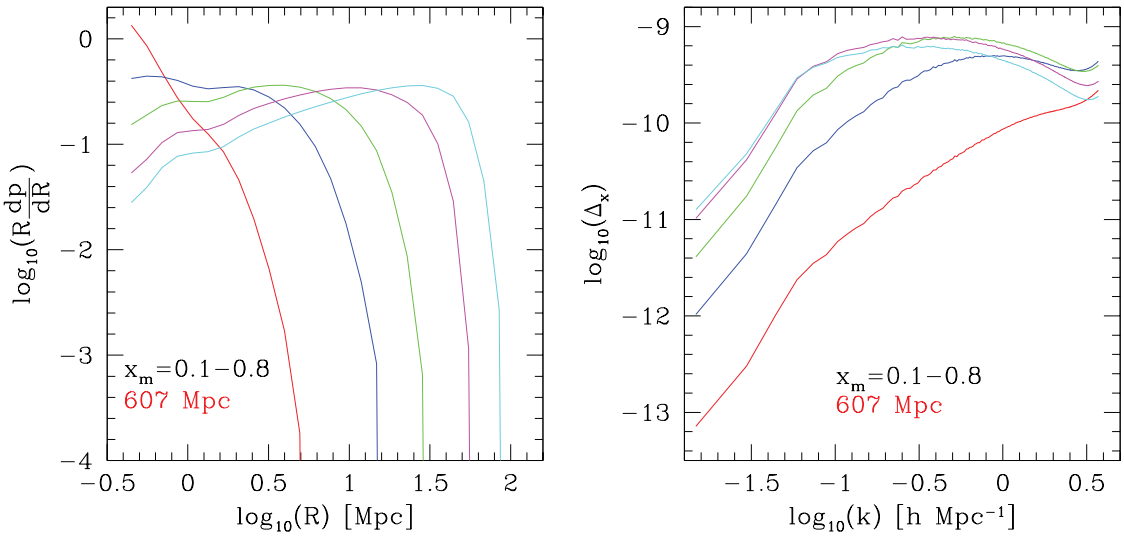

Figure 5: (left panel) Probability distribution function per logarithmic radial bin, $R\frac{dp}{dR}$, spherical regions with radius R as given by the Spherical Average method (Zahn et al., 2007) based on the ionized distribution given by a reionization simulation with volume of 607 Mpc and 504^3 grid (Iliev et al., 2014). Shown are results for different stages of the reionization process, for ionized fraction by mass $x_m = 0.1$ to 0.8 (left to right). (right panel) Dimensionless power spectra, Δ_x, of the volume-weighted ionized fraction, for H II regions extracted from the same reionization simulation and at the same EoR stages (bottom to top).

Consequently, these halos are strongly clustered, with bias with respect to the underlying mass distribution well above 1 (Figure 4, right). This strong clustering yields quick percolation of the individually small HII regions around each relatively weak source and thus the rapid growth to much larger scales. Furthermore, there is a notable power in the density fluctuations at fairly large scales, which required large simulation volumes to account for properly (Mesinger & Furlanetto, 2007b; Iliev et al., 2014). This additional power means that local photon output is modulated significantly, which is not modelled correctly in volumes smaller than about $\sim 100\,\mathrm{Mpc/h}$ per side, resulting in artificial suppression of the redshifted 21-cm fluctuations, among others. Different measures of the characteristic scales of the patchiness all yield typical peak sizes of tens of comoving Mpc (see Figure 5), which corresponds to tens of arcmin (see also Sobacchi & Mesinger, 2014). In summary, accurate modelling of all these physical processes again points to requirements of large, at least several hundred Mpc per side, volumes and sufficient resolution to reliably identify, either directly or sub-grid, the main sources and sinks driving the reionization process.

3.2 Computational Requirements

As mentioned above, reliable guidance and interpretation of the observations in terms of deriving the properties of the first galaxies requires the creation of large libraries of models sampling the available parameters space. At present a few full radiative transfer codes can be scaled up to the volumes and resolutions required for full SKA1 EoR simulation discussed in the previous section. This can only be achieved using massively-parallel approach (in some cases using accelerators like Graphical Processing Units, GPUs, and Intel Phi multicore processors) on the largest avail-

PoS(AASKA14)007

able computers and a single simulation of this size requires up to tens of millions of core-hours. Even with the expected advances in computing technology it is unlikely that a large number of such simulations could be practically performed. It is therefore most likely that more approximate methods like semi-numerical modelling would have to be employed, guided by fewer detailed full simulations.

Both approaches also require large amounts of data storage. The large N-body structure formation simulations (needed for precision and accuracy even in semi-numerical models, as explained in § 2.2), alone require up to several PB of storage per simulation, with further significant storage required for the reionization data itself. Accessing and using this data within the community will require also investment in databases and other efficient methods for data sharing.

4. Summary

We presented an overview of the current status and future prospects for simulations and modelling of the Epoch of Reionization, with focus on the specific requirements for SKA1-LOW. As discussed in detail, extensive modeling is particularly important for Cosmic Dawn and EoR science compared to other areas of study because as yet there is very limited direct observational data to guide us. Two basic approaches are available - full numerical simulations and semi-analytical/semi-numerical modeling. The simulations can handle the nonlinear dynamics, feedback effects and complex geometry, but are fairly computationally expensive. This drawback is being alleviated by innovative, efficient radiative transfer methods, some of which are able to efficiently utilise the latest Petascale computing facilities and specialist hardware (e.g. GPU accelerators). This now allows simulations which were impossible just a few years ago, with volumes and resolution matching both the intrinsic scales of the reionization process and the FOV and resolution expected for the SKA1 EoR experiment. Nonetheless, full simulations remain quite expensive and consequently a significant effort has been invested in the development of semi-numerical modelling and other faster modelling methods. These approaches are by nature more approximate, generally use simplified physics and are missing the non-linear effects. However, when they are carefully constructed they still can retain many of the key features, while at the same time introducing the option of constructing large libraries of models to be used for interpreting the data, which is not feasible for full simulations. Much additional work is still required on these models, as well as on the numerical simulations, particularly in adding important physical processes which are still missing and in calibration and verification of semi-analytical models against numerical simulations. We have also outlined the requirements for SKA1-LOW-specific simulations and provided estimates on the resources which will be required for this effort.

References

Ahn K., Iliev I. T., Shapiro P. R., Mellema G., Koda J., Mao Y., 2012, ApJL, 756, L16
Ahn K., Iliev I. T., Shapiro P. R., Srisawat C. B., 2014, ArXiv e-prints, 1407.2637
Alvarez M. A., Abel T., 2012, ApJ, 747, 126
Alvarez M. A., Busha M., Abel T., Wechsler R. H., 2009, ApJL, 703, L167
Baek S., di Matteo P., Semelin B., Combes F., Revaz Y., 2009, *A.&A*, 495, 389

PoS(AASKA14)007

Barkana R., Loeb A., 2005, ApJL, 624, L65
Battaglia N., Trac H., Cen R., Loeb A., 2013, ApJ, 776, 81
Choudhury T. R., Haehnelt M. G., Regan J., 2009, MNRAS, 394, 960
Ciardi B., Ferrara A., Governato F., Jenkins A., 2000, MNRAS, 314, 611
Ciardi B., Scannapieco E., Stoehr F., Ferrara A., Iliev I. T., Shapiro P. R., 2006, MNRAS, 366, 689
Couchman H. M. P., Rees M. J., 1986, MNRAS, 221, 53
Dijkstra M., Haiman Z., Rees M. J., Weinberg D. H., 2004, ApJ, 601, 666
Efstathiou G., 1992, MNRAS, 256, 43P
Friedrich M. M., Mellema G., Alvarez M. A., Shapiro P. R., Iliev I. T., 2011, MNRAS, 413, 1353
Furlanetto S. R., McQuinn M., Hernquist L., 2006, MNRAS, 365, 115
Furlanetto S. R., Zaldarriaga M., Hernquist L., 2004, ApJ, 613, 1
Geil P. M., Wyithe J. S. B., 2008, MNRAS, 386, 1683
Ghara R., Choudhury T. R., Datta K. K., 2014, ArXiv e-prints
Gnedin N. Y., 2000a, ApJ, 535, 530
Gnedin N. Y., 2000b, ApJ, 542, 535
Gnedin N. Y., Ostriker J. P., 1997, ApJ, 486, 581
Hoeft M., Yepes G., Gottlöber S., Springel V., 2006, MNRAS, 371, 401
Iliev I. T., Mellema G., Ahn K., Shapiro P. R., Mao Y., Pen U.-L., 2014, MNRAS, 439, 725
Iliev I. T., Mellema G., Pen U.-L., Merz H., Shapiro P. R., Alvarez M. A., 2006, MNRAS, 369, 1625
Iliev I. T., Mellema G., Shapiro P. R., Pen U.-L., 2007, MNRAS, 376, 534
Iliev I. T., Mellema G., Shapiro P. R., Pen U.-L., Mao Y., Koda J., Ahn K., 2012, MNRAS, 423, 2222
Jensen H. et al., 2013, MNRAS, 435, 460
Kitayama T., Tajiri Y., Umemura M., Susa H., Ikeuchi S., 2000, MNRAS, 315, L1
Kohler K., Gnedin N. Y., Hamilton A. J. S., 2007, ApJ, 657, 15
Majumdar S., Mellema G., Datta K. K., Jensen H., Choudhury T. R., Bharadwaj S., Friedrich M. M., 2014, ArXiv e-prints, arXiv:1403.0941
Mao Y., Tegmark M., McQuinn M., Zaldarriaga M., Zahn O., 2008, Phys Rev D, 78, 023529
McQuinn M., Lidz A., Zahn O., Dutta S., Hernquist L., Zaldarriaga M., 2007, MNRAS, 377, 1043
McQuinn M., Zahn O., Zaldarriaga M., Hernquist L., Furlanetto S. R., 2006, ApJ, 653, 815
Mesinger A., Ewall-Wice A., Hewitt J., 2014, MNRAS; arXiv:1310.0465
Mesinger A., Ferrara A., Spiegel D. S., 2013, MNRAS, 431, 621
Mesinger A., Furlanetto S., 2007a, ApJ, 669, 663
Mesinger A., Furlanetto S., 2007b, ApJ, 669, 663
Mesinger A., Furlanetto S., Cen R., 2011, MNRAS, 411, 955
Okamoto T., Gao L., Theuns T., 2008, MNRAS, 390, 920
O'Leary R. M., McQuinn M., 2012, ApJ, 760, 4
Park H., Shapiro P. R., Komatsu E., Iliev I. T., Ahn K., Mellema G., 2013, ApJ, 769, 93
Pober J. C., et al., 2013, The Astrophysical Journal Letters, 768, L36
Pritchard J. R., 2007, PhD thesis, California Institute of Technology
Rees M. J., 1986, MNRAS, 218, 25P
Ricotti M., Gnedin N. Y., Shull J. M., 2002, ApJ, 575, 33

PoS(AASKA14)007

Santos M. G., Amblard A., Pritchard J., Trac H., Cen R., Cooray A., 2008, ApJ, 689, 1
Santos M. G., Cooray A., 2006, Phys Rev D, 74, 083517
Santos M. G., Ferramacho L., Silva M. B., Amblard A., Cooray A., 2010, MNRAS, 406, 2421
Sethi S. K., 2005, MNRAS, 363, 818
Sobacchi E., Mesinger A., 2013, MNRAS, 432, 3340
Sobacchi E., Mesinger A., 2014, MNRAS, 440, 1662
Thomas R. M., et al., 2009, MNRAS, 393, 32
Thoul A. A., Weinberg D. H., 1995, ApJ, 442, 480
Thoul A. A., Weinberg D. H., 1996, ApJ, 465, 608
Trac H., Cen R., 2007, ApJ, 671, 1
Tseliakhovich D., Hirata C., 2010, Phys Rev D, 82, 083520
Wise J. H., Abel T., 2008, ApJ, 685, 40
Zahn O., Lidz A., McQuinn M., Dutta S., Hernquist L., Zaldarriaga M., Furlanetto S. R., 2007, ApJ, 654, 12
Zahn O., Mesinger A., McQuinn M., Trac H., Cen R., Hernquist L. E., 2011, MNRAS, 414, 727

PoS(AASKA14)007

PROCEEDINGS OF SCIENCE

SKA - EoR correlations and cross-correlations: kSZ, radio galaxies, and NIR background

Vibor Jelić[1,2]*, **Benedetta Ciardi**[3], **Elizabeth Fernandez**[1], **Hiroyuki Tashiro**[4], **Dijana Vrbanec**[3]

[1] *Kapteyn Astronomical Institute, University of Groningen, PO Box 800, 9700 AV Groningen, the Netherlands;*
[2] *ASTRON - the Netherlands Institute for Radio Astronomy, PO Box 2, 7990 AA Dwingeloo, the Netherlands;*
[3] *Max-Planck Institute for Astrophysics, Karl-Schwarzschild-Strasse 1, D-85748 Garching bei München, Germany;*
[4] *Department of Physics and Astrophysics, Nagoya University, Furocho, Chikusaku, Nagoya, 464-8602 Japan*

E-mail: vjelic@astro.rug.nl

The Universe's Cosmic Dawn (CD) and Epoch of Reionization (EoR) can be studied using a number of observational probes that provide complementary or corroborating information. Each of these probes suffers from its own systematic and statistical uncertainties. It is therefore useful to consider the mutual information that these data sets contain. In this paper, we discuss a potential of cross-correlations between the SKA cosmological 21 cm data with: (i) the kinetic Sunyaev-Zel'dovich (kSZ) effect in the CMB data; (ii) the galaxy surveys; and (iii) near infrared (NIR) backgrounds.

Advancing Astrophysics with the Square Kilometre Array
June 8-13, 2014
Giardini Naxos, Italy

*Speaker.

PoS(AASKA14)008

1. Introduction

Experiments designed to measure the redshifted 21 cm line from the Cosmic Dawn (CD) and Epoch of Reionization (EoR) are challenged by the strong astrophysical foreground contamination, ionospheric distortions, radio frequency interference and complex instrumental response. In order to reliably detect the cosmological signal from the observed data, it is essential to understand in detail all aspects of the experiment. For example, the cosmological signal has some characteristics which differentiates it from the foregrounds and noise. By use of proper statistics, it is possible to remove these components to extract signatures of reionization (see Chapman et al. 2014).

To alleviate some of the problems associated with the observations of the weak cosmological signal, several cross-correlation analyses with observations in other frequency windows have been proposed. In doing this, the noise/systematics in two observations of different frequencies and strategies may cancel out. Even if SKA may have a high enough sensitivity not to need cross-correlation techniques in order to detect the signal, cross-correlating with other probes will improve our understanding of the process of reionization (for an overview Mellema et al. 2013).

In this paper we present the potential of cross-correlation studies between the SKA cosmological 21 cm data, which reflects the neutral hydrogen content of the Universe as a function of redshift, with: (i) the kinetic Sunyaev-Zel'dovich (kSZ) effect in the Cosmic Microwave Background (CMB) data, produced by the scattering of CMB photons off free electrons produced during the reionization process (Sec. 2); (ii) galaxy surveys (Sec. 3); and (iii) the near infrared (NIR) backgrounds that reflect the primordial star formation (Sec. 4).

Throughout this study we consider three SKA configurations: early science SKA1-LOW, SKA1-LOW and SKA2-LOW. The SKA1-LOW (Dewdney et al. 2013) is our standard SKA configuration for the noise simulations, using the OSKAR simulator[1]. We assume full correlation between all 866 core stations of SKA1-LOW, where the maximum baseline length is 5.29 km. Baseline coordinates are generated for a 12-hour synthesis observation, with a 5-minute sampling interval. The noise is then re-normalised to reflect 1000 hours of integration. For early science SKA1-LOW we assume that the sensitivity is halved. For SKA2-LOW we assume that the sensitivity is quadrupled.

2. The Cross-Correlation with the kSZ

One of the leading sources of secondary anisotropies in the CMB is due to the scattering of CMB photons off free electrons (Zeldovich & Sunyaev 1969). The effect of anisotropies when induced by thermal motions of free electrons is called the thermal Sunyaev-Zel'dovich effect (tSZ) and when due to bulk motion of free electrons is called the kinetic Sunyaev-Zel'dovich effect (kSZ). The latter is far more dominant during reionization (for a review of secondary CMB anisotropies see, e.g. Aghanim et al. 2008).

The kSZ effect from a homogeneously ionized medium, i.e., with ionized fraction only as a function of redshift, has been studied both analytically and numerically by a number of authors; the linear regime of this effect was first calculated by Sunyaev & Zeldovich (1970) and subsequently revisited by Ostriker & Vishniac (1986) and Vishniac (1987) – hence also referred to as

[1] http://www.oerc.ox.ac.uk/ ska/oskar

PoS(AASKA14)008

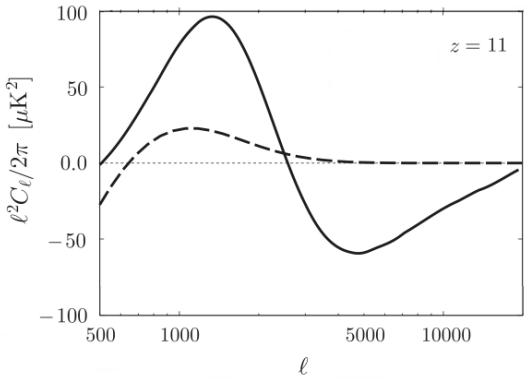

Figure 1: An example of the cross-power spectrum of the kSZ and the cosmological 21cm signal at $z = 11$. The solid line is for a 'patchy' reionization history, while the dashed line is for a 'homogenous' history. (Tashiro et al. 2011)

the Ostriker-Vishniac (OV) effect. In recent years various groups have calculated this effect in its non-linear regime using semi-analytical models and numerical simulations (Gnedin & Jaffe 2001; Santos et al. 2003; Zhang et al. 2004). These studies show that the contributions from non-linear effects are only important at small angular scales ($l > 1000$), while the OV effect dominates at larger angular scales.

The kSZ effect from patchy reionization was first estimated using simplified semi-analytical models by Santos et al. (2003), who concluded that it dominates over that of a homogeneously ionized medium. More detailed modeling of the effect of patchy reionization were subsequently performed using numerical simulations (Salvaterra et al. 2005; Iliev et al. 2007) and semi-analytical models (McQuinn et al. 2005; Zahn et al. 2005; Mesinger et al. 2012). Doré et al. (2007) used numerical simulations to derive the expected CMB polarization signals due to EoR patchiness. The CMB bolometric arrays Atacama Cosmology Telescope (ACT, Fowler et al. 2010) and South Pole Telescope (SPT, Shirokoff et al. 2011) are currently being used to measure the CMB anisotropies at the scales relevant to reionization ($3000 < \ell < 8000$). The SPT results are starting to put limits on the duration of reionization (Zahn et al. 2012).

Cross-correlation between the cosmological 21cm signal, as measured with SKA, and the secondary CMB anisotropies provide a potentially useful statistic. The cross-correlation has the advantage that the measured statistic is less sensitive to contaminants such as the foregrounds, systematics and noise in comparison to "auto-correlation" studies.

Analytical cross-correlation studies between the CMB temperature anisotropies and the EoR signal on large scales ($l \sim 100$) were carried out by Alvarez et al. (2006); Adshead & Furlanetto (2008); Lee (2009) and on small scales ($l > 1000$) by Cooray (2004); Salvaterra et al. (2005); Slosar et al. (2007); Tashiro et al. (2008, 2010, 2011). Cross-correlation between the E- and B-modes of CMB polarization with the redshifted 21cm signal was done by Tashiro et al. (2008); Dvorkin et al. (2009). Numerical studies of the cross-correlation were carried out by Salvaterra et al. (2005); Jelić et al. (2010).

These studies showed that the kSZ and the redshifted 21cm signal: (i) anti-correlate on the scales corresponding to the typical size of ionized bubbles; and (ii) correlate on the larger scales,

PoS(AASKA14)008

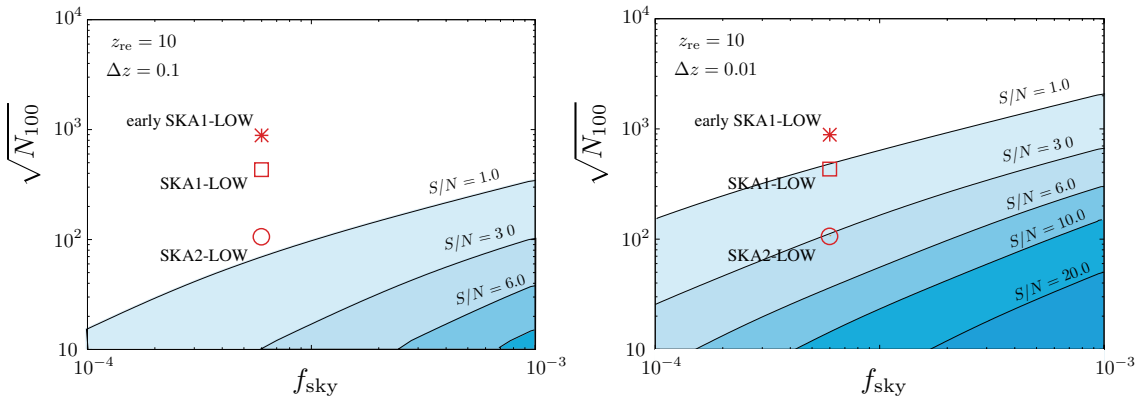

Figure 2: S/N of the 21cm cross-correlation with the kSZ for two different reionization models, defined with the redshift at which the ionized fraction equals 0.5 (z_{re}) and the reionization duration (Δz). The S/N is given as a function of the sky fraction and the normalised noise power spectrum. We assume 1000h of integration time with early SKA1-LOW, SKA1-LOW and SKA2-LOW and a field of view of 25 deg^2. For the CMB data we assume Planck sensitivity. (based on Tashiro et al. 2010)

where the patchiness of the ionization bubbles are averaged out (see Fig. 1). The significance of the anti-correlation signal depends on the reionization scenario (Salvaterra et al. 2005; Jelić et al. 2010; Tashiro et al. 2011).

The cross-correlation signal turns out to be difficult to detect (see Fig. 2). We might be able to make detection only with SKA2-LOW, assuming a very radical reionization duration of $\Delta z = 0.01$. If duration of reionization is longer, detection is not possible for all three SKA configurations. However, the kSZ signal induced during the EoR could possibly be detected in the power spectra of the CMB and used to place some additional constraints on this epoch in the history of our Universe.

3. The Cross-Correlation with Galaxy Surveys

Following Lidz et al. (2009), one can define the cross power spectrum between the 21cm emission and the galaxies as:

$$\begin{aligned}\Delta^2_{21,\mathrm{gal}}(k) &= \tilde{\Delta}^2_{21,\mathrm{gal}}(k)/\delta T_{b0} \\ &= x_{\mathrm{HI}}\left[\Delta^2_{x_{\mathrm{HI}},\mathrm{gal}}(k) + \Delta^2_{\rho,\mathrm{gal}}(k) \right. \\ &\quad \left. + \Delta^2_{\rho x_{\mathrm{HI}},\mathrm{gal}}(k)\right],\end{aligned} \tag{3.1}$$

where δT_{b0} is the 21cm brightness temperature relative to the CMB for neutral gas at the mean density of the universe, x_{HI} is the neutral fraction and $\Delta^2_{a,b}(k)$ is the dimensionless cross power spectrum between fields a and b. In order to construct the cross power spectrum, one therefore requires three fields, the density field (ρ), the neutral hydrogen field (x_{HI}), and the galaxy field (gal), which can be obtained via numerical simulations of galaxy formation and the reionization process.

It is found that the 21cm emission is initially correlated with galaxies on large scales, anti-correlated on intermediate scales, and uncorrelated on small scales. This picture quickly changes

PoS(AASKA14)008

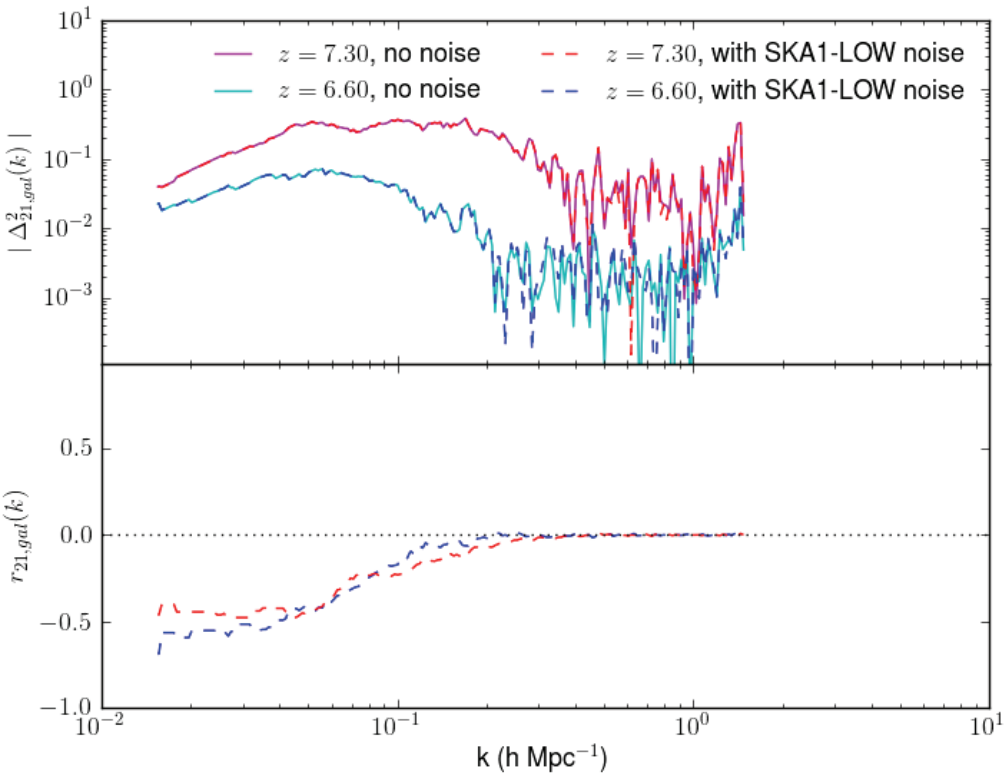

Figure 3: The circularly averaged, unnormalized 2D 21cm – galaxy cross power spectrum ($\tilde{\Delta}^2_{21,\mathrm{gal}}(k)$; and correlation coefficient for two redshifts. In the analysis we followed Wiersma et al. (2013).

as reionization proceeds and the two fields become anti-correlated on large scales (Lidz et al. 2009; Wiersma et al. 2013). These (anti-) correlations can be a powerful tool in indicating the topology of reionization and should form important diagnostic tools for SKA observations.

If the effect of observing and selecting real galaxies is taken into account, the result depends on the observational campaign considered. For example, for a drop-out technique (as in observations of Lyman Break Galaxies), the normalization of the cross power spectrum seems to be the most powerful tool for probing reionization. In particular, it is quite sensitive to the ionized fraction as different reionization histories yield similar cross power spectra for a fixed ionized fraction. When instead a more precise measurement of the galaxy redshifts is available (as in Ly-α Emitters surveys), which provides the three-dimensional position of the galaxy, much more information about the nature of reionization can be extracted, since the shape and the normalization of the cross power spectrum provide useful information. In addition, the observability of the Ly-α line from these galaxies is affected by neutral patches in the IGM and thus Ly-α Emitters surveys are particularly useful for EoR studies (McQuinn et al. 2007; Jensen et al. 2014).

Figure 3 shows the 21cm - Ly-α Emitters cross power spectrum (with and without SKA noise) and correlation coefficient for two redshifts. Here the noise assigned to the 21cm survey is the one

PoS(AASKA14)008

of the SKA telescope with SKA1-LOW configuration and noise for 1000 hours of integration time, while the Ly-α Emitters survey has the same characteristics of the one described in Jensen et al. (2014); Ouchi et al. (2010) with the Subaru telescope. As we can see, the 21cm - Ly-α Emitters cross power spectrum is not very sensitive to noise. Therefore, early SKA1-LOW and SKA2-LOW will show very similar results. The effect of neutral patches in the IGM on the observability of these Ly-α Emitters is not included here.

4. The Cross-Correlation with Near Infrared Backgrounds

Understanding star formation at high redshifts is fundamentally linked to our understanding of reionization history. In order for reionization to occur, a plentiful source of ionizing photons was needed. Stars are a likely candidate to produce these photons. Therefore, any attempt to understand reionization must be paired with an understanding of primordial star formation.

However, current observational constraints suggest that in order for the Universe to be reionized, a plentiful number of small galaxies beneath the detection limit of current surveys are most likely needed. Because they are so faint, it is difficult to obtain information about these galaxies directly. Instead, these galaxies can be observed using indirect means. For example, the cumulative light from these galaxies would be redshifted to the infrared, and therefore, any background in the infrared may provide clues to the nature of these galaxies. Many have suggested that the remnant light from these galaxies is indeed present in the excess emission in the Near Infrared Background (NIRB), and if this is true, looking at the mean intensity and the power spectrum of the NIRB can give information about these early stellar populations (e.g., Santos et al. 2002; Magliocchetti et al. 2003; Salvaterra & Ferrara 2003; Cooray 2004; Kashlinsky 2005; Fernandez & Komatsu 2006; Fernandez et al. 2010; Cooray et al. 2012; Fernandez et al. 2012; Kashlinsky et al. 2012; Fernandez & Zaroubi 2013; Yue et al. 2013).

On the other hand, 21cm emission originates from areas of neutral hydrogen, so it corresponds to regions that have not seen plentiful star formation and hence have not yet been ionized. Therefore, we should expect that regions that are bright in 21cm background emission should not be bright in the infrared. Conversely, regions that are bright in the infrared have plenty of star formation and therefore should be dim in the 21cm background. Because of this, these two observations should be anti-correlated.

In Fernandez et al. (2014), we predict the observational properties of both high redshift galaxies (which would be observable in the infrared) and the neutral regions that have yet to be ionized by galaxies (observable as part of the 21cm background). In order to do this, we combined large scale N-body simulations (Iliev et al. 2014), which included radiative transfer, with analytical models of the luminosities of the halos (Fernandez & Komatsu 2006). The brightness temperature of the 21cm background was also computed from the simulation, which depends on the density and neutral fraction of the IGM around the galaxies.

In Fernandez et al. (2014), we then produced simulated sky maps for both the 21cm emission and the emission in the infrared. These maps were created by combining the emission models and the simulation output to create luminosity cubes. These cubes were then randomly rotated and stacked along the line of sight to create a three dimensional cuboid. This was projected onto two dimensions to create a simulated sky map in both the radio and the infrared. In Fernandez et al.

PoS(AASKA14)008

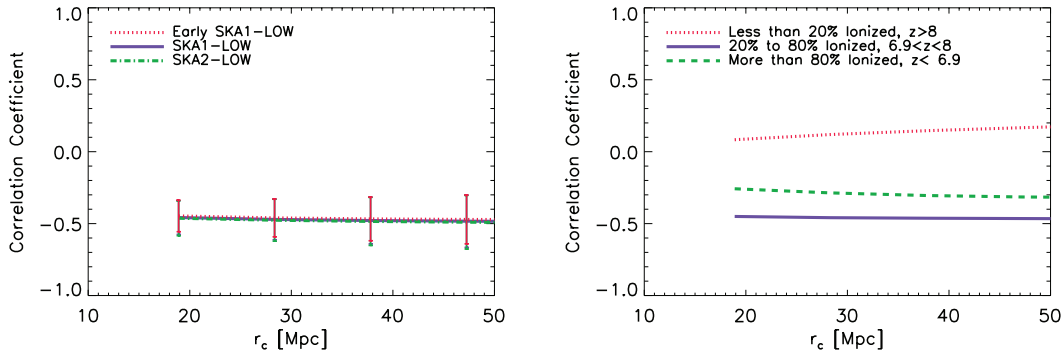

Figure 4: Left: The cross correlation of the entire NIRB against the 21cm background, assuming three SKA configurations with 1000h of integration time. The results do not depend heavily on noise levels, indicating that errors from unknowns in observation dominate over errors introduced from the noise. Right: The cross correlation at various redshifts: $6.4 < z < 7$, $7 < z < 8$, and $8 < z < 11$, assuming SKA1-LOW configuration.

(2014), we created sky maps specific for the LOFAR instrument; here, we present maps tailored for three SKA configurations: early science SKA1-LOW, SKA1-LOW and SKA2-LOW (assuming 1000h of integration).

For the radio map, since the 21cm background is line emission, each frequency corresponds to a different redshift, and observations can be adjusted to correspond to any arbitrary redshift range. On the other hand, since the emission in the infrared has a considerable amount of continuum, it is very difficult to extract redshift information for observations at any given wavelength. Therefore, the map in the infrared is created using the integrated light from a redshift of 6 to 30, or the entire simulation volume.

These two maps in the infrared and in the radio can then be cross-correlated using the Pearson correlation coefficient:

$$\rho_{21\mathrm{cm,NIRB}} = \frac{\mathrm{cov}((\delta T_\mathrm{b}), I_{NIRB})}{\sigma_{\delta T_\mathrm{b}} \sigma_{I_{NIRB}}}, \tag{4.1}$$

where I_{NIRB} is the intensity in the infrared and δT_b is the brightness temperature of the 21cm line. The results of this cross-correlation is shown in left panel of Fig. 4, which illustrates the cross-correlation between the integrated light from $6 < z < 30$ in the near-infrared against the entire 21cm map from $6.4 < z < 11$, assuming three SKA configurations. Error bars are generated from cross-correlating the 21cm emission with 1000 randomized maps in the infrared. The cross-correlation coefficient shows that these two maps are strongly anti-correlated, corresponding to the fact that the two emission maps are sensitive to emission from mutually exclusive areas. In addition, there is not a significant difference in result between Early SKA1-LOW, SKA1-LOW, and SKA2-LOW, indicating that the errors introduced from the noise is sub-dominant.

In addition, since the 21cm background is line emission, we can cross-correlate only specific slices of the 21cm background with the entire NIRB. Results of this for SKA1-LOW configuration are shown in the right panel of Fig. 4. The correlation coefficient is computed using radio maps for early ($z > 8$), mid ($6.9 < z < 8$) and late ($z < 6.9$) stages of reionization against the entire NIRB. The correlation coefficient is the most negative during mid stages of reionization. At early stages

PoS(AASKA14)008

of reionization, ionized bubbles around the host galaxies are too small, perhaps smaller than the smoothing length, and therefore no correlation is seen between the two maps. At late stages of reionization, most of the structure in the 21cm maps has disappeared.

5. Conclusions

In the view of presented results, cross-correlations with other probes will improve our understanding of the process of reionization. The cross-correlation with the galaxy surveys and NIR backgrounds will specifically help in answering the question which types of galaxies are mostly responsible for reionization. There is not a significant difference in results between Early SKA1-LOW, SKA1-LOW, and SKA2-LOW, indicating that the errors introduced from the noise is subdominant. Unfortunately, the cross-correlation signal in the case of the CMB turns out to be difficult to detect. There is only a possibility of detection in the case of a very short reionization scenario and using SKA2-LOW.

References

Adshead, P. J. & Furlanetto, S. R. 2008, MNRAS, 384, 291

Aghanim, N., Majumdar, S., & Silk, J. 2008, Reports on Progress in Physics, 71, 066902

Alvarez, M. A., Komatsu, E., Doré, O., & Shapiro, P. R. 2006, ApJ, 647, 840

Chapman, E., Bonaldi, A., Harker, G., Jelić, V., Abdalla, F., Bernardi, G., Bobin, J., Dulwich, F., Mort, B., Santos, M., & Starckh, J.-L. 2014, PoS(AASKA14)

Cooray, A. 2004, PhRvD, 70, 063509

Cooray, A., Gong, Y., Smidt, J., & Santos, M. G. 2012, ApJ, 756, 92

Dewdney, P., Turner, W., Millenaar, R., McCool, R., Lazio, J., & Cornwell, T. 2013, SKA-TEL-SKO-DD-001

Doré, O., Holder, G., Alvarez, M., Iliev, I. T., Mellema, G., Pen, U.-L., & Shapiro, P. R. 2007, PhRvD, 76, 043002

Dvorkin, C., Hu, W., & Smith, K. M. 2009, ArXiv e-prints

Fernandez, E. R., Iliev, I. T., Komatsu, E., & Shapiro, P. R. 2012, ApJ, 750, 20

Fernandez, E. R. & Komatsu, E. 2006, ApJ, 646, 703

Fernandez, E. R., Komatsu, E., Iliev, I. T., & Shapiro, P. R. 2010, ApJ, 710, 1089

Fernandez, E. R. & Zaroubi, S. 2013, MNRAS, 433, 2047

Fernandez, E. R., Zaroubi, S., Iliev, I. T., Mellema, G., & Jelić, V. 2014, MNRAS, 440, 298

Fowler, J. W., Acquaviva, V., Ade, P. A. R., Aguirre, P., Amiri, M., Appel, J. W., Barrientos, L. F., Battistelli, E. S., Bond, J. R., Brown, B., Burger, B., Chervenak, J., Das, S., Devlin, M. J., Dicker, S. R., Doriese, W. B., Dunkley, J., Dünner, R., Essinger-Hileman, T., Fisher, R. P., Hajian, A., Halpern, M., Hasselfield, M., Hernández-Monteagudo, C., Hilton, G. C., Hilton, M., Hincks, A. D., Hlozek, R., Huffenberger, K. M., Hughes, D. H., Hughes, J. P., Infante, L., Irwin, K. D., Jimenez, R., Juin, J. B., Kaul, M., Klein, J., Kosowsky, A., Lau, J. M., Limon, M., Lin, Y.-T., Lupton, R. H., Marriage, T. A., Marsden, D., Martocci, K., Mauskopf, P., Menanteau, F., Moodley, K., Moseley, H., Netterfield, C. B., Niemack, M. D., Nolta, M. R., Page, L. A., Parker, L., Partridge, B., Quintana, H., Reid, B., Sehgal, N., Sievers, J., Spergel, D. N., Staggs, S. T.,

PoS(AASKA14)008

Swetz, D. S., Switzer, E. R., Thornton, R., Trac, H., Tucker, C., Verde, L., Warne, R., Wilson, G., Wollack, E., & Zhao, Y. 2010, ApJ, 722, 1148
Gnedin, N. Y. & Jaffe, A. H. 2001, ApJ, 551, 3
Iliev, I. T., Mellema, G., Ahn, K., Shapiro, P. R., Mao, Y., & Pen, U.-L. 2014, MNRAS, 439, 725
Iliev, I. T., Pen, U.-L., Bond, J. R., Mellema, G., & Shapiro, P. R. 2007, ApJ, 660, 933
Jelić, V., Zaroubi, S., Aghanim, N., Douspis, M., Koopmans, L. V. E., Langer, M., Mellema, G., Tashiro, H., & Thomas, R. M. 2010, MNRAS, 402, 2279
Jensen, H., Hayes, M., Iliev, I., Laursen, P., Mellema, G., & Zackrisson, E. 2014, ArXiv e-prints
Kashlinsky, A. 2005, PhysRep, 409, 361
Kashlinsky, A., Arendt, R. G., Ashby, M. L. N., Fazio, G. G., Mather, J., & Moseley, S. H. 2012, ApJ, 753, 63
Lee, K. 2009, ArXiv e-prints
Lidz, A., Zahn, O., Furlanetto, S. R., McQuinn, M., Hernquist, L., & Zaldarriaga, M. 2009, ApJ, 690, 252
Magliocchetti, M., Salvaterra, R., & Ferrara, A. 2003, MNRAS, 342, L25
McQuinn, M., Furlanetto, S. R., Hernquist, L., Zahn, O., & Zaldarriaga, M. 2005, ApJ, 630, 643
McQuinn, M., Hernquist, L., Zaldarriaga, M., & Dutta, S. 2007, MNRAS, 381, 75
Mellema, G., Koopmans, L. V. E., Abdalla, F. A., Bernardi, G., Ciardi, B., Daiboo, S., de Bruyn, A. G., Datta, K. K., Falcke, H., Ferrara, A., Iliev, I. T., Iocco, F., Jelić, V., Jensen, H., Joseph, R., Labroupoulos, P., Meiksin, A., Mesinger, A., Offringa, A. R., Pandey, V. N., Pritchard, J. R., Santos, M. G., Schwarz, D. J., Semelin, B., Vedantham, H., Yatawatta, S., & Zaroubi, S. 2013, Experimental Astronomy, 36, 235
Mesinger, A., McQuinn, M., & Spergel, D. N. 2012, MNRAS, 422, 1403
Ostriker, J. P. & Vishniac, E. T. 1986, ApJL, 306, L51
Ouchi, M., Shimasaku, K., Furusawa, H., Saito, T., Yoshida, M., Akiyama, M., Ono, Y., Yamada, T., Ota, K., Kashikawa, N., Iye, M., Kodama, T., Okamura, S., Simpson, C., & Yoshida, M. 2010, ApJ, 723, 869
Salvaterra, R., Ciardi, B., Ferrara, A., & Baccigalupi, C. 2005, MNRAS, 360, 1063
Salvaterra, R. & Ferrara, A. 2003, MNRAS, 339, 973
Santos, M. G., Cooray, A., Haiman, Z., Knox, L., & Ma, C.-P. 2003, ApJ, 598, 756
Santos, M. R., Bromm, V., & Kamionkowski, M. 2002, MNRAS, 336, 1082
Shirokoff, E., Reichardt, C. L., Shaw, L., Millea, M., Ade, P. A. R., Aird, K. A., Benson, B. A., Bleem, L. E., Carlstrom, J. E., Chang, C. L., Cho, H. M., Crawford, T. M., Crites, A. T., de Haan, T., Dobbs, M. A., Dudley, J., George, E. M., Halverson, N. W., Holder, G. P., Holzapfel, W. L., Hrubes, J. D., Joy, M., Keisler, R., Knox, L., Lee, A. T., Leitch, E. M., Lueker, M., Luong-Van, D., McMahon, J. J., Mehl, J., Meyer, S. S., Mohr, J. J., Montroy, T. E., Padin, S., Plagge, T., Pryke, C., Ruhl, J. E., Schaffer, K. K., Spieler, H. G., Staniszewski, Z., Stark, A. A., Story, K., Vanderlinde, K., Vieira, J. D., Williamson, R., & Zahn, O. 2011, ApJ, 736, 61
Slosar, A., Cooray, A., & Silk, J. I. 2007, MNRAS, 377, 168
Sunyaev, R. A. & Zeldovich, Y. B. 1970, Astrophys. Space Sci., 7, 3
Tashiro, H., Aghanim, N., Langer, M., Douspis, M., & Zaroubi, S. 2008, MNRAS, 389, 469
Tashiro, H., Aghanim, N., Langer, M., Douspis, M., Zaroubi, S., & Jelic, V. 2010, MNRAS, 402, 2617

PoS(AASKA14)008

Tashiro, H., Aghanim, N., Langer, M., Douspis, M., Zaroubi, S., & Jelić, V. 2011, MNRAS, 414, 3424

Vishniac, E. T. 1987, ApJ, 322, 597

Wiersma, R. P. C., Ciardi, B., Thomas, R. M., Harker, G. J. A., Zaroubi, S., Bernardi, G., Brentjens, M., de Bruyn, A. G., Daiboo, S., Jelic, V., Kazemi, S., Koopmans, L. V. E., Labropoulos, P., Martinez, O., Mellema, G., Offringa, A., Pandey, V. N., Schaye, J., Veligatla, V., Vedantham, H., & Yatawatta, S. 2013, MNRAS, 432, 2615

Yue, B., Ferrara, A., Salvaterra, R., & Chen, X. 2013, MNRAS, 431, 383

Zahn, O., Reichardt, C. L., Shaw, L., Lidz, A., Aird, K. A., Benson, B. A., Bleem, L. E., Carlstrom, J. E., Chang, C. L., Cho, H. M., Crawford, T. M., Crites, A. T., de Haan, T., Dobbs, M. A., Doré, O., Dudley, J., George, E. M., Halverson, N. W., Holder, G. P., Holzapfel, W. L., Hoover, S., Hou, Z., Hrubes, J. D., Joy, M., Keisler, R., Knox, L., Lee, A. T., Leitch, E. M., Lueker, M., Luong-Van, D., McMahon, J. J., Mehl, J., Meyer, S. S., Millea, M., Mohr, J. J., Montroy, T. E., Natoli, T., Padin, S., Plagge, T., Pryke, C., Ruhl, J. E., Schaffer, K. K., Shirokoff, E., Spieler, H. G., Staniszewski, Z., Stark, A. A., Story, K., van Engelen, A., Vanderlinde, K., Vieira, J. D., & Williamson, R. 2012, ApJ, 756, 65

Zahn, O., Zaldarriaga, M., Hernquist, L., & McQuinn, M. 2005, ApJ, 630, 657

Zeldovich, Y. B. & Sunyaev, R. A. 1969, Astrophys. Space Sci., 4, 301

Zhang, P., Pen, U.-L., & Trac, H. 2004, MNRAS, 347, 1224

PoS(AASKA14)008

PROCEEDINGS OF SCIENCE

Bulk Flows and the End of the Dark Ages with the SKA

Umberto Maio[*1,2], **Benedetta Ciardi**[3], **Leon V. E. Koopmans**[4]

[1] *INAF – Osservatorio Astronomico di Trieste, via G. Tiepolo 11, Trieste, Italy; Marie Curie Fellow, E-mail:* maio@oats.inaf.it

[2] *Leibniz Institute for Astrophysics (AIP), An der Sternwarte 16, D-14482 Potsdam, Germany, E-mail:* umaio@aip.de

[3] *Max Planck Institute for Astrophysics, Karl-Schwarzshild-Straße 1, Garching b. Muenchen, Germany; E-mail:* ciardi@mpa-garching.mpg.de

[4] *Kapteyn Astronomical Institute of the University of Groeningen, Landleven 12, Groeningen, The Netherlands; E-mail:* koopmans@astro.rug.nl

The early Universe is a precious probe of the birth of primordial objects, first star formation events and consequent production of photons and heavy elements. Higher-order corrections to the cosmological linear perturbation theory predicts the formation of coherent supersonic gaseous streaming motions at decoupling time. These bulk flows impact the gas cooling process and determine a cascade effect on the whole baryon evolution. By analytical estimates and N-body hydrodynamical chemistry numerical simulations including atomic and molecular evolution, gas cooling, star formation, feedback effects and metal spreading for individual species from different stellar populations according to the proper yields and lifetimes, we discuss the role of these primordial bulk flows at the end of the dark ages and their detectable impacts during the first Gyr in view of the upcoming SKA mission. Early bulk flows can inhibit molecular gas cooling capabilities, suppressing star formation, metal spreading and the abundance of small primordial galaxies in the infant Universe. This can determine a delay in the re-ionization process and in the heating of neutral hydrogen making the observable HI signal during cosmic evolution patchier and noisier. The planned SKA mission will represent a major advance over existing instruments, since it will be able to probe the effects on HI 21-cm at $z \sim 6-20$ and on molecular line emissions from first collapsing sites at $z \sim 20-40$. Therefore, it will be optimal to address the effects of primordial streaming motions on early baryon evolution and to give constraints on structure formation in the first Gyr.

Advancing Astrophysics with the Square Kilometre Array
Giardini di Naxos, Sicily, Italy
June 8 - 13, 2014

[*]Speaker.

PoS(AASKA14)009

1. Introduction

The initial phases of the Universe are extremely interesting for modern astrophysics, because they are supposed to witness the birth of the first stars and galaxies. Features and details of the mechanisms leading to this event are still unknown and the properties of primordial generations are largely debated (Maio et al., 2011b; Biffi & Maio, 2013; de Souza et al., 2013, 2014; Wise et al., 2014). Primordial star formation processes determine the production of photons in different energy bands, marking the end of the dark ages and the start of the cosmic dawn. Ongoing feedback from stellar evolution impacts the following baryon history and cause the occurrence of the first heavy elements in the Universe. Such processes are crucial in the build-up of small primordial visible objects, such as gamma-ray-burst host galaxies (Campisi et al., 2011; Salvaterra et al., 2013; Ghirlanda et al., 2013; Maio & Barkov, 2014), gaseous damped Lyman-alpha absorption systems (Simcoe et al., 2012; Maio et al., 2013) and very early faint galaxies (Jeeson-Daniel et al., 2012; Dunlop et al., 2013; Ouchi et al., 2013; Maio & Viel, 2014).
In addition, the emission by atomic (Wouthuysen, 1952; Field, 1958; Bahcall & Ekers, 1969) and molecular (Shchekinov, 1986, 1991; Ciardi & Ferrara, 2001; Kamaya & Silk, 2002) lines in the pristine gas would be strongly dependent on the thermal state of the high-redshift (z) inter-galactic medium. This whole picture is affected by the properties of the initial perturbations that can leave their imprint in the infancy of primordial structures. Indeed, supersonic streaming motions are expected to be originated as a result of the relative velocities between dark matter and baryons following recombination, at $z \simeq 10^3$ (Tseliakhovich & Hirata, 2010). They are due to non-linear corrections to cosmological perturbation theory that predicts coherent gas motions on Mpc scales with typical velocities with a rms value of $\sim 30\,\mathrm{km/s}$. These bulk flows could be able to influence cosmic gas emission (McQuinn & O'Leary, 2012; Pritchard & Loeb, 2012) and star formation events at $z \sim 10-30$ (Maio et al., 2011a; Stacy et al., 2011; Greif et al., 2011; Maio & Iannuzzi, 2011; Fialkov, 2014), with possible consequences on the kinetic SZ effect and on the determination of the temperature-density equation of state (Dalal et al., 2010). Although direct observations are still very challenging and outside the possibilities of current facilities, they could be probed by the future Square Kilometre Array (SKA) (Carilli & Rawlings, 2004; Dewdney et al., 2013) that will detect radiative emissions by cosmic gas at redshift $z \sim 6-30$. At those epochs the Universe is largely pristine, dominated by H atoms that can form H_2 and HD and lead to gas cooling and collapse. Molecular-rich gas in dense regions is likely to emit through collisional excitations around ~ 533 GHz and such features can be used to identify the very first star forming sites. The following star formation processes would locally inject large amounts of entropy (e.g. Maio et al., 2013) and would produce energetic photons that will boost HI 21-cm (1.4 GHz) emission via Ly-α pumping, allowing the gas to be seen against the cosmic microwave background (Wouthuysen, 1952; Field, 1958; Madau et al., 1997; Wyithe & Loeb, 2003; Ciardi & Ferrara, 2001). The resulting temperature contrast in the optically thin limit depends on the optical depth, τ, which is a function of the neutral H fraction. Therefore, 21-cm analysis is a very suitable probe of the ages before reionization and can help place constraints on cosmic star formation, early galaxy evolution and on the implications of primordial bulk flows (Dalal et al., 2010; McQuinn & O'Leary, 2012; Visbal et al., 2012; Mellema et al., 2013). Given the fact that SKA will observe in different frequency ranges – between 50 MHz (SKA1-LOW) and 14 GHz (SKA1-MID) in Phase 1 and up to 24 GHz at 10

PoS(AASKA14)009

times larger sensitivity in Phase 2 – these radiative emissions will result within its instrumentational potential and, if detected, will represent a strong advancement for our theoretical understanding of primordial structures.
In the following, the impacts of baryon streaming motions for early gas emissions and structure formation will be outlined and the possibilities for the different frequency ranges of SKA will be discussed in more detail.

2. Streaming motions during the dark ages and perspectives for SKA

Streaming motions affect in the first place the primordial gas evolution, delaying its collapse and the subsequent star formation history. This is shown by *ad hoc* numerical simulations (Maio et al., 2011a) adopting a ΛCDM model with present-day geometrical parameters for total-matter, Λ, dark-matter and baryon density given by: $\Omega_{0,\mathrm{m}} = 0.3$, $\Omega_{0,\Lambda} = 0.7$, $\Omega_{0,\mathrm{dm}} = 0.26$, $\Omega_{0,\mathrm{b}} = 0.04$, and an expansion parameter at the present $H_0 = 100h\,\mathrm{km/s/Mpc}$ with $h = 0.7$. A simple way to take into account primordial bulk velocities in numerical simulations is to assume a velocity shift along the e.g. x-direction, $v_{\mathrm{b}x}$, given uniformly to each gas particle at initial time, according to magnitudes of $v_{\mathrm{b}x} = 0$, 30, 60 km/s at $z \simeq 1020$ – see (Naoz et al., 2011) for further studies. In this way we explore various streaming velocity scenarios by means of the numerical code Gadget (Springel, 2005), with subsequent modifications including: non-equilibrium cosmic chemistry (for e^-, H, H^+, H^-, He, He^+, He^{++}, H_2, H_2^+, D, D^+, HD, and HeH^+); stellar evolution of stars for different masses, metal yields (He, C, O, Mg, S, Si, Fe, N, etc.) and lifetimes (Maio et al., 2007; Tornatore et al., 2007; Maio et al., 2010); star formation led by H, He and H_2 radiative losses in pristine environments and by resonant or fine-structure metal transitions (such as CII 157.7 μm, SiII 34.8 μm, OI 145.5 and 63.18 μm, FeII 87.41, 51.28, 35.35, 25.99 μm) in enriched environments (Maio et al., 2007). Subsequent supernova and wind feedback are responsible for spreading heavy elements in the surrounding gas and for determining the transition from the primordial pristine (population III) star formation regime to the metal-enriched solar-like (population II-I) regime when a critical metallicity of $10^{-4}\,\mathrm{Z}_\odot$ is reached – see further details in Maio et al. (2010). Cosmic structures at different redshifts are identified by means of a friends-of-friends algorithm with a linking length of 20% the mean interparticle separation. For each object gas, dark and stellar properties are stored.

2.1 Implications for gas evolution

Fig. 1 displays the differential (left) and cumulative (right) distribution of gas clouds at redshift $z = 23$ (top) and 19 (bottom), corresponding to cosmic times of about 0.1 and 0.2 Gyr, respectively, in different parameter scenarios. They refer to four simulations run with initial conditions generated for a 0.5 Mpc/h-side box, sampling dark-matter and gaseous-matter fields with 2×320^3 particles and corresponding to a gas resolution of about 40 $\mathrm{M}_\odot$. A primordial spectral slope of $n = 1$ is assumed and the normalization is fixed by imposing $\sigma_8 = 0.9$. In order to test degeneracies with spectral parameters, results for a case of $\sigma_8 = 0.8$ are overplotted, as well. In general, streaming motions contribute in shaping the gaseous content and in lowering the typical clump masses and abundances. This is mostly evident at higher redshift when dark-matter haloes are smaller and the additional kinetic energy coming from the bulk flows make more difficult to trap the gas in the

PoS(AASKA14)009

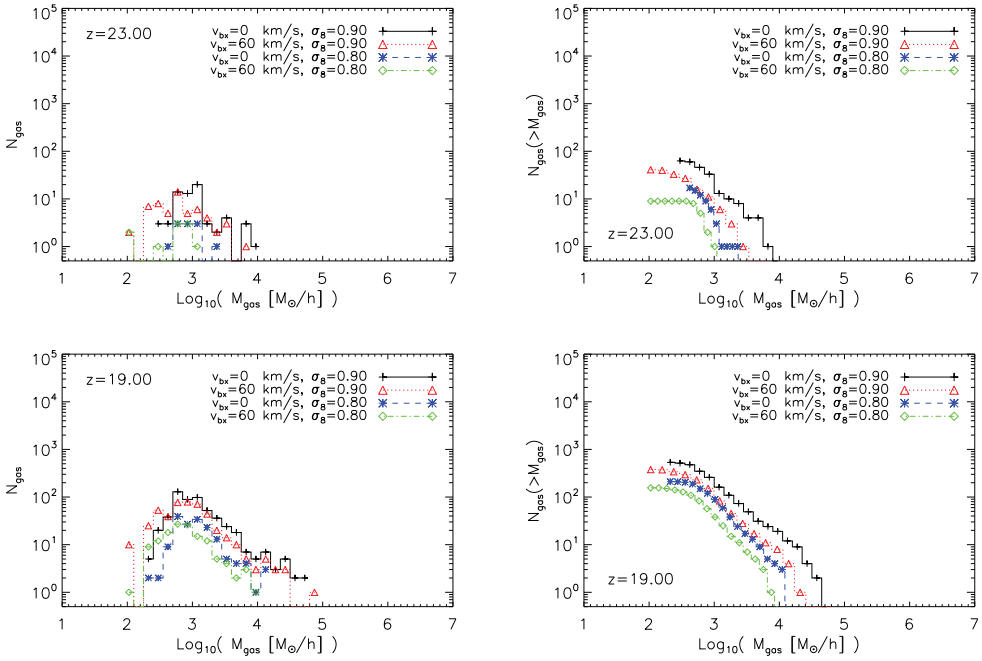

Figure 1: Expected differential (left column) and cumulative (right column) distributions for gas clouds at redshift $z = 23$ (top) and 19 (bottom). Data refer to simulations of $\sim$1 Mpc-size box run with different σ_8 and v_{bx}: $\sigma_8 = 0.9$ and $v_{bx} = 0\,\mathrm{km/s}$ (solid line and crosses); $\sigma_8 = 0.9$ and $v_{bx} = 60\,\mathrm{km/s}$ (dotted line and triangles); $\sigma_8 = 0.8$ and $v_{bx} = 0\,\mathrm{km/s}$ (dashed line and asterisks); $\sigma_8 = 0.8$ and $v_{bx} = 60\,\mathrm{km/s}$ (dot-dashed line and squares).

dark-matter potential wells. Panels referring to $z = 23$ highlight this effect very clearly. The differential distribution shows that, for any choice of σ_8, the $v_{bx} = 0\,\mathrm{km/s}$ case predicts larger and more abundant gaseous structures, while the $v_{bx} = 60\,\mathrm{km/s}$ scenario predicts typically lower-mass structures. This is due to the effects of bulk flows that cause gas evacuation from primordial objects. It is worth noting that the effects of streaming velocities is comparable to a significant decrease of σ_8 from 0.9 to 0.8. The overall changes of cosmic abundances are better displayed by the cumulative distribution at the same redshift. In the $v_{bx} = 0\,\mathrm{km/s}$ case variations in the high-mass tail of the number densities of up to 1 dex with respect to the limiting case of $v_{bx} = 60\,\mathrm{km/s}$ are reported. In the lower-mass end suppression of a factor of ~ 2 is visible. The slight excess of small clumps in the $v_{bx} > 0\,\mathrm{km/s}$ models is due to residual gas that collapses later with respect to the $v_{bx} = 0\,\mathrm{km/s}$ case. At later times, it is still possible to see similar trends, as shown in the $z = 19$ panels. There differences between different-v_{bx} models decrease slightly due to the simultaneous increase of typical dark-matter masses and the redshift decay of bulk flows. Thus, gas in-fall and collapse are less hindered. This leads to typical differences of a factor $\lesssim 2$ in the gas cloud differential distributions and of a factor of a few in the gas cloud cumulative distributions. The statistical behaviour shows a converging evolution of the gas cloud masses and abundances at later times ($z \sim 10-20$). At these epochs gas collapse is only marginally affected by primordial streaming motions (at $\sim 10\%$ level) and a major role is played by cosmological star formation and environments (see next). These trends suggest that the main effect on gas cloud evolution is a delay of the collapse redshift of $\Delta z \sim$

PoS(AASKA14)009

a few (corresponding to tens of Myr at the epoch of interest).
Since in these epochs there are no significant star formation events, yet, and forming structures are characterized by abundant pristine molecular gas, SKA could be able to detect H_2 and HD signatures from the first collapsing sites. E.g., H_2 $J = 2-0$ rotational transition and HD $J = 4-3$ rotational transition have rest-frame frequencies of 533.179 GHz and 533.388 GHz, respectively. During Phase 1 SKA1-MID will have frequency bands up to $\sim$ 14 GHz, hence observable (redshifted) signal from rare dense collapsing gas at very high redshift (around $z \sim 35-40$) will fall in the covered regime. However, the SKA operational range will reach 24 GHz in phase 2, and then SKA frequency bands will cover the frequencies of molecular lines emitted by cold gas clouds down to $z \gtrsim 20$. The emissivity of such lines should be detactable. Indeed, H_2 $J = 2-0$ emission is expected to be at level of $\sim 2\times10^{-7}$ Jy per each collapsing clump, while HD $J = 4-3$ line is expected to have a lower rate of $\sim 10^{-8}$ Jy (Kamaya & Silk, 2003). Roughly speaking, our theoretical estimates in Fig. 1 suggest a number of collapsing clumps ranging from some tens up to some thousands per Mpc^3 at $z \sim 23-19$, hence the total emissivity by a $\sim 1\,\mathrm{Mpc}^2$ patch (accounting for an area of $\vartheta \simeq 0.33\,\mathrm{deg}^2$ at $z \sim 19$)[1] should range from ~ 10 up to ~ 1000 times 2×10^{-7} Jy, i.e. $\sim 2-200\,\mu$Jy. Assuming field of view and sensitivity for SKA1-MID ($\Delta = 0.49\,\mathrm{deg}^2$ and $63\,\mu\mathrm{Jy}-\mathrm{hr}^{-1/2}$, respectively) the detectable emission turns out to be $\Delta/\vartheta = 0.49/0.33 \simeq 1.5$ times higher, i.e. around $\sim 3-300\,\mu$Jy. Therefore, the effects could be assessed by a-few-hours SKA1 observations of gas molecular lines. The signal should be more easily detected by SKA2-LOW that is going to have a 10-times better sensitivity in the $350-24000$ MHz frequency band.

2.2 Implications for star formation

After the condensation of first gas clumps, star formation processes start taking place and radiation from stars act on the thermodynamical state of the surrounding medium.
The top panel of Fig. 2 displays the effects of streaming motions on the whole cosmological star formation rate density and on the population III (pop III) contribution. In all the cases there is a cosmological effect on the trend and magnitude of the star formation activity. This suffers the delays in the gas collapse caused by streaming motions and shows a retarded onset for different v_{bx} values, up to $\Delta z \sim 3$. For the $v_{bx} = 0\,\mathrm{km/s}$ case the onset takes place at $z \simeq 20$, when the age of the Universe is about 0.17 Gyr, while for the cases including a velocity shift star formation kicks in at $z \simeq 19$ and $z \simeq 17.6$ for $v_{bx} = 30\,\mathrm{km/s}$ and $v_{bx} = 60\,\mathrm{km/s}$, respectively. The corresponding cosmological times are 0.19 Gyr, and 0.21 Gyr accounting for time delays of some ten Myr with respect to the $v_{bx} = 0\,\mathrm{km/s}$ case. Values for the star formation rate density differ at very early times of more than one order of magnitude and global trends show a converging behaviour only below $z \sim 14$, catching up at $z \lesssim 10$. The reason for this is related to gas cloud evolution that results delayed because of the higher kinetic energy gained at recombination. In larger-v_{bx} models, primordial mini-haloes can retain less material (see Fig. 1), the hosted gas condenses more slowly, molecule formation gets hindered, the consequent cooling is less efficient and the resulting star formation activity is delayed. This impacts mainly primordial haloes with masses $\sim 10^4 - 10^8$ M$_\odot$, as their dimensions are comparable to or smaller than the baryon Jeans length (Tseliakhovich &

[1] The (comoving) distance to $z \sim 19$ is about 10 Gpc, the corresponding angular separation of 1 (comoving) Mpc results to be 10^{-2} rad $\simeq 0.573$ deg and hence 1 Mpc^2 patch covers 0.33 deg^2. This is comparable to SKA1-MID resolution.

PoS(AASKA14)009

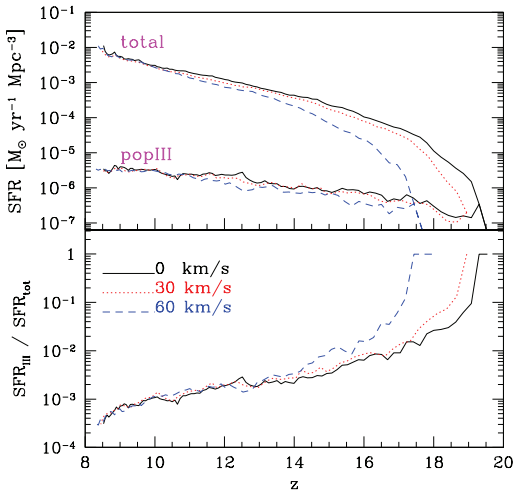

Figure 2: *Top panel:* Redshift evolution of the total cosmological star formation rate density and of the population III (pop III) star formation rate density for $v_{bx} = 0\,\mathrm{km/s}$ (solid lines), $v_{bx} = 30\,\mathrm{km/s}$ (dotted lines), $v_{bx} = 60\,\mathrm{km/s}$ (dashed lines). *Bottom panel:* Contribution of the pop III star formation regime ($\mathrm{SFR_{III}}$) to the cosmological star formation rate ($\mathrm{SFR_{tot}}$) for the different v_{bx} cases.

Hirata, 2010). Therefore, gas cannot fragment within the halo and partially or entirely flows out of it, as larger dark-matter potential wells would be needed to completely retain it. Basically, these processes start from small scales and cascade over the growth of larger objects suppressing gas condensation and subsequent star formation already before reionization. Photon production, feedback effects and the consequent occurrence of the first heavy elements in the Universe will be delayed, as well. This is better seen in the lower panel of Fig. 2 that highlights the contribution from the pristine pop III regime (whose evolution is dictated by ongoing metal production) to the cosmic star formation rate. It is evident that for larger v_{bx} the transition from the primordial pop III era to the metal-enriched pop II-I one takes place at later times due to the impacts of early bulk flows. At later times ($z \lesssim 10$) the trends converge and the imprints of the initial dynamical patterns are more difficult to recognize.

2.3 Implications for 21-cm signal

A valuable observable to investigate the cosmological response of baryons at the end of the dark ages ($z \sim 6-20$) is 21-cm signal from HI. This falls in the frequency range covered by SKA1-LOW ($50-350$ MHz), that could possibly map at a $3-\sigma$ level neutral gas from the dark ages and cosmic dawn until full re-ionization at $z \sim 6$ (Mellema et al., 2013).
The expected signal is usually described in terms of differential brightness temperature, δT_b, the extent of which depends mainly on the ionization and thermodynamical state of the (partially) neutral gas. The effect on star formation caused by primordial streaming motions will impact δT_b in different ways. In particular, by delaying the onset of star formation streaming motions would also shift the beginning of the re-ionization process towards lower redshift (i.e. higher frequencies), while by suppressing or reducing star formation within small mass halos they would

PoS(AASKA14)009

change the topology of re-ionization. As a consequence, an impact on the 21-cm signal is also expected. Semi-analytical arguments extrapolated to $\sim 100\,\mathrm{Mpc}$ scales (Dalal et al., 2010; Visbal et al., 2012; McQuinn & O'Leary, 2012; Ali-Haïmoud et al., 2014) suggest $v_{\mathrm{b}x}$ implications on the 21-cm signal from comoving distances of the order of $\sim 100\,\mathrm{kpc}$ (Visbal et al., 2012; McQuinn & O'Leary, 2012) down to $\sim 10\,\mathrm{kpc}$ (McQuinn & O'Leary, 2012; Ali-Haïmoud et al., 2014), with an overall effect on δT_{b} ranging from $\sim 2\,\mathrm{mK}$ (Dalal et al., 2010) to $\sim 10\,\mathrm{mK}$ (Visbal et al., 2012). On the other hand, implications from structure formation shocks can contribute at $\lesssim 10\%$ level, while enhancements to the ionization fraction due to X-rays, albeit very uncertain, seem to be negligible or almost irrelevant (e.g. McQuinn & O'Leary, 2012).
We finally note that the scenario commonly adopted for these estimates relies on standard cold dark matter, however, comparable or even larger suppressions of cosmic structure evolution might arise in presence of alternative background models, such as warm dark matter (see e.g. Maio & Viel, 2014, and references therein), non-Gaussian matter distributions (Maio & Iannuzzi, 2011; Maio et al., 2012; Maio & Khochfar, 2012; Pace & Maio, 2014) or early dark energy (Maio et al., 2006).

3. Conclusions

Higher-order corrections (Tseliakhovich & Hirata, 2010) to the cosmological linear perturbation theory predict the formation of coherent supersonic gaseous streaming motions at decoupling. These are relevant for primordial gas condensation, the birth of the first stars and the build-up of the lowest-mass objects and proto-galaxies. In view of the upcoming SKA, we have discussed the implications of such bulk flows via numerical N-body hydrodynamical chemistry simulations (Maio et al., 2011a) of early structure formation taking into account non-equilibrium cosmic chemistry, gas cooling (Maio et al., 2007), stellar evolution of stars for different masses, metal yields (He, C, O, Mg, S, Si, Fe, N, etc.) and lifetimes (Maio et al., 2007; Tornatore et al., 2007) and the transition (Maio et al., 2010) from the primordial pristine pop III star formation regime to the metal-enriched solar-like pop II-I. Primordial gas streaming motions can suppress gas collapse, with consequent delay of cosmological star formation, feedback effects, metal spreading and cosmic re-ionization. Their impacts on gas clouds are particularly evident at $z \sim 15-30$, when number densities and typical gas content in primordial haloes result lowered of up to a factor of 10. Hence, they affect molecular H_2 and/or HD emissions from overdense gaseous regions that will be observable by SKA1-MID. Subsequently, bulk flows delay star formation, metal pollution and feedback mechanisms of $\Delta z \sim$ a few at $z \sim 10-20$, influencing the cosmic HI thermal and chemical state, and making the 21-cm signal at the end of the dark ages patchier and noisier. The next SKA mission will represent a major advance over existing instruments, since it will be able to detect HI 21-cm (e.g. SKA1-LOW at $50-350\,\mathrm{MHz}$) and molecular-line (e.g. SKA1-MID up to $14-24\,\mathrm{GHz}$ in phase 1 – 2) emissions from early star forming sites at $z \sim 6-40$ (SKA2-LOW). Therefore, it will be possible to address the effects of primordial streaming motions on early baryon evolution and to give constraints on structure formation in the first Gyr.

References

Ali-Haïmoud, Y., Meerburg, P. D., & Yuan, S. 2014, Phys. Rev. D, 89, 083506

PoS(AASKA14)009

Bahcall, J. N., & Ekers, R. D. 1969, ApJ, 157, 1055
Biffi, V., & Maio, U. 2013, MNRAS, 436, 1621
Carilli, C. L., & Rawlings, S. 2004, New Astronomy Reviews, 48, 979
Campisi, M. A., Maio, U., Salvaterra, R., & Ciardi, B. 2011, MNRAS, 416, 2760
Ciardi, B., & Ferrara, A. 2001, MNRAS, 324, 648
Ciardi, B., & Madau, P. 2003, ApJ, 596, 1
Dalal, N., Pen, U.-L., & Seljak, U. 2010, J. of Cosm. and Astrop. Phys., 11, 7
de Souza, R. S., Ciardi, B., Maio, U., & Ferrara, A. 2013, MNRAS, 428, 2109
de Souza, R. S., Maio, U., Biffi, V., & Ciardi, B. 2014, MNRAS, 440, 240
Dewdney, P., Turner, W., Millenaar, R., McCool, R.,Lazio, J., Cornwell, T., 2013, "SKA1 System Baseline Design", Document number SKA—TEL—SKO—DD—001, Revision 1
Dunlop, J. S., Rogers, A. B., McLure, R. J., et al. 2013, MNRAS, 432, 3520
Fialkov, A. 2014, International Journal of Modern Physics D, 23, 1430017
Field, G. B. 1958, Proceedings of the IRE, 46, 240
Ghirlanda, G., Salvaterra, R., Burlon, D., et al. 2013, MNRAS, 435, 2543
Greif, T. H., White, S. D. M., Klessen, R. S., & Springel, V. 2011, ApJ, 736, 147
Jeeson-Daniel, A., Ciardi, B., Maio, U., et al. 2012, MNRAS, 424, 2193
Kamaya, H., & Silk, J. 2002, MNRAS, 332, 251
Kamaya, H., & Silk, J. 2003, MNRAS, 339, 1256
Loeb, A., & Zaldarriaga, M. 2004, Physical Review Letters, 92, 211301
Madau, P., Meiksin, A., & Rees, M. J. 1997, ApJ, 475, 429
Maio, U., Dolag, K., Meneghetti, M., et al. 2006, MNRAS, 373, 869
Maio, U., Dolag, K., Ciardi, B., & Tornatore, L. 2007, MNRAS, 379, 963
Maio, U., Ciardi, B., Dolag, K., Tornatore, L., & Khochfar, S. 2010, MNRAS, 407, 1003
Maio, U., Koopmans, L. V. E., & Ciardi, B. 2011, MNRAS, 412, L40
Maio, U., Khochfar, S., Johnson, J. L., & Ciardi, B. 2011, MNRAS, 414, 1145
Maio, U., & Khochfar, S. 2012, MNRAS, 421, 1113
Maio, U., Salvaterra, R., Moscardini, L., & Ciardi, B. 2012, MNRAS, 426, 2078
Maio, U., Ciardi, B., Mueller, V. 2013, MNRAS, 435, 1443
Maio, U., Dotti, M., Petkova, M., Perego, A., & Volonteri, M. 2013, ApJ, 767, 37
Maio, U., & Barkov, M. V. 2014, MNRAS, 439, 3520
Maio, U., & Iannuzzi, F. 2011, MNRAS, 415, 3021
Maio, U., & Viel, M. 2015, MNRAS, 446, 2760
McQuinn, M., & O'Leary, R. M. 2012, ApJ, 760, 3
Mellema, G., Koopmans, L. V. E., Abdalla, F. A., et al. 2013, Exp. Astr., 36, 235
Mesinger, A., Ewall-Wice, A., & Hewitt, J. 2014, MNRAS, 439, 3262
Naoz, S., Yoshida, N., & Barkana, R. 2011, MNRAS, 416, 232
Ouchi, M., Ellis, R., Ono, Y., et al. 2013, ApJ, 778, 102
Pace, F., & Maio, U. 2014, MNRAS, 437, 1308
Petkova, M., & Maio, U. 2012, MNRAS, 422, 3067
Pritchard, J. R., & Loeb, A. 2012, Reports on Progress in Physics, 75, 086901
Salvaterra, R., Maio, U., Ciardi, B., & Campisi, M. A. 2013, MNRAS, 429, 2718
Shchekinov, Y. A. 1986, Pisma v Astronomicheskii Zhurnal, 12, 499

PoS(AASKA14)009

Shchekinov, I. 1991, Ap&SS, 175, 57
Simcoe, R. A., Sullivan, P. W., Cooksey, K. L., et al. 2012, Nature, 492, 79
Springel, V. 2005, MNRAS, 364, 1105
Stacy, A., Bromm, V., & Loeb, A. 2011, ApJ, 730, L1
Tornatore, L., Borgani, S., Dolag, K., & Matteucci, F. 2007, MNRAS, 382, 1050
Tseliakhovich, D., & Hirata, C. , 2010, Phys. Rev. D, 82, 083520
Visbal, E., Barkana, R., Fialkov, A., Tseliakhovich, D., & Hirata, C. M. 2012, Nature, 487, 70
Wise, J. H., Demchenko, V. G., Halicek, M. T., et al. 2014, arXiv:1403.6123
Wouthuysen, S. A. 1952, AJ, 57, 31
Wyithe, J. S. B., & Loeb, A. 2003, ApJ, 586, 693

PoS(AASKA14)009

PROCEEDINGS OF SCIENCE

HI tomographic imaging of the Cosmic Dawn and Epoch of Reionization with SKA

Garrelt Mellema[*,1] **León Koopmans,**[2], **Hemant Shukla,**[3], **Kanan K. Datta,**[4], **Andrei Mesinger**[5], **Suman Majumdar**[1] **on behalf of the CD/EoR Science Working Group**

[a]Dept. of Astronomy & Oskar Klein Centre, Stockholm University, AlbaNova, SE-10691 Stockholm, Sweden; [b]Kapteyn Astronomical Institute, Universiity of Groningen, P.O. Box 9000, 9700 AA Groningen, The Netherlands; [c]Astronomy Centre, Department of Physics & Astronomy, Pevensey II Building, University of Sussex, Falmer, Brighton BN1 9QH, UK; [d]National Centre For Radio Astrophysics, Post Bag 3, Ganeshkhind, Pune 411 007, India; [e]Scuola Normale Superiore, Piazza dei Cavalieri 7, I-56126 Pisa, Italy

E-mail: garrelt@astro.su.se

We provide an overview of 21cm tomography of the Cosmic Dawn and Epoch of Reionization as possible with SKA-Low. We show why tomography is essential for studying CD/EoR and present the scales which can be imaged at different frequencies for the different phases of SKA-Low. Next we discuss the different ways in which tomographic data can be analyzed. We end with an overview of science questions which can only be answered by tomography, ranging from the characterization of individual objects to understanding the global processes shaping the Universe during the CD/EoR.

Advancing Astrophysics with the Square Kilometre Array
June 8-13, 2014
Giardini Naxos, Italy

[*]Speaker.

PoS(AASKA14)010

1. Introduction

SKA1-Low will provide enough sensitivity to deliver an image signal to noise larger than 1 for signals of order 1 mK on scales of a few arcminutes for a combination of bandwidth and integration time $Bt \approx 1000$ MHz hrs. This capability allows imaging of the redshifted 21cm signal from the Epoch of Reionization on these angular scales. SKA1-Low will be the first interferometer that will be able to do this as the precursors LOFAR, MWA and PAPER have at least an order of magnitude less sensitivity and thus can only hope to characterize the signals statistically, for example through the value of the 21cm power spectrum at certain scales or the variance of the signal at all observable scales or higher-order statistics such as skewness and kurtosis.

This chapter which forms part of the set of chapters from the Cosmic Dawn/Epoch of Reionization section of this volume discusses this imaging capability of SKA1-Low and how it can be used to improve our understanding of these two epochs.

Actually as first discussed in some detail by Madau et al. (1997), since the signal can be imaged in many adjacent frequency bins, it is better to speak of 21cm *tomography* when analysing the stacks of images, or image cube, at different frequencies. The frequency direction is of course special as along this line-of-sight direction the signal is seen from different look back times ('light cone effect') and also is affected by redshift space distortions introduced by the peculiar velocity field of the gas. Still, the three-dimensional data will provide a measurement of the distribution of the 21cm signal in three-dimensional space. In this the 21cm signal is more akin to galaxy redshift surveys at very much lower redshifts and very different from the Cosmic Microwave Background which only provides us with a snapshot from a single epoch.

The 21cm signal also differs in another fundamental way from the CMB signal. Whereas the CMB fluctuations reflect the tiny density fluctuations around the time of decoupling, the 21cm signal has strongly non-linear fluctuations. Furthermore, whereas the CMB fluctuations follow a Gaussian distribution and thus are statistically fully described by a power spectrum analysis, the same is not true for the 21cm signal whose probability distribution function (PDF) has been shown to be strongly non-Gaussian (Mellema et al. 2006). So, although a power spectrum analysis can reveal important properties of the signal, it does not fully describe it. This is illustrated in Fig. 1 which shows a 21cm image derived from a full numerical simulation of reionization and an image with the same power spectrum but a Gaussian PDF. The two images are very different but at the same time are indistinguishable in a power spectrum analysis.

2. The 21cm signal & sources of variations

As for the example described in more detail in Furlanetto et al. (2006), the redshifted 21cm signal from the intergalactic medium during the CD/EoR is the differential brightness temperature $\delta T_{\rm b}$ which when scaled to canonical values can be written as

$$\delta T_{\rm b} \approx 27 x_{\rm HI}(1+\delta)\left(\frac{1+z}{10}\right)^{\frac{1}{2}}\left(1-\frac{T_{\rm CMB}(z)}{T_{\rm s}}\right)\left(\frac{\Omega_{\rm b}}{0.044}\frac{h}{0.7}\right)\left(\frac{\Omega_{\rm m}}{0.27}\right)^{\frac{1}{2}} \left(\frac{1-Y_{\rm p}}{1-0.248}\right)\left(1+\frac{1}{H(z)}\frac{{\rm d}v_{\parallel}}{{\rm d}r_{\parallel}}\right)^{-1} \quad {\rm mK}, \tag{2.1}$$

PoS(AASKA14)010

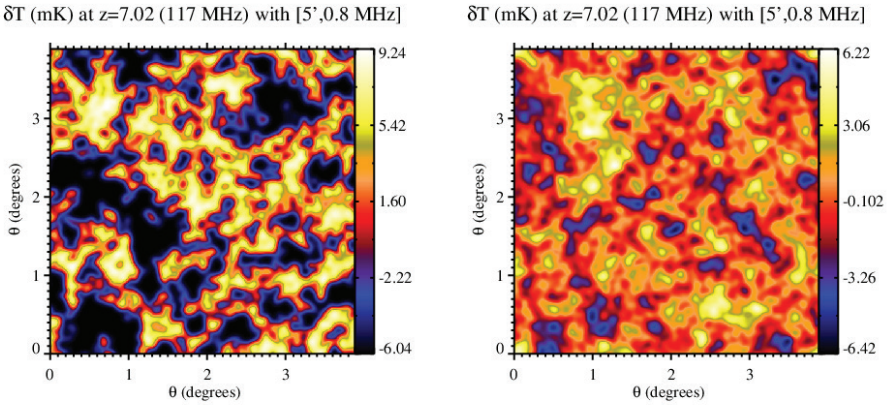

Figure 1: Left panel: 21cm image at $z = 7.02$ as derived from a full numerical simulation of reionization (XL2 from Iliev et al. 2014), convolved with a 5 arcminute FWHM Gaussian beam and 0.8 MHz bandwidth. The dark parts are large ionized regions. Right panel: a constructed 21cm signal with the same power spectrum as the signal in the left panel but a Gaussian PDF. These two images are very different but indistinguishable in a statistical power spectrum analysis.

with $x_{\rm HI}$ the neutral hydrogen fraction, $\delta = \rho/\langle\rho\rangle - 1$, the overdensity in the baryon distribution, $T_{\rm s}$ the spin (or excitation) temperature of the 21cm transition, $T_{\rm CMB}(z)$ the Cosmic Microwave Background (CMB) temperature, z the redshift of the signal, $\Omega_{\rm m}$ and $\Omega_{\rm b}$, the total matter and baryon density in terms of the critical density, h the Hubble parameter in units of 100 km s^{-1} Mpc^{-1}, $Y_{\rm p}$ the primordial helium abundance by mass, and $\mathrm{d}v_{\|}/\mathrm{d}r_{\|}$ the proper gradient of the peculiar velocity along the line of sight. This last term represents the effect of redshift space distortions.

From this expression one sees that the 21cm signal varies with position due to variations in the matter overdensity δ, the hydrogen neutral fraction $x_{\rm HI}$, the spin temperature $T_{\rm S}$ and line of sight velocity gradient $\mathrm{d}v_{\|}/\mathrm{d}r_{\|}$. This forms the basis of the analysis of the 21cm signal be it statistically or tomographically.

3. Regimes for Imaging

Imaging becomes possible once the signal to noise (S/N) for a certain size of spatial/spectral resolution element becomes larger than 1. Since the instrument noise will decrease when forming larger and larger resolution elements, even the first generation experiments such as LOFAR can in principle produce images, although with very poor resolution. This was worked out in detail in Zaroubi et al. (2012) where it was shown that LOFAR could produce images with a resolution of $\sim 20'$, whereas power spectrum analysis should be able to reach angular scales of $\sim 3'$.

Since the sensitivity of SKA1-Low varies with frequency, imaging will not be possible on the same scales at all frequencies. Specifically, as the sensitivity drops rapidly below the critical frequency the imaging capabilities for $\nu < 100$ MHz quickly deteriorate. In this regime larger image resolution elements will need to be used to reach the same noise levels. For those regimes in which imaging becomes unfeasible, statistical analysis with power spectra should be used.

PoS(AASKA14)010

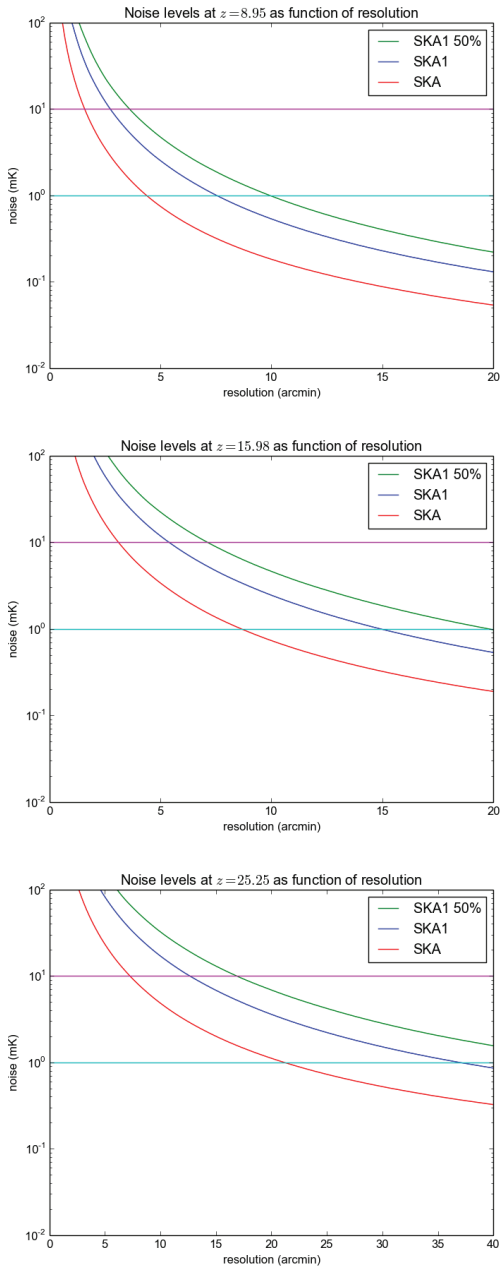

Figure 2: SKA-Low image noise levels as a function of imaging resolution for redshifts 8.95, 15.98 and 25.25. The assumed integration time is 1000 hrs and the frequency bandwidth is matched to the angular resolution. The different curves indicate the early science SKA1-Low, the full SKA1-Low and the final SKA2-Low. The horizontal lines are placed at 1 mK and 10 mK noise levels. These results can also be found in Koopmans & et al. (2015). The SKA1-Low configuration assumed is identical to the Baseline Design (Dewdney et al. 2013). Early science has half and the full SKA2-Low has four times the collecting area.

The three panels of Figure 2 illustrate the imaging capabilities of SKA-Low in three different stages: an early science 50% of the Baseline Design, the Baseline Design SKA1-Low (Dewdney

PoS(AASKA14)010

et al. 2013) and the full SKA2-Low at 4 times the sensitivity of SKA1-Low. All cases are for an integration time of 1000 hours and for a frequency bandwidth matched to the angular resolution. For tomography it is better if the frequency bandwidth matches the imaging scale so as to have fairly uniform resolution across the three-dimensional volume.

Concentrating on the full SKA1-Low case the figure shows that for $\nu \sim 140$ MHz ($z \sim 9$) imaging on scales down to $7'$ (19 comoving Mpc[1]) gives 1 mK noise levels. For the regime around 80 MHz this increases to scales of around $15'$ (47 cMpc) and only very coarse imaging at scales of 0.5 degree (100 cMpc) or worse is feasable for the lowest frequencies.

At noise levels of 1 mK it is possible to detect fluctuations in the neutral HI distribution. However, inspection of Eq. 2.1 shows that much larger amplitude variations can occur in the signal. For example, for the case of $T_{\rm s} \gg T_{\rm CMB}$ the contrast between fully ionized and fully neutral regions at mean density is given by

$$27 \left(\frac{1+z}{10}\right)^{\frac{1}{2}} \quad \text{mK}, \tag{3.1}$$

which should be detectable at higher noise levels than 1 mK. It is thus possible to map out the shapes of ionized regions at higher resolution. Figure 2 shows that for 10 mK noise, SKA1-Low could image ionized regions at $\sim 4'$ (11 cMpc) at $z \sim 9$.

Similarly, variations in the spin temperature during the Cosmic Dawn can result in more than 100 mK variations as can be seen from evaluating

$$27 \left(1 - \frac{T_{\rm CMB}(z)}{T_{\rm s}}\right) \left(\frac{1+z}{10}\right)^{\frac{1}{2}} \quad \text{mK}. \tag{3.2}$$

for $T_{\rm s}$ in the range 5 to 200 K. As can be seen from Figure 2 10 mK noise levels permit imaging with SKA1-Low at $\sim 6'$ (19 cMpc) scales around $z \sim 16$ and at $\sim 14'$ (47 cMpc) scales around $z \sim 25$.

For the other two configurations, the 50% SKA1-Low case requires roughly a 50% worse resolution and the SKA2-Low case allows roughly a factor 2 better resolution for the same noise levels, see Fig. 2.

To further illustrate the imaging capabilities of SKA1-Low, Figure 3 shows the result of an imaging pipeline in which an input image from a large scale reionization simulation has been observed by an interferometer with the same specifications as in the SKA1-Low Base Line Design (Dewdney et al. 2013) for 1000 hours. This pipeline is based on the MeqTrees software (Noordam & Smirnov 2010). The largest HII regions in this image are clearly visible (Shukla et al., in preparation).

4. Analyzing images

Once a tomographic data set has been obtained, it requires analysis to draw quantitative conclusions about the (astro)physics of the CD/EoR. Relying on the results of simulations several

[1]For these conversions the cosmological parameters from Eq. 2.1 are used.

[2]For computational reasons only 10% of the stations are used. To mimick the full SKA1-Low the noise is scaled down by a factor 10.

PoS(AASKA14)010

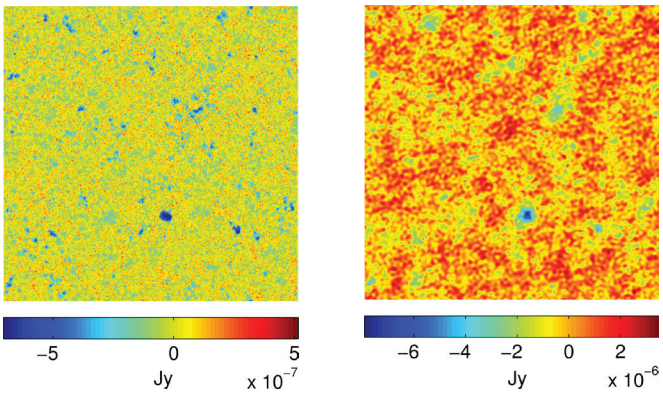

Figure 3: Left panel: The 21cm signal from a simulation of reionization in a 425 h^{-1} Mpc volume (Iliev et al. 2014). The redshift is $z = 8.515$ and it is assumed that $T_s \gg T_{\rm CMB}$. The field is 3.64×3.64 degrees on the sky. Right panel: the 21cm signal plus thermal noise when observed with SKA1-Low for 1000 hours.[2] The frequency is 150 Mhz, bandwidth 1 MHz and only baselines less than 2 km are used. This gives a synthesized beam of $3.7' \times 3.2'$. The large HII region in the lower half of the image is 18.55 h^{-1} Mpc or $9.5'$ in size and is clearly recovered in the observed image.

methods have been considered for analyzing such three-dimensional data sets. However, as the focus of the SKA precursors is on statistical measurements, the analysis of tomographic data is still very much a field in development. In this section, we summarize some of the techniques that can be used. Section 5 provides an overview of the science that can be done with tomographic data.

4.1 Regions around special objects

By targeting a region which contains a special object, such as a bright quasar or a group of bright galaxies, the 21cm signal shows how this object has influenced its environment, either through its ionizing radiation, or through its heating. The measurement would provide the size and geometry of features in the 21cm signal (e.g. a spherical HII region around a bright quasar). Such measurements would presumably employ rather ad hoc analysis methods motivated by the interest in a specific area.

For the cases when the S/N is insufficient for imaging, for example when the HII region is small or during the Cosmic Dawn when the noise is high, a matched filter based method can be used to optimally detect such regions using the visibilities directly, although this does require making assumptions about the shape of the region. This can then be used to estimate their sizes (Datta et al. 2007, 2008). Another technique that can be applied in the low S/N case is the stacking of observations of several (similar) objects.

4.2 Bubble size measures

When not considering a special region, some sort of statistic is needed to characterize the tomographic data set. For example, one might want to characterize the distribution of HII bubble sizes. Although this sounds quite straightforward, in reality this will not be so. The reason for this is that the geometry of ionized sources is unlikely to be a set of isolated nearly spherical bubbles of various sizes. Simulations show that rather there exists a complex network of ionized regions which partly overlap. The reason for this is that the sources of reionization live in the developing

PoS(AASKA14)010

cosmic web and thus are spread out like beads on connected strings. Simple two-dimensional cuts through this geometry do not do justice to its complexity.

Several methods to characterize bubble sizes in simulation results have been suggested. These include the "spherical average method" (Zahn et al. 2007), the power spectra of the ionized fraction P_{xx}, the Friends-of-Friends (FoF) method (Iliev et al. 2006) and PDFs (probability distribution functions) of path lengths through ionized regions (Mesinger & Furlanetto 2007; Hong et al. 2014). The results of the first three methods were compared in Friedrich et al. (2011). The conclusion was that each method measures different aspects and depending on what one is after, each provides a useful measurement of bubble sizes.

It has to be noted that all of these methods rely on the ionized or neutral fraction to characterize the bubble size distribution. The use of these or similar methods on the redshifted 21cm signal from an interferometer requires more investigation as the presence of density fluctuations, noise, synthesized beam shape and possibly residual foregrounds will affect their results.

4.3 Topological measures

A different property of the distribution of ionized regions is their geometry and topology. These are often described through the so-called Minkowski Functionals which provide the total volume, total surface, mean curvature and the so-called Euler Characteristic χ. The latter is a number characterizing the topology of the regions, sometimes also expressed as the *genus* g, where $g = 1 - \chi$. If $N_{\rm part}$ is the total number of isolated regions, $N_{\rm tunnel}$ the number of tunnels through these regions and $N_{\rm cavity}$ the number of cavities inside these regions, then

$$\chi = N_{\rm part} - N_{\rm tunnel} + N_{\rm cavity} \tag{4.1}$$

The work in Gleser et al. (2006); Lee et al. (2008); Friedrich et al. (2011); Hong et al. (2014) suggests that such topological measurements will be useful to characterize the reionization process and distinguish between different models. However, as for the bubble size methods discussed above, also here more work is needed to adapt these methods for use with real 21cm data.

4.4 Effects of finite resolution

Interferometers have both a minimum and maximum scale for which they are sensitive and this will impact the images. Starting with the minimum scale, finite resolution will limit the interpretation of the data. Fluctuations in density, neutral fraction and spin temperature below the resolution scale will not be separable. This means for example that a resolution element with a low value of the 21cm signal can be either a low density region or a high density region with several small, unresolved HII regions.

However, tomography does offer the possibility of analyzing this further by creating an ionization mask. Large ionized regions should be easily identifiable from their uniform, low flux level. Masking these out from a statistical analysis, one can then derive power spectra for the 'neutral' regions. These regions will still contain unresolved effects from small HII regions but comparing power spectra from different redshifts would allow detecting their effects on the density field. Note that such a masked analysis of the density field is only possible with tomographic data supplying the location of the masks.

PoS(AASKA14)010

As is well known, interferometers do not have baselines with zero separation and thus are unable to measure the average value of the signal within the FoV. In fact, there is a range of angular scales that cannot be measured, determined by the length of the smallest baseline. The smallest baseline for SKA1-Low has not yet been defined but will presumably lie in the range of $\sim$30 m implying that modes on scales of more than a few degrees will not be contained in the tomographic data. It is therefore important that these missing scales do not contain astrophysically or cosmologically essential structures as it would be impossible to reliably reconstruct these from the observations. Since we expect such information up to scales of a few degrees, shortest baselines of $\sim$30 m are required for the CD/EoR science case (Mellema et al. 2013). This implies station sizes of at least this size, although the availability of correlations between individual dipoles within stations would make it possible to capture even larger scales.

5. Science from images

In this section we discuss briefly some of the questions about Reionization and the Cosmic Dawn that can be answered by analysing the tomographic 21cm signal. Please also see Wyithe et al. (2015) in this volume for a case study of imaging with SKA1-Low.

5.1 QSO properties

By mapping out the shape of the ionized region around a bright quasar several properties of the quasar can be derived. A requirement for this is that the ionizing photon production from quasar dominates over the that of the local galaxy population. As quasars presumably live in biased, high density regions, this requirement is not trivially fulfilled. However, for optimistic assumptions about the radiation flux from a quasar, Datta et al. (2012) do find that a quasar can leave a clear imprint on its local environment.

As they are expected to be large and prominent features in the redshifted 21cm sky, the literature on quasar HII region in 21cm data is extensive (Wyithe et al. 2005; Geil & Wyithe 2008; Wyithe 2008; Furlanetto et al. 2008; Datta et al. 2012; Majumdar et al. 2012; Feng et al. 2013). The size of HII regions around the quasar can be used to put constraints on the quasar life time and luminosity, and possibly the mean neutral fraction of the surrounding IGM. The occurence of fossil HII regions will put constraints on the quasar population at high redshifts and will also measure the properties of the ionized IGM.

A growing quasar HII region that is spherical in shape in the quasar's rest frame, would appear to be distorted ('egg-shaped') along the line of sight in a tomographic data set due to the light cone effect (Shapiro & Giroux 1987; White et al. 2003; Wyithe & Loeb 2004; Yu 2005). From this apparent anisotropy of its shape, constraints on the quasar's ionizing luminosity, its age and neutral fraction of the local IGM can be derived (Geil & Wyithe 2008; Majumdar et al. 2012)[3] The constraints obtained from tomographic data will be more stringent than the ones currently avialable from the quasar absorption spectra (e.g. Bolton et al. 2011).

[3]We note that besides tomographic imaging the same can be achieved using an improved matched filter technique (Majumdar et al. 2012) acting directly on the actual visibilities. This will possibly provide a better handle on the noise than the image cube (Datta et al. 2007; Malloy & Lidz 2013) although the choice of the filter shape is important.

PoS(AASKA14)010

In addition such measurements will allow us to measure the possible anisotropy of the emission from the quasar itself. If the ionizing radiation only escapes in certain directions due to the presence of an obscuring torus, as is seen in many lower redshift quasars, the imprint on the surrounding medium will not be spherical. If such an anisotropy would be found in the 21cm data, it would be the first three-dimensional mapping of the radiative anisotropy of a high redshift active galactic nucleus.

If quasars are present during the Cosmic Dawn, heating of the surrounding IGM by their X-ray flux could leave strong imprints on the 21cm signal, creating 21cm emission regions against a background of absorption. The contrast between the absorption and emission regions could be as high as 200 mK which would make it possible to image these even at quite high redshifts (Alvarez et al. 2010), see also section 5.6 below.

5.2 Connection between galaxy population and HII regions

Determining the volume and shape of the ionized region around a group of optically detected galaxies would allow one to infer the connection between the ionizing radiation output of a galaxy population and the brightest members of this population. It is well-known that the galaxies we can currently detect are insufficient to reionize the Universe (see e.g. Schmidt et al. 2014) and references therein). However, the shape and extent of the luminosity function for the unobserved population remains a matter of contention. By measuring the specific examples of known galaxy groups, better constraints on this problem can be derived. In addition such observations would map the developing cosmic web.

As far as we know, no systematic exploration of such an approach has been performed. Most of the work connecting galaxies and the 21cm signal has focused on performing a cross-correlation between a galaxy survey and a 21cm observation. This technique can even be employed in noise regimes where imaging is not possible (Furlanetto & Lidz 2007; Wyithe & Loeb 2007; Lidz et al. 2009; Wiersma et al. 2013; Park et al. 2014).

5.3 Bubble size distribution & topology - breaking degeneracies in reionization models.

Although power spectrum analysis will be an important tool to determine the parameters of reionization, it can be expected that there will be certain degeneracies between key parameters. As the 21cm signal has a non-Gaussian distribution, power spectra do not fully describe it and quite different models could be consistent with the same power spectrum. It is likely although not proven that tomographic data can break some of the degeneracies in a pure power spectrum analysis.

Both from the point of view of cosmology and galaxy evolution, the important question is how to connect the measured size distribution of HII regions to the dark matter halo distribution. This correspondence will not be trivial as it involves a range of (astro)physical processes, such as the feedback (thermal, mechanical etc), recombinations etc. The measured bubble size distribution and topology will shed light on all these mechanisms. However, to date a detailed study of how to reliably extract this information from such measurements remains to be done.

5.4 Measurements of the cosmological density field

As explained in Section 4.4, knowing the location of large ionized regions would allow excluding these from the analysis of the remaining signal, which would then be a modified version

PoS(AASKA14)010

of the cosmological density field. Since reionization is likely to occur earlier in denser regions, the remaining signal would be dominated by lower density regions and affected by unresolved ionized regions. Still, a measurement such as this would provide useful information, especially if complemented by higher redshift power spectrum measurements. However, in order to produce high quality masks and to detect significant density fluctuations, high resolution is required. Likely this application will only become feasible with the full SKA2-Low[4].

5.5 Measuring the global 21cm signal

Since the intrinsic signal from the ionized regions will be zero or at least very close to zero, the presence of well resolved ionized regions could be used as a zero-point to determine the power contained in scales above those set by the minimum baseline of the interferometer, $> 3^\circ$ (at 150 MHz) for SKA-Low. We do not expect substantial power in the spectrum of 21cm fluctuations beyond these scales and consequently the value will be nearly equal to the mean 21cm signal in the Universe at that epoch. Measuring the flux from well-resolved HII regions will thus yield an independent measurement of the global 21cm signal. This technique does rely on the presence of large enough ionized regions with mininal contribution from unresolved neutral structures within them. A similar constant 'zero-point' could possibly also be found during the Cosmic Dawn if one assumes that the regions with the lowest signal are the coldest ones whose temperature can be derived from adiabatic cooling due to the expansion of the Universe.

5.6 Cosmic Dawn Science

Before $z \sim 12$, the spatial variations in the 21cm signal are expected to be mostly due to variations in the spin temperature. As explained in Section 3, cold regions could generate high amplitude signals (> 100 mK). Therefore higher image noise levels of 10 – 30 mK are acceptable, allowing for higher resolution images at these frequencies. The spin temperature evolution is thought to have two phases, an initial one during which UV photons from the first stars will decouple the spin temperature from the CMB temperature and couple it to the (cold) gas kinetic temperature, thus making the 21 cm signal observable against the background CMB. This phase is followed by a phase in which the cold IGM will be heated by X-ray radiation, turning the 21cm signal from absorption into emission. Both phases will likely be patchy and thus excellent targets for tomography (see e.g. Mesinger et al. 2014)).

To start with the heating phase, the heating profile and the 21 cm signal around X-ray sources will depend strongly on the flux and spectrum of the X-ray radiation reaching the IGM. This in its turn will depend on the intrinsic X-ray flux and spectrum and the level of absorption within the host galaxies. For mini-QSOs or a hot interstellar medium in star-forming galaxies, which emit substaintial amounts of soft X-ray (< 1 Kev) photons, heated regions will be smaller and the heating will be patchy (Pacucci et al. 2014; Ghara et al. 2014). On the other hand, heating will be more homogeneous and heated regions will be very large if the spectrum is dominated by hard X-ray photons, for example in the case of high mass X-ray binaries (Fialkov et al. 2014) and/or a

[4]We note that an alternative way to probe the large scale density distribution is to measure the dark matter power spectrum. It has been proposed that anisotropies in the HI 21 cm power spectra arising from the peculiar velocities ('redshift space distortions') can be used to extract the 'pure' dark matter power spectrum from the astrophysical HI power spectra (Barkana & Loeb 2005; Shapiro et al. 2013).

PoS(AASKA14)010

high level of absorption within the host galaxies. Thus the measurement of sizes of heated regions will be a direct probe of the first X-ray sources and their spectra. This measurement will also probe the level of the X-ray background (Christian & Loeb 2013; Mesinger et al. 2014).

During the earlier decoupling phase the patchiness is driven by the rarity and clustering of the sources of UV photons. Even though this phase is expected around $z \sim 20$, the decoupled regions around these sources may still be imaged with SKA-Low as the contrast between coupled and decoupled regions will be high ($\sim$ 100 mK, see for example Semelin et al. 2007; Santos et al. 2008; Mesinger et al. 2014; Ghara et al. 2014). Measurements of size and distribution of the decoupled regions would probe the nature of the very first stars and their environment.

One particularly interesting application of tomography for the early Cosmic Dawn would be to map out the effects of 'bulk flows', an expected large scale variation of the velocity difference between dark and baryonic matter (Tseliakhovich & Hirata 2010). This effect would modulate early star formation on scales of $\sim$100 Mpc, corresponding to $30'$ at $z = 20$. Both the modulation in the UV background and the heating could generate observable signatures (McQuinn & O'Leary 2012). In spite of the low sensitivity for imaging around 65 MHz, such a modulation would actually fall within the imaging possibilities of SKA-Low.

It should be pointed out that most of the papers cited above focus on power spectrum analysis of the 21cm signal from the Cosmic Dawn. More work is needed to establish the impact of different kinds of X-ray and UV sources on the 21cm signal and how well these phenomena could be imaged with SKA-Low.

6. Conclusions

SKA-Low will transform the study of the Cosmic Dawn and the Epoch of Reionization by allowing tomographic imaging of the 21cm signal. With this capability we will be able to address a range of questions not accessible to a statistical, power spectrum characterization of the signal. Deep observations of 1000 hours with SKA1-Low will provide $\sim$ 1 mK image noise levels at resolutions ranging from $\sim 7'$ at $\sim$ 200 MHz to $\sim 30'$ at $\sim$ 50 MHz, assuming a frequency bandwidth matching in physical size. However, many features such as isolated ionized regions during the EoR and isolated heated regions during the CD, can be imaged at $\sim$ 10 mK noise levels, allowing image resolution elements in the range $4'$ – $14'$ in the same frequency range.

Tomographic imaging will allow the characterization of individual bright quasars, including their isotropy or lack thereof. It will also make it possible to connect the 21cm observations to optical galaxy surveys, thus unravelling the connection between photon producing galaxies and the reionization process. The ionized bubble size distribution and the topology of ionized regions uniquely characterize the reionization process. Extracting these from the observations requires tomographic imaging as they are not described by the power spectrum of the 21cm signal, due to its inherent non-Gaussian signature. Furthermore, identifying the location of ionized regions will make it possible to study the baryonic density field during reionization and using the ionized regions as a zero-point can be used to determine the global 21cm signal. Tomographic imaging thus opens the door to a wide range of studies inaccessible to a power spectrum analysis and essential to understand the reionization process.

PoS(AASKA14)010

The relatively coarse imaging possible for the highest redshifts may still be able to characterize the sizes and distribution of 'heated' and'decoupled' regions and the effect of the velocity differences between dark matter and baryonic matter during the Cosmic Dawn. This will provide a unique and important probe of the very first X-ray and UV sources.

None of the existing low frequency precursors is capable of tomographically imaging the redshifted 21cm signal and even the planned HERA project will only attempt imaging at very large scales and during the EoR. This makes SKA-Low in all its phases a truly transformational telescope which will not only provide detailed 3D tomographic imaging of the EoR but also coarse, yet groundbraking imaging of the Cosmic Dawn. SKA-Low will be the only telescope on Earth capable of looking this far back in the history of our Universe and reveal the earliest phases of star and galaxy formation.

References

Alvarez, M. A., Pen, U.-L., & Chang, T.-C. 2010, ApJ, 723, L17
Barkana, R., & Loeb, A. 2005, ApJ, 624, L65
Bolton, J. S., Haehnelt, M. G., Warren, S. J., et al. 2011, MNRAS, 416, L70
Christian, P., & Loeb, A. 2013, JCAP, 9, 14
Datta, K. K., Bharadwaj, S., & Choudhury, T. R. 2007, MNRAS, 382, 809
Datta, K. K., Friedrich, M. M., Mellema, G., Iliev, I. T., & Shapiro, P. R. 2012, MNRAS, 424, 762
Datta, K. K., Majumdar, S., Bharadwaj, S., & Choudhury, T. R. 2008, MNRAS, 391, 1900
Dewdney, P., Turner, W., Millenaar, R., McCool, R. Lazio, J., & Cornwell, T. 2013, SKA1 System Baseline Design, Document number SKA–TEL–SKO–DD–001 Revision 1
Feng, Y., Croft, R. A. C., Di Matteo, T., & Khandai, N. 2013, MNRAS, 429, 1554
Fialkov, A., Barkana, R., & Visbal, E. 2014, Nature, 506, 197
Friedrich, M. M., Mellema, G., Alvarez, M. A., Shapiro, P. R., & Iliev, I. T. 2011, MNRAS, 413, 1353
Furlanetto, S. R., Haiman, Z., & Oh, S. P. 2008, ApJ, 686, 25
Furlanetto, S. R., & Lidz, A. 2007, ApJ, 660, 1030
Furlanetto, S. R., Oh, S. P., & Briggs, F. H. 2006, Phys. Rep., 433, 181
Geil, P. M., & Wyithe, J. S. B. 2008, MNRAS, 386, 1683
Ghara, R., Choudhury, T. R., & Datta, K. K. 2014, ArXiv:1406.4157, arXiv:1406.4157
Gleser, L., Nusser, A., Ciardi, B., & Desjacques, V. 2006, MNRAS, 370, 1329
Hong, S. E., S.Ahn, K., Park, C., et al. 2014, Journal of Korean Astronomical Society, 47, 49
Iliev, I. T., Mellema, G., Ahn, K., et al. 2014, MNRAS, 439, 725
Iliev, I. T., Mellema, G., Pen, U.-L., et al. 2006, MNRAS, 369, 1625
Koopmans, L. V. E., & et al. 2015, in Advancing Astrophysics with the Square Kilometre Array (Proceedings of Science), PoS(AASKA14)001
Lee, K.-G., Cen, R., Gott, III, J. R., & Trac, H. 2008, ApJ, 675, 8
Lidz, A., Zahn, O., Furlanetto, S. R., et al. 2009, ApJ, 690, 252
Madau, P., Meiksin, A., & Rees, M. J. 1997, ApJ, 475, 429
Majumdar, S., Bharadwaj, S., & Choudhury, T. R. 2012, MNRAS, 426, 3178
Malloy, M., & Lidz, A. 2013, ApJ, 767, 68

PoS(AASKA14)010

McQuinn, M., & O'Leary, R. M. 2012, ApJ, 760, 3
Mellema, G., Iliev, I. T., Pen, U.-L., & Shapiro, P. R. 2006, MNRAS, 372, 679
Mellema, G., Koopmans, L. V. E., Abdalla, F. A., et al. 2013, Experimental Astronomy, 36, 235
Mesinger, A., Ewall-Wice, A., & Hewitt, J. 2014, MNRAS, 439, 3262
Mesinger, A., & Furlanetto, S. 2007, ApJ, 669, 663
Noordam, J. E., & Smirnov, O. M. 2010, A&A, 524, A61
Pacucci, F., Mesinger, A., Mineo, S., & Ferrara, A. 2014, MNRAS, 443, 678
Park, J., Kim, H.-S., Wyithe, J. S. B., & Lacey, C. G. 2014, MNRAS, 438, 2474
Santos, M. G., Amblard, A., Pritchard, J., et al. 2008, ApJ, 689, 1
Schmidt, K. B., Treu, T., Trenti, M., et al. 2014, ApJ, 786, 57
Semelin, B., Combes, F., & Baek, S. 2007, A&A, 474, 365
Shapiro, P. R., & Giroux, M. L. 1987, ApJ, 321, L107
Shapiro, P. R., Mao, Y., Iliev, I. T., et al. 2013, Physical Review Letters, 110, 151301
Tseliakhovich, D., & Hirata, C. 2010, Phys. Rev. D, 82, 083520
White, R. L., Becker, R. H., Fan, X., & Strauss, M. A. 2003, AJ, 126, 1
Wiersma, R. P. C., Ciardi, B., Thomas, R. M., et al. 2013, MNRAS, 432, 2615
Wyithe, J. S. B. 2008, MNRAS, 387, 469
Wyithe, J. S. B., Geil, P. M., & Kim, H. 2015, in Advancing Astrophysics with the Square Kilometre Array (Proceedings of Science), PoS(AASKA14)015
Wyithe, J. S. B., & Loeb, A. 2004, ApJ, 610, 117
—. 2007, MNRAS, 375, 1034
Wyithe, J. S. B., Loeb, A., & Barnes, D. G. 2005, ApJ, 634, 715
Yu, Q. 2005, ApJ, 623, 683
Zahn, O., Lidz, A., McQuinn, M., et al. 2007, ApJ, 654, 12
Zaroubi, S., de Bruyn, A. G., Harker, G., et al. 2012, MNRAS, 425, 2964

PoS(AASKA14)010

PROCEEDINGS OF SCIENCE

Constraining the Astrophysics of the Cosmic Dawn and the Epoch of Reionization with the SKA

Andrei Mesinger[*1], **Andrea Ferrara**[1], **Bradley Greig**[1], **Ilian Iliev**[2], **Garrelt Mellema**[3], **Jonathan Pritchard**[4], **Mario G. Santos**[5,6,7], **on behalf of the EoR/CD Science Team**

[1]*Scuola Normale Superiore, Piazza dei Cavalieri, 7 56126 Pisa, Italy;* [2]*Astronomy Centre, Department of Physics and Astronomy, University of Sussex, Falmer, Brighton BN1 9QH, UK;* [3]*Dept. of Astronomy & Oskar Klein Centre, Stockholm University, AlbaNova, SE-10691 Stockholm, Sweden;* [4]*Department of Physics, Blackett Laboratory, Imperial College, London SW7 2AZ, UK;* [5]*Department of Physics, University of Western Cape, Cape Town 7535, South Africa;* [6]*SKA SA, 4rd Floor, The Park, Park Road, Pinelands, 7405, South Africa;* [7]*CENTRA, Departamento de Fisica, Instituto Superior Tecnico, 1049-001 Lisboa, Portugal*

E-mail: andrei.mesinger at sns.it

The Square Kilometre Array (SKA) will offer an unprecedented view onto the early Universe, using interferometric observations of the redshifted 21cm line. The 21cm line probes the thermal and ionization state of the cosmic gas, which is governed by the birth and evolution of the first structures in our Universe. Here we show how the evolution of the 21cm signal will allow us to study when the first generations of galaxies appeared, what were their properties, and what was the structure of the intergalactic medium. We highlight qualitative trends which will offer robust insights into the early Universe.

Advancing Astrophysics with the Square Kilometre Array
June 8-13, 2014
Giardini Naxos, Italy

[*]Speaker.

PoS(AASKA14)011

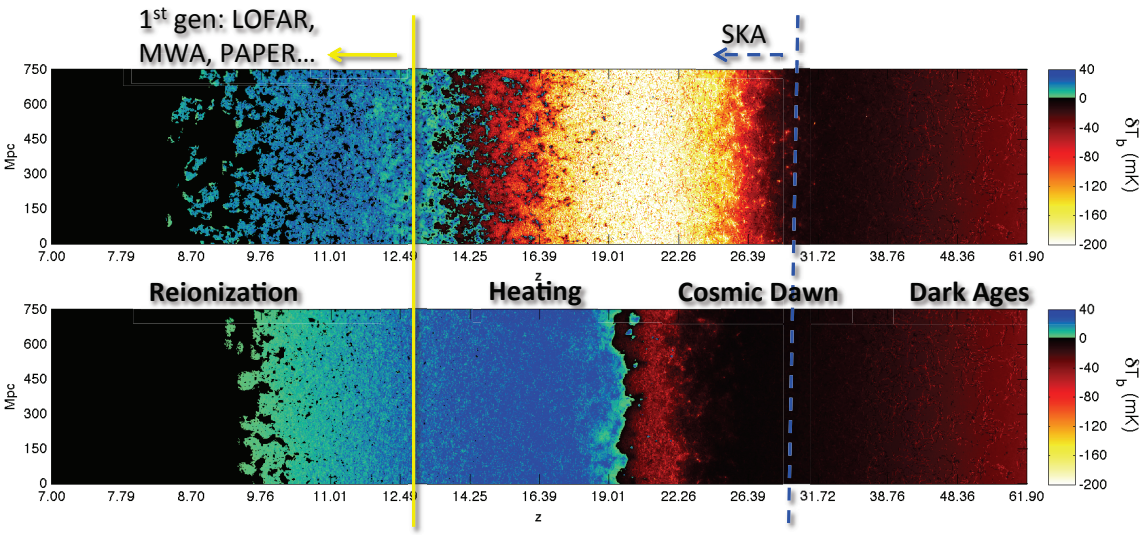

Figure 1: 21cm brightness temperature offset from the CMB (from Mesinger et al. (2013)). The horizontal axis shows evolution along the comoving line-of-sight coordinate, from $z \approx 62$ to $z \approx 7$. From right to left we see the expected major milestones in the signal: (i) collisional decoupling (*red*→*black*); (ii) WF coupling (*black*→*yellow*); (iii) IGM heating (*yellow*→*blue*); (iv) reionization (*blue*→*black*). The *top panel* corresponds to a "fiducial" model, while the *lower panel* corresponds to an "extreme X-ray" model in which primordial galaxies are much more efficient than local starbursts in generating X-rays (see, e.g. Mirabel et al. (2011)), saturating the unresolved soft X-ray background Hickox & Markevitch (2007) by $z \sim 10$. The lower panel further assumes that soft X-rays with energies $\lesssim$1keV are absorbed within the host galaxy. Although the models have comparable electron scattering optical depths, τ_e, the astrophysical milestones are very different in 21cm. The redshift limit accessible to first generation interferometers roughly corresponds to the vertical yellow line; the SKA-LOW should probe out to roughly the vertical blue line, opening-up a new window on the Cosmic Dawn. The slices are 750 Mpc in height and 1.5 Mpc thick.

1. Introduction

With unprecedented resolution and sensitivity, the SKA-LOW will enable ground-breaking studies of early Universe astrophysics through the 21cm line from neutral hydrogen. No other planned instrument will allow us to study baryons at high redshift in such detail. We will be able to trace the delicate, physics-rich interplay between the intergalactic medium (IGM) and the first galaxies.

As a cosmological probe, the signal is usually represented in terms of the offset of the 21cm brightness temperature from the cosmic microwave background (CMB) temperature, T_γ, along a line of sight at observed frequency ν (c.f. Furlanetto et al. (2006)):

$$\delta T_b(\nu) = \frac{T_S - T_\gamma}{1+z}(1-e^{-\tau_{\nu_0}}) \approx \tag{1.1}$$
$$27 x_{\rm HI}\left(1-\frac{T_\gamma}{T_S}\right)(1+\delta_{\rm nl})\left(\frac{H}{dv_r/dr+H}\right)\sqrt{\frac{1+z}{10}\frac{0.15}{\Omega_{\rm M}h^2}}\left(\frac{\Omega_b h^2}{0.023}\right)\left(\frac{1-Y_p}{0.75}\right)\text{mK},$$

where T_S is the gas spin temperature, τ_{ν_0} is the optical depth at the 21cm frequency ν_0, $\delta_{\rm nl}(\mathbf{x},z) \equiv \rho/\bar{\rho} - 1$ is the evolved (Eulerian) density contrast, Y_p is the Helium mass fraction, $H(z)$ is the Hubble parameter, dv_r/dr is the comoving gradient of the line of sight component of the comoving velocity, and all quantities are evaluated at redshift $z = \nu_0/\nu - 1$. The cosmological 21cm signal uses the CMB as a back-light: if $T_S < T_\gamma$, then the gas is seen in absorption, while if $T_S > T_\gamma$, the gas is seen in emission.

PoS(AASKA14)011

The spin temperature, T_S, interpolates between the CMB temperature, T_γ, and the gas kinetic temperature, T_K. Since we only observe the *contrast* of the gas against the CMB, a signal is only obtained if $T_S \to T_K$. This coupling is achieved through either: (i) collisions, which are effective in the intergalactic medium (IGM) at high redshifts, $z \gtrsim 50$; or (ii) a Lyman alpha background (so-called Wouthuysen-Field (WF) coupling; Wouthuysen (1952); Field (1958)), effective soon after the first sources turn on.

In the top panel of Fig. 1, we show a slice through the δT_b field in a "fiducial" model (below we use the term "fiducial" to refer to models in which atomically-cooled galaxies have similar X-ray and UV properties as local ones, with an ionizing emissivity such that the mid-point of reionization is at $z \sim 10$; for further details, see, e.g. Mesinger et al. (2013)). It is immediately obvious that the 21cm signal is a physics-rich probe, encoding information on various processes during the Cosmic Dawn (CD) and Epoch of Reionization (EoR). Although the exact timing of the cosmic epochs is uncertain, the relative order is robustly predicted (c.f. Furlanetto (2006); §2.1 in McQuinn & O'Leary (2012)):

1. **Collisional coupling**: The IGM is dense at high redshifts, so the spin temperature is uniformly collisionally coupled to the gas kinetic temperature, $T_K = T_S \lesssim T_\gamma$. Following thermal decoupling from the CMB ($z \lesssim 300$), the IGM cools adiabatically as $T_K \propto (1+z)^2$, faster than the CMB: $T_\gamma \propto (1+z)$. Thus $\delta\bar{T}_b$ is negative. This epoch, serving as a *clean probe of the matter power spectrum* at $z \gtrsim 100$, is not shown in Fig. 1.
2. **Collisional decoupling**: The IGM becomes less dense as the Universe expands. The spin temperature starts to decouple from the kinetic temperature, and begins to approach the CMB temperature again, $T_K < T_S \lesssim T_\gamma$. Thus $\delta\bar{T}_b$ starts rising towards zero. Decoupling from T_K occurs as a function of the local gas density, with underdense regions decoupling first. Fluctuations are sourced by the density field, and again *offer a direct probe of cosmology*. Eventually ($z \sim 25$), all of the IGM is decoupled and there is little or no signal. This epoch corresponds to the red→black transition on the right edge of Fig. 1.
3. **WF coupling (i.e. Lyα pumping)**: The first astrophysical sources turn on, and begin coupling T_S and T_K, this time through the Lyα background. $\delta\bar{T}_b$ becomes more negative, reaching values as low as $\delta\bar{T}_b \sim$-100 – -200 mK (depending on the offset of the WF coupling and X-ray heating epochs). Fluctuations are driven by the strength of the Lyα background. This epoch, offering a window on the *very first stars in our Universe*, corresponds to the black→yellow transition in Fig. 1.
4. **IGM heating**: The IGM is heated, with the spin temperature now coupled to the gas temperature, $T_K = T_S$. Fluctuations are sourced by the gas temperature. As the gas temperature surpasses T_γ, the 21cm signal changes from absorption to emission, becoming insensitive to the actual value of T_S (see eq. 1). This epoch probes all processes which heat the IGM, *both astrophysical and cosmological*. The dominant source of heating is likely the X-rays from early accreting black holes (e.g. Furlanetto (2006)) or from the hot interstellar medium (ISM; Pacucci et al. (2014)). This epoch corresponds to the yellow→blue transition in the panels of Fig. 1.
5. **Reionization**: as the abundance of *early galaxies* increases, the IGM gradually becomes ionized, a process which is inside-out on large scales. Fluctuations during the advanced

PoS(AASKA14)011

stages are dominated by the ionization field. The tomography of this process is sensitive to the nature and clustering of the dominant UV sources (e.g. McQuinn et al. (2007)), as well as the evolution of inhomogeneous recombinations (e.g. Sobacchi & Mesinger (2014)). The 21cm signal decreases, approaching zero. This epoch corresponds to the blue→black transition in the panels of Fig. 1.

The first two stages (the Dark Ages) allow us to probe cosmology at redshifts much lower than recombination, while the last three stages are sensitive to early astrophysical sources (and sinks) of cosmic radiation fields. These last three stages will be observable with SKA1-LOW. Below, we focus on the astrophysical insight which can be gained from the CD and EoR (for cosmological insights, see §Cosmology from the EoR/CD). As a foreshadowing of how astrophysics can impact the CD and EoR signals, in the bottom panel of Fig. 1, we show an alternate model, in which the early galaxies formed later, but were much more efficient at producing hard X-ray photons, saturating the unresolved X-ray background (XRB; Hickox & Markevitch (2007)) by $z \approx 10$; the CD and EoR are dramatically different in these two models.

As our observable, we focus on the 21cm power spectrum. Although alternate statistics can provide complimentary observations, the power spectrum serves to quantify the main impact of astrophysics on the morphology of the 21cm signal. We define the 3D power spectrum as $P_{21}(k,z) = k^3/(2\pi^2 V)\ \delta\bar{T}_b(z)^2 \langle|\delta_{21}(\mathbf{k},z)|^2\rangle_k$, where $\delta_{21}(\mathbf{x},z) \equiv \delta T_b(\mathbf{x},z)/\delta\bar{T}_b(z) - 1$. Moreover, when discussing detectability, we focus on the redshift evolution of large-scale power at $k \approx 0.2$ Mpc^{-1} (e.g. Baek et al. (2010)), roughly corresponding to the largest scales which should be relatively foreground free (e.g. Pober et al. (2013)). Our models of the SKA1-LOW thermal noise are described in Mesinger et al. (2014). In brief, we take a fiducial 1000h observation, with a $\Delta z = 0.5$ bandwidth and a frequency resolution of 1 kHz. 866 stations (each a 17x17 array of log-periodic dipoles) are placed using a Gaussian distribution with 75 % falling within 1000m of the center Dewdney et al. (2013). For most frequency bins and reasonable astrophysical parameters, the S/N can be dominated by cosmic variance (see Mesinger et al. (2014) and Fig. 3). This suggest significant results already with a 50% early-science phase with SKA1-LOW, and also motivates a multi-tiered strategy combining several, moderatly deep observations (as highlighted in the EoR/CD science goals; see also §7).

Unless stated otherwise, we quote all quantities in comoving units. The predictions below are consistent with recent Planck measurements of cosmological parameters Planck Collaboration (2013).

Below we highlight how SKA1-LOW will allow us to study the galaxies and IGM during the CD/EoR. It will allow us to answer some of the most fundamental questions in astrophysical cosmology: *When did the first generations of galaxies appear? What were their UV and X-ray properties? What was the small-scale structure of the IGM?*

2. First, molecularly-cooled galaxies

The first galaxies likely formed at high redshifts, $z > 30$ in very low mass halos $M_{\rm halo} = 10^{6-7} M_\odot$ (e.g. Haiman et al. (1996); Abel et al. (2002); Bromm et al. (2002)), sometimes referred to as minihalos. Since the gas was primordial in composition, accretion and star-formation was

PoS(AASKA14)011

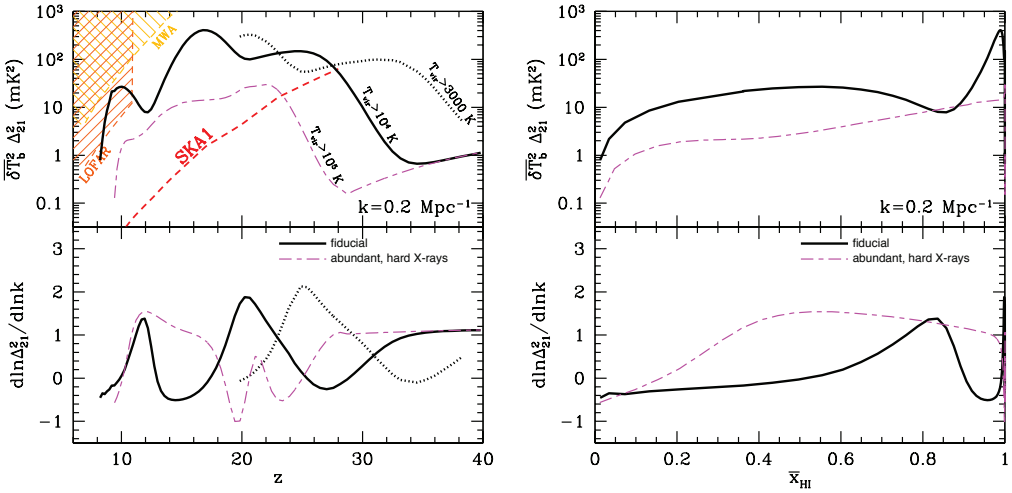

Figure 2: Evolution of the 21cm power spectrum amplitude (*top panels*) and slope (*bottom panels*) at $k = 0.2$ Mpc^{-1}. Evolution vs redshift ($\bar{x}_{\rm HI}$) is shown on the left (right). Solid black (dashed magenta) curves correspond to the fiducial (extreme X-ray) model shown in the top (bottom) panel of Fig. 1. The achievable thermal noise after a 1000h observation with SKA1-LOW is shown with the dashed red curve in the left panel; the analogous noise for the first generation instruments, LOFAR and MWA is marked by the checkered region in the top left corner of the panel. As discussed in the text, fiducial models show a three-peaked evolution in the large-scale 21cm power, corresponding to: (i) WF coupling, (ii) X-ray heating; and (iii) EoR. Models are taken from Mesinger et al. (2013). Also shown in the left panel is a model with an additional contribution at $z \geq 20$ from H_2 cooling halos with virial temperatures > 3000 K.

governed by H_2 cooling. Due to their shallow potential wells and inefficient cooling, the star formation inside minihalos is strongly susceptible to feedback effects, e.g.: (i) mechanical feedback from SNe explosions; (ii) X-ray heating; (iii) ionizing UV background (UVB); (iv) H_2 dissociative radiation. The later, so-called Lyman-Werner background (LWB) is expected to eventually sterilize star-formation inside minihalos (e.g. Haiman et al. (2000); Ricotti et al. (2001); Mesinger et al. (2006)). In fact, even galaxies hosted by more massive, atomically-cooled halos (which are more resilient to feedback) could be sufficiently-abundant to establish a LWB strong enough (e.g. O'Shea & Norman (2008)) to sterilize star-formation inside minihalos by $z \sim 20$ (e.g. Holzbauer & Furlanetto (2012); Fialkov et al. (2013); though see Ahn et al. (2012)).

Nevertheless, these fragile first galaxies are likely the ones which start the Cosmic Dawn. As mentioned above, this beginning is observable in 21cm through the WF coupling epoch, mostly driven by photons just redward of Lyβ which emerge from galaxies and redshift into Lyα resonance. These photons have mean free paths of $\gtrsim 100$ Mpc, and can efficiently couple the spin temperature to the gas temperature, with 21cm being seen in absorption against the CMB. 21cm fluctuations during this epoch are driven by fluctuations in the strength of this coupling, i.e. the Lyα background. Therefore, *the timing and duration of the initial rise and fall of the 21cm power tells us about the star-formation inside the very first, molecularly-cooled galaxies*.

This is highlighted by comparing the solid and dotted black curves in the left panels of Fig. 2. The solid black curve corresponds to a fiducial model, in which star formation only occurs in atomically-cooled galaxies. The dotted black curve assumes an additional contribution at $z \geq 20$ from minihalos with virial temperatures > 3000 K. The WF epoch starts earlier, and is more extended, driven by the slower evolution of the halo mass function on these scales. This delay is likely further extended by the feedback processes mentioned above. In this model, the peak in

PoS(AASKA14)011

power associated with WF coupling would occur too early (at low frequencies) to be detectable with SKA1-low. However, the trough between the WF coupling and X-ray heating epochs should be detectable. Hence, if we do *not* detect a third peak in power at $z \gtrsim 20$, it would imply that minihalos are driving WF coupling.

Moreover, the *shape* of the power-spectrum at a given astrophysical milestone can tell us which halos hosted the first galaxies (e.g. Santos et al. (2011)). As we shall also see below, radiation fields driven by more biased, rare galaxies result in less small-scale structure and associated 21cm power.

3. X-ray properties of early galaxies and IGM heating

As discussed above, X-rays from early galaxies are expected to heat the IGM to temperatures above the CMB well before the bulk of reionization. When the ionized fraction of the IGM surpasses a few percent, most of the X-ray energy gets deposited as heat through free-free interactions of the primary ionized electron (e.g. Shull & van Steenberg (1985); Furlanetto & Stoever (2010); Valdés et al. (2010)). This makes X-rays more efficient as sources of heating than ionization. However, they could still significantly contribute to the EoR (in addition to the heating epoch), since the first, metal-poor galaxies are likely more X-ray luminous than local ones (per unit star formation rate; e.g. Fragos et al. (2013); Basu-Zych et al. (2013). Current limits do not rule out a strong redshift evolution in this efficiency of X-ray production (e.g. Brorby et al. (2014)). X-rays could also indirectly impact the EoR by raising the Jeans mass in the IGM. The resulting photo-heating feedback on sources might delay the EoR (e.g. Ricotti & Ostriker (2004); Mesinger et al. (2013)), providing a window for a clean measurement of the matter power spectrum.

The interaction of X-rays with the IGM is characterized by a very large mean free path:

$$\lambda_{\rm X} \approx 20\, \bar{x}_{\rm HI}^{-1} \left(\frac{E_{\rm X}}{300{\rm eV}}\right)^{2.6} \left(\frac{1+z}{10}\right)^{-2} \ {\rm cMpc}\ , \tag{3.1}$$

where $\bar{x}_{\rm HI}$ is the (volume) mean neutral fraction of the IGM and $E_{\rm X}$ is the photon energy. This means that only soft X-rays ($E_{\rm X} \lesssim$ keV) interact with the IGM, making them relevant for 21cm studies. Without sub-keV X-rays, the EoR and IGM heating epochs would have dramatically different (smoother) morphologies (see the bottom panel of Fig. 1).

IGM heating during the CD is the most potent probe of early X-rays. X-rays from galaxies likely dominate the heating. First generation instruments will not detect this exciting epoch, for most reasonable scenarios Mesinger et al. (2014). The SKA1-LOW is poised to offer us the first glimpses into this exciting epoch, driven by the high-energy processes inside the first galaxies!

To further quantify this, in the top panels of Fig. 3, we show the peak amplitude and redshift of the peak amplitude of the large-scale 21cm power. We plot quantities in the parameter space of: (i) the minimum halo mass hosting star forming galaxies, $M_{\rm min}$, and (ii) their X-ray efficiency, f_X. The fiducial value, $f_X \equiv (N_{\rm X}/0.25) = 1$ corresponds to $N_{\rm X} = 0.25$ X-ray photons per stellar baryon, consistent with empirical scaling relations from nearby star-forming galaxies (e.g. Mineo et al. (2012a)). Similarly, the fiducial choice of $M_{\rm min} \sim 10^8 M_\odot$ corresponds to atomic-cooling galaxies (see §5 below). Increasing f_X shifts the X-ray heating epoch (and associated peak in power) towards higher redshifts, while increasing $M_{\rm min}$ shifts *all* astrophysical epochs towards

PoS (AASKA14) 011

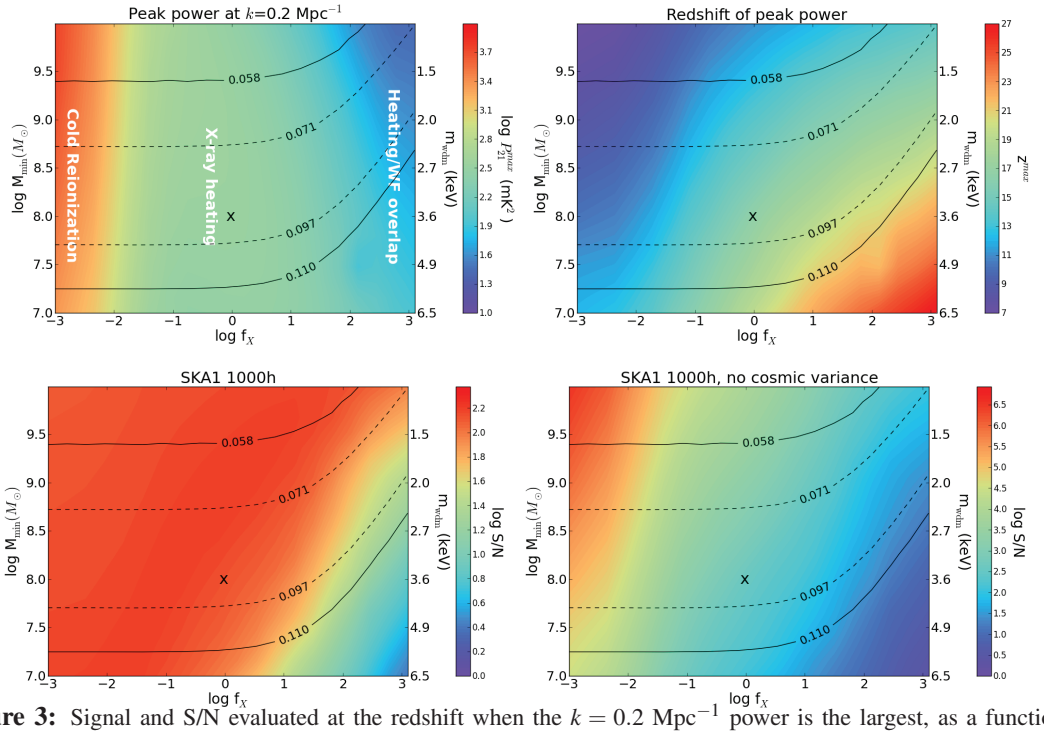

Figure 3: Signal and S/N evaluated at the redshift when the $k = 0.2$ Mpc^{-1} power is the largest, as a function of the minimum halo mass hosting star forming galaxies, $M_{\rm min}$, and their X-ray efficiency, f_X. *Top left:* peak signal, i.e. maximum amplitude of the 21cm power. *Top right:* redshift of the peak signal. *Bottom left:* corresponding S/N after 1000h with SKA1-LOW Phase 1. *Bottom right:* S/N neglecting the cosmic variance component: $P_{21}/\sqrt{N_k}$. A 'fiducial' model with $M_{\rm min} = 10^8 M_\odot$ and $f_X = 1$, is denoted with an 'x' in the panels. For the observing strategies used, see Mesinger et al. (2014).

lower redshifts (see top left panel of Fig. 2). Therefore, this 2D parameter space should span most of the variation in the signal.

Over a broad swath of parameter space, the large scale 21cm power during heating (driven by temperature fluctuations) peaks at a value of few hundred mK^2 (c.f. Baek et al. (2010)), an order of magnitude larger than the peak during the EoR (driven by ionization fluctuations). In the bottom panels of Fig. 3 we show the signal-to-noise (S/N) at which this signal can be detected with a 1000h observation of SKA1-LOW, with and without cosmic variance (left and right panels, respectively). *We see that the SKA1-LOW should easily detect X-ray heating throughout the parameter space*. Most scenarios are limited by cosmic variance, suggesting an observational strategy of sampling several independent fields, if higher S/N is desired, e.g. for imaging.

What are the likely sources of X-rays in the early galaxies? The bolometric X-ray luminosities of local, star-forming galaxies are dominated by bright, high mass X-ray binaries (HMXBs; e.g. Gilfanov et al. (2004); Mineo et al. (2012b)). However, the soft-bands relevant for X-ray heating, $E_X \lesssim 2$ keV, have a comparable contribution from the hot interstellar medium (ISM; Mineo et al. (2012c)). Because of the strong dependence of the X-ray mean free path on the photon energy (eq. 3.1), *the X-ray spectral energy distributions (SEDs) of the first galaxies have a strong imprint on the 21cm fluctuations during the CD.* In particular, scenarios in which X-ray heating is dominated by HMXBs should result in a factor of ~ 3 less large-scale 21cm power than those dominated by the hot ISM Pacucci et al. (2014). This difference is easily identifiable with the SKA1-LOW, and

PoS(AASKA14)011

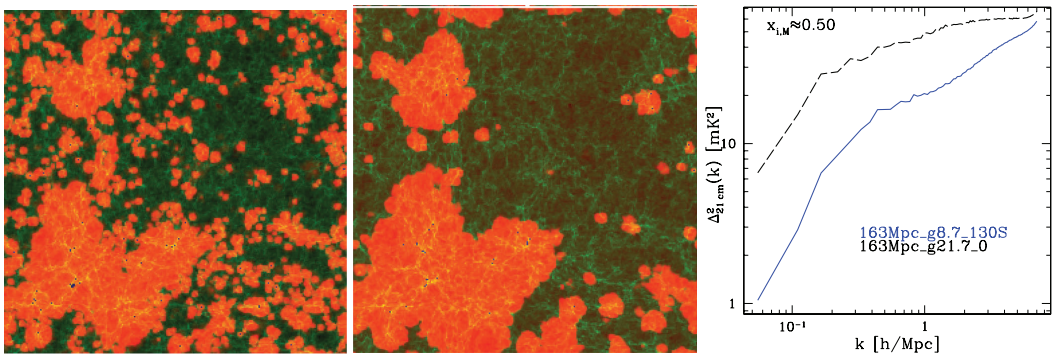

Figure 4: EoR morphologies driven by bursty star formation in atomically-cooled galaxies, $M_{\rm min} \gtrsim 10^8 M_\odot$, (*left panel*) compared to those driven by galaxies residing in $M_{\rm min} \gtrsim 10^9 M_\odot$ (*middle panel*). Slices are 53 Mpc on a side, and correspond to the mid-point of reionization. The power spectra in the right panel are generated from 163 Mpc simulations with analogous source prescriptions. The power spectra corresponding to the two source models differ by factors of ∼2–3 on large scales. Panels are from Iliev et al. (2012).

importantly, is not degenerate with the galaxies' X-ray luminosities. Hence, *the SKA will be a powerful tool for studying the first galaxies and their high-energy processes.*

4. Radio loud sources at high-redshifts

Before the Universe was heated to temperatures greater than the CMB, the IGM could be visible in absorption along sightlines to high-redshift radio sources. This is the 21cm analogy of the well-studied Lyα forest. Although detecting features in the forest will be challenging even for SKA1-LOW (e.g. Mack & Wyithe (2012)), integration time can be reduced if one is only after a statistical measure, such as the increased variance along a sightline (e.g. Carilli et al. (2004)). In any case, detecting the 21cm forest along individual sightlines requires a radio-loud QSO at redshifts before heating (e.g. Mack & Wyithe (2012); Ciardi et al. (2013)). It is not clear how likely this is, given that the population of bright QSOs declines rapidly towards high-z (e.g. Willott et al. (2007); Wilman et al. (2008)).

Chances can be improved however using the statistical imprint of a larger number of fainter QSOs. A high-redshift population of radio sources will introduce small-scale power in the 21cm power spectrum pre-heating. Temperature fluctuations driven by the X-ray emitting galaxies are expected to dominate the large-scale power, while the small-scale power ($k \gtrsim 0.5$ Mpc^{-1}) will allow us to constrain the population of radio loud active galactic nuclei at high redshifts Ewall-Wice et al. (2013).

Dense structures such as damped Lyman alpha systems (DLAs), or even sterilized minihalos (mentioned above), would aid in the detection of the 21cm forest, if they contain enough cold, neutral gas. The resulting increased absorption features would be strongly imprinted in both individual sightlines (e.g. Furlanetto & Loeb (2002); Mack & Wyithe (2012)) as well as statistical detections Ewall-Wice et al. (2013), allowing us to additionally constrain the abundance of cold gas clumps at high-z.

PoS(AASKA14)011

5. EoR sources

The SKA1-LOW we will map out the timing and duration of the EoR (see Fig. 2). The EoR is expected to be driven by UV photons from galaxies (e.g. McQuinn (2012)), and is characterized by some generic features in the evolution of 21cm power. Initially (following heating), there is a dramatic drop in large-scale amplitude and steepening of the slope during the early stages of reionization, $\bar{x}_{\rm HI} \gtrsim 0.8$, when the burgeoning HII regions 'cover-up' the densest IGM patches (solid curve in the right panel of Fig. 2). This evolution can be understood (to first order, assuming $T_S \gg T_\gamma$) as the transition of the 21cm power spectrum, $P_{21} \approx P_{xx} - 2\bar{x}_{\rm HI}P_{\rm xd} + \bar{x}^2_{\rm HI}P_{\rm dd}$, from being dominated by the density power, P_{dd}, to the ionization power, P_{xx}; the transition being governed by the negative contribution of the density-ionization cross spectrum, P_{xd} Lidz et al. (2008). Subsequently, the fluctuations in the ionization field, P_{xx}, drive the large-scale 21cm power to a peak value during the mid-point of reionization.

However, this evolution is qualitatively different if hard ($\gtrsim 1$ keV) X-rays play a dominant role. The resulting weaker density-ionization cross-power and ionization power results in a much more gradual fall in power during the EoR, as well as a much lower overall amplitude (dashed curve in the right panel of Fig. 2). Both of these scenarios are easily identifiable with SKA1-LOW. More reasonable models, in which (soft) X-rays play a sub-dominant role in the EoR still show a 21cm peak in large-scale power during the midpoint of reionization. However, the P_{xd} induced drop in power occurs earlier, $\bar{x}_{\rm HI} \sim 0.9$, due to the pre-ionization from X-ray sources Mesinger et al. (2013). The 21cm probability distribution function (PDF) can also be used as a diagnostic, with X-rays decreasing the bi-modality of the PDF Baek et al. (2010).

In addition to the timing and duration of the EoR, the 21cm signal can tell us about the nature of EoR galaxies. The EoR is likely driven by faint galaxies below the sensitivity limits of current and upcoming space telescopes, including *JWST*. The EoR galaxies formed through atomic cooling, requiring host halo virial temperatures of $T_{\rm vir} \gtrsim 10^4$ K ($\gtrsim 10^8 M_\odot$ at $z \sim 10$). However, the efficiency of star formation inside these dwarf galaxies at high-z is highly uncertain. Moreover, it is likely that feedback processes (either through internal mechanical feedback, e.g. Springel & Hernquist (2003), or photo-heating feedback from the UVB; e.g. Thoul & Weinberg (1996)), regulated the evolution of their star formation rate (SFR). The timing of the EoR signal, tells us when the dominant EoR sources appeared, which is a combination of their host halo masses and star formation efficiencies.

This degeneracy can be broken using the EoR morphology, which allows us to study the dominant host halo population of EoR galaxies. More massive host halos are more biased, with corresponding EoR morphologies with less small-scale ionization structure (see Fig. 4). This observation is however complicated by the fact that the bias of the halos evolves only weakly over this mass range McQuinn et al. (2007), and by the fact that sinks of ionizing photons can also strongly impact the EoR morphology (see next section).

6. EoR sinks

By depleting the ionizing photon budget available to expand cosmic HII regions, recombining systems (largely comprised of so-called Lyman limit systems; LLSs) can have a large impact dur-

PoS(AASKA14)011

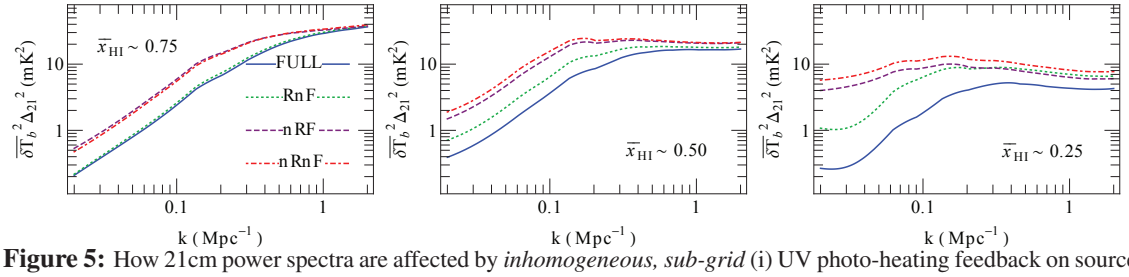

Figure 5: How 21cm power spectra are affected by *inhomogeneous, sub-grid* (i) UV photo-heating feedback on sources and (ii) recombinations in sinks. The FULL (*blue curves*) model includes both effects via calibrated, sub-grid models. The RnF (*green curves*) model includes only recombinations. The nRF (*purple curves*) model includes only UVB feedback. The nRnF (*red curves*) model includes neither effects, and is comparable to current large-scale RT simulations of reionization (e.g. Zahn et al. (2011); Majumdar et al. (2014)). Recombinations in sub-grid structures (and UVB photo-heating feedback to a lesser extent) can strongly suppress large-scale ionization structure (by factors of 2–5 throughout reionization). Figures are taken from Sobacchi & Mesinger (2014).

ing (and following) cosmic reionization. Unfortunately, directly resolving such small ($\lesssim$kpc) sinks of ionizing photons in large-scale reionization simulations is computationally impractical. Therefore, relatively untested sub-grid models must be used. SKA1-LOW will allow us to confront the predictions of such sub-grid models, offering insights into the small-scale baryonic physics of the IGM.

During reionization, gas is heated from low temperatures to $\sim 10^4$ K. Depending on the level of pre-heating by X-rays, this might have a strong impact on the clumpiness of gas in the IGM (e.g. Pawlik et al. (2009); Emberson et al. (2013)) and minihalos (e.g. Shapiro et al. (2004); Iliev et al. (2005)). Subsequently, the gas establishes photo-ionization equilibrium with the local ionizing background, with most recombinations occurring in systems with densities large enough to partially self-shield (e.g. McQuinn et al. (2011)). As a cosmological HII region grows, an increasing fraction of its ionizing photon budget is lost to balance recombinations, limiting its further growth Furlanetto & Oh (2005). This 'slowdown' is more dramatic for larger HII regions, since (i) they generally have a higher ionizing background, with ionization fronts driven into more dense, rapidly recombining systems; and (ii) their centers were the first to be reionized, thus having had enough time to recombine Sobacchi & Mesinger (2014). As large regions slow down, moderate HII regions can 'catch' up, further resulting in a more uniform size distribution even early in reionization.

As a result, recombinations strongly suppress the large scale ionization structure during the EoR. This can be seen from Fig. 5: comparing the green and red curves, we see that inhomogeneous recombinations can suppress the large-scale 21cm power by factors of 2–3. The effect is magnified by UVB feedback, which is also strongest inside large HII regions, whose cores ionized early enough for gas to respond to photo-heating. Comparing the blue and red curves, we see that the total impact of both (i) recombinations and (ii) UVB photo-heating feedback on sources results in a suppression of large-scale 21cm power by factors of 2–5. Neither effects are accounted for in most large-scale EoR simulations.

Although 'directly' detecting sinks through a corresponding rise in 21cm power on small-scales has been suggested Choudhury et al. (2009), realistic models of their sizes and neutral gas mass make this direct detection unlikely even with the SKA1-LOW Sobacchi & Mesinger (2014). However, the indirect detection via the above-mentioned steep slope of the 21cm power spectrum should be easy to detect and can tell us about small-scale IGM structure.

PoS(AASKA14)011

7. Observing Strategy

Different observing strategies can impact the scientific return from SKA1-LOW. For example, the large-scale modes are dominated by sample (cosmic) variance, while the small-scale modes are affected by the intrinsic detector (thermal) noise. Increasing the total integration time of a single observed patch of the sky decreases the noise on small-scales, while instead for N observations, the sample variance is be reduced by $\sqrt{N}$.

A quantitative analysis of EoR/CD constraints with different observing strategies has not been done yet. Qualitatively, we expect the largest constraining power to come from the redshift evolution of large-scale modes (e.g. Mesinger et al. (2014); Pober & other (2014)). From figures 2 and 3 we see that a single 1000h observation with SKA1-LOW, even with a possible 50% reduction in area, will be limited by cosmic variance on large-scales. This suggests that optimal science returns would benefit from an increase in the total field of view, at the expense of a modest reduction in integration time. These considerations motivate SKA1-LOW's current planned three-tiered observing strategy: (i) 1x1000h; (ii) 10x100h; (iii) 100x10h. The relative science gains from these strategies will depend on: (i) the effectiveness of foreground removal on large-scales; (ii) statistics used to characterize the cosmic signal; as well as (iii) the available instantaneous bandwidth probing the redshift evolution of the signal.

8. Conclusions

We summarize our main conclusions below.

- The timing and duration of the initial rise and fall of the 21cm power tell us about star-formation inside the very first, molecularly-cooled galaxies. Efficient star-formation inside these minihalos could source WF coupling fluctuations (driven by the Lyα background) as early as $z \gtrsim 30$. Hence if we do *not* detect a third peak in 21cm power at $z \lesssim 30$ with SKA1-LOW, it would imply that minihalos are driving WF coupling.
- The peak *amplitude* of the large-scale 21cm power during X-ray heating is sensitive to the SEDs of the first galaxies (at the factor of few level), while the *redshift* of the peak tells us about the nature of their X-ray luminosity and host DM halos.
- The early stages of reionization, $\bar{x}_{\rm HI} \approx$0.8-0.9, are characterized by a drop in large-scale 21cm power amplitude, and a steepening of the power spectrum. The timing and duration of this feature tells us about the contribution of X-rays to the EoR.
- The midpoint of the EoR is characterized by a local maximum in large-scale 21cm fluctuations (driven by the ionization field), except if hard X-rays dominate reionization.
- The morphology of the EoR encodes information about the efficiency of star-formation inside galaxies, feedback processes and absorption systems.
- Absorption systems inhibit the growth of large HII regions, and could result in a dramatic reduction of large-scale 21cm power (by factors of 2–5). Therefore the steepness of the EoR power spectrum can tell us about the structure and evolution of these small-scale gas clumps.

PoS(AASKA14)011

- Radiation fields driven by more biased, rare galaxies result in less small-scale structure. Thus the 21cm power on small-scales encodes information on the host halos which host the dominant sources.
- The 21cm forest, if detected either through individual sightlines or statistically through the rise in 21cm power towards small-scales ($k \gtrsim 0.5$ Mpc^{-1}), will constrain the population of radio-loud AGN as well as cold gas clumps at high-z.

References

Abel, T., Bryan, G. L., & Norman, M. L. 2002, Science, 295, 93
Ahn, K., Iliev, I. T., Shapiro, P. R., et al. 2012, ApJ, 756, L16
Baek, S., Semelin, B., Di Matteo, P., Revaz, Y., & Combes, F. 2010, A&A, 523, A4
Basu-Zych, A. R., et al. 2013, ApJ, 762, 45
Bromm, V., Coppi, P. S., & Larson, R. B. 2002, ApJ, 564, 23
Brorby, M., Kaaret, P., & Prestwich, A. 2014, ArXiv e-prints:1404.3132, arXiv:1404.3132
Carilli, C. L., Gnedin, N., Furlanetto, S., & Owen, F. 2004, NAR, 48, 1053
Choudhury, T. R., Haehnelt, M. G., & Regan, J. 2009, MNRAS, 394, 960
Ciardi, B., et al. 2013, MNRAS, 428, 1755
Dewdney, P., et al. 2013, SKA1 SYSTEM BASELINE DESIGN
`http://www.skatelescope.org/wp-content/uploads/2013/03/SKA-TEL-SKO-DD-001-1_BaselineDesign1.pdf`, 1
Emberson, J. D., Thomas, R. M., & Alvarez, M. A. 2013, ApJ, 763, 146
Ewall-Wice, A., Dillon, J. S., Mesinger, A., & Hewitt, J. 2013, ArXiv e-prints:1310.7936, arXiv:1310.7936
Fialkov, A., Barkana, R., Visbal, E., Tseliakhovich, D., & Hirata, C. M. 2013, MNRAS, 432, 2909
Field, G. B. 1958, Proceedings of the Institute of Radio Engineers, 46, 240
Fragos, T., et al. 2013, ApJ, 764, 41
Furlanetto, S. R. 2006, MNRAS, 371, 867
Furlanetto, S. R., & Loeb, A. 2002, ApJ, 579, 1
Furlanetto, S. R., & Oh, S. P. 2005, MNRAS, 363, 1031
Furlanetto, S. R., Oh, S. P., & Briggs, F. H. 2006, Physics Reports, 433, 181
Furlanetto, S. R., & Stoever, S. J. 2010, MNRAS, 404, 1869
Gilfanov, M., Grimm, H.-J., & Sunyaev, R. 2004, MNRAS, 347, L57
Haiman, Z., Abel, T., & Rees, M. J. 2000, ApJ, 534, 11
Haiman, Z., Thoul, A. A., & Loeb, A. 1996, ApJ, 464, 523
Hickox, R. C., & Markevitch, M. 2007, ApJ, 661, L117
Holzbauer, L. N., & Furlanetto, S. R. 2012, MNRAS, 419, 718
Iliev, I. T., Mellema, G., Shapiro, P. R., et al. 2012, MNRAS, 423, 2222
Iliev, I. T., Shapiro, P. R., & Raga, A. C. 2005, MNRAS, 361, 405
Lidz, A., Zahn, O., McQuinn, M., Zaldarriaga, M., & Hernquist, L. 2008, ApJ, 680, 962
Mack, K. J., & Wyithe, J. S. B. 2012, MNRAS, 425, 2988
Majumdar, S., Mellema, G., Datta, K. K., et al. 2014, ArXiv e-prints:1403.0941, arXiv:1403.0941
McQuinn, M. 2012, MNRAS, 426, 1349

PoS(AASKA14)011

McQuinn, M., Lidz, A., Zahn, O., et al. 2007, MNRAS, 377, 1043
McQuinn, M., Oh, S. P., & Faucher-Giguère, C.-A. 2011, ApJ, 743, 82
McQuinn, M., & O'Leary, R. M. 2012, ApJ, 760, 3
Mesinger, A., Bryan, G. L., & Haiman, Z. 2006, ApJ, 648, 835
Mesinger, A., Ewall-Wice, A., & Hewitt, J. 2014, MNRAS; arXiv:1310.0465, arXiv:1310.0465
Mesinger, A., Ferrara, A., & Spiegel, D. S. 2013, MNRAS, 431, 621
Mineo, S., Gilfanov, M., & Sunyaev, R. 2012a, MNRAS, 419, 2095
—. 2012b, MNRAS, 419, 2095
—. 2012c, MNRAS, 426, 1870
Mirabel, I. F., Dijkstra, M., Laurent, P., Loeb, A., & Pritchard, J. R. 2011, A&A, 528, A149
O'Shea, B. W., & Norman, M. L. 2008, ApJ, 673, 14
Pacucci, F., Mesinger, A., Mineo, S., & Ferrara, A. 2014, ArXiv e-prints, arXiv:1403.6125
Pawlik, A. H., Schaye, J., & van Scherpenzeel, E. 2009, MNRAS, 394, 1812
Planck Collaboration, . 2013, ArXiv e-prints:1303.5076, arXiv:1303.5076
Pober, J. C., & other. 2014, ApJ, 782, 66
Pober, J. C., et al. 2013, The Astrophysical Journal Letters, 768, L36
Ricotti, M., Gnedin, N. Y., & Shull, J. M. 2001, ApJ, 560, 580
Ricotti, M., & Ostriker, J. P. 2004, MNRAS, 352, 547
Santos, M. G., Silva, M. B., Pritchard, J. R., Cen, R., & Cooray, A. 2011, A&A, 527, A93
Shapiro, P. R., Iliev, I. T., & Raga, A. C. 2004, MNRAS, 348, 753
Shull, J. M., & van Steenberg, M. E. 1985, ApJ, 298, 268
Sobacchi, E., & Mesinger, A. 2014, MNRAS, 440, 1662
Springel, V., & Hernquist, L. 2003, MNRAS, 339, 312
Thoul, A. A., & Weinberg, D. H. 1996, ApJ, 465, 608
Valdés, M., Evoli, C., & Ferrara, A. 2010, MNRAS, 404, 1569
Willott, C. J., et al. 2007, ArXiv e-prints 0706.0914, 0706.0914
Wilman, R. J., et al. 2008, MNRAS, 388, 1335
Wouthuysen, S. A. 1952, AJ, 57, 31
Zahn, O., Mesinger, A., McQuinn, M., et al. 2011, MNRAS, 414, 727

PoS(AASKA14)011

PROCEEDINGS OF SCIENCE

Cosmology from EoR/Cosmic Dawn with the SKA

Jonathan Pritchard[*1], **Kiyotomo Ichiki**[2], **Andrei Mesinger**[3], **Robert Benton Metcalf**[4], **Alkistis Pourtsidou**[4], **Mario Santos**[5], **Filipe Abdalla**[6], **Tzu-Ching Chang**[7], **Xuelei Chen**[8], **Jochen Weller**[9], **Saleem Zaroubi**[10], **on behalf of the Cosmology-SWG and EoR/CD-SWG**

[1]*Imperial College London,* [2]*Nagoya University,* [3]*Scuola Normale Superiore, Pisa,* [4]*Universitá di Bologna,* [5]*University of the Western Cape,* [6]*University College London,* [7]*ASIAA,* [8]*National Astronomical Observatory of China,* [9] *Universitaets-Sternwarte Muenchen,* [10]*University of Groningen.*

E-mail: j.pritchard@imperial.ac.uk

SKA Phase 1 will build upon early detections of the EoR by precursor instruments, such as MWA, PAPER, and LOFAR, and planned instruments, such as HERA, to make the first high signal-to-noise measurements of fluctuations in the 21 cm brightness temperature from both reionization and the cosmic dawn. This will allow both imaging and statistical maps of the 21cm signal at redshifts $z = 6-27$ and constrain the underlying cosmology and evolution of the density field. This era includes nearly 60% of the (in principle) observable volume of the Universe and many more linear modes than the CMB, presenting an opportunity for SKA to usher in a new level of precision cosmology. This optimistic picture is complicated by the need to understand and remove the effect of astrophysics, so that systematics rather than statistics will limit constraints.

This chapter describes the cosmological, as opposed to astrophysical, information available to SKA Phase 1. Key areas for discussion include: cosmological parameters constraints using 21cm fluctuations as a tracer of the density field; lensing of the 21cm signal, constraints on heating via exotic physics such as decaying or annihilating dark matter; impact of fundamental physics such as non-Gaussianity or warm dark matter on the source population; and constraints on the bulk flows arising from the decoupling of baryons and photons at $z = 1000$. The chapter explores the path to separating cosmology from 'gastrophysics', for example via velocity space distortions and separation in redshift. We discuss new opportunities for extracting cosmology made possible by the sensitivity of SKA1 and explore the advances achievable with SKA2.

Advancing Astrophysics with the Square Kilometre Array
June 8-13, 2014
Giardini Naxos, Italy

[*]Speaker.

PoS(AASKA14)012

1. Introduction

The years since the COBE observations of the CMB have ushered in an age of precision cosmology. Key cosmological parameters have been determined by measurements of the distribution of matter in the Universe through WMAP and Planck observations of CMB anisotropies and large volume galaxy surveys such as SDSS. These surveys have made precision measurements of parameters describing the matter content of the Universe - the baryons Ω_b, dark matter Ω_c, dark energy Ω_Λ, radiation Ω_r, and neutrinos Ω_ν - and the physics of inflation - via the tilt n_s, amplitude A_s, running $\mathrm{d}n_s/\mathrm{d}\log k$ or the primordial potential power spectrum and r the ratio of tensor-to-scalar modes produced by inflation. These measurements have firmly established a working model of our Universe, known widely as the ΛCDM model of cosmology. The success of this model is despite our ignorance of the physics of key components, such as dark matter and dark energy, and deviations from the standard model could help refine our understanding.

Despite this precision, measuring model parameters is only the first step towards a deep understanding of the underlying physics. Our ignorance of the nature of the dark matter and the dark energy or how neutrinos acquire mass and what value that mass takes are just two questions that modern cosmology hopes to address. Over the next decade two paths will help shed light on this. The simplest is simply to measure these cosmological parameters ever more precisely and over a wider range of times and scales in the hope of gaining further insights. The exemplar of this is with dark energy, where attempts to measure the redshift evolution of the dark energy density, parameterised by an equation of state $w(z)$, might distinguish a true cosmological constant from more general dark energy or modified gravity. For others there are critical thresholds of precision required to distinguish physical scenarios - for example, measuring the sum of the neutrino masses $M_\nu \lesssim 0.1$ would determine the neutrino mass hierarchy. Clearly more precision is a good thing, but it is not the only path forward.

More generally, we can seek signatures of new physics in ways distinct from the distribution of large scale matter. For example, the processes that produce dark matter will also allow it to annihilate and maybe to decay. The associated release of energy could have impact on the surrounding environment, heating the intergalactic medium. Pursuing unique signatures of new physics in new regimes will be a key part of the next decade. The SKA is uniquely placed to probe cosmology in this way, as it is capable of mapping the Universe over wide volumes and an unprecedented range of redshifts (see Figure 1). In this chapter, we will focus on the new opportunities created by SKA observations of the epoch of reionization (EoR) and the cosmic dawn (CD). This period has never before been observed offering a unique opportunity to test the consistency of the ΛCDM model and search for new hints to the great unanswered questions of cosmology.

Fundamental physics in cosmology is generally associated with the density field, whose fluctuations are generated by inflation and which contains imprint of other physics such as neutrino mass. Astrophysics is a major challenge to getting at cosmology with SKA, but we can identify several key approaches to extracting cosmology: (1) directly from density fluctuations (2) via the presence of exotic sources of radiation (3) via the radiation fields produced by all sources since those sources will trace the density field in some biased fashion (4) via the weak lensing of the 21cm signal by structures between the observer and signal (5) miscellaneous other probes. Extracting cosmology from the 21cm signal during the EoR will require innovative new techniques

PoS(AASKA14)012

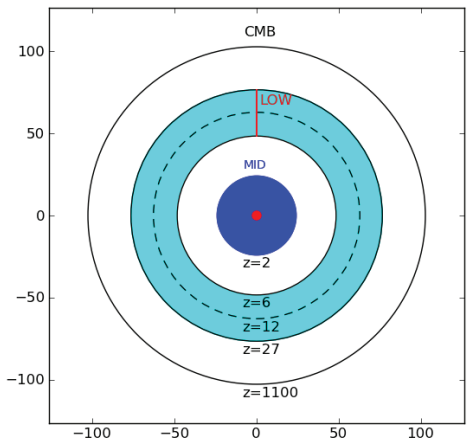

Figure 1: Illustration of the volume probed by SKA where 3D comoving volume has been mapped to a 2D disk. The volume probed by an all sky galaxy survey out to $z = 0.3$ (red circle, ∼SDSS) and $z = 2$ (blue circle, ∼SKA-MID) are marked as is the volume at the redshifts probed by SKA-LOW, $z = 6-27$ (cyan annulus). Existing cosmological parameters are derived using the CMB and relatively local galaxies, with an implicit assumption that nothing strange happens in between.

to separate astrophysics from cosmology. Nonetheless the sensitivity of the instruments, large volume probed, and new redshift regime accessible to SKA makes this a very interesting area for new science.

In this chapter, we will explore these different avenues for extracting cosmology from the 21cm signal and attempt to assess the sort of constraints that will be achievable by SKA Phase 1 and 2. However, we caution the reader that this is not a settled area and it is still unclear how well astrophysics can be dealt with. New ideas may improve the constraints, but new obstacles may render them optimistic.

2. Cosmological parameters from density fluctuations

In this section, we explore the ability of SKA to constrain cosmological parameters via observations of the density field. Just as galaxy surveys constrain cosmology by using galaxies as a tracer of the linear density field, SKA can constrain cosmology by using the 21 cm brightness temperature as a tracer of the density field. This is not an unproblematic assertion, since brightness temperature fluctuations may be sourced by variation in the spin temperature and neutral fraction in addition to the density field.

$$\delta T_B = 27 x_{HI}(1+\delta_b)\left(\frac{T_S - T_{\rm CMB}}{T_S}\right)\left(\frac{1+z}{10}\right)^{1/2}\left[\frac{\partial_r v_r}{(1+z)H(z)}\right]^{-1} \text{mK} \tag{2.1}$$

Equation 2.1 shows how these different terms come into play (Furlanetto et al. 2006). In a regime where $T_S \gg T_{\rm CMB}$ and $x_{HI} = 1$ then δT_B will be an unbiased tracer of the density field. At all other times the effects of astrophysics must be modelled and removed or somehow avoided. One

PoS(AASKA14)012

possibility might be to exploit redshift space distortions that produce an angular dependence of the power spectrum, which in the simplest linear theory models look like

$$P(k) = P_{\mu^0}(k) + P_{\mu^2}\mu^2 + P_{\mu^4}\mu^4. \tag{2.2}$$

In principle, measurement of this angular dependence of the power spectrum could separate cosmology and astrophysics since the $P_{\mu^4} = P_\delta$ so directly probes the density field. In practice, this separation is complicated by non-linear growth of structure (Shaw & Lewis 2008; Mao et al. 2012) and the motion of ionised regions themselves (McQuinn et al. 2006) and it is unclear how effective it can be. We will return to a discussion of separating astrophysics and cosmology in §3 as this is a critical point.

In this section, we take the optimistic view that there will be a regime in which $\delta T_b \propto (1+\delta)$ so that the 21cm signal provides a clean measurement of the density field. This approach enables us to evaluate the best case scenario for SKA in measuring cosmological parameters. By comparing this to galaxy surveys we get a sense of how competitive SKA could be, if astrophysics could be overcome. While we focus on standard cosmological parameters - energy density in baryons Ω_b, matter Ω_m, cosmological constant Ω_Λ; hubble parameter h; inflationary parameters A_S, n_s and $\mathrm{d}n_s/\mathrm{d}\log k$; neutrino mass M_ν and curvature Ω_k - SKA will open a new regime into exotic physics that can only be probed at high redshift, for example compensated isocurvature modes whose effect decreases with time (Gordon & Pritchard 2009). Cosmology is moving from simply wanting to measure cosmological parameters more accurately and instead becoming more focused on control of systematics and relaxing simplifying assumptions. SKA will test consistency of cosmological parameters in a new redshift range.

The sensitivity of a radio interferometer to the 21cm power spectrum has been well studied (e.g. Bowman et al. 2006; McQuinn et al. 2006; Mao et al. 2008; Mellema et al. 2013) and we follow the same approach here. The variance of a 21 cm power spectrum estimate for a single $\mathbf{k}$-mode with line of sight component $k_{||} = \mu k$ is given by (Lidz et al. 2008):

$$\sigma_P^2(k,\mu) = \frac{1}{N_{\rm field}}\left[\bar{T}_b^2 P_{21}(k,\mu) + T_{\rm sys}^2 \frac{1}{Bt_{\rm int}}\frac{D^2\Delta D}{n(k_\perp)}\left(\frac{\lambda^2}{A_e}\right)^2\right]^2. \tag{2.3}$$

The first term on the right-hand-side of the above expression provides the contribution from sample variance, while the second describes the thermal noise of the radio telescope. The thermal noise depends upon the system temperature $T_{\rm sys}$, the survey bandwidth B, the total observing time $t_{\rm int}$, the conformal distance $D(z)$ to the center of the survey at redshift z, the depth of the survey ΔD, the observed wavelength λ, and the effective collecting area of each antennae tile A_e. The effect of the configuration of the antennae is encoded in the number density of baselines $n_\perp(k)$ that observe a mode with transverse wavenumber $k_\perp$ (McQuinn et al. 2006). Observing a number of fields $N_{\rm field}$ further reduces the variance. Given the sensitivity of the instrument, the Fisher matrix formalism can be used to estimate $1-\sigma$ errors on the model parameter λ_i are $(\mathbf{F}_{ij}^{-1})^{1/2}$, where

$$F_{ij} = \sum_\mu \frac{\varepsilon k^3 V_{\rm survey}}{4\pi^2}\frac{1}{\sigma_P^2(k,\mu)}\frac{\partial P_{T_b}}{\partial \lambda_i}\frac{\partial P_{T_b}}{\partial \lambda_j}. \tag{2.4}$$

PoS(AASKA14)012

In this equation, $V_{\rm survey} = D^2 \Delta D(\lambda^2/A_e)$ denotes the effective survey volume of our radio telescopes and we assume wavenumber bins of width $\Delta k = \varepsilon k$. Key to determining cosmological parameters are the effective volume probed and the minimum wavenumber probed $k_{\rm min}$ where modes can still be assumed to be linear. SKA has a significant advantage over galaxy surveys as more modes are still in the linear regime at $z > 6$.

Table 1: Low-frequency radio telescopes and their parameters. We specify the number of antennae N_a, total collecting area $A_{\rm tot}$, bandwidth B, and total integration time $t_{\rm int}$ for each instrument. These values are fixed at $\nu = 110$MHz and extrapolated to other frequencies using $A_{\rm tot} = N_{\rm ant} N_{\rm dip} A_{\rm dip}$ with a physical station size of 35m and the number of antennae per station $N_{\rm dip} = 289$ and $A_{\rm dip} = \min(\lambda^2/3, 3.2\,{\rm m}^2)$.

Array	N_a	$A_{\rm tot}(10^3\,{\rm m}^2)$	B (MHz)	$t_{\rm int}$ (hr)	$R_{\rm min}(m)$	$R_{\rm max}(km)$
MWA	112	1.6	8	1000	4	0.75
LOFAR Core	48	38.6	8	1000	100	1.5
HERA	331	50.0	8	1000	14.3	0.3
SKA0	899×0.5	831×0.5	8	1000	35	2
SKA1	899	831	8	1000	35	2
SKA2	899×4	831×4	8	1000	35	2

We first illustrate the sensitivity of different iterations of SKA in Figure 2, where we take the parameters in Table 1 for SKA0 - with 50% of the SKA1 baseline collecting area, SKA1, and SKA2 - with x4 the collecting area of SKA1. For each of these we assume a filled core followed by r^{-2} distribution out to a maximum radius $R_{\rm max}$. HERA is assumed to have a uniform antennae distribution. SKA1 has 911 stations total with 899 in the core and 650 stations within a radius of 1km accounting for ∼75% of the total number of stations and collecting area (Dewdney 2013). At lower frequencies the array is densely packed and has constant collecting area, at higher frequencies the array becomes sparse.

Figure 2 illustrates a few key points governing parameter constraints. Here we have eliminated modes whose wavelength exceeds the instrument bandwidth removing sensitivity to the largest physical scales (smallest k modes). At $z = 8$, SKA0 is directly comparable in sensitivity to the proposed HERA experiment (Pober et al. 2014), which is more centrally concentrated to compensate for its small number of stations. Detection of the 21cm signal at $z \gtrsim 20$ with SKA1 is dependent upon either a strong 21cm absorption signal that boosts the amplitude of the 21cm power spectrum, e.g. $T_S \ll T_\gamma$ as expected before X-ray heating, or spin temperature fluctuations that add additional power over that of the density field. Unfortunately, it seems likely that during the absorption regime the details and spatial variation of the spin temperature will matter and complicated getting at cosmology.

Table 2 shows the cosmological parameters obtained with the listed experimental performances using a Fisher matrix approach following McQuinn et al. (2006). The key take home message of this is that SKA-LOW has the raw sensitivity to add useful information on cosmological parameters to Planck. The largest gains are on parameters that require small scale information, for example the running of the primordial power spectrum and related inflationary parameters (Barger et al. 2009; Adshead et al. 2011) and neutrino masses (Pritchard & Pierpaoli 2008). This

PoS(AASKA14)012

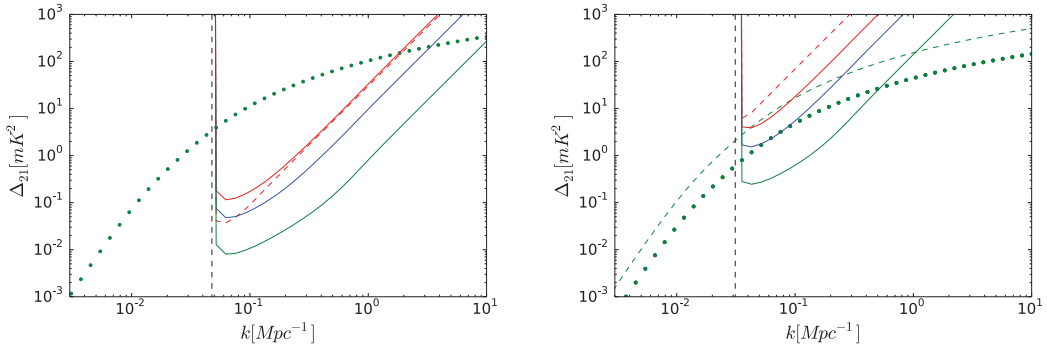

Figure 2: Sensitivity plots of HERA (red dashed curve), SKA0 (red), SKA1 (blue), and SKA2 (green). Dotted curve shows the predicted 21cm signal *from the density field alone* assuming $x_H = 1$ and $T_S \gg T_{\rm CMB}$. At $z = 20$, we also plot the case of $T_S = 20$K in the $z = 20$ panel to give a better sense of the expected 21 cm signal during absorption. Vertical black dashed line indicates the smallest wavenumber probed in the frequency direction $k = 2\pi/y$, which may limit foreground removal. *Left panel:* $z = 8$ *Right panel:* $z = 20$.

also indicates that SKA-LOW will have the sensitivity to provide a useful consistency check on cosmological parameters from the high redshift regime long before dark energy becomes important.

These numbers assume a single deep field designed to reduce thermal noise and so maximise sensitivity on the smallest scales. This tends to maximise the constraint on parameters like neutrino mass, which modify the power spectrum primarily on small scales. On large scales, cosmic variance dominates over thermal noise. This makes it useful to complement a single deep field with many shallower fields, which increase the survey volume and reduce the cosmic variance. The SKA-LOW survey strategy of shallow ~ 10000 deg^2, mid 1000 deg^2, and deep 100 deg^2 surveys provides a good mix to optimise for cosmology.

Table 2: Fiducial parameter values and $1-\sigma$ constraints on cosmological parameters. Non-cosmological parameters included in the analysis $\{\tau, x_H(z=7), x_H(z=7.5), x_H(z=8)\}$ are not shown. We take $k_{\rm min} = 2{\rm Mpc}^{-1}$ as the limit to linear modes.

	$\log\Omega_m h^2$	$\log\Omega_b h^2$	Ω_Λ	n_s	$\log(A_s/10^{-10})$	Ω_k	$dn_s/d\log k$	M_ν (eV)
Value	-1.9	-3.8	0.7	0.95	-0.19	0	0	0.3
Planck	0.028	0.0068	0.038	0.0035	0.0097	0.0022	0.0047	0.35
Hera	0.0091	0.0055	0.011	0.003	0.0088	0.0021	0.0036	0.12
SKA0	0.017	0.0058	0.023	0.0032	0.009	0.0022	0.0034	0.22
SKA1	0.0083	0.0051	0.01	0.003	0.0084	0.002	0.0018	0.12
SKA2	0.0016	0.0048	0.0026	0.0027	0.0081	0.0012	0.00092	0.084

We make no attempt here to model the effects of astrophysics on these constraints. Increasingly conservative assumptions can degrade these constraints arbitrarily far (Mao et al. 2008), so

PoS(AASKA14)012

these should be viewed as optimistic bounds on the constraints that might be achieved. Nonetheless it is clear that the attempt to extract cosmology from CD and EoR observations could be quite rewarding.

3. Separating "gastrophysics" and cosmology

The key challenge for extracting fundamental physics from the 21cm signal will be separating the effects of cosmology from "gastrophysics". A number of avenues have been studied in the literature, which broadly separate into (1) avoidance and (2) modelling and (3) redshift space distortions. The optimistic case in the previous section assumed the possibility of avoidance - a clean region in redshift where $T_S \gg T_{\rm CMB}$ and $x_H = 1$. Theoretical modelling of the 21cm signal (e.g. Pritchard & Loeb 2008; Thomas & Zaroubi 2011; Mesinger et al. 2013; Fialkov et al. 2014) suggests that we are unlikely to find such a region, although certain epochs may approach this limit. In the absence of a clean window, it might still be possible to avoid astrophysics via the angular dependence of the power spectrum induced by redshift space distortions. Focussing on the $P_{\mu^4} \approx P_\delta$ part could lead to clean cosmological measurements. Obtaining precision cosmology this way is hard and the literature suggests little improvement over Planck will be possible (McQuinn et al. 2006; Mao et al. 2008). Figure 3 shows predicted errors bars for SKA on the P_{μ^2} and P_{μ^4} parts of the power spectrum. A detection is possible with at wavenumbers $k = 0.1 - 1\,{\rm Mpc}^{-1}$, but with much less precision than the full 21 cm power spectrum.

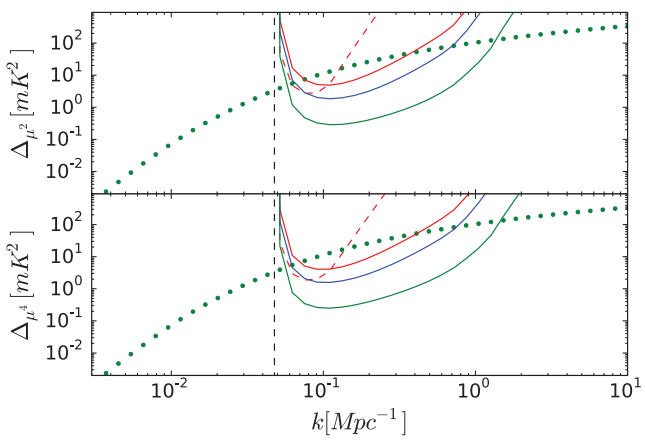

Figure 3: Sensitivity plots at $z = 8$ on P_{μ^2} (top panel) and P_{μ^4} (bottom panel) for HERA (red dashed curve), SKA0 (red), SKA1 (blue), and SKA2 (green). Dotted curve shows the predicted 21cm signal from the density field alone assuming $x_H = 1$ and $T_S \gg T_{\rm CMB}$. Vertical black dashed line indicates the smallest wavenumber probed in the frequency direction $k = 2\pi/y$, which may limit foreground removal.

The most likely path is to model the contribution of astrophysics. Compared with the CMB our theoretical understanding of the 21cm signal during reionization is poor. Predictions for the 21cm power spectrum do not exist at the same level of precision as the cosmology. Nonetheless, we

PoS(AASKA14)012

expect the contribution of astrophysics to be relatively broad band and determined by extra power about a characteristic scale, eg the bubble size during reionization. Mao et al. (2008) showed that relatively simple parametrisations capture the shape of ionisation contributions and so might be fitted for and marginalised out. Information from measurements of P_{μ^2} would complement this, as would information from different redshift slices. Given the large amount of information in 3D and the ability of SKA to image the signal - allowing ionised bubbles to be directly identified and masked out - it may be possible to characterise the astrophysics on large scales. This has yet to be examined in detail and it is unclear how far 21cm observations might be “cleaned" of astrophysics.

One thing to note is that reionization destroys information - ionised bubbles produce no 21cm signal - while heating and Lyα coupling merely overlay the density field with other information. It may be possible in the future to establish a way of separating spin temperature fluctuations from the density field in some other way, e.g. by using galaxy observations to reconstruct the Lyα flux on large scales, and so recover more of the cosmological information from observations in the cosmic dawn.

4. Constraining new physics from heating

The 21cm signal probes both the ionization and thermal state of the IGM. Although we do not know the precise timing and evolution of the signal, empirical scaling relations based on local star-forming galaxies (e.g. Mineo et al. 2012) suggest that the X-rays from early galaxies heat the IGM to temperatures above the CMB before the bulk of reionization (e.g. Furlanetto 2006; McQuinn & O'Leary 2012). This marks the transition of the 21cm signal from absorption to emission, with large-scale fluctuations in gas temperature likely driving the 21cm power to its largest amplitude (e.g. Pritchard & Furlanetto 2007; Baek et al. 2010). The epoch of IGM heating is a powerful probe of the high-energy processes in the early Universe, with could have both astrophysical and cosmological origins. Both can tell us about the nature of dark matter (DM).

In order to explain the apparent deficiencies of CDM on small (sub-Mpc) scales, Warm Dark Matter (WDM) models have recently gained in popularity. In these models, DM is assumed to consist of smaller mass particles, $\sim$ keV, such as the sterile neutrino or gravitino. The increased particle free-streaming and velocity dispersion (acting as a sort of effective pressure), can dramatically suppress structures on small-scales. This suppression is even more obvious in the early Universe, where typical halos hosting galaxies were much smaller, and larger structures did not have time to fragment. Current astrophysical lower limits on the WDM particle range from $m_x \gtrsim$ 1-3 keV (assuming a thermal relic relativistic at decoupling), with various degrees of astrophysical degeneracy (e.g. de Souza et al. 2013; Kang et al. 2013; Pacucci et al. 2014; Viel et al. 2013)

The resulting dearth of galaxies in the early Universe means that the astrophysical epochs in the 21cm signal were delayed. The challenge as always will be to disentangle the cosmological impact from astrophysical uncertainties, for example a lower than expected star formation efficiency in CDM would look superficially similar to a higher star formation efficiency in WDM. Since the fractional suppression of structure increases with redshift, this becomes much easier with the first galaxies observable with the SKA. For example, we only need to understand the astrophysics of the first galaxies to an order of magnitude in order to improve on current m_X constraints (Sitwell et al. 2014). Moreover, even if the star-formation efficiency in CDM is allowed to vary in order to

PoS(AASKA14)012

mimic the mean 21cm evolution in WDM models, the signal will still not be completely degenerate (see Fig. 4a). This is due to the fact that the galaxies driving the 21cm evolution in WDM should reside in higher mass, more rapidly evolving halos, than those in CDM. The increased bias of such halos results in larger 21cm fluctuations (see Fig. 4a).

The heating of the IGM could also have a cosmological component. In particular, annihilations of dark matter particles in the $\sim$ 10 GeV mass range (motivated by recent results from indirect experiments; (e.g. Adriani et al. 2009; Abdo et al. 2010; Aguilar et al. 2013) could provide a dominant source of heat, before the birth of the first galaxies. Driven by the evolution of $\sim M_\odot$ structures, several orders of magnitude smaller than those hosting galaxies, heating is expected to be much slower in such models, resulting in a smaller brightness temperature gradient $\mathrm{d}\delta T_b/\mathrm{d}\nu \sim$ 4mK MHz^{-1} in the range $\nu \sim 60-80$ MHz (Valdés et al. 2013). Moreover, DM annihilations would heat the IGM quite uniformly, which is not the case for heating driven by astrophysical sources residing in early galaxies. The resulting lack of temperature fluctuations (see Fig. 4b) would result in dramatic drop in 21cm power during heating, which would be easy to identify with the SKA (Evoli et al. 2014). Furthermore, the ensuing rise in 21cm power when the galaxies start contributing to heating the IGM should occur *when the IGM is already in emission*. The later is a qualitatively robust signature of DM annihilation heating, easily obtainable with the SKA.

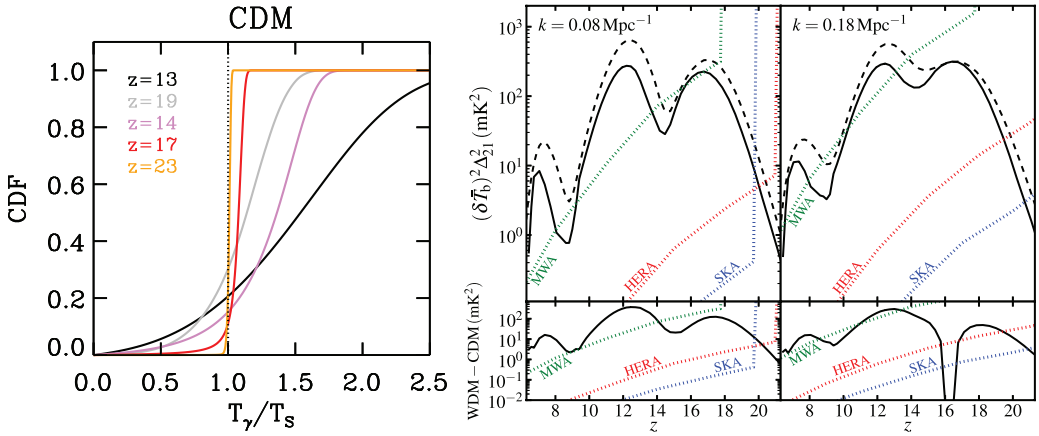

Figure 4: *Right panel:* Evolution of the power spectrum of δT_b for WDM with $m_X = 2$ keV. The top panels show power spectra at $k = 0.08, 0.18$ Mpc^{-1} for WDM (dashed) and the CDM model (solid). CDM models have f_*(z) (star-formation efficiency) chosen to reproduce the global 21-cm signal found for the respective WDM model. The bottom panels show the difference in the power spectrum between WDM and CDM models. Dotted curves show forecasts for the 21cm power spectrum thermal noise as computed in Mesinger et al. (2014) assuming 2000 h of observation time. The dotted green, blue and red curves are the forecasts for the MWA, SKA and HERA, respectively. This figure is from Sitwell et al. (2014). CDFs of T_γ/T_S corresponding to the fiducial and extreme astrophysical X-ray heating (black and gray curves respectively) from Mesinger et al. (2013). The colored curves correspond to models in which 10 GeV DM annihilations are also accounted for (in addition to fiducial astrophysical heating), with varying relative contribution. The curves correspond to the redshift for which $T_s \sim T_{\mathrm{CMB}}$. Figure is from (Evoli et al. 2014).

PoS (AASKA14) 012

4.1 21 cm signal from primordial magnetic fields

Primordial magnetic fields (PMFs) has been intensively investigated in the literature as possible seeds for large scale magnetic fields observed in galaxies and clusters of galaxies (for a recent review, see (Durrer & Neronov 2013)). Magnetic fields in galaxies in high redshifts (Bernet et al. 2008) and in void regions (Neronov & Vovk 2010; Ando & Kusenko 2010; Takahashi et al. 2013) can well be the pieces of evidence that the seed fields are of primordial origin. The primordial magnetic fields may be created in the very early universe, e.g., at the epoch of inflation, cosmological phase transition, and cosmological recombination. The Planck collaboration recently placed limits on the magnetic field strength smoothed on 1 Mpc scales $B_{\lambda=1\mathrm{Mpc}} < 3.4$ nG and the spectral index $n_B < 0$ of any PMFs from the temperature anisotropies on large and small angular scales (Planck Collaboration 2013).

The CMB brightness temperature fluctuations produced by the neutral hydrogen 21-cm line (21 cm) would offer a new probe of the primordial magnetic fields (PMFs) created in the early universe. For the 21 cm observation, aside from the early structure formation effect by the Lorentz force from the PMFs, one of the important effects is the dissipation process of the PMFs that increases the baryon temperature. The dissipation occurs mainly through ambipolar diffusion due to the velocity difference between neutral hydrogen (which is the dominant component in the dark ages) and ionized particles (whose trajectory is bent by the Lorentz force). The effect of the dissipation is rather significant. The gas temperature can reach 1000 K or even 10^4 K at $z = 30$ if the magnetic fields have the strength of $B_\lambda \sim 3$ nG (Sethi & Subramanian 2005; Tashiro & Sugiyama 2006; Schleicher et al. 2009; Kunze & Komatsu 2014).

This dissipation will give rise to a unique signature of the PMFs on the 21 cm observation. Because the spin temperature is closely coupled to the gas temperature at high redshift ($z > 30$), the 21 cm signal would come as 'emission' if the energy dissipation is efficient. In Fig. 5 the global HI signal with several magnetic field strengths are shown. For cases with sufficient magnetic fields, say $B \gtrsim 0.03$ nG, the signal is always emission against CMB while in the standard ΛCDM model the signal would be absorption for the frequency range of $f_\nu \lesssim 80$ MHz (corresponding to the signal from redshift $z \gtrsim 20$).

We show the angular power spectrum of the 21 cm brightness temperature including the PMFs in Fig. 5b (Shiraishi et al. 2014). Here we do not account for any (standard) heating effects (i.e., UV, X, and Lα background emissions) to isolate and clarify the effects from the PMFs. On large scales which may be relevant to SKA observations, there are two distinct contributions. One is from the standard (adiabatic) density fluctuations enhanced by the heating from the PMFs, and the other is from the PMF induced density fluctuations dominant on smaller scales (Tashiro & Sugiyama 2006; Schleicher et al. 2009). We can see from the figure that $B = 1$ nG magnetic fields are marginally within reach for a statistical detection of the power spectrum. Stacking observing channels in principle will add more statistical power.

The angular correlation function in real space including the effects from the PMFs is also studied in Sethi & Subramanian (2009). The function exhibits a distinct feature because the PMFs induce early structure formation and the small scale halos form more compared to the case in the standard ΛCDM model The signal from primordial magnetic fields shows oscillatory feature contrary to that in the standard ΛCDM since the matter power spectrum induced by the PMFs is

PoS(AASKA14)012

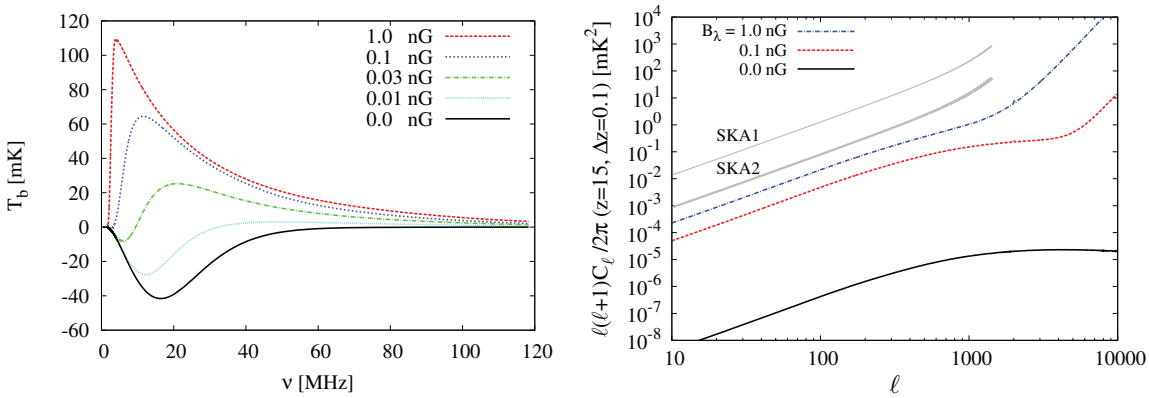

Figure 5: *Left panel:* The global 21 cm signal with magnetic field strength $B = 1$ 0.1, 0.03, and 0.01 nG (colored lines from top to bottom). The solid line corresponds to the model without primordial magnetic fields. Note that any other heating source than magnetic fields is neglected in the figure. *Right panel:* Angular power spectra for PMF strengths: $B = 0,\ 0.1,\ 1.0$ nG at $z = 15$. The bottom curve shows the power spectrum from the standard density perturbations for fully neutral medium without any heating and reionization processes. The red and blue curves correspond to the cases with heating by the PMFs with $B = 0.1$ nG and $B = 1.0$ nG, respectively. The heating induces deviations of the spin temperature from the CMB temperature and the signal is enhanced. The noise curves for SKA1 and SKA2 with 1MHz bandwidth are also shown as indicated. By courtesy of M. Shiraishi & H. Tashiro. For reference, at $z = 15$, $k \approx 0.2(l/1000)\,\mathrm{Mpc}^{-1}$.

blue and most of halos are formed at the scale close to the magnetic Jeans' length. It has been argued that 5 sigma detection of the 0.5 nG magnetic fields will be possible with less than one week integration of SKA observation (Sethi & Subramanian 2009).

5. Bulk flows

Tseliakhovich & Hirata (2010) demonstrated the existence of coherent supersonic velocity flows between baryons and dark matter after decoupling at $z \approx 1100$. This has the consequence of inhibiting the formation of star forming galaxies in low-mass halos ($M \lesssim 10^6\,\mathrm{M}_\odot$) (e.g. Maio et al. 2011; Stacy et al. 2011). If there is significant star formation in such halos, dependent upon H_2 cooling and the absence of Lyman-Werner background, then the radiation from such galaxies can lead to a significantly enhanced 21cm signal (Visbal et al. 2012; Fialkov et al. 2014; McQuinn & O'Leary 2012). The effect of bulk flows could then have a major effect on the 21cm signal during the period of Lyman alpha coupling and IGM heating.

Although the details of this are still quite uncertain, if this enhancement exists, it opens the possibility of measuring cosmology at $z = 20 - 27$ with SKA. The relative velocity flows trace the sound horizon and so especially enhance the baryon acoustic oscillation feature in the 21cm power spectrum (see e.g. McQuinn & O'Leary 2012). The BAO signature provides a standard ruler, calibratable with CMB observations, to form an inverse distance ladder stretching from $z = 1100$ through $z \sim 20$. Such measurements would strongly constrain the parameter space for departures from ΛCDM, such as early dark energy models (e.g. Bartelmann et al. 2006; Doran & Robbers 2006). Imaging the 21cm structures induced by these bulk flows will be possible with both SKA-

PoS(AASKA14)012

LOW Phase 1 and SKA2. This will be a truly novel probe of cosmology at high redshift vastly the reducing the possibility that non-standard dynamics could hide in the observational void between low redshift galaxy surveys and the CMB.

6. Cosmology on ultra-large scales with SKA-Low

The measurement of very large scales provides an unique way to probe modifications to the standard cosmological model. In particular it is on scales past the matter-radiation equality peak that General Relativistic corrections become important, at scales above ~ 5 comoving Gpc/h (Jeong et al. 2012). Probing this region would allow to check for any inconsistencies in General Relativity. However, current surveys are still far from probing this region - as an example, the BOSS survey only probes scales up to 200 Mpc/h (Anderson et al. 2012). In fact, the total volume contained at $z < 1$ is sufficient to probe only ~ 8 modes with $k = 2\pi/(5\mathrm{Gpc}/h)$ while at $6 < z < 30$ almost 200 modes could be constrained reducing cosmic variance.

Moreover, primordial non-Gaussianity will affect the clustering of biased tracers of dark matter, by adding an extra correction $\Delta b_X(z,k)$ to the Gaussian large-scale bias b_X^G of a given biased tracer X: $\Delta b_X(z,k) = 3[b_X^G(z) - 1]\Omega_m H_0^2 \delta_c/[c^2 k^2 T(k) D_+(z)] f_{nl}$. Here, $\Omega_m = \Omega_b + \Omega_{dm}$ is the total (baryons plus dark matter) matter fraction, H_0 is the Hubble constant, $\delta_c \simeq 1.686$ is the critical collapse density contrast of matter, $T(k)$ is the matter transfer function versus the physical wave number k, and $D_+(z)$ is the linear growth factor of density perturbations. Attempts at detecting this effect with redshift surveys have led to some constraints on f_{nl} (Giannantonio et al. 2014).

By observing at very high redshifts, a low frequency interferometer would be able to probe these large 3-dimensional scales during the Epoch of Reionization and beyond. Although astrophysics will generate model dependent features on the 21cm power spectrum, it is expected that on large enough scales the power spectrum should follow the dark matter one with a different amplitude. For instance, during the epoch of reionization, the ionisation power spectrum should be a biased linear tracer of the dark matter one on scales much larger than the bubble size (see Figure 6. Although the bias itself will depend on the assumed astrophysical model, measurements on these scales will allow to pick any scale dependence generated by primordial non-Gaussianity or General Relativistic corrections.

By accessing these large volumes, probes of the high-z 21cm signal will not only measure these large scales but also have enough modes to reduce cosmic variance on the scales of interest. Having large fields of view will therefore be a key factor for these experiments. The field of view of SKA1-Low ranges from 7 deg^2 at 220 MHz ($z \sim 5.5$) to 133 deg^2 at 50 MHz ($z \sim 27$), going basically as $(1+z)^2$. These correspond to scales of ~ 380 comoving Mpc at $z \sim 5.5$ to ~ 2.3 comoving Gpc at $z \sim 27$. As a further example, a fixed redshift bin of 0.1 would evolve on the same range from 50 Mpc to 5.5 Mpc (decreasing with z). We see therefore that, although the volumes accessible by SKA1-Low are quite large, especially at very high-z, we would require a telescope with about 100 deg^2 at $z \sim 8$ to probe Gpc scales. Something that will probably have to wait for SKA2. Figure 7 shows the constraints on the primordial non-Gaussianity parameter for different telescopes.

PoS(AASKA14)012

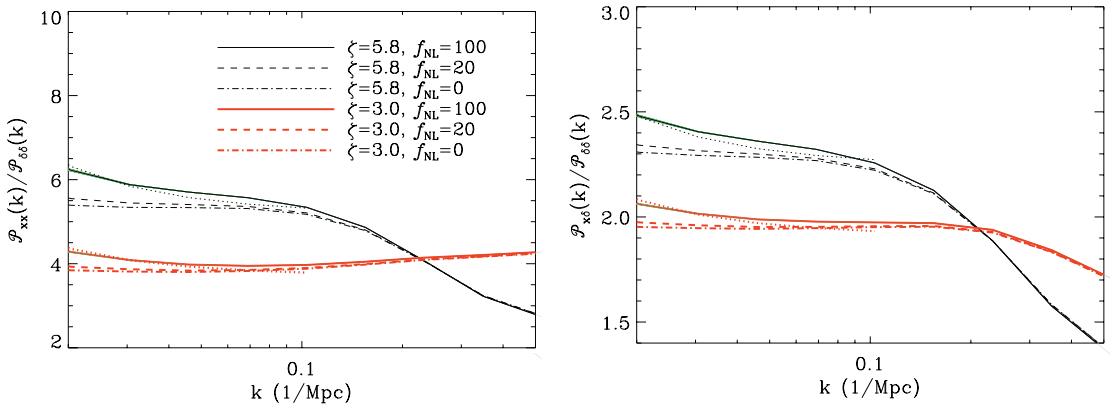

Figure 6: Ionization power spectra with non-Gaussianity of the local form from numerical simulations. We show $f_{nl} = (0, 20, 100)$ (dot-dashed, dashed, solid) for efficiency $\zeta = (5.8, 3.0)$ (thin black, thick red) at $z = 7.5$, where $x_{\rm HI} = (0.50, 0.75)$. Analytical fits are in dotted lines.

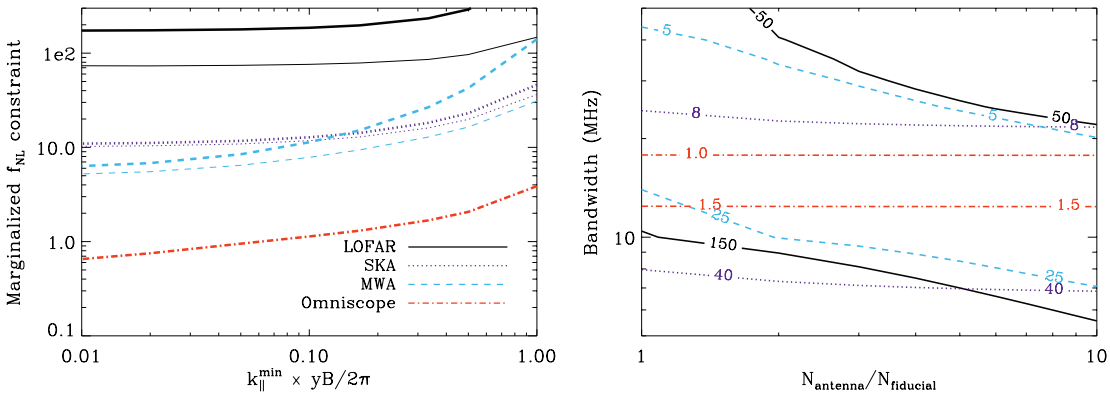

Figure 7: *Top*: Marginalized f_{nl} constraints for cases with noise (thick) and without noise (thin), which overlap for Omniscope. We consider a bandwidth of 6 MHz, but assume foregrounds can be removed on scales larger than $k_{\parallel} = 2\pi/(yB)$. *Bottom*: Marginalized f_{nl} constraints as function of bandwidth and number of antennae. The bandwidth limits the number of modes and largest scale probed along the LOS (via the survey volume $V \propto B$ and $k_{\parallel}^{\rm min} \propto 1/B$), whereas a larger number of antennae for fixed array density increases the survey resolution and number of perpendicular modes (via $n(u_{\perp})$, on large scales $\propto N_{\rm ant}$, and $u_{\perp}^{\rm max} \propto \sqrt{N_{\rm ant}}$). The color coding is the same as for the top panel.

7. Cosmic shear and the EoR

It is possible that the EoR signal could be used to measure weak gravitational lensing. In Zahn & Zaldarriaga (2006) and Metcalf & White (2009) it was shown that if the EoR is at redshift $z \sim 8$ or later, a large radio telescope such as the SKA could measure the lensing convergence power spectrum. However a very large $f_{\rm sky}$ and a very compact low frequency array was assumed by those authors. Here the calculation is repeated with parameters that are more consistent with current SKA baseline design.

The current plans for a 25 square degree survey with SKA1-Low will preclude making competitive measurements of the cosmological parameters through their effects on the weak lensing

PoS(AASKA14)012

power-spectrum because of sample variance (this is not true of the SKA1-Mid at lower redshift where the survey area will be much larger). It still might be possible to map the lensing convergence within the 25 square degree EoR survey area and a mix of wider-shallower and narrower-deeper observing modes can further optimise for weak lensing. This would allow us to actually "see" the distribution of dark matter in a typical region of the sky, something that is only possible with galaxy lensing around very atypical, large galaxy clusters. This would provide a great opportunity to correlate visible objects with mass and test the dark matter paradigm.

The previously mentioned authors extended the Fourier-space quadratic estimator technique, which was first developed in Hu (2001) for CMB lensing observations to three dimensional observables, i.e. the 21 cm intensity field $I(\theta, z)$. The convergence estimator and the corresponding variance on the lensing reconstruction are calculated assuming that the temperature (brightness) distribution is Gaussian. This will not be strictly true during the EoR, but serves as a reasonable approximation for these purposes. Note that the lensing reconstruction noise contains the thermal noise of the telescope which -assuming a uniform telescope distribution- is calculated using the formula

$$C_\ell^{\rm N} = \frac{(2\pi)^3 T_{\rm sys}^2}{B t_{\rm obs} f_{\rm cover}^2 \ell_{\rm max}(\nu)^2}\,, \tag{7.1}$$

where the system temperature $T_{\rm sys}$ at high redshifts is dominated by galactic synchrotron radiation and can be approximated by $T_{\rm sys} = 60 \times (\nu/300\,{\rm MHz})^{-2.55}\,{\rm K}$ (Dewdney 2013), B is the chosen frequency window, $t_{\rm obs}$ the total observation time, $D_{\rm tel}$ the diameter (maximum baseline) of the core array, $\ell_{\rm max}(\lambda) = 2\pi D_{\rm tel}/\lambda$ is the highest multipole that can be measured by the array at frequency ν (wavelength λ), and $f_{\rm cover}$ is the total collecting area of the core array $A_{\rm coll}$ divided by $\pi(D_{\rm tel}/2)^2$.

The advantage of 21cm lensing is that one is able to combine information from multiple redshift slices. In Fourier space, the temperature fluctuations are divided into perpendicular to the line of sight wave vectors $\mathbf{k}_\perp = \mathbf{l}/r$, with r the angular diameter distance to the source redshift, and a discretized version of the parallel wave vector $k_\parallel = \frac{2\pi}{\mathscr{L}} j$, where $\mathscr{L}$ is the depth of the observed volume. Considering modes with different j independent, an optimal estimator can be found by combining the individual estimators for different j modes without mixing them. The three-dimensional lensing reconstruction noise is then found to be (Zahn & Zaldarriaga 2006)

$$N(L,\nu) = \left[\sum_{j=1}^{j_{\rm max}} \frac{1}{L^2} \int \frac{d^2\ell}{(2\pi)^2} \frac{[\mathbf{l}\cdot\mathbf{L} C_{\ell,j} + \mathbf{L}\cdot(\mathbf{L}-\mathbf{l}) C_{|\ell-L|,j}]^2}{2 C_{\ell,j}^{\rm tot} C_{|\mathbf{l}-\mathbf{L}|,j}^{\rm tot}}\right]^{-1}. \tag{7.2}$$

Here, $C_{\ell,j}^{\rm tot} = C_{\ell,j} + C_\ell^{\rm N}$, where $C_{\ell,j} = [\bar{T}(z)]^2 P_{\ell,j}$ with $\bar{T}(z)$ the mean observed brightness temperature at redshift z due to the average HI density and $P_{\ell,j}$ the underlying dark matter power spectrum (Zahn & Zaldarriaga 2006). For SKA1-Low we can consider a $1,000$ hr observation time and we choose $B = 8\,{\rm MHz}$ and $j_{\rm max} \sim 40$, but with multiple bands ν that can be stacked to reduce the noise so that $N_L = 1/\sum_\nu [N(L,\nu)]^{-1}$.

At redshift $z_s \sim 8$, we can assume the SKA1-Low Baseline Design (Dewdney 2013) parameters of $A_{\rm coll} \simeq 0.3\,{\rm km}^2$ with maximum baseline $D_{\rm tel} = 4\,{\rm km}$, while for SKA we can consider $A_{\rm coll} \simeq 1.2\,{\rm km}^2$. The estimated lensing noise is shown in Figure 8 along with the estimated signal. Here

PoS(AASKA14)012

$C_L^{\kappa\kappa}$ is the convergence field power spectrum at $z_s = 8$ and N_L the lensing reconstruction noise assuming a reionization fraction $f_{\rm HI} = 1$.

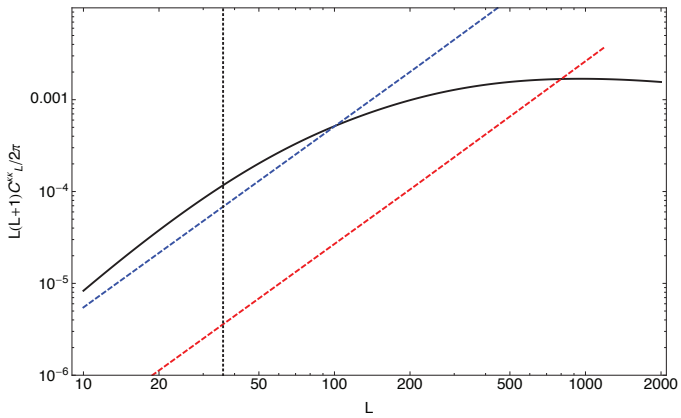

Figure 8: The lensing convergence field power spectrum, $C_L^{\kappa\kappa}$, for sources at $z = 8$ is shown as a solid black line and lensing reconstruction noise N_L as dashed lines. The blue dashed line is for SKA1-Low with 10 8 MHz frequency bins around $z = 8$ spanning the redshift range $z \simeq 6.5 - 11$. The red dashed line is for SKA2 and the same frequency bins. The vertical line is approximately the lowest L accessible with a 5-by-5 degree field. Where the noise curves are below $C_L^{\kappa\kappa}$, typical fluctuations in the lensing deflection should be recoverable in a map.

These results show that it might be possible to map the lensing signal over a range of angular scales. This measurement greatly benefits from the larger collecting area that will come with SKA2 (we also note that considering a more compact array, i.e. smaller $D_{\rm tel}$, also improves the signal-to-noise). Note that the sensitivity of SKA1-LOW is such that larger area surveys at lower integration time do not significantly improve this picture. Although multi-beaming to get larger area at fixed integration time would help with cosmic variance on large scales. For SKA-LOW an optimal observing strategy includes a mix of shallow-wide surveys to beat down cosmic variance on large scales and deep-narrow surveys to measure small scales. The weak lensing power spectrum can be better measured for redshifts after reionization using SKA-Mid and the same 21 cm intensity mapping technique discussed, but over a much larger area of sky (Pourtsidou & Metcalf 2014).

8. Conclusions

SKA-LOW will provide the first window onto cosmological information from the epoch of reionization and cosmic dawn at $z = 6 - 27$. This makes it unique among the diverse array of future cosmological experiments, which are typically limited to redshifts $z \lesssim 3$. This new view of the Universe will test the standard cosmological model deep in the matter dominated regime, where, in principle, we believe we know the evolution of the Universe. The absence of deviations from ΛCDM would observationally confirm our current assumption that a single cosmological model applies from the CMB to the present. Deviations from ΛCDM predictions would signal new physics and provide a new way of learning about the Universe.

Precision cosmology with SKA-LOW has potential to be very interesting, but is made difficult by astrophysical contamination. The large volume and number of linear modes of the density field

PoS(AASKA14)012

accessible at high redshift will one day lead to a revolution in precision cosmological constraints. SKA-LOW Phase 1 will take the first step in this direction and a mix of shallow-wide and deep-narrow observing fields can help optimise for cosmology; for example matching a narrow-deep 1000hr field over a single field with broad-shallow 10hr fields. The greater sensitivity of SKA2 will push significantly further. The key limitation will be our ability to separate astrophysics the density field to measure cosmological parameters. It is clear that the effort should be made, but our existing understanding of the astrophysics is still too crude to make robust predictions. SKA will contribute to more precise measurements of ΛCDM parameters, but crucially will test the parameters in a new regime.

Much clearer is the ability of both SKA-Low Phase 1 and 2 to measure the thermal history of the Universe at redshifts $z = 6 - 27$. Never before measured, the thermal history contains information about exotic physics - dark matter physics, primordial magnetic fields, and more. The time dependence and spatial variation of such heating is qualitatively different from that of galaxies providing a clear observational signature accessible to SKA. At the same time, SKA could measure the effect of supersonic relative velocity flows between baryons and dark matter. This probes much the same physics as the CMB and might allow BAO measurements of the sound horizon as a standard ruler to measure the geometry of the Universe.

As SKA1 becomes SKA2, greater sensitivity will allow wider sky surveys to fixed depth for a given integration time. These large volume observations will access super-horizon physics and, with the SKA2, it will be possible to search for relativistic corrections and primordial non-Gaussianity on $\gtrsim$ Gpc scales. Wider sky area and greater angular resolution also improves the ability of SKA to measure weak lensing of the 21cm background. Weak lensing will map the dark matter field in representative patches of the Universe on scales from degrees to tens of arc minutes providing a unique view of the growth of dark matter into the cosmic web.

In this chapter, we have focussed on the main paths to cosmology with SKA-LOW. Many more speculative ideas for cosmology exist. For example, constraining time evolution of the fine structure constant (Khatri & Wandelt 2007) or observing cosmic strong wakes (Brandenberger et al. 2010). 21cm observations over wide sky areas offer a way of probing distinct Hubble volumes in the same way as the CMB. Given the relative infancy of this field, it is likely that new ideas for probing cosmology will be developed during the development of SKA.

It is hopefully clear that SKA-LOW will have something to say on a wide range of cosmological topics. The 21cm signal offers more varied routes to cosmology than traditional probes of large scale structure. This means that the subtleties of extracting precision cosmology from 21cm observations are not fully understood and much work will be needed before SKA. SKA-LOW will transform our view of the astrophysics of the epoch of reionization and cosmic dawn, the same observations will add to our understanding of cosmology and provide new insights into the make up of the early Universe.

References

Abdo, A. A., et al. 2010, JCAP, 4, 14
Adriani, O., et al. 2009, Nat., 458, 607
Adshead, P., Easther, R., Pritchard, J., & Loeb, A. 2011, JCAP, 2, 21

PoS(AASKA14)012

Aguilar, M., et al. 2013, Physical Review Letters, 110, 141102
Anderson, L., et al. 2012, MNRAS, 427, 3435
Ando, S., & Kusenko, A. 2010, ApJ, 722, L39
Baek, S., Semelin, B., Di Matteo, P., Revaz, Y., & Combes, F. 2010, A & A, 523, A4
Barger, V., Gao, Y., Mao, Y., & Marfatia, D. 2009, Physics Letters B, 673, 173
Bartelmann, M., Doran, M., & Wetterich, C. 2006, A & A, 454, 27
Bernet, M. L., Miniati, F., Lilly, S. J., Kronberg, P. P., & Dessauges-Zavadsky, M. 2008, Nat., 454, 302
Bowman, J. D., Morales, M. F., & Hewitt, J. N. 2006, ApJ, 638, 20
Brandenberger, R. H., Danos, R. J., Hernández, O. F., & Holder, G. P. 2010, JCAP, 12, 28
de Souza, R. S., et al. 2013, MNRAS, 432, 3218
Dewdney, P. 2013, Document number SKA-TEL-SKO-DD-001 Revision 1
Doran, M., & Robbers, G. 2006, JCAP, 6, 26
Durrer, R., & Neronov, A. 2013, A & A Rev., 21, 62
Evoli, C., Mesinger, A., & Ferrara, A. 2014, ArXiv e-prints, arXiv:1408.1109
Fialkov, A., Barkana, R., Pinhas, A., & Visbal, E. 2014, MNRAS, 437, L36
Furlanetto, S. R. 2006, MNRAS, 371, 867
Furlanetto, S. R., Oh, S. P., & Briggs, F. H. 2006, Phys. Rep., 433, 181
Giannantonio, T., et al. 2014, PRD, 89, 023511
Gordon, C., & Pritchard, J. R. 2009, PRD, 80, 063535
Hu, W. 2001, ApJ, 557, L79
Jeong, D., Schmidt, F., & Hirata, C. M. 2012, PRD, 85, 023504
Kang, X., Macciò, A. V., & Dutton, A. A. 2013, ApJ, 767, 22
Khatri, R., & Wandelt, B. D. 2007, Physical Review Letters, 98, 111301
Kunze, K. E., & Komatsu, E. 2014, JCAP, 1, 9
Lidz, A., Zahn, O., McQuinn, M., Zaldarriaga, M., & Hernquist, L. 2008, ApJ, 680, 962
Maio, U., Koopmans, L. V. E., & Ciardi, B. 2011, MNRAS, 412, L40
Mao, Y., Shapiro, P. R., Mellema, G., et al. 2012, MNRAS, 422, 926
Mao, Y., Tegmark, M., McQuinn, M., Zaldarriaga, M., & Zahn, O. 2008, PRD, 78, 023529
McQuinn, M., & O'Leary, R. M. 2012, ApJ, 760, 3
McQuinn, M., Zahn, O., Zaldarriaga, M., Hernquist, L., & Furlanetto, S. R. 2006, ApJ, 653, 815
Mellema, G., Koopmans, L. V. E., Abdalla, F. A., et al. 2013, Experimental Astronomy, 36, 235
Mesinger, A., Ewall-Wice, A., & Hewitt, J. 2014, MNRAS, 439, 3262
Mesinger, A., Ferrara, A., & Spiegel, D. S. 2013, MNRAS, 431, 621
Metcalf, R. B., & White, S. D. M. 2009, MNRAS, 394, 704
Mineo, S., Gilfanov, M., & Sunyaev, R. 2012, MNRAS, 419, 2095
Neronov, A., & Vovk, I. 2010, Science, 328, 73
Pacucci, F., Mesinger, A., Mineo, S., & Ferrara, A. 2014, MNRAS, 443, 678
Planck Collaboration. 2013, ArXiv e-prints, arXiv:1303.5076
Pober, J. C., et al. 2014, ApJ, 782, 66
Pourtsidou, A., & Metcalf, R. B. 2014, MNRAS, 439, L36
Pritchard, J. R., & Furlanetto, S. R. 2007, MNRAS, 376, 1680
Pritchard, J. R., & Loeb, A. 2008, PRD, 78, 103511

PoS(AASKA14)012

Pritchard, J. R., & Pierpaoli, E. 2008, PRD, 78, 065009
Schleicher, D. R. G., Banerjee, R., & Klessen, R. S. 2009, ApJ, 692, 236
Sethi, S. K., & Subramanian, K. 2005, Mon. Not. Roy. Astron. Soc., 356, 778
—. 2009, Journal of Cosmology and Astro-Particle Physics, 11, 21
Shaw, J. R., & Lewis, A. 2008, PRD, 78, 103512
Shiraishi, M., Tashiro, H., & Ichiki, K. 2014, ArXiv e-prints, arXiv:1403.2608
Sitwell, M., Mesinger, A., Ma, Y.-Z., & Sigurdson, K. 2014, MNRAS, 438, 2664
Stacy, A., Bromm, V., & Loeb, A. 2011, ApJ, 730, L1
Takahashi, K., Mori, M., Ichiki, K., Inoue, S., & Takami, H. 2013, ApJ, 771, L42
Tashiro, H., & Sugiyama, N. 2006, Mon. Not. Roy. Astron. Soc., 372, 1060
Thomas, R. M., & Zaroubi, S. 2011, MNRAS, 410, 1377
Tseliakhovich, D., & Hirata, C. 2010, PRD, 82, 083520
Valdés, M., Evoli, C., Mesinger, A., Ferrara, A., & Yoshida, N. 2013, MNRAS, 429, 1705
Viel, M., Becker, G. D., Bolton, J. S., & Haehnelt, M. G. 2013, PRD, 88, 043502
Visbal, E., Barkana, R., Fialkov, A., Tseliakhovich, D., & Hirata, C. M. 2012, Nat., 487, 70
Zahn, O., & Zaldarriaga, M. 2006, ApJ, 653, 922

PoS(AASKA14)012

PROCEEDINGS OF SCIENCE

The physics of Reionization: processes relevant for SKA observations.

Benoît Semelin*
LERMA, Observatoire de Paris, UPMC, France
E-mail: benoit.semelin@obspm.fr

Ilian Iliev
Astronomy Centre, Department of Physics & Astronomy, Pevensey II Building, University of Sussex, Falmer, Brighton BN1 9QH, United Kingdom
E-mail: I.T.Iliev@sussex.ac.uk

The local intensity of the 21 cm signal emitted during the Epoch of Reionization that will be mapped by the SKA is modulated by the amount of neutral hydrogen. Consequently, understanding the process of reionization of the intergalactic medium (IGM) is crucial for predicting and interpreting the upcoming observations. After presenting the basic physics and most meaningful quantities pertaining to the process of reionization, we will review recent progress in our understanding of the production and escape of ionizing photons in primordial galaxies and of their absorption in the IGM especially in so-called minihalos and Lyman Limit Systems.

Advancing Astrophysics with the Square Kilometre Array
June 8-13, 2014
Giardini Naxos, Italy

*Speaker.

PoS(AASKA14)013

1. Introduction

The SKA will observe the Epoch of Reionization (EoR) through the redshifted 21 cm emission of Hydrogen. The intensity of the emitted signal depends on several local quantities but during most of the EoR the most important one is obviously the ionization state of the gas: only neutral atoms in the ground state can emit 21 cm radiation. Fully ionized regions will show up as null-signal areas in the tomographic data cube. While the basic physics of hydrogen ionization is simple, it takes place in a strongly inhomogeneous medium and thus involves vastly different scales and characteristic times, resulting in a complex geometry and evolution of the ionization field.

To discuss the important aspects of the reionization process we will first consider that the gas consists of pure hydrogen. The effects of the presence of helium and metals will be discussed as needed. If x_i is the local ionization fraction of hydrogen, it obeys the simple equation:

$$\frac{dx_i}{dt} = \gamma(T)(1-x_i)n_e - \alpha(T)x_i n_e + \Gamma(1-x_i) \qquad \text{with} \qquad \Gamma = \int d\Omega \int_{\nu_0}^{\infty} \frac{\sigma_\nu I_\nu}{h\nu} d\nu \tag{1.1}$$

where n_e is the number density of electrons, T is the temperature, γ is the collisional ionization coefficient, α is the recombination coefficient, Γ is the photoionization rate, ν is the frequency, I_ν is the local specific intensity, σ_ν is the ionization cross-section, and Ω the solid angle. Tightly coupled to the ionization equation is the energy equation:

$$\frac{dE}{dt} = \mathscr{H} - \Lambda \tag{1.2}$$

where E is the internal energy of the gas, $\mathscr{H}$ is the heating rate and Λ is the cooling rate. Both $\mathscr{H}$ and Λ include contributions from radiative processes (photo-heating, collisional ionization cooling, recombination cooling, collisional excitation cooling, Bremsstrahlung cooling and Compton cooling - heating) and from dynamical processes (adiabatic cooling or heating, heating from viscous dissipation). References for fitting functions of the various rates, that depend on temperature and ionization state and for the ionization cross-section that depends on the frequency can be found for example in Iliev et al. (2006).

2. Insights into the ionization process

Along with the equations above, the process of reionization is governed by the radiative transfer equation (Rybicki & Lightman 1986). In the general case, these equations are furthermore coupled to the hydrodynamics equation of the self-gravitating gas through the energy equation and the equation of state of the gas. However ionization by UV photons will only heat up the gas to $\sim 20\,000$ K, and the amount of X-rays produced during the EoR will not change this picture in the bulk of the IGM. The associated increase in the pressure of the gas will affect noticeably only structures with a virial temperature of the same order as the heated gas temperature or lower. If the radial density profile of real halos actually follow the numerical fit in Navarro et al. (1997) (the so-called NFW profile), structures with a virial temperature less than $\sim 20\,000$ K have a total masse $\lesssim 10^8 M_\odot$ (both dark matter and baryons included). The gas in these structures may be photo-evaporated by the arrival of an ionization front or will never fall into the potential well of

PoS(AASKA14)013

halos in ionized regions. On larger scales though, the coupling to the dynamics may safely be ignored as gravitation dominates over hydrodynamic pressure.

Evaluating a few physical quantities in typical EoR environments will help us to get a first idea on how reionization proceeds.

2.1 Mean free path of ionizing photons

In a homogeneous medium the mean free path of ionizing photons is defined by $l = \frac{1}{\sigma_\nu n_H}$, where $\sigma_\nu \simeq 6.3\ 10^{-18} \left(\frac{E}{E_0}\right)^{-3}$ cm^{-2} is the ionization cross-section (see Verner et al. (1996) for a more accurate formula), E_0 is the energy of the ionization threshold and n_H the number density of absorbers, here neutral hydrogen atoms. In a fully neutral IGM at the average density of the universe we find $l \simeq 2.\ \left(\frac{10}{1+z}\right)^2 \left(\frac{E}{E_0}\right)^3$ comoving kpc. In higher density regions the value will be even smaller. Consequently, a reionization fueled by stars that produce ionizing photons at energies not much higher than the ionization threshold will proceed in the form of fully ionized bubbles growing around the sources, separated from the neutral region by a sharp ionization front. On the other hand, the small amount of X-ray photons emitted above 1 keV have a mean free path in the 1 comoving Gpc range and will provide a weak (a few percent at most) and mostly uniform contribution to the ionization field (note that the associated heating has important consequences for the 21 cm signal). Photons with energies of a few keV have only a small probability of being absorbed in the IGM before reionization is complete.

2.2 Recombination time

Another important quantity is the typical recombination time. Or, in other words, how many times does an hydrogen atom in the IGM need to be ionized by the end of the EoR. The recombination time is defined as $t_{\rm rec} = \frac{1}{\alpha(T) n_H}$. At the average density of the universe and for a gas at $T = 10^4$K, we find, $t_{\rm rec} \simeq 240 \left(\frac{10}{1+z}\right)^3$Myr. Since the bulk of the IGM is likely reionized in the $6 < z < 10$ range, most atoms need to be ionized only once. At the same time, a moderate overdensity of $\frac{\delta\rho}{\rho} \sim 20$ will have a much shorter recombination time of ~ 10 Myr. Such structures (filaments, minihalos) will act as photon sinks until the ionizing flux is large enough to photoevaporate them (see, e. g. Sobacchi & Mesinger 2014). The recombination time in the interstellar medium will be even shorter and, most likely, only the clumpiness of the medium or holes blown by supernovae explosion or AGN feedback will allow ionizing photons to escape into the IGM (see next section).

2.3 Ideal Stromgren sphere model

Assuming sharp ionization fronts, neglecting recombinations in ionized regions and neglecting the coupling to the hydrodynamics are thus reasonable assumptions for building simple analytic models on how the IGM is reionized. If we further simplify by assuming an isolated point source in a homogeneous IGM and a constant temperature in the ionized region we get the well known Strömgren sphere model (Strömgren 1939). In this case the radius of the spherical ionized region grows as: $r(t) = r_s \left[1 - \exp(t/t_{\rm rec})\right]^{1/3}$ where $r_s = \left[\frac{3\dot{N}_\gamma}{4\pi\alpha(T) n_H^2}\right]^{1/3}$ is the asymptotic radius of the ionized sphere and $\dot{N}_\gamma$ is the number of ionizing photons produced per second by the source. From

PoS(AASKA14)013

this model we can estimate that the typical velocity of ionization fronts in the IGM during the EoR is $\gtrsim 10^3$ km.s^{-1}. Let us emphasize that during the EoR, the luminosity of proto-galaxies typically increases on time scales much shorter that $t_{\rm rec}$, and thus the asymptotic Strömgren radius is never reached.

Generalized solutions for the Strömgren sphere in an expanding universe have been formulated (Shapiro & Giroux 1987). In view of the future attempts to detect individual bubbles in the SKA tomographic data, it is also important to notice that the apparent shape of the bubbles along the light cone is not isotropic (Yu 2005; Majumdar et al. 2011).

3. Ionization processes in primordial galaxies

3.1 Escape of the ionizing continuum

The ionization history of the IGM is regulated by the number of ionizing photons escaping from primordial galaxies. From an observational point of view this number can be inferred from the galaxy luminosity function at various redshifts. The most recent data give us indications to the amplitude and shape of the luminosity function up to $z = 8$ (e.g. Bouwens et al. 2014). But then modeling comes in to connect the luminosity function to the mass function, through a M/L ratio that may depend on a number of parameters. For an in-depth understanding of the physics of primordial galaxies however, it is useful to break the M/L parameter in two parts: the star formation rate (SFR) and the radiation escape fraction $f_{\rm esc}$, and more specifically for our purpose the escape fraction of the ionizing continuum. Indeed, primordial galaxies host dense gas clouds with short recombination time that will consume a large fraction of the emitted photons before they ever reach the slowly-recombining diffuse IGM. Dust may also play a role in absorbing photons during the later phase of the EoR. In any case, $f_{\rm esc}$ and its dependence on the host galaxy and its environment is the result of complex radiative processes.

From an observational point of view, measuring $f_{\rm esc}$ during the EoR presents a challenge since the photons that do escape galaxies will be absorbed in the IGM and participate in the global reionization process, and thus will never reach us. Indirect probes can be used, such as the determination of the average photoionization rate in the IGM from Ly-α forest observations, or the Lyman-α emitters (LAE) luminosity since the intensity of the Lyman-α line is proportional to the recombination rate in the galaxy and thus to the amount of ionizing radiation that does not escape. Using such observations, a substantial level of modeling is needed to yield $f_{\rm esc}$. Observations provide some constraints for the relative escape fraction between ionizing and non-ionizing photons at $z \sim 3$ (e.g. Steidel et al. 2001; Iwata et al. 2009). A few studies focused on higher redshift provide only tentative results: an upper limit of 0.6 at z=5.6 (Ono et al. 2010) or an inferred value of 0.3 at z=6-8 (Finkelstein et al. 2012). However, there is a general agreement based on models that, if stellar sources are to be the main contributor to reionization, the escape fraction must increase toward higher redshifts and/or be higher in low mass galaxies (e.g. Alvarez et al. 2012; Haardt & Madau 2012; Kuhlen & Faucher-Giguère 2012; Mitra et al. 2012).

Another way to produce estimates of $f_{\rm esc}$ is to run numerical simulation that preferably include the coupling between the ionizing continuum radiative transfer and the dynamics. These simulations need to resolve to some extent the interstellar medium while preserving the cosmological

PoS(AASKA14)013

environment and have become possible only recently (Gnedin et al. 2008; Wise & Cen 2009; Razoumov & Sommer-Larsen 2010; Yajima et al. 2011, 2014; Paardekooper et al. 2013; Wise et al. 2014; Kimm & Cen 2014). They do not use similar resolution nor similar modeling, and thus do not quantitatively converge in terms of the mean value and scatter of $f_{\rm esc}$ as a function of redshift and host halo mass. One common trend seems to emerge however: $f_{\rm esc}$ decreases with the mass of the host halo (with Gnedin et al. (2008) finding the opposite trend however, and Kimm & Cen (2014) finding almost no dependence), and increases with redshift (weak opposite tend in Kimm & Cen (2014)). This seems to indicate that low mass galaxies made the largest contribution to the production of ionizing photons, at least at high redshift, before radiative feedback quenched their star formation rate.

3.2 Feedback on primordial galaxies

The second important aspect of ionizing radiative processes in primordial galaxies is the feedback on the gas (and thus star formation). This feedback is enacted through the photo-heating and photo-evaporation of the gas in galaxies and of the accreting gas clumps and filaments, but also to some extent through radiation pressure.

In a forming galaxy made of near-primordial gas, cooling processes below 10^4 K are rather inefficient (low metal content, uncertain H_2 formation). Thus photo-heating the cold gas back to $\sim 10^4$ K through ionization may substantially decrease the SFR. This is easily understood in $< 10^8$ $M_\odot$ galaxies that have a virial temperature below 10^4 K: the gas will be expelled from the galaxy (Petkova & Springel 2011; Dale et al. 2012; Hasegawa & Semelin 2013). But it may also be true in more massive galaxies where the gas is not expelled but merely prevented from fragmenting. Such an effect is found by Hasegawa & Semelin (2013) for example. Such small scale processes can be implemented in large scale reionization simulations using sub-grid recipes (Iliev et al. 2007)

On top of the feedback mediated by thermal pressure, radiation pressure may play a role in regulating star formation in primordial galaxies. Wise et al. (2012) observed, using numerical simulation, a significant quenching of the star formation rate when ionizing radiation pressure is included. This result has not been reproduced yet by other teams using different numerical techniques. It is definitely worth further investigation.

Last but not least, the feedback from supernovae explosions definitely regulates the escape fraction. Although not a pure radiative process, it shapes the gas distribution around the sources and influences the escape fraction of ionizing photons (Kimm & Cen 2014).

The relative importance of these different processes probably depends on the mass of the host halo and is not the object of a consensus. Further numerical investigation is needed.

4. Ionization processes in the IGM

As we have seen in section 2.1, the mean free path of ionizing photons in typical IGM conditions during the EoR is very small at the ionization energy threshold compared to typical cosmological distances. Consequently the ionization process sourced by UV photons takes the form of ionizing fronts sweeping through the IGM. The isothermal sound speed in the ionized gas behind the front is ~ 10 km.s^{-1}, and much lower in the neutral gas ahead of the front. The ionization front velocity (set by the local ionizing flux and baryon density alone if recombination is neglected) is

PoS(AASKA14)013

typically larger than 1000 km.s^{-1} in the IGM at $z \sim 10$ (see section 2.3). Consequently the gas is unable to respond dynamically, and the front is an extreme weak-R type (R for rarefied, see Spitzer 1978), with negligible compression of the gas behind the front. This is the main justification for not coupling radiative transfer to hydrodynamics in many EoR simulation. It is worth mentioning however, that the ionization front not only slows down but even stalls in structures with moderate overdensity (~ 30) due to recombinations (e. g. Sobacchi & Mesinger (2014) and references therein).

While there is little doubt that stars contributed a significant faction of the ionizing photons through their UV continuum, we have few constraints yet on the contribution of X-ray sources (X-ray binaries, Supernovas, AGN and more) to the reionization process. Because of their long mean free path, a reionization powered by X-rays only would show a diffuse and fluctuating ionization field without any fronts. It is however unlikely that X-rays contribute as much as the UV continuum to the ionization budget. Consequently the most likely picture is that of an IGM with fully ionized regions around the sources, separated by a sharp ionization front from near-neutral regions, ionized at most a few percent by X-rays. An important effect of X-ray penetrating into the neutral IGM however is the heating by secondary electrons (Furlanetto et al. 2006; Shull & van Steenberg 1985). Indeed when an X-ray photon ionizes an hydrogen atom, the energy in excess of the ionization threshold goes into kinetic energy for the freed electron. This electron then collides with neighboring atoms, producing secondary ionizations, excitations and heating. Heating up the cold IGM by a few K only has a strong impact on the 21 cm signal.

The presence of helium in the primordial gas has a moderate impact on the reionization of hydrogen. With first and second ionization energies at 24.6 eV and 54.4 eV respectively, Helium filters and hardens the spectrum of Pop III and Pop II stars. In practice the emissivity above 54.4 eV is small enough that the reionization of HeII is negligible at $z > 6$. On the other hand, HeI is reionized mostly at the same time as HI, moderately slowing the pace of the process by consuming a small part of the radiation (e.g. Ciardi et al. 2012). Behind the ionization fronts, the temperature of the ionized IGM is somewhat higher than if Helium is not considered. Overall, the impact of helium reionization on the 21 cm signal is small.

5. Recombination processes in the IGM

5.1 Minihalos

The very first stars formed in cosmological minihalos, much smaller than present-day galaxies, with total masses below $\sim 10^8 M_\odot$. The efficiency of this process is however uncertain. Indeed, the Jeans mass criterion for star formation requires that the gas be extremely cold, with temperatures of just a few hundred K. At primordial composition, consisting almost exclusively of Hydrogen and Helium, the gas in such small halos can only cool through H_2 molecular line cooling. These molecules are fragile, however, and easily dissociated by Lyman-Werner radiation. Moreover, minihalos are photoevaporated by ionizing radiation (Shapiro et al. 2004; Iliev et al. 2005b), which is a complex process that results in screening of the intergalactic medium by them and slowing down the large-scale ionization fronts (Iliev et al. 2005a; Ciardi et al. 2006).

Furthermore, due to their shallow gravitational potential wells, the minihalo abundance is influenced by heating of the IGM by e.g. X-rays, as well as modulated locally by baryon-dark

PoS(AASKA14)013

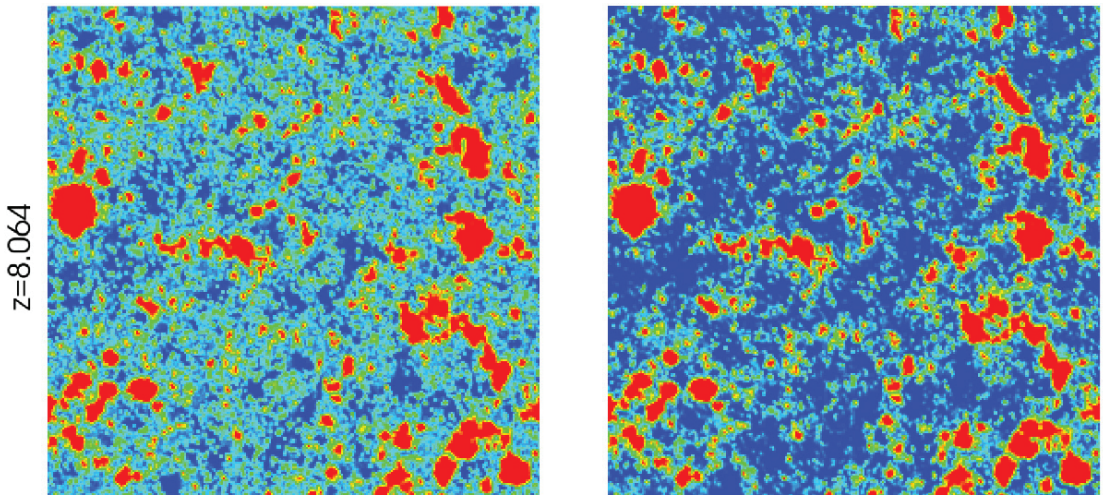

Figure 1: Maps of the ionization fraction color coded form 0. (blue) to 1. (red) in simulations modeling the effects of minihalos (left) or not (right). From Ahn et al. (2012).

matter velocity offsets (Tseliakhovich & Hirata 2010). The relative importance of these effects is still highly uncertain and requires much better knowledge than we currently possess of the early sources of X-rays and soft UV radiation: their nature, abundance and clustering. Nonetheless different aspects of this physics have been modeled in both simulations (Ahn et al. 2009; Baek et al. 2010; Ahn et al. 2012) and semi-analytical work (Santos et al. 2010). Both X-rays and Lyman-Werner photons have very long mean free paths, of order 100 Mpc or more, and the baryon-dark matter velocity modulation acts on similarly large scales, all of which could result in significant fluctuations in the local abundance of minihalos and their star formation rates (e.g. Fialkov & Loeb 2013). The first stars forming in cosmological minihalos likely dominated the early reionization, but eventually the Lyman-Werner radiation from those same stars suppresses further star formation, stalling the reionization history until the larger-mass, atomically-cooling halos take over (Ahn et al. 2012). This results in significantly different early reionization history compared to the case without minihalos, much higher electron-scattering optical depth for CMB photons and a different reionization geometry (see Figure 1).

5.2 Lyman Limit systems

Lyman Limit Systems (LLS) are structures of any mass that are optically thick to the UV background (in practice with column density larger than 10^{17} cm^{-3}). They act as screens for UV photons traveling in ionized regions. Analysis of QSO spectra show that LLS limit the mean free path of UV photons to ~ 50 cMpc at $z = 6$ (Songaila & Cowie 2010). Estimates at higher redshifts are uncertain. The main consequence of LLS would then be to slow down the end of reionization (in terms of the average ionization fraction reaching 1), by limiting the effective number of sources that contribute to the local ionizing flux.

LLS are difficult to take into account in full numerical simulations because it typically involves resolving the internal structure and internal ionization processes in dwarf galaxies. Subgrid models can be devised and implemented. Using semi-numerical simulations Crociani et al. (2011)

PoS(AASKA14)013

and Sobacchi & Mesinger (2014) find that LLS have an impact on the history and geometry of reionization and thus on the 21 cm signal power spectrum. Alvarez & Abel (2012) also implement the effect of LSS in simulations.

6. Conclusion

At first glance, the process of reionization is simple: ionized bubbles around primordial galaxies with sharp, supersonic ionization fronts expanding into a neutral IGM mildly heated and weakly ionized by X-rays. It is however regulated by two complex processes: the production and escape of ionizing photons from primordial galaxies, and the presence of dense, small scale structures in the IGM that act as photon sinks (minihalos and LLS). Both of these processes have an impact on the pace and geometry of reionization. On the one hand observations provide limited constraints on these processes at $z < 6$ whose extrapolation during the Eopch of Reionization is risky. On the other hand, simulations do not offer a consensus on these processes, mainly because they involve small scales that are difficult to resolve while keeping a statistically significant volume. Either significant progress will be made in the next few years or the interpretation of the observations of the 21 cm signal with the SKA will have to deal with models involving a large parameter space.

References

Ahn, K., Iliev, I. T., Shapiro, P. R., et al. 2012, ApJL, 756, L16
Ahn, K., Shapiro, P. R., Iliev, I. T., Mellema, G., & Pen, U.-L. 2009, ApJ, 695, 1430
Alvarez, M. A., & Abel, T. 2012, ApJ, 747, 126
Alvarez, M. A., Finlator, K., & Trenti, M. 2012, ApJL, 759, L38
Baek, S., Semelin, B., Di Matteo, P., Revaz, Y., & Combes, F. 2010, A&A, 523, A4
Bouwens, R. J., Illingworth, G. D., Oesch, P. A., et al. 2014, arXiv1403.4295
Ciardi, B., Bolton, J. S., Maselli, A., & Graziani, L. 2012, MNRAS, 423, 558
Ciardi, B., Scannapieco, E., Stoehr, F., et al. 2006, MNRAS, 366, 689
Crociani, D., Mesinger, A., Moscardini, L., & Furlanetto, S. 2011, MNRAS, 411, 289
Dale, J. E., Ercolano, B., & Bonnell, I. A. 2012, MNRAS, 424, 377
Fialkov, A., & Loeb, A. 2013, JCAP, 11, 66
Finkelstein, S. L., Papovich, C., Ryan, R. E., et al. 2012, ApJ, 758, 93
Furlanetto, S. R., Oh, S. P., & Briggs, F. H. 2006, PhR, 433, 181
Gnedin, N. Y., Kravtsov, A. V., & H.-W., C. 2008, ApJ, 672, 765
Haardt, F., & Madau, P. 2012, ApJ, 746, 125
Hasegawa, K., & Semelin, B. 2013, MNRAS, 428, 154
Iliev, I. T., Ciardi, B., Alvarez, M. A., et al. 2006, MNRAS, 371, 1057
Iliev, I. T., Mellema, G., Shapiro, P. R., & Pen, U. 2007, MNRAS, 376, 534
Iliev, I. T., Scannapieco, E., & Shapiro, P. R. 2005a, ApJ, 624, 491
Iliev, I. T., Shapiro, P. R., & Raga, A. C. 2005b, MNRAS, 361, 405
Iwata, I., Inoue, A. K., Matsuda, Y., et al. 2009, ApJ, 692, 1287
Kimm, T., & Cen, R. 2014, ApJ, 788, 121
Kuhlen, M., & Faucher-Giguère, C.-A. 2012, MNRAS, 423, 862

PoS(AASKA14)013

Majumdar, S., Bharadwaj, S., Datta, K. K., & Choudhury, T. R. 2011, MNRAS, 413, 1409
Mitra, S., Choudhury, T. R., & Ferrara, A. 2012, MNRAS, 419, 1480
Navarro, F., Frenk, C., & White, S. D. M. 1997, APJ, 490, 493
Ono, Y., Ouchi, M., Shimasaku, K., et al. 2010, ApJ, 724, 1524
Paardekooper, J.-P., Khochfar, S., & Dalla Vecchia, C. 2013, MNRAS, 429, L94
Petkova, M., & Springel, V. 2011, MNRAS, 412, 935
Razoumov, A. O., & Sommer-Larsen, J. 2010, ApJ, 710, 1239
Rybicki, G. B., & Lightman, A. P. 1986, Radiative Processes in Astrophysics
Santos, M. G., Ferramacho, L., Silva, M. B., Amblard, A., & Cooray, A. 2010, MNRAS, 406, 2421
Shapiro, P. R., & Giroux, M. L. 1987, ApJ, 321, L107
Shapiro, P. R., Iliev, I. T., & Raga, A. C. 2004, MNRAS, 348, 753
Shull, J. M., & van Steenberg, M. E. 1985, ApJ, 298, 268
Sobacchi, E., & Mesinger, A. 2014, MNRAS, 440, 1662
Songaila, A., & Cowie, L. L. 2010, ApJ, 721, 1448
Steidel, C. C., Pettini, M., & Adelberger, K. L. 2001, ApJ, 546, 665
Strömgren, B. 1939, ApJ, 89, 526
Tseliakhovich, D., & Hirata, C. 2010, Phys. Rev. D, 82, 083520
Verner, D. A., Ferland, G. J., Korista, K. T., & Yakovlev, D. G. 1996, ApJ, 465, 487
Wise, J. H., Abel, T., Turk, M. J., Norman, M. L., & Smith, B. D. 2012, MNRAS, 427, 311
Wise, J. H., & Cen, R. 2009, ApJ, 693, 984
Wise, J. H., Demchenko, V. G., Halicek, M. T., et al. 2014, MNRAS, 442, 2560
Yajima, H., Choi, J.-H., & Nagamine, K. 2011, MNRAS, 412, 411
Yajima, H., Li, Y., Zhu, Q., et al. 2014, MNRAS, 440, 776
Yu, Q. 2005, ApJ, 623, 683

PoS(AASKA14)013

PROCEEDINGS OF SCIENCE

All-sky signals from recombination to reionization with the SKA

Ravi Subrahmanyan
Raman Research Institute, C V Raman Avenue, Sadashivanagar, Bangalore 560080, India
E-mail: rsubrahm@rri.res.in

N Udaya Shankar
Raman Research Institute, C V Raman Avenue, Sadashivanagar, Bangalore 560080, India
E-mail: uday@rri.res.in

Jonathan Pritchard
Imperial College London, Astrophysics, Blackett Laboratory, Prince Consort Road, London SW7 2AZ, UK
E-mail: j.pritchard@imperial.ac.uk

Harish K Vedantham*
Kapteyn Astronomical Institute, Landleven 12, 9747 AD Groningen, The Netherlands
E-mail: h.k.vedantham@rug.nl

Cosmic evolution in the hydrogen content of the Universe through recombination and up to the end of reionization is expected to be revealed as subtle spectral features in the uniform extragalactic cosmic radio background. The redshift evolution in the excitation temperature of the 21-cm spin flip transition of neutral hydrogen appears as redshifted emission and absorption against the cosmic microwave background. The precise signature of the spectral trace from cosmic dawn and the epoch of reionization are dependent on the spectral radiance, abundance and distribution of the first bound systems of stars and early galaxies, which govern the evolution in the spin-flip level populations. Redshifted 21 cm from these epochs when the spin temperature deviates from the temperature of the ambient relic cosmic microwave background results in an all-sky spectral structure in the 40–200 MHz range, almost wholly within the band of SKA-Low. Another spectral structure from gas evolution is redshifted recombination lines from epoch of recombination of hydrogen and helium; the weak all-sky spectral structure arising from this event is best detected at the upper end of the 350–3050 MHz band of SKA-mid. Total power spectra of SKA interferometer elements form the measurement set for these faint signals from recombination and reionization; the inter-element interferometer visibilities form a calibration set. The challenge is in precision polarimetric calibration of the element spectral response and solving for additives and unwanted confusing leakages of sky angular structure modes into spectral modes. Herein we discuss observing methods and design requirements that make possible these all-sky SKA measurements of the cosmic evolution of hydrogen.

Advancing Astrophysics with the Square Kilometre Array
June 8-13, 2014
Giardini Naxos, Italy

*Speaker.

PoS(AASKA14)014

1. Introduction: the science case

From the time of big bang nucleosynthesis hydrogen gas makes up ∼75% of the mass of the baryons in the Universe. This makes atomic lines of neutral hydrogen in the intergalactic medium an ideal tracer of the evolution and history of the Universe over cosmic time. In this section, we review the physics affecting hydrogen over cosmic time and the resulting signals that SKA can measure. A number of useful reviews on this topic exist, including Furlanetto et al. (2006); Pritchard & Loeb (2012); Sunyaev & Chluba (2009).

Until the Universe cools to a temperature of ~ 0.3 eV photons from the radiation background keep hydrogen ionised. At a redshift of $z \approx 1100$ hydrogen recombines leading to physical decoupling of the photons. From that point on, the majority of photons free stream without scattering to the present day when they appear as the relic cosmic microwave background (CMB). Fully ionised helium (He III), with its higher binding energy, recombines somewhat earlier first to He II (at $z \approx$ 5000-8000) and then to He I (at $z \approx$ 1600-3500).

Although the photons decouple from the baryons at $z \approx 1100$, the large photon-to-baryon ratio (approximately 10^{10} photons per baryon) means that scattering of photons from the small residual ionised fraction of free electrons ($x_e \sim 10^{-5}$) maintains thermal equilibrium between the free electrons and the CMB. Collisions between free electrons and the remainder of the baryons maintains $T_K = T_{\rm CMB}$. This thermal coupling eventually ends at a redshift $z \approx 200$ as dilution of the gas with Hubble expansion reduces the photon-electron scattering rate below a critical threshold. With thermal decoupling, the gas begins to cool adiabatically with expansion and its temperature scales as $T_K \propto (1+z)^2$, cooling faster than the CMB, which evolves as $T_{\rm CMB} \propto (1+z)$. For the first time in the Universe's evolution there exist two separate temperature scales that dictate the level populations in the atomic gas - the gas kinetic temperature T_K and the CMB temperature $T_{\rm CMB}$. This temperature difference creates the opportunity for an interesting 21 cm signal.

Key to understanding the 21 cm signal is the evolution of the spin temperature T_S, which describes the ratio of atoms in the upper and lower hyperfine level $n_1/n_0 = 3\exp(-T_\star/T_S)$, where $T_\star \equiv hc/k\lambda_{21\rm cm} = 0.068\,$K. The spin temperature is set by the relative rate of spin-flip transitions driven by interaction with CMB photons, scattering Lyα photons, or collisions between the mix of neutral hydrogen atoms, free protons and free electrons. Formally it is determined by

$$T_S^{-1} = \frac{T_{\rm CMB}^{-1} + x_\alpha T_\alpha^{-1} + x_c T_K^{-1}}{1 + x_\alpha + x_c}, \tag{1.1}$$

where T_α is the color temperature of the Lyα radiation field at the Lyα frequency and x_c, x_α are coupling coefficients due to atomic collisions and scattering of Lyα photons, respectively. T_α is closely coupled to T_K by recoil during repeated scattering and the spin temperature becomes strongly coupled to the gas temperature when $x_{\rm tot} \equiv x_c + x_\alpha \gtrsim 1$. Combining the spin temperature with the amount of neutral hydrogen, which is parametrized by the neutral fraction $x_{\rm HI}$, gives the differential brightness temperature

$$T_b = 27\, x_{\rm HI} \left(\frac{\Omega_b h^2}{0.023}\right) \left(\frac{0.15}{\Omega_m h^2}\frac{1+z}{10}\right)^{1/2} \left(\frac{T_S - T_{\rm CMB}}{T_S}\right) \text{mK}. \tag{1.2}$$

The evolution of the all-sky 21 cm signal is illustrated in Fig. 1 and shows three key regimes - two absorption troughs and one emission feature.

PoS(AASKA14)014

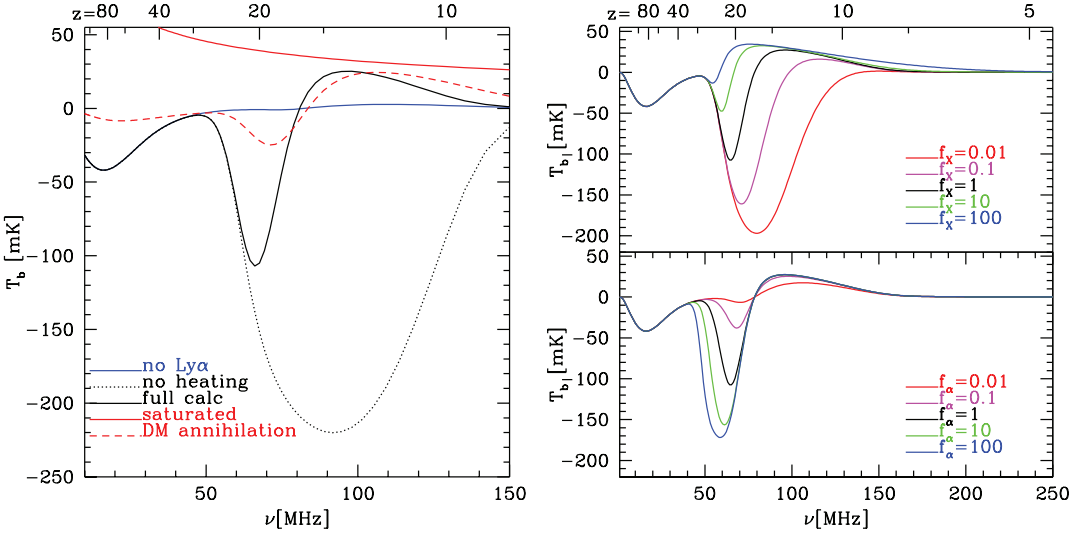

Figure 1: Example histories of the 21 cm all-sky signal. *Left panel:* Variation with different physics Burns et al. (2012a) *Right panel:* Variation with X-ray heating (top) and Lyα flux (bottom) Pritchard & Loeb (2010).

Working chronologically down from high redshift, we first see a 21 cm absorption signal during the cosmic dark ages. In the absence of exotic new physics, the evolution of this signal is determined by collisional coupling and the effect of adiabatic expansion on the temperature of the gas Loeb & Zaldarriaga (2004). However, it is possible that exotic physics and dark matter annihilation, for example, can heat the gas in this early phase changing this picture Burns et al. (2012a).

More generically, collisional coupling becomes ineffective as the gas becomes more diffuse and it is only when the first stars and galaxies form that the 21 cm signal becomes complex. Galaxies produce Lyα photons that couple $T_S \approx T_K$ leading to the second absorption feature at redshifts less than about 30. The start of this potentially deep second absorption feature occurs as Lyα coupling starts and the end is governed by the eventual heating of the Universe by UV and soft X-rays, which leads to the final emission feature. The right panel of Fig. 1 serves to illustrate some of the uncertainty on the all-sky signal with Lyα and X-ray emissivity for fixed star formation history and assuming atomic hydrogen cooling. The Lyα luminosity is relatively similar for Pop II and Pop III stars and so reasonably well understood. More difficult to predict is the star formation history itself. Recent work has shown that relative velocity between baryons and dark matter can suppress early star formation in low mass halos Maio & Khochfar (2012); Fialkov et al. (2014). The availability of molecular H_2 for gas cooling in mini halos is also significant in early star formation.

The production of X-rays and their absorption by the IGM, which is highly dependent on their energy, is still quite poorly understood. Candidate sources include mini-quasars, inverse-Compton scattering from supernova remnants and X-ray binaries in star forming galaxies Furlanetto (2006). Current predictions extrapolate based on local source populations, but evolution effects are to be expected Mirabel et al. (2011). Moreover, the SED of sources is variable being more or less like a power law at different energies. Hard X-rays (>2 keV) may have mean free paths comparable

PoS(AASKA14)014

with the size of the Universe and so fail to heat the IGM. The rising edge of the deep absorption feature provides a way to constrain this physics and has been a topic of considerable recent interest Pritchard & Loeb (2008); Mesinger et al. (2013).

Ultimately, the IGM is likely to enter a hot, Lyα coupled state where $T_S \gg T_{\rm CMB}$, although this is not guaranteed. This saturates the all-sky 21-cm signal removing any dependence on T_S, so that δT_B is completely determined by the mean density and neutral fraction x_{HI}. As ionizing UV photons from star-forming galaxies reionize the Universe the neutral fraction x_{HI} falls to zero. This is the final emission feature of the all-sky 21-cm signal, whose decline indicates the progression of reionization.

Another cosmological signal in the all-sky mean spectrum of the cosmic radio background is recombination lines from the epoch of recombination Sunyaev & Chluba (2009). In contrast to the 21-cm signatures of reionization, the predictions of the recombination spectrum are rather precise Rubiño-Martín et al. (2008) assuming standard recombination physics, and hence serve as an excellent test of the standard model. The recombination lines are expected to appear across SKA bands: in Fig. 2 we show the signature across the SKA-mid frequency range.

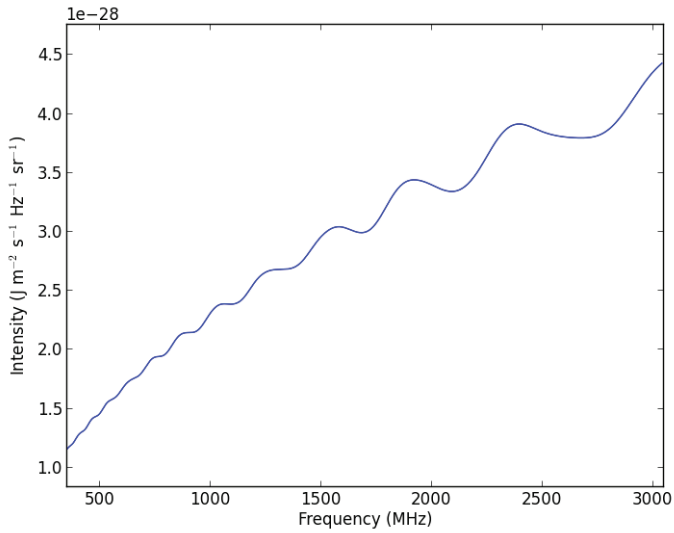

Figure 2: Spectrum of recombination lines from the epoch of cosmological recombination Rubiño-Martín et al. (2008) across the SKA-mid frequency range.

2. The motivation for all-sky wideband observations with the SKA

The generic all-sky spectral signature of reionization has an early cosmic time when Lyman-α from the first stars might cause a substantial absorption dip in the cosmic radio background, which is followed by reheating and late time ionization that is expected to manifest as 21-cm emission that progressively diminishes towards lower redshifts. The spatial distribution of ionizing sources and the density structure of the gas originating in the matter distribution power spectrum results in spatial structure in hydrogen spin temperature and ionization fraction; this manifests as an evolving

PoS(AASKA14)014

power spectrum of brightness temperature fluctuations about the evolving mean all-sky absorption or emission signature. A key science goal of SKA-Low is the interferometer imaging of the cosmic evolution of spatial structure in the ionization state and 21-cm spin-flip excitation temperature. The detection of the evolving power spectrum of this spatial structure is a diagnostic of the astrophysics in the reionization epoch, the radiation from the first stars and dwarf galaxies, and their distribution statistics.

In this context it is useful to ask whether the all-sky spectral signature contains any observables that are outside the horizon of the SKA observing in interferometer mode. The all-sky redshifted 21-cm signature provides, for all redshifts, the mean departure of the 21-cm brightness temperature from the ambient CMB. This measurement is the critical zero-spacing measurement of reionization that is vital for establishing the normalization or base level of the interferometer measurement of fluctuation power. The all-sky signature is a direct measure of the mass-averaged evolution in the state of the gas and establishes clearly whether the interferometer measurements of fluctuating power at any epoch refers to absorption or emission. The all-sky measurement unambiguously determines the 'turning points' in the all-sky spectrum that identifies epochs when the spin state of the gas is driven by Wouthuysen-Field mechanism of coupling to the gas kinetic temperature, when X-ray and UV reheating occur and finally when reionization proceeds.

Today, the relative roles of the UV and X-ray radiations from the earliest stellar populations, dwarf galaxies and galactic nuclei is poorly constrained and as a consequence substantial uncertainty exists in our knowledge of the redshifts at which 21-cm power might be detectable. Second, the detection of redshifted 21-cm power from these epochs is very dependent on our ability to precisely subtract the confusing power from Galactic and extragalactic foregrounds, which dominate the cosmological signal by orders of magnitude. For both these reasons, an independent and early detection of the all-sky signature of cosmic evolution in the gas is advantageous in that it aids in selecting optimum bands for SKA imaging of the evolving power spectrum and selecting control bands where the power is expected to be diminished. SKA measurements of the all-sky signatures are, therefore, to be viewed as an essential precursor to detection and imaging of spatio-temporal 21-cm power and a necessary zero-spacing measurement that provides the base level in which the fluctuation power resides.

In the measurement of the all-sky spectrum of the cosmic radio background with the aim of detecting the faint reionization signatures embedded therein, the effective collecting area of the sensor of the sky radiation is not of consequence. What is needed is a spectral radiometer that may be precisely calibrated, and a sensor that is ideally frequency independent so that sky brightness distribution structures do not result in confusing spectral structure in the measurement set. As expected, there are several ongoing and proposed experiments that aim to make precision measurements of the spectrum of the cosmic radio background: CoRE (Chippendale, PhD thesis, 2009), EDGES Bowman & Rogers (2010), LEDA Greenhill et al. (2012), DARE Burns et al. (2012b), SARAS Patra et al. (2013), SCI-HI Voytek et al. (2014) and ZEBRA (Mahesh et al. 2014, submitted). So the question arises as to why we even consider all-sky measurements with SKA elements or stations, when dedicated single-element spectral radiometers that are purpose built for the all-sky measurement might suffice!

The cosmological signal is embedded in a foreground that is expected to be smooth in the sense that it is a summation over numerous sources within the receptor beam pattern and along

PoS(AASKA14)014

the line of sight, each of which have spectra close to a power law but which may have a spread in their indices. The foreground spectrum would, therefore, be a *'complete monotone'* but might require a high order function for precise modeling (Rao et al., in preparation). The observing band must necessarily include multiple turning points of the predicted reionization signature so that the cosmological signal in the total observing band be indescribable as a complete monotone and hence separable from the foregrounds. The expected cosmological signatures from reionization are rather wideband signals, and hence separation of the cosmological signal from foregrounds requires observing with bandwidths exceeding an octave.

The spectral response of any total power spectral radiometer contains the spectrum of the radio background modulated by the spectral gains of the receptor and electronics. The response includes additive terms from ohmic losses in the receptor of the radiation and its interconnect to amplifier devices, amplifier noise, ground spillover etc. Depending on the magnitude of the dependence of the receptor beam pattern on frequency, the response also contains spectral structure arising from mode coupling of sky structure into spectral structure. Over observing bands exceeding an octave, design of receptors with frequency independence of the beam patterns at the precision required to avoid mode coupling is challenging. However, the SKA in interferometer mode solves simultaneously for sky structure, receptor pattern and hence provides calibration solutions for the mode-coupling; this is the prime motivation for SKA measurement of the all-sky signal.

Recombination lines from the epoch of recombination are expected to appear as an extremely weak ripple in the cosmic radio background. Their detection is likely best done at cm wavelengths, where the signal-to-noise is expected to be greatest considering the line intensities, background sky noise contribution to measurement errors and receiver technology (Rao et al., in preparation). Detection of the recombination spectral structure requires observing with about 10^3 elements for reasonable integration times. SKA-mid elements operating as spectral radiometers is perhaps the only instrument capable of detecting these features in the foreseeable future; as discussed above their operation as interferometers provides the calibrations for element bandpass and gains as well as solutions for mode coupling.

3. Observing all-sky cosmological signals with the SKA

The dark-ages and reionization signatures are from about 40 to 200 MHz, almost wholly in the band of SKA-Low Phase 1. Nominally, the interferometer elements in SKA-Low Phase 1 are phased arrays of 256 dual-polarized log-periodic antennas, referred to as stations. The measurement set for this science is the total power spectra of the interferometer elements of SKA-Low operating as spectral radiometers, which corresponds to the auto-correlation spectra of the station signals. Recombination lines are predicted to be present across all SKA bands; however, the optimum frequency range for SKA is at the top of the SKA-mid band, and the total power spectra of the dish elements that form the SKA-mid interferometer form the measurement set for that science.

Critical to the science is the calibration of these total-power spectral radiometers. Calibration consists of (a) determining the instrumental bandpass for the sky signal, (b) modeling the additive spectral contaminations from other sources of system noise: receiver noise, ground spillover etc., and (c) correcting the measurement set for mode-coupling. The interferometer visibility measurements form the calibration set that generate the all-sky model of the sky brightness distribution

PoS(AASKA14)014

while simultaneously solving for a model of the antenna pattern and the interferometer element bandpass and gains. These provide the bandpass for the sky signal in the station-based total power radiometers, and also provide model of the mode coupling of sky structure into spectral structure. Certain additive contaminants (receiver noise etc.) require special and separate calibration via engineering design of the interferometer elements.

Since collecting area is inconsequential for the all-sky signal, and simplicity and frequency invariance in the beam pattern is critical, the measurement set for the reionization signature may be derived using the sky signal from just one log-periodic antenna in each station of SKA-Low. In this case just that station array element may be outfitted with electronics for calibration of its auto-correlation spectra. Alternately, a separate precision element may form an outrigger to each station and provide a wide-field auto-correlation signal, which would serve as the measurement set for the EoR science. It may be noted here that an outrigger that is placed sufficiently isolated from the station elements would escape inter-element coupling effects that are highly chromatic.

3.1 Interferometric measurement of a global signal using lunar occultation

Interestingly, the all-sky 21-cm signal can also be measured interferometrically Shaver et al. (1999), thereby circumventing some of the calibration challenges in total-power measurements. Though an interferometer is in general insensitive to a uniform all-sky signal, the presence of an occulting object such as the Moon imposes spatial structure on an otherwise featureless all-sky signal. Interferometers being spatial differencing instruments are sensitive to this structure, and measure the brightness contrast between the occulted background (diffuse Galactic emission plus all-sky 21-cm signal) and the Moon. The Moon is expected to behave as a 230 K blackbody (spectrally featureless) at radio frequencies Heiles & Drake (1963) and provides a suitable constant temperature reference against which the spectral structure in temperature of the uniform background may be measured. The spectrum observed in synthetic beams of SKA-Low towards the Moon and over the full band of 50-350 MHz provide a difference measurement between the Moon and background, which would contain the reionization spectral structure. This technique has been demonstrated recently for the first time between 35 and 75 MHz using LoFAR Vedantham et al. (2014).

Reflected Earthshine (radio frequency interference or RFI) from the Moon was thought to be a limitation to this technique McKinley et al. (2013). However, recent work with LOFAR Vedantham et al. (2014) has shown that reflected Earthshine images to the center of the lunar disc due to the specular nature of reflection and, therefore, may be independently modeled and subtracted using longer baselines (> 100 spatial wavelengths) that have the resolution to isolate this contaminant. Another potential limitation of this technique stems from contamination of lunar flux by Galactic and Extragalactic emission because of mode-coupling due to chromatic sidelobes of the interferometer synthetic beam. Here again all-sky images of continuum structure that are observed along with solutions for the station gain and bandpass calibrations provide the models for subtracting the mode-coupling.

Apart from the primary cosmic dawn/EoR science goals, the lunar occultation technique is expected to yield extremely interesting early science results from the SKA via the combination of interferometer data on the Moon and total power spectra from absolute calibration of interferometer elements to accurately measure the brightness temperature of the Moon itself. Since the thermal

PoS(AASKA14)014

emission from the Moon comes from a depth of ~ 100 wavelengths, this technique facilitates an unprecedented measurement of the depth evolution (if any) of the lunar regolith temperature up to depths of ~ 1 km.

4. SKA design requirements for the science case

The SKA1-Low will consist of 1024 stations each containing 256 log-periodic dual-polarized antenna elements evenly distributed in an irregular-random configuration within a station diameter of 35 m. The stations are distributed in an array configuration that places 50% within a 600 m radius, 75% within a 1 km radius, and the remaining 25% in three spiral arms that give maximum baseline of 100 km. The array will operate from 50 to 350 MHz. All of the 256 log-periodic dipoles in each station are usually combined in a beam former and the dual polarization signals from 1024 stations will be transported to a central signal processing building where they will be channelized and cross-correlated to provide full Stokes measurements of the spectral visibilities. The station beams, when formed from all 256 elements, expose a field-of-view defined by a circularly symmetric beam of 5° at the half-power points at 100 MHz.

We have mentioned in Section 3 above three different and alternate approaches to generating the basic measurement sets for the all-sky reionization signal using SKA-Low. They are (a) to use as basic elements the 35 m diameter stations configured as phased arrays of the 256 dipoles, or (b) to derive the sky signal by enabling just one log periodic element in each station, or (c) to separately add, as an outrigger to each station, an antenna element with precision calibration capability that would provide the autocorrelation spectra.

In all the three approaches, the observing strategy is to measure the autocorrelations of both polarization signals (X & Y) from each of the stations—to serve as the measurement set—and also full Stokes correlations (XX, YY, XY & YX) between all pairs of station signals to serve as the calibration set. This may be done for only signals from stations in the central core. An obvious advantage of restricting EoR all-sky measurements to the core stations is that this restricts the baselines used to those that are not severely affected by ionosphere; therefore, element gains, phases and bandpass calibrations may be derived with greater accuracy. The SKA1-Low correlator is required to be configured to generate the total power autocorrelation spectra for the station signals from the central core, as well as the usual interferometer cross correlations. It may be noted here that the overhead to generate the autocorrelations is relatively small and the autocorrelations may be performed by the resources freed by omitting the correlations between station signals from the outer arms.

Strategy (a) above has the highest collecting area per station and hence maximum sensitivity in baselines; consequently, this option has minimum calibration errors and produces the best global sky model. It may be noted here that enabling recording of accurate and useful auto-correlation spectra from these station signals is critical to using their sky-scans for providing the short and zero-spacing information, which will be vital for making complete and absolutely-calibrated global sky models. This is no doubt important for Galactic and Extragalactic science. From the perspective of all-sky EoR science, making an excellent global sky model with all sky-structure modes represented is critical to subtracting the spectral structures in autocorrelation spectra arising from mode coupling.

PoS(AASKA14)014

Spectral confusion due to any chromatic variation in the beam, which would couple foreground structure to spectrum (the mode-coupling issue), indeed has a solution with the SKA. In option (a) above, where the entire SKA-Low station is phased to form the signal for the total power detector, the station beams are inevitably frequency dependent. In this case the relatively superior station sensitivity also has the capacity for creating global sky models with greater accuracy, and as we have discussed above, the stations may also provide measurements of large angular modes to make the global sky model more truly representative of the absolute sky brightness distribution. A frequency dependent weighting of the element voltages prior to combining to form the station beams could potentially reduce the frequency dependence of the station beams, but not exactly because the elements do not provide continuous coverage of the aperture field. Along with interferometer solutions for the bandpass of the station beams, the models also provide calibrations for the mode coupling. Option (b) above that deploys single log-periodic dipole elements as the total power detectors would also suffer mode-coupling owing to the frequency dependence in the beam (by definition, the antenna is log-periodic, which implies that it has periodic structure in antenna characteristics in log-frequency space). In this option the sky model and antenna response modeling that emerges from the interferometer data would provide relatively poorer calibration of the mode coupling. Option (c) above uses outriggers: these antennas may be designed to be wideband frequency-independent elements with relatively lower mode coupling. Even if the elements and station beams are frequency independent, it may be mentioned here that the ionosphere could make the effective beam chromatic.

The detection and mitigation of RFI will be far superior in all-sky measurements based on autocorrelation spectra of SKA stations, which simultaneously record interferometer data. The SKA-Low baselines between the core stations are relatively small in wavelength units and hence RFI is poorly rejected in the interferometer integration times. Therefore, the visibilities are excellent detectors of RFI, particularly when Stokes V visibilities are formed, and constitute a calibration set for RFI recognition in time-frequency space that may be used to reject RFI-corrupted station signals. Moreover, interferometer data that do not contain the uniform all-sky signal may also be used to model and subtract RFI from the station total power spectra, which constitute the measurement set. Real-time RFI rejection and mitigation algorithms that clean the SKA station autocorrelation spectra using visibility data is desirable.

Experiments to date with single receptors have shown that the calibration of additive bias in the auto-correlation data is challenging, and many methods have been proposed for their marginalization. The additive contributions to autocorrelation spectra arise from ground spillover, antenna and balun ohmic losses, losses in the analog electronics signal path, and amplifier noise, which has components that propagate along and against the nominal signal flow direction. Impedance mismatches within the signal path cause reflections and, therefore, these system temperature components appear in the spectra of measurement sets with frequency structure owing to multi-path propagation to the detector. The marginalization of additive bias requires special calibration techniques; some methods are discussed and demonstrated in designs of EDGES and SARAS.

Using station beams as in option (a) above requires designing all log-periodic dipoles to have additive terms that are smooth functions of frequency that are separable from EoR signatures, which have turning points. Possible solutions include restricting path lengths for multi-path propagation by, for example, integrating high-gain amplifiers with baluns at the antenna terminals and optically

PoS(AASKA14)014

isolating this front-end electronics from the rest of the receiver. Calibration of the response to amplifier noise requires either that the amplifier noise figure be switchable between high and low states, so that a differential response would provide the response to the amplifier noise. An alternate method that has been explored is including a bidirectional coupler with the amplifier so that a calibration noise may be injected at the same point in the signal path to measure the spectrometer response to a bidirectional noise that originates at the amplifier.

SARAS demonstrates the value of correlation receivers that yield difference measurements between the sky power spectra and that from an internal reference load. Switching in the correlation receiver cancels many internal systematics and additive contaminants downstream of the switch. The correlation receiver provides complex spectra in which the sky power is exclusively in the real part following bandpass calibration, and the additive contaminants from receiver noise appear in real and imaginary parts with quadrature phase offset allowing for modeling and marginalization of their effects. Switching of the internal load provides a means for separating its contribution. SARAS represents a purpose built complex calibration scheme that may hence be included in options (b) and (c).

Bandpass calibration of spectral radiometer elements that form SKA interferometers may be done using spectral visibilities to simultaneously solve for sky structure and element gains. Switched injection of flat-spectrum noise power via directional couplers is an alternate engineering approach to bandpass calibration—implemented in SARAS—that requires noise sources and couplers in every radiometer element. An alternate engineering solution for bandpass calibration of the radiometers is pulse calibration, which is the time domain equivalent of flat spectrum noise injection. By measuring the system response to pulses much narrower than inverse of the bandwidth, the bandpass calibration is derived and also different modes in the observed spectra may be tagged to reflections from different impedance discontinuities in the signal path. Yet another method for bandpass calibration is the injection of a swept frequency tone into the system path.

In addition to bandpass calibration and the marginalization of additives, precision polarimetric calibration to estimate the unwanted confusing leakages from the polarized structure in the sky into spectral modes is necessary. Linearly polarized sky emission will appear with spectral structure in total power spectra of linearly polarized antenna elements if Faraday rotation changes the plane of polarization arriving at the antenna over frequency. Improper instrumental calibration along with Faraday Rotation that causes the polarized signal to have frequency structure might confuse the all-sky EoR signature. In this context, once again we see the advantage of using the SKA for all-sky EoR signal detection because of the ability of an interferometer array to also yield solutions for precision polarimetric calibration for the interferometer elements, which in this case constitute the spectral radiometers that measure the all-sky 21-cm signature. Specifically, Faraday rotation-measure (RM) synthesis using interferometer visibilities offers a more complete and hence accurate polarimetric calibration, associating each pixel in the sky with Stokes I along with (Q, U, RM) sets and their spectral indices. The Stokes V data are also useful in setting the thermal noise level apart from providing an indicator for radio frequency interference. The off-axis polarization effects are smaller in strategy (a), which uses a narrow station beam of 5°, compared to strategies (b) and (c), which use single receptors with broad beams as basic elements.

All of the above discussions on the requirements for interferometer based calibration of element bandpass, and solving for the mode coupling of sky structure to spectral structure from

PoS(AASKA14)014

continuum radio sources as well as linearly polarized emission along with Faraday rotation, are also relevant to SKA-mid for detection of recombination lines. The SKA-mid antennas are dishes that form the interferometer elements: their autocorrelation spectra form the measurement set for the detection of recombination lines are hence the additives in these signals will require calibration. Dish-type antennas are electrically large structures and hence would have long lengths in the signal path arising from reflections off structural elements. For this reason, for the all-sky science it is desirable for the dishes to be off-axis reflector antennas.

5. The path to SKA-Low detection of all-sky 21-cm from reionization

It is often the case that effective use of a complex experimental system for a key science goal for which it is custom built requires a deep understanding of performance and systematics, which requires experience with the instrument and development of appropriate calibration methods in the commissioning phase. New telescopes that push frontiers of technology come with surprises beyond the imagination of its designers and builders.

The sensitivity of a spectral radiometer to the all-sky EoR signature is independent of collecting area and depends on the system temperature and integration time. Pilot observations, which could lead to useful science, could begin early in the commissioning phase with 128 stations once interferometer imaging to solve for the global sky model and system calibration is enabled. The expected system temperature at 110 MHz is about 800 K and this leads to the nominal requirement of about 1 hr observing time with 128 station beams to achieve 1 mK sensitivity with a 1 MHz bandwidth. The actual time required to achieve this sensitivity would be a factor of a few larger because of various switching schemes that are inevitably introduced for calibration. For example, EDGES has a three-way switching scheme while SARAS cycles through six states of the receiver to obtain measurement and calibration data products. The above bandwidth and sensitivity are adequate to characterize the turning points in the spin temperature evolution curve (see Fig. 1). The advantage as the buildout progresses towards completion of SKA Phase 1 is not in thermal-noise related sensitivity to all-sky EoR signal, but in increasing accuracy of the calibration of the individual radiometer elements.

It may be noted here that the foregrounds are of substantially greater brightness towards longer wavelengths since the cosmic radio background has a steep $T_b \sim \nu^{-2.5}$ dependence on frequency; therefore, successful imaging of the spatial structure in 21-cm spin flip is increasingly challenging towards earlier times in the evolution of the gas. The substantially greater calibration accuracy and confusion subtraction required for elucidating early-time evolution through interferometer imaging encourages designing for detection first of the wideband all-sky signature, which may be done in SKA Phase 1. All-sky detection of the absorption trough will serve as a motivation and prelude to later imaging of the spatial structure.

The experience with SKA Phase 1 would be critical to the design of the elements of SKA Phase 2: in the design of the antenna elements and calibration schemes for additives.

6. The path to SKA detection of the recombination era

The all-sky recombination spectral signature requires 10^3 spectral radiometers operating in

PoS(AASKA14)014

parallel, and whose calibrated spectra are co-added, for detection in reasonable time. As demonstrated in Rao et al. (in preparation), arrays of radiometers with about octave bandwidths within Band 4 of the SKA-mid frequency range would require about 25,000 antenna-days for a 1σ detection. SKA1-mid array of 190 antennas, with dual polarization, would require 66 days for such a detection. A genuine attempt at a detection of the recombination spectrum is really reserved for the full SKA, after completion of SKA2-mid in Phase 2. Long duration imaging campaigns, perhaps as a deep all-sky survey, would yield the data set that might serve for detection of the recombination line signature with SKA in Phase 1 and in Phase 2.

References

Bowman, J. D., & Rogers, A. E. E. 2010, Nat., 468, 796

Burns, J. O., Lazio, J., Bale, S., et al. 2012a, Advances in Space Research, 49, 433

—. 2012b, Advances in Space Research, 49, 433

Fialkov, A., Barkana, R., Pinhas, A., & Visbal, E. 2014, MNRAS, 437, L36

Furlanetto, S. R. 2006, MNRAS, 371, 867

Furlanetto, S. R., Oh, S. P., & Briggs, F. H. 2006, Phys. Rep., 433, 181

Greenhill, L. J., Werthimer, D., Taylor, G., Ellingson, S., & LEDA Collaboration. 2012, in American Astronomical Society Meeting Abstracts, Vol. 220, American Astronomical Society Meeting Abstracts #220, 104.03

Heiles, C. E., & Drake, F. D. 1963, Icarus, 2, 281

Loeb, A., & Zaldarriaga, M. 2004, Physical Review Letters, 92, 211301

Maio, U., & Khochfar, S. 2012, MNRAS, 421, 1113

McKinley, B., Briggs, F., Kaplan, D. L., et al. 2013, AJ, 145, 23

Mesinger, A., Ferrara, A., & Spiegel, D. S. 2013, MNRAS, 431, 621

Mirabel, I. F., Dijkstra, M., Laurent, P., Loeb, A., & Pritchard, J. R. 2011, A & A, 528, A149

Patra, N., Subrahmanyan, R., Raghunathan, A., & Udaya Shankar, N. 2013, Experimental Astronomy, 36, 319

Pritchard, J. R., & Loeb, A. 2008, PRD, 78, 103511

—. 2010, PRD, 82, 023006

—. 2012, Reports on Progress in Physics, 75, 086901

Rubiño-Martín, J. A., Chluba, J., & Sunyaev, R. A. 2008, A & A, 485, 377

Shaver, P. A., Windhorst, R. A., Madau, P., & de Bruyn, A. G. 1999, A&A, 345, 380

Sunyaev, R. A., & Chluba, J. 2009, Astronomische Nachrichten, 330, 657

Vedantham, H. K., Koopmans, L. V. E., de Bruyn, A. G., et al. 2014, ArXiv e-prints, arXiv:1407.4244

Voytek, T. C., Natarajan, A., Jáuregui García, J. M., Peterson, J. B., & López-Cruz, O. 2014, ApJ, 782, L9

PoS(AASKA14)014

PROCEEDINGS OF SCIENCE

Imaging HII Regions from Galaxies and Quasars During Reionisation with SKA

J. Stuart B. Wyithe*, **Paul M. Geil**, **Hansik Kim**
School of Physics, The University of Melbourne, Parkville, Vic 3010, Australia
E-mail: swyithe@unimelb.edu.au

The ionisation structure of the Intergalactic Medium (IGM) during reionisation is sensitive to the unknown galaxy formation physics that prevailed at that time. This structure introduces non-Gaussian statistics into the redshifted 21 cm fluctuation amplitudes that can only be studied through tomographic imaging, which will clearly discriminate between different galaxy formation scenarios. Imaging the ionisation structure and cosmological HII regions during reionisation is therefore a key goal for the SKA. For example, the SKA1-LOW baseline design with a 1 km diameter core will resolve HII regions expected from galaxy formation models which include strong feedback on low-mass galaxy formation. Imaging the smaller HII regions that result from galaxy formation in the absence of SNe feedback will also be possible for SKA1-LOW in the later stages of reionisation, but may require the greater sensitivity of SKA early in the reionisation era. In addition to having baselines long enough to resolve the HII regions, the field of view for SKA1-LOW reionisation experiments should be at least several degrees in order to image the largest HI structures towards the end of reionisation. The baseline design with 35 meter diameter stations has a field of view within a single primary pointing which is sufficient for this purpose.

Advancing Astrophysics with the Square Kilometre Array
June 8-13, 2014
Giardini Naxos, Italy

*Speaker.

PoS(AASKA14)015

1. Introduction

Redshifted 21 cm emission from HI in the intergalactic medium (IGM) offers several probes of the reionisation epoch. Owing to the low signal-to-noise expected for first generation telescopes, including the MWA and LOFAR, most attention has been focussed on statistical observations of the power-spectrum of 21 cm fluctuations together with its evolution. However several other observational signatures become more powerful probes of reionisation using the imaging capability of SKA1-LOW. These include *i*) the cross-correlation of 21 cm emission with galaxies, which would directly probe the connection between reionisation and the sources of ionising radiation (Wyithe & Loeb, 2007b; Furlanetto & Lidz, 2007; Lidz et al., 2009; Park et al., 2014), *ii*) the probability distribution of intensity fluctuations, which contains additional information about the non-Gaussian intensity fluctuations during reionisation (Wyithe & Loeb, 2007b; Harker et al., 2009a; Barkana, 2009), *iii*) the observation of individual HII regions, which will probe galaxy formation physics, and *iv*) the observation of quasar-dominated HII regions, which will probe quasar emission geometries as well as the evolution of the neutral IGM (Wyithe & Loeb, 2004a; Kohler et al., 2005; Valdés et al., 2006).

While the cross-correlation of 21 cm emission with galaxies may be possible with first generation arrays using the statistics of the cross power-spectrum (Wyithe & Loeb, 2007b; Furlanetto & Lidz, 2007; Lidz et al., 2009), direct observation of the correspondence between galaxies and ionisation structure will provide unambiguous evidence of the role of galaxies in reionisation. An important prediction from the various modelling studies concerns whether over-dense or under-dense regions become ionised first. Standard calculations of the expected cross-correlation between the distribution of galaxies and the intergalactic 21 cm emission at high redshifts show that over-dense regions will be ionised early (e.g. Wyithe & Loeb, 2007b), leading to an anti-correlation between 21 cm emission and the galaxy population. Redshifted 21 cm surveys should be able to discriminate between "outside-in" and "inside-out" reionisation, even when combined with galaxy surveys of only several square degrees.

The distribution of fluctuation amplitudes is expected to be Gaussian during the early phases of reionisation. At these early times the power-spectrum represents the natural quantity to describe fluctuations in 21 cm emission, since it contains all the statistical information. However the distribution of fluctuation amplitudes becomes non-Gaussian as reionisation progresses (Mellema et al., 2006; Wyithe & Morales, 2007; Harker et al., 2009b). This is particularly the case on small scales once HII regions have formed (Furlanetto et al., 2004). As a result, the power-spectrum does not provide a complete statistical description of the reionisation process, and instead the full probability distribution of intensity fluctuations should be considered. For example, additional information could be captured by measuring skewness in the probability distribution (Wyithe & Morales, 2007; Harker et al., 2009b). However, unlike the power-spectrum, the probability distribution for intensity fluctuations must be derived from images of the ionisation structure.

In this chapter we focus on the prospects for studying galaxy formation through the imaging of HII regions, both in the typical IGM as well as around quasars using SKA1-LOW. The direct imaging of the ionised structure during reionisation would be the most unambiguous measurement of reionisation. This represents the "holy grail" of 21 cm reionisation experiments, and is a key goal for the SKA. The importance of imaging with SKA for capturing the physics of reionisation

PoS(AASKA14)015

is discussed in more detail in Mellema et al. (2015). Discussion of the science potential of SKA1-LOW for imaging the ionised structure during reionisation requires modelling of ionised regions on very large scales, and we therefore begin this chapter with a brief discussion of the semi-numerical method used to calculate ionisation structure. A more detailed discussion of issues associated with simulation of reionisation can be found in Iliev et al. (2015).

2. Semi-numerical model for reionisation

In recent years approximate, but efficient semi-numerical methods for simulating the reionisation process have been developed (Mesinger & Furlanetto, 2007) in order to overcome the limitations of both analytic and numerical methods. These extend prior work (Bond & Myers, 1996; Zahn et al., 2007) to estimate the ionisation field based on a catalogue of sources by applying a filtering technique based on an analytic HII region model (Furlanetto et al., 2004). The resulting structure of the ionisation field is similar for different variations on the filtering method as well as for full radiative transfer, implying that semi-numerical models can be used to explore a larger range of reionisation scenarios than is possible with current numerical simulations (Mesinger & Furlanetto, 2007). Alternatively, rather than adopt a filtering scheme, ionising sources can be used used to generate HII regions based on the spherically averaged radial density profile (Thomas et al., 2009). A feature of this model is that overlap of neighbouring HII regions is treated self-consistently with respect to photon conservation. The model can also be easily adapted to compute ionisation structure for more complex galaxy formation models.

We use a combination of these techniques implemented within the semi-analytic model GALFORM (e.g. Lagos et al., 2012) in order to study the effect of galaxy formation properties on the ionisation structure of the IGM (Kim et al., 2013). Beginning with a relatively small (~ 100 Mpc$/h$ cubed) volume simulation of the ionisation structure in which the physics of the lowest mass sources thought to dominate reionisation are resolved, this method can be extended to very large volumes using the statistical distribution of ionising flux as a function of large-scale ($\sim$Mpc) over density (Kim 2014, in prep). This distribution is used to populate a much larger low resolution volume via a Monte-Carlo technique, thus producing simulations of ionisation structure in cubic Gpc volumes that contain the SKA1-LOW field of view, while retaining the effects of physics from the smallest-scale galaxies.

2.1 HII regions and galaxy formation

Examples of slices through simulated volumes of ionisation structure are shown in Figure 1. Several different volumes are shown at $z = 7.272$ to illustrate the scales involved. All simulations have the same mass-averaged neutral hydrogen fraction of $\langle x_{\rm HI} \rangle \sim 0.45$. From left to right we show the HII region structure resulting from the default GALFORM galaxy formation model implemented within the 100 Mpc$/h$ cubed volume of the Millennium-II simulation (Kim et al., 2013), as well as the extension via our Monte-Carlo method (Kim 2014 in prep) to the 500 Mpc$/h$ cubed volume of the Millennium simulation and 1Gpc$/h$ cubed volume of the GiggleZ simulation (Poole et al., 2014). Note that ionised volumes that are nearly as large as the 100 Mpc$/h$ cubed Millennium-II simulation can be seen in the larger 500 Mpc$/h$ cubed Millennium and 1 Gpc$/h$

PoS (AASKA14) 015

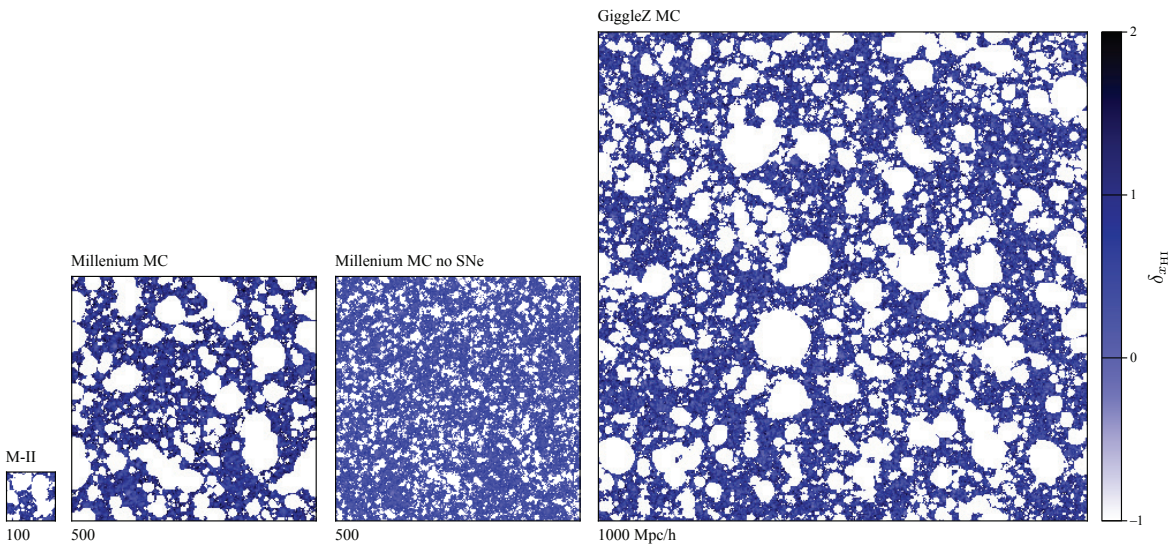

Figure 1: Simulations of the HII region structure in the Millennium-II simulation (left), with Monte-Carlo (MC) extension to the Millennium simulation (second and third panels) and the Gigglez 1Gpc cubed simulation (right panel). In each case simulations are shown for the default GALFORM galaxy formation model with SNe feedback, and reionisation was assumed to have progressed to a neutral fraction of 0.45. In the case of the Millennium simulation we also show the scenario where the galaxy formation model does not include SNe feedback (third panel from left). The model slices have a depth 2Mpc$/h$.

cubed GiggleZ simulation volumes. These very large HII regions indicate that Gpc-scale volumes are required to fully understand the large-scale power of reionisation (Iliev et al., 2014).

In addition to the default GALFORM galaxy formation model in which SNe feedback plays a significant role in regulating star formation, for the Millennium 500 Mpc$/h$ cubed simulation we also show a second example in which SNe feedback is absent. In each case the galaxy formation model produces an acceptable description of the high redshift galaxy luminosity function, and the mean neutral fraction of the IGM in both models is forced to be equal by construction. In the case of a galaxy formation model without SNe feedback, we find that much smaller HII regions are produced owing to the smaller luminosity-weighted mass of the ionising galaxies (Kim et al., 2013), requiring imaging at greater resolution in order to study the structure of the HII regions.

2.2 Quasar HII regions

Spectra of several of the most distant known quasars at $z \sim 6$ exhibit evidence for the presence of an HII region in a partially neutral IGM e.g. (Cen & Haiman, 2000; Wyithe & Loeb, 2004a), although this interpretation remains uncertain (Lidz et al., 2007; Bolton & Haehnelt, 2007). Recently, stronger evidence for a neutral IGM has been found at $z \sim 7$ (Bolton et al., 2011), where spectra show the possible detection of an IGM-generated Lyα damping wing in addition to a Lyα absorption trough. The redshifted 21 cm observation of quasar HII regions will probe quasar physics as well as the evolution of the neutral gas (Wyithe & Loeb, 2004a; Kohler et al., 2005). For example, Figure 2 shows a semi-numerical model of the evolving 3-dimensional ionisation structure of the IGM within a 500 Mpc cubed volume around a luminous $z > 6$ quasar (Geil et al., 2008) observed

PoS(AASKA14)015

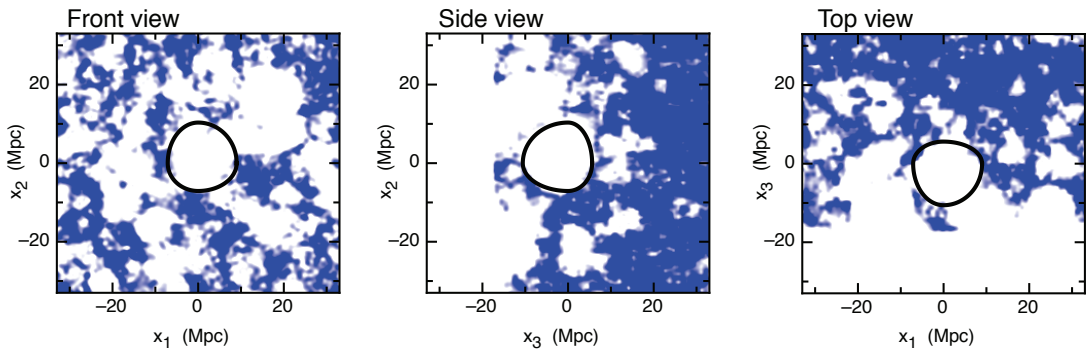

Figure 2: A quasar HII region in an evolving IGM (figure adapted from Geil et al., 2008). Three aspects of the HII region are shown, with slices through the centre of the box when viewed from the front, top and side. The quasar was assumed to contribute ionisation equivalent to an HII region of radius $R_{\rm q} = 34$ co-moving Mpc, and to be centred on $z = 6.65$, which is also the redshift at the centre of the simulation box. Each slice is 6 Mpc thick, which corresponds to ~ 3 MHz along the x_3-axis (units in this figure are shown in physical Mpc). In observed units, the cube is ~ 3.3 degrees on a side and 33 MHz deep. The shape of the HII region is also plotted (see Geil et al., 2008, for details). The mass-averaged IGM neutral fraction was assumed to be 0.15 at the quasar redshift.

near the end of reionisation. The evolution of the IGM, which is assumed to be quite rapid, is clearly seen in this figure with the percolation process completing between the "back" of the box and the "front" of the box. We note that in difference to galaxy HII regions which are driven by many sources over a long period of time, during the early phase quasar driven HII regions expand with a relativistic speed (Wyithe & Loeb, 2004b). Consequently, their measured sizes along and transverse to the line-of-sight should have different observed values due to relativistic time delay. A combined measurement of these sizes could therefore be used to directly constrain the neutral fraction of the surrounding IGM as well as the quasar lifetime (Wyithe & Loeb, 2004b). The figure also illustrates asymmetries perpendicular to the line of sight, which are a result of expansion of the spherical quasar driven HII region into an in homogeneously ionised IGM.

3. Imaging sensitivity of SKA1-LOW

In this section we estimate the sensitivity of the proposed SKA1-LOW baseline design with respect to imaging of cosmological HII regions. The baseline design for the SKA1-LOW will consist of 949 stations, of which approximately 400 are located within a uniform station density profile within a 500 m radius, with the remaining stations distributed in equal area per logarithm of radius in spiral arms beyond the core. Each station consists of 256 dual-polarisation antenna elements within a diameter of 35 m. The system temperature at $\nu < 200$ MHz is due to the combined sky and receiver temperatures, with a value $T_{\rm sys} = T_{\rm sky} + T_{\rm rcvr}$, where $T_{\rm sky} \sim 60\,[\lambda/m]^{2.55}$ K and $T_{\rm rcvr} = 0.1 T_{\rm sky} + 40\ K$. Simulations described in the document *SKA1 Imaging Science Performance*[1] yield a noise level that should be within a factor of 2 of the natural instrument sensitivity.

[1] Braun, R., "SKA1 Imaging Science Performance", Document no. SKA-TEL-SKO-DD-XXX Revision A Draft 2

PoS(AASKA14)015

The angular resolution corresponding to the 500 m radius core at 171 MHz is $\theta_{\rm b} = 7.3$ arc minutes, and the primary beam width for the 35 m station is $\Omega = 3.5$ degrees (defined as centre to first null). For reference, the resulting rms noise in an image constructed in the manner described, for a frequency channel $\Delta\nu$ has the form

$$\Delta T_{\rm b} \approx 0.05\,{\rm mK} + 0.66\,{\rm mK}\left(\frac{1+z}{8.5}\right)^{2.55}\left(\frac{\Delta\nu}{1\,{\rm MHz}}\frac{t_{\rm int}}{1000\,{\rm hr}}\right)^{-1/2}\left(\frac{\theta_{\rm b}}{7'}\right)^{-2}. \tag{3.1}$$

Radio interferometers do not directly image the full range of spatial scales, but rather measure a frequency-dependent, complex visibility for each frequency channel and baseline $\mathbf{U}$ in their configuration. The measured visibility is a linear combination of signal and noise, with the latter proportional to the square-root of the effective fraction of the array that can observe a particular visibility $\mathbf{U}$, which is in turn proportional to the number density of baselines $n(\mathbf{U})$ that can observe the visibility (McQuinn et al., 2006). We simulate the thermal noise in a 3-dimensional visibility-frequency cube (Geil et al., 2008), and then perform a 2-dimensional inverse Fourier transform in the *uv*-plane for each binned frequency in the bandwidth, which gives a realisation of the system noise in the image cube (i.e. sky coordinates). We scale the noise in each channel to have the variance described by equation (3.1). We construct the image using all baselines of up to 1000 m, including both core stations and stations along the spiral arms.

4. Simulated images of ionised structure with SKA1-LOW

In Figure 3 we estimate the SKA1-LOW response to the ionisation structure in the GiggleZ 1Gpc$/h$ cubed simulation in which galaxy formation is assumed to include an efficient SNe feedback. The top-left panel shows the model slice of depth 2 Mpc$/h$, which corresponds to 171 kHz along the line-of-sight, at a central frequency of 175MHz for HI at $z = 7.27$. As in Figure 1, our model has a neutral fraction of 0.45 at this redshift. In addition to the properties of the image noise, the array configuration directly impacts the features of the image that can be measured. On scales where the density of baselines is low or zero, features in the image cannot be observed. This includes image power on both small and large scales. Finite visibility coverage, determined by the baseline distribution, therefore truncates the visibilities that make up the observed image. Thus, in addition to dictating the behaviour of noise, the array configuration determines which properties of the HII regions can be imaged. The upper-right panel of Figure 3 shows an image of the simulation slice including only power on those scales measured by baselines of up to 1000 m. Here we have assumed an estimate of the primary beam gain using the Fourier transform of a filled circle aperture.

Foreground emission, from Galactic synchrotron and extra-galactic point sources, will provide the largest challenge to measurement of the signal from reionisation. In this discussion we assume that resolved sources can be successfully removed, which should be practical at the proposed sensitivity of SKA1-LOW (Liu et al., 2009). We estimate the effects of removing the diffuse Galactic foregrounds, which can lower the contrast of observed images (Geil et al., 2008) by modelling the foreground continuum using a 2nd-order polynomial in the logarithm of frequency which is appropriate in the absence instrumental polarisation leakage (Geil et al., 2008, 2011). We perform fits with this functional form along the line-of-sight within a 20 MHz bandwidth for each spatial pixel

PoS(AASKA14)015

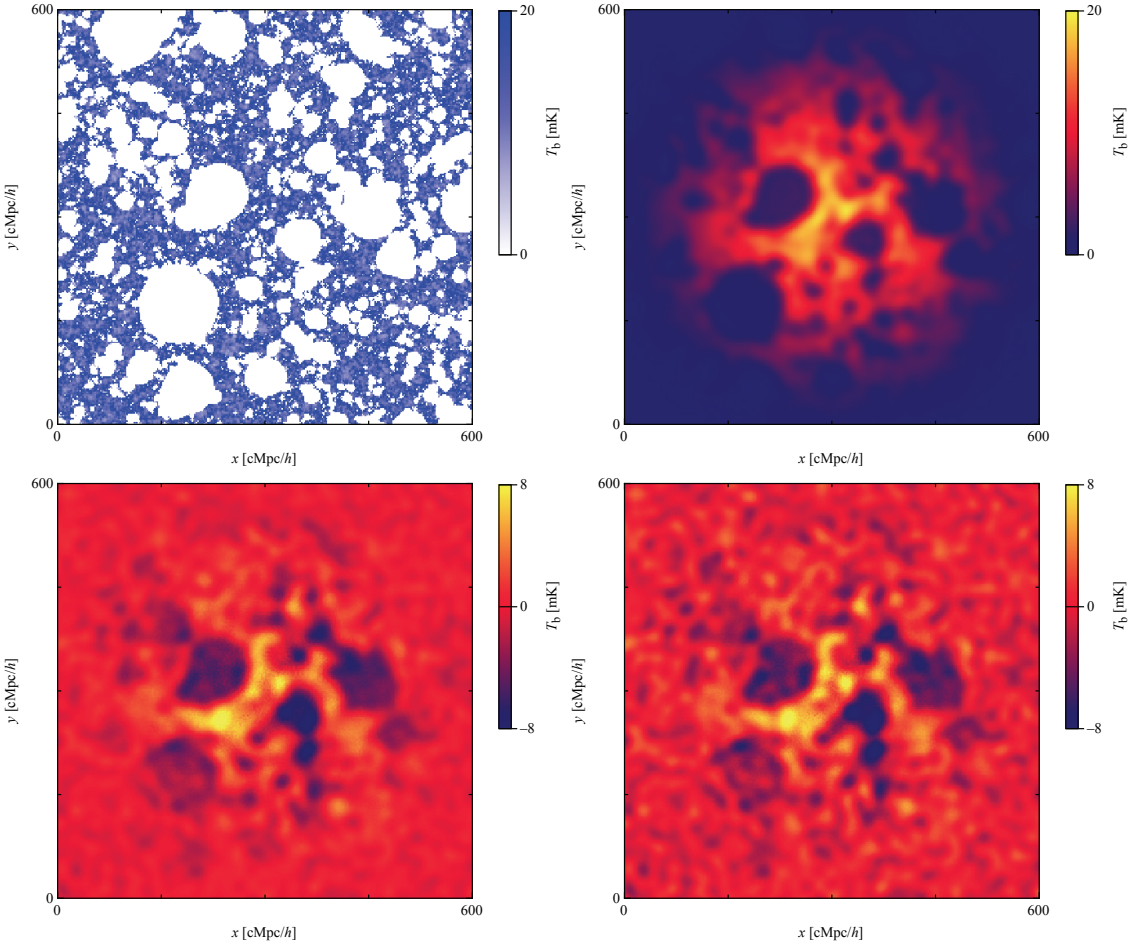

Figure 3: Simulations of the SKA1-LOW response to the ionisation structure in the Gigglez 1 Gpc$/h$ simulation in which galaxy formation is assumed to include an efficient SNe feedback, and reionisation has progressed to a neutral fraction of 0.45. The upper-left panel shows the model slice of depth 2 Mpc$/h$ (corresponding to 171 kHz at $z = 7.27$). The upper-right panel shows an image of this slice assuming an estimate of the primary beam gain, accounting only for the power on scales that can be observed by baselines shorter than 1000 m (corresponding to the diameter of the core). The lower-left and lower-right panels show simulations of observed maps (without a primary beam correction) assuming the base-line SKA1-LOW with 1000 hr integration and an early deployment where the collecting area is decreased by a factor of 2. The model observations have a depth of 1.2 MHz, which corresponds to 14 Mpc$/h$ along the line-of-sight, at a central frequency of 173 MHz for HI at $z = 7.27$, and is equivalent to the FWHP of the synthesised beam.

in the simulated image cube. We then subtract the best fit, leaving residual fluctuations around the foreground emission, which will include any residual continuum foregrounds, instrumental noise and the reionisation signal. The lower-left and lower-right panels of Figure 3 show simulated maps following diffuse foreground removal assuming 1000 hr integrations with the base-line SKA1-LOW design, and an early deployment of SKA1-LOW for which the sensitivity is decreased by a factor of 2 respectively. Here the slices are of depth 14 Mpc$/h$, which corresponds to 1.2 MHz along the line-of-sight, and is equivalent to the full-width at half power (FWHP) of the synthesised

PoS(AASKA14)015

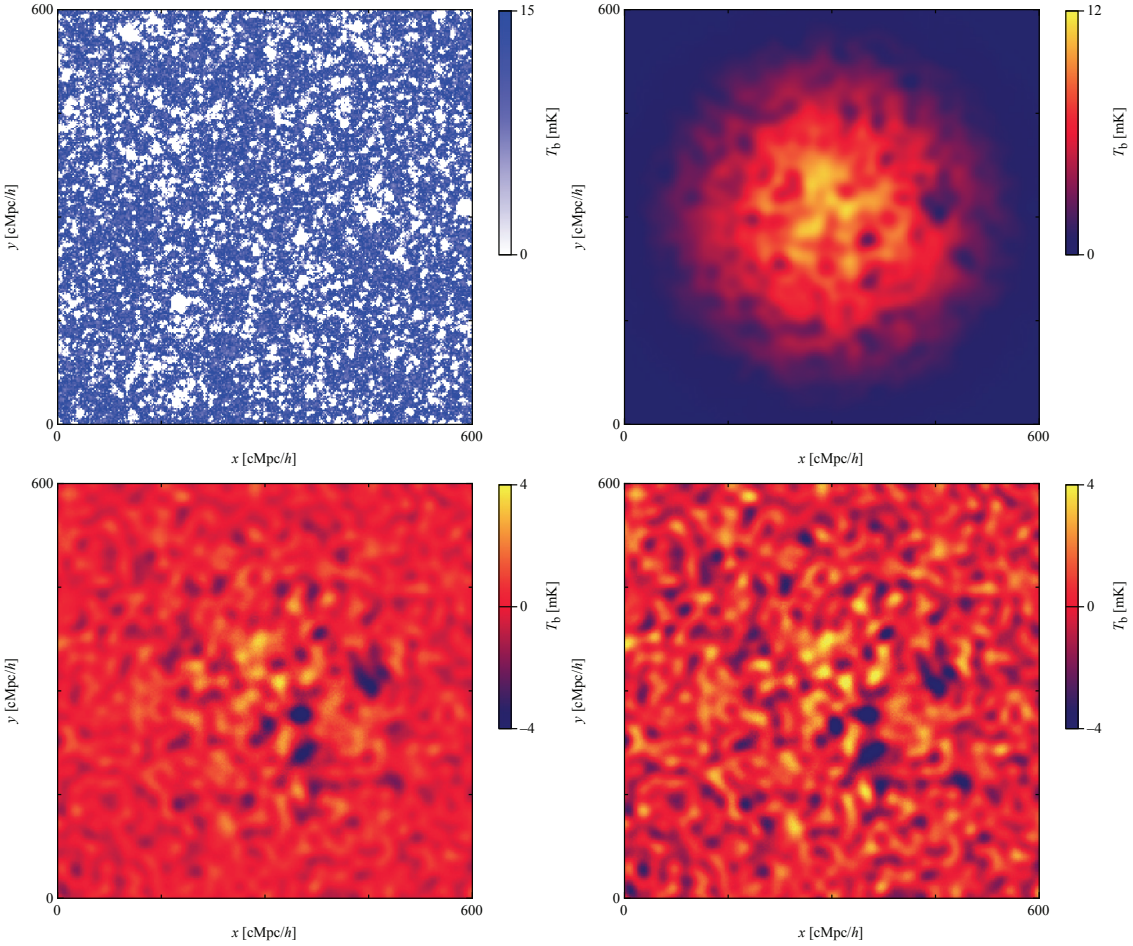

Figure 4: Simulations of the SKA1-LOW response to the ionisation structure in the GiggleZ 1Gpc$/h$ simulation in which star formation is assumed to proceed in the absence of a strong SNe feedback. Details are as per Figure 3.

beam. The large HII regions produced by a model with SNe feedback can be imaged well by the SKA1-LOW baseline design, and marginally imaged with an early deployment of SKA1-LOW having half the sensitivity of the baseline design. The consequence of removing the foreground continuum, together with the fact that interferometers do not make zero-spacing measurements, results in a decreased contrast between ionised and non-ionised regions, and a loss of power from large-scale modes (Geil et al., 2008).

In Figure 4, we show examples of simulated maps for the case where HII regions are produced by galaxies in which star formation is assumed to proceed in the absence of a strong SNe feedback. Panels in this figure correspond to those in Figure 3. We find that while the configuration of the SKA1-LOW baseline design can observe the largest of the smaller HII regions generated by a galaxy formation model without SNe feedback, these will in practice be difficult to observe owing to noise and the effects of foreground subtraction which lower the contrast of the observed HII regions. The SKA1-LOW baseline design appears to be the minimum configuration necessary

PoS(AASKA14)015

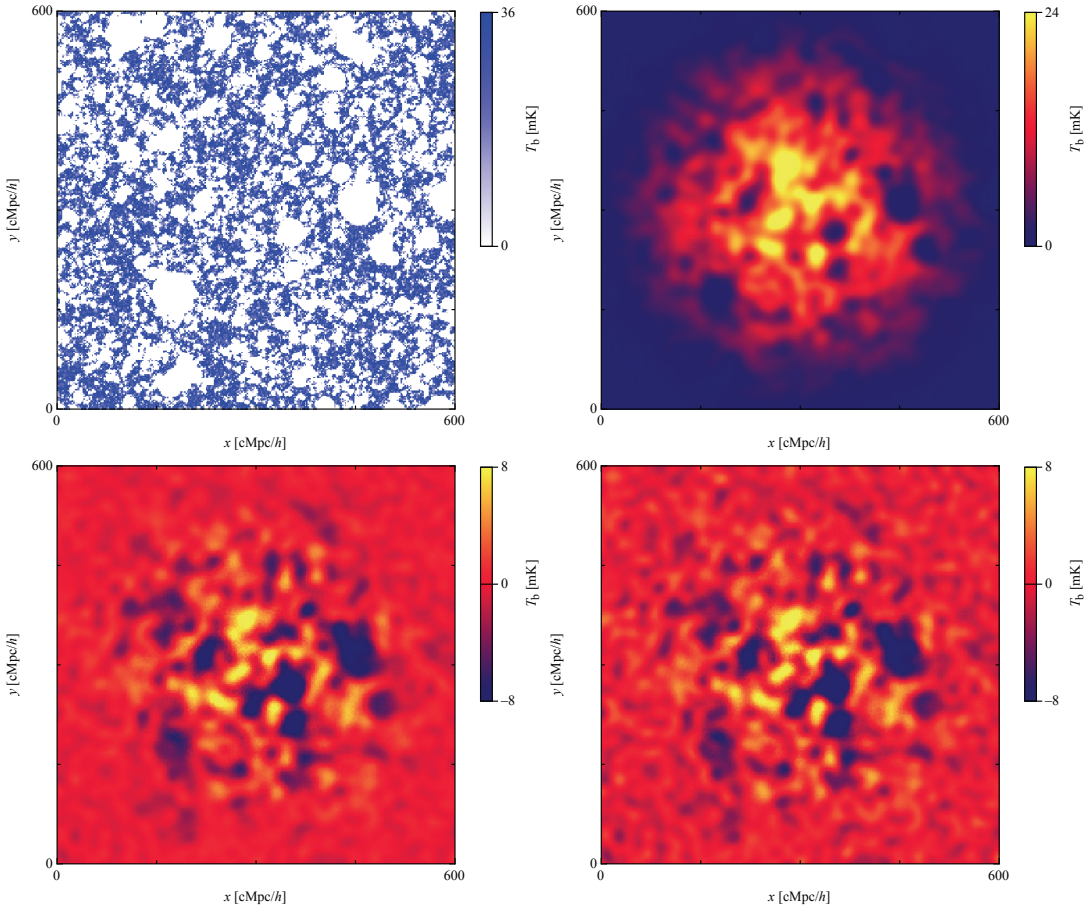

Figure 5: As per Figure 4, but assuming a more advanced stage of reionisation with a neutral fraction of 0.25 rather than 0.45.

to image HII regions generated by this second galaxy formation model during the early-to-mid portions of the reionisation era. Figure 5 shows the corresponding maps in the scenario of galaxy formation without strong SNe feedback, where reionisation is more advanced with a smaller neutral fraction of 0.25. The larger HII regions generated later in reionisation could be resolved by SKA1-LOW. Note that although the HII regions in Figure 5 are of similar size to the case of galaxy formation with SNe feedback at an earlier phase of reionisation (Figure 3), the sensitivity of SKA1-LOW would be sufficient to detect the excess of small-scale fluctuations seen in Figure 5, and would therefore provide a discriminant between these models.

The left and right panels of Figure 6 show simulated maps following diffuse foreground removal assuming 1000 hr integrations with an SKA for which the sensitivity is increased by a factor of 4 over the SKA1-LOW baseline design. This sensitivity is achieved by increasing the density of stations in the spiral arms and size of the core (since increasing the density of the core would lead to a station filling factor greater than unity). As a result of the reduced FWHP of the synthesised beam, the model slice has a smaller depth of 7.4 Mpc$/h$, which corresponds to 0.45 MHz along the line-of-sight (at a central frequency of 172MHz). We find that the greater sensitivity and resolution

PoS(AASKA14)015

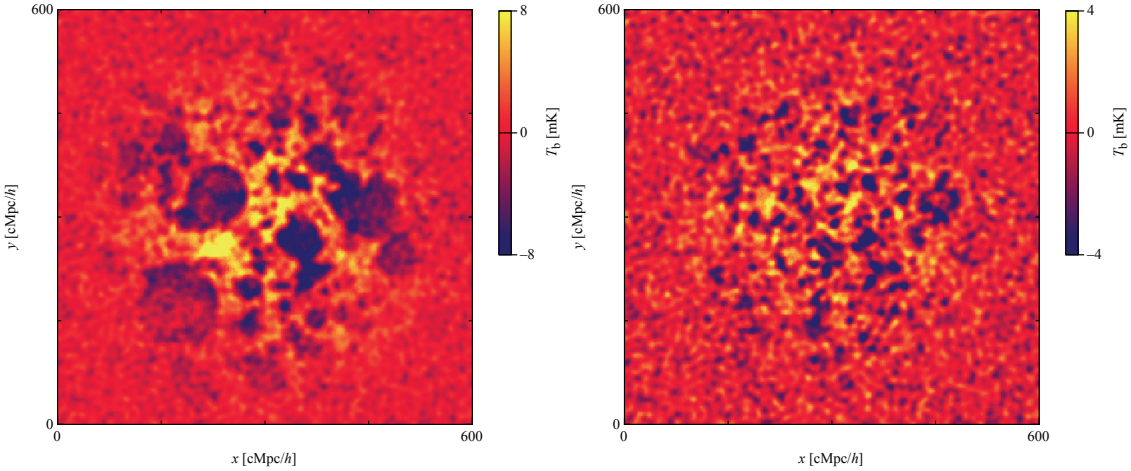

Figure 6: Simulations of the SKA response to the ionisation structure (without a primary beam correction) in the GiggleZ 1 Gpc$/h$ simulation in which star formation is assumed to include an efficient SNe feedback (left) and to proceed in the absence of a strong SNe feedback (right). In both cases reionisation is assumed to have progressed to a neutral fraction of 0.45. For SKA, the sensitivity is assumed to increase by a factor of 4 (increasing the radius of the core by a factor of 2, and the density of stations in the arms by a factor of 4). The model observation has a depth of 7 Mpc$/h$, which corresponds to 0.6 MHz along the line-of-sight (at a central frequency of 172 MHz).

of an SKA would allow more detailed imaging of HII regions generated by both the cases of galaxy formation with and without strong SNe feedback.

5. Sharpness of HII regions

Quasars have a harder spectrum than star forming galaxies, and this leads to thicker ionising fronts than is the case for a starburst driven HII region (Zaroubi & Silk, 2005; Kramer & Haiman, 2008). With sufficient angular resolution the contribution of hard ionising sources, such as mini-quasars to reionisation could therefore be inferred from the structure of ionising fronts at the edge of HII regions (Tozzi et al., 2000). Similarly, the distribution of ionising sources surrounding a massive galaxy at the centre of an HII region prevents the boundaries of such HII regions from being sharp when viewed at finite resolution (Wyithe & Loeb, 2007a). Rather, the clustering of sources near massive galaxies results in a spatially averaged neutral fraction that rises gradually towards large radii from an interior value near zero. As a result, a neutral hydrogen fraction corresponding to the global background value is typically reached only at a distance of 2–5 times the radius of the HII region around the central massive galaxy. This will lead to HII regions that look to have smooth edges unless observed at very high resolution. While detailed simulations remain to be done, inspection of Figures 3–6 implies that this science will require the sensitivity and resolution of SKA.

PoS(AASKA14)015

6. Field of view for SKA1-LOW

Direct imaging of the ionisation structure on small scales during reionisation is challenging because of reduced sensitivity at high resolution. However simulations suggest that very large structures of HI, with sizes of up to 100 Mpc will still be present during the later stages of reionisation (Zaroubi et al., 2012). Such large areas of patchy reionisation in the IGM result from the clustering of the large-scale structure on scales of up to $\sim 120h^{-1}$ Mpc, or ~ 1 degree (see Figure 1). Detection of these large-scale features may be possible at moderate significance with first generation arrays including LOFAR, and will be valuable for answering many cosmological questions (Zaroubi et al., 2012). However these expected large-scale features imply that the field of view for reionisation experiments performed with SKA1-LOW should have a size of at least several degrees.

At these very large scales, the light travel time can become comparable to the Hubble time, implying that light-cone effects become important. Thus, while HII regions can become arbitrarily large in a simulation at fixed proper time (as may be seen in Figure 1) during the brief period of overlap at the end of reionisation, the combined constraints of cosmic variance and light travel time imply a maximum observed HII region size at the end of the overlap epoch (as may be seen in Figure 2). This maximum size is found to have a value of ~ 100 Mpc (Wyithe & Loeb, 2004a). In agreement with the simulations of Zaroubi et al. (2012), this implies that reionisation experiments with SKA1-LOW should be sensitive to a characteristic angular scale of ~ 1 degree for detection of the largest-scale 21 cm flux fluctuations near the end of reionisation, and have a field of view sufficiently large to image these features.

7. Summary

The properties of the ionisation structure of the IGM are sensitive to the unknown galaxy formation physics that prevailed during reionisation. This ionisation structure introduces non-Gaussian statistics into the redshifted 21 cm fluctuation amplitudes which can only be studied through tomographic imaging, and will clearly discriminate between different galaxy formation scenarios. Imaging the ionisation structure of the IGM during reionisation is therefore a key goal for the SKA. As an example, we have shown that the SKA1-LOW baseline design with a 1 km diameter core would resolve HII regions expected from galaxy formation models that include strong feedback on low-mass galaxy formation. However detailed imaging of the smaller HII regions that result from galaxy formation in the absence of SNe feedback may require the greater sensitivity of SKA, particularly in the early-to-mid phases of reionisation. In addition to having baselines long enough to resolve the typical HII regions, the field of view for SKA1-LOW reionisation experiments should be at least several degrees across in order to image the largest HI structures towards the end of reionisation. The baseline design with 35 m diameter stations has a field of view within a single primary pointing which is marginally sufficient for this purpose.

References

Barkana, R. 2009, MNRAS, 397, 1454

PoS(AASKA14)015

Bolton, J. S. & Haehnelt, M. G. 2007, MNRAS, 381, L35
Bolton, J. S., Haehnelt, M. G., Warren, S. J., Hewett, P. C., Mortlock, D. J., Venemans, B. P., McMahon, R. G., & Simpson, C. 2011, MNRAS, 416, L70
Bond, J. R. & Myers, S. T. 1996, ApJS, 103, 1
Cen, R. & Haiman, Z. 2000, ApJL, 542, L75
Furlanetto, S. R. & Lidz, A. 2007, ApJ, 660, 1030
Furlanetto, S. R., Zaldarriaga, M., & Hernquist, L. 2004, ApJ, 613, 16
Geil, P. M., Gaensler, B. M., & Wyithe, J. S. B. 2011, MNRAS, 418, 516
Geil, P. M., Wyithe, J. S. B., Petrovic, N., & Oh, S. P. 2008, MNRAS, 390, 1496
Harker, G. et. al.. 2009a, MNRAS, 397, 1138
Harker, G. J. A. et. al.. 2009b, MNRAS, 393, 1449
Iliev, I. T., Mellema, G., Ahn, K., Shapiro, P. R., Mao, Y., & Pen, U.-L. 2014, MNRAS, 439, 725
Iliev et al. 2015, EoR modeling and simulations, in proceedings of "Advancing Astrophysics with the Square Kilometre Array", PoS(AASKA14)007
Kim, H.-S., Wyithe, J. S. B., Raskutti, S., Lacey, C. G., & Helly, J. C. 2013, MNRAS, 428, 2467
Kohler, K., Gnedin, N. Y., Miralda-Escudé, J., & Shaver, P. A. 2005, ApJ, 633, 552
Kramer, R. H. & Haiman, Z. 2008, MNRAS, 385, 1561
Lagos, C. d. P., Bayet, E., Baugh, C. M., Lacey, C. G., Bell, T. A., Fanidakis, N., & Geach, J. E. 2012, MNRAS, 426, 2142
Lidz, A., McQuinn, M., Zaldarriaga, M., Hernquist, L., & Dutta, S. 2007, ApJ, 670, 39
Lidz, A., Zahn, O., Furlanetto, S. R., McQuinn, M., Hernquist, L., & Zaldarriaga, M. 2009, ApJ, 690, 252
Liu, A., Tegmark, M., & Zaldarriaga, M. 2009, MNRAS, 394, 1575
McQuinn, M., Zahn, O., Zaldarriaga, M., Hernquist, L., & Furlanetto, S. R. 2006, ApJ, 653, 815
Mellema, G., Iliev, I. T., Pen, U.-L., & Shapiro, P. R. 2006, MNRAS, 372, 679
Mellema et al. 2015, in proceedings of "Advancing Astrophysics with the Square Kilometre Array", PoS(AASKA14)010
Mesinger, A. & Furlanetto, S. 2007, ApJ, 669, 663
Park, J., Kim, H.-S., Wyithe, J. S. B., & Lacey, C. G. 2014, MNRAS, 438, 2474
Poole, G. B. et. al.. 2014, ArXiv e-prints 1407.0390
Thomas, R. M. et. al.. 2009, MNRAS, 393, 32
Tozzi, P., Madau, P., Meiksin, A., & Rees, M. J. 2000, ApJ, 528, 597
Valdés, M., Ciardi, B., Ferrara, A., Johnston-Hollitt, M., & Röttgering, H. 2006, MNRAS, 369, L66
Wyithe, J. S. B. & Loeb, A. 2004a, *Nature*, 427, 815
—. 2004b, ApJ, 610, 117
—. 2007a, MNRAS, 374, 960
—. 2007b, MNRAS, 375, 1034
Wyithe, J. S. B. & Morales, M. F. 2007, MNRAS, 379, 1647
Zahn, O., Lidz, A., McQuinn, M., Dutta, S., Hernquist, L., Zaldarriaga, M., & Furlanetto, S. R. 2007, ApJ, 654, 12
Zaroubi, S. et. al.. 2012, MNRAS, 425, 2964
Zaroubi, S. & Silk, J. 2005, MNRAS, 360, L64

PoS(AASKA14)015

Synergies and Other Science

PROCEEDINGS OF SCIENCE

Very Long Baseline Interferometry with the SKA

Zsolt Paragi[*1], **Leith Godfrey**[2], **Cormac Reynolds**[3], **Maria Rioja**[4,5], **Adam Deller**[2], **Bo Zhang**[6], **Leonid Gurvits**[1,37], **Michael Bietenholz**[7,38], **Arpad Szomoru**[1], **Hayley Bignall**[3], **Paul Boven**[1], **Patrick Charlot**[8], **Richard Dodson**[9,10], **Sándor Frey**[11], **Michael Garrett**[2,12], **Hiroshi Imai**[13], **Andrei Lobanov**[14], **Mark Reid**[15], **Eduardo Ros**[14,39], **Huib van Langevelde**[1,12], **J. Anton Zensus**[14], **Xing Wu Zheng**[16], **Antxon Alberdi**[17], **Iván Agudo**[1], **Tao An**[6], **Megan Argo**[18], **Rob Beswick**[18], **Andy D. Biggs**[19], **Andreas Brunthaler**[14], **Robert M. Campbell**[1], **Giuseppe Cimó**[1], **Francisco Colomer**[4], **Stéphane Corbel**[20], **John Conway**[21], **David Cseh**[22], **Roger Deane**[23,33], **Heino Falcke**[22], **Krisztina Gabányi**[41,11], **Marcin Gawronski**[24], **Michael Gaylard**[7,†], **Gabriele Giovannini**[25], **Marcello Giroletti**[25], **Ciriaco Goddi**[1], **Sharmila Goedhart**[7], **José L. Gómez**[17], **Alastair Gunn**[18], **Taehyun Jung**[9], **Preeti Kharb**[26], **Hans-Rainer Klöckner**[14], **Elmar Körding**[22], **Yurii Yu. Kovalev**[27,14], **Magdalena Kunert-Bajraszewska**[24], **Michael Lindqvist**[21], **Matt Lister**[28], **Franco Mantovani**[14,25], **Iván Martí-Vidal**[21], **Mar Mezcua**[29], **John McKean**[2], **Enno Middelberg**[30], **James Miller-Jones**[3], **Javier Moldon**[2], **Tom Muxlow**[18], **Tim O'Brien**[18], **Miguel Pérez-Torres**[17], **Sergei Pogrebenko**[1], **Jonathan Quick**[7], **Anthony P. Rushton**[31,40], **Richard Schilizzi**[18], **Oleg Smirnov**[32,33], **Bong Won Sohn**[9], **Gabriele Surcis**[1], **Greg Taylor**[34], **Steven Tingay**[3], **Valeriu Tudose**[35], **Alexander van der Horst**[36], **Joeri van Leeuwen**[2,36], **Tiziana Venturi**[25], **René Vermeulen**[2], **Wouter Vlemmings**[21], **Aletha de Witt**[7], **Olaf Wucknitz**[14], **Jun Yang**[21]

[1]*JIVE,* [2]*Astron,* [3]*ICRAR-Curtin U.,* [4]*OAN,* [5]*ICRAR-UWA,* [6]*ShAO,* [7]*HartRAO,* [8]*U. Bordeaux,* [9]*KASI,* [10]*ICRAR-UWA,* [11]*FÖMI SGO,* [12] *U. Leiden,* [13]*Kagoshima U.,* [14]*MPIfR,* [15]*Harvard-Smithsonian CfA,* [16]*SASS-Nanjing U.,* [17]*IAA-CSIC,* [18]*JBO-U. Manchester,* [19]*ESO,* [20]*CEA Saclay,* [21]*OSO,* [22]*RU Nijmegen,* [23]*U. Cape Town,* [24]*Toruń CfA–Nicolaus Copernicus U.,* [25]*IRA–INAF,* [26]*IIA Bangalore,* [27]*ASC–Lebedev Phys. I.,* [28]*Purdue U.,* [29]*IAC,* [30]*Ruhr-U. Bochum,* [31]*U. Oxford,* [32] *Rhodes U.,* [33] *SKA South Africa,* [34]*UNM,* [35]*Inst. Sp. Sci.,* [36]*U. Amsterdam,* [37] *TU Delft,* [38] *York U., Toronto,* [39] *U. Valencia,* [40] *U. Southampton,* [41] *U. Szeged*

E-mail: zparagi@jive.nl

Adding VLBI capability to the SKA arrays will greatly broaden the science of the SKA, and is feasible within the current specifications. SKA-VLBI can be initially implemented by providing phased-array outputs for SKA1-MID and SKA1-SUR and using these extremely sensitive stations with other radio telescopes, and in SKA2 by realising a distributed configuration providing baselines up to thousands of km, merging it with existing VLBI networks. The motivation for and the possible realization of SKA-VLBI is described in this paper.

Advancing Astrophysics with the Square Kilometre Array
June 8-13, 2014
Giardini Naxos, Italy

[*]Speaker.
[†]Deceased

PoS(AASKA14)143

1. Introduction

A high angular resolution capability has long been considered an essential part of the Square Kilometre Array (SKA) concept (Garrett 2000; Gurvits 2004; Fomalont & Reid 2004; Schilizzi et al. 2007; Godfrey et al. 2012). Very long baseline interferometry with the SKA (hereafter SKA-VLBI) will provide very sensitive, milliarcsecond (mas) resolution imaging that is important, for example, to study active galactic nuclei (AGN) down to very low luminosities, to understand the detailed physics of jet formation and its coupling to the accretion process, as well as the growth of the first generation of massive black holes in the universe (Agudo et al. 2015), and their role in regulating star formation (a.k.a. feedback processes, see Prandoni & Seymour 2015; Morganti et al. 2015). The detection of a great number of tidal disruption events (TDE), and radio imaging at mas-scale, will be invaluable for the understanding of jet formation in a pristine environment, and will possibly reveal a new population of massive black holes (MBH, $M_{\rm BH} \sim 10^4 - 10^6 M_\odot$) that may resemble the black hole seeds in the early universe (Donnarumma et al. 2015). High-fidelity SKA-VLBI polarimetric observations will constrain the magnetic field structure close to the jet launch site, providing important constraints on the jet launch mechanism and related processes (Blandford & Znajek 1977; Blandford & Payne 1982). In connection with the Cherenkov Telescope Array (CTA), it will help reveal the nature of the large population of hitherto unidentified high-energy sources (Giroletti et al. 2015). The various "exotic" accreting black hole systems that will potentially be revealed by mas-scale deep SKA-VLBI imaging include low-power MBH in the centres of dwarf galaxies (Paragi et al. 2014), off-centre intermediate-mass black holes ($M_{\rm BH} \sim 10^2 - 10^4 M_\odot$, Wolter et al. 2015), and dual- or multiple supermassive black holes[1] (SMBH, $M_{\rm BH} \sim 10^6 - 10^{10} M_\odot$, Deane et al. 2015) in advanced stages of mergers. It will allow the detection of 10^6 $M_\odot$ dark matter haloes from high resolution imaging of gravitationally lensed arcs to investigate galaxy formation scenarios. It will also enable a test of models for dark energy from the measurement of geometric distances to high-redshift galaxies with nuclear water masers (McKean et al. 2015).

Ultra-precise astrometry at the microarcsecond level to determine distances and transverse velocities via the measurement of proper motions and parallaxes of Galactic objects will be possible out to a distance of tens of kpc. Achieving this for a large fraction of the radio pulsar population detected in the SKA Galactic pulsar census will enable strong field tests of gravity in a broad range of relativistic binary systems (Kramer & Stappers 2015; Shao et al. 2015), the detection of the gravitational wave background (Janssen et al. 2015), tomographic modelling of the large scale Galactic magnetic field and mapping the ionized interstellar plasma in the Galaxy (Han et al. 2015), and constraining the physics of neutron stars (Watts et al. 2015). Curiously, the gravitational wave background might be constrained independently by observing its subtle effect on the apparent position of quasars (e.g. Jaffe 2004, see also Sect. 4.2). Ultra-precise astrometry will be very important for many other classes of compact radio sources with emission in the SKA frequency range – for instance, masers (Green et al. 2015), protostellar objects (e.g. Loinard et al. 2007), and a variety of accreting stellar objects such as novae, isolated black holes, or accreting neutron stars and black holes in binary systems (a.k.a. microquasars, Corbel et al. 2015). Proper motion measurements of stellar-mass black holes will provide constraints on models of their formation,

[1] For two recently reported candidates awaiting confirmation see e.g. Gitti et al. (2013); Deane et al. (2014)

PoS(AASKA14)143

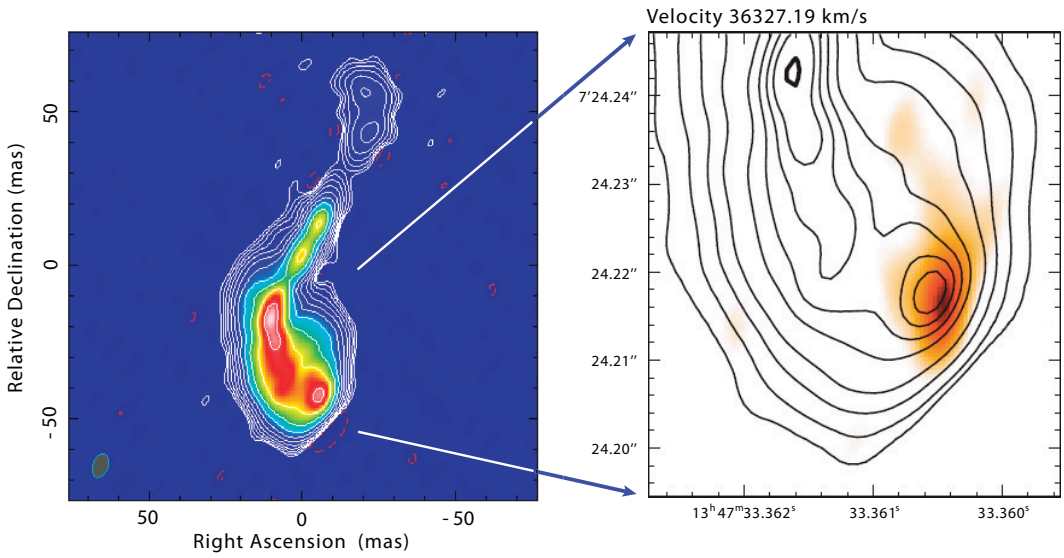

Figure 1: Left: global VLBI continuum image of the young, restarted AGN 4C12.50 at 1.27 GHz. Right: HI absorption (orange-white) superimposed on the continuum image (contours) of the southern lobe. The deepest HI absorption is co-spatial with the termination point of the jet; there is extended HI absorption detected as well. The jet drives a large-scale atomic (HI) and cold molecular (CO) outflow. This result demonstrates that jet-driven outflows may play an important role in AGN feedback mechanisms (Morganti et al. 2013).

while measuring their parallax distances will provide accurate luminosities which are important for tests of accretion physics (e.g. Miller-Jones et al. 2009). For radio-emitting stars, in addition to the distance via parallax, the presence of a planetary companion can be sought via the reflex motion of the star (e.g. Guirado & Ros 2007; Bower et al. 2009). The excellent sensitivity on very long baselines will mean that extragalactic stellar explosions like supernovae (Bietenholz 2008; Perez-Torres et al. 2015) and gamma-ray burst afterglows (GRB, Burlon et al. 2015, but see also Sect. 7) will be imaged, in total intensity as well as in polarization, in more detail than is possible today.

A number of high impact scientific results produced in the last few years demonstrate the potential of very sensitive and flexible SKA-VLBI with mas-scale imaging capability. These include global VLBI HI spectral line imaging of the AGN 4C12.50 (see Fig 1), demonstrating how AGN jets drive large-scale outflows and thus contribute to AGN feedback (Morganti et al. 2013); an accurate parallax measurement of SS Cyg in a series of triggered VLBI experiments (see Fig 3), proving that the disc instability model for accretion is correct (Miller-Jones et al. 2013); and the recent finding that binary orbits may be the driver of γ-ray emission and mass ejection in classical novae (Chomiuk et al. 2014). To fully explore the broad range of science cases we refer the reader to the various chapters mentioned above, as well as Godfrey et al. (2011, 2012). In this paper we focus on practical SKA-VLBI issues and highlight only a few SKA-VLBI science applications.

We describe possible realisations of SKA-VLBI in Sect. 2, along with expected sensitivities based on the SKA1 Baseline Design. Sect. 3 describes calibration requirements and explains the need for forming multiple phased-array beams (in one or more sub-arrays) and why simultaneous production of phased-array and local interferometer data is necessary. Astrometry with SKA-VLBI

PoS (AASKA14) 143

SKA Band	SKA-core SEFD [Jy]	Bandwidth [MHz]	Remote tel. SEFD [Jy]	Baseline sens. 60s [μJy]	Image noise 1hr [μJy/beam]
50% SKA1-MID	5.2	256	20	82	9
SKA1-MID	2.6	1024	20	29	3
Full SKA	0.26	2048	20	3	0.05

Table 1: Typical expected 1σ baseline and image sensitivities of various SKA-VLBI configurations at $\sim$3–8 GHz, with the inner 4 km of SKA core phased up. All the baseline sensitivities are given for a 100m-class remote telescope. 50% SKA1-MID (early operations): assuming an accompanying array of 5 25–30m dishes and a 100m-class antenna. SKA1-MID – same configuration. Note at $\sim$1–3 GHz and including SKA1-SUR as well will provide a similar sensitivity. Full SKA: 10x more sensitive than SKA1-MID.

will be described in Sect. 4. In Sect. 5 we will show how *Gaia* astrometry can be improved using SKA-VLBI, and how these complementary facilities may open up new fields of research. This will be followed by introducing the need and potential for SKA-VLBI surveys in Sect. 6. Highlighting the superior resolution of SKA-VLBI even for very faint targets, we will show in Sect. 7 that –in certain cases– it will be possible to resolve extreme GRB afterglows while these are still in the ultra-relativistic regime. Various issues with correlation and data transport will be described in Sect. 8.

2. VLBI configurations of SKA

There is a significant difference between the planned operation of the high angular resolution component for SKA1 and SKA2: in SKA1, the SKA core will be operated as a sensitive element (or elements) to be added to existing VLBI networks, increasing the sensitivity but not the resolution of those networks. In this case, the "remote stations" comprise existing facilities, and the SKA will participate as the most sensitive element in an otherwise conventional VLBI array (see Table 1). Key to the success of this approach will be the addition of a few (2–4) remote stations in Africa. Ideal locations for these stations would be the developing African VLBI Network (AVN) stations in Zambia, Ghana, Kenya and Madagascar (Gaylard et al. 2011). These additional stations will provide the short and medium length baselines to the SKA core to give good *uv*-coverage.

The left panel of Figure 2 shows the single-frequency, 12-hours *uv*-coverage that could be obtained at the Galactic centre with a global imaging array including a large number of telescopes. The right panel shows a more typical *uv*-coverage for a 4-hours track on a source at declination -20° using just a handful of the more sensitive telescopes available in the global array, but still providing baseline lengths up to 10,000 km in length. In the coming era of rapidly expanding e-VLBI capabilities the realisation of such an array should not present any significant logistical problems. Coordinated proposals and observations are already offered by the European VLBI Network (EVN), the Chinese VLBI Network (CVN), the Japanese VLBI Network (JVN), the Korean VLBI Network (KVN), the Long Baseline Array (LBA) the Very Long Baseline Array (VLBA), and the High Sensitivity Array (HSA). Table 1 gives the likely sensitivity of arrays that could be formed with SKA1 era assuming various configurations and bandwidths.

PoS (AASKA14) 143

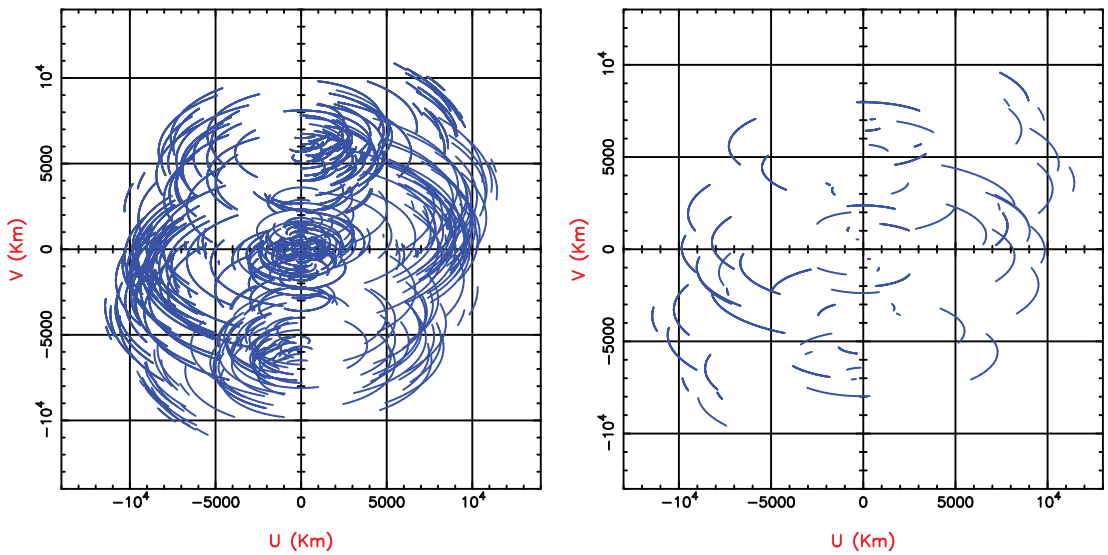

Figure 2: Left: *uv*-coverage of the Galactic Centre in a 12-hours observation with 24 telescopes combined in the EVN, CVN, LBA and the AVN with SKA1-MID. Right: *uv*-coverage of a more typical 4-hours observation of a DEC $-20°$ source with 9 telescopes selected from the above configuration.

There are, however, limitations to the approach described above (Garrett 2000). To address these limitations, in SKA2 the remote stations will be an integrated part of the array, with up to 25% of the collecting area distributed along spiral arms in remote stations, extending thousands of kilometres from the core, and the SKA will effectively operate as a real-time electronic-VLBI (e-VLBI) array. Merging with telescopes from existing VLBI networks will still be possible; note that in this case the SKA processor will have to act as the VLBI correlator (Table 1). Many of the technical requirements for implementation of SKA-VLBI in phase 1 will also be requirements for phase 2, and as such, implementation of the high angular resolution capability in phase 1 will be an essential step to realising the high angular resolution component in phase 2.

Even in the early science phase (50% SKA1-MID sensitivity) SKA-VLBI will match or exceed the current capabilities of the typical e-EVN configuration[2], but will be capable of accessing the entire southern sky, including tracking the Galactic center for many hours! SKA-VLBI with the full capacity SKA1-MID and/or SKA1-SUR, especially when adding FAST (Nan et al. 2011), will outperform current global VLBI arrays including the most sensitive telescopes. While we are not considering it further here, we note that VLBI with SKA1-LOW (ν<350 MHz) has the potential of using speckles of interstellar scattering to achieve sub-nano-arcsec resolution in certain cases. With current instruments this is possible for some bright pulsars (Pen et al. 2014), but the sensitivity of the SKA is required for more general applications.

3. SKA-VLBI calibration

Calibration of the VLBI datastream from the phased-up core of the SKA array would follow

[2]The e-EVN consists of EVN telescopes with real-time e-VLBI capability, streaming data at a rate of 1 Gbit s^{-1}. Here we assumed the e-EVN without Arecibo. See `http://www.evlbi.org/evlbi/e-vlbi_status.html`

PoS(AASKA14)143

much the same methods as currently used for phased arrays in VLBI. When connected element interferometers such as the Australia Telescope Compact Array (ATCA), The Karl G. Jansky Very Large Array (VLA) or the Westerbork Synthesis Radio Telescope (WSRT) are operated as an element of a VLBI network, the internal calibration of the array is used to measure the gains for the individual array antennas. The signals from these are then scaled and summed in a tied array output from the correlator. We assume that the SKA will function along these lines as part of VLBI operations. Besides forming a tied array beam (or rather beams, see below), another crucial requirement is the provision of the metadata, such as the system temperature and weather information, by the array. The gains of the phased-array sum need to be accurately determined and recorded. The metadata will be essential for the accurate conversion of the VLBI correlation into a measure of correlated flux density. These calibrations are particularly important as such data will be dominated by the baselines to the phased SKA because of the large weights these baselines will have due to the large collecting area.

One issue in VLBI is that primary flux density calibrators are not available to further improve on a-priori amplitude calibration. Primary calibrators are resolved on mas scales, while sources that are compact on baselines up to $\sim$10,000 km are variable. SKA-VLBI will offer a great solution to this by providing local interferometer and phased-array data simultaneously. The flux densities and polarization properties of compact calibrators can be measured using the local interferometer data during the VLBI observations, leading to very accurate flux density and polarization calibration (for both polarization leakage and polarization position angle) of the VLBI data product.

3.1 Multi-view calibration

To provide 10 μas astrometric accuracy using single source phase referencing at 1.6 GHz one would require an extremely nearby reference source. One can estimate from the expressions in Asaki et al. (2007) that the reference sources should be no more than 60 arcsec from the target to provide the required accuracy. The projected source counts suggest that there will not be sufficient calibrator source density to provide this, even at the sensitivities of SKA1-MID to SKA1-SUR baselines (see Table1).

However, using lines of sight to multiple calibrator sources (minimally 3) it is possible to solve for a full 2D correction to the spatial atmospheric distortions around the VLBI target, which will provide significantly improved calibration, imaging and astrometric precision compared to that from a single calibrator (see e.g. Rioja et al. 2009, and references therein). This is particularly important in the ionosphere-dominated regime ($<$5 GHz). The improvement arises from the fitting of a spatial function to the calibration residuals and interpolating this model to the target position, which allows a more accurate calibration solution in the target direction. Simulations show (Jimenez-Monferrer et al. 2010) that by using Multi-view approaches one can achieve an order of magnitude better astrometric accuracy than by using a single calibrator. The necessary calibrator-target separation is $\lesssim$5 arcminutes, and the probability of detecting suitable calibrators at such distances seems promising at least up to 5 GHz (Godfrey et al. 2011), making this band the best for SKA-VLBI astrometry (described below).

When SKA1-MID and SKA1-SUR are phased for use in SKA-VLBI, the resultant tied-array beams will be narrow ($\sim$10 arcseconds at 1.6 GHz if the inner 4 km of the core is phased up). This is much narrower than the field-of-view of the 25-100m class telescopes which will form the

PoS(AASKA14)143

remainder of the SKA1-VLBI array, and much smaller than the separation between potential SKA-VLBI calibrator sources. Accordingly, a different SKA tied array beam will typically be needed per calibrator source. This drives the requirement for a minimum of 4 SKA1-MID and SKA1-SUR VLBI beams.

4. Astrometry

4.1 Differential astrometry

Differential VLBI astrometry is obtained by carefully calibrating standard phase-referenced VLBI observations (see Reid & Honma 2014, and references therein). The calibration is derived from one source (or more sources, using Multi-view calibration) registered within the International Celestial Reference Frame (ICRF), and the same local frame is constructed over multiple observations, meaning that systematic contributions to positional errors remain constant to first order. Thus, while the absolute position of the target will be in error by a small but unknown amount, the changes between epochs – including, importantly, annual geometric parallax and source proper motion – are reliable. Compared to absolute astrometry (discussed below), differential astrometry can obtain higher relative precision and can target much fainter objects. Differential astrometry with VLBI provides the highest precision direct distance measurements of objects outside the solar system available in astronomy (see Figure 3), and as such it contributes a crucial rung to the distance ladder.

The attainable accuracy with differential astrometry can be limited by 4 factors: 1) the noise-limited position fit of the target (determined by array resolution and sensitivity and target brightness); 2) the registration of the target within the calibrator frame (limited by the proximity of the calibrator(s) and the calibration solution interval); 3) the stability of the calibrator frame itself (limited by the intrinsic nature of the source(s) used); and, in case of parallax measurements 4) the stability of the target emission centroid. The participation of SKA1-MID and SKA1-SUR in VLBI astrometric observations will lead to considerable reductions in the sum of these error contributions; so much so that the expected noise floor is difficult to extrapolate from present observations.

The instantaneous sensitivity of a VLBI array containing SKA1-MID and SKA1-SUR would be more than a factor of 10 better than the VLBA. This translates into a corresponding reduction in the first error component. Moreover, it means that fainter sources can be used as calibrators. As explained in Sect. 3, several calibrator sources within $\sim$5 arcminutes could be expected, that will result in up to an order of magnitude reduction in the second error component (which is usually the limiting factor with current astrometric observations). By virtue of the fact that many sources will be used to construct the calibrator frame, cross-checks will be possible allowing the removal of sources which demonstrate discernible structure evolution, mitigating the third error component. This is currently poorly constrained (Fomalont et al. 2011), as it is below the error floor for most current observations. The fourth error component is only relevant for certain targets (such as masers) and can be mitigated by compressing the campaign duration.

Astrometric observations with current instruments are capable of reaching parallax precisions of $\sim$10 μas (e.g. Deller et al. 2013; Nagayama et al. 2011; Zhang et al. 2013; Reid et al. 2011). SKA-VLBI has the potential to reach parallax accuracies of 3 μas or better, sufficient for a precise distance to any Galactic object along a line of sight that is not substantially affected by scattering.

PoS(AASKA14)143

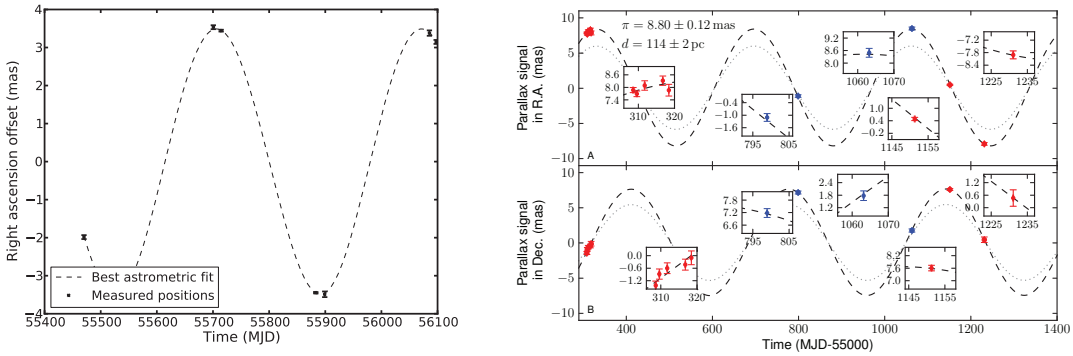

Figure 3: Left: the proper motion and parallax of the binary pulsar J2222-0137 as measured by the VLBA. The distance to this source was measured to 0.4% accuracy to be 267.3 pc, using 7 observations spread over 20 months (Deller et al. 2013, Fig. 5) Right: VLBA and e-EVN accurate parallax distance measurement of the dwarf nova SS Cyg from a series of triggered VLBI experiments, which removed a major challenge to our understanding of accretion theory (Miller-Jones et al. 2013, Fig. 2)

4.2 Absolute astrometry and geodesy

Improving the reference frames - both celestial and terrestrial - that are needed for differential astrometry is the domain of absolute astrometry and geodesy. Absolute astrometry can also be used to study very small secular effects such as the "Galactic aberration" introduced by the acceleration of the Solar System barycentre in the Galactic potential, and apparent quasar proper motions introduced by the low-frequency gravitational wave background (e.g. Gwinn et al. 1997; Titov et al. 2011, and references therein). For these observations, one cannot make use of a nearby calibrator or calibrators to largely eliminate the effect of the ionosphere or troposphere, and so they dominate the error and must be modeled as accurately as possible. As long as the spanned bandwidth is relatively wide, the ionospheric contribution can be precisely measured and compensated because it introduces a dispersive delay. To model the troposphere, observations of many sources at different locations are needed within a short period of time – ideally minutes. The SKA can provide multiple subarrays, but the efficiency will be dictated by the number of non-SKA antennas available to participate.

Unless the number of VLBI-capable antennas in the southern hemisphere is considerably expanded, the addition of SKA1-MID will not result in large improvements in the accuracy of the ICRF. However, SKA2 with intrinsic baselines up to thousands of kilometres as well as higher frequencies, will be able to make a significant improvement over the current ICRF accuracy. To achieve that, it will be necessary to correct for the opacity-shift in AGN jets for the ICRF defining sources (e.g. Paragi, Fejes & Frey 2000; Porcas 2012, and references therein), which will also be crucial for aligning the radio and the *Gaia* optical reference frames as explained below.

5. Synergies with Gaia

5.1 Calibrating Gaia parallaxes

Gaia — the successor to Hipparcos — was launched in the end of 2013, with an ambitious aim to chart a three-dimensional map of the Milky Way. *Gaia* will use twin telescopes to observe two

PoS(AASKA14)143

regions in the sky simultaneously to reach the expected parallax accuracy of $\sim$20 μas at magnitude $\sim$15. However, even very small periodic variations in the so-called basic angle between the two fields of view could lead to an undesirable global offset of the measured parallaxes (Mignard 2011).

Although the variations are monitored by an on-board metrology system, it is important to verify the *Gaia* parallaxes by independent methods. Among methods which are in principle available to verify the *Gaia* parallaxes, distant quasars with practically zero parallaxes are the most promising candidates, but the parallax zero point determined with this method would introduce a possible additional bias from foreground stars contaminating the sample (Windmark et al. 2011). Parallax measurements of stars with accuracy comparable to that of *Gaia* are possible with VLBI. However, due to the limited sensitivity, only a few stars with optical counterparts observable with *Gaia* have been measured with VLBI (e.g. Miller-Jones et al. 2013; Ratner et al. 2012). The number of objects detectable with current VLBI arrays is not high enough to calibrate *Gaia*, therefore we will need SKA-VLBI to accurately measure parallaxes for a significant number of Galactic *Gaia* targets.

As can be seen in Table 1, the image sensitivity of a moderate SKA-VLBI array is 3 μJy beam^{-1} hr$^{-0.5}$ at $\sim 3-8$ GHz. Assuming a baseline length up to 10,000 km (resolution $\sim$1 mas), this will ensure a noise-limited position fit with a theoretical precision of a few μas for stars with flux density exceeding $\sim$1 mJy (SNR>100), even if observed in a snapshot mode ($\sim$10 min. per target). As explained in previous sections, the systematic errors can be reduced significantly by using multiple calibrators within a few arcminutes. For verification of *Gaia* parallaxes, we need to observe radio targets which have optical counterparts with magnitude $6-15$, of which there are 3699 catalogued[3]. These stars could be first observed in a snapshot survey to measure their radio brightness and compactness; we expect to find hundreds of radio stars as targets for parallax measurements. As a next step, suitable mJy-level calibrators will be sought within a few arcminutes of the targets. All this work can be carried out with 50% SKA1-MID capabilities in a modest VLBI array (Table 1). It is expected that in phase 1, SKA-VLBI will provide parallaxes with $<$10 μas accuracy for hundreds of stars. To calibrate the *Gaia* parallax zero point with an uncertainty of 0.6 μas, we will need parallax measurements for $\sim$500 stars.

5.2 Possible science applications from comparing radio & optical astrometry

SKA-VLBI will significantly improve the connection between the celestial reference frames defined in the optical and radio bands. Currently, the most accurate fundamental celestial reference frame is ICRF2, the second realization of the International Celestial Reference Frame (Fey et al. 2009), constructed with dual-frequency (2.3/8.4 GHz) VLBI observations of selected radio-loud AGN. By about 2020, *Gaia* is expected to construct a reference frame with an accuracy similar to or better than that of VLBI, based directly on optical AGN measurements. For maintaining the consistency between the optical and radio frames, it will be essential to align the *Gaia* and VLBI frames with as many common high-quality reference objects as possible. However, the number of known optically bright AGN detectable with *Gaia* that also have compact mas-scale radio structures is low (e.g. Bourda et al. 2008). Increasing this number depends largely on having deeper VLBI observations (Bourda et al. 2010), and the high sensitivity SKA-VLBI on long baselines will play an important role here, at least in the southern sky (see Sect. 6).

[3] `http://www.hs.uni-hamburg.de/EN/For/Kat/radiost.html`

PoS(AASKA14)143

Pulsar – white dwarf binary systems provide further opportunity for reference frame ties with *Gaia*. There are currently ∼120 binary systems known that consist of a white dwarf and a radio pulsar (Manchester et al. 2005). With the SKA pulsar surveys that number could increase 5-fold. Comparison of the positions derived from *Gaia* and SKA VLBI would considerably enhance the reference frame tie provided by radio stars alone. Importantly, the majority of pulsars with a white dwarf companion are millisecond pulsars, for which $\sim \mu$as-precision position measurements are possible from timing data alone (Smits et al. 2011). Pulsar timing positions are based on the dynamic solar system frame, while interferometric positions are based on the inertial quasar reference frame therefore pulsars can be used to tie the different reference frames (Bartel et al. 1996). By combining positions derived from pulsar timing data with positions obtained with *Gaia* and SKA-VLBI, the pulsar-white dwarf binary systems will tie the three reference frames (*Gaia* frame, the quasar frame and solar system dynamical frame) with better than 10 μas precision.

To align the radio and optical reference frames using AGN as described above, one has to take into account that the radio and optical peak-brightness positions of compact AGN are not necessarily coincident at the accuracy offered by *Gaia* and VLBI, a phenomenon known as "core shift". To measure this effect requires observations over a wide range of frequencies, preferably extending to even above 10 GHz. With comparable astrometric accuracies in the radio and optical, *Gaia* will provide important constraints to this by accurately locating the position of the central engine with respect to the observed radio structure. SKA2 will be able to measure core shifts on sub-mas scales for large sample of AGN and thereby constrain AGN jet properties such as the magnetic field strength, the non-thermal particle density, jet power (Lobanov 1998; Kovalev et al. 2008) and even the accretion physics (Zamaninasab et al. 2014). The measurement of the jet power, combined with data at X-ray energies and/or at optical wavelengths, could provide an estimate of the accretion rate and black hole spin (Martínez-Sansigre & Rawlings et al. 2011).

Comparing *Gaia* and SKA-VLBI positions of the centres of galaxies will be a great tool for finding astrophysically interesting objects as well. Off-centre compact radio sources could be related to background quasars gravitationally lensed by the galaxy, or indicate dual active nuclei in merging galaxies where one of the components is radio-quiet while the other is optically obscured but radio-loud (e.g. Orosz & Frey 2013). The latter might be expected for example in minor mergers because the smaller black hole will undergo enhanced accretion episodes during the merger process (Callegari et al. 2011). A particularly interesting case would be the identification of recoiling supermassive black holes that are expelled from the centre of the host galaxy due to three-body interactions (Hoffman & Loeb 2007), or gravitational-wave recoil after binary coalescence in a galaxy merger (Blecha et al. 2011; Komossa 2012).

6. SKA-VLBI surveys

Large field of view (FoV) VLBI surveys have a number of important applications like exploring the AGN content of the universe (identified by their observed high brightness temperature, e.g. Chi, Barthel & Garrett 2013, see Fig. 4) and revealing the AGN physical properties down to very low accretion rates ($10^{-6} - 10^{-9} L_{\rm Edd}$) and masses ($< 10^6 M_\odot$). Most importantly, combining radio data products with the the "multicolor" sky view of the Large Synoptic Survey Telescope (LSST) will provide invaluable information on a huge number of individual objects; for example, accurate

PoS(AASKA14)143

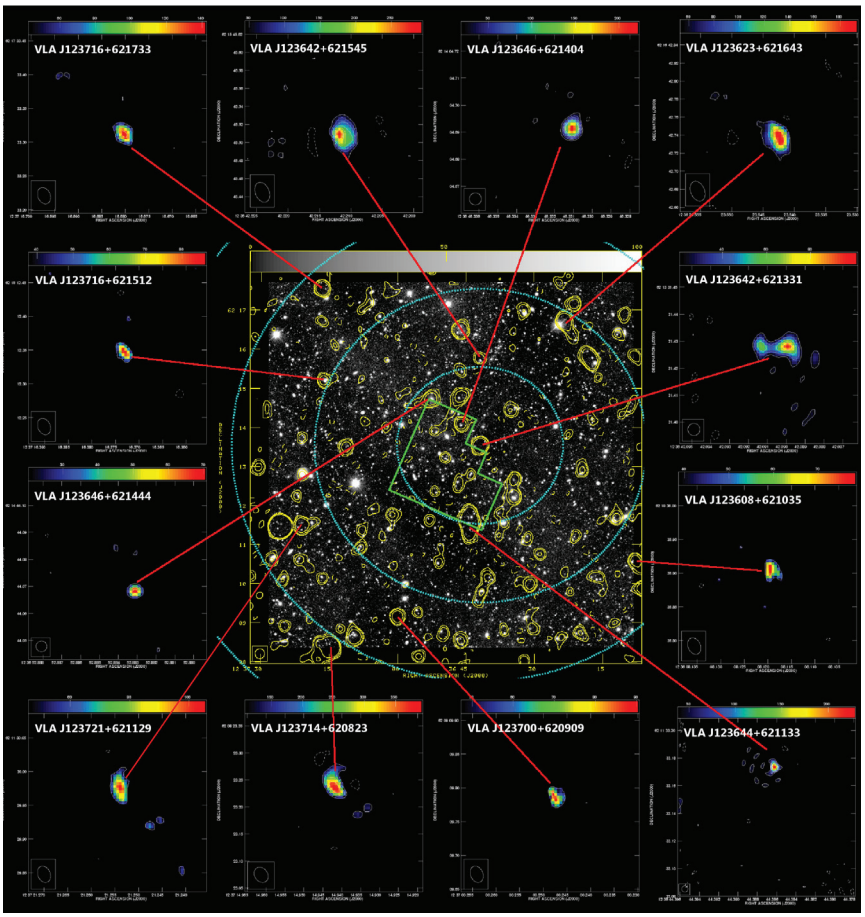

Figure 4: VLBI-detected AGN in the field of Hubble Deep Field North and Flanking Fields (grey scale: optical; yellow contours: WSRT 1.4 GHz). The cyan circles represent annuli of decreasing resolution and sensitivity, and are drawn at 2, 4, 6, and 8 arcmin radius w.r.t. the phase center which coincides with radio AGN VLA J123642+621331 (Chi, Barthel & Garrett 2013, Fig. 1).

photometric redshifts will be available for millions of faint targets out to $z > 2$, essential to understanding the evolution of activity in the universe as traced by radio emission (Lazio et al. 2014). Although at present, the FoV in VLBI observations has been strongly limited by data averaging in time and frequency, new techniques promise to allow the VLBI imaging of sources over most or all of the primary beam. Wide-field observations to map the full field of view of the primary beam of individual telescopes have been carried out, but this was a computationally challenging exercise (e.g. Lenc et al. 2008). The use of fast hierarchical widefield mapping procedures can reduce the computational burden significantly (Wucknitz 2010). However, in recent years the advent of "multifield" correlation in VLBI software correlators like DiFX (Deller et al. 2011) have provided an alternative and efficient means of imaging multiple targets within the FoV of the VLBI array. Internal to the correlator, visibilities are processed with high frequency resolution, and are shifted to the positions of the target sources with a high cadence ($\sim$100 Hz) before being heavily averaged (Morgan et al. 2011). In this way hundreds of previously-identified sources can be studied in a single observation at mas resolution, without the generation of an extremely large dataset.

PoS(AASKA14)143

The main limitation to SKA-VLBI survey science will be the small number of tied-array beams (N$\sim$4) available with SKA1. The relatively sparse nature of the SKA1-MID and SKA1-SUR cores means that only a small fraction of the full primary field of view will be visible to the tied array beams. A larger tied-array beam can be formed at the expense of sensitivity, by including fewer antennas to a shorter maximum diameter. In most cases, however, optimal sensitivity will be gained by using sensitive, narrow tied-array beams and switching between targets with a rapid cadence. Standard multi-field VLBI correlation targeting all sources within the primary beam would be used (since all targets would be visible at all times to the other, single-dish elements of the SKA-VLBI array) but only a subset of the targets would have a tied SKA beam contributing sensitivity at any given time. An important issue is how to calibrate the gain of the remote antennas accurately in the direction of the chosen VLBI phase centres, since the primary beam response of the individual telescopes is often poorly known (Middelberg et al. 2011; Cao et al. 2014; Deller & Middelberg 2014). This is unlikely to be a concern for tied array beams from SKA1-MID and SKA1-SUR, however, since the primary FoV of the dishes will be order of 1°, considerably larger than some other elements of the SKA-VLBI array (and hence the area from which targets will be drawn).

SKA2 will be capable of streaming and processing data from all individual elements to provide high resolution data for practically the full FoV, although it may still only be practical to provide the full resolution for limited areas, e.g. hundreds of independent phase-centers. The full SKA will thus provide a unique range of mas to arcsec angular scales that will help to distinguish between various interpretations of faint radio sources (unresolved AGN core, resolved emission powered by an AGN, star forming complexes etc.).

7. Resolving explosive outflows

SKA-VLBI will make possible (sub)-mas imaging of radio sources. In particular, for transient phenomena such us explosive outflows, SKA-VLBI monitoring will allow us to measure the expansion velocity, or proper motion of jetted ejecta, which is important to understanding the physics of the explosion as well as for studying the progenitor environments. The various Galactic (e.g. microquasars, magnetars, novae) and extragalactic (e.g. TDE) examples are discussed in other chapters. Here we describe a particular application of SKA-VLBI, as an example, in order to highlight the importance of improved sensitivity in global VLBI arrays.

Some of the most energetic events in the universe, supernovae (SNe) and long-duration gamma-ray bursts, involve explosive outflows of material from dying stars (the latter observed in the other parts of the electromagnetic spectrum as GRB afterglows). Supernovae are not only intrinsically spectacular, but they also have a significant effect on both the chemical evolution of galaxies and inject significant amounts of energy into the interstellar medium. Some supernovae, specifically those of Type Ib and Ic, which originate in stars that have lost most of their original H-rich stellar envelopes, can eject material at relativistic speeds. Long duration GRBs are known to be associated with Type Ic supernovae, and thought to be produced by ultra-relativistic jets launched in the collapsing star. Many details about these processes are still unknown. Why do only a small fraction of Type Ic SNe give rise to an observed GRB? How is the relativistic jet launched and how does it evolve? VLBI provides the best way of obtaining spatially resolved information about these sources, which would be of obvious benefit in attempting to understand the physics. Radio

PoS(AASKA14)143

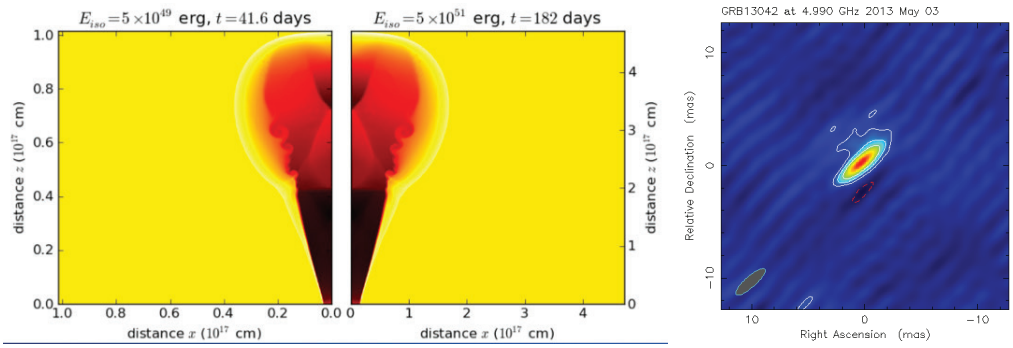

Figure 5: Left: 2D simulations of gamma-ray burst (GRB) jets. The scale invariance between relativistic jets of different energy allows easy reproduction of the jet dynamics. This provides a powerful method for fitting simulation results to observational data (van Eerten et al. 2012). With SKA-VLBI this will be possible for a large number of GRBs. Figure courtesy of Hendrik van Eerten. Right: Early e-EVN detection of the highest fluence GRB detected for decades, GRB 130427A (Paragi et al. 2013).

observations have the further advantage that radio emission generally traces the fastest outflows in GRB afterglows.

VLBI observations of GRBs and SNe are limited both by the available resolution and sensitivity. Although the SKA will provide no direct increase in resolution, it will provide an indirect increase in that the accuracy with which model-fitting can be used to constrain source sizes increases with increasing signal-to-noise ratio (SNR). In SKA1-MID Band 4–5, with a global array of VLBI telescopes where the longest baselines are ∼10,000 km (approximately the distance between the SKA core in South Africa and Australia or Europe), native imaging resolutions down to ∼1 mas (FWHM) would be obtained. For SNR∼50, the minimum detectable angular diameter is ∼0.2 mas[4]. This minimum detectable size corresponds to a length of ∼11 light-days (3×10^{16} cm) at distance 10 Mpc, and ∼1.6 light-years (8×10^{18} cm) at a redshift, z of 0.15. Interestingly, at $z=20$, it corresponds to the same length of ∼1.6 light years, so sources at very large cosmological distances can be resolved provided they are bright enough to be detected. Such measurements therefore have the exciting potential to directly measure the expansion of a nearby relativistic outflow in the first two weeks, and to possibly resolve outflows even at cosmological distances.

SKA-VLBI will allow us to observe sources below the detection limits of current instruments. Of all GRB afterglows, only ∼30% are bright enough to have been detected in the radio with present instrumentation (Chandra & Frail 2012), and only GRB 030329 has been resolved (e.g. Taylor et al. 2004). Similarly, only ∼30% of the observed core-collapse supernovae were detected in the radio, and only a handful have well-resolved images (Bietenholz 2008, 2014). The sensitivity of SKA would allow a significantly increased sample of both GRBs and SNe to be resolved with VLBI. We note that the minimum detectable source size could be significantly smaller than 0.1 mas for SNR∼1000. This SNR should be achieved for the most extreme and nearby >1 mJy sources with SKA1, and with SKA2 for practically all GRB afterglows with a flux density of a few hundred μJy known as "radio-loud" today (cf. Table 1). The resulting large GRB samples

[4]The theoretical resolving power of an interferometer is inversely proportional to the signal-to-noise ratio. The minimum detectable size depends weakly on the source geometry, and can vary by ∼30% for different source geometries such as a uniform disk or an optically thin sphere (Martí-Vidal et al. 2012).

PoS(AASKA14)143

will give the first opportunity to study GRBs in a model-independent fashion while they are still in their ultra-relativistic phase (that can last up to about two weeks for sources that are in a low-density environment), and directly compare the results with detailed simulations (see Fig. 5). This will however require extremely accurate calibration for all interferometer elements and flexible response to triggers; detailed simulation of SKA-VLBI configurations will provide more robust estimate of realistic expectations for "super-resolution" capability with SKA-VLBI.

A particularly exciting possibility is that of detecting and resolving the outflows from GRBs from the first generation of stars — Population III GRBs. GRB afterglows have already been detected at $z > 9$ (Cucchiara et al. 2011), and recent work (e.g. Ghirlanda et al. 2014; Mesler et al. 2014) has shown that the very massive stars expected to form in the early universe could give rise to spectacular GRBs, and their afterglows may be detectable by SKA despite being at $z \sim 20$.

8. SKA in VLBI observations: data transport, data formats and correlation

8.1 Status of global VLBI

The EVN currently operates at a bandwidth of 128 MHz and 2-bit sampling, resulting in data streams of 1 Gbit s^{-1} per telescope. The VLBA in the USA has recently completed an upgrade to 2 Gbit s^{-1}. The ongoing roll-out of new digital backends (DBBC) in the EVN will make 2 and 4 Gbit s^{-1} operations possible. After the completion of this roll-out, the only obstacles for high-bandwidth global VLBI will be the availability of suitable receiver systems (feeds etc.) at the telescopes, and of sufficient magnetic media for recording or sufficient networking bandwidth for real-time correlation of the data streams. The RFI environment at the different telescope sites will of course limit the usable bandwidth. Using phased-up arrays of radio telescopes (like the ATCA, the VLA and the WSRT) as elements in VLBI observations is common practice. Once beam forming has taken place, the output of the array is treated like that of any of the other VLBI stations.

8.2 SKA-VLBI

The cores of SKA1-MID and SKA1-SUR will produce very narrow beams. The practice of using in-beam calibrators in order to obtain the highest quality phase calibration will only be possible if at least four beams are formed, one for the target and additional three for the calibrators (see Sect. 3). With the usual caveats, one can reasonably assume that on the timescale of the construction of SKA1 most VLBI telescopes will move to 512 MHz bandwidth operations. Assuming 4 beams, 512 MHz bandwidth and 2-bit sampling, the total data rate of the phased-up SKA would be 16 Gbit s^{-1}. While current software correlators can easily deal with different bit representations, and a higher bit representation of the SKA data would yield some additional gain in sensitivity, it probably would make most sense to re-sample/truncate (depending on the exact representation) the SKA data at the telescope to 2 bits/sample, thus saving on data volume and storage/transport. The SKA data would also have to conform to the standard VLBI subband scheme, meaning that subbands of 32 MHz should be available. Care should be taken that the band can be tuned so as to be compatible with standard VLBI settings.

PoS(AASKA14)143

8.3 Data format

VLBI has known a variety of data formats. In recent years however a common format named VDIF (Whitney et al. 2009) has been accepted by most of the community. Most newly developed VLBI equipment now supports this data format. While dealing with different formats nowadays is far less problematic than in the days of ASIC-based hardware correlators, one common format is of course preferable. It is not yet known what SKA data will look like, but after beam forming, truncating and maybe re-filtering it should be possible to pack the data in any format desired. Related to this, the SPEAD (Manley et al. 2007) protocol which will be used for data exchange in MeerKAT, and maybe for SKA1-MID as well, actually supports the VDIF format. Hartebeesthoek Observatory in South Africa has participated in a successful 4 Gbit s^{-1} e-VLBI demonstration, streaming data in real time to the EVN correlator at JIVE in the Netherlands. Considering that 100 Gbit s^{-1} networking technology is being rolled out by national and international research networks, transporting a data stream of 16 Gbit s^{-1} from South Africa or Australia to Europe (or another correlator location) in real-time should be no problem at all in five years. Recording such data streams and trickling them to a correlator at lower speeds at a later time ("e-shipping") is already possible right now.

Finally, many VLBI arrays are configured using the VEX (VLBI EXperiment)[5] format, providing a complete description of a VLBI experiment, including scheduling, data-taking and correlation. Some sort of interface will be needed to translate VEX files into configuration files understandable by the SKA control system.

9. Conclusions

In this paper we described the scientific motivation and possible technical realisations of SKA-VLBI. The science goals are best achieved with SKA1 by forming phased-array elements from SKA1-MID and SKA1-SUR observing together with existing VLBI arrays in the 1-15 GHz frequency range (and up to 22 GHz in SKA2). In addition, the combination of local interferometry data from SKA1-MID and SKA-VLBI will provide the basis for very accurate amplitude and polarization calibration of the VLBI data products. A high resolution configuration of SKA2 (with a resolution of tens of mas to $\sim$100 mas, depending on frequency) will allow imaging of e.g. extragalactic sources from sub-pc to kpc scales simultaneously, a capability that is rarely available today. An important part of the requirements for the SKA is forming multiple VLBI beams for accurate phase calibration, targeting multiple sources within the primary beam. This mode of operation will be compatible with other multi-beam VLBI components such as the WSRT-APERTIF.

VLBI with the SKA1 will not be very different from that with other tied arrays, in terms of operations, data rates and computing. More beams will mean more data, but the numbers are reasonable, even in relation to today's technology. As observing at higher frequencies becomes possible with the SKA, increasing the instantaneous bandwidth will become increasingly important. Higher bandwidths, and the consequent higher data rates, should become feasible in the relevant time-frame.

[5] http://www.vlbi.org/vex/docs/vex%20definition%2015b1.pdf

PoS (AASKA14) 143

SKA-VLBI will have a profound effect on a large number of fields within astronomy. Accreting objects will be in reach at a range of accretion rates well below Eddington, providing a comprehensive view of compact objects such as neutron stars as well as the full range of masses from stellar- to supermassive black holes. Many of these will be discovered in transient surveys. Especially interesting candidates are TDEs that could provide clues to derive the low end of the SMBH mass-function, and extremely high redshift GRBs that would provide a line of sight through a large volume of the universe. These, along with the great number of newly discovered dual and multiple SMBH systems and recoiling BH will provide clues for understanding structure formation in the early universe. In addition, there will be a wealth of information about the feedback processes between the central AGN and their host galaxies from spectral line VLBI surveys at $\sim$1 GHz. At higher frequencies the study of star formation and stellar evolution, as well as resolving explosive outflows in the Galaxy and at cosmological distances will be among the most important applications. As explained in this work, VLBI astrometry will remain a very important tool for astrophysics. For example pulsar parallax measurements using SKA-VLBI will play an essential role in several high impact areas, including strong field tests of gravity in relativistic binary systems, tomographic mapping of the Galactic magnetic field and mapping the ionised interstellar plasma in the Galaxy, and the physics of neutron stars, as well as detecting the gravitational wave background. A particularly interesting idea is the detection of the gravitational wave background directly through measuring proper motions of a million of quasars with SKA2.

References

Agudo, I., Böttcher, M., Falcke, H. et al. 2015, "Studies of Relativistic Jets in Active Galactic Nuclei with SKA", in proc. *Advancing Astrophysics with the Square Kilometre Array*, PoS(AASKA14)093

Asaki, Y., Sudou, H., Kono, Y., et al. 2007, PASJ, 59, 397

Bartel, N., Chandler, J. F., Ratner, M. I., et al. 1996, AJ, 112, 1690

Bietenholz, M. 2008, PoS(IX EVN Symposium)064

Bietenholz, M. F. 2014, PASA, 31, 2

Blandford, R. D., & Payne, D. G. 1982, MNRAS, 199, 883

Blandford, R. D., & Znajek, R. L. 1977, MNRAS, 179, 433

Blecha, L., Cox, T. J., Loeb, A., & Hernquist, L. 2011, MNRAS, 412, 2154

Bourda, G., Charlot, P., & Le Campion, J.-F. 2008, A&A, 490, 403

Bourda, G., Charlot, P., Porcas R. W., & Garrington, S. T. 2010, A&A, 520, A113

Bower, G. C., Bolatto, A., Ford, E. B., & Kalas, P. 2009, ApJ, 701, 1922

Burlon, D., Ghirlanda, G., van der Horst, A., et al. 2015, "The SKA view of Gamma-ray Bursts", in proc. *Advancing Astrophysics with the Square Kilometre Array*, PoS(AASKA14)052

Callegari, S., Kazantzidis, S., Mayer, L. et al. 2011, ApJ, 729, 85

Cao, H.-M., Frey, S., Gurvits, L. I. et al. 2014, A&A, 563, A111

Chandra, P., & Frail, D. A. 2012, ApJ, 746, 156

Chi, S., Barthel, P. D., & Garrett, M. A. 2013, A&A, 550, A68

Chomiuk, L., Linford, J. D., Yang, J. et al. 2014, Nat, accepted

PoS(AASKA14)143

Corbel, S., Miller-Jones, J., Fender, R. P. et al. 2015, "Incoherent transient radio emission from stellar-mass compact objects in the SKA era", in proc. *Advancing Astrophysics with the Square Kilometre Array*, PoS(AASKA14)053

Cucchiara, A., Levan, A. J., Fox, D. B. et al. 2011, ApJ, 736, 7

Deane, R. P., Paragi, Z., Jarvis, M. J. et al. 2014, Nat, 511, 57

Deane, R., Paragi, Z., Jarvis, M., et al. 2015, "Multiple supermassive black holes systems: SKA's future leading role", in proc. *Advancing Astrophysics with the Square Kilometre Array*, PoS(AASKA14)151

Deller, A. T., & Middelberg, E. 2014, AJ, 147, 14

Deller, A. T., Brisken, W. F., Phillips, C. J. et al. 2011, PASP, 123, 275

Deller, A. T., Boyles, J., Lorimer, D. R. et al. 2013, ApJ, 770, 145

Donnarumma, I., Rossi, E. M., Fender, R. P., et al. 2015, "SKA as a powerful hunter of jetted Tidal Disruption Events", in proc. *Advancing Astrophysics with the Square Kilometre Array*, PoS(AASKA14)054

Fey, A., Boboltz, D., Charlot, P. et al. 2009, Bull. AAS, 41, 676

Fomalont, E., & Reid, M. 2004, New Astronomy Reviews, 48, 1473

Fomalont, E., Johnston, K., Fey, A. et al. 2011, AJ, 141, 91

Garrett, M. A. 2000, in M. P. van Haarlem (ed.) Perspectives on Radio Astronomy: Science with Large Antenna Arrays, 139 (Astron:Dwingeloo)

Gaylard, M. J., Bietenholz, M. F., Combrinck, L. et al. 2011, in I. Basson & A. E. Botha (eds.) Proc. SAIP2011, p. 425 (arXiv 1405.7214)

Giroletti, M., Orienti, M., D'Ammando, F. et al. 2015, "The connection between radio and high energy emission in black hole powered systems in the SKA era", in proc. *Advancing Astrophysics with the Square Kilometre Array*, PoS(AASKA14)153

Gitti, M., Giroletti, M., Giovannini, G., Feretti, L., & Liuzzo, E. 2013, A&A, 557, L14

Ghirlanda, G., Burlon, D., Ghisellini, G. 2014, PASA, 31, 22

Godfrey, L., Bignall, H. & Tingay, S. 2011, "Very High Angular Resolution Science with the SKA", SKA Memo No. 135

Godfrey, L. E. H., Bignall, H., Tingay, S. et al. 2012, PASA, 29, 42

Green, J. A., van Langevelde, H. J., Brunthaler, A. et al. 2015, "Maser Astrometry with VLBI and the SKA", in proc. *Advancing Astrophysics with the Square Kilometre Array*, PoS(AASKA14)119

Guirado, J. C., & Ros, E. 2007, "High-Precision Radio Astrometry: The Search for Extrasolar Planets", in A. Lobanov, A. Zensus, C. Cesarsky & P. Diamond (eds.) "Exploring the Cosmic Frontier: Astrophysical Instruments for the 21st Century", ESO Astrophysics Symposia, p. 257

Gurvits, L. I. 2004, New Astronomy Reviews, 48, 1211

Gwinn, C. R., Eubanks, T. M., Pyne, T., Birkinshaw, M., & Matsakis, D. N. 1997, ApJ, 485, 87

Han, J. L., van Straten, W., Lazio, T. J. W., et al. 2015, "Three-dimensional Tomography of the Galactic and Extragalactic Magnetoionic Medium with the SKA" in proc. *Advancing Astrophysics with the Square Kilometre Array*, PoS(AASKA14)041

Hoffman, L., & Loeb, A. 2007, MNRAS, 377, 957

Jaffe, A. H. 2004, New Astronomy Reviews, 48, 1482

Janssen, G., Hobbs, G., McLaughlin, M. et al. 2015, "Gravitational wave astronomy with the

PoS(AASKA14)143

SKA", in proc. *Advancing Astrophysics with the Square Kilometre Array*, PoS(AASKA14)037
Jimenez-Monferrer, S., Rioja, M. J., Dodson, R., Smirnov, O., & Guirado, J. C. 2010, PoS(10th EVN Symposium)084
Komossa, S. 2012, Advances in Astronomy, 2012, id. 364973
Kovalev, Y. Y., Lobanov, A. P., Pushkarev, A. B., & Zensus, J. A. 2008, A&A, 483, 759
Kramer, M., & Stappers, B. 2015, "Pulsar Science with the SKA — Overview", in proc. *Advancing Astrophysics with the Square Kilometre Array*, PoS(AASKA14)036
Lazio, J. W., Kimball, A., Barger, A. J. et al. 2014, PASP, 126, 196
Lenc, E., Garrett, M. A., Wucknitz, O., Anderson, J. M., & Tingay, S. J. 2008, ApJ, 673, 78
Lobanov, A. P. 1998, A&A, 330, 79
Loinard, L., Torres, R. M., Mioduszewski, A. J., et al. 2007, ApJ, 671, 546
Manchester, R. N., Hobbs, G. B., Teoh, A., & Hobbs, M. 2005, AJ, 129, 1993
Manley, J., Welz, M. Parsons, A., Ratcliffe, S., & van Rooyen, R. 2007, `http://casper.berkeley.edu/astrobaki/images/9/93/SPEADsignedRelease.pdf`
Martínez-Sansigre, A., & Rawlings, S. 2014, MNRAS, 414, 1937
Martí-Vidal, I., Pérez-Torres, M. A., & Lobanov, A. P. 2012, A&A, 541, A135
McKean, J. P., Jackson, N., Vegetti, S. et al. 2015, "Strong gravitational lensing with the SKA", in proc. *Advancing Astrophysics with the Square Kilometre Array*, PoS(AASKA14)084
Mesler, R. A., Whalen, J., Smidt, J. et al. 2014, ApJ, 787, 91
Middelberg, E., Deller, A., Morgan, J. et al. 2011, A&A, 526, A74
Mignard, F. 2011, Adv. Sp. Res., 47, 356
Miller-Jones, J. C. A., Jonker, P. G., Dhawan, V., et al. 2009, ApJL, 706, L230
Miller-Jones, J. C. A., Sivakoff, G. R., Knigge, C. et al. 2013, Sci, 340, 950
Morgan, J. S., Mantovani, F., Deller, A. T. et al. 2011, A&A, 526, A140
Morganti, R., Fogasy, J., Paragi, Z., Oosterloo, T., & Orienti, M. 2013, Sci, 341, 1082
Morganti, R., Sadler, E. & Curran, S. J. 2015, "Cool Outflows and HI absorbers with the SKA", in proc. *Advancing Astrophysics with the Square Kilometre Array*, PoS(AASKA14)134
Nagayama, T., Omodaka, T., Handa, T. et al. 2011, PASJ, 63, 719
Nan, R., Li, Di, Jin, C. et al. 2011, Int. J. Mod. Phys. D, 20, 989
Orosz, G. & Frey, S. 2013, A&A, 553, A13
Paragi, Z., Fejes, I., & Frey, S. 2000, "Indications for Frequency Dependent Radio Core Position in 1823+568", in Nancy R. Vandenberg & Karen D. Baver (eds.) "IVS 2000 General Meeting", p. 342
Paragi, Z., van der Horst, A. J., Yang, J. et al. 2013, ATel #5242
Paragi, Z., Frey, S., Kaaret, P. et al. 2014, ApJ, 791, 2
Pen, U.-L., Macquart, J.-P., Deller, A., & Brisken, W. 2014, MNRAS, 440, L36
Perez-Torres, M. A., Alberdi, A., Beswick, R. J. et al. 2015, "Core-collapse and Type Ia supernoave with the SKA", in proc. *Advancing Astrophysics with the Square Kilometre Array*, PoS(AASKA14)060
Porcas, R. W. 2012, Mem. Soc. Astron. Ital., 83, 970
Prandoni, I., & Seymour, N. 2015, "Revealing the Physics and Evolution of Galaxies and Galaxy Clusters with SKA Continuum Surveys" in proc. *Advancing Astrophysics with the Square Kilo-*

PoS(AASKA14)143

metre Array, PoS(AASKA14)067
Ratner, M. I., Bartel, N., Bietenholz, M. F. et al. 2012, ApJS, 201, 5
Reid, M. J., & Honma, M. 2014, ARA&A, 52, 339
Reid, M. J., McClintock, J. E., Narayan, R. et al. 2011, ApJ, 742, 83
Rioja, M., Dodson, R., Porcas, R. W. et al. 2009, PoS(EXPReS09)014
Schilizzi, R. T., Alexander, P., Cordes, J. M. et al. 2007, SKA Memo No. 100
Shao, L., Stairs, I. H., Antoniadis, J. et al. 2015, "Testing Gravity with Pulsars in the SKA Era", in proc. *Advancing Astrophysics with the Square Kilometre Array*, PoS(AASKA14)042
Smits, R., Tingay, S. J., Wex, N., Kramer, M., & Stappers, B. 2011, A&A, 528, A108
Taylor, G. B., Frail, D. A., Berger, E., & Kulkarni, S. V. 2004, ApJ, 609, L1
Titov, O., Lambert, S. B., & Gontier, A.-M. 2011, A&A, 529, A91
van Eerten, H., van der Horst, A. J., & MacFadyen, A. 2012, ApJ, 749, 44
Watts, A. L., Xu, R., Espinoza, C. et al. 2015, "Probing the neutron star interior and the Equation of State of cold dense matter with the SKA", in proc. *Advancing Astrophysics with the Square Kilometre Array*, PoS(AASKA14)043
Windmark, F., Lindegren, L., & Hobbs, D. 2011, A&A, 530, A76
Whitney, A., Kettenis, M., Phillips, C., & Sekido, M. 2009, PoS(EXPReS09)042.
Wolter, A., Rushton, A. P., Mezcua, M. et al. 2015, "Radio investigation of Ultra-Luminous X-ray (ULX) Sources in the SKA Era", in proc. *Advancing Astrophysics with the Square Kilometre Array*, PoS(AASKA14)091
Wucknitz, O. 2010, PoS(10th EVN Symposium)100
Zamaninasab, M., Clausen-Brown, E., Savolainen, T., & Tchekhovskoy, A. 2014, Nat, 510, 126
Zhang, B., Reid, M. J., Menten, K. M. et al. 2013, ApJ, 775, 79

PoS(AASKA14)143

PROCEEDINGS OF SCIENCE

Synergy between the Large Synoptic Survey Telescope and the Square Kilometre Array

David Bacon[*1], **Sarah Bridle**[2], **Filipe B. Abdalla**[3,4], **Michael Brown**[2], **Philip Bull**[5], **Stefano Camera**[2], **Rob Fender**[6], **Keith Grainge**[2], **Željko Ivezić**[7], **Matt Jarvis**[6,8], **Neal Jackson**[2], **Donnacha Kirk**[3], **Bob Mann**[9], **Jason McEwen**[10], **John McKean**[11], **Jeffrey Newman**[12], **Alvise Raccanelli**[13,14,15], **Martin Sahlén**[6], **Mario Santos**[8], **Anthony Tyson**[16], **Gong-Bo Zhao**[17,1]

[1] *University of Portsmouth, UK;* [2] *University of Manchester, UK;* [3] *University College London, UK;* [4] *Rhodes University, South Africa;* [5] *University of Oslo, Norway;* [6] *University of Oxford, UK;* [7] *University of Washington, USA;* [8] *University of the Western Cape, South Africa;* [9] *University of Edinburgh, UK;* [10] *Mullard Space Science Laboratory, University College London, UK;* [11] *ASTRON, The Netherlands;* [12] *University of Pittsburgh, USA;* [13] *Johns Hopkins University, USA;* [14] *Jet Propulsion Laboratory, Caltech, USA;* [15] *California Institute of Technology, USA;* [16] *University of California, Davis, USA;* [17] *National Astronomy Observatories, Beijing, China.*
E-mail: david.bacon at port.ac.uk

We provide an overview of the science benefits of combining information from the Square Kilometre Array (SKA) and the Large Synoptic Survey Telescope (LSST). We first summarise the capabilities and timeline of the LSST and overview its science goals. We then discuss the science questions in common between the two projects, and how they can be best addressed by combining the data from both telescopes. We describe how weak gravitational lensing and galaxy clustering studies with LSST and SKA can provide improved constraints on the causes of the cosmological acceleration. We summarise the benefits to galaxy evolution studies of combining deep optical multi-band imaging with radio observations. Finally, we discuss the excellent match between one of the most unique features of the LSST, its temporal cadence in the optical waveband, and the time resolution of the SKA.

Advancing Astrophysics with the Square Kilometre Array
June 8-13, 2014
Giardini Naxos, Italy

[*] Speaker.

PoS(AASKA14)145

1. The Large Synoptic Survey Telescope

1.1 The LSST system

The LSST system is designed to achieve multiple goals in four main science themes: (i) taking an inventory of the Solar System; (ii) mapping the Milky Way; (iii) exploring the transient optical sky; and (iv) probing dark energy and dark matter. These are just four of the many areas in which LSST will have enormous impact, but they span the space of technical challenges in the design of the system and survey, and have been used to focus the science requirements. The LSST will be a large, wide-field ground-based telescope, camera and data management system designed to obtain multi-band images over a substantial fraction of the sky every few nights. The observatory site will be located on Cerro Pachón in northern Chile (near the Gemini South and SOAR telescopes), with the first light expected in 2021 and the first public data releases mid-2023. The survey will yield contiguous overlapping imaging of over half the sky in six optical bands (*ugrizy*, covering the wavelength range 320–1050 nm).

The LSST telescope uses a novel three-mirror design (modified Paul-Baker) with a very fast f/1.234 beam (Figure 1). The optical design has been optimised to yield a large field of view (9.6 deg^2), with seeing-limited image quality, across a wide wavelength band. Incident light is collected by the primary mirror, which is an annulus with an outer diameter of 8.4m and inner diameter of 5.0m (an effective diameter of 6.5m), then reflected to a 3.4m convex secondary, onto a 5m concave tertiary, and finally into three refractive lenses in a camera. This is achieved with an innovative approach that positions the tertiary mirror inside the primary mirror annulus ring, making it possible to fabricate the mirror pair from a single monolithic blank using borosilicate technology. The secondary is a thin meniscus mirror, fabricated from an ultra-low expansion material. All three mirrors will be actively supported to control wavefront distortions introduced by gravity and environmental stresses on the telescope. The telescope sits on a concrete pier within a carousel dome that is 30m in diameter. The dome has been designed to reduce dome seeing (local air turbulence that can distort images) and to maintain a uniform thermal environment over the course of the night.

The LSST camera (Figure 1) provides a 3.2 Gigapixel flat focal plane array, tiled by 189 4K$\times$4K CCD science sensors with 10 μm pixels. This pixel count is a direct consequence of sampling the 9.6 deg^2 field-of-view (0.64m diameter) with 0.2$\times$0.2 arcsec^2 pixels (Nyquist sampling in the best expected seeing of $\sim$0.4 arcsec). The sensors are deep depleted high resistivity silicon back-illuminated devices with a highly segmented architecture that enables the entire array to be read in 2 seconds. The detectors are grouped into 3$\times$3 rafts; each contains its own dedicated front-end and back-end electronics boards. The rafts are mounted on a silicon carbide grid inside a vacuum cryostat, with an intricate thermal control system that maintains the CCDs at an operating temperature of 180 K. The entrance window to the cryostat is the third of the three refractive lenses in the camera. The other two lenses are mounted in an optics structure at the front of the camera body, which also contains a mechanical shutter, and a carousel assembly that holds five large optical filters. The sixth optical filter can replace any of the five via a procedure accomplished during daylight hours.

The rapid cadence of the LSST observing program will produce an enormous volume of data ($\sim$15 TB of raw imaging data per night), leading to a total database over the ten years of operations of 50 PB for the raw uncompressed imaging data (100PB with processed versions), and 15PB for

PoS(AASKA14)145

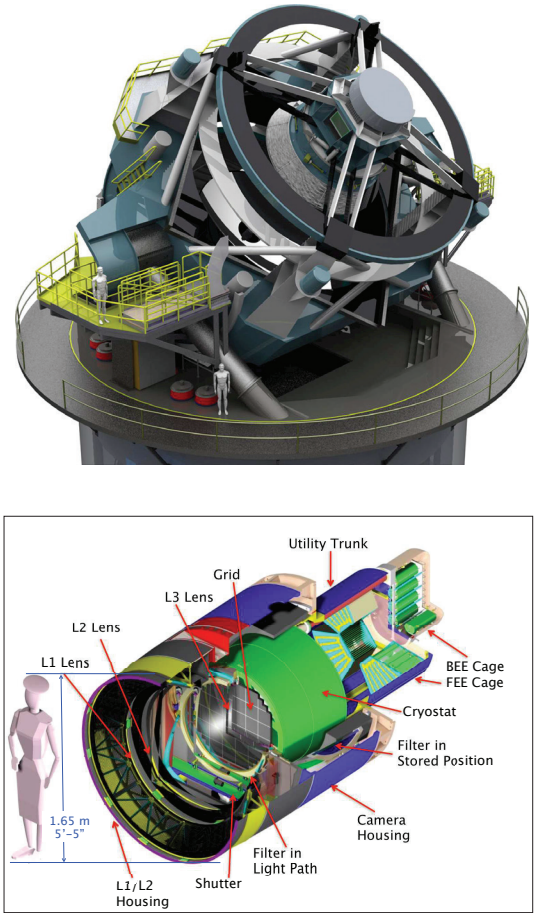

Figure 1: Upper panel: baseline design for the LSST telescope. Lower panel: the LSST camera layout. Credit: LSST Corporation.

the final catalog database. The computing power required to process the data grows as the survey progresses, starting at ∼100 TFlops and increasing to ∼400 TFlops by the end of the survey. Processing such a large volume of data, automated data quality assessment, and archiving the results in useful form for a broad community of users are major challenges. The data management system is configured in three levels: an infrastructure layer consisting of the computing, storage, and networking hardware and system software; a middleware layer, which handles distributed processing, data access, user interface and system operations services; and an applications layer, which includes the data pipelines and products and the science data archives.

The application layer is organised around the data products being produced. The nightly pipelines are based on image subtraction, and are designed to rapidly detect interesting transient events in the image stream and send out alerts to the community within 60 seconds of completing the image readout. The data release pipelines, in contrast, are intended to produce the most completely analysed data products of the survey, in particular those that measure very faint objects and cover long time scales. A new run will begin each year, processing the entire survey data set that is available to date. The data release pipelines consume most of the computing power of the data management system. The calibration products pipeline produces the wide variety of calibration data required by the other pipelines. All of these pipelines are designed to make efficient use of

PoS(AASKA14)145

computer clusters with thousands of nodes. There will be computing facilities at the base facility in La Serena, at a central archive facility, and at multiple data access centres. The data will be transported over existing high-speed optical fibre links from South America to the USA.

For a more detailed discussion, including optical design, the filter complement, the focal plane layout, and special science programs, please see the LSST overview paper (Ivezic et al. 2008) and the LSST Science Book[1] (Abell et al. 2009).

1.2 Planned survey strategy and delivered data products

The LSST observing strategy is designed to maximise scientific throughput by minimising slew and other downtime and by making appropriate choices of the filter bands given the real-time weather conditions. The fundamental basis of the LSST concept is to scan the sky deep, wide, and fast, and to obtain a dataset that simultaneously satisfies the majority of the science goals. This concept, the so-called "universal cadence", will yield the main deep-wide-fast survey and use about 90% of the observing time. The observing strategy for the main survey will be optimised for homogeneity of depth and number of visits. In times of good seeing and at low airmass, preference will be given to r-band and i-band observations. As often as possible, each field will be observed twice, with visits separated by 15-60 minutes. The ranking criteria also ensure that the visits to each field are widely distributed in position angle on the sky and rotation angle of the camera in order to minimise systematic effects in galaxy shape determination.

The current baseline design will allow about 10,000 deg^2 of sky to be covered using pairs of 15-second exposures in two photometric bands every three nights on average, with typical 5σ depth for point sources of $r \sim 24.5$. For example, these individual visits will be about 2 mag deeper than the SDSS data. The system will yield high image quality as well as excellent astrometric and photometric accuracy for a ground-based optical survey. The survey area will include 30,000 deg^2 with $\delta < +34.5°$, with the 18,000 deg^2 main survey footprint visited over 800 times during 10 years. The coadded data within the main survey footprint will be 5 mag deeper than SDSS ($r \sim 27.5$). The main survey will result in databases including 20 billion galaxies and a similar number of stars, which will serve the majority of science programs. The remaining 10% of observing time will be used to obtain improved coverage of parameter space such as very deep ($r \sim 26$) observations (e.g. optimised for SNe), observations with very short revisit times ($\sim$1 minute), and observations of "special" regions such as the Ecliptic, Galactic plane, and the Large and Small Magellanic Clouds.

The LSST data system is being designed to enable as wide a range of science as possible. Standard data products, including calibrated images and catalogs of detected objects and their attributes, will be provided both for individual exposures and the deep incremental data coaddition. About 20 billion objects will be routinely monitored for photometric and astrometric changes, and any transient events (non-recurrent objects with statistically significant photometric change; about 10,000 per night on average) will be distributed in less than 60 seconds via web portals. For the "static" sky, there will be yearly database releases listing many attributes for billions of objects and will include other metadata (parameter error estimates, system data, seeing summary etc).

[1] Available from www.lsst.org/lsst/SciBook

PoS(AASKA14)145

LSST has been conceived as a public facility: the database that it will produce, and the associated object catalogs that are generated from that database, will be made available to the U.S. and Chilean scientific communities and public with no proprietary period. Negotiations are under way with prospective international partners to make LSST data more broadly available.

It is expected that the scientific community will produce a rich harvest of discoveries with LSST data products. Many of the highest priority LSST science investigations will require organised teams of professionals working together to optimise science analyses and to assess the importance of systematic uncertainties on the derived results. To meet this need, eleven science collaborations have been established by the project in core science areas. As of the time of this contribution, there are over 500 participants in these collaborations, mostly from LSST member institutions. Through the science collaborations, the astronomical and physics communities are involved in the scientific planning of LSST deployment strategies.

2. Overview of Synergies

The SKA and LSST are the two major ground-based survey telescopes of the next decade. They offer significant synergies, in terms of both sky area and time-domain astrophysics, and are likely to be on the sky over much of the same time-period. The survey strategies for SKA1 and SKA2 are being developed in this book, but are likely to include 3π surveys over the same area as LSST, as well as thousands of square degrees to a greater depth than LSST.

The LSST will leverage a large range of science from the SKA by providing approximate (photometric) redshifts for about 40 galaxies per square arcminute. Many of the existing SKA science applications assume that such photometric redshift information will be available. LSST is the only foreseen survey covering a large fraction of the southern hemisphere at an appropriate depth to provide this information. Euclid can further improve the photometric redshifts from LSST by supplying infra-red information.

Conversely, the SKA can enable LSST to carry out additional exciting science. For instance, one of the challenges for LSST is to calibrate its photometric redshifts with precise redshift information. The SKA has the potential to provide a large amount of redshift information through observations of HI emission, which can then be used to calibrate LSST objects through cross-correlation (Newman 2008; McQuinn & White 2013). SKA will also provide direct redshifts for training photo-zs for highly extinguished or featureless sources that fail to yield emission lines or spectral breaks in the optical/near-IR.

The synergy between the LSST and SKA will have a major impact for several disciplines. In cosmology, much effort is focussed on understanding the apparent accelerated expansion of the Universe. Forecasts currently often take the form of constraints on the dark energy equation of state; however in a decade we may be more concerned with testing the laws of gravity, or investigating new surprises yet to come. In any case, it will be necessary to confront theory with observations of the statistics of cosmological probes, to a large distance. The SKA and LSST are well-suited to each other to obtain the necessary observational cosmology data.

In addition, cosmology in the next decade is likely to have reached the limit of what can be achieved simply by increasing the volume surveyed. Control of systematic errors will be paramount, and therefore cross-checks of quantities between the SKA and LSST will enable ad-

PoS(AASKA14)145

ditional science. For best results, the data from both surveys can be cross-correlated to reduce systematic effects specific to one survey or the other.

When it comes to our attempts to understand how galaxies form, again we find that this quest is intimately tied to both optical and radio observations. The pivotal role of AGN in galaxy formation (see McAlpine et al. (2015) and Smolčić et al. (2015) in this book), and the presence of neutral hydrogen, can only be understood at radio wavelengths, whereas the star formation history can be extracted from both multi-wavelength optical studies and in an extinction-free way using radio continuum observations (see Jarvis et al. (2015) in this book). LSST provides the necessary photometric redshift information that can be used to simultaneously extract approximate redshifts and star-formation rates.

The SKA and LSST both have unusually high time resolution for survey instruments; both are likely to be able to process data in a matter of seconds. They also have a similar size of instantaneous field of view or beam. Therefore the potential for coordinated surveys to find transients opens up an exciting new regime in observational parameter space.

The SKA and LSST will both benefit greatly from other major facilities that will be observing the southern sky. Facilities such as Euclid and WFIRST will provide key near-infrared wavelength data coupled with high resolution that will aid both strong and weak lensing studies, photometric redshift determination, and will allow estimates of the stellar mass of galaxies at $z > 1$. The addition of eROSITA will provide a complementary approach to disentangling the AGN in radio continuum surveys. Complementary to the cosmological studies described here, the proposed all-sky ACTPol survey and future SPT surveys will provide high-resolution CMB polarisation and lensing maps along with a large increase in the number of SZ selected clusters. There are many powerful three-way synergies; here we will concentrate on the SKA-LSST axis.

2.1 LSST-SKA Methodological Synergies

Although we focus predominantly on scientific synergies, the LSST and the SKA will also present many methodological synergies. Both experiments will provide petabyte-scale observational data-sets recorded over time. Extracting all of the astrophysical information contained in such big data-sets will be a considerable challenge. Although the raw observational data recorded by optical and radio interferometric telescopes exhibit quite different properties, the underlying techniques that will be used to analyse these data share many similarities. Bayesian analysis techniques are now of widespread use in astrophysics (e.g. Lewis & Bridle 2002; Feroz et al. 2009); sampling methods that scale to very high-dimensional settings, such as Gibbs and Hamiltonian sampling (e.g. Wandelt et al. 2004; Taylor et al. 2008), will be increasingly important in analysing big-data. Machine learning techniques (e.g. Ball & Brunner 2010) will also play an increasingly important role in tackling the curse of dimensionality that both LSST and SKA data will suffer. Supervised machine learning techniques can be exploited to efficiently navigate these high-dimensional data-sets, while unsupervised learning techniques can be used for dimensionality reduction, allowing the data to effectively speak for themselves.

The sparse structure of big data-sets can also be exploited. Compressive sensing (Candès 2006; Donoho 2006) is a recent ground-breaking development in information theory, going beyond the Shannon-Nyquist sampling theorem by exploiting sparsity, and which has the potential to revolutionise data acquisition in many fields (for a brief introduction see Baraniuk 2007). Although the

PoS(AASKA14)145

application of compressive sensing techniques in astrophysics is not yet mature, first applications for radio interferometric imaging have shown considerable promise (e.g. Carrillo et al. 2014). The effective application of all of these analysis methodologies will be instrumental in the extraction of scientific information from large observational data-sets, such as those recorded by LSST and the SKA. Both experiments will benefit greatly from sharing expertise, analysis techniques and open-source numerical codes.

3. Cosmology with LSST and SKA

Here we will discuss the synergies we expect for major cosmological probes, in particular galaxy clustering (including intensity mapping), weak lensing and strong lensing.

3.1 Weak lensing

LSST will have an unprecedented sample of 3 billion galaxies with high S/N and good colour-redshifts with which to generate dark matter tomographic maps. SKA1 can obtain 40 million galaxies for weak lensing, with SKA2 possibly matching LSST's number density (see Brown & et al. 2015, in this book). Overlapping optical and radio surveys such as those carried out by LSST, SKA1-MID and SKA2 have a particularly useful synergy in terms of reducing and quantifying the impact of systematic effects in weak gravitational lensing analyses (Brown & et al. 2015). By cross-correlating the shapes of galaxies as measured in the optical and radio surveys, one can eliminate instrumental systematic effects that are not correlated between the two telescopes (Patel et al. 2010). Given the very different designs and modes of operation of optical and radio telescopes, one would not expect their instrumental systematic effects to be correlated, and so this offers a route to measuring the cosmic shear signal in a very robust way.

In addition, radio surveys offer unique ways to measure the lensing signal that are not available to optical telescopes. In particular, both radio polarisation information and rotational velocity measurements from HI observations can provide estimates of the *intrinsic* position angles of the lensing source galaxies (Blain 2002; Morales 2006; Brown & Battye 2011). Such measurements offer great potential to (i) reduce the effects of galaxy "shape noise" (due to the intrinsic dispersion in galaxy shapes) and (ii) to mitigate the contaminating signal from the intrinsic alignments in galaxy orientations which is perhaps the most worrisome astrophysical systematic effect facing future weak lensing surveys. In addition to using this information in a combined analysis, one could potentially use the SKA-based estimates of the intrinsic alignment contamination to calibrate out the alignment signal in the LSST lensing survey.

Finally, the envisaged SKA1-MID and SKA2 surveys will probe a wider range of redshifts than will be reached by LSST. They therefore provide extra (high-redshift) tomographic slices with which the evolution of structure at relatively early times can be probed. SKA can also push to high redshift by measuring the lensing distortion signal in HI intensity mapping surveys (Pourtsidou & Metcalf 2014). Thus, these high-redshift SKA lensing experiments will naturally fill the gap between the traditional optical lensing probes (where sources are typically located at $z \sim 1$) and the ultimate lensing source of the CMB at $z \sim 1000$.

PoS(AASKA14)145

3.2 Galaxy clustering

The three approaches to SKA galaxy clustering benefit from LSST in distinct ways, which we will now describe.

3.2.1 HI galaxy survey

As discussed in the chapter on HI threshold surveys (Abdalla et al. 2015), one approach to galaxy clustering with SKA is to measure redshifts from the HI line for a sample of individually detected galaxies. This provides us with a galaxy survey where the redshifts are known to very high precision (we assume a Gaussian error of $\delta_z = 0.0001$). There is a powerful synergy here between this spectroscopic-quality large scale structure (LSS) survey from SKA and the weak gravitational lensing (WGL) surveys from LSST (with or without the further improvements in systematics from combining with the SKA weak lensing survey, see section 3.1 above). The LSST WGL survey has poor redshift resolution (due both to photometric-quality redshifts and the inherently broad WGL geometric kernel) but has direct access to the true matter distribution in the Universe. In contrast the SKA LSS survey has very good redshift resolution but uses galaxies as biased tracers of the mass distribution. Combination of the two surveys allows us to control for uncertainties in galaxy bias and improve our knowledge of how mass clustering evolves with redshift compared to WGL alone.

In Fig. 2 we present results combining a specimen SKA LSS survey with an LSST WGL survey. Our WGL survey is assumed to have a source density of $n_g = 50\text{arcmin}^{-2}$ and to cover a redshift range of $0 < z < 3.0$. The galaxy redshift distribution is given by Hojjati et al. (2012) and broken into 6 tomographic bins of approximately equal number density. The Gaussian scatter on the photo-z errors is $\delta_z = 0.03$.

We assume a LSS study with the full SKA2 survey over 30,000 deg^2. We have adopted the galaxy redshift distribution discussed in Santos et al. (2014); our forecasts assume 40 tomographic bins up to $z = 2.0$. We use the exact projected angular power spectrum, $C(\ell)$, formalism (not the Limber approximation) and include the effects of redshift space distortions (RSDs) according to the formalism of Kaiser (1987). Both these effects are neglected in the WL forecasts because the broad tomographic bins make their impact negligible. We use a maximum wavenumber of $\ell_{\max} = 3000$ for the WL analysis, and exclude non-linear scales in the LSS analysis using the cutoff $\ell_{\max}(z_{\text{med i}}) = k_{\text{lin max}}(z_{\text{med i}})\chi(z_{\text{med i}})$. Here $z_{\text{med i}}$ is the median redshift of tomographic bin i, $k_{\text{lin max}}(z_{\text{med i}}) = 0.132 z_{\text{med i}} h^{-1}$ Mpc, and χ represents comoving distance.

Our Figure of Merit analysis forecasts constraints for a set of cosmological parameters: $\{\Omega_m$, Ω_b, Ω_{DE}, w_0, w_a, h, σ_8, $n_s, b, Q_0, Q_0(1+R_0)/2\}$. As well as the standard wCDM parameters, b is a free amplitude on galaxy bias and $Q_0, Q_0(1+R_0)/2$ are parameterisations of deviations to General Relativity that modify the Poisson equation and the ratio of metric potentials; our ability to constrain these parameters quantifies our ability to test gravity on cosmic scales, see e.g. Kirk et al. (2013). When presenting constraints on dark energy we marginalise over the cosmological parameters and galaxy bias but keep the modified gravity parameters fixed. When presenting constraints on modified gravity we marginalise over cosmology, including w_0 and w_a, and galaxy bias. Priors consistent with the latest Planck temperature constraints are included.

PoS (AASKA14) 145

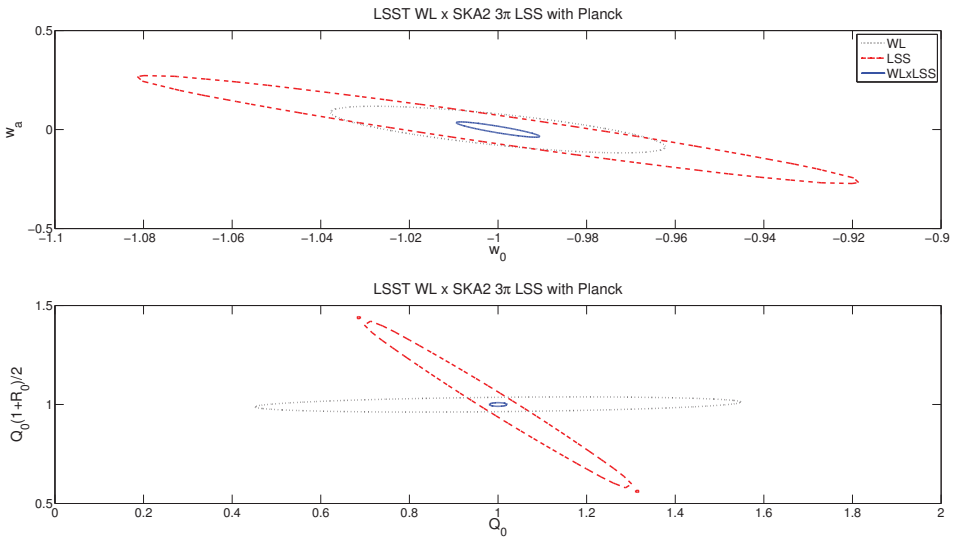

Figure 2: Constraints on dark energy (*top panel*) and gravity parameters (*bottom panel*) with SKA2 HI galaxy survey and LSST WGL survey, together with Planck priors.

It is clear from Fig. 2 that the combination of SKA2 and LSST yields an impressive constraining power. These probes are very complementary; the WGL survey responds directly to the presence of matter, but has poor discrimination in redshift due both to the reliance on photometric redshift and the irreducible width of the lensing kernel along the line of sight. In contrast the LSS survey uses galaxies as biased tracers of the underlying dark matter distribution but has much greater resolution in redshift. The combined analysis makes use of the best features of both probes, gaining redshift discrimination from LSS while directly probing the growth of structure and the geometry of expansion through WGL.

Of course it is possible that systematic effects might affect each probe differently and lead to mis-aligned probability ellipses in the upper panel of Fig. 2, so careful tests and cross-checks for systematics are essential. On the other hand, another benefit of combined probe analysis is the ability to "calibrate" systematics of one probe using another. For example, galaxy Intrinsic Alignments (IAs) could be an important astrophysical contaminant of WGL measurements; but information from spectroscopic LSS surveys can be used to down-weight physically close galaxy pairs and mitigate the impact of IAs.

The improvement over each probe alone is particularly pronounced in the modified gravity constraints; this is the result of combining one probe sensitive to the bending of light (WL, sensitive to the sum of metric potentials $\Psi + \Phi$) and another probe using galaxies as non-relativistic tracers (LSS, sensitive to the Newtonian potential Ψ). This combination of sensitivities breaks a pronounced degeneracy in the MG parameter space and produces constraints far stronger than either probe alone.

3.2.2 Principal Component Analysis

The dark energy and gravity parameters constrained above are constant physical quantities as a

PoS(AASKA14)145

function of time and scale. Instead, we can conduct the Principal Component Analysis (PCA) approach from the chapter by Zhao et al. (2015) to examine how sensitive the LSST and SKA are to physical quantities. In particular, we can examine the sensitivity to the time evolution of the dark energy equation of state, $w(z)$, and the time and scale dependence of the effective Newton's constant $\mu(k,z)$, and the gravitational slip, $\gamma(k,z)$.

The details of our approach are given in Zhao et al. (2015). We consider several LSST cosmological probes: weak gravitational lensing, clustering, and the clustering-lensing cross-correlation; we use the number density and bias models given in Hojjati et al. (2012). In addition, we use the HI clustering surveys for SKA1-MID and SKA2, with number density, bias and survey parameters as in Santos et al. (2014), Tables 2 and 4). We make PCA analyses for each telescope independently in combination with Planck constraints, or in combination with each other and with Planck.

Firstly, we work in the context of General Relativity ($\mu = 1, \gamma = 1$) and calculate the Fisher matrix for each telescope combination, with the cosmological parameters $\{\Omega_b h^2, \Omega_c h^2, h, \tau, n_s, A_s, w_i\}$. After marginalising over the other parameters, we perform PCA on the w_i bins. The results are shown in Figure 3; we see that LSST+Planck is already excellent at constraining eigenmodes of the dark energy equation of state, with 5 modes constrained at the $\sigma < 0.1$ level. SKA1 and SKA2 alone are not competitive for this purpose; however, SKA1 in combination with LSST substantially improves LSST constraints on the first few modes (by 70% for SKA1 and 75% for SKA2, for the best constrained mode).

Next, we allow μ and γ to vary as a function of time and scale, in addition to dark energy time variation. The results of the various PCA analyses, described in detail in Zhao et al. (2015), are shown in Figure 4; in this case, the synergy between LSST and SKA is very strong. While LSST+Planck alone can constrain 5 modes of the effective Newton constant μ at the $\sigma < 0.01$ level, even LSST+SKA1+Planck can constrain 7, and LSST+SKA2+Planck can constrain 11 - with errors on the first mode reduced by a factor of 5. The situation is equally impressive for the gravitational slip γ; the addition of SKA1 to LSST+Planck reduces errors on the first mode by 20%, and the addition of SKA2 reduces errors by a factor of 6.

As in Section 3.2.1, the cause of this improvement is the different physical effects of μ and γ on different cosmological probes. Weak lensing and the CMB are sensitive to combinations of the two metric potentials Φ and Ψ, which are affected by both μ and γ modes. On the other hand, redshift space distortions measured in the SKA HI surveys are only sensitive to Ψ, and hence μ. Thus we find that LSST+SKA are an excellent combination for future tests of gravity.

3.2.3 Continuum survey

As described in the chapter on cosmology with radio continuum surveys (Jarvis et al. 2015), a new era for continuum cosmology is close to becoming a reality. Among the numerous planned surveys are the LOFAR Surveys, the Evolutionary Map of the Universe (EMU), the MeerKAT-MIGHTEE survey and the Westerbork Observations of the Deep APERTIF Northern Sky (WODAN). These forthcoming experiments will provide us with a homogeneous all-sky continuum catalogue > 10 times larger than the largest one hitherto available, and SKA1 will be able to reach a factor an order of magnitude deeper over similar sky areas to these.

However, radio continuum surveys do not provide any redshift information for the sources. For cosmological purposes, this is a serious issue; to investigate cosmic acceleration, we require

PoS(AASKA14)145

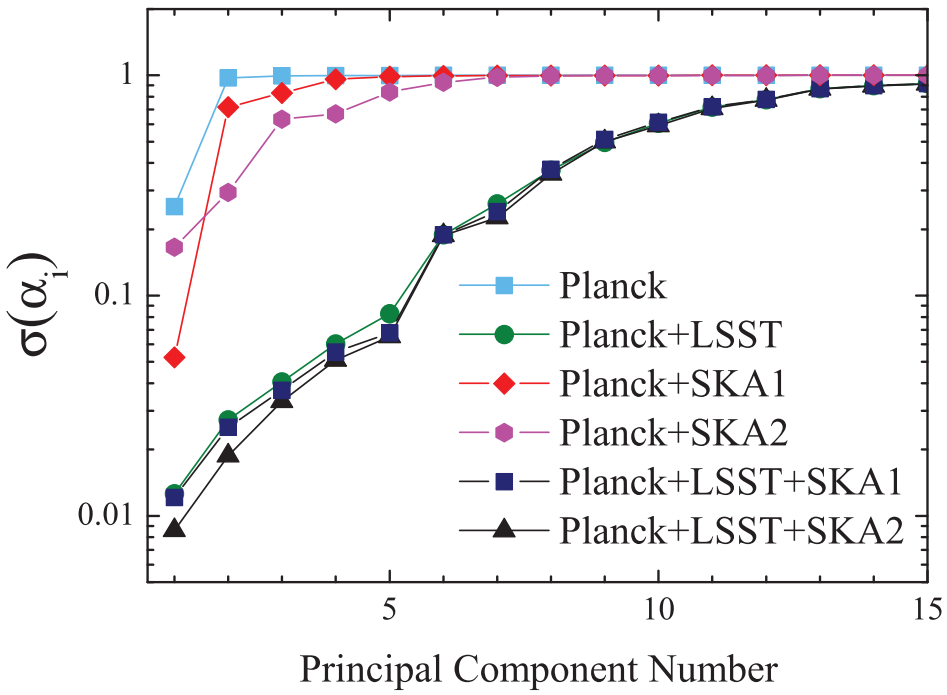

Figure 3: The forecast 68% CL measurement error of the principal components, for the dark energy equation of state, for different survey combinations listed in the legend.

information about the time evolution of the Universe's expansion and structure growth. For this purpose, Camera et al. (2012) proposed to cross-identify continuum radio sources with optical to near-infrared surveys (currently these include SkyMapper and SDSS). Even now such studies could be extended by incorporating data from other surveys, particularly at near/mid-infrared wavelengths where the VISTA Hemisphere Survey (McMahon et al. 2013), 2MASS (Skrutskie et al. 2006) and WISE (Wright et al. 2010) can provide robust detections of low-redshift sources. LSST will further improve the prospects for cross-identification at higher redshift. By making these cross-matches, one can separate the source distribution into a low- and a high-redshift sample, thus providing information on the evolution of cosmological parameters such as those related to dark energy. This approach yields constraints more than four times tighter than in the case without redshift information.

Using both the SKA and the LSST, we are also able to perform a cross-correlation of galaxy clustering with the Cosmic Microwave Background, probing the integrated Sachs-Wolfe (ISW) effect. Raccanelli et al. (2014) have provided promising forecasts for constraining the non-Gaussianity of primordial fluctuations using this probe with SKA and photometric surveys. This can be seen from Figure 5, where we show how having redshift information will enable a tomographic ISW, which will help in pinning down the constraints on the non-Gaussianity parameter $f_{\rm NL}$. We plot constraints for the SKA1 only case (no redshift information) for a 5μJy rms survey of 30000 sq deg, and where redshift information is provided by a photometric survey such as LSST for SKA

PoS(AASKA14)145

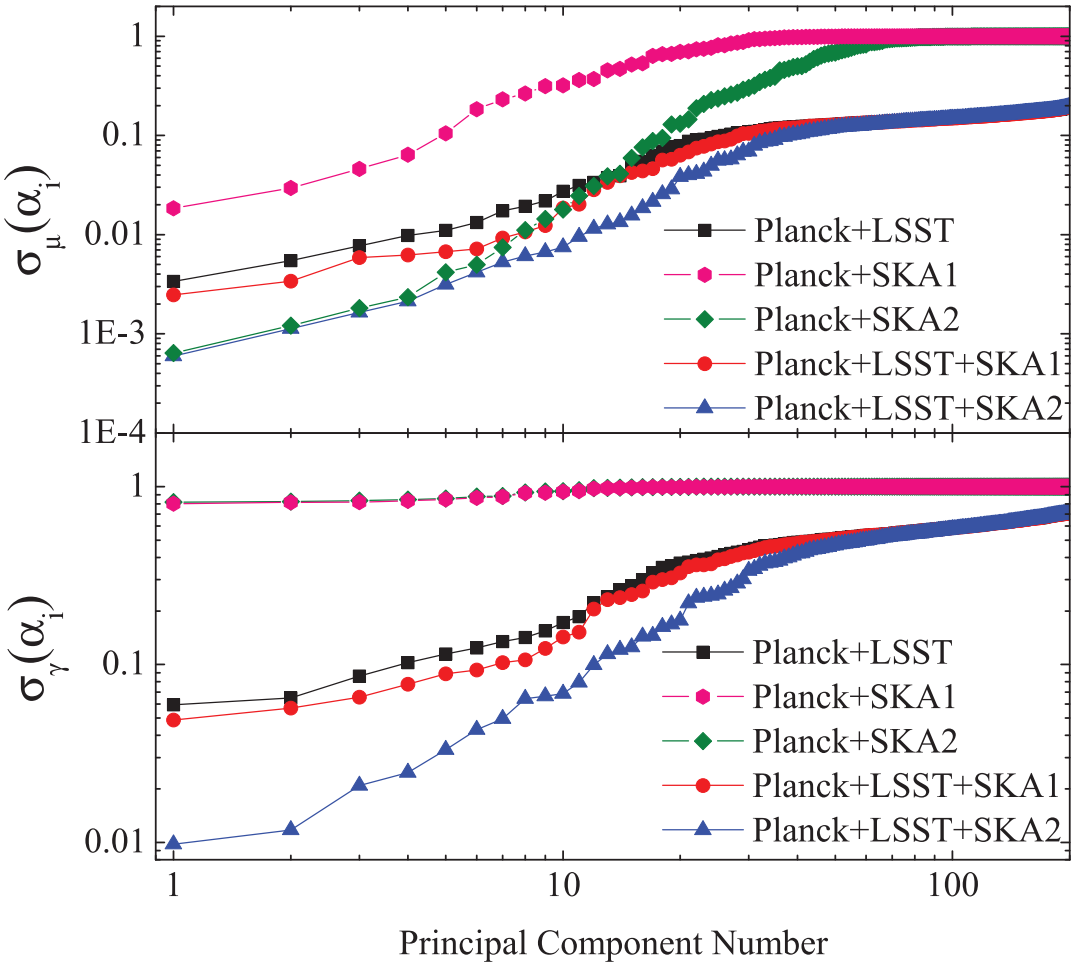

Figure 4: The forecast 68% CL error of the principal components of $\mu(k,z)$ (top panel) and $\gamma(k,z)$ (bottom panel), for different survey combinations listed in the legend.

sources, up to $z = 1$ and $z = 2$. The error on $f_{\rm NL}$ is reduced from 20 to $\simeq 1$, which compares favourably to the current current best constraint of $f_{\rm NL} = 2.7 \pm 5.8 (1\sigma)$ from Planck (Ade et al. 2014).

3.2.4 Intensity mapping

Intensity mapping of the redshifted neutral hydrogen 21cm emission line is an exciting new survey methodology for large scale structure. Instead of resolving many individual galaxies at high signal-to-noise, one instead uses low-resolution maps of the integrated emission from many unresolved

PoS(AASKA14)145

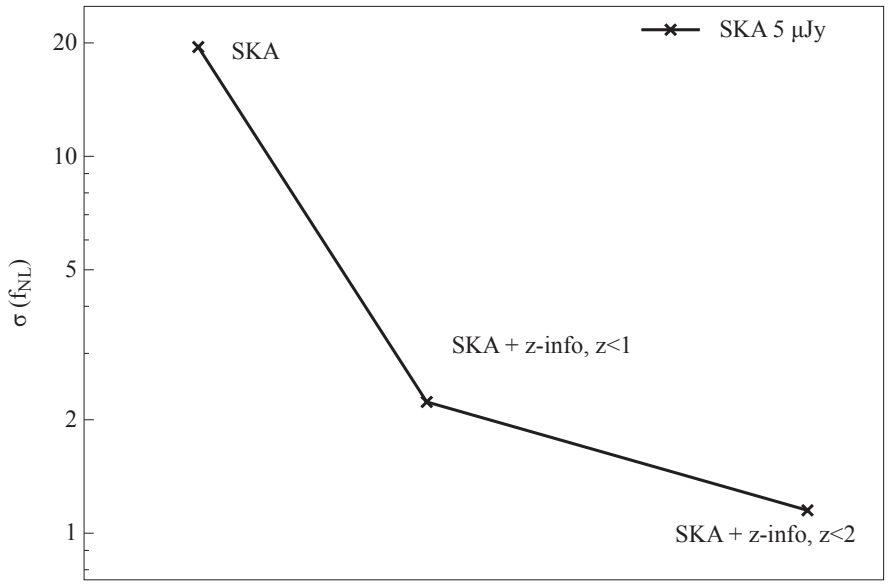

Figure 5: Constraints on the non-Gaussianity parameter $f_{\rm NL}$ from the cross-correlation SKA-CMB, with and without redshift information provided by a photometric survey such as LSST.

galaxies to probe the large scales ($\sim 1^\circ$) corresponding to the baryon acoustic oscillations. Since the galaxy population hosting the HI emitting regions is a biased tracer of the underlying dark matter distribution, so too is the integrated HI signal, and redshift information is trivially obtained by the frequency of the emission. By making low-resolution maps over a substantial fraction of the sky, for many channels over a wide band, intensity mapping (IM) surveys are therefore able to rapidly reconstruct the large-scale redshift-space matter distribution over extremely large cosmological volumes, out to high redshift (Santos et al. 2015).

While the IM methodology is not yet mature, a number of medium-size experiments that are either planned or in construction (e.g. CHIME, Bandura et al. (2014), BINGO, Battye et al. (2012)) are expected to yield cosmological results substantially before SKA1 sees first light. With SKA1, a 10,000 hour, 25,000 deg^2 IM survey on either the MID or SUR arrays are projected to yield dark energy constraints that are competitive with a Dark Energy Task Force Stage IV galaxy redshift survey (Bull et al. 2014; Bull & et al. 2015; Raccanelli et al. 2015). This could potentially be completed several years before LSST (and even Euclid), with a substantial overlap in survey area and redshift coverage.

While this would provide many of the same advantages as an overlapping galaxy survey in the radio, intensity mapping has a number of additional benefits in terms of synergies with LSST. Foremost is the significantly different set of systematic effects that one expects from making intensity maps rather than galaxy catalogues. A number of calibration and selection effects that are common to galaxy surveys, but not IM, can then be expected to drop out in cross-correlation, which will be especially powerful if, as expected, future large scale structure surveys are systematics-limited. IM surveys are also capable of spanning both lower and higher redshifts than LSST, and can potentially be used to 'anchor' the LSST data by filling in some information in missing redshift bins –

PoS(AASKA14)145

for example, SKA1-MID can cover $0.4 \lesssim z \lesssim 3$ with Band 1, and $0 \lesssim z \lesssim 0.5$ with Band 2.

Because IM surveys probe a differently-biased population of galaxies to LSST, one can also benefit from multi-tracer analysis (McDonald & Seljak 2009; Abramo & Leonard 2013; Camera & et al. 2015). For certain observables – most notably redshift space distortions – this allows the limits imposed by cosmic variance to be beaten, which is of particular importance for reconstructing the growth history of the Universe to high enough precision to test modifications to General Relativity (Raccanelli et al. 2015).

3.3 Strong lensing

The 2020s will be a new era for studying galaxy formation, the high redshift Universe and cosmology with strong gravitational lensing (see the chapter by McKean & et al. (2015) in this volume). Currently, ∼500 strong lens systems are known, of which about 10% are radio-loud. This sample will potentially increase with SKA and LSST to about 100000 in each waveband (e.g. Marshall et al. 2005; Oguri & Marshall 2010). SKA alone will detect lensed sources in abundance, with a few per square degree accessible to SKA1 and many more to SKA2. These will include AGN and star forming regions via their continuum synchrotron emission, and gas clouds out to high redshift via their molecular line emission. The latter are particularly interesting for providing source redshifts and velocity fields.

Detailed multi-band optical and infrared imaging will be important both for finding and using this new sample of gravitational lenses. Having two surveys at very different wavebands reduces the false positive rate, which is likely to be the main problem with the next generation of lens surveys, because the radio-optical flux ratio of potential multiple lensed images will be a much better discriminant than anything available within a single waveband. (0.3"-resolution optical data would have drastically reduced the necessary followup in radio surveys such as CLASS (Myers et al. 2003), for instance). A secondary consideration is that detecting the lensing galaxy allows probabilistic arguments to be made about the likelihood of a lensing model for any surrounding objects, versus the hypothesis that the surrounding objects are non-lensed features such as star-forming regions. The deep multi-band photometry from the LSST will enable the lensing galaxies to be detected and their photometric redshifts to be measured in most of the SKA systems; lens galaxy redshifts and positions are needed for accurate modelling of their mass distributions. Once we have confirmed lens systems with good lens models, we will be able to test galaxy formation models, and explore source populations at high magnification.

The synergy between the LSST and SKA is also important for the cosmological applications of strong lenses. Both telescopes will be capable of measuring independent gravitational time-delays from the variable optical and radio emitting regions, needed for the measurement of distances and so to test models for dark energy (e.g. Suyu et al. 2010). Multi-wavelength follow-up is very important in these studies, to characterise the properties of the lenses and their environment, which are needed to overcome systematics in the mass model. The radio monitoring is particularly powerful where the source is varying, since the lightcurves are not (or at least much less) affected by microlensing.

PoS(AASKA14)145

4. Galaxy evolution with LSST and SKA

With the onset of wide and deep field surveys across all wavebands, coupled with high-resolution cosmological hydrodynamic simulations, much progress has been made in understanding galaxy evolution over the past decade. However, there are clear deficiencies in our understanding of galaxies over the whole of cosmic time. At the bright end of the galaxy luminosity function, we need to understand better the role of AGN feedback (Fabian 2012), and how this may truncate or stimulate star formation in the AGN host itself or in the surrounding environment. At the faint end, we need to understand the influence of the environment, and how for instance hot and cold gas may get stripped from galaxy haloes as they fall into the deep potential wells of clusters.

The combination of deep optical imaging from LSST, coupled with both continuum and spectral line surveys with the SKA, offers a unique opportunity to significantly impact on our understanding of the formation and evolution of galaxies up to the highest redshifts. Here we highlight some of the key synergies that are also discussed at greater length in other chapters in this volume.

4.1 The evolution of activity in the Universe

One of the key goals of the SKA continuum surveys is to provide a complete census of the AGN and star-formation activity across cosmic time. Radio continuum observations play a unique role for both of these topics. For AGN, the radio traces highly energetic jets which provide the mechanical feedback in many semi-analytic models and hydrodynamic simulations of galaxy evolution. However, current radio surveys do not provide a full picture of the impact of such sources. In particular, more depth is required to obtain information on the detailed physics of distant radio sources, coupled with a full sampling of the uv-plane to ensure that both large and small spatial scales are sampled as required. On the other hand, the sources are rare and thus relatively wide surveys are also needed to ensure that all environments at all redshifts are fully sampled.

Radio emission may provide the most robust tracer of the star-formation rate in all galaxies. This is because the radio waveband does not suffer from dust extinction which is a limiting property of similar studies using the visible waveband. Furthermore, the high-resolution, sub-arcsecond imaging possible with the SKA ensures that AGN and star-formation activity can be distinguished, and that radio sources can be associated with optical and near-infrared counterpart galaxies.

Therefore, continuum surveys with the SKA provide the necessary depth and area to provide a complete census of AGN and star-formation activity across cosmic time. However, what is missing from radio observations is information on the redshift, stellar mass, and the many other properties associated with the stellar populations within galaxies (e.g. metallicity, age) which can be supplied by LSST. On the other hand, knowledge of the presence of an AGN from the SKA will ensure that AGN emission can be considered for modelling the SED at optical/near-infrared wavelengths. Thus it is only by combining the SKA continuum surveys with photometric redshifts and stellar properties from the LSST that we will gain the fullest picture of galaxy evolution.

The LSST Deep Drilling Fields will provide extremely deep imaging data (AB$\sim$ 28 mag) in four extragalactic fields, overlapping with deep near-infrared imaging from UltraVISTA (McCracken et al. 2012) and VIDEO (Jarvis et al. 2013) of LSST ($\sim$ 9.6 deg^2 each). The LSST Deep Drilling Fields combined with the proposed deep SKA continuum fields will allow us to trace Milky Way type galaxies up to the highest redshifts with both facilities, sampling enough cosmological

PoS(AASKA14)145

volume not to be dominated by sample variance issues for this purpose. In particular, these LSST deep fields will be sufficiently deep to find galaxies at $z > 6$, which will be ripe for CO redshift measurement with SKA Band 5. The LSST all-sky survey coupled with the SKA all-sky survey will provide a similar census of galaxy evolution at $z < 1$, again sampling all of the accessible volume.

4.2 The evolution of hydrogen

One of the unique aspects of the SKA is its ability to measure the evolution of neutral hydrogen in the Universe. With SKA1 this can be done in deep fields out to the limiting frequency for SKA-MID (350MHz corresponds to a redshift of $z \sim 3$). In the wider area surveys the ability to detect HI will probably be limited to around $z \sim 0.6$.

Together the SKA and LSST surveys could potentially provide the key information on how quickly gas is turned into stars. For example, in combination with ALMA, the surveys could provide a continuous view of the path from neutral (SKA) to molecular gas (ALMA) through to star formation (radio continuum and LSST). To be able to carry out such studies as a function of galaxy mass, galaxy type and environment, will strongly enhance our understanding of the evolution of galaxies.

4.3 High-redshift galaxies and reionization

The LSST galaxy sample at $z \sim 5$ will provide an important calibration of stellar mass density and galaxy clustering, as a function of galaxy properties and environment. These can anchor interpretations of measurements of the brightness temperature fluctuations from the epoch of reionization with SKA. During the later stages of reionization, the brightness temperature is dominated by fluctuations in the neutral hydrogen fraction, which in turn depend on reionization-source properties and their clustering statistics (Mellema et al. 2013). Measurements of such quantities during the epoch of reionization, $z = 6 - 15$, with instruments such as VISTA, James Webb Space Telescope, and Hyper-SuprimeCam, will need such a lower-redshift normalization around the end of reionization to realize their full statistical potential. Deep observations with the James Webb Space Telescope to detect samples of the first galaxies will particularly complement the LSST sample by providing an anchoring point at the start of, or before, the epoch of reionization. The combination of the LSST, SKA, and James Webb Space Telescope will be key for joint constraints on galaxy evolution and reionization.

The LSST Deep Drilling Fields will provide additional information during the epoch of reionization, $z > 6$, in principle allowing studies of cross-correlation and co-evolution between galaxies and the brightness temperature/neutral hydrogen fraction from SKA. In combination with potential deep SKA continuum fields and complementary near-infrared data, the Deep Drilling Fields will allow the determination of key source population observables such as UV luminosity, star formation rate, escape fraction of ionizing photons, metallicity, and stellar mass (e.g. in combination with Spitzer or Euclid). Additional redshift measurements from SKA would complement this.

As a baseline, by combining the source population data with the measured global brightness temperature signal from SKA, constraints can be placed on the fraction of reionization that is provided by galaxies. If reionization occurs late, at $z \sim 6 - 10$ as some evidence suggests, e.g. Pentericci (2012), such that the brightness temperature fluctuations still trace the source statistics,

PoS(AASKA14)145

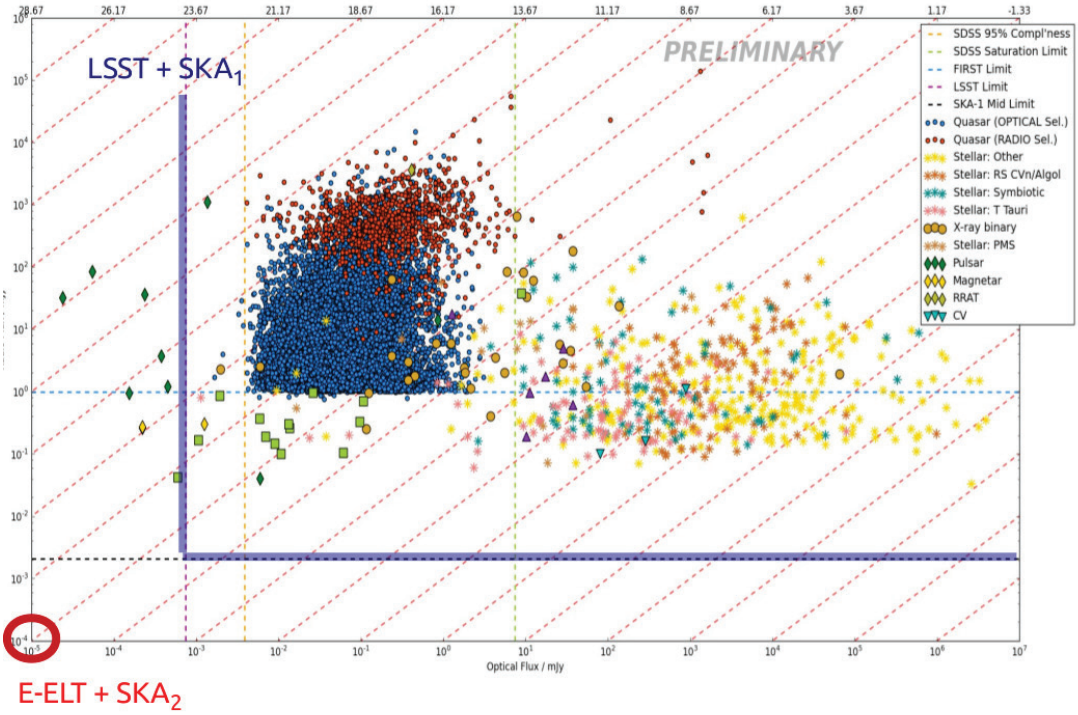

Figure 6: Radio vs optical flux density for a range of astrophysical variables, including a large set of SDSS AGN as well as stellar sources, pulsars and and active binaries. The sample is largely cut off by the limits of the SDSS and FIRST optical and radio surveys, respectively. Optical flux is immediately seen to be a good discriminator between the broad classes of source. The solid mauve lines indicate the typical nightly sensitivities of LSST and SKA1-MID for a given field, demonstrating how much further into parameter space they will routinely push. For example, stellar sources will be detectable throughout the galaxy instead of just locally. Also indicated are the flux limits for a typical joint observation of a field with E-ELT and the dish component of SKA2 (albeit rather uncertain). From Stewart et al., in prep.

cross-correlation of the LSST Deep Drilling Fields with SKA might be possible (Lidz et al. 2009; Wiersma et al. 2013). This would provide another way to constrain details of the reionization process, e.g. to what degree different galaxy types are responsible. Since LSST will characterise the source galaxy populations in great detail, the statistics of the brightness temperature field could also be directly correlated with galaxy properties. Such information is important for a full characterisation of the power spectrum of brightness temperature fluctuations, and hence for extracting the full cosmological information from SKA (Mellema et al. 2013).

5. Variables and transients

One of the key science drivers for the LSST is the time variable Universe and transient astrophysics.

PoS(AASKA14)145

In recent years this is an area which has also come to the fore in the key programmes being planned or implemented on the SKA and its pathfinders and precursors. LOFAR (Stappers et al. 2011), MeerKAT, ASKAP and the MWA all have approved key programmes in the area of radio transients, both 'fast' (coherent, found primarily in beamformed data) and 'slow' (incoherent synchrotron, found mainly in image stacks). The chapters in this book by Fender et al. (2015); Macquart et al. (2015); Corbel & et al. (2015) provide an overview of the science and likely performance of the SKA transients surveys in both modes, with further, more detailed, case studies in the following transient chapters. An earlier review of the prospects for radio transients with the SKA can be found in Fender & Bell (2011).

However, it is clear that the value of finding radio transients is severely reduced if counterparts at other wavelengths are not also identified. Since the sources are by definition ephemeral, this usually means rapid identification, reporting and follow-up of radio transients (hence the strong push for automated commensal transient searching in Fender et al. (2015)). Which wavelengths are best? In most cases, although X-ray and other counterparts will be important, the optical or infrared bands are most needed, as these can be readily compared against reference images and can identify candidates for spectroscopic follow-up (and possibly redshift measurement) in the most exciting cases. Probably the single highest priority, therefore, for radio transient follow-up, is to get an optical photometric measurement. Fig. 6 presents a wide sample of the optical and radio fluxes, from sources ranging from stars to supermassive black holes, which are likely radio variables.

Fortunately, in the era of parallel wide-field SKA and LSST observations, the optical data will be readily available for most fields. For the kind of surveys being envisaged with SKA1, and the nightly sky sweeps of LSST, several fields per night will get much deeper than the parameter space explored in Fig. 6 (mauve lines).

6. Conclusions

In this chapter we have examined the value of combining data and analyses with the SKA and LSST. We introduced the LSST, recognising it as one of the foremost survey telescopes of the next decade. We then discussed the synergies available between the SKA and LSST, at both the methodological and science result levels.

In the field of cosmology, we discussed how weak gravitational lensing benefits from the combination of optical and radio shape measurements with radically different systematic effects present. We showed how the combination of LSST lensing and clustering, and SKA galaxy clustering with spectroscopic redshifts, provide improved constraints on dark energy and gravity parameters. We discussed how the synergy between LSST and SKA continuum and intensity mapping measurements also provides improvements on cosmological parameters. Strong lensing studies benefit from the combined ability of SKA and LSST to characterise both the lenses and sources in detail.

We have also discussed the benefits to studies of galaxy evolution, where SKA can provide information on redshift, neutral hydrogen, AGN and star formation, while LSST can provide complementary information about star formation, galaxy age and metallicity. LSST will provide an important calibration of galaxy properties for interpreting brightness temperature fluctuation data

PoS(AASKA14)145

obtained with SKA from the epoch of reionization. The LSST Deep Drilling Fields in combination with SKA will help determine how galaxy populations reionize the Universe, thereby also providing information that will improve the SKA cosmology analysis.

Finally, we have discussed the value of combining the LSST and SKA time domain in order to understand and discover a wide range of astrophysical variables and transients.

In conclusion, using both surveys gives:

- Complementary physical constraints (e.g. the sensitivity of LSST lensing to both metric potentials, and the SKA RSD measurements to the Newtonian potential alone);
- Removal of systematics (e.g. cross-correlation of optical and radio lensing signals removing shape measurement systematics);
- Cross checks of results; in the forthcoming period of concern about systematic effects, even using the two machines independently will provide important verification of the science results (c.f. the experiments at the Large Hadron Collider);
- Mutual science support (e.g. LSST providing photometric redshifts for SKA continuum detections, and SKA calibration of LSST photo-zs via spectroscopic redshift cross-correlations);
- A more complete picture (e.g. in galaxy evolution, LSST and SKA are sensitive to different components of the galaxy such as neutral hydrogen and stellar populations; in the time domain, the telescopes inform us of different aspects of the transient physics.)

References

Abdalla, F. B., Bull, P., Camera, S., et al., 2015, "Cosmology from HI galaxy surveys with the SKA", in proc. *Advancing Astrophysics with the Square Kilometre Array*, PoS(AASKA14)017

Abell, P. A., Allison, J., Anderson, S. F., et al. 2009, arXiv:0912.0201

Abramo, L. R., & Leonard, K. E. 2013, MNRAS, 432, 318

Ade, P. A. R., Aghanim, N., Armitage-Caplan, C., et al. 2014, A&A, 571, A24

Ball, N. M., & Brunner, R. J. 2010, International Journal of Modern Physics D, 19, 1049

Bandura, K., Addison, G. E., Amiri, M., et al. 2014, in Society of Photo-Optical Instrumentation Engineers (SPIE) Conference Series, Vol. 9145, Society of Photo-Optical Instrumentation Engineers (SPIE) Conference Series, 22

Baraniuk, R. 2007, IEEE Signal Processing Magazine, 24, 118

Battye, R. A., Brown, M. L., Browne, I. W. A., et al. 2012, arXiv:1209.1041, arXiv:1209.1041

Blain, A. W. 2002, ApJLett, 570, L51

Brown, M., Bacon, D. J., Camera, S., et al., 2015, "Weak gravitational lensing with the Square Kilometre Array", in proc. *Advancing Astrophysics with the Square Kilometre Array*, PoS(AASKA14)023

Brown, M. L., & Battye, R. A. 2011, MNRAS, 410, 2057

Bull, P., Camera, S., Raccanelli, A., et al., 2015, "Measuring baryon acoustic oscillations with future SKA surveys", in proc. *Advancing Astrophysics with the Square Kilometre Array*, PoS(AASKA14)024

PoS(AASKA14)145

Bull, P., Ferreira, P. G., Patel, P., & Santos, M. G. 2014, arXiv:1405.1452, arXiv:1405.1452
Camera, S., Raccanelli, A., Bull, P., et al., 2015, "Cosmology on the Largest Scales with the SKA", in proc. *Advancing Astrophysics with the Square Kilometre Array*, PoS(AASKA14)025
Camera, S., Santos, M. G., Bacon, D. J., et al. 2012, MNRAS, 427, 2079
Candès, E. 2006, Proceedings of the International Congress of Mathematicians, 3, 1433
Carrillo, R. E., McEwen, J. D., & Wiaux, Y. 2014, MNRAS, 439, 3591
Corbel, S., Miller-Jones, J. C. A., Fender, R. P., et al., 2015, "Incoherent transient radio emission from stellar-mass compact objects in the SKA era", in proc. *Advancing Astrophysics with the Square Kilometre Array*, PoS(AASKA14)053
Donoho, D. 2006, IEEE Transactions on Information Theory, 52, 1289
Fabian, A. C. 2012, ARA&A, 50, 455
Fender, R. et al., 2015, "The Transient Universe with the Square Kilometre Array", in proc. *Advancing Astrophysics with the Square Kilometre Array*, PoS(AASKA14)051
Fender, R. P., & Bell, M. E. 2011, Bulletin of the Astronomical Society of India, 39, 315
Feroz, F., Hobson, M. P., & Bridges, M. 2009, MNRAS, 398, 1601
Hojjati, A., Zhao, G.-B., Pogosian, L., et al. 2012, PhysRevD, 85, 043508
Ivezic, Z., Tyson, J. A., Acosta, E., et al. 2008, arXiv:0805.2366, arXiv:0805.2366
Jarvis, M., et al. 2015, "Cosmology with SKA Radio Continuum Surveys", in proc. *Advancing Astrophysics with the Square Kilometre Array*, PoS(AASKA14)018
Jarvis, M. J., Bonfield, D. G., Bruce, V. A., et al. 2013, MNRAS, 428, 1281
Kaiser, N. 1987, MNRAS, 227, 1
Kirk, D., Laszlo, I., Bridle, S., & Bean, R. 2013, MNRAS, 430, 197
Lewis, A., & Bridle, S. 2002, PhysRevD, 66, 103511
Lidz, A., Zahn, O., Furlanetto, S. R., et al. 2009, The Astrophysical Journal, 690, 252
Macquart, J., Keane, E. F., Grainge, K., et al., 2015, "Fast Transients at Cosmological Distances with the SKA", in proc. *Advancing Astrophysics with the Square Kilometre Array*, PoS(AASKA14)055
Marshall, P., Blandford, R., & Sako, M. 2005, New Ast. Rev., 49, 387
McAlpine, M., Prandoni, I., Jarvis, M., et al., 2015, "The SKA view of the Interplay between SF and AGN Activity, and its role in Galaxy Evolution", in proc. *Advancing Astrophysics with the Square Kilometre Array*, PoS(AASKA14)083
McCracken, H. J., Milvang-Jensen, B., Dunlop, J., et al. 2012, A&A, 544, A156
McDonald, P., & Seljak, U. 2009, JCAP, 10, 7
McKean, J., Jackson, N., Vegetti, S., et al., 2015, "Strong gravitational lensing with the SKA", in proc. *Advancing Astrophysics with the Square Kilometre Array*, PoS(AASKA14)084
McMahon, R. G., Banerji, M., Gonzalez, E., et al. 2013, The Messenger, 154, 35
McQuinn, M., & White, M. 2013, MNRAS, 433, 2857
Mellema, G., Koopmans, L. V. E., Abdalla, F. A., et al. 2013, Experimental Astronomy, 36, 235
Morales, M. F. 2006, ApJLett, 650, L21
Newman, J. A. 2008, ApJ, 684, 88
Oguri, M., & Marshall, P. J. 2010, MNRAS, 405, 2579
Patel, P., Bacon, D. J., Beswick, R. J., Muxlow, T. W. B., & Hoyle, B. 2010, MNRAS, 401, 2572
Pentericci, L. 2012, Memorie della Societa Astronomica Italiana, 83, 1123

PoS(AASKA14)145

Pourtsidou, A., & Metcalf, R. B. 2014, MNRAS, 439, L36

Raccanelli, A., Bull, P., Camera, S., et al., 2015, "Measuring redshift-space distortions with future SKA surveys", in proc. *Advancing Astrophysics with the Square Kilometre Array*, PoS(AASKA14)031

Raccanelli, A., Doré, O., Bacon, D. J., et al. 2014, arXiv:1406.0010, arXiv:1406.0010

Santos, M. et al., 2014b, Proceedings of "Advancing Astrophysics with the Square Kilometre Array", PoS(AASKA14)021

Santos, M., Bull, P., Alonso, D., et al., 2015, "Cosmology with a SKA HI intensity mapping survey", in proc. *Advancing Astrophysics with the Square Kilometre Array*, PoS(AASKA14)019

Skrutskie, M. F., Cutri, R. M., Stiening, R., et al. 2006, AJ, 131, 1163

Smolčić, V., Padovani, P., Delhaize, J., et al., 2015, "Exploring AGN Activity over Cosmic Time with the SKA", in proc. *Advancing Astrophysics with the Square Kilometre Array*, PoS(AASKA14)069

Stappers, B. W., Hessels, J. W. T., Alexov, A., et al. 2011, A&A, 530, A80

Suyu, S. H., Marshall, P. J., Auger, M. W., et al. 2010, ApJ, 711, 201

Taylor, J. F., Ashdown, M. A. J., & Hobson, M. P. 2008, MNRAS, 389, 1284

Wandelt, B. D., Larson, D. L., & Lakshminarayanan, A. 2004, PhysRevD, 70, 083511

Wiersma, R. P. C., Ciardi, B., Thomas, R. M., et al. 2013, MNRAS, 432, 2615

Wright, E. L., Eisenhardt, P. R. M., Mainzer, A. K., et al. 2010, AJ, 140, 1868

Zhao, G.-B., Bacon, D., Maartens, R., et al., 2015, "Model-independent constraints on dark energy and modified gravity with the SKA", in proc. *Advancing Astrophysics with the Square Kilometre Array*, PoS(AASKA14)165

PoS(AASKA14)145

PROCEEDINGS OF SCIENCE

Euclid & SKA Synergies

Thomas D. Kitching[*1], **David Bacon**[2], **Michael L. Brown**[3], **Philip Bull**[4], **Jason D. McEwen**[1], **Masamune Oguri**[5], **Roberto Scaramella**[6], **Keitaro Takahashi**[7], **Kinwah Wu**[1], **Daisuke Yamauchi**[8]

[1]*University College London, Department of Space and Climate Physics;* [2]*ICG, University of Portsmouth;* [3]*Department of Physics, University of Manchester;* [4]*University of Oslo, Institute for Theoretical Astrophysics;* [5]*Graduate School of Science, University of Tokyo, Japan;* [6]*INAF-Osservatorio di Roma, I-00040 Monteporzio Catone, Italy;* [7]*Graduate School of Science and Technology, Kumamoto University, Japan;* [8]*Research Center for the Early Universe, University of Tokyo, Japan;*
E-mail: t.kitching@ucl.ac.uk

Over the past few years two of the largest and highest fidelity experiments conceived have been approved for construction: Euclid is an ESA M-Class mission that will map three-quarters of the extra galactic sky with Hubble Space Telescope resolution optical and NIR imaging, and NIR spectroscopy, it has scientific aims (amongst others) are to create a map of the dark Universe and to determine the nature of dark energy. The Square Kilometre Array (SKA) has similar scientific aims (and others) using radio wavelength observations. The two experiments are synergistic in several respects, both through the scientific objectives and through the control of systematic effects. SKA1 and Euclid will be commissioned on similar timescales offering an exciting opportunity to exploit synergies between these facilities.

Advancing Astrophysics with the Square Kilometre Array
June 8-13, 2014
Giardini Naxos, Italy

[*]Speaker.

PoS(AASKA14)146

1. Introduction

In this Chapter we will describe the ESA Euclid mission, and discuss some of the synergies that Euclid has with the SKA. Euclid probes the low redshift Universe, through both weak lensing and galaxy clustering measurements. The SKA has the potential to probe a higher redshift regime and a different range in scales of the matter power spectrum, linear scales rather than the quasi-non-linear scales that Euclid will be sensitive to, that will make the combination particularly sensitive to signatures of modified gravity and neutrino mass. In combination a longer baseline in redshift will improve expansion history and growth of structure measurements leading to improved measurements of the redshift bahaviour of the dark energy equation of state. The cross correlation between Euclid and SKA weak lensing (shape as well as size and flux magnification), Euclid and SKA galaxy clustering (BAO and redshift space distortions), SKA 21cm intensity mapping and Planck data (CMB, SZ and ISW) will provide a multitude of cross-correlation statistics.

As an example of the benefit of combining the experiments for systematic control for the primary science, the shape measurement from Euclid and SKA will be affected by systematics in different ways, meaning that a cross-correlation of the weak lensing data from both data sets will be less prone to shape measurement biases (see Brown et al, in this volume). Furthermore the intrinsic (un-lensed) ellipticity alignments measured by both Euclid and the SKA will have mutual benefit. Specifically, in addition to Euclid, for weak lensing SKA contributes i) depth, providing more source counts for weak lensing, ii) a way to cross-calibrate shape systematics, iii) a way to cross-calibrate intrinsic alignments, and iv) precise redshifts through 21cm line observations. And possibly the use of polarisation and 21cm rotational velocities for intrinsic shapes and lensing tomography of high redshift 21cm fluctuations.

In addition to the primary science objectives of Euclid there is a plethora of additional legacy and cosmology synergies. We can expect $> 10^5$ strong lens detections from Euclid and SKA, many with redshifts for the lenses and sources and high-resolution images. The combination of Euclid and SKA will better investigate the obscured cosmic star formation history as a function of redshift and environment thanks to their combination of areal coverage and sensitivity. For population III, hypernovae and Type II supernovae NIR emission will be detectable by Euclid from supermassive Pop III supernovae in dense 10^7-10^8 $M_\odot$ haloes out to $z = 10-15$, and radio synchrotron emission from Pop III supernova remnants detectable by SKA out to $z = 20$.

A further synergistic aspect is that each of these areas will require post-operation infrastructure development in terms of a very large number of hydrodynamical and n-body simulations to understand the effects of non-linear clustering and baryonic feedback. Finally the data analysis of giga-scale catalogues, peta-bytes of data, and post-operation simulations require astrostatistical and astroinformatics synergies for astronomers to access and visualise these data sets.

1.1 Euclid Overview

Euclid is one of the European Space Agency's (ESA) medium (M) class missions that has been selected as part of ESAs "cosmic visions" programme. Euclid was selected by ESA in October 2012, to take the second of the M-class mission places, M2, which means that there is a scheduled launch date for 2020. The science objective of Euclid is primarily to determine the nature of the the phenomenon that is causing the expansion rate of the Universe to accelerate; so-called 'dark

PoS(AASKA14)146

energy'. However the top-level science objectives are in fact four-fold and cover all current major open questions in cosmology:

- Dynamical Dark Energy: Is the dark energy simply a cosmological constant, or is it a field that evolves dynamically with the expansion of the Universe?
- Modification of Gravity: Alternatively, is the apparent acceleration instead a manifestation of a breakdown of General Relativity on the largest scales, or a failure of the cosmological assumptions of homogeneity and isotropy?
- Dark Matter: What is dark matter? What is the absolute neutrino mass scale and what is the number of relativistic species in the Universe?
- Initial Conditions: What is the power spectrum of primordial density fluctuations, which seeded large-scale structure, and are they described by a Gaussian probability distribution?

More quantitatively the objective of Euclid is to achieve a dark energy Figure of Merit (Albrecht et al. 2006) of ≥ 400 and to determine the growth index γ, that provides a simple parameterisation for deviations from general relativity, to an accuracy of 0.02. Euclid is designed to achieve these science objectives with support from ground-based observations. In combination with the SKA it is expected that the combined strength of these experiments will enable both to far exceed their singular goals. In order to achieve these science objectives Euclid will use two primary cosmological probes: weak lensing and galaxy clustering. These are given equal priority in the mission and indeed it is only through the combination of weak lensing and galaxy clustering that the science objectives can be achieved. In addition Euclid will provide the astronimcal community with a rich data set that will enable many astrophysical studies; areas in Euclid that are referred to as 'Legacy' science.

The SKA science goals are synergistic with those of Euclid. Whilst Euclid is a focussed experiment to address a particular goal, the SKA design allows for flexibility in the type of science questions that can be addressed. In this case proposals for SKA observations can be tailored to be in the best synergy with Euclid. The Euclid mission has been designed given particular constraints on the telescope size and overall cost of the mission and instrumentation. An optimisation during the Euclid Assesment Phase (Laureijs 2009) that was refined and elaborated during the Definition Phase (Laureijs et al. 2011) of the mission. This resulted in a nominal design of Euclid being a 1.2 meter Korsch, 3 mirror anasigmat telescope. There will be two instruments on board: the VISible focal plane instrument (VIS) (Cropper et al. 2012) and the Near Infrared SpectroPhotometric (NISP) instrument.

VIS will provide high-resolution optical imaging over a field of view of size 0.787×0.709 square degrees, with a resolution of 0.18 arseconds, over a single broad-band wavelength range of 550-900 nm (an optical band equivalent to an RIZ filter, although Euclid in fact does not have an optical filter on board). It will consist of 36 4k$\times$4k CCDs. The primary purpose of the VIS instrument is to provide imaging to enable the measurement of galaxy ellipticities to sufficient accuracy and precision for use in weak lensing. It will image approximately 1.5 billion galaxies with a limiting R-band magitude of 24.5 (10σ extended source).

PoS(AASKA14)146

NISP has a field of view of a similar size to VIS of 0.763×0.722 square degrees, these are matched to enable simultaneous/matched observations of the sky. The focal plane will contain 16 2k$\times$2k HgCdTe ("Mer-Ca-Tel") detectors. There will be 3 NIR filters, that will enable imaging, and 2 grism spectroscopic elements, that will enable slitless spectroscopy (with an approximate resolution of $R = 250$). The imaging is designed to enable photometric measurements of the same galaxies observed using the VIS instrument for the determination of photometric redshifts for weak lensing. The spectroscopy is designed to enable precision redshifts to be determined for galaxy clustering measurements.

In order to achieve the photometric redshift required for the weak lensing science Euclid will use ground-based optical imaging data from DES and KiDS, and any other available surveys; requiring normal broad-band imaging over the VIS wavelength range. Spectroscopic redshifts from ground-based surveys such as BOSS, DESI and MOONS will also be ingested and used for photometric redshift calibrations.

Every aspect of Euclid is designed using a systems engineering approach where the science requirements are translated into progressively more detailed requirements on survey, telescope and instrument design, as well as requirements on the algorithms used in the data processing. This flow of requirements is described in a series of ESA documents (for example Euclid SciRD) and related publications (for example (Cropper et al. 2013)). With regard to instrument designs, Euclid and the SKA are therefore synergistic in the sense that Euclid will observe in the optical and NIR wavelengths and SKA will observe at longer radio frequencies. As we will discuss in this article this enables unique scientific synergies to be exploited when combining the data between the two experiments.

1.2 Survey Synergies

The Euclid primary probes, weak lensing and galaxy clustering, will be carried our over the same area of sky in a wide-field survey of 15,000 square degrees. As described in Laureijs et al. (2011) the area is driven by an optimisation between the galaxy clustering (that prefers a wider area for a fixed observing time) and weak lensing (that can prefers a shallower deeper survey for intrinsic alignment mitigation), as well as efficiency in survey design whereby the lowest 30 degrees in ecliptic latitude are not observed to avoid zodiacal light contamination. In Figure 1 we show the Euclid reference survey from Amiaux et al. (2012) and how this builds as a function of time. It is self-evident that the areal coverage of Euclid and SKA is synergistic with both experiments expected to observe significant fractions of the extragalactic sky.

The synergy of the Euclid and SKA experiments in time is also self-evident. Euclid is a nominally 6 year mission that is scheduled to begin observations in 2020, SKA is scheduled to begin construction in 2018 and begin observations on a similar time scale to Euclid.

The depth of the Euclid and SKA surveys is also synergistic, Euclid will have a limiting magnitude in optical wavelengths that will mean it is sensitive to galaxies with redshifts over the range $0 < z < 2$, and the NIR spectroscopy will be sensitive to galaxies at slightly higher redshifts. In Figure 2 we show as an example the normalised distribution of weak lensing galaxies that SKA1 and SKA2 over 3π steradians, and the Euclid weak lensing survey will cover.

The Euclid weak lensing survey will have 30 galaxies per square arcminute with size larger than 1.5 times the PSF (R^2) and magnitude $RIZ \leq 24.5$. The SKA survey area and number density

PoS(AASKA14)146

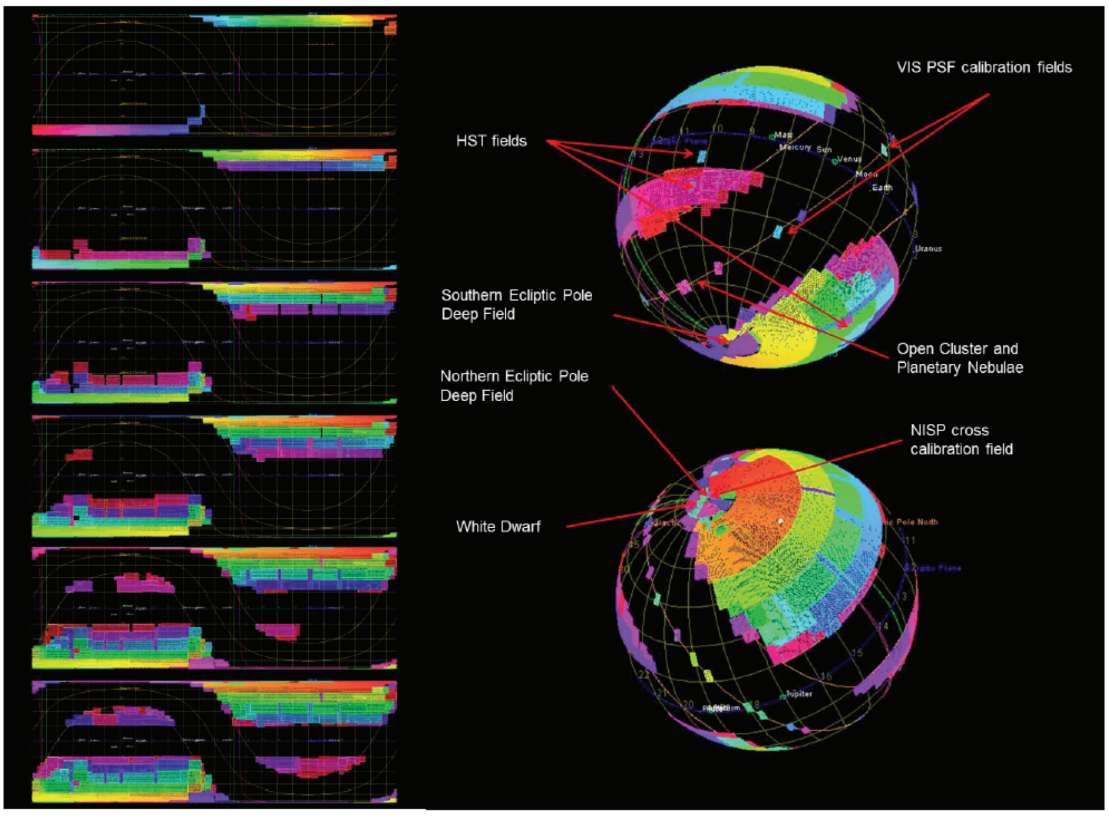

Figure 1: From Amiaux et al. (2012). Euclid Reference Survey construction from year 1 (top) to year 6 (bottom) in cylindrical (left) and orthographic projection. In the left panel, only the wide survey fields are shown. In the right panel, the calibration fields are also displayed.

has several possibilities, with various area and redshift overlap scenarios (see continuum survey overview, also Brown et al. and Jarvis et al. in this volume), for example for the full SKA (or SKA phase 2) there could be either

- 3π steradian survey: RMS noise $= 0.5$ micro-Jy, 10 gals arcmin^{-2}.
- 5000 sq. deg survey: RMS noise $= 0.2$ micro-Jy, 23 galaxies arcmin^{-2}.
- 1000 sq. deg survey: RMS noise $= 0.1$ micro-Jy, 37 galaxies arcmin^{-2}.

In the remainder of this article we will discuss the scientific synergies that instrument and survey designs of Euclid and the SKA enable.

2. Cosmological Synergies

The primary objectives of Euclid are cosmological in nature, in synergy with SKA these objectives can be supplemented and extended. Both the SKA and Euclid will be able to measure:

- Weak lensing shear g,

PoS(AASKA14)146

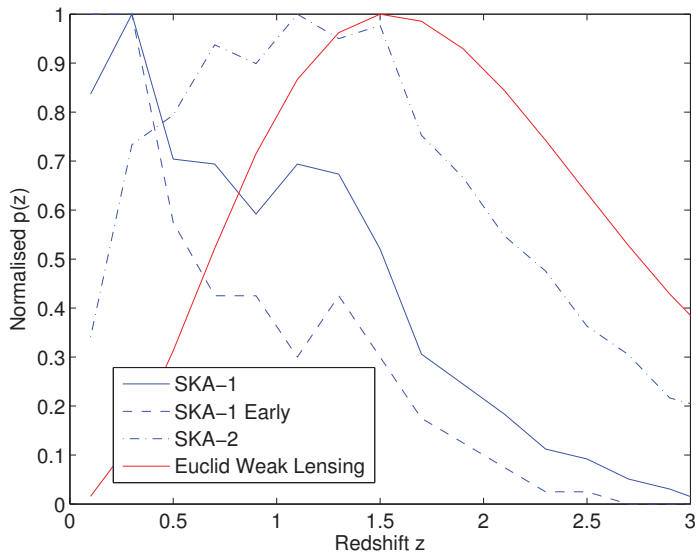

Figure 2: The normalised distributions of galaxies useable for weak lensing analyses in Euclid and the SKA, for the different phases. The numbers for SKA are derived from specifications quoted in the SKA Imaging Science Performance memo which is in turn based on the SKA1 Baseline Design and from the SKADS simulations of Wilman et al. (2008). The instrument of choice is SKA1-MID and it has been assumed Band 2 (950-1760 MHz) has been used which, under the current version of the SKA1 baseline design gives the best performance in terms of sensitivity at the required angular resolution.

- Weak lensing magnification; including size s and flux ($n(z)$),
- Galaxy positions, both photometric θ_p, and spectroscopic θ_s.

This results in 10 2-point observables, power spectra, in total that can be combined combinatorially to produce 55 cross and auto-correlation statistics. If, for example, a 'tomographic' approach is pursued and the galaxy populations are split into > 10 redshift bins then this results in over 5000 power spectra that could be computed including all inter and intra bin correlations. Some of these correlations can be used to reduced systematic effects, for example the correlation of galaxy shear with galaxy position can be used in infer the intrinsic alignment systematic in cosmic shear studies, see for example Joachimi et al. (2011), or the correlation between weak lensing shear in the radio and optical data sets can be used to reduce ellipticity measurement systematics. Some of these correlations can be used to increase the statistical precision of the combined data, for example the combination of weak lensing shear and size (Heavens et al. 2013). The SKA can also measure unresolved 21cm intensity to create maps that can then be included as an additional cosmological probe to be included in the synergistic combination of probes.

We will highlight just a few of these combinations as examples in this chapter.

2.1 21 cm Intensity Mapping

The principal advantage of 21cm intensity mapping (see Santos et al., in this volume) over traditional galaxy redshift surveys is that extremely large volumes can be surveyed in a relatively

PoS(AASKA14)146

short time; for example, SKA1 will be capable of surveying a total area of $\sim$30,000 deg^2 from $z = 0$ to 3 over the course of 1-2 years. This ability stems from the modest resolution requirements of the IM method; there is no need to resolve individual galaxies, and only the integrated HI emission on comparatively large angular scales matters. We refer to the Chapters on Intensity Mapping and RSD with SKA for more details of this science synergy.

At its most basic, a large IM survey with a SKA1 array would complement Euclid simply by increasing the total volume being probed. Consider a situation in which Euclid and the SKA targeted independent survey volumes. The sensitivity of SKA-IM to the first BAO acoustic peak is comparable to that of Euclid, which is practically cosmic variance-limited at these scales anyway; past-doubling the survey volume would therefore have a significant effect in beating down cosmic variance and increasing the precision of BAO distance indicators and other observables.

Preventing the surveys from overlapping would spoil a number of interesting opportunities, however. Probing the same volume with two almost cosmic variance-limited experiments is not redundant; as well as providing useful cross-checks for consistency between the two, one can also benefit from the 'multi-tracer' effect (see Section 2.3), whereby one can continue to gain information about some observables in spite of cosmic variance as long as different populations of tracers can be distinguished by each survey. This can be used to enhance the precision of redshift space distortion measurements, for example, which probe the growth of structure.

SKA IM surveys are capable of significantly extending the redshift range of Euclid, which covers $0 < z < 2$. By 'filling in' redshifts missed by the galaxy survey, one can gain a great deal of leverage on key cosmological functions such as the equation of state of dark energy and the linear growth rate; and could also be used for cross-correlations to get better photometric redshifts for Euclid. Figure 3 shows the joint constraints that can be achieved on w_0 and the growth index, γ, by the combination of Euclid and an SKA-IM survey with much wider redshift coverage. The additional information at low redshift helps to pin down the evolution of dark energy and possible deviations from the standard growth history, while constraints at higher redshift act as a useful 'anchor', by locating the transition from the matter-dominated era and putting limits on the spatial curvature, Ω_K.

2.2 Neutrino Physics

Measuring neutrino properties is potentially a particularly interesting area of Euclid-SKA science. Massive neutrino suppress the growth of structure via free-streaming effects introducing an effective pressure that acts in regions of higher density. This continues until the neutrinos become non-relativistic. This transition imprints a feature at a particular scale in the matter power spectrum. As shown in Jimenez et al. (2010) an all-sky Euclid-like survey combined with a galaxy clustering survey such as that could be achieved by the final SKA may even be able to determine the neutrino hierarchy.

2.3 Multi-Tracer Method

The SKA and Euclid will observe a huge number of galaxies, and the errors in power spectrum of galaxies will be dominated by cosmic variance, rather than shot noise, at cosmological scales. This is especially serious when we try to constrain primordial non-Gaussianity whose effect is

PoS(AASKA14)146

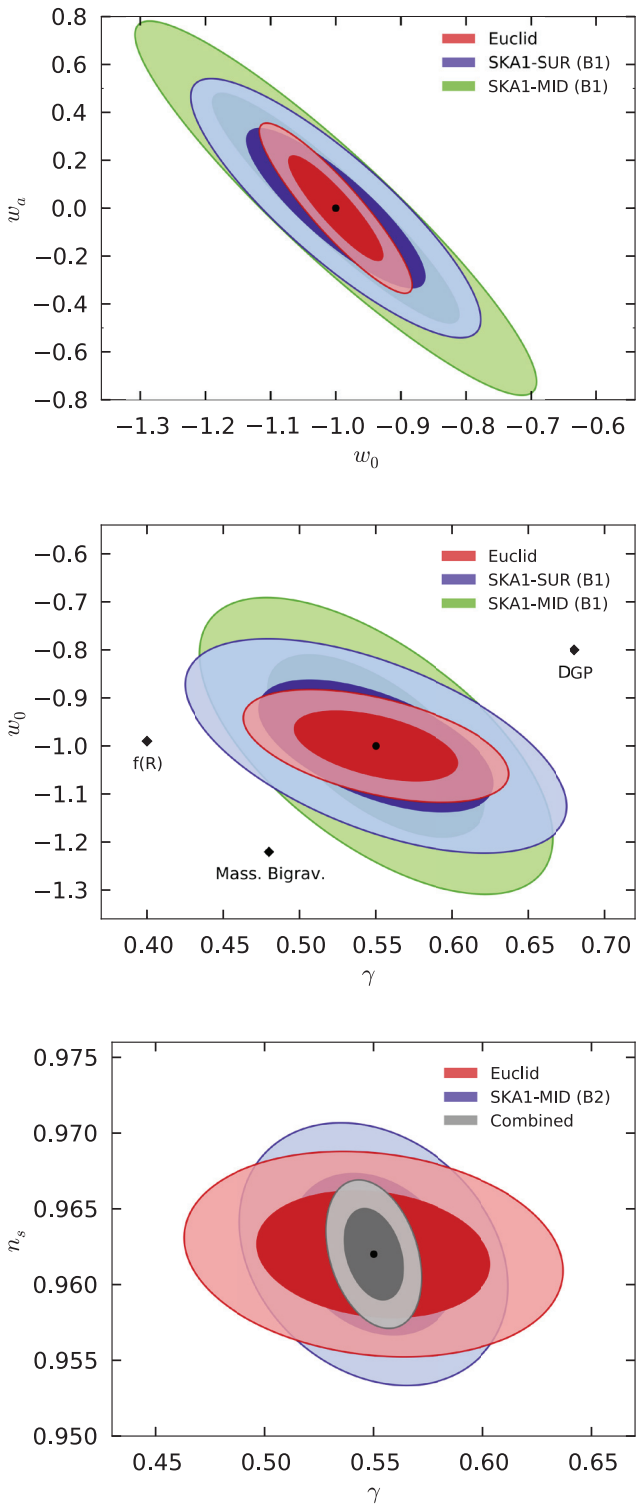

Figure 3: Predicted 1σ, 2 parameter, error contours for dark energy (w_0, w_a), modified gravity (γ), and initial condition (n_s) parameters for Euclid galaxy clustering and SKA1 design.

PoS(AASKA14)146

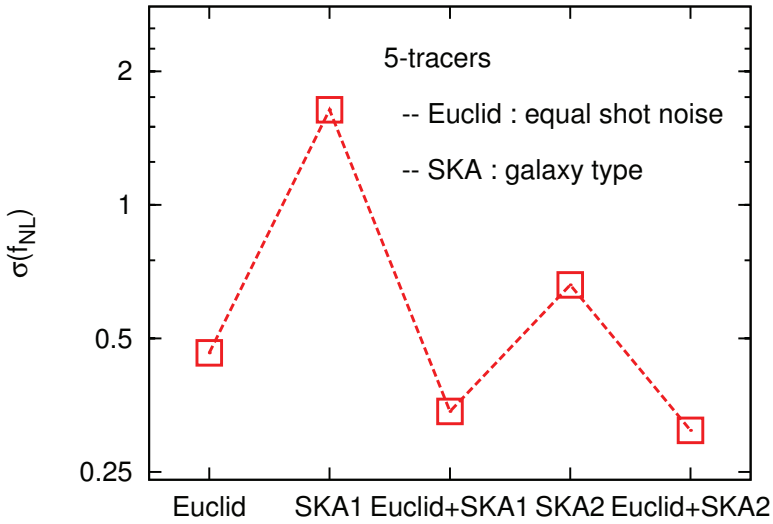

Figure 4: Expected constraints on $f_{\rm NL}$ from the SKA continuum survey, Euclid photometric survey and their combinations Yamauchi et al. (2014).

stronger at larger scales. Cosmic variance could be avoided with a the 'multi-tracer' method Seljak (2009) which uses multiple tracers of the dark matter distribution with different biases to cancel out sample variance. Although power spectra of tracers themselves are limited by cosmic variance, the ratio of the power spectra of two tracers, which represents the ralative bias, can evade cosmic variance and is limited only by shot noise. Because the mass and redshift dependences of bias are affected by non-Gaussianity ($f_{\rm NL}$), it can be constrained by the measurements of relative biases.

This multi-tracer method is effective when the bias difference, hence mass difference, is large between tracers and it is critically important to estimate the mass of dark halo hosting each galaxy. A deep survey is also important because bias evolves rapidly with redshift. The SKA and Euclid surveys will have different redshift-distributions of observed galaxies so that their combination enhances the power of multi-tracer method. Yamauchi et al. (2014) studied the potential of combination of the SKA continuum survey and Euclid photometric survey for the constraint on $f_{\rm NL}$. The SKA continuum survey reaches much further than the Euclid photometric survey, providing a larger redshift range in combination, while the number of galaxies observed by Euclid is larger than that by the SKA at low redshifts, so they are complementary to probe the evolution of bias. Figure 4 shows expected constraints on $f_{\rm NL}$ from Euclid, SKA1, SKA2 and their combinations. Here, it is assumed that galaxies observed by Euclid have photometric redshifts while SKA cannot obtain redshift information (it is a very conservative assumption that SKA has no redshift information, but see (Camera et al. 2014) for gains made by using optical near-if photozs). It is seen that the constraint on $f_{\rm NL}$ can reach below unity and approach $O(0.3)$.

2.4 Magnetic Fields

The two pressing questions regarding cosmic magnetism are: what is the origin of the cosmological magnetic fields and how do these magnetic fields affect (or were affected by) the structure

PoS(AASKA14)146

formation and evolution of the Universe? In a more practical perspective, we would like to know how the cosmological magnetic fields imprint observational signatures and how we can make use of these signatures to understand better the structural formation process in our Universe.

Charged particles in the presence of a magnetic field experience a Lorentz force. As such the presence of a primordial magnetic field would produce and amplify the density fluctuation in ionised gas (the baryons). Through gravitational coupling between the baryons and the dark matter, the magnetic field would imprint signatures in the dark matter density distributions. As magnetic fields alter the matter density power spectrum and the halo mass function, the magnification bias and the redshift distribution of galaxies are distorted (see Fedeli & Moscardini (2012); Camera et al. (2014)). The capability of Euclid weak lensing studies (and SKA weak lensing studies) together with the Faraday rotation measurements using the SKA will be able to quantify such a mechanism, which not only sets constraints on the strength of the magnetic fields in the early Universe but also determines the role of magnetic interaction in cosmological structure formation, which has been assumed to be solely gravitational.

Gravitational lensing, both weak and strong, are powerful tools in the studies of cosmological large-scale structures. Lensing calculations rely on ray tracing in a geometrical framework set upon by the theory of relativity. Absorption and scattering of photons emitted from the distant lensed sources along the ray are usually ignored. Gravitational lensing is therefore achromatic, at least in principle. This may well be a sensible first approximation, but if there are ongoing activities, such as merging of clusters and/or violent large-scale galactic outflows, the situation could be more complicated. Photons on different rays originating from a lensed source would have different frequency dependent attenuation, through absorption and/or scattering by the matter along the rays. Moreover, if there is a spatially inhomogeneous magnetic field permeating the lens and its surrounding, polarisation fluctuations would also be induced into the lensed images. The frequency dependent distortion in the lensed images could be problematic, such as, when the precision measurement of shears is required in gravitational weak lensing studies, which is a key science of Euclid. The matter and the magnetic properties along the line of sight can, however, be inferred through multi-wavelength polarisation observations of SKA. With the information of the matter distribution and the magnetic field along the line of slight, frequency dependent attenuation of photons can be modelled using radiative transfer calculations and hence prescriptions for correcting the corresponding distortion and biases can be derived.

3. Systematic Synergies

The combination of power spectra discussed in the previous section will enable a mitigation systematic to be performed at the statistical level. However because Euclid and the SKA will observe many of the same galaxies one can directly compare the measurement to gain an ever larger advantage. We refer here to systematic reductions discussed in the Chapter on Weak Lensing and Synergies, and highlight one particular aspect that is enabled through the weak lensing shape measurement that is only possible using both Euclid and SKA, due to the PSF stability and size available from space or very wide aperture radio telescopes (see Massey et al. (2013); such observations are not possible using ground-based optical telescopes).

PoS(AASKA14)146

Optical and radio surveys, such as Euclid and SKA, have a particularly useful synergy in reducing and quantifying the impact of systematic effects which may dominate each survey alone on some scales. By cross-correlating the shear estimators from one of these surveys with those of the other, several systematic errors are mitigated. We can see this by writing the contributions to an optical (o) or radio (r) shear estimator:

$$\gamma^{(o)} = \gamma_{\rm grav} + \gamma_{\rm int}^{(o)} + \gamma_{\rm sys}^{(o)} \tag{3.1}$$

$$\gamma^{(r)} = \gamma_{\rm grav} + \gamma_{\rm int}^{(r)} + \gamma_{\rm sys}^{(r)} \tag{3.2}$$

$$\tag{3.3}$$

where $\gamma_{\rm grav}$ is the gravitational shear we are seeking, $\gamma_{\rm int}$ is the intrinsic ellipticity of the object, and $\gamma_{\rm sys}$ are systematic errors induced by the telescope.

If we correlate optical shears with optical shears, or radio shears with radio shears, we obtain terms like

$$\langle\gamma\gamma\rangle = \langle\gamma_{\rm grav}\gamma_{\rm grav}\rangle + \langle\gamma_{\rm grav}\gamma_{\rm int}\rangle + \langle\gamma_{\rm int}\gamma_{\rm int}\rangle + \langle\gamma_{\rm sys}\gamma_{\rm sys}\rangle \tag{3.4}$$

where the first term is the gravitational signal we seek, the second term is the GI intrinsic alignment, the third term is the II intrinsic alignment, and the final term is the contribution from systematics. All of these terms could be similar size on certain scales, which is of damage to cosmological constraints. On the other hand, if we cross-correlate the optical shears with radio shears, we obtain

$$\langle\gamma^{(o)}\gamma^{(r)}\rangle = \langle\gamma_{\rm grav}\gamma_{\rm grav}\rangle + \langle\gamma_{\rm grav}\gamma_{\rm int}^{(o)}\rangle + \langle\gamma_{\rm grav}\gamma_{\rm int}^{(r)}\rangle + \langle\gamma_{\rm int}^{(o)}\gamma_{\rm int}^{(r)}\rangle + \langle\gamma_{\rm sys}^{(o)}\gamma_{\rm sys}^{(r)}\rangle \tag{3.5}$$

The second and third terms are the GI systematic alignment, which still survives. However, the fourth term involves the correlation between optical and radio shapes, which will be less than that between one frequency alone as the emission mechanisms are different (c.f. Patel et al. (2010) where no correlation at zero lag was found). This term is therefore reduced. Most importantly, the fifth term involving systematics is expected to be zero, as the systematics in these two telescopes of completely different design and function are not expected to be correlated at all. We are therefore able to remove the dangerous systematic correlations from our shear analysis - and to gain an estimate of its magnitude in the autocorrelation case.

4. Simulation Synergies

Both Euclid and the SKA will require a large number of N-body simulations in order to achieve their science objectives. These simulations will be used for a variety of purposes for example a small number of large box-size simulations can be used to generate mock catalogues that can be used in the development of data analysis agorithms by creating fake data with which to test the pipelines. In order to compute the likelihood functions used for cosmological analyses covariance matrices for data vectors will be needed. In order to characterise these realisations of data will be required (Taylor et al. 2013), and depending on the number of data points and parameters this could result in up to $\sim 10^6$ realisations. Because the covariance matrices for cosmological observable power spectra depend on cosmology themselves this results in the potential need for tens of thousands or millions of high resolution, small box-size, simulations.

PoS(AASKA14)146

This is a significant computational task and, because at small scales the impact of baryonic feedback will be important (see for example Kitching et al. (2014)), it is likely that these simulations will need to be hydrodynamical as well as N-body. The completion of this number of simulations by 2020, in time for both Euclid and the SKA, is a challenge but because the area and depth of both surveys is synergistic it is likely that well designed simulations will meet the needs of both experiments, providing a common resource for both. Whilst common simulations will reduce the overall resources required for this task, it will also require that these simulations are potentially more sophisticated than survey-specific ones. For example a single simulation that provided a resource for both 21cm mapping and lower redshift cosmic shear may need to perform ray tracing over a substantially larger redshift range that a simulation that was tailored to either cosmological probe alone.

5. Methodological Synergies

Not only will Euclid and the SKA have many scientific synergies, but they will both provide big (a large number of bytes) astrophysical data-sets, the analysis of which will also present many methodological synergies. In addition to the techniques already in use today to analyse optical and radio observations, recent experience from the analysis of cosmic microwave background (CMB) observations can be used to infer future methods of interest.

Bayesian statistics is the dominant paradigm for the analysis of CMB observations. Typically cosmological parameters are estimated from observational data in a Bayesian framework using Markov Chain Monte Carlo (MCMC) sampling techniques e.g. (e.g. Lewis & Bridle 2002), such as the Metropolis Hastings algorithm. If the parameter space is of moderate size, then nested sampling methods (Skilling 2004; Feroz & Hobson 2008; Feroz et al. 2009, 2013) are often used to enable the efficient calculation of the Bayesian evidence in order to distinguish between cosmological models. Such techniques are already common when analysing optical and radio observations. For high-dimensional problems, Gibbs and Hamiltonian sampling have been applied successfully to sample high-dimensional posterior distributions for CMB analysis (e.g. Wandelt et al. 2004; Taylor et al. 2008). These sampling techniques are already starting to be applied to mock galaxy surveys (Jasche et al. 2010; Jasche & Wandelt 2013a,b).

In addition to Bayesian analysis, sparsity-based approaches are gaining popularity as an alternative and complementary CMB analysis technique. First works in this area focused on the use of wavelets, which are a powerful signal analysis tool due to their ability to represent signal content in space and scale simultaneously. This property is particularly useful for the study of astrophysical signals, where the physical processes responsible for signals of interest are typically manifest on specific physical scales, while often also spatially localised. Wavelet transforms and fast algorithms defined on the sphere (e.g. Antoine & Vandergheynst 1999; Wiaux et al. 2005; McEwen et al. 2006; Starck et al. 2006; McEwen et al. 2007a; Wiaux et al. 2008; Marinucci et al. 2008; McEwen et al. 2013; Leistedt et al. 2013) were developed for the analysis of CMB data and have proved to be particularly effective McEwen et al. 2007b. More recently, the revolutionary new paradigm of compressive sensing has been exploited for CMB analysis. Compressive sensing (Candès et al. 2006; Donoho 2006) is a recent ground-breaking development in information theory, which goes beyond the Shannon-Nyquist sampling theorem by exploiting sparsity and which has the potential

PoS(AASKA14)146

to revolutionise data acquisition in many fields (for a brief introduction see Baraniuk 2007). At its heart, compressive sensing provides a powerful framework for solving inverse problems, typically exploiting the sparse representation of signals in a wavelet dictionary. Sparse component separation techniques that exploit these ideas have been developed to recover CMB maps from observations corrupted by foreground emission (Bobin et al. 2013). There is considerable scope to extend sparsity-based approaches to the analysis of both Euclid and SKA data, leading to numerous methodological synergies.

The galaxies that will be observed by Euclid live in 3D, hence to exploit sparsity-based techniques for the analysis of Euclid data suitable 3D wavelet transforms must be constructed. Recently, wavelet transforms have been constructed specifically for the analysis of such data by Lanusse et al. (2012) and Leistedt & McEwen (2012). These constructions are complementary, where the construction of Lanusse et al. (2012) yields isotropic 3D wavelets, whereas the construction of Leistedt & McEwen (2012) yields wavelets with angular and radial aperture that can be controlled separately. Application of these wavelet transforms to galaxy surveys is underway. Specifically, such wavelet representations should be particularly useful for 3D weak lensing. For example, compressive sensing approaches have been developed already to solve the inverse problem required to recover 3D density maps from weak lensing data using hybrid 2D-1D wavelets (Leonard et al. 2012, 2014).

Sparsity-based approaches have also shown considerable promise for imaging observations from radio interferometric telescopes, such as the SKA. Compressive sensing approaches have been developed to solve the inverse problem of recovering images from the raw Fourier measurements made by interferometric telescopes, starting from idealised applications (Wiaux et al. 2009a; McEwen & Wiaux 2011), to optimising telescope configurations (Wiaux et al. 2009b), to novel imaging methodologies (Carrillo et al. 2012), to realistic imaging scenarios (Carrillo et al. 2014), and to supporting wide fields-of-view (McEwen & Wiaux 2011; Wolz et al. 2013). In addition to imaging raw data, methods to exploit sparsity have been developed to separate the 21cm emission from the epoch of reionization from foreground emission (Chapman et al. 2013).

Sparsity and compressive sensing hence show considerable potential for the analysis of both Euclid and SKA observations. Although appropriate wavelets must be constructed on the space where the data live, the application of wavelet and compressive sensing techniques to both types of observations shares many similarities. A generic approach can be taken to solve inverse problems in a compressive sensing framework across different data domains. Furthermore, the underlying convex optimisation algorithms e.g. Combettes & Pesquet (2011) developed to solve these inverse problems are largely the same and hence the same underlying codes can be used or adapted.

In summary, the analysis of the large data-sets expected from both Euclid and the SKA will exhibit many methodological synergies and will benefit considerably by the sharing of expertise, techniques, and numerical codes, both for Bayesian and sparsity-based approaches.

6. Conclusion

The concurrent development of Euclid and the SKA over the next decade, with the near simultaneous observations of significant fractions of the sky in radio wavelengths and spaced-based optical and NIR imaging and spectra represents an unprecedented era in astronomy; and step-change

PoS(AASKA14)146

in data quantity and quality that is unlikely to surpassed in the foreseeable future. The synergies between these projects is manifest, and it almost goes without saying that the combination of the science from these projects will result in more than the sum of the parts.

The synergies are many-fold enabling the experiments to mutually reduce systematic effects; improve statistical constraints on parameters, in particular for cosmology; and enable new science. In addition there are synergies on the prepartory aspects, in particular on the production of simulations, and on the exploitation of the data through methodological overlap. Specifically

- **Survey synergies.** Euclid and SKA will observe the same sky, at complementary overlapping depths, over the same time period of observation, but crucially at different wavelengths which enables indepedent cross-validation of results and systematics.

- **Cosmology synergies.** The combination of the two experiments can improve cosmological constraints through the simple addition of the data, but extra information from the cross-correlation is likely to allow for further gains. In particular dark energy, modified gravity and non-Gaussianity measurement may be improved significantly through the combination of Euclid and the SKA.

- **Systematic synergies.** Euclid and SKA will measure some of the same properties from the same galaxies but at at different wavelengths and with different instrumental systematics. By cross-correlating it may be possible to construct estimators that have much lower (or even zero) sensitivity to particular systematics, for example those associated with galaxy weak lensing measurements.

- **Simulations & Methodological synergies.** Both Euclid and SKA will require many N-body simulations, and new methodological techniques, to support the theoretical interpretation of the observations. Given the finite resources available to the astronomy community there is an opportunity for cooperation in this area during and after the construction phases.

These synergies exist *now*, even in pre-construction, during prepartion, and will continue to grow as data is accumulated. These synergies will last for decades after data is collected, involving thousands of scientists world wide in mutual collaboration.

References

Albrecht, A., Bernstein, G., Cahn, R., et al. 2006, arXiv:0609591

Amiaux, J., Scaramella, R., Mellier, Y., et al. 2012, in Society of Photo-Optical Instrumentation Engineers (SPIE) Conference Series, Vol. 8442, Society of Photo-Optical Instrumentation Engineers (SPIE) Conference Series

Antoine, J.-P., & Vandergheynst, P. 1999, ACHA, 7, 1

Baraniuk, R. 2007, IEEE Sig. Proc. Mag., 24, 118

Bobin, J., Starck, J.-L., Sureau, F., & Basak, S. 2013, A&A, 550, A73

Camera, S., Fedeli, C., & Moscardini, L. 2014, JCAP, 3, 27

Candès, E., Romberg, J., & Tao, T. 2006, IEEE TIT, 52, 489

Carrillo, R. E., McEwen, J. D., & Wiaux, Y. 2012, MNRAS, 426, 1223

PoS(AASKA14)146

—. 2014, MNRAS, 439, 3591
Chapman, E., Abdalla, F. B., Bobin, J., et al. 2013, MNRAS, 429, 165
Combettes, P., & Pesquet, J.-C. 2011, Proximal splitting methods in signal processing (New York: Springer), 185–212
Cropper, M., Cole, R., James, A., et al. 2012, in Society of Photo-Optical Instrumentation Engineers (SPIE) Conference Series, Vol. 8442, Society of Photo-Optical Instrumentation Engineers (SPIE) Conference Series
Cropper, M., Hoekstra, H., Kitching, T., et al. 2013, MNRAS, 431, 3103
Donoho, D. 2006, IEEE TIT, 52, 1289
Fedeli, C., & Moscardini, L. 2012, JCAP, 11, 55
Feroz, F., & Hobson, M. P. 2008, MNRAS, 384, 449
Feroz, F., Hobson, M. P., & Bridges, M. 2009, MNRAS, 398, 1601
Feroz, F., Hobson, M. P., Cameron, E., & Pettitt, A. N. 2013, arXiv:1306.2144
Heavens, A., Alsing, J., & Jaffe, A. H. 2013, MNRAS, 433, L6
Jasche, J., Kitaura, F. S., Wandelt, B. D., & Enßlin, T. A. 2010, MNRAS, 406, 60
Jasche, J., & Wandelt, B. D. 2013a, MNRAS, 432, 894
—. 2013b, ApJ, 779, 15
Jimenez, R., Kitching, T., Peña-Garay, C., & Verde, L. 2010, JCAP, 5, 35
Joachimi, B., Mandelbaum, R., Abdalla, F. B., & Bridle, S. L. 2011, A&A, 527, A26
Kitching, T. D., Heavens, A. F., Alsing, J., et al. 2014, MNRAS, 442, 1326
Lanusse, F., Rassat, A., & Starck, J.-L. 2012, A&A, 540, A92
Laureijs, R. 2009, arXiv:0912.0914
Laureijs, R., Amiaux, J., Arduini, S., et al. 2011, arXiv:1110.3193
Leistedt, B., & McEwen, J. D. 2012, IEEE TSP, 60, 6257
Leistedt, B., McEwen, J. D., Vandergheynst, P., & Wiaux, Y. 2013, A&A, 558, 1
Leonard, A., Dupé, F.-X., & Starck, J.-L. 2012, A&A, 539, A85
Leonard, A., Lanusse, F., & Starck, J.-L. 2014, MNRAS, arXiv:1308.1353
Lewis, A., & Bridle, S. 2002, PRD, 66, 103511
Marinucci, D., Pietrobon, D., Balbi, A., et al. 2008, MNRAS, 383, 539
Massey, R., Hoekstra, H., Kitching, T., et al. 2013, MNRAS, 429, 661
McEwen, J. D., Hobson, M. P., & Lasenby, A. N. 2006, arXiv:0609159
McEwen, J. D., Hobson, M. P., Mortlock, D. J., & Lasenby, A. N. 2007a, IEEE TSP, 55, 520
McEwen, J. D., Vandergheynst, P., & Wiaux, Y. 2013, in SPIE Wavelets and Sparsity XV
McEwen, J. D., & Wiaux, Y. 2011, MNRAS, 413, 1318
McEwen, J. D., Vielva, P., Wiaux., Y., et al. 2007b, JFAA, 13, 495
Patel, P., Bacon, D. J., Beswick, R. J., Muxlow, T. W. B., & Hoyle, B. 2010, MNRAS, 401, 2572
Seljak, U. 2009, Physical Review Letters, 102, 021302
Skilling, J. 2004, in American Institute of Physics Conference Series, Vol. 735, American Institute of Physics Conference Series, ed. R. Fischer, R. Preuss, & U. V. Toussaint, 395–405
Starck, J.-L., Moudden, Y., Abrial, P., & Nguyen, M. 2006, A&A, 446, 1191
Taylor, A., Joachimi, B., & Kitching, T. 2013, MNRAS, 432, 1928
Taylor, J. F., Ashdown, M. A. J., & Hobson, M. P. 2008, MNRAS, 389, 1284
Wandelt, B. D., Larson, D. L., & Lakshminarayanan, A. 2004, PRD, 70, 083511

PoS(AASKA14)146

Wiaux, Y., Jacques, L., Puy, G., Scaife, A. M. M., & Vandergheynst, P. 2009a, MNRAS, 395, 1733
Wiaux, Y., Jacques, L., & Vandergheynst, P. 2005, ApJ, 632, 15
Wiaux, Y., McEwen, J. D., Vandergheynst, P., & Blanc, O. 2008, MNRAS, 388, 770
Wiaux, Y., Puy, G., Boursier, Y., & Vandergheynst, P. 2009b, MNRAS, 400, 1029
Wilman, R. J., Miller, L., Jarvis, M. J., et al. 2008, MNRAS, 388, 1335
Wolz, L., McEwen, J. D., Abdalla, F. B., Carrillo, R. E., & Wiaux, Y. 2013, MNRAS, 436, 1993
Yamauchi, D., Takahashi, K., & Oguri, M. 2014, arXiv:1407.5453

PoS(AASKA14)146

PROCEEDINGS OF SCIENCE

SKA synergy with Microwave Background studies

Carlo Burigana,[ab] **Paul Alexander,**[c] **Carlo Baccigalupi,**[d] **Domingos Barbosa,**[e] **Alain Blanchard,**[f] **Adriano De Rosa,**[a] **Gianfranco de Zotti,**[gd] **Fabio Finelli,**[a] **Alessandro Gruppuso,**[a] **Michael Jones,**[h] **Sabino Matarrese,**[i] **Alessandro Melchiorri,**[l] **Diego Molinari,**[j] **Mattia Negrello,**[g] **Daniela Paoletti,**[a] **Francesca Perrotta,**[d] **Roberto Scaramella,**[k] **and Tiziana Trombetti**[a]

[a] *INAF-IASF Bologna, Via Piero Gobetti 101, I-40129, Bologna, Italy*
[b] *Dipartimento di Fisica e Scienze della Terra, Università degli Studi di Ferrara, Via Giuseppe Saragat 1, I-44100 Ferrara, Italy*
[c] *Cavendish Laboratory, Cambridge, UK*
[d] *SISSA, Astrophysics Sector, Via Bonomea 265, 34136 Trieste, Italy*
[e] *Radioastronomy Group, Instituto de Telecomunicações, Campus Universitario de Aveiro, 3810-183 Aveiro, Portugal*
[f] *Université de Toulouse, UPS-OMP, IRAP, Toulouse, France*
[g] *INAF – Osservatorio Astronomico di Padova, Vicolo dellÕOsservatorio 5, Padova, Italy*
[h] *Department of Physics, Oxford University, Oxford, UK*
[i] *Dipartimento di Fisica e Astronomia G. Galilei, Università degli Studi di Padova, Via Marzolo 8, 35131 Padova, Italy*
[l] *Dipartimento di Fisica, Università La Sapienza, P. le A. Moro 2, Roma, Italy*
[j] *Instituto de Física de Cantabria (CSIC-Universidad de Cantabria), Avda. los Castros s/n, Santander, Spain*
[k] *INAF – Osservatorio Astronomico di Roma, Via Frascati 33, 00040 Monteporzio Catone (Roma), Italy*

E-mail: burigana@iasfbo.inaf.it

The extremely high sensitivity and resolution of the Square Kilometre Array (SKA) will be useful for addressing a wide set of themes relevant for cosmology, in synergy with current and future cosmic microwave background (CMB) projects. Many of these themes also have a link with future optical-IR and X-ray observations. We discuss the scientific perspectives for these goals, the instrumental requirements and the observational and data analysis approaches, and identify several topics that are important for cosmology and astrophysics at different cosmic epochs.

Advancing Astrophysics with the Square Kilometre Array
June 8-13, 2014
Giardini Naxos, Italy

PoS(AASKA14)149

1. Introduction

Although it is not specifically designed for cosmic microwave background (CMB) observations, because of its high resolution and limited high-frequency coverage, the extremely high sensitivity of the SKA (Dewdney et al. 2013, Braun 2014) may be used to address a wide set of themes relevant for cosmology, in synergy with current and future CMB projects. Many of these also have a strong link with the future *Euclid*[1] mission and *Athena*[2] observations (Takahashi et al. 2015).

In this chapter we will discuss several important themes: (i) the contribution to future high-precision CMB absolute temperature experiments aimed at detecting spectral distortion, including long wavelength free-free emission linked to cosmological reionization (Sect. 2); (ii) cross-correlation between CMB and SKA surveys for the analysis of Integrated Sachs-Wolfe (ISW) effect and constraining on dark energy (Sect. 3); (iii) constraining non-Gaussianity with joint analyses of CMB and radiosources (Sect. 3); (iv) primordial magnetic fields (Sect. 4); (v) Galactic foreground studies, linked to component separation in future CMB experiments (Sect. 5).

From the observational point of view, these topics can be divided into two broad categories (Burigana et al. 2004): those relying on precise point source observations and those that require sensitivity to extended structures. The former take advantage of the high resolution and point-source sensitivity naturally offered by interferometry, while the latter require a suitable array design and observational approach, such as a compact configuration implementing short baselines and a high *uv*-space filling factor, mosaicing techniques, and for the largest areas, methods such as the on-the-fly-mapping. These approaches, required by a wide set of SKA scientific projects, are still under definition and optimization.[3] We will identify the corresponding instrumental and observational requirements and data analysis approaches needed to carry out the proposed studies.

2. SKA contribution to future CMB spectrum experiments

The current limits on CMB spectral distortions and the constraints on energy dissipation processes in the plasma (Salvaterra & Burigana 2002) ($|\Delta\varepsilon/\varepsilon_i| \lesssim 10^{-4}$) are mainly set by the COsmic Background Explorer[4] (COBE) / Far InfraRed Absolute Spectrophotometer (FIRAS) experiment (Mather et al. 1990, Fixsen et al. 1996). High accuracy CMB spectrum experiments from space, such as the Diffuse Microwave Emission Survey (DIMES) (Kogut 1996, Kogut 2003) at $\lambda \gtrsim 1$ cm and FIRAS II (Fixsen & Mather 2002) at $\lambda \lesssim 1$ cm, have been proposed to constrain (or probably detect) energy exchanges 10–100 times smaller than the FIRAS upper limits. Experiments such as DIMES may probe dissipation processes at early times ($z \gtrsim 10^5$) resulting in Bose-Einstein-like distortions (Sunyaev & Zeldovich 1970, Danese & de Zotti 1980, Burigana et al. 1991) and free-free distortions (Bartlett & Stebbins 1991) possibly generated by heating mechanisms at late epochs ($z \lesssim 10^4$), before or after the recombination era (Burigana & Salvaterra 2003) (or possibly cooling processes, see Stebbins & Silk 1986, although these are disfavoured by Wilkinson Microwave Anisotropy Probe[5] (WMAP) data). These possibilities have been recently reconsidered in the context of new CMB space missions such as the Primordial Inflation Explorer (PIXIE) (Kogut et al.

[1] www.rssd.esa.int/euclid

[2] http://www.the-athena-x-ray-observatory.eu/

[3] See http://www-astro.physics.ox.ac.uk/ hrk/SKA_EXPOSURE.html for a numerical tool.

[4] http://lambda.gsfc.nasa.gov/product/cobe/

[5] http://lambda.gsfc.nasa.gov/product/map/current/

PoS(AASKA14)149

2011) proposed to NASA, which combines high-accuracy polarization and spectrum measurements at $\sim$ degree resolution, and in the possible inclusion of spectral measurements in highly sensitivite polarization CMB space missions with arcmin resolution, such as the Cosmic Origins Explorer[6] (COrE) (COrE Collaboration 2011) proposed to the ESA and its possible successors, such as the Polarized Radiation Imaging and Spectroscopy Mission[7] (PRISM) (PRISM Collaboration 2014).

Calculations of various types of typical distorted spectra (see left panel of Fig. 1) have been presented in various works (e.g. Danese & Burigana 1994, Procopio & Burigana 2009, Khatri & Sunyaev 2012). Improving CMB absolute temperature measures will give a corresponding strengthening of the constraints on physical parameters of various classes of processes (see e.g. PRISM Collaboration 2014 and references therein). Decaying and annihilating particles during the pre-recombination epoch may affect the CMB spectrum, with the exact distorted shape depending on the process timescale and, in some cases, being different from that produced by energy release. This is especially interesting for decaying particles with lifetimes $t_X \approx \text{few} \times 10^8 - 10^{11}$ sec (Danese & Burigana 1994, Chluba & Sunyaev 2012). Superconducting cosmic strings would also produce copious electromagnetic radiation, creating CMB spectral distortion shapes (Ostriker & Thompson 1987) that would be distinguishable with high accuracy measurements. Evaporating primordial black-holes provide another possible source of energy injection, with the shape of the resulting distortion depending on the black-hole mass function (Carr et al. 2010). CMB spectral distortion measurements could also be used to constrain the spin of non-evaporating black-holes (Pani & Loeb 2013). The CMB spectrum could also set constraints on the power spectrum of small-scale magnetic fields (Jedamzik et al. 2000), the decay of vacuum energy density (Bartlett & Silk 1990), axions (Ejlli & Dolgov 2014), and other new physics processes. Deciphering these signals is a challenge, but holds the potential for important new discoveries and constraining unexplored processes that cannot be probed by other means.

In addition to the processes discussed above, a certain level of departure of the CMB spectrum from a perfect blackbody is theoretically predicted due to some unavoidable fundamental processes. Cosmological reionization produces electron heating which causes a Comptonization distortion proportional to the fractional amount of energy exchanged during the interaction, characterized by the Comptonization parameter $y(t) = \int_{t_i}^{t} [(\phi - \phi_i)/\phi](k_B T_e/m_e c^2) n_e \sigma_T c dt \simeq (1/4)\Delta\varepsilon/\varepsilon_i$ (where the last equality holds in the limit of small energy injections and integrating over the relevant epochs). Here $\phi(z) = T_e(z)/T_{CMB}(z)$, and $\phi_i = \phi(z_i) = (1 + \Delta\varepsilon/\varepsilon_i)^{-1/4} \simeq 1 - y$ is the equilibrium matter temperature and radiation temperature ratio at the beginning of the heating process (i.e. at z_i). Typical values of y expected from reionization are $\approx 10^{-7}$. For example, for two astrophysical reionization scenarios based on different radiative feedback assumptions (*filtering* and *suppression* models) Burigana et al. (2008) found $y \simeq (0.965 - 1.69) \times 10^{-7}$. Other kinds of unavoidable spectral distortions are Bose-Einstein (BE)-like distorted spectra, produced by the dissipation of primordial perturbations at small scales, damped by photon diffusion and thus invisible in the CMB anisotropies, which produce a positive chemical potential, $\mu_0 \simeq 1.4\Delta\varepsilon/\varepsilon_i$, and Bose-Einstein condensation of the CMB by colder electrons associated with the faster decrease of matter temperature in the expanding Universe relative to than that of radiation, which gives a negative chemical poten-

[6] http://www.core-mission.org/

[7] http://www.prism-mission.org/

PoS(AASKA14)149

tial (for a recent review see Sunyaev & Khatri 2013, and references therein). These two kinds of distortions are characterized by an amplitude, respectively, in the range $10^{-9} - 10^{-7}$ (and in particular $\simeq 2.52 \times 10^{-8}$ for a primordial scalar perturbation spectral index $n_S = 0.96$, without running), and $\simeq 3 \times 10^{-9}$. Since very small scales not explored by current CMB anisotropy data are relevant in this context, a wide range of primordial spectral indexes needs to be explored. A wider range of chemical potentials is found by Chluba et al. (2012), allowing also for variations of the amplitude of primordial perturbations at very small scales, as motivated by different inflation models.

The free-free signal associated with cosmological reionization represents the most relevant type of low-frequency spectral distortion. The CMB brightness temperature, T_{br}, under the combined effect of Comptonization and free-free processes is approximated by $(T_{br} - T_{CMB}\phi_i)/T_{CMB} \simeq y_B/x^2 - 2y\phi_i$, where $x = h\nu/kT_{CMB}$, and y_B is the free-free distortion parameter. For a homogeneous ionized medium $y_B(x,t) = \int_{t_i}^{t}(\phi - \phi_i)\phi^{-3/2} g_B(x,\phi) K_{0B} dt$, where g_B is the Gaunt factor weighted over ionized atoms and the bremsstrahlung rate in a hydrogen-helium plasma is given by $K_{0B}(z) \simeq (8\pi/3)e^6 h^2 n_e^{free}(n_H^+ + n_{He}^+ + 4n_{He}^{++})\phi^{7/2}/[m(6\pi mkT_e)^{1/2}(kT_e)^3]$ (Burigana et al. 1991). The density of free electrons and ionized atoms is determined by the reionization history. Since structure formation is far from homogeneous, the dependence of free-free emission on the square of the baryon density implies a distortion amplification with respect to the case of homogeneous medium by a large factor, $\simeq 1 + \sigma^2$, where σ^2 is the matter distribution variance ($\gg 1$ at moderate and low redshifts), as found in Trombetti & Burigana (2014) who combine Boltzmann codes for the matter variance evaluation with a dedicated free-free distortion code. The results are shown in right panel of Fig. 1, where both free-free signal and Comptonization decrement are included.

The radio background, mainly contributed by the very bright Galactic synchrotron emission, is approximated (in terms of brightness temperature) by $(T/\mathrm{K}) \sim 2.8 \times (\nu/\mathrm{GHz})^{-2.55}$. The extragalactic background determined by the ARCADE 2 experiment (Seiffert et al. 2011) (expressed in terms of equivalent thermodynamic temperature) is also consistent with a power law with a very similar index, -2.57, but with an amplitude about two times smaller, plus a frequency-independent CMB contribution at $\simeq 2.725$ K. In order to accurately observe with dedicated experiments the tiny CMB spectral distortions discussed above, the problem of the modelling and subtraction of the contribution from Galactic emissions and extragalactic foreground needs to be solved. The high sensitivity and resolution of the SKA can be used to address this issue, as discussed below.

Current measurement of radio source counts at GHz frequencies (see e.g. Prandoni et al. 2001, Condon et al. 2012) have sensitivity levels of tens of μJy (a recent estimation of radio source background can be found in Gervasi et al. 2008). However, the very faint tail of radio source counts and their contribution to the radio background at very low brightness temperature is not accurately known. Exploiting the recent differential number counts at 0.153 GHz (Williams et al. 2014), 0.325 GHz (Mauch et al. 2013), 1.4 GHz (Condon et al. 2012), and 1.75 GHz (Vernstrom et al. 2014a) it is possible to evaluate the contribution, T_b, to the radio background from extragalactic sources in various ranges of flux densities. While these signals are clearly negligible compared to the accuracy of current CMB spectrum experiments, mostly at $\lambda \gtrsim 1$ cm, they can be significant at the accuracy level potentially achievable with future experiments. Assuming to have subtracted the sources brighter than several tens of nJy, T_b is found to be less than ~ 1 mK at frequencies above ~ 1 GHz, but larger than ~ 10 mK below ~ 0.3 GHz. The estimate of the minimum source detection threshold is given by the source confusion noise which, around 1.4 GHz, has been quoted by Condon et al.

PoS(AASKA14)149

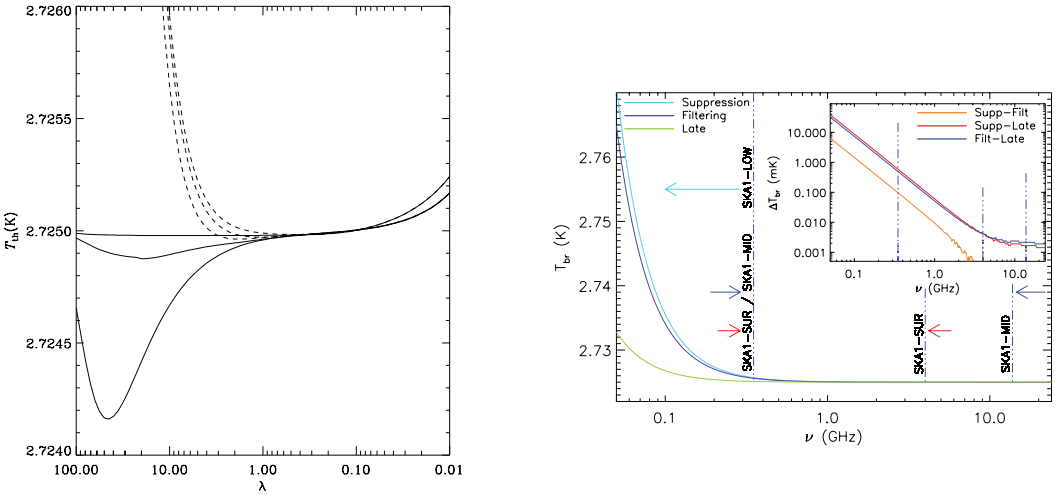

Figure 1: Left panel: CMB distorted spectra in terms of equivalent thermodynamic temperature as a function of the wavelength λ (in cm) in the presence of a late energy injection with $\Delta\varepsilon/\varepsilon_i \simeq 4y = 5\times10^{-6}$ plus an early/intermediate energy injection with $\Delta\varepsilon/\varepsilon_i = 5\times10^{-6}$ (about 20 times smaller than current upper limits) occurring at the "time" Comptonization parameter $y_h = 5, 1, 0.01$ (from the bottom to the top; in the figure the cases at $y_h = 5$ – when the relaxation to a Bose-Einstein modified spectrum with a dimensionless chemical potential given, in the limit of small distortions, by $\mu \simeq 1.4\Delta\varepsilon/\varepsilon_i$ is achieved – and at $y_h = 1$ are extremely similar at short wavelengths; solid lines) and plus a free-free distortion with $y_B = 10^{-6}$ (dashes). y_h is defined by y but with $T_e = T_{CMB}$ when the integral is computed from the time of the energy injection to the current time. From Burigana et al. (2004). Right panel: free-free distortion in the SKA2 frequency range produced by two astrophysical reionization histories (a reionization phenomenological model, *late* model, see Naselsky & Chiang 2004, with parameters given by Eq. (4) of Trombetti & Burigana 2012 is also displayed for comparison). The inset shows the absolute differences between the models. Vertical lines display the frequency ranges of the three SKA1 configurations.

(2012): $5\sigma_{conf} \simeq 5\times1.2(\nu/3\,\mathrm{GHz})^{-0.7}(\theta/8'')^{10/3}\mu$Jy, where θ defines the relevant resolution. According to the authors, the finite angular extension of faint galaxies, $\theta \sim 1''$, implies a "natural confusion limit" of about 10 nJy at frequencies around ~ 1.4 GHz, thus indicating that, for deep surveys such as those discussed below, source confusion will not represent a relevant limitation.

At 1 GHz $\lesssim \nu \lesssim$ some GHz ($\lambda \approx 1$ dm) the signal amplitudes found for CMB distorted spectra well below FIRAS constraints (see Fig. 1) are significantly larger than the estimates of the background from extragalactic sources fainter than some tens of nJy. Free-free distortion amplitude increases at decreasing frequencies, but source confusion noise may represent there a serious problem, possibly preventing the achievement of the faint detection threshold necessary to have a source contribution to the background significantly less than the CMB distortion amplitude.

Extragalactic source contribution is small compared to the Galactic radio emission, which currently represents the major astrophysical problem in CMB spectrum experiments, but, unlike the Galactic emission, it cannot be subtracted from the CMB monopole temperature by exploiting its angular correlation properties. Accurate absolute measurements with a wide frequency coverage can allow a joint fit of both CMB distorted spectra and astrophysical signals (see e.g. Salvaterra & Burigana 2002 for an application to FIRAS data) but a direct radio background estimate from precise number counts will certainly improve the robustness of this kind of analyses.

The relevance of this problem emerged in the detection by the Absolute Radiometer for Cos-

PoS(AASKA14)149

mology, Astrophysics, and Diffuse Emission 2[8] (ARCADE 2) of an excess in the CMB absolute temperature at 3.3 GHz (Singal et al. 2011, Seiffert et al. 2011), which is likely explained by a background of very faint sources or by residual emission from subtraction of the Galactic component. Singal et al. (2010) concluded that, for a radio background at the level reported, the majority of the total surface brightness would have to have been produced by ordinary star-forming galaxies at redshift $z \gtrsim 1$, characterized by an evolving radio–far-IR correlation, which changes towards the radio loud with increasing redshift. Using the JVLA at 3 GHz Vernstrom et al. (2014b) ruled out a new discrete population peaking brighter than 50 nJy while Vernstrom et al. (2014a) constrained the contribution to the ARCADE 2 excess from an extended population peaking above 1 μJy. Analyzing dedicated radio observations with the JVLA,[9] Condon et al. (2012) argued that the discrete sources possibly dominating the reported extragalactic background excess cannot be located in (or near) galaxies and must be typically fainter than 0.03 μJy at 1.4 GHz. The problem raised by this controversial 3.3 GHz excess underlines how crucial the precise estimation of very faint source counts is for the accurate exploitation of CMB spectrum measurements.

SKA continuum surveys, driven by a set of SKA top priority science cases and defined to provide significant advances over pre-SKA surveys, are described in Prandoni & Seymour (2015). Deep and ultra-deep surveys are clearly the most relevant ones to determine the very faint source counts, while $P(D)$ methods can be exploited to extract information on number counts below the survey sensitivity (Condon et al. 2012), particularly in low frequency continuum surveys, dedicated to non-thermal emission in clusters and filaments. The Ultra Deep survey dedicated to the Star Formation History of the Universe (SFHU), with their planned rms sensitivity of some tens of nJy per beam and arcsec or better resolution, will represent a great opportunity for an accurate determination of source number counts down to very faint fluxes, significantly helping the solution of one fundamental problem of the future generation of CMB spectrum experiments at long wavelengths.

2.1 Free-free localized emissions

The SKA will be able, for the first time, to trace the detailed distribution of neutral hydrogen before reionization, and the neutral-to-ionized transition state at the reionization epoch, through the 21-cm line (see e.g. Schneider et al. 2008). It is also possible to trace the development of ionized material directly by looking for the free-free emission from ionized halos. The expected signal can be calculated exploiting reionization phenomenological and astrophysical models through both semi-analytical methods (Naselsky & Chiang 2004, Trombetti & Burigana 2014), and numerical simulations (Ponente et al. 2011).

The direct observation of diffuse gas and Pop III objects in thermal bremsstrahlung has been investigated by Oh (1999). Observations at high resolution of dedicated sky areas are a natural way to distinguish free-free distortion by ionized halos rather than by diffuse ionized IGM. The SKA should be able to detect up to $\sim 10^4$ individual free-free emission sources with $z > 5$ in 1 square degree (see left panel of Fig. 2).

Simulations by Ponente et al. (2011) show that the expected individual halo signal should be $S_{\rm ff} \sim 3.67 \times 10^{-9}$ Jy, while the analytic β-model for halo density profiles predicts a signal a factor ~ 7.5 larger. In terms of ΔT, the maximum temperature distortion is about a few μK (at 1 GHz)

[8] http://asd.gsfc.nasa.gov/archive/arcade/
[9] http://www.nrao.edu/pr/2012/jansky/

PoS(AASKA14)149

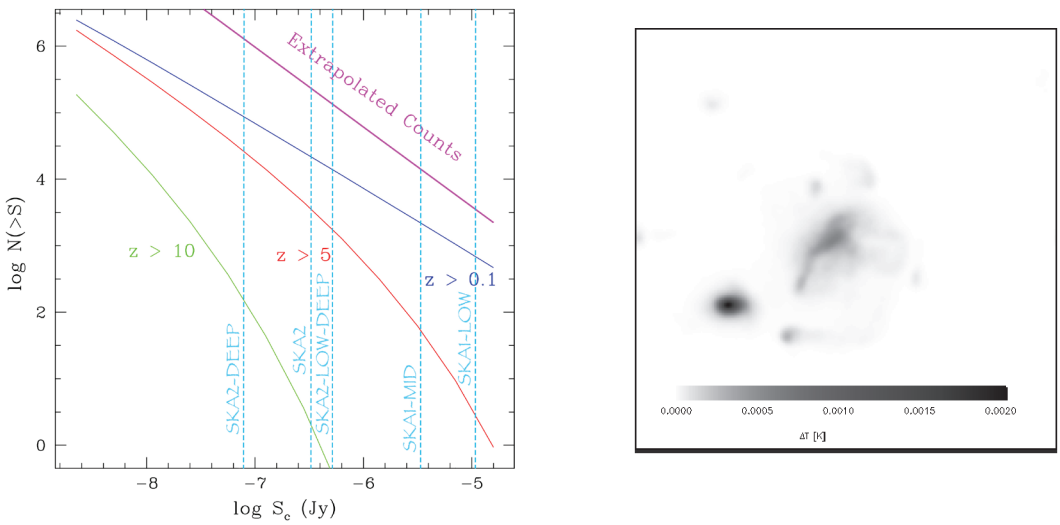

Figure 2: Left panel: number of sources which may be detected in 1 deg^2 by SKA, as a function of the threshold flux S_c (theoretical predictions from Oh 1999). Realistic limiting fluxes (5σ sensitivity levels achievable in one hour of integration on one field of view (FoV)) for point source detection are shown (vertical lines). We report also the (5σ) sensitivity achievable by SKA2 with a deep exposure (in $\sim$ one day of integration) at low and mid/high frequencies. Extrapolated source counts from Partridge et al. (1997). Right panel: free-free signal for a halo with $M = 6.6 \times 10^{14} h^{-1} M_\odot$ at $z = 0.15$. The greyscale shows the signal in K and at 1 GHz. The field of view is $\approx 40'$. The total flux in this region is $S_{\rm ff} = 2.83 \times 10^{-5}$ Jy. From Ponente et al. (2011).

at the center of the cluster. More massive and denser clusters would produce stronger signals, representing a useful way to study the intracluster medium. For a simulated massive cluster at redshift $z = 0.15$ the free-free distortion at 1 GHz is of the order of 1 mK in the cluster regions (see right panel of Fig. 2). Thus, the precise mapping of individual halos represents an interesting goal for the excellent imaging capabilities of the SKA.

3. Cross-correlation with CMB

High accuracy CMB surveys such as those carried out and expected by the *Planck* satellite[10] are designed to cover high sky fractions, f_{sky}, or the whole sky. The SKA is mainly designed to achieve very faint fluxes on limited sky fields, but its sensitivity is so high on typical FoVs of $\sim$ degree side at frequencies $\sim$ 1 GHz, that it is reasonable to expect to be able to cover a significant f_{sky} (thousands of square degrees) with unprecedented sensitivity in some months of integration. This will improve the cross-correlation analyses with CMB surveys and with surveys in other frequency bands (see also Takahashi et al. 2015).

3.1 Integrated Sachs-Wolfe effect and constraints on dark energy

The ISW effect comes from the line-of-sight integral in the Sachs Wolfe equation (Sachs & Wolfe 1967). It arises when CMB photons streaming across the Universe interact with the time-evolving gravitational potential wells associated with foreground large-scale structure (LSS). The evolution of the potential leads to a net change of the photon energies as they pass through the LSS. The ISW is a linear effect which depends the cosmological model, since it requires a change in the

[10] www.rssd.esa.int/planck

PoS(AASKA14)149

cosmic fluid equation of state. The evolution of the gravitational potential is related to the matter linear density perturbations; in the matter dominated regime, the growth of matter perturbation is proportional to the scale factor. This balances the dilution of matter due to the cosmic expansion and makes the gravitational potential variations negligible. They are relevant however at early times, when the Universe goes from being radiation dominated to matter dominated (*early ISW*), and at late times, as the dark energy (DE) (or curvature) takes over from the matter (*late ISW*). The ISW contribution to the CMB anisotropy in a direction $\hat{n}$ on the sky is approximately given by $\Delta^{ISW}(\hat{n}) \approx -2\int_{\text{Last Scattering}}^{\text{Today}} d\eta\ \dot{\Phi}[r\hat{n},\eta]$, where Φ is the Newtonian potential, the dot denoting a derivative with respect to the conformal time η, and $r(\eta)$ is the proper distance.

Unlike the early ISW, the late ISW is virtually uncorrelated with the CMB anisotropies generated at last scattering. Direct detection of late ISW is difficult because of its small amplitude and its dominance only on super-horizon (i.e. large) scales, where cosmic variance is large. However, it is possible to isolate the late ISW generated at low redshifts through the cross-correlation of the CMB maps with LSS surveys. Indeed, when CMB photons cross a time-varying potential, they become slightly hotter or colder: statistically, we expect a tiny correlation of hot spots in the CMB with LSS, an effect expected to be less than 1 μK, orders of magnitude smaller than the CMB correlations (Crittenden & Turok 1996, Peiris & Spergel 2000). Several measurements have been performed to detect the ISW signal: positive cross-correlations were measured using Sloan Digital Sky Survey[11] (SDSS) galaxy data and WMAP (Fosalba et al. 2003, Padmanabhan et al. 2005, Granett et al. 2008, Granett et al. 2009, Papai et al. 2011), on APM galaxies (Fosalba & Gaztanaga 2004), the 2MASS survey (Afshordi et al. 2004), and on radio data (see Nolta et al. 2004, Raccanelli et al. 2008 and Boughn & Crittenden 2004a,b where correlations with hard X-ray background were found). Also, Afshordi et al. (2004), Rassat et al. (2007), and Francis & Peacock (2010) used IR galaxy samples to characterize the ISW signal. The typical significance of ISW detections is currently quite low, around 2-3 σ. The cross-correlation detection of CMB with LSS requires a good CMB map on large scales and a deep enough galaxy distribution map with large f_{sky} to reduce the uncorrelated CMB map noise, with $S/N \propto f_{sky}^{1/2}$.

Given a CMB map in temperature and a galaxy survey $\mathbf{x} = (\mathbf{T},\mathbf{G})$ (vector in pixel space), the quadratic maximum likelihood (QML) estimator (Tegmark 1997) provides an estimate of the angular power spectrum (APS) $\hat{C}_\ell^X$, where $X = TT, TG, GG$. QML is well suited for such analysis, being optimal, i.e. unbiased and with minimum variance, an essential feature when the S/N ratio is low, as for the ISW effect. It is computationally demanding, but can be applied at relatively low resolution, i.e. for large scales, where the (late) ISW effect appears, and even for $f_{sky} < 1$, being a pixel based method. A set of estimators (Xia et al. 2009) exploiting the features of the redshift surveys considered has been developed: the correlation of WMAP7 CMB data with radio sources in the NRAO Very Large Array Sky Survey[12] (NVSS) and its implications on the cosmological perturbation statistics (Xia et al. 2010b); the foreground removal from CMB maps (Xia et al. 2010a) to improve auto and cross-correlation spectra (Xia et al. 2011); and WMAP7 maps and NVSS cross-correlations with dedicated methods to constrain the DE content (Schiavon et al. 2012).

From the 2013 data release, the *Planck* Collaboration detected the ISW effect with a 2σ –

[11] www.sdss.org

[12] http://www.cv.nrao.edu/nvss/

PoS(AASKA14)149

$4\,\sigma$ significance, depending on the adopted method (*Planck* Collaboration 2014a). The SKA will play a crucial role in improving the current large-scale galaxy dataset. The requirement to have a negligible shot noise in the galaxy power spectrum is β FoV $T_0 > 10\,\mathrm{deg}^2\mathrm{yr}$ (Abdalla & Rawling 2005); here β is the receiver bandwidth, T_0 is the survey duration and FoV is 1 deg^2 and 200 deg^2 for SKA1-MID and SKA2-LOW, respectively. It is foreseen that a 1-yr SKA survey will contain $> 10^9(f_{sky}/0.5)$ HI galaxies in a redshift range $0 < z < 1.5$. This makes the combination of SKA and *Planck* data a powerful tool for investigating the ISW correlation, offering the opportunity to achieve an independent measurement of the effect and increasing the confidence level in the detection from the present, marginal evidence. It will also be possible to improve constraints on the statistics of primordial perturbations and DE dynamics.

3.2 Non-Gaussianity from joint analyses of CMB and radiosources

Statistical analyses of the extragalactic source distribution can probe the Gaussianity of primordial perturbations through their imprints at the origin of LSS. Different kinds of non-Gaussianity, such as the local type (loc), equilateral (eq), enfolded (enf), orthogonal, have been predicted (Bartolo et al. 2004, Komatsu et al. 2010). For example, the local type is parameterized by a constant dimensionless parameter f_{NL} (see e.g. Verde et al. 2000, Komatsu & Spergel 2001, Babich et al. 2004), $\Phi = \phi + f_{NL}(\phi^2 - <\phi^2>)$, where Φ denotes Bardeen's gauge-invariant potential (evaluated deep in the matter era in the CMB convention) and ϕ is a Gaussian random field. Extragalactic radio sources are powerful tracers of the LSS, since they span a large volume extending out to substantial redshift. A global analysis of the constraints on the amplitude of primordial non-Gaussianity (PNG) from the APS obtained from extragalactic radio sources (the SDSS Release Six quasar catalogue), the final SDSS II Luminous Red Galaxy (LRG) photometric redshift survey, and cross-correlation with the WMAP CMB temperature map, has set limits of $f_{NL}^{loc} = 48 \pm 20$, $f_{NL}^{eq} = 50 \pm 265$ and $f_{NL}^{enf} = 183 \pm 95$ at 68% confidence level, almost stable with respect to potential systematic errors and analysis details (Xia et al. 2011). A recent, interesting analysis of PNG of local type using the clustering of 8×10^5 photometric quasars from the SDSS in the redshift range $0.5 < z < 3.5$ has been presented by Leisted et al. (2014). The authors separate the sample of quasars into four redshift bins by selecting objects with photometric redshift estimates and mitigate the impact of systematics in the estimate of power spectra with a novel technique, the extended mode projection, based on the measurement and mapping onto the sky of the most potential systematics (e.g. observing conditions, calibration) during SDSS observations. They obtain $-49 < f_{NL}^{loc} < 31$ and predict an error $\sigma(f_{NL}^{loc}) \simeq 5$ from the angular power spectra of galaxies in 20 tomographic bins in the redshift range 0.5 < z < 3.5 that will be obtained with the Large Synoptic Survey Telescope-like photometric survey (LSST DE Science Collaboration 2012). Furthermore, a robust constraint, $f_{NL}^{loc} = 5 \pm 21$, on PNG of local type has been derived by Giannantonio et al. (2014) cross-correlating a wide set of currently available catalogs of galaxy surveys and them with WMAP maps and performing an extended analysis of the possible systematics aimed at reducing their impact on the results. Tests of non–Gaussianity would have profound implications for inflationary mechanisms – such as single-field slow roll, multifields, curvaton (local type) – and for models whose effects on the halo clustering can be described by the equilateral template (related to higher-order derivative type non-Gaussianity) and by the enfolded template (related to modified initial state or higher-derivative interactions). *Planck* data already set strong limits on the non-Gaussianity parameter f_{NL}, namely

PoS(AASKA14)149

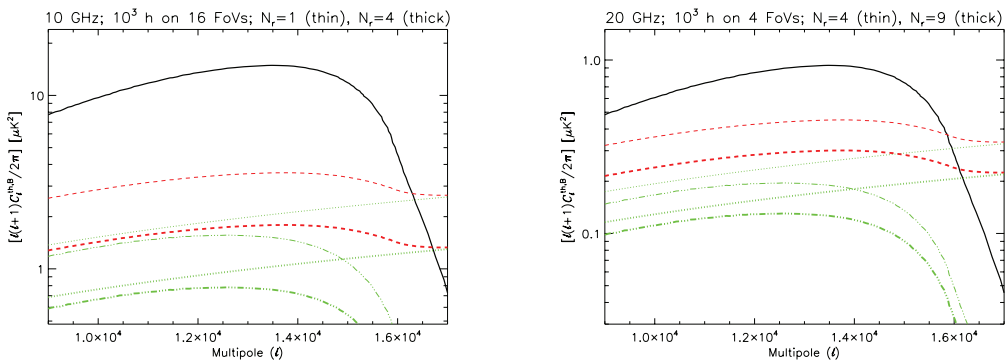

Figure 3: B-mode APS of the CMB at 10 GHz and 20 GHz induced by the Faraday rotation field with PMF normalization comoving scale $\lambda = 1$ Mpc and $n_B = 0$ (solid black line – adapted from Fig. 2 in Kosowsky et al. 2005) compared with SKA2 sensitivity (red dashes) achieved in $\sim 10^3$ hours of integration on a suitable number of FoVs, each of area $\simeq 0.49 \times (1.67\,\mathrm{GHz}/\nu)^2$ deg^2. Cosmic+sampling variance from this signal (green three-dots) and instrumental noise limitation (green dots) are also separately displayed. A 10% binning in ℓ is assumed. With relatively short baselines exploited here, the sharing of the same integration time on a number of FoVs may be more advantageous in terms of trade-off between the minimization of sampling and noise variances. The use of a focal-plane array with a number of receivers, N_r, allowing to observe a correspondingly larger sky area in the same time, will imply a better signal-to-noise ratio. See also the text.

$f_{NL}^{loc} = 2.7 \pm 5.8$, $f_{NL}^{eq} = -42 \pm 75$ and $f_{NL}^{enf} = -25 \pm 39$ at 68% confidence level (*Planck* Collaboration 2014b), significantly constraining or ruling out many classes of inflationary models.

Recent forecast works exploit the SKA radio continuum surveys (Prandoni & Seymour 2015) covering $\simeq 3.1 \times 10^4$ deg^2 out to high redshift. To mitigate the problem of lack of redshift data, Raccanelli et al. (2014) propose a combination of two methods: cross-correlation of the radio counts with CMB temperature anisotropies, i.e. the ISW effect, to reduce systematics on large scales which are particularly sensitive to PNG; and cross-identification of radio sources with optical data in order to split the radio sources into redshift bins. The authors show that even with only two redshift bins, a tomographic analysis could improve the constraints on f_{NL}^{loc} by an order of magnitude with respect to the case of a single redshift bin, achieving $\sigma(f_{NL}^{loc}) \simeq 2$, while including full redshift information will allow highly precise measurements of the non-Gaussianity parameter, with $\sigma(f_{NL}^{loc}) < 1$. General relativistic effects on the galaxy number counts, such as a non-linear primordial correction and linear projection effects from observing in redshift space on the past light-cone, have been included in the analysis of Camera et al. (2014). Their relevance emerges for a precise analysis of small values of f_{NL}^{loc}, necessary in the light of *Planck* results. Neglecting difficulties due to cosmological parameter degeneracies, since the inclusion of PNGs does not significantly broaden the constraints on other parameters, the standard approach is adopted of varying freely only the parameters one is interested in and fixing all the others to their fiducial values, as fitted for instance by *Planck*. The authors find that with SKA2 (in its full configuration) it will possible to constrain f_{NL}^{loc} down to $\sigma(f_{NL}^{loc}) \simeq 1.54$, thanks to the large number of HI galaxies that will be detected up to high redshift. These works indicate the possibility to improve with SKA the constraints on f_{NL}^{loc} of a factor ~ 3 with respect to *Planck* results.

The combination of high accuracy and deep extragalactic source surveys achievable with the SKA and the forthcoming and future CMB maps will provide a significant progress in this topic, at least for the local configuration.

PoS(AASKA14)149

4. Primordial magnetic fields versus seed magnetic field

The large-scale magnetic fields of the order of few μG observed in galaxies and galaxy clusters may be the product of the amplification, during structure formation, of primordial magnetic seeds (Ryu et al. 2012). Several early-universe models predict the generation of primordial magnetic fields (PMF), either during inflation or during cosmological phase transitions (see Widrow et al. 2012 for a review). The impact of PMF on Big Bang nucleosynthesis constrains their amplitude at the μG level (Kawasaki & Kusakabe 2012). Tighter constraints at the nG level come from CMB temperature APS (Paoletti & Finelli 2011, Shaw & Lewis 2012, Paoletti & Finelli 2013) and bispectrum (Caprini et al. 2009, Seshadri & Subramanian 2009, Trivedi et al. 2010, Trivedi et al. 2012, Shiraishi et al. 2012). PMF also impact structure formation. The presence of an extra component of anisotropic stress carried by the PMF and the Lorentz force induced on baryons modifies the evolution of matter perturbations, and impacts the small-scale matter power spectrum, and the formation and early evolution of structure. This effect, studied through magnetohydrodynamic N-body numerical simulations (Dolag 2006), is still at an early stage of development, especially concerning the analytical non-linear treatments. Data from the γ-ray observatory *Fermi* have recently added new intriguing observations in the context of cosmological magnetic fields which might be interpreted as a lower bound on the PMF amplitude. The data on γ-ray cascades from blazars show a lack of photons, which is compatible with diffuse extra-galactic magnetic fields in the intracluster medium (voids) with a lower bounds of the order of $10^{-15} - 10^{-16}$ G (Neronov & Vovk 2010, Taylor et al. 2011, Vovk et al. 2012). If this lower bound on the PMF is be confirmed, the SKA could perform crucial measurements towards probing the PMF generation mechanism. Current CMB constraints on the PMF are dominated by temperature anisotropy accuracy measurements, since PMF impact the high multipoles ($\ell \sim 1500$) without suppression by Silk damping. Recent measurements from WMAP combined with SPT and *Planck* were crucial in disentangling PMF contributions from high-ℓ foreground and secondary anisotropies (Paoletti & Finelli 2013). SKA measurements in temperature and polarization of very high-ℓ multipoles could improve these bounds on the PMF as well as the characterization of foreground and secondary anisotropies beyond the Silk damping tail. The PMF contribution to CMB anisotropies is generated either at the last-scattering surface or by Faraday rotation of the intervening magnetic fields of the stochastic background with the characteristic frequency dependence $\propto \nu^{-4}$ (Kosowsky & Loeb 1996). The smoking gun of the Faraday rotation from a stochastic background of PMF is a B-polarization signal at very high-ℓ multipoles, with a peak around $\ell \sim 1.4 \times 10^4$ (Kosowsky et al. 2005). SKA2 (in particular with the bands at $\sim 10 - 20$ GHz, because of their minor foreground contamination) can target such signal (see Fig. 3) in the multipole range $\ell \sim 10^4 - 1.5 \times 10^4$ for a magnetic field amplitude $\approx$ nG allowed by the temperature measurement. We exploit the flexibility of SKA to identify suitable conditions for detecting this signal, searching for configurations able to jointly minimize sampling and noise variances. We find that, even assuming a collecting area (and, correspondingly, receiver numbers) decreased to about 50%, relatively short baselines (around 5 km) are better suited to this aim. While the FoV at ~ 10 GHz is in principle large enough for a detection (or to improve current constraints on PMF models), the implementation of SKA2 with focal-plane arrays, allowing an increase the observed sky area in the same integration time, will be extremely useful for this research, particularly at 20 GHz. Obviously, the best configuration will be selected according to the

PoS(AASKA14)149

allocated time and actual implementation of SKA2. CMB polarization can be crucial to determine or constrain the nature of the stochastic background, given the different dependence of the Faraday effect on B_λ and the magnetic field power spectrum index n_B.

5. Galactic foregrounds

For many of the above topics the accurate study of Galactic emission is particularly crucial (see e.g. Burigana et al. 2013). The possibility of mapping intermediate and large scales with the SKA relies on the ability to merge different FoVs into maps with appropriate large-scale calibration and matching, possibly in combination with other radio surveys. On the other hand, the relatively bright Galactic radio signal does not require the extreme sensitivity demanded, for instance, by CMB fluctuation mapping at the SKA highest frequencies. SKA1 and SKA2 observations in the radio domain will allow us to test Galactic synchrotron emission models, 3D physical models of the Galaxy and the large scale coherent component of the Galactic magnetic field (Sun et al. 2008, Sun & Reich 2009, Sun & Reich 2010, Fauvet et al. 2011, Fauvet et al. 2012), based on advanced numerical codes (Strong & Moskalenko 1998, Waelkens et al. 2009) and including turbulence phenomena (Cho & Lazarian 2002).

For both Galactic science and the treatment of foregrounds in cosmology, it is also important to improve our understanding of the *anomalous microwave emission* (AME) and of the *haze* component. AME is the recently identified emission component which is well-correlated with far-IR dust emission. It is produced by rapidly spinning small dust grains having an electric dipole moment (Draine & Lazarian 1998) and its spectrum is expected to peak in the range 15–50 GHz. For the first time *Planck* was able to define the shape of the spectrum on the high frequency side of the emission peak in a number of dust/molecular/HII regions (*Planck* Collaboration 2011). In the frequency range 20–40 GHz AME is typically comparable in brightness to the free-free for the inner Galactic plane. SKA2 could provide precise mapping on the low frequency tail of this emission.

Planck was also able to identify and characterize the emission from the Galactic haze at microwave wavelengths (*Planck* Collaboration 2013). This is a distinct component of diffuse Galactic emission, roughly centered on the Galactic centre, extended to $|b| \sim 35^\circ$ in Galactic latitude and $|l| \sim 15^\circ$ in longitude. By combining WMAP and *Planck* data, *Planck* Collaboration (2013) were able to determine the spectrum of this emission to high accuracy, unhindered by the large systematic biases present in previous analyses. The derived spectrum is consistent with power-law emission with a spectral index of -2.55 ± 0.05, thus excluding free-free emission as the source and instead favoring hard-spectrum synchrotron radiation from an electron population with a distribution (number density per energy) $dN/dE \sim E^{-2.1}$. At Galactic latitudes $|b| < 30^\circ$, the microwave haze morphology is consistent with that of the Fermi γ-ray haze or bubbles (see also Carretti et al. 2012), indicating that we have a multi-wavelength view of a distinct component of our Galaxy. Given the very hard spectrum and the extended nature of the emission, it is unlikely that the haze electrons result from supernova shocks in the Galactic disk. Instead, a new mechanism for cosmic-ray acceleration in the centre of our Galaxy is implied. With the SKA multifrequency mapping in total intensity and polarization we will have the opportunity to firmly constrain these models.

In general, a large sky coverage is crucial for mapping Galactic radio emissions. Among the SKA continuum surveys (Prandoni & Seymour 2015), we compare the sensitivity (on the same

PoS(AASKA14)149

resolution element) of the $\simeq 75\%$ sky coverage surveys at 1.4 GHz and at 0.12 GHz, planned for 1–2 years of integration and dedicated respectively to strong gravitational lensing and legacy/rare serendipity and to non-thermal emission in clusters and filaments, with that of radio surveys (La Porta et al. 2008) currently adopted as ancillary maps in CMB experiment analyses. The former will have a sensitivity about 20 times better than the available all-sky radio survey at 1.4 GHz, the latter will have sensitivity about 4 times better than the Haslam map at 408 MHz (Haslam et al. 1982), thus representing a significant improvement with respect to current ancillary radio maps.

Summarizing, the SKA high resolution maps of the Galactic emission will contribute to a better understanding of the Galactic foreground and will provide key astrophysical information for the separation of CMB and the cosmological HI 21 cm emission.

Acknowledgements – It is a pleasure to thank Isabella Prandoni for useful discussions about SKA performance and flexibility. We warmly thank the reviewer and the SKA editors for constructive comments. Partial support by ASI/INAF Agreement 2014-024-R.0 for the *Planck* LFI Activity of Phase E2 is acknowledged.

References

Abdalla, F.B, Rawling, S., 2005, MNRAS, 360, 27
Afshordi, N., Loh, Y.S., Strauss, M.A., 2004, Phys. Rev. D, 69, 083524
Babich, D., Creminelli, P., Zaldarriaga, M., 2004, JCAP, 08, article id. 009
Bartlett, J.G., Silk, J., 1990, ApJ, 353, 399
Bartlett, J.G., Stebbins, A., 1991, ApJ, 371, 8
Bartolo, N., Komatsu, E., Matarrese, S., Riotto, A., 2010, Physics Report, 402, 103
Boughn, S., Crittenden, R., 2004a, Nature, 427, 45
Boughn, S.P., Crittenden, R.G., 2004b, ApJ, 612, L64
Braun, R., 2014, "SKA1 Imaging Science Performance", SKA-TEL-SKO-DD-XXX, Rev. A Draft 2
Burigana, C., Danese, L., de Zotti, G., 1991, A&A, 246, 59
Burigana, C., Davies, R.D., de Bernardis, P., et al., 2013, Int. J. Modern Phys. D, 22, 1330011
Burigana, C., de Zotti, G., Danese, L., 1995, A&A, 303, 323
Burigana, C., de Zotti, G., Feretti, L., 2004, New Astronomy Reviews, 48, 1107
Burigana, C., Popa, L.A., Salvaterra, R., et al., 2008, MNRAS, 385, 404
Burigana, C., Salvaterra, R., 2003, MNRAS, 342, 543
Camera, S., Santos, M.G., Maartens, R., 2014, arXiv:1409.8286v1
Caprini, C., Finelli, F., Paoletti, D., Riotto, A., 2009, JCAP, 06, article id. 21
Carretti, E., Crocker, R.M., Staveley-Smith, L., et al., 2012, Nature, 493, 66
Carr, B., Kohri,K., Sendouda, Y., Yokoyama, J., 2010, Phys. Rev. D, 81, 104019
Chluba, J., Erickcek, A.L., Ben-Dayan, I., 2012, ApJ, 758, 76
Chluba, J., Sunyaev, R.A., 2012, MNRAS, 419, 1294
Cho, J., Lazarian, A., 2002, ApJ, 575, L63
Condon, J.J., Cotton, W.D., Fomalont, E.B., et al., 2012, ApJ, 758, article id. 23
COrE Collaboration, 2011, "COrE – Cosmic Origins Explorer – A White Paper", arXiv:1102.2181
Crittenden, R.G., Turok, N., 1996, PRL, 76, 575

PoS(AASKA14)149

Danese, L., Burigana, C., 1994, Lect. Notes Phys., 429, 28
Danese, L., de Zotti, G., 1980, A&A, 84, 364
Dewdney, P., Turner, W., Millenaar, R., et al., 2013, "SKA1 System Baseline Design", SKA-TEL-SKO-DD-001, Rev. 1
Dolag, K., 2006, Astronomische Nachrichten, 327, 575
Draine, B.T., Lazarian, A., 1998, ApJ, 494, L19
Ejlli, D., Dolgov, A.D., 2014, Phys. Rev. D, 90, 063514
Fauvet, L., Macias-Perez, J.F., Aumont, J., et al., 2011, A&A, 526, A145
Fauvet, L., Macias-Perez, J.F., Désert, F.X., 2012, Astroparticle Physics, 36, 57
Fixsen, D.J., Cheng, E.S., Gales, J.M., et al., 1996, ApJ, 473, 576
Fixsen, D.J., Mather, J.C., 2002, ApJ, 581, 817
Fosalba, P., Gaztaœnaga, E., Castander, F.J., 2003, ApJ, 597, L89
Fosalba, P., Gaztanaga, E., 2004, MNRAS, 350, L37
Francis, C.L., Peacock, J.A., 2010, MNRAS, 406, 2
Gervasi, M., Tartari, A., Zannoni, M., Boella, G., Sironi, G., 2008, ApJ, 682, 223
Giannantonio, T., Ross, A.J., Percival, W.J., 2014, Phys. Rev. D, 89, 023511
Granett, B.R., Neyrinck, M.C., Szapudi, I., 2008, ApJ, 683, L99
Granett, B.R., Neyrinck, M.C., Szapudi, I., 2009, ApJ, 701, 414
Haslam, C.G.T., Salter, C.J., Stoffel, H., Wilson, W.E. 1982, A&AS, 47, 1
Jedamzik, K.,Katalinic V., Olinto, A.V., 2000, PRL, 85, 700
Kawasaki, M., Kusakabe, M., 2012, Phys. Rev. D, 86, 063003
Khatri, R., Sunyaev, R.A., 2012, JCAP, 09, article id. 016
Kogut, A., 1996, in XVI Moriond Astrophysics meeting, March 16-23, Les Arcs, France, astro-ph/9607100
Kogut, A., 2003, New Astronomy Reviews, 47, 945
Kogut, A., Fixsen, D.J., Chuss, D.T., et al., 2011, JCAP, 07, article id. 025
Komatsu, E., Afshordi, N., Bartolo, N., et al., 2010, in Astro2010: The Astronomy and Astrophysics Decadal Survey, Science White Papers, Vol. 158, arXiv:0902.4759
Komatsu, E., Spergel, D.N., 2001, Phys. Rev. D, 63, 063002
Kosowsky, A., Kahniashvili, T., Lavrelashvili, G., Ratra, B., 2005, Phys. Rev. D, 71, 043006
Kosowsky, A., Loeb, A., 1996, ApJ, 469, 1
Kurz, R., Shaver, P., 1999, Messenger, 96, 7
La Porta, L., Burigana, C., Reich, W., Reich, P., 2008, A&A, 479, 641
Leistedt, B, Hiranya, H.V., Roth, N., 2014, arXiv:1405.4315v3
LSST Dark Energy Science Collaboration, 2012, arXiv:1211.0310
Mather, J.C., Cheng, E.S., Eplee, R.E. Jr., et al., 1990, ApJ, 354, L37
Mauch, T., Klöckner, H.R., Rawlings, S., et al., 2013, MNRAS, 435, 650
Naselsky, P., Chiang, L.Y., 2004, MNRAS, 347, 921
Neronov, A., Vovk, I., 2010, Science, 328, 73
Nolta, M.R.,Wright, E.L., Page, L., et al., 2004, ApJ, 608, L10
Oh, S.P., 1999, ApJ, 527, 16
Ostriker, J.P., Thompson, C., ApJ, 323, L97
Padmanabhan, N., Hirata, C.M., Seljak, U., et al., 2005, Phys. Rev. D, 72, 043525

PoS(AASKA14)149

Pani, P., Loeb, A., 2013, Phys. Rev. D, 88, 041301
Paoletti, D., Finelli, F., 2011, Phys. Rev. D, 83, 123533
Paoletti, D., Finelli, F., 2013, Phys. Lett. B, 726, 45
Papai, P., Szapudi, I., Granett, B.R., 2011, ApJ, 732, L27
Partridge, R.B., Richards, E.A., Fomalont, E.B., Kellerman, K.I., Windhorst, R., 1997, ApJ, 483, 38
Peiris, H.V., Spergel, D.N., 2000, ApJ, 540, 605
Planck Collaboration, 2011, A&A, 536, A20
Planck Collaboration, 2013, A&A, 554, A139
Planck Collaboration, 2014a, *Planck* 2013 results. XIX, A&A, 571, A18
Planck Collaboration, 2014b, *Planck* 2013 results. XXIV, A&A, 571, A24
Ponente, P.P., Diego, J.M., Sheth, R.K., et al., 2011, MNRAS, 410, 2353
Prandoni, I., Gregorini, L., Parma, P., et al., 2001, A&A, 365, 392
Prandoni, I. & Seymour, N., 2015, "Revealing the Physics and Evolution of Galaxies and Galaxy Clusters with SKA Continuum Surveys", in proc. *Advancing Astrophysics with the Square Kilometre Array*, PoS(AASKA14)067
PRISM Collaboration, 2014, JCAP, 02, article id. 006
Procopio, P., Burigana, C., 2009, A&A, 507, 1243
Raccanelli, A., Bonaldi, A., Negrello, M., et al., 2008, MNRAS, 386, 2161
Raccanelli, A., Doré, O., David J. Bacon, D.J., et al., 2014, arXiv:1406.0010v1
Rassat, A., Land, K., Lahav, O., Abdalla, F.B., 2007, MNRAS, 377, 1085
Ryu, D., Schleicher, D.R.G., Treumann, R.A., Tsagas, C.G., Widrow, L.M., 2012, Space Sci. Rev., 166, 1
Sachs, R.K., Wolfe, A.M., 1967, ApJ, 147, 73
Salvaterra, R., Burigana, C., 2002, MNRAS, 336, 592
Schiavon, F., Finelli, F., Gruppuso, A., et al., 2012, MNRAS, 427, 3044
Schneider, R., Salvaterra, R., Choudhury, T.R., et al., 2008, MNRAS, 384, 1525
Seiffert, M.D., Fixsen, D.J., Kogut, A., et al., 2011, ApJ, 734, article id. 6
Seshadri, T.R., Subramanian, K., 2009, PRL, 103, 081303
Shaw, J.R., Lewis, A., 2012, Phys. Rev. D, 86, 043510
Shiraishi, M., Nitta, D., Yokoyama, S., Ichiki, K., 2012, JCAP, 03, article id. 41
Singal, J., Fixsen, D., Kogut, A., et al., 2011, ApJ, 730, article id. 138
Singal, J., Stawarz, L., Lawrence, A., Petrosian, V., 2010, MNRAS, 409, 1172
Stebbins, A., Silk, J., 1986, ApJ, 169, 1
Strong, A.W., Moskalenko, I.V., 1998, ApJ, 509, 212
Sun, X.H., Reich, W., Waelkens, A., Ensslin, T.A., 2008, A&A, 477, 573
Sun, X.H., Reich, W., 2009, A&A, 507, 1087
Sun, X.H., Reich, W., 2010, Research in Astron. Astrophys., 10, 1287
Sunyaev, R.A., Khatri, R., 2013, Int. J. Modern Phys. D, 22, 1330014
Sunyaev, R.A., Zeldovich, Ya.B., 1970, Ap&SS, 7, 20
Takahashi, K., Brown, M.L., Burigana, C., et al., 2015, "Overview of Complementarity and Synergy with Other Wavelengths in Cosmology in the SKA era", in proc. *Advancing Astrophysics with the Square Kilometre Array*, PoS(AASKA14)0159

PoS(AASKA14)149

Taylor, A.M., Vovk, I., Neronov, A., 2011, A&A, 529, A144
Tegmark, M., 1997, Phys. Rev. D, 55, 5895
Trivedi, P., Seshadri, T.R., Subramanian, K., 2012, PRL, 108, 231301
Trivedi, P., Subramanian, K., Seshadri, T.R., 2010, Phys. Rev. D, 82, 123006
Trombetti, T., Burigana, C., 2012, J. Modern Phys., 3, 1918
Trombetti, T., Burigana, C., 2014, MNRAS, 437, 2507
Verde, L., Wang, L.M., Heavens, A., Kamionkowski, M., 2000, MNRAS, 313, L141
Vernstrom, T., Norris, Ray P., Scott, D., Wall, J.V., 2014a, arXiv:1408.4160v1
Vernstrom, T., Scott, D., Wall, J.V., et al., 2014b, MNRAS, 404, 2791
Vovk, I., Taylor, A.M., Semikoz, D., Neronov, A., 2012, ApJ, 747, L14
Waelkens, A., Jaffe, T., Reinecke, M., Kitaura, F.S., Ensslin, T.A., et al., 2009, A&A, 495, 697
Widrow, L.M., Ryu, D., Schleicher, D.R.G., et al., 2012, Space Sci. Rev., 166, 37
Williams, W.L., Intema, H.T., Röttgering, H.J.A., 2013, A&A, 549, A55
Xia, J.Q., Baccigalupi, C., Matarrese, S., Verde, L., Viel, M., 2011, JCAP, 08, article id. 033
Xia, J.Q., Bonaldi, A., Baccigalupi, C., 2010a, JCAP, 08, article id. 013
Xia, J.Q., Viel, M., Baccigalupi, C., Matarrese, S., 2009, JCAP, 09, article id. 003
Xia, J.Q., Viel, M., Baccigalupi, C., et al., 2010b, ApJ, 717, L17

PoS(AASKA14)149

PROCEEDINGS OF SCIENCE

Synergistic science with Euclid and SKA: the nature and history of Star Formation

Paolo Ciliegi and Sandro Bardelli
INAF - Osservatorio Astronomico di Bologna, Via Ranzani 1, 40127 Bologna, Italy
E-mail: paolo.ciliegi@oabo.inaf.it

We explored the impact of the synergy between the Euclid near-infrared photometric surveys and the SKA radio continuum surveys on the studies of the cosmic star formation. The Euclid satellite is expected to perform a Wide and Deep photometric surveys to an infrared limit of H$\simeq$24 and H$\simeq$26 respectively and a spectroscopy survey with a flux limit of $\sim 3\times10^{-16}$ erg cm^{-2} s^{-1} in the H$_\alpha$ line. Combining the H band Euclid selected samples with the ground based ancillary data (fundamental for the SFR estimation) we will be able to detect the star forming galaxies down to SFRs of order of unit to z$\sim$2 and down to SFR$\simeq$10 to z$\sim$3, sampling the majority of the star forming galaxies up to z$\sim$3 and beyond and placing definitive constraints on the star formation history of the universe at z<4-5 (is there a peak a z$\sim$2 or a plateau at 1$\lesssim$z$\lesssim$5 ?) and on the galaxies evolution models. The only tools able to provide a accurate dust-free calculation of their SFR are the SKA continuum surveys.

The observational parameters of the Deep Tier SKA1 reference survey (a 0.2$''$ - 0.5$''$ resolution and a 5 σ detection limit of 1 μJy over 30 deg^2 at Band 1/2) are the perfect complement of the Euclid survey. We showed, in fact, that with this kind of SKA survey we will be able to determine a dust unbiased SFR for a huge fraction ($\sim$85%) of the Euclid SFG providing strong constraints on the star formation history of the Universe. Moreover, the high angular resolution will provide an important tool to study the star formation history not only without dust contamination but also without AGN contamination. Finally, we suggest that during the SKA2 configuration a similar survey must be conducted also at higher frequency ($\sim$10 GHz) in order to allow the identification and separation of thermal and non-thermal radio emission components in higher redshift star forming galaxies

Advancing Astrophysics with the Square Kilometre Array
June 8-13, 2014
Giardini Naxos, Italy

PoS(AASKA14)150

1. Introduction

Understanding how galaxies form and the physical processes that drive their evolution has been an active field of study ever since galaxies were observationally established as objects external to our Milk Way. Modern galaxy formation theory is developed within the cold dark matter plus dark energy scenario where galaxies form when gas condenses at the centre of dark matter halos, following the radiative cooling of baryons. This leads to the formation of neutral hydrogen clouds in which denser regions can cool further and form molecular clouds where, in turn, star formation takes place (see Bough 2006 and Benson 2010 for recent review on galaxy formation theory). However, how and when galaxies build up their stellar mass is still a major question in observational cosmology. While a general consensus has been reached in the last few years on the evolution of the galaxy stellar mass function (Dickinson et al. 2003, Fontana et al. 2006) the evolution of the star formation rate (SFR) as function of redshift and stellar mass SFR(M, z) still remains unclear.

Initial determinations of the evolution of the SFR in the universe were based on optical observations which reveal rest-frame ultraviolet luminosities of starbursts at high redshift (Madau et al. 1996, Lilly et al. 1996). Uncertain corrections for extinction are the greatest limitation of such studies, and the importance of dust obscuration has become increasingly emphasized by several factors : the dependence of obscuration on galaxy mass (more massive galaxies are more obscured) and on SFR (higher SFR means more obscuration) (Hopkins et al. 2001, Garn and Best 2010) and the discovery of a large population of starburst galaxies among the dusty sources found by the Spitzer Space Telescope (Dey et al. 2008). After about two decades of studies, it has now became clear that we cannot understand galaxy evolution and SFR without accounting for the energy absorbed by dust and re-emitted in the far-infrared (FIR) and sub-millimetre regions. More than 15 years ago using the SCUBA sub millimetre data, Hughes et al. (1998, 2002) found a star formation rate density (SFRD) that increases steeply to z$\sim$1, then flattens between z$\sim$1 and z$\sim$3 and decreases at z$\gtrsim$3. A very similar trend has been recently confirmed by Gruppioni et al. (2013) using the FIR data from the *Herschel* satellite. However, although an extinction-free measure, the interpretation of FIR and sub-millimetre emission is complex. Variations in the dust composition, content, temperatures and distribution along the line of sight affect the fraction of UV photon absorbed, while a portion of the FIR emission could arises from dust heated by older stars (Bendo et al. 2010, Li et al. 2010).

An independent estimate of the SFR in a galaxy, not biased by the galaxy's dust content, is provided by its radio continuum emission. This is due to processes such as the free-free emission from HII regions and the synchrotron radiation from relativistic electron from supernova (SN) remnants (Condon 1992). Over the last few years, several studies based on the radio emission (Seymour et al. 2008, Pannella et al. 2009, Karim et al. 2011) confirmed the rapid increase of the star formation rate density (SFRD) from z=0 to $z\sim$1 in very good agreement with the results already obtained at other wavelengths, while at redshift greater than $z\sim$1.5 there is still a significant discrepancy between the SFRD estimated from different wavelengths. These discrepancies do not allow us to establish unambiguously the presence of a peak in the SFRD at z$\sim$2 or a plateau at z$\gtrsim$1.5, severely limiting our conclusions on galaxies evolution models. These results are summarized in Fig. 1 from Ilbert et al. (2013) where the SFRD inferred from different wavelengths is plotted against the redshift.

PoS(AASKA14)150

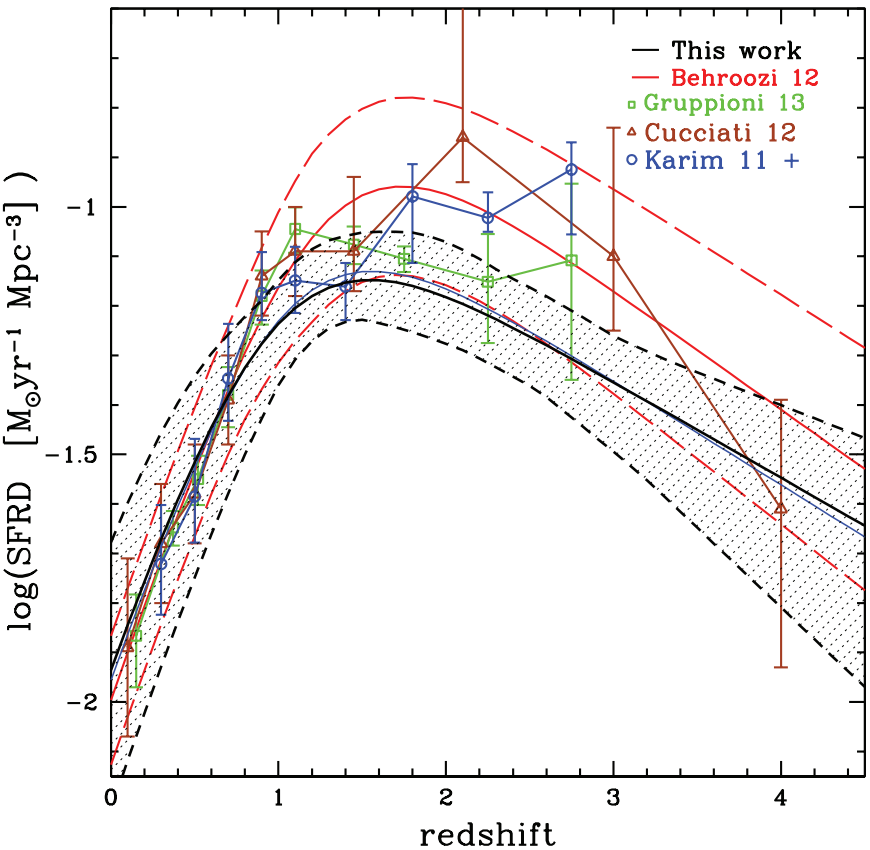

Figure 1: Star formation rate density inferred from different wavelengths (figure from Ilbert et al. 2013) including: direct measurements compiled by Behroozi et al. (2013) (red solid line with dashed lines for associate uncertainties), SFRD derived from the UV and IR luminosity function from Cucciati et al. (2012), and Gruppioni et al. (2013) (brown triangles and green squares, respectively), radio estimates from Karim et al. (2011) (blue open circle) and finally the SED fitting SFRD derived from the K-band selected UltraVISTA sample from Ilbert et al. (2013) (black solid line and dashed area corresponding to 1σ errors).

However, while the obvious advantage of the radio emission as a tracer for star formation is its independence on any correction for dust attenuation, there are two major drawbacks : i) the general low sensitivity to the normal galaxy population even in the deepest radio surveys to date which usually limits the analysis at high redshift to a stacking approach ; ii) as for the UV and far infrared wavelength, radio emission is not only produced by star formation but also by active galactic nuclei (AGNs) and therefore we need to separate the radio sources into those whose radio emission is AGN dominated and those that are consistent with being dominated by star formation (Seymour et al. 2008, Smolcic et al. 2008, Bardelli et al. 2010). To overtake these problems a new generation of multi-wavelengths surveys (in terms of sensitivity, resolution and area covered) are needed in order to detect the faintest radio sources and to uniquely characterize their physical properties (origin of radio emission, redshift, mass). The next two decades will open a new astronomical era to address the open questions discussed above. Several new generation facilities are, in fact, planned to be

PoS(AASKA14)150

realised and to work at different wavelengths. In the radio regime the advent of the revolutionary interferometer SKA will be preceded by a number of next-generation radio telescope and upgrade, including APERTIF, eMERLIN, JVLA, LOFAR and the two SKA precursors: ASKAP (Australia) and MeerKAT (South Africa). All these facilities are part of a wider context of new generation instruments, from the optical and near infrared band (LSST, E-ELT, TMT, GMT) to the X-ray band (eRosita, Athena), whose data will be able to provide a new panchromatic view of the Universe. However, the huge amount of data that will be produced by all these facilities forces to establish strong synergies in order to maximize the use of data.

For a more comprehensive discussion on the potential role played by the SKA in addressing the history of star formation we refer to Jarvis et al. (2015, this Volume). In this contribution we concentrate on how a synergy between the SKA continuum survey and the Euclid data (combined with the optical ancillary data for the SFR determination) will revolutionise our current knowledge on the nature and history of the star formation history, while for a description of the cosmological implication of the SKA-Euclid synergy see Kitching et al. (2015, this Volume).

2. The Euclid mission

Euclid (PI Y. Mellier) is a Medium Class mission selected by ESA within the Cosmic Vision programme and is aimed to "Understand the nature of Dark Energy and Dark Matter" using several cosmological probes. The launch is scheduled for 2020 and the end of the nominal mission is foreseen for late 2026.

For details of the mission, scientific goals and organization see the Euclid Red Book (Laureijs et al. 2011). The payload comprises two wide field instruments: a visible (VIS) and a near infrared photometric and spectroscopic instrument (NISP P and NISP S). The visible channel is aimed for weak lensing and will have a plate scale of 0.10 arcsec in a wide red band (R+I+Z, 0.55 to 0.92 μm). The NIR instrument in the photometric mode provides deep photometric data in three NIR bands (Y, J and H). The spectroscopic mode operates in the 1.0-2.0 μm range and provides slitless spectra at a spectral resolution of $R \sim 250$.

Euclid is expected to perform a Wide Survey of $\sim 15,000$ deg^2 to an infrared limit of mag=24 (Y,J,H at 5σ detection for a point source) and to a visible limit of 24.5 (at 10σ for extended sources). During this survey, the spectroscopy will have a flux limit of $\sim 3 \times 10^{-16}$ erg cm^{-2} s^{-1} (at 3.5σ) in the H$_\alpha$ line. A Deep Survey will be done on a 40 deg^2 area and will reach a limit ~ 2 magnitude deeper in the NIR bands. It is expected that Euclid will deliver a dataset with images and photometry of more than a billion galaxies and several million of spectra.

Finally, in order to achieve the photometric redshift error of $\sigma[(1+z)/z] \sim 0.04$ required from the cosmological studies and a reliable SED fitting and SFR, the Euclid photometric data in the Y, J and H bands will be combined with deep ground based optical data. During the Euclid mission several new optical ground - based instruments optimized for deep, large area photometric surveys will be available, both in the north (CFHT, Pan-STARRS, SUBARU/HSC, LSST-South) and south (Blanco 4m/DES) hemisphere. The combination of EUCLID and ground based data will provide a unique baseline of optical counterparts to study the star formation history of the universe with the SKA data, although we should keep in mind that a NIR (Euclid) selected sample of galaxies could be biased in favour of relatively massive galaxies at high redshift.

PoS(AASKA14)150

3. The Star Formation History

The cosmic star formation history has been studied thoroughly over the past decade and half. As shown in Fig. 1 the space density of the star formation rate declines by an order of magnitude between a redshift of unit and zero, while at higher redshift the SFRD is almost flat when estimated al longer wavelengths (far infrared and radio) and shows a decline when estimated at shorter wavelengths (optical and near-infrared). Since at redshift $1 \leq z \leq 3$ the star formation activity appears to be dominated by dusty, heavily obscured, star forming galaxies (Caputi et al. 2007, Murphy et al. 2011a), much of the discrepancy among these estimates could arise by a poor determination of the dust extinction in the optical near-infrared band and how SFRs in different galaxy populations are determined. Thus, deep radio continuum surveys can provide an important tool for measuring the cosmic star formation history of the Universe out to $z \sim$5, down to very modest SFRs. Moreover, because star-forming galaxies are discovered in various way, it is vital to compare various methods for measuring the SFR in galaxies.

In the next decade, facilities of new generation in the optical near infrared band (Euclid) and radio band (SKA) will give us a unique opportunity to open a new window on our knowledge of the star formation history of the Universe. In particular the availability of deep SKA radio continuum data and Euclid deep near infrared data (with its multi wavelengths ancillary data) will give us the opportunity to study with unprecedented accuracy and precision the following issues :

- **The Star Formation History out to $z \sim$5, down to very modest SFRs.** As recently shown by Rodighiero et al. 2011, starburst galaxies (defined as sources with SFR$\gtrsim$100-1000 $M_\odot$/yr in the mass range 10^{10} - 10^{11} $M_\odot$), *i.e.* sources that have a SFR - stellar mass ratio greater than 4 times the main sequence (MS) for star-forming galaxies defined by Daddi et al. (2007), represent only 2% of mass-selected star-forming galaxies and account for only 10% of the cosmic SFR density at the cosmic peak of the star formation activity (z$\sim$2) (Rodighiero et al. 2011). The bulk of the star formation history is driven by "normal" star forming galaxies (SFG) that have SFR $\sim$ 10-20 $M_\odot$/yr at a stellar mass $\sim 10^{10}$ $M_\odot$ and SFR$\sim$100 only for galaxies with stellar mass of $\sim 10^{11}$ $M_\odot$.

  Therefore, in order to have a direct, dusty unbiased measure of the bulk of the SFG responsible of SFR history of the Universe, a new generation of extremely deep continuum radio data are needed. In fact, as shown by Seymour et al. 2008 the actual generation of radio surveys are able to sample only the highest SFR objects at any given redshift. A radio survey with a 4σ detection limit of 30μJy is able to detect star forming galaxies with a SFR of $\sim$10-20 $M_\odot$/yr only locally (z$\lesssim$0.5), while at z$\gtrsim$ 1 only starburst galaxies with SFR $\gtrsim$100 $M_\odot$/yr are detected: the bulk of the SFG responsible of the Star Formation History of the Universe is completely missed. This is well represented in Fig. 2 from Seymour et al. (2008), where the SFR is plotted against the redshift for different stellar masses ranges.

  The photometric deep survey from the Euclid satellite will be able to detect normal star forming galaxies with low SFR (few $M_\odot$/yr) out to z $\sim$ 3-4 (see next section). However, considering that a new generation of FIR facilities are not scheduled so far, an accurate dust-unbiased estimate of the SFR of the SFG can be obtained only with deep radio surveys. The SKA deep continuum radio surveys are the perfect tool to achieve this goal. In the

PoS(AASKA14)150

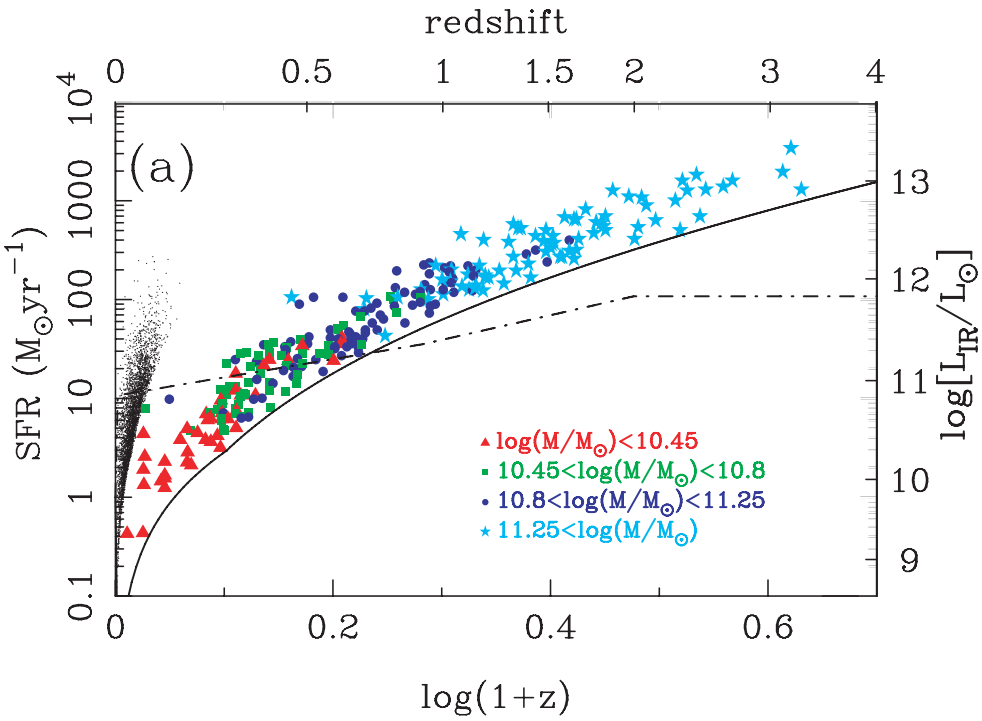

Figure 2: Star formation rate as function of redshift from the 13^H *XMM/Chandra Dee Field* (figure from Seymour et al. 2008), one of the deepest radio survey actually available with a 4σ detection limit of 30μJy. The different symbols represent different stellar masses ranges as indicated in the panel. The solid line represents the 1.4 GHz detection limit and the dot dashed line indicates the 10 times $L_\star$ of the radio star forming LF. The black dots are the SFGs from the local 6dF-NVSS sample. See Seymour et al. 2008 for more details.

next section we will consider different SKA surveys (in terms of depth, resolution and area covered) and we will investigate their impact (coupled with the Euclid data) on the study of the star formation history of the Universe.

- **Star Formation vs AGN activity in Radio Sources**

  In addition to the classification of the sources based on the Euclid plus ground based multi wavelength data (via SED fitting, Smolcic et al. 2008, Bardelli et al. 2010, see also McAlpine et al. 2015, this Volume), the availability of deep radio and NIR infrared surveys gives us the opportunity to test at very faint flux levels (both in the NIR and radio bands) the methods to separate star forming from AGN activity using the radio to NIR flux ratio used by Seymour et al. (2008) down to a radio flux level of 30μJy.

  In addition, the excellent high angular resolution of the SKA1 (from $\sim 0.2''$ to $\sim 1''$), corresponding to spatial resolution spanning sub-kpc to $\sim$10 kpc at z $>$1, will provide a unique opportunity to separate the core radio emission, likely associated to AGN activity, from more extended emission, likely associate to star forming regions, giving us the opportunity to study the star formation history not only without dust contamination but also without AGN con-

PoS(AASKA14)150

tamination.

- **The nature of radio emission in star-forming galaxies**

  Radio continuum emission from galaxies typically arises from two processes that are both tied to the SFR. At low frequency ($\leq$2 GHz), the radio continuum is dominated by non-thermal synchrotron emission arising from cosmic-ray electrons that have been accelerated by SN remnants and are propagating through the galaxy's magnetised interstellar medium. This physical link to massive star formation provides the foundation for the far infrared (FIR) - radio correlation. At high frequency ($\sim$10-100 GHz) the radio emission is dominated by thermal (free-free) radiation, which is directly proportional to the ionising photon rate of young, massive stars. However, while for the non-thermal radiation it is unclear how presumably unrelated physical processes (propagation of cosmic - ray electrons, magnetic field strength/structure, heating size and composition of dust grain) could conspire together to keep the FIR-radio relation intact, the free-free emission is largely extinction free and can be directly related to the star formation. Thus sensitive observations at radio frequency $\gtrsim$ 10 GHz , along with parallel deep observations at 1.4 GHz, will allow the identification and separation of thermal and non-thermal radio emission components in higher redshift star forming galaxies (Murphy et al. 2011b). The SKA1-MID instrument with its sensitivity up to $\sim$ 14 GHz (Dewdney et al. 2013) is the perfect instrument to perform such observations.

4. The Euclid and SKA synergetic view of the star formation history

4.1 The SKA surveys

In this section we will investigate the impact of different SKA continuum surveys (in terms of depth, resolution and area covered) on the study of the SFR as a function of redshift in combination with the Euclid data. As reference SKA1 continuum survey we used the three-tiered survey at Band 1/2 reported in Seymor and Prandoni (2014) : 1) a **Wide Tier** 1000-5000 deg^2 survey with 0.5$''$ resolution with a 5σ detection limit of 5 μJy/beam; 2) a **Deep Tier** 10-30 deg^2 survey with 0.5$''$ resolution with a 5σ detection limit of 1 μJy/beam and 3) an **Ultra-Deep Tier** survey of 1 deg^2 with 0.5$''$ resolution with a 5σ detection limit of 0.25 μJy/beam.

4.2 The Euclid survey

The Euclid wide survey down to a photometric limit 24 mag in the NIR band (see Section 2) has been assumed as our reference NIR survey. In order to simulate a reliable Euclid wide survey sample, we started from the deep photometric sample (version 1.8, Ilbert et al. 2009) available in the COSMOS field Scoville et al. (2007). This sample is a compilation of photometric data in the optical and NIR bands, covers an area of about 1.4 deg^2 and is limited to the optical magnitude $i \sim 28$ with completeness limit at $i \sim 26.5$. In Ilbert et al. (2009) all the intrinsic properties of the sources (like photometric redshift, star formation rate, mass) have been estimated through a Spectral Energy Distribution (SED) fitting procedure using 30 broad, intermediate and narrow bands from UV to mid-IR frequencies (see their Table 1). With the same catalogue and SED fitting procedure, we obtained an Euclid simulated sample in the J_{AB} and H_{AB} bands down to a magnitude limit of H_{AB}=24 (Ilbert, private communication).

PoS(AASKA14)150

4.3 The SFR with Euclid and SKA

In this section we test the capability of the simulated sample described above (ground based multi wavelength optical data down to $i \sim 28$ plus the Euclid simulated wide survey down to H_{AB}=24) to observe the bulk of the star forming galaxies up to z∼3. In Fig. 3 we plot the SFR obtained from SED fitting procedure (Ilbert et al. 2009) using all the available optical to NIR bands as a function of redshift: red dots show the SFR for the subsample with H_{AB} <24 (detectable in the Euclid wide survey) while the black dots show the entire photometric sample limited to $i \sim 28$ without limitation in the H band. As shown in the figure, the H_{AB} <24 limited sample ("Euclid sample") at a given redshift samples the region of higher SFR with respect the entire sample. This is due to the fact that with a NIR limited sample we favour the detection of relatively massive galaxies, losing low mass starburst galaxies. However, even though these mass and SFR limitations, the Euclid wide survey down to H_{AB}=24 (combined with the ground based ancillary data for the determination of the SFR values), will allow us to detect the SFG down to SFRs of order of unit to z∼2 and down to SFR≃10 to z∼3. Better results, of course, will be obtained using a sample selected from the Euclid deep survey that will reach a limit ∼ 2 magnitude deeper in the NIR bands over an area of ∼40 deg^2, combined with the ground based data for the SFR calculation. With these samples in our hands we are going to sample the majority of the massive star forming galaxies up to z∼3 and beyond, placing definitive constraints on the star formation history of the universe at z<4-5 (is there a peak a z∼2 or a plateau at $1 \lesssim z \lesssim 5$?) and on the galaxies evolution models.

However, while the Euclid data and its ancillary multi-wavelengths data will give us the opportunity to obtain informations on the intrinsic properties of the sources, including the SFR through the SED fitting procedure, an independent, dusty unbiased, estimation of the SFR of these sources is a fundamental step that must be obtained in order to ensure a clear picture of the cosmic star formation. Moreover a very deep radio continuum survey will ensure also the detection of the low mass starburst galaxies population that we could miss in a sample selected in the NIR band.

Considering the extremely low SFR of these sources (see Fig. 3) we have only one tool able to reach this scope : the SKA radio continuum survey. Following Bell (2003) we converted the radio flux detection limit of the four SKA surveys considered (see above) in SFR as function of the redshift, and we plot the relative curves in Fig. 3.

At a 5σ detection limit of 5 μJy (Wide Tier SKA1 survey, solid blue line in Fig. 3) we are able to detect only a small part of the Euclid objects, from ∼ 25% at $z < 1.4$ to ∼ 10% for higher redshifts, sampling only the region of the high SFR (the starburst region) and completely missing the sources (star forming galaxies) responsible of the bulk of the cosmic star formation (see Rodighiero et al. 2011). Therefore a radio survey at this flux level, similarly to the deepest radio survey actually available (see Fig. 2 and the black dashed line in Fig. 3 corresponding to the limit of the COSMOS radio survey of 50μJy, 5σ detection limit, Schinnerer et al. 2007) is not suitable to strongly constrain the galaxies evolutionary models, except through more uncertain statistical studies as the stacking analysis (see Pannella et al. 2009, Karim et al. 2011).

The 1 μJy 5σ detection limit survey (Deep Tier) perform much better, detecting ∼ 85% of the Euclid objects in the redshift range considered, (white long dashed line in Fig. 3) and sampling the region of the star forming galaxies with low SFR (few $M_\odot$/yr) responsible of the bulk of the cosmic star formation. The Ultra Deep Tier survey, corresponding to a 5σ detection limit of 0.25

PoS (AASKA14) 150

μJy is plotted in Fig. 3 as solid green line. At this flux limit we detect almost all the star forming Euclid objects.

Finally, as reference, in Fig. 3 we show also the line (dot dashed yellow) corresponding to the spectroscopic Euclid sample, where the H_α limit of 3×10^{-16} erg cm^{-2} s^{-1} is converted in star formation rate following the formula of Moustakas et al. (2006). This sample corresponds roughly to the radio flux limit of 10μJy, with the limitation in the derivation of the star formation history of the Universe discussed above. The limit in the SFR values sampled by the Euclid spectroscopic redshift strengthen the need for a strong synergy between Euclid and SKA, the latter being the only instrument able to provide a direct measure of the SFR for all the star forming galaxies (even with few $M_\odot$/yr up to z$\simeq$3-4) that will be detected in the Euclid photometric surveys.

The results presented in this section are summarised in Table 1, where for each survey considered, we report the 5σ detection flux limit (μJy/beam) , the area covered (in deg^2), an estimation of the total integration time needed to complete the survey with SKA, the value of the SFR sampled at z$\simeq$1 and z$\simeq$2-3 and the fraction of the Euclid SFGs that will be detected in the radio regime by the survey. Moreover, for comparison, we report also the values for the deepest already available surveys (VLA-COSMOS (Schinnerer et al. 2007) and 13^H *XMM/Chandra Deep Field* (Seymour et al. 2008)), for the ongoing surveys that will be obtained with the actual upgraded instrumentation (JVLA COSMOS 3GHz Large Project , PI V. Smolčić) and for the SKA precursors ASKAP-EMU (Norris et al. 2011), APERTIF-WODAN and MeerKAT-MIGHTEE. Finally, for the Deep Tier survey we considered also the values that can be reached during an "early-science" phase of deployment for each SKA1 component, where sensitivity has grown to about 50% of its fully specified level, and during the final SKA phase (SKA2), when the sensitivity, resolution and field of view will be improved by a factor 10-20 in comparison to SKA1.

5. Conclusion

The radio continuum surveys have been largely used over the past decade to study the star formation history of the Universe using their capacity to penetrate significant dust obscuration. However, even at the deepest radio flux limit of the available surveys, only the sources with the highest star forming rate ($\gtrsim$100-200 $M_\odot$/yr) are detected at redshift greater than z$\sim$1 and the bulk of the normal star forming galaxies responsible for $\sim$ 90% of the cosmic SFR density at z$\sim$2 are completely missed.

In this paper we showed how a strong synergy between two revolutionary facilities (Euclid and SKA), which will become operative during the next decade and the NIR and radio bands, will open a new window in our knowledge on the galaxies evolutionary models. In particular we showed that combining the H band Euclid selected samples with the ground based ancillary data (fundamental for the SFR calculation) we will be able to detect the majority of the SFG responsible of the cosmic SFR density and that the only tools able to provide an accurate dust-free calculation of their SFR are the SKA continuum surveys. Moreover a very deep radio continuum survey will ensure also the detection of the low mass starburst galaxies population that we could miss in a NIR selected sample.

We considered the SKA1 Reference Survey in Band 1/2 reported in Seymour and Prandoni (2014) and we showed that with the Deep Tier Survey (obtainable with a reasonable amount of time,

PoS(AASKA14)150

Table 1: Radio continuum survey and their SFR observability

Survey	Flux (μJy)	Resolution (arcsec)	Area (deg^2)	Time SKA	SFR sampled ($M_\odot$/yr)	% Euclid SFG
Already available surveys and SKA Precursors						
Deep Radio Survey already available	50	$\gtrsim$ 1	few ($\sim$ 2-3)	-	$\gtrsim$20 at z$\simeq$1 $\gtrsim$200 at z$\simeq$2-3	1-2
EMU + WODAN (SKA Precursors)	50	10	all sky	-	$\gtrsim$20 at z$\simeq$1 $\gtrsim$200 at z$\simeq$2-3	1-2
Ongoing deep survey (JVLA)	10	0.65	2	-	$\gtrsim$10 at z$\simeq$1 $\gtrsim$100 at z$\simeq$2-3	5-10
MeerKAT-MIGHTEE T2 (SKA Precursors)	5	3.5	35	1950	$\gtrsim$8 at z$\simeq$1 $\gtrsim$60 at z$\simeq$2-3	10-25
MeerKAT-MIGHTEE T3 (SKA Precursors)	0.5	3.5	1.0	1700	$\gtrsim$0.4 at z$\simeq$1 $\gtrsim$1-2 at z$\simeq$2-3	90
SKA1 reference surveys at Band 1/2 (Seymour and Prandoni 2014)						
Wide Tier	5	0.5	5000	$\sim$1 yr	$\gtrsim$8 at z$\simeq$1 $\gtrsim$60 at z$\simeq$2-3	10-25
Deep Tier	1	0.5	30	$\sim$ 2000 hrs	$\gtrsim$0.5 at z$\simeq$1 $\gtrsim$2-3 at z$\simeq$2-3	85
Ultra Deep Tier	0.25	0.5	1	$\sim$ 2000 hrs	$\gtrsim$0.2 z$\simeq$1 $\gtrsim$1 z$\simeq$2-3	100
SKA1 early science and SKA2						
Early Deep Tier (50% SKA1)	2	0.5	30	$\sim$1000 hrs	$\gtrsim$1 at z$\simeq$1 $\gtrsim$10 at z$\simeq$2-3	50
Deep SKA	0.1	$\lesssim$0.1	30	$\sim$40 hrs	$\gtrsim$0.1 z$\simeq$1 $\gtrsim$0.5 z$\simeq$2-3	100

$\sim$ 2000 hrs) we will be able to determine a dust unbiased SFR for a huge fraction ($\sim$85%) of the SFG detected by Euclid providing strong constraints on the star formation history of the Universe. Moreover the angular resolution of $\sim$ 0.2 - 0.5 arcsec will ensure an unambiguous identification of the radio sources and will provide an important tool to separate the core radio emission (likely associate to AGN activity) from the outer emission likely associate to star forming regions, giving us the opportunity to study the star formation history not only without dust contamination but also without AGN contamination.

Moreover we showed that during the early science phase, when the SKA1 sensitivity will be $\sim$50% of its fully specified level, we will be able to detect about 50% of the Euclid SFG (see Table 1), starting to shed a light on properties (in terms of SFR) of the galaxies responsible of the bulk of the cosmic star formation. Finally, during the SKA2 phase, when the sensitivity, resolution and field of view will be improved by a factor 10-20 in comparison to the SKA1 phase, this kind of radio survey could be easily obtained in less than 2 days. However, at that time it will be desirable to increase the area covered and, more important, to obtain an high frequency ($\sim$ 10 GHz) survey

PoS(AASKA14)150

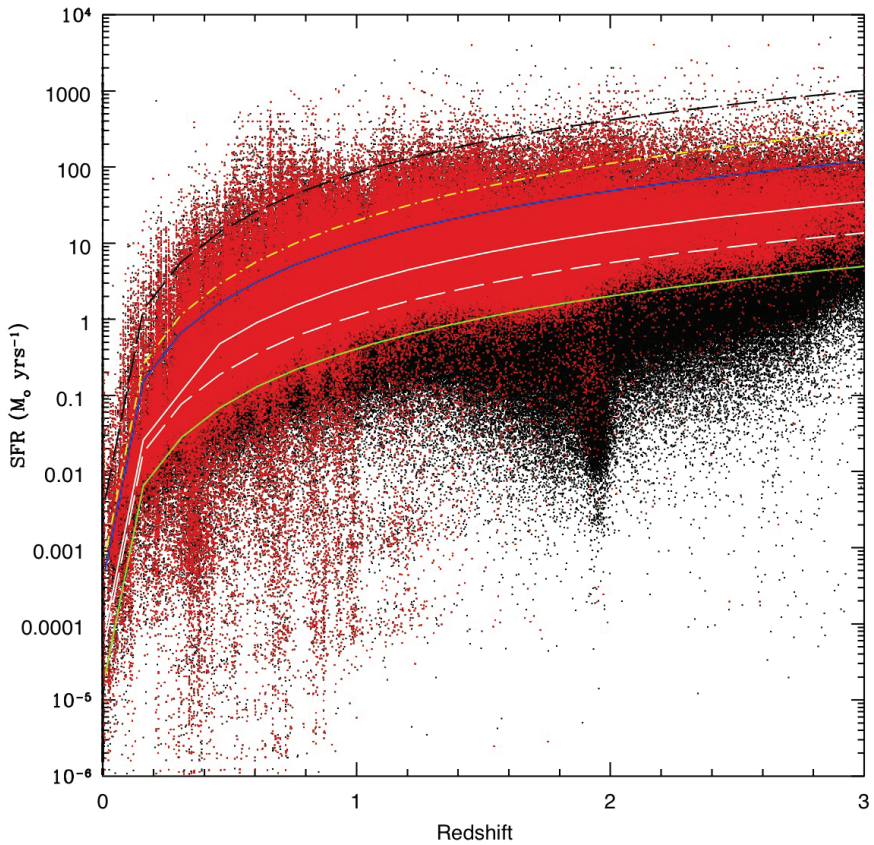

Figure 3: Star formation rate as function of redshift. SFR obtained from SED fitting procedure (Ilbert et al. 2009) for the simulated Euclid wide survey limited at $H < 24$ are plotted as red dots, while the entire photometric sample limited to $i \sim 28$ with a completeness limit at $i \sim 26.5$ is plotted as black dots. The curves represents the SFR detection limit as function of redshift for the Euclid spectroscopic sample (dot-dashed yellow line) and for different radio 5σ detection flux limits : 50μJy (dashed black line), 5μJy (solid blue line), 2μJy (solid white line), 1μJy (dashed white line) and 0.25 μJy (solid green line)

with a similar depth, resolution and area covered in order to identify and to separate the thermal and non-thermal radio emission components in higher redshift star forming galaxies.

0.0pt

REFERENCES

Bardelli, S, et al, 2010, A&A, 511,1
Behrooz,i P.S., Wechsler R.H. & Conroy C., 2013, ApJ, 770, 57
Bell, E.F., 2003, ApJ, 586, 794
Bendo, G.J., et al., 2010, A&A, 518,L65
Benson, A.J., 2010, Phys. Rep., 495, 33
Bough, C.M., 2006, Report on Progress in physics, 69, 3101

PoS(AASKA14)150

Braun, R., 2014, “SKA1 Imaging Science Performance”, Document number SKA-TEL-SKO-DD-XXX, Rev A, Draft 2
Caputi, K. I. , et al, 2007, ApJ, 660, 97
Condon J.J, 1992, ARAA, 30, 575
Cucciati O., et al., 2012, A&A, 548, 108
Daddi, E., et al., 2007, ApJ, 670, 156
Dey, A. et al, 2008, ApJ, 677, 943
Dewdney, P., Turner, W.,Millenaar, R., et al., 2013, "SKA1 System Baseline Design", Document number SKA-TEL-SKO-DD-001 Revision 1
Dickinson, M., et al., 2003, ApJ, 587, 25
Fontana, A., et al., 2006, A&A, 459, 745
Garn, T. and Best ,P.N., 2010, MNRAS, 409,421
Gruppioni, C., et al. , 2013, MNRAS, 436, 2875
Hopkins, A.M, et al., 2001, AJ, 122,288
Hughes, D.H. et al. 1998, Nature, 394, 241
Hughes, D.H. et al. 2002, MNRAS, 335, 871
Ilbert,. O., et al. , 2009, ApJ, 690, 1236
Ilbert, O. et al. 2013, A&A, 556,55
Jarvis M. J., Bacon, D., Blake, D., et al., 2015, “Cosmology with SKA Radio Continuum Surveys”, in proc. *Advancing Astrophysics with the Square Kilometre Array*, PoS(AASKA14)018
Kitching T. D., Bacon, D., Brown, M. L., et al., 2015, “Euclid-SKA Synergies”, in proc. *Advancing Astrophysics with the Square Kilometre Array*, Pos(AASKA14)146
Karim, A., et al., 2011, ApJ, 2011, 730, 61
Laureijs, R. et al. , 2011’, *Euclid Definition Study Report*, arXiv:1110.3193, [astro-ph.CO]
Li, Y., et al, 2010, ApJ, 725, 677
Lilly, S.J. et al., 1996, ApJL, 460, L1
McAlpine K., Prandoni, I., Jarvis, M., et al., 2015, “The SKA view of the Interplay between SF and AGN Activity, and its role in Galaxy Evolution”, in proc. *Advancing Astrophysics with the Square Kilometre Array*, PoS(AASKA14)083
Madau, P. et al., 1996, MNRAS, 283, 1388
Moustakas, J., Kennicutt R.C. & Tremonti C.A., 2006, ApJ 642, 775
Murphy, E. J., et al., 2011a, ApJ, 732, 126
Murphy, E. J., et al., 2011b, ApJ, 737, 67
Norris, R. , et al, 2011, PASA, 28, 215
Pannella, M. , et al., 2009, ApJ, 698, L116
Rodighiero, G., et al., 2011, ApJL, 739, L40
Schinnerer, E., et al, 2007, ApJS, 172, 46
Scoville, N., et al., 2007, ApJS, 172, 1
Seymour, N., et al., 2008, MNRAS, 386, 1695
Seymour, N. and Prandoni I., 2014, *Continuum Science Assessment Workshop Summary*, SKA-BD-09-05c
Smolčić V., et al., 2008, ApJS, 177,14

PoS(AASKA14)150

PROCEEDINGS OF SCIENCE

Multiple supermassive black hole systems: SKA's future leading role

Roger Deane[*1,2], **Zsolt Paragi**[3], **Matt Jarvis**[4,5], **Mickäel Coriat**[1,2], **Gianni Bernardi**[2,6,7], **Sandor Frey**[8], **Ian Heywood**[9,6], **Hans-Rainer Klöckner**[10]

[1] *University of Cape Town,* [2] *Square Kilometre Array South Africa,* [3] *Joint Institute for VLBI in Europe,* [4] *University of Oxford,* [5] *University of the Western Cape,* [6] *Rhodes University,* [7] *Harvard-Smithsonian Center for Astrophysics,* [8] *FÖMI Satellite Geodetic Observatory,* [9] *CSIRO Astronomy and Space Science,* [10] *Max-Planck-Institut für Radioastronomie*
E-mail: roger.deane [at] ast.uct.ac.za

Galaxies and supermassive black holes (SMBHs) are believed to evolve through a process of hierarchical merging and accretion. Through this paradigm, multiple SMBH systems are expected to be relatively common in the Universe. However, to date there are poor observational constraints on multiple SMBHs systems with separations comparable to a SMBH gravitational sphere of influence (« 1 kpc). In this chapter, we discuss how deep continuum observations with the SKA will make leading contributions towards understanding how multiple black hole systems impact galaxy evolution. In addition, these observations will provide constraints on and an understanding of stochastic gravitational wave background detections in the pulsar timing array sensitivity band (nHz -μHz). We also discuss how targets for pointed gravitational wave experiments (that cannot be resolved by VLBI) could potentially be found using the large-scale radio-jet morphology, which can be modulated by the presence of a close-pair binary SMBH system. The combination of direct imaging at high angular resolution; low-surface brightness radio-jet tracers; and pulsar timing arrays will allow the SKA to trace black hole binary evolution from separations of a galaxy virial radius down to the sub-parsec level. This large dynamic range in binary SMBH separation will ensure that the SKA plays a leading role in this observational frontier.

Advancing Astrophysics with the Square Kilometre Array
June 8-13, 2014
Giardini Naxos, Sicily, Italy

[*]Speaker.

PoS(AASKA14)151

1. Introduction

Binary supermassive black hole (SMBH) systems have long been predicted to be common in the Universe (Begelman, Blandford & Rees, 1980). Simulations suggest that they have a broad range of astrophysical impacts, including shallowing the inner density profiles of galactic halos as they eject stars via three-body interactions during in-spiral (e.g. Graham 2004, Merritt 2006); and an increase in bulge star formation and black hole accretion through disruption of cold gas angular momentum (e.g. Blecha et al. 2011, van Wassenhove et al. 2012). Furthermore, sub-parsec binary SMBHs are expected to dominate the stochastic gravitational wave background at nHz-μHz frequencies (Wyithe & Loeb 2003, Sesana 2013). Numerical simulations of the large-scale structure formation of the Universe reveal a process of hierarchical galaxy merging (e.g. Springel et al., 2005). Since every galaxy is expected to host a SMBH (Kormendy & Richstone 1995), each galaxy merger should include a merger of SMBHs. Despite this forecasted ubiquity and the broad range of predicted binary SMBH impacts, our observations of these systems remain very limited. Recently, there has been a resurgence in effort to find more dual/binary AGN[1], most notably by a hard X-ray census of the local Universe (Koss et al. 2012); a large-scale search through VLBI data archives for double flat-spectrum sources (Burke-Spolaor 2011); and 2D spectroscopic and near-infrared, adaptive-optics-assisted followup imaging of double-peaked narrow emission line AGN selected from SDSS (e.g. Rosario et al. 2010, 2011; McGurk et al. 2011; Fu et al. 2011, Comerford et al. 2011). This has resulted in an increase in the number of dual AGN on $\sim$1-100 kpc scales, however, to date there are only four strong candidate sub-kpc binary/dual AGN systems (Komossa et al. 2003, Rodriguez et al. 2006, Fabbiano et al. 2011, Deane et al. 2014). In this chapter we discuss how the SKA will take a leading role in exploring this observational frontier.

1.1 Observational status

In Fig. 1 we plot what could be considered as the strongest candidate binary SMBH systems. While there may be a degree of subjectivity on which sources should appear in this figure, it illustrates how few candidates there are, despite our expectations to the contrary. Nonetheless, progress has been made in the past decade considering that only three systems in this figure could be found in the literature at the time the first SKA science case was published (Carilli & Rawlings, 2004). In the next decade, large-scale surveys with the SKA will make significant contributions towards populating the sub-kpc parameter space in particular, driven by superior angular resolution and sensitivity, negligible dust and gas attenuation at GHz frequencies, and the enhanced nuclear accretion that appears to take place in kpc-scale dual and triple AGN (see Sec. 2.1). In Fig. 1 we show the approximate angular resolution at 1-2 GHz of SKA1-MID/SUR and SKA-VLBI (see Paragi et al. 2014, these proceedings), which illustrates its advantage to search for these systems, particularly when considering the wide-area surveys the SKA will perform in this frequency band.

1.2 Impact on Galaxy Evolution

The prevalence and evolution of multiple SMBH systems are predicted to have a broad range of astrophysical impacts, which have important galaxy evolution implications. Gravitational per-

[1]We call a SMBH system dual if the separation of its components is larger than their radii of gravitational influence, and binary otherwise (see Merritt 2013).

PoS(AASKA14)151

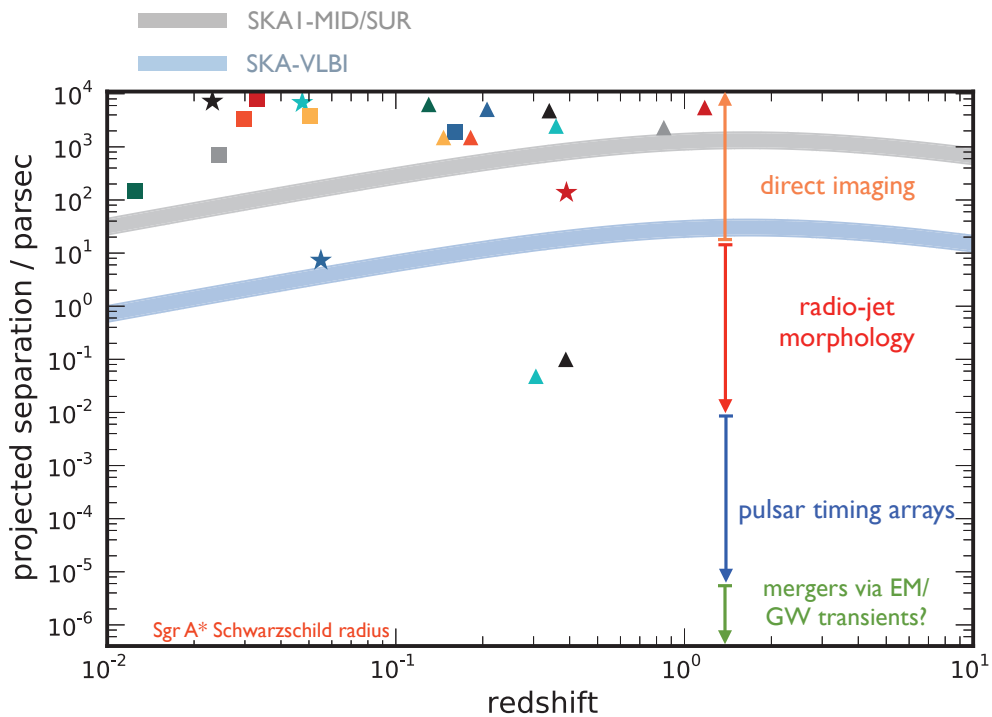

Figure 1: Sample of the strongest dual/binary AGN candidates as revealed by direct imaging at X-ray (squares), optical/infrared (triangles) and radio (stars) wavelengths. The two sub-pc triangles denote two spatially-unresolved candidates based on their double-peaked broad emission lines and quasi-periodic light curve. The grey and blue curves indicate the spatial resolution (for frequency range 1-2 GHz) that will be possible with SKA1-MID/SUR and SKA-VLBI. The labels on the right provide a rough sketch on how the SKA will explore $\gtrsim$6 decades of binary SMBH orbital separation and are elaborated on later in this contribution. The projected separation lower limit is set to the Schwarzschild radius of Sgr A* ($r_s \sim 4 \times 10^{-7}$ pc). Source names can be found in Deane et al. (2014)

turbations from binary systems are expected to increase both SMBH accretion and bulge star formation rates, and hence impact the well-correlated nuclear black hole to spheroid mass ratio (e.g. McConnell & Ma 2013). Additional scatter in this relation may result from the potential ejection of recoiling black holes (e.g. Blecha et al. 2011). Hydrodynamical simulations suggest that the separations of $\sim 10^8$ $M_\odot$ binary SMBHs can decrease from $\sim$100 parsec down to the sub-pc gravitational radiation dominated regime on a timescale of a few Myr if sufficient gas is present (e.g. van Wassenhove et al. 2012). As the orbital separation decreases, the binary SMBH system is predicted to eject of order 1-4 times their combined mass from the galaxy/bulge via three-body interactions (Merritt 2006). This mass is sufficient to flatten the inner density slope, as is measured in nearby galaxies (Merritt & Milosavljević 2005). Therefore, this appears to be an important consideration in the attempts to reconcile theoretically motivated central matter density cusps in a ΛCDM cosmology versus the observationally supported cores which have flat central density profiles (e.g. Mashchenko et al. 2006). The anisotropic gravitational wave emission from binary coalescence

PoS(AASKA14)151

is predicted to result in large recoil velocities and should enable the measurement of AGN offset from the host galaxy centre (e.g. Madau & Quataert 2004). However, apart from a number of strong individual candidates (e.g. Civano et al. 2010), a detailed analysis of 14 nearby cored elliptical galaxies suggests this offset (where measured) is not as large as predicted for plausible merger rates (Lena et al. 2014).

1.3 Linking with pulsar timing array experiments

While binary SMBHs are expected to dominate the low-frequency stochastic gravitational wave background, very little is known about the properties of low separation binaries themselves, such as the typical binary in-spiral rate, eccentricity evolution and environmental coupling at sub-kpc scales. These are important to constrain as they directly determine the low-frequency gravitational wave spectral normalization and shape. Indeed, stochastic gravitational wave background predictions assume that nature solves the so-called 'last parsec problem'. This arises from the estimate that binaries take of order a Hubble time to merge via gravitational radiation, following the ejection of most matter within binary orbital separations of $\sim$1 parsec (Merritt & Milosavljević 2005). Statistics from a large sample of binaries will measure the in-spiral rate and directly address the question of stalled binaries. However, eccentricity evolution will require further successes in the sophisticated simulations that have developed in the recent past (e.g. Mayer et al. 2007, Blecha et al. 2011, Kulkarni et al. 2012, van Wassenhove et al. 2012) as well as detailed ALMA observations of the molecular gas. Stellar scattering driven models predict that if typical binary SMBHs have an initial eccentricity of $e_0 \sim 0.7$ at formation, the expected characteristic strain at 1 nHz is suppressed by a factor of $\sim$5, while the effect is minimal at higher frequencies ($\sim$1-10 μHz, Sesana 2013, Ravi et al. 2014). Moreover, the presence of significant gas masses appears to increase the eccentricity (although, perhaps not to the extremely high values in the stellar driven case). Such eccentric systems are predicted to emit sharp spikes of gravitational wave radiation as the black holes reach the pericentre of their increasingly eccentric orbit. For eccentricities of $e \sim 0.9 - 0.95$, the characteristic strain will increase by 2-3 orders of magnitude for a constant semi-major axis. This implies that the highly eccentric inner binaries that result in simulated triple systems in particular (e.g. Hoffman & Loeb 2007) may result in detectable sources for pointed gravitational wave experiments (for a small fraction of their orbit). While this may be promising for detecting gravitational wave hotspots, it is likely to decrease the amplitude of the stochastic gravitational wave spectrum at nHz frequencies by significant factors. Therefore, the combination of a large sample of SKA-discovered binaries; the continued progress on sophisticated simulations; as well as molecular gas dynamics at high angular resolution with ALMA are important in understanding the characteristic binary in-spiral evolution and resultant nHz gravitational wave spectrum. See Burke-Spolaor (2013) for an excellent review on the multi-messenger astrophysics that will be ushered in by linking pulsar timing array results with electromagnetic probes.

2. Motivation: why the SKA will lead

The combination of depth, area and angular resolution of SKA continuum surveys will result in an unprecedented view of the faint radio Universe, and by extension, multiple SMBH systems.

PoS(AASKA14)151

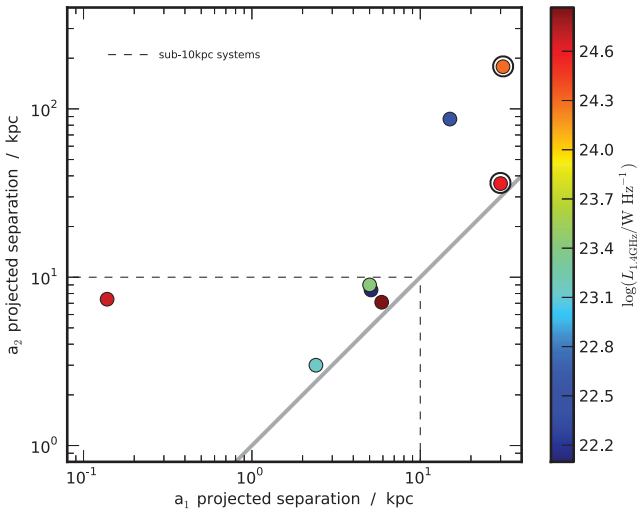

Figure 2: Projected separations of candidate triple active galactic nuclei. The axes denote the lowest and 2$^{\rm nd}$ lowest separations between AGN. The solid black line indicates a ratio of unity. The dashed lines isolate the sub-10kpc systems, which is roughly the effective stellar radius of an elliptical galaxy. The colours correspond to the total integrated radio luminosity of the AGN plus the host galaxy, since low angular resolution limits a fair AGN radio luminosity comparison. Nonetheless, the plot supports enhanced accretion within triple systems, particularly in the sub-10kpc systems. The two black circled points (which are triple quasar systems) indicate upper radio luminosity limits from archival observations. Figure reproduced from Deane et al. (2014), with references therein.

However, there are a number of attributes of these hitherto exotic systems that will further enable their detailed study with the SKA.

2.1 Enhanced radio-jet triggering in dual and triple AGN

It has been shown that galaxy-galaxy interactions are extremely efficient at triggering both nuclear star formation (e.g. Scudder et al. 2012; Patton et al. 2013) and AGN activity (e.g. Ellison et al. 2011), and that these trends continue well into the post-merger phase (Ellison et al. 2013). These results are consistent with predictions from hydrodynamical simulations (e.g. van Wassenhove et al. 2012, Blecha et al. 2011) and this implies that radio-jet triggering should become more prevalent amongst binary and triple SMBHs (see Fig. 2) . Following this (admittedly simplistic, yet plausible) argument would lead us to expect the efficiency of binary SMBHs to increase with decreasing orbital separation, provided sufficient angular resolution and survey sensitivity. If correct, the sub-arcsecond angular resolution and $\lesssim 1\,\mu$Jy beam^{-1} wide-area SKA surveys will undoubtedly enable the efficient discovery of a large population of sub-kpc binary/dual AGN.

Despite this increased discovery efficiency that would be enabled by the SKA, Fig. 3 suggests that direct imaging is unlikely to yield a large number of candidates for pointed gravitational wave experiments in the pulsar timing array band. However, as we discuss in the following section, the large-scale radio-jet morphology may provide an alternative method to discover close-pair binaries not resolvable at VLBI resolution. We note that the SKA is likely to be a 50+ year project and so the lower frequency limit in the pulsar timing band will increase in time. Halving the lower frequency limit results in roughly a factor of 8 larger cosmological volume 'surveyed', so a future

PoS(AASKA14)151

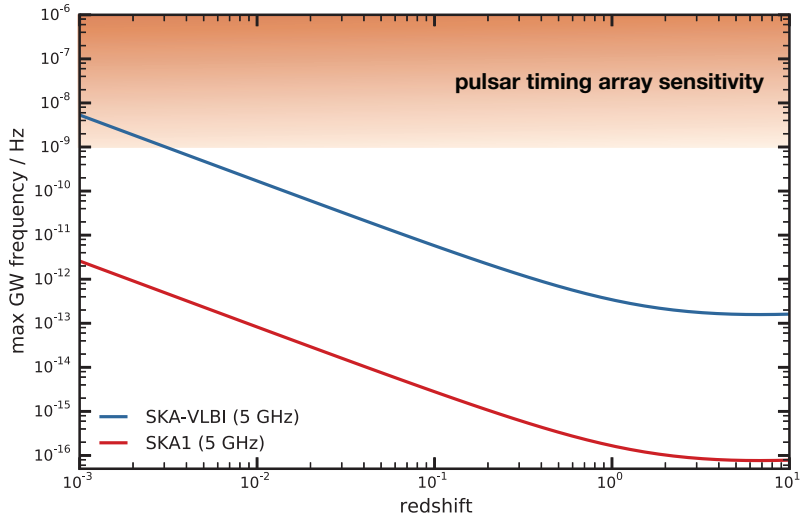

Figure 3: This plot shows the derived maximum gravitational wave frequency from a binary SMBH system that can be spatially-resolved by SKA1-MID/SUR and SKA-VLBI. We assume binaries with an angular separation equal to 2 PSF FWHM, masses of 10^9 $M_\odot$ and circular orbits. This plot demonstrates that even high sensitivity VLBI is unlikely to discover sources in the frequency band detectable by pulsar timing arrays, however, as discussed in Sec. 2.2, this may not be necessary to find so-called gravitational wave hotspots.

generation of astronomers may re-plot Fig. 3 with an updated lower frequency limit and come to a different conclusion.

2.2 Radio-jet morphology as a proxy

Even though SKA1-MID/SUR is only likely to detect dual AGN separations of $\lesssim$ 1 kpc *for all redshifts*, it may be able to select excellent close-pair ($<<$ 1 kpc) binary candidates via the large-scale radio-jet morphology, particularly given the unprecedented low surface brightness sensitivity. A number of studies have investigated the binary SMBH imprint on radio-jet morphology (e.g. Begelman et al. 1980, Kaastra & Roos 1992). Deane et al. (2014) show evidence of a $\sim$140 parsec binary SMBH in SDSS J1502+1115 using VLBI observations, as well as rotationally-symmetric "S"-shaped radio emission centered on the VLBI flat-spectrum cores. This suggests that the close-pair ($<<$1 kpc) binary SMBH could in principle be discovered using the rotationally-symmetric modulation imprinted onto the radio jets. The radio jets for the two lowest separation, spatially-resolved binary candidates (0402+379 and SDSS 1502+1115) are shown in Fig. 4, indicating the binary orbits may have a significant influence on their morphology. As discussed in the introduction, hydrodynamical simulations suggest that the separations of $\sim 10^8$ $M_\odot$ binary SMBHs can decrease from $\sim$100 parsec down to the gravitational radiation dominated regime ($<$1 parsec) on a timescale of a few Myr, particularly if sufficient gas is present (e.g. van Wassenhove et al. 2012). This is comparable to the typical lifetime of radio jets ($\sim$10 Myr), suggesting that these helical relics may provide arcsecond-scale signposts of close-pair binaries, some of which may not even be resolvable using VLBI. If that is the case, this may be a way to find gravitational wave 'hotspots'

PoS (AASKA14) 151

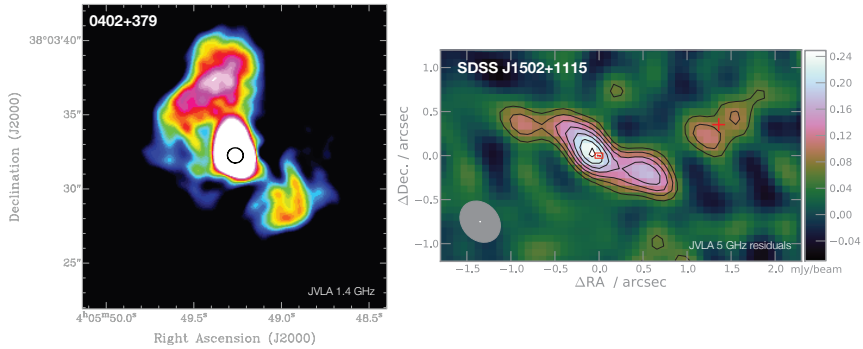

Figure 4: The above figures show the low surface brightness emission associated with the two lowest separation binary SMBH candidates (0402+379 and J1502+1115). This is to illustrate how arcsec-scale radio-jet morphology may reveal the presence of low separation binaries. **Left panel:** JVLA 1.4 GHz map of 0402+379, the lowest separation ($\sim$ 7 parsec) binary SMBH system known. The colour scale is clipped between 2-20 mJy beam^{-1} (1σ noise = 0.21 mJy beam^{-1}) to highlight the complex, potentially helical-like large-scale radio-jet emission centered on the VLBI cores which are within the 1.4 GHz PSF FWHM (shown by black ellipse in centre). VLBI observations resolve out all emission but the two radio cores and the innermost, few-parsec scale jets. Intermediate baselines ($\sim$200 km) are required to map the substantial 1.4 GHz jet emission at higher resolution. Figure from Deane et al. (in prep.). **Right panel:** Point-source subtracted JVLA 5 GHz residuals revealing rotationally symmetric "S"-shaped radio emission centred on VLBI components (within the red rectangle). There also appear to be small-scale jets centred on the third SMBH in the system to the west (J1502P, red cross). Over-plotted are the JVLA 5 GHz contours (black) starting at ± 60 μJy beam^{-1} ($\pm 4\sigma$) and increasing/decreasing in steps of $\pm 2\sigma$. The grey ellipse shows the JVLA 5 GHz PSF, while the white ellipse shows the 5 GHz EVN PSF. Modified figure to Fig. 1c in Deane et al. (2014).

where a nearby system with sufficiently high mass black holes may stand out above the stochastic gravitational wave background (e.g. Sesana 2014, Simon et al. 2014). Such targets would be very useful in understanding electromagnetic counterparts of gravitational wave sources. Therefore, radio-jet morphology may be a promising tool in binary SMBHs searches of the future, particularly given the expected SKA imaging fidelity and sensitivity at VLBI-scales. The above applies to 'static' jets (negligible variation over the timescale of years), however, monitoring variations of parsec-scale jets (e.g. Agudo et al. 2012) is an additional probe, particularly given the cadence that jet position angles may be measured at high angular resolution. These two radio jet morphology techniques may identify promising targets for millimetre VLBI observations with $<$40 μ-arcsecond angular resolution (e.g. Doeleman et al., 2008). This would in principle enable the direct imaging of a $z \lesssim 0.1$ binary SMBH that generates gravitational waves in the pulsar timing array band.

2.3 Binary SMBH insights from pulsar timing arrays

As described in Janssen et al. (2014, these proceedings), detection of the stochastic gravitational wave background is likely by the end of the decade. Pulsar timing arrays are sensitive to low-frequency (nHz-μHz) gravitational waves, limited roughly by the length of time astronomers have been accurately timing millisecond pulsars at the low end ($\sim$1-3 decades); and by the required time to achieve sufficient timing residuals signal-to-noise (of the full network of pulsars) at the high

PoS(AASKA14)151

end (~ 2 weeks). This frequency range is thought to be dominated by binary SMBHs and therefore, such a detection will prove the existence of a population of sub-pc separation systems of high mass ($\gtrsim 10^7$ $M_\odot$).

While pulsar timing arrays, radio-jet morphology and direct imaging of flat-spectrum sources are very different probes of binary SMBHs, these approaches will have to form a consistent picture. Each should in principle contribute to an overall understanding of the binary in-spiral evolution.

For binary separations and masses that correspond to $\sim$nHz frequency, environment coupling is thought to be particularly important in determining the in-spiral rate and orbital eccentricity – both of which have significant effects on the spectral shape of the stochastic gravitational wave background (as discussed in Sec. 1.3). Therefore, the spectral shape of the nHz detected stochastic gravitational wave background must be reconciled with the merger rate and constraints of radio-detected AGN fraction at sub-kpc scales. Measurements of stellar core deficits with the JWST and E-ELT, as well as ALMA-derived molecular gas kinematics will be critical ancillary data products for SKA-discovered binaries. Variability and transient events may indicate mergers and a synergy between LSST and SKA is also expected in this particular pursuit (see Fender et al. 2014, these proceedings, and references therein).

What sets the SKA apart from the major multi-wavelength facilities of the future is the dynamic range of binary black hole separation that it will probe. This will be several ($\gtrsim$6) orders of magnitude when considering the virial radius of a large elliptical galaxy ($\sim$10 kpc) down to the sub-pc separations of binaries in the gravitational radiation dominated zone.

3. Predictions for the SKA

As Fig. 1 illustrates, very few of the expected population of low separation binary SMBHs have been identified. Extrapolations to the number of systems the SKA will detect are therefore highly unconstrained. However, theoretical expectations suggest that 0.1-1 percent of galactic halos may host binary SMBHs, at least at intermediate to high redshift (e.g. Volonteri et al. 2003, Kulkarni & Loeb 2012). Given the enhanced AGN triggering at low separation, as well as the high number density of radio AGN to be detected with the SKA continuum surveys ($\sim 10^4$ per square degree at 1.4 GHz; $> 5\sigma$), we expect several orders of magnitude increase in the number of known binary SMBHs. We make no attempt to extrapolate from small number statistics, since the overwhelming message is that both phases of the SKA will open up a massive discovery space and will allow robust statistics of sub-kpc binary/dual AGN to be performed for the first time. This will enable constraints on the binary SMBH coalescence rate and correlations with their host galaxies via other multi-wavelength tracers to be explored. This revolutionary view of binary SMBHs in the Universe is critically dependent on high sensitivity on long baselines ($>$ 200 km) and VLBI capability for high angular resolution followup of the $\gtrsim 50\,\mu$Jy sources. Here SKA-VLBI refers to combining existing VLBI networks with the SKA in both phases.

3.1 SKA1 impact

Assuming the above indicative estimate on the sub-kpc AGN prevalence, we should in principle be able to detect a large fraction of those with radio counterparts with SKA1-MID/SUR sensitivity. This simple extrapolation therefore predicts that SKA1-MID/SUR will make of order a

PoS(AASKA14)151

few to a few hundred dual AGN detections per square degree. This will be a unique sample not only in size, but also in selection since it will be unbiased by dust and gas obscuration. Furthermore, SKA1-MID/SUR will be able to probe these scales (1-100 kpc) at all redshifts (see Fig. 1) and so will become a dominant driver of this field. A 50 percent decrease in SKA1-MID/SUR sensitivity will only impact the science output through the rough factor of $\sqrt{2}$ decrease in the number of dual AGN detected, assuming a comparable baseline distribution.

SKA1 is also expected to participate in VLBI sessions with existing networks (e.g. European and African VLBI Networks; Paragi et al. 2014, these proceedings). SKA1-MID/SUR will therefore already provide the opportunity to perform high sensitivity observations at milli-arcsecond angular resolution for a few weeks per year.

3.2 SKA2 impact

SKA2 will naturally lead to a significant increase in the sample of known parsec-scale binary AGN, through the dramatic increase in sensitivity on longer baselines ($>$ 200 km) for the majority of the available telescope observing time. SKA2-VLBI will be able to resolve binaries with separations of $\sim$ 20 pc at all redshifts and map associated jets with high fidelity. The wide-area ($\gtrsim$10 deg^2) mas-resolution surveys will open a completely new parameter space and discover a large number of systems of comparable and lower separation that the current record holder: 0402+379, the 7 pc separation binary at $z \sim 0.06$ (Rodriguez et al. 2006). This increased sample size at low separation will be key in bridging the black hole coalescence rate and environment coupling with the results from pulsar timing arrays. The latter requires the stochastic gravitational wave background nHz spectral shape to be measured from pulsar timing arrays, which may be possible by the time SKA2 is complete. In addition, these surveys will provide a large sample of high precision measurements of AGN positions, enabling a statistical study of the offset AGN predicted by gravitational recoil or the presence of binary SMBHs (e.g. Orosz & Frey 2013, Paragi et al., these proceedings).

This suggests that SKA2 (particularly when combined with existing VLBI arrays) will completely revolutionize this field once again (following SKA1-MID/SUR) in the low separation parameter space and bridge pulsar timing array results with what is gleaned from mas-scale continuum surveys. This naturally leads to the question: *will SKA2-VLBI resolve SMBH binaries that can be detected by pulsar timing arrays?* In Fig. 3 we have shown the maximum gravitational wave frequency of a binary that has a 10 milliarcsecond separation, mass of 2×10^9 M$_\odot$, and circular orbit. This demonstrates that even SKA2-VLBI is unlikely to discover binaries in the pulsar timing array sensitivity frequency band at 1-2 GHz. This places greater emphasis on higher frequency surveys and searching for low separation (sub-pc) binaries using the large-scale radio-jet morphology. We note the exciting possibility that the SKA may discover such systems purely through pulsar timing array experiments, however, the associated positional uncertainties ($\sigma_{\rm pos} >> 10$ deg^2) may prohibit electromagnetic counterpart determination.

4. Summary

This contribution discusses how the SKA will constrain the black hole merger rate at low separations ($<<$1 kpc). The preliminary evidence that radio-jet triggering is enhanced in dual and triple SMBH systems; negligible dust and gas attenuation at GHz frequencies; and unmatched

PoS(AASKA14)151

sensitivity and angular resolution suggests that the SKA will play a leading role in opening up the low separation parameter space. Identification of galaxies with binary SMBH systems by the SKA will have significant multi-wavelength synergy with current/future facilities such as ALMA, E-ELT, JWST and LSST, all of which will contribute to understanding the astrophysical impact thereof. Also of great importance will be the ability of high brightness temperature sensitivity observations to probe relic emission from precessing jets and hence provide arcsec-scale proxies of close-pair binary SMBH systems that cannot not be spatially resolved by VLBI. If sufficiently massive binaries are found, these may be detectable by directed gravitational wave experiments with pulsar timing arrays. The range of science possible with SMBHs is extensive and the SKA will play a leading role in their discovery, characterization and followup. These different observing modes are therefore expected to usher in the exciting era of multi-messenger astrophysics with a single facility.

0.0pt

REFERENCES

Blecha L., Cox T. J., Loeb A., et al., 2011, MNRAS, 412, 2154
Burke-Spolaor S., 2011, MNRAS, 410, 2113
Burke-Spolaor S., 2013, Classical and Quantum Gravity, 30, 224013
Carilli C. L., Rawlings S., 2004, New Ast. Reviews, 48, 979
Civano F., Elvis M., Lanzuisi G., et al., 2010, ApJ, 717, 209
Comerford J. M., Pooley D., Gerke B. F., et al., 2011, ApJL, 737, LL19
Deane R. P., Paragi Z., Jarvis M. J., et al., 2014, Nature, 511, 57
Doeleman S. S., Fish V. L., Schenck D. E., et al., 2012, Science, 338, 355
Ellison S. L., Mendel J. T., Patton D. R., et al., 2013, MNRAS, 435, 3627
Ellison S. L., Patton D. R., Mendel J. T., et al., 2011, MNRAS, 418, 2043
Fabbiano G., Wang J., Elvis M., et al., 2011, Nature, 477, 431
Fender, R. P., et al. 2015, "The Transient Universe with the Square Kilometre Array", in proc. *Advancing Astrophysics with the Square Kilometre Array*, PoS(AASKA14)051
Fu H., Myers A. D., Djorgovski S. G., et al., 2011, ApJ, 733, 103
Fu H., Zhang Z.-Y., Assef R. J., et al., 2011, ApJL, 740, LL44
Graham A. W., 2004, ApJL, 613, L33
Hoffman L., Loeb A., 2007, MNRAS, 377, 957
Janssen, G., Hobbs, G., McLaughlin, M., et al. 2015, "Gravitational Wave Astronomy with the SKA", in proc. *Advancing Astrophysics with the Square Kilometre Array*, PoS(AASKA14)037
Jiang L., Fan X., Ivezić Ž., et al., 2007, ApJ, 656, 680
Kaastra J. S., Roos N., 1992, A&A, 254, 96
Komossa S., Burwitz V., Hasinger G., et al., 2003, ApJL, 582, L15
Kormendy J., Richstone D., 1995, ARA&A, 33, 581
Koss M., Mushotzky R., Treister E., et al., 2012, ApJL, 746, LL22
Kulkarni G., Loeb A., 2012, MNRAS, 422, 1306
Lena D., Robinson A., Marconi A., et al., 2014, ApJ, 795, 146
Madau P., Quataert E., 2004, ApJL, 606, L17

PoS(AASKA14)151

Mashchenko S., Couchman H. M. P., Wadsley J., 2006, Nature, 442, 539
Mayer L., Kazantzidis S., Madau P., et al., 2007, Science, 316, 1874
McConnell N. J., Ma C.-P., 2013, ApJ, 764, 184
McGurk R. C., Max C. E., Rosario D. J., et al., 2011, ApJL, 738, LL2
Merritt D., 2013, Dynamics and Evolution of Galactic Nuclei, Princeton University Press, 2013
Merritt D., 2006, Reports on Progress in Physics, 69, 2513
Merritt D., Milosavljević M., 2005, Living Reviews in Relativity, 8, 8
Orosz G., Frey S., 2013, A&A, 553, AA13
Paragi, Z., Godfrey, L., Reynolds, C., et al. 2015, "Very Long Baseline Interferometry with the SKA", in proc. *Advancing Astrophysics with the Square Kilometre Array*, PoS(AASKA14)143
Patton D. R., Torrey P., Ellison S. L., et al., 2013, MNRAS, 433, L59
Ravi V., Wyithe J. S. B., Shannon R. M., et al., 2014, MNRAS, 442, 56
Rodriguez C., Taylor G. B., Zavala R. T., et al., 2006, ApJ, 646, 49
Rosario D. J., Shields G. A., Taylor G. B., et al., 2010, ApJ, 716, 131
Scudder J. M., Ellison S. L., Torrey P., et al., 2012, MNRAS, 426, 549
Sesana A., 2013, MNRAS, 433, L1
Sesana A., 2014, arXiv:1407.5693
Simon J., Polin A., Lommen A., et al., 2014, ApJ, 784, 60
Springel V., White S. D. M., Jenkins A., et al., 2005, Nature, 435, 629
Van Wassenhove S., Volonteri M., Mayer L., et al., 2012, ApJL, 748, LL7
Volonteri M., Haardt F., Madau P., 2003, ApJ, 582, 559
Wyithe J. S. B., Loeb A., 2003, ApJ, 590, 691

PoS(AASKA14)151

PROCEEDINGS OF SCIENCE

Star and Stellar Cluster Formation: ALMA-SKA Synergies

G. A. Fuller
Jodrell Bank Centre for Astrophysics & UK ALMA Regional Centre Node, School of Physics & Astronomy, University of Manchester, UK
E-mail: G.Fuller@manchester.ac.uk

J. Forbrich
Institute of Astronomy, University of Vienna, Austria
E-mail: jan.forbrich@univie.ac.at

J. M. Rathborne
CSIRO Astronomy and Space Science, Australia
E-mail: Jill.Rathborne@csiro.au

S. Longmore
Astrophysics Research Institute, Liverpool John Moores University, UK
E-mail: S.N.Longmore@ljmu.ac.uk

S. Molinari*
INAF-IFSI, Rome, Italy
E-mail: molinari@iaps.inaf.it

Over the next decade, observations conducted with ALMA and the SKA will reveal the process of mass assembly and accretion onto young stars and will be revolutionary for studies of star formation. Here we summarise the capabilities of ALMA and discuss recent results from its early science observations. We then review infrared and radio variability observations of both young low-mass and high-mass stars. A time domain SKA radio continuum survey of star forming regions is then outlined. This survey will produce radio light-curves for hundreds of young sources, providing for the first time a systematic survey of radio variability across the full range of stellar masses. These light-curves will probe the magnetospheric interactions of young binary systems, the origins of outflows, trace episodic accretion on the central sources and potentially constrain the rotation rates of embedded sources.

Advancing Astrophysics with the Square Kilometre Array
June 8-13, 2014
Giardini Naxos, Italy

*Speaker.

PoS(AASKA14)152

1. Introduction

The Atacama Large Millimeter/submillimeter Array (ALMA)[1] is the largest telescope yet constructed. Initial results from its early science observations span the range from the detection of a remarkable spiral patterned mass loss resulting from the interaction of an ABG star and its binary companion (Maercker et al. 2012) to constraining the density of extreme starburst galaxies at $z > 1$ (Karim et al. 2013). Here we focus on galactic star formation and the synergies provided by the complementarity of ALMA and SKA observations.

For studies of star formation, ALMA observations will trace how cold dust and gas is assembled on the small-scales within a molecular cloud and how disks around young stars are formed. SKA will be essential for complementing these studies by tracing the higher energy phenomena associated with the accretion of this material on to the star, probing the stellar and disk magnetospheres, and the ionising feedback from outflows and stellar winds. Combined, these cutting edge facilities will reveal the process of mass assembly and accretion onto young stars and will be revolutionary for studies of star formation.

2. Capabilities: ALMA and SKA

Comprising fifty four 12m diameter dishes plus twelve 7m diameter dishes, ALMA is an international collaboration between ESO, NRAO and NAOJ presenting Europe, North America and East Asia respectively in cooperation with the Republic of Chile. Operating between 30 GHz and 900 GHz (10 mm – 0.35 mm) in 10 frequency bands which span the available atmospheric windows to study the emission from cold dust and molecular gas, ALMA is located on the 5000m altitude Chajnantor plateau in northern Chile.

There were two key science drivers for the design of ALMA. The first is the imaging of the physical, chemical and magnetic structure of protostellar/protoplanetary disks around low mass protostars in the nearest star forming regions. The second is imaging of Milky Way-mass galaxies at $z = 3$ in CO or C^+ (the brightest tracers of molecular gas) in less than 24 hours. In parallel with these is the requirement to routinely deliver high precision images at an angular resolution of 0.1". With 8 GHz of instantaneous bandwidth, the ALMA correlator provides spectral resolutions up to maximum of 3.8 kHz, corresponding to a velocity resolution of 0.01 km/s at 110 GHz. In full operation ALMA with reach continuum noise levels of 1 mJy (at 110 GHz) in 1 second, corresponding to a mass of $\sim$0.004 $M_\odot$ per beam in the nearest star forming regions and $\sim 5\,M_\odot$ at 5 kpc. Figure 1 shows the angular size scale versus frequency coverage of ALMA compared with SKA1-Mid (and the NRAO Karl G. Jansky Very Large Array, JVLA). As the figure demonstrates, to probe similar angular scales as ALMA at frequencies above 60 GHz, requires frequency Band 5 on SKA1-Mid. As an indication of the range of physical scales relevant for studies of galactic star formation, the horizontal lines on the figure show the angular size required to image a hypercompact HII region, the earliest phase of massive star formation where ionised gas is detected, and a large circumstellar disk/toroid at the typical distance to molecular clouds in the molecular ring, ~ 5 kpc.

[1] www.almaobservatory.org

PoS(AASKA14)152

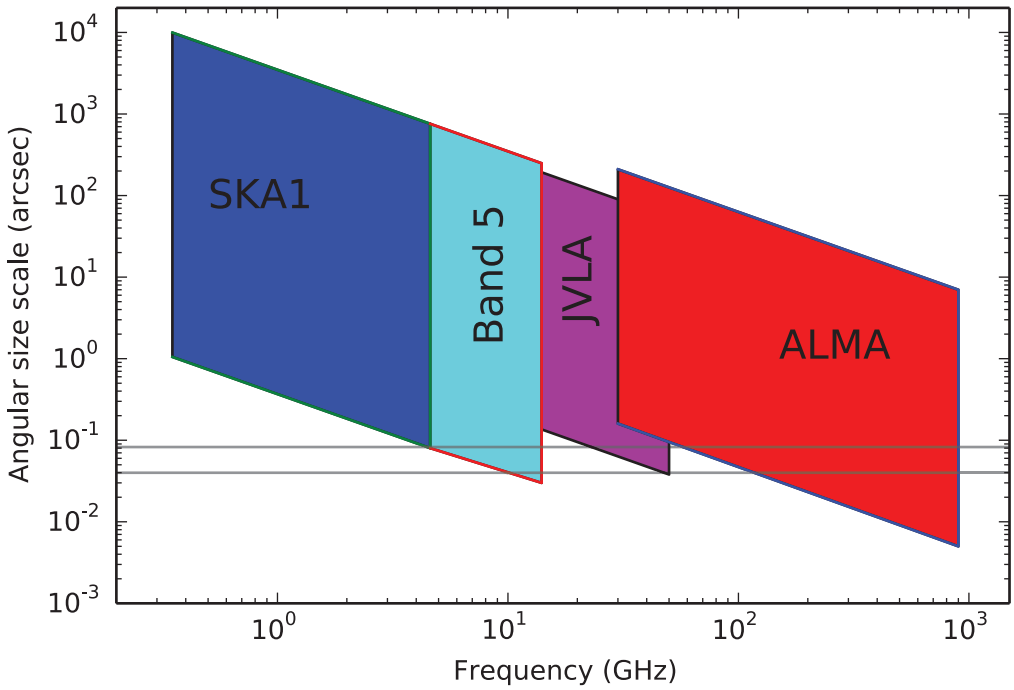

Figure 1: Angular size scale as a function of frequency for SKA1, JVLA and ALMA. Frequency band 5 on SKA1-Mid is identified separately. The shaded regions show the angular scale from the maximum resolution at each frequency to the instantaneous field of view. Larger angular size scales are of course accessible through mosaicing. The two horizontal lines indicate the resolution required to resolve a 0.01 pc-sized hypercompact HII region (upper) and a 1000 AU circumstellar disk/toroid (lower) at a distance of 5 kpc.

3. Tracing global collapse, disks and outflows

The ultimate fate of infalling material, and how stars actually gain mass, depends on the processes taking place on small spatial scales close to a forming star. Recent evidence suggests that the final stages of accretion on to the central star may be highly episodic. For example, ALMA observations of the chemical composition of the envelope around a low mass protostar shows evidence of heating associated with a burst of accretion 100-1000 years ago when the mass accretion rate was a factor of $\sim$ 100 above its current rate (Jørgensen et al. 2013).

On the large spatial scales, ALMA observations of the massive infrared dark cloud SDC335 (Peretto et al. 2013) show that the infalling dense gas seen in single dish images is confined to a number of filaments, allowing us to trace the large-scale global collapse. On the small scales, ALMA observations of high excitation lines of both complex organic species (Pineda et al. 2012) and simple species (Zapata et al. 2013) show infall profiles towards one component of the low mass protostellar binary IRAS16293. Indeed, measuring infall is a crucially important tool for understanding star formation: line profiles diagnostic of infalling gas (e.g. Anglada et al. 1987) have been identified towards starless cores (e.g. Lee et al. 1999), low mass protostars (e.g. Walsh et al. 2006), high mass young stellar objects (e.g. Fuller et al. 2005), UCHII regions (e.g. Ho &

PoS(AASKA14)152

Young 1996), and molecular filaments (e.g. Kirk et al. 2013).

Circumstellar disks are the mass reservoir out of which planets form. ALMA observations are elucidating the structure and composition of these disks with unprecedented detail. Observations of transition disks, relatively evolved disks with larger inner holes, have revealed large azimuthal asymmetries in the dust continuum emission at radii of $\sim 30-50$ AU (Casassus et al. 2013; van der Marel et al. 2013; Pérez et al. 2014). These asymmetries are interpreted as resulting from the trapping of dust in large anticyclonic vortices in the disk.

The growth of dust grains is a critical step towards planet formation which SKA will probe. Regions of disks where this growth may be occuring are revealed by ALMA observations, not only of the dust continuum emission, but also using molecular lines to trace the CO snowline, where CO condensed on to grain surfaces (Qi et al. 2013; Mathews et al. 2013). ALMA observations also reveal evidence for complex chemistry in a transition disk (van der Marel et al. 2014) as well the presence of a simple sugars (Jørgensen et al. 2012). Future SKA observations will be critical for the identification of complex organic species towards these objects.

Material in protoplanetary disks can be eroded by the winds and high energy radiation from nearby high-mass stars. To quantify this interaction, ALMA observations can probe molecular gas in the disk (Mann et al. 2014) while SKA can probe the photoionized gas flow from the disk as well as the interaction zone between the gas and the impinging stellar wind (e.g. Graham et al. 2002).

Outflows are an ubiquitous feature of star formation. Driven by winds and jets which originate from the inner disk/disk-star interface region (Li et al. 2014), they not only sculpt, and eventually clear the material around the protostar, but also inject energy into the surrounding medium and remove angular momentum. The bulk of the molecular line emission seen from outflows detected via ALMA observations (e.g. Arce et al. 2013) will trace material swept up by the stellar wind. The nature of the jets from stars evolves as the driving source evolves (Frank et al. 2014) but observations show the jets have a significant atomic component potentially observable by SKA in HI.

4. Accretion and Variability in Young Stars

Low-mass young stellar objects (YSOs) are thought to accrete mass via their circumstellar disks. Associated accretion shocks can be observed both when mass is accreted onto the disk and also when it is eventually accreted onto the central object (e.g. Hartmann 2009). The accretion process is observable at wavelengths ranging from the radio to the X-ray regime, including optical and infrared wavelengths. The connection of accretion and high-energy processes (e.g. Feigelson & Montmerle 1999) detected in both X-ray and radio emission has been highlighted by spectacular examples like V1647 Ori (Kastner et al. 2004), while spectral lines in the X-ray can provide an estimate of the the accretion rate (Brickhouse et al. 2012).

In the centimeter regime, accretion processes can be associated with both thermal (free-free) and nonthermal (gyrosynchrotron) radiation, as discriminated by their spectral and polarization properties. Generally, it is thought that the nonthermal radiation emanates from the magnetospheric structures in the innermost vicinity of YSOs while thermal emission most likely traces the bases of outflows and jets further away from the central object.

PoS(AASKA14)152

Recently there has been considerable observational progress in two relevant areas. First at centimeter wavelengths, new instrumentation, provided via the expanded capabilities of the JVLA, is rekindling protostellar radio astronomy. In tandem with these advances, a multi-wavelength, time-domain view of the dynamic processes in YSOs, including accretion is emerging. Well sampled time series datasets are now becoming available, in particular in the infrared. Simultaneously obtained multi-wavelength time series datasets are also becoming increasingly important to constrain the underlying physical processes.

4.1 Identifying radio counterparts to low-mass YSOs

Observations with the VLA initiated protostellar radio astronomy by providing excellent angular resolution to reliably identify radio counterparts to low-mass YSOs. While the first radio-detected YSOs identified by the VLA were found in the Orion Nebula Cluster (e.g. Moran et al. 1983; Garay et al. 1987), the radio sample remained incomplete, as indicated by the fraction of radio detected YSOs being consistently lower than the X-ray detection fraction (Forbrich & Wolk 2013).

Prior to the sensitivity upgrade of the VLA, only the most nearby star-forming regions could be studied in detail. The low-mass *Coronet* cluster at a distance of 130 pc is an example where almost all known YSOs in the inner cluster have radio counterparts (Brown 1987; Forbrich et al. 2006). This region was shown to host the first of only a few known protostars with confirmed nonthermal radio emission as inferred from circular polarization indicative of gyrosynchrotron emission (Feigelson et al. 1998; Choi et al. 2009).

The newly upgraded JVLA has already significantly advanced this research by providing a more complete census of YSOs detected at centimetre wavelengths (Dzib et al. 2013b; Kounkel et al. 2014). Indeed, with the improved JVLA, a more complete census of YSOs in nearby star-forming regions is emerging, both in terms of sensitivity and in area covered. Using rapid variability, negative spectral indices and polarization as indicators, a recent, large survey of ρ Oph revealed that about half of the identified YSOs show nonthermal emission (Dzib et al. 2013b).

Similarly, a recent large-scale (more than 2 square degrees) survey of the Orion Nebula Cluster, detected 374 sources at 4.5 GHz (Kounkel et al. 2014). Of these, 148 had been previously classified as YSOs and 86 additional sources are inferred to be new YSO candidates. With reliably determined spectral indices, these sources will be used as targets for follow-up VLBI observations to study parallaxes and proper motions. New and sensitive monitoring observations of the *Coronet* cluster show that the youngest sources in the sample are the brightest and least variable, possibly exhibiting mostly thermal wind emission (Liu et al. 2014).

4.2 Time variability

The significant increase in sensitivity provided by new JVLA observations is also starting to produce radio light-curves for YSOs. While YSO X-ray flares have been known for some time (e.g. Getman et al. 2008), very little is known about protostellar radio flares (Bower et al. 2003; Forbrich et al. 2008) and a possible X-ray–radio connection (e.g. Guedel & Benz 1993; Forbrich & Wolk 2013). As a result the physics of YSO radio flares is not currently well understood although they are thought to be produced by coronal-type activity in scenarios that also produce X-ray emission

PoS(AASKA14)152

(e.g. Drake et al. 1992). Some of the activity could also be directly or indirectly related to accretion. However, some YSO flares are thought to be due to the interaction of large magnetospheric features in close binary systems (e.g., V773 Tau: Massi et al. (2006) and DQ Tau: Salter et al. (2008); Getman et al. (2011) and references therein) or from periodic accretion bursts (Muzerolle et al. 2013; Balog et al. 2014; Bary & Petersen 2014).

Impressive time domain studies are now being carried out in the infrared. A 30-day *Spitzer* and *CoRot* photometric monitoring campaign of more than a thousand YSOs in NGC 2264 (Cody et al. 2014) classified a variety of different variability mechanisms in YSOs, mainly on timescales of days. Other recent work suggests that short-term optical variability may be due to enhanced accretion activity (Stauffer et al. 2014), while mid-infrared variability may be due to structural perturbations in the inner disk (Flaherty et al. 2013). Spectroscopic monitoring campaigns have also revealed a new level of complexity. Multi-epoch near-infrared spectroscopy of several accreting YSOs in ρ Oph observed as part of the *Spitzer* YSOVAR project, showed no correlation between the YSO mid-IR light curves and time-resolved veiling or mass accretion rates (Faesi et al. 2012).

4.3 Accretion onto high-mass stars

Strong magnetic fields and circumstellar disks are key drivers of the evolution of, and activity in, the inner circumstellar regions of low mass stars and there is growing evidence these important components are also present in young high-mass, $M > 8M_{\odot}$, stars. Keplerian disks have been detected through high angular resolution imaging of molecular lines around a number of B-type stars (e.g. Cesaroni et al. 2014; Beltrán et al. 2014) where, like their lower mass counterparts, they presumably play a role in the accretion of material on to the central star. Stellar magnetic fields in the range of hundreds to thousands of kG have also been measured towards OB stars (Nazé 2014). Since stellar magnetic fields are expected to decay away as the high-mass star evolves due to the absence of a convective zone, similar or stronger fields are likely present towards younger stars where they can play an important role in the rotational braking of the stars, setting their initial rotation rates (Meynet et al. 2011; Rosen et al. 2012). The presence of disks and strong magnetic fields suggest that young high-mass stars can show a similar range of circumstellar energetic phenomena as seen towards young low-mass stars, probing the final stages of mass inflow on to the central star as well as the launching of outflows.

Indeed non-thermal radio emission has been detected towards an increasing number of young high-mass stars (e.g. Andre et al. 1988; Rodríguez et al. 2012; Moscadelli et al. 2013; Rodríguez et al. 2014). This emission can arise from a range of phenomena including magnetospheric activity (such as due to variations in magnetically mediated accretion on to the central star), interacting winds in a massive binary system and synchrotron emission from a jet, all processes which are likely to be variable on a range of timescales as seen towards low mass sources (e.g. Dzib et al. 2013b). For example, a source in Orion has been seen to increase in flux by factor of 3 increase over 1 hour (Gómez et al. 2008).

Thermal radio emission from young high-mass stars arises from their ionised winds and their self-photoionised disks, envelopes and surroundings in the form of HII regions. The accretion flow into a HII region and on to forming massive stars will change the ionization balance and hence, flux and size of the ionised region. Such inflowing material will be clumpy and so the mass

PoS(AASKA14)152

accretion variable. This is borne out by simulations which show that the accretion rates onto stars has considerable time variability, with peak rates between 10 and 100 times higher than the time-averaged values (e.g. Klassen et al. 2012b). This variable inflow results in a flickering of the radio continuum emission of the HII regions around massive stars. The simulations by Galván-Madrid et al. (2011) found that about 10% of HII regions showed flux variations of 10% or more in 10 year timescales. A similar result was found by Klassen et al. (2012a). The radio variability of HII regions can therfore probe the structure and variability of the accretion into massive stars.

To date there have only been a very limited number of studies of the radio variability of HII regions. Galván-Madrid et al. (2008) identified a $\sim 45\%$ decrease in flux (at 5 GHz) of a hyper-compact HII (HCHII) region over a 5 year period due to enhanced accretion, while 10% of the ultracompact HII (UCHII) regions with Sgr B2 showed significant changes in flux over a timescale of 23 years (De Pree et al. 2014). The variable central source in W3(OH) has changed flux by a factor of 5 on timescales of 9 years (Dzib et al. 2013a) which is interpreted as due to changes in the ionised atmosphere of a circumstellar disk possibly due to changes in the accretion through the circumstellar disk.

The masers observed towards many embedded massive stars provide an additional sensitive probe of changes in the contiunuum emission of their exciting sources. For example, towards some sources the 6.7 GHz methanol maser emission varies periodically or quasi-periodically (Goedhart et al. 2014; Szymczak et al. 2014) which may reflect variations in either the free-free background radiation due to changes in the ionization of the circumstellar material or changes in the infrared pump radiation. Both of these effects may arise from periodic accretion from a circumstellar disk.

5. SKA1 Young Star Variability Survey

Both low- and high-mass young stars show centimetre radio continuum emission which is variable on a range of timescales from sub-hour to years and decades. This emission traces a range of phemonena associated with accretion, magnetospheric activity, and outflow which link the hot inner circumstellar regions with the infall and outflow of cooler material traced on larger scales by ALMA. SKA time domain continuum surveys of young stars will provide powerful probes of the inner circumstellar regions of young stars, opening new windows on the star formation process. For example, providing the first comprehensive studies of the properties of the episodic accretion in the inner circumstellar regions of forming massive stars.

In order to confirm the association of radio emission with a particular YSO in crowded cluster environments, as well as isolate the emission close to the central star, such a SKA survey will require sub-arcsecond angular resolution. In addition it will require near simultaneous wide multi-frequency coverage (Figure 2) to constrain the spectral index of the emission to discriminate between thermal and non-thermal emission as well as optically thick and optically thin emission. Measurements of the thermal emission in both the optically thick and thin regimes are important to distinguish between changes in size of the HII region and its ionization. Full Stokes synthesis will be important not only for confirmation of the presence of non-thermal emission, but also to allow the separation of thermal and non-thermal components of the emission.

Figure 2 shows the spectral flux distribution of young HII regions as well as thermal wind and synchrotron emission from lower mass stars. To distinguish between the possible emission

PoS(AASKA14)152

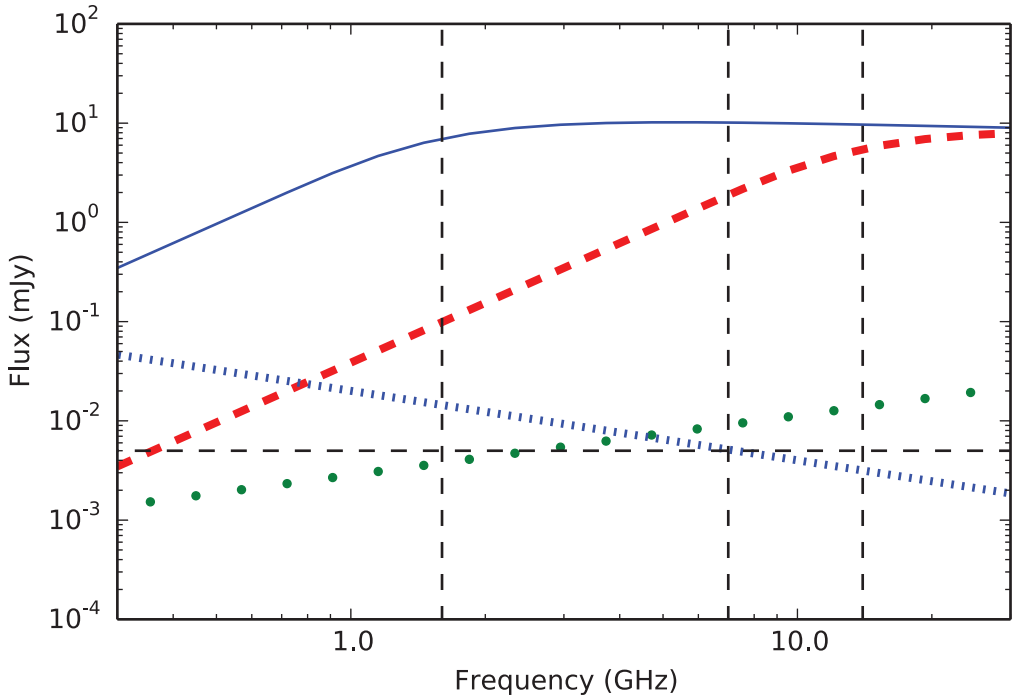

Figure 2: Spectral flux distribution for typical UCHII region (solid, blue curve) with an emission measure of 10^7 pc cm^{-6}, a typical HCHII region (dashed, red curve) with an emission measure of 10^9 pc cm^{-6}, a typical ionised wind (with the flux scaling as $\nu^{0.6}$) (green dots) and synchrotron emission $\propto \nu^{-0.7}$ (dotted, blue curve). The break in the spectrum of the UCHII and HCHII regions marks the transition between optically thin and optically thick emission. The wind and synchrotron emission are normalised to the 4.5 GHz measured flux of young stellar objects detected in Orion (Kounkel et al. 2014) scaled to a distance of 5 kpc. The vertical dashed lines indicate the survey frequencies while the horizontal dashed lines shows the survey 5-σ noise level (5 μJy).

mechanisms, observations at three frequencies are required. A proposed set of survey frequencies, 1.6 GHz, 7 GHz and 14 GHz, is shown on the figure. As well as providing good sampling of the continuum spectrum of the sources, these particular frequencies also cover several of the key maser transitions (ground state OH masers at 1.6 GHz, Class II methanol masers at 6.7 GHz and 12.2 GHz, and the H_2CO 2(1,1)– 2(1, 2) transition at 14.5 GHz[2]) which are themselves variable, in some cases periodically, and provide an additional, sensitive tracer of changes in the emission from the central sources. A summary of the parameters and the required observing time for a sample survey are given in Table 1.

To sample the range of physical phenomena which give rise to variable radio emission requires repeated observations with a wide range of cadences. Analysis of subsets of the observations will sample sub-hour variability due to flares arising from accretion or magnetospheric events (e.g. Salter et al. 2008; Massi et al. 2006) and rapidly rotating stars (Wolff et al. 2006) while daily to

[2]This line is not currently expected to be covered by SKA1 although this would be desirable. However, this frequency is expected to be available with the full SKA.

PoS(AASKA14)152

Frequency (GHz)	F_{src} (μJy)	σ (μJy)	θ (")	Time (hours/field)	Comments
1.6	14	1	0.5	5	Optically thick UCHII regions; synchrotron; OH ground state masers
7	9	1	0.5	2.5	Optically thin UCHII, thick HCHII; synchrotron-thermal wind cross over; 6.7 GHz methanol masers
14	14	1	0.5	2.5	Low optical depth HCHII; thermal wind emission; 12.2 GHz methanol masers; H_2CO transition

Table 1: SKA1 young star variability survey parameters. The columns show the frequency of observation, the target source flux (F_{src}) and rms flux noise levels (σ), the required angular resolution (θ) and the integration time per field. The comments indidate the emission probed and spectral lines which would be covered in the observations.

monthly observations will sample rotating stars and binary systems with longer periods. Longer observation intervals will sample processes ranging from outflow bursts to changes in the ionization, and therefore flickering, of HII regions due to accretion flows (Galván-Madrid et al. 2011).

The angular resolution of the survey is set by the requirement to isolate individual sources in crowded star forming regions and resolve the emission from individual HCHII regions with sizes ~ 0.02 pc out to at least the molecular ring at ~ 5 kpc. To connect the detailed studies which can be carried out in nearby star forming regions with the processes in the wider galactic plane requires that similar sources are detectable in both kinds of regions. Therefore the sensitivity required for each single observation is set by the need to sample a similar range of sources to those observed in nearby star forming regions such as Orion at the typical distance of a star forming region in the molecular ring, 5 kpc. To detect wind emission sources and synchrotron sources in the Orion star forming region (Kounkel et al. 2014) at 5 kpc implies a required noise level of 1 μJy at each of the observing frequencies (Fig. 2) which should provide detections of up to few hundred sources per star forming region.

Combining the observations at the different epochs will also provide a highly sensitive survey for faint sources including HII regions around relatively low mass stars. The combination of 14 GHz observations at 10 epochs would reach a noise level of $\sim 0.3\,\mu$Jy, sensitive at a 6-σ level to the HII regions from stars with masses as low as $6.5 M_\odot$ corresponding to a spectral type of B5 (Diaz-Miller et al. 1998).

6. Summary

A SKA time-domain survey of star forming regions will produce well sampled radio light-curves of hundreds of sources per star forming region. As is the case for infrared light-curves of young sources, these will undoubtably have a range of properties, tracing and constraining a range of phenomena. For example, the identification of rotationally modulated emission will provide the first observational constraints on the rotation rates of embedded protostars. Observations of the

PoS(AASKA14)152

flickering of HII regions will trace the inflow of material around the highest mass objects while flare activity in these, and other, sources can trace the final infall of material on to the central protostars. These observations can not only constrain the properties of the accretion but also the stochastic heating of the circumstellar regions which can surpress fragmentation (e.g. Krumholz et al. 2007), leading to the formation of more massive stars.

Looking forward to full SKA the factor 10 enhancement in sensitivity will enable studies of smaller (and therefore also shorter time scale) flux variations. Full SKA will also make stellar clusters to beyond the Galactic centre accessible to detailed time-domain studies, probing star formation over a much wider range of environments. The enhanced resolution of SKA will allow studies of the changes in morphology of the sources during their variation in flux, provide stronger constraints on the mechanisms involved and the models for the emission.

Building a comprehensive model for the formation of both low-mass and high-mass stars requires understanding the evolution of gas and dust from molecular clouds down through clumps and cores and eventually on to the forming stars. This is only possible with the combination of ALMA to trace the cool molecular gas and dust and SKA to follow this material into the inner circumstellar regions. The radio light-curves which SKA will produce for hundreds of sources in star forming regions out to 5 kpc will provide the first detailed insight across a wide range of stellar masses of the transient energetic phenomena occurring on the small spatial scales close to the central star. These light curves will for the first time provide a systematic survey which can study the magnetospheric interactions in young binary systems, tracing episodic accretion, the origin of outflows and potentially constrain the rotation rates of deeply embedded sources.

References

Andre, P., Montmerle, T., Feigelson, E. D., Stine, P. C., & Klein, K.-L. 1988, ApJ, 335, 940
Anglada, G., Rodriguez, L. F., Canto, J., Estalella, R., & Lopez, R. 1987, A&A, 186, 280
Arce, H. G., Mardones, D., Corder, S. A., et al. 2013, ApJ, 774, 39
Balog, Z., Muzerolle, J., Flaherty, K., et al. 2014, ApJ, 789, L38
Bary, J. S., & Petersen, M. S. 2014, ApJ, 792, 64
Beltrán, M. T., Sánchez-Monge, Á., Cesaroni, R., et al. 2014, A&A, 571, A52
Bower, G. C., Plambeck, R. L., Bolatto, A., et al. 2003, ApJ, 598, 1140
Brickhouse, N. S., Cranmer, S. R., Dupree, A. K., et al. 2012, ApJ, 760, L21
Brown, A. 1987, ApJ, 322, L31
Casassus, S., van der Plas, G., M, S. P., et al. 2013, Nature, 493, 191
Cesaroni, R., Galli, D., Neri, R., & Walmsley, C. M. 2014, A&A, 566, A73
Choi, M., Tatematsu, K., Hamaguchi, K., & Lee, J.-E. 2009, ApJ, 690, 1901
Cody, A. M., Stauffer, J., Baglin, A., et al. 2014, AJ, 147, 82
De Pree, C. G., Peters, T., Mac Low, M.-M., et al. 2014, ApJ, 781, L36
Diaz-Miller, R. I., Franco, J., & Shore, S. N. 1998, ApJ, 501, 192
Drake, S. A., Simon, T., & Linsky, J. L. 1992, ApJS, 82, 311
Dzib, S. A., Rodríguez-Garza, C. B., Rodríguez, L. F., et al. 2013a, ApJ, 772, 151
Dzib, S. A., Loinard, L., Mioduszewski, A. J., et al. 2013b, ApJ, 775, 63
Faesi, C. M., Covey, K. R., Gutermuth, R., et al. 2012, PASP, 124, 1137

PoS(AASKA14)152

Feigelson, E. D., Carkner, L., & Wilking, B. A. 1998, ApJ, 494, L215
Feigelson, E. D., & Montmerle, T. 1999, ARA&A, 37, 363
Flaherty, K. M., Muzerolle, J., Rieke, G., et al. 2013, AJ, 145, 66
Forbrich, J., Menten, K. M., & Reid, M. J. 2008, A&A, 477, 267
Forbrich, J., Preibisch, T., & Menten, K. M. 2006, A&A, 446, 155
Forbrich, J., & Wolk, S. J. 2013, A&A, 551, A56
Frank, A., Ray, T. P., Cabrit, S., et al. 2014, Protostars and Planets VI, 451
Fuller, G. A., Williams, S. J., & Sridharan, T. K. 2005, A&A, 442, 949
Galván-Madrid, R., Peters, T., Keto, E. R., et al. 2011, MNRAS, 416, 1033
Galván-Madrid, R., Rodríguez, L. F., Ho, P. T. P., & Keto, E. 2008, ApJ, 674, L33
Garay, G., Moran, J. M., & Reid, M. J. 1987, ApJ, 314, 535
Getman, K. V., Broos, P. S., Salter, D. M., Garmire, G. P., & Hogerheijde, M. R. 2011, ApJ, 730, 6
Getman, K. V., Feigelson, E. D., Broos, P. S., Micela, G., & Garmire, G. P. 2008, ApJ, 688, 418
Goedhart, S., Maswanganye, J. P., Gaylard, M. J., & van der Walt, D. J. 2014, MNRAS, 437, 1808
Gómez, L., Rodríguez, L. F., Loinard, L., et al. 2008, ApJ, 685, 333
Graham, M. F., Meaburn, J., Garrington, S. T., et al. 2002, ApJ, 570, 222
Guedel, M., & Benz, A. O. 1993, ApJ, 405, L63
Hartmann, L. 2009, Accretion Processes in Star Formation: Second Edition (Cambridge University Press)
Ho, P. T. P., & Young, L. M. 1996, ApJ, 472, 742
Jørgensen, J. K., Favre, C., Bisschop, S. E., et al. 2012, ApJ, 757, L4
Jørgensen, J. K., Visser, R., Sakai, N., et al. 2013, ApJ, 779, L22
Karim, A., Swinbank, A. M., Hodge, J. A., et al. 2013, MNRAS, 432, 2
Kastner, J. H., Richmond, M., Grosso, N., et al. 2004, Nature, 430, 429
Kirk, H., Myers, P. C., Bourke, T. L., et al. 2013, ApJ, 766, 115
Klassen, M., Peters, T., & Pudritz, R. E. 2012a, ApJ, 758, 137
Klassen, M., Pudritz, R. E., & Peters, T. 2012b, MNRAS, 421, 2861
Kounkel, M., Hartmann, L., Loinard, L., et al. 2014, ApJ, 790, 49
Krumholz, M. R., Klein, R. I., & McKee, C. F. 2007, ApJ, 656, 959
Lee, C. W., Myers, P. C., & Tafalla, M. 1999, ApJ, 526, 788
Li, Z.-Y., Banerjee, R., Pudritz, R. E., et al. 2014, Protostars and Planets VI, 173
Liu, H. B., Galván-Madrid, R., Forbrich, J., et al. 2014, ApJ, 780, 155
Maercker, M., Mohamed, S., Vlemmings, W. H. T., et al. 2012, Nature, 490, 232
Mann, R. K., Di Francesco, J., Johnstone, D., et al. 2014, ApJ, 784, 82
Massi, M., Forbrich, J., Menten, K. M., et al. 2006, A&A, 453, 959
Mathews, G. S., Klaassen, P. D., Juhász, A., et al. 2013, A&A, 557, A132
Meynet, G., Eggenberger, P., & Maeder, A. 2011, A&A, 525, L11
Moran, J. M., Garay, G., Reid, M. J., et al. 1983, ApJ, 271, L31
Moscadelli, L., Cesaroni, R., Sánchez-Monge, Á., et al. 2013, A&A, 558, A145
Muzerolle, J., Furlan, E., Flaherty, K., Balog, Z., & Gutermuth, R. 2013, Nature, 493, 378
Nazé, Y. 2014, in Putting A Stars into Context: Evolution, Environment, and Related Stars, ed. G. Mathys, E. R. Griffin, O. Kochukhov, R. Monier, & G. M. Wahlgren, 340–349
Peretto, N., Fuller, G. A., Duarte-Cabral, A., et al. 2013, A&A, 555, A112

PoS(AASKA14)152

Pérez, L. M., Isella, A., Carpenter, J. M., & Chandler, C. J. 2014, ApJ, 783, L13
Pineda, J. E., Maury, A. J., Fuller, G. A., et al. 2012, A&A, 544, L7
Qi, C., Öberg, K. I., Wilner, D. J., et al. 2013, Science, 341, 630
Rodríguez, L. F., González, R. F., Montes, G., et al. 2012, ApJ, 755, 152
Rodríguez, L. F., Masqué, J. M., Dzib, S. A., Loinard, L., & Kurtz, S. E. 2014, Rev. Mexicana Astron. Astrofis., 50, 3
Rosen, A. L., Krumholz, M. R., & Ramirez-Ruiz, E. 2012, ApJ, 748, 97
Salter, D. M., Hogerheijde, M. R., & Blake, G. A. 2008, A&A, 492, L21
Stauffer, J., Cody, A. M., Baglin, A., et al. 2014, AJ, 147, 83
Szymczak, M., Wolak, P., & Bartkiewicz, A. 2014, MNRAS, 439, 407
van der Marel, N., van Dishoeck, E. F., Bruderer, S., & van Kempen, T. A. 2014, A&A, 563, A113
van der Marel, N., van Dishoeck, E. F., Bruderer, S., et al. 2013, Science, 340, 1199
Walsh, A. J., Bourke, T. L., & Myers, P. C. 2006, ApJ, 637, 860
Wolff, S. C., Strom, S. E., Dror, D., Lanz, L., & Venn, K. 2006, AJ, 132, 749
Zapata, L. A., Loinard, L., Rodríguez, L. F., et al. 2013, ApJ, 764, L14

PoS(AASKA14)152

PROCEEDINGS OF SCIENCE

The connection between radio and high energy emission in black hole powered systems in the SKA era

M. Giroletti*[a], M. Orienti[a], F. D'Ammando[a,b], F. Massaro[c], G. Tosti[d] on behalf of the *Fermi*-LAT collaboration, and R. Lico[a,b], G. Giovannini[a,b], I. Agudo[e], A. Alberdi[f], H. Bignall[g], M. Pandey-Pommier[h], A. Wolter[i]

[a]*INAF Istituto di Radioastronomia, Bologna, Italy;* [b]*University of Bologna, Italy;* [c]*University of Turin, Italy;* [d]*University of Perugia, Italy;* [e]*Joint Institute for VLBI in Europe, The Netherlands;* [f]*Instituto de Astrofisica de Andalucia, Spain;* [g]*Curtin Institute of Radio Astronomy, Australia;* [h]*Observatoire de Lyon, France;* [i]*INAF-Osservatorio Astronomico di Brera, Italy*
E-mail: giroletti@ira.inaf.it

Strong evidence exists for a highly significant correlation between the radio flux density and $E >$ 100 MeV gamma-ray energy flux in blazars revealed by the *Fermi* Gamma-ray Space Telescope. However, there are central issues that need to be clarified in this field: what are the counterparts of the about 30% of gamma-ray sources that are as yet unidentified? Are they just blazars in disguise or they are something more exotic, possibly associated with dark matter? How would they fit in the radio-gamma ray connection studied so far? the radio-gamma ray connection, given that most gamma-ray sources are highly variable? With their superb sensitivity, SKA1-MID and SKA1-SUR will help to resolve all of these questions. Even more, while the radio-MeV/GeV connection has been firmly established, a radio-VHE (Very High Energy, $E > 0.1$ TeV) connection has been entirely elusive so far. The advent of CTA (Cherenkov Telescope Array) in the next few years and the expected CTA-SKA1 synergy will offer the chance to explore this connection, even more intriguing as it involves the opposite ends of the electromagnetic spectrum and the acceleration of particles up to the highest energies. We are already preparing to address these questions by exploiting data from the various SKA pathfinders and precursors. We have obtained 18 cm European VLBI Network observations of $E > 10$ GeV sources, with a detection rate of 83% (and higher than 50% for the unidentified sources). Moreover, we are cross correlating the *Fermi* catalogs with the Murchinson Widefield Array commissioning survey: when faint gamma-ray sources are considered, pure positional coincidence is not significant enough for selecting counterparts and we need an additional physical criterion to pinpoint the right object. It can be radio spectral index, variability, polarization, or compactness, needing high angular resolution in SKA1-MID; timing studies can also reveal pulsars, which are often found from dedicated searches of unidentified gamma-ray sources. SKA will be the ideal instrument for investigating these characteristics in conjunction with CTA. A proper classification of the unidentified gamma-ray sources and the study of the radio-gamma ray connection will be essential to constrain the processes at work in the vicinity of super massive black holes.

Advancing Astrophysics with the Square Kilometre Array
June 8-13, 2014
Giardini Naxos, Italy

*Speaker.

PoS(AASKA14)153

1. Introduction

Blazars are the rarest and most extreme class of Active Galactic Nuclei (AGN). They are radio loud sources, characterized by the presence of a relativistic pair of plasma jets whose axis is closely aligned with our line of sight. The ultimate source of their huge energetic output (bolometric isotropic luminosity reaching up to 10^{49} erg s^{-1} in the most extreme events) is the gravitational potential of a super massive black hole (SMBH, with mass up to $M_{\rm BH} \sim 10^9 M_\odot$). Blazars radiate across the entire electromagnetic spectrum, with a typical two-humped spectral energy distribution (SED). On the basis of their optical spectra, blazars are divided into flat spectrum radio quasars (FSRQs, with prominent emission lines) and BL Lac type objects (BL Lacs, with featureless optical spectra). Moreover, blazars are often classified according to the peak frequency of the synchrotron component of their SED, as low-synchrotron peaked (LSP, with $\nu_{\rm peak} \leq 10^{14}$ Hz), intermediate-synchrotron peaked (ISP, with 10^{14} Hz $\leq \nu_{\rm peak} \leq 10^{15}$ Hz), or high-synchrotron peaked (HSP, $\nu_{\rm peak} \geq 10^{15}$ Hz) sources, with FSRQs being in general of the LSP type. In addition to the different optical spectra and SED, the two subclasses have other differences in observational and evolutionary properties.

Despite being the rarest class of AGN, blazars dominate the census of the gamma-ray sky at high and very high energy (VHE, $E > 0.1$ TeV). In the last years, there has been a tremendous progress in the understanding of the physical properties of blazars thanks to the advent of the *Fermi*-Large Area Telescope (LAT) and its synergy with a large number of multi-wavelength (MWL) facilities across the electromagnetic spectrum. In particular, monitoring projects in the radio (MOJAVE, Boston University monitoring, F-GAMMA, VIPS) have provided strong information about blazar physics, and in some cases possibly imaged the gamma-ray emission zone itself (e.g. Agudo et al., 2011). With further advances expected thanks to the construction and operation of the Cherenkov Telescope Array (CTA) at VHE, significant efforts remain necessary for a conclusive answer on the many open questions in blazar physics, including fundamental issues such as where and how the gamma-ray emission is produced. Moreover, a significant fraction of gamma-ray sources, both at HE and VHE, lacks a proper association to known astrophysical objects; it is important to understand if these sources are just blazars in disguise or more intriguing kinds of objects, possibly related to dark matter annihilation or other exotic physical processes.

The Square Kilometre Array (SKA) will be a fantastic instrument to help address these points. Indeed, understanding the blazar phenomenon inevitably requires a characterization of the physical properties of relativistic jets, which are the subject of other Chapters of this book (e.g. Agudo et al., 2015). In the present Chapter, in particular, we plan to highlight how the SKA project will shed light on the properties of gamma-ray sources as a population, starting from ongoing and incipient works with pathfinders and precursors, continuing with the SKA itself in its phase 1 and ultimately with the full sensitivity and frequency range that will be available in phase 2. This Chapter is organized as follows: in Section 2, we present an outline of the current and planned HE and VHE surveys; in Section 3, we review the state of the art about the connection between radio and gamma-ray emission (3.1) and the search for unidentified gamma-ray source (UGS) counterparts (3.2); a sample ongoing topics are presented in Section 4; in Section 5, we finally deal with the prospects for SKA in these areas. Further topics are discussed in other Chapters of this book (Agudo et al., 2015; Bignall et al., 2015; Corbel et al., 2015; Donnarumma et al., 2015; Paragi et al., 2015;

PoS(AASKA14)153

Turriziani et al., 2015), as the connection between radio and high energy emission in black hole powered system (both stellar and super massive) is of great interest and has implications on many other areas of astrophysics.

2. Gamma-ray instruments and census

2.1 High energy gamma rays (10 MeV $< E <$ 300 GeV)

Blazars have dominated the census of gamma-ray sources (particularly at high galactic latitude) since the Compton Gamma Ray Observatory (CGRO) mission in the 1990's. This evidence has further strengthened in recent years, thanks to the ongoing AGILE (Tavani et al., 2009) and *Fermi* (Atwood et al., 2009) missions. In particular, the LAT onboard *Fermi* is a pair-conversion gamma-ray telescope sensitive to photon energies from about 20 MeV up to $>$ 300 GeV, with a large field of view (2.4 sr) and a relatively narrow point spread function (PSF) of $0^\circ.6$ (for a single photon, at 1 GeV). For most of its operations since launch, the LAT has operated in all-sky survey mode, completing a number of catalogs with increasing sensitivity (Abdo et al., 2009a, 2010a; Nolan et al., 2012) and providing the opportunity to study gamma-ray light curves and time resolved spectra at a variety of time scales for a large number ($\sim 10^3$) of sources. The next planned release is the third *Fermi* catalog of gamma-ray sources, based on 4 years of data, and consisting of $\sim$ 3 000 sources (Thompson et al., 2014).

The AGN population of each *Fermi* catalog is described in accompanying dedicated papers, the most recent of which is the second LAT AGN catalog (2LAC, Ackermann et al., 2011b). In the 2LAC "clean" sample[1], there are 886 active galaxies, accounting for 47% of the total number of *Fermi* sources. Of these 886, 395 are BL Lacs, 310 are FSRQs, 157 are blazars of unknown type (typically because of the lack of an optical spectrum of adequate quality), and 24 are AGNs of other type. The latter group includes 8 so-called misaligned AGNs (typically radio galaxies with small-to-intermediate jet viewing angle, see e.g. Abdo et al., 2010b), 4 radio loud narrow-line Seyfert 1 (NLS1, Abdo et al., 2009b), 2 galaxies dominated by starburst activity, and 10 more sources not yet fully characterized. *Fermi* BL Lacs and FSRQs differ in many observational properties, such as photon index (with the BL Lacs being on average harder than FSRQs), luminosity (with FSRQs being more powerful than BL Lacs), and variability; the most distant *Fermi* FSRQs in the 2LAC is located at a redshift $z = 3.10$, while BL Lacs have typically lower redshift, as HSP in particular show strong negative evolution (Ajello et al., 2014); a significant fraction of BL Lacs however lack a redshift measurement. When sources are classified according to the peak frequency of the synchrotron component of their SED, the numbers of LSP, ISP, and HSP blazars in the 2LAC are 301, 95, and 213, respectively.

Beside blazars, pulsars are the second largest population of associated gamma-ray sources in the 2FGL; interestingly, pulsars are also generally bright radio sources and they are indeed one major subject for SKA studies, as discussed in other Chapters. A few systems associated to accretion and ejection around stellar mass black holes (including microquasars, X-ray and gamma-ray binaries) are also found at high energy. However, the total number of pulsars and other associated

[1]The "clean" sample contains only high-latitude ($|b| > 10^\circ$) sources, with a single AGN association, and without analysis flags. The total number of 2FGL sources associated with AGNs is 1121, i.e. 60% of the total.

PoS(AASKA14)153

sources besides blazars reaches only 195 (55 at $|b| > 10°$), while the majority of the remaining sources are so far unassociated (31% of the total). The existence of a large fraction of UGSs has been around since the EGRET era, although its composition has changed a lot given the higher sensitivity and better localization provided by *Fermi*, and the vastly improved MWL catalogs at all other wavelength.

2.2 Very high energy gamma rays ($E > 100$ GeV)

At larger energies, the sensitivity of space detectors is not adequate and observations are carried out on the ground through the detection of Cherenkov radiation triggered by VHE photon interactions in the atmosphere. Current generation of VHE Imaging Atmospheric Cherenkov Telescopes (IACT) exploits the stereoscopic technique to improve sensitivity and characterization of the event, and is implemented in three major observing arrays MAGIC, HESS, and VERITAS. These arrays and their predecessors have so far detected 147 sources, which are listed in the so-called TeVCat catalog[2].

The census of VHE sources is again dominated by (occasionally misaligned) blazar sources, with BL Lacs, FSRQs, and FRI radio galaxies accounting for 38% (58/147) of the total population (a fraction that becomes significantly larger at high galactic latitudes). However, the overall properties of the VHE blazar population are markedly different from those at lower energy. BL Lacs, and in particular HSP blazars, are the most numerous class, with 50 detected sources, 42 of which are of the HSP type. Only 3 FSRQs are known, with the most distant one being 3C 279 at $z = 0.536$. The typical luminosity is much lower than for *Fermi* blazars, and the redshift distribution is also very different, being most sources at a very low redshift. This is both a consequence of their physics and of the absorption through photon-photon interaction with the extragalactic background light (EBL) being more pronounced for more distant sources.

The fraction of unidentified sources is 18%. One significant difference between IACTs and *Fermi* is that the latter operates in survey mode, while the formers generally do pointed observations. This generally produces a bias in the selection of the VHE targets, and it is to be expected that many more unidentified sources would be discovered in a blind survey, which could be possible with the advent of CTA.

3. State of the art

3.1 The radio-gamma ray connection

As radio loud sources dominate the extragalactic gamma-ray population, it is clear that there is a connection between radio and high energy emission, physically originated by the presence of a relativistically beamed jet emerging from a SMBH. However, not all blazars are detected in gamma rays, and in particular at VHE the most luminous radio sources are hardly, if ever, detected by current instruments. Several works since the 1990's have attempted to reveal the details of such a connection (e.g., Padovani et al., 1993; Stecker & Salamon, 1996; Mücke et al., 1997; Ghirlanda et al., 2010; Mahony et al., 2010). The most extensive work dealing with the radio/gamma-ray connection at MeV/GeV energy is the one by Ackermann et al. (2011a, see also Fig. 1, left panel),

[2] `http://tevcat.uchicago.edu/`

PoS(AASKA14)153

based on 599 sources detected in the first catalog of *Fermi* AGN (1LAC, Abdo et al., 2010c). In this work, we applied a dedicated statistical tool (Pavlidou et al., 2012) to establish the strength and significance of the correlation between radio flux density and gamma-ray energy flux using archival and concurrent radio data, considering different gamma-ray energy bands, and analysing the whole *Fermi* AGN population as well as all the different blazar sub-classes. The main findings are as follows: radio flux density and gamma-ray energy flux are correlated with a very high significance (chance probability $< 10^{-7}$) in the whole 1LAC blazar sample, as well as for BL Lacs and FSRQs separately; gamma-ray data correlate better with concurrent radio data than with archival ones; there is a low significance hint of a trend between blazar SED type and strength of the correlation in gamma-ray sub-bands.

However, even in the most significant cases, the correlation itself shows a large scatter, and the distribution of data points is very broad, especially at low fluxes and near the sensitivity limit of the *Fermi* survey. Therefore, it is misleading to use such correlation to extrapolate gamma-ray luminosity functions from the radio ones. Future improvements could be obtained through the use of substantially deeper gamma-ray data (such as those that will be available at the end of the *Fermi* mission) and/or shorter wavelength radio emission, which is produced on regions closer to the gamma ray emission site and could provide a tighter correlation (Agudo et al., 2014). In any case, direct use of the blazar gamma-ray luminosity function will remain more accurate, while estimate based on the radio-gamma correlation might apply to radio galaxies and star forming galaxies.

As far as the radio-VHE connection is concerned, the situation is even more complex. Physically, it is natural to expect an anti-correlation between VHE and radio luminosity, since the most powerful radio sources tend to have low-frequency peaked SEDs, soft gamma-ray photon indexes, and to suffer strong EBL absorption due to their large distance. Moreover, the IACTs operational mode introduces significant biases in the target selection, so that a complete survey and a statistically significant assessment of any radio-VHE correlation are precluded. In any case, it is still confirmed that the majority of VHE detected sources are indeed radio loud blazars.

3.2 Un-associated gamma-ray sources

Overall, about 30% of *Fermi* sources lack a high-confidence low-frequency counterpart. This fraction is not constant among gamma-ray flux bins, as it becomes larger for faint gamma-ray sources. First, the gamma-ray error ellipse is larger; moreover, on the basis of the radio-gamma ray correlation described above, faint gamma-ray sources are likely associated with low flux density radio sources, whose space density is larger and which often lack an optical spectrum. Therefore, it is likely that many weak gamma-ray blazars remain unrecognized because their low-frequency counterpart can not reach the statistical significance necessary to call a formal association. There are various ways to get around this difficulty at present. The logical approach would favour the use of all-sky high-frequency radio surveys, as radio sources other than blazars are rare at high frequency. However, large and deep high-frequency surveys are very difficult in practice: the most valuable resource so far in this field is the Australia Telescope 20 GHz (AT20G) survey, with its catalog going down however only to a flux-density limit of 40 mJy (Murphy et al., 2010).

A complementary approach aims to the selection of blazars based on some characteristic spectral features, such as the infrared colors or the low frequency spectral index. In this way, it is possible to exploit existing large and comparatively deep surveys, where blazars are generally a

PoS(AASKA14)153

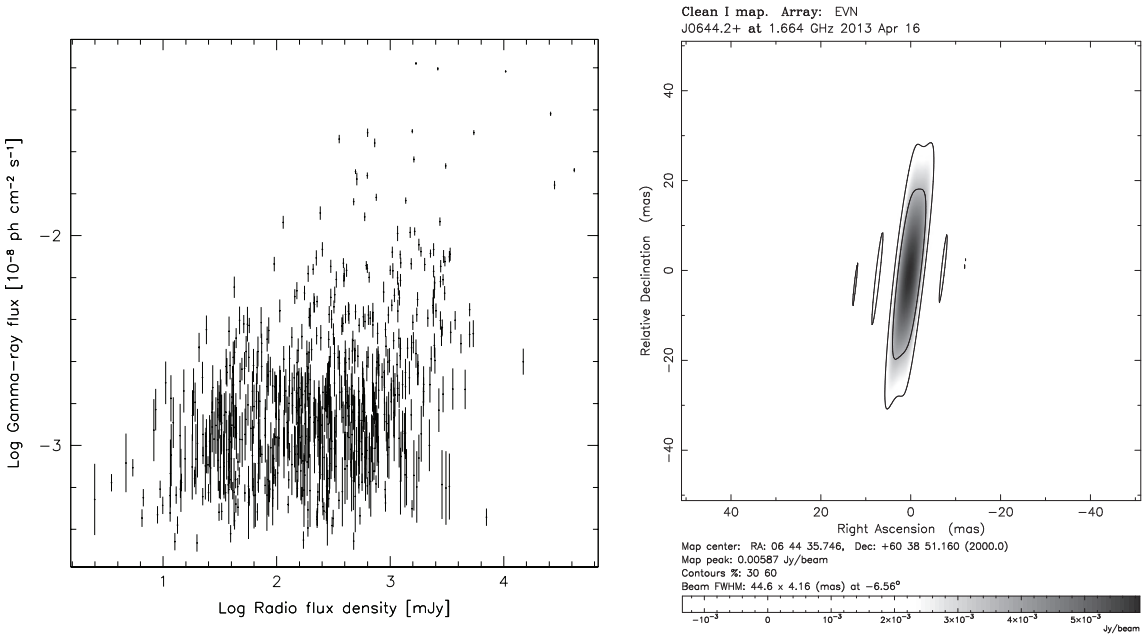

Figure 1: Left: gamma-ray vs radio flux for 1LAC sources, adapted from Ackermann et al. (2011a). Right: EVN 18cm image of NVSS J064435+603849, showing a compact source possibly associated to the UGS 2FGL J0644.2+6036.

minority population. For example, Massaro et al. (2011) and D'Abrusco et al. (2013) have shown how blazars form a so-called *strip* in the IR color space and have exploited this feature to propose new IR counterparts for $\sim 20\%$ of the UGSs investigated (Massaro et al., 2013a). Similarly, Massaro et al. (2013b,c) have demonstrated that blazars maintain a flat spectral index well below $\nu < 1$ GHz, and proposed 31 new blazar associations (see also Nori et al., 2014). We are also investigating the low frequency morphology of *Fermi* blazars through high angular resolution images obtained at the Giant Metrewave Radio Telescope (GMRT).

4. Some pathfinder projects

4.1 EVN survey of 1FHL sources

Before dealing with the SKA outcomes in this area, it is worthwhile to highlight some of the results that are being made possible by the SKA pathfinder and precursors. In section 3.1, we briefly discussed how the assessment of a correlation between radio and VHE emission is affected by the IACT observational mode. Eventually, CTA will offer the opportunity to overcome this difficulty thanks to a uniform survey simultaneous to the SKA operations; at present time, the most useful resource in this field is probably the first *Fermi*-LAT catalog of 514 sources detected above 10 GeV (1FHL, Ackermann et al., 2013), based on LAT data accumulated during the first three years of survey. While of course not being entirely representative of the VHE population, the 1FHL indeed provides a sample whose average properties are quite different from those of the full-band *Fermi* catalogs: the SED-based classification starts to lean towards HSP types (with 99, 71, and

PoS(AASKA14)153

162 sources of the LSP, ISP, and HSP types respectively); the redshift distribution only extends out to $z = 2.5$, and the overall luminosities are generally lower. The fraction of unidentified sources is low, just 13%.

We are now investigating the 284 1FHL sources at $\delta > 0^\circ$ with the use of high angular resolution Very Long Baseline Interferometry (VLBI) radio observations. We note that VHE blazars tend to display peculiar VLBI properties, e.g. comparatively low brightness temperature and lack of superluminal motions (Piner et al., 2008; Lico et al., 2012), which are otherwise common in MeV/GeV blazars. In particular, we have observed with the European VLBI Network (EVN) at 1.7 GHz the sky regions of the 71 northern 1FHL sources without any existing VLBI data but with at least one NVSS source in the *Fermi* error ellipse. Of these, 49 are classified as blazars, one is a supernova remnant, the remaining 21 are unassociated sources. While a detailed presentation of the observations and discussion of the results is given in a dedicated paper (Giroletti et al., 2014), we highlight here some of the most relevant finding, also in perspective of actual SKA observations. For sources classified as blazars, we have a detection rate of 100%, confirming that parsec scale cores are ubiquitous in gamma-ray blazars; eventually, this will allow us to explore the existence of a correlation between radio and $E > 10$ GeV gamma-ray flux using high resolution, concurrent data, which is clearly desirable. For the unassociated sources, we have a relatively high detection rate (preliminarily, 11/21) of compact components; given the low space density of milliarcsecond scale sources, they are most likely the true counterparts of the 1FHL sources, and our data provides important information for follow-up studies and a proper classification. Interestingly, among the unassociated sources there are four objects that are also present in the 2FGL and for which there is a blazar candidate selected with the low-frequency spectral index method described in 3.2: for all of them, we find a compact radio source, which further supports their blazar nature and the validity of the method (see e.g. NVSS J064435+603849 in the right panel of Fig. 1).

4.2 MWA-*Fermi* catalog cross correlation

Blazar catalogs become rather incomplete around ~ 10's mJy flux density levels, because of the technical difficulty in going deep at high radio frequency and of the large number of contaminating steep-spectrum radio sources at low radio frequency. Additional constraints can be used to narrow the number of blazar candidates at low frequency, like we did on the basis of the flat radio spectrum. Thanks to the SKA pathfinders and precursors, there will soon be several sensitive, wide area, low frequency surveys, ideal for this scope. In particular, even in its early commissioning phase, the Murchinson Widefield Array (MWA) has surveyed approximately 9 hr in R.A. over a declination range of 45° at three different frequencies (119, 150 and 180 MHz). Of order 10,000 sources were detected at 5σ above the confusion noise limit, determining a flux and spectral index for each of them (Hurley-Walker et al., 2014; Morgan et al., 2014). We are currently cross-correlating this catalog against the 2FGL and 3FGL, with the goals of (1) verifying whether the radio-gamma ray correlation extends at very low radio frequency, (2) characterizing the spectral properties of known blazars in this unexplored window of the electromagnetic spectrum, and (3) searching for counterparts to unidentified gamma-ray sources among the low frequency population.

PoS(AASKA14)153

5. SKA prospects

SKA will surely be a game changer for the topics described in this Chapter, starting from its Phase 1 (SKA1) and even in the early science phase. We can anticipate at least two major well-defined projects that shall be carried out in phase 1: the first one (5.1) deals with the identification and characterization of as large a fraction as possible of the MeV/GeV and the VHE populations, and the second one (5.2) does then address the implications on the physics of gamma-ray sources, and in particular of relativistic jets supported by SMBH.

For SKA1 specifications, we consider SKA1-MID observations in Bands 1, 3, and 5 (350-1050 MHz, 1.65-3.05 GHz, and 4.6-13.8 GHz), and SKA1-SUR data from Phased Array Feed (PAF) in the 1.5-4.0 GHz range. Since blazars are continuum emission sources with flat spectrum, the choice of bands can reasonably be adjusted; however, it would be highly desirable to keep the highest frequency bands (4.6-13.8 GHz for SKA1-MID, and possibly 1.5-4.0 GHz for SKA1-SUR), where there is less contamination from steep spectrum sources and de-polarization effects are less severe. Indeed, polarization has not been discussed so far in this Chapter but it will be a very important probe to the physics (see also the Chapter by Agudo et al. 2015). The full band and the longest baselines provided by SKA2 will provide further critical information (5.3).

5.1 SKA1 & the identification and characterization of gamma-ray sources

The fraction of UGS in the MeV/GeV domain is around 30% at present and it is essential to understand how many of these sources are known gamma-ray emitters yet to be identified and how many are related to unknown classes and/or to exotic physics. By the time SKA will be operational, *Fermi* shall have completed at least a 10 year survey, revealing $\sim 10^3$ UGS. At the same time, CTA will be starting its operation, and in particular if it will carry out even a moderately shallow wide area survey, it will reveal a large number (probably several $\times 10^2$) of new, possibly weak and/or transients VHE sources. While continuum sensitivity of existing interferometers is already reasonably suited for the detection of classical gamma-ray blazars, the SKA1 characteristics (wide field, polarimetry, bandwidth, timing) will be essential for a full characterization of the UGS sources.

A first, fundamental step will consist in the build up of a complete and deep blazar catalog, *based on SKA1-SUR in the band 1.5-4.0 GHz*. Sensible choices for selecting blazars in this frequency range would be a spectral index $\alpha < 0.5$ and a polarization fraction $p > 0.5\%$. Assuming an instantaneous bandwidth of 500 MHz and the typical PAF sensitivity, it will be possible to extend surveys such as the Combined Radio All-Sky Targeted Eight GHz Survey (CRATES, Healey et al., 2008) by at least one magnitude, going down to ~ 5 mJy completeness, with the additional benefit of polarization information. CRATES has been a powerful resource in identifying blazars in the early releases of the *Fermi* catalogs but it has become more and more incomplete as counterparts became fainter and fainter. In addition to pulsar searches which will further diminish the number of UGS, the fraction of UGS will be significantly reduced. Ackermann et al. (2012) used a statistical method to propose a blazar or pulsar origin for more than half of the 1FGL UGS, and MWL data generally confirm the proposed classifications. Similarly, we can predict that a significant fraction (possibly around 50%) of the still unassociated *Fermi* sources will be actually classified thanks to SKA1-SUR observations. We also expect a strong synergy with total intensity and polarization surveys from the radio continuum and cosmic magnetism working groups. Identification of transient

PoS(AASKA14)153

sources such as microquasars or novae star will also be facilitated by SKA1, already in its early operation phase.

The build up of a complete gamma-ray blazar (and pulsar) catalog will have important scientific implications by itself (see 5.2); moreover, it will allow us to select by difference a population of truly exotic gamma-ray sources, belonging to so far unknown classes of gamma-ray emitters. For both the newly discovered blazars and the remaining "exotic" UGS, dedicated *multi-λ, multi-epoch SKA1-MID observations* will provide a better characterization of their spectral, variability, structural, and polarization properties. The same approach will of course be adopted for VHE sources detected by CTA, with the additional benefit of simultaneous operations between the two instruments: SKA and CTA will have significant analogies, from the large collecting areas, the remarkable jump in sensitivity with respect to existing instrumentation, the capability to detect transient sources, the multi-fold design (with different parts of the instrument working with different specifications and science goals), the requirements in terms of computational and data storage resources, and the international nature of the projects themselves.

5.2 SKA1, the radio-gamma ray connection and its physical implications

As a result of a longer exposure as well as a better characterization of both the instrument response function and the diffuse background model (Grove et al., 2014), the final 10-yr catalog of *Fermi* blazars will likely reach a sensitivity limit nearly one magnitude deeper than the 1LAC. An even larger improvement is expected in the VHE band thanks to CTA. With high quality radio data from SKA1 it will thus be possible to clarify the still open points on the radio-gamma ray correlation in the MeV/GeV band and to address for the first time the one with VHE gamma rays. There are various issues for which a definite answer could be reached: the different trends obtained for blazar spectral types, redshift bins, gamma-ray energy bands, and epoch of multi-λ data will in turn provide constraints on the processes of high energy emission, blazar evolution, size of the emitting region, duty cycle and variability nature of blazars. For instance, the comparison of polarized radio flux density and gamma-ray energy flux can reveal if and how the magnetic field intensity is actually relevant for the gamma-ray emission (through inverse Compton scattering on synchrotron photons), a link that can not be studied systematically with the sensitivity of present instruments. Moreover, and in particular for the radio-VHE connection, simultaneous radio and gamma-ray observations should be relatively easy with an SKA-CTA synergy thanks to the sensitivity, flexibility, and sub-arraying capability of SKA1-MID; this will reveal how much of the scatter in the correlation is due to non-simultaneity, and therefore provide insights on the size and relative distance between the radio and gamma-ray emission regions. Additional statistical tests could be carried out by comparing the gamma-ray properties not only to the radio flux density but also to other properties such as the spectral index and the polarization percentage, which can trace the compactness, core dominance, and magnetic field configuration of the gamma-ray emitting zone.

For all the above goals it is critical to obtain radio data of high quality for a large number of sources: sub-mJy, polarization sensitive, arcsecond resolution, multi-frequency and possibly multi-epoch data for ~ 2000 sources (we focus only on the southern sky) will be necessary. It is important to note that the new sources with a low flux density could be either high redshift or low power sources. Either way, they would not just provide an increased statistic for existing studies but actually probe new regions of the space of parameters with respect to currently known gamma-ray

PoS(AASKA14)153

blazars. A full survey of this population would be well feasible with SKA1-MID: the faintest blazar in the 2LAC (2FGL J0912.5+2758) has a flux density $S = 4.2$ mJy; we can conservatively assume a value about $10\times$ lower for the faintest blazar detected by *Fermi* in its entire mission. Based on a 30 μJy s^{-1} minimum detectable flux density for SKA1-MID Band 5 (Dewdney et al., 2013, Table 9), the time requested for a survey of all the visible *Fermi* AGNs down to the faintest one would be mostly driven by slewing time. With clever scheduling and sub-arraying, no more than a few hours would be necessary. If we aim for detection of polarized emission at the 1% level, only the faintest ~ 100 or so of blazars would require non-negligible observing time, but the entire project would not be significantly expanded. Even in an early science phase providing $\sim 50\%$ of the SKA1 baseline design, this project could be carried out without significant trouble; actually, this is an ideal project for early SKA1 phases since it could permit (nearly) concurrent SKA1-*Fermi* observations.

Finally, we note that the radio-gamma ray scatter plot has a significant spread based on current data; therefore, it can not be used to constrain the blazar contribution to the extragalactic gamma-ray background based on radio luminosity function. However, with deeper surveys and better characterization of the variability in radio and gamma rays, it could become possible to improve our understanding of such connection (Bignall et al., 2015). Eventually, this would allow us also to constrain the available fraction for other more or less exotic contributors (from radio galaxies to dark matter).

5.3 Full SKA prospects

As suggested by variability time scales and SED model fit, the gamma-ray emission regions are typically very compact (sub-pc) and heavily self-absorbed at cm-λ. Therefore, it is critical to obtain high resolution and high frequency radio data as much as technically feasible. A direct approach of the gamma-ray region is beyond the scope of SKA and it requires (sub-)mm-VLBI. Nonetheless, the full SKA will provide the opportunity to get much closer to this region than SKA1 could. In this case, the critical requirements will be the completion of the longest SKA-MID baselines with $\nu > 10$ GHz, and possibly an integration with the African VLBI Network (AVN) and the EVN (Paragi et al., 2015). In particular, for very high redshift sources ($z \sim 5-8$), Band5 observations would correspond to millimetre wavelength emission in the source's rest frame, hence providing a tool to observe the innermost regions of blazars.

High resolution, time resolved, sensitive, polarimetric observations of individual sources will become possible, similar to what is currently being carried out only for a handful of special sources, like M87 (Giroletti et al., 2012) and 3C120 (Agudo et al., 2012).

References

Abdo, A. A., Ackermann, M., Ajello, M., et al. 2009a, ApJS, 183, 46
Abdo, A. A., Ackermann, M., Ajello, M., et al. 2009b, ApJ, 707, L142
Abdo, A. A., Ackermann, M., Ajello, M., et al. 2010a, ApJS, 188, 405
Abdo, A. A., Ackermann, M., Ajello, M., et al. 2010b, ApJ, 720, 912
Abdo, A. A., Ackermann, M., Ajello, M., et al. 2010c, ApJ, 715, 429
Ackermann, M., Ajello, M., Allafort, A., et al. 2011a, ApJ, 741, 30
Ackermann, M., Ajello, M., Allafort, A., et al. 2011b, ApJ, 743, 171

PoS(AASKA14)153

Ackermann, M., Ajello, M., Allafort, A., et al. 2012, ApJ, 753, 83
Ackermann, M., Ajello, M., Allafort, A., et al. 2013, ApJS, 209, 34
Agudo, I., Jorstad, S. G., Marscher, A. P., et al. 2011, ApJ, 726, L13
Agudo, I., Gómez, J. L., Casadio, C., Cawthorne, T. V., & Roca-Sogorb, M. 2012, ApJ, 752, 92
Agudo, I., Thum, C., Gómez, J. L., et al. 2014, A&A in prep.
Agudo, I., Böttcher, M., Falcke, H., et al. 2015, "Studies of Relativistic Jets in Active Galactic Nuclei with SKA", in proceedings of "Advancing Astrophysics with the Square Kilometre Array", PoS(AASKA14)093
Ajello, M., Romani, R. W., Gasparrini, D., et al. 2014, ApJ, 780, 73
Atwood, W. B., Abdo, A. A., Ackermann, M., et al. 2009, ApJ, 697, 1071
Bignall, H., Croft, S., Hovatta, T., et al. 2015, "Time domain studies of Active Galactic Nuclei with the Square Kilometre Array", in proceedings of "Advancing Astrophysics with the Square Kilometre Array", PoS(AASKA14)058
Corbel, S., Miller-Jones, J.C.A., Fender, R.P., et al. 2015, "Incoherent transient radio emission from stellar mass compact objects in the SKA era", in proceedings of "Advancing Astrophysics with the Square Kilometre Array", PoS(AASKA14)053
D'Abrusco, R., Massaro, F., Paggi, A., et al. 2013, ApJS, 206, 12
Dewdney, P., Turner, W., Millenaar, R., McCool, R., Lazio, J., Cornwell, T., 2013, "SKA1 System Baseline Design", Document number SKA-TEL-SKO-DD-001 Revision 1
Donnarumma, I., Rossi, E.M., Fender, R., et al. 2015, "SKA as a powerful hunter of jetted Tidal Disruption Events", in proceedings of "Advancing Astrophysics with the Square Kilometre Array", PoS(AASKA14)054
Ghirlanda, G., Ghisellini, G., Tavecchio, F., & Foschini, L. 2010, MNRAS, 407, 791
Giroletti, M., Hada, K., Giovannini, G., et al. 2012, A&A, 538, L10
Giroletti, M., Lico, R., Bignall, H., et al. 2014, A&A, in preparation
Grove, J. E., & on behalf of the Fermi LAT Collaboration 2014, AAS, 223, #256.03
Healey, S. E., Romani, R. W., Taylor, G. B., Sadler, E. M., Ricci, R., et al. 2008, ApJS, 175, 97
Hurley-Walker, N., Morgan, J., Wayth, R. B., et al. 2014, arXiv, arXiv:1410.0790
Lico, R., Giroletti, M., Orienti, M., et al. 2012, A&A, 545, A117
Mahony, E. K., Sadler, E. M., Murphy, T., et al. 2010, ApJ, 718, 587
Massaro, F., D'Abrusco, R., Ajello, M., Grindlay, J. E., & Smith, H. A. 2011, ApJ, 740, L48
Massaro, F., D'Abrusco, R., Paggi, A., et al. 2013a, ApJS, 206, 13
Massaro, F., D'Abrusco, R., Giroletti, M., et al. 2013b, ApJS, 207, 4
Massaro, F., Giroletti, M., Paggi, A., et al. 2013c, ApJS, 208, 15
Morgan, J., Hurley-Walker, N., Wayth, R., & MWA 2014, AAS, 223, #421.01
Murphy, T., Sadler, E. M., Ekers, R. D., et al. 2010, MNRAS, 402, 2403
Mücke, A., Pohl, M., Reich, P., et al. 1997, A&A, 320, 33
Nolan, P. L., Abdo, A. A., Ackermann, M., et al. 2012, ApJS, 199, 31
Nori, M., Giroletti, M., Massaro, F., et al. 2014, ApJS, 212, 3
Padovani, P., Ghisellini, G., Fabian, A. C., & Celotti, A. 1993, MNRAS, 260, L21
Paragi, Z., Godfrey, L., Reynolds, C., et al. 2015, "Very Long Baseline Interferometry with the SKA", in proceedings of "Advancing Astrophysics with the Square Kilometre Array", PoS(AASKA14)143

PoS(AASKA14)153

Pavlidou, V., Richards, J. L., Max-Moerbeck, W., et al. 2012, ApJ, 751, 149
Piner, B. G., Pant, N., & Edwards, P. G. 2008, ApJ, 678, 64
Stecker, F. W., & Salamon, M. H. 1996, ApJ, 464, 600
Tavani, M., Barbiellini, G., Argan, A., et al. 2009, A&A, 502, 995
Thompson, D. J., Ballet, J., Burnett, T., & Fermi LAT Collaboration 2014, AAS, 223, #256.01
Turriziani, S., 2015, "Extragalactic jets in the SKA era: solving the mystery of Ultra High Energy Cosmic Rays?", in proceedings of "Advancing Astrophysics with the Square Kilometre Array", PoS(AASKA14)160

PoS(AASKA14)153

PROCEEDINGS OF SCIENCE

Synergies between SKA and ALMA: observations of Nearby Galaxies

Rosita Paladino[*1,2], **Jan Brand**[2], **Emanuela Orrú**[3], **Viviana Casasola**[2], **Elisabetta Liuzzo**[2], **Marcella Massardi**[2], **Arturo Mignano**[2]

[1] *Università di Bologna;* [2] *INAF-Istituto di Radioastronomia - Italian ALMA regional center;*
[3] *ASTRON*
E-mail: paladino@ira.inaf.it

The past decade has seen amazing advances in radioastronomy, which led to the construction of brand-new instruments such as LOFAR and ALMA, and the updating of existing ones, e. g. JVLA and e-MERLIN. The SKA will be the spearhead of a future technological development and it will change the way astrophysical topics have been studied so far by opening up new frequency windows with unprecedented spatial resolution and sensitivity. The SKA location in the southern hemisphere makes it particularly suitable to complement ALMA, which is already giving exciting results both on the local and the more distant Universe.
Among the possible synergies between SKA and ALMA, we focus on the observations of nearby star forming galaxies. Star formation processes in galaxies involve all the components of the interstellar medium, so the only way to have a complete picture of them is through multifrequency observations.
ALMA observes gas and dust emission, while the SKA will trace both the free-free thermal and the non-thermal synchrotron emission. The spatial comparison between these components gives information about the contribution to star formation processes provided by magnetic fields and cosmic rays. The high spatial resolution achievable with ALMA and SKA will make it possible to compare these emissions on very small spatial scales, by resolving single molecular clouds in nearby galaxies.
By the time the SKA will start observing, ALMA will have already imaged many nearby galaxies in the southern hemisphere, for which no low frequency data at comparably high spatial resolution will be available. The SKA will fill this gap, and have a profound impact on the studies of nearby galaxies, making valuable contributions to our understanding of star formation processes, and of the role of magnetic fields and cosmic rays in them.

Advancing Astrophysics with the Square Kilometre Array
June 8-13, 2014
Giardini Naxos, Italy

[*]Speaker.

PoS(AASKA14)156

1. Introduction

Star formation (SF) is a key astrophysical process, being the principal agent of galaxy formation and evolution. It is however difficult to formulate general theories about it, due to the wide range of physical processes involved. In the past decades, observational information has been obtained expanding the range of physical scales explored from individual protostellar and protoplanetary systems to molecular clouds and star clusters, to entire galaxies and systems of galaxies, see Krumholz (2014) for a comprehensive review on the current status of the field. Detailed observations of individual star-forming regions have been possible so far only in the Milky Way, while the extragalactic studies have been focused on characterizing the collective effects of star-formation processes on galactic and cosmological scales (see Kennicutt & Evans, 2012, and references therein).

It is now clear that the large-scale star formation rate (SFR) is determined both by physical processes on galactic or extragalactic scales (such as the accretion of gas onto disks from satellite objects and intergalactic medium), and by processes operating on local cloud scales (from the cooling of the gas on kpc scales, to the formation of molecular clouds on pc scales, and the subsequent fragmentation and accretion of this molecular gas to form denser structures), for a recent review see Dobbs et al. (2013). The key processes influencing SF lie in the boundary between these physical scales. At present, there are no models that include all the physical processes necessary to simulate the transformation of the ISM from the galactic to the stellar scale, and future theories will certainly benefit from input from comparison with observations.

Nearby galaxies provide the opportunity to study galaxy processes on large scales, while still being close enough to reveal the local details, if high resolution and sensitivity are achieved. The advent of new observational facilities providing so far unattainable resolutions will make nearby galaxies key targets to address important questions, such as what is the importance of local (disk or cloud instability) and global effects (spiral density waves, tidal forces) in triggering SF, which is the role of magnetic fields, or how do environmental conditions or galaxy properties influence SF.

2. Multi frequency studies

Star formation processes take place in the cold gaseous medium of galaxies, but they involve in a very complex way all the components of the interstellar medium (ISM).

- **Gas**

  The cold gas component can be observed in its atomic phase through the hyper-fine transition of hydrogen, occurring in the rest frame at 21 cm, and in the molecular phase, mostly observable through molecular transitions in the millimetric domain. The most commonly used tracer of the molecular gas so far has been the carbon monoxide (CO): despite many drawbacks, its lines are the easiest to observe (see Bolatto et al. 2013 for a review). Essentially, CO emission traces molecular gas only over a limited dynamic range: since a minimum density is required to excite it, it does not trace all the molecular gas, especially if the metallicity is low; on the other end, CO becomes optically thick at very low total column densities. The use of CO isotopologues provides lower optical depths at the cost of weaker lines. Higher-J

PoS(AASKA14)156

CO transitions and other molecular lines, such as HCN or CS, are more suitable to trace warmer and denser gas.

- **Dust**

  Despite containing only 1% of the total mass content in the ISM, dust plays an important role in SF since it helps in the gravitational collapse of molecular clouds, by acting as a cooling agent. In return, it is severely affected by the proximity of star formation, modifying the chemical composition of the circumstellar environs. From the observational point of view: dust absorbs radiation at higher frequencies where it can be optically thick, and reprocesses the energy, emitting at longer wavelengths, from IR to millimeter. Transformational results have been obtained with the *Spitzer Space Telescope* (Werner et al. 2004) and the *Herschel Space Observatory* (Pilbratt et al. 2010). At $\sim$ 1 mm the emission is close to the Rayleigh-Jeans limit, so the mm continuum emission provides a good tracer of dust column density and mass.

- **Cosmic rays and magnetic field**

  In addition to the thermal gas and dust components, the ISM is permeated by a background of highly energetic particles, the cosmic ray component, consisting mainly of relativistic electrons and ions, tied to the galaxy by magnetic field.

  It has become increasingly clear that cosmic rays and magnetic fields play a significant role in the star formation process, even though this role is far from being understood.

  The tight FIR/radio continuum (RC) correlation (e.g. Condon 1992, Yun et al. 2001) is generally interpreted as a manifestation of the link between cosmic ray electrons (CRe) and star formation. CRe, responsible for diffuse synchrotron emission, are thought to be produced in expanding supernova remnants (SNRs), which are generally associated with massive star formation. The study of the origins and propagation mechanisms of the CRe is directly linked to the understanding of SF processes.

  The role of magnetic fields at almost all stages of SF remains highly controversial (see Crutcher et al., 2012), in large part as a result of the lack of observational constraints. It is however clear that processes opposing gravitational collapse of the molecular clouds have to take place to justify the low efficiency of molecular clouds in forming stars.

Empirical relations between observational tracers of these different components have been exploited to study star formation rates in external galaxies (see Kennicutt & Evans 2012 for a recent review). Radio continuum emission, which is not affected by dust obscuration, is widely used as a tracer of star formation in galaxies both at low and high redshifts. It will be particularly useful in the redshift range between 1 and 3, where the galaxies appear to be mostly dusty starbursts (e.g., Bouwens et al. 2009; Murphy et al. 2011). In order to calibrate radio continuum emission as a star formation tracer, observations of star forming regions in a large range of conditions, in the nearby Universe, will provide essential constraints. Furthermore, studies of low metallicity systems, such as dwarf irregular galaxies, can be used to extrapolate star formation laws in the unenriched early Universe.

PoS(AASKA14)156

Table 1: SKA1-SUR and SKA1-MID parameters

	Freq* GHz	Max res* arcsec	Cont rms* μJy·hr$^{-1/2}$	scale @ 10 Mpc pc
SKA1-SUR PAF2	0.650 −1.67	1.9−0.8	5.6	92−39
SKA1-MID Band 2	0.950−1.76	0.32−0.17	0.96	15.5−8.3
SKA1-MID Band 4	2.8−5.2	0.11−0.06	0.45	5.4−2.9
SKA1-MID Band 5	4.6−13.8	0.07−0.02	0.52	3.4−0.97

*From tables 6 and 7 of the SKA1 system baseline design (Dewdney et al., 2013)

Table 2: Some interesting lines observable with ALMA and the range of resolutions achievable

Line	restfreq GHz	Band	res range arcsec	range of scales @ 10 Mpc (in pc)
CO(1-0)	115.27	3	13 − 0.1	630 − 5
CO(2-1)	230.58	6	11 − 0.02	533 − 1
HCN(1-0)	88.63	3	13 − 0.1	630 − 5
HCN(3-2)	265.88	6	11 − 0.02	533 − 1
HCO^+(1-0)	85.16	3	13 − 0.1	630 − 5
HCO^+(3-2)	267.55	6	11 − 0.02	533 − 1
DCO^+(1-0)	70.73	2	6 − 0.05	290 −2.4
DCO^+(2-1)	141.46	4	3 − 0.03	145−1.4

3. Synergies between SKA and ALMA

3.1 Radio continuum and molecular emissions correlation

The radio emission from galaxies at centimetric wavelengths is a combination of thermal and non-thermal radiation: both arising from massive star formation. Thermal emission, due to bremstrahlung radiation from star forming regions, is dominant at short wavelengths (< 20 cm). At 3.6 cm, 30% of emission is thermal and can be directly related to the ionizing photon rate arising from newly formed massive stars (Condon 1992). In the low frequency range (wavelengths larger than $\sim$ 20 cm), the dominant component is the non-thermal synchrotron emission from CR electrons accelerated by supernovae and spiraling in galactic magnetic fields.

The high resolution and sensitivity provided by SKA allow the observation of both the free-free thermal component and the non-thermal synchrotron emission in nearby galaxies, and the separation of their contribution on local scales. It will be possible to study the details of gas processing and to get a clear and detailed picture of star formation on large (kpc) scales, by decomposing the galaxies into individual sources and disentangling the contribution from AGNs. Furthermore, the high sensitivity provided by SKA will make it possible to observe the relativistic phase (magnetic

PoS(AASKA14)156

field and cosmic rays) in faint regions, so far invisible, helping in clarifying which role this phase plays in SF processes.

ALMA allows observations of the molecular emission with comparable resolution and sensitivity. A correlation between radio continuum and CO emission has been found to hold in nearby galaxies, both on global (Adler et al, 1991; Murgia et al. 2002) and local scales (e.g. Murgia et al. 2005; Paladino et al. 2006, 2008; Schinnerer et al. 2013), but its origin is still not understood. The combination of SKA and ALMA will allow the study of this correlation down to spatial scales of the order of few parsecs (last columns of tables 1 and 2 list the range of spatial scales covered by SKA1 and ALMA). Emission from molecules such as HCN, HCO+, CN, less abundant than CO but tracing much denser gas, will be observable in nearby galaxies with the unprecedented sensitivity offered by ALMA. In very nearby galaxies (closer than 10 Mpc), even the internal structures of giant molecular clouds (GMCs) can be studied, and, thanks to ALMA polarization capabilities, it will be also possible to determine magnitude and direction of magnetic field in GMCs. A recent study on M33 GMCs (Li & Henning 2011) has proven the possibility to determine the magnetic field orientation from the polarization of molecular lines. The comparison between large-scale galactic magnetic field (obtained from synchrotron polarization observations with SKA), and the clouds' magnetic fields is essential to clarify the origin and distribution of magnetic fields in GMCs, and hence their role in star formation processes.

ALMA also provides continuum observations in the millimetric range. These observations, complementing RC, IR and molecular line observations, allow the spatially resolved study of the spectral energy distribution, from centimeter to sub-millimeter wavelengths, allowing the investigation of the interaction between SF and nuclear activity. Furthermore, the dust is a particularly relevant tracer of interstellar matter with low heavy elements abundance.

3.2 Observations of giant molecular clouds in nearby galaxies

SKA and ALMA, when fully operational, will allow the extension of studies currently done only on galactic H II regions to nearby spiral and faint irregular galaxies.

One of the still open questions about star formation processes is whether they *care* about the galactic structure in which they happen. Star formation can be thought of as a localized process: the coldest gas in GMCs, at least three orders of magnitude smaller in size than a galaxy, collapses to form stars in cores, another order of magnitude smaller; however, large-scale dynamics may drive the evolution of GMCs (Koda et al. 2009).

Some of the properties of GMCs have been observed to be similar in different galaxies (Blitz et al. 2007; Bolatto et al. 2008; Donovan Meyer et al., 2013), suggesting that GMCs are unaware of the global environment. Evidence to the contrary has also been gathered during the past years: systematic variations in the Kennicutt-Schmidt relation (Schmidt 1959, Kennicutt 1998) have been found and interpreted as influence on star formation activity of global structural variations, such as galaxy type (Daddi et al. 2010; Leroy et al. 2013), condition in the galactic central region (Oka et al. 2001) and the morphology (Sheth et al. 2002; Momose et al. 2010).

On the theoretical side, various studies have found a dependence of GMC properties on galactic structures (Dobbs & Bonnell 2006; Koda et al. 2009; Fujimoto et al. 2014). High spatial resolution radio observations of nearby galaxies with VLA or ATCA have allowed the study of compact sources such as HII regions and SNRs in starburst galaxies at distances up to 5 Mpc (e. g.

PoS(AASKA14)156

Table 3: Scaled flux of Cas A and W49A at 1.4 and 5 GHz, at various distances

Distance	Cas A (μJy)			W49A (μJy)		
Mpc	1.4	5	8 GHz	1.4	5	8 GHz
10	177	58	48	93	114	131
25	28	9	8	15	18	21
50	7	2.3	2	3.7	4.6	5
75	3	1	0.8	1.7	2	2.3
100	2	0.6	0.5	0.9	1.1	1.3

Lacey et al. 1997; Gordon et al. 1999). To fully understand massive star formation and supernova evolution though, different types of galaxies with different properties must be surveyed in order to understand the effects of gas density and metallicity on star formation.

If star formation is really influenced by environmental effects, there must be a variation of GMCs properties. Obviously, GMCs in the Milky Way have been studied to a high level of precision (Larson 1981; Garcia et al. 2014), but observations in our own Galaxy are often hampered by our location inside its disk. Current observing facilities allow the study of GMCs in only a few galaxies (e.g. Hughes et al 2013) close enough to get the necessary resolution, while current limits in sensitivity prevent the observations of CO-faint dwarf galaxies.

Aversa et al. (2011) recently studied a sample of star forming galaxies within 10 Mpc, to identify candidate star-forming regions in them. Due to current sensitivity limits only a few thermal sources have been detected. Higher sensitivity and spatial resolution will allow this kind of studies in more distant galaxies.

4. SKA foreseen contribution to the field

To estimate the capabilities of the SKA in detecting thermal and non-thermal compact sources in external galaxies, we use two prototypical sources in the Milky Way as benchmarks for analogous ones in external galaxies. The core-collapse SNR Cas A, with the highest luminosity and youngest age in the Galaxy (Baars et al. 1977; Fesen et al. 2006) will be our model for non-thermal sources, while W49A, the most luminous starforming region in the Milky Way (e.g. Galvan-Madrid 2013), will be our standard thermal source.

Cas A, at a distance of 2.8 kpc, has a flux density of 2260, 740 and 612 Jy, at 1.4, 5 and 8 GHz, respectively (Baars et al, 1977), and W49A (at 14.1 kpc) has a flux density of 47.2, 57.5, 66 Jy at 1.4, 5 and 8 GHz, respectively (Mezger, Schraml & Terzian 1967). We scaled these fluxes at distances up to 100 Mpc, results are reported in Table 3.

SKA1-MID – The SKA1-MID is particularly suitable for this kind of studies. Assuming that the available bands will be Band 2 (0.950-1.76 GHz), Band 4 (2.8-5.2 GHz), and Band 5 (4.6-13.8 GHz), the continuum sensitivity achievable (reported in Table 1) is enough to ensure 4σ detections of thermal sources up to 75 Mpc in $\sim$ 2 hrs at 1.4 GHz, and $\sim$ 3 hrs at 5 GHz. 4σ detections of non-thermal sources will be possible in $\sim$ 5 hrs at 1.4 GHz, and $<$ 1 hr at 5 GHz.

PoS(AASKA14)156

In terms of spatial resolution, SKA1-MID will allow spatial resolution of the order of ∼50 pc in 50 Mpc distant galaxies at 1.4 GHz. The spatial scales will be smaller at higher frequencies. These resolutions are high enough to identify compact sources with sizes typical of the galactic GMCs ∼ 40 pc (ranging from 20 to 100 pc; Solomon et al., 1987).

In SKA "early science" phase, with sensitivity about 50% of the full SKA1 specified level, the observations of these kinds of objects will be already feasible in a reasonable amount of time, compared to the current existing facilities. In less than four hours of observations it will be already possible to detect, with S/N larger than 4, thermal and non-thermal sources in galaxies at distances up to 50 Mpc.

SKA2 – Obviously, SKA2 sensitivity, 10 times higher than what is obtained in phase 1, and its resolution, 20 times better, will bring about a significant leap in the current way we study nearby galaxies. Thermal and non-thermal compact sources up to distances of ∼100 Mpc will be detected, with a 4σ S/N, in few minutes. In galaxies at distances < 10 Mpc, SKA2 resolution will correspond to spatial scales of the order of a few tenths of a pc. Relatively face-on spirals such as M 33 present an excellent environment in which to examine the global aspects of massive star formation as traced through their HII region populations. The SKA2 resolution of ∼15 milli-arcsec at 5 GHz corresponds to nearly 0.05 pc in M 33. This is the scale of ultra-compact H II regions, which are not accessible to optical or even near-IR observations, since they are deeply embedded in their parent molecular cloud. In galaxies of the Local Group, the SKA2 will access scales explored so far only in our own Galaxy.

ALMA will observe with comparable resolution the millimetric counterpart of these sources. Scaling the millimetric flux of W49A (Galvan-Madrid et al. 2014) to larger distances, we verified the possibility to detect dust in typical starforming regions with continuum observations. Detection of lines will be possible for the more abundant species, such as CO and its isotopologues, up to 10 Mpc distances. If the ratio between molecular species is the same as in our own Galaxy, a few relatively abundant molecules (HCO^+, DCO^+, etc.) will also be detected, with low S/N. However, ALMA will provide information on the chemistry of faint regions and in low metallicity environments, which is still not well known. In particular, ALMA band 2, not yet available but possibly operational when SKA2 will start observing, will allow observations of deuterated molecules (some of them are listed in Table 2). These molecules drive the chemistry in highly embedded regions, where CO is depleted, in addition in cold, dark clouds, where some molecules are highly enriched in deuterium due to chemical fractionation. For these reasons, observations of them in external galaxies are extremely interesting but so far impossible due to sensitivity limits.

REFERENCES

Adler, D. S., Allen, R. J., & Lo, K. Y. 1991, ApJ, 382, 475
Aversa, A. G., Johnson, K. E., Brogan, C. L. et al., 2011, AJ, 141, 125
Baars, J. W. M., Genzel, R., Pauliny-Toth, I. I. K., & Witzel, A., 1977, A&A, 61, 99
Blitz, L., Fukui, Y., Kawamura, A. et al., 2007, prpl.conf 81B
Bolatto, A. D., Leroy, A. K., Rosolowsky, E. et al., 2008, IAU Symposium, 255, 274
Bolatto, A. D., Wolfire, M., Leroy, A. K., 2013,ARA&A, 51, 207B
Bouwens, R. J., Illingworth, G. D., Franx, M. et al., 2009, ApJ, 705, 936

PoS(AASKA14)156

Condon, J. J., 1992, ARA&A, 30, 575
Crutcher, R. M., 2012, ARA&A, 50, 29
Daddi, E., Elbaz, D., Walter, F. et al., 2010, ApJ, 714, L118
Dewdney, P., Turner, W., Millenaar, R., McCool, R., Lazio, J., Cornwell, T., 2013, "SKA1 System Baseline Design", Document number SKA-TEL-SKO-DD-001 Revision 1
Dobbs, C. L., Bonnell, I. A., Pringle, J. E., 2006, MNRAS, 371,1663
Dobbs, C. L., Krumholz, M. R., Ballesteros-Paredes, J. et al., 2013, arXiv1312.3223
Donovan Meyer, J., Koda, J., Momose, R., et al., 2013, ApJ, 772, 107
Fesen, R. A., Hammell, M. C., Morse, J. et al., 2006, ApJ, 645, 283
Fujimoto, Y., Tasker, E. J., Wakayama, M. et al., 2014, MNRAS, 439, 936
Galván-Madrid, R., Liu, H. B., Zhang, Z.-Y. et al., 2013, ApJ, 779, 121
Galván-Madrid, R., Liu, H. B., Manara, C.-F. et al., 2014, ApJ, 570, L9
García, P., Bronfman, L., Nyman, L.-Å., 2014, ApJS, 212, 2
Gordon, S. M., Duric, N., Kirshner, R. P., 1999, ApJS, 120, 247
Hughes, A., Meidt, S. E., Colombo, D. et al., 2013, ApJ, 779, 46
Kennicutt, R. C. 1998, ApJ, 498, 541
Kennicutt, R. C., Evans, N. J., 2012, ARA&A, 50, 531
Koda, J., Scoville, N., Sawada, T., et al., 2009, ApJ, 700, L132
Krumholz, M. R., 2014, arXiv1402.0867
Lacey, C., Duric, N., Goss, W. M., 1997, ApJS, 109, 417
Larson, R. B., 1981, MNRAS, 194, 809
Leroy, A. K., Walter, F., Sandstrom, K. et al., 2013, AJ, 146, 19
Li, H.-B., Henning, T., 2011, Nature, 479, 499
Mezger, P. G., Schraml, J., Terzian, Y., 1967, AJ, 72, 817
Momose, R., Okumura, S. K., Koda, J. et al, 2010, ApJ, 721, 383
Murgia, M., Crapsi, A., Moscadelli, L., & Gregorini, L., 2002, A&A, 385, 412
Murgia, M., Helfer, T. T., Ekers, R., et al., 2005, A&A, 437, 389
Murphy, E. J., Chary, R.-R., Dickinson, M.,et al., 2011, ApJ, 732, 126
Oka, T., Hasegawa, T., Sato, F., 2001, ApJ, 562, 348
Paladino, R., Murgia, M., Helfer, T. T., et al., 2006, A&A, 456, 779
Paladino, R., Murgia, M., Tarchi, A., et al, 2008, A&A, 485, 679
Pilbratt, G. L., Riedinger, J. R., Passvogel, T. et al., 2010, A&A, 26A, 518L
Schmidt, M., 1959, ApJ, 129, 243
Schinnerer, E., Meidt, S. E., Pety, J., et al., 2013, ApJ, 779, 42
Sheth, K., Vogel, S. N., Regan, M. W. et al., 2002, AJ, 124, 2581
Solomon, P. M., Rivolo, A. R., Barrett, J. et al., 1987, ApJ, 319, 730
Werner, M. W,, Roellig, T. L., Low, F. J. et al., 2004, ApJS, 154, 1
Yun, M. S., Reddy, N. A., & Condon, J. J. 2001, ApJ, 554, 803

PoS(AASKA14)156

PROCEEDINGS OF SCIENCE

Multi-wavelength, Multi-Messenger Pulsar Science in the SKA Era

John Antoniadis,[1,2] **Lucas Guillemot,**[3] **Andrea Possenti**[*,4] **Slavko Bogdanov,**[5] **Josef D. Gelfand,**[6] **Michael Kramer,**[1,7] **Roberto Mignani,**[8,9] **Benjamin Stappers**[7] **& Pablo Torne**[1]

[1]*Max-Planck-Institut für Radioastronomie, Bonn, Germany;* [2]*Dunlap Institute for Astronomy and Astrophysics University of Toronto;* [3]*Laboratoire de Physique et Chimie de l'Environnement, Orléans, France Station de radioastronomie de Nançay, Obs. de Paris, CNRS/INSU, Nançay, France;* [4] *INAF-Osservatorio Astronomico di Cagliari, Selargius (CA), Italy;* [5] *Columbia Astrophysics Laboratory, Columbia University, New York, USA;* [6] *New York University, Abu Dhabi;* [7] *Jodrell Bank Center for Astrophysics, University of Manchester, UK;* [8] *INAF - Istituto di Astrofisica Spaziale e Fisica Cosmica Milano, Milano, Italy;* [9] *Kepler Institute of Astronomy, University of Zielona Góra, Zielona Góra, Poland*
email: antoniadis@dunlap.utoronto.ca

The Square Kilometre Array (SKA) is an integral part of the next-generation observatories that will survey the Universe across the electromagnetic spectrum, and beyond, revolutionizing our view of fundamental physics, astrophysics and cosmology. Owing to their extreme nature and clock-like properties, pulsars discovered and monitored by SKA will enable a broad range of scientific endeavour and play a key role in this quest. This chapter summarizes the pulsar-related science goals that will be reached with coordinated efforts among SKA and other next-generation astronomical facilities.

Advancing Astrophysics with the Square Kilometre Array
June 8-13, 2014
Giardini Naxos, Italy

*Speaker.

PoS(AASKA14)157

1. Introduction

One of the key science goals for the SKA is to provide a nearly complete census of radio pulsars in the Milky Way and its Globular Clusters (Keane et al. 2015; Hessels et al. 2015). The large number of pulsar discoveries and the unprecedented timing precision of the instrument will enable a broad spectrum of science, ranging from characterization of stochastic gravitational wave (GW) signals (Janssen et al. 2015) to probing all possible outcomes of massive-star evolution (Tauris et al. 2015).

As the SKA will be detecting its first light, a fleet of sensitive telescopes will be gathering photons at all wavelengths and second generation GW detectors will be making sensitive observations. This multi-wavelength, multi-messenger frontier in astronomy will allow to tackle many remaining open problems in neutron star (NS) physics, and study with unprecedented detail the Galactic structure and content, the nature of the strong interaction, strong-field gravity and the large-scale structure of the Universe.

Figure 1 sketches an approximate timeline (design–construction–operations) for observatories that will be of particular importance for pulsar science. At radio and sub-mm wavelengths, ALMA[1] and EHT[2]/BlackHoleCam[3], will study the pulsar emission mechanism and magnetic structure and, jointly with pulsar-timing observations, probe the nature of strong-field gravity around the supermassive black hole (SMBH) at the center of the Milky Way.

Ground-based and space-borne instruments such as GAIA[4], LSST[5], JWST [6] and E-ELT [7] will provide a thorough census of the Galaxy's stellar content, including the companions of pulsars discovered and monitored with the SKA. Similarly, studies of NS X-ray binaries with next-generation X-ray telescopes such as NICER[8], eROSITA [9] and LOFT[10] and precise timing of binary millisecond pulsars will constrain the super-dense matter equation-of-state (EoS) (Watts et al. 2015) and further enrich the ensemble of laboratories for strong-field gravity (Shao et al. 2015). In $\gamma-$rays, pulsar searches in *Fermi*[11] and CTA[12] unidentified sources will allow a better understanding of the NS environment, pulsar emission and binary evolution. Beyond the electromagnetic spectrum, Advanced-LIGO[13], VIRGO[14], eLISA[15] and the Pulsar Timing Array (PTA) monitored by the SKA will open a new window to the GW Universe.

[1] Atacama Large Millimeter/submillimeter Array, http://www.almaobservatory.org/
[2] Event-Horizon Telescope, http://www.eventhorizontelescope.org/
[3] http://www.space.com/24002-black-hole-image-event-horizon.html
[4] Global Astrometric Interferometer for Astrophysics, http://sci.esa.int/gaia/
[5] Large Synoptic Survey Telescope, http://www.lsst.org/lsst/
[6] James Webb Space Telescope, http://www.jwst.nasa.gov/
[7] The European Extremely Large Telescope, https://www.eso.org/public/teles-instr/e-elt/
[8] Neutron star Interior Composition Explorer; http://heasarc.gsfc.nasa.gov/docs/nicer/
[9] extended ROentgen Survey with an Imaging Telescope Array, http://www.mpe.mpg.de/eROSITA
[10] Large Observatory For X-ray Timing; http://sci.esa.int/loft
[11] http://fermi.gsfc.nasa.gov
[12] Cherenkov Telescope Array, https://www.cta-observatory.org
[13] https://www.advancedligo.mit.edu
[14] http://www.ego- gw.it/public/about/whatis.aspx
[15] https://www.elisascience.org

PoS(AASKA14)157

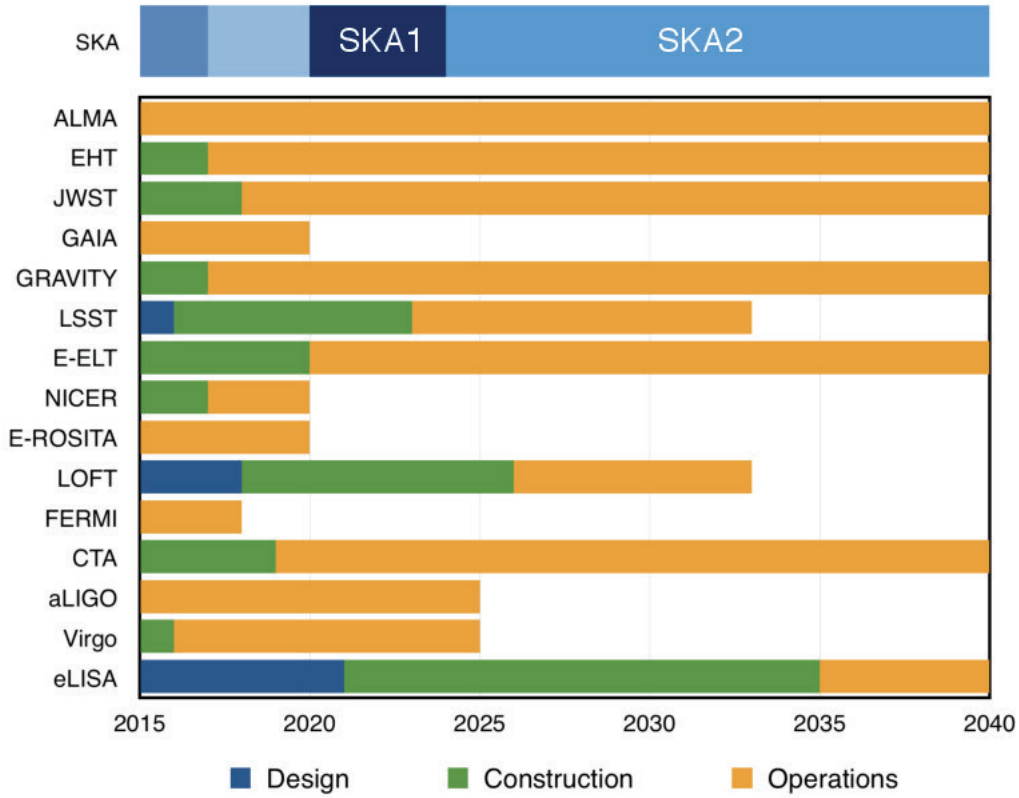

Figure 1: Approximate timeline for observatories of interest for synergistic neutron star science with the SKA.

In this chapter we elaborate on a selected number of topics, for which coordination between different observatories will provide the greatest benefits. The text is organized as follows: Section 2 covers the Galactic structure and content, focusing on studies of the Milky Way's kinematics and multi-wavelength pulsar surveys. Section 3 discusses the added benefits for stellar evolution and NS population studies. In section 4 we elaborate on the NS EoS and the nature of the Strong Interaction and in section 5 on NS-related transient phenomena. Finally, section 6 covers the multi-messenger efforts in the GW detection era and section 7 concludes with some final remarks. Given space limitations, this chapter is not meant to be an in-depth review of each topic nor does it exhaust the complete potential of the multi-wavelength approach. For details on specific topics the reader is encouraged to skim through the other chapters of this book cited throughout the text.

2. The Galactic Structure and Content

2.1 Targeted multi-wavelength searches for pulsars

One of the great achievements of *Fermi* was the discovery by its main instrument, the Large Area Telescope (LAT), of a large number of γ-ray sources with no previously known counterparts, the so-called unassociated sources. The 2FGL catalogue (Nolan et al. 2012), a catalogue of *Fermi* LAT sources based on two years of data, contained 1873 sources in total, of which about 30%

PoS(AASKA14)157

have not yet been associated with a known class of gamma-ray source; the recently published 3FGL catalogue, which is based on four years of LAT data, contains a total number of sources close to 3000. Many of these could be $\gamma-$ray pulsars, the most numerous class of Galactic $\gamma-$ray sources. Indeed, searches for pulsations at the locations of LAT unassociated sources with pulsar-like $\gamma-$ray emission properties have led to the discovery of many new pulsars, either by directly blind searching the photon data (Pletsch et al. 2012), or by conducting deep radio observations (Ray et al. 2012).

Radio searches of pulsations in LAT sources have led to the discovery of a very large number of previously unknown MSPs (Ray et al. 2012) – currently about 25% of all known in the Galaxy[16]. A good fraction of these new pulsars would probably have *eventually* been found in standard radio-pulsar surveys. However, the LAT accelerated their discovery by showing radio telescopes where to look. Until the end of its mission, *Fermi* will continue to discover new sources and the SKA will be extremely useful in the quest for the identification of the unassociated ones. Similarly, other instruments covering different wavelengths that have started operating (e.g., GAIA or ALMA) or will start in the future (e.g., LSST, eROSITA, or the CTA), will find new sources across the spectrum that could be searched for pulsars with the SKA. To quote some examples: faint, variable optical stars detected by GAIA could point to white dwarfs orbiting unknown radio pulsars (e.g. Antoniadis et al. 2013), or "black widow" systems, with millisecond pulsars ablating their companion stars with their strong particle winds, generating optical emission modulated at the orbital period (e.g. Romani 2012). Another example is the possibility to search for young radio-emitting pulsars with the SKA, at the locations of supernova remnants, pulsar wind nebulae (PWNe) or unassociated sources discovered by CTA, in its future surveys of the very high energy γ-ray sky (Dubus et al. 2013).

2.2 Probing the Dynamics and Structure of the Galaxy

Regardless of the discovery method, measured positions, distances and proper motions of radio pulsars, have allowed to broadly outline the structure of the Galactic disk and, among others, unveiled the presence of a warp (Yusifov 2004). However, to date, out of $\sim$2200 known radio pulsars, only $\sim$150 (i.e. about 7%) have measured proper motions and even less have measured parallaxes, fundamental in determining their actual location in the Galaxy.

The large number of pulsar discoveries expected by the SKA, both in Phase-1 (SKA1) and later in Phase-2 (Keane et al. 2015; Hessels et al. 2015), and the manifold increase in sensitivity, will improve the accuracy of previous results and allow to look for new features like humps or depletions in the Galactic disk that might have escaped previous searches. Furthermore, binary pulsars with optical counterparts, where both the proper motion and systemic radial velocity can be measured, will provide their full three- dimensional motion in the Galaxy (Lazaridis et al. 2009) enabling the reconstruction of the Milky-Way's structure and possibly unveiling thin and thick disk pulsar populations. Similarly, precise knowledge of pulsar proper motions (Smits et al. 2011) will allow to discriminate between pulsars born in the warped regions of the Galaxy from those born in the Galactic plane. In all these respects, the SKA will complement the work done by GAIA which will sample different stellar populations.

[16]See http://astro.phys.wvu.edu/GalacticMSPs/GalacticMSPs.txt for an up-to-date list of known Galactic disk MSPs.

PoS(AASKA14)157

2.3 The Interstellar and Intergalactic Medium

In addition to the above, effects like dispersion measure, Faraday rotation, scattering and scintillation, routinely measured in pulsar observations, provide valuable information about the interstellar medium (ISM). Since pulsars are typically very faint, until now, mostly those located in the vicinity of the Sun have been used for studies of the ISM (Cordes & Lazio 2002). The superb sensitivity of the full SKA will extend precision ISM studies to greater distances (Han et al. 2015) and further enable studies of the intergalactic medium (IGM) through the detection of pulsars and fast radio bursts (FRBs) in other galaxies.

If the distance to the host galaxy is known by e.g. optical and near-infrared studies of standard candles and Cepheid variables, the electron column density and magnetic field parallel to the line-of-sight to the pulsar can be calculated. These distances to nearby galaxies have been historically difficult to measure with precision (Jacoby et al. 1992), but the new and more powerful optical and infrared telescopes such as E-ELT and JWST will significantly improve distance measurements.

3. Extreme Astrophysics and Stellar Evolution

3.1 Studies of the pulsar emission mechanism across the electromagnetic spectrum

While the general concept of pulsar electromagnetic emission is fairly well established, the complex details of the radiation processes such as the exact emission heights and the relevant importance of various emission mechanisms are still unclear. Different approaches and models attempting to explain the geometry and physical processes responsible for pulsar emission rely on a broad range of assumptions that lead to different predictions (Lyne & Graham-Smith 2012). The different techniques utilized to study the physical processes in emission regions, e.g., profile shape studies and polarimetry, make use of information at multiple frequencies across the radio spectrum (Lyne & Graham-Smith 2012). As the radiation from pulsars is broadband, and produced presumably by several distinct radiative mechanisms, the coverage of the multiple wavelengths across the electromagnetic spectrum is required to build a complete analysis of the problem. With the SKA and the new ground and space borne observatories covering virtually the entire electromagnetic spectrum with unprecedented sensitivity and time resolution, a much better understanding of the emission processes from pulsars is possible. This new era of cutting-edge instrumentation may answer many of the related questions, that last now more than 45 years.

Beyond that, population analyses of $\gamma-$ray pulsars will yield information on the fraction of "Geminga-like" pulsars: pulsars that are only visible from high- energy observations or with extremely low radio luminosities, presumably because the radio emission beams do not cross or only graze our line of sight. The ratio of radio-loud to radio-quiet pulsars is a key observable of high-energy emission models (Watters & Romani 2011) and the SKA's great sensitivity will be particularly useful for constraining this ratio, and thus understanding pulsar emission across the spectrum.

3.2 Pulsar Wind Nebulae

There will also be significant synergies between the SKA and upcoming high-energy facilities like the Cerenkov Telescope Array (CTA) regarding the study of PWNe. Powered by the rota-

PoS(AASKA14)157

tional energy of their central NS, these objects are detected across the electromagnetic spectrum, and currently dominate the Galactic population of TeV γ-ray sources (e.g. Hartman et al. 1999). The radio emission from PWNe is believed to be synchrotron emission from the electrons and positrons created in the pulsar magnetosphere interacting with the PWN's magnetic field, while its γ-ray emission is believed to result from these high-energy lepton inverse Compton scattering of background photons. Detecting both the radio and γ-ray emission from a PWN allows one to measure the electron particle spectrum, magnetic field strength, and energy density of the background photon field – critical for understanding the generation and acceleration of leptons in these objects (Gaensler & Slane 2006; Gelfand et al. 2009). However, such an analysis is currently possible for only few sources, since many TeV PWNe remain undetected at radio wavelengths. This is likely the result of a low magnetic field strength and large angular size, resulting in a radio surface brightness too low to be detected with current facilities. However, the significant improvement in sensitivity of the SKA, especially on large angular scales, will allow us to detect radio emission from existing TeV PWNe as well as any new PWN candidate detected by CTA. Additionally, the SKA will also have the sensitivity to discover PWN and pulsars in currently unidentified TeV sources (Gelfand et al. 2015). Together, the CTA and SKA have the potential for revolutionizing our understanding of these sources.

3.3 A multi-wavelength view of stellar evolution

The advent of sensitive multi-wavelength surveys described above will uncover a diverse population of binary NSs. This rich NS ensemble will greatly increase the chances for revision, and ultimately unification of the stellar formation and evolution paradigm (Tauris et al. 2015). For example, the SKA will enable extremely precise mass measurements for a large number of pulsars in binaries, allowing a thorough statistical study of the mass-transfer mechanics and the distribution of NS masses at birth (Kiziltan et al. 2013; Özel et al. 2012). At the same time, sensitive optical instruments such as GAIA, LSST and E-ELT will measure the radial velocities, atmospheric composition, proper motions and parallaxes for several pulsar companions with optical counterparts, providing further information for the evolutionary history of the systems (e.g. Antoniadis et al. 2012). Furthermore, as described above, a joint optical/radio effort might increase the chances for finding unique systems. Just to give an example, intermediate-mass binary pulsars may be ideal places to look for faint, ultra-cool white dwarfs, which constraint the stellar formation history of the Milky Way and might contribute to its "dark" baryonic content (Kaplan et al. 2014). Similarly, X-ray observatories such as LOFT may help to identify more low-mass X-ray binary/MSP transition objects which would help to understand the details of pulsar recycling models (Archibald et al. 2009; Patruno et al. 2014; Tauris et al. 2015). Deep radio observations of pulsars discovered in X-ray or γ-ray blind searches are also key for understanding the NS luminosity distribution. Unlike high- energy signals, radio waves are dispersed by free electrons in the propagation path. The dispersion measure of pulsars inferred with radio observations yields their (approximate) distance (Cordes & Lazio 2002), which is impossible to determine from the high-energy observations alone.

4. Nuclear Physics and the Strong Interaction

NSs are extremely compact objects; denser than any other object in the current Universe, and

PoS(AASKA14)157

anything that has ever been since ~ 3 ms after the Big Bang (Lattimer 2012). Owing to their extreme properties, they are of fundamental importance for studying the nature of the Strong Interaction which dictates the behaviour of matter at densities reaching and exceeding the nuclear saturation density (Watts et al. 2015). The EoS describing the bulk properties of matter can theoretically be inferred from first-principle QCD calculations. Practically however, the complicated many-body interactions at play render this approach unfeasible. Over the past few decades, numerous different approximations have been developed, leading to diverse EoS predictions that span a large space of parameters (Lattimer 2012).

The EoS of cold nuclear matter, and the way it joins up with the EoS of hot matter, uniquely determine several NS observables such as the NS mass-radius relation, moment of inertia, cooling rate, maximum spin and maximum mass above which NSs collapse to black holes. For the first time, these observables will be significantly constrained in a range of NS populations with the SKA and next-generation X-ray observatories (Watts et al. 2015). The SKA will measure masses for several hundreds of binary pulsars and significantly increase the chances for finding rapidly spinning pulsars (Watts et al. 2015; Hessels et al. 2015). Furthermore it will provide, for the first time, a direct measurement of the moment-of-inertia for pulsars in relativistic double-NS systems like J0737−3039 (Watts et al. 2015; Keane et al. 2015; Shao et al. 2015). At the same time X-ray missions such as LOFT and Athena will provide simultaneous mass and radius measurements for a handful of NSs residing in X-ray binaries and potentially measure the cooling rates of nearby, thermally emitting NSs such as Cas A (Watts et al. 2015).

Multi-wavelength targeted survey approaches may also significantly speed-up the search for EoS-constraining pulsars, by telling us where to look: fast-spinning pulsars for example are energetic and most likely radiate the bulk of their spin-down energy in the form of $\gamma-$rays (Keane et al. 2015). Furthermore, there has been increasing evidence that "black-widow" and "redback" binary pulsars that have optical, X-ray and γ-ray counterparts, might host massive NSs (van Kerkwijk et al. 2011; Romani et al. 2012). Today, precise mass measurements in these systems are challenging, mostly due to sensitivity limits of radio and optical telescopes.

5. Transient Phenomena and the Dynamic Sky

5.1 Synergies between the SKA and optical telescopes

The identification of radio transients, such as Rotating Radio Transients (RRATs) and microquasars, through the interaction with the LSST and LOFT (Feroci et al. 2012; Lazio et al. 2014), or any other X-ray sky monitor to fly in the 2020s, will be one of the main science goals of the SKA (Fenderet al. 2015). Thanks to their location in the southern hemisphere, the synergies between LSST and the SKA will be crucial to elucidate the nature of thousands of transients in the restless radio and optical sky. With its continuous monitoring of 20000 square degrees of the sky and its different observing cadence, LSST will discover thousands of transient events on time scales ranging from tens of seconds to hours over 9 decades in flux (Ivezic et al. 2008). Furthermore, the LSST will be able to respond to targets-of-opportunity (ToOs) from other facilities with a reaction time of 60s in its Rapid Response Mode. Due to its large field of view of almost 10 square degrees, the LSST will provide colour information in six bands for several fast transients at each time, following the light curve evolution before, during, and after the event and provide quick localisation

PoS(AASKA14)157

for follow-ups with other facilities (Ivezic et al. 2008). Spectral information in the optical (including photometric redshifts for AGNs) will be crucial to complement the spectral coverage in the radio provided by the SKA and elucidate the nature of the transient, discriminating, e.g. a Galactic microquasar from an AGN. Inversely, an SKA trigger of a fast radio transient for LSST follow-up may be crucial for determining its nature. RRATs and other sort of bursting NSs would be probably undetectable in optical integration much longer than the length of the radio burst (typically a fraction of a second for the RRATs (Keane et al. 2011)), with the signal from a possible optical burst (assuming that it lasts as long as the radio burst) being washed out. While the non-detection of a candidate RRAT in the optical down to mag$\sim$24.5 (the typical sensitivity of 2×15 s-long LSST snapshot integration) would still be provide information to help identify its NS, more intriguing synergies would emerge with the E-ELT if it is equipped with suited instruments to fully exploit its potentials in time-domain astronomy down to the ms time scales. The detection of simultaneous optical and radio bursts from RRATs in coincidence with the radio burst, a goal that we missed so far, will shed light on the origin of these events and will allow to test the proposed models by, e.g. comparing the optical and radio fluence, the profile of the burst light curve, and the characteristics of the radio and optical pulsations (typically detected during a RRAT burst), including possible time lags.

5.2 Transients with the SKA and X-ray Telescopes

The real-time identification of Galactic X-ray transients and follow-up of variable sources discovered by LOFT, eROSITA and, a posteriori, by *Fermi* is another field that will greatly benefit from the synergy with the SKA. For example LOFT, with its Wide Field Monitor (WFM), which will cover at least 50% of the sky simultaneously in the 2-50 keV energy band, will be a perfect discovery machine of X-ray transients, such as magnetars, which have been well known and extensively studied for the past three decades. However, well known does not necessarily mean well understood. After the discovery of the prototype source back in 1979, only 30 magnetars have been found (including candidates) and we are still in a position where better understanding would benefit from the discovery of more sources. The recent discovery of both radio-loud (e.g. Shannon & Johnston 2013) and low magnetic field magnetars (Rea et al. 2010), has triggered a profound rethinking of the nature of these objects. Most magnetars have been identified by their transient X-ray emission. Previous large field-of-view telescopes, such as the All-Sky Monitor aboard RXTE, were instrumental in this role, spotting several candidates. With a factor of 20 larger collecting area, the WFM will discover many more magnetar candidates, triggering alerts for other new facilities, including the SKA. Following-up magnetars in radio during, but not only, their bursting phase is key to solve the long-standing dichotomy on the magnetar radio-quietness or radio-loudness and peer deep into the very nature of magnetars.

Other types of erratic variability in radio pulsars can be explored by the LOFT and SKA. A few pulsars tend to emit Giant Radio Pulses (GRPs) and, so far, similar phenomena at different energies (Giant Optical Pulses; Strader et al. 2013) have been observed to occur simultaneously in the Crab pulsar. Do they occur in the X rays as well? Only the SKA and LOFT will be able to answer this question. Phenomena discovered only recently in radio pulsars are the mode switches observed synchronously in X rays and in radio, like e.g. in PSR B0943+10 (Hermsen et al. 2013). How many other radio pulsars show a similar behaviour? The SKA and LOFT will certainly find

PoS(AASKA14)157

more of such cases. On longer time scales, the nature of the many variable X-ray sources that eROSITA will discover in its 4 year all-sky survey (8 scans in total) could be clarified by the SKA and optical facilities.

5.3 Fast Radio Bursts

Finally, an emerging field where synergy may be proven useful is the discovery and characterization of FRBs. FRBs are temporary isolated impulsive bursts of radio emission with very short duration of a few milliseconds. An initial discovery by Lorimer et al. (2007) was followed by a small number of detections (Keane et al. 2012; Thornton et al. 2013; Spitler et al. 2014) which dissipated the initial doubts about the astrophysical origin of the bursts. The sources of FRBs remain elusive but their large measured dispersion measures and sky locations suggest a possible extragalactic origin. If this is the case, apart from the importance of discovering a likely new population of astronomical sources at cosmological distances, they will become important tools for the study of the intergalactic medium (Ginzburg 1973). The inherent short duration of FRBs make their detection very difficult in current radio surveys, where a big single-dish telescope with its small field of view is scanning the whole sky on many-year timescales. Additionally, the commonly adopted off-line processing of survey data usually leads to detection of events well after they have occurred on the sky. What makes these phenomena even more intriguing is that no long-lasting counterpart in radio or other wavelengths is found in the direction of the detected bursts. This could mean that additional radiation of the burst at other wavelengths, if any, is also short-lived. The SKA's wide field of view will allow to monitor big portions of the sky at once, increasing significantly the detection rate for these FRBs, which are thought to occur several thousand times-per-day per-sky (Thornton et al. 2013; Spitler et al. 2014). In addition, the proposed real-time processing back-end for the survey data in search of short radio bursts enable the necessary rapid follow-up of the detected events. A real-time warning from an SKA detection could trigger rapid ToO observations at other wavelengths in the burst direction. The SKA in combination with the observatories at all other wavelengths will be key to resolve the mystery of the origin of FRBs and let us study in detail the sources and the physical processes producing these unexpected bursts of radiation.

6. Strong-Field Gravity and the Large-Scale Structure

6.1 Studies of the Galactic-Centre black hole across the spectrum

Observations of the orbits of the so-called "S-stars" have provided detailed information about the object in the centre of our Galaxy. The observations provide the most convincing case for it being a super-massive black hole (Genzel et al. 2010; Melia & Falcke 2001). First detected in the radio as a point source named Sgr A* (Sagittarius A*), the source is now being studied also at near-infrared and X-ray wavelengths. Tracing the orbits of the S-stars, one can derive the distance to the Galactic Centre (8 kpc) and the mass of the black hole (4 million solar masses). Finding (even normal) pulsars orbiting Sgr A*, the spin and the quadrupole moment can be determined with high precision (Eatough et al. 2015). These measurements can be compared with constraints to be derived with high-precision optical astrometry of the inner-most stars. Measuring for instance the mass of Sgr A* with radio pulsars to a precision of one solar mass (Eatough et al. 2015), we

PoS(AASKA14)157

can determine the distance to the Galactic Centre using the optical observation with a precision to about 1 pc, providing a firm anchor for our understanding of the Galactic dynamics.

6.2 Multi-Messenger Gravitational Wave Science

Precision timing with the SKA will start an era of GW astronomy with pulsars. SKA1 will virtually guarantee the detection of a stochastic GW background that has emerged from a population of super-massive binary black holes that was present in processes of early galaxy formation (Janssen et al. 2015). Full SKA will allow studying this background in great detail, thereby, for instance, providing insight into the fundamental properties of gravitons such as their spin and mass (Lee et al. 2010). In general, the SMBH population that is detectable with a PTA experiment is of higher mass than those of sources detectable with the space- based GW detector eLISA. With PTAs being sensitive to SMBHs with 10^7 solar masses and orbital periods between 10 and 20 years, SKA observations provide a truly complementary window to the SMBH population. Moreover, observations with the SKA can provide measurements of the amplitude and spectral shape of the GW background, which encodes information about galaxy merger and SMBH accretion processes. As for instance pointed out by Sesana (2013), the amplitude of the signal tracks the number of occurred mergers integrated over the redshift range, while the spectral shape should contain a break frequency where contribution of individual systems becomes important. Indeed, some individual sources may produce a signal that is significantly larger than indicated by the average spectrum, allowing the detection of a single source which will eventually evolve into the eLISA frequency band.

In a comprehensive review Burke-Spolaor (2013) discusses in more detail the possibilities, and importance, of electromagnetic identification of the sources of GWs, which could be from continuous-wave, burst or GW memory sources. PTAs are already being used to dis-prove the identification of supermassive black hole binaries in the local neighbourhood Jenet et al. (2004). As the sensitivity of PTAs improves dramatically with the SKA, improved limits and ultimately detections will be possible. Localising these sources by use of an electromagnetic counterpart such as might be possible with current surveys in optical and X-ray wavelengths and using future facilities like LSST, IXO/Athena, Astro-H combined with the GW signature will allow significantly more detailed information about the binary system to be determined.

For compact relativistic binaries with sufficiently small orbital periods, it is possible that GWs may be directly detectable with eLISA. The orbital frequency of the Double Pulsar, for instance, is 1.16×10^{-4} Hz, so that we can expect to observe a strain of about 5×10^{-21} at 2.3×10^{-4} Hz (Kramer & Stairs 2008). Realistically, a detection may be aggravated by the large expected background of double-white-dwarf systems with similar orbital periods (Nelemans et al. 2001). However, if the orbital ephemerides are well known from radio timing with the SKA, and because the systems should also produce power at the next orbital harmonic, it should be possible to detect the appropriate sources in a coherent search that takes advantage of the known direction to the source (S. Sigurdsson & C. Miller, private communication). If detection is made, it is possible to combine the observations obtained from the radio with those obtained with eLISA. This combination should in principle be able to provide the exact distance to the source, the true inclination angle of the system (rather than either sine or cosine of the inclination angle) and the masses. Therefore,

PoS(AASKA14)157

the system should be vastly over-determined, allowing to provide unprecedented tests of theories of gravity.

Isolated neutron stars may also be the source of GWs if they are deformed in such a way as to make them axi-symmetric. The GW amplitude will depend on the size of the asymmetry which in turn is strongly dependent on the nature of the equation of state of the neutron star and the strength of the internal magnetic fields. Significant and important limits on the degree of deformation and the fraction of the spin-down energy loss of pulsars that might manifest as GW emission have been obtained with current generation GW observatories (e.g. Aasi et al. 2014; The LIGO Scientific Collaboration et al. 2014) however the SKA will be operating at the same time as the much more sensitive advanced LIGO and VIRGO detectors. To be able to undertake these searches for GWs typically involves long integration times and it is therefore necessary to have good models of the rotational history of the pulsars. The SKA will help by discovering many more pulsars, thus improving chances of finding even just one deformed source and also be enabling the monitoring of even larger numbers of pulsars. Moreover we will also be sensitive to systems that might exhibit GW bursts. This is only the tip of what might be possible though synergies between the ground-based gravitational wave observatories and the SKA.

7. Conclusions

In this chapter we elaborated on various aspects of the multi-wavelength, multi-messenger NS science that will be enabled in the SKA era. Current simulations show that even SKA1 can discover a total of about 10000 normal pulsars and perhaps as many as 1800 millisecond pulsars (MSPs), with SKA1-LOW surveying the sky with the Galactic latitude $|b| \geq 5^{o}$, and SKA1-MID surveying the sky with the Galactic latitude $|b| \leq 10^{o}$ (Keane et al. 2015). Full SKA will provide a complete census of radio pulsars and with its Aperture Array systems should allow for an optimum combination of sensitivity, field-of-view and number of beams to be able to obtain exceptional cadence on a very large number of sources. These key features will allow for significant advances in our understanding of NSs, which could be further accelerated by coordinated efforts with other next-generation telescopes. As demonstrated here, synergies across the electromagnetic-spectrum and beyond could provide a better understanding of (I) the Galactic structure and content, (II) extreme astrophysics and stellar evolution, (III) nuclear physics and the strong interaction, (IV) transient phenomena and (V) strong-field gravity and the large-scale structure of the Universe.

References

Aasi, J., Abadie, J., Abbott, B. P., et al. 2014, ApJ, 785, 119
Antoniadis, J., Freire, P. C. C., Wex, N., & et al. 2013, Science, 340, 448
Antoniadis, J., van Kerkwijk, M. H., Koester, D., & et al. 2012, MNRAS, 423, 3316
Archibald, A. M., Stairs, I. H., Ransom, S. M., & et al. 2009, Science, 324, 1411
Burke-Spolaor, S. 2013, Classical and Quantum Gravity, 30, 224013
Cordes, J. M., & Lazio, T. J. W. 2002, ArXiv Astrophysics e-prints, ArXiv:0207156
Dubus, G., Contreras, J. L., Funk, S., et al. 2013, Astroparticle Physics, 43, 317

PoS(AASKA14)157

Eatough, R. P., Lazio, T. J. W., Casanellas, J., et al. 2015, "Observing Radio Pulsars in the Galactic Centre with the Square Kilometre Array", in proc. *Advancing Astrophysics with the Square Kilometre Array*, PoS(AASKA)045

Fender, R. et al. 2015, "The Transient Universe with the Square Kilometre Array", in proc. *Advancing Astrophysics with the Square Kilometre Array*, PoS(AASKA)051

Feroci, M., Stella, L., van der Klis, & et al. 2012, Experimental Astronomy, 34, 415

Gaensler, B. M., & Slane, P. O. 2006, ARA&A, 44, 17

Gelfand, J. D., Breton, R. P., Ng, C.-Y., et al. 2015, "Pulsar Wind Nebulae in the SKA era", in proc. *Advancing Astrophysics with the Square Kilometre Array*, PoS(AASKA)046

Gelfand, J. D., Slane, P. O., & Zhang, W. 2009, ApJ, 703, 2051

Genzel, R., Eisenhauer, F., & Gillessen, S. 2010, Reviews of Modern Physics, 82, 3121

Ginzburg, V. L. 1973, Nature, 246, 415

Han, J. L., van Straten, W., Lazio, T. J. W., et al. 2015, "Three-dimensional Tomography of the Galactic and Extragalactic Magnetoionic Medium with the SKA", in proc. *Advancing Astrophysics with the Square Kilometre Array*, PoS(AASKA)043

Hartman, R. C., Bertsch, D. L., Bloom, & et al. 1999, ApJS, 123, 79

Hermsen, W., Hessels, J. W. T., & Kuiper, e. 2013, Science, 339, 436

Hessels, J. W. T., Possenti, A., Bailes, M., et al. 2015, "Pulsars in Globular Clusters with the SKA", in proc. *Advancing Astrophysics with the Square Kilometre Array*, PoS(AASKA)047

Ivezic, Z., Tyson, J. A., Acosta, E., et al. 2008, ArXiv e-prints, arXiv:arXiv:0805.2366

Jacoby, G. H., Branch, D., Ciardullo, R., Davies, R. L., & et al. 1992, PASP, 104, 599

Janssen, G. H., Hobbs, G., McLaughlin, M., et al. 2015, "Gravitational Wave Astronomy with the SKA", in proc. *Advancing Astrophysics with the Square Kilometre Array*, PoS(AASKA)037

Jenet, F. A., Lommen, A., Larson, S. L., & Wen, L. 2004, ApJ, 606, 799

Kaplan, D. L., Boyles, J., Dunlap, B. H., & et al. 2014, ApJ, 789, 119

Keane, E. F., Kramer, M., Lyne, A. G., Stappers, B. W., & McLaughlin, M. A. 2011, MNRAS, 415, 3065

Keane, E. F., Stappers, B. W., Kramer, M., & Lyne, A. G. 2012, MNRAS, 425, L71

Keane, E. F., Bhattacharyya, B., Kramer, M., et al. 2015, "A Cosmic Census of Radio Pulsars with the SKA", in proc. *Advancing Astrophysics with the Square Kilometre Array*, PoS(AASKA)040

Kiziltan, B., Kottas, A., De Yoreo, M., & Thorsett, S. E. 2013, ApJ, 778, 66

Kramer, M., & Stairs, I. H. 2008, ARA&A, 46, 541

Lattimer, J. M. 2012, Annual Review of Nuclear and Particle Science, 62, 485

Lazaridis, K., Wex, N., Jessner, A., & et al. 2009, MNRAS, 400, 805

Lazio, J. W., Kimball, A., Barger, A. J., & et al. 2014, PASP, 126, 196

Lee, K., Jenet, F. A., Price, R. H., Wex, N., & Kramer, M. 2010, ApJ, 722, 1589

Lorimer, D. R., Bailes, M., McLaughlin, M. A., Narkevic, D. J., & Crawford, F. 2007, Science, 318, 777

Lyne, A., & Graham-Smith, F. 2012, Pulsar Astronomy

Melia, F., & Falcke, H. 2001, ARA&A, 39, 309

Nelemans, G., Yungelson, L. R., & Portegies Zwart, S. F. 2001, A&A, 375, 890

Nolan, P. L., Abdo, A. A., Ackermann, M., et al. 2012, ApJS, 199, 31

Özel, F., Psaltis, D., Narayan, R., & Santos Villarreal, A. 2012, ApJ, 757, 55

PoS(AASKA14)157

Patruno, A., Archibald, A. M., Hessels, J. W. T., & et al. 2014, ApJ, 781, L3
Pletsch, H. J., Guillemot, L., Allen, B., & et al. 2012, ApJ, 744, 105
Ray, P. S., Abdo, A. A., Parent, D., & et al. 2012, ArXiv e-prints, arXiv:ArXiv:1205.3089
Rea, N., Esposito, P., Turolla, R., & et al. 2010, Science, 330, 944
Romani, R. W. 2012, ApJ, 754, L25
Romani, R. W., Filippenko, A. V., Silverman, J. M., & et al. 2012, ApJ, 760, L36
Sesana, A. 2013, MNRAS, 433, L1
Shannon, R. M., & Johnston, S. 2013, MNRAS, 435, L29
Shao, L., Stairs, I. H., Antoniadis, J., et al. 2015, "Testing Gravity with Pulsars in the SKA Era", in proc. *Advancing Astrophysics with the Square Kilometre Array*, PoS(AASKA14)042
Smits, R., Tingay, S. J., Wex, N., Kramer, M., & Stappers, B. 2011, A&A, 528, A108
Spitler, L. G., Cordes, J. M., Hessels, J. W. T., & et al. 2014, ArXiv e-prints, arXiv:ArXiv:1404.2934
Strader, M. J., Johnson, M. D., Mazin, B. A., & et al. 2013, ApJ, 779, L12
Tauris, T. M., Kaspi, V. M., Breton, R. P., et al. 2015, "Understanding the Neutron Star Population with the SKA", in proc. *Advancing Astrophysics with the Square Kilometre Array*, PoS(AASKA)039
The LIGO Scientific Collaboration, the Virgo Collaboration, Aasi, J., et al. 2014, ArXiv e-prints, arXiv:1410.8310
Thornton, D., Stappers, B., Bailes, M., & et al. 2013, Science, 341, 53
van Kerkwijk, M. H., Breton, R. P., & Kulkarni, S. R. 2011, ApJ, 728, 95
Watters, K. P., & Romani, R. W. 2011, ApJ, 727, 123
Watts, A., Xu, R., Espinoza, C., et al. 2015, "Probing the neutron star interior and the Equation of State of cold dense matter with the SKA", in proc. *Advancing Astrophysics with the Square Kilometre Array*, PoS(AASKA14)043
Yusifov, I. 2004, in The Magnetized Interstellar Medium, ed. B. Uyaniker, W. Reich, & R. Wielebinski, 165–169

PoS(AASKA14)157

PROCEEDINGS OF SCIENCE

Overview of Complementarity and Synergy with Other Wavelengths in Cosmology in the SKA era

Keitaro Takahashi[*1], **Michael L. Brown**[2], **Carlo Burigana**[3,4], **Carole A. Jackson**[5], **Matt Jarvis**[6], **Thomas D. Kitching**[7], **Jean-Paul Kneib**[8], **Masamune Oguri**[9], **Simon Prunet**[10], **Huanyuan Shan**[8], **Jean-Luc Starck**[11], **Daisuke Yamauchi**[12]

[1]*Graduate School of Science and Technology, Kumamoto University, Japan* [2]*Jodrell Bank Centre for Astrophysics, University of Manchester, Oxford Road, Manchester M139PL, UK* [3]*INAF-IASF Bologna, Via Piero Gobetti 101, I-40129, Bologna, Italy* [4]*Dipartimento di Fisica e Scienze della Terra, Università degli Studi di Ferrara, Via Giuseppe Saragat 1, I-44100 Ferrara, Italy* [5]*ICRAR, Curtin University, GPO Box U1987, Perth 6845, Australia* [6]*Astrophysics Department, University of Oxford, UK* [7]*Mullard Space Science Laboratory, University College London, Holmbury St Mary, Dorking, Surrey RH5 6NT, UK* [8]*Ecole Polytechnique Fédérale de Lausanne Laboratoire d'Astrophysique, Observatoire de Sauverny, CH-1290 Versoix, Switzerland* [9]*Graduate School of Science, University of Tokyo, Japan* [10]*Canada-France-Hawaii Telescope* [11]*Laboratoire AIM, UMR CEA-CNRS-Paris 7, Irfu, SAp, CEA Saclay, F-91191 Gif sur Yvette cedex, France* [12]*Research Center for the Early Universe, University of Tokyo, Japan*
E-mail: keitaro@sci.kumamoto-u.ac.jp

We give an overview of complementarity and synergy in cosmology between the Square Kilometre Array and future survey projects in other wavelengths. In the SKA era, precision cosmology will be limited by systematic errors and cosmic variance, rather than statistical errors. However, combining and/or cross-correlating multi-wavelength data, from the SKA to the cosmic microwave background, optical/infrared and X-ray, substantially reduce these limiting factors. In this chapter, we summarize future survey projects and show highlights of complementarity and synergy, which can be very powerful to probe major cosmological problems such as dark energy, modified gravity and primordial non-Gaussianity.

Advancing Astrophysics with the Square Kilometre Array
June 8-13, 2014
Giardini Naxos, Italy

[*]Speaker.

PoS(AASKA14)159

1. Introduction

In the era of SKA operations, astronomy will be fully in the realm of Ąebig dataĄf science. Observational data will have been accumulated from millions of discrete objects across the electromagnetic spectrum by a large number of ground and space-based missions. In addition there will be existing and evolving detailed simulated data: all of which the SKA will contribute to and provide a unique insight to its interpretation.

Whilst significant sets of data may be complete from a number of other facilities ahead of, and during early SKA operations, the challenge will be to fully exploit its scientific yield. This requires that observational integrity and repeatability are maintained across the build phases to realize the full SKA (SKA2). This alignment of the data is critical because many SKA-complementary facilities will only have limited lifetimes, and as such it relies on the *SKA* meeting these requirements not vice-versa. It should also be noted that the SKA will come into operation in an era where we will have moved beyond multiple simultaneous space missions as we do now due to increasing costs. Even today, some of the SKA-complementary facilities are of limited-lifetime (even single-experiment) facilities.

So far cosmology has been developed by extracting statistical information from the distribution of a large number of objects such as galaxies and galaxy clusters. Errors in cosmological parameters are, in many cases, dominated by statistical errors, which can be reduced by increasing the number of objects. However, in the SKA era with huge optical/infrared surveys by Euclid, LSST and WFIRST, systematic errors and cosmic variance, rather than statistical errors, will become the limiting factors to advance cosmology further. Thus, it is of vital importance to reduce systematics and cosmic variance.

Instrumental systematics will be independent for different wavelength observations so that combining or cross-correlating multi-wavelength data is expected to be able to reduce systematics substantially. This is a major way of synergy and weak lensing is a typical example as we describe briefly later. Cross-correlation is also effective between the CMB anisotropies and large scale structure. Although the CMB anisotropies contain a lot of cosmological information such as initial condition and evolution of primordial fluctuations, geometry of the universe and history of cosmic expansion, it is not easy to disentangle them. Cross-correlation with the distribution of galaxy is a powerful way to extract low-redshift information, which allows us to investigate dark energy and modified gravity.

In this chapter, we give an overview of synergies in cosmology between the SKA and surveys in other wavelengths. Each topic will be briefly described and we refer to other chapters in for the details.

2. Future Survey Projects

In this section we briefly summarise the major surveys that are, or will, take place until routine SKA1 operations. In writing about the future potential, we have to bear in mind that timelines can slip and missions change in scope and focus; however what follows is a summary of the cosmology-relevant landscape that SKA will inhabit. We must also consider SKA as it evolves: the initial build

PoS(AASKA14)159

phase (SKA1) will have a limited operational window, followed by potential build interruptions to evolve into the full SKA (SKA2).

2.1 Surveys in the pre-construction SKA era

There are many SKA pathfinding surveys during the pre-construction and early build era; these use existing and precursor/pathfinder telescopes. Many of these are major wide-field and/or deep surveys in themselves. They will deliver important results as well as informing both the design and science directions of the SKA. These surveys are discussed in Norris et al. (2014) and their details are not presented here. A characteristic of these pathfinding surveys is the preparatory work being undertaken by large international teams ahead of observations. Not only will this work tackle some of the data management and SKA-era compatibility issues but it will also ensure the systematics of these surveys is well understood, ready for even deeper cosmological analyses.

Across the rest of the spectrum there are a number of major new facilities that will yield data to progress SKA-cosmology experiments. In the optical these include SDSS, JWST, DESI and VST/KiDS. In the infrared WISE and HERSCHEL have already contributed massive information which SKA observations will draw on. At higher energies eROSITA (X-ray) will detect clusters as a probe of dark energy and primordial density fluctuations Colafrancesco et al. (2015)) and GALEX (UV) are expected to have completed observations by the first operations of SKA.

2.2 Surveys in the SKA era $\sim$ 2020 onwards

At the time that the SKA is operational, there will be additional survey data flowing from a number of new ground-based telescopes and space missions that we now briefly discuss.

Euclid Laureijs et al. (2011) is expected to be launched in 2020 and will perform imaging and spectroscopic surveys in optical and infrared bands. The survey area is about 15,000 deg^2 and the primary sciences are weak lensing and baryon acoustic oscillation. The synergies between the SKA and Euclid are discussed in the other chapter Kitching et al. (2015).

The large synoptic survey telescope (LSST) Ivezić (2008) is an ground-based optical wide-field survey telescope that will observe the entire available sky every few nights and anticipated to be operational from 2022. It will observe 18000 square degrees of the southern hemisphere and provide photometric redshifts and optical shapes. The synergies between the SKA and LSST are discussed in the other chapter Bacon et al. (2015).

Great efforts are being pursued in the CMB community to prepare a next generation of experiments. These are space missions and include the following.

In response to the ESA Cosmic Vision (2015-2025) Call for Proposals, a medium-size mission, B-Pol (http://www.b-pol.org) has been proposed. This is targeted to ultra-accurate CMB polarization measurements up to a moderate resolution (about 1 degree) at six frequency bands between 45 GHz and 353 GHz de Bernardis et al. (2009) to primarily identify primordial B-modes. B-pol is proposed to be realized as a set of eight small telescopes co-aligned within the spacecraft axis with an array of about 1000 single mode corrugated feed horns in each telescopeĄfs focal plane, designed to be well-matched with the optics and only minimal aberrations.

Building on *Planck*'s success the Cosmic Origins Explorer (COrE: http://www.core-mission.org) COrE Collaboration (2011) has been proposed in response to the ESA call. About 6400 dual-polarisation receivers at the focal plane of a 1.5 - 2 m class telescope would achieve a resolution of

PoS(AASKA14)159

a few arcmin with excellent polarization sensitivity, across a wide (45 GHz - 795 GHz) frequency range (15 bands). The goal of COrE is to extend CMB polarization studies through to higher multipoles, probing a variety of cosmological and fundamental physics along with a providing a new generation of all-sky polarization surveys.

In the other critical aspect of CMB cosmology, i.e. the detailed study of the frequency spectrum, little progress has been made since the stunning results from COBE/FIRAS. There are two ambitious projects now proposed which would have impact in the SKA era. The Primordial Inflation Explorer (PIXIE) Kogut et al. (2011) has been presented to NASA as an Explorer-class proposal. It would be equipped with receivers operating between 30 GHz and 6 THz, sensitive to polarization and coupled to an advanced cryogenic calibration system to achieve the required precise measurements. The main goal is to reveal the fine details of the CMB spectrum as well as addressing the extremely small scales of primordial perturbations that are otherwise damped and unobservable in anisotropies. The second, and by far most ambitious mission, the Polarized Radiation Imaging and Spectroscopy Mission (PRISM: http://www.prism.org) PRISM Collaboration (2014) was first proposed in 2013 as an ESA Science Programme. PRISM is aimed at ultra-accurate CMB mapping in both temperature and polarization, limited only be cosmic variance and foregrounds. PRISM would have imaging accuracy to a few arcmin over a very wide frequency range (30 GHz to 6 THz), and with these capabilities it would map the distribution of galaxy clusters through to the IR. Furthermore, PRISM sensitivity to CMB spectrum is about one order of magnitude better than PIXIE.

LiteBird (JAXA proposed future mission: http://litebird.jp/eng/) which will undertake a full sky CMB polarization survey at degree scale; 50 GHz - 320 GHz (with 30 arcmin resolution at 150 GHz). Planned launch in the early 2020s.

3. Weak Lensing

3.1 Weak Lensing survey efficiency

Weak lensing is made possible by the statistical study of the shapes of distant sources and brings information on the mass distribution located between us and these distant sources. The weak lensing measurements thus requires shape information and redshift information. Shape information is essential, however for some application redshift information can be used on a statistical basis.

The weak lensing information will scale with the number density of distant sources, and is limited by the intrinsic ellipticity distribution of the background sources and our (limited) knowledge of the PSF and its possible variation across the survey. This can be seen in the shear measurement error that can be written as:

$$\sigma_\gamma^2 \propto \frac{\sigma_{\varepsilon-int}^2 + \sigma_{meas}^2}{N} \tag{3.1}$$

where N is the number of galaxies over which the shape is measured, $\sigma_{\varepsilon-int}$ is the intrinsic shape dispersion and depends only on the intrinsic nature of the sources observed and σ_{meas} is the noise added by the measurement techniques and includes information (or lack of) of the PSF and the photon noise. Note that PSF issues are much more critical at optical wavelength (specially for ground based observatory, less for space mission) than radio wavelength.

PoS(AASKA14)159

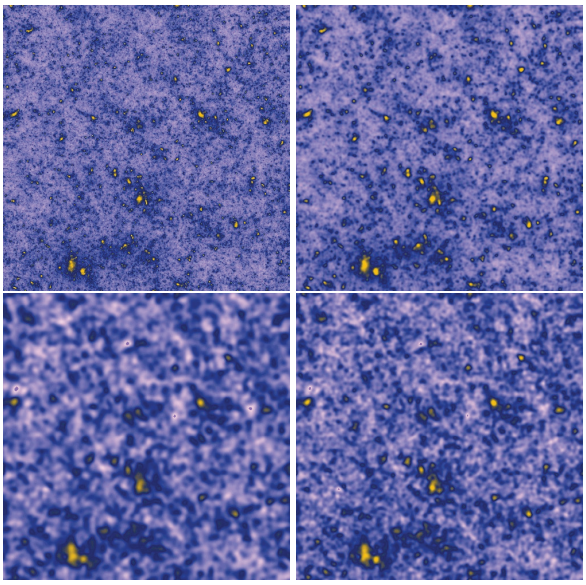

Figure 1: Simulation of 3 square degrees converence maps. The top-left panel is the input mass map, the top-right panel is the smoothed mass map. The bottom-left panel shows the recovery for a Euclid-like survey with effective galaxy number density $n_g \sim 30$ gals/arcmin^2. The bottom-right panel shows the simulated recovery for the SKA plus Euclid with $n_g \sim 100$ gals/arcmin^2. It shows that SKA information will help increase both the weak lensing S/N measurement as well as better resolving smaller-scale mass structure.

Because distant sources are small (of the order of $\sim$1 arcsec or smaller), cosmological weak lensing survey efficiency will scale with the total number of sources for which one can resolve their shape.

Different weak lensing techniques can inform us on the matter distribution on different scales.

- Cosmic shear allows to probe the matter power spectrum, and is very efficient in probing the very large scales. Yet, ground based weak lensing power has been quite limited on large scale ($>$ 100 Mpc) because of systematic limitations.
- Weak lensing mass mapping and peak statistics: blind search of structure, sensitive to cosmological parameters.
- Cluster weak lensing: need cluster survey sample
- Galaxy-galaxy lensing: need foreground galaxy sample

3.2 Weak lensing survey complementarity

Wide-field radio and optical survey differs significantly by the nature of the sources found the continuum imaging. Radio sources are good tracers of star-formation activities while I-band selected galaxies used in optical are more of a tracer of stellar masses (at least to $z < 1$). Radio sources are thus likely less biased system than optical sources, and possibly have a more homogeneous distribution on the sky.

PoS(AASKA14)159

Because of this, the redshift distribution of continuum radio and optical galaxies are somewhat different. Optically I-band selected sources will mostly lie at $z < 1$, while radio sources are more broadly distributed in redshift with a more prominent tail at high redshift.

Radio surveys will thus allow to probe mass distribution and the large-scale structure at higher redshift than can possibly be done with optical surveys. They will also be more efficient in probing high density region such as galaxy clusters as the cluster light is blocking somewhat the signal of background galaxies.

Overlapping optical and radio surveys have a particularly useful synergy in terms of reducing and quantifying the impact of systematic effects in weak gravitational lensing analyses (Fig. 1). By cross-correlating the shapes of galaxies as measured in the optical and radio surveys, one can eliminate instrumental systematic effects that are not correlated between the two telescopes. Given the very different designs and modes of operation of optical and radio telescopes, one would not expect their instrumental systematic effects to be correlated and so this offers a route to measuring the cosmic shear signal in a very robust way.

Moreover, radio surveys offer unique additional ways to measure the lensing signal that are not available to optical telescopes. In particular, both radio polarization information and rotational velocity measurements from HI observations can provide estimates of the *intrinsic* position angles of the lensing source galaxies. Such measurements offer great potential to (i) reduce the effects of galaxy "shape noise" due to the intrinsic dispersion in galaxy shapes Morales (2006) and (ii) to mitigate the contaminating signal from the intrinsic alignments in galaxy orientations which is perhaps the most worrisome astrophysical systematic effect facing future weak lensing surveys Patel et al. (2010). In addition to using this information in a combined analysis, one could potentially use the SKA-based estimates of the intrinsic alignment contamination to calibrate out the alignment signal in the LSST lensing survey.

Finally, the envisaged SKA surveys will probe a wider range of redshifts than will be reached by LSST. The SKA surveys thus provide extra (high-redshift) tomographic slices with which the evolution of structre at relatively early times can be probed. SKA can push to even higher reshift by measuring the lensing distortion signal in HI intensity mapping surveys. Thus, these high-redshift SKA lensing experiments will naturally help fill the gap between the traditional optical lensing probes (where sources are typically located at $z \sim 1$) and the ultimate lensing source of the CMB at $z \sim 1000$.

4. Cosmic Microwave Background

The Cosmic Microwave Background is a very powerful probe to constrain cosmological parameters that are dynamically relevant at the epoch of recombination ($z \sim 1080$). Recent high-sensitivity, high-angular resolution measurements of the CMB temperature anisotropies by *Planck* Planck Collaboration (2014a,b) over the nominal 14 month mission show that the now standard ΛCDM model is an excellent fit to the data. By the end of this year, the full temperature data, as well as results from polarisation data should be made public. If the quality of the CMB data is now good enough to break degeneracies between parameters that were plaguing earlier datasets, it cannot nevertheless tell us much about the precise dynamical behaviour of the Universe at low

PoS(AASKA14)159

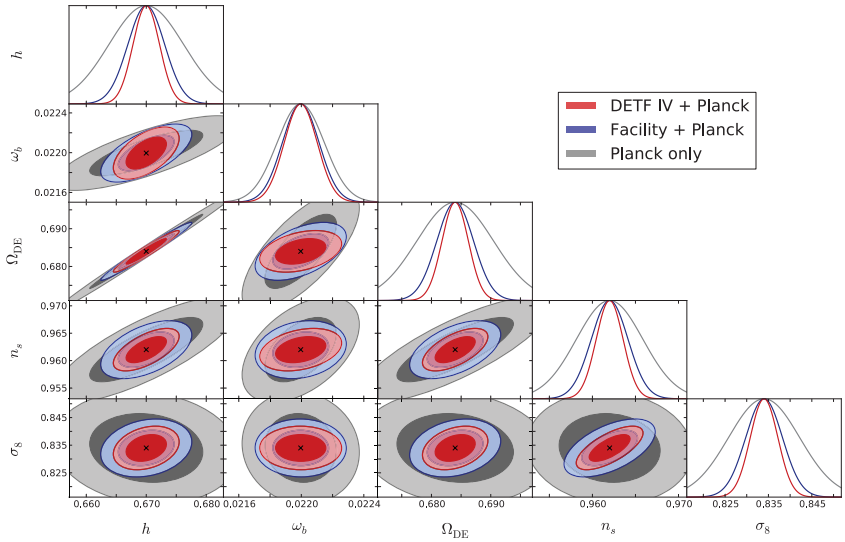

Figure 2: Compared constraints from a Fisher matrix analysis on ΛCDM parameters using different probe combinations Bull et al. (2014). "Facility" is representative of the SKA1 survey in combined (single dish plus interferometric) mode, and "DETF IV" is representative of e.g. the Euclid redshift survey. Both SKA1 and Euclid should come on similar time frames (around 2020) and have similar power on this model.

redshifts, in particular it cannot give any precise constraints on dark energy or modified gravity models.

On the other hand, future giant radio surveys with the SKA will provide an exquisite view of the low redshift universe, with the first phase surveys at the horizon of 2020, i.e. on a similar time frame to the next generation of optical/near-infrared galaxy surveys, e.g. Euclid and LSST. These low-redshift probes however cannot constrain by themselves the full cosmological model, but they will have a tremendous impact on the study of dark-energy models Blake et al. (2004). Therefore, the primary synergy of CMB and SKA data will come from a joint analysis of the cosmological parameters including dark energy and/or modified gravity models on linear scales where the theoretical predictions are well understood.

For such an analysis on linear scales, it has been shown that an Intensity Mapping (IM) of the HI fine-structure line emission that does not resolve individual galaxies should provide powerful cosmological constraints Mao et al. (2008). A recent, detailed forecasting of a joint Planck+SKA1 IM survey Bull et al. (2014), making full use of the redshift information available, shows that this particular combination of probes should be competitive with e.g. Planck+Euclid redshift survey combinations not only on the standard ΛCDM model parameters (see Fig. 2), but also on dark energy model parameters (see Fig. 3).

It will also be competitive on constraining the curvature parameter Ω_K, which exhibits a degeneracy with other parameters in CMB data taken alone Efstathiou & Bond (1999), by tightening the constraint by more than a factor of 3. In this analysis, the value of the HI bias has been conservatively marginalised over in each redshift bin. However, a large uncertainty lies in the value of the comoving HI fraction $\Omega_{\rm HI}$ which is poorly known today, and which directly impacts the signal-to-noise of the measured HI emission. This translates into an overall uncertainty of the constraints

PoS(AASKA14)159

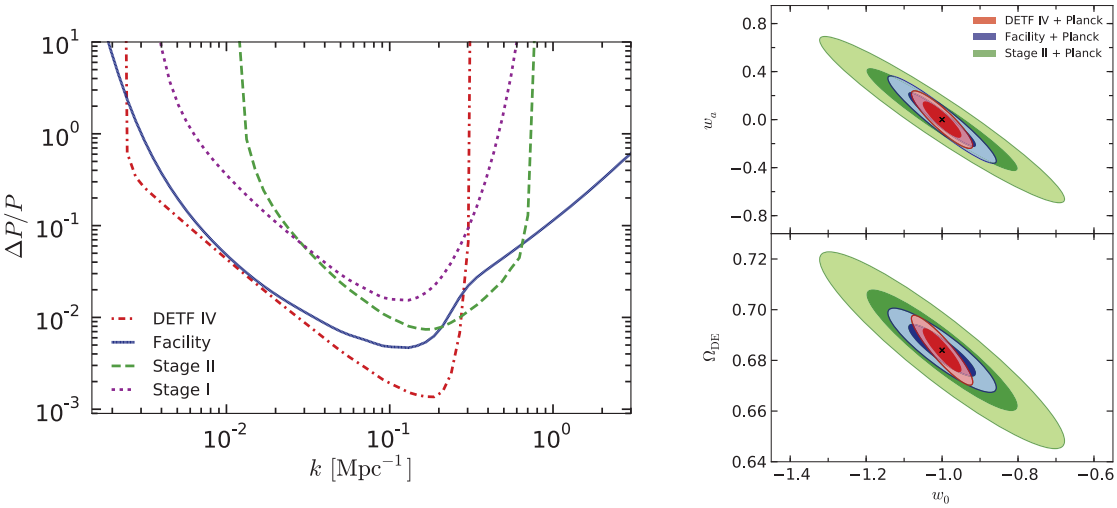

Figure 3: *Left panel:* Fractional constraints on the dark matter power spectrum $P(k)$ of different planned surveys, combined over the full range over their respective redshift coverage, with 20 bins per decade Bull et al. (2014). We can see that the "Facility" survey (representative of SKA1 in combined mode) and the "DETF IV" survey (representative of Euclid redshift survey) have comparable measurement power on linear scales ($k \lesssim 0.1\,\mathrm{Mpc}$). *Right panel:* Constrains from a Fisher matrix analysis of different combinations of *Planck* CMB data with either the "Facility" of "DETF IV" surveys. Again, we see that both combinations have comparable constraining power. Here the dark energy equation of state is parametrised as $w(a) \simeq w_0 + (1-a)w_a$, where a is the scale factor.

shown in Figs. 2,3.

We should also note that HI emission is strongly contaminated by Galactic (synchrotron, free-free) and extragalactic (free-free, point sources) foreground emissions Mao et al. (2008). The constraints shown in Figs. 2,3 are obtained under the assumption that these foreground emissions, due to their smooth spectral emission properties, can be reduced by 10^3 in amplitude with foreground-cleaning techniques, which represents a significant challenge in itself.

A more direct way to jointly analyse CMB and low-redshift probes is to investigate their cross-correlation, sourced by the correlation of the dark matter fluctuations and the late ISW effect Sachs & Wolfe (1967); Boughn et al. (1998, 2004), possibly using the redshift information Giannantonio et al. (2008); Ho et al. (2008). While this correlation is limited to very large scales and should be therefore cosmic variance limited when using SKA1 data Raccanelli et al. (2012), it provides a different way of constraining dark energy models, and has a linear (rather than quadratic) dependence on the HI bias. It is therefore an important consistency check of the cosmological model, despite its reduced constraining power. Another way of looking at the correlation of CMB and LSS probes is spatially correlating the extrema of the CMB and LSS on very large scales, possibly assigning the ISW-LSS correlation to the largest supervoids/superclusters around us Granett et al. (2008). A detailed analysis of these extrema with Planck and SKA1 data will shed a new light on the largest structures around us.

On smaller scales, high frequency SKA measurements of galaxy clusters will provide high-resolution maps of the Sunyaev-Zel'dovich effect Sunyaev & Zel'dovich (1972); Subhramanian

PoS(AASKA14)159

& Eckers (2002) with a very precise subtraction of radio sources (a major contaminant of today's measurements), for up to 10^3 sources per field of view. Other CMB+SKA synergies include primordial non-gaussianity, high-redshift free-free emission, magnetic fields at cosmological scales are discussed in the other chapter Burigana et al. (2015).

Finally, CMB fluctuations have a Gaussian distribution at a very accurate level Planck Collaboration (2014d). It is thus possible to estimate, through careful resummation of its trispectrum Seljak (1996); Okamoto & Hu (2003); Lewis & Challinor (2006); Benoit-Lévy et al. (2013), the convergence map of the matter up to $z \sim 1080$ Das et al. (2011); van Engelen et al. (2012); Planck Collaboration (2014c). The correlation of these CMB convergence maps with the more traditional weak-lensing measurements of background galaxies has been measured recently Hand et al. (2013). This method, when applied to SKA weak-lensing measurements (see Section 3) together with CMB data (at large and small scales) will allow to constrain the matter distribution at redshifts unreachable by SKA alone.

The synergies between CMB and SKA data are, in summary, very diverse, and extremely powerful to constrain cosmological parameters, and the first phase SKA1 survey, in combined (single dish plus interferometric) mode, will be competitive with Euclid and LSST for the study of dark energy models.

5. Galaxy Power Spectrum and Multi-Tracer Method

In 2020's, the SKA and optical/infrared surveys will perform ultimate observations of large-scale structure of the universe. With huge number of galaxies, the errors in power spectrum of galaxies will be dominated by cosmic variance, rather than shot noise, at cosmological scales. This is especially serious when we try to constrain primordial non-Gaussianity whose effect is stronger at larger scales.

Seljak (2009) proposed a novel method, called multi-tracer method, to defeat cosmic variance using multiple tracers of the dark matter distribution with different bias. Although power spectra of tracers themselves are limited by cosmic variance, the ratio of the power spectra of two tracers, which represents the ralative bias, can evade cosmic variance and is limited only by shot noise. Because the mass and redshift dependences of bias are affected by non-Gaussianity ($f_{\rm NL}$), it can be constrained by the measurements of relative biases.

This multi-tracer method is effective when the bias difference, hence mass difference, is large between tracers and it is critically important to estimate the mass of the dark halo hosting each galaxy. Ferramacho et al. (2014) considers using different radio galaxy populations (star forming galaxies, starburst galaxies, radio-quiet quasar, FRI and FRII AGN galaxies) as tracers of dark halos of different mass. Although it would not be easy to distinguish these populations observationally, especially between star forming galaxies and starburst, they showed that the SKA continuum survey could ideally reach $f_{\rm NL} \lesssim 1$.

Another key is the redshift evolution of bias. Because the SKA and optical/IR surveys will have different redshift-distribution of observed galaxies, their combination enhances the power of multi-tracer method. Yamauchi et al. (2014) studied the potential of combination of the SKA continuum survey and Euclid photometric survey for the constraint on $f_{\rm NL}$. The SKA continuum survey reaches much further than the Euclid photometric survey while the number of galaxies ob-

PoS(AASKA14)159

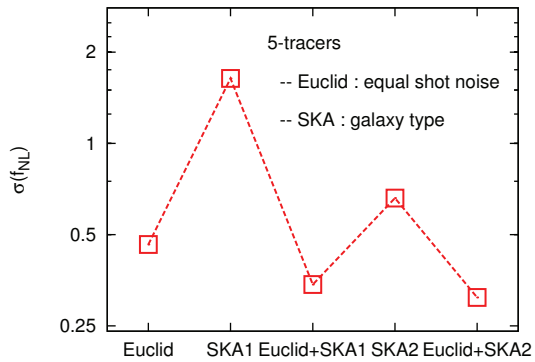

Figure 4: Expected constraints on $f_{\rm NL}$ using multi-tracer method assuming observations of the SKA continuum survey, Euclid photometric survey and their combinations Yamauchi et al. (2014).

served by Euclid is larger than that by the SKA at low redshifts, so they are complementary to probe the evolution of bias. Fig. 4 shows the expected constraints on $f_{\rm NL}$ from Euclid, SKA1, SKA2 and their combinations. Here, it is assumed that galaxies observed by Euclid have photometric redshift while SKA cannot obtain redshift information. It is seen that the constraint on $f_{\rm NL}$ can reach below unity and it would be possible to approach to $O(0.1)$.

6. Cluster Cosmology

The formation of galaxy clusters is seeded by density fluctuations of $10h^{-1}$ Mpc comoving scale. This is dominated by the gravitational processes and is relatively simple, and thus the halo mass function and its evolution depend strongly on the properties of density fluctuations at the scale. In fact, they have been used as probes for the amplitude of density fluctuations and dark energy. An X-ray satellite eROSITA is expected to be launched in 2016 and will observe about 10^5 clusters including 10^3 high-redshift ($z > 1$) clusters.

A critical ingredient when we use clusters as a cosmological tool is the estimation of halo mass. There is a scaling relation between halo mass and X-ray observables such as temperature and mass of the intracluster gas. However, because the X-ray observables are sensitive to non-gravitational processes such as radiative cooling Kravtsov et al. (2005); Stanek et al. (2010), the scaling relation has relatively large intrinsic scatter. Thus, it is crucial to calibrate the scaling relation and understand intrinsic scatter in order to do precision cosmology with clusters.

On the other hand, halo mass can be estimated directly by weak lensing of the background galaxies. The optical observations thus far did not have enough sensitivity and, due to the lack of background galaxies, the estimation of halo mass has been successful only for nearby clusters. With a weak lensing survey by the SKA, the estimation of halo mass will become possible for drastically large number of clusters and we will be able to calibrate the scaling relation much more precisely Colafrancesco et al. (2015).

PoS(AASKA14)159

7. Summary

In this chapter, we summarized future survey projects in other wavelengths and showed complementarity and possible synergy with the SKA. In the SKA era with huge number of samples, we need to defeat systematic errors and cosmic variance to advance presicion cosmology.

- In the case of weak lensing, the instrumental systematics can be reduced by cross-correlating shear signals from the radio and optical surveys. Further, the intrinsic alignment of galaxies, which is difficult to model, can also be probed by their integrated radio polarization.
- The information on low-redshift universe provided by The galaxy survey of the SKA breaks degeneracies in the estimation of cosmological parameters by the CMB anisotropies. Dark energy can be probed by directly cross-correlating the CMB and galaxy distribution.
- Euclid and the SKA are complementary in the redshift distribution and so their combination is very effective to study evolution of biases and then constrain primordial non-Gaussianity of density fluctuations.
- As to cluster cosmology, scaling relation between halo mass and X-ray observables is critical and this can be accurately calibrated by estimation of halo mas with the weak lensing observation of the cluster.

K.T. is supported by Grant-in-Aid from the Ministry of Education, Culture, Sports, Science and Technology (MEXT) of Japan, Nos. 24340048 and 26610048. C.B. acknowledge partial support by ASI for *Euclid* activities and for the *Planck* LFI Activity of Phase E2 (ASI/INAF Agreement 2014-024-R.0). D.Y. is supported by Grant-in-Aid for JSPS Fellows (No.259800).

References

Bacon, D., Bridle, S., Abdalla, F.B., et al., 2015, “Synergy between the Large Synoptic Survey Telescope and the Square Kilometre Array”, in proceedings of "Advancing Astrophysics with the Square Kilometre Array", PoS(AASKA14)145

Benoit-Lévy, A., Dchelette, T., Benabed, K. et al. 2013, Astron. & Astrophys., 555, 37

de Bernardis, P., Bucher, M., Burigana, C., Piccirillo, L., for the P-Pol Collaboration, 2009, Exp. Astron., 23, 5

Blake, C., Abdalla, F., Bridle, S. & Rawlings, S. 2004, New Astron. Rev., 48, 1063

Boughn, S. P., Crittenden, R. G. & Turok, N. G. 1998, New Astron. 3, 275

Boughn, S. P. & Crittenden, R. G. 2004, Nature, 427, 45

Bull, P., Ferreira, P., Patel, P. & Santos, M. G. 2014, arXiv:1405.1452

Burigana, C., Alexander, P., Baccigalupi, C. et al., 2015, “SKA synergy with CMB studies”, in proceedings of "Advancing Astrophysics with the Square Kilometre Array", PoS(AASKA14)149

Colafrancesco, S., Marchegiani, P. & Emritte, M. S., 2015, “Cosmology with galaxy clusters: studying the Dark Ages and the Epoch of Reionization in the SKA era”, in proceedings of "Advancing Astrophysics with the Square Kilometre Array", PoS(AASKA14)034

COrE Collaboration, COrE – Cosmic Origins Explorer – A White Paper, 2011, arXiv:1102.2181

PoS(AASKA14)159

Das, S., Sherwin, B. D., Aguirre, P. et al. 2011, Phys. Rev. Lett., 107, 021301
Efstathiou, G. & Bond., J. R. 1999, MNRAS, 304, 75
van Engelen, A., Keisler, R., Zahn, O. et al. 2012, ApJ, 756, 142
Ferramacho, L. D., Santos, M. G., Jarvis, M. J., & Camera, S. 2014, MNRAS, 442, 2511
Giannantonio, T., Scranton R., Crittenden, R. G., et al. 2008, Phys. Rev. D 77, 123520
Granett, B., Neyrinck, M. C. & Szapudi, I. 2008, Astrophys. J., 683, L99
Hand, N., Leauthaud, A., Das, S. et al. 2013, arXiv:1311.6200
Ho, S., Hirata, C., Padmanabhan, et al. 2008, Phys. Rev. D 78, 043519
Ivezić, Ž., Tyson, J. A., Abel, B., et al., arXiv:0805.2366
Kitching, T. D., Bacon, D., Brown, M.L., et al., 2015, "Euclid-SKA Synergies", in proceedings of "Advancing Astrophysics with the Square Kilometre Array", PoS(AASKA14)146
Kogut, A., Fixsen, D. J., Chuss, D. T., et al., 2011, JCAP, 07, article id. 025
Kravtsov, A. V., Nagai, D., & Vikhlinin, A. A., 2005, Astrophys. J., 625, 588
Laureijs, R., Amiaux, J., Arduini, S., et al., 2011, ESA/SRE, 12, arXiv:1110.3193
Lewis, A. & Challinor, A. 2006, Phys. Rep, 429, 1
Mao, Y., Tegmark, M., McQuinn, M., Zaldarriaga, M. & Zahn, O. 2008, Phys. Rev. D. 78, 023529
Morales, M. F. 2006, Astrophys. J., 650, L21
Norris, R., Basu, K., Brown, M., et al., 2015, "The SKA Mid-frequency All-sky Continuum Survey: Discovering the unexpected and transforming radio-astronomy", in proceedings of "Advancing Astrophysics with the Square Kilometre Array", PoS(AASKA14)086
Okamoto, T. & Hu, W. 2003, Phys. Rev. D, 67, 083002
Patel, P., Bacon, D. J., Beswick, R. J., Muxlow, T. W. B., & Hoyle, B. 2010, MNRAS, 401, 2572
Planck Collaboration I. 2014a, Astronomy & Astrophysics, 571, A1
Planck Collaboration XV. 2014, Astronomy & Astrophysics, 571, A15
Planck Collaboration XVII. 2014, Astronomy & Astrophysics, 571, A17
Planck Collaboration XXIV. 2014, Astronomy & Astrophysics, 571, A24
PRISM Collaboration, 2014, JCAP, Issue 02, article id. 006
Raccanelli, A., Zhao, G.-B., Bacon, D., et al. 2012, MNRAS, 424, 801
Sachs, R. K. & Wolfe, A. M., 1967, Astrophys. J., 147, 73
Seljak, U. 1996, Astrophys. J., 463, 1
Seljak, U. 2009, Phys. Rev. Lett., 102, 021302
Stanek, R., Rasia, E., Evrard, A. E., Pearce, F., & Gazzola, L. 2010, Astrophys. J., 715, 1508
Subhramanian, R., & Eckers, R. D. 2002, in the XXVIIth General Assenbly of the URSI, Maastricht, The Nederlands, arXiv:0209569v1
Sunyaev, R. A. & Zel'dovich, Y. B. 1972, Comm. Astrophys. Space Phys., 4. 173
Yamauchi, D., Takahashi, K., & Oguri, M. 2014, Phys. Rev. D, 90, 083520

PoS(AASKA14)159

PROCEEDINGS OF SCIENCE

Solar and Heliospheric Physics with the Square Kilometre Array

Valery M. Nakariakov[1], **Mario M. Bisi**[2], **Philippa K. Browning**[3], **Dalmiro Maia**[4], **Eduard P. Kontar**[5], **Divya Oberoi**[6], **Peter T. Gallagher**[7], **Iver H. Cairns**[8], **Heather Ratcliffe**[1]

[1] *Centre for Fusion, Space and Astrophysics, Physics Department, University of Warwick, Coventry CV4 7AL, UK;* [2]*RAL Space, Science & Technology Facilities Council – Rutherford Appleton Laboratory, Harwell Oxford, Oxfordshire, OX11 0QX, England, UK;* [3] *Jodrell Bank Centre for Astrophysics, University of Manchester, Manchester, M13 9PL, UK;* [4]*CICGE, Observatorio Astronomico Professor Manuel de Barros, Faculdade de Ciencias da Universidade do Porto, Vila Nova de Gaia, Portugal;* [5] *School of Physics and Astronomy, University of Glasgow, Glasgow, G12 8QQ, UK;* [6]*National Centre for Radio Astrophysics, Tata Institute of Fundamental Research, India;* [7] *School of Physics, Trinity College Dublin, 2, Dublin, Ireland;* [8]*School of Physics, University of Sydney, Sydney, NSW 2006, Australia.*

E-mail: V.Nakariakov at warwick.ac.uk; Mario.Bisi at stfc.ac.uk

The fields of solar radiophysics and solar system radio physics, or radio heliophysics, will benefit immensely from an instrument with the capabilities projected for SKA. Potential applications include interplanetary scintillation (IPS), radio-burst tracking, and solar spectral radio imaging with a superior sensitivity. These will provide breakthrough new insights and results in topics of fundamental importance, such as the physics of impulsive energy releases, magnetohydrodynamic oscillations and turbulence, the dynamics of post-eruptive processes, energetic particle acceleration, the structure of the solar wind and the development and evolution of solar wind transients at distances up to and beyond the orbit of the Earth. The combination of the high spectral, time and spatial resolution and the unprecedented sensitivity of the SKA will radically advance our understanding of basic physical processes operating in solar and heliospheric plasmas and provide a solid foundation for the forecasting of space weather events.

Advancing Astrophysics with the Square Kilometre Array
June 8-13, 2014
Giardini Naxos, Sicily, Italy

PoS(AASKA14)169

1. Introduction

The Sun is the brightest radio object in the Universe visible from the Earth. In powerful flares, the radio flux density may exceed 10^9 Jy. The wide variety of mechanisms, both coherent and incoherent, for solar and heliospheric radio emission provide us with unique information required for understanding the basic physical processes operating in natural and laboratory plasmas, at both microscopic and macroscopic levels. The topics of ongoing intensive investigations are the fundamental problems of plasma astrophysics: the release of magnetic energy, acceleration of charged particles, magnetohydrodynamic (MHD) waves and turbulence, wave-particle interaction, etc. The proximity of the Sun to the Earth allows for its study with an unprecedented combination of time, spatial and spectral resolution, and a unique opportunity to study fundamental plasma physics processes both in situ and remotely. Finally, plasma physics processes in the solar atmosphere are directly relevant to geophysical challenges such as climate change and space weather; a strong additional motivation for the intensive development of solar and heliospheric radio physics.

Observations of solar and heliospheric radio emission are mainly performed with dedicated instruments, such as radio interferometers. However these are rather limited. For example the highest spatial resolution in the microwave band currently achieved by the Nobeyama Radioheliograph (NoRH, Nakajima et al. 1994), 5" at 34 GHz, is much lower than the spatial scale of plasma structures in the solar corona as resolved in the EUV and X-ray bands (smaller than 1"). Not even the upcoming new generation of state-of-the-art specialised solar radio interferometers, namely the Chinese Spectral Radioheliograph (CSRH, frequency range 0.4–15 GHz, longest baseline 3 km, Yan et al. 2009), the upgraded Siberian Solar Radio Telescope (SSRT, frequency range 4–8 GHz, longest baseline 622.3 m, Lesovoi et al. 2014) and the Expanded Owens Valley Solar Array (e-OVSA, frequency range 1–18 GHz, longest baseline 1.8 km, Gary et al. 2012) will reach the SKA's spatial resolution and sensitivity. In short, as well as providing simultaneously high spectral and spatial resolution unavailable with current instruments, the SKA will radically (by two orders of magnitude) improve on their sensitivity, allowing for the detection of a number of physical phenomena predicted theoretically. The breakthrough potential of SKA in solar and heliospheric studies in the low frequency band has already been demonstrated in frames of the LOw Frequency ARray (LOFAR) and Murchison Widefield Array (MWA), both of which are SKA pathfinder projects. These instruments include solar and heliospheric physics, and space weather amongst their key science objectives and have already lead to several interesting publications (e.g. Mann et al. 2011; Oberoi et al. 2011; Bowman et al. 2013).

A further interesting opportunity is connected with the fact that for a 300 km baseline, the proximity of the Sun to the interferometer puts it in the near-field zone of the instrument at higher frequencies. The sphericity of the waves coming from spatially localised solar sources can be measured and the radial distance to the source can be estimated, providing us with 3D information: both angular coordinates on the plane-of-the-sky and the distance to the source (e.g. giving radial resolution of 0.1 $R_\odot$ at 1.5 GHz on a 300 km baseline, Braun 1997).

For imaging purposes, solar observations are particularly challenging. First of all there is the immense dynamic range. During major outbursts the flux can be dominated by very spatially-localised sources and simultaneously there are elongated features whose brightness temperature over the same spatial extent as the narrow source could be nine orders of magnitude lower. The

PoS(AASKA14)169

spatial scales of those emissions vary widely, with the thermal emission from the corona exceeding the size of the solar disk, and loop gyrosynchrotron emissions reaching even larger sizes, while the emission from noise storms is close to the minimum size defined by scattering in the solar atmosphere e.g. the effect of plasma turbulence in the meter wave range, (Bastian et al. 1998)). The temporal scales also vary widely. Thermal emission can be stable on the order of hours or days, but many outbursts or quasi-periodic pulsations (QPP) require better than 0.1-second time resolution, and the typical eruptive event will develop through a series of outbursts during a time interval of less than 10 minutes. This means that although aperture synthesis could be used for the quiet Sun, it is not an option for solar radio burst science, for which instantaneous imaging is required.

The various heliospheric phenomena are associated with radio emission covering a wide range of frequencies. The frequency range from 50 MHz to 3 GHz (or higher) suffices to monitor a wide range of solar phenomena of fundamental interest, in particular relating to flare physics, CME initiation, shock propagation, and energetic particle acceleration. In this Chapter we present several research topics that would specifically benefit from the high resolution and sensitivity to be provided by the SKA, and which are expected to bring us new results of transformative nature.

2. Magnetic reconnection diagnostics

Solar flares produce high-energy radiation, non-thermal energetic particles and (sometimes) clouds of magnetised plasma known as Coronal Mass Ejections (CMEs) (e.g. Benz 2008; Fletcher et al. 2011). Each of these are major events of space weather, and can have significant effects on technological systems on Earth and on satellites in the terrestrial environment (Schwenn 2006). They are increasingly identified as a major societal risk, with high economic impact. Radio observations with the SKA could play an important role in elucidating the underlying processes in flares, building towards predictive capacity, as well as in space weather monitoring. The latter issue requires the SKA operation planning team to dedicate several time slots to heliospheric observations daily. Furthermore, understanding solar flares is a challenging problem in fundamental plasma physics, with implications for other astrophysical transients including stellar flares, which have recently been shown to be common across many types of stars (Maehara et al. 2012).

Flares almost certainly represent the release of stored magnetic energy through the process of magnetic reconnection (Priest & Forbes 2002; Shibata & Magara 2011). However, there are many unsolved problems concerning the physical processes involved. The reconnection in a flare may be triggered by a filament eruption, as in the “standard” flare model - or by another process such as newly-emerging flux or an instability. One crucial task is thus to determine the magnetic field configuration. However, the coronal magnetic field cannot be directly measured and is usually inferred by e.g. a force-free extrapolation from measured fields at the photosphere (De Rosa et al. 2009). There are a number of difficulties with this approach even for steady fields, such as the non-force-free nature of the lower atmospheric layers, and it certainly does not apply to rapidly-changing fields during a flare. Indeed, current quantitative estimates of the changes in magnetic energy during a flare are inconsistent with the overall energy budget (Sun et al. 2012), probably due to these uncertainties in field extrapolations. Analysis of gyrosynchrotron emission during flares can be used to constrain the coronal magnetic field (Fleishman et al. 2009) and so studies combining

PoS(AASKA14)169

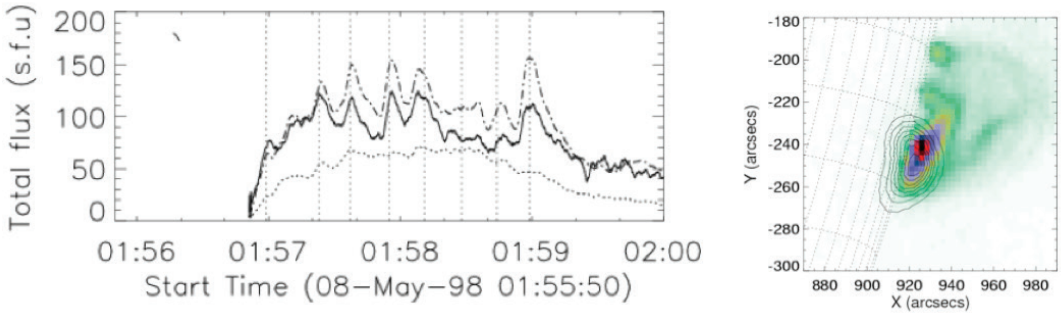

Figure 1: Quasi-periodic pulsations in the solar flare of 8th May 1998. *Left:* Solar flux time profiles of microwave emission at 9.4 GHz (dot-dashed line), 17 GHz (solid line) and 3.75 GHz (dotted line). *Right:* Soft X-ray image from Yohkoh. Contour: microwave emission source for the same flare, observed by NoRH at 17 GHz intensity (from Inglis et al. 2008).

the high spatial and spectral resolution of the SKA will provide far more detailed information about the magnetic field.

The magnetic reconnection site in flares cannot be directly observed, and indeed, the scale lengths of the dissipation region are likely to be extremely small, probably of the order of tens of metres. However, in order to understand the energy-release processes, it is essential to determine the location and spatial extent of this site. In the standard model this is a single monolithic current sheet, but there is increasingly strong evidence that the reconnection site is fragmented, either into a chain of magnetic islands or plasmoids, or into even more complex three-dimensional (3D) structures (Cargill et al. 2012; Gordovskyy et al. 2013), and reconnection and turbulence interact on many scales in flares (Browning & Lazarian 2013). Non-thermal particles produced during flares are a crucial tool for indirectly observing the reconnection site (Zharkova et al. 2011), and are discussed further in Section 4. Their diagnostic capabilities will benefit greatly from the improved spatial resolution offered by the SKA.

3. Quasi-periodic pulsations in flares

The radio, white light, X-ray and gamma-ray light curves of solar and stellar flares are often found to have pronounced quasi-oscillatory patterns called quasi-periodic pulsations (QPP; see Fig. 1, and Nakariakov & Melnikov 2009, for a comprehensive review). The detected periodicities range from a fraction of a second to tens of minutes and the modulation depth of the main flaring signal varies significantly between events, from a few percent to a hundred percent.

The strong correlations typically seen between the microwave and X-ray emission indicate that the phenomenon is associated with non-thermal electrons (Section 4), but the physical mechanisms for QPP in flares are still uncertain. Theoretical studies show that the detected periodicities may be caused by MHD oscillations of the flaring active regions or nearby plasma structures. This interpretation is supported by the recent discovery of ubiquitous MHD wave activity in the solar corona (see De Moortel & Nakariakov 2012, for a recent review), as space and time resolved MHD waves and oscillations in coronal plasma structures in the EUV band have periods in the same range

PoS(AASKA14)169

as long-period QPP. However, the shorter-period QPP (< 1 min) are not time-resolved in the EUV band.

Coronal MHD waves are intensively used for diagnostics of the plasma in MHD seismology (e.g. Stepanov et al. 2012). The confident identification of MHD oscillations in flaring QPP will lead to the transformative change in the application of this method, as the superior time resolution intrinsic to the radio band allows the detection of phenomena on the time scale of the transverse Alfvén transit time, of the order of one second. Such observations require the combination of high sensitivity with high spatial and time resolution, and hence are a natural task for the SKA. Moreover, the broad spectral coverage would allow simultaneous resolution of the processes associated with the non-thermal electrons propagating from the flare site downwards into dense plasma, seen in the high-frequency band (> 1 GHz), and upwards, into rarified plasma, seen in the low-frequency band, again a transformative improvement for coronal seismology.

The knowledge gained from the study of QPP in solar flares can be applied to the interpretation of QPP in stellar flares, providing us with an important tool for MHD seismology of stellar coronae. Short-period QPP have been confidently detected in stellar flares in the radio band (e.g. Zaitsev et al. 2004); and even occasionally in the white light and X-ray bands, despite the lack of the necessary resolution and sensitivity. This issue demonstrates clearly the synergetic potential of this research - the SKA sensitivity will allow radical improvements to the detection of QPP in stellar flares and hence the statistical significance of the results.

4. Particle acceleration and transport in solar flares

Solar flares are known to efficiently accelerate electrons in large numbers (Holman et al. 2011), but the detailed physics of the process is not known. At high frequencies (above a few GHz), flare radio emission is often dominated by gyrosynchrotron radiation from such energetic ($\simeq 100$ keV) electrons in flaring loops (e.g. White et al. 2011, for a recent review). As noted in Section 2, this emission can be used to constrain the coronal magnetic field, while non-thermal particles are a crucial tool to diagnose the flare reconnection site. New observations (e.g. Fleishman et al. 2011) suggest that radio emission can even be used as a unique tool to diagnose the region where energetic electrons are accelerated when traditional X-ray techniques are insensitive. In addition, optically thin gyrosynchrotron emission provides a powerful tool to infer the poorly understood properties of the energetic electrons. Spatially and spectrally resolved observations are key to this understanding. The two fixed frequencies (17 and 34 GHz) currently offered by NoRH, are not sufficient to disentangle features of the acceleration from the effects of electron transport. The SKA will allow the simultaneous imaging of various regions of the flaring atmosphere, and therefore significantly improve our understanding of these processes, and by extension magnetic reconnection.

Radio emission is also seen with rather short (sub-second) duration and very narrow bandwidth (Benz 2008, as a review). Although in a few such cases, the spatial relation between coronal X-ray sources and such coherent radio emissions (called decimetric spikes) has been investigated, the origin and the driver of such bursts is largely unknown. Metric spikes are also sometimes associated with the acceleration of electrons (e.g. Paesold et al. 2001) which lead to Type III radio bursts (see below). High sensitivity observations can substantially improve our knowledge of radio signatures, often associated with microscopic processes in the solar atmosphere (e.g. Karlický 2004).

PoS(AASKA14)169

Non-thermal electrons are also observed to escape the solar atmosphere and travel into interplanetary space, producing radio bursts of several kinds (e.g. Pick & Vilmer 2008, as a review). Radio observations at frequencies of around 50-300 MHz therefore provide a unique tool to probe the high solar corona and are often the only means by which to observe such escaping particles as well as CMEs and shocks (discussed in the next section) in this region (e.g. Bastian et al. 1998).

Although we have a basic physical picture of electron transport from the Sun to the Earth, there are still many open questions concerning energetic electron acceleration, storage, and release in the corona, and transport in interplanetary space (e.g. Kontar & Reid 2009, and references therein). So called Type III solar radio bursts can be produced by the propagating electrons at the local plasma frequency which ranges from hundreds of MHz in the high corona to kHz near and beyond the Earth (e.g. Sinclair Reid & Ratcliffe 2014). A Type III burst observed at steadily decreasing frequency thus implies a population of fast electrons injected onto an open magnetic field line in the corona and travelling outwards. SKA observations of radio signatures at decimetric/metric wavelengths thus provide essential tools for studying not only energetic particles, but also the magnetic field geometry near flares and magnetic connections from the flare site to the interplanetary medium.

5. Shocks and particle acceleration in the solar atmosphere

CMEs are spectacular eruptions of plasma and magnetic field from the surface of the Sun into the heliosphere, which can travel at speeds of up to 2,500 km s^{-1} and have masses $\sim 10^{15}$ g. CMEs often produce shocks in the solar atmosphere and thereby accelerate electrons and other particles into interplanetary space. The MHz and GHz radio emission from these accelerated electrons can be used to diagnose the acceleration mechanism, which may include magnetic reconnection and coronal shock waves (e.g. Gary & Keller 2004), although the precise details of these mechanisms remain unclear. The SKA will enable us to address these questions using its extremely high sensitivity, spectral coverage, and imaging capabilities. These results will not only give us a new insight into the fundamental physics of CMEs and CME shocks, but will enable us to improve the forecasting of adverse space weather at Earth.

Recently, Carley et al. (2013) studied shocks and particle acceleration associated with the eruption of a CME using EUV, radio and white-light imaging. The CME-induced shock was coincident with a coronal ("EIT") wave and an intense metric radio burst (known as a Type II solar radio burst) generated by intermittent acceleration of electrons to kinetic energies of 2-46 keV (0.1-0.4c). Their results indicate that CME-driven quasi-perpendicular shocks are capable of producing quasi-periodic acceleration of electrons, an effect consistent with a turbulent or rippled plasma shock surface.

The Nançay Radioheliograph used in that study provides imaging at a few discrete frequencies in the 10's to 100's of MHz, while the Birr Callisto radio-spectrometer (e.g. Zucca et al. 2012) offers good spectral coverage, but the combined superior spatial and spectral resolution offered by the SKA would radically advance these topics. For example, the high spatial, spectral and temporal resolution offered by LOFAR (van Haarlem et al. 2013) was exploited by Morosan et al. (2014) to study solar Type III radio bursts and their association with CMEs (see Figure 2). The non-radial high altitude Type III bursts were associated with the expanding flank of a CME which may have compressed neighbouring streamer plasma producing larger electron densities at high altitudes,

PoS(AASKA14)169

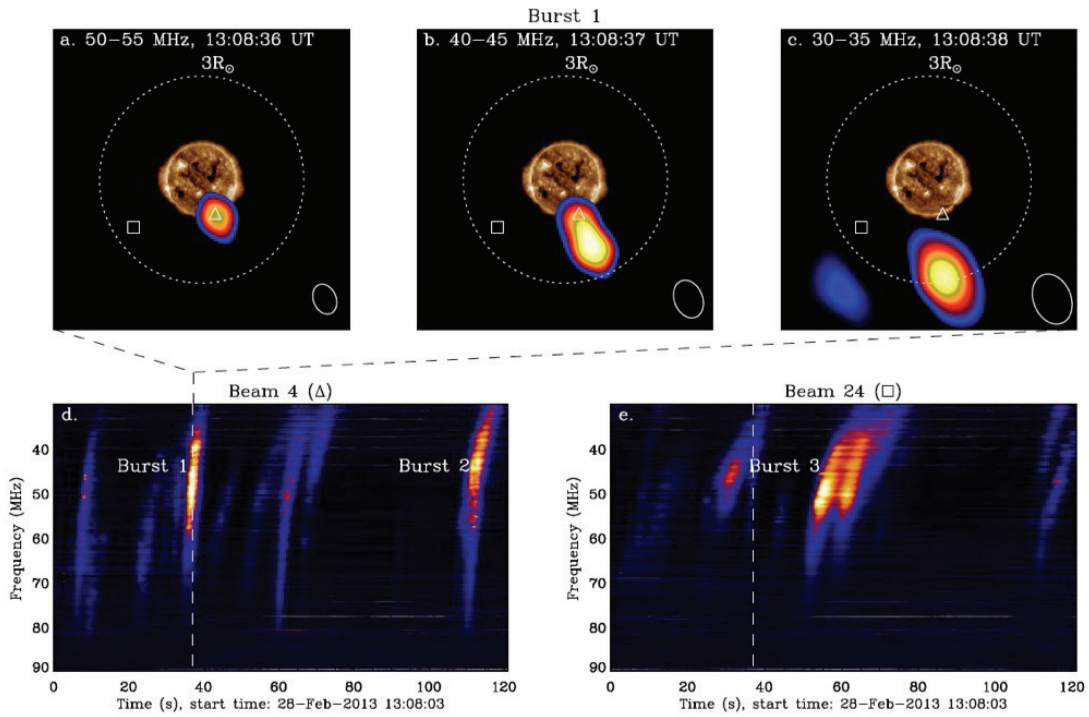

Figure 2: LOFAR tied-array images of a Type III radio burst at (a) 50-55 MHz (b) 40-45 MHz and (c) 30-35 MHz, separated by 1 s. The inset is an SDO/AIA (19.3 nm) image of the EUV Sun. The dynamic spectra corresponding to two different beams, Beam 4 and Beam 24, are shown in panels d and e. The full evolution of the radio sources in the dynamic spectra (Bursts 1, 2 and 3) can be viewed in Morosan et al. (2014)

while the non-radial burst trajectories can be explained by the deflection of radial magnetic fields as the CME expanded in the low corona. New discoveries, such as the short-duration, fast-drift metric bursts recently found with the MWA (e.g. Oberoi et al. 2011, and references therein) also demonstrate the potential of the SKA.

Newly-available theory and simulation capabilities offer great promise to explain the detailed properties of Type II and III bursts. For instance, impressive agreement exists between the observed and predicted dynamic spectra of several type II bursts below about 15 MHz (Schmidt & Cairns 2014). These combine 3D MHD simulation of a particular CME moving through the event-specific corona (using the BATS-R-US code with data-driven models) with detailed emission physics, and show multiple radio sources distributed across the 3D shock front. Type III simulations have also been developed which can predict the basic properties of emission including its fine structures in frequency, associated bremsstrahlung X-rays in the chromosphere (Hannah et al. 2013), and intensification when the electron beam crosses a shock (Li & Cairns 2012). Fully 3D theories for type III bursts, as well as enhanced theories for decimetric events (Cairns 2011) are expected to be available before SKA1 is operational.

The SKA therefore offers the ability to address some of the many fundamental and important

PoS(AASKA14)169

issues, both observational and theoretical, for solar radio bursts (see also the related discussion for the MWA; Bowman et al. 2013), by allowing high time, spatial and spectral resolution imaging. Correlations with data from other wavelengths, such as EUV and X-ray images of solar flares, magnetic reconnection, and CMEs from multiple spacecraft (e.g. SDO, STEREO, and RHESSI) and also detailed comparison with new theory and simulations will allow new and unanticipated discoveries, as well as illuminating such issues as the detailed source structure and sizes of Type II and III bursts, their evolution, polarisation characteristics, and their relation with other processes during flares.

6. Interplanetary Scintillation

Interplanetary scintillation (IPS) is caused by small-scale ($\sim$80 km to 500 km) density variations in the solar wind crossing the line of sight (LOS) from distant, compact astronomical radio sources (or occasionally, spacecraft beacons) to the radio receiver and scattering their radio signal (e.g. Hewish et al. 1964; Bisi et al. 2010b, and references therein). Such measurements led to fundamental discoveries of solar wind structuring and the first heliospheric remote-sensing results, only confirmed much later by spacecraft. IPS of a compact radio source gives fast (typically $\sim$0.1 Hz to $\sim$20 Hz) fluctuations of radio intensity/amplitude and phase, containing information about both solar wind and radio source. When simultaneous observations of IPS are undertaken at a range of observing frequencies, say f to $5f$, (i.e. say 60 MHz to 300 MHz – a capability of SKA1-LOW), such data would be extremely useful in examining the scale size of density irregularities, shape of the density and cross-frequency spectra. A mathematical description of IPS is available in e.g. Salpeter (1967); Fallows et al. (2006); Bisi (2006) and references therein.

Simultaneous observations at a range of observing frequencies, for example 60 MHz to 300 MHz with SKA1-LOW, would be extremely useful in examining the scale size of density irregularities, shape of the density and cross-frequency spectra, and studying the transition between weak and strong scattering of the interplanetary (IP) medium. These effects are also important in relation to other radio observations, such as Type II and III bursts (Section 5) as scattering can strongly affect their source sizes and directionality, and smear out any fine structure within the source. Density irregularities can also change the frequency fine structuring of Type III emission (Li et al. 2012). The smallest scale size of density irregularities (in the case of IPS, the cut-off scale or inner-scale size (e.g. Coles & Harmon 1978)) present in the solar wind will determine the typical scale size of radio emission. Further from the Sun this scale will be within reach with SKA1-LOW, but closer in, it may require the MID or SURVEY ranges.

More robust methods for obtaining solar wind parameters are generally based on the cross-correlation of two simultaneous observations of the same radio source (e.g. Coles 1996; Breen et al. 1996; Bisi et al. 2010a, and references therein). Figure 3 provides a simplified overview of a multi-site IPS experiment. Typically both receivers operate at the same frequency, but Bisi (2006) and Fallows et al. (2006) have shown that multi-frequency cross-correlations are also possible and can produce much interesting science (as described earlier in this section). The SKA can potentially open up such possibilities in investigating the turbulence scale and spectrum of the solar wind.

In addition, multiple observations of IPS over several weeks or months will allow for the 3D tomographic reconstruction of the detailed structure of solar-wind outflows in the heliosphere,

PoS(AASKA14)169

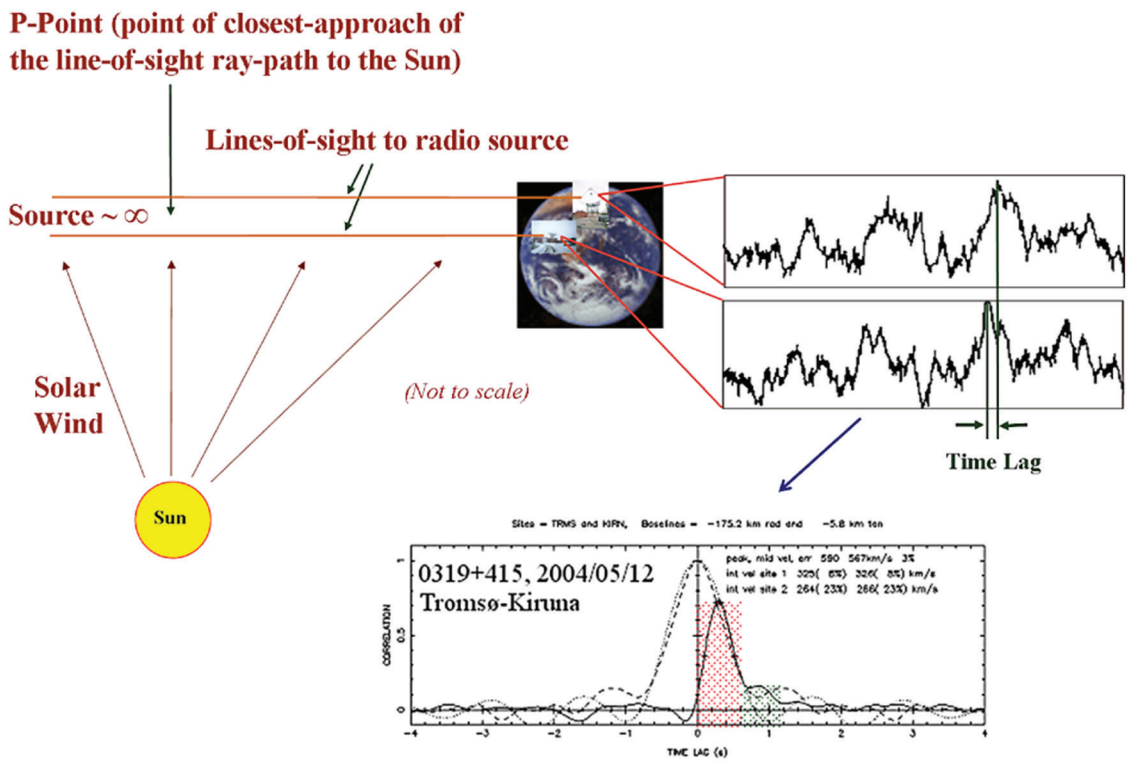

Figure 3: The basic principles of multi-site (in this case two European Incoherent SCATter, EISCAT, radar antennas, located in Tromsø and Kiruna) IPS through the simultaneous observation of a single radio source as described in the text. The signal's variation in amplitude as recorded is directly related to turbulence and density variation in the solar-wind outflow crossing the LOS. A cross-correlation analysis of the two simultaneous signals received yields what is known as a cross-correlation function (CCF) which can be used as a first estimate of the velocity or velocities crossing the LOS. (From Bisi et al. (2010a)).

using, for example, the University of California, San Diego (UCSD) algorithms (e.g. Jackson et al. 2013, and references therein). SKA1-LOW will allow a sufficient number of observations per day to reconstruct the temporal evolution of the outflows in unprecedented detail, and the application of SKA2 in the future will allow us to access new physics on the turbulence-scale of the solar wind (scales that are currently too small to be sampled fast enough with current and upcoming in-situ instrumentation), as well as improved and higher-resolution 3D reconstructions of the inner heliosphere to allow us to better visualise and reconstruct a complete picture of the solar wind as it propagates from the Sun to the Earth's orbit and beyond.

7. Heliospheric Faraday Rotation

Space weather forecasting is of considerable interest socioeconomically, particularly for highly geo-effective events like CMEs. The impact of these depends strongly on the presence of a southwardly-directed magnetic field, either in the CME itself or behind the CME driven shock (in the CME sheath region). Hence, information on the magnetic field topology within a CME,

PoS(AASKA14)169

especially the strength of the B_z component, as it is usually referred to, is necessarily required to determine its geo-effectiveness. At present, our earliest information of **B** within a CME comes from in-situ measurements from space-based observatories located in orbit about the Sun-Earth L_1 point. However, these offer at best tens of minutes early warning, and tend to be disrupted by the CME (or indeed the shocked plasma ahead of the fast CMEs).

Faraday rotation (FR) of background linearly-polarised sources allows remote sensing of the magnitude and orientation of magnetic field along the observing LOS. The technique was pioneered using the telemetry signals from Pioneer 6 and Helios spacecraft (e.g Stelzried et al. 1970; Bird et al. 1985, and references therein), and remains a highly productive approach (e.g. Jensen et al. 2013, and references therein). Astronomical radio sources may also be used to detect coronal FR (e.g. Mancuso & Spangler 2000; Spangler & Whiting 2009, and references therein).

Applied to CMEs, a large number of background sources should be observed along the projected path of the CME in the sky plane before, during, and after the passage of a CME, while tracking the CME as it ploughs its way out. Each measurement provides information only on the LOS component of **B**, integrated along the entire LOS. However, the observations of a large number (> 100) of lines of sight through the CME as it evolves and travels through the heliosphere provide a large number of independent constraints.

Moreover, the currently-favoured flux-rope based models of CME magnetic fields require only $\sim$10 degrees of freedom in even the most general models. Therefore, self-consistent modelling of the observed FR, especially when exploiting the continuities along time and space axes, in the time-evolving CME model will yield a very-tightly constrained model for the CME flux rope. In fact, using the time series of FR observed along a single LOS (provided by satellite beacons) (Jensen & Russell 2008; Bisi et al. 2010b, and references therein) have successfully constrained the flux-rope orientation, position, size, velocity, rate of change of rope radius and pitch angle. Multiple LOS measurements will allow much more detailed characterisation.

Indeed, in anticipation of instruments such as LOFAR and the MWA, Liu et al. (2007) and Jensen et al. (2010) showed that simultaneous observations along multiple lines of sight can indeed be used to uniquely determine the **B** field in the CME flux rope. If the turn-around time on this analysis can be reduced to a few hours, this technique can provide an early warning one-to-two days in advance, as opposed to the present warning time of a few hours at best.

FR is quadratically dependent on wavelength, and so is easier to discern at lower frequencies. However, at lower frequencies the fractional polarisation of most extra-galactic sources drops significantly, the Galactic background becomes steadily brighter (e.g. Rogers & Bowman 2008) and the FR due to the terrestrial ionosphere also increases. Additional complications arise because the lines of sight passing close to the active Sun are required, and the solar radio emission is strongly and rapidly varying and shows strong spectral features. Nonetheless, recent instruments such as the MWA and LOFAR do intend to explore this possibility.

We expect there to be a sufficiently-dense grid of sources radiating linearly-polarised light to serve as a background grid to against which to observe the CME plasma. WSRT observations in the range of 340 MHz to 370 MHz found extra-galactic sources with typical linearly-polarised fluxes of 20 mJy and readily measurable rotation measures (RMs) with an angular density of about one suitable polarised source every $\sim$4 square degrees (e.g. Haverkorn et al. 2003, and references therein). These observations also found the Galactic synchrotron background emission to be significantly

PoS(AASKA14)169

linearly polarised. Recent work with the new-generation instruments has confirmed the presence of this practically ubiquitous diffuse polarised background emission at even lower frequencies (e.g. Jelic et al. 2014, and references therein). Simultaneous (or near simultaneous) observations of IPS alongside those of heliospheric FR will also provide additional context information on the structure(s) within the heliosphere to enable a better understanding of what exactly is causing the FR or the changes in FR recorded say, during the passage of a CME.

The optimal observing frequencies lie in the upper part of the SKA1-LOW range. In practise, triggered observing will be required for these hard-to-predict events, most likely using a space-based observatory, which can provide information of the launch time, direction, and speed of a CME. Heliospheric imagers, such as those aboard the twin STEREO spacecraft, can provide additional information determining the patch of sky to be monitored. The observations ideally require good time resolution, and angular resolution of order tens of arc seconds to an arc minute in the spectral line mode, with a spectral resolution of a few 10s of kHz. To maximise the benefit from the use of technique of RM synthesis (e.g. Brentjens & de Bruyn 2005), these observations should cover the widest bandwidth possible. Contamination from the ionospheric FR signal is a problem over much of the region of interest, and will require calibrating down to a few percent, but Sotomayor-Beltran et al. (2013) have already shown good progress in this respect. The SKA1-LOW projected sensitivity and dynamic range will offer exciting new observations using this technique, both for forecasting, and for the improved understanding of CMEs in general.

8. Summary

The impact and usefulness of SKA1 for coronal observations will depend on the imaging capabilities available and their adaptation for solar observations. The first criterion to consider is the frequency coverage and the type of instrument. SKA1-LOW will cover part of the range of LOFAR, with a denser coverage for the short baselines, which is an important factor for solar imaging since LOFAR is somewhat sparse in the tens of meters to a few hundred meter baselines necessary to define the shape of the solar disk at meter wavelengths. SKA1-LOW, if observing during daytime, will need to include in its operating mode a way to deal with the rather high fluxes originating from solar outbursts so solar imaging using SKA-LOW is more likely than with SKA1-SUR and SKA1-MID which we will discuss later. Unfortunately SKA1-LOW will be placed far from the instrument which offers the best complement in terms of frequency range, SKA1-MID. This means that although SKA1-MID and SKA1-LOW together will cover the frequency range from 50 MHz to 3,050 MHz a given solar radio outburst which is a short feature on the scale of minutes or seconds will either be observed by one or the other but not both. Simultaneity may not always be possible due to the Earth's longitudinal separation of the two antenna types. However, solar observations with SKA1-LOW will well overlap in time with the NoRH, and the upcoming high-frequency spectral radio heliographs of the new generation, CSRH and SSRT.

SKA1-SUR can still provide some complementary measures, but the fact that it provides lower resolution with a much sparser field of view than SKA1-MID and in particular the fact that it will not be upgraded for SKA2 mean that SKA1-MID plus LOFAR would jointly outperform SKA1-SUR plus SKA1-LOW. We thus expect SKA1-LOW to essentially overlap the solar science case for LOFAR, likely with better image performance for the Sun and with NoRH, CSRH and SSRT

PoS(AASKA14)169

as complementary instruments at higher frequencies. This in particular opens up an interesting possibility for simultaneous tracing of the emission of non-thermal particles going up and down from a flare site.

Since for solar purposes the case for SKA1-SUR is reasonably similar to the case for SKA1-MID and since SKA1-MID will the only one to be significantly upgraded for SKA2 we concentrate the further discussion on SKA-MID. The frequency range range for SKA1-MID, from 350 MHz to 3,050 MHz, means we could study the range from 450 MHz to 1 GHz where there has been a noticeable lack of imaging on the Sun. That alone would be a major contribution for solar physics from SKA1. We note a couple of issues on the possibility of imaging with SKA1-MID as defined for SKA1.

First there is the fact that the dish size (15 metres) and the single beam means that at the highest frequencies the antenna field of view is smaller than the angular size of the Sun (the synthetic field of view will be even smaller). Below 1 GHz the size of the field of view should be adequate if particular attention is taken to ensure that the short baseline coverage is enough for the Sun to be effectively imaged out to about two solar radii from the Sun's centre. This field of view aspect will be less of an issue if the SKA1-MID dishes are equipped with phased array feeds and probably will not be an issue for SKA2 if dense aperture arrays are to be implemented.

The greatest problem in using SKA1-MID to observe the solar corona relates to the very large fluxes involved. Solar radiastronomers define their flux in terms of solar flux units (SFU) such that 1 SFU = 10,000 Jy. Solar fluxes in the decimeter wavelength range are often close to 100 SFU, and in large events such as the Halloween 2003 events, the solar emission in the decimeter to meter wavelength can exceed 10^5 SFU (Pick et al. 2005). The dense aperture array systems to be installed during SKA2, if performing operations during daytime, will need to handle such fluxes in their normal operating modes, so even major solar outbursts can readily be included in the science topics for SKA2. The dishes that will be used for SKA1 do not need to handle solar like fluxes even during daytime operations since the observing schedule can always be defined in order to maintain the Sun outside of the antenna field of view. If pointed at the Sun there will be a major departure from the sub-Jansky modes typical of non-solar observations. On the other hand, observations of IPS will be possible using SKA1-MID, and FR could also be attempted within respectable elongation angles from the Sun, and we feel that this, together with imaging observations with SKA1-LOW, atop of the IPS and FR prospects with SKA1-LOW, will be the most important contributions from SKA1 for Heliophysics including solar and space weather studies.

Despite some challenges and potential cost implications involved with coronal imaging using SKA1-MID, we note that such high fluxes must be handled during any daytime operation by the dense aperture arrays during SKA2. Also, the multi-beam characteristics of the dense aperture arrays will then facilitate allocation of time for solar operation. IPS observations with SKA1-MID are not affected by these issues, and these, alongside imaging observations with SKA1-LOW, will certainly make important contributions from SKA1 to radio heliophysics and space weather studies.

We conclude that the observational parameters of both SKA1 and SKA2 will provide a major breakthrough in solar and heliospheric radiophysics, bringing new discoveries and qualitatively advancing solar and heliospheric physics, fundamental plasma astrophysics, and space weather.

PoS(AASKA14)169

References

Bastian, T. S., Benz, A. O., & Gary, D. E. 1998, ARA&A, 36, 131
Benz, A. O. 2008, Living Reviews in Solar Physics, 5, 1
Bird, M. K., Volland, H., Howard, R. A., et al. 1985, Sol. Phys., 98, 341
Bisi, M. M. 2006, Ph.D. Thesis (http://cadair.aber.ac.uk/dspace/handle/2160/4064), The University of Wales, Aberystwyth
Bisi, M. M., Fallows, R. A., Breen, A. R., & O'Neill, I. J. 2010a, Sol. Phys., 261, 149
Bisi, M. M., Breen, A. R., Jackson, B. V., et al. 2010b, Sol. Phys., 265, 49
Bowman, J. D., Cairns, I., Kaplan, D. L., et al. 2013, PASA, 30, 31
Braun, R. 1997, in Lecture Notes in Physics, Berlin Springer Verlag, Vol. 483, Coronal Physics from Radio and Space Observations, ed. G. Trottet, 207
Breen, A. R., Coles, W. A., Grall, R., et al. 1996, Journal of Atmospheric and Terrestrial Physics, 58, 507
Brentjens, M. A., & de Bruyn, A. G. 2005, A&A, 441, 1217
Browning, P., & Lazarian, A. 2013, Space Sci. Rev., 178, 325
Cairns, I. H. 2011, Coherent Radio Emissions Associated with Star System Shocks, ed. M. P. Miralles & J. Sánchez Almeida, 267
Cargill, P. J., Vlahos, L., Baumann, G., Drake, J. F., & Nordlund, Å. 2012, Space Sci. Rev., 173, 223
Carley, E. P., Long, D. M., Byrne, J. P., et al. 2013, Nature Physics, 9, 811
Coles, W. A. 1996, Ap&SS, 243, 87
Coles, W. A., & Harmon, J. K. 1978, J. Geophys. Res., 83, 1413
De Moortel, I., & Nakariakov, V. M. 2012, Royal Society of London Philosophical Transactions Series A, 370, 3193
De Rosa, M. L., Schrijver, C. J., Barnes, G., et al. 2009, ApJ, 696, 1780
Fallows, R. A., Breen, A. R., Bisi, M. M., Jones, R. A., & Wannberg, G. 2006, Geophys. Res. Lett., 33, 11106
Fleishman, G. D., Kontar, E. P., Nita, G. M., & Gary, D. E. 2011, ApJLett, 731, L19
Fleishman, G. D., Nita, G. M., & Gary, D. E. 2009, ApJLett, 698, L183
Fletcher, L., Dennis, B. R., Hudson, H. S., et al. 2011, Space Sci. Rev., 159, 19
Gary, D. E., & Keller, C. U., eds. 2004, Astrophysics and Space Science Library, Vol. 314, Solar and Space Weather Radiophysics - Current Status and Future Developments
Gary, D. E., Nita, G. M., & Sane, N. 2012, in American Astronomical Society Meeting Abstracts, Vol. 220, American Astronomical Society Meeting Abstracts #220, #204.30
Gordovskyy, M., Browning, P. K., Kontar, E. P., & Bian, N. H. 2013, Sol. Phys., 284, 489
Hannah, I. G., Kontar, E. P., & Reid, H. A. S. 2013, A&A, 550, A51
Haverkorn, M., Katgert, P., & de Bruyn, A. G. 2003, A&A, 404, 233
Hewish, A., Scott, P. F., & Wills, D. 1964, Nature, 203, 1214
Holman, G. D., Aschwanden, M. J., Aurass, H., et al. 2011, Space Sci. Rev., 159, 107
Inglis, A. R., Nakariakov, V. M., & Melnikov, V. F. 2008, A&A, 487, 1147
Jackson, B. V., Clover, J. M., Hick, P. P., et al. 2013, Sol. Phys., 285, 151
Jelic, V., de Bruyn, A. G., Mevius, M., et al. 2014, ArXiv e-prints, arXiv:1407.2093

PoS(AASKA14)169

Jensen, E. A., Bisi, M. M., Breen, A. R., et al. 2013, Sol. Phys., 285, 83
Jensen, E. A., Hick, P. P., Bisi, M. M., et al. 2010, Sol. Phys., 265, 31
Jensen, E. A., & Russell, C. T. 2008, Geophys. Res. Lett., 35, 2103
Karlický, M. 2004, A&A, 417, 325
Kontar, E. P., & Reid, H. A. S. 2009, ApJLett, 695, L140
Lesovoi, S. V., Altyntsev, A. T., Ivanov, E. F., & Gubin, A. V. 2014, Research in Astronomy and Astrophysics, 14, 864
Li, B., & Cairns, I. H. 2012, ApJ, 753, 124
Li, B., Cairns, I. H., & Robinson, P. A. 2012, Sol. Phys., 279, 173
Liu, Y., Manchester, IV, W. B., Kasper, J. C., Richardson, J. D., & Belcher, J. W. 2007, ApJ, 665, 1439
Maehara, H., Shibayama, T., Notsu, S., et al. 2012, Nature, 485, 478
Mancuso, S., & Spangler, S. R. 2000, ApJ, 539, 480
Mann, G., Vocks, C., & Breitling, F. 2011, Planetary, Solar and Heliospheric Radio Emissions (PRE VII), 507
Morosan, D. E., Gallagher, P. T., Zucca, P., et al. 2014, A&A, 568, A67
Nakajima, H., Nishio, M., Enome, S., et al. 1994, IEEE Proceedings, 82, 705
Nakariakov, V. M., & Melnikov, V. F. 2009, Space Sci. Rev., 149, 119
Oberoi, D., Matthews, L. D., Cairns, I. H., et al. 2011, ApJLett, 728, L27
Paesold, G., Benz, A. O., Klein, K.-L., & Vilmer, N. 2001, A&A, 371, 333
Pick, M., Malherbe, J.-M., Kerdraon, A., & Maia, D. J. F. 2005, ApJLett, 631, L97
Pick, M., & Vilmer, N. 2008, A&A Rev., 16, 1
Priest, E. R., & Forbes, T. G. 2002, A&A Rev., 10, doi:10.1007/s001590100013
Rogers, A. E. E., & Bowman, J. D. 2008, AJ, 136, 641
Salpeter, E. E. 1967, ApJ, 147, 433
Schmidt, J. M., & Cairns, I. H. 2014, Journal of Geophysical Research (Space Physics), 119, 69
Schwenn, R. 2006, Living Reviews in Solar Physics, 3, 2
Shibata, K., & Magara, T. 2011, Living Reviews in Solar Physics, 8, 6
Sinclair Reid, H. A., & Ratcliffe, H. 2014, Research in Astronomy and Astrophysics, 14, 773
Sotomayor-Beltran, C., Sobey, C., Hessels, J. W. T., et al. 2013, A&A, 552, A58
Spangler, S. R., & Whiting, C. A. 2009, in IAU Symposium, Vol. 257, IAU Symposium, ed. N. Gopalswamy & D. F. Webb, 529–541
Stelzried, C. T., Levy, G. S., Sato, T., et al. 1970, Sol. Phys., 14, 440
Stepanov, A. V., Zaitsev, V. V., & Nakariakov, V. M. 2012, Physics Uspekhi, 55, A4
Sun, X., Hoeksema, J. T., Liu, Y., et al. 2012, ApJ, 748, 77
van Haarlem, M. P., Wise, M. W., Gunst, A. W., et al. 2013, A&A, 556, A2
White, S. M., Benz, A. O., Christe, S., et al. 2011, Space Sci. Rev., 159, 225
Yan, Y., Zhang, J., Wang, W., et al. 2009, Earth Moon and Planets, 104, 97
Zaitsev, V. V., Kislyakov, A. G., Stepanov, A. V., Kliem, B., & Furst, E. 2004, Astronomy Letters, 30, 319
Zharkova, V. V., Arzner, K., Benz, A. O., et al. 2011, Space Sci. Rev., 159, 357
Zucca, P., Carley, E. P., McCauley, J., et al. 2012, Sol. Phys., 280, 591

PoS(AASKA14)169

PROCEEDINGS OF SCIENCE

Extragalactic jets in the SKA era: solving the mystery of Ultra High Energy Cosmic Rays?

Sara Turriziani[*†]
University of Rome Tor Vergata
E-mail: sara.turriziani@roma2.infn.it

The extreme properties shown by supermassive black holes at the centres of galaxies (active galactic nuclei; AGN) make them obvious candidates for producing Ultra High Energy Cosmic Rays (UHECRs), the most energetic particles known in the Universe.
AGN can exhibit outflows in the form of powerful, collimated jets of particles, accelerated in some cases close to the speed of light. Although AGN jets dimension and magnetic field could in principle accelerate particles to extreme energies, it is not easy to develop a model which describes an efficient acceleration mechanism. Different solutions have been proposed, but they need further investigation from both observational and theoretical point of view: in fact, two pieces of astrophysical understanding would need revision, namely the parameters (size and magnetic fields) in jets of AGN, and the strength of the magnetic field in the local region of the Universe.
The capabilities offered by the Square Kilometre Array (SKA) in improving current measures of the jet physical parameters will permit a better characterization of the magnetic field strength ,and its structure within the jet itself. This will be crucial to refine our estimations for the key parameters of the nearby γ-ray AGN, which are to date the best candidate sources of UHECRs.

Advancing Astrophysics with the Square Kilometre Array
June 8-13, 2014
Giardini Naxos, Italy

[*]Speaker.

[†]The author is grateful to S. Cristiani for his encouragement, to M. Hardcastle, A. Marscher, A. Tramacere, S. Markoff, M. Giroletti and M. Casolino among others for fruitful discussions

PoS(AASKA14)160

1. Introduction

In 2002, the U.S. National Research Council's Committee on Physics of the Universe composed a list of 11 particularly direct questions about the cosmos. "Where do ultra-energy particles come from?" is one of these fundamental but still unanswered questions. After many decades of investigation, this fascinating enigma is still attracting several theoretical efforts, as there are severe limitations to the properties of astrophysical candidates for accelerating cosmic rays beyond 10^{20} eV (see e.g. Kotera & Olinto 2011). Among the possible candidates, much theoretical attention have been given in particular to AGN (e.g. Ginzburg & Syrovatskii 1964; Hillas 1984; Biermann & Strittmatter 1987; Berezinsky et al. 2006; Berezhko 2008). In fact, the dimension and magnetic field of an AGN jet could in principle accelerate particles to extreme energies (Halzen & Zas 1997); however, it is not easy to develop a model which describes an efficient acceleration mechanism (see Letessier-Selvon & Stanev 2011, and references therein). Although different solutions have been proposed, there are many aspects that need further investigation from both observational and theoretical point of view. As already suggested in Nagano & Watson (2000), we need to revise the parameters (size and magnetic fields) in jets/lobes of AGN, and the strength of the magnetic field in the local region of the Universe. To date, the latter is quite hard to estimate, but the SKA will open a new window in the study of cosmic magnetism, especially regarding the poor-known extragalactic magnetic field (Beck et al. 2007; Beck et al. 2015; Johnston-Hollitt & et al. 2015). Moreover, the SKA will enable a deeper understanding of the properties and energetics of AGN jets and lobes.

This Chapter focus on the advances we can achieve in jet physics with the SKA and is organized as follows: Sect. 2 shows the current state-of-the-art characterization of relativistic jets associated with AGN, comparing observations made at different angular scale with the structure predicted by numerical simulations; Sect. 3 discuss the long-term search for astrophysical sources of ultra high energy cosmic rays (UHECRs), giving particular attention to AGN as candidate sources; Sect. 4 illustrate how the SKA will shed light on this fascinating enigma. Further related topics are discussed in other Chapters of this book, as relativistic jets are amazing laboratories to test both general relativistic (or special relativistic) magnetohydrodynamic and radiation microphysics at work (e.g. Agudo et al. 2015; Gaensler et al. 2015; Giroletti et al. 2015).

2. AGN Jets

The process of accretion powers the most energetic phenomena known in the Universe, such as AGN, their stellar-mass analogues (X-ray binaries), and gamma-ray bursts (GRBs). In all cases, the accretion process is directly coupled to outflows from the systems in the form of powerful, collimated jets (in some cases accelerated close to the speed of light). The presence of relativistic electrons and magnetic fields in jets implies that they emit synchrotron radiation, which is the dominant emission process in the radio regime. The rapid injection of kinetic energy into ambient media universally results in outbursts of synchrotron radiation resulting from the acceleration of particles and compression of magnetic fields. These outbursts are observed from a variety of sources (e.g. van der Laan 1966; Marscher & Gear 1985; Cawthorne & Wardle 1988; Hughes et al. 1989). Detection and monitoring of such outbursts serves several purposes. In fact, it allows us to estimate the feedback of kinetic energy from the central source, to compare this to the available

PoS(AASKA14)160

energy (whether, e.g., from accretion, rearrangement of magnetic fields, etc), in order to understand how this feedback affects the surrounding medium. To date, the studies in the field of AGN relativistic jets benefit on a fertile sinergy between multi-frequency studies in the high-energy (X ray, γ-ray, TeV) domain, and high resolution radio (and sometimes optical) observations. To proper investigate how jets themselves and their host system work, it is crucial to know their energy, mass, velocity, composition, and any possible connection between the power in the jet and the power associated with the release of gravitational energy of mass accreting on the central black hole. However, the estimate of power transported in jets from the observed radiation can be affected by large uncertainties. These mainly include our ignorance on: i) the jet composition (whether the plasma is dominated by a proton-electron component, or electron-positron pairs one); ii) the filling factor, i.e. the fraction of the volume actually permeated by the emitting plasma; iii) the extension of the emitting particle distribution - as this is typically steep, the low energy part is crucial in determining the total number of particles, but self-absorption in the radio band[1] makes it hard to directly observe it. The widely used approach is to compare estimates on different scales, derived by independent data sets, information and modeling and to see if a quantitative consistent picture emerges (e.g. Celotti & Ghisellini 2008).

The combination of multi-frequency monitoring data with regular VLBI observations, as available with e.g. the MOJAVE project (Lister et al. 2009), is essential to understand the nature of the extreme variability and therefore the structure and dynamics of parsec-scale relativistic jets (e.g. Marscher et al. (2010)). There is now growing evidence of a close connection between γ-ray emission and pc-scale radio jet properties of blazars and radio galaxies. However, we are still missing answers (even at least partial) to the following questions: i) what is the role of magnetic fields? More specifically, what is the magnitude of the magnetic fields? what is the configuration of magnetic field in jets? ii) what is the influence of the jet on the surrounding matter? is an AGN jet capable to accelerate particles up to the highest energies?

To date, the acceleration, collimation and stability of the observed jets remain key issues. Theoretical modeling of these jets demands to combine general (or special) relativistic magnetohydrodynamics with radiation microphysics, in order to associate the observed emission features to both the radiation microphysics and macroscopic dynamics. So far, numerical simulations revealed that the highly collimated AGN jets are subject to the Kevin-Helmholts (KH) instability when kinetically dominated, whereas they are disposed to current driven (CD) instability, where the current flows are high and jets are magnetically dominated (e.g. Hardee (2011)). The simulations predict how the structures associated to those instabilities develop and which structures dominate the jet dynamics, thus comparing the observed jet features with theoretically predicted structures can shed light on macroscopic jet properties, and, at the smallest scales, on the conditions in the jet launching region. In fact, at the largest angular scales the jets are kinetically dominated; although they may contain pressure equipartition magnetic fields, strong magnetic fields should exist close to the acceleration and collimation zone, as suggested by several theoretical works (see e.g. Blandford (1976); Blandford & Znajek (1977); Blandford & Payne (1982); Lovelace (1976); Koide et al.

[1] At low enough frequencies (e.g. $\sim$ 100 MHz), any synchrotron source will become opaque to radiation. However, compact radio sources (e.g. AGN with size much less than 1 Kpc) with very high synchrotron electron densities start to self-absorb yet at higher frequencies (see Marscher 1987, for details). On the other hand, the relativistic particle densities in the extended radio components are low enough that they can remain optically thin even at very low radio frequencies.

PoS(AASKA14)160

(2000); Nishikawa et al. (2005); De Villiers et al. (2003, 2005); Hawley & Krolik (2006); McKinney & Gammie (2004); McKinney (2006); Mizuno et al. (2007)). At the largest scales, jets are useful as probes of the external environment: large angular structure such as those seen in Virgo A or NCG 1265 imply that jets are less dense than the intra-cluster medium and are carrier of a huge energy flux (De Young 2006).

Radio source morphology starts to show differences at intermediate spatial and angular scales, and those differences give hints on the properties of jets in these objects: namely, the basic two source classes were first classified by Fanaroff & Riley (1974) and are now known as FR-I (whose jets decollimate to form long tails) and FR-II (where jets remain highly collimated to the outer edge of large radio lobes). The morphology is connected to the jet power as on average FR-II jets are more powerful. Furthermore, the morphology can be related to the properties of stability of their jets: in FR-I the jet loses its collimation from interactions with the surrounding environment as the KH instability develops at the interface with the external medium and outer mass is pulled into the jet. Many theoretical works focused on determining the physical conditions which suppress the onset of KH instability in order to keep the jets highly collimated as in FR-II (see Hardee (2011) and references therein for further details). Numerical simulations revealed that organized magnetic fields in pressure equipartition also enable sensible stabilization and reduce mass entrainment (Rosen et al. 1999). However, detailed understanding of the flow properties are still elusive at intermediate scales, even if they can still provide useful constrains on stability requirements.

Finally, at the smallest scales (i.e. tens to hundred of parsecs) the detection of twisted emission structures permits to determine more precisely the jet properties. The analysis of internal jet structure combined with motions allows for identifying macroscopic properties of kinetically dominated jet flows: this technique has been considerably used so far to extract the jet parameters in M87, the most well-studied extragalactic jet (see e.g. Lobanov et al. (2003)). Moreover, the presence of a spine-shear jet morphology is suggested in TeV BL Lacs as they require extreme relativistic bulk motions in the γ-ray emission region while observed proper motion are much slower (Ghisellini et al. 2005). Organized magnetic fields become crucial to explain jet dynamics and structure at those scales, as theoretical and numerical works showed that jets are expected to exhibit (potentially observable) helical structures driven by instability.

This excursus on AGN jets at all angular scales shows how magnetic fields are ubiquitous in these astrophysical objects, and how MHD-formed structures are important to explain the dynamics of the jet itself. A proper knowledge of the magnetic field distribution along the jet is fundamental, also because variations of magnetic fields in space and time imply the existence of transient electric fields, which can possibly accelerate charged particles in the jet to the highest energies (see sect. 3). Thus, understanding magnetic field structure in jets is crucial to put constraints on the UHECRs production models in AGN.

3. The long standing search for sources of UHECRs

How to accelerate cosmic rays up to 10^{20} eV is a pending question since their very first detection in the 1960s. Although the extragalactic nature of UHECRs is widely accepted, their actual origin is still far from being understood (Allard 2012). It is crucial to recognize that the energy in a source capable of accelerating particles to 10^{20} eV and beyond must be extremely large. The

PoS(AASKA14)160

size of the acceleration region R is assumed to be comparable to the Larmor radius of the particle in the magnetic field B, which must in turn be sufficiently weak to avoid that synchrotron losses overcome the energy gain. It can be shown easily that the total magnetic energy in the source scales as the Lorenz factor of the particle to the fifth power; for 10^{20} eV the magnetic field energy must be greater than 10^{57} erg, with $B < 0.1G$. Such sources are likely to be strong radio emitters with radio power exceeding 10^{41} $erg\ s^{-1}$, unless hadrons are being accelerated and electrons are not. This general argument does not specify which acceleration mechanism is invoked. The conditions on potential acceleration sources are summarized in the Hillas plot (Hillas 1984), which relates the maximum energy of a charged particle and the size and strength of the magnetic field of the astrophysical object. A quick look at the Hillas plot shows clearly that only a few astrophysical sources are capable to satisfy this necessary, even if not sufficient, requirement. The list of possible candidates includes neutron stars and other similar compact objects, large-scale shocks due to merging galaxies or clusters of galaxies, the core and the jets of AGN, hot spots of FR-II radio galaxies, and processes associated with GRBs. In particular, AGN have long been investigated as potential origin of such extreme energetic particles (e.g. Biermann et al. 2009; Gizani 2012; Bykov et al. 2012; Tavecchio 2014). Although the properties of core of AGN could in principle lead to accelerate protons to a few tens of EeV, the high radiation field around the central engine is likely to interact with the accelerated protons while energy losses due to synchrotron radiation, Compton processes, and adiabatic losses will take place. Bhattacharjee & Sigl (2000) show that such processes may reduce the maximum energy to only a small fraction of EeV, particularly in the case of nuclei as they will photodisintegrate faster. To overcome this problem, the acceleration must take place in a region with lower radiation density, away from the active center, such as in the terminal shock sites of the jets, a requirement possibly fulfilled by FR-II galaxies, which combine a very powerful engine and relativistic blast waves (with Lorentz factor of the order 2-10) together with a relatively scarce environment (Letessier-Selvon & Stanev 2011). Hence, their hot spots (where the jets terminate) satisfy the acceleration requirement but also the criterion that the accelerated particles does not loose all of the energy gained on the way out of the source (Rachen & Biermann 1993; Hardcastle 2010). In particular, Hardcastle (2010) details how stocastic acceleration in the large-scale lobes of radio galaxies is viable to produce UHECRs, but acceleration to the highest energies put strong constrains on the properties of the cosmic sources, indicating only a small number of local radio galaxies as plausible candidates (if UHECRs are protons).

Although the diffusive shock acceleration (Malkov & O'C Drury 2001), based on the Fermi process, is the most invoked mechanism, several alternative models have been proposed. This list comprises: unipolar inductors (Berezinskii et al. 1990; McKinney et al. 2012), magnetic reconnection acceleration (Zweibel & Yamada 2009; Giannios 2010), wakefield acceleration (often related to ponderomotive acceleration; Tajima & Dawson (1979)), re-acceleration in sheared jets (Lyutikov & Ouyed 2007), and "magnetoluminescence"(Blandford et al. 2014). None of this model is free of open issues, especially regarding their efficiency. For example, Pelletier et al. (2009) state that the Fermi 1st order mechanism is not so efficient around ultra-relativistic shocks, unless amplification is provided by effects outside the MHD range (Pelletier et al. 2009) or shear acceleration (Lyutikov & Ouyed 2007). Recently, Giannios (2013) shows how reconnection-driven plasmoids in blazars can effectively dissipate magnetic energy in the flow and power blazar emission, if the magnetic field is appropriate. On the other hand, Blandford et al. (2014) point out that the rela-

PoS(AASKA14)160

tivistic magnetic reconnection is unfortunately an unproved possibility of acceleration, even if it remains an attractive one. Ebisuzaki & Tajima (2014) show instead that wakefield acceleration mechanism arising from the Alfvénic pulse incurred by an accretion disk around the central supermassive black hole could be a viable way to accelerate particle well beyond 10^{20} eV. Moreover, the production rate of UHECRs in this model is found to be consistent with the observed γ-ray luminosity function of blazars and makes predictions on their time variability.

In this pletora of models, it is clear that several aspects demand dedicated studies. In particular, we need to revise both the parameters (size and magnetic fields) in jet/lobes of AGN, and the strength of the magnetic field in the local supercluster, as several models still rely on quite generous hypotesis on the value of these parameters. Moreover, it is worth noting that to-date there is no robust or direct measurement of the magnetic field in the jets and lobes of FRI sources, which constitute the numerically dominant population of radio galaxies in the local universe.

The SKA promises to move a huge step forward in the study of cosmic magnetism and will be able to address these issues. In particular, the SKA and its pathfinders will allow for a better characterization of: i) the magnetic field strength and its structure within the jet of an AGN; ii) the overall jet properties and energetics. These efforts will improve our knowledge in this class of cosmic accelerators, in particular regarding how they contribute to the observable flux of UHECRs.

4. Relativistic Jets in the SKA era

The SKA will dramatically improve our understanding of AGN jet with respect to both structure and dynamics: in fact, it will permit not only to image the full extent of the radio emission coming from the jet, but also to characterize polarization and to track the evolution of emission features within the jet (Bicknell et al. 2004). The unprecedented sensitivity and VLBI-scale angular resolution will allow the SKA to study in details the parameters of the nearby γ-ray AGN, which are to date the best candidate sources of UHECRs.

4.1 SKA1

Due to its relative proximity (d $\sim$ 16 Mpc), the jet of M87 has been used so far as a suitable laboratory to constrain jet structure and dynamics. The SKA will permit to extent these kind of studies to a larger sample of objects, since the SKA1 early science phase (see 4.1.1). In fact, SKA1-MID can detect features similar to the HST-1 seen in M87 jet up to 100 Mpc, with observing time of few minutes (Wolter et al. 2013). The resolution needed is of the order of 0.1 arcsec that will be achieved with the largest SKA1 planned baseline. This more detailed census of the properties of "local" AGN jets is fundamental as the effect of interactions between extragalactic cosmic rays and the cosmic background radiation causes the Greisen-Zatsepin-Kuzmin (GZK) cutoff in UHECRs spectrum (Greisen 1966; Zatsepin & Kuz'min 1966), implying that the observable sources of UHECRs lie within 100 Mpc (if UHECRs are mainly protons). Therefore, we can simply interpret the results from the Pierre Auger Observatory (i.e. correlations between UHECRs above 55 EeV and the distribution of nearby AGN, Abraham et al. (2007)) as protons from nearby sources within the so-called GZK sphere. Thus, SKA capabilities, especially resolution and sensitivity, will shed light on this topic, with the detailed characterization of all the AGN jets within the GZK horizon in

PoS(AASKA14)160

the southern sky. All these findings will be essential to develop more refined models for the origin and the acceleration of UHECRs, constraining their flux produced at AGN sites.

The simultaneous multifrequency capabilities offered by SKA1 will be crucial to investigate deeply different jet parameters. For Phase 1 specification, SKA1-MID observations in Band 1, Band 4, Band 5 (350-1050 MHz, 1.65-3.05 GHz, and 4.6-13.8 GHz) will characterize the source spectrum from the MHz to the GHz. Using all the baselines available, the observations will determine the angular size of features in the jets. At lower frequencies and hence lower energies the electrons start to self absorb the emitted photons and the spectral index changes accordingly. Once the size of a source and its spectrum are known, it is straightforward to calculate the strength of the magnetic field (Marscher 1983). For *Chandra*-detected jets, other useful constraints on the magnetic field will come from the interaction of the jet emission with the CMB (see Jorstad & Marscher 2004). Moreover, the comparison of MHz and GHz studies of energy budget (via SED[2] modeling) can tell us if it implies the existence of a strong magnetic field gradient. This will permit also to get information on the minimum electron energy, which is currently one of the less constrained parameter in the analysis of jets.

Besides the magnetic fields, the data will provide contraints on the bulk and particle Lorentz factors, the Doppler factor, and the jet viewing angle. These parameters will also improve our knowledge on the poorly-constrained low energy end of the particle energy spectrum.

Furthermore, the measurement of linear polarization allows for mapping the magnetic field direction in extended jets, such as those of FRI radio galaxies. Then, the polarization capabilities offered by SKA1 will give us a more defined and precise description of the magnetic fields role in jets. The comparison between the measured percentages of linear and circular polarization will then put constrains on different models: for example, a conversion of part of linear to circular polarization is expected in optically thick regions.

SKA1-LOW and SKA1-SUR observations can add data to built complete radio spectra and SEDs for the sources, even if their capabilities will not allow for the detection for HST-1-like feature up to 100 Mpc. In particular, we could better characterize the source spectrum if SKA1-SUR data cover a Band not available at this stage with SKA1-MID.

Among the greatest capabilities offered by the SKA there is the chance of doing repeated observations, as these will make feasible to address several key issues in jet physics: in fact, individual snapshots of SEDs can probe only a partial picture of the underlying physical mechanisms. In fact, a common feature of many jet models is that emission at different frequencies comes from different regions in the jet. This implies that the instantaneous SED measured in the observer's reference frame plausibly originates from spatially separated zones. If we fit an individual SED in terms of a single population of energetic particles, we are not considering that the energy distribution may evolve as particles are moving through the jet. Indeed, if the particle energy distribution does vary temporally, and thus spatially, it may be impraticable to really reproduce each individual instantaneous SED with a single particle distribution. Time dependent modeling becomes therefore clearly essential for understanding jet physics. This necessarily increases the complexity of the modeling, and demands for extensive computing resources. However, theorists are currently at work to incorporate time-dependence in jet modeling (e.g. Maitra et al. (2009)). Moreover, jet monitoring

[2]Spectral Energy Distribution

PoS(AASKA14)160

will allow us also to test theoretical predictions on variability structures. It is worth to point out here that on-going efforts in improving simulations will sensibly reduce the risks of being stuck by immature and weak models when we will be plenty of data in the SKA era.

4.1.1 Early science with SKA1

To address this topic, we consider as early science the SKA1 phase when only the 50% of the full SKA1 capabilities will be deployed. For example, if only half of the maximum programmed baseline is available during early science, this will prevent detection of an HST-1-like feature up to 100 Mpc with the SKA1-MID, and of course it will lower the possible detections even more if considering SKA1-SUR and SKA1-LOW observations. Thus, in this phase only the closest sources will be studied, postponing the complete census of the local AGN when the full maximum baseline will become available. On the other hand, a cut in sensitivity of 50% will imply simply the need for longer observations to detect HST-1-like features up to 100 Mpc (providing that we have only a reduction of sensitivity but we retain the maximum baseline). In the least favourable case, i.e. a simultaneous cut of 50% in both sensitivity and maximum available baseline, we can focus on the closest and brightest source, to test for example different observational strategies (to determine e.g. the optimal cadence for repeated observations), and to obtain a set of observations that will serve as a proof of principle of what will be done when the array will reach it full capabilities.

However, it would be desirable to have available even at these early stages at least Band 1 and Band 5 for the SKA1-MID: in fact, Band 1 will allow us to get MHz fluxes for the sources, where their spectrum is expected to be more self-absorbed, whereas Band 5 will be less contamined by steep spectrum sources and suffer of lower depolarization effects. Moreover, Band 1 probes older electrons in the external part of the jet, since MHz frequencies sample kpc spatial scales. This allows us to study extended emission at large distances from the compact object driving the jets and possibily obtain hints on the interaction between the jet and circumnuclear regions, or jet-feedback, thus helping us to determine the impact of the jets on their surroundings. Combining observations made at different wavelengths will trace the structure of the jets.

4.2 SKA Phase 2

The SKA superb improvement in sensitivity will make possible to monitor “local” AGN with really short snapshots with an unprecedented angular resolutions. Moreover, the extention up to 30 GHz of Band 5 is important as the highest frequencies probe closer to the AGN radio core, that is detected so far at 43 GHz. Moreover, the longest baseline available with the SKA-MID highest band (and possibly an integration with other arrays providing longer baselines) will allow us to observe the nearby AGN at smaller angular scale and measure: (i) structures such as helical twists or shock transitions, (ii) proper motions, (iii) polarization and so characterize the magnetic geometry within the jet, (iv) the spectral and temporal evolution of the emission. All of them are required to understand both the dynamics and the microphysics of AGN jets (Hardee 2008). Polarization data will trace changes in the magnetic geometry that will allow us to better identify transition points. If longer baselines will be available, thanks to the integration of SKA with the African VLBI, in the case of exemplary obiects such as M87, new observations will locate beyond any doubt the base of the kinetically dominated region, and this will permit to set robust constrains on jet formation models using the spatial distance from the origin and the rate of collimation out to

PoS(AASKA14)160

this point. Moreover, the eventual detection of deceleration or acceleration in proper motions along the jet at these spatial and angular scales will have impact on high energy emission models, notably in the TeV band. Among other importante observables, transverse emission structures will play a key role in reconstructing the jet spine-sheath structure, when combinated with proper motion measures. This will give us an unique view of the jet of M87.

Furthermore, as stated earlier, the SKA will permit for the first time to extent the present studies on individual sources as M87 to a more statistically significant sample of objects, also covering a wider range in redshift and evolution. This unprecedented data set will be fundamental in hunting answers for the following open questions: has M87 just a peculiar jet of its own or is it the perfect prototype for jets in radio galaxies? More generally, what kind of jets the nature makes? Is there simply a dichotomy as the radio galaxy morphology points out? Which are the parameters that preserve jet stability? More specifically, is it more a matter of galaxy/enviroment in which the AGN lie or is it related mainly to jet power? Is there any evolution in the jet key parameters in the local Universe? Which jets can accelerate particles to extreme energies?

However, a complete jet picture can be achieved only integrating SKA obervations with VLBI-(sub)mm information, and this implies to plan synergies between SKA and ALMA. Moreover, synergies with the Cherenkov Telescope Array (CTA) will allow us to perform radio/VHE correlation studies with greatly improved VHE sensitivity, thus giving major contributions in particle acceleration in nearby γ-ray AGN, improving our knowledge of the jet-structure and jet-composition at different locations from the main engine. All these studies inform ongoing efforts to improve our understanding of the particle acceleration mechanisms in AGN jets, and possibly solving the long-standing enigma of the origin of ultra-energetic particles.

References

Abraham, J., Abreu, P., Aglietta, M., et al. 2007, Science, 318, 938

Agudo, I., Boettcher, M., Falcke, H., et al. 2015, "Studies of Relativistic Jets in Active Galactic Nuclei with SKA", in proceedings of "Advancing Astrophysics with the Square Kilometre Array", PoS(AASKA14)093

Allard, D. 2012, Astroparticle Physics, 39, 33

Beck, R., Bomans, D., Colafrancesco, S., & et al. 2015, "Structure, dynamical impact and origin of magnetic fields in nearby galaxies in the SKA era", in proceedings of "Advancing Astrophysics with the Square Kilometre Array", PoS(AASKA14)094

Beck, R., Gaensler, B., & Feretti, L. 2007, in Exploring the Cosmic Frontier: Astrophysical Instruments for the 21st Century, ed. A. P. Lobanov, J. A. Zensus, C. Cesarsky, & P. J. Diamond (Springer-Verlag), 103

Berezhko, E. G. 2008, ApJ, 684, L69

Berezinskii, V. S., Bulanov, S. V., Dogiel, V. A., & Ptuskin, V. S. 1990, Astrophysics of cosmic rays

Berezinsky, V., Gazizov, A., & Grigorieva, S. 2006, Phys. Rev. D, 74, 043005

Bhattacharjee, P., & Sigl, G. 2000, Phys. Rep., 327, 109

Bicknell, G. V., Jones, D. L., & Lister, M. 2004, New A Rev., 48, 1151

Biermann, P. L., & Strittmatter, P. A. 1987, ApJ, 322, 643

PoS(AASKA14)160

Biermann, P. L., Becker, J. K., Caramete, L., et al. 2009, Nuclear Physics B Proceedings Supplements, 190, 61
Blandford, R., Simeon, P., & Yuan, Y. 2014, arXiv:1409.2589, "Cosmic Ray Origins: An Introduction", in Proceedings of the "Cosmic Ray Origin - Beyond the Standard Models" International Conference, Nuclear Physics B Proceedings Supplement. Eds. O. Tibolla, L. Drury, M. Persic, S. Kaufmann, H. Völk, K. Mannheim and A. de Angelis
Blandford, R. D. 1976, MNRAS, 176, 465
Blandford, R. D., & Payne, D. G. 1982, MNRAS, 199, 883
Blandford, R. D., & Znajek, R. L. 1977, MNRAS, 179, 433
Bykov, A., Gehrels, N., Krawczynski, H., et al. 2012, Space Sci. Rev., 173, 309
Cawthorne, T. V., & Wardle, J. F. C. 1988, ApJ, 332, 696
Celotti, A., & Ghisellini, G. 2008, MNRAS, 385, 283
De Villiers, J.-P., Hawley, J. F., & Krolik, J. H. 2003, ApJ, 599, 1238
De Villiers, J.-P., Hawley, J. F., Krolik, J. H., & Hirose, S. 2005, ApJ, 620, 878
De Young, D. S. 2006, ApJ, 648, 200
Ebisuzaki, T., & Tajima, T. 2014, Astroparticle Physics, 56, 9
Fanaroff, B. L., & Riley, J. M. 1974, MNRAS, 167, 31P
Gaensler, B., Agudo, I., Akahori, T., et al. 2015, "Broadband Polarimetry with the Square Kilometre Array: A Unique Astrophysical Probe", in proceedings of "Advancing Astrophysics with the Square Kilometre Array", PoS(AASKA14)103
Ghisellini, G., Tavecchio, F., & Chiaberge, M. 2005, A&A, 432, 401
Giannios, D. 2010, MNRAS, 408, L46
—. 2013, MNRAS, 431, 355
Ginzburg, V. L., & Syrovatskii, S. I. 1964, The Origin of Cosmic Rays (Macmillan, New York)
Giroletti, M., Orienti, M., D'Ammando, F., et al. 2015, "The connection between radio and high energy emission in black hole powered systems in the SKA era", in proceedings of "Advancing Astrophysics with the Square Kilometre Array", PoS(AASKA14)153
Gizani, N. A. B. 2012, Nuclear Instruments and Methods in Physics Research A, 692, 280
Greisen, K. 1966, Physical Review Letters, 16, 748
Halzen, F., & Zas, E. 1997, ApJ, 488, 669
Hardcastle, M. J. 2010, MNRAS, 405, 2810
Hardee, P. 2008, Journal of Physics Conference Series, 131, 012052
Hardee, P. E. 2011, in IAU Symposium, Vol. 275, IAU Symposium, ed. G. E. Romero, R. A. Sunyaev, & T. Belloni, 41–49
Hawley, J. F., & Krolik, J. H. 2006, ApJ, 641, 103
Hillas, A. M. 1984, ARA&A, 22, 425
Hughes, P. A., Aller, H. D., & Aller, M. F. 1989, ApJ, 341, 54
Johnston-Hollitt, M., & et al. 2015, "Using SKA Rotation Measures to Reveal the Mysteries of the Magnetised Universe" in proceedings of "Advancing Astrophysics with the Square Kilometre Array", PoS(AASKA14)092
Jorstad, S. G., & Marscher, A. P. 2004, ApJ, 614, 615
Koide, S., Meier, D. L., Shibata, K., & Kudoh, T. 2000, ApJ, 536, 668
Kotera, K., & Olinto, A. V. 2011, ARA&A, 49, 119

PoS(AASKA14)160

Letessier-Selvon, A., & Stanev, T. 2011, Reviews of Modern Physics, 83, 907
Lister, M. L., Cohen, M. H., Homan, D. C., et al. 2009, AJ, 138, 1874
Lobanov, A., Hardee, P., & Eilek, J. 2003, New A Rev., 47, 629
Lovelace, R. V. E. 1976, Nature, 262, 649
Lyutikov, M., & Ouyed, R. 2007, Astroparticle Physics, 27, 473
Maitra, D., Markoff, S., & Falcke, H. 2009, A&A, 508, L13
Malkov, M. A., & O'C Drury, L. 2001, Reports on Progress in Physics, 64, 429
Marscher, A. P. 1983, ApJ, 264, 296
Marscher, A. P. 1987, in Superluminal Radio Sources, ed. J. A. Zensus & T. J. Pearson, 280–300
Marscher, A. P., & Gear, W. K. 1985, ApJ, 298, 114
Marscher, A. P., Jorstad, S. G., Larionov, V. M., et al. 2010, ApJ, 710, L126
McKinney, J. C. 2006, MNRAS, 368, 1561
McKinney, J. C., & Gammie, C. F. 2004, ApJ, 611, 977
McKinney, J. C., Tchekhovskoy, A., & Blandford, R. D. 2012, MNRAS, 423, 3083
Mizuno, Y., Hardee, P., & Nishikawa, K.-I. 2007, ApJ, 662, 835
Nagano, M., & Watson, A. A. 2000, Reviews of Modern Physics, 72, 689
Nishikawa, K.-I., Richardson, G., Koide, S., et al. 2005, ApJ, 625, 60
Pelletier, G., Lemoine, M., & Marcowith, A. 2009, MNRAS, 393, 587
Rachen, J. P., & Biermann, P. L. 1993, A&A, 272, 161
Rosen, A., Hardee, P. E., Clarke, D. A., & Johnson, A. 1999, ApJ, 510, 136
Tajima, T., & Dawson, J. M. 1979, Physical Review Letters, 43, 267
Tavecchio, F. 2014, MNRAS, 438, 3255
van der Laan, H. 1966, Nature, 211, 1131
Wolter, A., Tavecchio, F., Bonnoli, G., et al. 2013, "Relativistic Jets with SKA" in "Italian SKA White Book", INAF Press
Zatsepin, G. T., & Kuz'min, V. A. 1966, Soviet Journal of Experimental and Theoretical Physics Letters, 4, 78
Zweibel, E. G., & Yamada, M. 2009, ARA&A, 47, 291

PoS(AASKA14)160

PROCEEDINGS OF SCIENCE

Enabling the next generation of cm-wavelength studies of high-redshift molecular gas with the SKA

Jeff Wagg[*1], **Elisabete Da Cunha**[2], **Chris Carilli**[3,4], **Fabian Walter**[2], **Manuel Aravena**[5], **Ian Heywood**[6,7], **Jacqueline Hodge**[8], **Eric Murphy**[9], **Dominik Riechers**[10], **Mark Sargent**[11], **and Ran Wang**[12]

[1]*SKA Organisation, Lower Withington, UK;* [2]*MPIA, Heidelberg, Germany;* [3]*NRAO, Socorro, USA;* [4]*Cavendish Astrophysics Group, Cambridge, UK;* [5]*U. Diego Portales, Santiago, Chile;* [6]*CASS, Sydney, Australia;* [7]*RATT, Dept. of Physics and Electronics, Rhodes University, Grahamstown, South Africa;* [8]*NRAO, Charlottesville, USA;* [9]*IPAC, Caltech, Pasadena, USA;* [10]*Cornell University, Ithaca, USA;* [11]*Astronomy Centre, Department of Physics and Astronomy, University of Sussex, Brighton, UK;* [12]*KIAA, Peking, Beijing, China*

E-mail: j.wagg@skatelescope.org

The Square Kilometre Array will be a revolutionary instrument for the study of gas in the distant Universe. SKA1 will be among the first facilities with sufficient sensitivity to detect and image atomic 21 cm HI in individual galaxies at significant cosmological distances, complementing ongoing ALMA imaging of redshifted high-J CO line emission and far-infrared interstellar medium lines such as [CII] 157.7μm. At frequencies below $\sim$50 GHz, observations of redshifted emission from low-J transitions of CO, HCN, HCO^+, HNC, H_2O and CS provide insight into the kinematics and mass budget of the cold, dense star-forming gas in galaxies. In advance of ALMA band 1 deployment (35 to 52 GHz), the most sensitive facility for high-redshift studies of molecular gas operating below 50 GHz is the Karl G. Jansky Very Large Array (VLA). Here, we present an overview of the role that the SKA could play in molecular emission line studies during SKA1 and SKA2, with an emphasis on studies of the dense gas tracers directly probing regions of active star-formation.

Advancing Astrophysics with the Square Kilometre Array
June 8-13, 2014
Giardini Naxos, Italy

[*]Speaker.

PoS(AASKA14)161

1. Gas in galaxies: 2020 and beyond

Studies of the dense star-forming gas in high-redshift galaxies have been transformed in recent years owing to the increased sensitivity and bandwidth of new submm through cm-wavelenth facilities like the Karl G. Jansky Very Large Array (VLA), the Plateau de Bure Interferometer (PdBI) and the Atacama Large Millimeter/submm Array (ALMA). A few highlights include observations of molecular gas through ^{12}CO (hereafter CO) line emission in main sequence star-forming galaxies at $z \sim 1.5 - 2.0$ (Daddi et al. 2008, 2010; Dannerbauer et al. 2009; Tacconi et al. 2010, 2013; Aravena et al. 2010, 2014), the detection and imaging of CO and [CII] line emission in quasar host galaxies during the epoch of reionization (Walter et al. 2003, 2004; Carilli et al. 2007; Wang et al. 2013; Willott et al. 2013), and the first blank-field CO emission line surveys for gas-rich galaxies over significant cosmological volumes (Walter et al. 2014; Decarli et al. 2014). These new surveys greatly expand our knowledge of the gas content of galaxies in the distant Universe, which had been based primarily on detections of CO in far-infrared luminous AGN host galaxies and submm/mm-selected star-forming galaxies (see Carilli & Walter 2013 for a recent review). The emerging picture is that, with the exception of atomic HI, the cool gas content of main sequence star-forming galaxies is now accessible with current facilities across the peak in cosmic star-formation. Here, we summarize the molecular gas studies of high-redshift galaxies that could be enabled by the SKA.

In 2020 and beyond, the SKA will operate in parallel with major new facilities covering much of the electromagnetic spectrum, collaboratively conducting sensitive studies of gas and star-formation in galaxies well into the epoch of reionization (EoR) at $z > 6$. These facilities include optical telescopes like the European Extremely Large Telescope (E-ELT), the Thirty Meter Telescope (TMT), and the Large Synoptic Survey Telescope (LSST), and infrared facilities such as the *James Webb Space Telescope* (*JWST*) and *Euclid*. At long submm/mm-wavelengths, ALMA, NOEMA, the Cerro Chajnantor Atacama Telescope (CCAT) and the Large Millimeter Telescope (LMT) will shed light on Galactic and extragalactic regions of the Universe obscured by molecular gas and dust. The long wavelength complement to these facilities will be the SKA.

One of the main science drivers for the SKA has always been the study of 21 cm HI line emission in normal galaxies out to redshifts $z \gtrsim 1$. Predictions and science drivers for future SKA extragalactic HI surveys are presented by other authors in this volume (e.g. Morganti et al. 2015; Obreschkow et al. 2015; Santos et al. 2015; Staveley-Smith et al. 2015). Similarly, the SKA will provide the unique ability to survey thermal and non-thermal (synchrotron) radio emission at low radio frequencies covering 10s to 1000s of square degrees in order to probe the evolution of obscured star-formation out to redshifts approaching the end of reionization at $z \sim 6$ (see Prandoni & Seymour 2015, Jarvis et al. 2015, and Murphy et al. 2015 in this volume). Over fields much smaller than one square degree, this obscured star-formation will be probed to very sensitive depths by ALMA, which has already been successful in imaging far-infrared continuum emission in star-forming galaxies during the epoch of reionization (e.g. Wang et al. 2013). For galaxy evolution studies, the wide field imaging capabilities of the SKA will be complemented at optical/infrared wavelengths by LSST and *Euclid*. Finally, ALMA is sensitive to the high-J CO, HCN, HCO^+ and CS line emission in the distant Universe at frequencies $\nu > 86$ GHz ($\nu > 35$ GHz once band 1 is deployed), leaving open the need for a sensitive facility able to conduct surveys of the low-

PoS(AASKA14)161

J transitions of these molecules that provide an anchor for the spectral line energy distribution. Without this anchor, there will be degeneracies in the models fit to derive gas properties such as density and temperature. Measurements of only the high-J CO emission lines may lead to a bias in molecular gas mass estimates as their intensities will depend on the excitation conditions of the gas.

2. Molecular CO line emission with the SKA

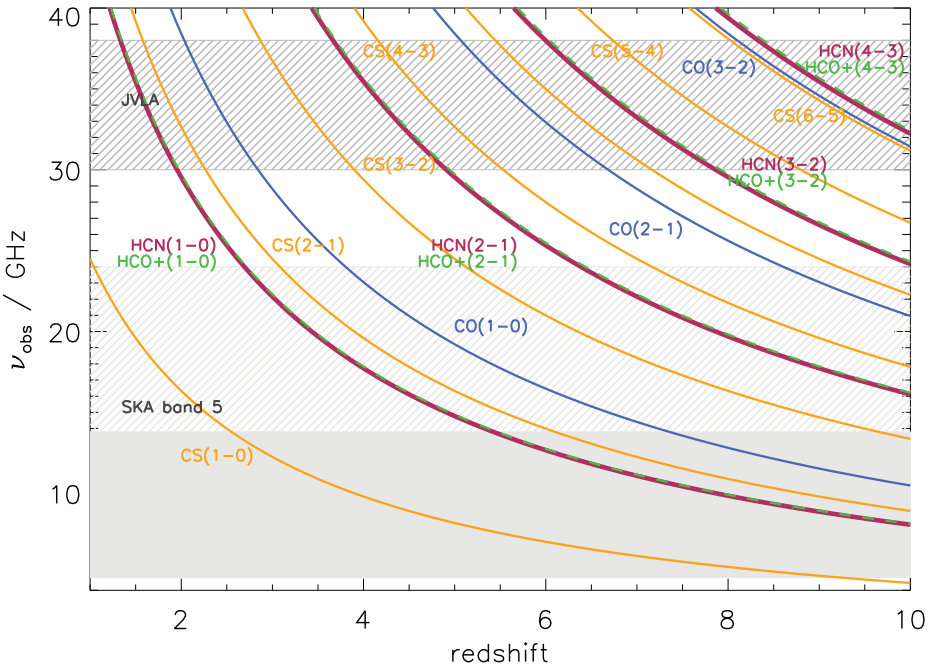

Figure 1: Redshifted line frequencies for multiple low-J transitions of CO, CS, HCN, and HCO^+. The *grey* region shows the currently defined frequency range of band 5 on SKA1-MID, and the proposed extension to 24 GHz for SKA2 is shown as a *hatched* region. At higher frequencies we show the frequency coverage provided by an 8 GHz bandwidth VLA survey with the Ka-band receivers (26.5 to 40 GHz). ALMA band 1 is expected to cover 35 to 52 GHz (Di Francesco et al. 2013).

Among the outstanding challenges for galaxy formation studies is to quantify the kinematic properties and to measure the gas content of star-forming galaxies over the history of the Universe. Aided by the typical increase in line flux density with increasing rotational transition in star-forming molecular gas, interferometric observations of CO line emission provide a means of estimating dynamical masses through the linewidths and source sizes in galaxies out to the very early Universe (e.g. Walter et al. 2004; Riechers et al. 2013). At cm-wavelengths, one is sensitive to the low-J transitions of this line, the luminosity of which has traditionally been used as a means of estimating the total cold molecular ($= H_2$) mass that is available to fuel star-formation by adopting a CO-to-H_2 conversion factor, α_{CO} (e.g Downes & Solomon 1998; Bolatto et al. 2013). As such, observations of high-redshift molecular CO line emission have naturally become one of

PoS(AASKA14)161

the main science drivers for current and future cm-wavelength interferometers operating above $\sim$20 GHz. Figure 1 shows the redshifted frequencies of the low-*J* CO lines, along with those of dense gas tracing molecular line species.

Here, we consider the likelihood that CO *J*=1-0 line emission will be either a viable tracer of galaxy dynamics or a tool for estimating cold molecular gas masses with the current plans for SKA1-MID and SKA2. The possibility of CO intensity mapping with the SKA is discussed in another chapter (Chang et al.). Five bands are currently defined for SKA1-MID, although only three are expected to be deployed in the first phase. Band 5 would extend up to 13.8 GHz, corresponding to CO *J*=1-0 line emission redshifted to $z = 7.35$. The most luminous metal-enriched quasar host galaxy at $z = 7.1$ is undetected in CO *J*=6-5 line emission with the PdBI (Venemans et al. 2012), which should benefit from a factor of $\sim$36$\times$ increase in flux density with respect to the CO *J*=1-0 line emission owing to the ν^2 dependance of flux density on rest frequency. Molecular line emission from transitions where the excitation temperature is similar to the CMB background temperature ($\mathrm{T_{CMB}(z) = 2.7(1+z)}$) should not be detectable (e.g. Papadopoulos et al. 2000; Obreschkow et al. 2009; Da Cunha et al. 2013b). In the case of a $z = 7.5$ star-forming galaxy (similar to a submm galaxy or a far-infrared luminous quasar host galaxy) with molecular gas at an average kinetic temperature of $\mathrm{T_k} = 40$ K (at $z = 0$), the CO *J*=1-0 line is predicted to exhibit $\sim$40% of the flux density it would have in the absence of the CMB. In the case of more quiescent star-formation where the kinetic temperature of the gas would be $\mathrm{T_k} = 18$ K , the integrated CO *J*=1-0 line flux density of that galaxy at $z = 7.5$ would be down to 5% of its $z = 0$ value. Such effects likely contributed to the (sensitive) Green Bank Telescope (GBT) non-detections of CO *J*=1-0 in two star-forming Lyα emitters (LAEs) at $z > 6.5$ by Wagg, Kanekar & Carilli (2009), including the gravitationally lensed LAE HCM6A, which may have a star-formation rate $\gtrsim 100$ $\mathrm{M_\odot\ yr^{-1}}$ (Chary et al. 2005). During these early cosmic times, corresponding to the epoch of reionization (EoR), measuring the kinematic properties (dynamical mass estimates) of quasar host galaxies, or redshifts for the lower luminosity galaxy population, would best be achieved through observations of the redshifted [CII] line emission at mm-wavelengths (e.g. Maiolino et al. 2005; Walter et al. 2009; Wagg et al. 2012a; Carilli et al. 2013; Wang et al. 2013; Riechers et al. 2014).

Adding to the inherent difficulty in detecting the low-*J* CO lines during the EoR, the average metallicity of galaxies is expected to be lower, and recent observational and theoretical work suggests that α_{CO} may be higher in low metallicity gas clouds (e.g. Genzel et al. 2012; Leroy et al. 2009; Narayanan et al. 2012). Larger α_{CO} naturally leads to a lower CO line flux density per unit mass of $\mathrm{H_2}$. The $z > 6$ population of star-forming Lyα emitters have typical star-formation rates of 5-10 $M_\odot$ $\mathrm{yr^{-1}}$. Their metallicities cannot be measured with current facilities (except possibly with ALMA, which is sensitive to redshifted FIR lines like [CII] and [NII]), although these are likely to have sub-solar metallicties given the timescales needed for metal enrichment (the Universe is $\sim$710 Myr old at $z = 7.5$). Wagg et al. (2012b) obtained a sensitive GBT upper-limit on CO *J*=2-1 line emission in the Lyα blob (LAB) 'Himiko' at $z = 6.6$. It is likely that the low expected metallicities of typical $z > 6$ star-forming galaxy populations like the LABs and LAEs will mean that SKA1-MID band 5 surveys of CO *J*=1-0 line emission will only be sensitive to more massive and rare starburst galaxies (see Murphy et al. in this edition). The only high-redshift galaxy currently detected in molecular CO line emission at frequencies below 20 GHz is a gravitationally lensed star-forming submm galaxy at $z = 6.34$ (Riechers et al. 2013). The surface density of similarly

PoS(AASKA14)161

luminous quasar host galaxies detected in CO line emission at $z > 6$ is $\sim$1 per 500 square degrees.

During SKA2, the situation would be improved by the expected order of magnitude increase in collecting area and extended frequency coverage up to 24 GHz (or 30 GHz, as proposed by Murphy et al. (2015), who also present the science case for $\nu > 10$ GHz extragalactic continuum studies). Such studies would be sensitive to CO J=1-0 line emission at $z > 3.8$ ($z > 2.8$ for $\nu < 30$ GHz), covering the epoch when massive $z \sim 2$ galaxies should have formed their stars, likely in obscured bursts of star-formation. For the case of cold, quiescent gas at a kinetic temperature of 18 K in a $z > 4$ galaxy, the prediction is that the measured flux density should be less than 25% of what would be measured in the absence of the CMB (Da Cunha et al. 2013b). For warm star-forming gas at $T_k = 40$ K, one would measure $\sim$65% of the $z = 0$ intensity at a redshift of $z = 4$. We expect that SKA2-MID should provide a powerful means of quantifying the cosmic evolution of the molecular H_2 gas density over the epoch of massive galaxy formation.

3. Dense star-forming gas

Dense star-forming gas tracers such as HCN and CS hold the promise for future SKA studies of the high-redshift interstellar medium (ISM), as their emission lines directly probe sites of active star-formation with densities in excess of 10^4 cm^{-3}. Although they are typically an order of magnitude fainter than the CO lines, the luminosity in the 88.6 GHz HCN J=1-0 line correlates linearly with infrared luminosity in star-forming gas over nearly eight orders of magnitude in luminosity (Gao & Solomon 2004; Wu et al. 2005). As such, emission from lines like HCN J=1-0 should be a good proxy for the total mass in dense molecular gas directly involved in ongoing star-formation activity. The HCN J=1-0 line traces gas at kinetic temperatures of 40 to 50 K in luminous infrared star-forming galaxies, much higher than the CMB temperature at redshifts below $z \sim 6$. Current cm-wavelength facilites lack the sensivity to detect HCN J=1-0 line emission at $\nu \lesssim 24$ GHz in even the most luminous, known star-forming galaxies and quasar host galaxies. Previous attempts to detect low-J HCN line emission in $z > 2$ galaxies have only been successful for a handful of lensed objects (Solomon et al. 2003; Vanden Bout et al. 2005; Carilli et al. 2005; Gao et al. 2007; Riechers et al. 2007), while high-J HCN line emission remains a promising tool for ALMA studies (Wagg et al. 2005; Weiss et al. 2007; Danielson et al. 2011). The HCO^+ line may also hold promise as a dense gas tracer in high-redshift galaxies (e.g. Riechers et al. 2006; Garcia-Burillo et al. 2006), although the possible decrease in abundance of HCO^+ in regions of high electron density has brought into question its effectiveness as a proxy for dense molecular gas mass in starburst galaxies (e.g Papadopoulos et al. 2007).

In the case of CS, the J=1-0 transition occurs at a rest frequency of 49 GHz, close to the atmospheric O_2 line, which limits the sensitivity for surveys of CS line emission in the local Universe. CS is a more common tracer of dense star-forming cores in our Galaxy (e.g. Evans 1999), however it has not been widely studied in the high-redshift Universe given the sensitivity of current cm-wavelength instruments.

If band 5 were deployed on SKA1-MID, it would be sensitive to HCN J=1-0 and HCO^+ J=1-0 line emission at $z > 5.4$ and CS J=1-0 line emission at $z > 2.6$. However, a more significant advance will be made with the increased sensitivity and extended frequency coverage of SKA2, which should be an excellent facility for the study of low-J transitions of dense gas tracers in

PoS(AASKA14)161

high-redshift galaxies. It would be the first interferometer capable of resolving the emission from the low-J dense gas tracers at redshifts between $z \sim 1$ (roughly half the present-day age of the Universe), and to the end of the epoch of reionization at $z \sim 6$. In Section 5, we make predictions for the expected number of dense gas emitters that might be detected in future SKA1 and SKA2 spectral line surveys.

4. OH and H_2O megamaser emission

Another potentially interesting probe of star-formation and the molecular ISM of high-redshift galaxies is redshifted emission from OH or H_2O megamaser emission. Although it may be that the luminosity in the OH megamaser line is correlated with star-formation activity, this emission has not been detected in far-infrared luminous galaxies at high-redshift (e.g. Ivison 2006). Similarly, early searches for H_2O megamasers at high-redshift (e.g. Wilner et al. 1999; Ivison 2006; Edmonds et al. 2009; Wagg & Momjian 2009), resulted in only a pair of detections at $z = 0.66$ (Barvainis & Antonucci 2005) and $z = 2.64$ (Impellizzeri et al. 2008). It is therefore difficult to predict the expected number density of these line emitters with the increased sensitivity of the SKA. Murphy et al. (this edition) discuss the use of H_2O megamaser line emission for studying AGN at high-redshift.

5. Predictions for SKA spectral line surveys

For the purpose of predicting the expected detectability of molecular emission lines in future SKA observations, we first assume a Λ-dominated cosmological model with $\Omega_\Lambda = 0.7$, $\Omega_M = 0.3$, and $H_0 = 70$ km s^{-1} Mpc^{-1}. The standard definition of line luminosity is given by Solomon, Downes & Radford (1992), and we assume a linewidth, $FWHM = 300$ km s^{-1} throughout. For both SKA1 and SKA2, we consider two scenarios, one where targeted observations of known ultraluminous infrared galaxies (ULIRGs) are made ($L_{IR} = 10^{12}$ L$_\odot$, $SFR \sim 100$ M$_\odot$ yr^{-1}), and a second where pointed deep field observations are conducted, sensitive to less luminous galaxies. In the latter case, we adopt the models of da Cunha et al. (2013a), who make empirical predictions for the observed molecular line properties of star-forming galaxies in the observed *Hubble* Ultra Deep Field (UDF). In the original models, the expected CO line luminosity is predicted from the infrared luminosity, and here we extend this prediction to HCN, HCO^+, and CS which we convert from the CO J=1-0 line luminosity by adopting the relationship to dense gas tracer line luminosity measured by Gao & Solomon (2004).

For the purposes of SKA1 band 5 (4.6 to 13.8 GHz) predictions, we do not consider CO J=1-0 line emission at $z > 7.4$, due to the effects discussed in the previous section. ALMA observations of higher-J CO lines would be sensitive to the same star-forming molecular gas, while also benefitting from an increase in flux density that depends on ν^2. For targeted observations of HCN J=1-0 or CS J=1-0 line emission in ULIRGs at $z \sim 5.4$ (HCN) or $z \sim 2.6$ (CS), the expected peak flux density in both cases would be $\sim$1.5 μJy. A 5-σ detection of such a line would take $\sim$1000 hours of integration time with the full SKA1, or $\sim$4000 hours if SKA1 had 50% less sensitivity. Now considering predictions for blind surveys, Figure 2 shows the expected number density of CS J=1-0 line emitters as a function of flux density, where we also indicate the expected sensitity after

PoS(AASKA14)161

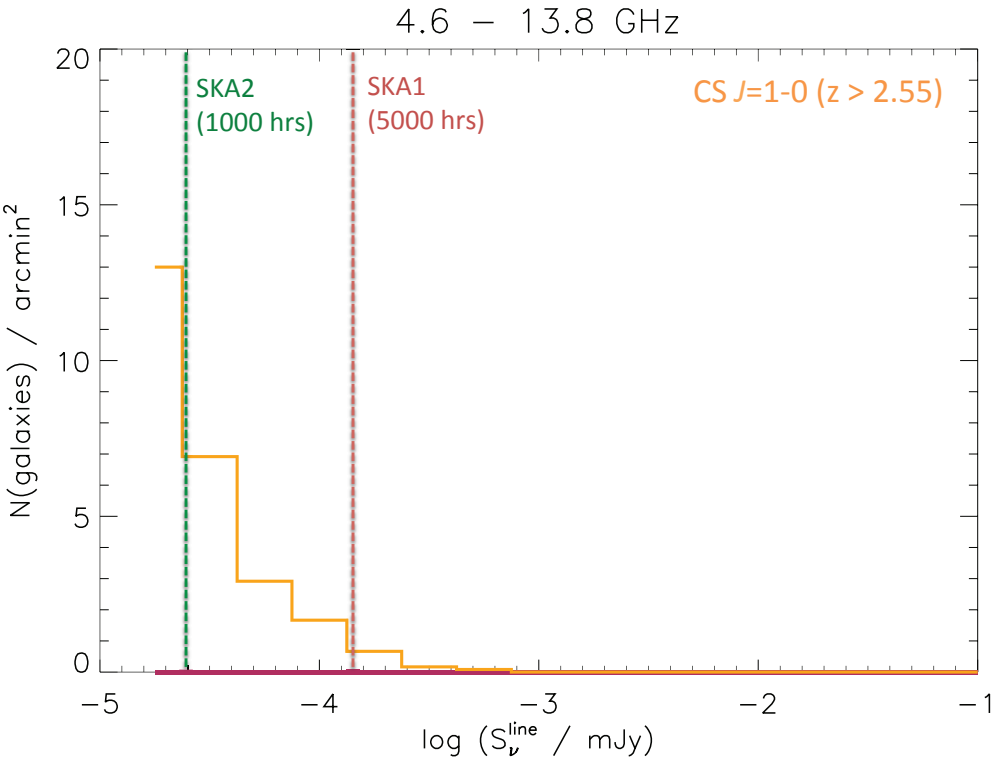

Figure 2: Predicted number density of CS J=1-0 line emitters (orange curve) as a function of peak flux density, assuming a 300 km s^{-1} linewidth. In a deep SKA1 survey (5000 hours integration time), one would expect to detect approximately one source per square arcminute over the field of view at 13.8 GHz. That number decreases to zero for SKA1 with half the sensitivity of the baseline design, but increases to 10 to 13 per square arcminute for an SKA2 survey (1000 hours integration time).

5000 hours with the full SKA1. In that case, one might expect to detect $\sim$ 1 source per square arcminute over the field of view at the highest frequency end of the band.

SKA2 should enable a revolution in high-redshift molecular gas studies, not only because of the extended frequency coverage (up to 24 GHz), but also due to the increase from 190 to 2500 in the number of band 5 MID antennas. In assessing the potential for SKA2 studies, we only assume blank-field searches for molecular line emitting galaxies. We note that the expected rms in a 300 km s^{-1} channel after 1000 hours of on-source integration time is expected to be $\sim$24 nJy at frequencies above $\sim$10 GHz. Figure 3 shows the predictions for two tunings, each covering 5 GHz of bandwidth over the upper-end of SKA2-MID band 5. We only consider CO J=1-0 line emitters detected in the upper tuning ($z < 5$), when the emission from cold molecular gas is not expected to be dramatically effected by the CMB effects discussed previously. We note that at these redshifts metallicity evolution may have an impact on the detectability of CO line emission in galaxies with low metallicities. A deep integration covering the 19 to 24 GHz frequency range is expected to detect more than 50 CO line emitters per square arcminute. Such a survey would provide the first strong constraint on the evolution of the CO J=1-0 line luminosity function at $z > 4$.

PoS(AASKA14)161

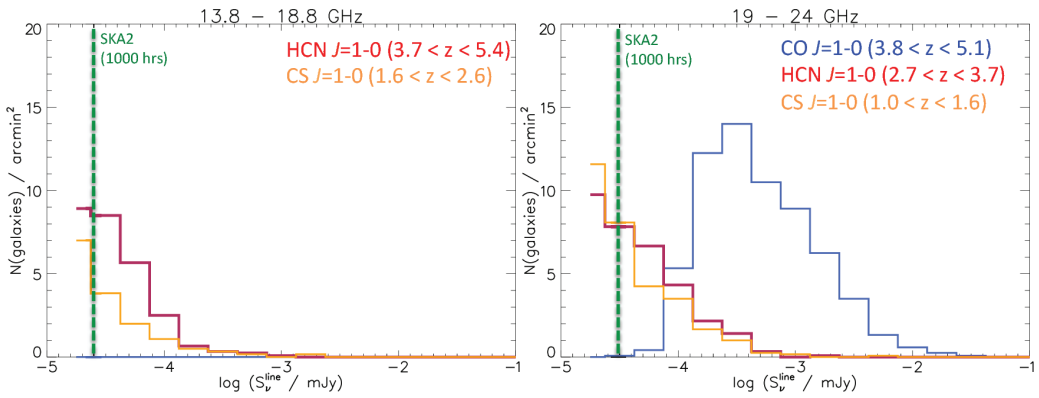

Figure 3: Predictions for the number density density of molecular line emitters as a function of peak line flux density (assuming a 300 km s^{-1} linewidth). The *left* panel shows the prediction for a 5 GHz wide tuning between 13.8 and 18.8 GHz, while the *right* panel shows the same for a 5 GHz wide tuning extending up to 24 GHz. CS *J*=1-0 line emitters are indicated by the orange curves, while the red curves show HCN *J*=1-0 (or HCO$^+$ *J*=1-0) and the blue curve in the right-hand panel indicates the expected number density of CO *J*=1-0 line emitters. Note that the decline in the number density of low luminosity CO line emitters is artificial, as it is based on the observed number density of low luminosity optically selected galaxies in the UDF.

6. Summary

The SKA has the potential to be a powerful facility for the detection and imaging of low-*J* transitions of molecular line emission in high-redshift galaxies. During SKA1, it could be possible to detect faint CS *J*=1-0 line emission associated with $z > 2.6$ luminous infrared galaxies ($L_{FIR} > 10^{12}$ L$_\odot$). At $z > 5.4$, HCN *J*=1-0 could be observed in order to quantify the total dense molecular gas mass in galaxies. Our models predict that with the increased sensitivity and frequency coverage of SKA2 extending up to ∼24 GHz, we expect to detect significant numbers of $z > 3.8$ CO line emitters in blank-field surveys. Such galaxies may be significant contributors to the total star-formation rate density of the Universe at these early cosmic epochs.

REFERENCES

Aravena, M., Carilli, C., Daddi, E., et al. 2010, ApJ, 718, 177
Aravena, M., Hodge, J. A., Wagg, J., et al. 2014, MNRAS, 442, 558
Barvainis, R., & Antonucci, R. 2005, ApJL, 628, L89
Bolatto, A. D., Wolfire, M., & Leroy, A. K. 2013, ARA&A, 51, 207
Carilli, C. L., & Rawlings, S. 2004, New Astronomy Reviews, 48, 979
Carilli, C. L., Solomon, P., Vanden Bout, P., et al. 2005, ApJ, 618, 586
Carilli, C. L., Neri, R., Wang, R., et al. 2007, ApJL, 666, L9
Carilli, C. L., & Walter, F. 2013, ARA&A, 51, 105
Carilli, C. L., Riechers, D., Walter, F., et al. 2013, ApJ, 763, 120
Chary, R.-R., Stern, D., & Eisenhardt, P. 2005, ApJL, 635, L5
da Cunha, E., Walter, F., Decarli, R., et al. 2013a, ApJ, 765, 9
da Cunha, E., Groves, B., Walter, F., et al. 2013b, ApJ, 766, 13

PoS (AASKA14) 161

Daddi, E., Dannerbauer, H., Elbaz, D., et al. 2008, ApJL, 673, L21
Daddi, E., Bournaud, F., Walter, F., et al. 2010, ApJ, 713, 686
Danielson, A. L. R., Swinbank, A. M., Smail, I., et al. 2011, MNRAS, 410, 1687
Dannerbauer, H., Daddi, E., Riechers, D. A., et al. 2009, ApJL, 698, L178
Decarli, R., Walter, F., Carilli, C., et al. 2014, ApJ, 782, 78
Di Francesco, J., Johnstone, D., Matthews, B. C., et al. 2013, arXiv:1310.1604
Downes, D., & Solomon, P. M. 1998, ApJ, 507, 615
Edmonds, R., Wagg, J., Momjian, E., et al. 2009, AJ, 137, 3293
Evans, N. J., II 1999, ARA&A, 37, 311
Gao, Y., & Solomon, P. M. 2004, ApJS, 152, 63
Gao, Y., Carilli, C. L., Solomon, P. M., & Vanden Bout, P. A. 2007, ApJL, 660, L93
García-Burillo, S., Graciá-Carpio, J., Guélin, M., et al. 2006, ApJL, 645, L17
Genzel, R., Tacconi, L. J., Combes, F., et al. 2012, ApJ, 746, 69
Impellizzeri, C. M. V., McKean, J. P., Castangia, P., et al. 2008, Nature, 456, 927
Ivison, R. J. 2006, MNRAS, 370, 495
Jarvis, M., Seymour, N., Afonso, J., et al., 2015, "The star-formation history of the Universe with the SKA", in Advancing Astrophysics with the SKA, PoS(AASKA14)068
Leroy, A. K., Bolatto, A., Bot, C., et al. 2009, ApJ, 702, 352
Maiolino, R., Cox, P., Caselli, P., et al. 2005, A&A, 440, L51
Morganti, R., Sadler, E.M., and Curran, S.J., 2015, "Cool Outflows and HI absorbers with the SKA", in Advancing Astrophysics with the SKA, PoS(AASKA14)134
Murphy, E.J., Sargent, M.T., Beswick, R.J., et al., 2015, "The Astrophysics of Star Formation Across Cosmic Time at >10 GHz with the Square Kilometre Array", in Advancing Astrophysics with the SKA, PoS(AASKA14)085
Narayanan, D., et al. 2012, MNRAS, 421, 3127
Obreschkow, D., Heywood, I., Klöckner, H.-R., & Rawlings, S. 2009, ApJ, 702, 1321
Obreschkow, D., Meyer, M., Popping, A., 2015, "The SKA as a Doorway to Angular Momentum", in Advancing Astrophysics with the SKA, PoS(AASKA14)138
Papadopoulos, P. P., Röttgering, H. J. A., van der Werf, P. P., et al. 2000, ApJ, 528, 626
Papadopoulos, P. P. 2007, ApJ, 656, 792
Prandoni, I., & Seymour, N., 2015, "Revealing the Physics and Evolution of Galaxies and Galaxy Clusters with SKA Continuum Surveys", in Advancing Astrophysics with the SKA, PoS(AASKA14)067
Riechers, D. A., Walter, F., Carilli, C. L., et al. 2006, ApJL, 645, L13
Riechers, D. A., Walter, F., Carilli, C. L., & Bertoldi, F. 2007, ApJL, 671, L13
Riechers, D. A., Bradford, C. M., Clements, D. L., et al. 2013, Nature, 496, 329
Riechers, D. A., Carilli, C. L., Capak, P. L., et al. 2014, arXiv:1404.7159
Santos, M., Bull, P., Alonso, D., et al., 2015, "Cosmology with a SKA HI intensity mapping survey" in Advancing Astrophysics with the SKA, PoS(AASKA14)019
Solomon, P., Vanden Bout, P., Carilli, C., & Guelin, M. 2003, Nature, 426, 636
Staveley-Smith, L., et al., 2015, "The Hydrogen Universe with the SKA" in Advancing Astrophysics with the SKA, PoS(AASKA14)167
Tacconi, L. J., Genzel, R., Neri, R., et al. 2010, Nature, 463, 781

PoS(AASKA14)161

Tacconi, L. J., Neri, R., Genzel, R., et al. 2013, ApJ, 768, 74
Vanden Bout, P. A., Solomon, P. M., & Maddalena, R. J. 2004, ApJL, 614, L97
Venemans, B. P., McMahon, R. G., Walter, F., et al. 2012, ApJL, 751, L25
Wagg, J., Wilner, D. J., Neri, R., Downes, D., & Wiklind, T. 2005, ApJL, 634, L13
Wagg, J., Kanekar, N., & Carilli, C. L. 2009a, ApJL, 697, L33
Wagg, J., & Momjian, E. 2009b, AJ, 138, 895
Wagg, J., Carilli, C. L., Wilner, D. J., et al. 2010, A&A, 519, L1
Wagg, J., Wiklind, T., Carilli, C. L., et al. 2012a, ApJL, 752, L30
Wagg, J., & Kanekar, N. 2012b, ApJL, 751, L24
Walter, F., Bertoldi, F., Carilli, C., et al. 2003, Nature, 424, 406
Walter, F., Carilli, C., Bertoldi, F., et al. 2004, ApJL, 615, L17
Walter, F., Decarli, R., Sargent, M., et al. 2014, ApJ, 782, 79
Wang, R., Carilli, C. L., Neri, R., et al. 2010, ApJ, 714, 699
Wang, R., Wagg, J., Carilli, C. L., et al. 2013, ApJ, 773, 44
Weiß, A., Downes, D., Neri, R., et al. 2007, A&A, 467, 955
Willott, C. J., Omont, A., & Bergeron, J. 2013, ApJ, 770, 13
Wilner, D. J., Bourke, T. L., Ho, P. T. P., Killeen, N. E. B., & Calabretta, M. 1999, AJ, 117, 1139
Wu, J., Evans, N. J., II, Gao, Y., et al. 2005, ApJL, 635, L173

PoS(AASKA14)161

PROCEEDINGS OF SCIENCE

Enhancing Science from Future Space Missions and Planetary Radar with the SKA

Dayton L. Jones[1], **Joseph Lazio**[1]

[1] *Jet Propulsion Laboratory, California Institute of Technology*

E-mail: dayton.jones at jpl.nasa.gov

Both Phase 1 of the Square Kilometre Array (SKA1) and the full SKA have the potential to dramatically increase the science return from future astrophysics, heliophysics, and especially planetary missions, primarily due to the greater sensitivity (A_{EFF} / T_{SYS}) compared with existing or planned spacecraft tracking facilities. While this is not traditional radio astronomy, it is an opportunity for productive synergy between the large investment in the SKA and the even larger investments in space missions to maximize the total scientific value returned to society. Specific applications include short-term increases in downlink data rate during critical mission phases or spacecraft emergencies, enabling new mission concepts based on small probes with low power and small antennas, high precision angular tracking via VLBI phase referencing using in-beam calibrators, and greater range and signal/noise ratio for bi-static planetary radar observations. Future use of higher frequencies (e.g., 32 GHz and optical) for spacecraft communications will not eliminate the need for high sensitivities at lower frequencies. Many atmospheric probes and any spacecraft using low gain antennas require frequencies below a few GHz.

The SKA1 baseline design covers VHF/UHF frequencies appropriate for some planetary atmospheric probes (band 1) as well as the standard 2.3 GHz deep space downlink frequency allocation (band 3). SKA1-MID also covers the most widely used deep space downlink allocation at 8.4 GHz (band 5). Even a 50% deployment of SKA1-MID will still result in a factor of several increase in sensitivity compared to the current 70-m Deep Space Network tracking antennas, along with an advantageous geographic location. The assumptions of a 10X increase in sensitivity and 20X increase in angular resolution for SKA result in a truly unique and spectacular future spacecraft tracking capability.

Advancing Astrophysics with the Square Kilometre Array
June 8-13, 2014
Giardini Naxos, Sicily, Italy

PoS(AASKA14)154

1. Introduction

Ever since the dramatic increase in sensitivity afforded by the SKA was widely recognized, it has been clear that, in addition to the multitude of astronomical applications described in this book, such capability could provide valuable benefits in other fields as well. One example is enhancing the science return from planetary exploration missions. The sensitivity of SKA will greatly exceed that of any existing or planned dedicated spacecraft tracking facility. This suggests the possibility of inter-agency collaborations that help both the radio astronomy and space science communities to make the most productive use of their major investments.

2. Telemetry Reception

The most obvious use of increased sensitivity in the context of scientific space missions is a potentially large increase in downlink data rate, particularly from distant spacecraft. Previous examples of this include the use of Parkes and the VLA to receive telemetry during the Voyager flybys of Uranus and Neptune (Brown et al. 1986; Ulvestad et al. 1988; Brown et al. 1990). This can be utilized to support faster data return during short-duration, high priority events or to increase the total data return through periodic tracking of longer duration missions. In both cases, higher ground antenna sensitivity will help reduce the mismatch between the very high data rates produced by current and future flight instruments and the more limited data rates that can be supported by dedicated spacecraft tracking antennas. This generic problem, and the importance of downlink data rate in terms in observational capabilities, is illustrated in Figure 1. It should be noted that investments to improve the sensitivity of telemetry reception antennas on the ground benefit all future space missions, while investments to improve the transmitter power or antenna size on a spacecraft benefit only a specific mission. Thus, maximizing the available sensitivity of ground tracking antennas through shared use of SKA is the more cost-effective approach to increasing the total science return from future missions, and thereby maximizing the scientific value of these expensive programs.

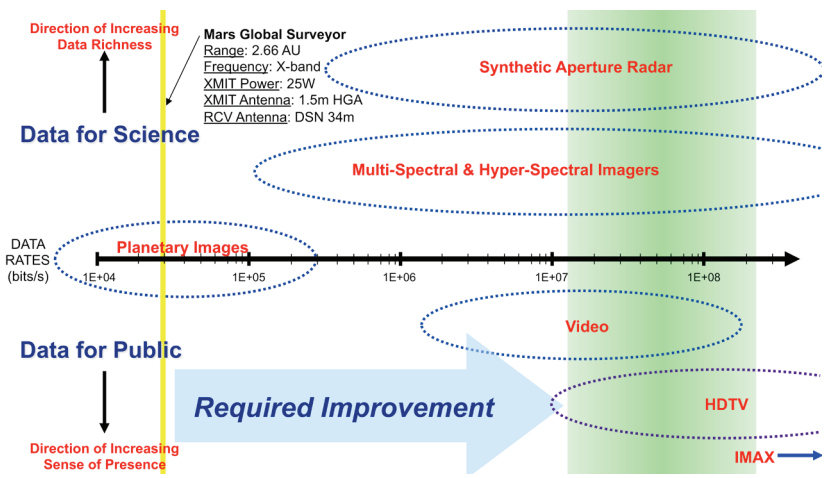

Figure 1: Different types of observation possible with different data rates. The Voyager data rates were $\sim$ 10 kb/s, while observing other planets as we do Earth requires data rates $>$ 10 Mb/s.

PoS(AASKA14)154

2.1 Small Probes

Small probes of planetary atmospheres and surfaces tend to have low power, low-gain antennas, and often very limited lifetimes. A few specific examples are Venus surface probes, probes of the inner solar corona, icy moon surface probes, clusters of probes descending into gas giant atmospheres, networks of small surface probes, atmospheric balloons/gliders/aircraft, boats on Titan lakes, and probes in extreme radiation environments. For most of these concepts optical communication is not an option because accurate pointing is not possible or because of atmospheric absorption. Consequently it can be challenging to obtain the desired quantity of data from such probes.

A common feature of all mission concepts of this type is the need to get data from the probes as rapidly as possible, before they die. In the past this has been done by transmitting data from a probe to a relatively nearby (and much larger) orbiting or flyby spacecraft, which then relays the data to Earth over a high-bandwidth downlink. This operational approach has been done successfully several times in the past (e.g., the Galileo and Cassini/Huygens missions), but always at the cost of increased mission risk and complexity. In addition, the fuel required to put a data relay spacecraft into orbit about the target solar system body can be a significant fraction of the total spacecraft mass, and thus a significant cost driver.

The SKA will allow some future small probe missions to downlink data directly to Earth, avoiding the need for a local relay spacecraft. As an example, Figure 2 shows the direct-to-Earth data rates that could be obtained from a probe with a 25 W transmitter (similar to the Huygens probe to the surface of Titan) and a low gain (4 dBi) antenna. The Huygens probe transmitted data at 8 kb/s, but only to the nearby Cassini orbiter. Huygens telemetry could not be received directly on Earth, although the carrier signal was detected. Figure 2 incorporates some optimistic assumptions, but still illustrates the large improvement possible in the SKA era. This improvement could enable entirely new classes of missions involving large numbers of small probes transmitting simultaneously.

A somewhat more extreme example is show in Figure 3, which is based on a probe with a very

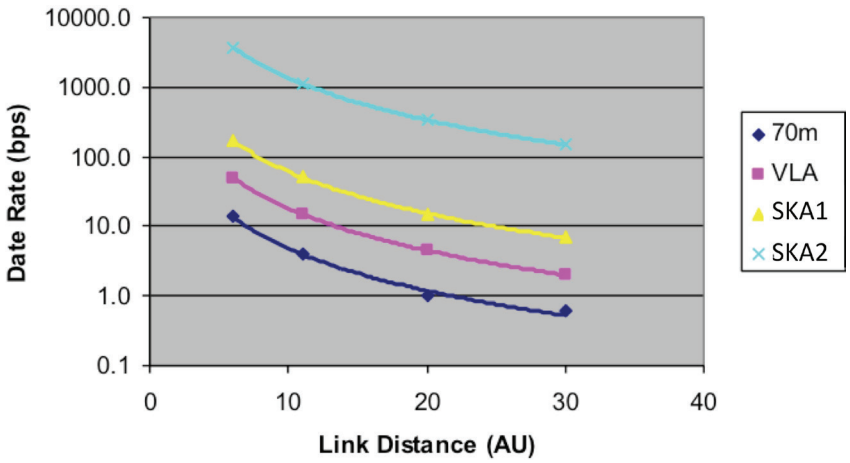

Figure 2: Predicted data rates to Earth as a function of distance for several ground arrays. These data rates are for a Huygens-like probe with a 25 W transmitter and 4 dBi gain antenna.

PoS (AASKA14) 154

low power (5 W) transmitter. Even in this case the SKA allows small but useful data rates to Earth even from the outer planets.

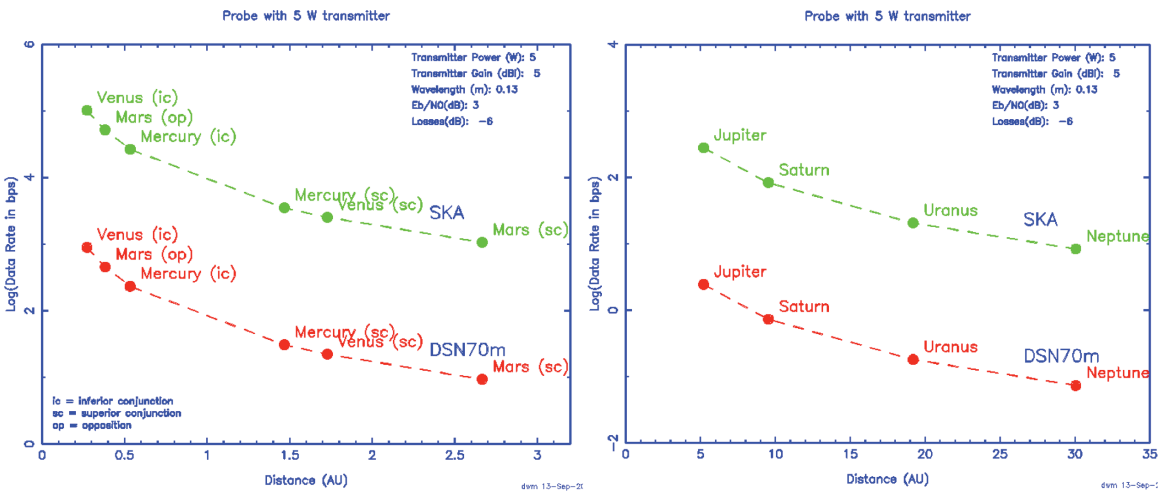

Figure 3: Data rates to Earth as a function of distance for the inner planets (left panel) and outer planets (right panel). In the left panel, ic = inferior conjunction, sc = superior conjunction, and op = opposition, the minimum and maximum distances from Earth for each planet. The curves in both panels assume a 5 W transmitter and low gain antenna at 2.3 GHz.

Table 1 shows similar information in a more quantitative format. The differences in data rates are large enough to make direct-to-Earth downlink for small probe missions viable in many cases where they would not be viable without use of the SKA.

Telemetry from	DSN 70-m	SKA
Venus (0.3 AU)	11 kb/s	1.3 Mb/s
Venus (2.4 AU)	180 b/s	21 kb/s
Mars (0.6 AU)	2.9 kb/s	340 kb/s
Mars (2.6 AU)	150 b/s	17 kb/s
Jupiter	35 b/s	4.1 kb/s
Saturn	10 b/s	1.1 kb/s
Uranus	3 b/s	330 b/s
Neptune	1 b/s	130 b/s

Of course larger spacecraft could benefit in the same way, especially those at extreme distances from Earth such as future interstellar probe missions (e.g., Wallace et al. 2000; McNutt et al. 2002).

2.2 Spacecraft Emergencies

One of the standard components of a safe-mode response to unexpected events or errors on spacecraft is to switch to a low-gain antenna for Earth communication. This procedure is used because, in an emergency, one cannot assume that the spacecraft will retain the ability to point a high gain antenna at Earth. Switching from a high gain antenna to a low gain spacecraft antenna can

PoS(AASKA14)154

reduce the received signal level by up to several orders of magnitude. In order to compensate for this the transmitted data rate must be reduced to very low levels, often only a few hundred or even tens of bits per second. But during a spacecraft emergency there is a great need for engineering data as rapidly and with as much detail as possible to allow problems to be diagnosed before the situation becomes unsalvageable. Use of the SKA, with its unequaled sensitivity, would substantially improve the chances of recovering at least one expensive mission during the SKA's planned lifetime.

2.3 Observing Duty Cycle

The SKA will be built as an astronomical research facility, and its use for spacecraft tracking support will necessarily need to be limited. Many situations that most benefit from higher ground antenna sensitivity are intrinsically of short duration, and can usually be scheduled to allow visibility from a particular site on Earth. Such situations include planetary atmospheric entry and landing phases, short-lived small probes, occultations of spacecraft signals, or bi-static planetary radar experiments. Consequently an operational scenario involving infrequent but high priority observations should be viable.

3. Radio Science

Precise tracking of the characteristics of signals from spacecraft has enabled study of the properties of solar system bodies, including their rings, atmospheres, and interiors; has advanced our understanding of the solar wind; and has provided limits on gravitational waves at frequencies complementary to those that will be probed by the SKA Pulsar Timing Array (Asmar et al. 2005; Tellmann et al. 2009). In many cases, particularly occultations and other dynamic events near solar system bodies or in studying the solar wind, increasing the integration time to obtain a high signal-to-noise ratio is not an option. Only high instantaneous sensitivity can provide the requisite signal-to-noise ratio. For short-duration radio science measurements, SKA1-MID would enhance, or even enable, observations through its increase in A_{EFF} / T_{SYS} over current spacecraft tracking facilities.

4. Tracking and Navigation

Interplanetary spacecraft navigation is an essential component of all planetary science missions. The accuracy with which spacecraft trajectories can be predicted determines the viability of some mission concepts, and can have a large influence on the mass of fuel that must be carried. Spacecraft tracking and navigation relies on an accurate planetary ephemeris, and three types of observational data: Doppler (one-way or multi-way), range, and very long baseline interferometry (VLBI). Together these provide the three position and three velocity values that define spacecraft motion. Range provides the radial (line-of-sight) component of position, Doppler the radial component of velocity, and VLBI the two plane-of-sky components of position and velocity. In general Doppler and range measurements can be made with narrow bandwidths, and are less likely to need the higher sensitivity offered by SKA. VLBI, on the other hand, is often sensitivity limited and would greatly benefit from use of the SKA.

PoS(AASKA14)154

Most VLBI spacecraft tracking is currently done with single baselines using group delays (delta differential one-way ranging or ΔDOR in the spacecraft tracking community). Narrow signals widely separated in frequency are broadcast from the spacecraft, and the observed phase slope between these signals gives the group delay on the baseline between antennas. This works well for single baselines because phase cycle ambiguities are much easier to resolve for group delays, but the phase delay is an intrinsically more accurate observable. A multi-baseline VLBI array using phase referencing to an angularly nearby position calibration source can measure spacecraft positions with higher accuracy (e.g., Jones et al. 2011).

Neither SKA1-MID nor SKA1-SUR provide long baselines for VLBI, but it should be possible to use the long and sensitive baseline between South Africa and Australia for astrometry at overlapping frequencies (see Figure 4). For astrometry of spacecraft, the overlapping frequency range must include band 3 (see section 6 for more details on relevant frequency bands). A sufficiently sensitive single baseline can measure phase delays with respect to a compact calibration source if the angular distance between the calibration source and the spacecraft is close enough that the phase ambiguities can be resolved (e.g., Gabor 2011), and the baseline between South Africa and Australia arrays should be sensitive enough to allow this. The large field of view provided by small antenna diameters helps greatly here because it increases the probability of having a suitable phase calibration source within the field of view. Having an in-beam calibrator avoids errors associated time interpolation of phases between two pointing positions, and also allows VLBI to occur simultaneously with telemetry reception. The still larger field of view of SKA1-SUR could be combined with sub-arraying of the SKA1-MID antennas.

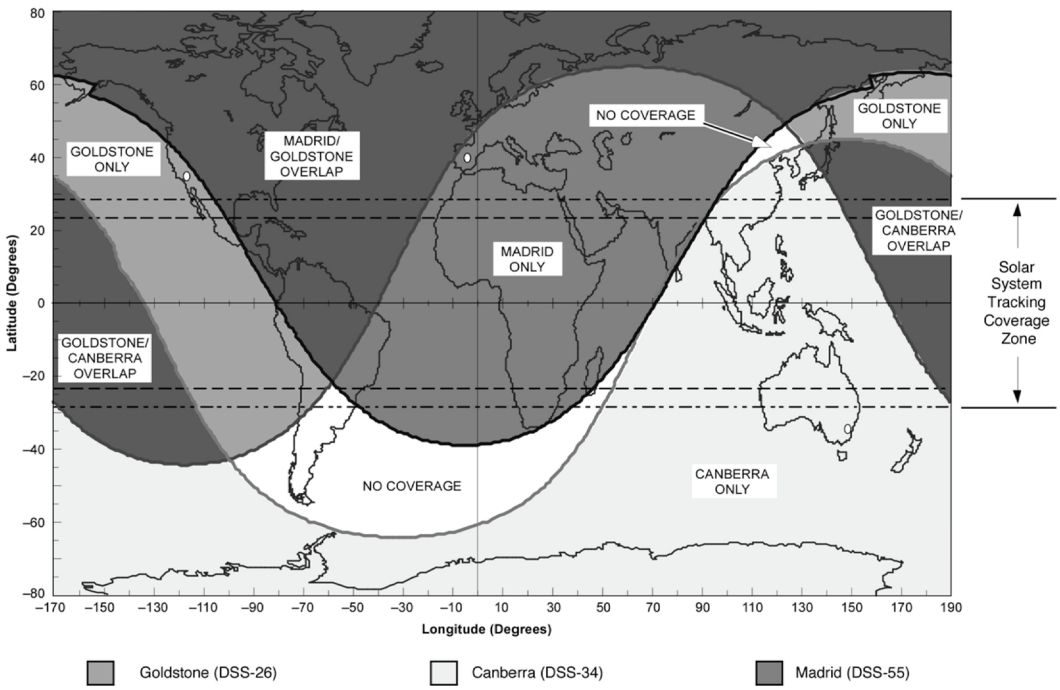

Figure 4: The darkest shaded areas show where VLBI coverage is possible between DSN sites. Lighter shaded areas show where there is visibility from only a single DSN site and VLBI tracking by the DSN is not possible. Most deep space tracking occurs within 30 degrees of the equator (Sniffin 2012).

PoS(AASKA14)154

Figure 4 shows the regions of mutual sky visibility between the three sites of the NASA Deep Space Network (DSN). Note the large area around Australia and Africa where there is no VLBI coverage possible by the DSN, only visibility from a single DSN site or from no sites. Recently cooperative observations between the DSN and a European Space Agency tracking antenna in Argentina have filled in some of the VLBI coverage gaps, but with reduced sensitivity. SKA1-MID and SKA1-SUR would completely fill the gaps in coverage while providing higher sensitivity. The full SKA, of course, will provide multiple long, very high sensitivity baselines and consequently it will be possible to obtain high precision astrometric positions for spacecraft in near-real time. Most importantly, SKA will have calibration sources within its field of view at all times.

5. Planetary Radar

The signal-to-noise ratio for radar observations decreases as distance to the fourth power, and with radar cross-section. A large increase in antenna sensitivity would increase the range and decrease the size of solar system object that could be detected, enhance the quality of polarization measurements and orbital solutions, and improve the resolution of radar imaging (Butler et al. 2004; De Pater 1999).

5.1 Range and Orbit Determination

One of the most important results from planetary radar is highly accurate orbit determinations for near-Earth objects (asteroids and comets). Especially when an asteroid is detected only a short time before closest approach to Earth, the orbit uncertainty from optical astrometry can be large. A single set of radar range and Doppler measurements can reduce this uncertainty by up to three orders of magnitude (Ostro and Giorgini 2004), allowing much better predictions of potential impact hazard and more reliable recovery of the object on subsequent approaches to Earth (see Figure 5).

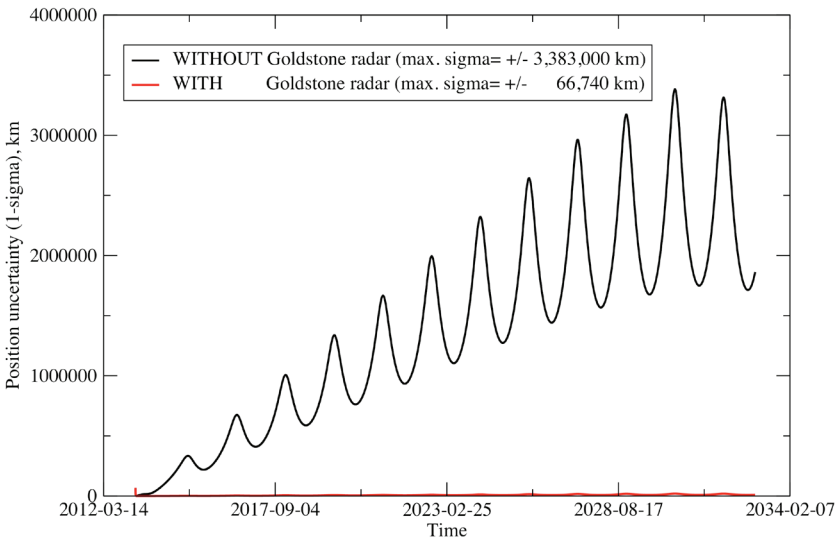

Figure 5: Example of asteroid orbit uncertainty (Asteroid 2013 FB8, gravity dynamics only). Note that the red line showing the uncertainty after a single epoch of radar range and Doppler measurements is nearly invisible along the bottom axis.

PoS(AASKA14)154

5.2 Imaging

In addition to the detection and tracking of near-earth objects, radar can be used to image the shape and surface features of these objects (see Figure 6). More generally, radar has been used to improve the planetary ephemeris through high accuracy range measurements to solar system bodies, and to study the surface properties of Venus, Mercury, the Galilean moons of Jupiter, and Titan, among other targets. Imaging observations of asteroids help define the orientation of their rotation axes, an important component of orbit modeling. All radar imaging observations would benefit from an increase in ground antenna sensitivity, even if only on the receive end of bi-static experiments.

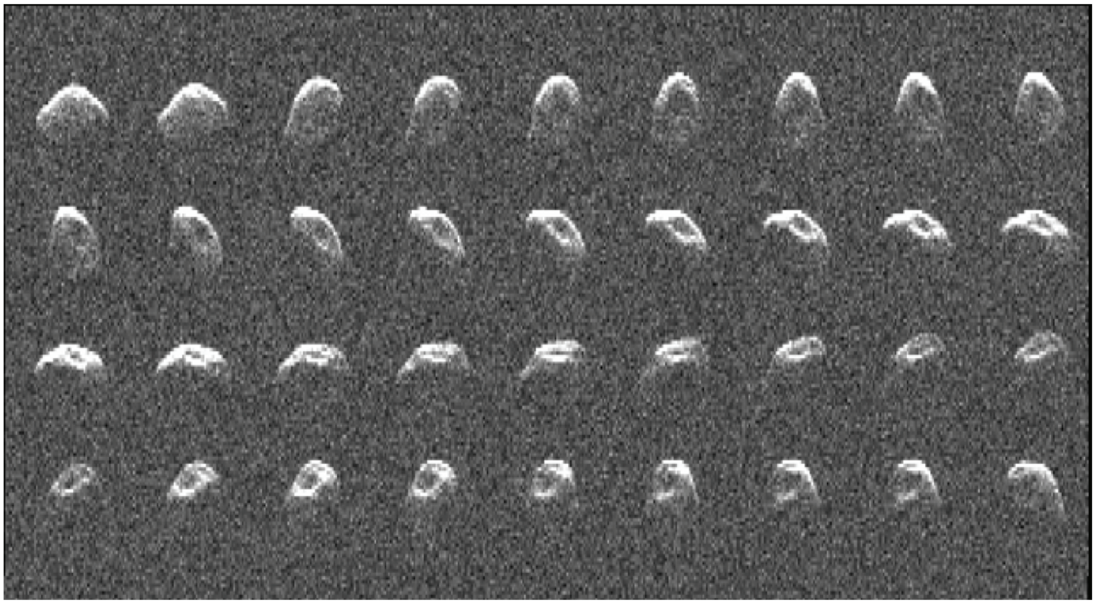

Figure 6: Planetary radar images of asteroid 2010 JL33 (NASA/JPL-Caltech).

As an example, the current Arecibo planetary radar system is able to detect Titan with an SNR approaching 100 at 2.4 GHz. Using the full SKA in a bi-static radar observation with Arecibo would increase the SNR to $\sim$1000, and a bi-static observation with the Goldstone planetary radar at 8.4 GHz would give an SNR $\sim$10,000. This is high enough to allow the multiple long SKA baselines to provide detailed images of the disk with a spatial resolution less than 100 km. It also implies that Neptune's moon Triton and even Pluto could be detected with SNR $\sim$ 10-20, adequate for studies of the bulk properties of their surfaces.

6. Summary of SKA1-MID Requirements

The primary requirement for SKA telemetry reception or tracking of science missions is receiver coverage of the allocated space-to-Earth downlink bands. For deep space missions the frequency allocations are near 2300, 8400, and 32000 MHz. The first two of these fall near the centers of receiver band 3 (1650-3050 MHz) and band 5 (4600-13800 MHz), respectively (Dewdney et al. 2013). Band 3 of SKA1-SUR also covers the 2.3 GHz downlink band. In some circumstances

PoS(AASKA14)154

it is necessary to use UHF frequencies for data from probes, and in those cases receiver band 1 (350-1050 MHz) of SKA1-MID will be appropriate.

Telemetry reception and spacecraft tracking require beamforming rather than cross-correlation of signals from the array antennas (see Figure 7). The cost of beamforming scales linearly with the number of antennas N, compared to the N^2 cost scaling of cross-correlation. In addition, spacecraft signals occupy relatively narrow bandwidths and signal processing costs scale linearly with bandwidth as well. Only a single telemetry receiver (labeled Integrated Demodulator in Figure 7) is required independent of the number of antennas in the array. JPL has developed portable telemetry receivers that are designed to be used at non-DSN sites.

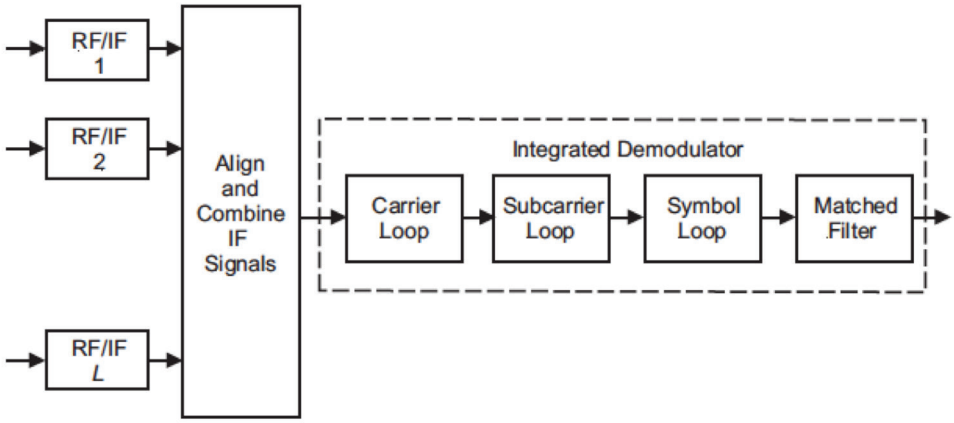

Figure 7: Typical telemetry receiver architecture for an array (Rogstad et al. 2003). Signal combining is done with the same type of beamformer used for SKA pulsar observations. The subsystem within the dashed lines would be provided by individual space missions.

Although SKA will eventually cover the primary 2.3 GHz and 8.4 GHz downlink frequency bands, it is also interesting to speculate on the possibility of a future generation of high frequency receivers extending coverage up to the 32 GHz downlink band. This band has a wider bandwidth allocation for space missions than the lower frequency bands, and will be more heavily used by future missions. Since the SKA1-MID and SKA1-SUR antennas are designed to work well up to at least 20 GHz, it is quite possible that they will still have usable efficiency at 32 GHz. Even an aperture efficiency of 10% would provide a higher sensitivity than existing DSN 34-m antennas at 32 GHz. Antenna blind pointing accuracy is often more of a limitation than surface accuracy in determining the high frequency limit of a radio antenna, but this is less of a concern when there is a spacecraft signal that can be used to derive real-time pointing corrections. Thus, it is plausible that SKA could eventually receive all three of the deep space downlink frequency bands, thereby enabling tracking and telemetry reception support for future science missions to any target from any space agency.

This work was carried out at the Jet Propulsion Laboratory, California Institute of Technology, under contract with the US National Aeronautics and Space Administration. We thank D. S. Abraham and R. A. Preston at JPL for providing Figure 1, D. W. Murphy at JPL for producing Figures 2 and 3, and J. D. Girogini at JPL for Figure 5.

PoS(AASKA14)154

REFERENCES

Asmar, S.W., Armstrong, J. W., Iess, L., and Tortora, P., 2005, "Spacecraft Doppler tracking: Noise budget and accuracy achievable in precision radio science observations", Radio Science, 40, RS2001, doi:10.1029/2004RS003101.

Brown, D. W., Cooper, H. W., Armstrong, J. W., Kent, S. S., 1986, "Parkes-CDSCC Telemetry Array: Equipment Design", TDA Progress Report (JPL), 42-85.

Brown, D. W., Brundage, W. D., Ulvestad, J. S., Kent, S. S., Bartos, K. P., 1990, "Interagency Telemetry Arraying for Voyager-Neptune Encounter", TDA Progress Report (JPL), 42-102.

Butler, B. J., Campbell, D. B., de Pater, I., and Gary, D. E., 2004, "Solar system science with SKA", New Astronomy Reviews, 48, 1511-1535.

De Pater, I., 1999, "Solar System Studies with SKA", in Perspectives on Radio Astronomy - Science with Large Antenna Arrays, van Haarlem, M.P. (Ed.), Netherlands Foundation for Research in Astronomy, p. 333.

Dewdney, P. E, Turner, W., Millenaar, R., McCool, R., Lazio, J., and Cornwell, T., 2013, "SKA1 System Baseline Design", Document number SKA-TEL-SKO-DD-001 Revision 1, SKA Organisation

Jones, D. L., Fomalont, E., Dhawan, V., Romney, J., Folkner, W. M., Lanyi, G., Border, J., and Jacobson, R. A., 2011, "VLBA Astrometric Observations of the Cassini Spacecraft at Saturn", Astronomical Journal, 141, 29-38.

McNutt, R. L., Andrews, G. B., Gold, R. E., Santo, A. G., Bokulic, R. S., Boone, B. G., Haley, D. R., McAdams, J. V., Feaeman, M. E., Williams, B. D., Boyle, M. P., Lester, D., Lyman, R., Ewing, M., Krishnan, R., Read, D., Naes, L., McPherson, M., and Deters, R., 2002, "Interstellar Explorer", presented at the First International ASI Workshop on Futuristic Space Technologies (Session: Beyond 2025), Trieste, Italy, May 2002.

Ostro, S. J., and Giorgini, J. D., 2004, "The role of radar in predicting and preventing asteroid and comet collisions with Earth", ch. 3 in Mitigation of Hazardous Comets and Asteroids, ed. M. J. S. Belton, T. H. Morgan, N. H. Samarasinah, and D. K. Yeomans (Cambridge Univ. Press).

Rogstad, D. H., Mileant, A., Pham, T. T., 2003, "Arraying Techniques", ch. 6 in Antenna Arraying Techniques in the Deep Space Network, Yuen, J. H., (Ed.), Monograph 5, Deep Space Communications and Navigation Series, JPL Publication 03-001, p. 45.

Sniffin, R. W., 2012, "Coverage and Geometry", DSN Document 810-005 301, Rev. H, p. 27.

Tellmann, S., Patzold, M., Hausler, B., Bird, M. K., and Tyler, G. L., 2009, "Structure fn the Venus neutral atmosphere as observed by the Radio Science experiment VeRa on Venus Express", Journal of Geophysical Research, 114, E00B36, doi:10.1029/2008JE003204.

Ulvestad, J. S., 1988, "Phasing the Antennas of the Very Large Array for Reception of Telemetry from Voyager 2 at Neptune Encounter", TDA Progress Report (JPL), 257, 42-94.

Wallace, R. A., Ayon, J. A., and Sprague, G. A., 2000, "Interstellar Probe mission/system concept", in Proc. 2000 IEEE Aerospace Conference, Big Sky, MT.

PoS(AASKA14)154

PROCEEDINGS OF SCIENCE

Delivering SKA Science

P.J. Quinn[1,2], T. Axelrod[3], I. Bird[4], R. Dodson[2], A. Szalay[5], A. Wicenec[2]
[2]International Centre for Radio Astronomy Research (ICRAR), [3]LSST Project, [4]LHC Computing Grid Project, CERN, [5]Institute for Data Intensive Science, Johns Hopkins University
E-mail: peter.quinn@icrar.org

The SKA will be capable of producing a stream of science data products that are Exa-scale in terms of their storage and processing requirements. This Google-scale enterprise is attracting considerable international interest and excitement from within the industrial and academic communities. In this chapter we examine the data flow, storage and processing requirements of a number of key SKA survey science projects to be executed on the baseline SKA1 configuration. Based on a set of conservative assumptions about trends for HPC and storage costs, and the data flow process within the SKA Observatory, it is apparent that survey projects of the scale proposed will potentially drive construction and operations costs beyond the current anticipated SKA1 budget. This implies a sharing of the resources and costs to deliver SKA science between the community and what is contained within the SKA Observatory. A similar situation was apparent to the designers of the LHC more than 10 years ago. We propose that it is time for the SKA project and community to consider the effort and process needed to design and implement a distributed SKA science data system that leans on the lessons of other projects and looks to recent developments in Cloud technologies to ensure an affordable, effective and global achievement of SKA science goals.

Advancing Astrophysics with the Square Kilometre Array
June 8-13, 2014
Giardini Naxos, Italy

[1] Speaker

PoS(AASKA14)147

1. Introduction

Over the past 20 years, the concept of what constitutes an observatory has grown to combine three central elements – the collectors, the detectors and the data. The delivery of data to astronomers in a form and variety that enables and accelerates the research process has become part of the fabric of new facilities in an attempt to achieve a maximal scientific return on an ever increase commitment of public funds. The capture and delivery of data of the right type, with the right quality, at the right time and with the right volume is a complex dance between collectors, detectors, those responsible for a facility and astronomers responsible for doing and communicating science. This complex network of relationships and resources needs to be identified, costed, prioritized and addressed as part of designing and building the SKA facility. The data and processing systems that enable SKA science (collectively called SKA-Data) should be regarded at the same level of scientific importance, visibility and criticality as the collectors/detectors known as SKA-LOW, SKA-MID and SKA-SUR. The ultimate scientific impact of SKA will be determined by the way in which we assign priorities and resources to all four of these elements of the SKA, recognizing that SKA-data supports all three collecting/detecting systems.

SKA is being showcased internationally as an Exa-scale computing project and considerable excitement and expectation is being generated in the scientific and industrial community by the associated technological and discovery opportunities. Today we know that Exa-scale enterprises require Google-like resources and we need to understand how astronomy will scale to, and afford, challenges of this magnitude. In this chapter we will examine the SKA-data requirements as determined by the set of SKA Key Science Projects. The existing SKA Phase 1 baseline design coupled with HI survey requirements already implies data volumes of processed and accumulated products for a single survey to be in excess of 1 ExB. We will discuss the projected costs and challenges for the production and delivery of SKA science products. This analysis will draw upon the experience gained across a number of major research efforts (Sloan Digital Sky Survey, Large Hadron Collider and the Large Synoptic Survey Telescope). We will draw attention to choices that may need to be made on the scope and capabilities of SKA-data and what those choices may imply for funding sources and operational models. Finally we will outline technological trends and innovations that may create new opportunities to do science with the SKA and which could change the design approach we take to SKA-data within this decade.

2. SKA Data Requirement

We begin our assessment of the scale of SKA's data requirements with an analysis of the data production for SKA1 based on a set of Key Science Projects (KSP, Lazio, 2011). For the 3 component arrays, SKA-LOW, SKA-MID and SKA-SUR, we take the following global parameters from the baseline design plus the addendum:

PoS(AASKA14)147

	SKA-LOW	SKA-MID	SKA-SUR
Nant	1024	254	96
Bmax (km)	100	200	50
Dstation (m)	35	15	15
BWmax(MHz)	250	1024	500
Nbeams	1	1	36

Table 1: Assumed baseline design parameters

For each KSP, the fiducial frequency is calculated based on the maximum and minimum frequency requested. This calculation produces figures that are reasonably close to the fiducial frequencies used in the baseline design. The figures are then used to calculate the sampling times and channel widths for the array to prevent temporal or bandwidth smearing. Oversampling factors for the time, frequency and images are ε_τ 11.2, ε_ν 8 and ε_{image} 4, respectively. The bytes per sample for the raw data, the visibilities and images are B_{raw} 1, B_{vis} 8 and B_{image} 4, respectively. Dual polarisations are recorded in all cases. The antennas are assumed to be distributed following the configurations proposed in the baseline design. This configuration affects the possible gains from the differential averaging based on baseline lengths. Based on these inputs, we have settled on averaging factors of 14.7, 13.8 and 4.81 for SKA-LOW, SKA-MID and SKA-SUR respectively. We assume in all cases that 6 hours of data is used for each image and that projects all receive 1 kHr for the SKA-LOW observations and 10 kHr for the SKA-MID and SKA-SUR observations in order to produce comparable results. Where only postage-stamps are required we have retained 100 pixels (or 25 resolution samples) around the target in the two on-sky dimensions and 1000 channels in velocity. Where only the continuum data is required the number of channels is reduced to 1000, to allow recovery of Rotation Measures. In the baseline design there is a limit of 2^{18} for the number of channels that can be formed. Therefore for some of the cases with narrow velocity channel width requirements, we have limited the correlated bandwidth to that which can be supported. This affects the sensitivity that can be obtained in the given observing time. For the correlator output we have retained all 4 polarizations and then assigned polarization data to projects/products as required. We have studied 14 science cases, with the parameters guided by the SKA design reference mission (DRM) document (Lazio, 2011) in most cases.

2.1 SKA-LOW KSP

Probing the Neutral IGM: This is the EOR experiment in Chapter 2 of the DRM. Frequencies between 50 and 200 MHz (Fiducial Frequency 93MHz) are observed, with channel widths of 150 km/s (10kHz). The required resolution in the image cubes is 120" and only stokes I is retained. In this line case the number of correlator channels is actually set by the bandwidth smearing. 1kHr of observations spread over 2π steradians is expected to deliver a sensitivity of 10 mJy/channel.

PoS(AASKA14)147

Low Frequency Continuum: A generic all-sky continuum imaging experiment at low frequencies. Frequencies between 50 and 300 MHz (Fiducial Frequency 109MHz) are observed. The required resolution in the image cubes is 15" and all four stokes products are retained. 1kHr of observations spread over 2π steradians is expected to deliver a sensitivity of 1.8 μJy.
Probing EOR with the Lyman Forest: This is the EOR experiment in Chapter 4 of the DRM, which covers redshifts of 6 to 20. It is a spectral line, postage stamp, experiment to detect the Hα forest at low frequencies. Only one field per beam is expected, on average. Frequencies between 50 and 200 MHz (Fiducial Frequency 93MHz) are observed, with channel widths of 0.2 km/s (which limits the instantaneous bandwidth to be 9MHz). The required resolution in the image cubes is 10" and only stokes I is retained. 1kHr of observations spread over 2π steradians is expected to deliver a sensitivity of 0.6 mJy/channel.
HI Absorption: This is the DRM Chapter 3 KSP to track Galaxy Evolution over redshifts from 0 (1420MHz) to 6 (200MHz) by detecting the absorption line of HI against high red-shift galaxies. It will be a spectral line, postage stamp, experiment. Ten fields per beam are expected, on average. For SKA-LOW this will be at frequencies between 200 and 350 MHz (Fiducial Frequency 261 MHz), with channel widths of 1 km/s. The required resolution in the image cubes is 5" and all four stokes products are retained. 1kHr of observations spread over 2π steradians is expected to deliver a sensitivity of 0.3 mJy/channel.

2.2 SKA-MID KSP

Galaxy evolution from Nearby HI: The HI galaxy evolution and large scale structure experiment for redshifts between 0 and 0.1. Frequencies between 1290 and 1420 MHz (Fiducial Frequency 1353 MHz) are observed, with channel widths of 3.3 km/s. The required resolution in the image cubes is 3" and all four stokes products are retained. 10kHr of observations spread over 2π steradians is expected to deliver a sensitivity of 0.3 mJy/channel.
Band 3 Continuum: A generic continuum experiment on SKA-MID. Frequencies between 1650 and 3050 MHz (Fiducial Frequency 2208 MHz) are observed. The required resolution in the image cubes is 0.2" and all four stokes products are retained. 10kHr of observations spread over 2π steradians is expected to deliver a sensitivity of 3 μJy.
Pulsar Timing/VLBI: The KSP pulsar projects are discussed in DRM Chapter 5. Pulsar timing and VLBI are combined as both of these experiments require a number of pointed phased array beams from the correlator (that is the tied array mode) of the inner core. We have allowed for 10 phased beams. Frequencies between 1000 and 3050 MHz (Fiducial Frequency 2208 MHz) are observed, with the output being the time domain signal with two polarisations for VLBI or a filterbank signal with all four stokes products retained. The correlator requirements follow the usual relationships to the inputs but the data product is small. 10kHr of observations spread over 2π steradians would deliver a sensitivity of 0.9 μJy, but as this experiment would be targeted this estimate is not applicable.
Pulsar Search: For pulsar searching the targets are unknown and therefore pointed approaches are not suitable. The requirement is to produced phased array filterbank

PoS (AASKA14) 147

averages (10MHz and 100 nsec integrations) of the inner core, which cover a larger area of the sky. We have allowed for 100 phased beams. Note that the gains for integrating down to 100 nsec samples and 10MHz channels for a 1GHz bandwidth are minor compared to retaining the Nyquist sampled data. Frequencies between 1000 and 3050 MHz (Fiducial Frequency 1662 MHz) are observed. The correlator requirements follow the usual relationships to the inputs but the data product is small. 10kHr of observations spread evenly over 2π steradians is expected to deliver a sensitivity of 0.6 μJy.
HI Absorption: The KSP to track Galaxy Evolution over redshifts from 0 (1420MHz) to 6 (200MHz) by detecting the absorption line of HI against high red-shift galaxies. It will be a spectral line, postage stamp, experiment. Ten fields per beam are expected, on average. For SKA-MID this will be at frequencies between 350 and 1420 MHz (Fiducial Frequency 578 MHz), with channel widths of 1 km/s. The required resolution in the image cubes is 3" and all four stokes products are retained. 10kHr of observations spread over 2π steradians is expected to deliver a sensitivity of 0.2 mJy/channel.
Deep HI: We have included a deep HI experiment that would aim to directly detect all HI galaxies to much higher redshifts than those in the nearby survey. We have selected a redshift limit of ~1. Frequencies between 650 and 1420 MHz (Fiducial Frequency 937 MHz) are observed, with channel widths of 1 km/s. The required resolution in the image cubes is 3" and only stokes I is retained. 10kHr of observations spread over 200 sq. deg. is expected to deliver a sensitivity of 30 μJy/channel.

2.3 SKA-SUR KSP

Wide and Shallow HI: We have included a wide (all sky) and shallow (z<0.05) HI experiment such as would be ideal for the SKA-SUR. Frequencies between 1350 and 1420 MHz (Fiducial Frequency 1,384 MHz) are observed, with channel widths of 1 km/s. The required resolution in the image cubes is 10" and only stokes I is retained. 10kHr of observations spread over 2π steradians is expected to deliver a sensitivity of 0.3 mJy/channel.
Continuum: A generic all-sky continuum survey on SKA-SUR. Frequencies between 650 and 1670 MHz (Fiducial Frequency 1005MHz) are observed. The required resolution in the image cubes is 2" and all four stokes products are retained. 10kHr of observations spread over 2π steradians is expected to deliver a sensitivity of 2 μJy.
HI Absorption: The KSP to track Galaxy Evolution over redshifts from 0 (1420MHz) to 6 (200MHz) by detecting the absorption line of HI against high red-shift galaxies. It will be a spectral line, postage stamp, experiment. Ten fields per beam are expected, on average. For SKA-SUR this will be at frequencies between 650 and 1420 MHz (Fiducial Frequency 937 MHz), with channel widths of 1 km/s. The required resolution in the image cubes is 10" and all four stokes products are retained. 10kHr of observations spread over 2π steradians is expected to deliver a sensitivity of 0.6 mJy/channel.
Deep HI: We have included a SKA-SUR deep HI experiment that would aim to directly detect all HI galaxies to much higher redshifts than those in the nearby survey. Frequencies between 650 and 1420 MHz (Fiducial Frequency 937 MHz) are observed, with channel widths of 1 km/s. The required resolution in the image cubes is 10" and only stokes I is retained. 10kHr of observations spread over 200 sq. deg. is expected to deliver a sensitivity of 60 μJy/channel.

PoS (AASKA14) 147

2.4 The Data Products, Scaling and Processing Power Requirements

The correlator output data rate (both total and baseline averaged) and the accumulated total volume of science data has been computed for each of the 14 survey projects listed in section 2.3. The following table gives example results in Log10 of data product values in Bytes/s or Bytes.

Project	Cont	Cont Band 3	Cont	Neut IGM	Deep HI
Telescope	Low	Mid	Survey	Low	Survey
Corr. Out (B/s)	12.86	12.22	12.66	12.05	12.53
Av. Corr. Out (B/s)	10.52	10.24	11.3	10.88	11.85
Sci Image Tot (B)	15.17	15.99	18.66	13.37	18.45
Project	HI Abs	HI Abs	HI Abs	EOR Forest	HI Deep
Telescope	Low	Mid	Survey	Low	Mid
Corr. Out (B/s)	12.64	12.17	12.23	12.71	11.85
Av. Corr. Out (B/s)	11.48	11.03	11.54	11.54	10.71
Sci Image Tot (B)	12.73	13.73	15.28	11.33	16.78
Project	HI Nearby	HI Wide	Pulsar Time	Pulsar Search	
Telescope	Mid	Survey	Mid	Mid	
Corr. Out (B/s)	10.78	11.36	12.79	13.79	
Av. Corr. Out (B/s)	9.64	10.67	10.51	11.51	
Sci Image Tot (B)	13.73	16.04	13.07	18.93	

Table 2: KSP data rates (Bytes/sec) and volumes (Bytes) for the projects listed in 2.3

PoS(AASKA14)147

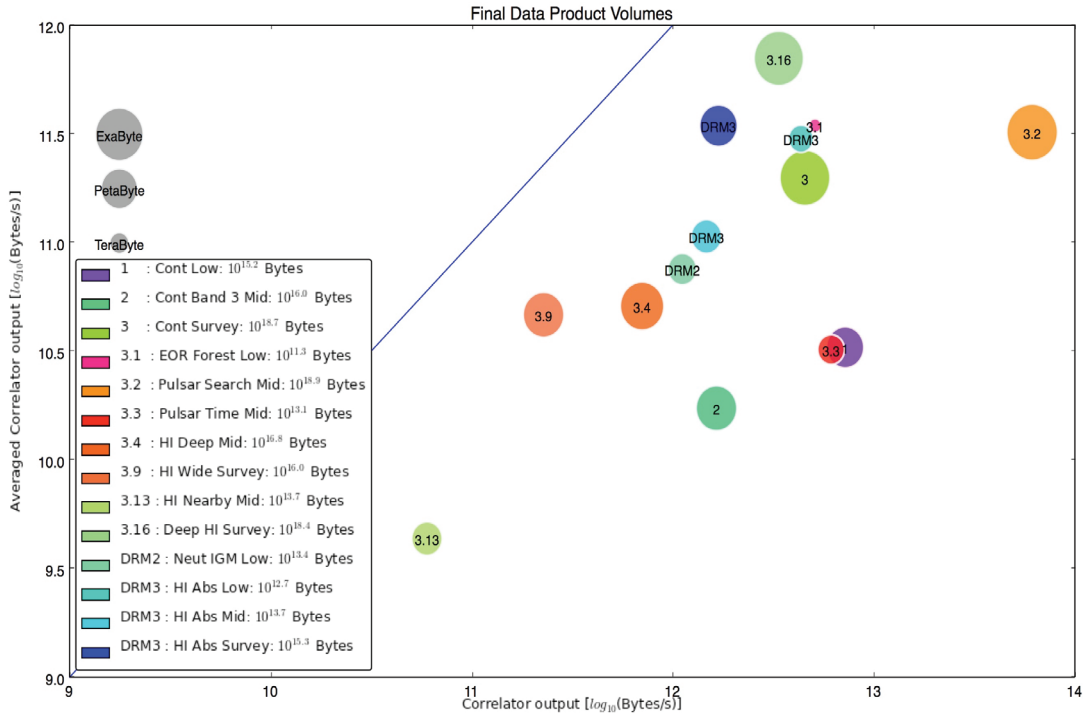

Figure 1: This diagram shows the optimally baseline Averaged Correlator Output (Level 3 Data) vs. the full, not averaged Correlator Output averaged to the longest baseline (both in Bytes/s) and the Final Data Product (Level 6 Data) volume (in Bytes) for 14 SKA1 KSPs. Note that all three parameters are plotted in Log10 units. The diameter of the circles is scaled by log10 of the total number of bytes of the science data products requested for those KSPs. The scale of the circles is indicated by the grey circles above the legend for Terabytes, Petabytes and Exabytes, respectively. The values are taken from the Table 2.

For the assumed exposure times and correlator buffer hold time (10^5 sec), the distribution of total exposure and data storage requirements for each array is given in Figure 2.

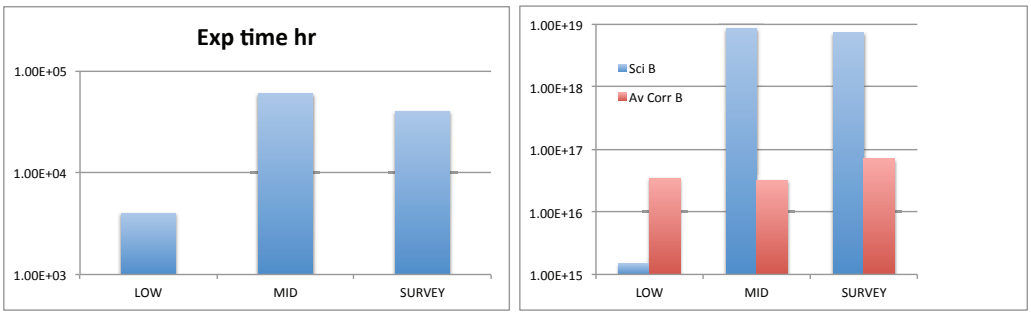

Figure 2: Total exposure time in Hours (left panel) and total science data volumes (Bytes) for the KPSs on the LOW, MID and SURVEY arrays. Correlator sizes referred to averaged outputs for the largest project on each array and 10^5 second hold times.

These results scale following simple relationships under the assumption of fixed maximum baseline length. Increasing the number of antennas increases the raw input by the same factor and the correlator output by that factor squared. It has no effect on the

PoS(AASKA14)147

science data product, given a fixed observation time, as the number of visibilities that form the image improves the sensitivity but not the size of that image. Increasing the observing time does not change the correlator inputs or outputs, but directly increases the size of the final data product by the same factor. Not included in this analysis, because of our starting assumptions, is that increasing the number of antennas and thereby increasing the instantaneous collecting area would reduce the required observing time by the same factor. This in turn would reduce the data product size. That is, if costs were dominated by storage factors, increasing the number of antennas reduces the overall storage costs, provided the science goals are not changed. These relationship are shown in Table 3. It is important to note that the cost of servicing a particular data rate or data volume can be switched between capital construction costs (size of storage facility) and operational costs (number of days of operations needed to deliver the KSP) depending on what observational parameters are held fixed.

Data	Exposure time fixed (**T**)	Number of Antenna fixed (**N**)	NT fixed: **NT=x**
Raw (B/s)	N^1	T^0	xT^{-1}
Corr (B/s)	N^2	T^0	x^2T^{-2}
Products	N^0	T^1	xN^{-1}

Table 3: The dependence of the Raw and Correlator data rates and the final data product size, on the number of antenna (N) and the exposure time (T) assuming fixed N, fixed T or fixed sensitivity measure (x) under ***the assumption of a fixed maximum baseline****. Green indicates a construction cost driver and red indicates an operations cost driver.*

Current radio astronomy calibration algorithms are iterative and thus require keeping all the data of an observation on a buffer storage and allowing for several reads over the whole data set. Given the estimated input data rates in the table above, this translates into several 100 PB storage buffers with a sustained random I/O speed of approximately 30 TB/s, for an observation duration of 12h.

The computational complexity (i.e. operations/Byte) in radio astronomy processing is typically fairly low and that does not fit well with current computing architectures. The expected number of real (delivered to applications) FLOPs required is of order 100 PetaFLOPs across all three telescopes. In addition, the efficiency of typical current day super-computers is optimised towards very high Linpack performance, but Radio Astronomy is dominated by FFTs and the efficiency is far lower. The average efficiency shown in Figure 3 below is just 6.9% (Wu, 2014). ***This means that we would need either super-computers, which are optimised for our compute tasks, or we would need super-computers with a Linpack performance (in FLOPS) about 10 times higher than our actual compute requirements***. The latter would imply much higher capital and operational (power) costs.

PoS (AASKA14) 147

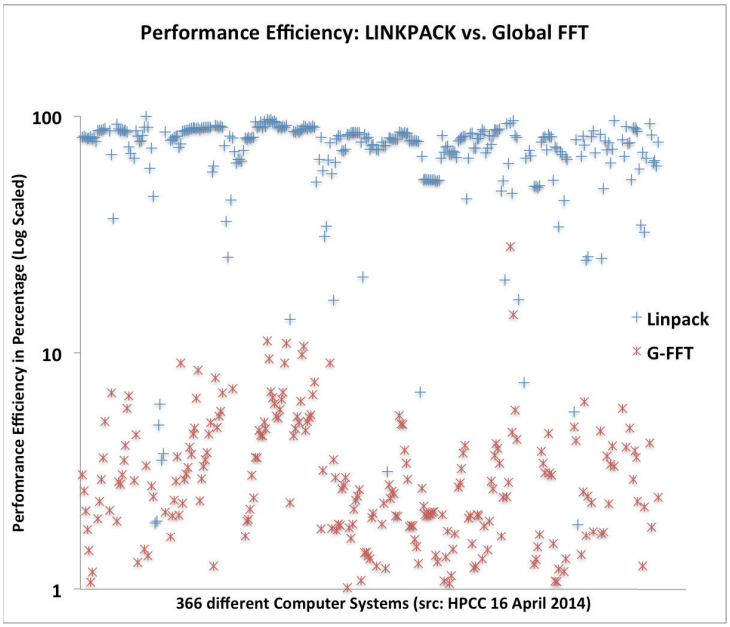

Figure 3: Performance efficiency of 366 different HPC systems. Blue crosses are Linpack, red stars are FFT. The average FFT efficiency is just 6.9%. [1]

3. SKA Data Flow – construction and operations

How will the SKA manage the flow of these data volumes through the Observatory? Where will the flow of data start and stop and what will be the resultant construction and operational consequences for the SKA project? Who has responsibility for the various processes and products involved in doing SKA science? In this section we will outline a likely model of the SKA Observatory data and process flow in order to identify the interfaces and processes that need to be scaled and costed for ExB astronomy. We will then analyse the scale of operational and construction requirements based on the data requirements of the SKA KSPs.

3.1 The SKA Observatory and Data Flow

The international SKA Organization (SKAO) is now working towards the creation of telescopes and observing facilities in Australia and South Africa as part of SKA Phase 1. With the SKAO headquarters at JBO, these facilities will form the SKA Observatory that will deliver a ground-breaking observational capabilities for global astronomy in the second decade of this century. Like many transformational observatories of the past, the SKA Observatory will consist of complementary capabilities in frequency and sky coverage that enable a range of survey and pointed programs to the depth afforded by the square kilometre aperture.

PoS(AASKA14)147

While the planning for the technical and scientific operations of the SKA is still to be finalized, the SKA Observatory will most probably execute processes and generate products that are similar to other successful international "public" observatories on the ground and in space. Over the past 20+ years, a similar science operational paradigm has been adopted by optical/IR (e.g. Hubble, VLT, Gemini, CFHT) and radio (e.g. ALMA) observatories as documented in the ongoing SPIE series on Observatory Operations (Ed. Quinn; 1998, 2000, 2002). Within this end-to-end paradigm, the Observatory takes responsibility to accept and adjudicate proposals, schedule resource, collect data, provide calibrations, exercise quality control and deliver data packages (see

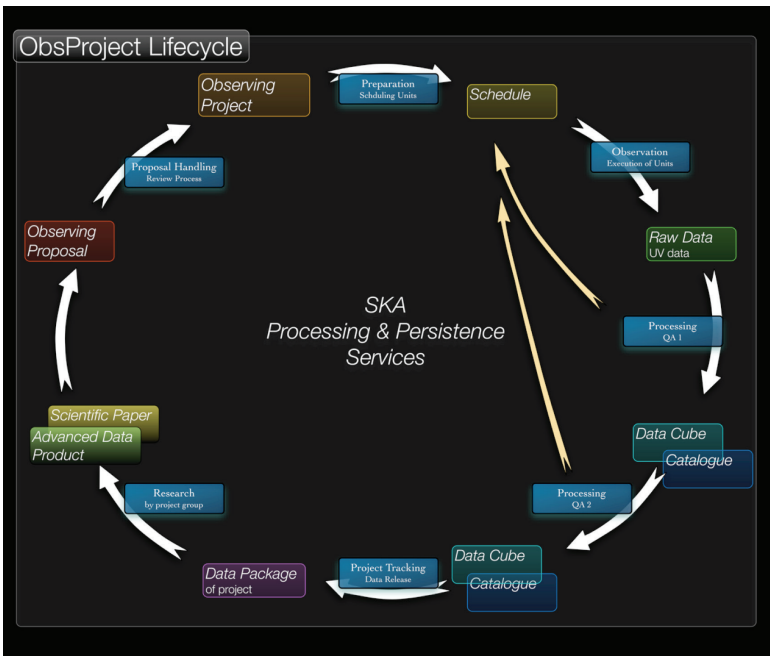

Figure 4).

Figure 4: Possible SKA end-to-end process and data flow (the "egg") based on similar systems implemented at ESO and elsewhere.

These delivered data packages could be rudimentary or advanced depending on the obligations and resources of the Observatory as well as the agreed boundary line between the Observatory and the community in terms of the total effort required to deliver scientific results. Where is this boundary for the SKA Observatory? What does the Observatory deliver and what does the community have to undertake? How should it be defined? Is it different for different types of programs (e.g. survey verses pointed verses target of opportunity)? These are clearly fundamental questions that need to be addressed as we plan the construction and operations of the SKA.

The flow of processes and products surrounding the lifecycle of an SKA project can be divided into 4 domains.

PoS(AASKA14)147

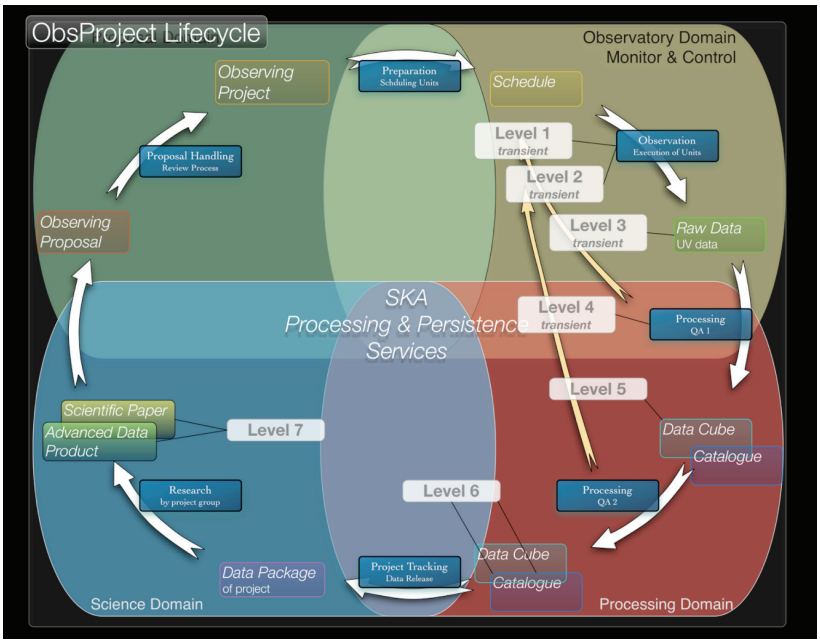

Figure 5: Operational domains and associated levels of data produced – see Figure 6

In the Proposal Domain proposals are prepared by the community, submitted and judged by the Observatory TAC process leading to the award of time and the preparation of a project description (sometimes called Phase 2 Proposal Preparation) in a form that can be scheduled and executed. In the Observatory Domain the observations are scheduled, executed and raw data is generated and captured. The Processing Domain turns raw data into images and catalogs and involves calibration and quality control at multiple stages. Finally the Science Domain defines and delivers data to users and facilitates the creation of advanced data products from input cubes and catalogs. The Observatory and Processing Domains are clearly central to the functioning of the SKA and will be assumed from here on to be part of the construction and operations cost of the SKA. Proposals are clearly defined and submitted by the community and the community will be doing science with SKA released data cubes and catalogs. Under these assumptions, the SKA will need to manage and deliver a number of different data products specified as data levels. These levels are shown in Figure 6.

PoS(AASKA14)147

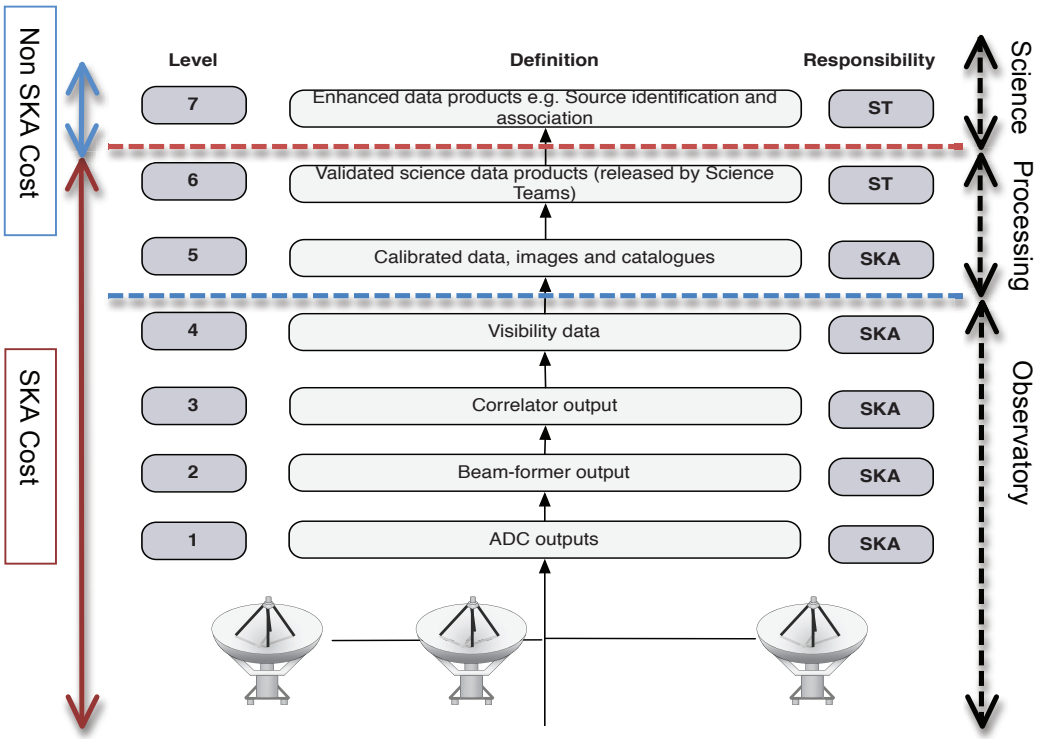

Figure 6: SKA data product levels (shown in Figure 5 from Cornwall, 2013) The blue and red dashed lines show the boundaries of the Observatory, Processing and Science Domains of Figure 5. The SKA Organization currently assigns responsibility to the KSP science teams (ST) to validate products to Level 6 and initiate the development of enhanced data products (Level 7).

At this point in time, the SKA Organization has indicated a transition from SKA Observatory responsibility for the data flow, to community responsibility between Level 5 and Level 6 data products. Whether this change of responsibility involves the utilization of SKA Observatory resources by the community to execute a quality control process and create validated products at Level 6, or whether it requires additional resources, is not determined at this time. The additional resources needed for the creation of Level 6 products will most likely be small compared to those required for Level 5. For this study, we will assume the Level 5 and 6 resources are within the construction and operations budgets of the SKA Observatory.

3.2 Construction and Operations Resources for Level 1 to Level 6

Based on the data volumes and rates in Table 2 for the assumed exposure time and telescope, Figure 7 shows the predicted volume of data products (Level 6) and Corrleator output buffer sizes assuming a buffer hold time of 100,000 seconds.

PoS(AASKA14)147

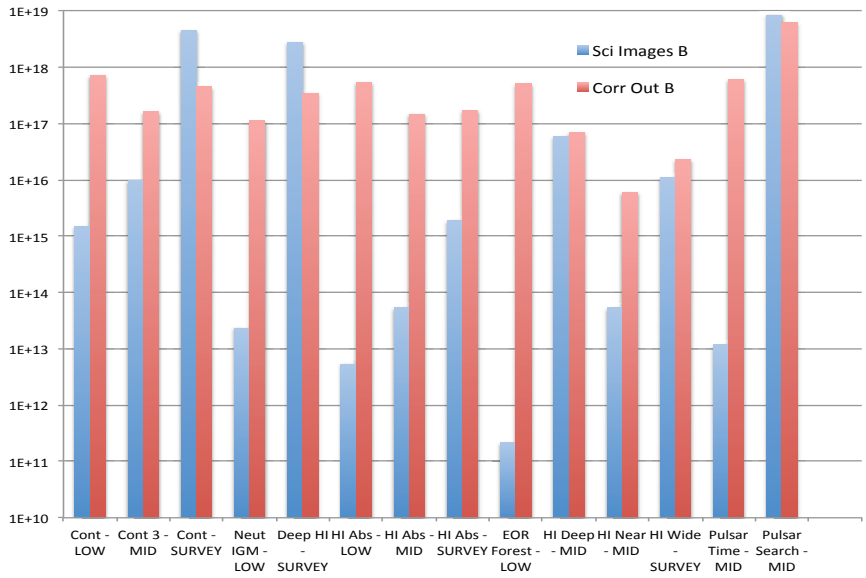

Figure 7: Total bytes generated at Level 6 for each KSP and the associated Correlator buffer size (without averaging) with a buffer hold time of 10^5 seconds.

If all KSPs were completed and the Level 6 products held on storage, the total science storage volume would be **16 Exabytes** with the largest buffer being **6.2 Exabytes** required by the Pulsar Search (MID) KSP. Figure 8 shows the effect of using averaged correlator outputs. In this case the required maximum buffer size is **71 PBytes** for the Deep HI Survey (SURVEY).

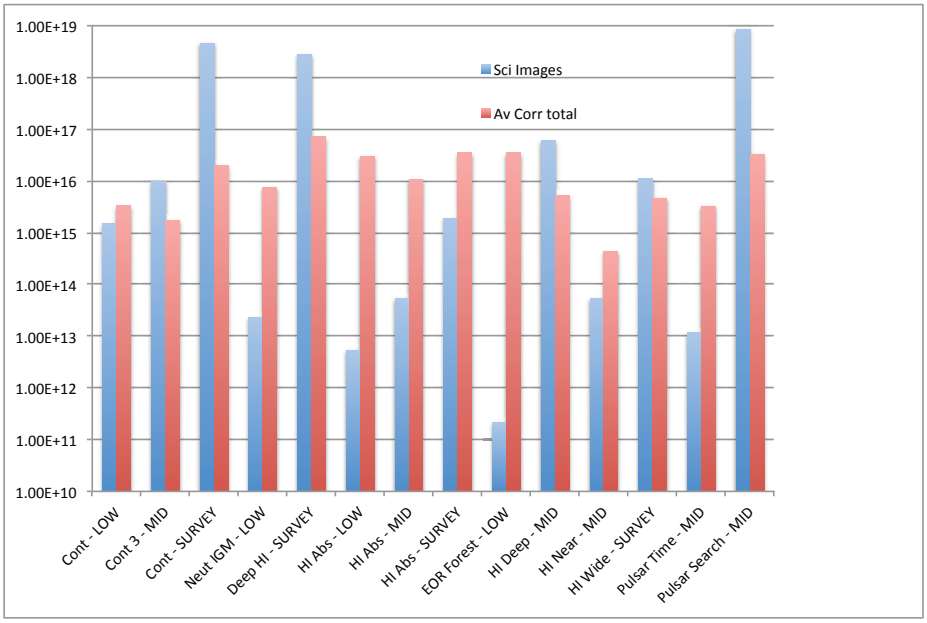

Figure 8: Total bytes generated at Level 6 for each KSP and the associated Correlator buffer size (averaged) with a buffer hold time of 10^5 seconds.

PoS (AASKA14) 147

The approximate cost of storage can be estimated from recently constructed HPC centres (e.g. Pawsey Centre in Australia) and from published industry trends for disks, tape robotics and hierarchical storage management systems given in the table below.

Year	$ HPC Doubling Exponent (yrs)	$ Tape Media Doubling Exponent (yrs)	$ Disk Doubling Exponent (yrs)	Tape media cost $/GB	Total Tape System $/GB	Disk $/GB
2014	-1.5	-2.3	-3	0.06	0.3	0.07

Table 4: Current trends (doubling exponents) and media costs for HPC, disk and tape systems based on HPC centre construction costs and industry trends.

Based on this analysis, and assuming correlator averaging, the storage costs on the timescale of 2020 are dominated by the tape storage systems (not correlator buffers) for the three largest surveys (Continuum, Deep HI and Pulsar Search) each of which will require investments of order 100 MEuro. The associated HPC cost (assume 100 PFlop off-the-shelf performance) will be approximately 80 MEuro by 2020.

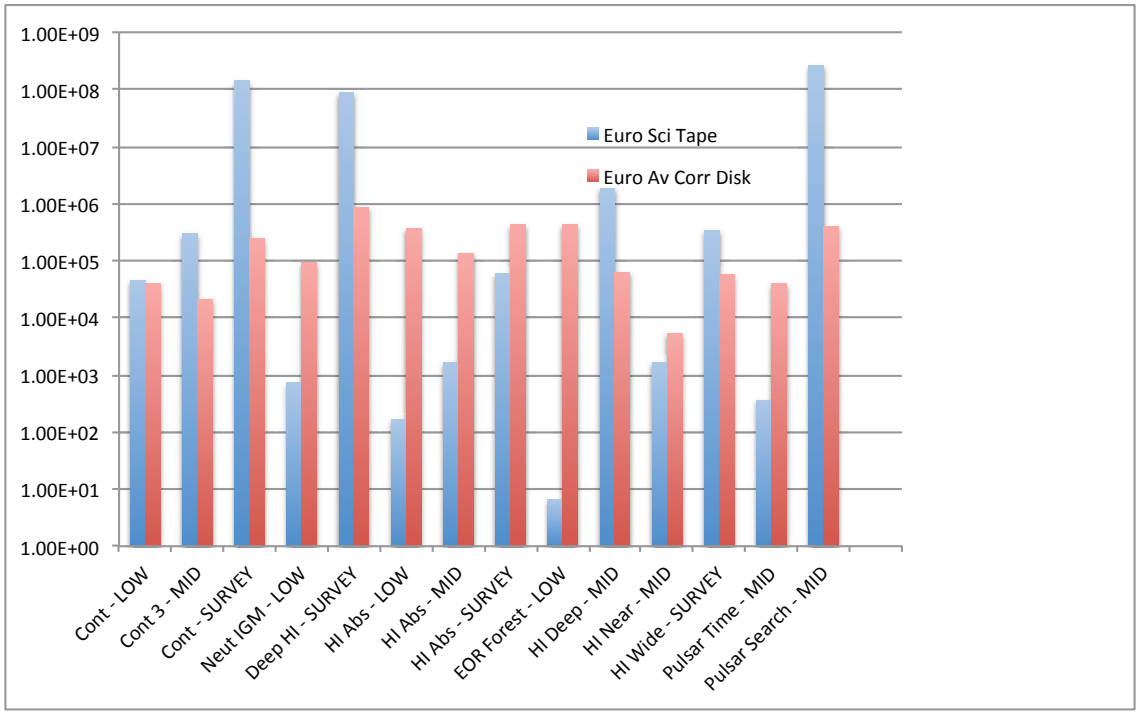

Figure 9: The cost in Euros of tape and disk storage systems for each of the KSPs projected to 2020 using the parameters in table 4.

The operational costs associated with these storage systems, along with the associated HPC, can also be estimated based on the recent HPC centre completion costs and industry trends in the power performance of HPC. Taking the power cost as a **lower limit** to the operational cost and assuming a Green500 mean doubling timescale for improvement in watts/mflop of 1.6 years, the lower limit operational cost of a 100

PoS (AASKA14) 147

PFlop facility is approximately 30 MEuro/yr on the timescale of 2020 at fixed unit electrical price. Figure 10 shows the construction cost and operational cost (over the total exposure time) for the combined set of KSPs as well as the three largest surveys under the assumptions above. The Figure also indicates the expected operational and construction costs for SKA1 based on the 650M Euro cost cap, a 100 MEuro allocation to HPC/Storage/Software, a total operational budget of 65 MEuro split equally among the three sites (UK, RSA and AUS) with a 50:50 split of operational costs between a site and a HPC/Data Centre.

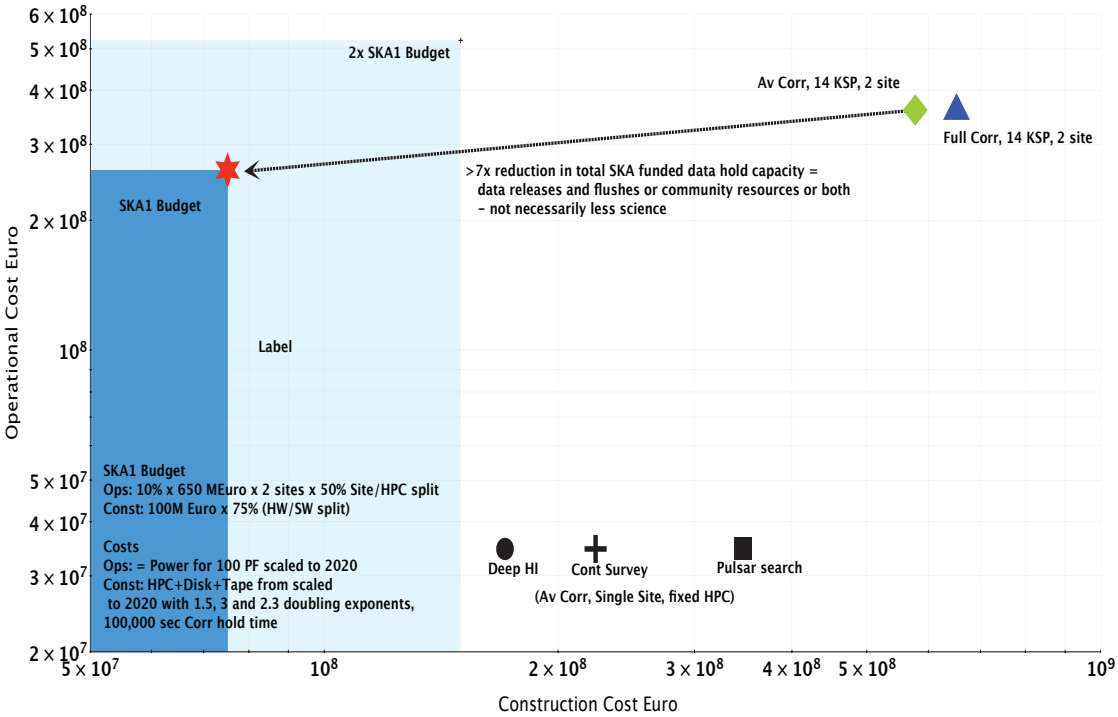

Figure 10: Projected operational and construction costs for KSP projects over the required exposure time, compared to estimated SKA1 budgets.

From Figure 10 it is apparent that the scale of the storage and processing/power requirements for SKA1 KSPs will exceed SKA1 expected budgets by a factor of at least 7 given the operational costs are lower limits. If the scale of the science requirements remains unchanged (survey sensitivity/depth) then the SKA funded data holding capacity needs to be reduced by at least the same factor of 7, or more, for Level 6 products. This could be achieved by instituting 7 or more data releases in the life cycle of a survey with a subsequence flush/reuse of the SKA funded resources. This would place the long term storage responsibility for SKA science data into community hands. Furthermore, the resources needed for Level 7 science are clearly of the same order, or larger than, Level 6 requirements. We are therefore facing a situation in which a significant community commitment, outside of the funding to construct and operation SKA1, will be required to deliver SKA1 science. This situation has been faced before by projects like the Large Hadron Collider and there is now clearly a need to initiate a significant effort in planning and resourcing the delivery of SKA science by the SKA community, working closely with SKAO.

PoS(AASKA14)147

4. The SDSS, LSST and LHC Science Data Systems

As pointed out in Section 3, the delivery of SKA science is going to require an SKA-Data system that is focused on delivering science from surveys in the most efficient manner possible and which is a distributed and shared facility across the SKA Observatory and the community. In the past 20 years, there are several important projects from astronomy and particle physics that have shared the mission of delivering maximal science impact to a distributed community within limited construction and operations resources. In this section we will examine three such projects. In each case we will look at the approach, the costs/challenges and whether these approaches will scale to the SKA needs.

4.1 The Sloan Digital Sky Survey (SDSS)

The SDSS (www.sdss.org) has made a significant contribution to international astronomy over the past 10+ years. This scientific return has resulted primarily from the development of a specific database and data management system that allowed the community to launch queries on a final set of catalogs and images (Level 6). The SDSS system is therefore a role model for the types of facilities we would expect to see in the Science Domain of SKA and dealing with the generation of Level 7 and beyond products.

4.1.1 Approach

The group at the Johns Hopkins University (Alex Szalay and Ani Thakar, in collaboration with Jim Gray) have spent much of the last two decades working on the archive for the SDSS. Opening in 2001, the archive has been issuing new data releases yearly. The most recent version of the database has a 12TB queryable public core, with about 120TB additional raw and calibrated files. The collaborative CasJobs interface has more than 6,820 registered users − almost half of the professional astronomy community.

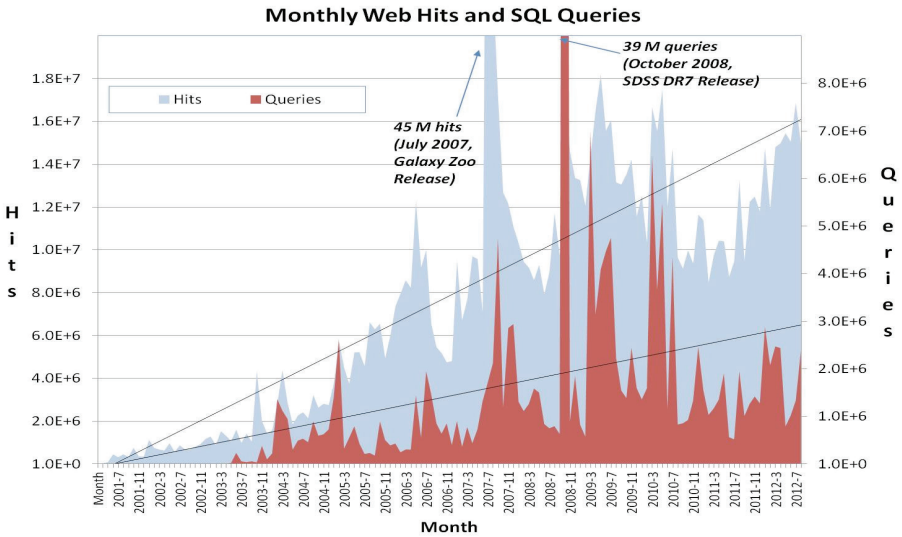

Figure 11: Monthly traffic of the SDSS SkyServer [provided by SDSS]

PoS (AASKA14) 147

SDSS (2000-2005) and its successors SDSS-II (2005-2008) and SDSS-III (2008-2014) surveys have produced data to support 5,000 papers with more than 200,000 citations. Within the Collaboration there have been over 120 SDSS-based PhD theses, and outside the Collaboration there have been many more.

4.1.2 Challenges and Costs

As traffic on the SDSS archive grew, many users were running repeated queries extracting a few million rows of data. The DB server delivered such data sets in 10 sec, but it took several minutes to transmit the data through the slow wide-area networks. It was realized that if users had their own databases at the server, then the query outputs could go through a high-speed connection, directly into their local databases, improving system throughput by a factor of 10. During the same time, typical query execution times and result sets kept growing, thus synchronous, browser-based access was no longer enough, especially for the rapidly growing segment of "power users". There had to be an asynchronous (batch) mode that enabled queries to be queued for execution and results to be retrieved later at will.

The CasJobs/MyDB batch query workbench environment was born as a result of combining these "take the analysis to the data" and asynchronous query execution concepts. CasJobs builds a flexible shell on top of the large SDSS database. Users are able to conduct sophisticated database operations within their own space: they can create new tables, perform joins with the main DB, write their own functions, upload their own tables, and extract existing value-added data sets that they can take to their home environment, to be used with the familiar tools they have been using since their graduate years. Their data and query history is always available to them through their user id, and they do not need to remember things like "how did I create this data set?"

As users became familiar with the system, there were requests for data sharing. As a result, the ability to create groups and to make individual tables accessible to certain groups was added. This led to a natural self-organization, as groups working on a collaborative research project used this environment to explore and build their final, value-added data for eventual publication. GalaxyZoo (www.galaxyzoo.org), which classified over a million SDSS galaxies though a user community of 300,000, used CasJobs to make the final results world-visible, and CasJobs also became a de-facto platform for publishing data.

An additional challenge was in dealing with regular data releases, in essence a versioning problem. As the project moved along, data was constantly collected, processed and ingested into an internal database. However, it would have been very confusing for the public to access this database, as the same query could have easily returned a different result every day, due to changes in the underlying data. Thus the project adapted a yearly data release. These happened usually coincident with the summer meeting of the American Astronomical Society. Data releases were accompanied by a short paper in the Astronomical Journal, which made citations to the data particularly easy through a conventional mechanism.

Older data releases were still kept alive, even today, as a research project that has been started with a given data release would have to rely on consistency and reproducibility. It is best to think of the Data Releases as ever newer editions of a book, where we do not throw away the old ones, they are still kept on the bookshelf.

PoS (AASKA14) 147

The original costs of the data infrastructure for SDSS have been grossly underestimated. The original budget for the whole project was about $25M in 1992, of which about **$2M** was the projection for the software and the archive. The estimated raw data was expected to be around 10TB, with a 0.5TB catalog database. Much of the software was going to be recycled from existing modules and data management tools from high energy physics. It was gradually realized that all of these costs and data sizes were highly underestimated. In the end, the project took more than 16 years to complete, and the total cost exceeded $100M, of which the software, the computational hardware and the archive were approximately 30%.

	Raw Data	**Database**	**Project Cost**	**HW/SW cost**
Initial	10 TB	0.5 TB	$25M	$2M
Current	120 TB	12 TB	$100M	$30M

Table 5: Predicted and actual costs and sizes for SDSS data systems

However, as the final data sets for the original SDSS-I and SDSS-II surveys are archived for the long term, it is clear that the data that needs to be stored is at least 120TB, the main database is over 12TB, with 25TB of additional databases (Stripe 82, Target, etc). So it is fair to say that the final data products were considerably more ambitious than the original vision. Nevertheless, the task was made easier by the exponentials: Moore's Law, and Kryder's Law. Both the speed of computing at a fixed yearly cost, and the capacity of disks at a fixed budget was growing exponentially, and the delays in the project enabled a much more ambitious data management outcome.

4.1.3 Scaling to ExBs

The current system with its 12TB database does not need a distributed system, so taken directly it would not scale to even a Petabyte. However, the different modifications of the SkyServer are now approaching a Petabyte in a single database, but spread over many servers, similar to the shared approach of LSST. If there was a lot of time pressure, one could build a 10PB astronomy database based on today's version of the SDSS software without much difficulty, probably at a cost of a few $M.

4.2 The Large Synoptic Survey Telescope (LSST)

The LSST is the highest priority of the US Decadal Survey of Astronomy for the period from 2010-2020. It will be an unprecedented optical survey facility capable of imaging the entire hemisphere every three nights and producing catalogs with billions of entries. The program of the LSST utilizes one telescope and one instrument to execute a number of well-defined surveys with community science focused around released catalogs and images. It is therefore has a more specialized approach to dataflow than the ESO-like system and is conceptually similar to SDSS.

4.2.1 Approach

LSST is a wide-field imaging survey that repeatedly images about 20000 sq deg of sky in 6 broadband filters over a 10 year period. Individual images are 3.5 gigapixels, and are collected at roughly 20 sec intervals. While LSST will be used to address a wide variety of science areas, there is a single survey with a uniform set of

PoS(AASKA14)147

data products which will be used for all of them. In many ways LSST can be thought of as a mega-SDSS, although without a spectroscopy component. Its major differences from SDSS are a much greater image depth (single exposures reach approximately 24.5 mag in r-band), and an emphasis on time dependent phenomena.

As was the case with SDSS, LSST expects that most science will be done with catalogs produced by the data pipelines, rather than directly from the images. The catalogs are implemented as a relational database, and one of the major design challenges of the data management system has been to ensure that this database is scalable to a large number of nodes that efficiently process database queries in parallel. This is required to support database queries that scan the entire database, as is required for many science use cases. A second challenge is to design the data processing pipelines so that they produce the catalog quantities that are required by the science use cases, and that they do so with a verified data quality that makes it unnecessary for science users to recompute them on their own from the image data.

LSST's image storage approach leverages the fact that most science that does require going beyond the catalogs to the actual images will do so by processing the deep coadds rather than individual exposures of a field. An example is searching for gravitationally lensed galaxies. Current processing pipelines are unable to reliably identify gravitational lenses, so images must be processed by a combination of specialized catalog-based selection in conjunction with human eyes. These lenses are static on LSST time scales, however, and the science need is for maximum depth and resolution, so the coadds will be utilized.

Since LSST images a typical field 200 times in each band, the coadds account for only about 0.5 percent of the total image data. This allows the vast majority of the image data to be archived on tape, which is inexpensive but slow compared to rotating disk. The typical image, therefore, is accessed only by the pipelines during the production of a data release, of which there are a total of 11 during the survey. The rest of the time, it can quietly reside on tape, available if needed, but with the expectation that it will not be.

4.2.2 Challenges and Costs

In considering the scalability of LSST's data management system to SKA size, we begin with a simple estimate of how big the scaling factor is. The overall size of the LSST data products is within an order of magnitude of SKA's. At the end of its 10 year survey, LSST will have archived roughly 500 PB of images. This is comparable to the deep HI survey, and roughly one tenth the size of the continuum survey, which together dominate the overall size of the SKA data products. The size of the LSST catalogs will certainly be substantially larger than SKA's, simply because of the difference in the total number of objects detected (roughly 45 billion objects for LSST vs 10s of millions for SKA). Considering only storage, the LSST's infrastructure cost is estimated at $6.3M and its operating costs (mainly in purchase of tapes and replacement disks) is $1.3M/yr. These costs are in FY15 year dollars, with projected component costs appropriate for operations beginning in 2022. This would suggest an SKA cost of perhaps $60M and $10M/year for data systems alone. These numbers are consistent with values in Figures 8 and 9.

PoS(AASKA14)147

4.2.3 Scaling to ExBs

From that simple perspective, then, it would seem that LSST's approach could scale to the SKA without unreasonable cost or difficulty. In fact, however, this scaling argument is of limited value because the SKA's will use its data in a very different pattern than does LSST. The patterns differ in at least two ways. First, while most LSST science will be based on catalog data, SKA science will mostly directly access images. Second, while most LSST image access outside of the pipelines themselves will be to a very limited subset (the deep coadds), the SKA will require much more uniform access to images. This is in good part a reflection of the fact that the typical SKA "image" is a three dimensional image cube of substantial depth, while an LSST "image" is basically two dimensional (or three dimensional with negligible depth to cover the six filter bands).

These considerations suggest that the LSST's approach of keeping the majority of its images stored on tape will not be practical for the SKA, and that the consequent cost of the required SKA infrastructure will be much larger than implied by the simple scaling argument.

4.3 The Large Hadron Collider (LHC)

The LHC is an international facility that was one of the first science endeavours to venture into the PetaScale of data and processing power. In facing this challenge, the LHC has split its data flow, responsibilities and costs into a number of tiers. A similar structure may be essential and desirable for SKA, for a number of community and cost-cap related reasons.

4.3.1 Approach

There are four large detectors at the LHC, which in the first 3 years of LHC running (Run 1) produced around 70 PB of raw data between them. This is significantly more than the 15 PB/year originally anticipated. Over the next 10 years the LHC and the experiments will all see significant upgrades, increasing luminosity and resolution, resulting in significantly increased data rates and volumes. For the "High Luminosity LHC" (HL-LHC) starting in 2023 or so, some 400 PB/year of raw data are anticipated; already in LHC Run 2 (2015-2018) double the Run 1 data volumes are expected, with intermediate increases for the run in 2019-22. Although today's raw data is of order 25 PB/year, the total data quantities are much larger; taking into account the needs of simulation, the various processing passes, and analysis data, the large experiments (ATLAS and CMS) each have a managed dataset of the order of 200 PB. Thus on the HL-LHC timescale – very close to the SKA timescale – each of ATLAS and CMS are likely to have (multi-)Exabyte scale datasets.

When the planning for LHC computing began in earnest around 2001, it was clear that the cost of computing, storage, and networking for LHC would be significant, and would approach the cost of building the large detectors. Thus CERN decided that the LHC computing project would be treated in terms of scientific and funding review, in the same way that the large experiments are managed. ***Thus, for the first time in High Energy Physics, the computing was recognized as one of the key components of enabling the science, together with the accelerator and the detectors***. ***It was also clear***

PoS(AASKA14)147

that the only way that sufficient computing and storage resources would be available would be by direct contributions from the countries participating in LHC experiments. It was also clear that those contributions would be through computing infrastructures in the funding countries. This funding reality then drove the need for building a globally distributed computing infrastructure.

The Worldwide Computing Grid (WLCG) collaboration was created to manage this computing infrastructure, and the reporting and reviewing requirements. It is a collaboration bound through a Memorandum of Understanding (MoU) between CERN and each of the participating funding agencies. This is the model of the LHC experiment collaborations themselves. An important feature of this MoU is that this is the mechanism through which the funding agencies pledge funding for the computing and storage resources. This is done through a yearly review and pledging process. It should be noted that the pledges are in terms of resources and not as money. As part of the MoU the computer centres agree to provide the services and service levels defined for the various Tiers.

High Energy Physics (HEP), and thus, LHC data processing and analysis differs from astronomy in several ways. In HEP there is no concept of a "science data product" in the sense of the output of an observatory (or a LHC detector). The output of the detectors is raw data, which must go through a series of data reconstruction, processing and selection stages, producing condensed summary data that is used for physics analysis. However, there may be different such analysis data sets, depending on the types of analysis to be performed. All of these steps are performed on the globally distributed computing infrastructure (the WLCG). In addition, a significant amount of simulation is needed, recognized as part of the analysis chain, and also performed on the distributed infrastructure. CERN, as the accelerator laboratory has a special role in that it archives on tape all of the raw data, and performs the necessary quasi-online calibration tasks. In terms of overall capacity CERN provides between 15-20% of computing and active storage needs of the experiments.

The computing model adopted for all LHC experiments initially is the following. All raw data is archived at CERN (the Tier 0), and a second copy distributed between 11 large (Tier 1) computing centres worldwide (7 in Europe, 2 in USA, 1 in Canada, and 1 in Taipei). The Tier 0 provides first-pass data reconstruction (particle track-finding), and urgent calibration tasks.

The Tier 1 centres provide reprocessing of the raw data once the calibrations have improved, creating the analysis data sets. These are distributed to the Tier 2 analysis centres.

The many Tier 2 centres (today ~150), often University Physics departments, provide compute clusters for physics analysis, with appropriate amounts of storage to host the physics data sets. All collaborators in an experiment have the right to access resources at any site, and indeed should not need to know where the data and compute is located.

There are also local resources available to national groups, out of scope of the WLCG collaboration.

4.3.2 Challenges and Costs

One of the early concerns was the adequacy of the networking, in particular being able to ensure the rapid distribution of raw data to the Tier 1s to ensure data

PoS(AASKA14)147

safety. This was addressed by provisioning dedicated 10 Gb/s connections from CERN to each Tier 1. This rapidly evolved to a redundant set of connections with backup paths between Tier 1s. This is the LHC Optical Private Network (LHCOPN), funded primarily by the Tier 1s and provisioned by the NRENs and Geant (in Europe), and a DOE-funded project in the USA. This was often seen by the NRENs as an important thing to help with as the LHC science was so visible. The costs of building LHCOPN were well within the computing budgets of the Tier 1s.

The experience in the run-up to LHC start, and the subsequent 3 years of Run 1 is that the network not only performs as needed, but is in fact a resource that can be used to reduce the eventual storage costs. This has led to an evolution of the strict hierarchical model, with data moving between sites as peers, and networking developing to allow this. The LHC experience, and the rapid evolution of network technology lead us to believe that over the next 10 years this will not be a technology concern, and that on the timescale of HL-LHC and SKA 1-10 Tbps networks will be available and affordable.

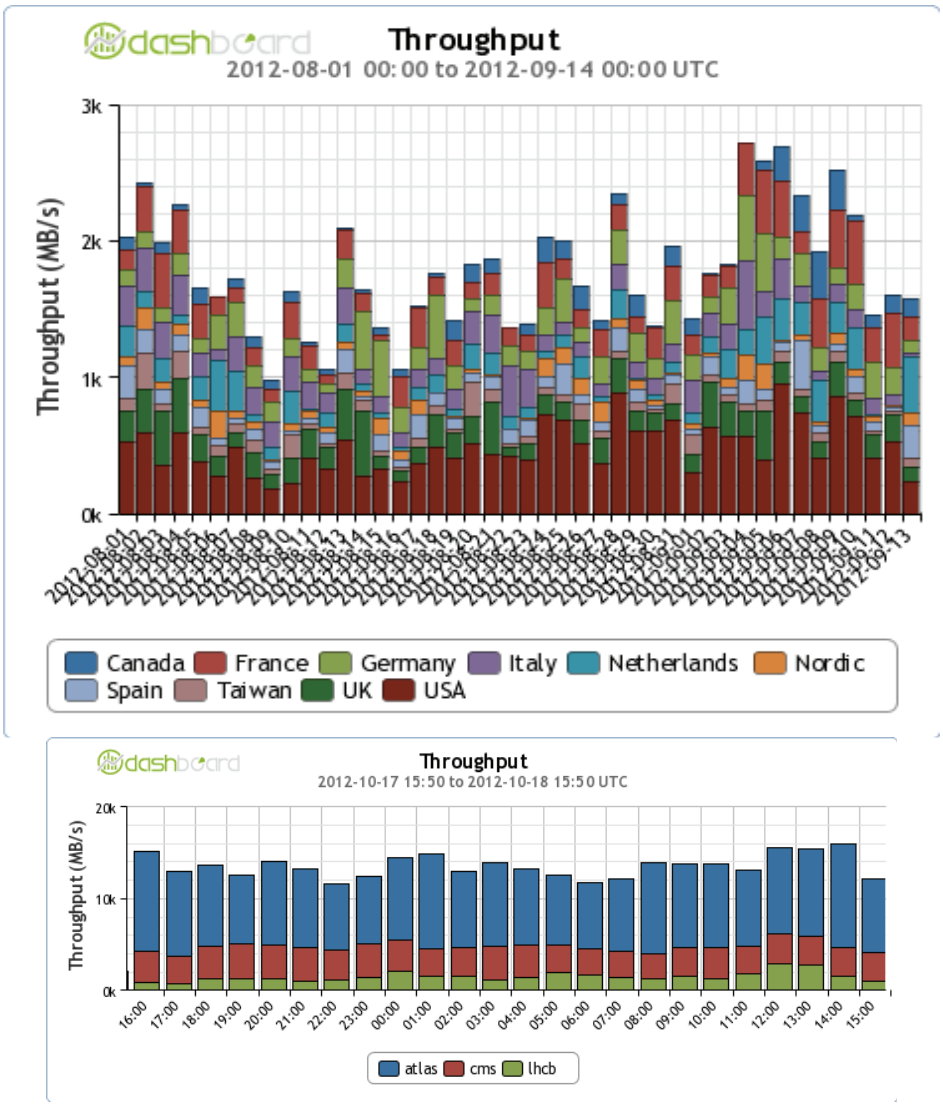

Figure 12: Examples of sustained network performance for LHC: top: 2 GB/s data export from CERN; bottom: global data transfers at 15 GB/s [data provided by CERN]

PoS(AASKA14)147

Today LHC spends around 60% of its computing budget globally on disk storage, a lot of this driven by the distributed nature, and the need to have many data copies to be able to utilize available compute resources. In the last year or so, the experiments have started to make use of accessing data remotely: pre-placing it "just-in-time", fetching it from a remote site if needed and not available locally, and in some cases realtime remote I/O. These strategies can be used in different cases, based on the observation that moving data today is cheaper than storing it. Thus, rather than storing many copies, there will many more network accesses to fewer copies of the data. This is at an early stage, but is likely to be the basis of the computing models in the coming years.

4.3.3 Scaling to ExBs

In the longer term – on the SKA timescale, this computing model must evolve significantly to make better use of economies of scale. It is clear that a highly distributed system such as the WLCG is more expensive than a more centralized large-scale system could be. Until now, this consideration has been outweighed by the considerable advantage of funding national institutions to provide the resources, allowing a real sense of ownership of the data, and complete engagement of the physicists in the analysis. Particularly for institutes outside of Europe and North America, this aspect has been essential, as has been the aspect of hands-on training of young scientists in managing large scale data and the associated technologies. In the future, however, we must make much more effective use of the available funding, building on technology evolution to federate national computing structures as they also evolve. It is also clear that on this timescale the actual computing models must evolve, to reduce the overall amount of processing necessary, making early decisions about which data to keep and which to reject. There are also ideas following the astronomy model of better defining the boundary between processing to produce a science data product and the use of those to do science. It is clear that the system will be highly distributed but that the model must evolve to better hide that nature from the scientist.

5. Delivering SKA science 2020+

The analysis of the scope and cost of SKA1 KSPs in sections 2 and 3, and the experience of SDSS, LSST and LHC outlines in section 4, contains some important messages for delivering SKA science and the size and nature of SKA-Data.

1. SKA surveys will produce a large range of data volumes that extend into the multi-Exabyte range. The 2020+ pricing of tape systems to manage the entirety of these surveys to Level 6, plus associated HPC costs, will exceed the anticipated SKA operational and construction budgets by factors of order 5-10. This fact alone implies multiple data release and flush cycles, and a shift of the long-term responsibility for storage to outside of SKA Observatory resources. An early realization of a similar challenge led the LHC to propose a new distributed approach to delivering science.
2. Both SDSS and LHC are examples of projects that have underestimated their data sizes and software/hardware costs. The factors involved are 4-24. There are potentially similar factors lurking in the SKA effort:

PoS(AASKA14)147

   a. The radio astronomy delivered performance of HPC verses Linpack benchmarks (factor of 14 – Figure 3)
   b. The resources needed beyond Level 6 to curate and deliver SKA science based on surveys (at least 7x Level 6)
3. SDSS is the most productive astronomical project of all time as measured by publications, citations and studentships. This was achieved by the design and development of a high performance and distributed database system that enabled collaboration between science teams. If SKA is to achieve the same success, then we need to leverage this experience and invest in a distributed and database focused, SKA survey science capability.
4. LHC realized and faced the same challenges to distribute data and do science that are now confronting the SKA. To do this, they took 10 years to design and implement an independent, distributed and complex collaborative network of research organizations (the WLCG = "the grid"). SKA will need to seriously consider this distributed concept, with all of its costs, benefits and complexity.
5. A distributed approach to doing challenging and expensive science, while complex, has been recognized by the LHC to have significant advantages in engaging and developing the community that built and operate the facility.

Is it feasible to considering distributing a large fraction of the SKA data flow and data management responsibility on the timescale of 2020+? The following figure shows the mean data flow rate in TB/s for KSP science products over the duration of a given project.

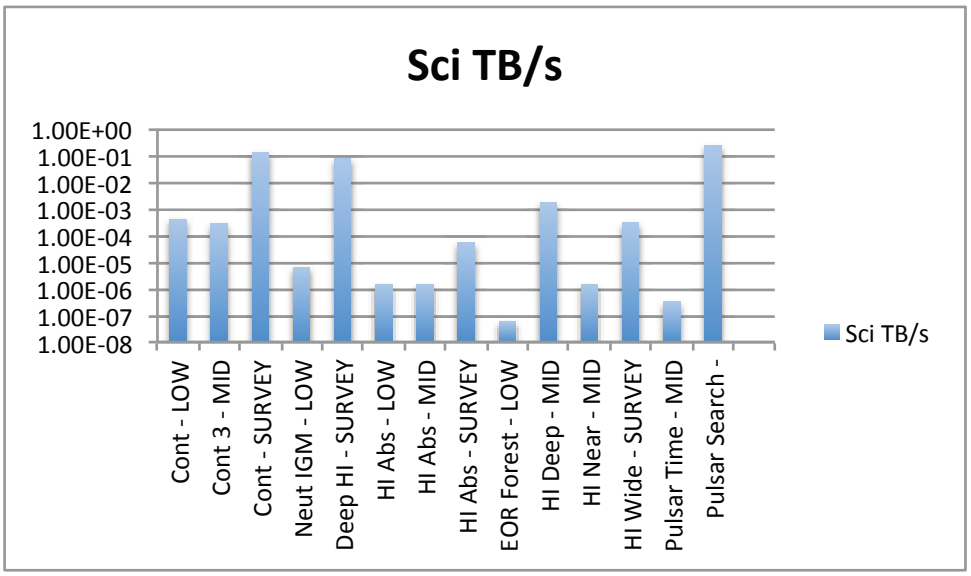

Figure 13: The mean data flow rate in TB/sec for the KSP set averaged over each projects exposure time.

Even for the largest surveys, the mean data flow rates are approximately 1 Tb/s. These data rates are expected to be widely available internationally and affordable on the timescale of 2020.

PoS (AASKA14) 147

Will SKA need to reinvent an infrastructure like WLCG to do SKA science? Since the first planning for the WLCG in 2001, and the subsequent operational roll-out of "the grid" in the past 5-10 years, there has been a growing trend to industrialize, simplify and commercialize distributed computing through the creation of "Cloud Computing and Storage". Cloud resources have now evolved from the simple decentralize storage of flat files, to reconfigurable arrays of processing and storage capabilities of significant scale. The Amazon Web Services (AWS) set of capabilities extends from modest backup for individual desktops to entire data and processing environments for US government agencies including NSA and NASA. The SkyNet community computing projects in radio astronomy (www.theskynet.org) (Vinsen 2013), based on AWS servers and storage, has already demonstrated the possibility of delivering Top500 class computing resources to astronomy applications. The cost of Cloud-based storage and processing is also evolving rapidly. Figure 14 shows the cost trends and models for AWS storage that are projected to be comparable to tape system costs per gigabyte by 2020.

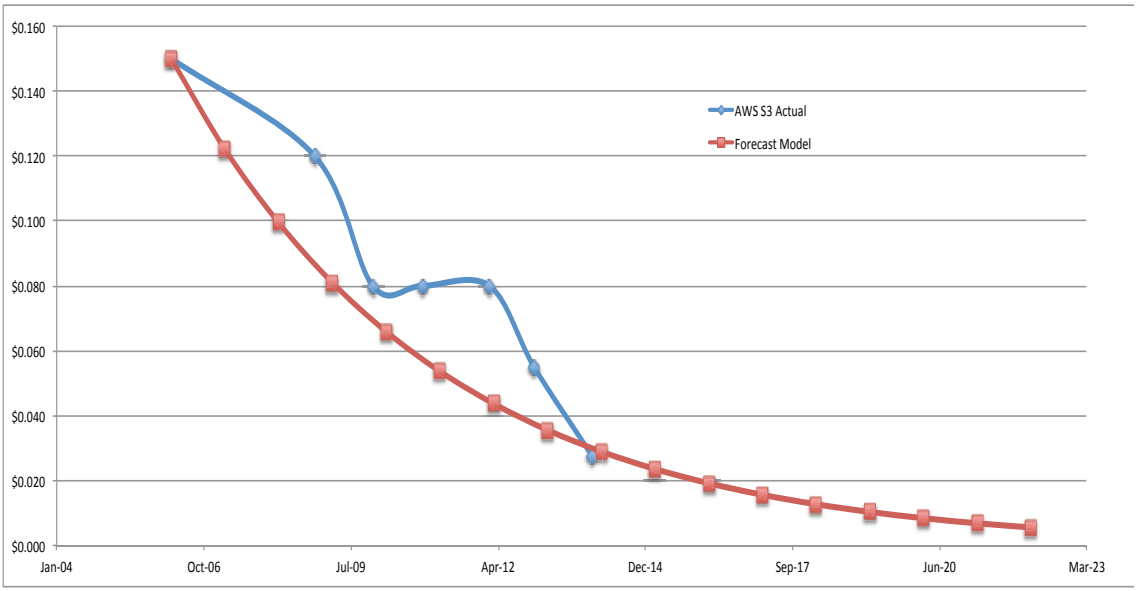

Figure 14: The projected and actual costs of AWS storage in dollars per gigabyte (source: AmazonWebServices.com).

The Cloud model for resources also shifts cost centres from capital expenses (initial investments in hardware) to ongoing operational costs. This strategy avoids the overheads and the direct costs associated with aging hardware, local fluctuations and growth in power costs, staffing and management investment, depreciation and the migration of content as technologies evolve. It also allows a uniform data access and analysis environment (part of AWS and others) in which physically separate research teams can simultaneously utilize the same astronomer-developed code-base, data and processing resources. While some measure of HPC and storage needs to be within the SKA Observatory and "plumbed into" the telescopes (Tier 0 in the LHC model), the distribution of analysis and survey science effort across the SKA community, may well benefit from appropriate utilization of Cloud resources, and the experience of cloud

PoS(AASKA14)147

providers who are currently rolling out top 20-scale machines every few days. At ICRAR, we are currently undertaking a trial Cloud implementation of a radio astronomy survey project (the CHILES JVLA deep HI survey, PI Jacqueline van Gorkom, Columbia U) in collaboration with Amazon Web Services to better understand Cloud based work flows and performance relevant to the SKA-data design process.

6. Conclusions

Based on an assessment of the data flow and storage requirements of a set of SKA Key Science Projects, and their projected operational and construction costs, it would appear likely that the resources needed for the full development of SKA science data products, and the long-term storage and access to science data, will require significant community involvement and commitment. That commitment, while technically necessary and financially significant, will also strongly bind and engage the diverse SKA international community into the scientific mission and success of the SKA. The developments undertaken by the SDSS and LHC projects, to facilitate distributed research, are highly relevant to the task that the SKA community should now undertake. That task is to design and build a SKA-data system that will, through working in close coordination with the SKA Observatory, enable survey science teams to delivery on the potential of the SKA for major astronomical breakthroughs in the coming decade. We feel that this task will be significantly assisted by the roll-out of globally available Cloud technologies and services.

References

Cornwell, T., 2013, *Data Products for SKA and SKA Low*, http://www.skatelescope.org/wp-content/uploads/2013/04/Cornwell-SKA_Lowscienceassessmentdataproducts.pdf

Lazio, J., 2011, *The Square Kilometre Array Design Reference Mission: SKA Phase 1,* Document number SCI-020.010.020.DRM-002.3a

Quinn, P. (Ed), 1998*, Observatory Operations to Optimize Science Return I,* SPIE Conference Series, Vol 3349

Quinn, P. (Ed), 2000, *Observatory Operations to Optimize Science Return II,* SPIE Conference Series, Vol 4010

Quinn, P. (Ed), 2002, *Observatory Operations to Optimize Science Return III*, SPIE Conference Series, Vol 4844

Vinsen, K., Thilker, D., 2013, *A BOINC based, citizen-science project for pixel spectral energy distribution fitting of resolved galaxies in multi-wavelength surveys*, *Astronomy and Computing*, Volumes **3–4**, 1-12, ISSN 2213-1337, http://dx.doi.org/10.1016/j.ascom.2013.10.001.

Wu, Chen, 2014, ICRAR report, based on data from *HPC Challenge site* (http://icl.cs.utk.edu/hpcc/hpcc_results.cgi?display=combo) supported by the Innovative Computing Laboratory (ICL) at the University of Tennessee (http://icl.cs.utk.edu/),

PoS(AASKA14)147

Summary and Future Directions

PROCEEDINGS OF SCIENCE

Square Kilometre Array key science: a progressive retrospective

Christopher L. Carilli[*1,2]

[1]*National Radio Astronomy Observatory, Socorro, NM,USA* [2]*Cavendish Astrophysics, Cambridge, UK*

E-mail: ccarilli@nrao.edu

I summarize the science drivers presented at the workshop for Phase I of the Square Kilometre Array: "Advancing Astrophysics with the Square Kilometre Array". I build from the historical perspective of the original Key Science programs: *"Science with a Square Kilometre Array"*, and consider progress in astrophysics since 2004. I then present my "score card" of the primary science drivers proposed by the Science Working Groups, and further developed in the white papers and presentations at the meeting. The science case for the SKA phase I is compelling, with the right mix of killer applications (eg. pulsars and gravity, 21cm cosmology), foundational radio astronomy (eg. cosmic magnetism, baryon cycle, high energy phenomena, large molecule chemistry and protoplanetary disks), and high risk-high return "game-changing" programs (eg. fast radio bursts, BAO intensity mapping, SETI). The case for real-time data spigots that allow for commensal observing is also strong. Ultimately, the greatest discoveries that will come from the SKA are likely even richer still, and beyond prognostication.

Advancing Astrophysics with the Square Kilometre Array
June 8-13, 2014
Giardini Naxos, Sicily, Italy

[*]Speaker.

PoS(AASKA14)171

1. Introduction

1.1 History and Approach

The concept of an interferometric array with a square kilometre of collecting area (SKA) at decimeter wavelengths has been discussed since the early 1990s, as a means of detecting HI 21cm emission from galaxies back to the "epoch of galaxy assembly" ($z \sim 2$; Wilkinson 1991). In 2004, a major international community effort was initiated to define and quantify the primary science program enabled by the SKA (Carilli & Rawlings 2004). The discussion was purposefully very broad, and considered the impact of a next generation radio mega-facility on the biggest questions in modern astronomy. Investigators were instructed to go beyond the classic areas of radio astronomy, and consider new applications, such as dark energy, gravity waves, reionization, the cosmic web, planets and planet formation, and extraterrestrial life. The telescope parameters were also broad, with observing wavelengths from 1cm to a few meters, and baselines from 1km to a few thousand km. The breadth of the discussion was both a blessing and a curse: new and exciting applications were established and pursued. However, the demands on the telescope design led to an instrument that was not plausible at the time, given budget and technical realities. In essence, as pointed out by Joe Lazio, the SKA became an Observatory, not a telescope.

In parallel, a committee was established to identify the Key Science Projects (KSPs) from this broad list of programs (Gaensler et al. 2004). The KSPs would be the programs that lead to the greatest scientific advances, and drive the design of the telescope. The resulting list was impressive (see below), but still required a telescope that would be difficult to realize in practice.

In the ensuing decade, a number of path-finder and precusor telescopes have been spawned to pursue many of the KSPs in advance of the full SKA:

- At low frequencies (< 200 MHz), the search for the HI 21cm signal from the epoch of reionization has re-energized the low frequency radio astronomy community, growing a new generation of talented young experts in radio techniques and cosmology. Telescopes such as LOFAR, PAPER, and the MWA, are now performing deep cosmological observations, and providing the first limits on the reionization HI 21cm signal.

- At mid-frequencies ($\sim$ 1GHz), numerous wide field survey telescopes have been constructed, including ASKAP and Apertif on the WSRT, as well as sensitive arrays such as MeerKAT. The VLA Sky Survey is now being designed, and will provide an important testing ground for both the science and techniques appropriate to SKA phase I. The GMRT, WSRT, and the VLA are performing deep integrations to detect HI in galaxies out to $z \sim 0.3$ to 0.5. Likewise, major pulsar search instrumentation has been developed and deployed on existing facilities, such as the GBT, Parkes, and Effelsberg. International teams have been established to search for gravity waves and test strong field General Relativity (GR), including NANOgrav, EPTA, PPTA, and the IPTA. The newest addition to the arsenal will be FAST, a ten times Arecibo-area single dish telescope under construction in China.

- At high frequencies (3 GHz to 50 GHz), a quantum leap in capabilities has been realized through the full operation of the Jansky Very Large Array. The JVLA is producing the first deep, wide-band searches for molecular gas in distant galaxies. These surveys provide unique insight into the cosmic evolution of the molecular gas content of galaxies – the fuel for star formation. The JVLA is also providing a unique look into terrestrial planet formation and the origin of stellar multiplicity.

PoS(AASKA14)171

The SKA is now in a critical development phase in which Phase I of the array is being designed as a first major step toward the full array. The 2014 meeting "Advancing Astrophysics with the SKA" (AASKA14) culminates a two year effort by the SKA Organization and international SKA science working groups (SWG), to refine the SKA science case based on the capabilities of phase I, but keeping in mind the long-term goal of the full SKA in collecting area, frequency coverage, and array lay-out.

When first asked to summarize AASKA14, I inspected the 150 or so science white papers submitted prior to the meeting, and the comparable number of talks scheduled at the meeting, and realized a full summary was problematic. However, I was reminded of the process Steve Rawlings and I, and the SKA International Science Advisory Committee, went through a decade ago in developing the KSPs. I thought it would be entertaining to consider progress on the KSPs over the past decade, and place these in the light of the science program proposed for SKA Phase I at AASKA14. Which areas have seen major progress? Which areas remain relevant? Are there new areas ripe for discovery? And in which areas will SKA Phase I make the most impact?

I would have worked on this summary with Steve Rawlings, but tragically, Steve passed away in 2012. I have tried to remain cognizant of his views throughout, in particular in the area of cosmological applications of deep radio surveys – an area he championed in 2004. Still, I must admit this is, by definition, a subjective assessment, based on my reading of the science working group reports and science white papers submitted prior to the meeting, and revised based on the excellent presentations given at the meeting.

1.2 Key Science Projects 2004: mapping to current Science Working Groups

The SKA KSPs were originally predicated in the SKA memo 44 (Gaensler et al. 2004), and summarized in the introduction to *"Science with the Square Kilometre Array"* (SSKA; Carilli & Rawlings 2004). More detailed analysis of each project can be found in the first 5 chapters of SSKA. It is interesting to reconsider the criteria that defined a KSP:

- Address important questions in fundamental astrophysics
- Emphasize contributions unique to SKA/radio, or in which the SKA plays a crucial complementary role
- Excites broader community and funding agencies

Figure 1 shows a mapping of the SKA KSPs from 2004 to the current SKA science working groups. The mapping is very close, with a few differences arising due to the more technique oriented SWGs in some areas. The area of time domain was considered in 2004 (Cordes et al. 2004), but did not reach the level of a KSP at the time. Clearly that has changed in the last decade.

1.3 Score Card

I have developed a "score card" to keep track of my assessment of the progress in given areas, and the relevance of SKA Phase I (Table 1). This score-card is clearly the most subjective aspect to my analysis. I use a simple rating system on a scale of 0 (zero) to 5 (high), for the following areas:

PoS(AASKA14)171

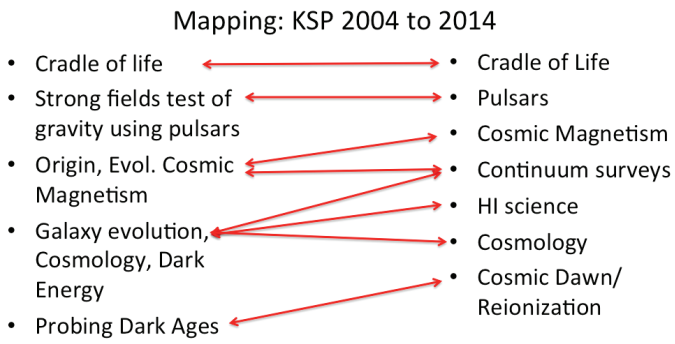

Figure 1: Mapping the SKA key science projects from 2004 to the current science working groups.

- Progress: how much has been learned over the last decade that is directly relevant to the SKA KSP, either through radio pathfinders (Prog.-R), or through observations at other wavelengths (Prog.-G)?
- SKA phase I role: what impact will SKA Phase I have on progress in the field?

To define the role of SKA Phase I, I adopt the basic criteria:

- SF = Science Facility. Major progress in key science expected using SKA Phase I
- SD = Science Demonstrator. Some progress in KSP, while informing phase II design/techniques
- TD = Technical Demonstrator. Minor progress in KSP, mostly inform phase II
- N/A = No progress in KSP w. SKA Phase I

I note that only three programs reach level 5 in the table. First is for "general progress on extrasolar planets". While there have been profound advances in many areas of astrophysics over the last decade, including precision cosmology, strong field GR, tracing galaxy formation back to the first galaxies, Galactic structure, star formation, I feel the area of extrasolar planets stands-out as a field that went from essentially zero to a mature field in the space of a few years, and a field that has profound sociological as well as scientific impact. Level 5 is thereby set by general progress on extra-solar planets. If SKA Phase I can successfully exploit the physics of gravity waves, and/or the HI 21cm signal from cosmic reionization, these would also be level 5 contributions, opening new cosmic vistas.

Table 1 also lists the SKA phase I facilities that are relevant to a given program. It is important to note that, in my assessment, I only considered Phase I of the SKA (construction beginning 2018, full-science beginning 2023), not the full SKA. I assume the specifications for Phase I as currently given in the rebaselined design:

- SKA1-LOW: 40% of a square kilometre in collecting area, with about half the area in a core of 0.3 km radius, and maximum baselines of about 65 km, operating from 50MHz to 350 MHz. Station beams will be formed with a FoV of 20 deg^2.
- SKA1-MID: 133 offset Gregorian dishes of 15m diameter, and 64 MeerKAT antennas of 13.5m diameter, with about half of the total collecting area within a 1-km radius, and three spiral arms providing a maximum baseline length of about 150km. MID will initially operate from 350MHz to 1760MHz (bands 1 and 2), and 4.6 GHz to 13.8 GHz (band 5).

PoS (AASKA14) 171

Table 1: Score Card: SKA Phase I Key Science Projects

KSP	Prog.-R[a]	Prog.-G[b]	SKA Fac.[c]	SKA Phase I[d]
Reionization: Precision HI 21cm cosmology	2	3	L	SF (5)
Reionization: 1st galaxies/AGN	3	4	M	TD (2)
Cosmology: DE/BAO intensity mapping	2	3	M	TD (2)
Cosmology: DE/DM/weak lensing, non-Gaussianity	1	3	M	TD (2)
Galaxy Evolution/nearby: Baryon cycle, SF laws	3	3	M	SF (4)
Galaxy Evolution/distant: HI, SF	4	4	M	SD (3)
Cosmic Magnetism: Objects – unique role	4	1	L, M	SF (4)
Cosmic Magnetism: All sky RM	3	0	M	SD (3)
Pulsars: Gravitational waves	3	3	M	SF (5)
Pulsars: double precision gravity	4	2	L, M	SF (4)
Pulsars: EoS neutron stars	4	0	L, M	SF (4)
Cradle of Life: prebio molecules, SETI	3	1	M	SD (3)
Cradle of Life: planets (B fields), P-P disks	3	5	L, M	SD (3)
Time Domain: LSST/Fermi... (min – days)	3	4	L, M	SF (4)
Time Domain: FRBs++ (msec – sec)	2	0	L, M	SD (3)

[a]Progress in radio (scoring: 0=low, 5=high); [b]Progress in general; [c]Relevant SKA facility: L = SKA1-LOW; M = SKA1-MID [d]Role SKA phase I (SF = Sci.Facility, SD = Sci.Demo., TD = Tech.Demo., N/A)

In the following sections, I describe in detail the rating for each KSP. References are given to the relevant white papers throughout. The ordering is roughly from the distant Universe to nearby. I conclude with some editorial remarks on the Phase I design and the SKA future.

2. Key science programs

2.1 Cosmic reionization and the first galaxies

Precision 21cm cosmology Probing the neutral intergalactic medium that pervaded the Universe during, and prior to, the formation of the first galaxies and cosmic reionization, is one of the paramount goals of 21st century astrophysics. Substantial progress has been made in constraining the Inter-galactic Medium (IGM) neutral fraction through Gunn-Peterson and related phenomena (Fan et al. 2006; Robertson et al. 2013). The most stringent constraints to date are based on the demographics of Lyα emission from early galaxies, which may indicate a rapidly increasing IGM neutral fraction, from $< 10^{-4}$ at $z < 5$, to possibly as high as 0.5 at $z \sim 8$ (Konno et al. 2014; Bouwens et al. 2015). Unfortunately, diagnostics related to the Lyα line saturate at low neutral fractions, and hence are most useful toward the end of cosmic reioinzation.

Imaging in the redshifted HI 21cm line provides the most direct means of probing the evolution of large scale structure and the neutral IGM through cosmic reionization into the preceding dark ages (Koopmans et al. 2015, Wyithe et al. 2015). A major push is underway to discover the HI 21cm emission from the IGM during cosmic reionization. LOFAR, PAPER, and the MWA are now performing deep integrations, and first limits have appeared in press (eg. Parsons et al. 2014; Pober et al. 2015; Ali et al. 2015). There is the real potential for a first detection of the signal by 2017. Just as importantly, techniques have been developed to mitigate the limitations imposed by the strong continuum foregrounds. These techniques are now being incorporated in optimal

PoS(AASKA14)171

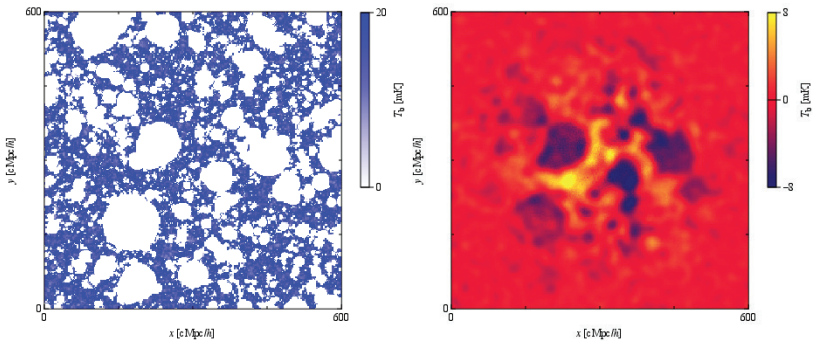

Figure 2: Left: Simulations of the SKA1-LOW response to the ionisation structure in the Gigglez 1 Gpc simulation with a neutral fraction of 0.45 at z=7.3 and depth of 2 Mpc over 6°. The right panel shows simulations of observed maps for the baseline SKA1-LOW with 4000 hr integration (Wyithe et al. 2015).

designs for the next wave of reionization experiments, such as HERA (Pober et al. 2014). It is just a matter of time before the signal is detected (hopefully a short time!), and initial power spectral characterization is performed.

The SKA1-LOW is required to go well beyond detection, to imaging of the evolution of large scale structure during reionization, and into the Dark Ages. Figure 2 shows the ability of phase 1 to image more typical structures in the IGM during reionization. These measurements are key to unlocking the secrets of the evolution of large scale structure within a few hundred Myr of the Big Bang, and to setting the environmental context for the formation of the first galaxies.

First galaxies: Study of the earliest galaxies is an area in which remarkable progress has been made over the last decade, principally through deep fields in the near-IR. We now know of hundreds of spectroscopically confirmed star forming galaxies at $z \sim 6$, and similar numbers of candidate drop out galaxies at $z \sim 7$ to 10 (eg. Bouwens et al. 2014, 2015; Trenti et al. 2014). These results have enabled a census of the galaxies required to reionize the IGM. Current estimates suggest that the constraints on the evolution of the IGM neutral fraction are consistent with the number of $z > 7$ galaxies required to reionize the Universe around $z \sim 8$ (Bouwens et al. 2015; Robertson et al. 2013). A major difficulty is obtaining spectroscopic redshifts for $z > 7$ galaxies – something that may have to wait for the JWST, or ALMA using the [CII] 158um line.

The role of cm radio astronomy in these studies is to observe the cool molecular gas (eg. CO and other dense gas tracers) in z > 6 galaxies. Using the JVLA, ATCA, GBT, Plateau de Bure, and now ALMA, CO has been detected in extreme starburst galaxies at z > 6 (see Carilli & Walter 2013 for a review). However, pushing down the luminosity function requires more sensitivity than the JVLA currently affords. Most recently, ALMA has detected [CII] 158um emission from a number of "normal" star forming galaxies from z = 5 to 7 (eg. Capak et al. 2015).

Unfortunately, study of CO at high redshift requires frequencies 25 GHz to 50 GHz, in particular given the weakness of the 1-0 transition caused by the warmer CMB at $z > 5$ (de Cuna et al. 2014), and hence is not possible with the SKA1.

2.2 Cosmology

Precision cosmology: The age of precision cosmology was entered with the first WMAP

PoS(AASKA14)171

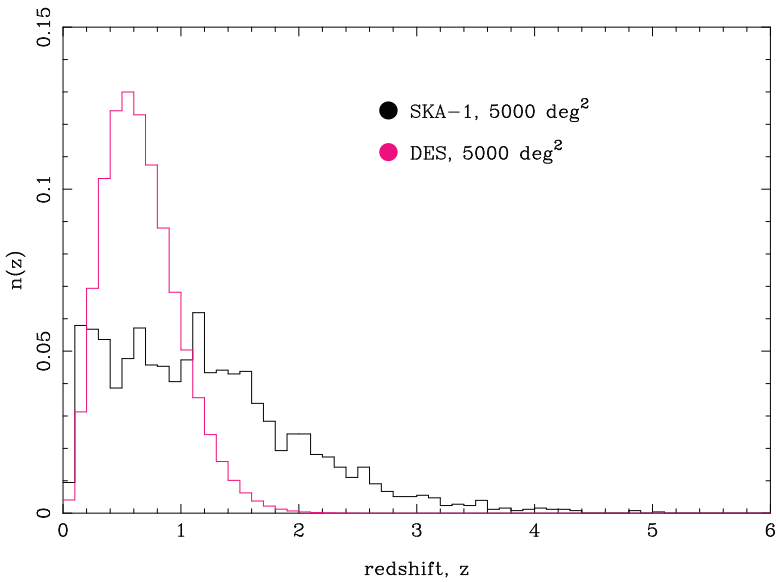

Figure 3: The predicted redshift distribution for galaxies in a deep survey for weak lensing for the SKA phase I and optical DES (Brown et al. 2015)

results, just as the SKA KSPs were established. Planck has now pushed us to double-precision cosmology (Ade et al. 2014). Cosmology is one of the three areas in astrophysics relevant to the SKA that I feel has made the biggest strides in the last decade, along with first galaxies and planets.

The idea of addressing some of the paramount questions in cosmology using the SKA, such as the nature of Dark Energy, was first championed by Steve Rawlings in SSKA. The current SKA SWG on cosmology has embraced this challenge through a remarkably creative set of experiments that have tremendous potential to contribute to this rapidly advancing field (Maartens et al. 2015; Brown et al. 2015).

Dark energy: A major question at the time of the KSPs, and one that remains paramount today, is that of the nature of Dark Energy and the accelerating Universe. The discovery of the imprint of the BAO in the SDSS galaxy distribution at z < 0.5 (Eisenstein et al. 2005), was published one year after Rawlings et al. proposed the SKA1-MID KSP on very large scale HI surveys to $z \sim 1$.

In the subsequent years, further studies of type Ia SNe, as well as the double-precision cosmology from Planck, have supported the conclusion of a late-time accelerating Universe. However, questions have been raised as to the effects of dust and evolving physical conditions on high z SNe, making for an interesting continuing debate on dark energy. Major optical redshift surveys (BOSS), to be followed by LSST and Euclid, should clarify the evolution of the BAO scale over the redshift range relevant to cosmic acceleration.

The SWG points out that the SKA phase I HI survey, while detecting 10^7 galaxies, will not be competitive with the optical surveys in constraining BAOs, and should be considered a technical demonstrator (TD). However, the group made a strong case for the use of HI intensity mapping (mean surface brightness on large scale), with SKA phase I (Santos et al. 2015). Using this technique, the SKA phase I has the potential to map out the BAO signal to a level easily competitive with the optical surveys, perhaps into the dark matter dominated era ($z > 1.5$). However, serious

PoS(AASKA14)171

technical challenges remain, most notably, obtaining accurate total power spectral measurements with the SKA1-MID dishes, hence I also rated this a TD. The galaxy HI survey itself will provide important checks on optical BAO surveys, in terms of clustering bias and the reliability of photometric redshifts (Abdalla et al. 2015).

Weak lensing and other cosmological problems: Weak lensing can determine the redshift evolution of the dark matter power spectrum over the epoch of cosmic acceleration. These results provide a complementary view of cosmic acceleration and the nature of dark energy to those obtained by type 1A SNe. According to the SWG, a continuum survey over 500 deg^2 with a resolution of $\sim 0.5''$ is required to constrain weak lensing substantially better than will be done with LSST. An SKA1-MID continuum survey has the potential to perform these measurements (Brown et al. 2015; Jarvis et al. 2015a). A unique aspect of the SKA weak lensing study is the redshift distribution of sources: the SKA will probe systematically higher redshifts than eg. Euclid (Fig. 3).

A wide field SKA continuum survey may also contribute to the study of the non-Gaussianity of structure on the largest angular scales, by probing a unique combination of very wide fields and very high redshifts. Likewise, SKA phase I may impact studies of the integrated Sachs-Wolfe effect, through cross correlation with the CMB.

The main challenge for the cosmology SWG remains the competition. All of these areas are under intense investigation using other techniques. The SWG make the case that phase I could be competitive in some areas, with some technical development, and possibly even lead others (non-Gaussianity). The case really hinges on the strength of "uniqueness" arguments, such as (i) the need for alternative measures of the cosmological parameters with different systematics, (ii) the power of cross-correlations of different techniques, and (iii) the unique parameter space explored by the SKA (eg. wider field of view, higher redshifts).

Finally, I note that the original SKA KSP role in precision cosmology concerned the determination of H_0 using water masers. Determining H_0 is an important prior needed to break degeneracies between the low z expansion rate and the equation of state of dark energy (Greenhill 2004). In the last few years, dedicated VLBA and single dish monitoring of water megamasers has brought the H_0 measurements to a few percent accuracy (Reid et al. 2013). The refinement of the CMB power spectrum through Planck has also narrowed the allowed range of H_o. The need for much higher precision using water masers was not discussed in AASKA14, and, perhaps more importantly, this experiment requires $\geq$ 20GHz, which is not at present in SKA Phase I.

2.3 Galaxy Evolution

Nearby galaxies: Study of nearby galaxies, and "late-time" galaxy evolution, is one of the foundational areas of radio astronomy. Strong cases were made at the meeting over a broad range of topics, including: ISM physics, star formation "laws", stellar photospheres and stellar evolution, SNe, SNR, and "non-HI line" science (Beswick et al. 2015).

A critical area that has come to the fore in the last few years is the baryon cycle through galaxies, and the realization that, to maintain star formation over a Hubble time, galaxies require resupply of cool gas, both at low and high redshift. Telescopes such as the GBT, WSRT, and Arecibo are now identifying low column, low mass neutral gas clouds around nearby galaxies, possibly comprising the neutral element of the "cosmic web". Evidence suggests that we are observing directly

PoS(AASKA14)171

the outflow, and infall, of cool gas as part of this baryon cycle of galaxies in the local Universe (Blyth et al. 2015).

An important question that has arisen in galaxy formation is: why do galaxies stop growing? One solution that has been proposed is "radio-mode feedback" in late-time galaxy formation, in which large scale radio jets heat the intercluster medium. Jets appear to be required to heat the intercluster medium around massive galaxies, thereby inhibiting further accretion and galaxy growth. These studies build on a strong connection between Xray and radio astronomy (Govoni et al. 2015). On even larger scales, a key observation will be delineation of the cosmic web through low surface brightness radio continuum emission (Vazza et al. 2015).

The SKA phase I will have major impact in all of these areas, through its sensitivity to very low surface brightness emission, and wide field of view.

Continuum deep fields: The continuum deep fields proposed for SKA phase I have multiple applications, from the Rotation Measure (RM) grid, to Galactic science, to cosmology (Prandoni & Seymour 2015; Johnson-Hollitt et al. 2015; Umana et al. 2015). In the area of galaxy formation, radio continuum deep fields are now a standard tool for the study of both the evolution of radio loud AGN, as well as a dust-unbiased means of determining the star formation history of the Universe (Jarvis et al. 2015b). Radio data have proven critical in both identifying distant, dusty starbursts, and determining sizes for star forming galaxies at early times. Deep fields with the JVLA are now routinely reaching $\sim 1\mu$Jy sensitivity at sub-arcsecond resolution. The VLA Sky Survey, a synoptic, full (observable) sky survey to tens of μJy sensitivity with arcsecond resolution and full polarization, is currently in the implementation stage. These results will inform the proposed deep fields for SKA phase I.

The SKA1-MID will take the next step in sensitivity and field of view in continuum deep fields. The sensitivity should be adequate to delineate the normal star forming galaxy population back to the peak epoch of cosmic star formation ($z \sim 2$). A case was made for detecting the Free-Free emission from early galaxies at (rest-frame) 50GHz or so, thereby obtaining the most direct measure of star formation rates in early galaxies (Murphy et al. 2015). Such a program requires ~ 20 GHz on the SKA, and must surmount the problem of separating the synchrotron, free-free, and cold dust emission in the SEDs.

HI deep fields: Detecting HI 21cm emission from distant galaxies was the first KSP for the SKA, and remains a key science area today. This is an area in which only slow progress has been made, due to limited collecting area of current facilities. Still, HI 21cm emission has now been detected with the JVLA, GMRT, and WSRT from large galaxies out to $z \sim 0.2$ (eg. Fernandez et al. 2013; Lah et al. 2007), and through stacking or intensity mapping, mean HI properties of galaxies have been infered out to $z \sim 0.4$ to 1 (eg. Switzer et al. 2013; Lah et al. 2011).

The SKA phase I remains the required device to determine the evolution of the HI mass function to $z \sim 1$. Deep, wide surveys with MID, will detect millions of galaxies to substantial redshifts (Fig. 4). These surveys will also detect 21cm absorption toward distant radio sources, and possibly OH masers in active galaxies. The resolution will typically not be adequate to image galaxy dynamics at high redshift, but certainly will allow for analysis of integrated galaxy properties, such as the Fisher-Tully relation (Blyth et al. 2015).

Molecular gas: One of the most important advances in the study of galaxy formation over the last decade has been the delineation of the cosmic star formation and stellar mass build-up, as

PoS(AASKA14)171

a function of galaxy type and environment, back through the "epoch of galaxy assembly" ($z \sim 1$ to 3), during which half the stars in the Universe form, back to first light and cosmic reionization at $z \sim 7$. However, these studies provide only half the story of galaxy formation, ie. the stars and star formation. Studies of the cool molecular gas – the fuel for star formation, are the required complement to the stellar studies, thereby completing the baryonic picture of galaxy formation.

The study of the cool molecular gas in distant galaxies has improved steadily in the past few years, principally through improvements with the PdBI, GBT, and ATCA, and more recently, with the advent of the JVLA and ALMA. There are now hundreds of CO detections at $z > 1$, with CO being the main diagnostic for total molecular gas mass in early galaxies. There have also been a number of detections of higher dipole moment, denser gas tracers, such as HCN, CS, HCO^+. Studies have moved beyond mere detection, to detailed gas dynamical imaging at kpc resolution, and multi-line, multi-species analysis of ISM physics. ALMA has also opened the field of detailed imaging studies of atomic fine structure lines in early galaxies – key diagnostics on ISM gas heating, cooling, and dynamics (see Carilli & Walter 2013).

The most remarkable result from these studies is the realization that "normal" star forming galaxies at high redshift (ie. those that dominate the cosmic star formation rate density at a given epoch), are likely gas-dominated in their baryonic content. The average ratio of molecular gas mass to stellar mass rises from $M_{gas}/M_{stars} \leq 0.1$ at $z \sim 0$, to $M_{gas}/M_{stars} \geq 1$ at $z \sim 2$ (see Carilli & Walter 2013 and references therein). This rise represents a profound change in galaxy properties with cosmic time, and likely drives the commensurate rise in cosmic star formation rate density.

In terms of the HI content of galaxies, SKA phase I will certainly add to the picture at $z \leq 0.5$ for individual galaxies, and possibly higher redshifts through stacking. However, given the "flat" cosmic evolution of the HI cosmic density inferred from Damped Lyα absorption systems, and the well documented fact that the star formation rate in galaxies depends on principally the molecular gas content, it appears that HI is a transition phase in the gas-star cycle. As stated in section 2.1 above, study of the molecular content of early galaxies requires frequencies between 20GHz and 50GHz (or higher), and are not part of the SKA-1 science case.

2.4 Cosmic Magnetism

Sources: The study of magnetic fields in the Universe from scales of AU to Mpc, is another unique and foundational aspects of radio astronomy. Impressive results were presented at the meeting from the VLA, GMRT, and the WSRT, on magnetic structures in star forming regions, AGN, spiral galaxies, and in Mpc-scale shocks and filaments in galaxy clusters. The SKA phase I will continue this important legacy into the coming decades, at higher sensitivity and angular scale.

All Sky RM survey: The original KSP for cosmic magnetic fields centered on an all-sky polarization survey, out of which would come a detailed map of the Faraday rotation across the sky. Such a map would have myriad applications, from mapping the Galactic magnetic field, to probing the fields in the intergalactic medium, to the evolution of cosmic magnetism back to the first galaxies. A first pass at such a very wide field RM survey will come through the VLASS, which should inform the SKA program (Johnston-Hollitt et al. 2015).

A particularly impressive calculation of the role an RM survey can play in studying cosmic magnetism was the delineation of the Cosmic web via the RM grid (Fig. 4; Akahori & Ryu 2011). I rate this as SD in Table 1, since it wasn't clear in the SWG report as to the relative impact of SKA

PoS(AASKA14)171

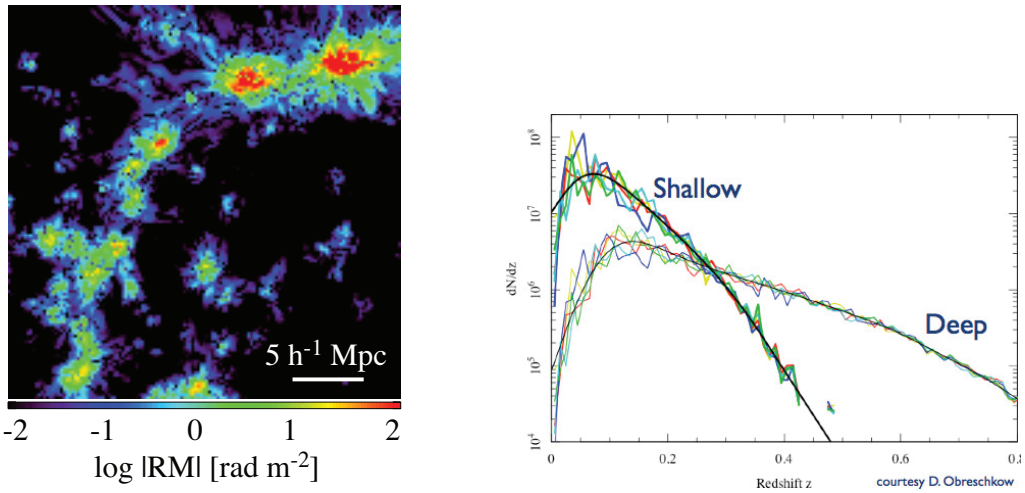

Figure 4: Left: Simulated image of rotation measure of 28 Mpc area in the local universe of depth of L = 100 Mpc (Akahori & Ryu 2011). Right: Predicted number counts versus redshift for an HI 21cm surveys (Blyth et al. 2015; Obreschkow et al. 2009).

phase I vs. the full SKA on the realization of the RM grid science. For instance, Akahori et al. (2014) show that SKA I should determine the strength of magnetic fields in the cosmic web, but the full SKA is needed to study the detailed structure of magnetic fields.

2.5 Pulsars and Gravity

Double precision gravity Pulsar timing remains at the forefront of studies of strong field gravity (Kramer & Stappers 2015). This field never fails to impress, with the discovery of exotic pairings, like binary msec pulsars (MSPs). Strong field GR has been validated to better than 0.01% using MSPs, and the triple MSP will provide the best-ever test of the Strong Equivalence Principle, eclipsing by a factor 20-100 the accuracy of measurements resulting from Lunar laser ranging.

Neutron star equation of state: Studies of msp – stellar binaries are setting new constraints on the nature of degenerate matter. These studies present a challenge to degenerate matter physics, including the recent discovery of a neutron star of 2.01(4) $M_\odot$, violating substantially the Chandrasekar limit (Tauris et al. 2015).

SKA Phase I will greatly facilitate the study of gravity using pulsars. The discovery of a black hole – pulsar binary seems inevitable. There is the exciting possibility of discovering pulsars orbiting the Galactic center SMBH with Band 5. Lastly, the SKA phase I may have the ability to extend pulsar studies to nearby galaxies, with untold consequences.

Gravitational waves: The existence of gravitational waves seems secure, through studies of pulsar spin-down rates. However, these observations indicate the effects of gravitational waves, but do not constitute a direct detection of a gravitational wave. LIGO is now searching for Hz-frequency gravitational waves that might arise from solar mass binary black holes.

Pulsar timing arrays have the potential to detect nano-Hz gravity waves, possibly from super-massive black hole binaries at cosmological distances, or cosmic strings at the inflationary epoch (Janssen et al. 2015). Figure 5 shows the expected GW background and current limits of PTAs

PoS(AASKA14)171

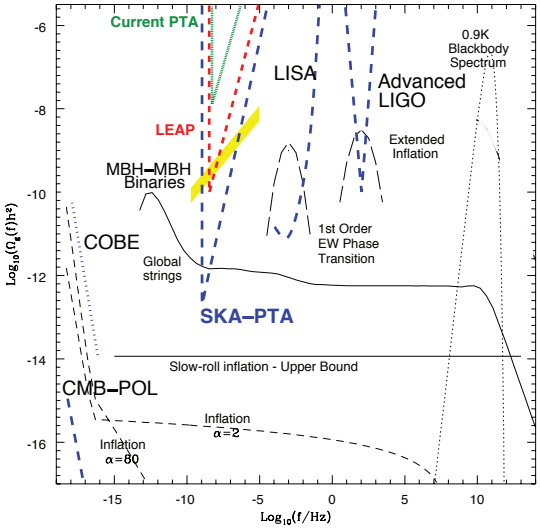

Figure 5: Expected signal and limits of experiments to search for cosmic gravitational waves. The most relevant predicted signal for the pulsar timing arrays (PTA) is the yellow region delineating the expected background due to coalescing binary super-massive black holes (Kramer & Stappers 2015). The best recent limit for PTAs is shown in green, and the red dash curve shows the expected limits in the coming two years.

and interferometric devices. The current PTAs are approaching the background of GW expected in vanilla models of SMBH and galaxy formation.

The SKA phase I will go well beyond detection, ushering in the era in which gravitational waves become a new window on the Cosmos. The SKA phase I has the potential to characterize the background in detail, and the sensitivity to detect individual GW events associated with SMBH binary mergers.

2.6 Cradle of Life

Planets and protoplanets: Our knowledge of extrasolar planets has gone from effectively zero, to a detailed classification of hundreds of planets, some possibly Earth-like and in the habitable zone. This work is driven by Kepler plus ground-based optical spectroscopy and photometry.

The study of protoplanets and protoplanetary disks is going through a similar revolution with the advent of high resolution imaging of dust and molecular gas with ALMA and the JVLA. Initial results already highlight the excitement and importance of direct imaging of planet formation on Solar system scales. In particular, the recent ALMA image of the protoplanetary disk around the Solar mass protostar, HL Tau, show the power of millimeter imaging in studies of planet formation (Brogan et al. 2015), while JVLA imaging at 40 GHz with μJy sensitivity and AU-resolution, have set the first constraints on a "circumplanetary disk", ie. accretion on to a forming planet itself (Isella et al. 2015).

The SKA phase I operating up to 14GHz provides an important tool to study the cm-sized "pebbles" in disks. Working in conjunction with the JVLA at 30GHz to 50GHz, and ALMA at higher frequencies, these telescopes will allow for the study of the poorly understood transition from dust to pebbles to planetesimals (Hoare et al. 2015; Testi et al. 2015).

PoS(AASKA14)171

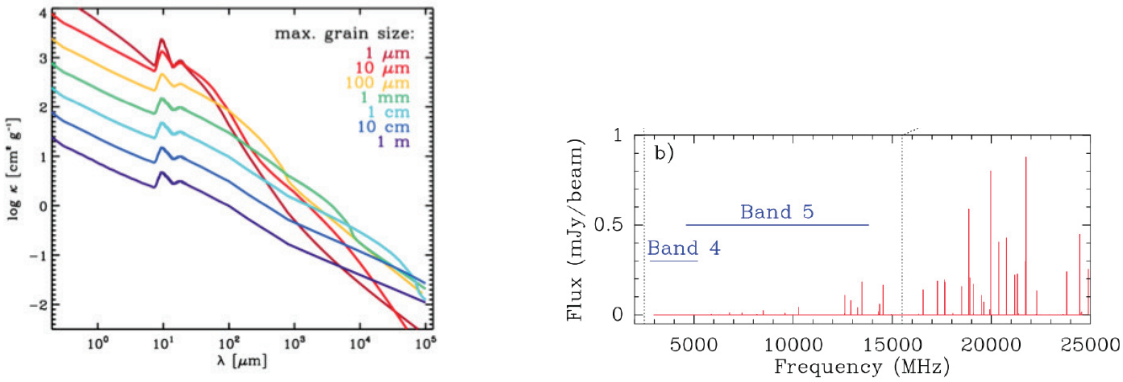

Figure 6: Left: Emissivity of dust grains versus frequency and grain size (Testi et al. 2015). Right: The spectrum of the simple amino acid, glycine, with the SKA band coverage (Codella et al. 2015).

The role of the SKA in the direct discovery of planets remains unclear. The search for Jupiter-type bursts, or possibly auroral-type emission, has the potential to probe planetary magnetic fields – a key ingredient in the development of life. However, the case remains exploratory (Zarka et al. 2015).

Pre-biotic molecules and SETI: Significant effort has gone into the search for large, pre-biotic molecules in the Galaxy (Codella et al. 2015). The biggest gains have come from the PRIMOS program at the GBT, where amino acid precursors are now routinely identified. Most of the characteristic lines from large molecules arise well above 3 GHz, and hence require band 5 in phase I (Fig 6).

The SETI program continues, principally at the SETI institute, with efforts in the optical through radio wavebands. The SKA phase I LOW has the potential to detect airport radar signals to distances of 10pc, within which there are 10^5 stars, most of which, we now know, have planets. SETI is clearly the most exploratory program with the highest return for the SKA, but it seems to me, must be pursued (Siemion et al. 2015).

2.7 Time domain

Synoptic surveys (long timescale variability) (min to days): Study of source variations over minutes to days or years has been another of the foundational aspects of radio astronomy. Non-thermal sources, and in particular, coherent sources, by their nature (high brightness temperature), are more naturally inclined to vary, relative to thermal processes. In the next few years, synpotic studies of the sky will increase in importance in astronomy, with the advent of LSST and Euclid. The SKA is the required element to maintain pace at radio wavelengths (Fender et al. 2015).

An area where radio astronomy has played a particularly important role is through the physical analysis of high energy sources, such as those identified with the Fermi gamma-ray observatory. VLBI imaging has proven to be the most incisive method with which to probe the physics behind extreme high energy phenomena and the engines driving the process, from Galactic XRBs and related, to distant Blazar AGN gamma-ray sources.

Bursting radio sky (msec to sec): The biggest discovery in the field of transients in the last decade may be the Fast Radio Bursts (FRBs). If these are really extragalactic and common as

PoS(AASKA14)171

suggested, the FRBs are a game-changer in the study of the transient sky, with many important implications for the source physics (stellar collapse to black holes?), and cosmology (eg. Dark energy, missing baryons). Unfortunately, there remains the issue of verifying and locating these sources, and identifying their host galaxies (if they are extragalactic). Numerous efforts are underway to answer these questions. Clearly, phase I of the SKA, both LOW and MID, would make order-of-magnitude steps in the study of such bursty cosmic radio sources, through the improved sensitivity and field of view (Macquart et al. 2015).

Beyond the FRBs, the msec radio sky remains wide-open for discovery. An excellent example is the recent discovery of kilo-Jy low frequency cyclotron emission from meteor fireballs by the LWA (Odenberger et al. 2014). Another application with broad implications is the difficult and important question of localizing the electromagnetic counter-parts of gravitational wave sources seen by LIGO. There are some models of LIGO-events that would lead to low frequency EM radiation – ideal for the very wide field of view of SKA1-LOW. Lastly, the case was made at the meeting for tracking space debris with the SKA (Jones & Lazio 2015). Reflected terrestrial interference might be used to track the debris over the whole sky using the SKA1-LOW. This application may be of interest to space funding agencies.

It was emphasized at the meeting that the study of the time domain is greatly facilitated by commensal observing and the possibility of time-buffering of the voltages. Commensal observing certainly seems like a must-have for the SKA, and may bring with it alternative funding sources from the specific projects.

3. Concluding remarks

3.1 What was missing?

There were a few areas that I am aware of that were not covered at the meeting, which I feel bear mentioning.

Precision astrometry seemed to be under-represented (Paragi et al. 2015; Loinard et al. 2015; Green et al. 2015). Over the last decade, the VLBA and EVN have demonstrated the power of precision astrometry in areas of Galactic structure, star formation, pulsars, and cosmology. There is the potential with such programs to determine the three dimensional motion of local group galaxies, and thereby obtain a full mass-model of the nearby Universe.

Another area that was missing was Solar system science (although see Nakariakov et al. 2015). Certainly, ALMA, JVLA, GBT, Arecibo have seen a steady demand for Solar system work, including Solar physics, radar studies of planetary sub-surfaces, Kuiper Belt objects, planetary atmospheres, comets, space weather, and ionospheric physics. The discovery of extrasolar planets has increased the interest in the study of our own Solar system. Likewise, space weather has become a major issue for Mankind, and the SKA1-LOW could be a powerful tool in the study of Solar activity and its effect on the Earth.

Lastly, a strong case was made for commensal observing. Options for commensal observing should be reconsidered in light of the rebaselined design. Alternative spigots for real time data access provide a dramatic means to increase the science output of the telescopes. Alternative approaches to data processing may bring with them alternative funding sources.

PoS(AASKA14)171

3.2 Concluding remarks

A remarkable degree of creative thought and hard work have gone into SKA science planning over the last decade, and the vibrancy of youth was clear at this meeting. One might argue that the SKA revolution is already in-progress, through science programs on the JVLA, WSRT, and other path-finder telescopes coming on-line today.

The SKA phase I has the right mix of "killer applications", "foundational applications", and "high-risk/high-return" programs that clearly justify the expense. Following is a far-from-complete listing of some of these programs. Ultimately, as Peter Wilkinson rightly points out (Wilkinson 2015), the greatest discoveries that will come from the SKA are likely even richer still, and beyond prognostication.

- Killer applications
  - Pulsars: double precision gravity and gravitational waves
  - HI 21cm cosmology: Imaging reionization and first light
- Foundational applications of radio astronomy
  - Cosmic magnetism
  - Milky way and nearby galaxies: eg. star formation, cool gas and baryon cycle, cosmic web
  - Galaxy formation (eg. star formation through deep fields, HI mass function, dark matter)
  - AGN, XRBs, and other high energy phenomena
  - Time domain and synoptic surveys
  - Planet formation and large molecule chemistry
- Possible game changers (high risk/high return)
  - FRBs: as profound impact as pulsars?
  - BAO intensity mapping and other cosmology apps: beat the Boss?
  - Dark ages and linear HI 21cm cosmology
  - SETI

Acknowledgements I would like to thank J. Wagg and R. Braun for inviting me to the conference, and M. Hoare, M. Kramer, M. Brown, T. van der Hulst, T. Akahori, M. Jarvis, S. Wyithe, C. Codella, and P. Diamond for figures and/or comments on the draft.

References

Abdalla, F. et al. 2015, "Cosmology from HI galaxy surveys with the SKA", in *Advancing Astrophysics with a Square Kilometre Array*, PoS(AASKA14)017

Akahori, T. & Ryu, D., 2011, ApJ, 738,134

Akahori, T., Gaensler, B. M., & Ryu D. 2014, ApJ, 790, 123

Ade, et al., 2014, Ph.Rev.Let, 112, 241101

Ali, Z. et al. 2014, arXiv1502.06016A

PoS(AASKA14)171

Beswick, R., et al. 2015, "SKA studies of nearby galaxies: star-formation, accretion processes and molecular gas across all environments", in *Advancing Astrophysics with a Square Kilometre Array*, PoS(AASKA14)070

Blyth, S. et al. 2015, "Exploring Neutral Hydrogen and Galaxy Evolution with the SKA", in *Advancing Astrophysics with a Square Kilometre Array*, PoS(AASKA14)128

Bouwens et al. 2015, arXiv1503.08228B

Bouwens, R. et al. 2014, ApJ, 795, 126

Brogan, C. et al. 2015, arXiv1503.02649P

Brown, M. et al. 2015, "Weak gravitational lensing with the Square Kilometre Array", in *Advancing Astrophysics with a Square Kilometre Array*, PoS(AASKA14)023

Capak, P. et al. 2015, arXiv1503.07596C

Carilli, C. L., & Rawlings, S. 2004, "Motivation, key science projects, standards and assumptions", in "Science with the Square Kilometre Array", New AR, 48, 979

Carilli, C.L., & Walter, F. 2013, ARAA, 51, 105

Codella, C., et al. 2015, "Complex organic molecules in protostellar environments in the SKA era", in *Advancing Astrophysics with a Square Kilometre Array*, PoS(AASKA14)123

Cordes, J. et al., 2004, New AR, 48, 1413

de Cuhna, E. et al. 2013, ApJ, 766, 13

Eisenstein, D. et al. 2005, ApJ, 633, 560

Fan, X., Carilli, C., Keating, B. ARAA, 2006, 44, 415

Fender, R. et al. 2015, "The Transient Universe with the Square Kilometre Array", in *Advancing Astrophysics with a Square Kilometre Array*, PoS(AASKA14)051

Fernandez, X. et al. 2014, ApJ, 770, L29

Gaensler, B et al. 2004, SKA memo series No. 44

Greenhill, L. 2004, NewAR, 48, 1079

Green, J., et al. 2015, "Maser Astrometry with VLBI and the SKA", in *Advancing Astrophysics with a Square Kilometre Array*, PoS(AASKA14)119

Govoni, F. et al. 2015, "Cluster magnetic fields through the study of polarized radio halos in the SKA era", in *Advancing Astrophysics with a Square Kilometre Array*, PoS(AASKA14)105

Hoare, M. et al. 2015, "SKA and the Cradle of Life", in *Advancing Astrophysics with a Square Kilometre Array*, PoS(AASKA14)115

Isella, A. et al. 2015, ApJ, 788, 129

Janssen, G. et al., 2015, "Gravitational Wave Astronomy with the SKA", in *Advancing Astrophysics with a Square Kilometre Array*, PoS(AASKA14)037

Jarvis, M. et al. 2015a, "Cosmology with SKA Radio Continuum Surveys", in *Advancing Astrophysics with a Square Kilometre Array*, PoS(AASKA14)018

Jarvis, M. et al. 2015b, "The star-formation history of the Universe with the SKA", in *Advancing Astrophysics with a Square Kilometre Array*, PoS(AASKA14)068

Johnston-Hollitt, M. et al. 2015, "Using SKA Rotation Measures to Reveal the Mysteries of the Magnetised Universe", in *Advancing Astrophysics with a Square Kilometre Array*, PoS(AASKA14)092

Jones, D., & Lazio, J. et al. 2015, "Enhancing Science from Future Space Missions and Planetary Radar with the SKA", in *Advancing Astrophysics with a Square Kilometre Array*, PoS(AASKA14)154

PoS(AASKA14)171

Kramer, M. & Stappers, B., 2015, "An overview of pulsar science with the SKA", in *Advancing Astrophysics with a Square Kilometre Array*, PoS(AASKA14)036

Konno, A. et al. 2014, ApJ, in press (arXiv:1404:6066)

Koopmans, L. et al. 2015, "The Cosmic Dawn and Epoch of Reionisation with SKA", in *Advancing Astrophysics with a Square Kilometre Array*, PoS(AASKA14)001

Lah, P. et al. 2009, MNRAS, 399, 1447

Lah, P. et al. 2007, MNRAS, 376, 1357

Loinard, L. et al. 2015, "SKA tomography of Galactic star-forming regions and spiral arms", in *Advancing Astrophysics with a Square Kilometre Array*, PoS(AASKA14)166

Maartens, R. et al. 2015, "Overview of Cosmology with the SKA", in *Advancing Astrophysics with a Square Kilometre Array*, PoS(AASKA14)016

Macquart, J.P., et al. 2015, "Fast Transients at Cosmological Distances with the SKA", in *Advancing Astrophysics with a Square Kilometre Array*, PoS(AASKA14)055

Murphy, E., et al. 2015, "The Astrophysics of Star Formation Across Cosmic Time at $\geq$10 GHz with the Square Kilometre Array", in *Advancing Astrophysics with a Square Kilometre Array*, PoS(AASKA14)085

Odenberger, K. et al. 2014, ApJ, 788, L26

Obreschkow, D. et al. 2009, ApJ, 703, 1890

Paragi, Z., et al. 2015, "Very Long Baseline Interferometry with the SKA", in *Advancing Astrophysics with a Square Kilometre Array*, PoS(AASKA14)143

Parsons, A. et al. 2014, ApJ, 788, 106

Pober, J. et al. 2014, ApJ, 782, 62

Pober, J. et al. 2015, arXiv1503.00045P

Prandori, I. & Seymour, N., 2015, "Revealing the Physics and Evolution of Galaxies and Galaxy Clusters with SKA Continuum Surveys", in *Advancing Astrophysics with a Square Kilometre Array*, PoS(AASKA14)067

Reid, M. et al. 2013, ApJ, 767, 154

Robertson, B. et al. 2013, ApJ, 768, 71

Santos, M. et al. 2015, "Cosmology from a SKA HI intensity mapping survey", in *Advancing Astrophysics with a Square Kilometre Array*, PoS(AASKA14)019

Siemion, A. et al., 2015, "Searching for Extraterrestrial Intelligence with the Square Kilometre Array", in *Advancing Astrophysics with a Square Kilometre Array*, PoS(AASKA14)116

Switzer, E. et al. 2014, MNRAS, 434, L46

Tauris, T., et al. 2015, "Understanding the Neutron Star Population with the SKA", in *Advancing Astrophysics with a Square Kilometre Array*, PoS(AASKA14)039

Testi L.. et al. 2015, "Protoplanetary disks and the dawn of planets with SKA", in *Advancing Astrophysics with a Square Kilometre Array*, PoS(AASKA14)117

Trenti, M. et al. 2012, ApJ, 746, 55

Umana, G. et al. 2015, "The impact of SKA on Galactic Radioastronomy: continuum observations", in *Advancing Astrophysics with a Square Kilometre Array*, PoS(AASKA14)118

Vazza, V. et al. 2015, "Filaments of the radio cosmic web: opportunities and challenges for SKA", in *Advancing Astrophysics with a Square Kilometre Array*, PoS(AASKA14)097

Wilkinson, P. 1991, IAU 131, ASP Conf series 19, 428

PoS(AASKA14)171

Wilkinson, P., 2015, "The SKA and the Unknown Unknowns", in *Advancing Astrophysics with a Square Kilometre Array*, PoS(AASKA14)065

Wyithe, S. et al. 2015, "Imaging HII Regions from Galaxies and Quasars During Reionisation with SKA", in *Advancing Astrophysics with a Square Kilometre Array*, PoS(AASKA14)015

Zarka, P. et al. 2015, "Magnetospheric Radio Emissions from Exoplanets with the SKA", in *Advancing Astrophysics with a Square Kilometre Array*, PoS(AASKA14)120

PoS(AASKA14)171